Thermodynamic Model for Tourmaline

Stan Roozen

April 20, 2025

Department of Earth and Planetary Sciences

McGill University

Montreal, Quebec, Canada

A thesis submitted to McGill University in partial fulfilment of the requirements of the degree of Doctor of Philosophy.

Use "entropy" and you can never lose a debate, von Neumann told Shannon - because no one really knows what "entropy" is.

Table of Contents

ABSTRACT **7**

RÉSUMÉ **9**

ACKNOWLEDGEMENTS **11**

CONTRIBUTION TO ORIGINAL KNOWLEDGE **17**

CONTRIBUTIONS OF AUTHORS **19**

LIST OF FIGURES **22**

LIST OF TABLES **38**

LIST OF ABBREVIATIONS **46**

Chapter 0. Introduction **53**

1. INTRODUCTION 54

1.1. Tourmaline supergroup mineral 54

1.2. Tourmaline: Net transfer reactions determine the stability 58

1.3. Tourmaline: External effect on element exchange 59

1.4. Tourmaline: Internal influences on element exchange 61

1.5. Need for a Thermodynamic model 62

1.6. Thermodynamic Modelling 62

1.7. Gibbs Free Energy Minimisation in Multi-Component Systems 67

2. OBJECTIVES 69

Chapter 1. Creating a consistently characterised tourmaline sample set with uncertainties for thermodynamic model calibration **79**

1. INTRODUCTION 80

2. DATABASE SAMPLE SELECTION AND SYNTHESIS 83

2.1 Natural tourmaline sample collection 83

2.2 Synthetic tourmalines 83

3. COMPOSITIONAL CHARACTERISATION 84

3.1 Wavelength Dispersive Electron Microprobe (WD-EMPA) 85

3.2 Laser-Ablation Inductively Coupled Plasma Mass Spectroscopy (LA-ICP-MS) 86

3.3 Karl Fisher Titration 88

4. VALENCY CHARACTERISATION 89

4.1 ^{57}Fe Mossbauer Spectroscopy 89

5. CRYSTALLOGRAPHIC CHARACTERISATION 91

5.1 Single crystal x-ray diffraction (SC-XRD) 91

5.2 Powder XRD (pXRD) 94
6. BOND VALENCE THEORY 97
7. TOURMALINE MINERAL FORMULA OPTIMISATION AND UNCERTAINTY ANALYSIS 98
8. POST-OPTIMISATION BOND VALENCE ANALYSIS 104
9. OUTPUT AND FINAL FOURIER SYNTHESIS 108
10. COMPARISON TO ALTERNATIVE OPTIMISATION SCHEMES 109
11. BOND VALANCE LIMITING COMPOSITION/SPECIATION SPACE 115
12. SAMPLE CHARACTERISATION DISCUSSION 118
13. CONCLUSIONS 125
Bridging Text Between Manuscripts (Chapter 1-Chapter 2) 134
Chapter 2. Thermodynamic model for Tourmaline. Model derivation and calibration of the molar volumes 137
1. INTRODUCTION 139
2. DEFINING THE THERMODYNAMIC MODEL FOR TOURMALINE 141
2.1 Tourmaline Speciation Model 142
2.2 Tourmaline Bulk Compositional Model 154
2.3 Other uses for the independent bulk parameters and site fractions 158
3. TRAINING SET ENDMEMBER FRACTIONS 159
4. TEST SET: ENDMEMBER FRACTIONS 170
5. REGRESSION METHODS 179
6. SOLID SOLUTIONS MODELS AND HIERARCHICAL SUBSET SELECTION 183
7. TRAINING DATASET REGRESSION: ORDINARY LEAST SQUARES 187
8. MODEL SELECTION 189
9. MODEL ASSESSMENT 202
10. COMBINED DATASET. ORDINARY LEAST SQUARES 208
11. CONCLUSIONS 214
Bridging Text Between Manuscripts (Chapter 2-Chapter 3) 224
Chapter 3. Thermodynamic model for Tourmaline. Entropy and Heat Capacity 226
1. INTRODUCTION 227
2. METHODS 228
2.1 Relaxation Calorimetry (Heat Capacity below 298.15K) 229
2.1 Differential Scanning Calorimetry (DSC) (above 298.15K) 230
2.2 Extrapolation from 2.5 K to 0K 233

3. RESULTS 235
4. TRAINING DATASET REGRESSION: ORDINARY LEAST SQUARES 246
4.1 Bulk Compositional Model: Low-T CP (Method 1) 248
4.2 Bulk Compositional Model High-T Cp (Method 1) 257
4.3 Speciation Model 269
1. DISCUSSION ORDINARY LEAST SQUARES MODELS 274
2. ALTERNATIVE REGRESSION METHODS 281
3. COMPARISON TO ESTIMATION MODELS BASED ON THE POLYHEDRON APPROACH 281
4. CORRELATIONS BETWEEN STATE VARIABLES 295
5. QUALITATIVE ASSESSMENT OF ENTROPY DIFFERENCES IN TOURMALINE 298
6. CONCLUSION 302
Bridging Text Between Manuscripts (Chapter 3-Chapter 4) 307
Chapter 4. Thermodynamic model for Tourmaline. Enthalpy 309
1. INTRODUCTION 310
2. METHODS 311
2.1 Thermogravimetric Analysis (TGA) 312
2.2 Drop Solution Calorimetry 313
2.3 FTIR powder absorption spectra 314
3. THERMOGRAVIMETRIC ANALYSIS (TGA) 318
4. ENTHALPIC THERMODYNAMIC CYCLES OF TOURMALINE 324
5. BULK COMPOSITIONAL MODEL 338
6. CORRELATION ANALYSIS 343
7. CHALLENGES IN DERIVING ENTHALPIES OF MIXING: INSIGHT FROM FTIR SPECTRA BROADENING 344
8. MODEL VALIDATION AND COMPARISON 347
9. CONCLUSIONS 351
Bridging Text Between Manuscripts (Chapter 4-Chapter 5) 359
Chapter 5. Model Integration and Conclusions 361
1. SUMMARY OF THERMODYNAMIC DATA 362
1.1 Speciation model standard state properties and caloric EoS 362
1.2 Bulk compositional model, standard state properties and caloric EoS 364
2. SOLUTION MODEL INTEGRATION 366
2.1 Configurational entropy 367

3. CONCLUSION AND SUMMARY 389
4. IMPLICATIONS AND FUTURE DIRECTIONS 390
Appendices Chapter 1 406
APPENDIX 1B. EMPA Details 407
APPENDIX 1D. Karl fisher titration details 410
APPENDIX 1E. Mossbauer details 411
APPENDIX 1E. Mossbauer Figures 413
APPENDIX 1F. p-XRD details 452
APPENDIX 1K1. Bond Valence Table 453
APPENDIX 1K2. Bond Valence Table for X-vacant tourmaline 454
APPENDIX 1L. Stability indices Bond Valence Theory 455
APPENDIX 1M. Bosi and Lucchesi (2004) method 455
Appendix 1N. A-priory bond lengths 458
Appendices Chapter 2 466
Appendix 2A. Endmember fraction Box and Violin plots 467
Appendix 2B. Details of regression methods 479
Appendix 2C. OLS Regression Analysis 487
Appendix 2D. Model Selection Bulk Model 500
Appendix 2E. Model Selection Speciation model 508
Appendix 2F. Model Assessment 514
Appendices Chapter 3 517
Appendix 3A. Theoretical framework Entropy and Cp(T) 518
Appendix 3B. Theoretical framework Calorimetry 530
Appendix 3C. Magnetic Spin Glass Transition Proof 536
Appendix 3D. Method 2 Bulk and Speciation Model 541
Appendix 3E. Bulk Model endmember curves 557
Appendix 3F. Method 1 Statistics Summary Bulk and Speciation 561
Appendix 3G. Bulk Model. 4 Temperature Zoom in Predicted vs Measured 563
Appendix 3H. Speciation Model Regression 567
Appendix 3I. Speciation Model 4 Temperature Zoom in Predicted vs Measured 584
Appendix 3J. Speciation Model endmember curves 588
Appendix 3K. Alternative Regression Methods 595
Appendix 3L. Derivation of Holland and Powell (1990) Landau tricritical 610

Appendix 3M. Improvements suggestions for the Polyhedron Method 615
Appendix 3N. State Variable Correlations 622
Appendices Chapter 4 628
Appendix 4A. Theoretical Framework: Empirical Link Between Broadening of FTIR Spectra and Enthalpy of Mixing and Disorder 629
Appendix 4B. TGA-DSC signals 640
Appendices Chapter 5 645
Appendix 5A. Bulk model exchange reactions relating the endmembers 646
Appendix 5B. Speciation model exchange reactions relating the endmembers 647
MASTER REFERENCE LIST 650

ABSTRACT

Tourmaline, $XY_3Z_6T_6O_{18}(BO_3)_3V_3W$, is a common borosilicate in crustal settings, recording phase relationships with minerals, fluids, and melts across tectonic environments. Its diverse sites enable elemental incorporation, while stability and low diffusivity preserve zoning, which is crucial for reconstructing P-T-X histories. Accurate interpretation requires a thermodynamic model, which this thesis develops through crystal-chemical and calorimetric measurements.

A tourmaline set of ~50 natural and synthetic samples was assembled within the Na-Ca-B-Fe^{2+}-Fe^{3+}-Mg-Al-Si-Ti-O-H-F system. Natural samples capture real-world variability, while synthetic samples reduce multicollinearity. Tourmalines were characterised by EMPA (main elements), LA-ICP-MS (trace), Karl-Fischer titration (H_2O) and Mössbauer spectroscopy ($Fe^{2+/3+}$). Single-crystal XRD provided structural constraints for formula optimisation using composition, site electrons, bond valence sums, and crystal-chemical assumptions. A uniform methodology including uncertainty assessment ensured internal consistency.

Two models were developed: 1. The bulk model, $X(YZ)_9Si_xAl_{(1-x)}(VW)_4$, defines a polytope with 9 independent endmembers and applies when only bulk composition is available; 2. The speciation model, $XY_3Z_6T_6V_3W$, uses 14 independent endmembers and requires site assignments. For both models, entropy (S), molar volume (V_M), and heat capacity (C_P) were measured and regressed to endmembers, while enthalpy (ΔH) was determined only for the bulk model due to data scarcity.

Molar volume was calculated from SC-XRD data. Given tourmaline's complexity, 50 samples were insufficient to assign endmember V_M conclusively, so 21 methods, including OLS, errors-in-variables, and robust regression, were compared to find best estimates. Robust regression minimised outlier effects for the bulk model, while EIV regression worked best for the speciation model, mitigating multicollinearity. Hierarchical subset selection identified interaction parameters, but test validation showed insignificance.

Heat capacity was measured from 2 to 774 K and integrated to entropy using linear interpolation (to 298 K) and a Berman fit for high-T data. S_0 is dominated by a low-T spin-glass transition. Enthalpy was measured for 15 samples in lead-borate drop-calorimetry at 700°C under O_2

flushing and converted to ΔH_f^{ox} through a thermodynamic cycle of oxidation, devolatilization, and reference oxide formation. Major uncertainty sources included Fe^{2+}/Fe^{3+} ratios, reference oxides, and mineral normalization. Bulk model H exhibited multicollinearity due to data scarcity. No excess S or ΔH was found. Configurational S was modelled using Bragg-Williams long-range order or molecular short-range order models. The SRO model with limited dimensions provides the simplest S^{conf} description but leads to fixed element correlations from missing polytope dimensions.

The model enables forward modelling of net-transfer and exchange equilibria, allowing tourmaline to be used in thermobarometry, provenance studies, mineral exploration, and fluid and magma reconstructions.

RÉSUMÉ

La tourmaline, $XY_3Z_6T_6O_{18}(BO_3)_3V_3W$, est un borosilicate commun dans les environnements crustaux, enregistrant les relations de phase avec minéraux, fluides et liquides magmatiques dans divers contextes tectoniques. La diversité de ses sites cristallographiques permet l'incorporation d'éléments, tandis que sa stabilité et faible diffusivité préservent la zonation, paramètres essentiels pour reconstruire les historiques P-T-X. Une interprétation précise nécessite un modèle thermodynamique, développé dans cette thèse à partir de mesures cristallochimiques et calorimétriques.

Un ensemble d'environ 50 échantillons naturels et synthétiques de tourmaline a été constitué dans le système Na-Ca-B-Fe^{2+}-Fe^{3+}-Mg-Al-Si-Ti-O-H-F. Les échantillons naturels capturent la variabilité réelle des compositions, tandis que les échantillons synthétiques réduisent la multicolinéarité. Les tourmalines ont été caractérisées par EMPA (éléments majeurs), LA-ICP-MS (traces), titrage Karl-Fischer (H_2O) et spectroscopie Mössbauer ($Fe^{2+/3+}$). La diffraction des rayons X sur monocristal (SC-XRD) a fourni des contraintes structurales permettant l'optimisation des formules à partir de la composition chimique, du nombre d'électrons par site, des sommes de valence de liaison et d'hypothèses cristallochimiques. Une méthodologie uniforme avec évaluation des incertitudes a assuré la cohérence interne.

Deux modèles ont été développés : 1. Le modèle global, $X(YZ)_9Si_xAl_{(1-x)}(VW)_4$, définit un polytope à 9 pôles indépendants et s'applique lorsque seule la composition totale est disponible ; 2. le modèle de spéciation, $XY_3Z_6T_6V_3W$, utilise 14 pôles indépendants et requiert une affectation des sites cristallographiques. Pour les deux modèles, l'entropie (S), le volume molaire (V_M) et la capacité calorifique (C_P) ont été mesurés et régressés sur les pôles, tandis que l'enthalpie (ΔH) n'a été déterminée que pour le modèle global en raison du manque de données.

Le volume molaire a été calculé à partir des données SC-XRD. Compte tenu de la complexité de la tourmaline, 50 échantillons étaient insuffisants pour assigner un V_M précis aux pôles. Par conséquent, 21 méthodes, incluant la régression des moindres carrés ordinaires (OLS), la régression avec erreurs sur les variables (EIV) et la régression robuste, ont été comparées pour obtenir les meilleures estimations. La régression robuste a minimisé l'effet des valeurs aberrantes dans le modèle global, tandis que la régression EIV a été plus efficace pour le modèle de

spéciation en atténuant la multicolinéarité. Une sélection hiérarchique de sous-ensembles a permis d'identifier les paramètres d'interaction, mais leur validation statistique a révélé une insignifiance.

La capacité calorifique a été mesurée entre 2 et 774 K, puis intégrée à l'entropie par interpolation linéaire jusqu'à 298 K et par un ajustement de Berman pour les données à haute température. S_0 est dominée par une transition des verres de spin à basse température. L'enthalpie a été mesurée pour 15 échantillons par calorimétrie à chute au borate de plomb à 700°C sous flux d'O_2, puis convertie en ΔH_f^{ox} par un cycle thermodynamique d'oxydation, dévolatilisation et formation d'oxydes de référence. Les principales sources d'incertitude incluaient les rapports Fe^{2+}/Fe^{3+}, les oxydes de référence et la normalisation minérale. Le modèle global a montré une multicolinéarité de ΔH, due à la rareté des données. Aucun excès de S ou ΔH n'a été trouvé. L'entropie configurationnelle (S^{conf}) a été modélisée à l'aide des modèles d'ordre à longue portée de Bragg-Williams ou d'ordre à courte portée moléculaire (SRO). Le modèle SRO à dimensions limitées offre la description la plus simple de S^{conf}, mais impose des corrélations fixes entre éléments en raison de dimensions manquantes dans le polytope.

Le modèle permet de modéliser les équilibres de transfert net et d'échange, permettant l'utilisation de la tourmaline en thermobarométrie, études de provenance, exploration minérale et reconstructions de fluides et magmas.

ACKNOWLEDGEMENTS

I express my deepest gratitude to those who have supported and contributed to this research.

First and foremost, I sincerely thank **Vincent van Hinsberg** for his outstanding supervision throughout this project. His enthusiasm for thermodynamics, statistics, and the mineral tourmaline was truly contagious, and I am grateful for his patience and clear explanations. As someone with dyslexia, I once struggled even to spell "thermodynamics" but Vincent's guidance opened the door for me to explore the fascinating world of phase equilibria. He was always available for discussions and I greatly appreciated being able to knock on his office anytime. It was truly inspiring to have a supervisor whose passion for the subject matched my own, as this was also your PhD topic. It has been an honour to continue your work, standing on your shoulders so that together we take another step toward making tourmaline an even more versatile tool for geoscientists. I have also always admired his mindset: that nothing is impossible and that with the right focus, solutions can be found for any obstacle on the road.

The author extends his gratitude to **Edgar Dachs** from the University of Salzburg. What was supposed to be a two-month lab visit unexpectedly turned into a ten-month stay due to the COVID19 pandemic and sudden border closures. This meant being separated from my wife for nearly a year, a difficult time, yet Edgar made it a period I now look back on fondly. He introduced me to the mountains of Austria, shared lunches and beers at the local beer garden, and even took me deep into the caves of the Alps, showing me an underground world that I had never seen before. Introduced me to the temperatures where the oxygen we breath would crystallise. From him, I learnt a great deal about thermodynamic model making and I am grateful for the small job he provided in my time of need, which allowed me to sustain myself while also gaining insight into biotite thermodynamics which would become the blueprint for my own work on tourmaline.

A special thanks to **Artur Benisek** for introducing me to the intricacies of density functional theory and sparking my enthusiasm for its power in predicting thermodynamic properties. His insights were invaluable, and he also motivated the FTIR and differential scanning calorimetry work. Both Edgar and Artur made my 30th birthday during the pandemic an occasion to remember. I sincerely thank **Günther Redhammer** for performing single-crystal X-ray

diffraction and for his expert guidance on refinements, which deepened my understanding of crystallography. **Gerold Tippelt** for XRD and Mossbauer measurements. Additional work on Mössbauer spectroscopy was greatly appreciated. **Christian Pruner** is thanked for his help with FTIR spectroscopy and for sharing many schnitzels and barbecues near his home, always in great company. **Claudia Hessl** for helping me integrate into Austrian culture and **Noreen Mary Vielreicher** for sharing an office with me. A special mention goes to **Gärtnerwirt Salzburg-Itzling**, where countless lunches were shared over those ten months. Finally, I am grateful to Charles Geiger for insightful discussions and for being excellent company for this *unterwasser-German*. You all made me feel like part of the team.

Klaus-Dieter Grevel is thanked for the synthesis experiments and for sparking my interest in drop-solution enthalpy. **Thomas Fockenberg** is thanked for Karl Fischer measurements; I hope the printer is still running! **Jeffrey Ovens** for SC-XRD analysis. **Kristoffer Szilas** is acknowledged for valuable discussions and for his support in fuelling my enthusiasm for studying the oldest of the old on Earth**.** I sincerely thank Christoph Heinrich, Albrecht von Quadt, and Yannick Buret, my master's supervisors, for providing the foundational guidance that became the stepping stone for my PhD, as did Kenneth Rijsdijk and Sjoerd Kluiving for my Bachelor Thesis.

To **Xiaofeng Guo**, thank you for your guidance on solution enthalpy measurements, X-ray absorption, and PDF analysis. This experience marked my first time living in the USA for two months. I also appreciate the camaraderie of your students, **Maggie Reece, Xiaodong Zhao, and Vitaliy Goncharov**, who shared long days and nights in *the bunker* working through calorimetry experiments together.

My sincere thanks to **Jamie Connolly** for taking the time to answer my (often research paper-sized) emails about the intricacies of polytopes. Your thermodynamics class during my time at the ETH Zurich during my master's degree sparked my enthusiasm so profoundly that I pursued a PhD in it. Your jokes in formal and informal texts made my day every time, and I’m convinced that the fact that your first *perplex* paper starts on page 666 is no coincidence! **Robert Myhill** for his help with my burning Burnman questions.

At **McGill University**, I extend my gratitude to **Lang Shi** for help with electron microprobe analysis**, Dominic Ryan** for performing the Mössbauer experiments**,** and **Anna Katharina Jung** for assistance with **LA-ICP-MS.** Special thanks to **Jeanne Paquette** for helping me understand the mineralogical aspects and for giving me access to the Department's tourmaline collection. Many of the tourmalines you provided are incorporated into the model. The author thanks **Anthony Williams-Jones**, who taught me how to critically evaluate research papers, learning that not everything written is the absolute truth. **Robert Martin** is acknowledged for insightful discussions and **Don Baker** is thanked for tailoring one of his classes in his course to solid solution models. I hope you like the result. **Kim Berlo** is thanked for valuable discussions during lab meetings. A heartfelt thanks to **Anne Kosowski**, **Angela Di Nino**, and **Kristy Thornton** at McGill's Planetary Sciences Department for keeping me on track and ensuring that I always had the support I needed. Anne also made sure I somehow always got paid, and together with Kristy, they created an excellent department culture. Thanks to **Yajing Liu** and **Brigitte Dionne** for giving me access to computational resources. I sincerely thank **Galen Halverson, Peter Douglas,** and **Jamie Kirkpatrick** for their support in getting me through the final stages of my studies and ensuring the completion of this thesis. Your help in the last stretch made all the difference. The **Redpath Museum** is acknowledged for providing tourmaline samples **and Peter Tarassoff** for their sample preparation.

This project would not have been possible without financial support from **FRQNT Geotop, the Geological Society of America, McGill University Financial Aid, Graduate Mobility Award, Robert Wares, NSERC, the Mineralogical Association of Canada, the Society of Economic Geologists, Vrijvrouwe van Renswoude, and the Postgraduate Students' Society of McGill University**. These funding sources allowed me to attend international conferences and paid for many of side projects which enriched this thesis.

To the **tourmaline family**, I am grateful for the insightful discussions on tourmaline with **Peter Bačík, Darrell Henry, Barbara Dutrow, Federico Pezzotta, Eleanor Berryman, Robert Trumbull, Jan Cempirek, Alessandra Altieri, Marko Bermanec, Beatrice Celata, Ferdinando Bosi, Giovanni Andreozzi, Oleg Vereshchagrin, and Horst Marschall**. **Jan Filip** is thanked for his help on Mossbauer Fitting.

I also extend my gratitude to the **FlexPet group** for fostering a supportive and open environment where academic and personal matters could be discussed freely. **Jill Kendrick, Miguel Cruz, Longbo Yang, Juliette Gomes, Haylea Nisbet, Marion Saby, Haihao Guo, Majken Poulsen, Charlie Beard, Romain Lauzeral, Bruno Alemão**, **Dominic D'Amato** and, especially, **Bernardo Filgueiras** for help and guidance in various steps during the thesis period**.** Special thanks to **Catherine Crotty**, it seems wherever I go, I am linked to the Irish. My Master's and Ph.D. projects both had Irish collaborators, which must have been due to the cover 4 I picked.

From the Graduates at McGill, Special thanks to **Nick Ogasa, Jethro Sanz-Robinson, and the Fight-Club** for always making me laugh and being there for the easy and difficult times. **Noah Phillips** for organizing our first conference session. I am grateful to **Regina Gonzalez, Ingá Boianju, Florentine Zwillich, David Martineau, and Julia Mattioli** for their friendship and for supporting me with my thesis until the very last minute. Thanks also to **Stephan Kolzenburg, Jessica Sales, Julia Morales, Moses Angombe, Melanie Burnett, Keavin Moore, Meghomita Das, Sam Metteer, Tim Howell, Samantha Carruthers, Lauren Somers, Caroline Seyler, Carly Faber, William Fajzel, Arvid Gonzalez, Duncan McLeish, Kevin Ng, Robert Collar, Holly Han, Robert Bogue, Jeannette Wan, Anna Hayden, Erin Eves, Kiera Broda, Phillipe Drouin, Pascale Daoust, Erin Gibbons, Kyle Henderson, Melanie King, Marko Prasek, Aube Gourdeau, Debarati Das, Sarah Bodeving, Gary Fung, Javier Bustamante, Jake Lone, Phoebe Nkansa, Andres Castro, and many others** for their support and companionship throughout this journey.

To friends, who have formed me over the years, **Thomas Heerma van Voss, Govert ter Mors, Ruben van Dijk, Laurens van der Schoot, Milo Buur, Reuben Moore, Thijs Faber, Abel Ranzijn, Pim Witkop, Melle Vogels, Aranka van der Schoot, Jana de Vries, Wietske Yntema, Rutger Kamphuis, Boris Popma, Laurens Eversmann, Sven van Ewijk, Tom Renema, Joost Veenkamp, Linda van der Waart, Rens Poesse, Henrique Franssens, Simon Berger, Sjoerd Visser and Schiller Café, Gaby Langendijk, Zita Hegger, Giel van der Grind, Klaas Sorgedrager, Araya Negash, Vera de Ruijter, Tiemen Gordijn, Venice Akker, Maria Froystein, Erik Koene, Jochem Braakhekke, Lydia Bailey, Siem Rouwendaal, Tim Suhrhoff, Joep van Dijk, Yarazai Simbron, Alberto Trujillo, Kristof Alonzo, Jose Navarro, Alfonso and Maria Teresa Urbina, Kuntideva Band, Lily Dabdoub, Ayanda Keith, Isabela**

Moreno, Juliana Camargo, Dany Racine, Nitzan Diskin, Fabrice Traore, Wasim Hamzi, Isaumir Borges, Marcella Santiago, Tiago Kaniak, Petra Schumann, Jamie Demperio, Victor Costa, Meagan, Maria Felix, Bernard and Lucie, Hector Baranda, Lidia Vasconcelos, Henning Zorn, Anna Mora, Piet Tromp, Ingrid Feenstra, Bop Dijkstra, Ineke van Rosenmalen, Coby Jelsma, Joep and Ulrike Sterman, Rosalien Derkinderen, Maria, Niek and Hans Roozen, Aeilko, Fenna and Harry Timersma, Bernadette Laudy, Onno, Yp and Abe de Lange, Patricia Ide, Werner Bichler, Suellen and Carlos, Tom and Max, Lysmar, Souza Family: Elenice, Hudson, Ingrid, Francianne, Marly, Pollyanna. Elias, Adenilson, and Ademir Lira, and many others. Jose Roozen, your tourmaline (tm28) is now part of science.

Eric Gaudry is especially thanked for his unwavering support, kindness, and friendship during crucial moments in our lives. His generosity and encouragement were deeply felt, and we are incredibly grateful to have him by our side.

To my **family**:
Ronald Roozen, thank you for always being there for me—I am happy to be part of the *Drie Musketiers*. I learnt from you that when you commit to something, you give it everything. You taught me that putting energy into subjects you love will give energy back, encourage perseverance, and find happiness in life. Without seeing the results of the many projects you started, Vézézoux, NL100, this thesis would never have been completed. You built monuments and helped me to build one for myself. **Helma Tilleman**, **Ruben Roozen, Lisa Roelofs, and now little Lova**, just born a few weeks ago. For all of our time in Vezézoux, where my passion for rocks began while searching for amethyst. Without your support, this thesis would not exist. **Priscilla Souza de Lira** and **Hugo Chauvet**, for giving us a home in *La Bella Italia* during the pandemic.

To **Naira Souza de Lira**, my love and companion in life. From one magical night in Belém, dancing by the river, a kiss under the stars, and a sunrise departure, you became my greatest adventure. That unforgettable summer night in the Amazon bloomed into seven beautiful winters together in Canada, warmed by your love. You are my balance, my inspiration, and my rock in

the sea. Thank you for your unwavering love and support over the past decade. It has been a fantastic ride.

To **Rio Roozen de Lira**, my son. You were born while I was working on this thesis - just after I sent off the first version of Chapter Three, after a sleepless night of writing, when your mother's water broke. It was a long night, but one of the happiest days of my life. We will all pass one day, but part of me will always live on in you. *We are one.*

Finally, to those who have passed: to **Jeannette Timersma**, my mother, and **Remmer Muller**, my friend, this thesis is dedicated to your memory.

CONTRIBUTION TO ORIGINAL KNOWLEDGE

Albert Einstein once remarked on thermodynamics, stating, "*A theory is the more impressive the greater the simplicity of its premises, the more different things it relates, and the more extended its area of applicability. Therefore, the deep impression that classical thermodynamics made upon me. It is the only physical theory of universal content which I am convinced will never be overthrown, within the framework of applicability of its basic concepts.*"

In the spirit of Einstein's perspective, this thesis provides a foundational thermodynamic model for tourmaline, designed with the aspiration that it will serve as a robust and enduring basis for future studies. Given that computational modelling of phase equilibria must be constrained by real thermodynamic data, the original contributions of this thesis are significant and manifold.

Firstly, it provides an extensive dataset of previously unavailable thermodynamic properties for tourmaline, including molar volumes, entropies, and heat capacities for approximately 50 samples. Additionally, 15 new enthalpy measurements are presented, which represent a notable enhancement to existing knowledge. This thesis also introduces critical advancements in mineral formula optimisation, extending techniques to accurately account for minor elements and anions, and incorporating rigorous uncertainty propagation methods. This approach addresses compositional uncertainties in thermodynamic data and emphasises the importance of maintaining normalisation consistency within thermodynamic datasets.

Furthermore, this work contributes to an internally consistent and integrated thermodynamic model for tourmaline, the first of its kind based on direct measurements. Detailed descriptions of the derivation of model parameters are included, enabling future researchers to reproduce, refine, and expand upon this model. Before this thesis, only a limited set of isolated measurements were available, which required earlier studies to largely depend on estimation methods. This research marks a significant advancement by providing a foundational framework that enables tourmaline integration into internally consistent thermodynamic databases. This inclusion enables forward modelling of tourmaline net transfer and exchange equilibria across pressure, temperature, and chemical potentials via Gibbs free energy minimisation. Given tourmaline's ubiquity as an accessory mineral, this significantly broadens its application in pseudosection thermobarometry, provenance studies, ore exploration, and tracing fluid and magma evolution as its mineral record

in the form of compositional zoning can finally be read. We hope that this model excites geoscientists about tourmaline's potential as a valuable petrogenetic indicator.

CONTRIBUTIONS OF AUTHORS

Chapter 1. Creating a consistently characterised tourmaline sample set with uncertainties for thermodynamic model calibration

Co-authors:

• Stan Roozen: Performed the initial reconnaissance study, collected all tourmaline samples, and performed initial analyses on approximately 200 tourmalines. For the subset for the thermodynamic model (~50 samples) conducted EMPA analysis, LA-ICP-MS, and data refinement. Performed final refinement of Mössbauer spectroscopy data initially measured and refined by Dominic Ryan, Jan Filip, and Günther Redhammer to ensure internal consistency. Completed final single-crystal X-ray diffraction (SC-XRD) refinements and mineral formula optimisation for all samples, including those initially refined by Günther Redhammer, Lee Groat, and Rhiana Elizabeth Henry. Performed Rietveld refinements of the powder XRD data. Implemented changes to the mineral formula optimisation code, including the bond valence analysis. Led the overall planning and design of the study in collaboration with Vincent van Hinsberg.

• Vincent van Hinsberg: Collaborated on the overall planning and design of the study and assisted with the refinement of the EMPA and LA-ICP-MS data. Reviewed the manuscript, correcting and refining its scientific accuracy.

• Günther Redhammer: Performed the majority of SC-XRD measurements, 36 samples of which are included in this thesis, conducted the three powder XRD measurements and performed initial refinements. Additionally, Mössbauer spectroscopy was performed on 8 of the samples and initial refinement.

• Dominic Ryan: Conducted 21 Mössbauer measurements and performed their initial data refinement.

• Klaus-Dieter Grevel: Conducted synthesis experiments on dravite, uvite, and oxyuvite, and additionally provided synthetic olenite from Ulrich Wodara and 3 natural samples.

Other Contributors:

• Ulrich Wodara: Performed the synthesis of the synthetic B-olenite sample.

• Gerold Tippelt: Assisted Günther Redhammer with SC-XRD, powder XRD, and Mossbauer measurements.

• Lee Groat and Rhiana Elizabeth Henry: Conducted SC-XRD measurements and initial refinements on a subset of 9 tourmaline samples in the context of a related trace element standard project; portions of these standards were used in this thermodynamic study.

• Jeffrey Ovens: SC-XRD measurements on 6 tourmaline samples.

• Jan Filip: Mössbauer spectroscopy measurements and initial refinement were conducted for the same subset of 9 tourmaline samples analysed by Lee Groat and Rhiana Elizabeth Henry.

• Thomas Fockenberg: Conducted Karl Fischer titration to measure volatile components for all tourmaline samples.

• Jeanne Paquette: Made natural samples available for this study.

• Redpath Museum: Provided additional natural samples for this study, with sample preparation conducted by Peter Tarasoff.

• Lang Shi: Assisted with the EMPA measurements.

Chapter 2. Thermodynamic Model for Tourmaline – Model Derivation and Calibration of Molar Volumes

Co-authors:

• Stan Roozen: Performed all model definitions, fit the mineral formula to the bulk and speciation endmember models, performed the regression methods to determine endmember molar volumes, and carried out fitting of training and test sets. Led the overall planning and design of the study in collaboration with Vincent van Hinsberg.

• Günther Redhammer: Performed the majority of SC-XRD measurements and all three powder XRD measurements from which the molar volumes were derived (see detailed contributions in Chapter 1).

• Vincent van Hinsberg: Collaborated in the overall planning and design of the study and collected all the literature data for the test case. Reviewed the manuscript, correcting and refining its scientific accuracy.

• Edgar Dachs: Assisted with setting up the model definitions.

Chapter 3. Thermodynamic Model for Tourmaline: Entropy and Heat Capacity

Co-authors:

• Stan Roozen: Performed all DSC measurements. Developed the thermodynamic model under the guidance of Edgar Dachs, performed all regressions, and performed the overall planning and design of the study.

• Edgar Dachs: Performed all PPMS measurements, instructed Stan Roozen in thermodynamic model development, and assisted in coding for the complete Cp curve regression.

• Vincent van Hinsberg: Collaborated in the overall planning and design of the study, calculated the estimated entropy and heat capacity using a polyhedron model for comparison with our model. Reviewed the manuscript, correcting and refining its scientific accuracy.

• Artur Benisek: Assisted with differential scanning calorimetry and provided codes for data normalisation.

Chapter 4. Thermodynamic Model for Tourmaline – Enthalpy

Co-authors:

• Stan Roozen: Developed the thermodynamic model and performed all regressions, Monte Carlo uncertainty calculations, and sensitivity analyses. Conducted most of the FTIR analyses under the guidance of Christian Pruner. Performed solution calorimetry under the guidance of Maggie Reece, Xiaodong Zhao, Vitaly Goncharov, and Xiaofeng Guo. Conducted the overall planning and design of the study.

• Vincent van Hinsberg: Collaborated in the overall planning and design of the study. Reviewed the manuscript, correcting, and refining its scientific accuracy.

• Xiaofeng Guo: Aided with drop solution enthalpy measurements, TGA-DSC analyses, and assisted in setting up the thermodynamic cycles.

• Artur Benisek: Assisted with FTIR sample preparation and provided codes for autocorrelation analysis.

• Christian Pruner: Provided guidance for FTIR analyses and performed FTIR measurements on approximately half of the samples (~20 samples).

Other Contributors:

• Maggie Reece, Xiaodong Zhao, and Vitaliy Goncharov: Provided guidance for solution calorimetry experiments and the TGA-DSC experiments and aided in setting up the thermodynamic cycles.

LIST OF FIGURES

Chapter 0. Introduction

- **Figure 0A.** Schematic representation of tourmaline's crystal structure, shown normal (A) and parallel (B) to the c-axis. The X site (purple) is positioned above the tetrahedral ring (blue), bonding to the inner corners of T sites and trigonally coordinated B sites (green). The O1 (W) site (red) is linked to three Y sites (yellow), with its O1-H1 bond directed toward the X site (H in light blue). The O3 (V) sites (red) each coordinate one Y (yellow) and two Z sites (orange), while the O3-H3 bond is oriented in the c^- direction, where H3 shares an H-bond with the O5 site (dashed circle) in the tetrahedral ring. (Figure after Berryman et al.(2016))
- **Figure 0B.** This master equation describes the molar Gibbs free energy G(P,T,**X**) of a multicomponent solid solution as a function of pressure P, temperature T, and endmember vector **X** with endmember mole fractions components X_i. The ▢ standard-state properties include the reference enthalpy H_i^0, entropy S_i^0, and molar volume V_i^0, at 298.15 K and 1 bar with enthalpies referenced to the elements. The ● caloric EoS captures temperature effects through heat capacity integrals: $C_{p,i}(T)$ is used to correct both enthalpy and entropy, respectively. The ● volumetric component captures pressure effects through direct integration of the volume function V(P,T). Thermal expansion α(T) is required to evaluate $V(P^0,T)$ at elevated temperatures, but it is not integrated as a separate energy contribution. Instead, it adjusts the temperature-dependent volume, which is then used in the pressure integral. Only the pressure integral $\int V(P,T)\,dP$ contributes cumulatively to Gibbs free energy. The ▢ compositional EoS includes the ideal configurational entropy, calculated from species (j) site (s) occupancies $x_{j,s}$, site multiplicities M_s, and total number of independent species $n_{ind,s}$. The $n_{ind,s}$ reflect the system's degrees of freedom+1 and can be expressed as linear combinations of the independent endmember fractions. The excess Gibbs energy forms from non-ideal interactions here as example modelled via regular parameters $W_{ij}(P,T)$. The final term, $G_{other}(P,T,\mathbf{X})$, accounts for energetic contributions not captured by endmember-based mixing, such as magnetic ordering or electronic transitions. These effects are typically

non-linear in composition and cannot be expressed as separable functions of P, T, and X; for example, Curie or Néel temperatures may vary non-trivially with Fe content.

Chapter 1. Creating a consistently characterised tourmaline sample set with uncertainties for thermodynamic model calibration.

Figure 1A. Mössbauer spectrum for tourmaline sample Tm72, illustrating one of the more complex cases encountered in the dataset.The fitted model includes Fe^{2+} doublets assigned to Y1, Y2, and Y3 sites, Fe^{3+} doublets representing Y or Z site occupancy, and a $Fe^{2.5+}$ mixed-valence component to account for broadening effects. The addition of the $Fe^{2.5+}$ component improves the fit but increases the uncertainty of precise site and valence assignments. Residuals remain within ±2σ limits, confirming the quality of the fit.

Figure 1B. Stacked bar chart showing the bulk compositions of all analysed tourmaline samples. Cationic abundances were calculated by summing all measured elements and renormalizing to 100% for each sample. Major components include Si, Al consistent with the expected framework of tourmaline. Significant proportions of Na, Mg, Fe^{2+}, and Fe^{3+} reflect substitutions at the X and Y sites, while minor amounts of Ca, Ti^{4+}, F and trace elements (e.g., Li, Cr, V, Mn, Zn, REEs) are also observed. The renormalization emphasizes compositional trends across major and minor elements and facilitates direct comparison between samples. You excluded boron, ogygen and water from the bulk plot to improve the visibility of the variation in minor and trace elements.

Figure 1C. Stacked bar chart showing the X site occupancies for all analysed tourmaline samples. The occupancies of Na^X, Ca^X, K^X, Sr^X, Ba^X, La^X, Ce^X, Nd^X, $Pb(II)^X$, $Bi(III)^X$, and $Vacancy^X$ are displayed as a percentage of total X site occupancy. Na is the dominant occupant in most samples, with varying proportions of Ca and minor K, Sr, and rare earth elements (REEs). Site vacancies are significant in some samples, reflecting incomplete X-site occupancy.

Figure 1D. Stacked bar chart showing the Y site occupancies for all analysed tourmaline samples. The occupancies of Mg^Y, $Fe(II)^Y$, $Fe(III)^Y$, Al^Y, $Mn(II)^Y$, $Ti(IV)^Y$, Li^Y, $Cr(III)^Y$, $V(III)^Y$, Zn^Y, $Sn(IV)^Y$, $Cu(II)^Y$, $Ni(II)^Y$, $Co(II)^Y$, Sc^Y, Ga^Y, $Nb(V)^Y$, and VacancyY are shown. The Y site is primarily occupied by Mg, Fe^{2+}, and Al, with significant contributions from Fe^{3+} and Ti^{4+} in

some samples. Minor trace element substitutions (e.g., Zn, Cr, V) and vacancies are present but generally subordinate.

Figure 1E. Stacked bar chart showing the Z site occupancies for all analysed tourmaline samples. The occupancies of Mg^{Z}, $Fe(II)^{Z}$, $Fe(III)^{Z}$, Al^{Z}, $Mn(II)^{Z}$, $Ti(IV)^{Z}$, Li^{Z}, $Cr(III)^{Z}$, $V(III)^{Z}$, Zn^{Z}, $Sn(IV)^{Z}$, $Cu(II)^{Z}$, $Ni(II)^{Z}$, $Co(II)^{Z}$, Sc^{Z}, Ga^{Z}, and $Nb(V)^{Z}$ are plotted.
The Z site is overwhelmingly dominated by Al, typically exceeding 80% occupancy in all samples. Minor Mg, Fe^{2+}, and Fe^{3+} substitutions are observed, with very low contributions from trace elements.

Appendix 1E: Contains all Mossbauer Figures.

Appendix 1K1: Bond Valence Table Figure.

Appendix 1K2: Bond Valence Table Figure for tourmaline with X-vacancy.

Chapter 2. Thermodynamic model for Tourmaline. Model derivation and calibration of the molar volumes

- **Figure 2A**. Scree plot showing the variance explained by each principal component for the speciation model. Principal component analysis (PCA) reveals that the first two principal components (PC1 and PC2) capture the majority of the variance across the dataset, while higher components contribute progressively less. The sharp drop in explained variance indicates that sample variability is largely confined to a low-dimensional subspace in X-space, and highlights directions that are poorly sampled, contributing to multicollinearity in model parameters
- **Figure 2B**. PCA biplot of PC1 versus PC2 for the distribution of samples and endmember loadings in the speciation model. Samples are primarily distributed along PC1, with limited spread along PC2. Loading vectors show that endmembers such as odrv**,** foi**,** and drvdis dominate the primary sampled variability, whereas endmembers like pov**,** mdtw**,** bu**,** and bole exhibit minimal independent variance. This confirms that certain directions in endmember X-space are poorly represented, weakening parameter resolution.

- **Figure 2C.** PCA biplot of PC1 versus PC3 for the distribution of samples and endmember loadings in the speciation model. The PC1 vs PC3 projection further illustrates the confinement of samples along dominant axes, with minimal independent variability along PC3. Endmember loadings in this plane reinforce those key compositional directions involving pov**,** mdtw**,** bu**,** and related endmembers are underexplored in the current dataset.
- **Figure 2D.** PCA biplot of PC1 versus PC4 for the distribution of samples and endmember loadings in the speciation model. Samples show almost no meaningful spread along PC4, confirming that this direction is extremely poorly sampled. Endmember contributions to PC4 are negligible, supporting the conclusion that multicollinearity stems from missing coverage in certain compositional vectors, which should guide future synthesis and sample acquisition strategies.
- **Figure 2E**. Scree plot showing the variance explained by each principal component for the bulk model. Principal component analysis (PCA) shows that the first two principal components capture most of the variance, while higher components contribute little, indicating poor sampling across certain endmember directions in X-space.
- **Figure 2F.** PCA biplot of PC1 versus PC2 for the distribution of samples and endmember loadings in the bulk model. Samples are strongly clustered along PC1, with limited spread along PC2. Endmember loadings show that drvB**,** foiB**,** and oleB dominate the primary variability, while endmembers like buB**,** mdtwB**,** and aosrmB contribute little, revealing underexplored directions.
- **Figure 2G**. PCA biplot of PC1 versus PC3 for the distribution of samples and endmember loadings in the bulk model. PC1 vs PC3 projections confirm that sample spread along PC3 is minimal, reinforcing that much of the X-space is poorly sampled beyond the dominant PC1 direction.
- **Figure 2H**. PCA biplot of PC1 versus PC4 for the distribution of samples and endmember loadings in the bulk model. Samples show negligible spread along PC4. This further demonstrates that poor coverage along specific compositional directions leads to multicollinearity and uncertainty in the associated thermodynamic parameters.
- **Figure 2I.** Scatter plot showing the projection of the training and test sets of the Bulk model onto the first two principal components (PC1 and PC2). Convex hulls in PCA1-

PCA2 space encapsulate the boundary of each set, highlighting areas of overlap and potential extrapolation where samples from one set fall outside the convex hull of the other. Sample labels are included to identify specific data points. Percentage of training samples in test convex hull: 80.77%. Percentage of test samples in training convex hull: 72.16%.

- **Figure 2J.** Histogram displaying the Mahalanobis distances of test samples from the centroid of the training set for the Bulk model. The distances quantify how well the test samples align with the core distribution of the training set, with larger distances indicating potential outliers or regions of poor coverage.
- **Figure 2K.** Comparing composition space for the training and test set for the Bulk model. Multivariate visualization comparing the standardized distributions of predictors between the training and test sets. Standardization (zero mean and unit variance) ensures comparability across variables with different units and scales. Each line represents a sample crossing axes for the predictors, highlighting variables where the test set significantly diverges from the training set.
- **Figure 2L.** Scatter plot showing the projection of the training and test sets of the Bulk model onto the first two principal components (PC1 and PC2). Convex hulls in PCA_1-PCA_2 space encapsulate the boundary of each set. Percentage of training samples in test convex hull: 100%. Percentage of test samples in training convex hull: 46.60%
- **Figure 2M.** Histogram displaying the Mahalanobis distances of test samples from the centroid of the training set for the speciation model.
- **Figure 2N.** Parallel coordinate plot comparing composition space for the training and test set for the speciation model. Each line represents a sample crossing axes for the predictors, highlighting variables where the test set significantly diverges from the training set.
- **Figure 2O.** Illustration demonstrating the general effect of the Bias-Variance Tradeoff. Modified from Hastie et al. (2017)
- **Figure 2P.** buB endmember fraction versus molar volume. Combined training and test set.
- **Figure 2Q.** The Cauchy robust model fit to the training set data. Green bands show confidence intervals for the mean response, while blue bands represent prediction

intervals for individual measurements. The increased estimation bias is mainly due to worsen fit to F-buergerite (tm64).

- **Figure 2R.** The Cauchy robust model fit to the test set data. Green bands show confidence intervals for the mean response, while blue bands represent prediction intervals for individual measurements. The centroid of data is fit well but compositional bias is high.
- **Figure 2S.** The CWTLS model fit to the training set data. Green bands show confidence intervals for the mean response, while blue bands represent prediction intervals for individual measurements.
- **Figure 2T.** The CWTLS model fit to the test set data. Dark grey bands show confidence intervals for the mean response, while blue dotted lines represent prediction intervals for individual measurements.
- **Figure 2U.** Combined dataset and the bulk model. Scatter plot of measured vs. predicted molar volume (J/bar·mol) with error bars from covariance matrix propagation. WLS regression (green) accounts for uncertainty variations, while the 1:1 line (dashed red) indicates perfect agreement.
- **Figure 2V.** Combined dataset and the **s**peciation model. Scatter plot of measured vs. predicted molar volume (J/bar·mol) with error bars from covariance matrix propagation. WLS regression (green) accounts for uncertainty variations, while the 1:1 line (dashed red) indicates perfect agreement.

Appendix 2A. Endmember Fraction Box and Violin Plots

- **Figure 2A.1.** Bulk compositional model training set endmember fractions.
- **Figure 2A.2.** Violin plots showing the distributions of the bulk compositional model training set endmember fractions.
- **Figure 2A.3.** Speciation model training set endmember fractions.
- **Figure 2A.4.** Violin plots showing the distributions of the speciation model training set endmember fractions.
- **Figure 2A.5.** Bulk compositional model test set endmember fractions.

- **Figure 2A.6.** Violin plots showing the distributions of the bulk composition model test set endmember fractions.
- **Figure 2A.7.** Speciation model test set endmember fractions.
- **Figure 2A.8.** Violin plots showing the distributions of the speciation model test set endmember fractions.
- **Figure 2A.9.** Bulk composition model combined dataset endmember fractions.
- **Figure 2A.10.** Violin plots showing the distributions of the bulk compositional model combined dataset endmember fractions.
- **Figure 2A.11.** Speciation model combined dataset endmember fractions.
- **Figure 2A.12.** Violin plots showing the distributions of the speciation model combined dataset endmember fractions.

Appendix 2D. Model Selection Bulk Model

- **Figure 2D.1.** Bulk model. OLS without interaction parameters and tm164. A) Training set fit. B) Test set fit. Green bands show confidence intervals for the mean response, while blue bands represent prediction intervals for individual measurements.

- **Figure 2D.2.** Bulk model. CWTLS without interaction parameters and tm164. A) Training set fit. B) Test set fit. Green bands show confidence intervals for the mean response, while blue bands represent prediction intervals for individual measurements.

- **Figure 2D.3.** Bulk model. Cauchy robust fit without interaction parameters. A) Training set fit. B) Test set fit. Green bands show confidence intervals for the mean response, while blue bands represent prediction intervals for individual measurements.

Appendix 2E. Model Selection Speciation Model

- **Figure 2E.1.** Speciation model. OLS without interaction parameters. A) Training set fit. B) Test set fit. Green bands show confidence intervals for the mean response, while blue bands represent prediction intervals for individual measurements.

- **Figure 2E.2.** Speciation model. OLS without interaction parameters. A) Training set fit. B) Test set fit. Green bands show confidence intervals for the mean response, while blue bands represent prediction intervals for individual measurements.

Chapter 3. Thermodynamic model for Tourmaline. Entropy and Heat Capacity

- **Figure 3A**. Heat capacity of Foitite sample (Tm 6) between 0-17K as measured using the PPMS and the uneven power series extrapolation to 0K.
- **Figure 3B**. Heat capacity of F-buergerite sample (tm64) between 0-17K as measured using the PPMS and the uneven power series extrapolation to 0K.
- **Figure 3C**. Specific heat capacity (Cp) of tourmalines. Buergerite (red) has the highest Cp at low T but the lowest above ~250 K, while uvite (blue) shows the highest Cp at high T. Other tourmalines are intermediate. The uncertainties are smaller than the thickness of the lines. The inset highlights the Cp behavior at the lowest temperatures, which disproportionately influences the integrated entropy.
- **Figure 3D**. Cp/T curves (coloured) and Interquartile Range (blue) showing that the mid-range (50–200 K) dominates entropy but has low variance, while the magnetic contribution at low temperatures, with high Cp variability, most influences entropy differences.
- **Figure 3E**. The Cp difference between foitite (tm6) and dravite (tm23) highlights significant variability in the 0–50 K T range, driven primarily by magnetic contributions. This range has the largest impact on Cp curve differences and dominates uncertainty in both Cp and integrated entropy, as entropy is highly sensitive to 1/T at low T. Measurements were conducted down to 2 K.
- **Figure 3F**. Heatmap of training set samples showing Cp Z-scores per T compared to the dataset mean, with white indicating values near the mean, blue lower, and red higher, illustrating how relative differences vary with T.
- **Figure 3G**. Heatmap of training set samples showing Cp uncertainties Z-scores per T compared to the dataset mean uncertainty.
- **Figure 3H**. The jump between PPMS and DSC data at 298.15K in terms of relative percentages.

- **Figure 3I**. Relative percentage % differences between PPMS-DSC.
- **Figure 3J**. Predicted $S_{298.15K}^{773.15\,K}$ using uncorrected DSC Berman fits. Samples with overestimated values correspond to positive jumps, while underestimated ones show negative jumps, indicating inaccuracies in the DSC data. A vertical correction was applied, assuming accurate slope determination.
- **Figure 3K**. Bulk compositional endmember low-T Cp curves with their confidence intervals.
- **Figure 3L**. Heatmap of bulk compositional model Cp curves Z-scores at 0.1 K intervals, comparing each endmember to the mean of all endmembers. White indicates Cp near the mean, blue lower than the mean, and red higher. The plot highlights how relative differences between curves vary with T.
- **Figure 3M**. The relative uncertainty in endmember in low-T Cp (J/K/mol) and its dependence on T.
- **Figure 3N**. VIF factors for the bulk compositional model. VIF factors depend on the designer matrix and are therefore equal for all regressions relating to the bulk compositional model.
- **Figure 3O**. Mean Squared Error (MSE) of Cp curve versus Measured Entropy (J/K/mol) for the low-T Cp curve regression of the Bulk Compositional Model.
- **Figure 3P**. Relative residuals (%) between measured and predicted low-T Cp curves for the bulk compositional model, plotted on a log scale. Higher uncertainties (>1%) occur below 100 K, while they remain <2% above 100 K.
- **Figure 3Q**. Measured versus predicted entropy using Method 1.
- **Figure 3R**. Bulk compositional endmember high-T Cp curves with their CI. $X(YZ)9Si_xAl_{(1-x)}(VW)_4$
- **Figure 3S**. Heatmap of bulk compositional model high-T Cp curves Z-scores at 1 K intervals, comparing each endmember to the mean of all endmembers. X(YZ)9SixAl(1-x)(VW)4.
- **Figure 3T**. The relative uncertainty in Cp (J/K/mol) dependence on T. $X(YZ)9Si_xAl_{(1-x)}(VW)_4$. Residuals from the OLS fit are randomly distributed.

- **Figure 3U**. Measured versus predicted entropy using Method 1. Uncertainties are propagated from the polynomial model fit and therefore assumed a 'perfect' Berman model.
- **Figure 3V**. Distribution of ΔG differences at 773.15 K arising from discrepancies between measured and predicted Cp for the bulk compositional model. The figure highlights the contributions from differences in S^0, integrated entropy along the high-T Cp curve ($S_{298.15K}^{773.15\,K}$), and their combined impact on ΔG values at 773.15 K.
- **Figure 3W**. Relative deviations between training set data and model for high-T Cp. $X(YZ)9Si_xAl_{(1-x)}(VW)_4$.
- **Figure 3X**. Predicted versus measured Cp at four different T with the 1:1 line. Note the increasingly horizontal distribution of samples around the 1:1 line at higher T.
- **Figure 3Y**. Slope weighted linear regression where the weight was multiplied with a factor of 20.
- **Figure 3Z**. S_0 versus buB fraction. Two distinct trends are evident: one toward buergerite (bu) and another toward povondraite (pov), reflecting differences in Fe^{3+} speciation and Z-site substitution (Al versus Fe^{3+}+Mg) in tourmalines. Arrows qualitatively indicate samples that, in the speciation model, have either high pov–low bu or high bu–low pov contents.
- **Figure 3AA**. $S_{298.15K}^{773.15\,K}$ versus buB fraction. The data show two separate trends toward bu and pov compositions, highlighting how Fe^{3+} speciation coupled with Z-site substitution influences entropy evolution. Arrows qualitatively indicate samples with dominant pov or bu components based on the speciation model.
- **Figure 3AB**. Molar volume versus buB fraction. Two distinct trends emerge corresponding to bu and pov behavior, underscoring the effects of Z-site chemical differences in addition to Fe^{3+} speciation. Arrows qualitatively point to samples enriched in pov or bu in the speciation model; light green points indicate intermediate compositions (pov-bu mixtures).
- **Figure 3AC**. Measured vs Predicted Entropy with Uncertainties, York Regression, and Integral Difference for the Polyhedron method with OHO polyhedra without Sconf. The method underpredicts by 25 J/(K·mol).

- **Figure 3AD**. Relative difference between measured Cp values and predictions from the polyhedron method, where negative values indicate overprediction. Both measured and predicted Cp data were fitted using the Berman model for consistency.
- **Figure 3AE**. Cp curves from the polyhedron model vs. measured Cp, both fitted using the Berman model. The 1:1 line indicates a perfect fit. Measured data is available up to ~1200 J/mol·K, with the remainder extrapolated.
- **Figure 3AF**. ΔG differences at 1000 K resulting from discrepancies between measured and predicted high-T Cp in the polyhedron model, highlighting the impact of model simplifications.
- **Figure 3AG**. Relative difference between measured Cp values and predictions from the bulk compositional method, where negative values indicate overprediction. Both measured and predicted Cp data were fitted using the Berman model for consistency and extrapolated up to 1200 K.
- **Figure 3AH.** ΔG differences at 1000 K resulting from discrepancies between measured and predicted high-T Cp in the bulk compositional model, highlighting the impact of model simplifications.
- **Figure 3AI.** Extrapolated Cp curves from the bulk compositional model compared to extrapolated measured Cp curves, with the 1:1 line indicating a perfect fit. Measured data is available up to ~1200 J/mol·K, with the remainder extrapolated.
- **Figure 3AJ.** Relationship between FeTotal (apfu) and standard-state entropy (S_0) for tourmaline samples. Sample labels are shown. The strong positive correlation reflects the dominant role of Fe^{2+} and Fe^{3+} spin disorder in contributing to magnetic entropy. Additionally, the high mass of Fe enhances acoustic phonon contributions, while weaker Fe^{2+} bonds allow more optical phonon modes, further increasing entropy.

Appendix 3B. Theoretical Framework Calorimetry

- **Figure A3B.1**. DSC signal before drift correction. Isothermal sections should be the same for blank (black), reference (green), and sample (red). The fact they are not the same indicates instrumental drift.
- **Figure A3B.2**. DSC signal after drift correction. Isothermal sections are made the same for blank (black), reference (green), and sample (red).

Appendix 3C. Magnetic Spin Glass Transition Proof

- **Figure A3C.1**. Mössbauer spectra of tourmaline samples Pa (Fe: 2.73 apfu), Y (Fe: 1.92 apfu), MC (Fe: 0.795 apfu), and UM (Fe: 0.6 apfu). Downward-pointing arrows indicate a magnetic sextet, possibly from magnetic ordering in tourmaline at 5 K. However, oxide inclusions can also be the culprit. Figure (4.18) and sample spectra from the thesis of Saegusa (1978).

Appendix 3D. Method 2 Bulk and Speciation

- **Figure A3D.1**. Measured versus predicted entropy using Method 2. A) Using the SE of the confidence interval. B) Using the SE of the prediction interval.
- **Figure A3D.2**. Measured versus predicted $S_{298.15K}^{773.15\,K}$ using Method 2. Prediction uncertainty based on the confidence interval. This figure is identical to Method 1 (Figure 3U), showing that the order of integration and regression does not matter for high-T Cp data.
- **Figure A3D.3**. Measured versus predicted entropy using Method 2 using CI and PI uncertainties.

Appendix 3E. Bulk Model endmember curves

- This Appendix contains all the Bulk model endmember Cp curves.

Appendix 3G. Bulk Model. 4 Temperature Zoom in Predicted vs Measured

- This Appendix contains all the Bulk Model. 4 Temperature Zoom in Predicted vs Measured for 298.15, 373.15, 573.15 and 773.15K.

Appendix 3H. Speciation Model Regression

- **Figure A3H.1.** Speciation endmember low-T Cp curves with their confidence intervals.
- **Figure A3H.2**. Heatmap of speciation model Cp curves Z-scores at 0.1 K intervals, comparing each endmember to the mean of all endmembers. White indicates Cp near the mean, blue lower than the mean, and red higher. The plot highlights how relative differences between curves vary with temperature.

- **Figure A3H.3**. The relative uncertainty in endmember in low-T Cp (J/K/mol) and its dependence on T.
- **Figure A3H.4**. VIF factors for the speciation model. VIF factors depend on the designer matrix and are therefore equal for all regressions relating to the speciation model.
- **Figure A3H.5**. Mean Squared Error (MSE) of Cp curve versus Measured Entropy (J/K/mol) for the low-T Cp curve regression of the speciation model.
- **Figure A3H.6**. Relative residuals (%) between measured and predicted low-T Cp curves for the speciation model, plotted on a log scale. Higher uncertainties (>1%) occur below 100 K, while they remain <2% above 100 K.
- **Figure A3H.7**. Measured versus predicted entropy using Method 1.
- **Figure A3H.8**. Speciation endmember high-T Cp curves with their confidence intervals. $XY_3Z_6T_6V_3W$
- **Figure A3H.9:** Heatmap of speciation model high-T Cp curves Z-scores at 1 K intervals, comparing each endmember to the mean of all endmembers. $XY_3Z_6T_6V_3W$
- **Figure A3H.10**. The relative uncertainty in Cp (J/K/mol) dependence on T. $XY_3Z_6T_6V_3W$. Uncertainty is high for the pov endmember.
- **Figure A3H.11**. Measured versus predicted entropy using Method 1. Uncertainties are propagated from the polynomial model fit and therefore assumed a 'perfect' Berman model.
- **Figure A3H.12.** Distribution of ΔG differences at 773.15 K arising from discrepancies between measured and predicted Cp for the speciation model. The figure highlights the contributions from differences in standard state entropy (S_0), integrated entropy along the high-T Cp curve ($S_{298.15K}^{773.15\,K}$), and their combined impact on ΔG values at 773.15 K.
- **Figure A3H.13.** Relative deviations between training set data and model for high-T Cp. $XY_3Z_6T_6V_3W$.
- **Figure A3H.14**. Predicted versus measured Cp at four different T with the 1:1 line, highlighting the more horizontal distribution of samples at higher T, though less pronounced than in the bulk compositional model.
- **Figure A3H.15**. Pov versus bu endmember fraction. Size of points indicate molar volume whereas the colour indicates in a) standard state entropy and in b) $S_{298.15K}^{773.15\,K}$. Note

the difference in scale for the pov and bu axis. The figures do show how pov and bu have drastically different properties.

Appendix 3I. Speciation Model 4 Temperature Zoom in Predicted vs Measured

This Appendix contains all the Speciation Model. 4 Temperature Zoom in Predicted vs Measured for 298.15, 373.15, 573.15 and 773.15K.

Appendix 3J. Speciation Model endmember curves

- This Appendix contains all the Speciation model endmember cp curves.

Appendix 3K. Alternative Regression Methods

- **Figure 3K.1**. Bulk model measured entropy versus LOOCV Entropy with Uncertainties, York Regression, and Integral Difference for OLS. Notice the high LOOCV MSE of F-buergerite (tm64).
- **Figure 3K.2**. Bulk model measured entropy versus LOOCV Entropy with Uncertainties, York Regression, and Integral Difference for CWTLS using the Full weight matrix with block diagonal covariances of each sample and covariances of the covariances. While overall fit is good, there is compositional bias as demonstrated by the high integral difference between the York line and the 1:1 line.
- **Figure 3K.3**. Bulk model measured entropy versus LOOCV Entropy with Uncertainties, York Regression, and Integral Difference for robust regression using the Cauchy weight function. The most robust method.
- **Figure 3K.4**. Speciation model measured entropy versus LOOCV Entropy with Uncertainties, York Regression, and Integral Difference for OLS. Notice the high LOOCV MSE of F-buergerite (tm64).

Appendix 3N. State Variable Correlations.

- This Appendix contains all the state variables correlations.

Chapter 4. Thermodynamic model for Tourmaline. Enthalpy

- **Figure 4A.** Independent endmember fractions of the Bulk model for the 15 natural samples selected for enthalpy measurements. Chapter 2 outlines their calculation and defines the Bulk model endmember abbreviations.
- **Figure 4B. Thermodynamic Cycle for Formation Enthalpy of Tourmaline** This diagram outlines the thermodynamic cycle used to derive the enthalpy of formation of tourmaline. The cycle begins with drop-solution calorimetry measurements of tourmaline and its reference oxides. The formation enthalpy from oxides is calculated as the difference between product and reactant solution enthalpies, using the sign convention appropriate for dissolution (opposite to formation). To obtain the formation enthalpy from the elements, standard enthalpies of formation for the oxides (from Robie and Hemingway, 1995) are added. An oxidation correction is applied via Hess's Law to account for transition metal oxidation during dissolution in lead borate. For example, FeO is oxidized to Fe_2O_3, corrected to 973 K using Cp integrals, and hematite's solution enthalpy is incorporated. Dividing the total corrected enthalpy by 4 yields the drop solution enthalpy of FeO. This cycle leverages the state function nature of enthalpy to isolate measurable steps while highlighting the complexity and error accumulation when multiple oxide references are required.
- **Figure 4C.** Independent endmember fractions of the Bulk model for the 49 natural samples selected for FTIR measurements. Chapter 2 outlines their calculation and defines the Bulk model endmember abbreviations.
- **Figure 4D.** Measured versus Predicted $\Delta H_f°_{el}$ of our training set tourmalines. Uncertainties are the Monte Carlo 2 standard deviations in case of the measured values.
- **Figure 4E.** Measured versus predicted standard-state enthalpies of formation ($\Delta Hf°$) for tourmaline test samples. Error bars represent the propagated uncertainty from the endmember regression model. The dashed line indicates the 1:1 line for perfect agreement between predicted and measured values.

Appendix 4B. TGA-DSC

- This Appendix contains all the TGA-DSC Figures.

Chapter 5. Model Integration and Conclusions

- **Figure 5A**. **Comparison of Configurational Entropy (S^{conf})** The four bars per sample represent independently calculated entropy contributions from different models: LRO S^{conf} Speciation (blue), LRO S^{conf} Bulk (orange), SRO S^{conf} Speciation (green), and SRO S^{conf} Bulk (red). Each bar shows the calculated S^{conf} value in J/(mol·K), with its exact value labeled at the right end of the bar. At 1000 K, differences in S^{conf} translate into Gibbs free energy differences of ~40–60 kJ/mol, comparable to many mineral reaction energies, emphasizing that the choice of configurational entropy model can significantly affect thermodynamic predictions.

LIST OF TABLES

Chapter 0. Introduction

Table 0A. Tourmaline nomenclature endmembers of this study. The endmembers relate to each other by homo- and hetero-valent coupled substitutions and their associated exchange vectors, as mentioned at the bottom of the table.

Chapter 1. Creating a consistently characterised tourmaline sample set with uncertainties for thermodynamic model calibration

Table 1A. Nomenclature tourmalines within the Na-Ca-Fe-Mg-Al-Ti-Si-B-H-F for which we estimate the atomic radii based on the a-priory BV matrix method.

Table 1B. List of tourmaline endmembers considered unstable based on first-order bond-valence stability analysis. Instabilities predominantly affect compositions with elevated Ti, B, Al at the T site, or ferric iron (Fef) content, as well as those with partial Ca–vacancy occupancy on the X site. The endmember $[Na][Al]_3[Al]_6[B_{1/2}Si_{1/2}]_6[OH]_3[OH]$ from the speciation-based model is also predicted to be unstable.

Appendix 1M: A-priory bond length

Table A1N.1. A-priory bond length of LRO endmembers.

Chapter 2: Thermodynamic model for Tourmaline. Model derivation and calibration of the molar volumes

Table 2A. Combined evaluation of compositional overlap, predictor constraints, and multicollinearity for the speciation model. Train in Test (%) and Test in Train (%) indicate the percentage of samples covered by the opposing set. VIF measure multicollinearity, with higher values reflecting stronger predictor correlations and inflated variance. Diagonal of X'X indicate predictor constraints, where smaller values reflect broader coverage and reduced redundancy, and larger values indicate poor constraints and limited variability.

Table 2B. Combined evaluation of compositional overlap, predictor constraints, and multicollinearity for the second model. Column definitions and interpretations are the same as described in Table 2A**.**

Table 2C. Regression Method Categories

Table 2D. Structural Formulas and Molar Volumes for Buergerite and Bosiite

Table 2E. Cauchy robust endmember molar volumes for the $X(YZ)_9Si_xAl_{(1-x)}(VW)$ model and the SD based on the covariance matrix. Regression model without interaction parameters. The correlation matrix is plotted directly below the table for visual reference, with correlation coefficients annotated inside each coloured cell to illustrate the strength and direction of relationships between endmembers.

Table 2F. CWTLS endmember molar volumes for the $XY_3Z_6T_6V_3W$ model and the SD based on the covariance matrix obtained from the Hessian at the nonlinear minimisation surface. Regression model without interaction parameters. The correlation matrix is plotted directly below the table for visual reference, with correlation coefficients annotated inside each coloured cell to illustrate the strength and direction of relationships between endmembers.

Appendix 2B. Statistical Methods Appendix

- **Table 2B.1.** Weight functions used by the robustfit algorithm in Matlab2022a.

Appendix 2C. OLS Regression Analysis

- **Table 2C.1.** $X(YZ)_9Si_xAl(1-x)(VW)_4$ model without interaction parameters.
- **Table 2C.2.** $X(YZ)_9Si_xAl(1-x)(VW)_4$ model with interaction parameters.
- **Table 2C.3.** $X(YZ)_9Si_xAl(1-x)(VW)_4$ model without interaction parameters using the combined dataset.
- **Table 2C.4.** $X(YZ)_9Si_xAl(1-x)(VW)_4$ model with interaction parameters using the combined dataset.
- **Table 2C.5.** $X(YZ)_9Si_xAl(1-x)(VW)_4$ model with subregular interaction parameters using the combined dataset.
- **Table 2C.6.** $XY_3Z_6T_6V_3W$ model without interaction parameters.

- **Table 2C.7.** $XY_3Z_6T_6V_3W$ model without interaction parameters using the combined dataset.

Appendix 2D. Model Selection Bulk Model

- **Table 2D.1.** Bulk Model. Best performing models based on a single statistic.
- **Table 2D.2.** Bulk model Z-score heuristics combining the sample-amount averaged index performance on the training and test sets. For the meaning of the different Z scores and how they are summed into one heuristic, see main text. Best performing robust regression method and x-uncertainty regression methods with lowest sum Z scores are in bold and yellow.

Appendix 2E. Model Selection Speciation Model

- **Table 2E.1.** Speciation Model. Best performing models based on a single statistic.
- **Table 2E.2.** Speciation model. Top 10 Model-method combinations based on total Z-score minimisation. Z-score heuristics combining the sample-amount averaged index performance on the training and test sets. For the meaning of the different Z scores and how they are summed into one heuristic, see main text. Best performing robust regression method and x-uncertainty regression methods with lowest sum Z scores are in bold and yellow.

Appendix 2F. Model Assessment

- **Table 2F.1.** Cauchy Robust Regression without interaction parameters including outlier tm164; Internal and External validation. Internal validation using the training data. The results of the internal validation of the $X(YZ)_9Si_xAl_{(1-x)}(VW)$ model.
- **Table 2F.2.** CWTLS without interaction parameters with outlier tm164. Internal validation using the training data. The results of the internal validation of the $XY_3Z_6T_6V_3W$ model, including output from the Matlab script and figures, are included in Appendix X.

Chapter 3. Thermodynamic model for Tourmaline. Entropy and Heat Capacity.

- **Table 3A**. S^0 of the endmembers obtained using method 1 for the bulk compositional model. Correlation matrix of the S0 bulk model endmembers. Correlation matrix figure for S^0 bulk model.
- **Table 3B.** Bulk model Berman polynomial regression coefficients for the endmember high-T Cp. The high number of significant figures are given as there are strong parameter correlations, rendering standard significance rules inapplicable.
- **Table 3C**. Bulk model covariance matrices for the Berman fit to endmember high-T Cp. Due to the high correlation between the Berman polynomial coefficients, uncertainty propagation should utilize the covariance matrices instead of the standard deviations of individual coefficients to avoid overinflating uncertainties. Additionally, the correlation matrices of the parameters are plotted. The correlation matrix of the heat capacity at 600 K (Cp_{600}) is also provided.
- **Table 3D.** Standard State Entropy of the endmembers obtained using method 1 for the speciation model. Additionally, the correlation matrices of the parameters are plotted.
- **Table 3E.** Speciation model Berman polynomial regression coefficients for endmember high-T Cp. The high number of significant figures are given as there are strong parameter correlations, rendering standard significance rules inapplicable.
- **Table 3F**. Speciation model covariance matrices for the Berman fit to endmember high-T Cp. Due to the high correlation between the Berman polynomial coefficients, uncertainty propagation should utilize the covariance matrices instead of the standard deviations of individual coefficients to avoid overinflating uncertainties. Additionally, the correlation matrices of the parameters are plotted. The correlation matrix of the heat capacity at 600 K (Cp_{600}) is also provided.
- **Table 3G**. Polyhedral Calculation in Tourmaline: Ordered vs. OH-Disordered Model for example tourmaline (fschorl).
- **Table 3H**. Polyhedral entropies for oct and OHO polyhedra (van Hinsberg et al. 2005a).
- **Table 3I.** Comparing the measured versus predicted of the speciation and all polyhedral models.

Appendix 3H. Speciation Model Regression.

Table A3H.1. Standard State Entropy of the endmembers obtained using method 1 for the speciation model.

Appendix 3K. Alternative Regression Methods.

Table 3K.1. Bulk Model: LOOCV MSE and Mean Residual Analysis. The LOOCV MSE and mean residuals assess the performance and robustness of different regression methods. Negative mean residuals indicate general underestimation, while positive values suggest general overestimation. LOOCV MSE highlights model sensitivity to extreme outliers, reflecting method robustness. The most robust models balance low MSE with minimal bias in residual means and are indicated with yellow. OLS is the reference method.

Table 3K.2. Bulk model Z-score heuristics using the LOOCV as an estimate for the test set show which models have lowest training set uncertainty and is most robust. For the meaning of the different Z scores and how they are summed into one heuristic, see Chapter 3. Best performing robust regression method and x-uncertainty regression methods with lowest sum Z scores are in bold and yellow.

Table 3K.3. Speciation Model: LOOCV MSE and Mean Residual Analysis.

Table 3K.4. Speciation model Z-score heuristics using the LOOCV as an estimate for the test set show which models have lowest training set uncertainty and is most robust. For the meaning of the different Z scores and how they are summed into one heuristic, see Chapter 3. Best performing robust regression method and x-uncertainty regression methods with lowest sum Z scores are in bold and yellow.

Appendix 3M: Improvements suggestions for the Polyhedron Method.

Table 3M.1. Adding molecular (SRO) model S^{conf} to the polyhedron method estimates.

Chapter 4. Thermodynamic model for Tourmaline. Enthalpy.

- **Table 4A.** Thermogravimetric analysis (TGA) results for selected tourmaline samples. Each sample was heated under either inert (N_2) or oxidative (air) conditions, and mass

loss was monitored as a function of temperature. Three distinct mass loss intervals (T1, T2, T3) are reported where applicable, corresponding to devolatilization events observed during heating. The table lists the temperature range (°C) and associated weight loss (%) for each step. The melting temperature indicates the onset of endothermic melting from differential scanning calorimetry (DSC) where available. Total weight loss is the cumulative mass loss over the full TGA run, and values corrected to exclude physically adsorbed water are given in the adjacent column. Karl-Fisher titration values from Chapter 1 provide an independent estimate of structural water. Samples measured in air (oxidizing conditions) are indicated with "air" in the name. Bolded values highlight measurements outside the expected dehydration behavior, possibly indicating experimental artifacts or compositional variability.

- **Table 4B.** Melting temperatures extrapolated to the bulk compositional model endmembers using ordinary least squares multiple linear regression on the 14 samples for which melting temperatures were obtained. The regression coefficient for each variable represents the predicted melting temperature (in °C) of the pure endmember. The 95% confidence intervals indicate the uncertainty in this extrapolation, based on the standard error of each coefficient.
- **Table 4C.** Drop-solution enthalpy measurements of tourmaline samples in lead-borate solvent at 700 °C. The first column lists the number of drops used per sample for calculating the mean and the total number of drops. Drops which gave inconsistent results were not used for the calculation of the mean. The second and third columns report the measured enthalpies of solution in kJ/g. These were converted to molar values using the molar mass of each sample (not shown). The fourth and fifth columns give the heat contents (Hº(700 °C) – Hº(25 °C)) in kJ/mol, obtained by integrating the caloric equations of state (Cp) from 25 °C up to 700 °C.
- **Table 4D**. Measured enthalpies of formation from the elements for our sample tourmalines. The first column lists $\Delta H^{\circ\text{tourmaline}}_{f,\text{ oxides}}$ using preferred values for composition and reference oxide enthalpies. The second column is the $\Delta H^{\circ\text{tourmaline}}_{f,\text{ element}}$. The MC mean $\Delta H^{\circ\text{tourmaline}}_{f,\text{ element}}$ is the average from 2000 Monte Carlo trials, incorporating the mean and

2SE of compositions and $\Delta H^{\circ}_{f,\,\text{oxides}}^{\text{tourmaline}}$ measurements. 2SD represents the standard deviation of the MC trials. All enthalpy values are at standard state (298.15 K, 1bar)

- **Table 4E.** $\Delta H_f°_{el}$ extrapolated to the bulk compositional model endmembers by ordinary least squares multiple linear regression of the 16 samples for with drop enthalpies were obtained. Figure of the correlation matrix of the bulk model $\Delta H_f°_{el}$ is found below.
- **Table 4F.** Summary of the most important statistical parameters of the $\Delta H_f°_{el}$ extrapolation to the bulk compositional model endmembers by ordinary least squares multiple linear regression of the 16 samples for with drop enthalpies were obtained. Correlations show relationships between variables, VIF measures how multicollinearity inflates the variance of regression coefficients, R^2 versus IVs indicates variance explained by other variables, tolerance reflects unexplained variance (1 - R^2), and diagonal (X'X inverse) reflects sensitivity of coefficients to data changes, with larger values suggesting higher instability.
- **Table 4G.** Comparison between measured and predicted standard-state enthalpies of formation (ΔHf°) for the tourmaline samples *schorl_Ogo*, *dravite_Ogo*, and *kuyunko*. Predicted values and their propagated uncertainties are based on regression from endmember enthalpies. The difference column shows predicted minus measured ΔHf° values.
- **Table 4H.** $\Delta H_f°_{el}$ of select bulk model endmembers compared with the same endmembers as derived from the polyhedron method of van Hinsberg and Schumacher (2007c).

Chapter 5. Model Integration and Conclusions

Table 5A. Speciation independent endmember definitions and independent site fractions**.**

Table 5B. Speciation model standard state molar volume and Entropy. Note that due to multicollinearity present in the data the uncertainties are not independent and it is better to use the covariance matrix which for molar volume can be found in Electronic Appendix 2D and the

correlation matrix for entropy can be found in Appendix 3D3 (which is the correlation matrix of method 2 but only minimal changes are assumed for method 1)

Table 5C. Heat capacity coefficients of a Berman and Brown (1985) model fit to speciation endmember curves. Cp polynomial was calibrated using measured Cp between 298-778K. Due to strong correlations in the Berman polynomial equations, individual variance uncertainties are not meaningful. Instead, uncertainties must be assessed using the covariance matrix, provided in Chapter 3.

Table 5D. Bulk independent endmember definitions and independent bulk parameters.

Table 5E. Bulk model standard state molar volume and Entropy. Note that due to multicollinearity present in the data the uncertainties are not independent and it is better to use the covariance matrix which for molar volume can be found in Electronic Appendix 2E and the correlation matrix for entropy can be found in Appendix 3D2 (which is the covariance matrix of method 2 but only minimal changes are assumed for method 1). For the Enthalpy data with strong multicollinearity due to the sparse dataset the correlation matrix can be found in Appendix 4F.

Table 5F. Heat capacity coefficients of a Berman and Brown (1985) model fit to bulk endmember curves. Cp polynomial was calibrated using measured Cp between 298-778K. Due to strong correlations in the Berman polynomial equations, individual variance uncertainties are not meaningful. Instead, uncertainties must be assessed using the covariance matrix, provided in Chapter 3.

Appendix 5A. Bulk Model exchange reactions between endmembers

- This Appendix contains all exchange reaction between endmembers in the Bulk model.

Appendix 5B. Speciation Model exchange reactions between endmembers

- This Appendix contains all exchange reaction between endmembers in the Speciation model.

LIST OF ABBREVIATIONS

Abbreviation	Definition
$AdjR^2$	Adjusted R-Squared
AFM	Antiferromagnetism
aorsm	Alumino-oxy-rossmanite
aorsmB	Bulk model Alumino-oxy-rossmanite
bu	Buergerite
buB	Bulk Model Buergerite
BV	Bond Valence
BVS	Bond Valence Sum
CALPHAD	Computer Coupling of Phase Diagrams and Thermochemistry
CI	Confidence Interval
Cmol	Curie Constant (Magnetic Susceptibility)
Cp	Heat Capacity
Cp(T)	Heat Capacity as a Function of Temperature
CWTLS	Correlated Weighted Total Least Squares
DFBETAS	Difference in Betas
DFFITS	Difference in Fits
DFT	Density Functional Theory
DM	Dzyaloshinskii-Moriya Interaction
drv	Dravite
drvB	Bulk Model Dravite
dravsyn	Synthetic Dravite
drvdis	Disordered Dravite
DSC	Differential Scanning Calorimetry
e-DOS	Electronic Density of States

Abbreviation	Definition
ED	Electron Density
EFG	Electric Field Gradient
EoS	Equation of State
E∥c	Electric Field Parallel to the c-axis
E⊥c	Electric Field Perpendicular to the c-axis
F0	Standard Free Energy in the Absence of Phase Transition
fluvt	Fluor-uvite
fluvtB	Bulk Model Fluor-Uvite
FM	Ferromagnetism
foi	Foitite
foiB	Bulk Model Foitite
FTIR	Fourier Transform Infrared
G	Gibbs Free Energy
G(Q)	Free Energy as a Function of Q
Ga	Giga annum
gtls	Generalized Total Least Squares
gtls-block-diag	Constrained Weighted TLS using block-diagonal covariance structure
gtls-cov-data	Generalized TLS using covariance matrix from full dataset
gtls-row-column	Generalized TLS using row-column structure
H	Enthalpy
H_o	Standard Enthalpy
H°f	Standard Enthalpy of formation
HFSE	High Field Strength Elements
HKF	Helgeson-Kirkham-Flowers model
HP	Holland and Powell
ICP-MS	Inductively Coupled Plasma Mass Spectrometry

Abbreviation	Definition
IMA	International Mineralogical Association
IWLS	Iteratively Weighted Least Squares
J	Exchange Interaction Constant
J′	Secondary Exchange Constant
J″	Tertiary Exchange Constant
kB	Boltzmann Constant
LA	Laser Ablation
Leff	Effective Orbital Angular Momentum
LOOCV	Leave-One-Out Cross-Validation
LRO	Long-Range Order
MAD	Median Absolute Deviation
MAE	Mean Absolute Error
mdtw	Midway Tourmaline
mdtwB	Bulk Model Midway Tourmaline
Ms	Equivalent Mixing Sites in Configurational Entropy
MSE	Mean Squared Error
NCSS	Statistical software used for regression analysis
nind	Independent Component Count for Configurational Entropy
NNLS	Non-Negative Least Squares
odrv	Oxy-Dravite
ole	Olenite
oleB	Bulk Model Olenite
OLS	Ordinary Least Squares
P	Pressure
PE	Polyethylene
PCA	Principal Component Analysis

Abbreviation	Definition
pov	Povondraite
PPMS	Physical Property Measurement System
pXRD	Powder X-Ray Diffraction
Q	Order Parameter in Landau Theory
QSD	Quadrupole Splitting Distribution
R	Gas Constant
RMSE	Root Mean Square Error
$RPRESS^2$	Predictive Residual Sum of Squares
RT	Room Temperature
R^2 Press	Cross-Validation R-Squared
S	Entropy
S_0	Standard Entropy
SC-XRD	Single Crystal X-Ray Diffraction
SE	Standard Error
SEM	Scanning Electron Microscope
Smag	Magnetic Entropy
Smax	Maximum Entropy
Sconf	Configurational Entropy
SRO	Short-Range Order
Svib	Vibrational Entropy
srl	Schorl
srlB	Bulk Model Schorl
T	Temperature
Tc	Critical Temperature
TGA	Thermogravimetric Analysis
TLS	Total Least Squares

Abbreviation	Definition
TN	Néel Temperature
V	Molar Volume
V_0	Standard Molar Volume
V-DOS	Vibrational Density of States
VIF	Variance Inflation Factor
VM	Molar Volume
Weiss T	Weiss Temperature
wMSE	Weighted Mean Squared Error
WLS	Weighted Least Squares
X	Composition
XPS	X-ray Photoelectron Spectroscopy
XRD	X-Ray Diffraction
Z-score	Standard Score for Statistical Analysis
Δ	Energy Gap
ΔCorr	Autocorrelated FTIR linewidth
$\delta\Delta$Corr	Excess FTIR line width compared to mechanical mixing
ΔQ	Differential Heat Flow
ΔH_{drop}	Drop solution enthalpies
$\Delta H_f°_{el}$	Enthalpy of formation from the elements
$\Delta H_f°_{ox}$	Enthalpy of formation from the oxides
θ	Curie-Weiss Temperature
θD	Debye Temperature
θE	Einstein Temperature
τ	Relaxation Time Constant
Ω	Number of Microstates
ω	Angular Frequency

Abbreviation	Definition
$^{3}(\omega)$	Phonon Density of States Function

Thermodynamic model for Tourmaline

Computational phase diagrams need real thermodynamic anchors—without them, they drift into uncertainty.

Chapter 0. Introduction

Stan Roozen

1. INTRODUCTION

Tourmaline is an exceptional geochemical recorder due to its ability to incorporate a wide range of elements across diverse crystallographic sites (van Hinsberg et al. 2011a), It is resistant to chemical weathering, has low volume diffusivity (Hawthorne and Dirlam 2011), and remains stable across extensive PTX conditions (Dutrow and Henry 2011). Its record is preserved from diagenesis (Henry and Dutrow 2012) to deep crustal levels (Lussier et al. 2016), and from recent to Archean times (Appel 1984). As an accessory phase, it does not significantly control host rock or fluid compositions (van Hinsberg et al. 2011a) and instead acts to capture its host rock's signature while zoning patterns track transient changes in fluid or magma (van Hinsberg et al. 2011b). While other minerals may reset, and fluids can enter and leave the system, tourmaline retains a record of their former chemical presence, preserving geochemical signatures across diverse geological environments.

Predicting exchange reactions between tourmaline, minerals, and internally or externally buffered fluids or melts during reactive fluid flow requires a high-quality, internally consistent thermodynamic model. This model must include standard-state properties and caloric, volumetric, and compositional equations of state (EoS) to describe PTX dependencies. Forward modelling, integrating mineral, fluid, melt, and aqueous speciation models (e.g., HKF (Helgeson et al. 1981)), enables the reconstruction of past fluid or melt compositions and the prediction of mineral exchange and net transfer reactions. Given tourmaline's widespread occurrence, such a model supports thermobarometry, provenance studies, mineral exploration, and fluid and magma reconstructions in metamorphic, igneous, and hydrothermal systems.

1.1. Tourmaline supergroup mineral

The tourmaline chemical composition is the result of external (temperature, pressure, mineral assemblage, fluid and magma composition) and internal influences (crystallographic constrains) and these controls need to be critically evaluated before tourmaline can be used as a mineral probe. The generalized structural formula for Tourmaline is $XY_3Z_6(T_6O_{18})(BO_3)_3V_3W$ where:

X = Na^{1+}, Ca^{2+}, K^{1+}, vacancy
Y = Fe^{2+}, Mg^{2+}, Mn^{2+}, Al^{3+}, Li^{1+}, Fe^{3+}, V^{3+}, Cr^{3++}, Ti^{4+}
Z = Al^{3+}, Fe^{3+}, Mg^{2+}, V^{3+}, Fe^{2+}, Cr^{3+}

T = Si^{4+}, Al^{3+}, B^{3+}

B = B^{3+}

V = OH^{1-}, O^{2-}

W = OH^{1-}, F^{1-}, O^{2-}

Most of the compositional variability in tourmaline occurs at the X, Y, Z, W, and V sites. Its structure, based on a rhombohedral lattice (R3m) with trigonal symmetry, consists of a 3D network of octahedral ZO_6 sites interwoven with columns of XO_9, YO_6, BO_3, and TO_4 polyhedra (Bosi 2018). The tetrahedral ring aligns with the c-axis, imparting noncentrosymmetry and a polar character responsible for its pyro- and piezoelectric properties (Hawthorne and Dirlam 2011). This influences growth, morphology, and zoning, with the slower-growing c^- ('analogous pole') and faster-growing c^+ ('antilogous pole') exhibiting hemimorphism (Henry and Dutrow 1996). Diffusion is negligible, as shown by H-diffusion experiments (Desbois and Ingrin 2007) and sharp compositional and isotopic zoning in high-temperature-experienced tourmaline (van Hinsberg and Marschall 2007a).

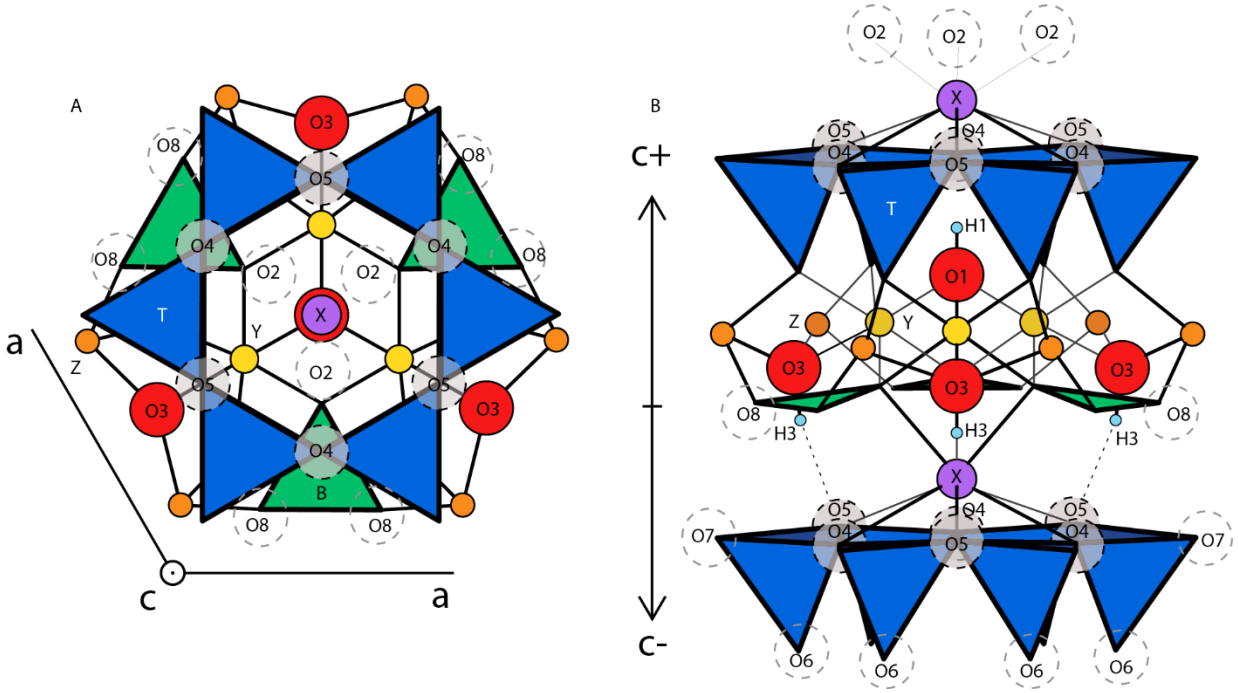

Figure 0A. Schematic representation of tourmaline's crystal structure, shown normal (A) and parallel (B) to the hexagonal c-axis. The X site (purple) is positioned above the tetrahedral ring (blue), bonding to the inner corners of the T sites and trigonally coordinated B sites (green). The O1 (W) site (red) is linked to three Y sites (yellow), with its O1-H1 bond directed toward the X

site (H in light blue). The O3 (V) sites (red) each coordinate one Y (yellow) and two Z sites (orange), while the O3-H3 bond is oriented in the c^- direction, where H3 shares an H bond with the O5 site (dashed circle) in the tetrahedral ring. (Figure modified after Berryman et al.(2016))

Table 0A. Tourmaline nomenclature endmembers of this study. The endmembers relate to each other by homo- and hetero-valent coupled substitutions and their associated exchange vectors, as mentioned at the bottom of the table.

Species	**(X)**	**(Y_3)**	**(Z_6)**	**T_6O_{18}**	**$(BO_3)_3$**	**V_3**	**W**
Alkali tourmaline, subgroup 1							
Schorl	Na	Fe^{2+}_3	Al_6	Si_6O_{18}	$(BO_3)_3$	$(OH)_3$	(OH)
Dravite	Na	Mg_3	Al_6	Si_6O_{18}	$(BO_3)_3$	$(OH)_3$	(OH)
Alkali tourmaline, subgroup 3							
Oxy-dravite	Na	Al_2Mg_1	MgAl5	Si_6O_{18}	$(BO_3)_3$	$(OH)_3$	(O)
Povondraite	Na	Fe^{3+}_3	Fe^{3+}_4 Al_2	Si_6O_{18}	$(BO_3)_3$	$(OH)_3$	(O)
Magnesium-Dutrowite	Na	$Mg_{2.5}Ti_{0.5}$	Al_6	Si_6O_{18}	$(BO_3)_3$	$(OH)_3$	(O)
Alkali tourmaline, subgroup 5							
Olenite	Na	Al_3	Al_6	Si_6O_{18}	$(BO_3)_3$	$(O)_3$	(OH)
Buergerite	Na	Fe^{3+}_3	Al_6	Si_6O_{18}	$(BO_3)_3$	$(O)_3$	(OH)
Alkali tourmaline, subgroup 6							
Na-Al-Al-B root name	Na	Al_3	Al_6	$Si_3B_3O_{18}$	$(BO_3)_3$	$(OH)_3$	(OH)
Calcic tourmaline, subgroup 1							
Uvite	Ca	Mg_3	$MgAl_5$	Si_6O_{18}	$(BO_3)_3$	$(OH)_3$	(OH)
Feruvite	Ca	Fe^{2+}_3	$MgAl_5$	Si_6O_{18}	$(BO_3)_3$	$(OH)_3$	(OH)
Fluor-uvite	Ca	Mg_3	$MgAl_5$	Si_6O_{18}	$(BO_3)_3$	$(OH)_3$	F
X-site vacant tourmaline, subgroup 1							
Foitite	□	Fe^{2+}_2Al	Al_6	Si_6O_{18}	$(BO_3)_3$	$(OH)_3$	(OH)

X-site vacant tourmaline, subgroup 7 (?)

Alumino-oxy-rossmanite	□	Al_3	Al_6	$Si_5Al_1O_{18}$	$(BO_3)_3$	$(OH)_3$	(O)

Generalized coupled substitutions	Resulting actions
$^{X}R^{1+} + R^{2+} \leftrightarrow {}^{X}\square + R^{3+}$	relates alkali-vacant groups
$^{X}R^{1+} + R^{3+} \leftrightarrow {}^{X}Ca + R^{2+}$	relates alkali-calcic groups
$R^{2+} + OH^{1-} \leftrightarrow R^{3+} + O^{2-}$	relates deprotonation in all groups
$R^{2+} + {}^{T}Si^{4+} \leftrightarrow R^{3+} + {}^{T}R^{3+}$	relates Tschermak-like tetrahedral-octahedral substitution in all groups

Note: R represents generalised cations such that XR1+ = Na1+; R2+ = Mg2+, Fe2+; R3+ = Al3+, TB3+ and no site designation reflects possibilities involving multiple sites.

The Nomenclature and Classification Committee (CNMNC) of the International Mineralogical Association (IMA) recognises 41 natural tourmaline species, with many additional synthetic and hypothetical end members (Henry et al. 2011). The primary classification is based on occupancy at X site, dividing tourmalines into alkali, calcic and X-vacant groups. Heterovalent coupled substitutions link these groups and their subgroups, while homovalent cation or anion substitutions define species within subgroups, indicated by prefixes (Henry et al. 2011).

This study focusses on tourmaline species within the Na-Ca-Mg-Fe^{2+}-Fe^{3+}-Ti-Al-B-O-H-F system, which are the most commonly found tourmalines in hydrothermal, igneous, and metamorphic environments. Li-bearing tourmalines are excluded as these are much rarer and essentially restricted to evolved igneous rocks and due to the apparent presence of a significant solvus separating dravite-elbaite and possibly schorl-elbaite, which would require extensive experiments to properly characterise (London 2011). Tourmalines with atypical enrichment in elements such as K, Mn, Cr, V, Zn, Ni, Co, or Cu, as well as those with non-rhombohedral symmetry (orthorhombic, monoclinic, or triclinic), are also omitted. Such tourmalines are rare, and deviations from rhombohedral symmetry typically result from minimal atomic displacements off symmetry positions, often explainable by compositional inhomogeneity or slight positional

disorder caused by short-range ordering (SRO) effects. With these exclusions, the study focusses on the following end-member species:

1.2. Tourmaline: Net transfer reactions determine the stability.

Experimental studies have explored the P-T-X stability range of tourmaline. Its upper thermal limit varies by endmember species, mineral assemblage, and fluid composition. Dravite-schorl in a natural assemblage undergoes incongruent melting at 725–800 ° C and 4–4.5 kbar (Von Goerne et al. 1999; Ota et al. 2008), while as a single-phase tourmaline without coexisting minerals, it remains stable up to 950 °C, i.e., showing no melting or breakdown (Robbins and Yoder Jr. 1962). The upper pressure limit for single-phase dravite is ~60–80 kbar (Krosse 1995) but stability depends on composition, with olenite and K-dravite stable at 40–50 kbar (Schreyer et al. 2000; Berryman et al. 2014) and influenced by mineral assemblage (Ota et al. 2008). The lower stability limit is uncertain but may be as low as 150°C and 1 kbar, as X-vacant tourmaline occurs in meta-evaporites and oceanic alteration (Byerly and Palmer 1991; Henry et al. 2008). Dravite has been synthesised at 0.5 kbar and 350 ° C (Palmer et al. 1992).

The breakdown products depend on the composition of the system. At high temperatures, tourmaline melts incongruently to cordierite, sillimanite, and B-bearing fluids or melts, sometimes with quartz or albite (von Goerne et al. 1999). In Fe–Al-rich systems, it may yield kornerupine, grandidierite, or sapphirine (Robbins and Yoder 1962; Werding and Schreyer 1978). Breakdown also occurs in calc-silicates (to serendibite, datolite, danburite) (Grew and Anovitz 1996) and in retrograde settings to muscovite, biotite, chlorite, or albite (Slack et al. 1996), especially under high-pH, boron-undersaturated fluids (Morgan and London 1989). In fluorine-rich granitic melts, tourmaline can dissolve entirely (Wolf and London 1997). In all cases, boron is released into fluid, melt, or new B-bearing phases.

Tourmaline growth and dissolution depend on the cation/anion activity ratio of its major elements (Dutrow et al. 1999). Its stability is influenced by the activity product of the oxide components, weighted by the stoichiometric exponent (London 2011). The oxide with the smallest activities, which also depend on other phases, has the largest role in its solubility. While silica is not a limiting factor, as evidenced by tourmaline's presence of tourmaline in mafic

rocks, alumina is, given tourmaline's peraluminous nature (London 2011). The activities of other Y site cations are often sufficient in many rocks, and tourmaline seems to be stable under a wide range of oxygen fugacities. Boron activity is critical, as tourmaline forms only in B-rich environments or through B-metasomatism. It stabilizes in neutral to acidic fluids, while alkaline conditions promote dissolution by forming tetrahedral $B(OH)_4^-$ complexes, whereas at lower pH, boron remains in the trigonal $B(OH)_3$ form, matching its coordination in tourmaline (Morgan and London 1989; Henry and Dutrow 1996).

Experimental studies indicate that tourmaline formation generally requires a minimum of 0.5–1.0 wt% B_2O_3 in acidic fluids at 600 °C and 200 MPa (Morgan and London 1989). At higher temperatures, this threshold increases; for instance, ~2.0 wt% B_2O_3 is needed at 700 °C and 100 MPa to stabilize tourmaline in a granitic system (London 2011). Below these concentrations, boron remains in the fluid, and tourmaline is unstable or does not nucleate. These thresholds may also vary depending on fluid pH, cation availability, and the presence of nucleation surfaces.

1.3. Tourmaline: External effect on element exchange

Tourmaline's potential for thermobarometry has been explored in tourmaline-biotite experiments and equilibrium mineral assemblages. The Mg-Fe exchange between tourmaline and biotite, staurolite, garnet, chlorite, and muscovite shows a wide distribution coefficients, $K_d^{\mathrm{Fe-Mg}} = \frac{(Fe/Mg)^{\mathrm{tourmaline}}}{(Fe/Mg)^{\mathrm{biotite}}}$, range due to inter-site partitioning at the Y and Z sites, affecting P-T-X dependencies (van Hinsberg and Schumacher 2009). Ca-Na exchange with plagioclase occurs at the X-site but is influenced by coupled substitutions involving the Y or Z site. K-based barometry remains semi-quantitative due to the lack of a K-saturating phase in experiments (Berryman et al. 2015). Other experiments show that K/Na ratios in tourmaline increase with pressure when buffered by biotite, but data scarcity prevents calibration of a reliable barometer (van Hinsberg et al. 2011b). Tourmaline exhibits sector zoning along the c-axis (Henry and Dutrow 1996) with the c+ sector enriched in Al and depleted in Ti, Ca, Mg, and Na, while the c- sector shows the opposite trend (van Hinsberg et al. 2006). Surface charge and morphology influence charged species' incorporation, with vacancies preferentially forming at the antilogous pole, and light elements like B and H fractionate as charge-balancing cations (van Hinsberg and

Marschall 2007). The a-sector does not exhibit sector zoning as it is oriented perpendicular to the asymmetry in the crystal structure (see Figure 0A for sector axes).

Inter-sector partitioning of ^{X}Ca and ^{Y}Ti has been empirically calibrated, providing a single-crystal thermometer for rocks above 350°C, independent of element concentration and pressure (van Hinsberg and Schumacher 2007b). Furthermore, BT concentrations in Al-rich tourmalines correlate with P-T conditions (Ertl et al. 2010).

Tourmaline's X-site occupancy of Ca and Na provides insight into fluid composition. ^{X}Na reflects fluid Na^{+} content but is assemblage- and temperature-dependent, and this empirical correlation works best for Na-rich tourmaline endmembers. ^{X}Ca is a more robust proxy for Ca^{2+} concentration in equilibrium with tourmaline, albite, and quartz at ~300°C and 2 kbar (von Goerne et al. 2011; Berryman et al. 2016), allowing estimation of the Ca, Na equivalent salt content of a fluid when the appropriate buffers are in place (van Hinsberg et al. 2017). Late-stage fibrous tourmalines in open veins are highly responsive to fluid changes, with alkali tourmalines stable in Na^{+}-rich fluids and foitite forming in Na^{+}-poor conditions (Dutrow and Henry 2016). Fluorine incorporation depends on fluid F content but is also influenced by X-site charge and crystal chemistry (Henry and Dutrow 2011). The Fe^{3+}/Fe^{t} ratio in tourmaline is a promising redox proxy, based on limited experimental data (Fuchs et al. 1998; Williamson et al. 2000). At fixed temperature, the ratio increases with fO_2 across buffers (Magnetite-Hematite (MH) < Ni-NiO < Quartz-Fayalite-Magnetite (QFM)), confirming redox sensitivity. Within a single buffer, it rises also with temperature to ~550 °C, then declines, likely due to dehydrogenation or structural changes. The correllation remains empirical and may be influenced by crystal-chemical and pressure effects (Celata et al., 2023). Broader calibration is needed for reliable application.

Tourmaline composition reflects rock chemistry, as it exchanges elements with a buffering mineral assemblage, a principle widely applied in provenance studies (Henry and Guidotti 1985). Some chemical variation arises from the host rock rather than the fluid (Slack 1996). The fluid:rock ratio determines the relative influence of host rock and external fluid. Fluid-buffered elements, controlled by solubility, remain independent of bulk composition until a saturating phase is exhausted, whereas rock-buffered systems imprint their chemistry onto tourmaline (van Hinsberg et al. 2017).

Compositional features such as concentric, patchy, and hourglass zoning, recrystallisation after brecciation, overgrowth, replacement, and crack- or vein-filling textures are recognised in multistage ore-forming processes (Slack and Trumbull 2011). Combined with exchange equilibria, these zoning patterns record the evolution of tourmaline's growth environment, including temperature, host rock, fluid composition, and occasionally pressure.

These empirical trends in tourmaline composition seem to reliably track external conditions, but many can also result from crystal chemical controls such as charge balance, site occupancy, and structural preferences. Inter-site partitioning, sector zoning, and coupled substitutions influence element incorporation, making it difficult to fully separate intrinsic effects from external availability.

1.4. Tourmaline: Internal influences on element exchange

Element exchange in tourmaline is strongly governed by crystallographic constraints, as structure and local charge compensation dictate coupled substitutions among endmembers (London 2011). Chemical variation is limited by what can fit within the crystal lattice rather than directly mirroring the surrounding chemistry.

Tourmaline's structure influences exchange at both the short- and long-range scales (Bosi 2018). Short-range structure clusters atoms in non-translational symmetry, governed by charge balance which can be estimated via the Bond Valence Model, where bond valences approximate formal valence (Brown 2016). This stabilizes specific cation arrangements around the O1 (V) and O3 (W) sites (Bosi 2018) and affects heterovalent order-disorder reactions linked to anion charge changes. These short-range structures contribute to low diffusivities (Bosi 2018). The long-range structure in tourmaline arises from stable short-range structures, maintaining mineral symmetry and controlling intra-crystalline LRO order-disorder reactions. Disorder of R^{2+} and R^{3+} over Y and Z sites helps minimize structural misfit by keeping the Y-O and Z-O bond length difference below 0.15 Å (Bosi and Lucchesi 2007). A similar mechanism may explain misfit between the Y and T sites, as tetragonal B has been observed in Al-rich tourmalines from <300°C environments (Ertl et al. 2008, 2010). Since Y-O bonds are consistently longer than Z-O bonds, larger ions preferentially occupy the Y site, while smaller ions favor Z. Despite advances in understanding cation and anion site distribution, uncertainties remain, particularly in assigning Mg^{2+}, Al^{3+}, and Fe^{2+} to Y and Z sites, especially in tourmalines with deprotonated coupled substitutions.

Structural refinement data indicate that position of crystal sites and their respective sizes vary with composition (Bačík 2015).

1.5. Need for a Thermodynamic model

A single thermodynamic model for tourmaline provides a physically grounded alternative to empirical calibrations described so far, which are constrained by small experimental datasets and have uncertain general applicability. Empirical thermobarometry and fluid reconstructions assume equilibrium P-T conditions, an assumption often invalid due to kinetics and bulk composition effects, leading to oversimplified stability models and potential biases. By selecting a single reaction, empirical methods neglect other coexisting equilibria that may be equally or more important in defining phase stability (Connolly 2016). This partial equilibrium approach, i.e., $\mu_i^{\alpha}=\mu_i^{\beta}$, where the chemical potential μ_i of component i is equal between phases α and β, is defined as $\mu_i = \left(\frac{\partial G}{\partial n_i}\right)_{T,P,n_{j\neq i}}$ with G as the extensive Gibbs free energy, n_i the number of moles of component i, T temperature, and P pressure. The subscript $n_{j\neq i}$ indicates that the mole numbers of all other components are held constant during differentiation. This criterion, when applied to only one component while allowing others to remain out of equilibrium, risks misrepresenting mineral compositions—particularly in multi-component systems where multiple reactions jointly govern the equilibrium state (Connolly 2016). In contrast, a thermodynamic model considers the full set of potential reactions, ensuring internal consistency and more accurate predictions.

The key advantage is that well calibrated thermodynamic models generalize beyond experimental conditions, enabling forward modelling of net-transfer and exchange reactions across P-T-X space while reducing reliance on specific chemical subspaces. However, their accuracy depends on the completeness of thermodynamic data and equilibrium assumptions, necessitating continuous refinement and validation against experimental and natural observations.

1.6. Thermodynamic Modelling

Thermodynamic databases in the Earth Sciences describe phase equilibria under high temperatures and pressures by modelling the extensive Gibbs free energy G as a function of pressure, temperature, and composition $G = f(P, T, n_1...n_n)$ (Connolly 2016)**,** where n_i represents

the number of moles of each i component or endmember. This formulation captures the extensive nature of G and allows for the computation of stable mineral assemblages and their evolution by minimizing G under specified P–T–X conditions. Since only a limited portion of phase space can be experimentally measured, thermodynamic models serve as low-parameter fits, linking discrete energetic observations to estimate the energy of minerals like tourmaline. The key requirement is that the model parameters retain physical significance, ensuring robust extrapolation beyond the calibration range. Without this constraint, alternative data-driven methods like neural networks could interpolate effectively but lack predictive extrapolation capability.

To obtain extensive G = f(P, T, $n_1 ... n_n$) requires integrating the differential:$dG = -SdT + VdP + \sum_i \mu_i dn_i$ from a reference state **(**P_r, T_r**)** where mineral thermodynamic properties are tabulated (Connolly 2016). Since standard-state properties refer to an ordered endmember composition, μdn term vanishes during integration because the composition is constant and dn_i=0; hence, only temperature and pressure integrals contribute to changes in G. The differential dG can be split into isothermal and isobaric components because entropy S and molar volume V are state functions, meaning their integrals depend only on initial and final states, not the integration path. By first integrating the caloric EoS over T at constant P, evaluating thermal expansivity at T to obtain V at T and then integrating the pressure dependent) volumetric EoS (containing the compressibility) over P at constant T, we obtain (Connolly 2016):

$$G(P,T) = G(P_r,T_r) - \int_{T_r}^{T} S(P_r,T)dT + \int_{P_r}^{P} V(P,T)\,dP \qquad \text{(eq 1)}$$

In case of Gibbs free energy the Maxwell relation relationships $\left(\frac{\partial S}{\partial P}\right)_T = -\left(\frac{\partial V}{\partial T}\right)_P$ ensures that entropy's pressure dependence does not need to be integrated to add their cumulative addition to Gibbs free energy as this integral is exactly offset by the volume's temperature integral (Berman 1988). This maintains thermodynamic consistency and ensures that $\left(\frac{\partial G}{\partial P}\right)_T = V$ and $\left(\frac{\partial G}{\partial T}\right)_P = -S$. Semi-Empirical functions for the volumetric V(P,T) and caloric S(T) EoS's must, however, be carefully selected.

In geosciences, the isobaric portion is traditionally rewritten using G= H - TS for convenience (Connolly 2016).

$$G(P_r, T) = H(P_r, T_r) + \int_{T_r}^{T} C_P \mathrm{d}T - TS(P_r, T)$$

(eq 2)

The $S(P_r, T)$ is the third-law entropy.

$$S(P_r, T) = S(P_r, T_r) + \int_{T_r}^{T} \frac{C_P}{T} dT$$

(eq 3)

Putting eq 2 and eq 3 in eq 1 and taken the enthalpy compared to a reference enthalpy of the elements one obtains for homogenous ordered endmember phase:

$$\Delta G = \Delta H^0 + \int_{T_0}^{T} Cp(T) dT - T\left\{S^0 + \int_{T_0}^{T} \frac{Cp(T)}{T} dT\right\} + \int_{P_0}^{P} V(P,T)\, dP$$

(eq 4)

(Anderson 2005). Here, all terms refer to per-mole quantities, i.e., the molar Gibbs free energy, which is intensive. $C_p(T)$ and V(P) must be parameterized for integration, and V^0 corrected to T using the V(T) (thermal expansion) EoS evaluation at T to compute ΔG at given P and T. ΔH°, S°, and V° are listed in databases, with several studies providing optimised thermodynamic parameters for rock-forming minerals (Holland and Powell 1985, 1990, 1998, 2011; Berman 1988; Powell and Holland 1988; Gottschalk 1996; Chatterjee et al. 1998). Each database applies specific thermodynamic models and mathematical optimisation methods, but all adhere to the fundamental requirement that a thermodynamic cycle must sum to zero energy within uncertainty, *i.e* are internally consistent. The $C_p(T)$ and V(P,T) equations of state vary between databases, requiring caution when combining sources. Frequent updates reflect the dynamic nature of these datasets, as additional constraints or more precise measurements can lead to shifts in linked phases. This is not a problem as long as internal consistency is maintained and improves model accuracy, but does mean that absolute values are not fixed.

Solution phases are represented as mixtures of endmember components and generally stored in separate thermodynamic databases. The total free energy of a solution G_{sol} consists of three components:

$$G_{sol} = G_{\mathrm{mech}} + G_{\mathrm{conf}} + G_{ex}$$

where G_{mech} is the mechanical mixing energy which is eq 4 for each respective endmember, G_{conf} Gconf accounts for residual atomic disorder not explicitly represented by the endmember model. This remaining disorder is assumed to be random and is quantified using statistical mechanics. The associated configurational entropy S^{conf} reflects the number of ways atoms can be arranged across crystallographic sites, following Boltzmann's equation:

$$S_{\text{conf}} = \text{k} \ln W$$

where k is Boltzmann constant and W is the number of microstates. For multi-site solid solutions, S^{conf} becomes in molar basis:

$$S_{\text{conf}} = -R \sum_{s} M_s \sum_{i=1}^{n_{\text{ind}}s} x_{i,s} \ln x_{i,s}$$

where:

- s: index for crystallographic site types
- Ms: number of equivalent sites of type s per formula unit (Multiplicity)
- $x_{i,s}$: site fraction of species i on site s
- n_{ind}: number of independent species on site s

This equation assumes ideal configurational entropy, meaning all arrangements are energetically equivalent and neglects any enthalpic interactions. In real systems, energetic interactions, such as differences in bond strength or atomic size, can make certain configurations more favorable, reducing the entropy below the ideal value and introducing an enthalpic component to mixing. The configurational contribution to Gibbs free energy is then:

$$G_{\text{conf}} = -TS_{\text{conf}}$$

For more detail, see Blundell and Blundell (2009).

G_{ex} represents excess energy, which is often associated with the enthalpy of mixing. In many cases, it primarily compensates for oversimplifying assumptions made in configurational entropy calculations, although the G_{ex} also captures non-ideal interactions between mixing components

that lead to asymmetry in the S_{conf} or development of a solvus. $G_{ex}(P,T,X)$ is the compositional EoS and its exact form depends on the type of solution model, *e.g.* regular solution model is $G_{ex} = WX_1X_2$ and for a subregular model is $G_{ex} = (W_1X_2 + W_2X_1)X_1X_2$ and these W terms can be P, T dependent. Figure 0B shows the complete integral molar Gibbs free energy equation colour coded for all the standard state properties and EoS needed for a thermodynamic model.

$$G(P,T,\mathbf{X}) = \sum_i X_i [\underbrace{H_i^0 - TS_i^0}_{\text{Standard-state properties}} + \underbrace{\int_{T_0}^{T} C_{p,i}(T)dT - T\int_{T_0}^{T} \frac{C_{p,i}(T)}{T}dT}_{\text{Caloric equations of state}} + \underbrace{\int_{P_0}^{P} V_i(P,T)dP}_{\text{Volumetric equation of state (V0 inside)}}] - TR\sum_s M_s \sum_{j=1}^{n_{\text{ind},s}} x_{j,s} \ln x_{j,s}$$

Ideal configurational interactions

$$+ \underbrace{\sum_{i<j} X_i X_j W_{ij}(P,T)}_{\text{Excess (non-ideal) interactions}} + \underbrace{G_{\text{other}}(P,T,\mathbf{X})}_{\text{Other contributions (e.g., magnetic)}}$$

Figure 0B. This master equation describes the molar Gibbs free energy G(P,T,**X**) of a multicomponent solid solution as a function of pressure P, temperature T, and endmember vector **X** with endmember mole fractions components X_i. The ▢ standard-state properties include the reference enthalpy H_i^0, entropy S_i^0, and molar volume V_i^0, at 298.15 K and 1 bar with enthalpies referenced to the elements. The ● caloric EoS captures temperature effects through heat capacity integrals: $C_{p,i}(T)$ is used to correct both enthalpy and entropy, respectivly. The ● volumetric component captures pressure effects through direct integration of the volume function V(P,T). Thermal expansion α(T) is required to evaluate $V(P^0,T)$ at elevated temperatures, but it is not integrated as a separate energy contribution. Instead, it adjusts the temperature-dependent

volume, which is then used in the pressure integral. Only the pressure integral $\int V(P,T)\, dP$ contributes cumulatively to Gibbs free energy. The ■ compositional EoS includes the ideal configurational entropy, calculated from species (j) site (s) occupancies $x_{j,s}$, site multiplicities M_s , and total number of independent species $n_{ind,s}$. The $n_{ind,s}$ reflect the system's degrees of freedom+1 and can be expressed as linear combinations of the independent endmember fractions. The excess Gibbs energy forms from non-ideal interactions here as example modelled via regular parameters $W_{ij}(P,T)$. The final term, $G_{other}(P,T,\mathbf{X})$, accounts for energetic contributions not captured by endmember-based mixing, such as magnetic ordering or electronic transitions. These effects are typically non-linear in composition and cannot be expressed as separable functions of P, T, and X; for example, Curie or Néel temperatures may vary non-trivially with Fe content.

The equation gives the molar Gibbs free energy $G(P,T,\mathbf{X})$, of a solution, where X_i are endmember mole fractions. The molar Gibbs free energy $G = \sum_i \mu_i X_i$ as a composition-weighted average of chemical potentials. Geometrically, the tangent plane to the G (X) surface at a given composition defines the set of μ_i, where each chemical potential corresponds to the constrained partial derivative of G with respect to Xi, under the condition $\sum_i X_i = 1$.

1.7. Gibbs Free Energy Minimisation in Multi-Component Systems

In a c-component system with p coexisting phases (e. g. , α and β)**,** equilibrium requires that the total Gibbs free energy of the system is minimised across all phases, ensuring no further spontaneous transformations (Connolly 2005). This defines the minimum free energy surface, where the chemical potentials of each component remain equal across phases (Connolly 1990):

$$\mu_1^{\alpha} = \mu_1^{\beta}, \mu_2^{\alpha} = \mu_2^{\beta}, \ldots, \mu_c^{\alpha} = \mu_c^{\beta}$$

Although solution phases are described internally by endmember mole fractions, they follow the same thermodynamic principles. In these models, the molar Gibbs energy G(P,T,X) is a function of endmember proportions, and the chemical potentials of system components are obtained by projecting the endmember derivatives through the phase's stoichiometric matrix A:

$$\boldsymbol{\mu}^{\text{components}} = \mathbf{A}^{\mathrm{T}} \cdot \left(\frac{\partial \bar{G}}{\partial \mathbf{X}}\right)_{\sum X_i = 1} .$$

At equilibrium, these component potentials correspond to the tangent plane slopes of the molar Gibbs free energy surface with respect to conserved system components (Connolly 2016). At equilibrium, chemical potentials correspond to the slopes (gradients) of the minimum Gibbs free energy surface with respect to component amounts, and can be extracted by projecting the tangent plane onto the respective composition axes (Connolly 2016).

Mass balance constraints ensure that the total number of moles of each component remains fixed across all phases: $\sum_{\alpha=1}^{p} n_i^{\alpha} = n_i^{\text{total}}$, where n_i^{α} is the number of moles of component i in phase α, p is the number of phases, n_i^{total} is the bulk composition of the system (Connolly 2005). Additionally, all component amounts must satisfy the non-negativity constraint**:** $n_i^{\alpha} \geq 0$, which prevents unphysical negative concentrations (Connolly 2005).

Gibbs free energy minimisation ensures stability only if the Gibbs function is convex; the stability criterion requires that the second derivative of G with respect to composition is positive definite, i.e.,

$$\left(\frac{\partial^2 G}{\partial n_i \partial n_j}\right)_{P,T} > 0$$

which prevents metastable solutions and ensures that any small compositional perturbation increases G. In the pseudocompound approach (Connolly 2005), Gibbs free energy minimisation inherently ensures stability by selecting only stable phase assemblages. If the free energy surface has negative curvature, the system decomposes into coexisting phases that restore convexity. By discretizing a solid solution into virtual endmembers, this method ensures selection from the convex hull of free energy, making explicit convexity checks unnecessary (Connolly 2005). Unlike polynomial models, which require stability verification, this approach inherently enforces it.

1.8. Tourmaline thermodynamics

Thermodynamic data for tourmaline are limited, except for V^0 and V(P,T). High-T Cp and $\Delta H°_f$ were measured for several natural elbaite, schorl, and dravite grains via high-T drop solution and DSC (Ogorodova et al. 2004, 2012), with additional High-T Cp data presented in Anovitz and

Hemingway (1996). A single low-T entropy measurement exists for a poorly characterised dravitic tourmaline (Kuyunko et al. 1984).

Limited thermodynamic data for tourmaline led to use of estimation models to estimate the thermodynamic properties, including the polyhedron method, where properties are derived as linear combinations of averaged polyhedral contributions (Garofalo et al. 2000; van Hinsberg et al. 2005b, 2005a; Van Hinsberg and Schumacher 2007c). These fractions are obtained via multiple linear regression on a database of endmembers with diverse polyhedral sizes, structures, polymerization levels, and crystal family classes, then summed into the required endmember. This method averages polyhedral properties across minerals that may share the same coordination number but have vastly different polyhedral sizes, shapes, and distortions, leading to oversimplified estimates.

2. OBJECTIVES

The primary objective of this study is to develop a comprehensive thermodynamic model for tourmaline that accurately describes its stability, and phase equilibria in geological systems. This model integrates internal controls—crystallographic constraints, site occupancy, and charge balance—determined by the definition of the endmember compositions, along with thermodynamic properties (standard state and EoS). By comparing solution energetics with those of coexisting phases, it allows for predicting tourmaline compositional evolution in response to external controls like pressure, temperature, mineral assemblages, and fluid/magma interactions.

To achieve this, the following sub-objectives will be addressed:

1. Characterizing Tourmaline with Internal Consistency (Chapter 1)

- Assemble a dataset of natural and synthetic tourmalines within the Na-Ca-B-Fe^{2+}-Fe^{3+}-Mg-Al-Si-Ti-O-H-F system.
- Use a multi-instrument approach to fully characterize tourmaline: EMPA for major elements, LA-ICP-MS for trace elements, Karl-Fischer titration for H_2O content, and Mössbauer spectroscopy for $Fe^{2+/3+}$ ratios.

- Determine site partitioning since elements can independently occupy multiple crystallographic sites. Single-crystal XRD provides structural constraints, but with more than three elements per site, formula optimisation is required which incorporates composition, site electrons, bond valence sums, and crystal-chemical constraints to refine order-disorder relationships.
- Ensure internal consistency by standardizing all methodologies. Thermodynamic properties are highly sensitive to normalization, requiring coherence across measurements to maintain reliability.
- Conduct an uncertainty analysis to quantify measurement precision, allowing for sensitivity analysis of thermodynamic properties and robust regression modelling.

2. Defining a Thermodynamic Model (Chapter 2)

- Develop a **bulk compositional model** for users relying only on chemical analyses.
- Develop a **speciation model** based on optimised mineral formulas, incorporating site-specific occupancies and structural constraints.

3. Obtaining Key Thermodynamic Properties

- **Molar Volume (V) (Chapter 2):** Calculate from single-crystal XRD measurements and extrapolate to endmembers using regression techniques. Given the abundance of published tourmaline molar volumes, test different regression methods, including robust regression and errors-in-variables (EIV) approaches, to manage multicollinearity and outliers and to test how sensitive parameter extraction is to compositional uncertainty.
- **Entropy (S°) and Heat Capacity (Cp) (Chapter 3):** Measure absolute entropy by integrating low-temperature heat capacity data from relaxation calorimetry. Fit high-temperature Cp data from differential calorimetry using polynomial functions. Endmember entropies and caloric equations of state are derived through regression of the full dataset.
- **Enthalpy (ΔH) (Chapter 4):** Determine enthalpy values using high-temperature lead-borate drop solution calorimetry at 700°C under O_2 flushing. Integrate results into a

thermodynamic cycle, accounting for oxidation, devolatilization, and reference oxide formation. A sensitivity analysis will assess uncertainties.

4. Model Integration and conclusions (Chapter 5)

- **Configurational Entropy Model:** Develop a statistical mechanics-based model for configurational entropy, incorporating Bragg-Williams long-range order and molecular short-range order models to capture disorder effects that are not explicitly included in the thermodynamic model.

- Integrate all components into a comprehensive thermodynamic solution model for tourmaline, suitable for incorporation into existing thermodynamic databases.

By addressing these sub-objectives, this study will establish a thermodynamic foundation for modelling tourmaline stability and compositional evolution across P-T-X conditions. The model will support pseudosection thermobarometry, provenance studies, mineral exploration, and fluid and magma evolution reconstructions by providing internally consistent thermodynamic parameters for phase equilibrium modelling.

References.

Anderson, G.M. (2005) Thermodynamics of natural systems, 2nd ed., 648 p. Cambridge University Press, Cambridge.

Anovitz, L.M., and Hemingway, B.S. (1996) Thermodynamics of boron minerals; summary of structural, volumetric and thermochemical data. Reviews in Mineralogy and Geochemistry, 33, 181–261.

Appel, P.W.U. (1984) Tourmaline in the early Archaean Isua supracrustal belt, West Greenland. The Journal of Geology, 92, 599–605.

Bačík, P. (2015) Cation ordering at octahedral sites in schorl-dravite series tourmalines. The Canadian Mineralogist, 53, 571–590.

Berman, R.G. (1988) Internally-consistent thermodynamic data for minerals in the system Na2O-K2O-CaO-MgO-FeO-Fe2O3-Al2O3-SiO2-TiO2-H2O-CO2. Journal of petrology, 29, 445–522.

Berryman, Wunder, B., Rhede, D., Schettler, G., Franz, G., and Heinrich, W. (2016) P-T-X controls on Ca and Na distribution between Mg–Al tourmaline and fluid. Contributions to Mineralogy and Petrology, 171, 31.

Berryman, E., Wunder, B., and Rhede, D. (2014) Synthesis of K-dominant tourmaline. American Mineralogist, 99, 539–542.

Berryman, E.J., Wunder, B., Wirth, R., Rhede, D., Schettler, G., Franz, G., and Heinrich, W. (2015) An experimental study on K and Na incorporation in dravitic tourmaline and insight into the origin of diamondiferous tourmaline from the Kokchetav Massif, Kazakhstan. Contributions to Mineralogy and Petrology, 169, 28.

Bosi, F. (2018) Tourmaline crystal chemistry. American Mineralogist, 103, 298–306.

Bosi, F., and Lucchesi, S. (2007) Crystal chemical relationships in the tourmaline group: Structural constraints on chemical variability. American Mineralogist, 92, 1054–1063.

Brown, I.D. (2016) The Chemical Bond in Inorganic Chemistry: The Bond Valence Model, Second Edition., 336 p. Oxford University Press, Oxford, New York.

Byerly, G.R., and Palmer, M.R. (1991) Tourmaline mineralization in the Barberton greenstone belt, South Africa: early Archean metasomatism by evaporite-derived boron. Contributions to Mineralogy and Petrology, 107, 387–402.

Chatterjee, N.D., Krüger, R., Haller, G., and Olbricht, W. (1998) The Bayesian approach to an internally consistent thermodynamic database: theory, database, and generation of phase diagrams. Contributions to Mineralogy and Petrology, 133, 149–168.

Celata, B., Stagno, V., Capizzi, L.S., Bosi, F., Ballirano, P., D'Arco, A., Stopponi, V., Lupi, S., Scarlato, P., Skogby, H. and Andreozzi, G.B., 2023. Schorl breakdown at upper mantle conditions: Insights from an experimental study at 3.5 GPa. Lithos, 438, p.106999.

Connolly, J. a. D. (1990) Multivariable phase diagrams; an algorithm based on generalized thermodynamics. American Journal of Science, 290, 666–718.

Connolly, J.A. (2005) Computation of phase equilibria by linear programming: a tool for geodynamic modelling and its application to subduction zone decarbonation. Earth and Planetary Science Letters, 236, 524–541.

Connolly, J.A.D. (2016) Thermodynamics applied to earth materials, 68 p. Lecture Notes, ETH Zurich.

Desbois, G., and Ingrin, J. (2007) Anisotropy of hydrogen diffusion in tourmaline. Geochimica et Cosmochimica Acta, 71, 5233–5243.

Dutrow, B.L., and Henry, D.J. (2016) Fibrous tourmaline: a sensitive probe of fluid compositions and petrologic environments. The Canadian Mineralogist, 54, 311–335.

Dutrow, B.L., Foster, C.T., and Henry, D.J. (1999) Tourmaline-rich pseudomorphs in sillimanite zone metapelites: Demarcation of an infiltration front. American Mineralogist, 84, 794–805.

Ertl, A., Tillmanns, E., Ntaflos, T., Francis, C., Giester, G., Körner, W., Hughes, J.M., Lengauer, C., and Prem, M. (2008) Tetrahedrally coordinated boron in Al-rich tourmaline and its relationship to the pressure–temperature conditions of formation. European Journal of Mineralogy, 20, 881–888.

Ertl, A., Marschall, H.R., Giester, G., Henry, D.J., Schertl, H.-P., Ntaflos, T., Luvizotto, G.L., Nasdala, L., and Tillmanns, E. (2010) Metamorphic ultrahigh-pressure tourmaline: Structure, chemistry, and correlations to PT conditions. American Mineralogist, 95, 1–10.

Fuchs, Y., Lagache, M., and Lixares, J. (1998) Fe-tourmaline synthesis under different T and fO_2 conditions. American Mineralogist, 83, 525–534.

Garofalo, P., Audétat, A., Gunther, D., Heinrich, C.A., and Ridley, J. (2000) Estimation and testing of standard molar thermodynamic properties of tourmaline end-members using data of natural samples. American Mineralogist, 85, 78–88.

Gottschalk, M. (1996) Internally consistent thermodynamic data for rock-forming minerals in the system SiO2-TiO2-Al2O3-Fe2O3-CaO-MgO-FeO-K2O-Na2O-H2O-CO2. European Journal of Mineralogy, 175–223.

Grew, E. S., & Anovitz, L. M. (1996). Borosilicates (exclusive of tourmaline) and boron in rock-forming minerals in metamorphic environments. Reviews in Mineralogy, 33, 387-502.

Hawthorne, F.C., and Dirlam, D.M. (2011) Tourmaline the indicator mineral: From atomic arrangement to Viking navigation. Elements, 7, 307–312.

Helgeson, H.C., Kirkham, D.H., and Flowers, G.C. (1981) Theoretical prediction of the thermodynamic behavior of aqueous electrolytes by high pressures and temperatures; IV, Calculation of activity coefficients, osmotic coefficients, and apparent molal and standard and relative partial molal properties to 600 degrees C and 5kb. American Journal of Science, 281, 1249–1516.

Henry, D.J., and Dutrow, B.L. (1996) Metamorphic tourmaline and its petrologic applications. Reviews in Mineralogy and Geochemistry, 33, 503–557.

——— (2011) The incorporation of fluorine in tourmaline: internal crystallographic controls or external environmental influences? The Canadian Mineralogist, 49, 41–56.

Henry, D.J., and Dutrow, B.L. Tourmaline at diagenetic to low-grade metamorphic conditions: Its petrologic applicability. , 154 Lithos 16–32 (Elsevier 2012). Elsevier.

Henry, D.J., and Guidotti, C.V. (1985) Tourmaline as a petrogenetic indicator mineral- An example from the staurolite-grade metapelites of NW Maine. American mineralogist, 70, 1–15.

Henry, D.J., Sun, H., Slack, J.F., and Dutrow, B.L. (2008) Tourmaline in meta-evaporites and highly magnesian rocks: perspectives from Namibian tourmalinites. European Journal of Mineralogy, 20, 889–904.

Henry, D.J., Novák, M., Hawthorne, F.C., Ertl, A., Dutrow, B.L., Uher, P., and Pezzotta, F. (2011) Nomenclature of the tourmaline-supergroup minerals. American Mineralogist, 96, 895–913.

Holland, T.J.B., and Powell, R. (1985) An internally consistent thermodynamic dataset with uncertainties and correlations: 2. Data and results. Journal of metamorphic Geology, 3, 343–370.

Holland, T.J.B., and Powell, R. (1990) An enlarged and updated internally consistent thermodynamic dataset with uncertainties and correlations: the system K2O–Na2O–CaO–MgO–MnO–FeO–Fe2O3–Al2O3–TiO2–SiO2–C–H2–O2. Journal of metamorphic Geology, 8, 89–124.

Holland, T.J.B., and Powell, R. (1998) An internally consistent thermodynamic data set for phases of petrological interest. Journal of metamorphic Geology, 16, 309–343.

Holland, T.J.B., and Powell, R. (2011) An improved and extended internally consistent thermodynamic dataset for phases of petrological interest, involving a new equation of state for solids. Journal of Metamorphic Geology, 29, 333–383.

Krosse, S. (1995) Hochdrucksynthese, stabilität und eigenschaften der borsilikate dravit und kornerupin sowie darstellung und stabilitätsverhalten eines neuen Mg-Al-borates. PhD Thesis.

Kuyunko, N.S., Semenov, Ë.V., Gurevich, V.M., Kuz'min, V.I., Topor, N.D., and Gorbunov, V.E. (1984) Experimental determination of thermodynamic properties of tourmaline dravite. Geokhimiya, 10, 1458–1465.

Liu, X., Vinograd, V.L., Nichenko, S., Kulik, D.A., Lu, X., and Winkler, B. (2019) Emulation of short-range ordering within the Compound Energy Formalism: Application to the calcite-magnesite solid solution. Calphad, 64, 115–125.

London, D. (2011) Experimental synthesis and stability of tourmaline: a historical overview. The Canadian Mineralogist, 49, 117–136.

Lussier, A., Ball, N.A., Hawthorne, F.C., Henry, D.J., Shimizu, R., Ogasawara, Y., and Ota, T. (2016) Maruyamaite, K (MgAl2)(Al5Mg) Si6O18 (BO3) 3 (OH) 3O, a potassium-dominant tourmaline from the ultrahigh-pressure Kokchetav massif, northern Kazakhstan: Description and crystal structure. American Mineralogist, 101, 355–361.

Morgan, G.B., and London, D. (1989) Experimental reactions of amphibolite with boron-bearing aqueous fluids at 200 MPa: implications for tourmaline stability and partial melting in mafic rocks. Contributions to Mineralogy and Petrology, 102, 281–297.

Ogorodova, L.P., Melchakova, L.V., Kiseleva, I.A., and Peretyazhko, I.S. (2004) Thermodynamics of natural tourmaline–elbaite. Thermochimica acta, 419, 211–214.

——— (2012) Thermodynamics of natural tourmalines—Dravite and schorl. Thermochimica acta, 539, 1–6.

Ota, T., Kobayashi, K., Katsura, T., and Nakamura, E. (2008) Tourmaline breakdown in a pelitic system: implications for boron cycling through subduction zones. Contributions to Mineralogy and Petrology, 155, 19–32.

Palmer, M.R., London, D., Morgan, G.B., and Babb, H.A. (1992) Experimental determination of fractionation of11B/10B between tourmaline and aqueous vapor: A temperature- and pressure-dependent isotopic system. Chemical Geology: Isotope Geoscience section, 101, 123–129.

Powell, R., and Holland, T.J.B. (1988) An internally consistent dataset with uncertainties and correlations: 3. Applications to geobarometry, worked examples and a computer program. Journal of metamorphic Geology, 6, 173–204.

Robbins, C.R., and Yoder Jr, H.S. (1962) Stability relations of dravite, a tourmaline. Carnegie Inst. Wash. Yearbook, 61, 106–108.

Schreyer, W., Wodara, U., Marler, B., Van Aken, P.A., Seifert, F., and Robert, J.-L. (2000) Synthetic tourmaline (olenite) with excess boron replacing silicon in the tetrahedral site: I. Synthesis conditions, chemical and spectroscopic evidence. European Journal of Mineralogy, 12, 529–541.

Slack, J.F. (1996) Tourmaline associations with hydrothermal ore deposits. Reviews in Mineralogy and Geochemistry, 33, 559–643.

Slack, J.F., and Trumbull, R.B. (2011) Tourmaline as a recorder of ore-forming processes. Elements, 7, 321–326.

van Hinsberg, V.J. (2011) Preliminary experimental data on trace-element partitioning between tourmaline and silicate melt. The Canadian Mineralogist, 49, 153–163.

van Hinsberg, V.J., and Marschall, H.R. (2007a) Boron isotope and light element sector zoning in tourmaline: Implications for the formation of B-isotopic signatures. Chemical Geology, 238, 141–148.

van Hinsberg, V.J. van, and Schumacher, J.C. (2007b) Intersector element partitioning in tourmaline: a potentially powerful single crystal thermometer. Contributions to Mineralogy and Petrology, 153, 289–301.

van Hinsberg, V.J., and Schumacher, J.C. (2007c) Using estimated thermodynamic properties to model accessory phases: the case of tourmaline. Journal of metamorphic Geology, 25, 769–779.

van Hinsberg, V.J., and Schumacher, J.C. (2009) The geothermobarometric potential of tourmaline, based on experimental and natural data. American Mineralogist, 94, 761–770.

van Hinsberg, V.J., Vriend, S.P., and Schumacher, J.C. (2005a) A new method to calculate end-member thermodynamic properties of minerals from their constituent polyhedra I: enthalpy, entropy and molar volume. Journal of Metamorphic Geology, 23, 165–179.

——— (2005b) A new method to calculate end-member thermodynamic properties of minerals from their constituent polyhedra II: heat capacity, compressibility and thermal expansion. Journal of Metamorphic Geology, 23, 681–693.

van Hinsberg, V.J., Schumacher, J.C., Kearns, S., Mason, P.R., and Franz, G. (2006) Hourglass sector zoning in metamorphic tourmaline and resultant major and trace-element fractionation. American Mineralogist, 91, 717–728.

van Hinsberg, V.J., Henry, D.J., and Marschall, H.R. (2011a) Tourmaline: an ideal indicator of its host environment. The Canadian Mineralogist, 49, 1–16.

van Hinsberg, V.J., Henry, D.J., and Dutrow, B.L. (2011b) Tourmaline as a petrologic forensic mineral: A unique recorder of its geologic past. Elements, 7, 327–332.

van Hinsberg, V.J., Franz, G., and Wood, B.J. (2017) Determining subduction-zone fluid composition using a tourmaline mineral probe. Geochemical Perspectives Letters, 3, 160–168.

von Goerne, G., Franz, G., and Robert, J.L. (1999) Upper thermal stability of tourmaline + quartz in the system MgO-Al2O3-SiO2-B2O3-H2O and Na2O-MgO-Al2O3-SiO2-B2O3-H2O-HCl in hydrothermal solutions and siliceous melts. The Canadian Mineralogist, 37, 1025–1039.

von Goerne, G., Franz, G., and van Hinsberg, V.J. (2011) Experimental determination of Na–Ca distribution between tourmaline and fluid in the system CaO–Na2O–MgO–Al2O3–SiO2–B2O3–H2O. The Canadian Mineralogist, 49, 137–152.

Warding, G., & Schreyer, W. (1978). Synthesis and crystal chemistry of kornerupine in the system MgO-Al2O3-SiO2-B2O3-H2O. Contributions to Mineralogy and Petrology. 67(3), 247-259.

Williamson, B.J., Spratt, J., Adams, J.T., Tindle, A.G., and Stanley, C.J. (2000) Geochemical Constraints from Zoned Hydrothermal Tourmalines on Fluid Evolution and Sn Mineralization: an Example from Fault Breccias at Roche, SW England. Journal of Petrology, 41, 1439–1453.

Wolf, M. B., & London, D. (1997). Boron in granitic magmas: stability of tourmaline in equilibrium with biotite and cordierite. Contributions to Mineralogy and Petrology, 130, 12-30.

Thermodynamic model for Tourmaline

"Crystallography is the experimental science of determining the arrangement of atoms in solids. In a way, crystallography is the mother of all materials science."

— *William Lawrence Bragg*

The Nobel laureate also called Tourmaline a '*Garbage can mineral*'. (Bragg, 1937)

one person's trash really is another one's treasure.

Bragg (1937) Atom Structure of Minerals. Cornell University Press, NY, 292 p.

Chapter 1. Creating a consistently characterised tourmaline sample set with uncertainties for thermodynamic model calibration

Stan Roozen, Vincent van Hinsberg, Gunther Redhammer, Klaus-Dieter Grevel, and Dominic Ryan

ABSTRACT

Tourmaline, a complex mineral phase, serves as a key geochemical archive for reconstructing P-T-X histories across tectonic settings. A thermodynamic model is essential for interpreting its chemical record, enabling phase equilibria and elemental exchange predictions. Here, we present an internally consistent, normalization-coherent tourmaline sample set of natural solid solutions and selected synthetic samples for thermodynamic property measurement (molar volume, entropy, heat capacity, enthalpy) within the Na_2O-CaO-B_2O_3-FeO-Fe_2O_3-MgO-Al_2O_3-SiO_2-TiO_2-H_2O-F system. To determine tourmaline's compositional complexity a multi-instrumental approach is needed: wavelength-dispersive electron microprobe for major elements, Karl-Fischer titration for H_2O, laser ablation ICP-MS for trace elements, and Mössbauer spectroscopy for Fe valence. In addition, single-crystal X-ray diffraction provides electron densities, which, combined with composition, bond valence sums, charge balance and site occupancy constraints reveals site-specific speciation. Existing code for crystal formula refinement (Wright et al. 2000) is extended to include minor elements, V and W anion sites, and mixed anion/cation environments, with Monte Carlo error propagation capturing sample heterogeneity and analytical uncertainties to determine the final optimised formula. Sensitivity analysis shows that crystal chemical assumptions dominantly control the obtained site fractions. Including these compositional and speciation uncertainties in subsequent thermodynamic model development prevents model overfitting.

1. INTRODUCTION

Tourmaline, a prevalent borosilicate in crustal settings, is widely used in petrology as a record of phase relationships with mineral assemblages, internal and external buffered fluids and melts across tectonic environments (Henry and Dutrow 1996). Its diverse crystallographic sites allow for diverse elemental incorporation, while its large P-T-X stability and low diffusivity preserve compositional records, often as growth zoning (van Hinsberg et al. 2011). Formed in boron-rich environments, tourmaline is a valuable geochemical archive for reconstructing P-T-X histories, essential in petrogenetic and provenance studies (Henry and Dutrow 1996; van Hinsberg et al. 2011).

A thermodynamic model is necessary to interpret tourmaline's chemical record, consisting of an independent, internally consistent set of thermodynamic end-member properties at standard state and caloric, volumetric, and compositional equations of state. Such a model allows phase equilibria and elemental exchange predictions across pressure, temperature, and chemical potentials, essential for phase equilibrium modelling tools like Perplex (Connolly 2005), Theriak-Domino (Capitani and Petrakakis 2010), MELTS (Asimow and Ghiorso 1998) and Gems-selector (Kulik et al. 2013). Despite increased tourmaline research in the past decade (Henry and Dutrow 2018), thermodynamic models for theoretical support remain limited, and were identified as one of the principal targets for future tourmaline research (van Hinsberg 2011). At present, only a handful of isolated thermodynamic data exist (Kuyunko et al. 1984; Hemingway and Evans Jr 1996; Ogorodova et al. 2004, 2012), which formed the basis of the estimated properties based model of van Hinsberg and Schumacher (2007).

Tourmaline's composition spans a wide range, requiring at least seven endmembers to describe each natural composition. Its generalized formula, $XY_3Z_6(T_6O_{18})(BO_3)_3V_3W$, includes major elements on the following sites (Henry et al. 2011, 2013):

X = Na^{1+}, Ca^{2+}, K^{1+}, □ = vacancy
Y = Fe^{2+}, Mg^{2+}, Mn^{2+}, Al^{3+}, Li^{1+}, Fe^{3+}, V^{3+}, Cr^{3+}, Ti^{4+}
B = B^{3+}
Z = Al^{3+}, Fe^{3+}, Mg^{2+}, V^{3+}, Fe^{2+}, Cr^{3+}
T = Si^{4+}, Al^{3+}, B^{3+}
V = OH^{1-}, O^{2-}
W = OH^{1-}, F^{1-}, O^{2-}

This study focuses on the Na-Ca-Mg-Fe^{2+}-Fe^{3+}-Ti-Al-B-O-H-F system, omitting the elements Li, K, Mn, V, and Cr, which are less common in typical hydrothermal, igneous and metamorphic tourmalines.

In this study, a thermodynamic tourmaline model is developed from directly measuring properties including molar volume (V), heat capacity (Cp(T)), and enthalpy from the oxides (ΔH_f°). S is derived from the low (T) Cp(T) measurement. While direct measurements of absolute

thermodynamic values may have higher uncertainties than phase equilibria fitting, they provide complimentary constraints. A tourmaline sample set that has been consistently characterised for composition and structure is critical for this approach. Without consistent composition, valence, and structural data, discrepancies in normalization, calibration, and analysis can lead to significant errors in correlating composition with thermodynamic properties. Indeed, compositional uncertainty is a major concern for the previously published thermodynamic data for tourmaline (see Hemingway et al. 1996; van Hinsberg and Schumacher 2007). Moreover, careful uncertainty analysis is crucial to identify the nature and sources of uncertainty in thermodynamic measurements and tourmaline compositions, as it determines where flexibility is justified and prevents overfitting in thermodynamic model calibration.

Creating a consistent tourmaline database from literature data is challenging due to inconsistencies in instrumentation, normalization, and evolving crystal chemical assumptions, which means that reported mineral formulae are not consistent. Given that mineral formulae are the critical step in converting the per mass calorimetric measurements to their molar equivalent, this is of crucial importance in thermodynamic studies. Existing guidelines (Henry et al. 2011, 2013) need updating, by first assigning Al^{3+} to the Z site using an empirical equation, then allocating Mg^{2+} (up to 2 apfu), Cr^{3+}, V^{3+}, and Fe^{3+}, with any excess trivalent cations placed in Y (Bosi 2018). This improves consistency between empirical and calculated formulas, ensuring accurate species identification. This study assembles a tourmaline sample set for subsequent thermodynamic study and proposes a detailed approach towards consistency, essential for deriving statistically significant generalisations. Future renormalization may be necessary as tourmaline chemistry knowledge advances, and integrating this database with others will require community collaboration. Currently, no uncertainty propagation is conducted during tourmaline mineral formula optimisation, giving the misleading impression that these formulas are extremely well constrained. By explicitly including uncertainty envelopes, it becomes clear that tourmaline compositions are significantly less well characterised than previously assumed.

To assemble a tourmaline sample set, we primarily used natural crystal with an intermediate solid solution composition, with a few synthetic samples to reduce the multicollinearity inherent in natural samples as dictated by the dominant exchange vectors. Since all tourmaline end members are hypothetical and tourmaline exists only as solid solutions, this approach reflects its

natural stability. We favor this over synthesizing tourmaline endmembers for thermodynamic measurement as their synthesis is challenging and rarely produces end-member compositions (von Goerne et al. 2011), complex crystal Short Range Order (SRO) (Hawthorne 1996, 2002; Bosi 2010, 2011, 2013) and Long Range Order (LRO) (Bosi and Lucchesi 2007; Henry and Dutrow 2011; Vereshchagin et al. 2018) chemical controls, and external factors that hinder formation of pure endmembers or binary solutions.

Tourmaline is one of several minerals exhibiting structural and compositional complexity comparable to that of amphiboles, micas, and high-entropy ceramics. The rigorous normalization procedures and uncertainty analyses presented here can serve as a template for studies on these similarly complex solid solutions, thus offering broader applicability in mineralogy and materials science (McCormack and Navrotsky 2021).

2. DATABASE SAMPLE SELECTION AND SYNTHESIS

2.1 Natural tourmaline sample collection

Approximately 220–250 natural tourmalines were assembled from the McGill University Department of Earth and Planetary Science and Redpath Museum collections, Tourmaline 2017 and 2021 conference excursions, and purchased at several mineral shows. Samples were visually inspected for inclusions and homogeneity using SEM imaging, and analysed by EMPA along well-distributed points across the mounted sections. Measurements were performed along both the *c*- and *a*-axes of the hexagonal cell to assess compositional variation. A subset of about 50 samples from metamorphic, igneous, and hydrothermal settings was selected to establish a network within the Na-Ca-Fe-Mg-Al-Ti-Si-B-H-F system, focusing on pseudobinary and some ternary/quaternary compositions. Inclusion criteria encompassed homogeneity, with no variation over 0.2 apfu for major elements and 0.10 apfu for minors, and no samples with impurities over 0.2 apfu for Li, K, Mn, V, and Cr. Sample details are in Electronic Appendix (e-Appendix) 1A.

2.2 Synthetic tourmalines

Three previously synthesized near-monophase synthetic tourmalines (dravite, uvite, and oxyuvite) were included to fill compositional gaps and reduce elemental correlations, while B-

olenite from Wodara (1996) adds a composition with a high fraction of tetrahedrally coordinated boron (B^{IV}) that allows for assessing this component.

Dravite, Uvite, and Oxyuvite synthesis Dravite ("Dr 14-1") was synthesized using Krosse's (1995) gel method with stoichiometric Na_2O, Al_2O_3, SiO_2, and MgO, along with H_2O and excess B_2O_3. Gold-encapsulated gels were subjected to 2.5 GPa and 800°C in a piston cylinder (Boyd and England 1960) at Ruhr University Bochum, using NaCl as the pressure medium in a steel/graphite resistor oven (Massonne and Schreyer 1986) with a Ni/NiCr thermocouple for temperature control. The process produced ~10 µm tourmaline crystals with minor (<1%) corundum, spinel ($MgAl_2O_4$), and pseudosinhalite as identified by XRD.

Uvite and oxyuvite were synthesized following Henry and Dutrow (1990) with stoichiometric $CaCO_3$, MgO, γ-Al_2O_3, and SiO_2, plus excess boric acid and H_2O. Gold-encapsulated mixtures were annealed at 700°C, then subjected to 2 GPa and 820 °C in a piston cyllinder for two weeks at the Steinmann Institute, University of Bonn. Near-monophase crystals of uvite (~20 µm) formed, with SEM imaging and EDX analyses showing minor <5% enstatite (see P-XRD results)

B-Olenite synthesis Wodara (1996) synthesized mono-phase boron-rich olenite (sample V81) using a gel composed of 0.625 Na_2O, 4.5 Al_2O_3, and 6 SiO_2, with 100% excess B_2O_3. Gel preparation followed Hamilton and Henderson (1968): elemental Al and sodium carbonate were mixed, converted to nitrates with water and diluted nitric acid, evaporated, then dissolved in deionized water and 50% ethanol. TEOS ($Si(C_2H_5O)_4$) was added for silica, with ethanol aiding miscibility. Ammonium hydroxide induced gel formation, decomposed in a platinum crucible under a Bunsen burner, then heated to 700°C and ground. The amorphous nature of the gel was confirmed by P-XRD. This material was loaded in gold capsules, sealed, and subjected to 25 kbar and 750°C for 96 hours in an end-loaded piston cylinder (Renner et al. 1997) at Ruhr University Bochum (Wodara 1996; Schreyer et al. 2000).

This dataset spans the targeted tourmaline compositional space with sufficient samples to independently constrain thermodynamically relevant properties in the following chapters.

3. COMPOSITIONAL CHARACTERISATION

3.1 Wavelength Dispersive Electron Microprobe (WD-EMPA)

Data Acquisition Natural tourmaline samples (±0.5 cm diameter, cut perpendicular and parallel to the c-axis) and synthetic powders were epoxy-mounted, polished, and carbon-coated. Major elements were measured on a Cameca SX100 FE microprobe using wavelength dispersive (WD) spectrometry at McGill University, predominantly with a 3 μm defocused beam with the remainder at 20 μm, a 20 nA current, and 20 kV voltage. WD monochromator crystals and Kα peak counting times were F (140 s), Si (20 s), Mg (30 s) on LTAP; Na (30 s), Al (20 s) on TAP; K (50 s), Ca (40 s), Ti (40 s) on LPET; and Fe (30 s), Mn (30 s), Cr (60 s) on LLIF. Background times were set at half the peak times and linearly interpolated. Despite long counting times, beam damage was minimal, and no time-dependent intensity correction was needed as determined by repeated analyses on a single point for 10 minutes. Primary standards were Fluorite for F, Diopside for Si, Mg, and Ca, Albite for Na, Sanidine for Al and K, Rutile for Ti, Magnetite for Fe, Spessartine for Mn, and Chromite for Cr. Homogeneity and variance were assessed by measuring 20 points per sample. In-house secondary tourmaline standards TM40, TM42, and TM49 were measured five times every 20 hours for drift and accuracy monitoring.

Data Normalisation Averaged k-ratios deviating from 1 and density differences between primary standards and tourmaline necessitated matrix corrections. Second-generation X-Phi ZAF corrections (Merlet 1992, 1994) were used to linearize calibration curves and link k-ratios to concentration ratios accurately. Fixed B_2O_3 (10%) and H_2O (2.5%) values were included as rough estimates for the matrix correction; these oxide components will be measured and/or refined later for greater accuracy. Tourmaline is sensitive to matrix correction methods due to differences in mass absorption coefficients for its light elements. Average detection limits for major elements were determined using the Goldstein method (Goldstein et al. 2003). Based on secondary standards, we applied post-processing corrections for both instrumental drift and bias. Drift in SiO_2 (the only element with consistent drift) was corrected using a linear model. Bias corrections for all elements, based on secondary standards, included concentration-dependent adjustments when the slope was significant, and fixed corrections when only the intercept was significant or for extrapolations beyond 20% (α=0.05). Consistent results between 5 μm and 20

μm beams confirmed the effectiveness of these corrections, allowing for dataset merging. The small grain size (10–20 μm) of synthetic tourmalines complicated achieving high totals due to matrix correction issues like mixed tourmaline-epoxy interaction volumes, non-flatness, and non-homogeneity. Only measurements with totals exceeding 90% for olenite (n=19) and 98% for oxyuvite (n=27), uvite (n=7), and dravite (n=9) were used. These totals included fixed values of 2.5 wt% H_2O and 10 wt% B_2O_3, with olenite's low total suggesting higher-than-average boron content.

Results and Uncertainties E-Appendices 1B1(natural samples)–1B2 (synthetics) provide mean and SD for parallel and perpendicular sections, merged values, and sample uncertainty. Matrix corrections (e-Appendix 1B3), standards (e-Appendix 1B4), and instrument settings (Appendix 1A2) are further discussed in Appendix 1B and accuracy in Appendix 1B5 and limits of detection (LOD) in e-Appendix 1B6. Merged values were used to calculate mineral formulas, with accuracy estimated from the average difference in measured secondary standards after bias corrections and their accepted values. This EMPA uncertainty does not take uncertainty in the accepted values of the primary standards into account.

Millimeter-scale sample heterogeneity is equivalent to total uncertainty, justifying standard deviation on the mean of the 20 measured points as the total compositional uncertainty from EPMA.

3.2 Laser-Ablation Inductively Coupled Plasma Mass Spectroscopy (LA-ICP-MS)

Data Acquisition Epoxy-mounted tourmalines were repolished and analysed with a NewWave 213 nm Nd-YAG laser (140 μm spot size (preablation 160 μm), 3.78 J/cm² at 10 Hz) coupled to a Thermo Finnigan iCapQc Quadrupole ICP-MS. We used a 70 s washout, 20 s warmup and gas blank, and 40 s measurement. Helium (0.8 L/min) and Argon (1 L/min) carrier gases transported the aerosols to the ICP-MS. Ions passed through a Ni-sample cone. ICP-MS optimisation gave 0.34% $^{238}U/^{238}U^{16}O$ oxide formation and 0.25% $^{137}Ba^{1+}/^{137}Ba^{2+}$ double-charged ion formation (Kent and Ungerer 2005), as determined on NIST SRM 610, requiring no interference corrections. The $^{238}U/^{232}Th$ ratio (~1) indicated minimal fractionation and complete evaporation (Günther and Hattendorf 2005).

Isotopes measured included: ^{7}Li, ^{23}Na, ^{24}Mg, ^{27}Al, ^{29}Si, ^{39}K, ^{43}Ca, ^{45}Sc, ^{47}Ti, ^{51}V, ^{53}Cr, ^{55}Mn, ^{57}Fe, ^{59}Co, ^{60}Ni, ^{63}Cu, ^{66}Zn, ^{71}Ga, ^{88}Sr, ^{93}Nb, ^{118}Sn, ^{137}Ba, ^{139}La, ^{140}Ce, ^{143}Nd, ^{208}Pb, ^{209}Bi. analysed with synthetic (NIST SRM 610) and natural glass standards (StH6-80, BIR-1G, BCR-2G). Each tourmaline's perpendicular and parallel sections were measured six times. Further details are in Appendix 3.

Data Normalization Data processing in Iolite 4 (Paton et al. 2011; Paul et al. 2023) involved setting integration windows to avoid surface contamination, large particle generation, inclusions, and washout tails. Windows with stable element ratios were selected and adjusted for each sample, and background (gas blank) was subtracted using a step-forward method. External calibration and drift correction were performed in Iolite using the multi-standard 3D trace element function, with NIST SRM 610 and natural standards (StH6-80, BIR-1G, BCR-2G) calibrated to GEOREM preferred values (as of 09-07-2018) (Jochum et al. 2005). Weighted least squares regression with a zero intercept (except for ^{118}Sn due to He-gas contamination) was applied. Median yield normalization factors corrected ablation yield differences for each RM relative to NIST SRM 610 based on shared elements. RMs measured at the session's start and end provided step-linear interpolation to correct for temporal drift, converting counts to concentrations for all samples.

Matrix differences in ablation yield, influenced by laser coupling, aerosol transport, particle size, and plasma volatility (Kuhn and Günther 2004) varied among RM glasses and tourmalines. ^{27}Al served as an internal standard (Longerich et al. 1996) due to its stable concentration and correlation with colour in tourmaline. In Excel, secondary internal standardization compared ^{27}Al-corrected concentrations of ^{23}Na, ^{24}Mg, ^{43}Ca, and ^{47}Ti to electron microprobe values, generating four correction factors per sample averaged into a single mean factor, applied to all elements. This step was essential, as single internal standard corrections can vary by over 30% and apply effectively only to adjacent periodic groups (Liu et al. 2008). No downhole fractionation correction was needed, as element ratios with internal standards remained flat during ablation.

A bias correction was applied using nine in-house secondary tourmaline standards measured three times initially, with TM40, TM42, and TM44 repeated at session end. A concentration-

dependent correction curve was determined via ordinary linear regression on all samples. Ordinary linear regression estimates the best-fitting straight line through a set of data points by minimizing the sum of squared differences between observed and predicted values. No correction was applied if regression coefficients were insignificant; a fixed correction was used if only the intercept was significant or if extrapolation exceeded 20%.

Results and Uncertainties Statistics (mean, median, SD, and SE, with and without propagated RM errors) and detection limits are in e-Appendix 1C2 for parallel and perpendicular sections, and in e-Appendix 1C3 for merged values with the non-Iolite normalization procedure. Final normalised means and SD are in e-Appendix 1C2, and tourmaline standard compositions in e-Appendix 1C4. Tourmaline standard TM39, excluded from bias correction, showed a median relative difference of 13%, totaling 150 ppm for trace and 3.2 wt% for major elements. Final bias-corrected secondary standards showed cumulative residuals of 235 ppm for trace and 1.9 wt% for majors. Due to greater uncertainty in major elements, EMPA data was used for mineral formula optimisation, while LA-ICP-MS data was used for elements <0.5 wt%.

3.3 Karl Fisher Titration

Structural water (OH) concentrations in tourmaline were measured via vaporization coulometric Karl Fischer titration (Meyer and Boyd 1959) at Ruhr University Bochum. Samples were powdered in acetone, dried at 150°C, and heated to 1000°C in platinum crucibles within an argon-purged induction furnace. Volatiles were carried to the titration cell, where water content was measured using a CA-200 moisture meter (Mitsubishi Chemical). Precision from five repeats of TM23 (10-50 mg), was $1\sigma = 0.08$ wt% H_2O. At 1000°C, tourmaline releases H_2O, with possible inflation from decomposing inclusions or unreacted phases. Volatile species containing F, Li, Na, and Zn may also be released; in F-rich samples, fluorine (likely as F_2 or HF) can oxidize iodide, potentially leading to an underestimation of H_2O. The results and details of the method can be found in Appendix 1D and e-Appendix 1D.

The missing elements Boron measurement was attempted by EMPA by peak scanning, but results were unsatisfactory with large uncertainty for the McGill EPMA instrument due to low atomic number, weak X-ray emission, and matrix sensitivity (Handt and Mosenfelder 2019;

Llovet et al. 2023). LA-ICP-MS, suited for trace boron, struggles with high concentrations due to boron's high ionization potential, matrix effects, retention in tubing, and calibration challenges, limiting precision at the 10% wt. level required to detect B beyond that on B^{III} sites. Boron was instead estimated by charge balance, adding uncertainty from propagated errors. Oxygen was assumed to be stoichiometric.

4. VALENCY CHARACTERISATION

Iron is the only major element in our samples with variable valence and more than 0.2 apfu.

4.1 ^{57}Fe Mossbauer Spectroscopy

Data Acquisition Tourmaline samples with >0.5 wt% FeO^{Total} were analysed for Fe^{3+}/Fe^{2+} ratios using Mössbauer spectroscopy at McGill University, Paris-Lodron University Salzburg, and Palacký University. Samples, adjusted to contain 8 mg Fe, were hand-ground in acetone for 10 minutes and loaded into 2 cm² sample holders. McGill and Palacký used 10 μm Kapton windows with boron nitride for high-iron samples, while Salzburg used a Cu ring with Al-foil and epoxy. Low-iron samples were directly loaded. The final absorber thickness was 3-5 mg/cm² Fe. Room-temperature Mössbauer spectra were collected in transmission mode at all labs with constant-acceleration spectrometers, using a triangular waveform and ±4 mm/s velocity range. Calibration with a 25 μm α-Fe foil set the velocity scale and zero-velocity at the Zeeman-split centroid using the data of Violet and Pipkorn (1971), defining the nuclear ground state reference for all nuclear transitions. Mirror-image spectra from bidirectional velocities were folded to improve signal-to-noise, with no observed issues in velocity linearity.

Laboratory-Specific Instrumentation Configurations McGill and Palacký used a 1.85 GBq ^{57}Co(Rh) source, while Salzburg used a 0.925 GBq source, both emitting 14.4125 keV gamma rays. McGill employed a 2" Kr-CO_2(5%) proportional counter at 1 atm and an 8 cm source-detector distance to balance count rates with minimal cosine smearing, achieving 4×10^6 off-resonance background counts with a 512-channel scalar. Palacký and Salzburg used 1024-channel analysers for higher resolution. Palacký used an MS2006 spectrometer (Pechoušek et al. 2012) with a $YAlO_3$:Ce scintillation detector, reaching 6×10^6 counts. Salzburg used a Halder

Electronics instrument with a Xe-filled counter and a 5 cm source-absorber distance, achieving 2×10^6 counts.

Model Fitting We used the Voigt-based Quadrupole Splitting Distribution (QSD) model (Rancourt and Ping 1991) in the fast relaxation limit, treating Quadrupole Splitting (QS) as a fit parameter sensitive to Electric Field Gradient (EFG) changes in each SRO structure, while assuming the Isomer Shift (IS) remains stable across clusters due to its dependence on mean bond distances (Grodzicki and Lebernegg 2011). Gaussian broadening was applied to QS of Lorentzian peaks, using multiple smaller Gaussians to approximate the true, likely lognormal site distribution suggestive of cluster preference of Fe, for comparison with earlier literature. Doublets were added incrementally, using initial parameters from Andreozzi et al. (2008), until a realistic fit was achieved. We optimised fits using the Levenberg-Marquardt algorithm in Recoil software (Lagarec and Rancourt 1998) to minimize the chi² function, with the Voigt line shape numerically approximated by Puerta and Martin (1981) achieving better results ($\chi^2 < 2$) than single Lorentzian doublets. Fit errors were derived from the covariance matrix (Hessian inversion of the χ^2 function), excluding overlap or misidentification effects, with standard error propagation used to estimate uncertainty in the Fe^{3+}/Fe^{2+} doublet ratio. No matrix corrections were applied. Full results for linewidths (Γ), isomer shift (δ), QS, and resonance areas (A) are found in e-Appendix 1E and are further detailed in Appendix 1E. Figures of the Mossbauer spectra can be found in Appendix 1E.

Uncertainty and Need for Ab Initio Calculations Main uncertainties in Fe^{3+}/Fe^{2+} ratios in tourmaline are described in Appendix 1E, and arise from spectral overlap, InterValence Charge Transfer (IVCT) interpretation, and missing recoil-free fractions, each adding 5-10% error (De Grave and Van Alboom, 1991), and, along with minor thickness effects (Rancourt et al., 1993) total 15-30%. This challenges Mössbauer spectroscopy's reliability for Fe valence/site fraction determination, highlighting the need for a multi-spectroscopy approach with theoretical support from ab initio calculations (Filatov 2009). These methods can predict Mössbauer parameters for iron in SRO structures, partial v-DOS to address recoil-free fraction and activation energies for electron hopping. Simultaneous fitting of spectra using ab initio constraints would reduce overlap issues and uncertainties, making Mössbauer more robust for iron analysis in tourmaline.

Current fit uncertainties are minimal, but are therefore with Fe^{3+}/Fe^{2+} ratios as best estimates based on present methods.

5. CRYSTALLOGRAPHIC CHARACTERISATION

5.1 Single crystal x-ray diffraction (SC-XRD)

Data Acquisition

Salzburg Room temperature (RT**)** SC-XRD of tourmaline was conducted at the University of Salzburg using a Bruker SMART APEX 3-circle CCD diffractometer. Crystal fragments (0.1-0.2 mm) were selected for homogeneity and glued onto 0.1 mm boron-silicate-glass capillaries. Data were collected with graphite-monochromatized Mo Kα radiation (λ = 0.71073 Å) at 50 kV, 20 mA, and a 30 mm crystal-to-detector distance. The APEX I CCD detector was calibrated at -30° and -50° 2θ positions. Data were acquired via ω-scan at four φ positions, achieving >95% completeness. Each run collected 630 frames (Δω = 0.3°) with 3-10 s exposure. Data processing used Bruker APEX3 software with SAINT for peak integration, dynamic box refinement, and Gaussian profile fitting. Spot shape correlation exceeded 0.8, with automated background subtraction.

Ottawa RT SC-XRD data were collected at the University of Ottawa using a Bruker Kappa ApexII diffractometer (50 kV, 30 mA, Mo Kα source, 4-circle goniometer, Triumph graphite monochromator, ApexII CCD detector). The Apex3 suite facilitated data acquisition, initial solution, and unit cell determination from 36 images with 3 omega scans. Scanning angles (2θ, Ω, χ, and φ) were optimised per crystal, using omega and phi scans with 0.5° image widths. Integration used SAINT with dynamic box refinement.

British Columbia Crystal fragments (0.1-0.2 mm) were mounted on glass fibers with quick-set epoxy. Data were collected at RT using either a Bruker X8 diffractometer with an Incoatec MoKα microsource or a Bruker DUO APEX II diffractometer with Triumph graphite monochromated MoKα radiation. Maximum 2θ values ranged from 2.6° to 36.4°, using φ and ω scans in 0.3° or 0.5° oscillations with 3–10 s exposures depending on sample intensity, and a crystal-to-detector distance of 38, 40, 50, or 60 mm was adjusted based on sample quality, diffraction intensity, and resolution requirements, with shorter distances enhancing low-angle

reflection coverage and longer distances improving spot separation and high-resolution data collection.

Data Normalization Measured intensities were converted to $|F(hkl)|^2_{obs}$ using $I(hkl) = K \cdot A \cdot L \cdot P \cdot |F(hkl)|^2$, where K scales intensities, A corrects for absorption, L accounts for Lorentz effects, and P corrects for polarization. APEX 3 applied Lorentz and polarization corrections. High redundancy of symmetry-equivalent reflections improved intensity precision, normalised exposure variations, and enhanced absorption corrections. SADABS' multi-scan method further refined absorption modelling by analyzing intensity variations across crystal orientations using spherical harmonics. Mass attenuation coefficients were chosen based on the bulk composition (Creagh and Hubbell 2006), with absorption coefficients and transmission factors in the cif files. The scale factor K was estimated via the Wilson plot in SCALE (APEX 3). High-angle data were used to reduce Fourier truncation and electron density noise, with reflections down to 0.60 Å included for precise anisotropic displacement and minimised parameter correlations.

Cell refinement Auto-indexing in XPREP (APEX 3) determined unit cell parameters by analyzing the positions and symmetry of the 3D reflection grid (hkl). Reflections with an intensity-to-noise ratio $I/\sigma(I)>2$ were used, where I is the measured reflection intensity and $\sigma(I)$ its standard deviation. Each reciprocal lattice point represents a specific crystallographic direction and d-spacing, defining the crystal structure. Normalised structure factors ($|E|$) were calculated using the Wilson method to remove thermal and $\sin(\vartheta)/\lambda$ effects. Space group R3m was confirmed by absence analysis and $|E|$ distribution, yielding the lowest merit figure. Non-linear least squares refined the orientation matrix, determining unit cell dimensions from up to 1865 reflections. R_{int} were generally below 3%, with no violations or discrepancies among equivalent reflections.

Structural Solution The crystal's diffraction pattern intensities, weighted by structure factor F(hkl) with amplitude $|F(hkl)|$ and phase $\Phi(hkl)$, reveal the unit cell's internal structure. Real-space electron density was reconstructed by summing F(hkl) in a Fourier series, with $|F(hkl)|_{obs}$ and initial $\Phi(hkl)_{calc}$ estimated by SHELXL (Sheldrick 2015)'s "intrinsic phasing" through probabilistic correlations and Monte Carlo simulations, producing a preliminary map revealing atomicity, symmetry, and non-negativity.

Structure Refinement by Fourier Synthesis Using Single Atomic Scattering Factor per Site

This map guided model building with the Independent Atom Model (IAM) in Olex2 for SHELXL 2018/3 (Sheldrick 2015), using neutral atomic scattering factors from Maslen et al. (2006). These scattering factors, Fourier transforms of atomistic electron density, decrease with atomic radius and $\sin(\vartheta)/\lambda$. Anomalous dispersion near absorption edges was corrected using $\Delta f'$ (real part) and $\Delta f''$ (imaginary part), which account for changes in X-ray scattering and absorption effects, respectively (Creagh 2006). $F(hkl)_{calc}$ were generated by summing neutral atomic scattering factors and deriving new $\Phi(hkl)_{calc}$ from atomic positions in the model. Refinement iteratively minimised differences between $|F(hkl)|_{calc}$ and $|F(hkl)|_{obs}$ in a Fourier cycle using weighted least squares until $\rho(xyz)$ converged and all non-hydrogen positions were refined.

Electron density smearing from thermal vibration and positional disorder, differing from atomic electron density in their dependence on $\sin(\vartheta)/\lambda$, was initially refined for non-hydrogen atoms using isotropic displacement parameters, then refined anisotropically. Structural sites in tourmaline were modelled with a single representative element, typically the dominant one, or larger minor elements if they improved the fit. H atoms on 3V sites were located using the $F(hkl)_{obs}$ - $F(hkl)_{calc}$ difference electron density map (Fo−Fc map), which highlights unmodelled electron density and aids in locating weakly scattering atoms such as hydrogen. Their displacement parameters were set as isotropic. We used the measured H position in SHELXL instead of fixing it to better capture true electron density. The H atom at the W site was not directly observed. Except for the Fe-rich O1 site, displacement parameters were below 0.01.

Absolute configuration was determined using Bijvoet differences, and van Hooft/Flack parameters. SHELXL suggested twinning early, but PLATON's TwinRotMat analysis ruled it out. An isotropic extinction parameter was applied in the final refinement as $F(hkl)_{obs} < F(hkl)_{calc}$. Convergence was reached with a shift/error <0.001, yielding favorable R1, Rw2, and GooF values. Refining site occupancies involved adjusting the scattering power of a model element per site to match experimental structure factors, analogous to comparing time- and space-averaged electron density with model atom densities to estimate LRO site occupancies. Full results are detailed in supplementary CIFs (e-Appendix 1F).

Final Fo−Fc maps showed unexplained density due to occupational disorder at X, Y, O1, sometimes Z sites, bonding electrons at B-O and Si-O, and notable O1 displacement in Fe-rich samples. Electron density magnitudes depend on measured Fobs and resolution, while localization relies on unmeasured phases of the structure factors and model assumptions. Site occupancies and displacement parameters, influenced by the extinction parameter, were highly correlated and dependent on Fourier synthesis assumptions. While the extinction parameter enhanced refinement, it may act as a compensatory factor, with discrepancies potentially arising from delocalisation, disorder, absorption, or thermal motion, underscoring the limitations of single-element modelling and the Independent Atom Model (IAM), which misses valence electron deformation.

Method limitations This method approximates electron density by focusing only on the orbital space of the reference spherical atom, excluding contributions from other orbitals influenced by the crystal potential or from other mixed elements on the site, which may have different orbital configurations (reflected in Rw2 or thermal displacement parameters). While robust against changes to the site model element, they remain IAM-based approximations. Defining site volume is subjective due to shared valence electrons and unclear boundaries. The neutral atom scattering factor underestimates electron density, particularly for covalently bonded elements like Si, B, and Al, and does not consider positional disorder (e.g., Na, Ca on the X site), potentially leading to occupancies >1 or missed valence charge on bonds. We considered adding residual electron density (ED) peaks from Fourier maps to T and B site occupancies, but the changes were minimal, so this was not pursued further. Results represent the best achievable approximation with current SHELXL models.

5.2 Powder XRD (pXRD)

pXRD was used for the synthetic tourmalines due to their small crystal size.

Data Acquisition Samples were ground in an agate mortar with alcohol for 5 minutes, visible contaminants removed, and placed in 16 mm metal cups or silicon zero-background holders for XRD. Step-scan pXRD data were collected at RT using a Bruker D8 Advance diffractometer (DaVinci Design, 280 mm goniometer radius, Lynxeye I detector, automatic sample changer) in

θ–θ reflection mode with Cu $K\alpha_{1,2}$ radiation ($K\alpha_1$ λ = 1.540590 Å), 40 kV, and 40 mA. Cu radiation's larger Ewald sphere captures fewer, better-separated reciprocal points. Measurements ranged from 10° to 90° 2θ, with 0.015° steps and 1 s integration time per step. Beam spill and divergence were minimised with 0.3 mm divergence and 2.5 mm receiving slits, and 2.5° Soller slits, and a 2.93° detector window. The sample was rotated, and detector energy filtering eliminated the need for a monochromator or K-beta filter. Alignment checked with corundum showed peak deviations within 0.002°.

Peak search/match PowderDLL was used to convert .raw data to XY format for Fullprof compatibility, and peaks were identified with QualX using the Crystallography Open Database (COD) and Hanawalt index. Tourmaline was confirmed as the main phase in all synthetic samples. Uvite samples had additional peaks at 20.145°, 28.163°, and 31.112° 2θ, while oxyuvite had peaks at 16.597°, 20.160°, 28.163°, and 31.112° 2θ. These persisted after Kα2 stripping. EMPA showed a rare phase with Si = 57%, Mg = 39%, Al = 1.8%, and Ca = 0.73%, consistent with clino-enstatite, confirmed by search/match algorithms. Multiphase Rietveld refinement with uvite and enstatite in Fullprof diverged, typical for phases <5 wt%. As this minor phase minimally obscured tourmaline peak centroids and volume, it was ignored from molar volume calculations but may affect specific heat capacity or entropy in later work (see chapters 3 and 4).

Rietveld refinement Rietveld refinement was conducted in the FullProf suite (Rodríguez-Carvajal 1993) to determine unit cell size and shape based on peak positions and symmetry of the powder diffraction pattern. Lattice centering and atomic distribution were inferred from peak intensities, though these are less constrained due to peak overlap in powder spectra compared to 3D patterns. Instrumental zero, unit cell dimensions, peak shape, and asymmetry affect peak positions, while fractional coordinates, displacement parameters, site occupancy, and preferred orientation impact intensities. Preliminary background points were calculated in Winplotr with a 0.01 tolerance and 11 iterations, then refined in EdPCR. Structural models from Kutzschbach et al. (2016) for olenite and Bosi et al. (2022) for uvite were used. The 2θ range from 0–12° was excluded due to beam stop interference.

Peak broadening was modelled with an empirical Voigt line shape**,** defined by η (Gaussian/Lorentzian ratio) and its 2θ dependence via X, without separating instrumental, size,

or strain effects. The total peak width followed Caglioti formula: $H_k = U\tan^2\ \theta + V\tan\ \theta + W$. Preliminary background points were imported into EdPCR and refined and linearly interpolated. The initial Rietveld refinement was performed using a tourmaline CIF file as a single phase in space group R3m over 10 refinement cycles with isotropic thermal parameters. Profile and line asymmetry were set before optimizing fractional coordinates. Parameters were refined sequentially: scaling factor, zero-shift, Caglioti W, lattice parameters, Gaussian/Lorentzian ratio η, Caglioti U, V, and atomic positions (excluding H), monitored to prevent excessive shifts. Refining individual atom displacements (B) resulted in unphysical values, so an overall (Debye-Waller) B for the unit cell was used. Background heights were then refined, yielding R-factors for the synthetic samples:

Olenite: Pattern: Rp: 10.4, Rwp: 11.0. Rexp: 6.11, χ2: 3.24,

Global user-weighted χ2 (Bragg contrib.): 3.380

Phase: Bragg R-factor: 3.064, RF-factor: 1.454

Uvite: Pattern: Rp: 25.9, Rwp: 28.0. Rexp: 7.41, χ2: 14.3,

Global user-weighted C χ2 (Bragg contrib.): 15.54

Phase: Bragg R-factor: 10.76, RF-factor: 7.260

Oxyuvite: Pattern: Rp: 24.4, Rwp: 26.6. Rexp: 6.39, χ2: 17.3,

Global user-weighted χ2 (Bragg contrib.): 19.09

Phase: Bragg R-factor: 9.016, RF-factor: 5.926

where Rwp is the weighted profile R-value, Rexp indicates observed data quality, and χ2 is defined as χ2=Rwp/Rexp. The RF-value, like the SC-XRD R-factor, compares observed and calculated structure factors, while the Bragg R-factor compares Bragg intensities, $I = m \cdot |F|^2$, where $|F|^2$ is the squared structure factor, representing the electron density contribution from a set of atomic planes, and m accounts for reflection multiplicity. High R-values in the uvite

samples stem from the missing enstatite phase, leaving unexplained peaks. Rietveld refinement is reliable only for phases over 5 wt%, so this issue could not be resolved. Refined parameter summaries are in .sum files (e-Appendix 1G). The final isotropic displacement parameter was reasonable, and standard deviations were scaled using the scor factor in FullProf, which adjusts uncertainties based on the goodness-of-fit (χ^2) to ensure they reflect the true quality of the refinement.

pXRD spectra preserve d-spacings and Bragg angles from the 3D diffraction pattern but average directional data. If Φ(hkl) were known, a Fourier transform of the structure factors would yield a spherically averaged 3D electron density centered on the unit cell origin. Although Rietveld refinement operates solely in reciprocal space, this highlights its strength in determining unit cell parameters but its limitations in providing detailed insights into internal unit cell structure.

6. BOND VALENCE THEORY

Bond Valence (BV) theory (Brown 2016), building on Pauling's rules, models solids by simplifying 3D electron density into a bond network analysed with electrostatics and graph theory. It treats bonds like an electrical circuit, where valence sums follow Kirchhoff's law to align bond strengths with atomic charges. Bond strength relates to bond length via the empirical equation $s_{i,a} = \exp\left(\frac{\left(r_0^{i,a} d_{i,a}\right)}{b^{i,a}}\right)$. This empirical expression relates the bond strength $s_{i,a}$ (also called bond valence**)** between a cation i and an anion a to their bond length $d_{i,a}$. Bond strength reflects the contribution of a single bond to the oxidation state of an atom, with the sum of all bond valences ideally matching the formal valence. The bond valence model parameters $r_0^{i,a}$ and $b^{i,a}$ are empirically derived from a large database of "unstrained" endmember structures. Here, $r_0^{i,a}$ is the reference bond length for a bond valence of 1 valence unit (v.u.), and $b^{i,a}$ controls the rate at which bond strength decreases with distance, influenced by the polarizability and anisotropy of the bonded atoms' electron clouds.

BV theory, formally applicable only to the SRO structure, can also approximate LRO structure with simplifications (Bosi 2014a). While BV analysis using topology overlooks electronic and

structural strain from quantum mechanical and symmetry needs (Bosi 2014b; Brown 2016), it effectively predicts structural stability in complex minerals.

7. TOURMALINE MINERAL FORMULA OPTIMISATION AND UNCERTAINTY ANALYSIS

Limitations of Crystallography Software Assigning site occupancies in high-entropy solid solutions is essential in materials science and petrology. While binary substitutions involving two species on a site can often be successfully refined using crystallographic software like SHELXL, introducing three or more substituents (or allowing vacancies) creates an underdetermined problem. In these cases, the number of unknown site fractions exceeds the number of independent constraints provided by diffraction data, such as total site scattering power or bond lengths. As a result, multiple sets of occupancies can fit the observed data equally well, and the refinement cannot converge to a unique physical solution without imposing additional assumptions or external constraints.

Due to these limitations, in this study, site occupancy optimisation was performed using constrained optimisation methods in Matlab, where physical and chemical constraints were explicitly enforced to produce chemically meaningful and internally consistent site distributions. Given the imperfect nature of both compositional and crystallographic data, as well as the underlying theoretical and crystal-chemical assumptions and constraints, the optimisation treated all inputs as minimisation goals rather than strictly enforced hard values, allowing flexibility to achieve the best overall fit.

Preparation of input files Custom Python scripts were used to generate 2000 MATLAB input files for OccQP's quadratic programming method (Wright et al. 2000) to determine optimal cation site occupancies within the crystal structure and evaluate the impact of measurement uncertainties on tourmaline formula optimisation. The optimal number of trials was determined in Matlab by stabilizing the inverse cumulative relative standard error. Two input files were: bulk compositional data as apfu values and uncertainties without site assignments, and a .cif file containing structural constraints for tourmaline.

Chemical constraints: Conversion to Bulk apfu Tourmaline compositional data (EMPA, LA-ICP-MS, Mössbauer) were converted to bulk apfu using a 31-oxygen normalization (Henry et al. 2011). A 2000-trial Monte Carlo (MC) simulation in Excel sampled Gaussian distributions based on mean and standard deviation, incorporating sample inhomogeneity. Boron was estimated via charge balance, with uncertainty from propagated MC errors (e-Appendix 1H2-3). Apfu values for site occupancy optimisation (eAppendix 1H1) excluded elements <0.001 apfu to simplify optimisation. Total ionic charge was calculated as $60 + F + (1 - F) \times 2$, highlighting the importance of precise fluorine measurements.

Structural constraints Structural constraints were obtained by parsing .cif data with Python scripts and Gemmi (Wojdyr 2022) to provide bond lengths and convert SHELXL crystal occupancies to chemical occupancies by multiplying by their Wyckoff multiplicities. Electrons per site for X, Y, Z, T, B, and O1 sites were calculated by multiplying chemical occupancies by the electron count of a neutral model atom, yielding electrons per formula unit (epfu) (Hawthorne et al. 1995). Crystal occupancy uncertainties were converted to site electron uncertainties. epfu are projections of measured averaged density onto model atom orbitals. SC-XRD-derived O-H bond lengths at V and W sites were replaced with neutron diffraction values (V: 0.972 Å, W: 0.958 Å) from oxydravite, as SC-XRD H's electron density is concentrated in the bonding region rather than at the nucleus. Despite fractional coordinate variation, these fixed lengths are optimal H-bond constraints for optimisation. O1 anion site electrons were used to validate EMPA fluorine apfu via $x=O1-8$.

Tourmaline CIF files often use inconsistent names for equivalent sites (e.g., NaX, Na1, X) and vary site order, complicating data parsing and requiring script adjustments. Standardizing site names in future nomenclature papers would simplify data processing and enhance consistency.

Bond valence sum constraints for mixed anionic and cationic sites Optimisation used metal-oxygen and metal-fluorine BV parameters from Gagné and Hawthorne (2015) and Brese and O'Keeffe (1991) where b is fixed in the latter and both b and R vary in the former, yielding similar bond strengths through correlated changes. Uncertainties were recorded to the second decimal for Brese and O'Keeffe (1991) and to the third for Gagné and Hawthorne (2015), reflecting fitting errors but not accounting for systematic issues like isotopic or anisotropic strain

in reference structures. Additional tests with Brown and Altermatt (1985) showed minimal differences, except for H.

We modified OccQP (Wright et al. 2000) to include mixed anionic sites. The Bond Valence Sum (BVS) for mixed cationic sites surrounded by different anions is calculated as:

$$\text{BVS} = \sum_{k=1}^{n_{\text{conrl}}} \left(\sum_{i=1}^{m} X_{\text{cation},i} \left[\sum_{a=1}^{p} \exp\left(\frac{\left(r_0^{i,a} - d_{i,a} \right)}{b^{i,a}} \right) X_{a,k} \right] \right)$$

where ncoord is the total number of bonds, m the cations, and p the anions and Xcation,i and Xa,k their fractions. The exponential in the brackets are the bond valences, $s_{i,a} = \exp\left(\frac{\left(r_0^{i,a} d_{i,a} \right)}{b^{i,a}} \right)$, depends on ideal ($r_0$) and observed ($d_{i,a}$) bond lengths and the bond softness parameter b.

This approach models BVS for Y cations with mixed O/F occupancy at O1 in tourmaline. No H-bonding to F at O1 was allowed. Due to EMPA uncertainty, F content was fixed, and Monte Carlo (MC) methods recalculated site occupancies at varying F concentrations. Cation sums were used for optimisation, and anion sums validated results. Path equations were excluded as they are sensitive to electronic or anisotropic strain, while BVS is mainly affected by isotropic strain and missing H-bond interactions.

In tourmaline, diverse SRO configurations create varied bond lengths and valences that, when averaged into LRO, do not accurately reflect local charge distributions, leading to systematic BVS errors, particularly in regular polyhedra (Bosi 2014a). These errors arise from the nonlinear bond valence-length relationships specific to each element and are most pronounced at 50/50 mixed occupancy, influenced by BV parameters and valence differences between mixed-site occupants, thus reducing BVS accuracy in solid solutions. Unfortunately, systematic uncertainties for nonregular sites have not been derived. Minimizing the BVS residual from V is an optimisation goal but need not be exact.

Hard-coded crystal chemical constraints The following element site assignments were hard coded: Na, K, Ca, Sr, Ba, La, Ce, Nd, Pb(II), Bi(III) to X; Mg, Fe(II/III), Mn(II), Cr(III), Li, Sc,

V(III), Co(II), Ni(II), Cu(II), Zn, Ga, Nb(V), Sn(IV) to Y/Z; H to V/W; Si to T; Al to Y/Z/T; Ti(IV) to Y. These are based on the minimum mismatch relative to the site properties (cf. (van Hinsberg et al. 2017)) Relaxing Ti's restriction to Y showed potential Z site occupation, suggesting further study (e.g., Ti-Kα XAFS) is needed for clarity. Boron was set to fully occupy the B site, and transition metals were assigned assumed oxidation states.

Weighting scheme for the constraints Initial optimisation with equal weights failed for minor elements due to data heteroscedasticity and differing variable units (e.g., wt%, electrons per site, bond lengths). Unweighted runs had the lowest residuals but drove minor elements to 0 wt%, which is unphysical. Various weighting schemes were tested (1/amount, 1/amount², $1/s^2$, 1/RSD, 1/RSD²), with 1/s (standard deviation) yielding the best results and aligning with Bosi and Lucchesi (2004), despite the theoretical preference for 1/s² (variance) (Bevington and Robinson, 2002), where the sample standard deviation is $s = \sqrt{\frac{1}{n-1}\sum_{i=1}^{n} (x_i - \bar{x})^2}$ and s^2 is the sample variance. This suggested correlations in the 31-O normalised compositional input data. Fixing minor elements led to unrealistic fits. Weights were prepared using 1/std for bulk composition parameters (apfu) (W_{chem},), charge balance (W_i (based on F uncertainty)), site electrons (W_q), and bond valence sums (W_{val}), adopting a 0.05 valence units (vu) uncertainty per Bosi et al. (2017) due to H-bonding exclusion. Weights were normalised, with zero weights for apfu B (charge-balance derived). Infinite weights were set for full Z, T, B occupancies (Ertl 2023), allowing X, Y, V, W vacancies. Weighting choice impacted site distributions more than analytical errors. Thus, rather than prioritizing analytical precision for each instrument, it is crucial to consider the relative importance of each measurement type and carefully evaluate the crystal chemical assumptions applied during data normalization or optimisation.

Tourmaline mineral formula optimisation in OccQP The final disordered tourmaline formula was determined using a constrained Non-Negative Least Squares (NNLS) algorithm following convex quadratic programming principles (Lawson and Hanson 1974), optimizing site occupancies based on 1/standard deviation weighted site electron density, bulk apfu, electroneutrality, and bond valence sums. This modified NNLS algorithm (adapted from Wright et al (2000)) incorporated Monte Carlo (MC) propagation, heteroligand polyhedra, minor elements, hydrogen sites, and output additional structural proxies. The objective function

minimised weighted residuals for electrons per site, chemical composition, and BVS, yielding optimal non-negative occupancies:

$$T^* = \sum_{j=1}^{m} W_Q^{(j)} \left(\sum_{k=1}^{n} x_k^{(j)} Q_k - Q_{\text{obs}}^{(j)} \right)^2 + \sum_{k=1}^{n} W_k^C \left(\sum_{j=1}^{m} x_k^{(j)} C^{(j)} - C_k^{\text{obs}} \right)^2 + \sum_{j=1}^{m} W_V^{(j)} \left[\sum_{k=1}^{n} x_k^{(j)} \left(Z_k - V_k^{(j)} \right) \right]^2 + \sum_{j=1}^{m} W_O^{(j)} \left(1 - \sum_{k=0}^{n} x_k^{(j)} \right)^2 + \sum_{k=1}^{m} \sum_{k=1}^{n} x_k^{(i)} C^{(i)} Z_k (= I_A)$$

Here, $x_k^{(j)}$represents the target occupancy fraction of species k at site j, with residuals calculated as the difference between calculated and observed values. Weights $W_Q^{(j)}, W_k^C, W_V^{(j)}$, and $W_O^{(j)}$controlled deviations in electron per site, composition, BVS, and full site occupancy, respectively. The variable I_A enforced charge balance (Z= formal ionic valence).

Traditional crystallographic refinement fails for complex minerals like tourmaline because diffraction data constrain only total site scattering and average bond lengths, not the detailed distribution of cations and vacancies. When more than two substituents share a site, the system becomes underdetermined, allowing multiple plausible solutions to fit the observed data (Wright et al. 2000). Bond Valence analysis was employed as a physical constraint to assist in resolving this underdetermination. By requiring that the average formal site valence (sum of occupancies × ionic valences) and the calculated bond-valence sums match, it introduces an additional independent constraint tied to local bonding environments. This approach is theoretically justified because ideal bond-valence sums reflect local electrostatic stability: in a stable crystal structure, the sum of bond valences at each site should match the formal ionic charge. Bond-valence theory replaces detailed electron density with a graph of discrete bond strengths, where the total charge is distributed across bonds, and the site bond-valence sums approximate the correct first-order charge distribution around each atom (Brown, 2016). Enforcing bond-valence sums thus guides occupancies toward chemically reasonable and energetically favorable configurations, even when diffraction data alone are insufficient to resolve species distributions.

However, bond valence theory also has intrinsic limitations. The empirical bond-valence parameters (R_0 and b) used to relate bond length to bond strength are derived by averaging over many minerals, often under the assumption that similar cations behave similarly across different structures. In reality, bond valence parameters may be mineral-specific, and tourmaline , with its complex, flexible, and multi-site structure, might deviate from average calibrations. Consequently, bond-valence matching provides a useful but imperfect constraint, reinforcing chemical plausibility without guaranteeing unique or fully accurate site assignments.

Additionaly, charge balance and site occupancy constraints offer powerful ways to regularize the solution space. In principle, crystallographic refinement software such as SHELXL allows certain constraints to be imposed, such as restraining site occupancies to sum to full site occupancy (SUMP constraints) or using EADP/SIMU to tie displacement parameters. However, enforcing exact electroneutrality or detailed site-specific charge constraints during refinement is not straightforward in SHELXL. These typically require either external post-processing or custom refinement protocols, and are not automatically handled within standard least-squares cycles. For complex solid solutions like tourmaline, direct incorporation of full charge balance and multi-site occupancy constraints into crystallographic refinement remains difficult, supporting the need for external constrained optimisation approaches as used here.

In this optimisation approach, all constraints , site electron densities, chemical compositions, bond valence sums, and full site occupancy, were treated as flexible minimisation goals rather than strict hard conditions, acknowledging the combined uncertainties from experimental data and theoretical approximations. The goal was to find the most chemically meaningful and internally consistent site distributions while allowing for realistic deviations. Relative occupancy differences between tourmalines are more reliable than absolute values due to error cancellation when internally consistent. The modified program can be found in e-Appendix 1I.

Mean MC and lowest Z score formula The first MC run used mean values, while subsequent runs sampled from Gaussian distributions defined by mean and standard deviations of apfu, F content, ionic totals, bond lengths, electrons per site and BV parameters. Comparing uncertainties in bulk apfu based on MC runs of the 31O normalisation based solely on chemistry

and electroneutrality to those recalculated from the optimised disordered formula reduced uncertainties by half.

The MC run with the lowest total absolute Z-score from 2500 trials was identified by converting optimised values to Z-scores based on original means and standard deviations. Z-scores were calculated for apfu, ionic totals, disordered formula, vacancies, valences, BVS, anion sums, bond valences, BSI, site charges, and bond lengths (e-Appendix 1J). The Excel sheet lists the lowest Z-score formula, MC mean formula, standard deviation, and the Z-score difference between the two formulae.

The final disordered tourmaline formula used the mean of all MC runs as it has an uncertainty estimate, despite slight inconsistencies with the ionic balance equation.

8. POST-OPTIMISATION BOND VALENCE ANALYSIS

Using BV theory, we derived stability indices and strain calculations as first-order approximations to assess structural trends and deviations from regularity. These values serve as qualitative stability indicators rather than precise measures.

Pauling Local Bond lengths The mean Pauling bond length Rj for any hypothetical polyhedron can be calculated using BV parameters and formal valences Z:

$$R_j = \frac{1}{n_{\text{coord}}} \sum_{k=1}^{n_{\text{corrd}}} \left(\left[\left(rR_{i,a} - b_{i,a} \ln \left(\frac{Z}{n_{\text{coord}}} \right) \right) \right] \right)$$

This equation is derived from solving the BV equation for Rj using the Pauling bond strength, Z/n_{coord} , as $s_{i,a}$. Rj represents hypothetical regular polyhedral bond lengths. This is an approximation, as BV parameters themselves were calibrated on a broad database of strained crystal structures and represent ‘average’ not ‘ideal’ valence-bond length relationships. Fixed ionic radii (e.g., Shannon (1976)'s) or regular Pauling local bond lengths fail to estimate bond lengths in strained structures with distorted polyhedral due to polymerization, isotropic steric strain, and anisotropic electronic/steric strains (Bosi 2014b), making them unsuitable as optimisation constraints (Wright et al. 2000; Bosi and Lucchesi 2004).

Pauling bond lengths can be calculated post-optimisation. Using occupancies from the disordered tourmaline formula, average site valences were derived to obtain Pauling bond strengths, allowing for bond length estimation as if tourmaline were composed of a set of hypothetical structures of isolated regular polyhedral with different coordination numbers:

$$R_j = \frac{1}{n_{\text{coord}}} \sum_{k=1}^{n_{\text{corrd}}} \left(\sum_{i=1}^{m} X_{\text{cation},i} \left[\sum_{a=1}^{p} \left(rR_{i,a} - b_{i,a} \ln \left(\frac{Z}{n_{\text{coord}}} \right) \right) X_{a,k} \right] \right)$$

This method averages fluorine, oxygen, and cation contributions within the coordination shell

Post-optimisation a-priori bond valences Post-optimisation topological (a-priori) bond valences can estimate local bond lengths using bond topology and average site valences as a validation step to make stability proxies which can identify compositional stability limits. This method improves on Pauling bond lengths by considering topology effects, however isotropic steric strain (affecting BVS) and electronic/steric anisotropic strains (influencing path equations) can still cause deviations.

Network equations We present an algebraic solution (Gagné et al. 2018) to Bacik's graphical method (Bačík 2015, 2018; Bačík and Fridrichová 2021), adapted for solid solutions, applying averaged valences to the bond topology's network equations. Appendix 1K presents the bond valence table, with cation BVS derived from rows and anion BVS from columns. A network equation matrix G was built from these BVS, with the T-site BVS removed as linearly dependent due to the electroneutrality constraint, leaving 14 BVS equations for 19 symmetry unique bond valences. 5 path equations representing closed paths through the bond valence table were added to solve this. This matrix is valid when X, Y, Z, T, B are at least partially occupied and not completely vacant, as this would change the topology. V and W site vacancies do not affect this, as their bonding is terminal when H-bonding is excluded. The matrix equation was then inverted to obtain the topological bond valences for the full 3D topology.

$$G = \begin{pmatrix}
\text{a} & \text{b} & \text{c} & \text{d} & \text{e} & \text{f} & \text{g} & \text{h} & \text{i} & \text{j} & \text{k} & \text{l} & \text{m} & \text{n} & \text{o} & \text{p} & \text{q} & \text{r} & \text{s} & \text{Comments} \\
3 & 1 & 0 & 0 & 0 & 0 & 0 & 0 & 0 & 0 & 0 & 0 & 0 & 0 & 0 & 0 & 0 & 0 & 0 & \text{O1} \\
0 & 0 & 1 & 2 & 1 & 0 & 0 & 0 & 0 & 0 & 0 & 0 & 0 & 0 & 0 & 0 & 0 & 0 & 0 & \text{O2} \\
0 & 0 & 0 & 0 & 0 & 1 & 2 & 1 & 0 & 0 & 0 & 0 & 0 & 0 & 0 & 0 & 0 & 0 & 0 & \text{O3} \\
0 & 0 & 0 & 0 & 0 & 0 & 0 & 0 & 1 & 2 & 0 & 0 & 0 & 0 & 0 & 0 & 0 & 0 & 0 & \text{O4} \\
0 & 0 & 0 & 0 & 0 & 0 & 0 & 0 & 0 & 0 & 1 & 2 & 0 & 0 & 0 & 0 & 0 & 0 & 0 & \text{O5} \\
0 & 0 & 0 & 0 & 0 & 0 & 0 & 0 & 0 & 0 & 0 & 0 & 1 & 1 & 1 & 0 & 0 & 0 & 0 & \text{O6} \\
0 & 0 & 0 & 0 & 0 & 0 & 0 & 0 & 0 & 0 & 0 & 0 & 0 & 0 & 0 & 2 & 1 & 0 & 0 & \text{O7} \\
0 & 0 & 0 & 0 & 0 & 0 & 0 & 0 & 0 & 0 & 0 & 0 & 0 & 0 & 0 & 0 & 0 & 2 & 1 & \text{O8} \\
0 & 0 & 3 & 0 & 0 & 0 & 0 & 0 & 3 & 0 & 3 & 0 & 0 & 0 & 0 & 0 & 0 & 0 & 0 & \text{X} \\
1 & 0 & 0 & 2 & 0 & 1 & 0 & 0 & 0 & 0 & 0 & 0 & 2 & 0 & 0 & 0 & 0 & 0 & 0 & \text{Y} \\
0 & 0 & 0 & 0 & 0 & 0 & 1 & 0 & 0 & 0 & 0 & 0 & 0 & 1 & 0 & 2 & 0 & 2 & 0 & \text{Z} \\
0 & 0 & 0 & 0 & 1 & 0 & 0 & 0 & 0 & 0 & 0 & 0 & 0 & 0 & 0 & 0 & 0 & 0 & 2 & \text{B} \\
\sout{0} & \sout{0} & \sout{0} & \sout{0} & \sout{0} & \sout{0} & \sout{0} & \sout{0} & \sout{0} & \sout{1} & \sout{0} & \sout{1} & \sout{0} & \sout{0} & \sout{1} & \sout{0} & \sout{1} & \sout{0} & \sout{0} & \sout{T\text{(linear dependent)}} \\
0 & 0 & 0 & 0 & 0 & 0 & 0 & 1 & 0 & 0 & 0 & 0 & 0 & 0 & 0 & 0 & 0 & 0 & 0 & \text{V} \\
0 & 1 & 0 & 0 & 0 & 0 & 0 & 0 & 0 & 0 & 0 & 0 & 0 & 0 & 0 & 0 & 0 & 0 & 0 & \text{W} \\
0 & 0 & 0 & 0 & 0 & 0 & 0 & 0 & 1 & -1 & -1 & 1 & 0 & 0 & 0 & 0 & 0 & 0 & 0 & \text{Path 1} \\
0 & 0 & 0 & 0 & 0 & 0 & 0 & 0 & 0 & 0 & 0 & 0 & 0 & 1 & -1 & -1 & 1 & 0 & 0 & \text{Path 2} \\
0 & 0 & 0 & 0 & 0 & 1 & -1 & 0 & 0 & 0 & 0 & 0 & -1 & 1 & 0 & 0 & 0 & 0 & 0 & \text{Path 3} \\
0 & 0 & 0 & 1 & -1 & 0 & 0 & 0 & 0 & 0 & 0 & 0 & -1 & 1 & 0 & 0 & 0 & -1 & 1 & \text{Path 4} \\
0 & 0 & 1 & -1 & 0 & 0 & 0 & 0 & -1 & 1 & 0 & 0 & 1 & 0 & -1 & 0 & 0 & 0 & 0 & \text{Path 5}
\end{pmatrix}$$

To solve for individual bond valences vector I we use: $\mathbf{G} \cdot \mathbf{I} = \mathbf{H}$, where matrix **G** encodes BVS and path equations, and **H** is the average site valence vector with zeros for the paths.

$$\mathbf{H} = \begin{pmatrix}
\text{avO1} \\ 2 \\ 2 \\ 2 \\ 2 \\ 2 \\ 2 \\ 2 \\ \text{avX} \\ \text{avY} \\ \text{avZ} \\ \text{avB} \\ \text{avV} \\ \text{avW} \\ 0 \\ 0 \\ 0 \\ 0 \\ 0
\end{pmatrix}$$

The solution is $\mathbf{I} = \mathbf{G}^{-1} \cdot \mathbf{H}$.

Empirical bond Valences Subsequently, bond valences derived from empirical bond lengths, calculated using $s_{i,a} = \sum_{i=1}^{m} X_{\text{cation},i} \left[\sum_{a=1}^{p} \exp\left(\frac{\left(r_0^{i,a} - d_{i,a}\right)}{b^{i,a}} \right) X_{a,k} \right]$ where rearranged in order to

get unique bond valences for each topologic different bond (e.g. sX-O2, sX-O4). The bond valence table was defined as:

$$\mathbf{BVtable}_1 = [a, b, c, d, e, f, g, h, i, j, k, l, m, n, o, p, q, r, s]$$

Stability Indices Topological bond valence analysis provides a first-order check on the structural and chemical validity of optimised tourmaline formulas by modelling electron density as a charge distribution over the bond network, ensuring valence sums match formal site charges. Low bond valences indicate weak bonding and local strain and derived proxies quantifies deviations from ideal geometry. This method highlights chemically implausible site occupancies, flags overfitting in optimisation routines, and identifies substitutions that approach structural instability.

Pauling bond strengths, topological bond valences, and empirical bond valences were used to derive stability proxies (Gagné and Hawthorne 2020).

Topological bond strain (Topostrain) was calculated as: $\text{Topostrain}_1 = I - \text{Pauling}_1^T$, and the average Topological Bond Strain Index (Δ_{topo}) for the unit cell was computed using cation site multiplicities (**C**atmult $_1 = [3,1,1,3,3,3,6,3,1,6,1,6,3,6,6,6,6,3]$, columns BV table) and bond multiplicities to the cation as weights ($w_1 =$ $[1,1,3,2,1,1,1,1,3,1,3,1,2,1,1,2,1,2,2]$, arrows down in BV table).

$$\Delta_{\text{topo}} = \sqrt{\frac{\sum\left(\text{Catmult}_i \cdot w_i \cdot \left(I_i - \text{Pauling}_i\right)^2\right)}{\sum(\text{Catmult}_i \cdot w_i)}}$$

This represents the difference between the topological structure and the hypothetical structure made out of regular polyhedra.

Electrosteric bond strain was calculated as: Electrostericstrain = I - BVtable^T, measuring steric and electronic strains. The average Bond Strain Index (BSI) for the unit cell was computed using the same cation site multiplicities and bond multiplicity weights:

$$\Delta_{\text{electrosteric}} = \text{BSI} = \sqrt{\frac{\sum(\text{Catmult}_1^T \cdot w_1^T \cdot (I - \text{BVtable}_1^T)^2)}{\sum(\text{Catmult}_1^T \cdot w_1^T)}}$$

We calculated the polyhedral versions of Δtopo and Δelectrosteric where multiPoly indicates how often the topological distinct bonds occur in the polyhedron:

$$\Delta_{\text{topo\_poly}}(j) = \sqrt{\frac{\sum\left(\text{multiPoly} \cdot \left(\text{I}_{\text{Poly}} - \text{Pauling}_{\text{Poly}}\right)^2\right)}{n_{\text{coord}}}}$$

$$\Delta_{\text{electrosteric\_poly}}(j) = \sqrt{\frac{\sum\left(\text{multiPoly} \cdot \left(I_{\text{Poly}} - \text{BVtable}_{\text{Poly}}\right)^2\right)}{n_{\text{coord}}}}$$

Our equations extend and slightly modify the Gagné & Hawthorne's (2020) formulation, with detailed method comparison in Appendix 1L. Correlations over 0.6 showed bond strain interdependencies, especially within polyhedra (e.g., Y, T) and between X and Y sites. Occupancy-bond strain correlations were generally low, except for O1 by W due to terminal bonding. Polyhedral strain indices could serve as rough correction factors for topology and steric/electronic effects in hard sphere models. The BV table, Stability indices, Bond distortion and GII index (which serves as a unit cell version of the BVS residuals in the optimisation) can be found in Appendix 1L.

9. OUTPUT AND FINAL FOURIER SYNTHESIS

Final output The final data includes average input variables and SD, such as electrons per site (Q_obs), O1 electrons per site (Q_O1), F, ionic total, bond lengths, and apfu. Optimised outputs averaged from MC runs and their SD included bulk apfu, ionic totals, site fractions, vacancies, BVS (sole occupant element), BVS per site, anion valence sums, empirical bond valences, electrosteric bond strains, electrosteric strain unit cell (BSI), site charge, local/mean bond lengths, and residuals for apfu, Q, bond length, valence, and ionic total. Z-scores for apfu, Q, bond length, valence, and ionic total, along with Z-scores using fixed SD (0.003 for bond length,

0.05 for valence), were provided. Post-processing metrics included mean bond length, bond distortion, Global Instability Index (GII), unit cell Δ_{topo} , Δelectrosteric, and polyhedral equivalents of these formulations (e.g., this chapter, Gagné and Hawthorne (2020)). See e-Appendix 1J.

Final Fourier synthesis Optimised occupancies were exported and converted to crystal occupancies and ShelXL SFAC cards using a custom Python script (e-Appendix 1I) and resulted in optimised site occupancies for the CIF files (E-Appendix 1F2). Directly imposing all fixed site occupancies during Fourier synthesis led to divergence during structure refinement, likely due to the model being over-constrained by too many changes introduced simultaneously. Instead, iterative manual addition of site occupancies was required to maintain refinement stability and achieve convergence. Refining fractional coordinates and thermal ellipses improved the final Φ(hkl) of the structure factors and led to slightly lower R values. In the future, incorporating the current methodology for high-entropy solids including bond valence and electroneutrality constraints directly into ShelXL refinements, would help minimize differences between calculated and observed structure factors in the Fourier synthesis.

Combined, this results in the final molecular formula for each of the tourmalines characterised in this study, its molecular weight and its molar volume as converted from the unit cell volume. This molecular formula is essential to convert measured calorimetric data from units per mass to units per mole, and is the basis for endmember deconvolution necessary to extrapolate measured intermediate compositions to endmember thermodynamic properties.

10. COMPARISON TO ALTERNATIVE OPTIMISATION SCHEMES

Bosi and Lucchesi (2004) method Most tourmaline studies currently use the method of Bosi and Lucchesi (2004), which differs somewhat from ours. The following compares the two methods. Bosi and Lucchesi (2004), minimised squared residuals normalised by uncertainties using:

$$\mathrm{F}(X_i) = \frac{1}{\mathrm{n}} \sum_{\mathrm{j}=1}^{\mathrm{n}} \left(\frac{\mathrm{O_j} - \mathrm{C_j}(X_i)}{\sigma_{\mathrm{j}}} \right)^2$$

Where O_j represents an observed structural or chemical parameter, and $C_j(Xi)$ is the calculated equivalent based on trial site occupancies X_i and σj is the SD. The observed quatition Oj include mean bond distance, apfu, site electrons, bond valance sums, and site occupancy and charge balance constrains. This approach, similar to our 1/σj weighting, converts each residual into a Z-score, $Z_j = \frac{O_j - C_j(X_i)}{\sigma_j}$, in contrast, averages over n, and minimises the mean of squared Z-scores, ensuring equal contribution of each measurement. The residual is calculated as (obs - calc).

Our method differs by using:

$$F(X_i) = \sum_{j=1}^{n} w_j \cdot \left(C_j(X_i) - O_j\right)^2, \text{ where } w_j = \frac{1/\sigma_j}{\sum_{k=1}^{n} 1/\sigma_k}$$

Each observation is weighted individually by the inverse of its own standard deviation. The weights are normalised to sum to one, preserving the relative influence of each observation while reducing sensitivity to the absolute scale of uncertainties. This approach gives proportionally more influence to observations with lower uncertainties and mitigates heteroscedasticity, particularly from minor or poorly constrained elements. We extended the optimisation to also obtain uncertainties using the MC method.

Including minor elements and hydrogen sites in optimisation adds parameters, often surpassing available data for constraining them independently. Despite sufficient degrees of freedom, multicollinearity persists, as indicated by a variance-covariance matrix of MC optimised apfu, electrons per site, valences, bond lengths, and ionic totals showing correlations over ±0.6, highlighting the need for additional constraints to reduce it.

Bosi and Lucchesi (2004) introduced 'size' constraints using empirically derived mean local bond lengths at specific sites by optimizing local bond lengths and unit cell dimensions with symmetry-compliant equations, based on a small tourmaline database pre-optimised with Shannon (1976) radii. Details are in the Appendix 1M. They assume fixed bond lengths across tourmaline chemistries, an assumption questioned in the next paragraph. Bosi and Lucchesi (2004) exclude minor elements, due to missing local bond lengths (Bosi 2018), fixing their occupancies and leaving it unclear if their contributions are subtracted from total electrons, bond

length, or ionic total. Minor elements influence partitioning, shown by residual variations when assigning infinite weight or making them optimizable.

While both our method and that of Bosi and Lucchesi (2004) aim to minimize uncertainty-weighted residuals, it is not claimed that our optimisation formulation is inherently better in minimizing residuals. Rather, the key advantage of our approach lies in its flexibility: it allows minor elements and anionic site occupancies to be included as optimizable variables within the same least-squares framework. In contrast, the Bosi and Lucchesi (2004) formulation, which relies on fixed local bond lengths calibrated from major elements, makes it difficult to incorporate species like minor cations and H-bearing anions for which reliable bond parameters are unavailable. Therefore, our formulation expands the range of site occupancies that can be optimised while maintaining internal consistency, particularly important for chemically complex tourmalines where minor elements and anionic substitutions significantly impact the structure.

Bond Length Variance in Tourmaline The a-priori BV matrix method (matrix G) can also be used on hypothetical endmember structures, providing a back-of-the-envelope framework to qualitatively estimate atomic radii and bond lengths ranges for elements. To demonstrates such use we apply method on Na-Ca-Fe-Mg-Al-Ti-Si-B-H-F nomenclature endmembers (Table 1A). This will calculate approximate atomic radii which illustrate general trends, not precise measurements.

Table 1A. Nomenclature tourmalines within the Na-Ca-Fe-Mg-Al-Ti-Si-B-H-F for which we estimate the atomic radii based on the a-priory BV matrix method.

Formula	**Name**
[Ca][Fe]3[Al]6[Si5/6Al1/6]6[OH]3[OH]	Adachiite
[V][Al]3[Al]6[Si5/6Al1/6]6[OH]3[O]	Alumino-oxy-rossmanite
[Na][Fef]3[Al4/6Mg2/6]6[Si]6[OH]3[O]	Bosiite
[Na][Mg]3[Al]6[Si]6[OH]3[OH]	Dravite
[Na][Fe5/6Ti1/6]3[Al]6[Si]6[OH]3[O]	Dutrowite
[Na][Al]3[Al]6[Si4/6B2/6]6[OH]3[O]	Ertlite
[Na][Fef]3[Al4/6Fe2/6]6[Si]6[OH]3[O]	Ferro-bosiite
[Ca][Fe]3[Mg1/6Al5/6]6[Si]6[OH]3[OH]	Feruvite
[Na][Fef]3[Al]6[Si]6[O]3[F]	Fluor-buergerite
[Na][Mg]3[Al]6[Si]6[OH]3[F]	Fluor-dravite
[Na][Fe]3[Al]6[Si]6[OH]3[F]	Fluor-schorl
[Ca][Mg]3[Al5/6Mg1/6]6[Si]6[OH]3[F]	Fluor-uvite
[V][Fe2/3Al1/3]3[Al]6[Si]6[OH]3[OH]	Foitite
[Ca][Fe]3[Al]6[Si]6[OH]3[O]	Lucchesiite
[Na][Mg5/6Ti1/6]3[Al]6[Si]6[OH]3[O]	Magnesio-dutrowite
[V][Mg2/3Al1/3]3[Al]6[Si]6[OH]3[OH]	Magnesio-foitite
[Ca][Mg]3[Al]6[Si]6[OH]3[O]	Magnesio-lucchesite
[Na][Al]3[Al]6[Si]6[O]3[OH]	Olenite
[Na][Al2/3Mg1/3]3[Al5/6Mg1/6]6[Si]6[OH]3[O]	Oxy-dravite
[V][Fe1/3Al2/3]3[Al]6[Si]6[OH]3[O]	Oxy-foitite
[Na][Fe2/3Al1/3]3[Al]6[Si]6[OH]3[O]	Oxy-schorl
[Na][Fef]3[Fef4/6Mg2/6]6[Si]6[OH]3[O]	Povondraite
[Na][Fe]3[Al]6[Si]6[OH]3[OH]	Schorl
[Ca][Mg]3[Al5/6Mg1/6]6[Si]6[OH]3[OH]	Uvite

The previous network equation matrix applies when all sites except V and W are at least partly occupied. X-site vacancies in the nomenclature dataset alter the bond topology by eliminating

X-O2 (c), X-O4 (i), and X-O5 (k) bonds, requiring adjustments to remove these columns, the X mean valence row, and "loop 1" and "loop 5" involving X bonds. The new BV Table can be found in Appendix 1K2.The updated matrix incorporates these changes.

$$G = \begin{pmatrix} a & b & d & e & f & g & h & j & l & m & n & o & p & q & r & s & \\ 3 & 1 & 0 & 0 & 0 & 0 & 0 & 0 & 0 & 0 & 0 & 0 & 0 & 0 & 0 & 0 & \text{O1} \\ 0 & 0 & 2 & 1 & 0 & 0 & 0 & 0 & 0 & 0 & 0 & 0 & 0 & 0 & 0 & 0 & \text{O2} \\ 0 & 0 & 0 & 0 & 1 & 2 & 1 & 0 & 0 & 0 & 0 & 0 & 0 & 0 & 0 & 0 & \text{O3} \\ 0 & 0 & 0 & 0 & 0 & 0 & 0 & 1 & 2 & 0 & 0 & 0 & 0 & 0 & 0 & 0 & \text{O4} \\ 0 & 0 & 0 & 0 & 0 & 0 & 0 & 0 & 0 & 1 & 2 & 0 & 0 & 0 & 0 & 0 & \text{O5} \\ 0 & 0 & 0 & 0 & 0 & 0 & 0 & 0 & 0 & 0 & 0 & 1 & 1 & 1 & 0 & 0 & \text{O6} \\ 0 & 0 & 0 & 0 & 0 & 0 & 0 & 0 & 0 & 0 & 0 & 0 & 0 & 0 & 2 & 1 & \text{O7} \\ 1 & 0 & 2 & 0 & 1 & 0 & 0 & 0 & 0 & 2 & 0 & 0 & 0 & 0 & 0 & 0 & \text{Y} \\ 0 & 0 & 0 & 0 & 0 & 1 & 0 & 0 & 0 & 0 & 1 & 0 & 2 & 0 & 2 & 0 & \text{Z} \\ 0 & 0 & 0 & 1 & 0 & 0 & 0 & 0 & 0 & 0 & 0 & 0 & 0 & 0 & 0 & 2 & \text{B} \\ 0 & 1 & 0 & 0 & 0 & 0 & 0 & 0 & 0 & 0 & 0 & 0 & 0 & 0 & 0 & 0 & \text{V} \\ 0 & 0 & 0 & 0 & 1 & -1 & 0 & 0 & 0 & -1 & 1 & 0 & 0 & 0 & 0 & 0 & \text{W} \\ 0 & 0 & 1 & -1 & 0 & 0 & 0 & -1 & 1 & 0 & 0 & 0 & -1 & 1 & 0 & 0 & \text{loop2} \\ 0 & 0 & 0 & 0 & 0 & 1 & -1 & 0 & 0 & 0 & -1 & 1 & 0 & 0 & 0 & 0 & \text{loop3} \\ & & & & & & & & & & & & & & & & \text{loop4} \end{pmatrix}$$

The modified **H** vector of the average site valences is:

$$H = \begin{pmatrix} \text{avO1} \\ 2 \\ 2 \\ 2 \\ 2 \\ 2 \\ 2 \\ 2 \\ \text{avY} \\ \text{avZ} \\ \text{avB} \\ \text{avV} \\ \text{avW} \\ 0 \\ 0 \\ 0 \end{pmatrix}$$

Bond valences from matrix inversion were reordered to compute bond lengths in the sequence: c,c,c,i,i,i,k,k,k,a,d,d,f,m,m,g,n,p,p,r,r,j,l,o,q,e,s,s,h,b for X, Y, Z, T, B, V, and W sites (see BV table). The average bond length for each site $\overline{R_j}$ is computed as

$$\overline{R_j} = \frac{1}{n_{\text{coord}}} \sum_{k=1}^{n_{\text{corrd}}} \left(\sum_{i=1}^{m} X_{\text{cation},i} \left[\sum_{a=1}^{p} \left(rR_{i,a} - b_{i,a} \ln(s_k) \right) X_{a,k} \right] \right)$$

This method models bond lengths in tourmaline with mixed oxygen, fluorine, and cation occupancy. Our LRO analysis of ordered and disordered nomenclature endmembers focuses on bond lengths where an element solely occupies a site, with neighboring mixed sites exerting averaged inductive effects. In tourmaline, a-priori bond lengths vary per endmember, even under full site occupancy. Appendix 1N summarizes these ranges for X, Y, Z, and T site cations across nomenclature endmember structures. The tables report minimum and maximum bond lengths, total range, and the endmembers contributing to these extremes. Bond length variability is most pronounced for larger, more polarizable cations such as Na, Ca, and Mg, and minimal for rigidly bonded cations like Al and Si. Valence ranges between the different endmembers indicate a bond length variability of up to ±0.05 Å at the X site. The Y-site cations Fe^{2+} and Mg exhibit similar bond length variability, while $^{Y}Fe^{3+}$ shows a ±0.01 Å. In contrast, Al and Si maintain more consistent bond lengths (<0.01 Å).

This qualitative analysis highlights topology and nearest neighbour effects on mean bond lengths of elements in different endmember. This analysis is simplified because BV parameters are derived from a broad set of crystal structures and represent average bond behavior, omitting structure-specific steric and electronic constraints—such as those required for *R3m* symmetry or quantum mechanical effects—which both can be significant (Gagné and Hawthorne 2017). Crystals consist of various short-range ordered (SRO) configurations forming an average unit cell where local symmetry breaks but R3m symmetry is restored at the LRO scale. LRO average charges may not reflect true SRO distribution averages, where valence graphs differ. Locally, atoms form bonds with distinct valences and lengths, and mean valence does not match the average bond length's due to the non-linear bond length-valence relationship, introducing systematic errors (Bosi 2014a). SRO structures show greater bond length variability, with BV analysis of SRO clusters revealing wide bond length ranges and using extremes to assess SRO stability (Hawthorne 1996, 2002; Bosi 2010, 2011, 2013).

Empirical mean local bond lengths (Bosi and Lucchesi 2004) vary with similar magnitude due to experimental error, neighboring effects, partial occupancy, and atomic polarizability (Bosi 2018). BV analysis using LRO topology suggests next-nearest neighbor effects, however the variance likely falls within method error, comparable to errors from mean valence in mixed sites or electronic/steric strain (Bosi 2014a). Observing these patterns empirically and in BV analysis

implies minor electronic/steric effects. Whatever the true origin of the bond length variance, this variance exceeds Bosi et al. (2017)'s 0.003 Å assumed variance, challenging the unimodal Gaussian assumption and indicating bond lengths, both SRO and LRO, may be multimodal. Optimizing tourmaline formulas with flexible size constraints better captures natural variability where fractional site coordinates vary, avoiding fixed size assumptions that ignore next-neighbor effects and lead to statistical averages that may misrepresent true bond distances ranges and guides optimisation toward a false minimum. Using mean local bond lengths to predict order-disorder while the mean bond length itself is influenced by order-disorder creates a circular issue. Until this issue is resolved, we exclude size constraints in our approach, though this unfortunately introduces correlations between some elements in the optimised mineral formula due to lack of constraint for the optimisation.

Accurate bond lengths across tourmaline compositions are essential to evaluate the effects of ordering on structural metrics. This involves distinguishing between two key concepts: (1) mean bond lengths at crystallographic sites (e.g., ⟨Y–O⟩ or ⟨Z–O⟩), which are averaged over the unit cell and reflect the effects of long-range order (LRO), and (2) local bond lengths in individual atomic configurations or clusters, which can vary due to short-range order (SRO), even when the average site occupancy (and thus the mean bond length) remains constant. Testing whether SRO induces systematic deviations from the LRO-defined mean bond lengths requires high-resolution techniques such as XANES, XAFS, diffuse x-ray scattering (PDF), or DFT with Bader analysis (Gibbs et al. 2014, 2022), though peak overlap and accuracy of ab initio bondlength remain challenging. Estimated atomic radii (e.g., Shannon (1976), Bosi (2018), Bačík and Fridrichová (2021)) may suffice for partitioning studies but are inadequate for precise site occupancy optimisation due to local strain, topology, partial occupancy, polarizability, neighboring effects, symmetry, and electron delocalisation.

Therefore, we consider that bond lengths are composition-dependent and vary systematically across the tourmaline compositional space.

11. BOND VALANCE LIMITING COMPOSITION/SPECIATION SPACE.

In the last paragraph, we perform bond-valence analysis on a small subset of tourmalines corresponding to established nomenclature species. However, the flexibility of charge configurations within the tourmaline structure permits the existence of many more hypothetical compositions beyond those currently recognised. To comprehensively explore this expanded chemical space, a complete list of 606 hypothetical, charge-balanced dependent endmembers was generated; the theoretical framework and enumeration procedure for deriving these endmembers is detailed in Chapter 2. We then apply a priori bond-valence analysis to this full set to assess their structural plausibility: any hypothetical endmember exhibiting negative bond valences at any site is classified as unstable. Out of the 660 candidate endmembers, 120 are considered unstable based on this analysis. The relatively small proportion of rejected compositions likely reflects the first-order nature of the bond-valence stability criterion applied. Most of the unstable compositions correspond to unusual tourmalines with elevated Ti, B, Al at the T site (AlT), or ferric iron (Fef) contents. Instability is also predicted for some more regular compositions, notably tourmalines with $[Ca_{0.5}Vac_{0.5}]$ occupancy on the X site, suggesting the existence of a miscibility gap in this region of the compositional space. Furthermore, $[Na][Al]_3[Al]_6[B_{1/2}Si_{1/2}]_6[OH]_3[OH]$, an endmember of the speciation-based model (discussed in the next chapter), is also predicted to be unstable. This allows a first-order delineation of the composition space, highlighting regions that are unlikely to yield stable or naturally occurring tourmalines. The code can be found in Electronic Appendix 1K1 and 1K2.

Table 1B. List of tourmaline endmembers considered unstable based on first-order bond-valence stability analysis. Instabilities predominantly affect compositions with elevated Ti, B, Al at the T site, or ferric iron (Fef) content, as well as those with partial Ca–vacancy occupancy on the X site. The endmember $[Na][Al]_3[Al]_6[B_{1/2}Si_{1/2}]_6[OH]_3[OH]$ from the speciation-based model is also predicted to be unstable.

[Na][Al]3[Al]6[B1/2Si1/2]6[OH]3[OH]	[Na][Ti]3[Fef]6[B]6[OH]3[F]	[Na][Ti]3[Fef]6[B]6[OH]3[OH]
[Na][Ti]3[Fef]6[Al]6[OH]3[F]	[Na][Ti]3[Fef]6[Al]6[OH]3[OH]	[Na][Ti]3[Al]6[B]6[OH]3[F]
[Na][Ti]3[Al]6[B]6[OH]3[OH]	[Na][Ti]3[Al]6[Al]6[OH]3[F]	[Na][Ti]3[Al]6[Al]6[OH]3[OH]
[Na][Ti]3[Fef]6[B5/6Si1/6]6[OH]3[O]	[Na][Ti]3[Fef]6[Al5/6Si1/6]6[OH]3[O]	[Na][Ti]3[Fef]6[B1/2Si1/2]6[O]3[F]
[Na][Ti]3[Fef]6[Al1/2Si1/2]6[O]3[F]	[Na][Ti]3[Fef]6[B1/3Si2/3]6[O]3[O]	[Na][Ti]3[Fef]6[Al1/3Si2/3]6[O]3[O]
[Na][Ti]3[Fef]6[B1/2Si1/2]6[O]3[OH]	[Na][Ti]3[Fef]6[Al1/2Si1/2]6[O]3[OH]	[Na][Fef]3[Fef]6[B1/2Si1/2]6[OH]3[F]
[Na][Fef]3[Fef]6[Al1/2Si1/2]6[OH]3[F]	[Na][Fef]3[Fef]6[B1/2Si1/2]6[OH]3[OH]	[Na][Fef]3[Fef]6[Al1/2Si1/2]6[OH]3[OH]
[Na][Al]3[Fef]6[B1/2Si1/2]6[OH]3[F]	[Na][Al]3[Fef]6[Al1/2Si1/2]6[OH]3[F]	[Na][Al]3[Fef]6[B1/2Si1/2]6[OH]3[OH]
[Na][Al]3[Fef]6[Al1/2Si1/2]6[OH]3[OH]	[Na][Ti]3[Al]6[B1/2Si1/2]6[O]3[F]	[Na][Ti]3[Al]6[Al1/2Si1/2]6[O]3[F]
[Na][Ti]3[Al]6[B1/3Si2/3]6[O]3[O]	[Na][Ti]3[Al]6[Al1/3Si2/3]6[O]3[O]	[Na][Ti]3[Al]6[B1/2Si1/2]6[O]3[OH]
[Na][Ti]3[Al]6[Al1/2Si1/2]6[O]3[OH]	[Na][Ti]3[Al]6[B5/6Si1/6]6[OH]3[O]	[Na][Ti]3[Al]6[Al5/6Si1/6]6[OH]3[O]
[Na][Fef]3[Al]6[B1/2Si1/2]6[OH]3[F]	[Na][Fef]3[Al]6[Al1/2Si1/2]6[OH]3[F]	[Na][Fef]3[Al]6[B1/2Si1/2]6[OH]3[OH]
[Na][Fef]3[Al]6[Al1/2Si1/2]6[OH]3[OH]	[Na][Al]3[Al]6[B1/2Si1/2]6[OH]3[F]	[Na][Al]3[Al]6[Al1/2Si1/2]6[OH]3[F]
[Na][Al]3[Al]6[B1/2Si1/2]6[OH]3[OH]	[Na][Al]3[Al]6[Al1/2Si1/2]6[OH]3[OH]	**[Ca1/2V1/2][Fe]3[Al]6[Si]6[OH]3[OH]**
[Ca1/2V1/2][Fe]3[Al]6[Si]6[OH]3[F]	[Ca1/2V1/2][Fe]3[Fef]6[Si]6[OH]3[OH]	[Ca1/2V1/2][Fe]3[Fef]6[Si]6[OH]3[F]
[Ca][Ti5/6Fe1/6]3[Fef]6[B]6[OH]3[F]	[Ca][Ti5/6Fe1/6]3[Fef]6[B]6[OH]3[OH]	[Ca][Ti5/6Fe1/6]3[Fef]6[Al]6[OH]3[F]
[Ca][Ti5/6Fe1/6]3[Fef]6[Al]6[OH]3[OH]	[Ca][Ti5/6Fe1/6]3[Al]6[B]6[OH]3[F]	[Ca][Ti5/6Fe1/6]3[Al]6[B]6[OH]3[OH]
[Ca][Ti5/6Fe1/6]3[Al]6[Al]6[OH]3[F]	[Ca][Ti5/6Fe1/6]3[Al]6[Al]6[OH]3[OH]	[Ca][Mg1/6Ti5/6]3[Al]6[Al]6[OH]3[OH]
[Ca][Mg1/6Ti5/6]3[Al]6[Al]6[OH]3[F]	[Ca][Mg1/6Ti5/6]3[Al]6[B]6[OH]3[OH]	[Ca][Mg1/6Ti5/6]3[Al]6[B]6[OH]3[F]
[Ca][Ti2/3Al1/3]3[Al]6[Al]6[OH]3[OH]	[Ca][Ti2/3Al1/3]3[Al]6[Al]6[OH]3[F]	[Ca][Ti2/3Al1/3]3[Al]6[B]6[OH]3[OH]
[Ca][Ti2/3Al1/3]3[Al]6[B]6[OH]3[F]	[Ca][Ti2/3Fef1/3]3[Al]6[Al]6[OH]3[OH]	[Ca][Ti2/3Fef1/3]3[Al]6[Al]6[OH]3[F]
[Ca][Ti2/3Fef1/3]3[Al]6[B]6[OH]3[OH]	[Ca][Ti2/3Fef1/3]3[Al]6[B]6[OH]3[F]	[Ca][Mg1/6Ti5/6]3[Fef]6[Al]6[OH]3[OH]
[Ca][Mg1/6Ti5/6]3[Fef]6[Al]6[OH]3[F]	[Ca][Mg1/6Ti5/6]3[Fef]6[B]6[OH]3[OH]	[Ca][Mg1/6Ti5/6]3[Fef]6[B]6[OH]3[F]
[Ca][Ti2/3Al1/3]3[Fef]6[Al]6[OH]3[OH]	[Ca][Ti2/3Al1/3]3[Fef]6[Al]6[OH]3[F]	[Ca][Ti2/3Al1/3]3[Fef]6[B]6[OH]3[OH]
[Ca][Ti2/3Al1/3]3[Fef]6[B]6[OH]3[F]	[Ca][Ti2/3Fef1/3]3[Fef]6[Al]6[OH]3[OH]	[Ca][Ti2/3Fef1/3]3[Fef]6[Al]6[OH]3[F]
[Ca][Ti2/3Fef1/3]3[Fef]6[B]6[OH]3[OH]	[Ca][Ti2/3Fef1/3]3[Fef]6[B]6[OH]3[F]	[Ca][Ti]3[Mg1/6Al5/6]6[Al]6[OH]3[OH]
[Ca][Ti]3[Mg1/6Fef5/6]6[Al]6[OH]3[OH]	[Ca][Ti]3[Mg1/6Al5/6]6[Al]6[OH]3[F]	[Ca][Ti]3[Mg1/6Fef5/6]6[Al]6[OH]3[F]
[Ca][Ti]3[Mg1/6Al5/6]6[B]6[OH]3[OH]	[Ca][Ti]3[Mg1/6Fef5/6]6[B]6[OH]3[OH]	[Ca][Ti]3[Mg1/6Al5/6]6[B]6[OH]3[F]
[Ca][Ti]3[Mg1/6Fef5/6]6[B]6[OH]3[F]	[Ca][Ti]3[Fe1/6Al5/6]6[Al]6[OH]3[OH]	[Ca][Ti]3[Fe1/6Fef5/6]6[Al]6[OH]3[OH]
[Ca][Ti]3[Fe1/6Al5/6]6[Al]6[OH]3[F]	[Ca][Ti]3[Fe1/6Fef5/6]6[Al]6[OH]3[F]	[Ca][Ti]3[Fe1/6Al5/6]6[B]6[OH]3[OH]
[Ca][Ti]3[Fe1/6Fef5/6]6[B]6[OH]3[OH]	[Ca][Ti]3[Fe1/6Al5/6]6[B]6[OH]3[F]	[Ca][Ti]3[Fe1/6Fef5/6]6[B]6[OH]3[F]
[Ca1/2V1/2][Mg]3[Al]6[Si]6[OH]3[OH]	[Ca1/2V1/2][Mg]3[Al]6[Si]6[OH]3[F]	[Ca1/2V1/2][Al]3[Al]6[Si]6[O]3[OH]
[Ca1/2V1/2][Al]3[Al]6[Si]6[O]3[F]	[Ca1/2V1/2][Fef]3[Al]6[Si]6[O]3[OH]	[Ca1/2V1/2][Fef]3[Al]6[Si]6[O]3[F]
[Ca1/2V1/2][Ti]3[Al]6[Al]6[OH]3[OH]	[Ca1/2V1/2][Ti]3[Al]6[Al]6[OH]3[F]	[Ca1/2V1/2][Ti]3[Al]6[B]6[OH]3[OH]
[Ca1/2V1/2][Ti]3[Al]6[B]6[OH]3[F]	[Ca1/2V1/2][Mg]3[Fef]6[Si]6[OH]3[OH]	[Ca1/2V1/2][Mg]3[Fef]6[Si]6[OH]3[F]
[Ca1/2V1/2][Al]3[Fef]6[Si]6[O]3[OH]	[Ca1/2V1/2][Al]3[Fef]6[Si]6[O]3[F]	[Ca1/2V1/2][Fef]3[Fef]6[Si]6[O]3[OH]
[Ca1/2V1/2][Fef]3[Fef]6[Si]6[O]3[F]	[Ca1/2V1/2][Ti]3[Mg]6[Si]6[OH]3[OH]	[Ca1/2V1/2][Ti]3[Mg]6[Si]6[OH]3[F]
[Ca1/2V1/2][Ti]3[Fe]6[Si]6[OH]3[OH]	[Ca1/2V1/2][Ti]3[Fe]6[Si]6[OH]3[F]	[Ca1/2V1/2][Ti]3[Fef]6[Al]6[OH]3[OH]
[Ca1/2V1/2][Ti]3[Fef]6[Al]6[OH]3[F]	[Ca1/2V1/2][Ti]3[Fef]6[B]6[OH]3[OH]	[Ca1/2V1/2][Ti]3[Fef]6[B]6[OH]3[F]
[Ca][Ti]3[Fef]6[B]6[OH]3[O]	[Ca][Ti]3[Fef]6[Al]6[OH]3[O]	[Ca][Ti]3[Al]6[B]6[OH]3[O]
[Ca][Ti]3[Al]6[Al]6[OH]3[O]		

12. SAMPLE CHARACTERISATION DISCUSSION

Sample Coverage over composition and site-occupancy space Optimised site occupancies and bulk compositions are provided in Electronic Appendix 1J. Due to document size restrictions and formatting limitations, these large data tables are not included directly in the main body of the thesis but are made available electronically for reference and reproducibility.

Bulk compositions were determined for all tourmaline samples and are reported as atom proportions per formula unit (apfu). These apfu values were summed (excluding boron and water) and renormalised to 100% solely for illustrative purposes, to better visualize the broad chemical variability captured across the sample set (Figure 1B). Major elements, including Si, Al, Na, Mg, and Fe, dominate the bulk chemistry. Minor elements, such as Ca and Ti^{4+}, contribute to secondary substitution mechanisms. Trace elements, including Li, Mn, Zn, Cr, and rare earth elements (La, Ce, Nd), occur at low concentrations and reflect localized geochemical variations within the samples. The consistent structural framework provided by high Si and Al contents, combined with the compositional spread in transition metals and alkalis, ensures that the samples comprehensively represent the natural chemical diversity observed in tourmaline.

The most precise measurements were obtained for Si, Al, Na, and Mg, with absolute uncertainties between 0.01 and 0.03 apfu, corresponding to relative uncertainties of less than 4%. The partitioning between Fe^{2+} and Fe^{3+}, constrained by Mössbauer spectroscopy, yielded relatively high internal precision, with absolute uncertainties around 0.01 apfu and relative uncertainties of 5–10%; however, uncertainties related to the absolute accuracy of the site assignments are not propagated here, and thus the reported values represent a minimal estimate of the true uncertainty (see Figure 1A). Moderately precise measurements were obtained for Ti^{4+}, and Ca, which exhibit relative uncertainties of approximately 10%, and 18%, respectively, reflecting their lower abundances in most samples. Minor and trace elements such as Li, Mn, Cr, and Zn display substantially larger relative uncertainties, often exceeding 50%, due to their low concentrations near detection limits. Overall, the high precision obtained for major elements ensures that the bulk compositions are robust and suitable for reliable thermodynamic model calibration, despite larger uncertainties in minor-element concentrations.

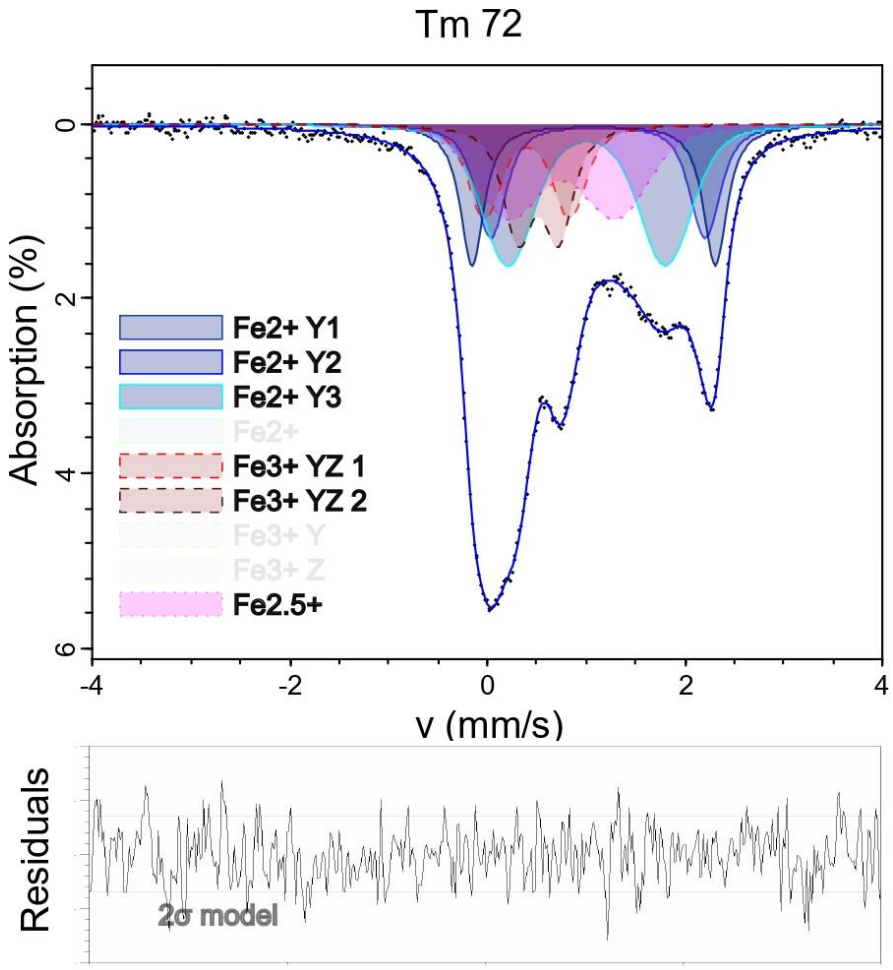

Figure 1A. Mössbauer spectrum for tourmaline sample Tm72, illustrating one of the more complex cases encountered in the dataset. The fitted model includes Fe^{2+} doublets assigned to Y1, Y2, and Y3 sites, Fe^{3+} doublets representing Y or Z site occupancy, and a $Fe^{2.5+}$ mixed-valence component to account for broadening effects. The addition of the $Fe^{2.5+}$ component improves the fit but increases the uncertainty of precise site and valence assignments. Residuals remain within ±2σ limits, confirming the quality of the fit.

Mössbauer Mössbauer spectra were interpreted using a multi-component doublet distribution fitting approach, allowing for the resolution of Fe^{2+}, Fe^{3+}, and intermediate $Fe^{2.5+}$ (mixed valence) components. Fe^{2+} doublets were modelled separately for distinct crystallographic environments (Y1, Y2, Y3 sites) based on variations in center shift and quadrupole splitting parameters. Fe^{3+} doublets were attributed to shared Y and Z site occupancy (YZ1, YZ2) reflecting partial site disorder between octahedral sites. An additional $Fe^{2.5+}$ component was incorporated where

necessary to account for broadened distributions indicative of mixed valence or electron delocalisation effects. Residuals between the modelled and observed spectra were evaluated to confirm the quality of fits, with the majority of fits remaining within ±2σ confidence intervals. This deconvolution approach enables quantitative partitioning of Fe^{2+} and Fe^{3+} across crystallographic sites, providing critical input for site-occupancy refinements and charge-balance calculations. Rest of the Mossbauer figures can be found in Appendix 1E.

Site occupancies The characterised samples span a wide range of crystallographic site occupancies, providing extensive coverage across the major chemical substitution vectors in natural tourmaline. Detailed site occupancy distributions for the X, Y, and Z sites, the principal crystallographic sites where substitution affects thermodynamic behavior, are illustrated in Figures 1C, 1D, and 1E, respectively. X-site occupancies vary from Na-dominant compositions to mixed Na–Ca–vacancy fields, reflecting substitution mechanisms along the alkali–vacancy and alkali–earth exchange vectors. Y-site compositions are dominated by Fe^{2+}- and Mg-rich endmembers, with additional contributions from Al, spanning a broad range of Fe–Mg–Al substitution space. Z-site occupancies are consistently Al-rich, with minor Mg substitution observed in selected samples, providing excellent coverage along the Al–Mg substitution vector. The T site is characterised by near-ideal Si occupancy, with minor Al-for-Si and B-for-Si substitutions captured across the sample set. The V and W sites are primarily OH-dominant, with systematic variation in F and O contents at the W site. This compositional spread ensures that the samples collectively occupy a wide volume of site-occupancy space, necessary for reliable calibration of thermodynamic models across diverse tourmaline compositions.

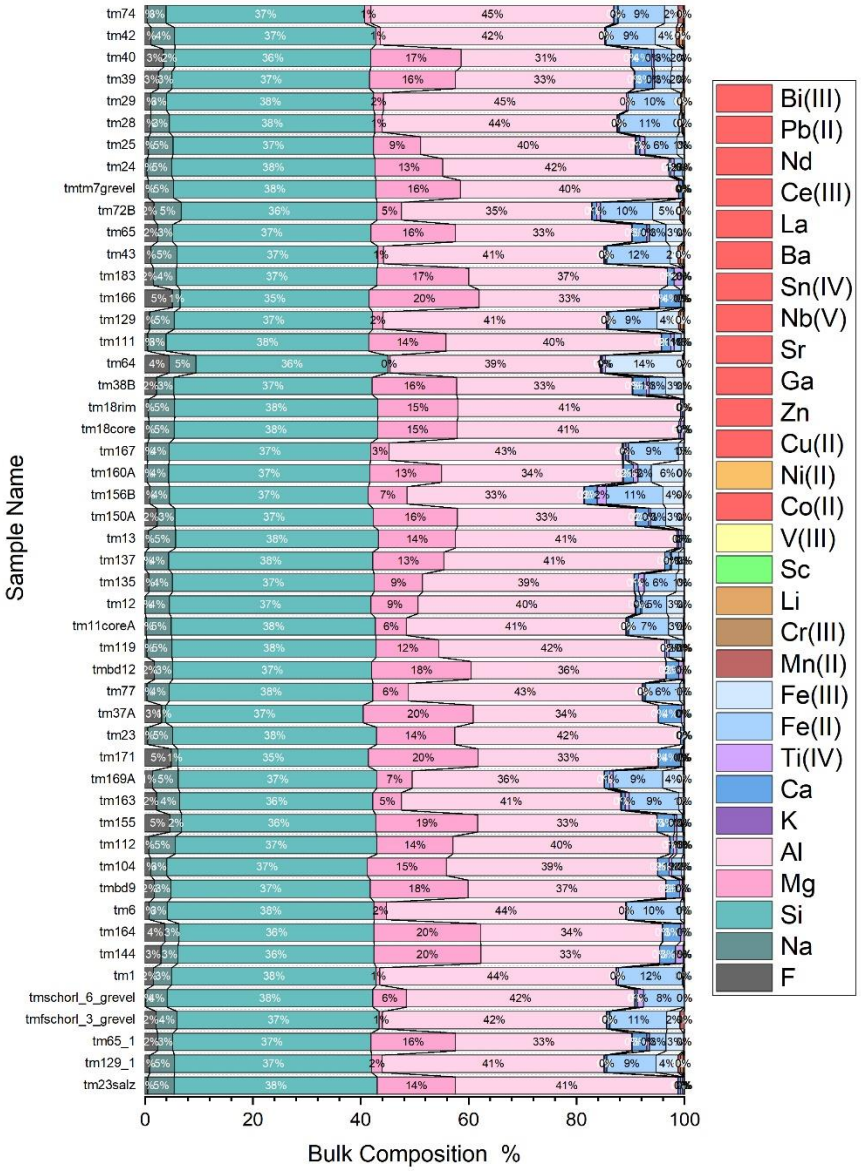

Figure 1B. Stacked bar chart showing the bulk compositions of all analysed tourmaline samples. Cationic abundances were calculated by summing all measured elements and renormalizing to 100% for each sample. Major components include Si, Al consistent with the expected framework of tourmaline. Significant proportions of Na, Mg, Fe^{2+}, and Fe^{3+} reflect substitutions at the X and Y sites, while minor amounts of Ca, Ti^{4+}, F and trace elements (e.g., Li, Cr, V, Mn, Zn, REEs) are also observed. The renormalization emphasizes compositional trends across major and minor elements and facilitates direct comparison between samples. You excluded boron, oxygen and water from the bulk plot to improve the visibility of the variation in minor and trace elements.

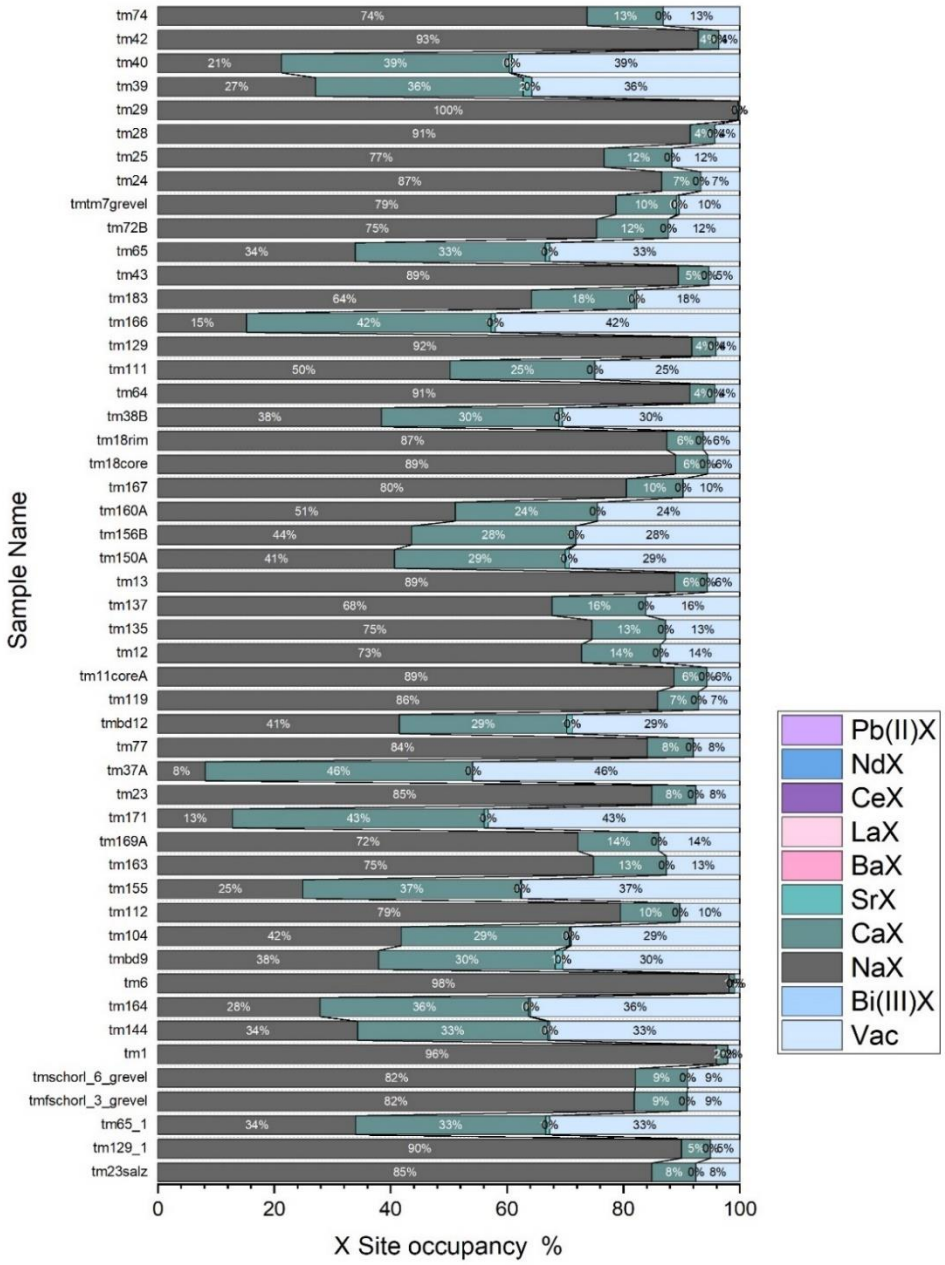

Figure 1C. Stacked bar chart showing the X site occupancies for all analysed tourmaline samples. The occupancies of Na^X, Ca^X, K^X, Sr^X, Ba^X, La^X, Ce^X, Nd^X, $Pb(II)^X$, $Bi(III)^X$, and $Vacancy^X$ are displayed as a percentage of total X site occupancy. Na is the dominant occupant in most samples, with varying proportions of Ca and minor K, Sr, and rare earth elements (REEs). Site vacancies are significant in some samples, reflecting incomplete X-site occupancy.

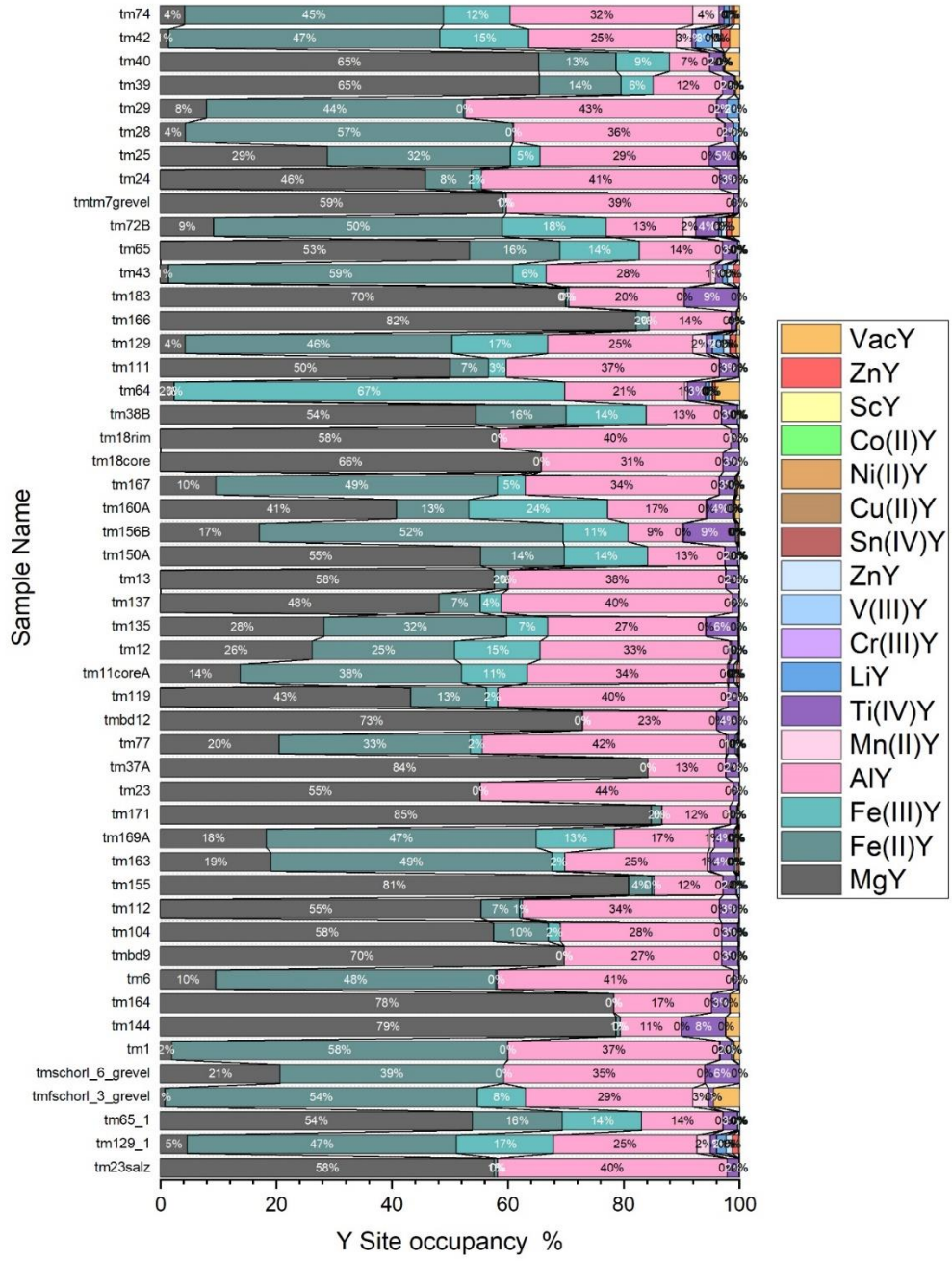

Figure 1D. Stacked bar chart showing the Y site occupancies for all analysed tourmaline samples. The occupancies of Mg^{Y}, $Fe(II)^{Y}$, $Fe(III)^{Y}$, Al^{Y}, $Mn(II)^{Y}$, $Ti(IV)^{Y}$, Li^{Y}, $Cr(III)^{Y}$, $V(III)^{Y}$, Zn^{Y}, $Sn(IV)^{Y}$, $Cu(II)^{Y}$, $Ni(II)^{Y}$, $Co(II)^{Y}$, Sc^{Y}, Ga^{Y}, $Nb(V)^{Y}$, and VacancyY are shown. The Y site is primarily occupied by Mg, Fe^{2+}, and Al, with significant contributions from Fe^{3+} and Ti^{4+} in some samples. Minor trace element substitutions (e.g., Zn, Cr, V) and vacancies are present but generally subordinate.

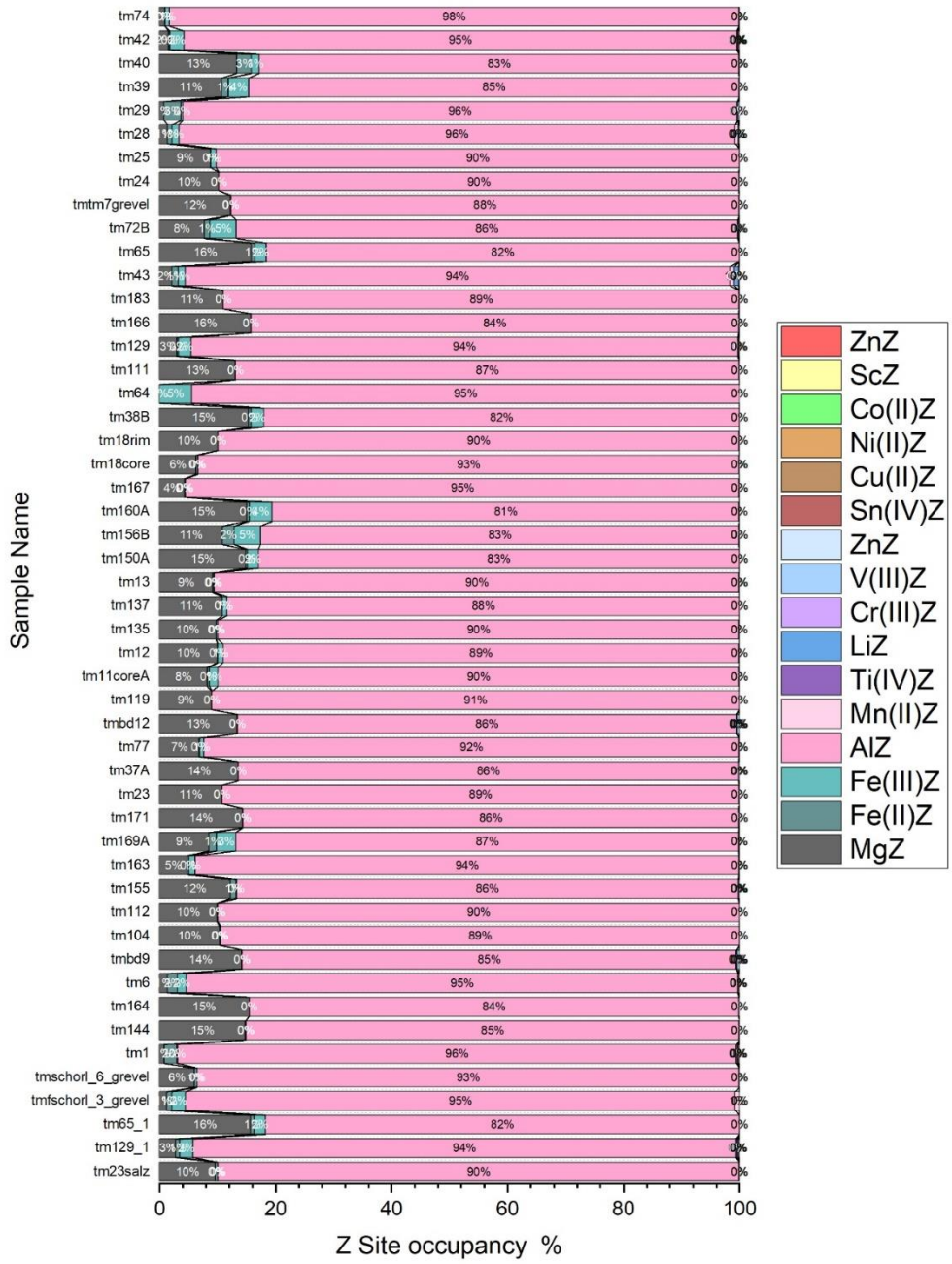

Figure 1E. Stacked bar chart showing the Z site occupancies for all analysed tourmaline samples. The occupancies of Mg^{Z}, $Fe(II)^{Z}$, $Fe(III)^{Z}$, Al^{Z}, $Mn(II)^{Z}$, $Ti(IV)^{Z}$, Li^{Z}, $Cr(III)^{Z}$, $V(III)^{Z}$, Zn^{Z}, $Sn(IV)^{Z}$, $Cu(II)^{Z}$, $Ni(II)^{Z}$, $Co(II)^{Z}$, Sc^{Z}, Ga^{Z}, and $Nb(V)^{Z}$ are plotted.

The Z site is overwhelmingly dominated by Al, typically exceeding 80% occupancy in all samples. Minor Mg, Fe^{2+}, and Fe^{3+} substitutions are observed, with very low contributions from trace elements.

Site occupancy uncertainties A total of 50 tourmaline samples were characterised for their complete site occupancies based on optimised chemical formula recalculations and, where available, Mössbauer spectroscopy-derived Fe^{2+}/Fe^{3+} distributions. Occupancies were determined for the X, Y, Z, T, V, W, and O1 crystallographic sites, with each value paired with a quantitative uncertainty estimate propagated from analytical and stoichiometric errors. Uncertainties vary systematically across sites: T-site occupancies (Si, Al, B) are the most tightly constrained, typically exhibiting absolute uncertainties below ±0.015 atoms per formula unit (apfu), with relative uncertainties for SiT consistently below 1%. Y- and Z-site occupancies (e.g., Mg, Al, Fe) show moderate absolute uncertainties around ±0.05 apfu, corresponding to relative uncertainties of approximately 18% for Mg and below 10% for Al. X-site occupancies (Na, Ca, vacancy) have intermediate uncertainties, generally below ±0.03 apfu, with Ca showing a mean relative uncertainty of approximately 18%. Minor and trace elements at the X, Y, and Z sites, such as K, Sr, Li, Zn, and Ga, exhibit significantly larger relative uncertainties (typically >100%) due to their low occupancies, although their absolute uncertainties remain small (typically <±0.01 apfu).

The V and W sites, associated with OH, O, and F groups, are generally well constrained, with V-site absolute uncertainties around ±0.008 apfu (relative uncertainty ~0.5%) and W-site absolute uncertainties around ±0.004 apfu (relative uncertainty ~14%), although greater variability is observed at the O1 site where F–OH partitioning introduces relative uncertainties up t**o** ~19%.

Overall, the uncertainties on major cations (Si, Al, Mg, Fe, Ca) are sufficiently small—typically better than ±0.05 apfu absolute and below 20% relative error, to ensure the data's robustness for subsequent thermodynamic modelling. The characterised samples span a broad range of site-occupancy space, including Na- to Ca-dominant X sites, Fe^{2+}- to Mg-rich Y sites, and near-ideal Si occupancy at the T site, providing a comprehensive representation of natural tourmaline compositional variability.

13.CONCLUSIONS

This study assembles a tourmaline sample set from natural and synthetic samples to future thermodynamic property measurement and compositionally and structurally characterises these tourmalines using a consistent multi-method analytical strategy and approach. Standardized

characterisation ensures accurate property-composition correlations. This compositional characterisation is combined with crystal-structure measurements by XRD and their Rietveld refinement, and subsequently analysed and optimised using bond-valence modelling. This allows elements to be assigned to the sites of the tourmaline structure, provides information on the bond network, and validates structural stability. In post-processing, we compared bond lengths from Rietveld refinement with those predicted by valence-distributed topology and regular polyhedra, using anion/cation bond valence sums and a loop equation-containing matrix method. Qualitative analysis of these results suggests that mean bond lengths in tourmaline may not be fixed. This combined structural and compositional characterisation of the tourmaline set results in obtaining the best estimate of their molecular formulae, which is the essential information needed to convert measured per mass thermodynamic properties to per mole values, and to deconvolute intermediate compositions to endmember fractions. Careful propagation of uncertainties shows that significant uncertainty in site assignment, and hence molecular formula, exists, even for the best practice analytical methods applied here, and this finding is directly applicable to other mineral groups with complex crystal-chemistry. As will be shown in subsequent chapters, uncertainties in this molecular formula represent a major component of the total uncertainty on endmember thermodynamic properties.

- **REFERENCES**

Andreozzi, G.B., Bosi, F., and Longo, M. (2008) Linking Mossbauer and structural parameters in elbaite-schorl-dravite tourmalines. American Mineralogist, 93, 658–666.

Asimow, P.D., and Ghiorso, M.S. (1998) Algorithmic modifications extending MELTS to calculate subsolidus phase relations. American Mineralogist, 83, 1127–1132.

Bačík, P. (2015) Cation ordering at octahedral sites in schorl-dravite series tourmalines. The Canadian Mineralogist, 53, 571–590.

——— (2018) The crystal-chemical autopsy of octahedral sites in Na-dominant tourmalines: Octahedral metrics model unconstrained by the Y, Z-site disorder assignment. Journal of Geosciences, 63, 137–154.

Bačík, P., and Fridrichová, J. (2021) Cation partitioning among crystallographic sites based on bond-length constraints in tourmaline-supergroup minerals. American Mineralogist, 106, 851–861.

Bosi, F. (2010) Octahedrally coordinated vacancies in tourmaline: a theoretical approach. Mineralogical Magazine, 74, 1037–1044.

——— (2011) Stereochemical constraints in tourmaline: from a short-range to a long-range structure. The Canadian Mineralogist, 49, 17–27.

——— (2013) Bond-valence constraints around the O1 site of tourmaline. Mineralogical Magazine, 77, 343–351.

——— (2014a) Bond valence at mixed occupancy sites. I. Regular polyhedra. Acta Crystallographica Section B Structural Science, Crystal Engineering and Materials, 70, 864–870.

——— (2014b) Mean bond-length variation in crystal structures: a bond-valence approach. Acta Crystallographica Section B Structural Science, Crystal Engineering and Materials, 70, 697–704.

——— (2018) Tourmaline crystal chemistry. American Mineralogist, 103, 298–306.

Bosi, F., and Lucchesi, S. (2004) Crystal chemistry of the schorl-dravite series. European Journal of Mineralogy, 16, 335–344.

——— (2007) Crystal chemical relationships in the tourmaline group: Structural constraints on chemical variability. American Mineralogist, 92, 1054–1063.

Bosi, F., Reznitskii, L., Hålenius, U., and Skogby, H. (2017) Crystal chemistry of Al–V–Cr oxy-tourmalines from Sludyanka complex, Lake Baikal, Russia. European Journal of Mineralogy, 29, 457–472.

Bosi, F., Biagioni, C., Pezzotta, F., Skogby, H., Hålenius, U., Cempírek, J., Hawthorne, F.C., Lussier, A.J., Abdu, Y.A., and Day, M.C. (2022) Uvite, CaMg3 (Al5Mg)(Si6O18)(BO3) 3 (OH) 3 (OH), a new, but long-anticipated mineral species of the tourmaline supergroup from San Piero in Campo, Elba Island, Italy. Mineralogical Magazine, 86, 767–776.

Boyd, F.R., and England, J.L. (1960) Apparatus for Phase-Equilibrium Measurements at Pressures up to 50 Kilobars and Temperatures up to 1750°C. Journal of Geophysical Research, 65, 741.

Brese, N.E., and O'Keeffe, M. (1991) Bond-valence parameters for solids. Acta Crystallographica Section B: Structural Science, 47, 192–197.

Brown, I.D. (2016) The Chemical Bond in Inorganic Chemistry: The Bond Valence Model, Second Edition., 336 p. Oxford University Press, Oxford, New York.

Brown, I.D., and Altermatt, D. (1985) Bond-valence parameters obtained from a systematic analysis of the inorganic crystal structure database. Acta Crystallographica Section B: Structural Science, 41, 244–247.

Capitani, C. de, and Petrakakis, K. (2010) The computation of equilibrium assemblage diagrams with Theriak/Domino software. American Mineralogist, 95, 1006–1016.

Connolly, J.A. (2005) Computation of phase equilibria by linear programming: a tool for geodynamic modelling and its application to subduction zone decarbonation. Earth and Planetary Science Letters, 236, 524–541.

Creagh, D.C. (2006) X-ray Dispersion corrections. In International Tables for Crystallography Vol. C, Table 4.2.6.8, pp. 255–257. Springer, Dordrecht.

Creagh, D.C., and Hubbell, J.H. (2006) X-Ray Absorption (or Attenuation) Coefficients. In International Tables for Crystallography Vol. C, Table 4.2.4.3, pp. 230–236. Springer, Dordrecht.

De Grave, E., and Van Alboom, A. (1991). Evaluation of ferrous and ferric Mössbauer fractions. Physics and chemistry of minerals, 18, 337-342

Ertl, A. (2023) Are the [6]-coordinated sites in tourmaline in certain cases partially vacant? Mineralogy and Petrology, 117, 201–207.

Filatov, M. (2009) First principles calculation of Mössbauer isomer shift. Coordination Chemistry Reviews, 253, 594–605.

Gagné, O.C., and Hawthorne, F.C. (2015) Comprehensive derivation of bond-valence parameters for ion pairs involving oxygen. Acta Crystallographica Section B: Structural Science, Crystal Engineering and Materials, 71, 562–578.

——— (2017) Mean bond-length variations in crystals for ions bonded to oxygen. Acta Crystallographica Section B: Structural Science, Crystal Engineering and Materials, 73, 1019–1031.

——— (2020) Bond-length distributions for ions bonded to oxygen: Results for the transition metals and quantification of the factors underlying bond-length variation in inorganic solids. IUCrJ, 7, 581–629.

Gagné, O.C., Mercier, P.H., and Hawthorne, F.C. (2018) A priori bond-valence and bond-length calculations in rock-forming minerals. Acta Crystallographica Section B: Structural Science, Crystal Engineering and Materials, 74, 470–482.

Gibbs, G.V., Ross, N.L., Cox, D.F., and Rosso, K.M. (2014) Insights into the crystal chemistry of Earth materials rendered by electron density distributions: Pauling's rules revisited. American Mineralogist, 99, 1071–1084.

Gibbs, G.V., Hawthorne, F.C., and Brown, G.E. (2022) Pauling's rules for oxide-based minerals: A re-examination based on quantum mechanical constraints and modern applications of bond-valence theory to Earth materials. American Mineralogist, 107, 1219–1248.

Goldstein, J.I., Newbury, D.E., Echlin, P., Joy, D.C., Lyman, C.E., Lifshin, E., Sawyer, L., and Michael, J.R. (2003) Scanning Electron Microscopy and X-ray Microanalysis: Third Edition. Springer US, Boston, MA.

Grodzicki, M., and Lebernegg, S. (2011) Computation and interpretation of Mössbauer parameters of Fe-bearing compounds. In Mössbauer spectroscopy and transition metal chemistry. Springer, Berlin.

Günther, D., and Hattendorf, B. (2005) Solid sample analysis using laser ablation inductively coupled plasma mass spectrometry. TrAC Trends in Analytical Chemistry, 24, 255–265.

Hamilton, D. t, and Henderson, C.M.B. (1968) The preparation of silicate compositions by a gelling method. Mineralogical magazine and journal of the Mineralogical Society, 36, 832–838.

Handt, A. von der, and Mosenfelder, J. (2019) Soft X-ray Emission Spectroscopy of Borosilicate Glasses and Minerals by SXES and EPMA-WDS. Microscopy and Microanalysis, 25, 270–271.

Hawthorne, F.C. (1996) Structural mechanisms for light-element variations in tourmaline. The Canadian Mineralogist, 34, 123–132.

——— (2002) Bond-valence constraints on the chemical composition of tourmaline. The Canadian Mineralogist, 40, 789–797.

Hawthorne, F.C., Ungaretti, L., and Oberti, R. (1995) Site populations in minerals; terminology and presentation of results of crystal-structure refinement. The Canadian Mineralogist, 33, 907–911.

Hemingway, B.S., and Evans Jr, H.T. (1996) Thermal expansion of some borate and borosilicate minerals (fluoborite, danburite, sinhalite, datolite, elbaite, dravite, kornerupine, dumortierite, ferro-axinite, and manganaxinite) between 25 and about 1200 degrees C. US Geological Survey.

Henry, D.J., and Dutrow, B.L. (1990) Ca substitution in Li-poor aluminous tourmaline. The Canadian Mineralogist, 28, 111–124.

——— (1996) Metamorphic tourmaline and its petrologic applications. Reviews in Mineralogy and Geochemistry, 33, 503–557.

——— (2011) The incorporation of fluorine in tourmaline: internal crystallographic controls or external environmental influences? The Canadian Mineralogist, 49, 41–56.

——— (2018) Tourmaline studies through time: contributions to scientific advancements. Journal of Geosciences, 63, 77–98.

Henry, D.J., Novák, M., Hawthorne, F.C., Ertl, A., Dutrow, B.L., Uher, P., and Pezzotta, F. (2011) Nomenclature of the tourmaline-supergroup minerals. American Mineralogist, 96, 895–913.

——— (2013) Erratum: Nomenclature of the tourmaline-supergroup minerals (American Mineralogist (2011) 96 (895-913. American Mineralogist, 98, 524.

Jochum, K.P., Nohl, U., Herwig, K., Lammel, E., Stoll, B., and Hofmann, A.W. (2005) GeoReM: A New Geochemical Database for Reference Materials and Isotopic Standards. Geostandards and Geoanalytical Research, 29, 333–338.

Kent, A., and Ungerer, A. (2005) Production of barium and light rare earth element oxides during LA-ICP-MS microanalysis. Journal of Analytical Atomic Spectrometry, 20.

Krosse, S. (1995) Hochdrucksynthese, stabilität und eigenschaften der borsilikate dravit und kornerupin sowie darstellung und stabilitätsverhalten eines neuen Mg-Al-borates. PhD Thesis.

Kuhn, H.-R., and Günther, D. (2004) Laser ablation-ICP-MS: particle size dependent elemental composition studies on filter-collected and online measured aerosols from glass. Journal of Analytical Atomic Spectrometry, 19, 1158–1164.

Kulik, D.A., Wagner, T., Dmytrieva, S.V., Kosakowski, G., Hingerl, F.F., Chudnenko, K.V., and Berner, U.R. (2013) GEM-Selektor geochemical modelling package: revised algorithm and GEMS3K numerical kernel for coupled simulation codes. Computational Geosciences, 17, 1–24.

Kutzschbach, M., Wunder, B., Rhede, D., Koch-Müller, M., Ertl, A., Giester, G., Heinrich, W., and Franz, G. (2016) Tetrahedral boron in natural and synthetic HP/UHP tourmaline: evidence from Raman spectroscopy, EMPA, and single-crystal XRD. American Mineralogist, 101, 93–104.

Kuyunko, N.S., Semenov, Ë.V., Gurevich, V.M., Kuz'min, V.I., Topor, N.D., and Gorbunov, V.E. (1984) Experimental determination of thermodynamic properties of tourmaline dravite. Geokhimiya, 10, 1458–1465.

Lagarec, K., and Rancourt, D. (1998) Recoil User Manual -- Mossbauer spectral analysis software for Windows.

Lawson, C.L., and Hanson, R.J. (1974) Solving Least Squares Problems. Society for Industrial and Applied Mathematics.

Liu, Y., Hu, Z., Gao, S., Günther, D., Xu, J., Gao, C., and Chen, H. (2008) In situ analysis of major and trace elements of anhydrous minerals by LA-ICP-MS without applying an internal standard. Chemical Geology, 257, 34–43.

Llovet, X., Pöml, P., Moy, A., and Fournelle, J.H. (2023) Assessing the Accuracy of Mass Attenuation Coefficients for Soft X-ray EPMA. Microscopy and Microanalysis, 29, 540–551.

Longerich, H.P., Jackson, S.E., and Günther, D. (1996) Inter-laboratory note. Laser ablation inductively coupled plasma mass spectrometric transient signal data acquisition and analyte concentration calculation. Journal of analytical atomic spectrometry, 11, 899–904.

Maslen, E.N., Fox, A.G., and O'Keefe, M.A. (2006) X-Ray Scattering. In International Tables for X-ray Crystallography Vol. C, Tables 6.1.1.4, pp. 555–564. Dordrecht, Springer.

Massonne, H.J., and Schreyer, W. (1986) High-pressure syntheses and X-ray properties of white micas in the system K2O-MgO-Al2O3-SiO2-H2O. Neues Jahrbuch Für Mineralogie. Abhandlungen, 153, 177–215.

McCormack, S.J., and Navrotsky, A. (2021) Thermodynamics of high entropy oxides. Acta Materialia, 202, 1–21.

Merlet, C. (1992) Quantitative Electron Probe Microanalysis: New Accurate Φ (ρz) Description. In A. Boekestein and M.K. Pavićević, Eds., Electron Microbeam Analysis pp. 107–115. Springer, Vienna.

——— (1994) An Accurate Computer Correction Program for Quantitative Electron Probe Microanalysis. Mikrochimica Acta, 114, 363–376.

Meyer, A.S., and Boyd, C.M. (1959) Determination of Water by Titration with Coulometrically Generated Karl Fischer Reagent. Analytical Chemistry, 31, 215–219.

Ogorodova, L.P., Melchakova, L.V., Kiseleva, I.A., and Peretyazhko, I.S. (2004) Thermodynamics of natural tourmaline–elbaite. Thermochimica acta, 419, 211–214.

Ogorodova, L.P., Melchakova, L.V., Kiseleva, I.A., and Peretyazhko, I.S. (2012) Thermodynamics of natural tourmalines—Dravite and schorl. Thermochimica Acta, 539, 1–6.

Paton, C., Hellstrom, J., Paul, B., Woodhead, J., and Hergt, J. (2011) Iolite: Freeware for the visualisation and processing of mass spectrometric data. Journal of Analytical Atomic Spectrometry, 26, 2508–2518.

Paul, B., Petrus, J., Savard, D., Woodhead, J., Hergt, J., Greig, A., Paton, C., and Rayner, P. (2023) Time resolved trace element calibration strategies for LA-ICP-MS. Journal of Analytical Atomic Spectrometry, 38, 1995–2006.

Pechoušek, J., Jančík, D., Frydrych, J., Navařík, J., and Novák, P. (2012) Setup of Mössbauer spectrometers at RCPTM pp. 186–193. Presented at the MOSSBAUER SPECTROSCOPY IN MATERIALS SCIENCE - 2012: Proceedings of the International Conference MSMS-12, Olomouc, Czech Republic.

Puerta, J., and Martin, P. (1981) Three and four generalized Lorentzian approximations for the Voigt line shape. Applied optics, 20, 3923–3928.

Rancourt, D.G., and Ping, J.Y. (1991) Voigt-based methods for arbitrary-shape static hyperfine parameter distributions in Mössbauer spectroscopy. Nuclear Instruments and Methods in Physics Research Section B: Beam Interactions with Materials and Atoms, 58, 85–97.

Rancourt, D.G., McDonald, A.M., Lalonde, A.E., and Ping, J.Y. (1993) Mössbauer absorber thicknesses for accurate site populations in Fe-bearing minerals. American Mineralogist, 78, 1–7.

Renner, J., Zerbian, A., and Stöckhert, B. (1997) Microstructures of synthetic polycrystalline coesite aggregates. The effect of pressure, temperature, and time. Lithos, 41, 169–184.

Rodríguez-Carvajal, J. (1993) Recent advances in magnetic structure determination by neutron powder diffraction. Physica B: Condensed Matter, 192, 55–69.

Schreyer, W., Wodara, U., Marler, B., Van Aken, P.A., Seifert, F., and Robert, J.-L. (2000) Synthetic tourmaline (olenite) with excess boron replacing silicon in the tetrahedral site: I. Synthesis conditions, chemical and spectroscopic evidence. European Journal of Mineralogy, 12, 529–541.

Shannon, R. D. (1976) Revised effective ionic radii and systematic studies of interatomic distances in halides and chalcogenides. Foundations of Crystallography, 32, 751–767.

Sheldrick, G.M. (2015) Crystal structure refinement with SHELXL. Acta Crystallographica Section C: Structural Chemistry, 71, 3–8.

van Hinsberg, V.J., and Schumacher, J.C. (2007) Intersector element partitioning in tourmaline: a potentially powerful single crystal thermometer. Contributions to Mineralogy and Petrology, 153, 289–301.

van Hinsberg, V.J. (2011) Preliminary experimental data on trace-element partitioning between tourmaline and silicate melt. The Canadian Mineralogist, 49, 153–163.

van Hinsberg, V.J., Henry, D.J., and Marschall, H.R. (2011) Tourmaline: an ideal indicator of its host environment. The Canadian Mineralogist, 49, 1–16.

van Hinsberg, V.J., Schumacher, J.C., Slack, J.F., and Marschall, H.R. (2017) Trace elements in tourmaline. Tourmaline 2017 conference, Czech Republic.

Vereshchagin, O.S., Frank-Kamenetskaya, O.V., Rozhdestvenskaya, I.V., and Zolotarev, A.A. (2018) Incorporation of 3d elements in tourmalines: structural adjustments and stability. European Journal of Mineralogy, 30, 917–928.

Violet, C.E., and Pipkorn, D.N. (1971) Mössbauer line positions and hyperfine interactions in α iron. Journal of Applied Physics, 42, 4339–4342.

von Goerne, G., Franz, G., and van Hinsberg, V.J. (2011) Experimental determination of Na–Ca distribution between tourmaline and fluid in the system CaO–Na2O–MgO–Al2O3–SiO2–B2O3–H2O. The Canadian Mineralogist, 49, 137–152.

Wodara, U. (1996) Synthese und Eigenschaften von Turmalinen im System Na2O-Al2O3-SiO2-B2O3-H2O. Unpublished Diploma thesis, Ruhr Universitat Bochum.

Wojdyr, M. (2022) GEMMI: A library for structural biology. Journal of Open Source Software, 7, 4200.

Wright, S.E., Foley, J.A., and Hughes, J.M. (2000) Optimisation of site occupancies in minerals using quadratic programming. American Mineralogist, 85, 524–531.

Bridging Text Between Manuscripts (Chapter 1-Chapter 2)

From Composition Space Definition (Characterisation and Endmember Basis) to Initial Energy Equation Calibration (Molar Volume)

The tourmaline sample set developed in Chapter 1, fully characterised using an internally consistent data normalization scheme, provides the foundation for the thermodynamic model calibration presented in Chapter 2. Natural and synthetic samples were analysed using a multi-technique approach, electron microprobe, Mössbauer spectroscopy, single-crystal X-ray diffraction (or powder XRD for synthetics), and Karl-Fischer titration, to derive optimised mineral formulas. These were refined through quadratic programming, using a weighted scheme that incorporated composition, site occupancy constraints, bond valence sums, electron densities, and charge balance. Monte Carlo-based error propagation accounted for analytical uncertainties and sample heterogeneity, resulting in a dataset that captures both compositional variability and its uncertainty structure.

Chapter 2 builds directly upon this framework by formally defining the compositional and speciation space for tourmaline, the first ingredient for a thermodynamic model. Two model formulations are introduced:

1. A bulk compositional model, suitable when only chemical analyses are available.
2. A speciation model, applicable when complete site occupancy data from structural analyses are provided.

The optimised formulas from Chapter 1 are mapped from bulk parameters/site fractions into composition/speciation endmember space. Together, these mappings define the compositional/speciation domain over which the thermodynamic energy equations operate.

The second ingredient, the energy equations themselves, begins here with the calibration of one of their key parameters: the molar volume. As a primary contributor to the pressure term in Gibbs free energy, molar volume plays a crucial role in phase stability modelling. Regression calibration was performed using the internally consistent dataset, with careful evaluation of multicollinearity, endmember independence, the uncertainty structure and model robustness.

The methodological continuity between chapters ensures that the derived thermodynamic properties and resulting energy equations are firmly anchored in a well-defined composition and speciation space. The approach not only underpins the molar volume model presented here but also establishes the compositional framework for calibrating entropy, heat capacity, and enthalpy in subsequent chapters. This progression from mineral characterisation to thermodynamic model construction reflects a central objective of this thesis: to develop a data-driven, experimentally constrained thermodynamic model for tourmaline solid solutions.

Thermodynamic model for Tourmaline

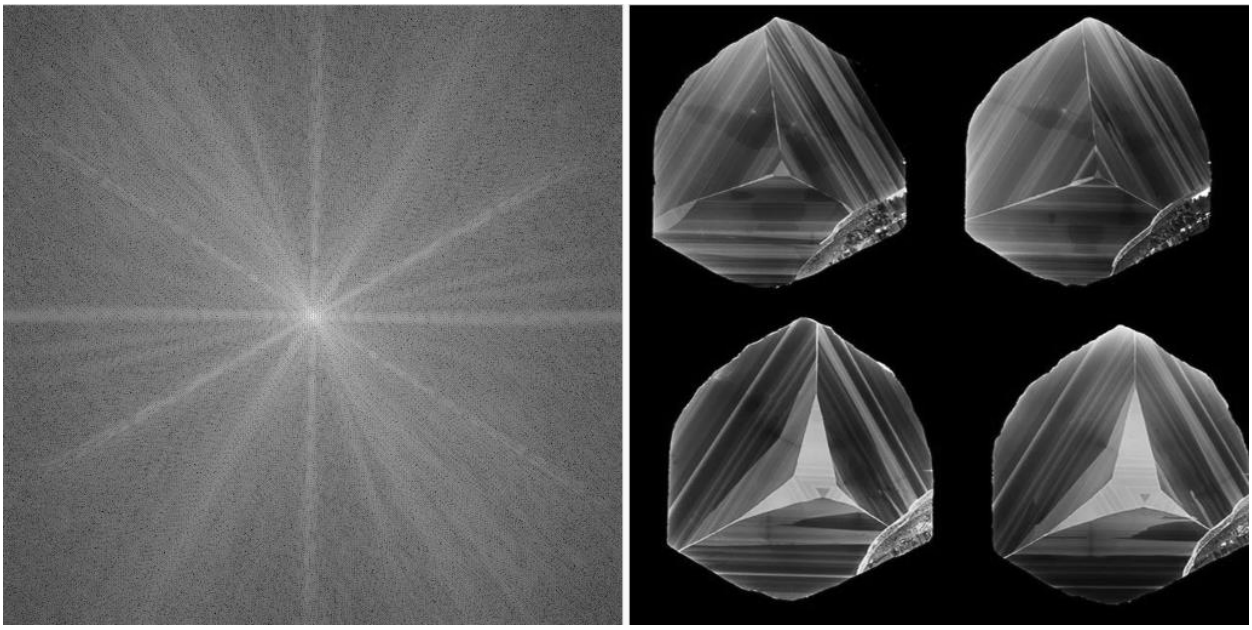

Tourmalines (Modified from Rustemeyer (2022) *The inner architecture of tourmaline crystals, as inferred from the morphology of colour zones in thin slices.* Journal of geosciences 67), at the right, and the Fourier Transform of the same image, at the left.

Do it for any image of your chose:

https://bigwww.epfl.ch/demo/ip/demos/FFT/

Chapter 2. Thermodynamic model for Tourmaline. Model derivation and calibration of the molar volumes

Stan Roozen, Vincent van Hinsberg, Gunther Redhammer, Edgar Dachs,

ABSTRACT Tourmaline, the most common crustal borosilicate, records phase relationships with minerals, fluids, and melts across divers tectonic settings. Its elemental flexibility, stability under wide P-T conditions, and low diffusivity preserve compositional zoning, making it a key archive of P-T-X histories for petrogenesis and provenance studies. Accurate interpretation of this record requires a thermodynamic model to predict its compositional response to changing conditions. This chapter formulates a molar volume model based on crystal-chemical measurements.

Two thermodynamic models were developed: a bulk model for cases with limited data, such as EMPA-only characterisation, and a speciation model requiring element site assignments from crystal-structure refinements. The bulk model, $X(YZ)_9Si_xAl_{(1-x)}(VW)_4$, a reciprocal model with dependent speciation, was derived using valences, site occupancy, and charge balance constraints to define a convex polytope with 9 independent endmembers and related independent bulk parameters. Stoichiometry matrices linked endmembers to bulk variables, with the nullspace revealing linear dependencies. A robust, independent bulk parameter set was selected to prevent negative dependent parameters or non-summing-to-1 endmember fractions caused by measurement imperfections, since any uncertainty propagates to the dependent parameters. The stoichiometry matrix using only independent bulk parameters formed a square matrix, and its inversion yielded linear mapping equations to the endmembers. For the speciation model, $XY_3Z_6T_6V_3W$, linear mapping equations link 14 independent speciation endmembers to independent site fractions. An implicit order-disorder formulation is also provided for convenience. Monte Carlo simulations propagated analytical and sample uncertainties into the endmember fractions.

Molar volume (V_M) was derived from SC-XRD crystal-structure refinements and linked to the optimised mineral formulas, normalised for internal consistency (Chapter 1). Multiple linear regression was used to extrapolate endmember V_M but due to tourmaline's complexity and limited sample size (50 samples), 21 regression methods, including OLS, x-uncertainty, and robust regression, were compared to identify the most reliable estimates. The methods were assessed using a reference database as a test set to balance bias, variance, and total error. Robust

regression provided the best results for the bulk model by minimizing the impact of outliers that needed speciation to be captured (F-buergerite), Correlated Weighted Total Least Squares (CWTLS), with block-diagonal weight matrices based on sample covariance worked best for the speciation model, mitigating multicollinearity. This approach ensures accuracy in well-sampled regions while maintaining reasonable extrapolation capabilities. Hierarchical subset selection identified interaction parameters, but test set validation showed they often overfit by capturing noise instead of real physical interactions.

A molar volume model is presented, essential for determining Gibbs free energy, as pressure variations strongly affect the stability of minerals with different molar volumes. In this work the first step to a comprehensive thermodynamic model for tourmaline is made by integrating direct measurements of key properties, including molar volume (this chapter), entropy and heat capacity (chapter 3), and enthalpy (chapter 4).

1. INTRODUCTION

Tourmaline's structural flexibility, reflected in its generalized formula $XY_3Z_6(T_6O_{18})(BO_3)_3V_3W$, accommodates extensive compositional variability (Henry et al. 2011):

X = Na^{1+}, Ca^{2+}, K^{1+}, □ = vacancy
Y = Fe^{2+}, Mg^{2+}, Mn^{2+}, Al^{3+}, Li^{1+}, Fe^{3+}, V^{3+}, Cr^{3+}, Ti^{4+}
B = B^{3+}
Z = Al^{3+}, Fe^{3+}, Mg^{2+}, V^{3+}, Fe^{2+}, Cr^{3+}
T = Si^{4+}, Al^{3+}, B^{3+}
V = OH^{1-}, O^{2-}
W = OH^{1-}, F^{1-}, O^{2-}

Its chemical diversity arises from homovalent substitutions (e.g., $R^{2+} \leftrightarrow R^{2+}$), coupled substitutions (e.g., $^{X}R^{+} + {}^{Y}R^{2+} \leftrightarrow {}^{X}\square + {}^{Y}R^{3+}$) and order-disorder relationships (Bosi 2018). However, the resistance to weathering, abrasion, and diffusion allows it to remain stable across a wide pressure-temperature-composition range, preserving records from the Archean to the present (Dutrow and Henry 2011). Its zoning patterns reflect phase relationships with surrounding minerals and internally or externally buffered fluids or melts, even when other

minerals reset (van Hinsberg 2011). Stable in acidic environments, its formation depends on boron and aluminum availability (Henry and Dutrow 1996). Despite increased research on tourmaline petrogenesis (Henry and Dutrow 2018), theoretical support remains limited. A thermodynamic model would provide a quantitative framework to test and refine proposed petrogenetic processes. This study develops the first part for a comprehensive thermodynamic model of tourmaline, addressing the absence of such a model in major databases. It is essential for predicting tourmaline's phase behavior, elemental exchange, and interpreting zoning patterns. The model focuses on the Na-Ca-Mg-Fe^{2+}-Fe^{3+}-Ti-Al-B-O-H-F chemical system, which encompasses the most common Li-K-Mn-V-Cr-poor tourmaline solid solution chemistries

Molar volume is particularly critical for determining Gibbs free energy, as pressure variations significantly impact the relative stability of minerals with differing molar volumes. Tourmaline has been documented across a wide P–T range, from diagenetic settings (Biernacka 2019) to ultra-high-pressure conditions (Ertl et al. 2010), and experiments conducted at room temperature revealed it can withstand pressures up to 60 GPa (Berryman et al. 2019).

Previous research on tourmaline, including single-crystal and powder XRD studies, primarily emphasized mineralogical aspects, often treating molar volume data as secondary (Bosi and Lucchesi 2007; Lussier et al. 2011, p. 333; Ertl et al. 2018; Vereshchagin et al. 2018). Thermodynamic models like Van Hinsberg and Schumacher (2007), refining Garofalo et al.'s (2000) work, used the polyhedron method to estimate molar volumes but are limited by oversimplified assumptions. The method poorly predicts tourmaline's molar volume due to its reliance on average polyhedral properties from diverse minerals, overlooking its highly polymerized structure with extensive edge- and face-sharing (Ertl et al. 2002; Bosi 2018). This omission is critical, as bond valence theory highlights polymerization as a dominant energetic factor (Brown 2016). Normalization inconsistencies affect molar volume accuracy in a more indirect but critical way. While the molar volume itself is derived primarily from the unit cell parameters and symmetry determined by SC-XRD, and is thus not strongly influenced by the mineral formula, the positioning of this volume in composition or speciation space depends entirely on an accurately optimised formula. Inaccurate normalization affects how the volume is assigned to a given endmember or solid solution configuration, which in turn impacts its contribution to thermodynamic regressions. As a result, even if the measured volume is precise,

its interpretation and integration into the model can be significantly biased by formula inconsistencies.

In this chapter we calibrate a model for tourmaline's molar volume, using direct crystal chemical measurements and optimised mineral formula of an internally consistent database from Chapter 1 with ~50 natural and synthetic samples. The model includes a bulk version for users with only compositional data and a speciation version for those with site occupancies from SC-XRD. This work is part of a broader effort to develop a comprehensive thermodynamic model by incorporating direct measurements of key properties, including enthalpy (ΔH), entropy (S), heat capacity (Cp), and molar volume (V).

2. DEFINING THE THERMODYNAMIC MODEL FOR TOURMALINE

Mean field model The generalized Bragg-Williams model, a mean field theory, describes solid solutions by averaging site occupancies and neglecting individual site and local interactions focusing instead on the long range order (LRO) (Bragg and Williams 1934, 1935). This approach applies when site multiplicities represent averaged sites and partial, rather than full, occupancies describe the solid solution. Chemical components are defined based on a LRO averaged unit cell constrained by space group symmetry, determined via single-crystal X-ray diffraction (SC-XRD). It is essential to note that the unit cell, sites and partial occupancies are modelling constructs, and such occupancies do not physically exist. Defining endmembers as chemical components accounts for the averaged electron density, transcending a purely ionic model. The model assumes a random distribution of elements across equivalent sites.

Endmembers incorporate element exchange and charge balance constraints, with endmember reactions describing (combinations of) coupled substitutions. While the Bragg-Williams model captures long-range order, it is less effective for systems with significant short-range order or clustering due to its neglect of local interactions (Will 1998).

Tourmaline thermodynamic model We present two mean field tourmaline models: a speciation model, which defines endmembers through site fractions, and a compositional model, which uses bulk compositional parameters to define endmembers. Both models apply the Myhill and Connolly (2021) mathematical framework, utilising geometry, set theory, and linear algebra via

Burman (Myhill et al. 2023), to establish independent endmembers for a Bragg-Williams-type solid solution model (Thompson (1967; 1969), Powell and Holland (1999)). The polytope for tourmaline is constrained by site occupancy and charge, allowing for the enumeration of all possible endmembers of its chemical space by specifying species identity, valences, and total charge of non-exchanging species (Myhill and Connolly 2021).

2.1 Tourmaline Speciation Model

We begin with the definition of the most complex model, as it closely aligns with the original mineral structural formula.

Tourmaline speciation model: $XY_3Z_6T_6V_3W$ The tourmaline speciation model operates as a charge-balanced order-disorder system. To utilize this model, the complete structural formula of tourmaline, expressed in terms of site fractions, is essential. The charge balance constraint and the requirement that site fractions sum to 1 make some site fractions linearly dependent (Powell and Holland 1993, 1999). Both explicit and implicit order-disorder models are derived, differing in computational approach yet structurally identical (Myhill and Connolly 2021). Explicit models compute the full speciation space by assigning real site occupancies to each endmember, requiring global Gibbs free minimisation across all species—a robust but computationally intensive method (Myhill and Connolly 2021). Implicit models, however, simplify calculations by transforming independent endmembers in speciation space (site fractions) into bulk compositional endmembers, using Q ordering vectors to distribute bulk parameters across sites (Holland and Powell 1996a, 1996b) . By discretizing the composition space and performing local Gibbs minimisation for each composition, this method can reduce computational costs. As speciation is not known beforehand, the composition space must be defined by a set of fully disordered endmembers that span the compositional range (disordered limit, see Tajčmanová et al (2009)).

Explicit order-disorder model

Derivation of the speciation polytope In thermodynamic modelling of ionic solutions, defining crystallographic sites and the valences of ionic species occupying each site is essential for establishing linear constraints and inequalities. These include non-negative occupancies, complete site filling, charge balance, and site multiplicities, all of which form a convex polytope

(generalized polyhedron). (Myhill and Connolly 2021). This high-dimensional geometric shape represents all feasible configurations of site-species occupancies that comply with these constraints. Each polytope vertex is an endmember, a unique site population arrangement that collectively defines the bounds of the speciation space (Myhill and Connolly 2021). The polytope's dimensionality corresponds to the number of independent site-species configurations, each dimension representing a unique degree of freedom, plus one to make the sum of independent endmembers 1 (Myhill and Connolly 2021). Independent endmembers define these degrees of freedom as distinct axes, while dependent endmembers are combinations of these, positioned along edges or faces without adding dimensions (Myhill and Connolly 2021). The choice of independent endmembers is arbitrary and interchangeable, a result of the linearity assumption, which ensures that combinations of endmembers satisfy constraints while preserving convexity and dimensionality (Helffrich and Wood 1989; Holland and Powell 2003; Myhill and Connolly 2021). Convexity here refers to the requirement that all physically meaningful compositions lie within the convex hull formed by linear combinations of the chosen endmembers, ensuring the composition space is continuous and mathematically well-defined. Based on Gibbs' (1957) (reprint from his work from 1873) definition of a "component" as the minimum set of chemical entities needed to define the composition of all phases, tourmaline's variability is described by independent endmembers spanning its solid solution space. Connolly's (1990) generalized linearity assumption ensures any valid set of endmembers satisfies mass balance, preserves convexity, and maintains dimensionality, making their choice interchangeable. Convexity ensures all endmember combinations stay within the solid solution's compositional limits, capturing the full range of possible compositions and interactions. (Myhill and Connolly 2021). Defining site multiplicities assumes species are randomly distributed across equivalent sites, resulting in a polytope that represents a long-range ordered subset (generalized Bragg-Williams). In contrast, the complete polytope, which represents the full configurational space, would treat each site uniquely and include all possible configurations, capturing both long-range and short-range order (see Discussion chapter).

The original tourmaline formula is expressed as $\mathbf{XY_3Z_6(T_6O_{18})(BO_3)_3V_3W}$, capturing the crystallographic site topology. For the speciation model this formula is reduced to include only the variable sites, those that allow chemical substitution. Fixed sites, such as the $[B]_3$ triangle (occupied solely by B^{3+}) and the framework oxygen atoms $[O]_{18}+ 3 *[O]_3 = [O]_{27}$, are excluded

from the model. The reduced speciation model includes the following variable site populations $XY_3Z_6T_6V_3W$:

[Na Ca Vac][Fe^{2+} Mg Al Fe^{3+} Ti]$_3$[Al Mg Fe^{2+} Fe^{3+}]$_6$[Si Al B]$_6$[OH O]$_3$[OH O F]

Site occupancy constraints are represented by the matrix equation Px=b (Myhill and Connolly 2021). Matrix P specifies allowable species (elements, OH, or vacancies) at each crystallographic site, with rows for sites, columns for species. The last row of P captures species valences times site multiplicity (e^-) for charge balance. Vector b enforces total occupancy of 1 per site and overall charge neutrality. The site charge composition is balanced to 45 e^-, derived from 62 e^- for 31 O^{2-} minus charges for 4 anionic oxygens (V_3, W) and 3 fixed borons: $62 - (4 * 2) - (3 * 3) = 45e^-$. In the case of tourmaline, the charge balance constraint is independent and cannot be derived from other occupancy constraints; thus, P is a full-rank matrix**.** Solving the equation Px=b gives the set of linear equality constraints that the occupancy vector x must satisfy. Together with the inequality constraints $x_i \geq 0$, these equations define a convex polytope representing the entire accessible speciation space (Myhill and Connolly 2021).

$$P = \begin{Bmatrix} & \mathbf{Na} & \mathbf{Ca} & \mathbf{Vac} & \mathbf{Fe^{2+}} & \mathbf{Mg} & \mathbf{Al} & \mathbf{Fe^{3+}} & \mathbf{Ti} & \mathbf{Al} & \mathbf{Mg} & \mathbf{Fe^{2+}} & \mathbf{Fe^{3+}} & \mathbf{Si} & \mathbf{Al} & \mathbf{B} & \mathbf{OH} & \mathbf{O} & \mathbf{OH} & \mathbf{O} & \mathbf{F} \\ X & 1 & 1 & 1 & 0 & 0 & 0 & 0 & 0 & 0 & 0 & 0 & 0 & 0 & 0 & 0 & 0 & 0 & 0 & 0 & 0 \\ Y & 0 & 0 & 0 & 1 & 1 & 1 & 1 & 1 & 0 & 0 & 0 & 0 & 0 & 0 & 0 & 0 & 0 & 0 & 0 & 0 \\ Z & 0 & 0 & 0 & 0 & 0 & 0 & 0 & 0 & 1 & 1 & 1 & 1 & 0 & 0 & 0 & 0 & 0 & 0 & 0 & 0 \\ T & 0 & 0 & 0 & 0 & 0 & 0 & 0 & 0 & 0 & 0 & 0 & 0 & 1 & 1 & 1 & 0 & 0 & 0 & 0 & 0 \\ V & 0 & 0 & 0 & 0 & 0 & 0 & 0 & 0 & 0 & 0 & 0 & 0 & 0 & 0 & 0 & 1 & 1 & 0 & 0 & 0 \\ W & 0 & 0 & 0 & 0 & 0 & 0 & 0 & 0 & 0 & 0 & 0 & 0 & 0 & 0 & 0 & 0 & 0 & 1 & 1 & 1 \\ e^- & 1 & 2 & 0 & 6 & 6 & 9 & 9 & 12 & 18 & 12 & 12 & 18 & 24 & 18 & 18 & -3 & -6 & -1 & -2 & -1 \end{Bmatrix}$$

$$b = \begin{Bmatrix} X & Y & Z & T & V & W & e^- \\ 1 & 1 & 1 & 1 & 1 & 1 & 45 \end{Bmatrix}$$

The polytope defined by these constraints enables the use of geometric algorithms (e.g., vertex enumeration) to derive all possible endmembers, which are stored in matrix E (Myhill and Connolly 2021). Without a charge constraint, this approach would simply enumerate all site-species combinations, but tourmaline's charge constraint restricts the vertices to a hyperplane, resulting that some endmembers are disordered. The Python script solution_polytope_from_charge_balance (Burnman Software (Myhill et al. 2023)) was used to enumerate all possible endmembers of the polytope, creating the endmember matrix E, this process yielded 606 total endmembers (dependent and independent). Hawthorne (2012) applied these principles in Chemographic Exploration (Gagné and Hawthorne 2016), with a mathematical proof (Hawthorne 2021) showing that a dominant endmember formula can always

be defined for any mineral or crystal structure. However, handling 606 endmembers in thermodynamics (or possibly nomenclature) remains impractical.

Independent endmembers The number of independent endmembers is determined by the matrix P, where columns represent site species and rows represent site constraints. If the charge balance constraint is linearly independent of the site constraints, it adds one additional row (c = 1); if not, c = 0. The number of independent endmembers is then given by: $N_{\text{ind}} - 1 = n_{\text{site-species}} - (n_{\text{sites}} + c)$ (Myhill and Connolly 2021). This represents the number of degrees of freedom (DOF), defined as the number of variables (site species) minus the number of constraints (site occupancy plus charge). One additional endmember is required to close the compositional simplex. For the $XY_3Z_6T_6V_3W$ tourmaline model, with $n_{\text{site-species}} = 20$, nsites = 6 and c=1, so there are 14 independent endmembers. This means that the polytope has a dimension of 14, requiring only 14 independent endmembers to fully describe it, despite being bounded by 606 total endmembers. This significantly reduces complexity, as dependent endmembers grow geometrically while independent endmembers grow linearly with the number of sites (Myhill and Connolly 2021).

Independent endmembers can be obtained by row-reducing matrix E (e.g., via Gaussian elimination), however, to control the selection, we chose endmembers in E closest to known nomenclature, forming our preferred basis E_{ind}, and confirmed that its rank matched the number of independent endmembers to ensure linear independence. We aimed to use established nomenclature endmembers as the axes of our polytope. These components naturally occur in tourmalines with at least 50% abundance. This aids direct measurement, reduces the need for extrapolation, and limits the associated increase in uncertainty. The independent speciation endmember in terms of the original tourmaline formula in apfu K_{ind}:

$$K_{ind} = \begin{pmatrix} \text{Endmember} & 1X & 3Y & 6Z & 6T & 3B & 27O & 3V & W \\ \text{schorl (srl)} & Na & Fe_3 & Al_6 & Si_6 & B_3 & O_{27} & OH_3 & OH \\ \text{dravite (drv)} & Na & Mg_3 & Al_6 & Si_6 & B_3 & O_{27} & OH_3 & OH \\ \text{uvite (uvt)} & Ca & Mg_3 & MgAl_5 & Si_6 & B_3 & O_{27} & OH_3 & OH \\ \text{feruvite (fuvt)*} & Ca & Fe_3 & FeAl_5 & Si_6 & B_3 & O_{27} & OH_3 & OH \\ \text{foitite (foi)} & Vac & Fe_2Al & Al_6 & Si_6 & B_3 & O_{27} & OH_3 & OH \\ \text{olenite (ole)} & Na & Al_3 & Al_6 & Si_6 & B_3 & O_{27} & O_3 & OH \\ \text{dravite-disordered (drvdis)*} & Na & Mg_2Al & MgAl_5 & Si_6 & B_3 & O_{27} & OH_3 & OH \\ \text{oxy-dravite (odrv)} & Na & Al_2Mg_1 & MgAl_5 & Si_6 & B_3 & O_{27} & OH_3 & O \\ \text{fluor-uvite (fluvt)} & Ca & Mg_3 & MgAl_5 & Si_6 & B_3 & O_{27} & OH_3 & F \\ \text{buergerite (bu)*} & Na & Fef_3 & Al_6 & Si_6 & B_3 & O_{27} & O_3 & OH \\ \text{magnesium-dutrowite (mdtw)*} & Na & MgTi_2 & Al_6 & Si_6 & B_3 & O_{27} & O_3 & O \\ \text{boron-olenite (bole)} & Na & Al_3 & Al_6 & Si_3B_3 & B_3 & O_{27} & OH_3 & OH \\ \text{alumina-oxy-rossmanite (aorsm)} & Vac & Al_3 & Al_6 & Si_5Al_1 & B_3 & O_{27} & OH_3 & O \\ \text{povondraite (pov)} & Na & Fef_3 & Fef_4Mg_2 & Si_6 & B_3 & O_{27} & OH_3 & O \end{pmatrix}$$

*Adjustments included: placing Fe^{2+} on Z in fuvt to allow Fe^{2+} occupancy there and ensure linear independence; selecting bu-OH over fluor-buergerite (Fbu) to decouple F and Fe^{3+}, to ease projection of the model to lower chemical subspaces; and reconfiguring mdtw with maximized Ti on Y, leaving V and W vacant to avoid fractional occupancies. Dravite-disordered (drvdis) is linearly independent and was included to separate Al–Mg and OH–O disordering across the Y/Z and V/W sites, which are both combined in the odrv endmember. It was retained despite not being an endmember under IMM rules (Bosi et al., 2019).(Bosi et al. 2019). This example highlights that mineral nomenclature, while essential for classification, imposes constraints that limit its usefulness in thermodynamic modelling. These include artificial boundaries like the 50% rule, which fails to capture continuous occupancy variations in solid solutions below this threshold, and arbitrary restrictions that prevent naming new species for disordered states—limiting full representation of site-species interactions.

The nomenclature fuvt, mdtw, bu-F are derivable as linear combinations as are the rest of the nomenclature tourmaline within the [Na Ca Vac][Fe^{2+} Mg Al Fe^{3+} Ti]$_3$[Al Mg Fe^{2+} Fe^{3+}]$_6$[Si Al B]$_6$*[B]$_3$[O]$_{27}$*[OH O]$_3$[OH O F] system, and are not further considered here (e.g. Lucchesite, adachiite, bosiite, dutrowite, ect). This shows that many nomenclature endmembers under linearity assumptions are dependent and redundant. This highlights a problem with current nomenclature: with 606 potential endmembers in our chemical subsystem, many meeting IMA-CNMNC rules, we would quickly run out of names honoring distinguished mineralogists often used to name new mineral species. Instead, these polytope endmembers could be more efficiently described using a compact, independent set, provided negative endmember fractions

are accepted. If positive fractions are needed one can always recast the independent endmember fractions into linear combinations which are always positive (see Chapter 5).

Each independent endmember is essential to the model; removing even an unusual one would reduce the polytope's dimensionality, making dependent endmembers on that dimension inaccessible. This impacts projections to subchemical systems: if a certain independent endmember does not exist within restricted bulk compositions but other dependent endmembers along that same dimension do exist, the independent basis of the solution model must be recalculated using the methods from Myhill & Connolly (2021).

The stoichiometry matrix E_{ind} in terms of site fractions of the complete set of site-species is:

Eind

$$
= \begin{array}{c}
\begin{array}{cccccccccccccccccccc}
 & x_{\mathrm{nax}} & x_{\mathrm{cax}} & x_{\mathrm{vx}} & x_{\mathrm{fey}} & x_{\mathrm{mgy}} & x_{\mathrm{aly}} & x_{\mathrm{fefy}} & x_{\mathrm{Tiy}} & x_{\mathrm{alz}} & x_{\mathrm{mgz}} & x_{\mathrm{fez}} & x_{\mathrm{fefz}} & x_{\mathrm{sit}} & x_{\mathrm{alt}} & x_{\mathrm{bt}} & x_{\mathrm{OHv}} & x_{\mathrm{Ov}} & x_{\mathrm{OHw}} & x_{\mathrm{Ow}} & x_{\mathrm{Fw}}
\end{array} \\
\begin{array}{c}
\mathrm{srl} \\ \mathrm{drv} \\ \mathrm{uvt} \\ \mathrm{fuvt} \\ \mathrm{foi} \\ \mathrm{ole} \\ \mathrm{drv\text{-}dis} \\ \mathrm{odrv} \\ \mathrm{fluvt} \\ \mathrm{bu} \\ \mathrm{mdtw} \\ \mathrm{bole} \\ \mathrm{aorsm} \\ \mathrm{pov}
\end{array}
\begin{pmatrix}
1 & 0 & 0 & 1 & 0 & 0 & 0 & 0 & 1 & 0 & 0 & 0 & 1 & 0 & 0 & 1 & 0 & 1 & 0 & 0 \\
1 & 0 & 0 & 0 & 1 & 0 & 0 & 0 & 1 & 0 & 0 & 0 & 1 & 0 & 0 & 1 & 0 & 1 & 0 & 0 \\
0 & 1 & 0 & 0 & 1 & 0 & 0 & 0 & \frac{5}{6} & \frac{1}{6} & 0 & 0 & 1 & 0 & 0 & 1 & 0 & 1 & 0 & 0 \\
0 & 1 & 0 & 1 & 0 & 0 & 0 & 0 & \frac{5}{6} & 0 & \frac{1}{6} & 0 & 1 & 0 & 0 & 1 & 0 & 1 & 0 & 0 \\
0 & 0 & 1 & \frac{2}{3} & 0 & \frac{1}{3} & 0 & 0 & 1 & 0 & 0 & 0 & 1 & 0 & 0 & 1 & 0 & 1 & 0 & 0 \\
1 & 0 & 0 & 0 & 0 & 1 & 0 & 0 & 1 & 0 & 0 & 0 & 1 & 0 & 0 & 0 & 1 & 1 & 0 & 0 \\
1 & 0 & 0 & 0 & \frac{2}{3} & \frac{1}{3} & 0 & 0 & \frac{5}{6} & \frac{1}{6} & 0 & 0 & 1 & 0 & 0 & 1 & 0 & 1 & 0 & 0 \\
1 & 0 & 0 & 0 & \frac{1}{3} & \frac{2}{3} & 0 & 0 & \frac{5}{6} & \frac{1}{6} & 0 & 0 & 1 & 0 & 0 & 1 & 0 & 0 & 1 & 0 \\
0 & 1 & 0 & 0 & 1 & 0 & 0 & 0 & \frac{5}{6} & \frac{1}{6} & 0 & 0 & 1 & 0 & 0 & 1 & 0 & 0 & 0 & 1 \\
1 & 0 & 0 & 0 & 0 & 0 & 1 & 0 & 1 & 0 & 0 & 0 & 1 & 0 & 0 & 0 & 1 & 1 & 0 & 0 \\
1 & 0 & 0 & 0 & \frac{1}{3} & 0 & 0 & \frac{2}{3} & 1 & 0 & 0 & 0 & 1 & 0 & 0 & 0 & 1 & 0 & 1 & 0 \\
1 & 0 & 0 & 0 & 0 & 1 & 0 & 0 & 1 & 0 & 0 & 0 & \frac{1}{2} & 0 & \frac{1}{2} & 1 & 0 & 1 & 0 & 0 \\
0 & 0 & 1 & 0 & 0 & 1 & 0 & 0 & 1 & 0 & 0 & 0 & \frac{5}{6} & \frac{1}{6} & 0 & 1 & 0 & 0 & 1 & 0 \\
1 & 0 & 0 & 0 & 0 & 0 & 1 & 0 & 0 & \frac{2}{6} & 0 & \frac{4}{6} & 1 & 0 & 0 & 1 & 0 & 0 & 1 & 0
\end{pmatrix}
\end{array}
$$

Selection of Robust Independent Site Fraction Set for Endmember Description To describe the independent endmember set, we have to select 14 site fractions from $n_{\text{site-species}}$=20, as these uniquely map to the 14 independent endmembers and satisfy all constraints (occupancy and -charge balance). The remaining 6 fractions are dependent and add no new information. This is

shown by converting the nonsquare stoichiometry matrix to an apfu matrix via site multiplicities, where its Nullspace reveals 14 degrees of freedom, yielding 6 dependency equations:

$$-\mathrm{aly} - 3\mathrm{cax} - \mathrm{fefy} - 2\mathrm{fey} - \mathrm{fez} + \mathrm{Fw} - 2\mathrm{mgy} - \mathrm{mgz} - 4\mathrm{nax} + \mathrm{OHv} + \mathrm{OHw} + \mathrm{sit} - 5\mathrm{vx}$$

$$\mathrm{aly} + 2\mathrm{cax} + \mathrm{fefy} + 2\mathrm{fey} + \mathrm{fez} + 2\mathrm{mgy} + \mathrm{mgz} + 3\mathrm{nax} - \mathrm{OHv} + \mathrm{Ow} - \mathrm{sit} + 4\mathrm{vx}$$

$$-3\mathrm{cax} - 3\mathrm{nax} + \mathrm{OHv} + \mathrm{Ov} - 3\mathrm{vx}$$

$$\mathrm{alt} + \mathrm{bt} - 6\mathrm{cax} - 6\mathrm{nax} + \mathrm{sit} - 6\mathrm{vx}$$

$$\mathrm{alz} - 6\mathrm{cax} + \mathrm{fefz} + \mathrm{fez} + \mathrm{mgz} - 6\mathrm{nax} - 6\mathrm{vx}$$

$$\mathrm{aly} - 3\mathrm{cax} + \mathrm{fefy} + \mathrm{fey} + \mathrm{mgy} - 3\mathrm{nax} + \mathrm{tiy} - 3\mathrm{vx}$$

Ideally, any independent set would work if tourmaline chemistry were perfectly measured and the model matched chemistries and charge balance exactly; however, given practical measurement limitations, we sought a robust set. Using our database, we tested measured tourmaline formulas (normalised projected) and enumerated 20,639 possible independent site fraction sets with a Mathematica script. After filtering for consistency (removing sets for which our measured compositions gave rise to negative or non-summing-to-1 endmember fractions), 9,541 robust sets remained. We calculated the mean and standard deviation of endmember fractions across the 9,541 robust sets to assess uncertainty in choosing different robust independent site fraction sets (see Electronic Appendix 2A). Our final selected set is:

$$\{x_{\mathrm{NaX}}, x_{\mathrm{CaX}}, x_{\mathrm{FeY}}, x_{\mathrm{MgY}}, x_{\mathrm{AlY}}, x_{\mathrm{FefY}}, x_{\mathrm{TiY}}, x_{\mathrm{AlZ}}, x_{\mathrm{MgZ}}, x_{\mathrm{FeFZ}}, x_{\mathrm{SiT}}, x_{\mathrm{AlT}}, x_{\mathrm{OHV}}, x_{\mathrm{FW}}\}$$

where Fe is ferrous and Fef is ferric iron (and therefore require Mossbauer or equivalent techniques).

In a later step, we apply a projection method in which charge balance is explicitly enforced, ensuring all sets yield valid model inputs. However, the robust set above is provided for cases where users prefer to work without projection, or when model applications require independently specified site occupancies.

Alternatively, measured tourmaline formulas can be fit using multiple linear regression, but this often yields lengthy equations with insignificant coefficients. We chose analytical equations as fixed site fractions to map site fractions to independent endmember space, meeting thermodynamic software requirements, reducing uncertainty in well-constrained sites, and concentrating it in dependent ones, unlike least squares, which distributes uncertainty evenly.

Mapping from Site Fraction Space to Independent Endmember Space The square independent endmember stoichiometry matrix using these 14 independent site fractions is (Find):

$$\text{Find} = \begin{array}{c|cccccccccccccc} & x_{nax} & x_{\text{cax}} & x_{\text{fey}} & x_{\text{mgy}} & x_{\text{aly}} & x_{\text{fefy}} & x_{\text{tiy}} & x_{\text{alz}} & x_{\text{mgz}} & x_{\text{fefz}} & x_{\text{sit}} & x_{\text{alt}} & x_{\text{OHv}} & x_{\text{Fw}} \\ \hline \text{srl} & 1 & 0 & 1 & 0 & 0 & 0 & 0 & 1 & 0 & 0 & 1 & 0 & 1 & 0 \\ \text{drv} & 1 & 0 & 0 & 1 & 0 & 0 & 0 & 1 & 0 & 0 & 1 & 0 & 1 & 0 \\ \text{uvt} & 0 & 1 & 0 & 1 & 0 & 0 & 0 & \left(\frac{5}{6}\right) & \left(\frac{1}{6}\right) & 0 & 1 & 0 & 1 & 0 \\ \text{fuvt} & 0 & 1 & 1 & 0 & 0 & 0 & 0 & \left(\frac{5}{6}\right) & 0 & 0 & 1 & 0 & 1 & 0 \\ \text{foi} & 0 & 0 & \left(\frac{2}{3}\right) & 0 & \left(\frac{1}{3}\right) & 0 & 0 & 1 & 0 & 0 & 1 & 0 & 1 & 0 \\ \text{ole} & 1 & 0 & 0 & 0 & 1 & 0 & 0 & 1 & 0 & 0 & 1 & 0 & 0 & 0 \\ \text{drvdis} & 1 & 0 & 0 & \left(\frac{2}{3}\right) & \left(\frac{1}{3}\right) & 0 & 0 & \left(\frac{5}{6}\right) & \left(\frac{1}{6}\right) & 0 & 1 & 0 & 1 & 0 \\ \text{odrv} & 1 & 0 & 0 & \left(\frac{1}{3}\right) & \left(\frac{2}{3}\right) & 0 & 0 & \left(\frac{5}{6}\right) & \left(\frac{1}{6}\right) & 0 & 1 & 0 & 1 & 0 \\ \text{fluvt} & 0 & 1 & 0 & 1 & 0 & 0 & 0 & \left(\frac{5}{6}\right) & \left(\frac{1}{6}\right) & 0 & 1 & 0 & 1 & 1 \\ \text{bu} & 1 & 0 & 0 & 0 & 0 & 1 & 0 & 1 & 0 & 0 & 1 & 0 & 0 & 0 \\ \text{mdtw} & 1 & 0 & 0 & \left(\frac{1}{3}\right) & 0 & 0 & \left(\frac{2}{3}\right) & 1 & 0 & 0 & 1 & 0 & 0 & 0 \\ \text{bole} & 1 & 0 & 0 & 0 & 1 & 0 & 0 & 1 & 0 & 0 & \left(\frac{1}{2}\right) & 0 & 1 & 0 \\ \text{aorsm} & 0 & 0 & 0 & 0 & 1 & 0 & 0 & 1 & 0 & 0 & \left(\frac{5}{6}\right) & \left(\frac{1}{6}\right) & 1 & 0 \\ \text{pov} & 1 & 0 & 0 & 0 & 0 & 1 & 0 & 0 & \left(\frac{2}{6}\right) & \left(\frac{4}{6}\right) & 1 & 0 & 1 & 0 \end{array}$$

We derived the mapping equations from the site fraction to the independent endmember coordinate system by obtaining the inverse of the independent endmember matrix in terms of independent site fractions.

$$y_{\mathrm{slr}} = 4 \cdot x_{\mathrm{alt}} - \frac{20 \cdot x_{\mathrm{aly}}}{3} + 6 \cdot x_{\mathrm{alz}} + \frac{2 \cdot x_{\mathrm{cax}}}{3} - \frac{20 \cdot x_{\mathrm{fefy}}}{3} + 6 \cdot x_{\mathrm{fefz}} - \frac{17 \cdot x_{\mathrm{fey}}}{3} - \frac{20 \cdot x_{\mathrm{mgy}}}{3} + 6 \cdot x_{\mathrm{mgz}} + \frac{2 \cdot x_{\mathrm{max}}}{3} - \frac{20 \cdot x_{\mathrm{tiy}}}{3}$$

$$y_{\mathrm{drv}} = -2 \cdot x_{\mathrm{alt}} - \frac{7 \cdot x_{\mathrm{aly}}}{3} + \frac{x_{\mathrm{cax}}}{3} - \frac{7 \cdot x_{\mathrm{fcfy}}}{3} + \frac{3 \cdot x_{\mathrm{fefz}}}{2} - \frac{10 \cdot x_{\mathrm{fcy}}}{3} - \frac{7 \cdot x_{\mathrm{mgy}}}{3} - 6 \cdot x_{\mathrm{mgz}} + \frac{x_{\mathrm{nax}}}{3} + x_{\mathrm{OHv}} + 2 \cdot x_{\mathrm{sit}} - \frac{7 \cdot x_{\mathrm{tiy}}}{3}$$

$$y_{\mathrm{uvt}} = -6 \cdot x_{\mathrm{aly}} + 6 \cdot x_{\mathrm{alz}} + x_{\mathrm{cax}} - 6 \cdot x_{\mathrm{fefy}} + 6 \cdot x_{\mathrm{fcfz}} - 6 \cdot x_{\mathrm{fey}} - x_{\mathrm{Fw}} - 6 \cdot x_{\mathrm{mgy}} + 6 \cdot x_{\mathrm{mgz}} - 6 \cdot x_{\mathrm{tiy}}$$

$$y_{\mathrm{fuvt}} = 6 \cdot x_{\mathrm{aly}} - 6 \cdot x_{\mathrm{alz}} + 6 \cdot x_{\mathrm{fefy}} - 6 \cdot x_{\mathrm{fefz}} + 6 \cdot x_{\mathrm{fey}} + 6 \cdot x_{\mathrm{mgy}} - 6 \cdot x_{\mathrm{mgz}} + 6 \cdot x_{\mathrm{tiy}}$$

$$y_{\mathrm{foi}} = -6 \cdot x_{\mathrm{alt}} + x_{\mathrm{aly}} - x_{\mathrm{cax}} + x_{\mathrm{fefy}} + x_{\mathrm{fey}} + x_{\mathrm{mgy}} - x_{\mathrm{nax}} + x_{\mathrm{tiy}}$$

$$y_{\mathrm{ole}} = x_{\mathrm{aly}} + \frac{3 \cdot x_{\mathrm{fefz}}}{2} + x_{\mathrm{fey}} + x_{\mathrm{mgy}} - x_{\mathrm{OHv}} - \frac{x_{\mathrm{tiy}}}{2}$$

$$y_{\mathrm{drvdis}} = 6 \cdot x_{\mathrm{alt}} + 19 \cdot x_{\mathrm{aly}} - 12 \cdot x_{\mathrm{alz}} - 3 \cdot x_{\mathrm{cax}} + 19 \cdot x_{\mathrm{fefy}} - \frac{27 \cdot x_{\mathrm{fefz}}}{2} + 22 \cdot x_{\mathrm{fcy}} + 22 \cdot x_{\mathrm{mgy}} - x_{\mathrm{max}} - 3 \cdot x_{\mathrm{OHv}} - 6 \cdot x_{\mathrm{sit}} + \frac{35 \cdot x_{\mathrm{tiy}}}{2}$$

$$y_{\mathrm{odrv}} = -6 \cdot x_{\mathrm{alt}} - 13 \cdot x_{\mathrm{aly}} + 6 \cdot x_{\mathrm{alz}} + 2 \cdot x_{\mathrm{cax}} - 13 \cdot x_{\mathrm{fefy}} + \frac{9 \cdot x_{\mathrm{fefz}}}{2} - 16 \cdot x_{\mathrm{fey}} - 16 \cdot x_{\mathrm{mgy}} + x_{\mathrm{nax}} + 3 \cdot x_{\mathrm{OHv}} + 6 \cdot x_{\mathrm{sit}} - \frac{23 \cdot x_{\mathrm{tiy}}}{2}$$

$$y_{\mathrm{fluvt}} = x_{\mathrm{Fw}}$$

$$y_{\mathrm{bu}} = x_{\mathrm{fefy}} - \frac{3 \cdot x_{\mathrm{fefz}}}{2}$$

$$y_{\mathrm{mdtw}} = \frac{3 \cdot x_{\mathrm{tiy}}}{2}$$

$$y_{\mathrm{bole}} = -2 \cdot x_{\mathrm{alt}} + 2 \cdot x_{\mathrm{aly}} + 2 \cdot x_{\mathrm{fefy}} + 2 \cdot x_{\mathrm{fey}} + 2 \cdot x_{\mathrm{mgy}} - 2 \cdot x_{\mathrm{sit}} + 2 \cdot x_{\mathrm{tiy}}$$

$$y_{\mathrm{aorsm}} = 6 \cdot x_{\mathrm{alt}}$$

$$y_{\mathrm{pov}} = \frac{3 \cdot x_{\mathrm{fefz}}}{2}$$

In this model, species mix across multiple sites (e.g., Fe^{2+}, Mg, and Fe^{3+} across Y and Z; Al across Y, Z, and T; OH and O across V and W), forming an order-disorder solution where composition and speciation spaces are non-equivalent. Here, we define an ordered endmember as

one where each site is occupied by a single species. Thus, slr, drv, ole and bu are ordered endmembers, while all others are disordered.

Implicit order-disorder model In the speciation model, species can redistribute across sites while keeping bulk composition fixed, making the site speciation space larger than the compositional space. Order-disorder reactions are described by isochemical reactions within or between endmembers. An implicit order-disorder model is achieved by transforming a complete set of independent endmembers in speciation space (site fractions) into a combination of compositional endmembers (bulk parameters) in composition space, along with Q ordering vectors to partition bulk parameters across sites (Holland and Powell 1996a, 1996b). This demonstrates that the basis can alternatively be described by isochemical reactions rather than endmembers (Myhill and Connolly 2021). The basis of independent reactions is found by calculating the nullspace of the stoichiometric matrix S_{ind}, which expresses the compositions of the independent endmembers in terms of bulk components (atoms per formula unit). This nullspace identifies linear dependencies among the endmembers—i.e., combinations that sum to zero change in total composition—and represents internal isochemical reactions among them (Myhill and Connolly 2021).

Sind =

	na	ca	vac	fe	mg	al	fef	ti	si	B	OH	F	O
srl	1	0	0	3	0	6	0	0	6	3	4	0	0
drv	1	0	0	0	3	6	0	0	6	3	4	0	0
uvt	0	1	0	0	4	5	0	0	6	3	4	0	0
fuvt	0	1	0	4	0	5	0	0	6	3	4	0	0
foi	0	0	1	2	0	7	0	0	6	3	4	0	0
ole	1	0	0	0	0	9	0	0	6	3	1	0	3
drvdis	1	0	0	0	3	6	0	0	6	3	4	0	0
odrv	1	0	0	0	2	7	0	0	6	3	3	0	1
fluvt	0	1	0	0	4	5	0	0	6	3	3	1	0
bu	1	0	0	0	0	6	3	0	6	3	1	0	3
mdtw	1	0	0	0	1	6	0	2	6	3	0	0	4
bole	1	0	0	0	0	9	0	0	3	6	4	0	0
aorsm	0	0	1	0	0	10	0	0	5	3	3	0	1
pov	1	0	0	0	2	0	7	0	6	3	3	0	1

Mathematically, any vector R_{ind} in the nullspace satisfies: $S_{\text{ind}} \cdot R_{\text{ind}} = 0$. Each row vector in R_{ind} is a balanced reaction: the left-hand side (negative coefficients) and right-hand side

(positive coefficients) consist of different combinations of endmembers that together conserve the total number of atoms of each bulk component. This gives 4 reactions R_{ind}:

$$\text{-2 drv - 7 bu + 6 ole + 3 pov}$$
$$\text{-2 drv - ole + 3 odrv}$$
$$\text{-drv+ drvdis}$$
$$\text{4 drv + 3 fuvt - 4 srl- 3 uvt}$$

Each of these reflects redistribution of atoms within the solid solution space (e.g., order–disorder or coupled substitutions), without changing the overall bulk chemistry. In analyzing site-species redistribution within R_{ind}, the dot product of reaction vectors R_{ind} with the transpose of the stoichiometry matrix in site fractions $Eind^T$ generates isochemical reactions in terms of site exchanges, represented as ordering vectors Q (Myhill and Connolly 2021):

$$Q1 = 6\text{aly} - 3\text{alz} - 4\text{fefy} + 2\text{fefz} - 2\text{mgy} + \text{mgz} + 0\text{Hv} - 3\text{OHw} - 0\text{v} + 3\text{Ow}$$

$$\text{Q2} = \text{aly} - \frac{\text{alz}}{2} - \text{mgy} + \frac{\text{mgz}}{2} + \text{OHv} - 3\text{OHw} - \text{Ov} + 3\text{Ow}$$

$$Q3 = \frac{\text{aly}}{3} - \frac{\text{alz}}{6} - \frac{\text{mgy}}{3} + \frac{\text{mgz}}{6}$$

$$Q4 = -\text{fey} + \frac{\text{fez}}{2} + \text{mgy} - \frac{\text{mgz}}{2}$$

Ordering vectors simplify speciation space by projecting it into bulk compositional space, reducing dimensions. This approach projects the site species polytope along ordering vectors onto a bulk composition hyperplane, allowing the model to be represented through bulk compositionally independent endmembers and order parameters. The resulting shape remains convex because linear projections of convex sets are themselves convex, ensuring the thermodynamic model maintains a physically meaningful, stable solution space. Four speciation endmembers are replaced by ordering vectors Q, with remaining endmembers derived from bulk parameters instead of site fractions. The maximum disordered limit is obtained by setting Q =0. Holland and Powell solid solution models commonly define speciation endmembers in order-disorder models using bulk parameters and Q vectors (Powell and Holland 1999; White et al.

2007; Green et al. 2016; Weller et al. 2024), and other authors have since adopted this formulation (Dachs and Benisek 2019, 2021, 2024; Dachs et al. 2021).

Isochemical Q vectors indicate how bulk parameters are distributed across sites to reproduce independent speciation endmembers, which appear dependent in terms of bulk parameters. Our model includes isochemical homogeneous reactions between endmembers with identical bulk compositions (e.g., -drv + drvdis, reaction 3) and heterogeneous isochemical reactions among multiple endmembers which individually have distinct bulk compositions (e.g., 4 “drv” + 3 “fuvt” - 4 “srl” - 3 “uvt”, reaction 4). All Q vectors must be retained when projecting to lower chemical subsystems. One unfortunate consequence of using heterogeneous isochemical reactions is for instance, that projecting to an Mg-free system would eliminate Al-Fe and Fe-Al substitutions, requiring a basis transformation. Homogeneous isochemical reactions are simpler to interpreted as the Q vector is directly related to the ordering/disordering of elements among sites, as disordered endmembers share bulk composition with ordered counterparts, which facilitates easy projections to lower chemical subsystems. However, we prioritised naturally occurring disordered endmembers over theoretical ones, as these can be physically measured and have been observed in nature at ≥50% concentrations, the IMA-CNMNC requirement for designation as a nomenclature endmember

Homogeneous Q3 involves Mg-Al disorder among Y-Z sites (drvdis = drv, disordered = ordered). Heterogeneous isochemical reactions are more complex to interpret and require a basis change to yield homogeneous isochemical reactions; however, by qualitatively analyzing and removing redundancies across the Q vectors, we can identify the site-specific ordering reactions represented. Although each isochemical reaction corrects for bulk composition differences between ordered and disordered endmembers using additional endmembers, the main order-disorder interactions are as follows: Fe^{2+}-Al ordering among Y-Z aligns with Q4 (fuvt = uvt), Fe^{3+}-Al ordering among Y-Z with Q1 (pov = bu), and OH-O ordering among V-W with Q2 (odrv = drv). Fe-Mg ordering among Y-Z sites is dependent, as is order-disorder on the T site, constrained by site fraction summing to 1. B^T is any B > 3 apfu, and $Al^T=6-Si-B^T$. In natural samples, BT was fixed at 3 apfu (no B on T), but in the synthetic olenite, BT > 3, indicating B–Si substitution at T. AlT was adjusted accordingly to maintain a total T-site occupancy of 6 apfu.

2.2 Tourmaline Bulk Compositional Model

Many users of the thermodynamic model will only have bulk compositional data, without detailed site occupancy information from techniques such as single-crystal XRD. Because site distributions control key thermodynamic properties like entropy and free energy, traditional thermodynamic modelling requires more than just bulk chemistry. To overcome this, the bulk compositional model simplifies the problem by removing endmembers which become invariant in bulk compositional parameters by grouping chemically active sites which are similar. This allows thermodynamic properties to be modelled directly from bulk compositions without assuming specific site assignments. It avoids large errors associated with heuristic site-distribution rules and enables modelling of phase stability and compositional trends even when ordering is unknown. In addition, by merging sites together, the model effectively reduces the dimensionality of composition space, allowing a lower-parameter thermodynamic model to be calibrated. This loosening of compositional constraints increases the robustness of the fit, not by introducing greater uncertainty in thermodynamic properties, but by allowing greater flexibility in composition space to accommodate natural variations across a broad range of samples.

Tourmaline reciprocal model with dependent speciation: $X(YZ)_9Si_xAl_{(1-x)}(VW)_4$ The compositional model aids thermodynamic modelling for users with only chemical data, providing insights into property variations despite incomplete structural information. The original tourmaline formula is expressed as $\mathbf{XY_3Z_6(T_6O_{18})(BO_3)_3V_3W}$. To obtain the reciprocal formula from the original tourmaline formula, we remove all atoms that are structurally fixed and do not participate in substitution or disorder. These include:

- B at the $[BO_3]_3$ group: B is always present as 3 apfu and does not vary.
- Framework oxygen atoms: 18 from T_6O_{18} and 9 from $[BO_3]_3$ groups, totaling 27 O atoms that are not substitutable.

Excluding these leaves only the X, Y, Z, T, V, and W sites with variable cation and anion occupancy. To express this in reciprocal form:

1. **Combine $Y_3 + Z_6 = (YZ)_9$**: These are the octahedral sites that can accommodate various cations (e.g., Mg, Fe^{2+}, Al, Ti, Fe^{3+}).

2. **Reduce T_6 to SixAl(1–x)**: Since T-site occupancy is constrained to Si and Al only, and total T = 6, Al content is directly dependent on Si (i.e., $Al_t = 6 - Si$).
3. **Merge the V_3 and W sites into $(VW)_4$**: these sites host anions (OH, O, F), but in most tourmaline compositions, the substitution is across the combined (VW) group due to crystallographic and energetic similarities.

Thus, the simplified **reciprocal formula** (Wood and Nicholls 1978; Powell and Holland 1993; Connolly 2016) with dependent speciation becomes:

$X(YZ)_9Si_xAl_{(1-x)}(VW)_4$

Aluminium occurs twice across two sites, typically indicating order-disorder, but here, T-site Al depends directly on Si in $Si_xAl_{(1-x)}$ and cannot independently order. Thus, speciation is fixed by the site occupancy constraint. In the rest of the model, $X(YZ)_9(VW)_4$, each species is confined to a single site, so each speciation point is uniquely defined by a bulk composition, making composition and speciation spaces identical, a pure reciprocal model described by bulk parameters.

Derivation of the reciprocal model with dependent speciation Derivation of the bulk model follows the same steps as the speciation model and thus references are not duplicated.

$X(YZ)_9Si_xAl_{(1-x)}(VW)_4$ with: [Na, Ca, Vac][Fe^{2+},Mg, Al, Fe^{3+},Ti]$_9$[Si,Al]$_6$[OH, O, F]$_4$.

Site charges are as follows: [1,2,0],[18,18,27,27,36],[24,18],[−4,−8,−4], balanced again to 45 e^-. B is excluded from the T site; though theoretically constrained by bulk composition, it was omitted in this model for robustness. The P matrix and b vector are:

$$P = \begin{pmatrix} & \text{Na} & \text{Ca} & \text{Vac} & \text{Fe}^{2+} & \text{Mg} & \text{Al} & \text{Fc}^{3+} & \text{Ti} & \text{Si} & \text{Al} & \text{OH} & \text{O} & \text{F} \\ X & 1 & 1 & 1 & 0 & 0 & 0 & 0 & 0 & 0 & 0 & 0 & 0 & 0 \\ (YZ) & 0 & 0 & 0 & 1 & 1 & 1 & 1 & 1 & 0 & 0 & 0 & 0 & 0 \\ T & 0 & 0 & 0 & 0 & 0 & 0 & 0 & 0 & 1 & 1 & 0 & 0 & 0 \\ (VW) & 0 & 0 & 0 & 0 & 0 & 0 & 0 & 0 & 0 & 0 & 1 & 1 & 1 \\ e- & 1 & 2 & 0 & 18 & 18 & 27 & 27 & 36 & 24 & 18 & -4 & -8 & -4 \end{pmatrix}$$

$$b = \begin{pmatrix} X & (YZ) & T & (VW) & e^- \\ 1 & 1 & 1 & 1 & 45 \end{pmatrix}$$

These equality constraints were used in vertex enumeration to obtain a polytope with 104 endmembers. The charge balance constraint, independent of composition, defines a hyperplane in bulk composition polytope, as occupancy of unequal valences occurs on three sites $X(YZ)_9(VW)_4$ and are interdependent. For the $X(YZ)_9Si_xAl_{(1-x)}(VW)_4$ model, $n_{site\text{-}species}$ = 13, nsites = 4 and c=1, so there are 9 independent endmembers. We selected the following 9 independent endmembers to describe the dimensions of the 9D hyperplane in the composition polytope. The complete bulk formulas of the independent endmemeber set for the bulk model including the sites with fixed occupancy are:

K_{ind} =

	1X	9(YZ)	6T	3B	27O	4(VW)
schorl (srlB)	Na	Fe_3Al_6	Si_6	B_3	O_{27}	OH_4
dravite (drvB)	Na	Mg_3Al_6	Si_6	B_3	O_{27}	OH_4
uvite (uvtB)	Ca	Mg_4Al_5	Si_6	B_3	O_{27}	OH_4
foitite (foiB)	Vac	Fe_2Al_7	Si_6	B_3	O_{27}	OH_4
olenite (oleB)	Na	Al_9	Si_6	B_3	O_{27}	OH_3
fluor-uvite (fluvtB)	Ca	Mg_4Al_5	Si_6	B_3	O_{27}	OH_3F
buergerite (buB)*	Na	Fef_3Al_6	Si_6	B_3	O_{27}	OH_3
magnesium-dutrowite (mdtwB)*	Na	$MgTi_2Al_6$	Si_6	B_3	O_{27}	O_4
alumina-oxy-rossmanite (aorsmB)	Vac	Al_9	Si_5Al	B_3	O_{27}	OH_3O

Asterix indicate the same modifications compared to the nomenclature endmembers as in the speciation model. We added an additional B to the abbreviation to indicate that it is an endmember defined using bulk parameters.

The stoichiometry matrix in terms of the complete set of bulk parameters is:

E_{ind} =

	na	ca	vac	fe	mg	al	fef	ti	si	B	OH	F	O
shlB	1	0	0	3	0	6	0	0	6	3	4	0	0
drvB	1	0	0	0	3	6	0	0	6	3	4	0	0
uvtB	0	1	0	0	4	5	0	0	6	3	4	0	0
foiB	0	0	1	2	0	7	0	0	6	3	4	0	0
oleB	1	0	0	0	0	9	0	0	6	3	1	0	3
fluvtB	0	1	0	0	4	5	0	0	6	3	3	1	0
buB	1	0	0	0	0	6	3	0	6	3	1	0	3
mdtwB	1	0	0	0	1	6	0	2	6	3	0	0	4
aorsmB	0	0	1	0	0	10	0	0	5	3	3	0	1

Selection of Robust Independent Bulk Parameter Set for Endmember Description The null space of the stoichiometry matrix reveals 4 linear dependencies among bulk parameters in the bulk composition model:

$$\mathrm{al} - 13\mathrm{ca} + 2\mathrm{fe} + \mathrm{fef} + 2\mathrm{mg} - 12\mathrm{na} + \mathrm{O} - 11\mathrm{vac}$$

$$-\mathrm{al} + 9\mathrm{ca} + \mathrm{F} - 2\mathrm{fe} - \mathrm{fef} - 2\mathrm{mg} + 8\mathrm{na} + \mathrm{OH} + 7\mathrm{vac}$$

$$\mathrm{B} - 3\mathrm{ca} - 3\mathrm{na} - 3\mathrm{vac}$$

$$\mathrm{al} - 15\mathrm{ca} + \mathrm{fe} + \mathrm{fef} + \mathrm{mg} - 15\mathrm{na} + \mathrm{si} + \mathrm{ti} - 15\mathrm{vac}$$

Using our database, we tested measured tourmaline formulas (normalised projected*)* in terms of bulk parameters and enumerated 512 possible independent bulk parameter sets. 250 robust parameters sets remains which did not give rise to negative bulk parameters after back transformation or gave rise to non-summing-to-1 endmember fractions. Electronic Appendix 2A provides the mean and standard deviation of endmember fractions for these sets. We selected the independent bulk parameter set:

$$\{\mathrm{na}, \mathrm{ca}, \mathrm{fe}, \mathrm{mg}, \mathrm{al}, \mathrm{fef}, \mathrm{ti}, \mathrm{si}, \mathrm{F}\}.$$

Mapping from bulk parameter space to independent endmember space. The square independent endmember stoichiometry matrix using these 9 independent bulk parameters is (F_{ind}):

$F_{ind} =$

	na	ca	fe	mg	al	fef	ti	si	F
srlB	1	0	3	0	6	0	0	6	0
drvB	1	0	0	3	6	0	0	6	0
uvtB	0	1	0	4	5	0	0	6	0
foiB	0	0	2	0	7	0	0	6	0
oleB	1	0	0	0	9	0	0	6	0
fluvtB	0	1	0	4	5	0	0	6	1
buB	1	0	0	0	6	3	0	6	0
mdtwB	1	0	0	1	6	0	2	6	0
aorsmB	0	0	0	0	10	0	0	5	0

Which resulted in these linear mapping equations by matrix inversion:

$$\mathrm{srlB} = \frac{2 \cdot \mathrm{al}}{9} + \frac{2 \cdot \mathrm{ca}}{3} + \frac{5 \cdot \mathrm{fe}}{9} + \frac{2 \cdot \mathrm{fef}}{9} + \frac{2 \cdot \mathrm{mg}}{9} + \frac{2 \cdot \mathrm{na}}{3} - \frac{4 \cdot \mathrm{si}}{9} + \frac{2 \cdot \mathrm{ti}}{9}$$

$$\mathrm{drvB} = -\frac{4 \cdot \mathrm{ca}}{3} + \frac{\mathrm{mg}}{3} - \frac{\mathrm{ti}}{6}$$

$$\mathrm{uvtB} = \mathrm{ca} - \mathrm{f}$$

$$\mathrm{foiB} = -\frac{2 \cdot \mathrm{al}}{3} - \mathrm{ca} - \frac{\mathrm{fe}}{3} - \frac{\mathrm{fef}}{3} - \frac{\mathrm{mg}}{3} - \mathrm{na} + \frac{2 \cdot \mathrm{si}}{3} - \frac{\mathrm{ti}}{3}$$

$$\mathrm{oleB} = -\frac{2 \cdot \mathrm{al}}{9} + \frac{2 \cdot \mathrm{ca}}{3} - \frac{5 \cdot \mathrm{fe}}{9} - \frac{5 \cdot \mathrm{fef}}{9} - \frac{5 \cdot \mathrm{mg}}{9} + \frac{\mathrm{na}}{3} + \frac{4 \cdot \mathrm{si}}{9} - \frac{5 \cdot \mathrm{ti}}{9}$$

$$\mathrm{fluvtB} = \mathrm{f}$$

$$\mathrm{buB} = \frac{\mathrm{fef}}{3}$$

$$\mathrm{mdtwB} = \frac{\mathrm{ti}}{2}$$

$$\mathrm{aorsmB} = \frac{2 \cdot \mathrm{al}}{5} + \frac{2 \cdot \mathrm{fe}}{5} + \frac{2 \cdot \mathrm{fef}}{5} + \frac{2 \cdot \mathrm{mg}}{5} - \frac{3 \cdot \mathrm{si}}{5} + \frac{2 \cdot \mathrm{ti}}{5}$$

2.3 Other uses for the independent bulk parameters and site fractions

Beyond thermodynamics, independent endmember and bulk/site fraction spaces improve mineral classification, simplify solid solutions, and enhance statistical analyses by removing constant-sum constraints. In geochemistry, they isolate environmental signals in provenance studies, and in machine learning, they provide independent variables for predictive modelling.

Independent bulk /site fractions as a way to remove crystal chemical control Independent bulk/site fractions can replace all site fractions, removing variance from crystal chemical control (Thompson Jr 1969) and isolating zoning patterns driven by external factors like P-T conditions and chemical potentials. This approach assumes selected endmembers capture all exchange reactions in the tourmaline system. It aids multivariate analysis (e.g., principal component analysis (PCA)) in provenance studies by eliminating crystal chemical effects, ensuring environmental signals remain distinct (Spear et al. 1982; Thompson Jr. 1982a, 1982b). Additionally, transforming independent endmembers removes constant-sum constraints, allowing direct application of traditional statistical methods without having to resort to complicated compositional statistics.

Concise Nomenclature A concise thermodynamic mineral nomenclature can be based on independent bulk/site fractions, which are always positive linear combinations of independent endmembers. This avoids the issue of negative endmembers while providing a practical way to classify solid solutions. For example, all tourmalines with Mg as dominant independent site fraction/bulk parameter tourmalines could be labeled as dravite, simplifying tourmaline nomenclature from 40+ endmembers to just 9 in bulk models or 14 in speciation models.

3. TRAINING SET ENDMEMBER FRACTIONS

In Chapter 1, we developed a set of internally consistent tourmalines which we used as training set for thermodynamic model calibration. Tourmalines in this set were characterised using identical instruments and lab procedures to ensure coherent normalization. They cover a broad compositional range, with uncertainties incorporated from analytical methods, sample heterogeneity, and assumptions. The database includes natural solid solutions and select synthetic samples. Monte Carlo simulations provided 2000 optimised formulas, with uncertainties derived from their mean and standard deviation.

Cell volumes and their uncertainties were extracted from the structure solution of the SC-XRD (natural samples) and Rietveld refinement of P-XRD (synthetics). To obtain molar volumes (V_m) we converted V_{cell} ($Å^3$) to cm^3 by multiplying by 10^{-24}, calculated $V_m = \frac{N_A V_{cell}}{Z}$, with Z=3 as there are 3 formula units of tourmaline in the hexagonal cell, and converted cm^3/mol to J/mol/bar using 1 cm^3/mol = 1 J/mol/kPa, because 1 Pa = 1 J/m^3. Since 1 bar = 100 kPa, this implies 1 cm^3/mol = 0.01 J/mol/bar. While not SI, this unit is conventional in geosciences for expressing molar volume.

Projection and mineral re-optimisation Samples with >0.2 apfu impurities were excluded. Tourmalines with <0.2 apfu impurities were projected, their formulas were renormalised for charge balance and full site occupancy.

Projection and re-optimisation simplified the formulas to fit the charge-balanced thermodynamic model, reducing dimensionality, assuming they have minimal (though untested) influence. Charge balance (I=60+F+(1−F)×2) was an optimisation goal but was not strictly constrained in the initial formula optimisation in chapter 1 due to F measurement uncertainty. Projection was

chosen over least-squares fitting to map the higher-order composition space to a lower-order model, providing cleaner equations for linking site fractions and bulk parameters to endmembers.

In MATLAB, re-optimisation fixed the fluor content (F) in each Monte Carlo run, as it determined charge balance in the objective function. This objective function minimised deviations from initial estimates while enforcing charge balance and site occupancy. The objective function,

$$\mathrm{Obj}(x) = \sum \left(\frac{x - x_{\mathrm{init}}}{x_{\mathrm{init}} + \epsilon}\right)^2 \cdot (1 - \ \mathrm{ZeroMask}\ ) + \left(\frac{\sum x_i \cdot V_i - I}{F + \epsilon}\right)^2 + \sum \mathrm{SiteConstr}(x)^2$$

includes three squared terms: deviation from the initial composition, charge balance, and site occupancy constraints. Here, x is the composition vector, x_{init} the initial composition, V the site species valences, and I the target charge. Weighting by $1/x_{init}$ emphasizes smaller components in proportion to their initial amounts. The `ZeroMask` is a logical array that flags variables set to zero in the initial composition /speciation and ensures they remain unchanged during optimisation by excluding them from the deviation penalty. It ensures these variables are excluded from the penalty term in the objective function, preventing division by zero and avoiding unnecessary penalization of values already fixed by the bounds. The charge balance target, I=60+F+(1−F)×2, is similarly weighted by 1/F, strengthening charge balance for samples with low fluorine. The site constraints differ between models**:**

Bulk composition model:

$$\mathrm{na} + \mathrm{ca} + \mathrm{vac} = 1, \mathrm{fe} + \mathrm{mg} + \mathrm{al} + \mathrm{fef} + \mathrm{ti} + \mathrm{si} = 15, \mathrm{b} = 3, \mathrm{h} + \mathrm{o} = 4 - F$$

with a lower bound of 0 on each variable.

Speciation model:

$$\mathrm{nax} + \mathrm{cax} + \mathrm{vx} = 1, \mathrm{fey}\ + \mathrm{mgy} + \mathrm{aly} + \mathrm{fefy} + \mathrm{Tiy} = 1, \mathrm{alz} + \mathrm{mgz} + \mathrm{fez} + \mathrm{fefz} = 1$$
$$\mathrm{sit}\ + \mathrm{alt} + \mathrm{bt} = 1, \mathrm{OHv} + \mathrm{Ov} = 1, \mathrm{Ow} + \mathrm{OHw} = 1 - \mathrm{F_w}$$

with each variable constrained between 0 and 1.

With a quadratic objective and linear constraints, this convex problem ensures any local minimum is global (Boyd and Vandenberghe 2004) . MATLAB 2022a's fmincon efficiently handles constraints, with site fractions adjusted for projected elements of varying valences to ensure both cation (summing to 1, including vacancies) and anion (charge balance) totals are closely met. For reoptimizing bulk parameters, we used the interior-point algorithm for its efficient convergence in smaller, well-constrained problems. For the larger, complex site fraction reoptimisation, we applied sequential quadratic programming, which handles extensive constraints through iterative approximations. This combination ensured efficient, accurate optimisation across scales.

The initial formula optimiser was not used because the electrons per site and bond valences derived from bond lengths included the impurities. Reoptimised bulk parameters and site fractions, charge residuals, and discrepancies between measured and reoptimised tourmaline compositions are detailed in Electronic Appendix 2B.

All 2000 MC reoptimised bulk parameters and site fractions were used to calculate endmember fractions and their uncertainties for both the speciation and bulk compositional models using the mapping equations derived in paragraph 2.1 and 2.2, respectively.

To concisely describe the solution polytope, endmembers must be linearly independent, which inherently allows negative endmember fractions, as the description using all polytope vertices requires hundreds of endmembers and thousands of interactions. Negative fractions, though mathematically valid, can bias regression and hinder extrapolation if training data is poorly distributed. This leads to interdependent fractions, such as uvt and fluvt or odvt and drvdis, which describe F content and OH-O disordering, respectively, even in cases where the solid solution lacks a uvit or dvt component. Balanced datasets, careful calibration, and rigorous validation are therefore essential for consistent and reliable thermodynamic models. Bar plots of the endmember fractions for each sample and violin plots illustrating their distributions in the training set are provided in the Appendix 2A.

Data Screening Multivariate outliers were identified using the Mahalanobis distance (Mahalanobis 1936) (reprint), measuring each observation's distance from the mean while

accounting for variable correlations, and flagged via Hotelling's T^2 test with a critical F-distribution threshold ($p<0.05$). A minimum of five observations per variable was required. Outliers included F-buergerite (tm64) for the **$X(YZ)_9Si_xAl_{(1-x)}(VW)_4$** model and F-buergerite (tm64) along with the synthetic B-olenite for the complete speciation model **$XY_3Z_6T_6V_3W$**.

Principal Component Analysis of Sample Distribution in X-Space (Speciation Model) To directly assess multicollinearity and identify which thermodynamic parameters are poorly resolved due to insufficient sampling of endmember X-space, principal component analysis (PCA) was performed on the distribution of samples in independent endmember fraction space for the speciation model.

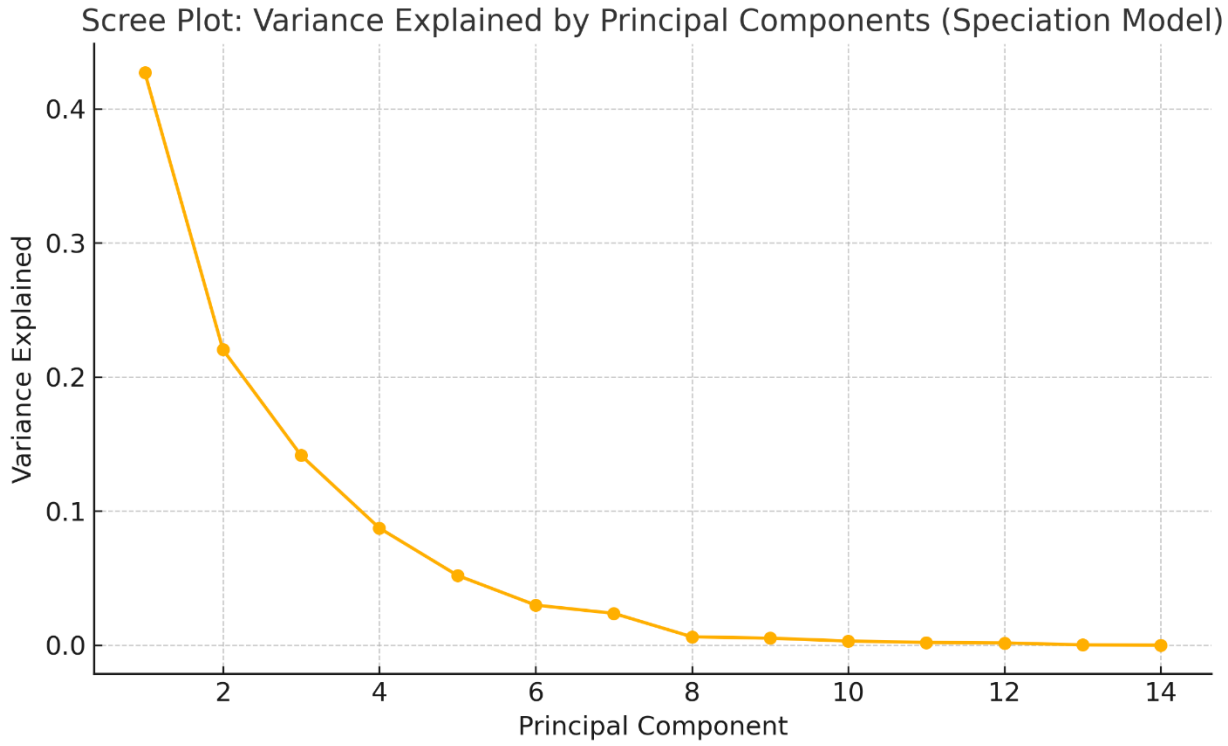

Figure 2A. Scree plot showing the variance explained by each principal component for the speciation model. Principal component analysis (PCA) reveals that the first two principal components (PC1 and PC2) capture the majority of the variance across the dataset, while higher components contribute progressively less. The sharp drop in explained variance indicates that sample variability is largely confined to a low-dimensional subspace in X-space, and highlights directions that are poorly sampled, contributing to multicollinearity in model parameters

The scree plot (Figure 2A) shows that the first two principal components (PC1 and PC2) capture the majority of the variance, while higher-order components contribute minimally, indicating that variation is confined to a lower-dimensional subspace. The biplots for PC1 vs PC2, PC1 vs PC3, and PC1 vs PC4 (Figures 2B–2D) illustrate that samples are primarily distributed along a dominant axis (PC1), with progressively less spread in subsequent principal component directions.

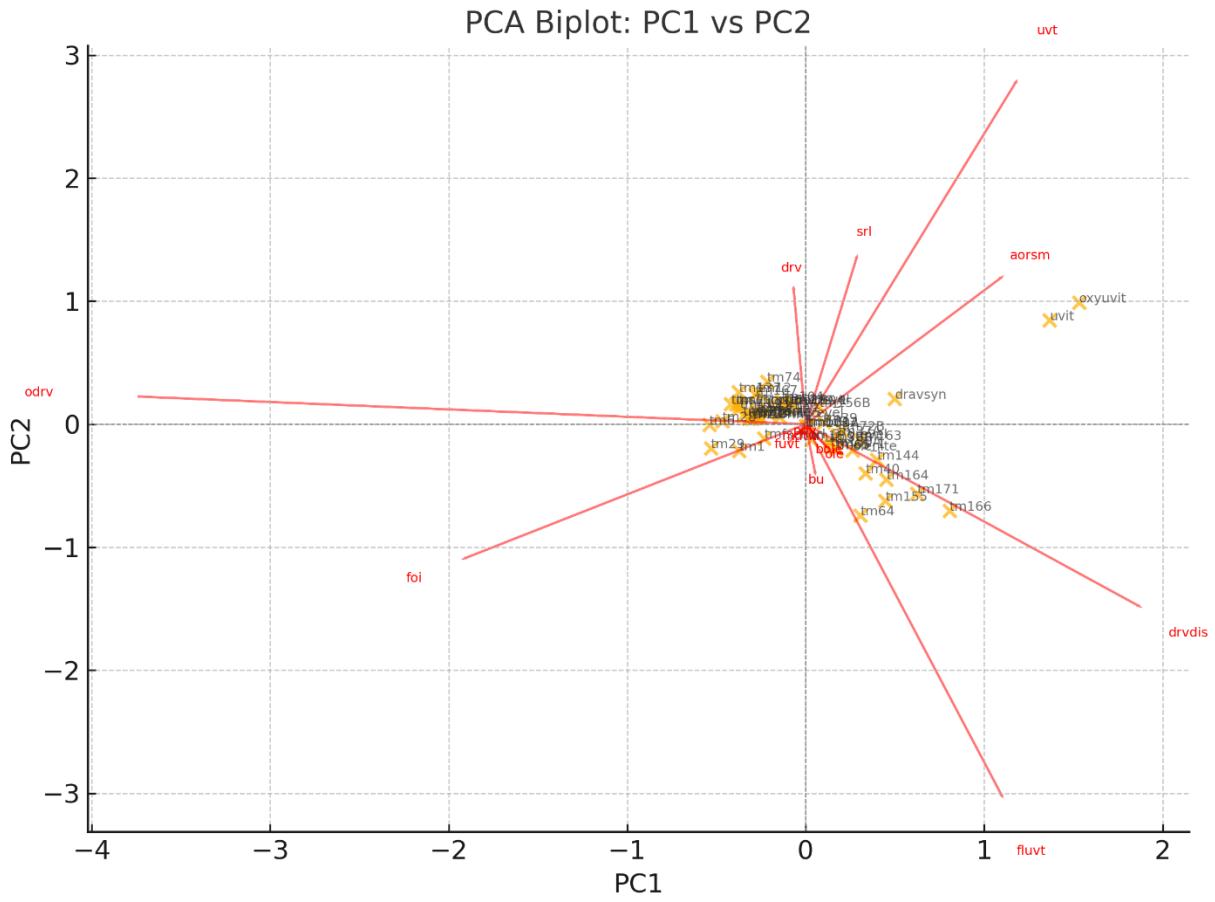

Figure 2B. PCA biplot of PC1 versus PC2 for the distribution of samples and endmember loadings in the speciation model. Samples are primarily distributed along PC1, with limited spread along PC2. Loading vectors show that endmembers such as odrv**,** foi**,** and drvdis dominate the primary sampled variability, whereas endmembers like pov**,** mdtw**,** bu**,** and bole exhibit minimal independent variance. This confirms that certain directions in endmember X-space are poorly represented, weakening parameter resolution.

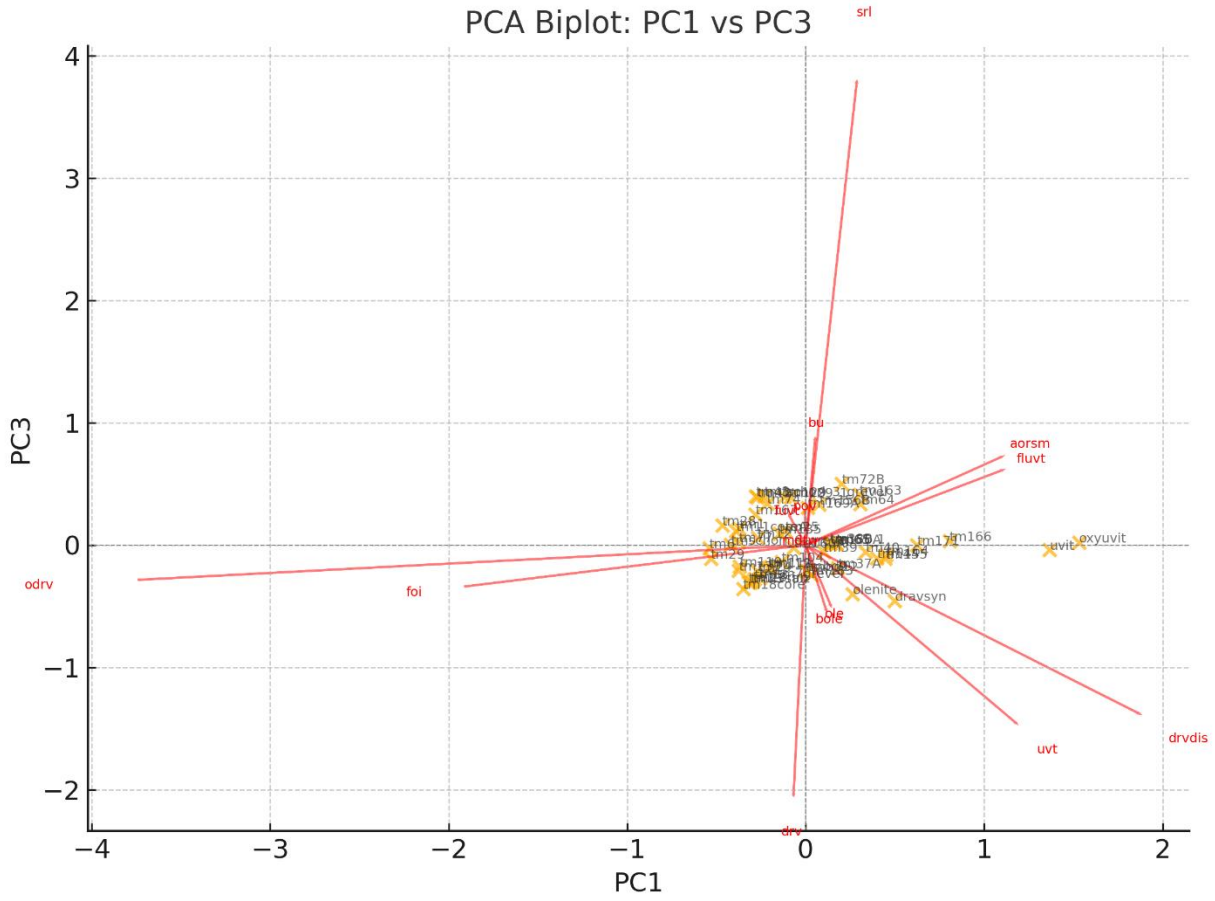

Figure 2C. PCA biplot of PC1 versus PC3 for the distribution of samples and endmember loadings in the speciation model. The PC1 vs PC3 projection further illustrates the confinement of samples along dominant axes, with minimal independent variability along PC3. Endmember loadings in this plane reinforce those key compositional directions involving pov**,** mdtw**,** bu**,** and related endmembers are underexplored in the current dataset.

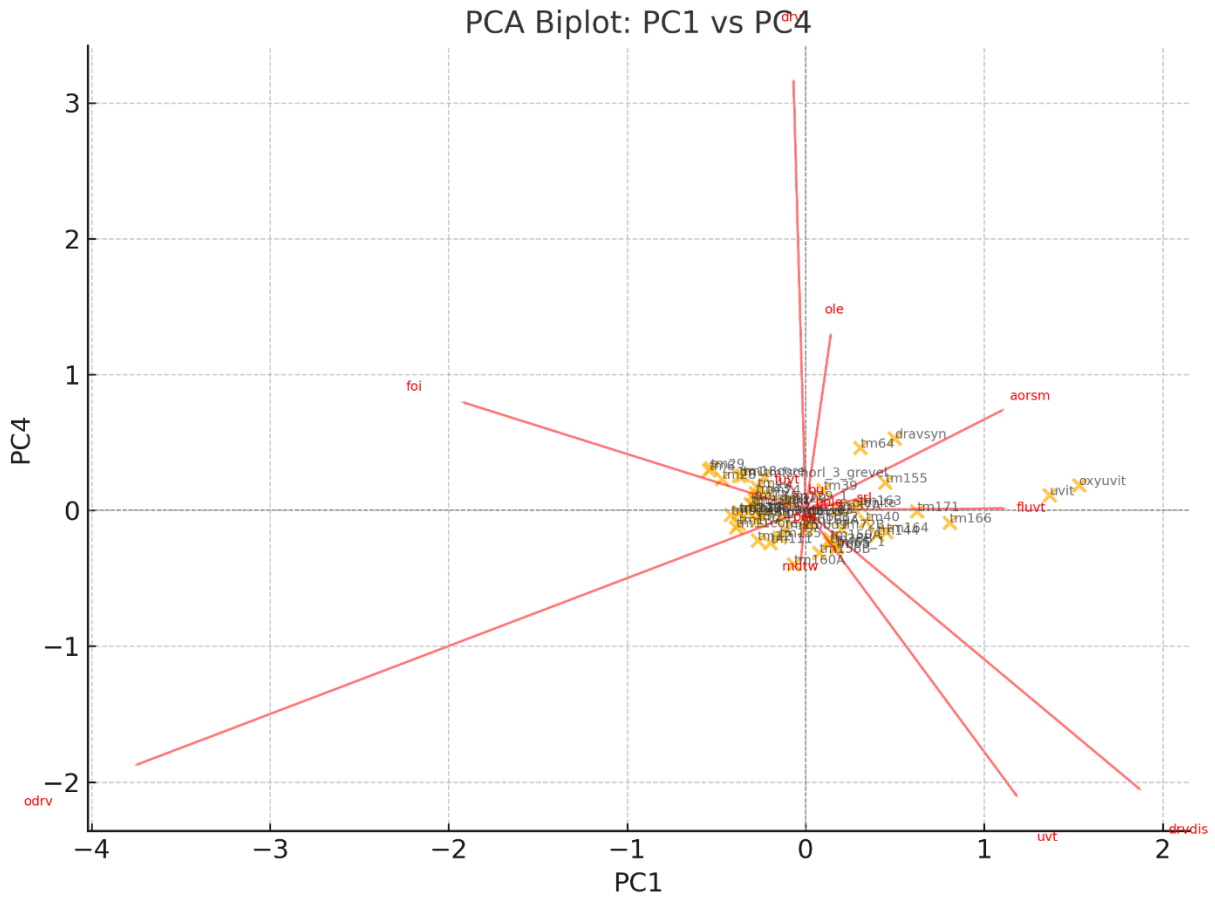

Figure 2D. PCA biplot of PC1 versus PC4 for the distribution of samples and endmember loadings in the speciation model. Samples show almost no meaningful spread along PC4, confirming that this direction is extremely poorly sampled. Endmember contributions to PC4 are negligible, supporting the conclusion that multicollinearity stems from missing coverage in certain compositional vectors, which should guide future synthesis and sample acquisition strategies.

PCA loadings reveal that endmembers such as odrv, foi, and drvdis dominate the major sampled directions (PC1 and PC2), whereas endmembers like pov, mdtw, bu, and bole show very low variance across the dataset. These poorly sampled vectors correspond to parameter directions that are weakly constrained and contribute strongly to multicollinearity in the model calibration.

Thus, PCA analysis clearly shows that multicollinearity arises not simply from model structure, but from incomplete coverage of endmember space. Poor resolution along specific compositional directions are directly linked to the instability of the associated thermodynamic parameters.

To address this, targeted synthesis or selection of future samples should prioritise compositions enriched in pov, mdtw, bu, and bole, and compositions that decouple the strong covariation observed between fluvt, uvt, and drvdis. Expanding the dataset into these poorly sampled regions of X-space would systematically reduce multicollinearity, improve parameter resolution, and enhance the predictive robustness of the thermodynamic model.

Principal Component Analysis of Sample Distribution in X-Space (Bulk Model) To further assess multicollinearity and incomplete sampling in X-space, principal component analysis (PCA) was also applied to the distribution of samples in the bulk endmember fraction model. The scree plot (Figure 2E) shows that variance is strongly concentrated in the first two principal components (PC1 and PC2), with subsequent components contributing minimally, indicating confinement to a low-dimensional subspace.

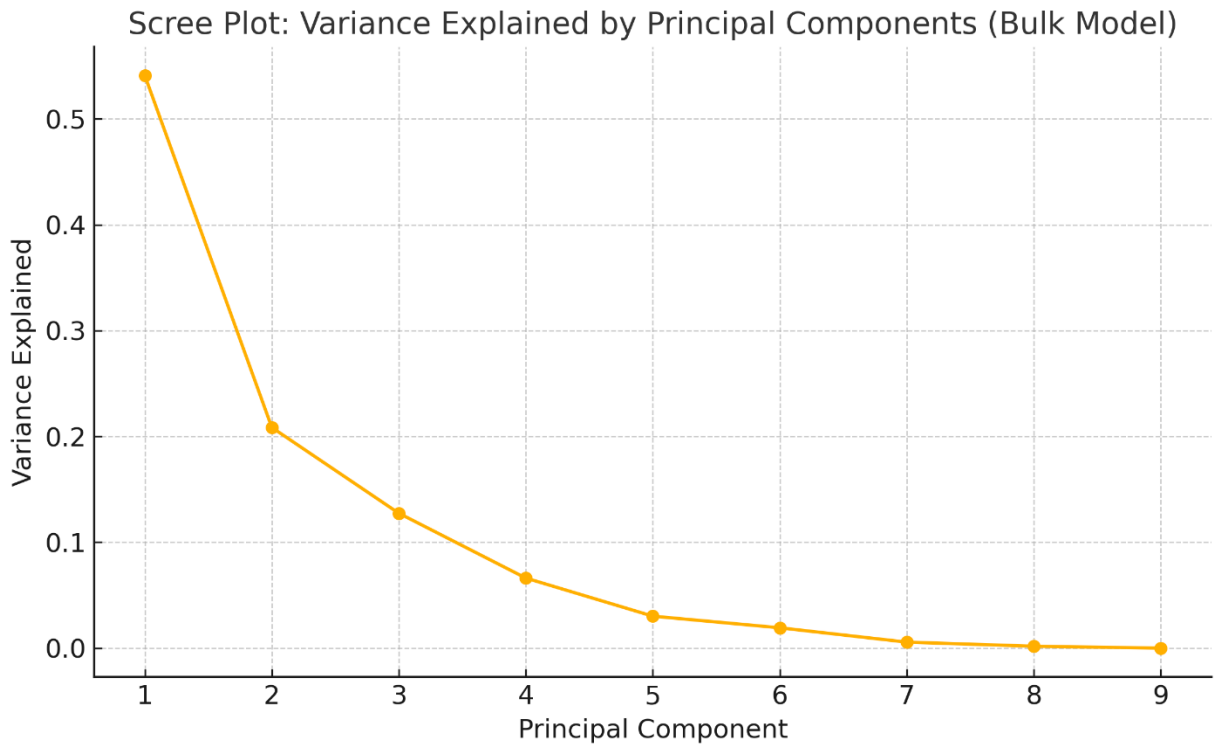

Figure 2E. Scree plot showing the variance explained by each principal component for the bulk model. Principal component analysis (PCA) shows that the first two principal components capture most of the variance, while higher components contribute little, indicating poor sampling across certain endmember directions in X-space.

The PCA biplots for PC1 vs PC2, PC1 vs PC3, and PC1 vs PC4 (Figures 2F–2H) illustrate that sample variability is again dominated by a primary direction (PC1), with limited independent variation along higher principal components.

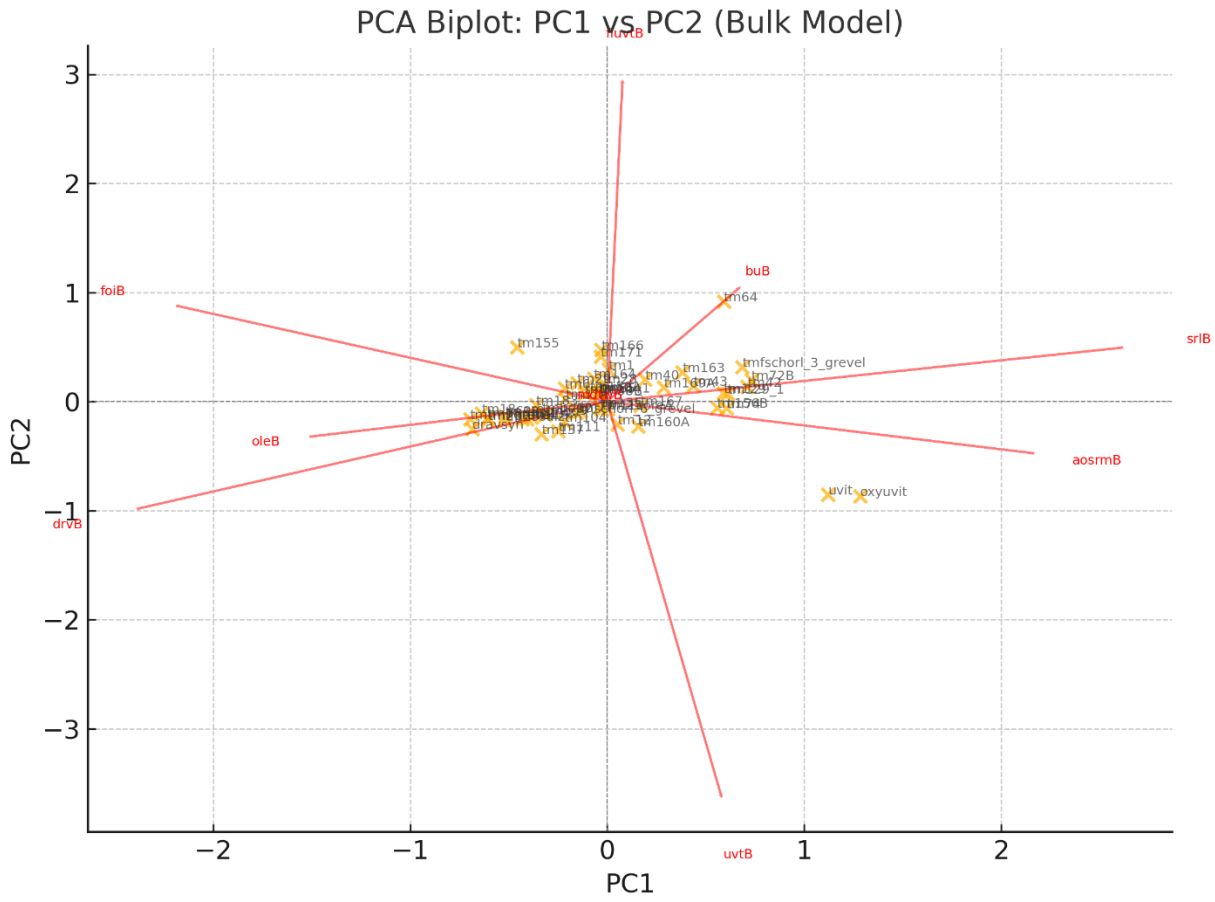

Figure 2F. PCA biplot of PC1 versus PC2 for the distribution of samples and endmember loadings in the bulk model. Samples are strongly clustered along PC1, with limited spread along PC2. Endmember loadings show that drvB**,** foiB**,** and oleB dominate the primary variability, while endmembers like buB**,** mdtwB**,** and aosrmB contribute little, revealing underexplored directions.

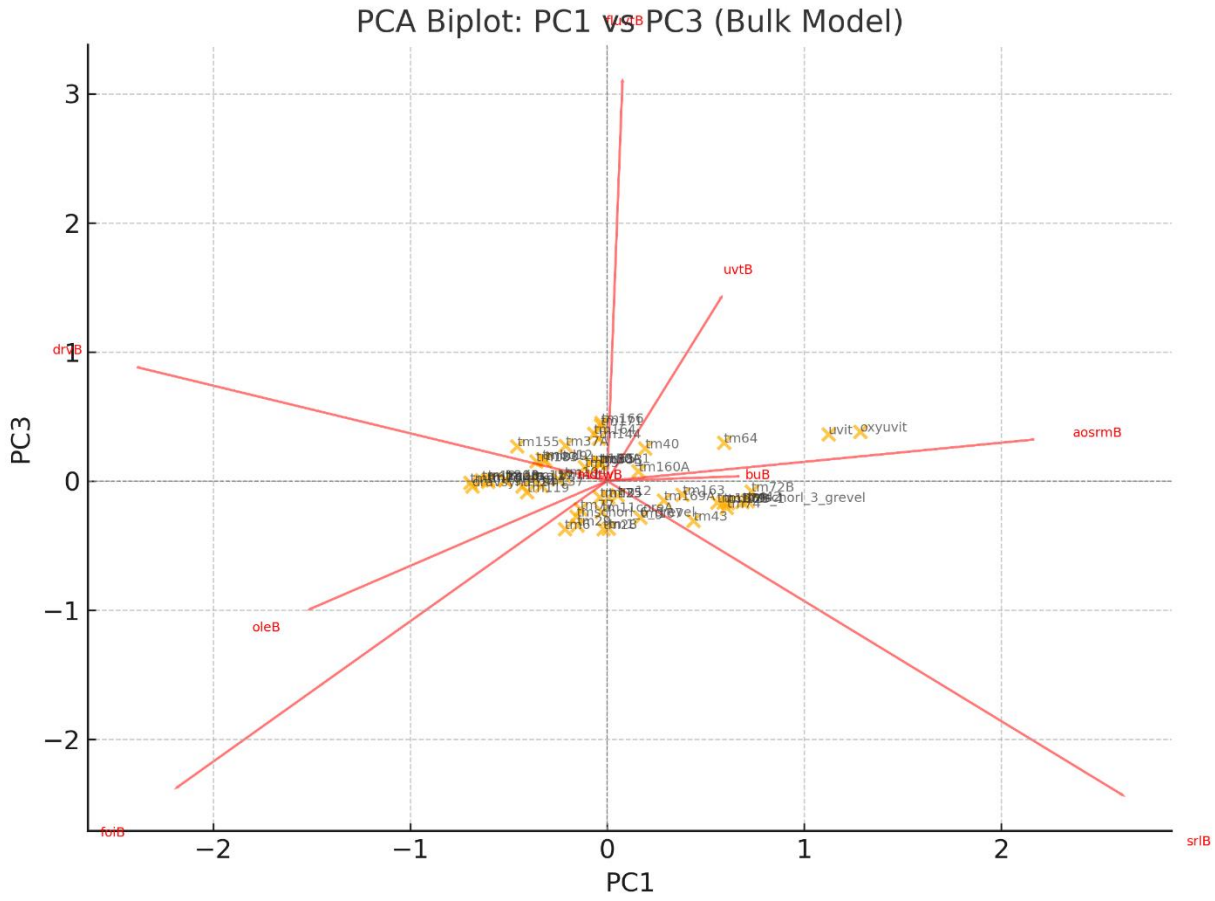

Figure 2G. PCA biplot of PC1 versus PC3 for the distribution of samples and endmember loadings in the bulk model. PC1 vs PC3 projections confirm that sample spread along PC3 is minimal, reinforcing that much of the X-space is poorly sampled beyond the dominant PC1 direction.

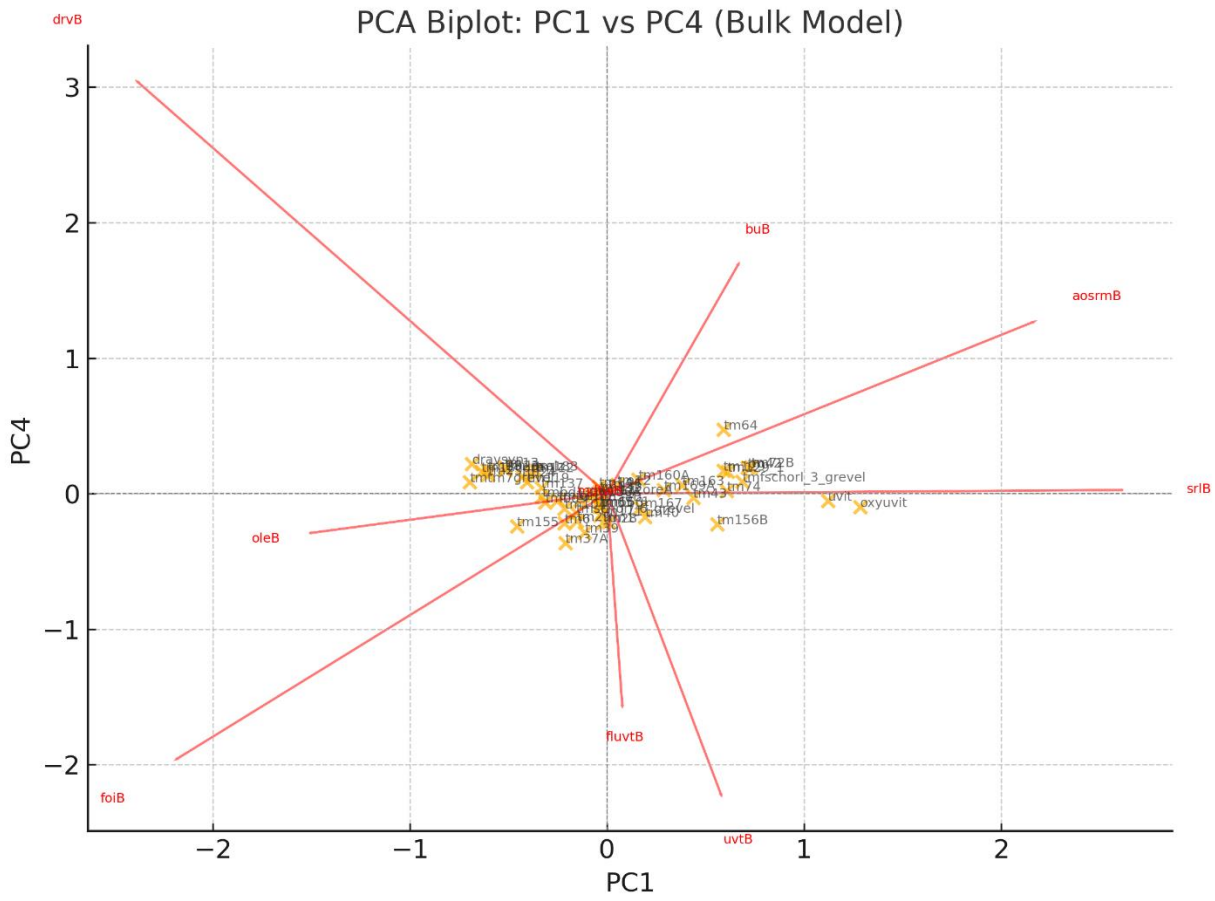

Figure 2H. PCA biplot of PC1 versus PC4 for the distribution of samples and endmember loadings in the bulk model. Samples show negligible spread along PC4. This further demonstrates that poor coverage along specific compositional directions leads to multicollinearity and uncertainty in the associated thermodynamic parameters.

Examination of the loading vectors reveals that endmembers such as drvB, foiB, and oleB dominate PC1 and PC2, while endmembers like buB, mdtwB, and aosrmB contribute very little to the major axes. Poor sampling of these latter directions explains instability and correlation of parameters associated with these endmembers in the thermodynamic model.

Thus, the PCA for the bulk model confirms that multicollinearity results from limited exploration of X-space, not solely model structure. Future synthesis efforts should target compositions enriched in buB, mdtwB, and aosrmB, and attempt to better separate substitutions involving oleB

and foiB. Expanding the sampling coverage in these poorly represented directions would significantly improve parameter resolution and model robustness.

4. TEST SET: ENDMEMBER FRACTIONS

Literature dataset molar volume For molar volume, SC-XRD data provides a literature-based test set, but inconsistencies in preprocessing, instrumentation, and assumptions limit its ability to fully evaluate model performance. The mineral formulas were taken directly from the papers, projected and renormalised as described in the former paragraph, and fitted to the same endmember equations as the training set. Ideally, an internally consistent dataset would be split into training, validation, and test sets (50-25-25%) (Hastie et al. 2017), but data scarcity necessitates reusing an (inconsistent) test set for both selection and assessment. Using the test set for both purposes introduce data leakage and inflates performance estimates. Despite its imperfections, the test set spans the predictor and feature space, balancing central regions with sparse outliers to evaluate interpolation and extrapolation. Extreme compositions are a strong test for the predictive power as they likely reflect chemical differences rather than normalization inconsistencies. It simulates real-world scenarios with incomplete or inconsistent inputs, offering insights into both predictive power and robustness. Performance proxies help to identify models that balance robustness and accuracy for thermodynamic modelling. Future improvements should involve creating an internally consistent test set using the same mineral optimisation. This would separate robustness, evaluated using inconsistent test sets, from generalisation, assessed through the consistent test set, ensuring a clearer distinction between the two.

Bulk model The test database for the bulk composition model included 97 SC-XRD tourmalines that comply with the same selection criteria as our training dataset within the modelled chemical system, sourced from 31 literature references (MacDonold and Hawthorne 1995; Taylor et al. 1995; Pieczka 1996; Bloodaxe et al. 1999; Cámara et al. 2002; Ertl et al. 2003, 2010, 2012, 2016; Bosi and Lucchesi 2004; Pieczka and Kraczka 2004; Bosi et al. 2005, 2010, 2015, 2017, 2022; Cempírek et al. 2006; Bosi 2008; Bačík et al. 2012, 2013; Bosi and Skogby 2013; Gadas et al. 2014; Gatta et al. 2014; Bačík 2015; Pieczka et al. 2018; Vereshchagin et al. 2018; Berryman et al. 2019; Andreozzi et al. 2020; Scribner et al. 2021; Ballirano et al. 2022; Biagioni et al. 2023). Bar plots of the endmember fractions for each sample and violin plots illustrating their distributions in the test set are provided in the Appendix 2A.

In Table 2A, the inverse Gram matrix, $(XX')^{-1}$ compares compositional spaces by indicating predictor constraints. Smaller diagonal values reflect broader coverage and better independence, while larger values indicate redundancy or poor constraints (Montgomery et al. 2021). In the test set, smaller diagonal values (e.g., srlB=0.41 vs. 1.20, mdtwB=15.26 vs. 29.47) indicate broader coverage and better validation capability, though some predictors (fluvtB=0.56 vs. 0.40, buB=2.72 vs. 1.9) are better constrained in the training set, reducing their validation power. Overall, the test set reduces redundancy and offers a more diverse validation range.

The Variance Inflation Factor (VIF) measures how much a predictor's coefficient variance is inflated due to multicollinearity, given by: $\mathrm{VIF}(X_j) = \frac{1}{1-R_j^2}$ where R_j^2 is the coefficient of determination from regressing Xj on other predictors (Montgomery et al. 2021). The VIF values reveal that multicollinearity is generally reduced in the test set. For example, oleB drops from 9.16 in training to 6.05 in the test, and foiB from 9.78 to 1.76, suggesting improved predictor independence. However, some predictors, like uvtB, experience an increase in VIF (1.70 to 3.59), indicating higher correlation under test conditions (see also Figure 2I).

Compositional overlap, measured by Train in Test (%) and Test in Train (%), shows that most predictors maintain high coverage across both sets (e.g., srlB, drvB, and foiB exceed 90% in both metrics). However, aormsB shows limited overlap, with only 63.46% of training samples within the test range, suggesting novel compositional combinations in the test set. Overall, the test set offers broader coverage and reduced multicollinearity and tighter constraints for certain predictors.

Table 2A. Combined evaluation of compositional overlap, predictor constraints, and multicollinearity for the speciation model. Train in Test (%) and Test in Train (%) indicate the percentage of samples covered by the opposing set. VIF measure multicollinearity, with higher values reflecting stronger predictor correlations and inflated variance. Diagonal of X'X indicate predictor constraints, where smaller values reflect broader coverage and reduced redundancy, and larger values indicate poor constraints and limited variability.

Independent Variable	VIF (Training)	Diagonal of X'X (Training)	Train in Test (%)	VIF (Test)	Diagonal of X'X (Test)	Test in Train (%)
srlB	4.3557	1.2017	100.00	1.9391	0.4113	95.88
drvB	2.5402	0.8536	100.00	1.1385	0.1786	92.78
uvtB	1.6999	0.6050	96.15	3.5908	0.4415	86.60
foiB	9.7840	3.2866	100.00	1.7587	0.4030	96.91
oleB	9.1576	7.8468	100.00	6.0527	3.0180	95.88
fluvtB	1.0072	0.4023	100.00	4.3375	0.5602	85.57
buB	1.7345	1.9030	100.00	5.3988	2.7165	98.97
mdtwB	1.3731	29.4688	100.00	1.9665	15.2566	97.94
aormsB	7.3938	3.2235	63.46	2.6157	1.7879	98.97

To visualize these relationships, we used Principal Component Analysis (PCA); see Hastie et al (2017) for technical details. PCA reduces the data to two dominant components (PC1 and PC2) (Figure 2I), providing a visual representation of the overlap. Convex hulls are constructed to define the boundaries of each set, with test samples falling outside the training convex hull indicating potential extrapolation. For the bulk model, PC1 and PC2 explain 65.6% of the variance in the training set and 57.6% in the test set.

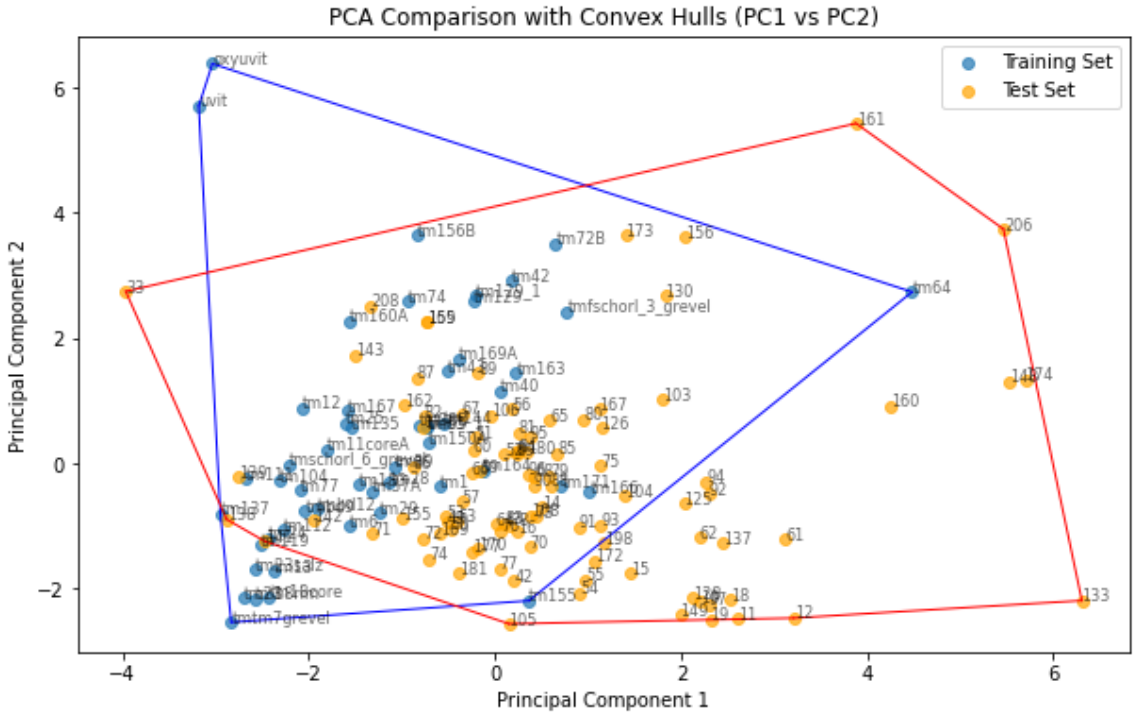

Figure 2I. Scatter plot showing the projection of the training and test sets of the Bulk model onto the first two principal components (PC1 and PC2). Convex hulls in PCA_1-PCA_2 space encapsulate the boundary of each set, highlighting areas of overlap and potential extrapolation where samples from one set fall outside the convex hull of the other. Sample labels are included to identify specific data points. Percentage of training samples in test convex hull: 80.77%. Percentage of test samples in training convex hull: 72.16%

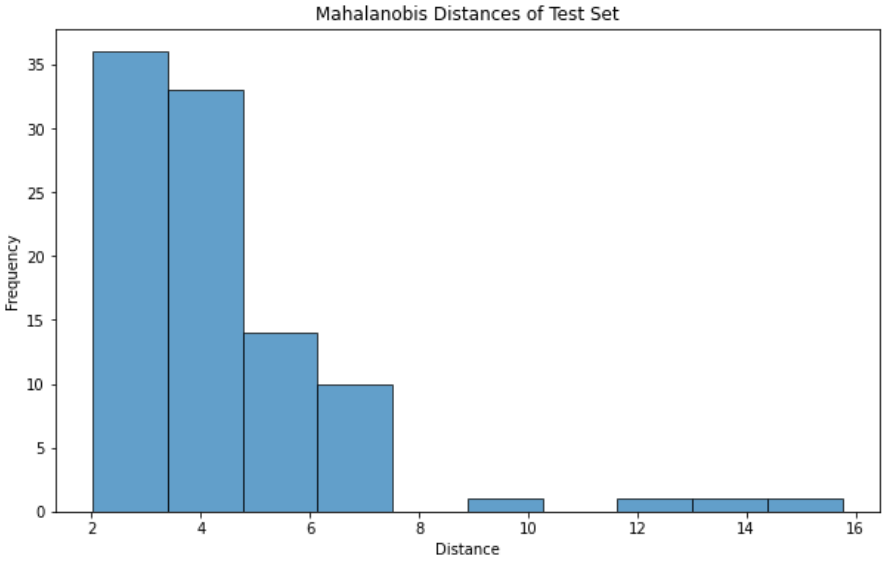

Figure 2J. Histogram displaying the Mahalanobis distances of test samples from the centroid of the training set for the Bulk model. The distances quantify how well the test samples align with the core distribution of the training set, with larger distances indicating potential outliers or regions of poor coverage.

The Mahalanobis distance (Figure 2J) further quantifies the degree of overlap by measuring how far each test sample deviates from the center of the training distribution, accounting for correlations among variables. A histogram of these distances highlights potential outliers and assesses whether the test set is well-covered within the training space.

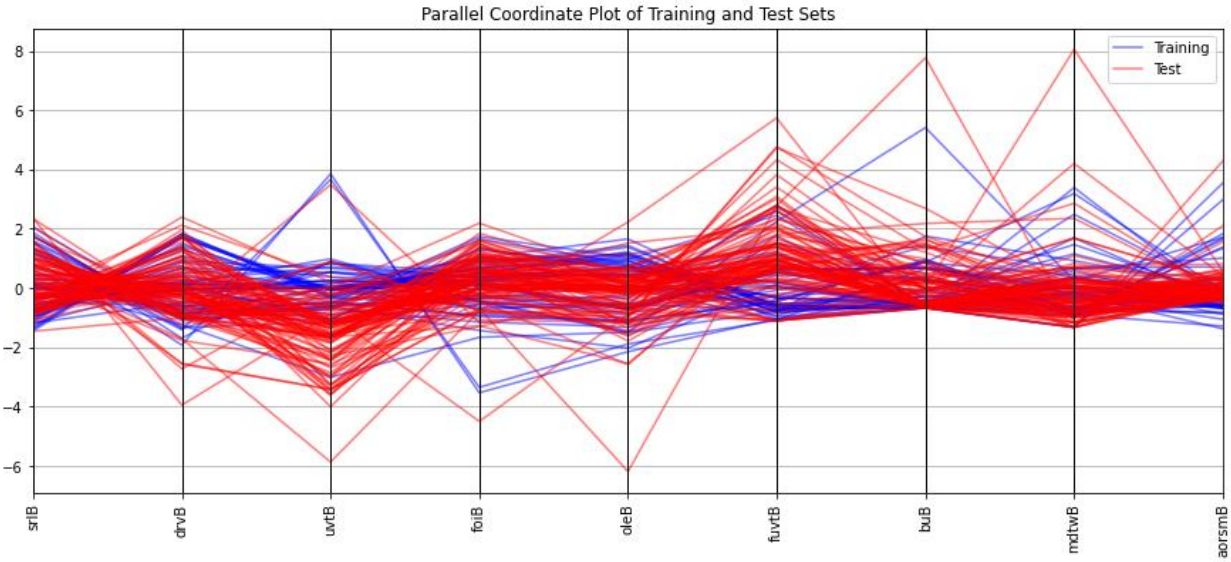

Figure 2K. Comparing of composition space for the training and test set for the Bulk model Multivariate visualization comparing the standardized distributions of predictors between the training and test sets. Standardization (zero mean and unit variance) ensures comparability across variables with different units and scales. Each line represents a sample crossing axes for the predictors, highlighting variables where the test set significantly diverges from the training set.

A parallel coordinate plot (Figure 2K) visualizes these overlaps and divergences, offering a comprehensive view of both global and variable-level coverage. Together, these analyses show relatively good compositional overlap, ensuring that model validation reflects meaningful generalisation rather than extrapolation artifacts.

Speciation model The speciation model test set comprised the same 97 SC-XRD tourmalines as the bulk composition model test set, supplemented by 7 additional tourmalines, and 3 extra literature sources, totalling 104 tourmalines (Ertl and Hughes 2002; Marler et al. 2002; Marschall et al. 2004) . Bar plots of the endmember fractions for each sample and violin plots illustrating their distributions in the test set are provided in the Appendix 2A.

The smaller $(XX')^{-1}$ diagonal values in the speciation test set (Table 2B) indicate broader speciation space, better constraints and reduced redundancy compared to the training set. This enables more independent molar volume validation, though predictors like ole, bu and mdtw remain weakly constrained.

VIF values reveal that multicollinearity is generally lower in the test set. For example, srl drops from 24.86 in training to 4.42 in the test, and foi from 28.42 to 1.52, indicating reduced interdependence and more stable coefficient estimation. However, certain predictors, such as uvt (4.60 in the test vs. 15.56 in training) and drvdis (5.31 in the test vs. 22.99 in training), retain moderate VIFs probably due to near-equality of drv and drvdis endmembers which might indicate mineral formula optimisation challenges.

Compositional overlap shows that most predictors have near-complete overlap, with srl, drv, foi, and fuvt covering 100% of training samples in the test set and over 90% of test samples in the training set. However, drvdis shows limited overlap (64.08% Test in Train), and bole highlights novel conditions with only 52.83% Train in Test. Overall, the test set improves coverage and

reduces redundancy, but predictors with high VIFs or limited overlap, such as drvdis and bole, require careful consideration for validation robustness.

Table 2B. Combined evaluation of compositional overlap, predictor constraints, and multicollinearity for the second model. Column definitions and interpretations are the same as described in Table 2A**.**

Independent Variable	VIF (Training)	Diagonal of X'X (Training)	Train in Test (%)	VIF (Test)	Diagonal of X'X (Test)	Test in Train (%)
srl	24.8593	10.8686	100.00	4.4226	0.7042	91.26
drv	8.8975	7.4539	100.00	3.4534	0.3355	73.79
uvt	15.5622	5.5483	100.00	4.5981	0.6230	97.09
fuvt	2.3110	25.3038	100.00	2.5523	2.6074	90.29
foi	28.4230	14.4832	100.00	1.5208	0.3168	97.09
ole	6.1399	24.3884	100.00	12.8605	16.8221	93.20
drvdis	22.9906	9.2240	100.00	5.3057	0.1887	64.08
odrv	8.0786	1.4863	100.00	1.5770	0.1747	91.26
fluvt	1.8073	0.7100	100.00	1.9574	0.6208	86.41
bu	9.2310	18.4398	98.11	13.1603	18.1288	90.29
mdtw	1.3892	27.7116	98.11	3.4332	25.4434	98.06
bole	2.4609	3.6161	52.83	1.3377	1.2142	100.00
aorms	16.7683	18.1755	100.00	2.5404	1.6376	99.03
pov	5.1553	221.7398	100.00	1.1743	3.8737	95.15

The low VIF of pov in the training set (5.1553) indicates minimal multicollinearity with other predictors, but its high diagonal value in the inverse Gram matrix (221.7398) reveals poor constraint. This suggests that pov is sensitive to small data changes, likely due to limited coverage or narrow variance, causing instability in its coefficient estimation.

Additionally compositional overlap between the training and test sets is shown in Figures 2D, 2E, and 2F. PCA (Figure 2L) visualizes the overlap, with convex hulls indicating that the test set is much larger than the training set, see also the Mahalanobis distance (Figure 2M). For the speciation model, these two PCA components account for 43.6% of the variance in the training set and 50.1% in the test set. The parallel coordinate plot (Figure 2N) highlights variable-level coverage, showing the test outliers are mainly in the pov and fuvt species. These results confirm sufficient overlap for reliable model validation, while significant extrapolation allows for a more thorough evaluation of the model's generalisation.

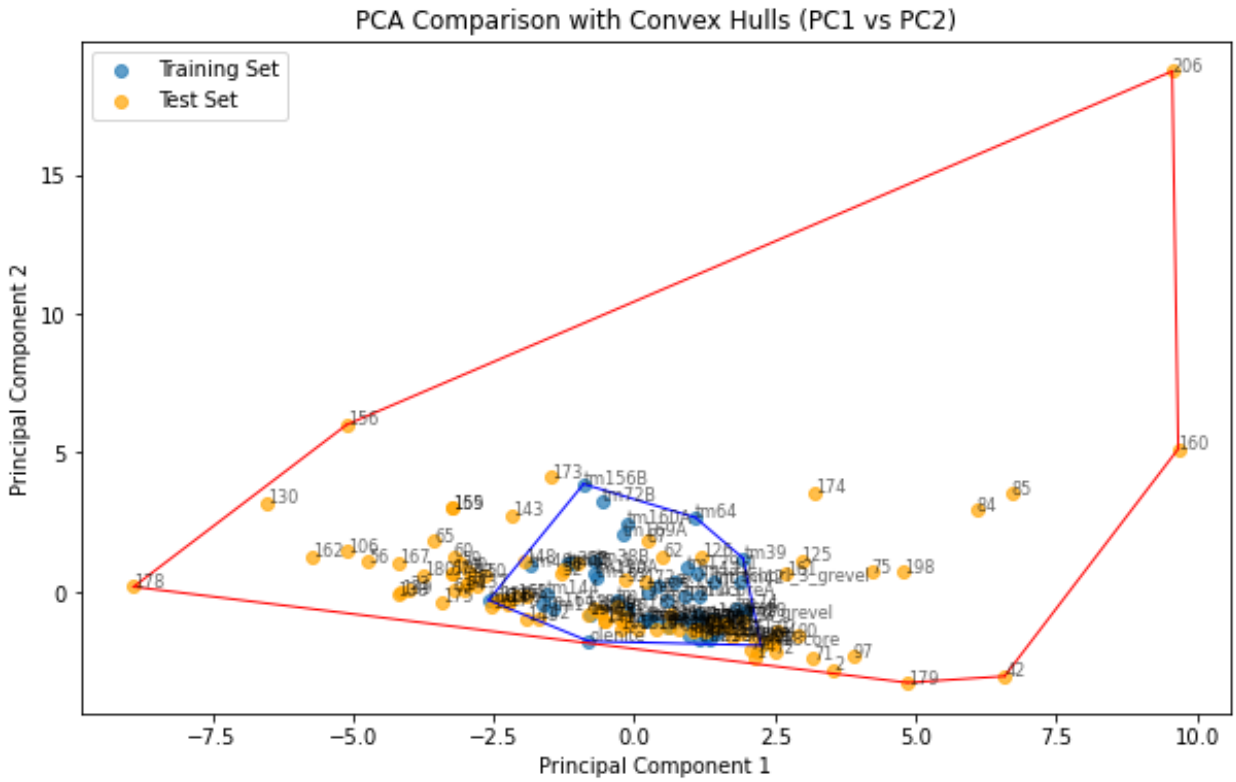

Figure 2L. Scatter plot showing the projection of the training and test sets of the Bulk model onto the first two principal components (PC1 and PC2). Convex hulls in PCA_1-PCA_2 space

encapsulate the boundary of each set. Percentage of training samples in test convex hull: 100%. Percentage of test samples in training convex hull: 46.60%

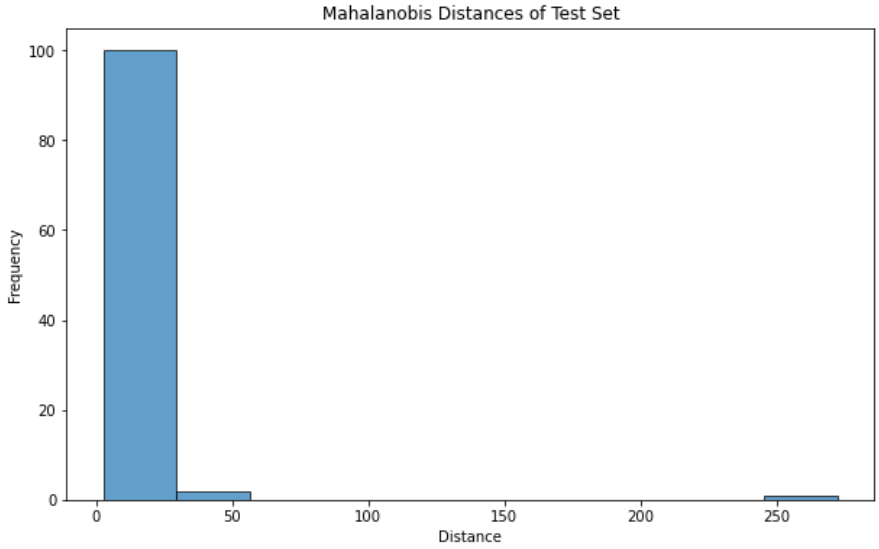

Figure 2M. Histogram displaying the Mahalanobis distances of test samples from the centroid of the training set for the speciation model

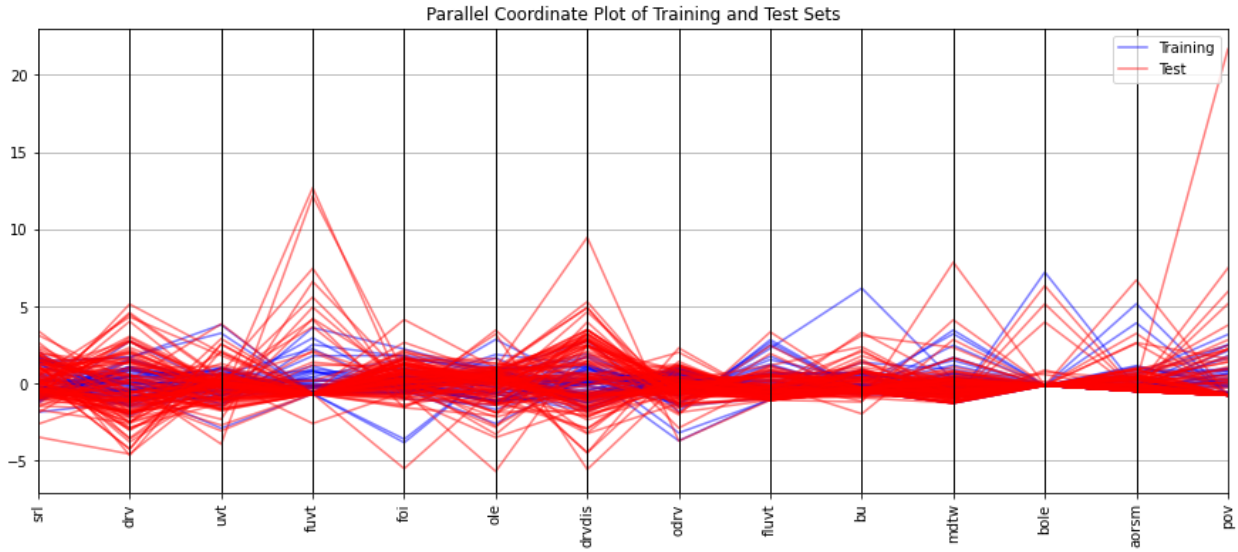

Figure 2N. Parallel coordinate plot comparing of composition space for the training and test set for the speciation model. Each line represents a sample crossing axes for the predictors, highlighting variables where the test set significantly diverges from the training set

5. REGRESSION METHODS

Extrapolation of molar volumes to endmembers

Since measured molar volumes of tourmalines are of mixed compositions, extrapolation to endmembers is necessary. Multiple linear regression was used for this extrapolation, but due to tourmaline's complexity and limited sample size (50 samples), reliable endmember data could not conclusively be obtained from a single method. To calibrate the thermodynamic model for tourmaline's molar volume, we applied 21 regression methods, including OLS, WLS, 11 total least squares (errors-in-variables), and 8 robust regression methods, leveraging the full uncertainty structure of endmember fractions and molar volumes from Monte Carlo simulations to balance bias, variance, and total error. These regression methods model thermodynamic systems with a global linear function $Y=X\beta+\varepsilon$ (Hastie et al. 2017), capturing endmember fractions and additive interactions. In this formulation, Y is the molar volume, X the endmember fractions, β the endmember volumes, and $\boldsymbol{\varepsilon}$ the residuals. A linear model is appropriate as molar volume is additive and expected to scale linearly with composition. Even when including interaction terms, the model remains linear in its parameters, allowing robust estimation of endmember contributions and interaction effects. However, since endmember fractions sum to 1 and cannot all be zero, the intercept, representing Y when all variables are zero, is physically meaningless. Comprehensive explanations of all analytical regression methods are included in Appendix 2B.

Regression methods considering molar volume uncertainties Ordinary Least Squares (OLS) provided a baseline by minimizing squared differences assumed only in molar volumes, while Weighted Least Squares (WLS) addressed molar volume heteroscedasticity by applying inverse variance weights to $(XX')^{-1}$ (Hastie et al. 2017).

Regression methods considering molar volume and endmember fraction uncertainties

Analytical methods Total Least Squares (TLS) accounts for errors in both endmember fractions (X) and molar volumes (y), providing greater flexibility by introducing 'wiggle room' as X values are no longer assumed to be perfect, allowing adjustments in both dimensions, accommodating uncertainties, and potential lead to better generalisation (Markovsky and Van Huffel 2007; Markovsky 2010). TLS redistributes variance between predictors and response variables, addressing training set constraints differently than OLS/WLS. We used MATLAB script of Wurm (2021) to apply various TLS methods. X-Scaled and XY-Scaled TLS apply column-wise scaling to equalize variances while ensuring homoscedasticity within X and Y, addressing differing magnitudes and greater uncertainty in some endmember fractions (Wurm 2021).

Generalized Total Least Squares (GTLS) assumes a single, constant covariance matrix that applies uniformly across all data points. We performed five GTLS versions: (1) using the mean covariance matrix derived from all individual covariance matrices obtained from sample optimisations across 2000 MC repetitions, (2) applying this matrix with additional scaling for Y, (3) using a covariance matrix directly from the standard deviations across all samples, rather than individually for each sample, (4) the same matrix with y scaling, and (5) Incorporating row- and column-wise correlations by deriving two covariance matrices: one for variables and one for samples (Wurm 2021).

Numerical methods While exact analytical solutions are available for the above methods, they are limited in the error structures they can handle. Ideally, we would use weighted TLS with individual covariance matrices per observation, forming a block-diagonal structure. With no analytical solution available, we applied the nonlinear optimisation from Wurm (2021) via MATLAB's lsqnonlin using the trust-region reflective algorithm to solve the Correlated Weights Total Least Squares (CWTLS). CWTLS extends GTLS by weighting each observation individually by its covariance matrix (block-diagonal) and, alternatively, using additionally the covariances of the covariance matrices of each individual observation (full W) to account for all uncertainties and correlations (Wurm 2021). Second-order covariances were calculated as matrix products of each pair of covariance matrices $(i, j), i \neq j$, reflect the combined variability and interaction between variables across the samples. Zero uncertainties in the weight matrix (e.g., due to absent Fe^{3+} or B-olenite endmember fractions) were handled using an indicator matrix. To set initial conditions, we used the nearest GTLS solution (Wurm 2021). This involved matrix

decomposition, deriving the column matrix P_C and row matrix P_R, which are closest to the weight matrix W, by solving the nearest Kronecker product problem (Loan and Pitsianis 1993): $min\|W^{-1} - P_C \otimes P_R\|_F^2$, where $\|\cdot\|_F$, is the Frobenius norm. The Kronecker product ($P_C \otimes P_R$) combines P_C (m×n) and P_R (p×q) into an mp×nq matrix, with each element of P_C scaled by P_R. These GTLS (block-diagonal) and GTLS (full W) starting value solutions are also provided. To ensure CWTLS convergence to a global minimum, we calculated CWTLS-equivalent solutions for all LS, TLS, and GTLS methods (Wurm 2021). Differences in regression coefficients were negligible, with no impact on predicted volumes to at least three decimal places. Covariance matrices for nonlinear least squares were numerically computed using the Hessian matrix (second-order partial derivatives) at the estimated global minimum (Wurm 2021). These covariance matrices, which are minimal uncertainty estimates, propagated uncertainties to the predicted endmember molar volumes.

Use of β^{TLS} in OLS framework Formally, TLS cannot be directly used as a predictive model because the solution it provides is in terms of an adjusted basis that incorporates small perturbations, denoted $X + \tilde{X}$, which corrects X for measurement errors (Gavin 2025). This means that the regression coefficients β^{TLS} obtained through TLS depend on the adjusted data matrix, rather than the original X alone. Consequently, any predicted values $\hat{y}_{TLS}$ would theoretically need to be calculated using this modified basis $X + \tilde{X}$, which perturbation is not directly applicable to new or unseen values of X. However, in practice, the basis changes $\tilde{X}$ in our case are often very small (perturbed endmember sums between [0.98–1.01]), allowing the TLS coefficients to be used approximately within an OLS framework for prediction if the data deviations are minimal.

Use of β^{TLS} in OLS framework is a form of Regularisation To address the documented multicollinearity and underconstrained nature of the observations, a regularisation strategy was adopted. Specifically, using TLS-derived coefficients within an OLS prediction framework constitutes a form of regularisation, stabilizing the model by introducing fit flexibility that accommodates measurement uncertainty in the predictor space. This approach suppresses noise amplification by preventing large or unstable coefficients, thereby improving predictive robustness without overfitting. Critically, regularisation here is grounded in true compositional uncertainties—specifically, uncertainties in endmember fractions—rather than arbitrary model

heuristics. By incorporating these uncertainties, the TLS-corrected coefficients are applied in a statistically and physically meaningful way, systematically reducing multicollinearity among thermodynamic parameters.

Robust regression methods Robust regression methods, including Iteratively Reweighted Least Squares (IRLS), reduce outlier influence by iteratively reweighting $(XX')^{-1}$ indirectly using residual-based weight functions (e.g., Huber, Tukey bisquare) (Huber 1981). These methods excel at fitting data centroids but may generalize poorly in the presence of extreme outliers. Detailed descriptions of each method are provided in Appendix 2B and in MATLAB 2022a Help file for *robustfit*.

Regularisation and Covariance Matrix Adjustment in Regression Methods Weight matrices in all methods must be symmetric, full rank, non-singular, and positive definite (Hastie et al. 2017). Covariance matrices from tourmaline chemical formula optimisation, being estimates, may occasionally fail these criteria. To address this, we implemented a MATLAB code that adjusts a regularisation parameter incrementally until the weight matrix has a nonzero determinant, positive eigenvalues, and full rank within a tolerance of 1×10^{-45}. This tolerance ensures the regulation parameter remains at least an order of magnitude smaller than the original variances and covariances, preserving regression accuracy. Regularisation parameters, listed in Electronic Appendix 2C, are approximately 1×10^{-6}. Note**:** The regularisation applied here was used solely to adjust the covariance matrices into a valid form for regression, ensuring they are symmetric, full rank, and positive definite. This adjustment is <u>not</u> a regularisation method in the sense of least-squares regularisation or coefficient penalization (i.e., the use of β^{TLS} in OLS framework is in essence a form of such regularisation), but purely a technical correction to meet matrix requirements.

Table 2C. Regression Method Categories

Category	Methods
LS Methods	LS, WLS
TLS Methods	TLS, Xscaled TLS, Xyscaled TLS, gtls y scaled, gtls cov data, gtls cov data y scaled, gtls row column, gtls block diag, cwtls block diag, gtls fullW, cwtls fullW
Robust Methods	andrews, bisquare, cauchy, fair, huber, logistic, talwar, welsch

6. SOLID SOLUTIONS MODELS AND HIERARCHICAL SUBSET SELECTION

Molar volume depends not only on fractional contributions from the partial volumes of endmembers but also on non-ideal interactions between elements on crystallographic sites and their associated endmembers. In geosciences, these interactions are typically described using the Margules formalism (Margules 1895). To identify and quantify such interactions within the dataset, we applied hierarchical subset selection (NCSS 2023b).

Hierarchical subset selection Hierarchical subset selection evaluates variables systematically to identify key predictors of molar volume. Interaction parameters (W), representing combined endmember effects beyond individual contributions, are included only when their lower-order terms, endmember volumes, are present and explain additional variance. These interaction parameters are linear with respect to their coefficients. Using OLS in NCSS 2023, we tested all possible interactions between endmembers, adding significant terms and removing redundant variables at each iteration to optimize model accuracy and prevent overfitting.

Interactions in the Generalized Bragg-Williams model The Bragg–Williams model is a mean-field theory that assumes a random distribution of components over site multiplicities. This assumption of random mixing applies equally to both the microscopic and macroscopic formulations of Bragg-Williams solid solution models. Microscopic Bragg-Williams models treat individual sites as chemical components, considering only nearest-neighbor interactions (intra-site and cross-site) while neglecting next-nearest and longer-range interactions (Ghiorso and Sack 1991; Sack and Ghiorso 1994; Sack 2017). In contrast, macroscopic models use

endmembers as components, averaging these interactions to describe collective energetics (Powell and Holland 1993). Critically, both models must respect the same fundamental degree of freedom (DOF) dictated by the crystallographic structure. These DOF are determined by the total number of variable site-species minus the number of site balance and charge balance constraints, and define the dimensionality of the thermodynamic model.

In the macroscopic model, random mixing applies to endmembers, long-range ordered combinations of site occupancies. The configuration space is spanned by independent endmember fractions, from which independent site-species occupancies are derived as linear combinations to compute configurational entropy using strictly positive values

In the microscopic model, entropy is computed from a minimal set of independent site-species fractions that define the configuration space. All variables represent physically meaningful, strictly positive site occupancies, eliminating the need to handle negative component fractions.

Thus, while the microscopic and macroscopic models differ in how they represent composition, independent site-species versus independent endmembers, they are mathematically equivalent representations of the same solution space. The Bragg–Williams assumption of ideal configurational entropy applies to both, as long as it is implemented over the appropriate independent variables that preserve the crystal-chemical constraints of the mineral system.

While both models describe the same number of compositional degrees of freedom, the microscopic model resolves interactions at a lower structural scale.

- In the **macroscopic model**, each endmember is a weighted combination of site-species across the structure. So, when two endmembers interact, the interaction energy is an averaged or "bulk" value, essentially a composite of all underlying site-species interactions

- In the **microscopic model**, each site-species is treated explicitly. This allows the model to distinguish between:
    - Intra-site interactions (e.g., Fe^{2+}–Mg on site Y),
    - Cross-site interactions (e.g., Al on site T interacting with Fe^{3+} on site Z),

- Charge-compensating or coupling substitutions across sites.

Although this microscopic representation appears more detailed, the number of independent W parameters is mathematically equivalent in both models. That's because the total number of unique pairwise interactions between independent degrees of freedom, whether endmembers or site-species, is the same. However, the microscopic model provides more interpretability and flexibility, as it separates contributions from specific crystallographic sites and enables clearer mapping to local substitution mechanisms.

Basis transformations, as described by Myhill and Connolly (2021), link the two approaches, allowing macroscopic W parameters to be interpreted in terms of their microscopic origins within the generalized Bragg-Williams framework in the same way as basis transformations between set of independent endmembers (Powell and Holland 1999) .

Power series solution models for mean field endmember thermodynamic models Energy in multicomponent systems, like V^{ex}, is described by a power series that represents interactions as a sum of mole- endmember fraction terms (Thompson 1967; Helffrich and Wood 1989). A Taylor series, derived by centering the expansion around pure endmembers where $V^{ex}=0$, replaces the general coefficients with derivatives of V^{ex} evaluated at those points, ensuring thermodynamic consistency (Wohl 1953; Helffrich and Wood 1989; Mukhopadhyay et al. 1993; Cheng and Ganguly 1994). Interaction parameters derived from the power series are accurate near endmembers, dictated by slopes at endmember fractions and reflecting infinite dilution behavior . (Sluiter and Kawazoe 2000; Vinograd et al. 2009; Li et al. 2014; Benisek and Dachs 2020). It's the difference between Henry's law and Raoult standard state chemical potential (Spear 1993) and therefore should connect to trace element geochemistry, capturing effects at low concentrations. Truncating higher-order terms reduces accuracy for intermediate compositions.

Regular Model For 2-way interactions, self-interaction terms were excluded, testing only single regular solution interaction parameters. The regular model (Hildebrand 1929) is derived from the Taylor series truncated at the second degree, and assumes constant, symmetric, composition-independent binary interactions: $V^{\mathrm{ex}} = \frac{1}{2}\sum_{i=1}^{n} \sum_{j=1}^{n} X_i X_j W_{V,ij}$where $W_{V,ij}=W_{V,ji}$ and X_i, X_j are endmember mole fractions (Ganguly 2001).

Subregular Model Extending the Taylor series to the third degree, the subregular model (Andersen and Lindsley 1988; Helffrich and Wood 1989; Cheng and Ganguly 1994) introduces compositional dependence of w_{ij}, capturing asymmetry: $V^{\text{ex}} = \frac{1}{2}\sum_{i=1}^{n} \sum_{j=1}^{n} X_i X_j \left(W_{V,ij} X_i + W_{V,ji} X_j\right) + \frac{1}{6}\sum_{i=1}^{n} \sum_{j=1}^{n} \sum_{k=1}^{n} X_i X_j X_k W_{V,ijk}$, where $W_{V,ij} \neq W_{V,ji}$, involving cubic terms ($X_i^2 X_j$ and $X_i X_j^2$).

Despite the first term describing asymmetric binary interactions, subregular terms act as 3-way interactions in subset selection due to the cubic dependence on endmember fractions, where one endmember composition repeats to reflect compositional changes in interaction parameters. The model inherently includes ternary interactions, as demonstrated by a basis transformation applied to a subregular model without ternary terms introduces nonzero ternary terms, making conventional zero-ternary assumptions thermodynamically implausible (Myhill and Connolly 2021). The truncation eliminates quaternary terms (Cheng and Ganguly 1994). For a statistical interpretation of the subregular model see Gottschalk (2016).

Assumptions and Linear Regression Fit Both models assume Taylor series can represent interactions and rely on Muggianu's projection for multicomponent systems (Muggianu et al. 1975). Despite the non-linear dependence on composition and the resulting non-linear extrapolation to endmembers, the interaction parameters $W_{V,ij}$ and $W_{V,ji}$ remaining linear coefficients in the regression framework, as they directly scale the mole-fraction terms, allows the usage of standard regression techniques. Other series solution models differ in truncation, projection, and interaction scaling assumptions, leading to varying results based on these assumptions (Ganguly 2001). In our case, only one binary subregular w terms were significant, so ternary interactions were avoided to minimize the risk of multicollinearity.

Fundamental Differences Between Regular and Subregular Models: The Role of Compositional Constraints in Their Equivalence The equivalence of the second-order term $w_{\text{reg}}\, x_1 x_2$ with the third-order subregular terms is valid under the constraint:$w_{\text{reg}}\, x_1 x_2 = w_{\text{sub}}\, x_1 x_2 x_2 + w_{\text{sub}}\, x_1 x_1 x_2$. This implies that $w_{\text{sub}} = \frac{w_{\text{reg}}}{x_1 + x_2}$ when x1+x2=1 (as in a binary system where x1 and x2 are mole fractions summing to unity). If x1+x2≠1 (e.g., in a system where other components exist or the fractions deviate from the constraint), $w_{sub} \neq w_{reg}$. This demonstrates that

the equivalence depends on the specific compositional constraints (Connolly, personal communication).

Number of parameters In a regular model, only binary interactions (w_{ij}) are considered, with 36 binomial combinations for a 9-endmember model and 91 for a 14-endmember model ($\binom{n}{2} = n(n-1)/2$) (Tucker 1994). In a subregular model, binary interactions are doubled (72 for 9 endmembers, 182 for 14), and ternary interactions (C_{ijk}) are included, with 84 for 9 endmembers and 364 for 14 ($\binom{n}{3} = n(n-1)(n-2)/6$). These parameter counts far exceed the calibration capacity of a limited training set, necessitating hierarchical subset selection. However, this approach is nonunique, as combinations of interaction parameters could equally explain a single interaction, making the final subset inclusion merely empirical in origin.

7. TRAINING DATASET REGRESSION: ORDINARY LEAST SQUARES

We begin with least squares regressions (OLS) on the training data in Number Cruncher Statitical Systems (NCSS) software by single inversion, providing the best fit per the Gauss-Markov theorem and ensuring unbiased estimates (Gauss 1823; Hastie et al. 2017). Least squares is chosen for its minimal assumptions, robustness to dataset changes as each observation is treated equally, and as a reference for evaluating more complex, potentially biased models. Subset selection in NCSS using least squares determined the hierarchical predictor subsets. Although formally valid only for least squares, the obtained interaction parameters were applied to other regression models to assess robustness. Detailed statistical summaries of OLS fits both the bulk composition and the speciation model and their subset predictors in NCSS can be found in Appendix 2C.

Bulk compositional model The bulk composition model has 9 endmembers across 52 samples. Poorly sampled endmembers like oleB, foiB, and aorsmB required extrapolation, yielding broader standard errors than well-sampled ones like drvB. The bulk compositional model was analysed with and without additional subset interaction parameters, including WdrvB-fluvtB (-1.28) and WfoiB-fluvtB (0.71), significant at $\alpha = 0.05$. Including more predictors reduced MSE (0.0048 to 0.0039), their R^2 contributions modest (0.07–0.03), but did not ensure better generalisation with PressR^2 (0.65 to 0.66). Interaction terms shifted drvB and fluvtB (~31.95 to

~32.15) beyond original confidence intervals, driven by the Wdrv-fluvt effect (-1.28), while changes in other endmembers, though larger in magnitude, were less significant due to wider confidence intervals. These binaries, linked to coupled substitutions, suggest potential nonideality, but it remains unclear whether the fitting parameters represent genuine interactions or fit noise.

Including interaction parameters increased multicollinearity, with VIF values (Appendix 2C) rising for foiB (9.78 to 12.54), oleB (9.16 to 11.03), aorsmB (7.39 to 7.54), and WdrvB-fluvtB (9.89). Strong correlations, such as srlB-drvB (-0.83), oleB and aorsmB with multiple endmembers, persisted, while new weak ones between W parameters and endmembers emerged. This highlights that the enhancing model fit comes at the cost of greater redundancy among predictors, complicating interpretability. The correlations between endmembers and interaction parameters were not strong enough for subregular parameterizations to be significant.

The W parameters fit tm164, reducing its residual from -0.27 to -0.18, but became insignificant without it. Residuals become normal with w parameters or exclusion of tm164. Leave-one-out-cross validation shows that our fluor-buergerite sample (tm64) is the most influential point in both models, strongly affecting fluvtB, drvB, and oleB, while tm164 influenced drvB, uvtB, and foiB.

Speciation model The speciation model, with 14 endmembers, includes 53 samples, adding synthetic B-olenite to constrain its extremely small molar volume despite a 0.2 apfu Y-site vacancy before projection. No additional interaction parameter was found significant during subset selection. Direct comparison is challenging due to differing training datasets and the shift from bulk parameters to site fractions in endmember definitions. The training set shows uneven coverage, with pov, fuvt, ole, and mdtw observed only in trace to minor amounts, increasing extrapolation uncertainty. The model achieves a mean squared error (MSE) of 0.0058, a slightly worse fit than the bulk composition model (MSE: 0.0048). Uvt and fluvt are similar between models. Foi, ole, and mdtw remain within 95% confidence intervals, while aor is higher (30.76→31.12) and ordered srl (32.26→31.94), drv (31.95→31.75), and bu (31.91→31.40) are lower, all outside the bulk compositional model's limits. Disordered drvdis (31.87) aligns with drvB's confidence range, indicating drvB is dominated by disordered drv. Ordered endmembers

generally predict lower volumes than disordered ones, though this trend is unclear for the other disordered endmembers that are combinations of ordered (pov, odrv) or mixed (fuvt) compositions.

However, these trends must be taken with a grain of salt as the fit suffers from extreme multicollinearity, see Table 2B. Very high VIFs (foi 28.42, srl 24.86, drvdis 22.99, aorsm 16.76) and strong correlations (foi-uvt -0.62, foi-aorsm -0.76, bole-molar volume -0.86) arise from fitting 14 highly interdependent endmembers with only 53 samples, far below the recommended sample-to-parameter ratio, severely impacting robustness ($R^2Press=0$). Using chemically similar endmembers, like odrv, drvdis, drv, or aorsm and olenite, increases multicollinearity, inflating VIFs and reducing robustness. Choosing distinct endmembers avoids this but can lead to negative fractions, which are acceptable in principle but may cause poor extrapolations with poorly distributed data. Thus, selecting independent endmembers requires balancing distinctiveness and compositional plausibility.

Residuals are not normally distributed, with tm164 (-0.31) as a significant outlier. Removing it reduces MSE by nearly 2 orders of magnitude to 0.00003 and normalizes residuals. tm164, an outlier in both reciprocal and speciation models, is unlikely an order-disorder effect. Interaction parameters primarily serve to fit this outlier, as no W terms remain significant without it. Its uncertainty, an order of magnitude higher than the training average, suggests a potential analytical error (e.g., inclusions) but is within the test dataset's normal range. This highlights that when extracting W interaction parameters from natural solid solutions, the regression often reduces to fitting outliers—data points that may reflect true physical effects or simply analytical error. Influential points include tm64, tm164, and olenite, with high Cook's D, DFFITS, and DFBETAS (see NCSS (2023a) for their definitions).

8. MODEL SELECTION

Models We performed all 21 regression methods on both the bulk and speciation models without any interaction parameters, with regular significant interaction parameters found by the subset selection using OLS, and with subregular significant interaction parameters found by the subset selection using OLS. We also performed the regression method with and without tm164 as this sample was the dominant contributor to the interaction parameters.

Model Bias–Variance Trade-off Total uncertainty in regression models comes from bias, variance, and irreducible error, such as noise and distribution shifts (Hastie et al. 2017). Due to data scarcity, we do not use formal definitions which includes cross validations but rely on simplified estimates to illustrate the concept and overall model behavior. Bias², estimated by training set MSE, reflects underfitting, while variance, measured by the gap between test and training errors, captures overfitting (but is inflated by noise in inconsistent test sets). Balancing bias and variance is crucial to minimizing error (Figure 2O). Robust methods, like x-uncertainty-weighted regressions, reduce variance by introducing bias to improve generalisation. Bias includes model bias (difference between estimates and true values) and estimation bias (difference between robust and OLS) (Hastie et al. 2017). Model complexity depends on parameters relative to data points and loss function constraints (Hastie et al. 2017). In thermodynamic databases, too many parameters and limited training data often lead to overfitting and poor generalisation. To control variance, we selected subsets capturing key effects. Using an inconsistent test dataset increases variance and error due to test set inconsistencies, but partial error cancellation from using the test set for both selection and assessment leads to generally underestimated uncertainty and model quality estimates.

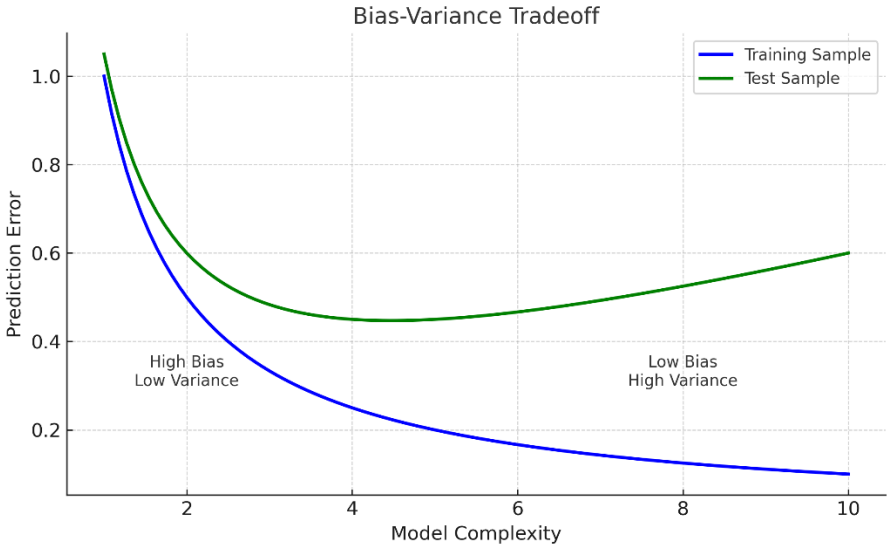

Figure 2O. Illustration demonstrating the general effect of the Bias-Variance Tradeoff. Modified from Hastie et al. (2017)

Selecting the correct degrees of freedom (df) top determine complexity is challenging because it is not well-defined across all regression types used. In OLS, df equals the number of observations minus parameters, but for total least squares (TLS) and robust regressions, where uncertainties exist in predictors and residuals are adaptively weighted, the effective df is unclear as is the use of some df in subset selection. TLS adjusts both predictors and responses, increasing model flexibility beyond the parameter count, while robust methods alter data influence through weighting. Classical df assumptions, fixed predictors and homoscedastic errors, do not fully apply, making it difficult to penalize complexity or accurately estimate variance inflation. As a result, the bias–variance versus complexity graph (Figure 2O) illustrates the concept qualitatively, and no formal curve was calculated for our set due to ambiguity in defining degrees of freedom across methods.

Train Error: Internal Validation Using Calibration Data All regression techniques minimize a quadratic loss function as a χ^2-based goodness-of-fit statistic (Bevington and Robinson 2003). OLS minimises unweighted vertical residuals, WLS weights deviations by y-variances, robust methods down-weight outliers, and TLS minimises the Frobenius norm of the residual matrix, capturing perpendicular distances with weighting schemes like S-TLS, GTLS, and CWTLS (see Appendix 2B). While traditional goodness-of-fit metrics are incompatible across methods due to differences in residual definitions, all regression coefficients are applied in an OLS predictor model, enabling a uniform comparison based on unweighted vertical y-residuals. These residuals, rather than the original fitting methods or minimised loss functions, are used for all goodness-of-fit metrics, assumption checks, confidence intervals, outlier and regression analyses, providing a consistent evaluation of each method's fit to the training dataset in terms of model and estimation bias. A self-written MATLAB script was used for this internal validation. OLS achieves the best fit per the Gauss-Markov theorem, ensuring unbiased estimates, while biased methods like weighted TLS coefficients in an OLS predictor model reduce complexity, increasing training bias but potentially lowering variance and test errors (Hastie et al. 2017). To test if tm164 is an unphysical outlier we perform the model selection using different regression methods with and without tm164 included in the training dataset.

Test Error: External Validation Using Literature Data The predictive OLS model with the regression coefficients from the various methods was used to predict the molar volumes of the

test set tourmalines and compared to their measured values. The same MATLAB script was used for the external validation of the test dataset. For external validation, the goodness of fit parameters represents the total test set errors. Subtracting the training error from the test error estimates the model variance. Z-score regression of the residuals against the predictors identifies the endmember contributing to high variance. Jackknife resampling (Quenouille 1956) highlights test samples inflating test errors, identifying compositions poorly fit by the model.

Scatterplot Analysis and York Regression To assess test and train errors of regression models (OLS, WLS, TLS, weighted TLS, IRLS) with and without interaction parameters, scatterplots of predicted vs. measured values were analysed. A good fit aligns points along the 1:1 line, while deviations indicate disagreement. Scatterplots include prediction uncertainties from covariance matrices and (underestimated) SC-XRD analytical uncertainties, which omit sample variability, systematic errors, and X-uncertainties. These y-$\hat{y}$ plots provide a comprehensive visual and quantitative assessment of model performance.

Goodness-of-fit metrics use unweighted y-residuals, representing the vertical distance of each point from the 1:1 line. Standard goodness of fit statistics are used (NCSS 2023a). R^2 and adjusted R^2 compare the model's performance against the mean, while Mean Squared Errors (MSE) captures overall error; all three are sensitive to outliers due to their reliance on squared residuals. In contrast, Mean Absolute Error (MAE) highlights typical prediction error by treating all residuals equally, and Median Absolute Deviation (MAD) robustly measures central error by minimizing the influence of outliers. These metrics provide a comprehensive assessment of overall, typical, and central residual trends in model performance but ignore uncertainties.

A York regression (York et al. 2004), accounting for uncertainties in both y-$\hat{y}$, was performed on the scatterplots, see Appendix 2B for details. York regression adds flexibility to fit the data, but with larger prediction errors at extremes and smaller errors for central data, it primarily fits central data while increasing bias at extremes due to higher uncertainties and sparse samples. The Bias Integral measures the area between the York fit and the 1:1 line, reflecting composition-dependent error. A high Bias Integral indicates large errors at extremes, while a low value signifies consistent performance across compositions, making it essential for model

comparison. In internal validation, the integral reflects compositional dependent training bias, while in external validation, it captures compositional dependent total error (bias + variance).

The metrics wMSE, wRMSE, wMAE, and their robust equivalent wMAD measure variance around the York line, while wR and AdjwR assess model performance relative to the mean. By focusing on weighted residuals, these metrics primarily evaluate the strength of composition-dependent bias in the dataset, with R^2PRESS (Allen 1974) indicating its robustness.

Model selection heuristic To select the final regression model for molar volumes, we used a heuristic based on the weighted average of training and test errors. Goodness-of-fit statistics (MSE, MAE, MAD, Adj_R^2, wMSE, IntegralBetweenYorkand1_1, AdjR^2, R^2PRESS) were standardized into Z-scores, with maximized metrics inverted. Training and test data statistics were weighted by observation counts to balance internal fit and generalisation. The model with the lowest Z-score sum was selected, minimizing residuals (MSE, MAE, MAD, Adj_R^2) and compositional bias (wMSE, IntegralBetweenYorkand1_1, AdjR^2, R^2PRESS). Using four indicators for each aimed to balance fit and generalisation for both the central samples and the extremes. This was implemented using custom Matlab code.

Although final molar volume predictions use an OLS framework, comparison based solely on the generalized chi-squared misfit

$$\chi^2 = (x_{\text{obs}} - x_{\text{model}})^T \text{COV}^{-1} (x_{\text{obs}} - x_{\text{model}})$$

is not inappropriate, but it is limited. This misfit assumes BLUE conditions—linearity, perfectly known predictors, and correctly modelled error covariances—which are only partially satisfied across OLS, error-in-variables, and robust regression methods. As a result, residuals differ systematically across models. The heuristic model selection, combining standardized goodness-of-fit and bias metrics, provides a more multidimensional and holistic assessment of model quality, rather than relying on a single statistic whose assumptions may not fully align with all regression approaches evaluated.

While effective, the approach has weaknesses: test set reuse risks data leakage, equal Z-score weighting may misrepresent metric importance, the heuristic lacks theoretical grounding, and

metric correlations could bias results (dimension reduction could help). But overall, this methodology offers a practical, adaptable framework for balancing residual minimisation and generalisation in complex datasets.

Bulk compositional model $X(YZ)_9Si_xAl_{(1-x)}(VW)$ Appendix 2D summarizes the minimisation of Z-score sums for eight weighted statistics across training and test sets. The best results were obtained without interaction parameters. No single model performs best overall; instead, three models focus on different aspects of the fit:

1. **CWTLS (block diagonal weight matrix):** Best for generalisation, with low bias integral and reliable extrapolation to extremes. However, it poorly fits bulk data, with samples distributed far from the 1:1 line, indicating high residuals.
2. **Robust models (Cauchy, Welsch, Bisquare, Andrews):** Fit centroid samples well but struggle with extremes due to compositional bias and slope changes near the 1:1 line, making them unreliable for extrapolation.
3. **Ordinary Least Squares (OLS):** Strikes a balance, fitting bulk data almost as well as robust models and generalizing moderately well.

The results highlight the challenge of fitting extreme samples without sacrificing precision for central data. For bulk compositional models, OLS provides a robust option, while CWTLS is preferred for generalisation, and robust models excel in centroid-focused fits. The choice depends on whether the priority is overall fit or generalisation. Bulk compositional models, common in older thermodynamic solution models, are robust against endmember fraction uncertainties. They perform well within the calibration range but poorly at extremes. Statistically significant interaction parameters from subset selection likely fit noise, increasing test dataset variance without improving the model fit.

Limitations of the Bulk Model for order-disorder effects on Molar volume The reciprocal bulk composition model merges Y/Z and V/W sites into bulk parameters, failing to distinguish ordered buergerite from disordered bosiite. Both are assigned similarly high buB components, despite F-buergerite having one of the smallest molar volumes in the dataset (larger only than ole, bole, and aorsm), while bosiite (Ertl et al. 2016) (the largest in the test set) and similarly disordered povondraite (Bosi et al. 2023) (not in test set) have the largest molar volumes in the

tourmaline system (Table 2D). This failure to capture speciation differences results in large residuals, with subset selection identifying W parameters that reflect the model's inability to address speciation effects or explain the extreme molar volume variations.

Table 2D. Structural Formulas and Molar Volumes for Buergerite and Bosiite

Mineral	Speciation	Projected and Renormalised Bulk Compositional model	Molar Volume (J/mol/bar)	Uncertainty (J/mol/bar)
F-Buergerite	$NaFef_3(Al_6)(Si_6O_{18})(BO3)_3(O_3)(F)$	$(Na_{0.821}\,Ca_{0.04}Vac_{0.14})(Al_{6.42}Fef_{2.41}Ti_{0.09}\,Mg_{0.07})(Si_{5.59}Al_{0.41})(B_3)(F_{0.73}H_{0.75}\,O_{2.52})\,O_{27.75}$	31.512	±0.001
Bosiite	$NaFef_3(Al_4Mg_2)(Si_6O_{18})(BO3)_3(OH_3)(O)$	$(Na_{0.73}\,Ca_{0.23}Vac_{0.04})(Al_{3.36}Fef_{3.35}Ti_{0.01}\,Mg_{1.69})(Si_{5.92}Al_{0.08})(B_3)\,(H_{3.16}\,O_{0.84})\,O_{30.16}$	33.02	±0.01

In the molar volume vs. buB plot (Figure 2P) of the combined training and test datasets, most Fe^{3+}-rich samples trend toward bosiite, while F-buergerite stands out as a true outlier in the bulk compositional model. The limited sample trending towards buergerite may indicate a miscibility gap or an island of stability for ordered buergerite, though further sampling is required to confirm this hypothesis. In principle, poorly fitting elements initially can increase molar volume due to strain but can stabilize the structure at higher concentrations, reducing molar volume. Removing F-buergerite (tm64) from the training dataset renders all buB-related W parameters insignificant.

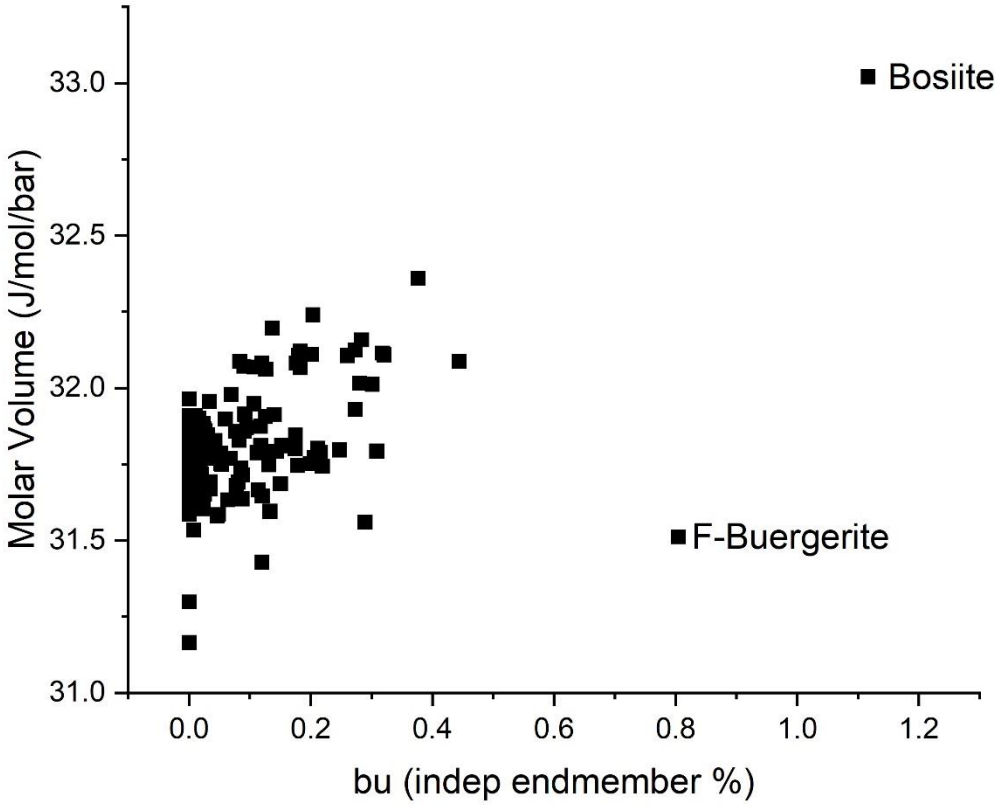

Figure 2P. buB endmember fraction versus molar volume. Combined training and test set.

The residuals for F-buergerite and bosiite disappear in the speciation model, allowing distinct molar volumes for ordered and disordered endmembers. The crystal chemical origin of the molar volume difference between buergerite and povondraite remains unclear. Bosi et al. (2023) observed a general trend of increasing molar volume with higher Fe^{3+} and decreasing volume with $^{VI}Al^{3+}$, but their Figure 6 oversimplifies the compositional space and fails to explain slope changes or why Fe^{3+}-rich buergerite has such a small molar volume. Molar volume differences stem from site occupancy, vacancies, and Y/Z and V/W disorder.

Bulk Compositional model with Cauchy Robust Regression

OLS rigidly fits outliers, CWTLS offers intermediate flexibility, and robust regression focuses on the data centroid. Cauchy robust regression is preferred for the bulk compositional model as it

assigns low weight to the small molar volume of F-buergerite, present only in the training set. This resolves its incompatibility with bosiite and improves the fit for the buB centroid, which primarily aligns with bosiite with only a minor trend toward buergerite in the combined dataset (Figure 2P). This make the resulting bulk compositional model unsuitable for buergerites, which require a speciation solid solution model and should be added as a separate pure endmember phase in the database. Table 2E shows the bulk endmember molar volumes.

Table 2E. Cauchy robust endmember molar volumes for the $X(YZ)_9Si_xAl_{(1-x)}(VW)$ model and the SD based on the covariance matrix. Regression model without interaction parameters. The correlation matrix is plotted directly below the table for visual reference, with correlation coefficients annotated inside each coloured cell to illustrate the strength and direction of relationships between endmembers.

Mineral	Molar Volume	SD	Difference with OLS	Outside OLS CI
srlB	32.1075	0.0672	-0.1525	Yes
drvB	31.8568	0.0567	-0.0991	No
uvtB	32.0976	0.0477	-0.0948	No
foiB	31.6362	0.1112	-0.1943	No
oleB	31.1157	0.1718	+0.3252	Yes
fluvtB	32.0113	0.0389	+0.0569	No
buB	32.1980	0.0846	+0.2810	Yes
mdtwB	31.9796	0.3330	+0.4790	Yes
aorsmB	30.8704	0.1101	+0.1015	No

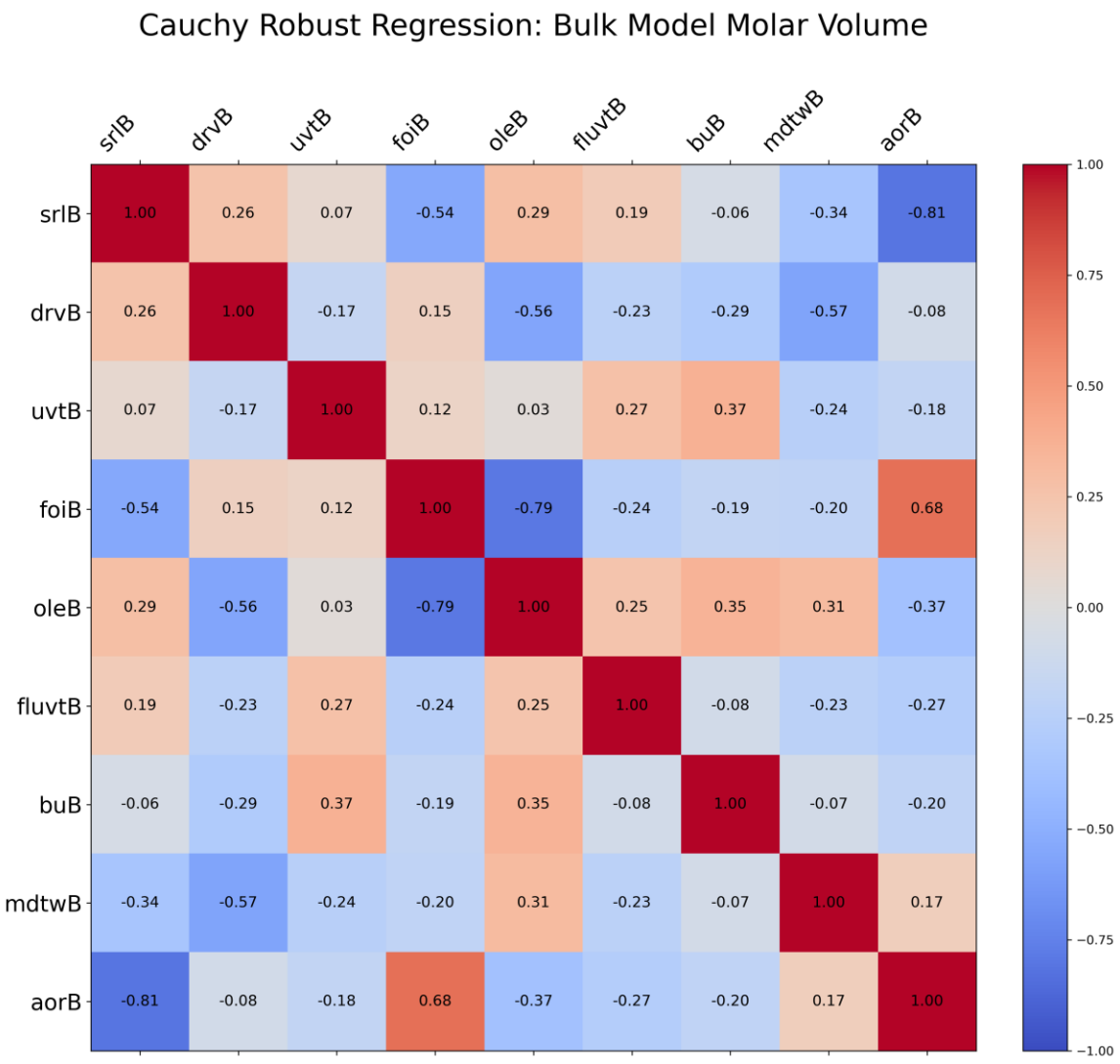

Compared to the OLS correlation matrix (Electronic Appendix 2C2), many of the strong correlations are broken in the robust regression. The largest differences in the regression coefficients relative to OLS, exceeding the OLS confidence intervals, are observed for mdtwB (+0.4790) and oleB (+0.3252), both of which are strongly extrapolated. and buB (+0.2810), due to the robust regression's lower fit hardness to F-buergerite. More detail on the internal and external validation of the robust Cauchy fit to the $X(YZ)_9Si_xAl_{1-x}(VW)$ model is detailed in Appendix 2D.

Speciation model $XY_3Z_6T_6V_3W$ Appendix 2E summarizes the minimisation of Z-score sums for eight weighted statistics. For the $XY_3Z_6T_6V_3W$ model, the best results were achieved without interaction parameters using CWTLS (block diagonal) with individual covariance matrices as

weights, making it the most reliable model due to its balance of fit, generalisation, and compositional robustness. CWTLS outperforms other methods for speciation modelling, unlike the bulk compositional model where several methods performed similarly.

As shown in Figure 2L, the test set had more outliers for the speciation model than the bulk compositional model, allowing direct extrapolation testing. This is common in speciation models, where the larger speciation space shifts minerals away from the compositional centroid sue to the increase in dimensions. Endmember fraction uncertainties are larger in speciation models than in bulk models. TLS methods outperform OLS and robust regression by addressing Y- and X-uncertainty, multicollinearity, and extremes, achieving strong generalisation and low bias integrals. However, some compositional bias exists particularly low-volume, B-rich tourmalines (e.g., samples 1, 2, and 179), likely due to deficiencies in Al-rich and B^{IV}-rich tourmalines in the training set. The dominance of Y-scaling methods likely arises from their ability to adding flexibility to the fit, making data points less stringent. This suggests the hypothesis that weighted least squares (WLS), with weights based on total x uncertainty, could be equally effective in adding flexibility to the fit—essentially functioning as a multivariate equivalent of York regression (York et al. 2004). However, testing this hypothesis remains a task for future work.

CWTLS excels but is sensitive to training data, with reduced performance without sample tm164. Errors-in-variables methods weigh data points differently, making them highly data-dependent. In contrast, least squares treat all points equally, offering more stability but less adaptability. While uncertainty-based methods like CWTLS improve generalisation, their performance relies heavily on the dataset's specific composition. Model success depends on the number of parameters, degrees of freedom, the scaling and magnitudes of X and Y, their sensitivity (partial derivatives), and data distribution, highlighting the data-dependent nature of performance and the importance of a test set for validation.

Speciation model with CWTLS and Block-Diagonal Weights

The CWTLS speciation model without interaction parameters provides regression coefficients, their covariance matrix, residuals in endmember fractions and molar volumes, total residuals

(Frobenius norm of combined x and y residuals), and a misfit parameter (Frobenius norm of all total residuals, 0.03), comparable to other TLS models (~0.005–0.05). Matrix correction of the covariance matrices (~1×10^{-5} regularisation) ensures positive definiteness for this type of regression. TLS mitigates multicollinearity better than OLS, WLS, or robust regression by minimizing errors orthogonally using SVD, though very small singular values can still cause instability. Results are in Appendix 2E. Table 2F shows the molar volumes of the speciation endmembers.

Table 2F. CWTLS endmember molar volumes for the $XY_3Z_6T_6V_3W$ model and the SD based on the covariance matrix obtained from the Hessian at the nonlinear minimisation surface. Regression model without interaction parameters. The correlation matrix is plotted directly below the table for visual reference, with correlation coefficients annotated inside each coloured cell to illustrate the strength and direction of relationships between endmembers.

Mineral	CWTLS Molar Volume	Standard Deviation	Difference with OLS	Outside OLS CI
srl	32.037	0.0422	-0.0898	No
drv	31.826	0.0465	-0.0671	No
uvt	32.087	0.0490	-0.0698	No
fuvt	32.362	0.0398	+0.2128	No
foi	31.612	0.0410	-0.0950	No
ole	30.854	0.0986	-0.1241	No
drvdis	31.913	0.0728	+0.0401	No
odrv	31.713	0.0319	+0.0156	No
fluvt	31.915	0.0391	-0.0695	No
bu	31.648	0.1131	+0.2444	No
mdtw	31.910	0.0650	+0.1264	No
bole	29.596	0.0297	+0.0518	No
aorsm	30.964	0.0586	-0.1568	No
pov	34.557	0.0301	-1.0704	No

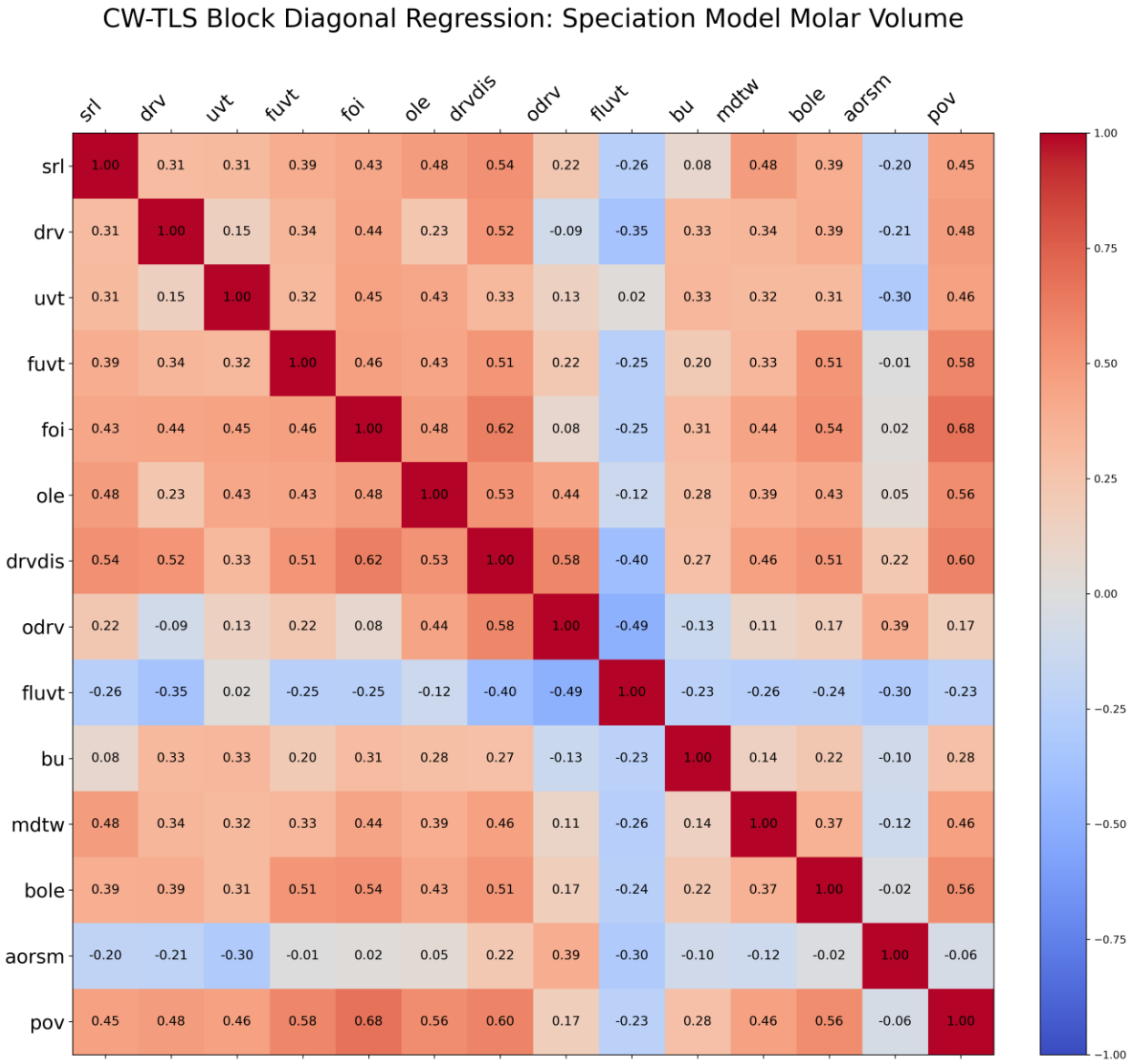

The CWTLS fit closely matches OLS for most endmembers, except for pov (−1.0704 J/mol·bar) and bu (+0.2444), fuvt (+0.2128) and aorsm (−0.1568), but remain within the (large) SE of the OLS coefficient. CWTLS uncertainties are likely underestimated because the Hessian, relying on local curvature and assuming a quadratic surface, ignores residual variance, predictor scaling, and global variability, which the covariance matrix accounts for, providing more realistic estimates.

The largest molar volume differences between the bulk compositional model (Cauchy robust) and the CWTLS speciation model are for bu (-0.5500), ole (-0.2617), and fluvt (-0.0963), with

bu and fluvt falling outside the SD's, indicating significant discrepancies. The speciation model predicts much lower bu volumes as it better separates the buergerite effect and distinguishes trends toward the buergerite and povondraite endmembers.

Isochemical ordering changes with molar volume Drv and drvdis fall within each other's uncertainty range and show no clear evidence of a molar volume increase from Mg–Al disordering at constant bulk composition. In contrast, other ordered/disordered pairs involve isochemical reactions but differ in bulk composition, complicating separation of disordering effects from compositional effects. Isolating the ordering effect would require base-transforming the model to include only ordered and disordered endmembers at identical compositions. Hydrogen disorder may slightly reduce molar volume, as suggested by the lower volume of odrv compared to drvdis, although W-site vacancies may also contribute. For Fe endmembers, the larger volume of fuvt relative to its ordered analog may indicate that Fe^{2+} disorder increases molar volume, while the much larger volume of povondraite compared to buergerite may similarly reflect Fe^{3+} disorder, though bulk composition effects cannot be excluded in either case.

9. MODEL ASSESSMENT

The test set was used for model assessment, slightly overestimating due to internal consistency but underestimating as it was partly used for model selection. By cancelling these errors, it provides a semi-quantitative estimate of the overall uncertainty expected from this molar volume model.

Bulk Compositional model with Cauchy Robust Regression

Model assessment statistics can be found in Appendix 2F (Table 2F.1).

Internal Validation The estimation bias of the Cauchy fit compared to OLS is 0.003 (MSE 0.007 vs 0.004). F-buergerite (tm64), previously tightly fit by OLS, now shows high residuals (0.3–0.4) alongside tm164, marking the only major difference in residuals (Figure 2Q).

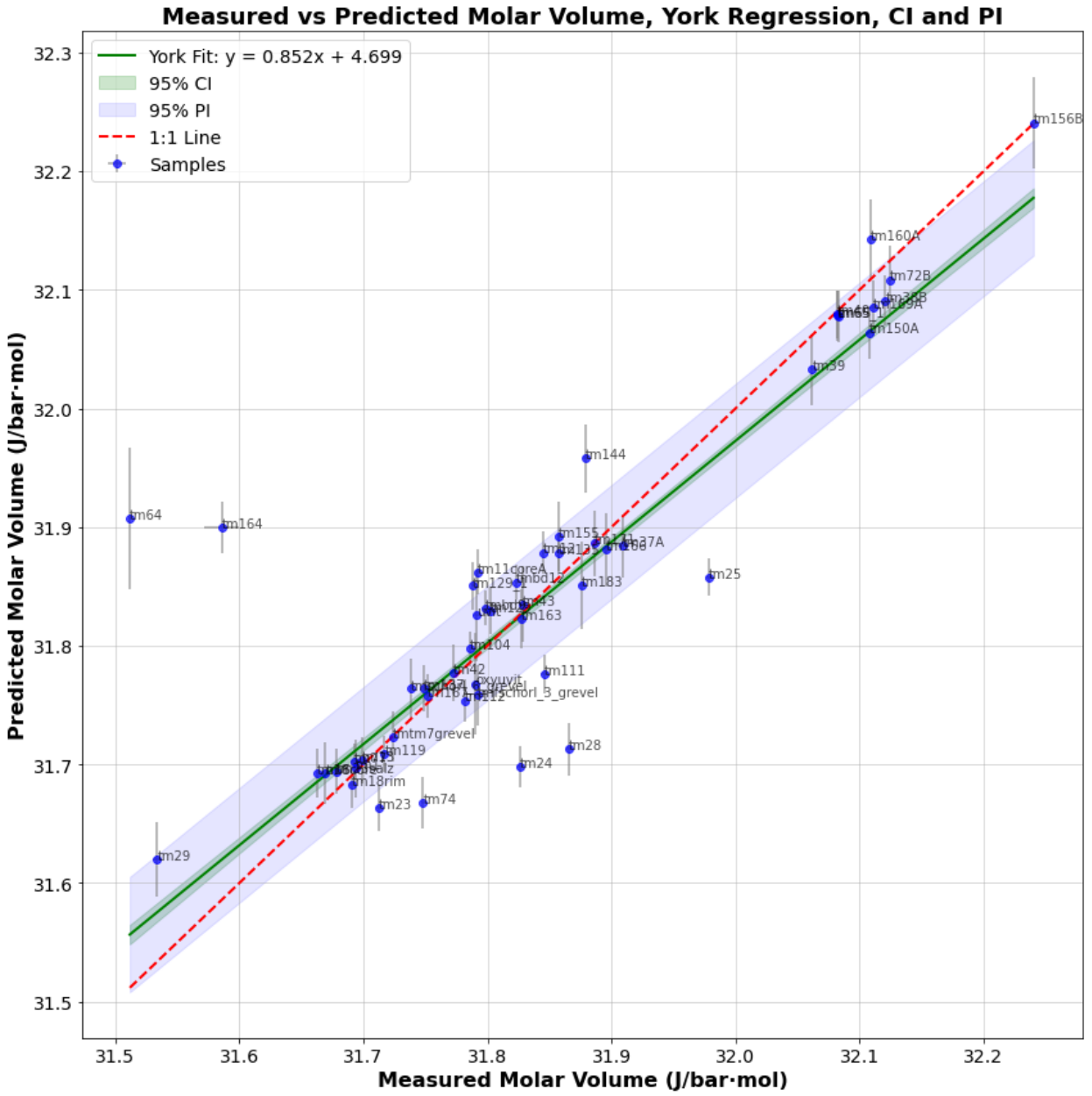

Figure 2Q. The Cauchy robust model fit to the training set data. Green bands show confidence intervals for the mean response, while blue bands represent prediction intervals for individual measurements. The increased estimation bias is mainly due to worsen fit to F-buergerite (tm64). Regression model without interaction parameters

External Validation The Cauchy robust fit model achieves an MSE of 0.007 for both internal and external validation, with zero model variance, demonstrating better generalisation. In this case, the bias-variance tradeoff, with a slight increase in estimation bias (0.003), resulted in a

better model compared to the OLS model, which has lower model bias (0.004) but higher variance (0.009) and total error (0.013), indicating overfitting. Schorl-dravite (sample 9 (Bloodaxe et al. 1999)) is a clear outlier (Figure 2R). The model performs well near the data centroid (31.5–32.5 J/mol·bar) but shows systematic composition-dependent bias, overestimating low and underestimating high molar volumes, demonstrated by a higher bias integral than the OLS/CWTLS fits.

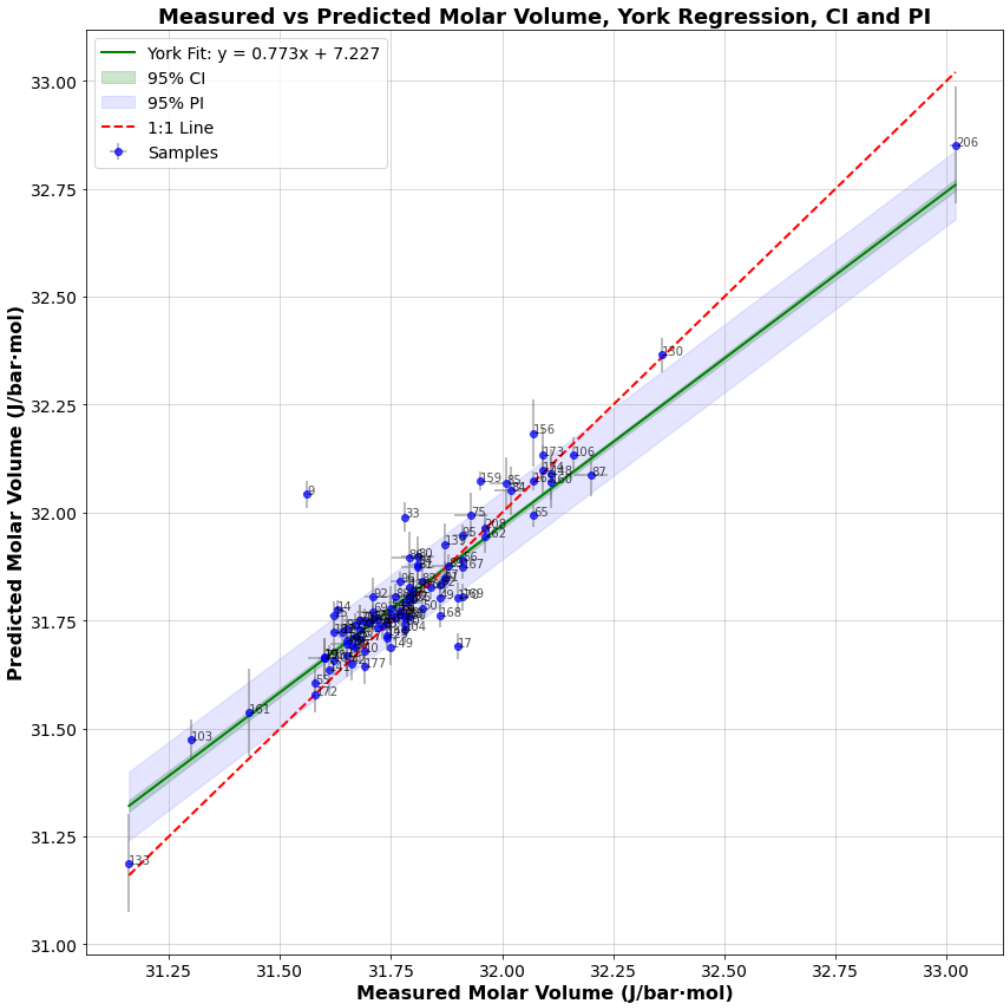

Figure 2R. The Cauchy robust model fit to the test set data. Green bands show confidence intervals for the mean response, while blue bands represent prediction intervals for individual measurements. The centroid of data is fit well but compositional bias is high. Regression model without interaction parameters

Speciation model with CWTLS and Block-Diagonal Weights

Model assessment statistics can be found in Appendix 2F (Table 2F.2).

Internal Validation The training fit is similar to the bulk composition model with the same outliers (tm164), except F-buergerite (tm64) is well fit (Figure 2S). The higher R^2 results from the high-leverage synthetic B-olenite sample.

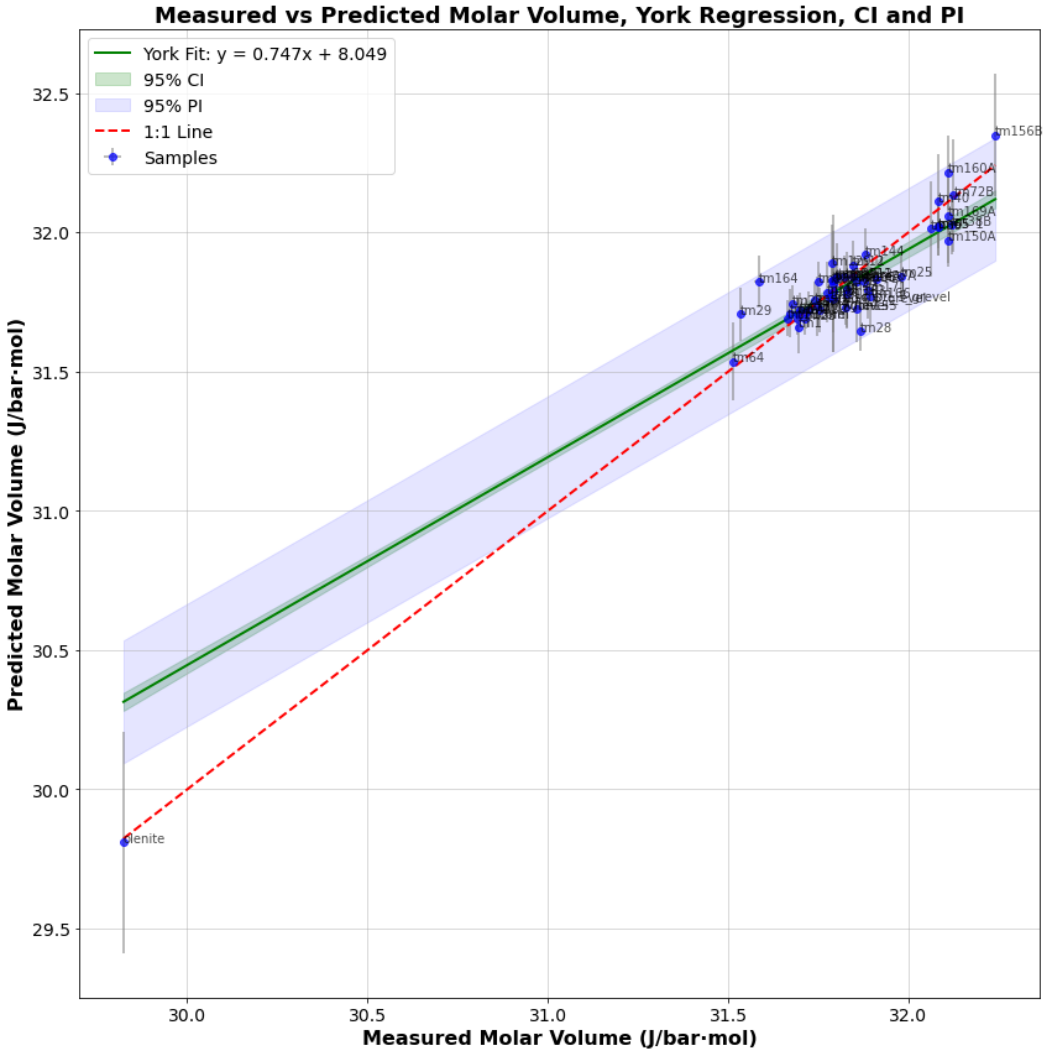

Figure 2S. The CWTLS model fit to the training set data. Green bands show confidence intervals for the mean response, while blue bands represent prediction intervals for individual measurements. Regression model without interaction parameters

External Validation The external validation of the $XY_3Z_6T_6V_3W$ model is detailed in Figure 2T. Comparison with the OLS fit for both training and test set can be found in Appendix 2E which clearly shows the bias-variance tradeoff.

The CWTLS model has low bias (training MSE: 0.005) and lower total error (test MSE: 0.017), yielding a model variance of 0.012, while the OLS model, with similar bias (0.004), has higher total error (0.028) and variance (0.024). A slight bias increase (0.001) in CWTLS improves model performance with lower variance. The bulk composition model fits better (test MSE: 0.007, MAE: 0.055) due to fewer extreme samples but still shows greater composition-dependent bias (bias integral: 0.51 vs. 0.276). The speciation model, though less tightly fit, generalizes better across compositions, performing well on extreme samples with smaller bias (Figure 2T).

Compositional bias in the speciation model persists for low-volume, B-rich tourmalines (e.g., samples 1, 2, and 179) due to the lack of Al-rich and B^{IV}-rich tourmalines in the training set. CWTLS excels in generalisation but is highly sensitive to training data, with reduced performance without sample tm164 demonstrating its data-dependence.

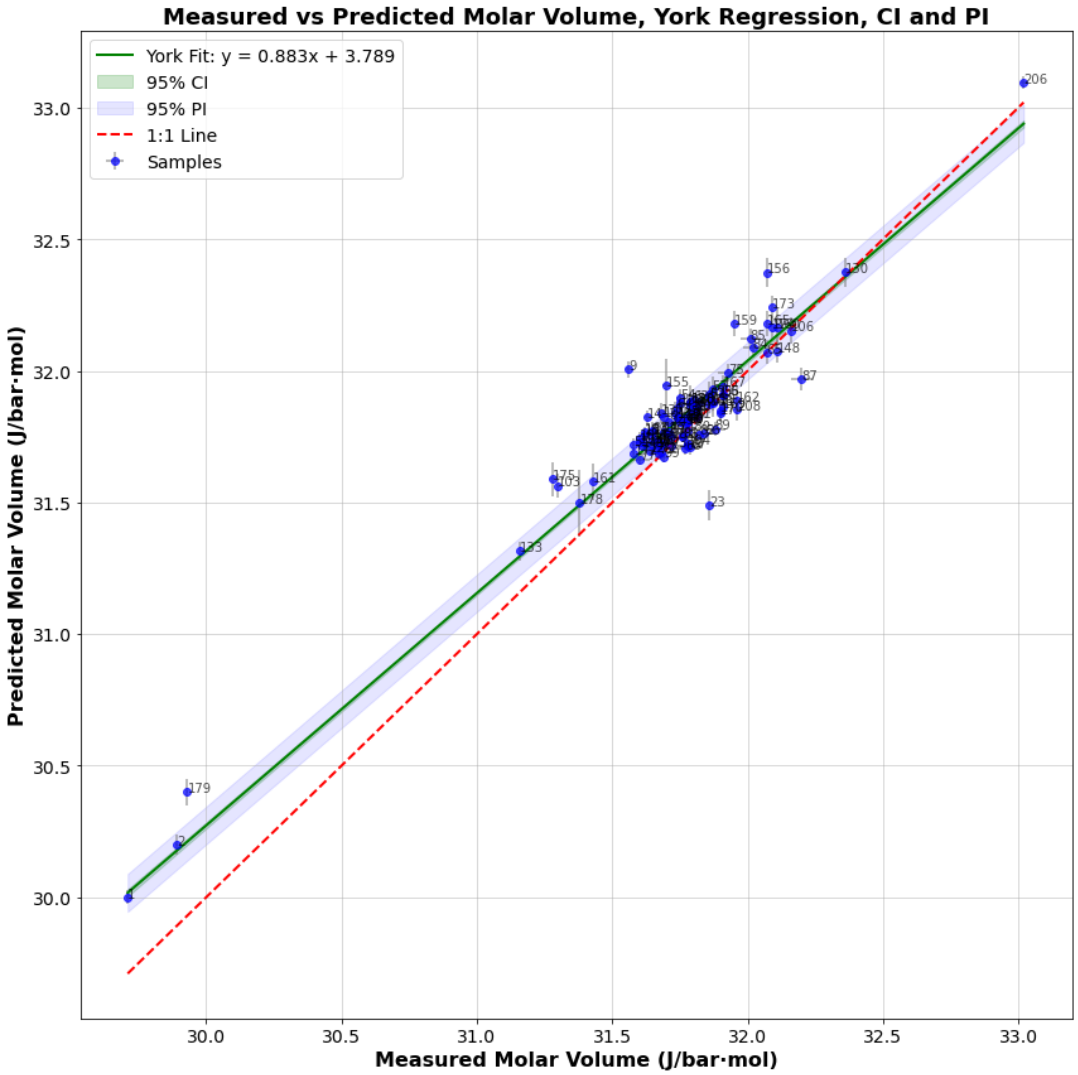

Figure 2T. The CWTLS model fit to the test set data. Dark grey bands show confidence intervals for the mean response, while blue dotted lines represent prediction intervals for individual measurements. Regression model without interaction parameters

Model uncertainty estimation The external validation plots of the bulk and speciation models can be used for uncertainty estimation of the predicted molar volumes**.** The York regression confidence intervals in the y-$\hat{y}$ plot estimate a minimal uncertainty in predicted molar volumes, while wider prediction intervals include individual variability for single observations, providing a maximum estimation (dark green and blue bands, respectively, in Figure 2Q to 2L), see theoretical details NCSS Helpfile (NCSS 2023a). Error propagation from the covariance matrix

of the regression coefficients offers an alternative, but likewise may overestimate uncertainty due to its worst-case-scenario nature (Bevington and Robinson 2003).

Multicollinearity Multicollinearity in bulk and compositional models arises primarily from limited sampling of the endmember space. This issue results in correlated regression coefficients, as many of the parameters are poorly resolved. The root of the problem lies in the inherent limitations of the sample space, which does not encompass the full diversity of possible compositions. Factors such as crystal-chemical controls, site and charge balance constraints from mineral formula optimisation, and natural alignment of samples along dominant exchange vectors due to common bulk compositions contribute to this issue. These natural alignments reinforce multicollinearity, making it difficult to eliminate entirely. Robust regression and CW-TLS help mitigate some of this multicollinearity by weighting the data, thereby reducing the influence of correlated variables. However, the most effective solution is to synthesize additional samples that break these natural trends. Principal component analysis (PCA) vectors (e.g., Figure 2I) can guide the synthesis of new samples by identifying compositional regions where these trends can be disrupted.

10. COMBINED DATASET. ORDINARY LEAST SQUARES

For both the $X(YZ)_9Si_xAl_{1-x}(VW)_4$ bulk composition and $XY_3Z_6T_6V_3W$ speciation models, high VIF factors indicate multicollinearity and data scarcity lead to broad OLS confidence intervals for the endmember molar volumes. Correlated endmember molar volumes reduce independence and applicability, making the models heavily data-dependent. This limits model use, as removing an endmember for smaller chemical systems requires refitting the entire model. The need to refit thermodynamic models with correlated endmember sets is a crucial yet often overlooked issue when projecting models to smaller chemical subsystems. Projection is only valid when the chosen endmembers are statistically independent, meaning they do not exhibit multicollinearity. In this case, the model can be directly reduced without introducing bias or instability. However, when endmembers are correlated, projection without refitting can distort model behavior, and reparameterization is required to maintain thermodynamic consistency. Although the CWTLS method mitigated some multicollinearity by increasing fit flexibility, it did not eliminate data dependence, as weighting altered the influence of each data point. To mitigate these issues, we

calibrated regression coefficients using the combined training and test datasets. However, merging the training and test datasets eliminates any independent validation set, precluding meaningful model assessment. In addition, the model lacks internal consistency, as the tourmaline compositions in the test data were not normalised using the same crystal-chemical assumptions as the training set, leading to compositional incompatibility. Furthermore, the absence of covariance matrices prevents the application of total least squares (TLS), which is required to account for uncertainty in both variables. Regression was therefore conducted using OLS in NCSS and details of the regressions can be found in Appendix 2C.

Bulk composition model The regression model based on the combined dataset of 149 observations demonstrates improved robustness compared to the original training dataset of 52 observations, primarily due to the increased sample size and reduced multicollinearity. The combined dataset shows broader predictor ranges, especially for drvB, aorsmB, fluvt, bu, and mdtw. Except for (hypothetical) mdtw, all $(XX')^{-1}$ diagonal values are below 1. Standard errors halved, tightening confidence intervals and improving model reliability. Significant shifts in foiB (-0.24), buB (+0.24), and oleB (+0.32) exceeded the original confidence intervals and standard errors, while other predictors, despite a large shift; mdtwB (+0.1747), remained within bounds.

Multicollinearity was substantially reduced in the combined dataset, with all VIF factors falling below 3.3 compared to values exceeding 9 in the training set model. In the combined dataset, several correlations from the original model disappeared, particularly those involving aorsmB, while new correlations emerged, notably between uvtB and fluvtB**,** oleB and buB, and oleB and Molar Volume**.**

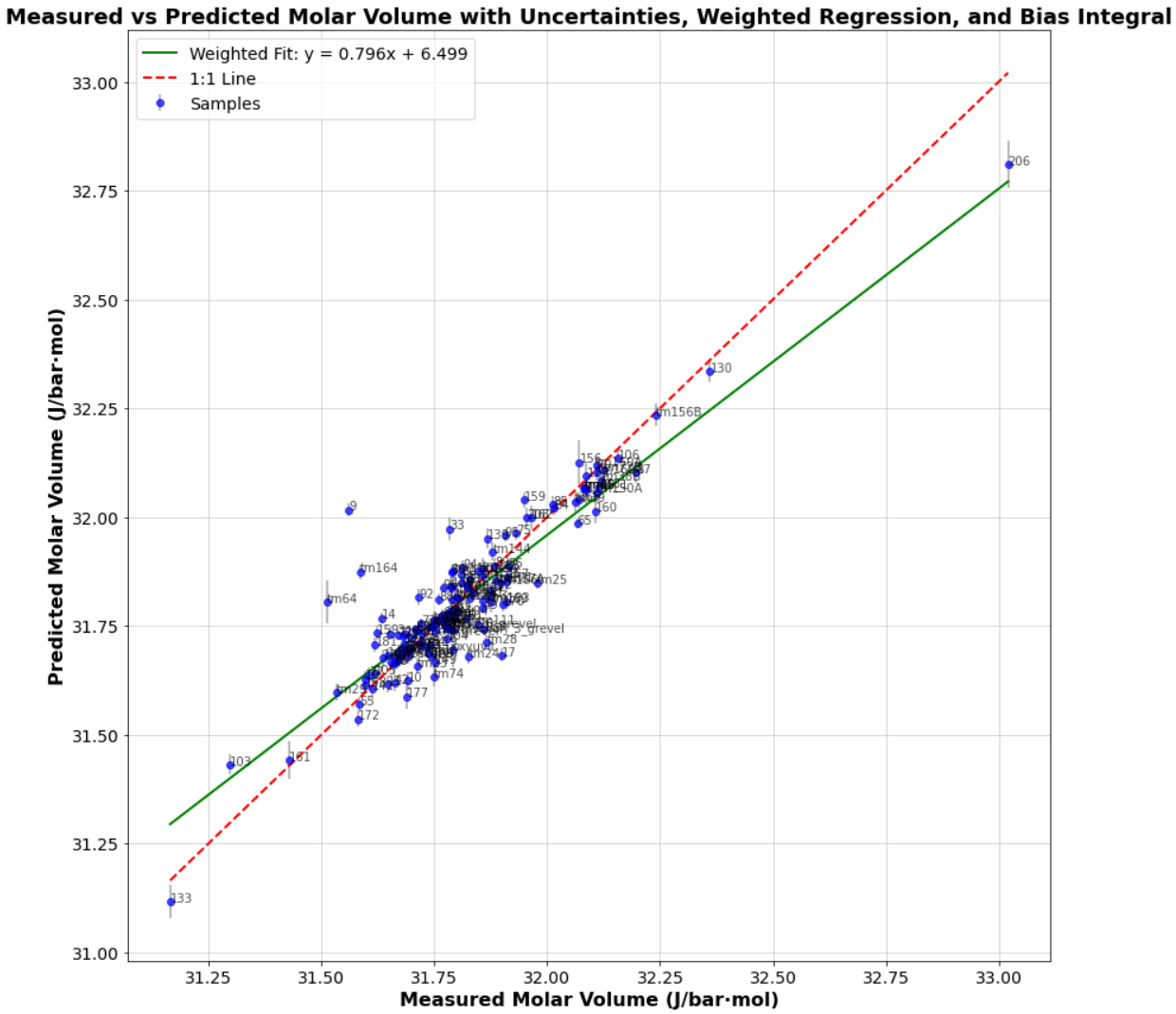

Figure 2U. Combined dataset and the bulk model. Scatter plot of measured vs. predicted molar volume (J/bar·mol) with error bars from covariance matrix propagation. WLS regression (green) accounts for uncertainty variations, while the 1:1 line (dashed red) indicates perfect agreement. Regression model without interaction parameters

In the combined dataset, fluor-buergerite (tm64, -0.29 residual, Cook's D 1.35, DFFITS -3.77) and bosiite (206, 0.20 residual, Cook's D 1.07, DFFITS 3.24) are significant influential outliers which affect multiple predictors, but specifically buB, while high residuals of tm164**,** dutrowite 156**,** 33**,** and 17 show reduced or minor influence with Cook's D values of 0.06, 0.05, 0.08, and 0.03, respectively (Figure 2U).

Subset selection identified five significant binaries to address outlier influence. Two extreme ones involving bu: $W_{srl\text{-}bu}$ (1.64), $W_{drv\text{-}bu}$ (1.19), and moderate negatives for W involving drv: $W_{drv\text{-}fluvt}$ (-0.66), $W_{drv\text{-}uvt}$ (-0.64), and $W_{drv\text{-}foi}$ (-0.47). Interaction parameters improved model fit (MSE 0.0065 to 0.005, R^2Press 0.79 to 0.83) but introduced severe multicollinearity, with VIFs for $W_{drvB\text{-}fluvtB}$ (21.73) and $W_{drvB\text{-}uvtB}$ (12.66), buB (7.38), $W_{srlB\text{-}buB}$ (6.71) exceeding the previous threshold of 3.3. Molar volume shifts beyond confidence intervals were observed for srl (smaller), drv, uvt, fluvt (larger), and bu (much larger). New correlations, such as $W_{drvB\text{-}uvtB}$ (-0.85) and $W_{srlB\text{-}buB}$ (0.75), suggest subregular interactions, with $W_{srlB\text{-}buB}$ replaced with $W_{srl\text{-}bu\text{-}bu}$ and $W_{srl\text{-}srl\text{-}bu}$ proven significant.

Unlike the training model, removing tm164 did not affect drv W's, indicating tm164 is not the sole driver, and the excess volumes in drv W's likely result from coupled substitutions involving X-site cations. However, none of the interaction parameters from the training model performed well on the test set, and strong multicollinearity suggests they may reflect inaccuracies in endmember properties, with their inclusion likely leading to overfitting.

The extreme (subregular) bu interaction terms primarily addressed discrepancies in F-buergerite (tm64) and bosiite (206). tm64 maintained a residual of -0.29 but saw its Cook's D drop from 1.35 to -0.7, reducing influence. Similarly, 206's residual decreased from 0.20 to 0.11, with Cook's D falling from 1.07 to -0.7. Removing tm64 rendered all bu-related interaction parameters insignificant proving that the bulk compositional model cannot deal with Fe3+-Al order-disorder effects.

$XY_3Z_6T_6V_3W$ model The speciation model calibrated with the combined dataset (157 tourmalines) shows significant improvements in precision, coverage, and multicollinearity compared to the training dataset (53 tourmalines). The combined dataset broadens compositional coverage, extending endmember ranges for srl, drv, fuvt, foi, drvdis, mdtw, aorsm, and pov. Molar volume ranges expand from 29.82–32.24 J/mol/bar to 29.71–33.02 J/mol/bar, incorporating more small-volume olenites and large-volume bossiites, enhancing representativeness. The combined dataset achieves a higher RPress2 (0.91 vs. 0) but slightly higher MSE (0.0089 vs. 0.0058). Endmember molar volumes vary from povondraite (34.23 J/mol/bar) to B-olenite (29.41 J/mol/bar), with intermediate values for foi (31.53), drv (31.93),

uvt (32.14), and fluvt (32.61). Drv and drvdis share volumes (31.9), while odrv (31.64) reflects protonation/deprotonation effects.

Regression coefficients remain within original confidence intervals, but pov decreased (-1.40), while fluvt (+0.46), srl (+0.27), and aorsm (-0.58) exceeded standard deviations. Standard errors decreased 2–7x with tighter confidence intervals. Multicollinearity improved significantly, with VIF values dropping below 5.0 (e.g., srl from 24.86 to 3.3). Most correlations are broken except for foi and aorsm (-0.69) and bole and molar volume (-0.83) and a new correlation emerged between drv and drvdis (-0.73) which explains the interdependence demonstrated by the intermediate high VIF factor of drvdis (5). An interaction parameter could decouple shared variance between correlated endmembers.

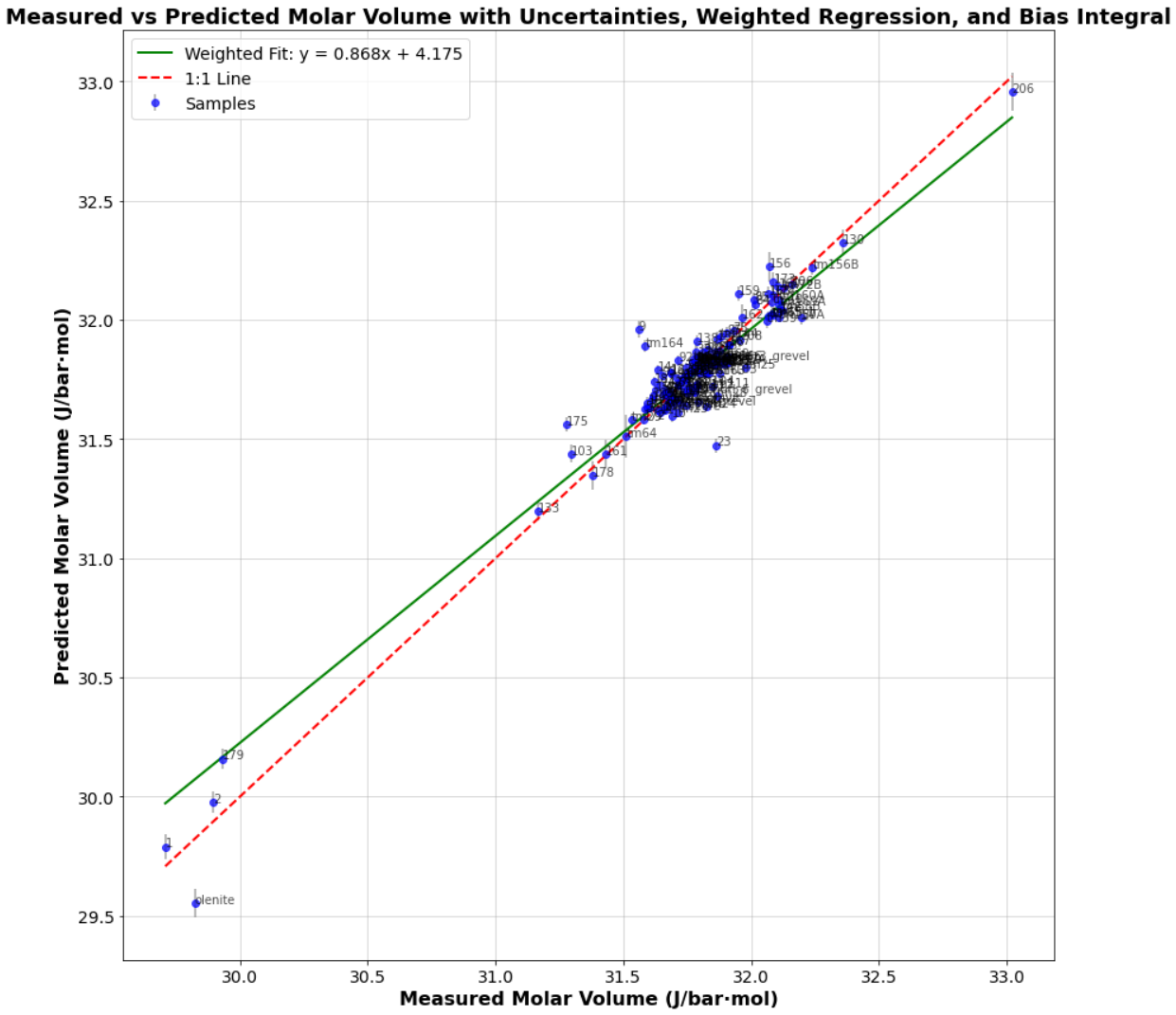

Figure 2V. Combined dataset and the **s**peciation model. Scatter plot of measured vs. predicted molar volume (J/bar·mol) with error bars from covariance matrix propagation. WLS regression (green) accounts for uncertainty variations, while the 1:1 line (dashed red) indicates perfect agreement. Regression model without interaction parameters

Residuals remain non-normal due to outliers. F-buergerite (tm64) and bosiite (206) are fit well in the speciation model (Figure 2V). Tm164 remains an outlier but with reduced influence. Synthetic B-olenite residual increased, likely due to its 0.2 apfu Y vacancy. High residuals for schorl-dravite 9 (Bloodaxe et al. 1999) and dravite 23 (Marschall et al. 2004) suggest potential internal consistency issues or unmodelled ^{IV}B. Large residuals of high ^{IV}B -tourmalines (175, 179) indicate the model's bole endmember requires refinement.

Comparing bulk composition and speciation models reveals notable coefficient differences: bu (0.4627) reflects buergerite-povondraite incompatibility, while mdtw (0.2450) and ole (0.1508) result from large extrapolations.

Combined dataset verdict Regression on the combined dataset improved robustness and tightened confidence intervals for the regression coefficients, highlighting the bulk model's inability to capture Fe^{3+}-Al speciation effects. It also suggests a potential interaction effect between dravite and uvite (~-0.5 J/bar·mol). It also showed that for the speciation model, ~150 samples are needed to better constrain all endmembers, though the absence of significant interaction parameters in the larger model indicates that a few extreme compositions could break the multicollinearities. Regression on the combined dataset demonstrably improved robustness and tightened confidence intervals for the thermodynamic parameters. However, the training and test sets were not normalised consistently, leading to compositional inconsistencies between them. Addressing this issue would require re-normalizing the test set according to the current normalization scheme and retraining the combined model. Until such a reanalysis is performed, we do not recommend using the regression values of the combined dataset due to these compositional inconsistencies, even though the parameter constraints are markedly improved.

11. CONCLUSIONS

This study presents two models for predicting the molar volume (V) of tourmaline: a bulk compositional model (based on bulk parameters) and a speciation model (using site fractions). We provide a detailed explanation of their derivation, strengths, and limitations, highlighting their ability to achieve accurate predictions against test sets. These models represent a significant advancement, offering the first validated tourmaline molar volume framework based on an internally consistent dataset of natural and synthetic samples.

The two models have strengths and limitations that must be carefully considered. The bulk model effectively captures general trends but fails to represent order-disorder effects and compositional extremes, such as distinguishing buergerite from bosiite. The speciation model accounts for site-specific interactions and order-disorder processes, making it better suited for complex compositions but more sensitive to input uncertainties as small changes in the chemical composition can lead to large changes in the endmember fractions. A critical takeaway is the need to balance the bias-variance trade-off between centroid and extreme compositions. The bulk model's failure at extremes indicates that prioritizing interpolation over generalisation limits its applicability beyond the calibration range. Conversely, the speciation model generalizes effectively but risks higher variance when the thermodynamics is dominated by noisy extremes. Therefore, models intended for extrapolation must tolerate higher variance, while those focused-on interpolation require stricter bias control.

Overfitting, a common issue in thermodynamic modelling, often arises from noisy data and outliers due to analytical artifacts, improper characterisation, model limitations, or impurities. In this study, reducing the influence of outliers—through robust techniques for the bulk model or flexible fitting for the speciation model—improved performance by reducing model variance and enhancing predictive accuracy. Overfitting was evident in the behavior of the W interaction parameters. While W terms improved fits within the training set, they significantly worsened prediction accuracy on test sets. As a result, no non-ideal W terms were retained in the final models. This emphasizes the critical importance of test set validation to identify and eliminate overfitted parameters that lack generalizability.

Multicollinearity is another issue in fitting thermodynamic models, affecting both the bulk model and, more significantly, the speciation model. Strong correlations between endmember properties and interaction terms obscure independent parameter contributions and compromise model accuracy. This emphasizes the need for recalibration of the model in smaller chemical spaces as endmembers can no longer be independently projected out. While it may be tempting to apply the most complex solid-solution model, the speciation model, simply because it is the most "up-to-date" option, data scarcity and multicollinearity issues can prevent such models from providing reliable, independent parameter estimates upon projection, limiting their effectiveness in simpler chemical systems and one is better off using the bulk model. These characteristics should be explicitly reported in thermodynamic models to highlight calibration gaps.

Overall, by addressing these challenges and leveraging the strengths of both models, this study provides a solid foundation for advancing tourmaline molar volume predictions, with future improvements achievable by breaking residual correlations, such as Mg-Fe, through controlled synthesis in iron-rich systems under strict oxygen fugacity or computational studies.

REFERENCES

Allen, D.M. (1974) The Relationship Between Variable Selection and Data Augumentation and a Method for Prediction. Technometrics, 16, 125–127.

Andersen, D.J., and Lindsley, D.H. (1988) Internally consistent solution models for Fe-Mg-Mn-Ti oxides; Fe-Ti oxides. American Mineralogist, 73, 714–726.

Andreozzi, G.B., Bosi, F., Celata, B., Capizzi, L.S., Stagno, V., and Beckett-Brown, C.E. (2020) Crystal-chemical behavior of Fe2+ in tourmaline dictated by structural stability: insights from a schorl with formula NaY(Fe2+2Al)Z(Al5Fe2+)(Si6O18)(BO3)3(OH)3(OH,F) from Seagull batholith (Yukon Territory, Canada). Physics and Chemistry of Minerals, 47, 25.

Bačík, P. (2015) Cation ordering at octahedral sites in schorl-dravite series tourmalines. The Canadian Mineralogist, 53, 571–590.

Bačík, P., Uher, P., Ertl, A., Jonsson, E., Nysten, P., Kanickỳ, V., and Vaculovič, T. (2012) Zoned Ree Enriched Dravite from a Granitic Pegmatite in Forshammar Bergslagen Province, Sweden an EMPA XRD and LA–ICP-MS Study. The Canadian Mineralogist, 50, 825–841.

Bačík, P., CemPírek, J., Uher, P., Novák, M., Ozdín, D., Filip, J., Škoda, R., Breiter, K., Klementová, M., and ĎuĎa, R. (2013) Oxy-schorl, Na (Fe2+ 2Al) Al6Si6O18 (BO3) 3

(OH) 3O, a new mineral from Zlatá Idka, Slovak Republic and Přibyslavice, Czech Republic. American Mineralogist, 98, 485–492.

Ballirano, P., Celata, B., and Bosi, F. (2022) In situ high-temperature behaviour and breakdown conditions of uvite at room pressure. Physics and Chemistry of Minerals, 49, 40.

Benisek, A., and Dachs, E. (2020) Excess enthalpy of mixing of mineral solid solutions derived from density-functional calculations. Physics and Chemistry of Minerals, 47, 15.

Berryman, E.J., Zhang, D., Wunder, B., and Duffy, T.S. (2019) Compressibility of synthetic Mg-Al tourmalines to 60 GPa. American Mineralogist, 104, 1005–1015.

Bevington, P.R., and Robinson, D.K. (2003) Data reduction and error analysis. McGraw-Hill, New York, 320.

Biagioni, C., Bosi, F., Mauro, D., Skogby, H., Dini, A., and Zaccarini, F. (2023) Dutrowite, Na (Fe2.52+Ti0.5)Al6(Si6O18)(BO3)3(OH)3O, a new mineral from the Apuan Alps (Tuscany, Italy): the first member of the tourmaline supergroup with Ti as a species-forming chemical constituent. European Journal of Mineralogy, 35, 81–94.

Biernacka, J. (2019) Insight into diagenetic processes from authigenic tourmaline: An example from Carboniferous and Permian siliciclastic rocks of western Poland. Sedimentary geology, 389, 73–90.

Bloodaxe, E.S., Hughes, J.M., Dyar, M.D., Grew, E.S., and Guidotti, C.V. (1999) Linking structure and chemistry in the Schorl-Dravite series. American Mineralogist, 84, 922–928.

Bosi, F. (2008) Disordering of Fe2+ over octahedrally coordinated sites of tourmaline. American Mineralogist, 93, 1647–1653.

——— (2018) Tourmaline crystal chemistry. American Mineralogist, 103, 298–306.

Bosi, F., and Lucchesi, S. (2004) Crystal chemistry of the schorl-dravite series. European Journal of Mineralogy, 16, 335–344.

——— (2007) Crystal chemical relationships in the tourmaline group: Structural constraints on chemical variability. American Mineralogist, 92, 1054–1063.

Bosi, F., and Skogby, H. Oxy-dravite, Na(Al2Mg)(Al5Mg)(Si6O18)(BO3)3(OH)3O, a new mineral species of the tourmaline supergroup. American Mineralogist, 98, 1442–1448.

Bosi, F., Andreozzi, G.B., Federico, M., Graziani, G., and Lucchesi, S. (2005) Crystal chemistry of the elbaite-schorl series. American Mineralogist, 90, 1784–1792.

Bosi, F., Balić-Žunić, T., and Surour, A.A. (2010) Crystal structure analyses of four tourmaline specimens from the Cleopatra's Mines (Egypt) and Jabal Zalm (Saudi Arabia), and the role of Al in the tourmaline group. American Mineralogist, 95, 510–518.

Bosi, F., Andreozzi, G.B., Hålenius, U., and Skogby, H. (2015) Experimental evidence for partial Fe2+ disorder at the Y and Z sites of tourmaline: a combined EMP, SREF, MS, IR and OAS study of schorl. Mineralogical Magazine, 79, 515–528.

Bosi, F., Skogby, H., Ciriotti, M.E., Gadas, P., Novák, M., Cempírek, J., Všianskỳ, D., and Filip, J. (2017) Lucchesiite, CaFe2+3Al6(Si6O18)(BO3)3(OH)3O, a new mineral species of the tourmaline supergroup. Mineralogical Magazine, 81, 1–14.

Bosi, F., Biagioni, C., and Oberti, R. (2019) On the Chemical Identification and Classification of Minerals. Minerals, 9, 591.

Bosi, F., Biagioni, C., Pezzotta, F., Skogby, H., Hålenius, U., Cempírek, J., Hawthorne, F.C., Lussier, A.J., Abdu, Y.A., and Day, M.C. (2022) Uvite, CaMg3(Al5Mg)(Si6O18)(BO3)3(OH)3(OH), a new, but long-anticipated mineral species of the tourmaline supergroup from San Piero in Campo, Elba Island, Italy. Mineralogical Magazine, 86, 767–776.

Bosi, F., Skogby, H., and Hovis, G.L. (2023) Crystal chemistry of povondraite by single-crystal XRD, EMPA, Mössbauer spectroscopy and FTIR. Mineralogical Magazine, 87, 178–185.

Boyd, S.P., and Vandenberghe, L. (2004) Convex optimisation, 716 p. Cambridge University Press, Cambridge, UK.

Bragg, W.L., and Williams, E.J. (1934) The effect of thermal agitation on atomic arrangement in alloys. Proceedings of the Royal Society of London. Series A, Containing Papers of a Mathematical and Physical Character, 145, 699–730.

——— (1935) The effect of thermal agitation on atomic arrangement in alloys—II. Proceedings of the Royal Society of London. Series A - Mathematical and Physical Sciences, 151, 540–566.

Brown, I.D. (2016) The Chemical Bond in Inorganic Chemistry: The Bond Valence Model, Second Edition., 336 p. Oxford University Press, Oxford, New York.

Cámara, F., Ottolini, L., and Hawthorne, F.C. (2002) Crystal chemistry of three tourmalines by SREF, EMPA, and SIMS. American Mineralogist, 87, 1437–1442.

Cempírek, J., Novák, M., Ertl, A., Hughes, J.M., Rossman, G.R., and Dyar, M.D. (2006) Fe-bearing olenite with tetrahedrally coordinated Al from an abyssal pegmatite at Kutná Hora, Czech Republic: structure, crystal chemistry, optical and XANES spectra. The Canadian Mineralogist, 44, 23–30.

Cheng, W., and Ganguly, J. (1994) Some aspects of multicomponent excess free energy models with subregular binaries. Geochimica et cosmochimica acta, 58, 3763–3767.

Connolly, J. a. D. (1990) Multivariable phase diagrams; an algorithm based on generalized thermodynamics. American Journal of Science, 290, 666–718.

Connolly, J.A.D. (2016) Thermodynamics applied to earth materials, 68 p. Lecture Notes, ETH Zurich.

Dachs, E., and Benisek, A. (2019) A new activity model for Mg–Al biotites determined through an integrated approach. Contributions to Mineralogy and Petrology, 174, 76.

——— (2021) A new activity model for Fe–Mg–Al biotites: I—Derivation and calibration of mixing parameters. Contributions to Mineralogy and Petrology, 176, 22.

——— (2024) A new activity model for biotite and its application. Contributions to Mineralogy and Petrology, 179, 93.

Dachs, E., Roozen, S., and Benisek, A. (2021) A new activity model for Fe–Mg–Al biotites: II—Applications in the K2O–FeO–MgO–Al2O3–SiO2–H2O (KFMASH) system. Contributions to Mineralogy and Petrology, 176, 23.

Dutrow, B.L., and Henry, D.J. (2011) Tourmaline: a geologic DVD. Elements, 7, 301–306.

Ertl, A., and Hughes, J.M. (2002) The crystal structure of an aluminum-rich schorl overgrown by boron-rich olenite from Koralpe, Styria, Austria. Mineralogy and Petrology, 75, 69–78.

Ertl, A., Hughes, J.M., Pertlik, F., Foit, F.F., Wright, S.E., Brandstätter, F., and Marler, B. (2002) Polyhedron Distortions in Tourmaline. The Canadian Mineralogist, 40, 153–162.

Ertl, A., Hughes, J.M., Brandstätter, F., Dyar, M.D., and Prasad, P.S.R. (2003) Disordered mg-bearing olenite from a granitic pegmatite at goslarn, austria: a chemical, structural, and infrared spectroscopic study. The Canadian Mineralogist, 41, 1363–1370.

Ertl, A., Marschall, H.R., Giester, G., Henry, D.J., Schertl, H.-P., Ntaflos, T., Luvizotto, G.L., Nasdala, L., and Tillmanns, E. (2010) Metamorphic ultrahigh-pressure tourmaline: Structure, chemistry, and correlations to PT conditions. American Mineralogist, 95, 1–10.

Ertl, A., Schuster, R., Hughes, J.M., Ludwig, T., Meyer, H.-P., Finger, F., Dyar, M.D., Ruschel, K., Rossman, G.R., and Klötzli, U. (2012) Li-bearing tourmalines in Variscan granitic pegmatites from the Moldanubian nappes, Lower Austria. European Journal of Mineralogy, 24, 695–715.

Ertl, A., Baksheev, I.A., Giester, G., Lengauer, C.L., Prokofiev, V.Y., and Zorina, L.D. Bosiite, NaFe^(Al4Mg2)(Si6O18)(BO3) 3 (OH) 3O, a new ferric member of the tourmaline supergroup from the Darasun gold deposit, Transbaikalia, Russia., 28 European Journal of Mineralogy 581–591 (2016).

Ertl, A., Henry, D.J., and Tillmanns, E. (2018) Tetrahedral substitutions in tourmaline: a review. European Journal of Mineralogy, 30, 465–470.

Gadas, P., Novák, M., Cempírek, J., Filip, J., Vašinová Galiová, M., Groat, L.A., and Všianskỳ, D. (2014) Mineral assemblages, compositional variation, and crystal structure of feruvitic

tourmaline from a contaminated anatectic pegmatite at Mirošov near Strážek, Moldanubian Zone, Czech Republic. The Canadian Mineralogist, 52, 285–301.

Ganguly, J. (2001) Thermodynamic modelling of solid solutions. In Solid Solutions in Silicate and Oxide Systems. Eotvos University Press.

Garofalo, P., Audétat, A., Gunther, D., Heinrich, C.A., and Ridley, J. (2000) Estimation and testing of standard molar thermodynamic properties of tourmaline end-members using data of natural samples. American Mineralogist, 85, 78–88.

Gatta, G.D., Bosi, F., McIntyre, G.J., and Skogby, H. (2014) First accurate location of two proton sites in tourmaline: A single-crystal neutron diffraction study of oxy-dravite. Mineralogical Magazine, 78, 681–692.

Gauss, C.F. (1823) Theoria combinationis observationum erroribus minimis obnoxiae. Henricus Dieterich.

Gavin, H.P. (2025) Total Least Squares, 11 p. Lecture Notes CEE 629 System Identification, Duke University.

Ghiorso, M.S., and Sack, O. (1991) Fe-Ti oxide geothermometry: thermodynamic formulation and the estimation of intensive variables in silicic magmas. Contributions to Mineralogy and Petrology, 108, 485–510.

Gibbs, J.W. (1957) The Collected Works of J. Willard Gibbs: In Two Volumes, 925 p. Yale University Press.

Gottschalk, M. (2016) Beyond the Margules equation: a universal thermodynamic equation for solid solutions including coupled substitution, long- and short-range order. European Journal of Mineralogy, 28, 219–244.

Green, E.C.R., White, R.W., Diener, J.F.A., Powell, R., Holland, T.J.B., and Palin, R.M. (2016) Activity-composition relations for the calculation of partial melting equilibria in metabasic rocks. Journal of Metamorphic Geology, 34, 845–869.

Hastie, T., Tibshirani, R., and Friedman, J. (2017) The elements of statistical learning: data mining, inference, and prediction, 715 p. Springer.

Hawthorne, F.C. (2012) The use of end-member charge arrangements in defining new mineral species and hetrovalent substitutions in complex minerals. Canadian Mineralogist, 40, 699–710.

Hawthorne, F.C. (2021) Proof that a dominant endmember formula can always be written for a mineral or a crystal structure. The Canadian Mineralogist, 59, 159–167.

Helffrich, G., and Wood, B.J. (1989) Subregular model for multicomponent solutions. American Mineralogist, 74, 1016–1022.

Henry, D.J., and Dutrow, B.L. (1996) Metamorphic tourmaline and its petrologic applications. Reviews in Mineralogy and Geochemistry, 33, 503–557.

——— (2018) Tourmaline studies through time: contributions to scientific advancements. Journal of Geosciences, 63, 77–98.

Henry, D.J., Novák, M., Hawthorne, F.C., Ertl, A., Dutrow, B.L., Uher, P., and Pezzotta, F. (2011) Nomenclature of the tourmaline-supergroup minerals. American Mineralogist, 96, 895–913.

Hildebrand, J.H. (1929) Solubility XII. Regular Solutions. Journal of the American Chemical Society, 51, 66–80.

Holland, T., and Powell, R. (1996a) Thermodynamics of order-disorder in minerals; I, Symmetric formalism applied to minerals of fixed composition. American Mineralogist, 81, 1413–1424.

——— (1996b) Thermodynamics of order-disorder in minerals; II, Symmetric formalism applied to solid solutions. American Mineralogist, 81, 1425–1437.

——— (2003) Activity–composition relations for phases in petrological calculations: an asymmetric multicomponent formulation. Contributions to Mineralogy and Petrology, 145, 492–501.

Huber, P.J. (1981) Robust Statistics., 320 p. John Wiley & Sons, Inc, New York.

Li, Y., Kowalski, P.M., Blanca-Romero, A., Vinograd, V., and Bosbach, D. (2014) Ab initio calculation of excess properties of La1−x(Ln,An)xPO4 solid solutions. Journal of Solid State Chemistry, 220, 137–141.

Loan, C.F., and Pitsianis, N. (1993) Approximation with Kronecker Products. In M.S. Moonen, G.H. Golub, and B.L.R. Moor, Eds., Linear Algebra for Large Scale and Real-Time Applications pp. 293–314. Springer Netherlands, Dordrecht.

Lussier, A.J., Abdu, Y., Hawthorne, F.C., Michaelis, V.K., Aguiar, P.M., and Kroeker, S. (2011) Oscillatory zoned liddicoatite from Anjanabonoina, central Madagascar. I. Crystal chemistry and structure by SREF and 11B and 27Al MAS NMR spectroscopy. The Canadian Mineralogist, 49, 63–88.

MacDonold, D.J., and Hawthorne, F.C. (1995) The crystal chemistry of Si= AI substitution in tourmaline. Canadian Mineralogist, 33, 849–858.

Mahalanobis, P.C. (1936) On the generalized distance in statistics. Proceedings of the National Institute of Science of India, 2, 49–55.

Margules, M.S. (1895) On the composition of saturated vapors of mixtures. Akademie der Wissenschaften in Wien, Mathematisch-Naturwissenschaftliche Klasse Abteilung II, 104, 1234–1239.

Markovsky, I. (2010) Bibliography on total least squares and related methods. Statistics and its interface, 3, 329–334.

Markovsky, I., and Van Huffel, S. (2007) Overview of total least-squares methods. Signal processing, 87, 2283–2302.

Marler, B., Borowski, M., Wodara, U., and Schreyer, W. (2002) Synthetic tourmaline (olenite) with excess boron replacing silicon in the tetrahedral site: II. Structure analysis. European Journal of Mineralogy, 14, 763–771.

Marschall, H.R., Ertl, A., Hughes, J.M., and McCammon, C. (2004) Metamorphic Na- and OH-rich disordered dravite with tetrahedral boron, associated with omphacite, from Syros, Greece: chemistry and structure. European Journal of Mineralogy, 16, 817–823.

Montgomery, D.C., Peck, E.A., and Vining, G.G. (2021) Introduction to linear regression analysis, 672 p. John Wiley & Sons.

Muggianu, Y.-M., Gambino, M., and JP, B. (1975) Enthalpies de formation des alliages liquides bismuth-étain-gallium à 723 K. Choix d'une représentation analytique des grandeurs d'excès intégrales et partielles de mélange. Journal de Chimie Physique, 83–88.

Mukhopadhyay, B., Basu, S., and Holdaway, M.J. (1993) A discussion of Margules-type formulations for multicomponent solutions with a generalized approach. Geochimica et Cosmochimica Acta, 57, 277–283.

Myhill, R., and Connolly, J. (2021) Notes on the creation and manipulation of solid solution models. Contributions to Mineralogy and Petrology, 176.

Myhill, R., Cottaar, S., Heister, T., Rose, I., Unterborn, C., Dannberg, J., and Gassmoeller, R. (2023) BurnMan–a Python toolkit for planetary geophysics, geochemistry and thermodynamics. Journal of Open Source Software, 8, 5389.

NCSS (2023a) Multiple Regression, 72 p. NCSS Helpfile, chapter 305.

——— (2023b) Subset Selection in Multiple Regression. NCSS Helpfile, chapter 307.

Pieczka, A. (1996) Studium mineralogiczne turmalinów Polski: Mineralogical study of Polish tourmalines. Wydawnictwo Oddziału Polskiej Akademii Nauk, Kraków.

Pieczka, A., and Kraczka, J. (2004) Oxidized tourmalines—a combined chemical, XRD and Mossbauer study. European Journal of Mineralogy, 16, 309–321.

Pieczka, A., Ertl, A., Sęk, M.P., Twardak, D., Zelek, S., Szełęg, E., and Giester, G. (2018) Oxy-dravite from Wołowa Góra Mountain, Karkonosze massif, SW Poland: Crystallochemical and structural studies. Mineralogical Magazine, 82, 913–928.

Powell, R., and Holland, T. (1993) On the formulation of simple mixing models for complex phases. American Mineralogist, 78, 1174–1180.

——— (1999) Relating formulations of the thermodynamics of mineral solid solutions; activity modelling of pyroxenes, amphiboles, and micas. American Mineralogist, 84, 1–14.

Quenouille, M.H. (1956) Notes on bias in estimation. Biometrika, 43, 353–360.

Sack, R.O. (2017) Fahlore thermochemistry: Gaps inside the (Cu,Ag)10(Fe,Zn)2(Sb,As)4S13 cube. Petrology, 25, 498–515.

Sack, R.O., and Ghiorso, M.S. (1994) Thermodynamics of multicomponent pyroxenes: I. Formulation of a general model. Contributions to Mineralogy and Petrology, 116, 277–286.

Scribner, E.D., Cempírek, J., Groat, L.A., Evans, R.J., Biagioni, C., Bosi, F., Dini, A., Hålenius, U., Orlandi, P., and Pasero, M. (2021) Magnesio-lucchesiite, CaMg3Al6(Si6O18)(BO3)3(OH)3O, a new species of the tourmaline supergroup. American Mineralogist, 106, 862–871.

Sluiter, M.H., and Kawazoe, Y. (2000) Prediction of solution enthalpies of substitutional impurities in aluminium. Modelling and Simulation in Materials Science and Engineering, 8, 221.

Spear, F.S. (1993) Metamorphic phase equilibria and pressure–temperature–time paths. Mineralogical Society of America Monograph., 799.

Tajčmanová, L., Connolly, J. a. D., and Cesare, B. (2009) A thermodynamic model for titanium and ferric iron solution in biotite. Journal of Metamorphic Geology, 27, 153–165.

Taylor, M.C., Copper, M.A., and Hawthorne, F.C. (1995) Local change-compensation in hydroxyl-deficient uvite. The Canadian Mineralogist, 33, 1215–1221.

Thompson, J.B. (1967) Thermodynamic properties of simple solutions. In P.H. Abelson, Ed., Researches in geochemistry vol. 2 Vol. 2, pp. 340–361. J. Wiley and Sons, New York, NY.

Thompson Jr, J.B. (1969) Chemical reactions in crystals. American Mineralogist: Journal of Earth and Planetary Materials, 54, 341–375.

Tucker, A. (1994) Applied combinatorics, 447 p. John Wiley & Sons, Inc.

van Hinsberg, V.J., and Schumacher, J.C. (2007) Using estimated thermodynamic properties to model accessory phases: the case of tourmaline. Journal of Metamorphic Geology, 25, 769–779.

van Hinsberg, V.J. (2011) Preliminary experimental data on trace-element partitioning between tourmaline and silicate melt. The Canadian Mineralogist, 49, 153–163.

Vereshchagin, O.S., Frank-Kamenetskaya, O.V., Rozhdestvenskaya, I.V., and Zolotarev, A.A. (2018) Incorporation of 3d elements in tourmalines: structural adjustments and stability. European Journal of Mineralogy, 30, 917–928.

Vinograd, V.L., Sluiter, M.H.F., and Winkler, B. (2009) Subsolidus phase relations in the CaCO 3 – MgCO 3 system predicted from the excess enthalpies of supercell structures with single and double defects. Physical Review B, 79, 104201.

Weller, O.M., Holland, T.J., Soderman, C.R., Green, E.C., Powell, R., Beard, C.D., and Riel, N. (2024) New thermodynamic models for anhydrous alkaline-silicate magmatic systems. Journal of Petrology, 65, egae098.

White, R.W., Powell, R., and Holland, T.J.B. (2007) Progress relating to calculation of partial melting equilibria for metapelites. Journal of metamorphic Geology, 25, 511–527.

Will, T.M. (1998) Phase Equilibria in Metamorphic Rocks, 315 p. Vol. 71. Springer, Berlin, Heidelberg.

Wohl, K. (1953) Thermodynamic evaluation of binary and ternary liquid systems. Chemical Engineering Progress, 49, 218–221.

Wood, B.J., and Nicholls, J. (1978) The thermodynamic properties of reciprocal solid solutions. Contributions to Mineralogy and Petrology, 66, 389–400.

Wurm, M. (2021) A universal and fast method to solve linear systems with correlated coefficients using weighted total least squares. Measurement Science and Technology, 33, 015017.

York, D., Evensen, N.M., Martínez, M.L., and De Basabe Delgado, J. (2004) Unified equations for the slope, intercept, and standard errors of the best straight line. American journal of physics, 72, 367–375.

Bridging Text Between Manuscripts (Chapter 2-Chapter 3)

Energy Equation Calibration: Molar Volume to Entropy and Heat Capacity Calibration

The thermodynamic model developed in Chapter 2 establishes the composition and speciation space for tourmaline and calibrates one of the key parameters of the energy equation: molar volume. This parameter, derived from crystal-chemical measurements controls the pressure sensitivity of Gibbs free energy and is thus essential for describing phase stability and exchange equilibria as function of pressure. Using internally consistent mineral formulas in terms of bulk parameters and site occupancies, two models were constructed: a bulk compositional model and a site-based speciation model. The calibration applied multivariate regression techniques to a dataset of ~50 samples, rigorously tested for multicollinearity, model robustness, and predictive accuracy using a molar volume literature test set. Together, the composition/speciation space and the molar volume calibration define the first components of the tourmaline thermodynamic framework—bounding the system both compositionally and volumetrically.

Chapter 3 extends this foundation by addressing the temperature dependence of the Gibbs free energy through direct measurement of heat capacity and entropy. Using the same internally consistent tourmaline dataset, high-precision calorimetric experiments were conducted from 2 to 773 K. These data enable regression of endmember entropies and Cp(T) functions in both bulk compositional and speciation models, applying the same structural and compositional framework used in the molar volume calibration. In contrast to molar volume, where a separate literature-based test set was available for model validation, no such dataset exists for entropy or heat capacity. As a result, model performance is assessed by comparing the fit of our new models to the training set against the fit of the previously published estimation model—using the same dataset as a proxy test set for the latter. This chapter therefore adds the thermal component to the energy equations, capturing both vibrational and magnetic entropy contributions, while ensuring physical consistency through rigorous uncertainty propagation. The integrated treatment of entropy, heat capacity, and molar volume across Chapters 2 and 3 represents a significant advance over estimation-based approaches and marks the next step toward a fully experimentally calibrated thermodynamic model for tourmaline solid solution.

Thermodynamic model for Tourmaline

"Entropy isn't what it used to be."

Chapter 3. Thermodynamic model for Tourmaline. Entropy and Heat Capacity

Stan Roozen, Vincent van Hinsberg, Edgar Dachs, Artur Benisek

ABSTRACT Tourmaline is a critical accessory mineral in igneous, metamorphic, and hydrothermal environments, serving as a geochemical recorder due to its compositional flexibility and large stability range in physical and chemical parameter space. However, the existing thermodynamic model for tourmaline, based on estimation methods, is insufficient for accurately predicting its phase equilibria and energetic behavior. To address this gap, we developed a solution model for entropy and high-temperature heat capacity in tourmaline, focusing on the Na-Ca-Mg-Fe^{2+}-Fe^{3+}-Ti-Al-B-O-H-F chemical system, which encompasses the most common tourmaline solid solution chemistries in typical igneous, metamorphic and hydrothermal settings, which are Li, K, Mn, V and Cr poor. The model is based on direct calorimetric measurements from 2 to 773.15 K, combining relaxation calorimetry and differential scanning calorimetry data, using the consistently characterised tourmaline database of chapter 2.

Two models were developed: a bulk compositional model, requiring only chemical composition with endmembers defined by bulk parameters, and a speciation model, relying on additional single crystal-XRD data with site fractions defining endmembers. This work builds on the molar volume models of chapter 3 and extends these to entropy and high-T heat capacity.

1. INTRODUCTION

Tourmaline is the most abundant borosilicate in Earth's crust and an exceptional geochemical recorder due to its structural flexibility, stability over a wide P–T–X range, and resistance to alteration and diffusion Hinsberg et al. (2011). Its $XY_3Z_6(T_6O_{18})(BO_3)_3V_3W$ structure supports diverse homovalent and coupled substitutions, allowing it to preserve compositional zoning and record interactions with minerals, fluids, and melts from diagenesis to ultrahigh-pressure metamorphism. This makes tourmaline a key tracer for reconstructing fluid histories (van Hinsberg et al. 2017), metamorphic reactions (Henry and Dutrow 1996), and P–T conditions (Hinsberg and Schumacher 2007). Yet, the rapid increase in tourmaline-based studies (Henry and Dutrow 2018) often outpaces the development of robust theoretical frameworks needed for quantitative interpretation.

The existing thermodynamic model for tourmaline is based on an estimation method. The polyhedron estimation method determines fractional polyhedral thermodynamic properties using

regression on databases containing minerals from diverse structures, polymerization levels, and crystal family classes (Van Hinsberg et al. 2005a, 2005b). These polyhedra are then stoichiometrically summed to estimate the thermodynamic properties of unknown, including tourmaline endmembers. The resulting endmembers were optimised by calibrating them against a limited set of natural and experimental phase assemblages (van Hinsberg 2006). This method only provides average polyhedral properties, combining data from minerals with vastly different sizes, shapes, distortions, and structural densities, leading to oversimplified and generalized estimates. Moreover, the "fitting the rock" approach without experimental constraints produces empirically tuned parameters that are highly correlated and lack physical significance, limiting their predictive power beyond the calibration range. As a result, these models are primarily capable of predicting the general order of net transfer reactions but offer little accuracy in describing more detailed thermodynamic processes, such as order-disorder relationships or local site interactions, as stated for tourmaline in van Hinsberg and Schumacher (2007).

This study presents two improved models for entropy (S) and heat capacity Cp(T) in tourmaline (bulk compositional and site-specific) derived from direct calorimetric measurements of synthetic and natural compositions using the tourmaline database of chapter 2 Endmember entropy and high-T Cp are determined by regressing and integrating the samples vibrational and magnetic contributions. Using these tourmaline specific endmember components as chemical units, instead of general polyhedra, enhances predictive accuracy. Incorporating order-disorder and site-specific interactions, they outperform estimation methods, offering a reliable framework for phase equilibria and petrological applications. The methodology allows the model parameters to retain physical meaning while avoiding overfitting and parameter correlation problems. This approach not only advances the thermodynamic modelling of tourmaline but also offers a transferable methodology for addressing similarly complex mineral systems. We will compare the performance of the bulk compositional and speciation models against the polyhedron model and show that these new models improve on S and Cp(T) predictions.

2. METHODS

The tourmaline dataset of chapter 2 provides detailed compositional characterisation and uncertainty analysis for natural single-crystal solid solutions and select synthetic samples,

ensuring robust normalization and data consistency. This dataset was used to calibrate a molar volume model in chapter 3, and in this study, it is utilized to directly measure entropy and heat capacity.

Theoretical Background Theoretical background about all the physical phenomena which give rise to Cp (T) curve can be found in Appendix 3A.

2.1 Relaxation Calorimetry (Heat Capacity below 298.15K)

Natural tourmaline single crystals (~3 × 3 mm) with polished bottoms were prepared to ensure optimal thermal contact and inspected under a binocular microscope for major inclusions. For samples that lacked sufficiently sized crystals for single crystal determination, powdered samples (5–25 mg) were used instead. These were finely ground in an agate mortar (under acetone to minimize oxidation of transition metals), packed into high-purity aluminum pans (~5.5 mg, 0.025 mm foil pre-formed with a 4 mm drill bit), sealed by folding the edges, and compressed to ~0.5 mm thickness using a hydraulic press at 1.5 tons for 1–2 minutes to eliminate voids and obtain pellets with parallel upper and lower surfaces, enhancing thermal conductivity (Dachs and Benisek 2011; Dachs et al. 2014). The pellet was reweighed to confirm integrity. The Quantum Design Physical Property Measurement System (PPMS) Cp Option setup consists of a helium-filled dewar, a thermally isolated vacuum chamber, and a puck containing a sapphire sample mounting platform with a heater and thermometer suspended by thin wires for precise thermal links (Lashley et al. 2003; Dachs and Bertoldi 2005; Kennedy et al. 2007). The platform was first cleaned with toluene and coated with a thin, uniform layer of Apiezon N grease to ensure good thermal contact with the sample. To isolate the sample's heat capacity, separate *addenda* measurements—referring to the combined heat capacity of the empty platform and grease—were performed and later subtracted from the total signal during sample runs. For the subsequent sample measurement, the polished side of the single crystal or the prepared pan was mounted on the platform. Measurements were performed on cooling from 300 K to 2 K using a ^{4}He system, with 60 logarithmically spaced T points, denser at low T. At each T point during the same cooling run, the heat capacity was measured three consecutive times to determine the analytical uncertainty. Heat capacity values were derived by subtracting addenda measurements (platform, grease) from the total, and subtracting the Al pan contributions which whose empirical Cp(T)

was determined prior and was fit with a cubic spline. Sample coupling was estimated by $\frac{100K_g}{(K_g+K_w)}$, where Kg and Kw are the thermal conductance's of the sample-platform interface and wires, respectively. Further theoretical detail about the method can be found in Appendix 3B.

Relaxation Calorimetry Data Processing Heat capacity was converted from μJ/K to J/mol·K by scaling to joules, normalizing by sample mass J/g·K, and multiplying by the molar mass, which depends on the precision of the tourmaline formula from compositional analysis. A ±0.02 mg weight uncertainty was assumed for this conversion. Linear interpolation was applied between measured data points to obtain a smooth Cp curve, though this simplification slightly underestimates the true, nonlinear curve. Using second-order instead of piecewise linear interpolation changes the entropy at 298.15 K by only 0.2 J/mol·K. Heat capacity uncertainty was determined via piecewise linear interpolation of the analytical uncertainty, and entropy uncertainty was derived by integrating this uncertainty function divided by T. Entropy calculations employed the equation $S = \int_{T_0}^{T} \frac{C_p}{T} dT$ evaluated using Mathematica's NIntegrate function over the range 2–298.15 K. Error propagation included analytical uncertainties from repeated measurements but did not account for sample-related or hysteresis-induced uncertainties. Accuracy and precision of the PPMS have been previously evaluated using standards and will be discussed in the Result section.

2.1 Differential Scanning Calorimetry (DSC) (above 298.15K)

Above 298.15K, heat capacity was measured using DSC. A Perkin Elmer Diamond DSC measured Cp from 243.3 to 773.15 K (high-T Cp signal) for powders and polished single crystals in Perkin Elmer aluminum pans (kit No. 0219-0041) with lids. Proper thermal coupling minimised T lag, with powdered samples exhibiting slightly more lag than single crystals. For one sample, Cp values from powders and single crystals were within uncertainty and merged. Samples were preheated to 500 °C to eliminate absorbed water and ensure no phase transitions occurred, then cooled and reweighed post-run to check for mass loss due to evaporation. DSC was performed before PPMS to ensure the same quenched state from 500°C was measured in both techniques. Most weight changes measured before and after DSC were below the 0.02 mg uncertainty, except for tm23, tm29, tm13 (0.03 mg), tm171 (0.04 mg), tm160A (0.08 mg), tm42

(0.13 mg), uvite (0.21 mg), and oxyuvite (0.50 mg), indicating possible evaporation of inclusions or experimental impurity phases.

Measurements began after stabilizing the calorimeter block at 243.3 K for 5 minutes using a Perkin Elmer Intracooler with a dried air flow (200 ml/min) to prevent ice formation. Runs were conducted under argon gas in step-scanning mode at a 10 K/min heating rate, with 50 K intervals and 2 minutes of isothermal time per step. Three runs were performed for each sample: blank (empty pans), reference (31.764 mg corundum crystal), and sample. Calibration used NIST Cp(T) values for sapphire, with a sapphire run calculating the calibration factor F=Cp(lit)/Cp(obs). Runs were accepted if within 1% of literature values, and each set (empty, sapphire, and sample) was repeated three times. DSC, as a dynamic heating method, can introduce hysteresis errors, highlighting the need for calibration, which is performed using indium's melting point and enthalpy of fusion. Further theoretical detail about the method can be found in Appendix 3B.

DSC Data Processing The data were analysed using a custom Mathematica script (Dachs and Benisek 2011) based on Mraw (1988)'s method. Ideally, isothermal baselines, representing the power required to maintain constant T at zero scan rate, should be identical for the empty pan, reference, and sample, but corrections were applied to account for system drift. These baselines were aligned by averaging data points within each isothermal section i, excluding dynamic equilibration periods. Mean T ($\bar{T}_i$) and heat flows ($\bar{Q}_i$) were calculated as: $\bar{T}_i = \frac{1}{n}\sum_{j=1}^{n} T_{ij}$, and $\bar{Q}_i = \frac{1}{n}\sum_{j=1}^{n} Q_{ij}$, where j indexes data points, and n is the number of points in section i. Scalar correction factors for the isothermal sections were computed as: $\Delta Q_{\mathrm{ref},i} = \bar{Q}_{\mathrm{empty},i} - \bar{Q}_{\mathrm{ref},i}$, $\Delta Q_{\mathrm{sample},i} = \bar{Q}_{\mathrm{empty},i} - \bar{Q}_{\mathrm{sample},i}$.

Polynomial fits (up to cubic terms) are applied to the averaged isothermal corrections across all sections to derive T-dependent bias correction functions:

$$\Delta Q_{\mathrm{ref}}(T) \approx a_{\mathrm{ref}} + b_{\mathrm{ref}} T + c_{\mathrm{ref}} T^2 + d_{\mathrm{ref}} T^3$$
$$\Delta Q_{\mathrm{sample}}(T) \approx a_{\mathrm{sample}} + b_{\mathrm{sample}} T + c_{\mathrm{sample}} T^2 + d_{\mathrm{sample}} T^3$$

and are applied to drift correct both isothermal and non-isothermal heat flow data of the reference and sample heat flow data, aligning them with the empty pan baseline:

$$Q_{\text{corrected,ref}}(T) = Q_{\text{original,ref}}(T) + \Delta Q_{\text{ref}}(T)$$
$$Q_{\text{corrected,sample}}(T) = Q_{\text{original,sample}}(T) + \Delta Q_{\text{sample}}(T)$$

Figures of the heat signal before and after drift correction can be found in Appendix 3B (Figure A3B.1 and A3B.2). The sample Cp was calculated as:

$$C_{\text{p sample}} = \frac{Q_{\text{sample}} - Q_{\text{empty}}}{\text{heating rate}} \cdot \frac{1}{60}$$

by subtracting the baseline heat flow (Q_{empty}) from the measured heat flow (Q_{sample}), normalizing it by the heating rate to account for T change over time. The 1/60 converts from seconds to minutes. The Cp differences of the aluminum DSC pan between empty and ref/sample, and for powders, the additional Cp of the aluminum foil, were subtracted using a polynomial expression for the heat capacity of the Al pan material (Dachs and Benisek 2011), whose heat capacity was taken from the JANAF-Tables (Chase, 1998):

$$C_{\text{pan, diff}} = \frac{135.18 - 0.139983T + 0.000117942T^2 - 3.2767\times10^{-8}T^3 - 1478\cdot T^{-0.5} + 595094\cdot T^{-2}}{\text{mass pan}} \cdot \text{ mass diff}$$

Here, T is the T, and the coefficients are specific to the pan material.

This correction ensures high accuracy and reproducibility, with DSC measurements accurate to within ±1%.

The data were averaged with SD calculated and fit to the empirical Berman & Brown (1985) Cp polynomial for cp data without λ transitions (further called the “Berman fit”):

$$Cp = k_0 + k_1 T^{-0.5} + k_2 T^{-2} + k_3 T^{-3}$$

in Mathematica using LinearFit with singular value decomposition, as the equation is linear in its coefficients. The covariance matrix of fit parameters was computed. Fit quality was assessed using the chi-square probability from the chi-squared statistic and degrees of freedom. With k_1

and $k_2 \leq 0$, inflections are avoided in the Cp(T) function above 298.15 K ensuring reliable extrapolation of Cp to higher T, crucial for tourmaline which is stable beyond current calorimetric limits. The equation cannot be used below 298.15 K due to potential inflections caused by the positive k_3 term at lower T.

This method minimises thermal lag, corrects baseline drift, and ensures accuracy through a uniform heating rate.

2.2 Extrapolation from 2.5 K to 0K

PPMS Cp measurements using ^{4}He cooling down to 2 K revealed a low-T Cp anomaly in iron-rich tourmaline, interpreted as a second-order magnetic spin glass transition (see Appendix 3A for details and Appendix 3C for proof). Unlike first-order transitions, where relaxation calorimetry struggles with profile fitting, second-order transitions can be accurately measured. (Rosen and Woodfield 2020). Measurements were taken up to the transition onset, avoiding direct magnon detection, and Cp was extrapolated from 0 K to 5 K using a series expansion with uneven powers ($Cp=aT+bT^3+cT^5+dT^7$) (Rosen and Woodfield 2020). The uncertainty was fixed at 0.01 for the 0–5 K range. The Cp and vibrational entropy S^{vib} are extrapolated to 0 J/(K·mol) at 0 K to satisfy the third law of thermodynamics (see Appendix 3A for a detailed explanation).

In antiferromagnetic tourmaline, spin wave contributions can be estimated using a linear magnon dispersion ($\omega \propto k$) leads to a DOS scaling as ω^2, resulting in a $Cp \propto T^3$ behavior at low-T(Gopal 1966; Miller 1988). Since the Néel T is low, the magnon T^3 behavior dominates over the phonon T^3 contribution in this range. The T^5 and T^7 terms provide fit flexibility, capturing non-standard behaviors such as critical fluctuations, nonlinear magnon interactions, anisotropies, or higher-order exchange effects near the critical T, beyond mean-field theory.

However, fitting with only $bT^3+cT^5+dT^7$ did not produce accurate results, necessitating the addition of a linear term. Linear terms are rare in low-T Cp for insulators but common in metals due to conduction electron contributions (Gopal 1966). In tourmaline, this linear term may indicate a low-T Schottky anomaly with a small energy level separation such as due to vacancies an/or impurities (Schliesser and Woodfield 2015), short-range spin-glass behavior, the low-T tail of the magnetic transition (Miller 1988). In Figure 3A and Figure 3B**,** the series expansion fit is

demonstrated for foitite and F-buergerite, respectively. In F-buergerite, Cp between 2–5 K shows two peaks, with the second likely at lower T, supported by relatively high Cp at 2.5 K.

The integral of Cp/T from 0–5 K is a maximum of 5J/mol·K using extrapolation, a small but significant contribution (~0.5–1%) to the entropy at 298.15 K, comparable to the total integrated uncertainty of Cp//T up to standard state conditions.

The <5 K empirical function, PPMS interpolation, and Berman fit were combined into a single Mathematica function covering 0–798.15 K for each sample, enabling calculation of Cp and S and their uncertainties at any T

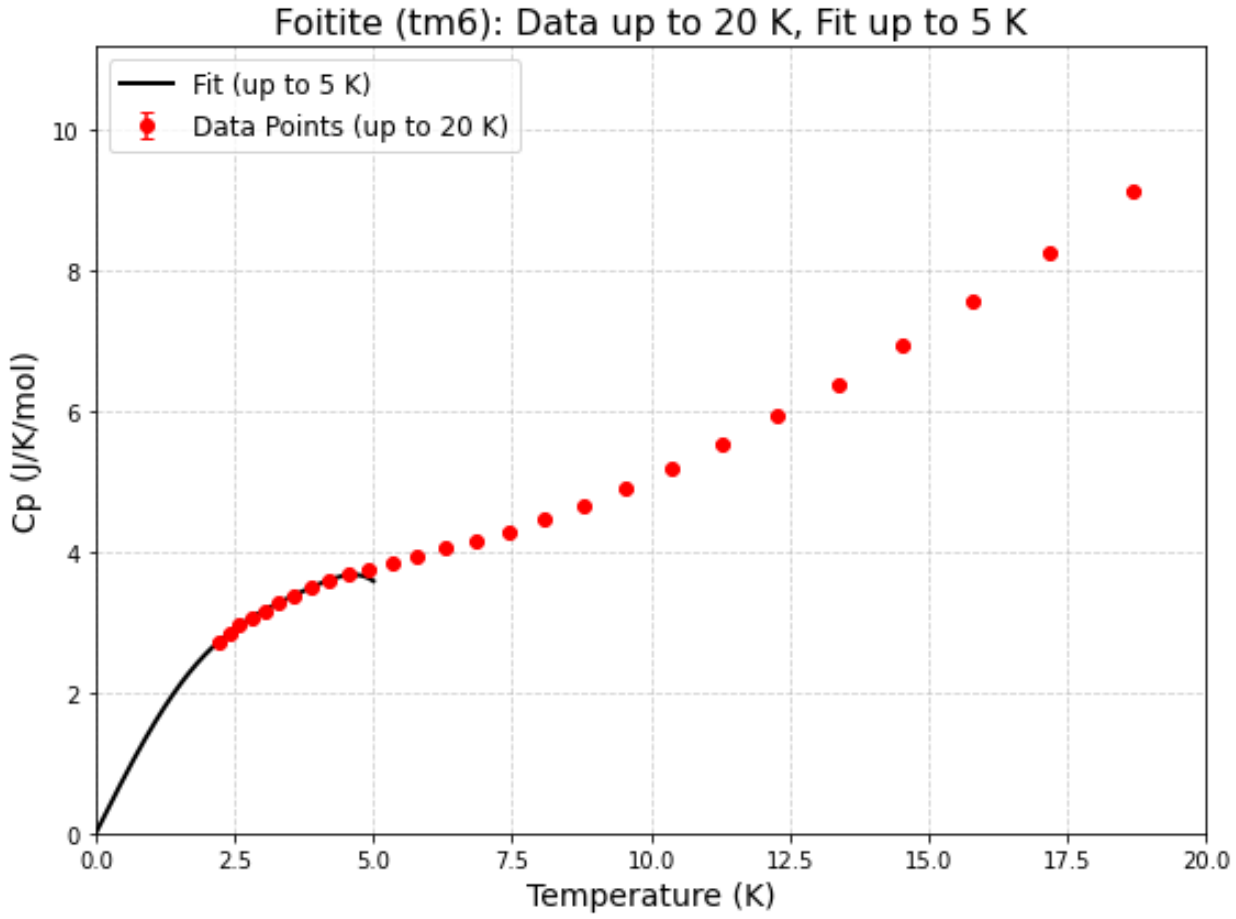

Figure 3A. Heat capacity of Foitite sample (Tm 6) between 0-17K as measured using the PPMS and the uneven power series extrapolation to 0K.

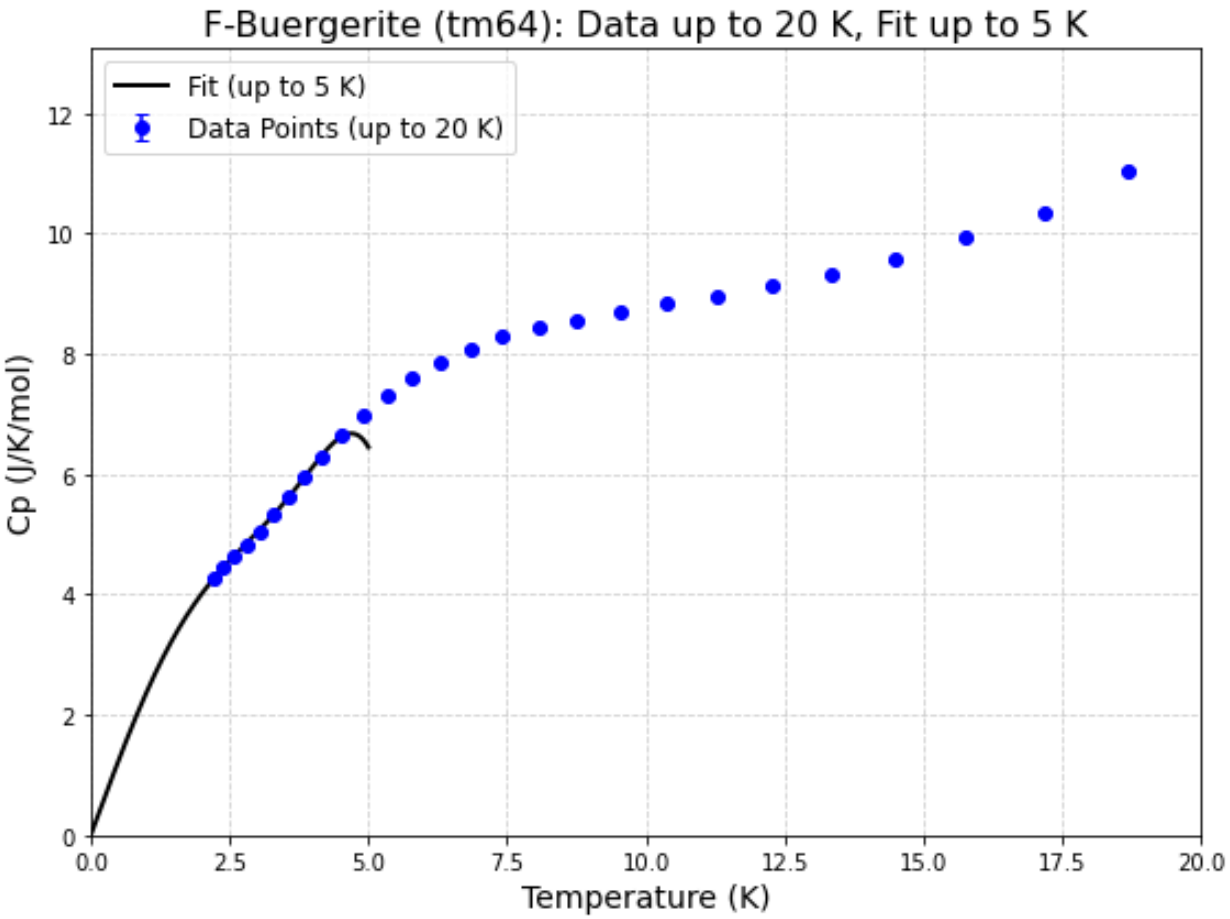

Figure 3B. Heat capacity of F-buergerite sample (tm64) between 0-17K as measured using the PPMS and the uneven power series extrapolation to 0K.

3. RESULTS

Combined heat capacity function and uncertainty propagation The heat capacity Cp(T) curve, spanning 0–774.15 K, is represented as a single Mathematica function combining three sections. The low temperature range (0-5K) is modelled using a power series $C_p(T) = aT + bT^3 + cT^5 + dT^7$. The intermediate range (5–298.15 K) is based on linearly interpolated relaxation calorimetry data. The high temperature range (298.15–774.15 K) follows a Berman and Brown (1985) fit $C_p(T) = k0 + k1T^{-2} + k2T^{-0.5} + k3T^2$, applied to the DSC data, were k0-k3 are fit coefficients.

A constant uncertainty (0.01 J/mol·K) was assumed for the low temperature range (Cp <5 K). Entropy (S) is computed as $S = \int \frac{C_p}{T} dT$, with uncertainty propagated via $\sigma_S = \int \frac{\sigma_{C_p}}{T} dT$, evaluated numerically using NIntegrate. To address the known issues with large swings in $\frac{C_p}{T}$ at low temperatures, we also tested the entropy calculation using $\int C_p d(\ln T)$ formulation. However, the differences between the standard $\int \frac{C_p}{T} dT$ and the $\int C_p d(\ln T)$ integrals were found to be extremely small (changes < 0.0001), and thus negligible for the purposes of this study.

In the intermediate T range ($5 < t \leq 298.15$K), uncertainty of Cp is obtained by a linear interpolation function trough the Cp uncertainties at each point, $\sigma_{C_p(T)} = \frac{T - T_{\text{lower}}}{T_{\text{upper}} - T_{\text{lower}}} \cdot \sigma_{\text{upper}} + \frac{T_{\text{upper}} - T}{T_{\text{upper}} - T_{\text{lower}}}$, where σ_{upper} and σ_{lower} are uncertainties of the bounding data points. The PPMS measured Cp three times per T during cooling without moving the sample, yielding higher apparent analytical precision. However, the lack of duplicate measurements in the PPMS likely underestimates true uncertainty While the calculation is independent of the number of points along the Cp curve due to continuous integration, the accuracy of the fit, and consequently the propagated uncertainty, depends on the sampling density of the raw Cp data used to derive the coefficients and their covariance and simplicity assumptions of the linear interpolation.

Accuracy and precision of the PPMS have been previously evaluated with studies showing that polished single crystals provide better thermal coupling and precision than powders (Dachs and Bertoldi 2005; Benisek and Dachs 2008). Studies using materials like synthetic corundum (SRM-720), fayalite, sanidine, and various silicates (e.g., anorthite, albite, forsterite) report PPMS accuracy for single crystals at ±0.1–0.2% above 50 K, with precision around ±0.3%. Powders exhibit lower accuracy (1–2% deviation above 50 K) and precision (±0.5% for 10–20 mg samples) (Geiger and Dachs 2018). Below 50 K, uncertainties increase to ±3–5%, reaching ±10% below 5 K due to thermal conductance changes. The PPMS matches adiabatic calorimetry precision with smaller sample sizes (~5–25 mg vs. 5–50 g), yielding S^0 uncertainties of 0.2–0.5% for powders and ~0.1% for single crystals. Our standard deviations are higher because we estimate uncertainties by integrating the interpolated uncertainty function over T, rather than deriving them from the covariance matrix of a fitted Cp polynomial or lattice model. Fit uncertainties are smaller because they assume the model perfectly represents the data, limiting

errors to fitting parameters, while propagated uncertainties capture variability across the dataset. However, we consider these propagated uncertainties reasonable, as they account only for analytical error based on triplicate measurements of a single sample at each temperature, and do not include variability from different sample preparations, such as mounting flatness or sample inhomogeneity, providing a conservative but realistic error estimate

The uncertainty of Cp at the Berman fit, $Cp = k_0 + k_1T^{-0.5} + k_2T^{-2} + k_3T^{-3}$, (high temperature range; 298.15–774.15 K) is propagated as in eq 1 with partial derivatives as: $\frac{\partial C_p}{\partial k_0} = 1, \frac{\partial C_p}{\partial k_1} = T^{-0.5}, \frac{\partial C_p}{\partial k_2} = T^{-2}$, and $\frac{\partial C_p}{\partial k_3} = T^{-3}$.

$$\sqrt{\sum_{i=1}^{4} \left(\frac{\partial C_p}{\partial k_i}\sigma_{k_i}\right)^2 + 2\sum_{i<j} \frac{\partial C_p}{\partial k_i}\frac{\partial C_p}{\partial k_j}\mathrm{Cov}(k_i, k_j)} \text{ (eq1)}$$

To propagate uncertainties in entropy calculations, we evaluated the variance of $\frac{C_p}{T}$ at each T using the covariance matrix (Cov(ki,kj)) of the fitted heat capacity coefficients {k0,k1,k2,k3}, and the partial derivatives in eq 2:

$$\frac{\partial\left(\frac{C_p}{T}\right)}{\partial k_0} = \frac{1}{T}, \frac{\partial\left(\frac{C_p}{T}\right)}{\partial k_1} = \frac{T^{-0.5}}{T}, \frac{\partial\left(\frac{C_p}{T}\right)}{\partial k_2} = \frac{T^{-2}}{T}, \frac{\partial\left(\frac{C_p}{T}\right)}{\partial k_3} = \frac{T^{-3}}{T} \text{ (eq2)}$$

The variance was computed as in eq 3 where $\mathbf{p}(T) = \left[\frac{1}{T}, \frac{T^{-0.5}}{T}, \frac{T^{-2}}{T}, \frac{T^{-3}}{T}\right]$ is the vector of partial derivatives.

$$\mathrm{Var}\left(\frac{C_p}{T}\right) = \mathbf{p}(T) \cdot \mathrm{Cov}(k_i, k_j) \cdot \mathbf{p}(T)^T \text{ (eq3)}$$

The total propagated uncertainty in entropy was obtained by integrating the variance over the T range and taking the square root (eq4):

$$S_{\text{Uncertainty}} = \sqrt{\int_{T_1}^{T_2} \mathrm{Var}\left(\frac{C_p}{T}\right) dT} \text{ (eq 4)}$$

This method fully accounts for contributions from both diagonal and cross-term elements of the covariance matrix, incorporating correlations between coefficients which are high for Berman polynomial coefficients and so without the crossterms the uncertainty would get inflated.

In the DSC, sample uncertainty matched analytical uncertainty due to repositioning, with ±1% accuracy and ±1% precision for single crystals and ±2% for powders. Final Cp uncertainty from the Berman fit covariance matrix was 0.1%, reflecting order of magnitude improvement of precision when the physical form of Cp is known. This assumes the Berman fit is error-free and accurately represents Cp, with uncertainties derived solely from the fit's covariance matrix, valid only if the model is physically correct.

Observed trends in sample heat capacities The entropy (S) and specific heat (Cp) of tourmalines exhibit notable variability, with the mean entropy calculated as 658.62J/mol·K and ranging from 617.76J/mol·K in synthetic Mg-foitite (dravsyn) to 709.54J/mol·K in for Ca-Fe^{3+} rich schorl (tm156B). The propagated analytical uncertainty in entropy (Ssd) has a mean of 9.55J/mol·K (~1.4 %) and a standard deviation of 2.78J/mol·K. For Cp at 600 K, the mean value is 1127.53 J/mol·K, spanning a range of 1092.80 J/mol·K in F-buergerite (tm64*)* (blue line in Fig. X) to 1165.54 J/mol·K in synthetic uvite (red line in Fig X.). The analytical uncertainty in Cp (Cp,sd) averages 0.70 J/mol·K (0.06%) with a standard deviation of 0.55 J/mol·K, emphasizing the precision of the data. Tourmaline entropies (621.78–709.54 J/mol·K) exceed simpler phases like amphiboles such as tremolite (553 J/mol·K) but are lower than sanidine (835 J/mol·K) and hydrated phases like lawsonite (876 J/mol·K), reflecting their intermediate thermodynamic complexity. Individual measured sample Cp curves and standard errors are shown in Figure 3C and further detailed in Electronic Appendix 3A and 3B, respectively.

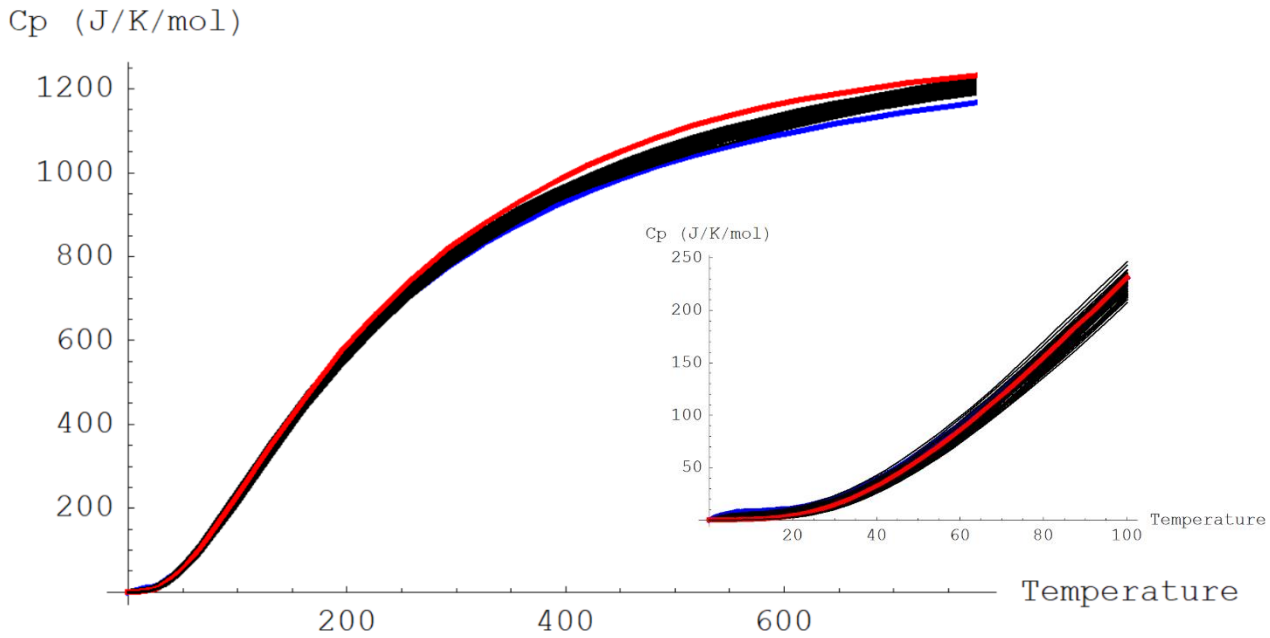

Figure 3C. Specific heat capacity (Cp) of tourmalines. *Buergerite* (blue) has the highest Cp at low T but the lowest above ~250 K, while *uvite* (red) shows the highest Cp at high T. Other tourmalines are intermediate. The uncertainties are smaller than the thickness of the lines. The inset highlights the Cp behavior at the lowest temperatures, which disproportionately influences the integrated entropy.

Notably, F-buergerite shows distinct behavior, with a high Cp at low T but becoming the lowest among all samples at higher T, such as 600 K. This highlights a significant T-dependent shift in its thermodynamic behavior. As shown in Figure 3D, entropy—calculated as the integral of Cp /T—accumulates most significantly between 100 and 200 K, with a significant magnetic contribution at low temperatures.

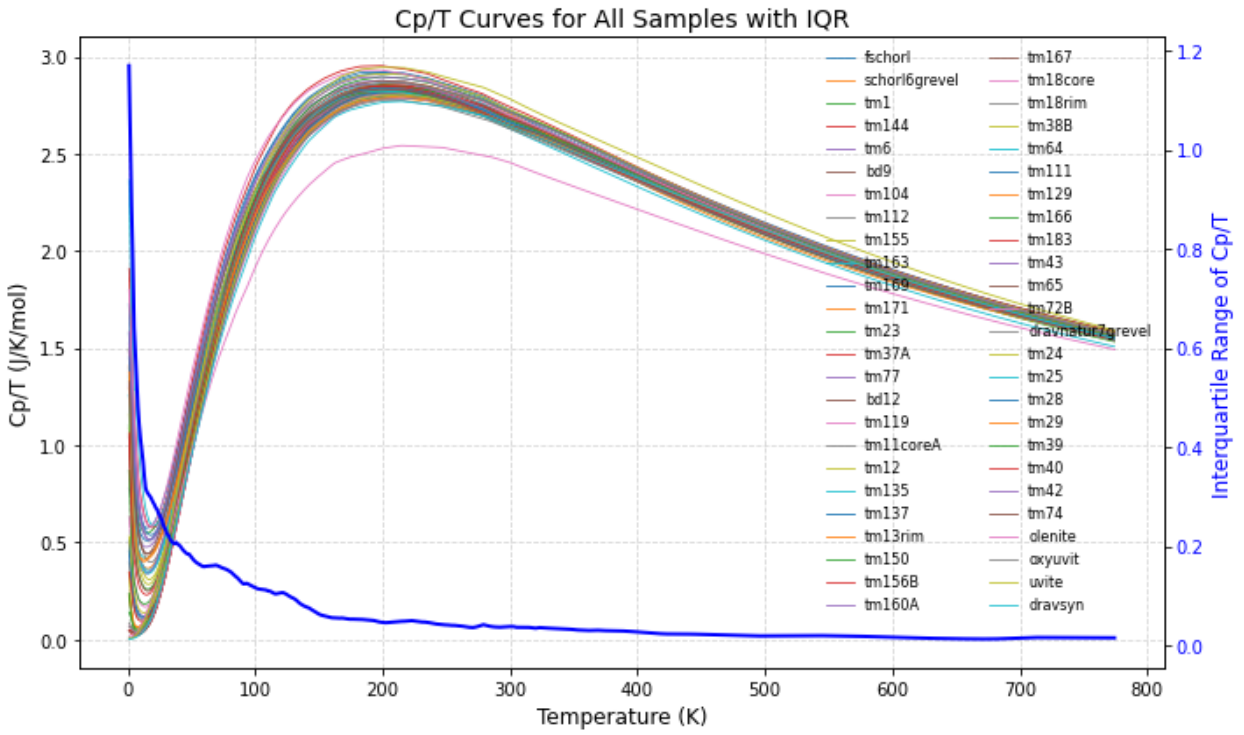

Figure 3D. Cp/T curves (coloured) and Interquartile Range (blue) showing that the mid-range (50–200 K) dominates entropy but has low variance, while the magnetic contribution at low temperatures, with high Cp variability, most influences entropy differences.

While the upward peak in Cp/T below 20 K may appear small, the 0–50 K range shows significant Cp variance between tourmalines, such as dravite-rich (TM23) and foitite-rich (TM6), Figure 3E, highlighting where most relative differences in Cp arise, mainly due to magnetic effects, see Appendix 3C. Accurate measurement and modelling of this low temperature behaviour are crucial, as it this range dictates tourmaline's S^{o} variance. Our study extends measurements down to 2 K, capturing critical low-T contributions often missed in older datasets, as adiabatic calorimetry historically was limited to 5–10 K (Westrum 1988). Geological thermodynamic databases based on these older measurements might not be entirely inconsistent with PPMS data especially for iron containing phases. For example, the Robie and Hemingway (1995) is mainly based on adiabatic calorimetry which also is the base for the Holland and

Powell database (2011).

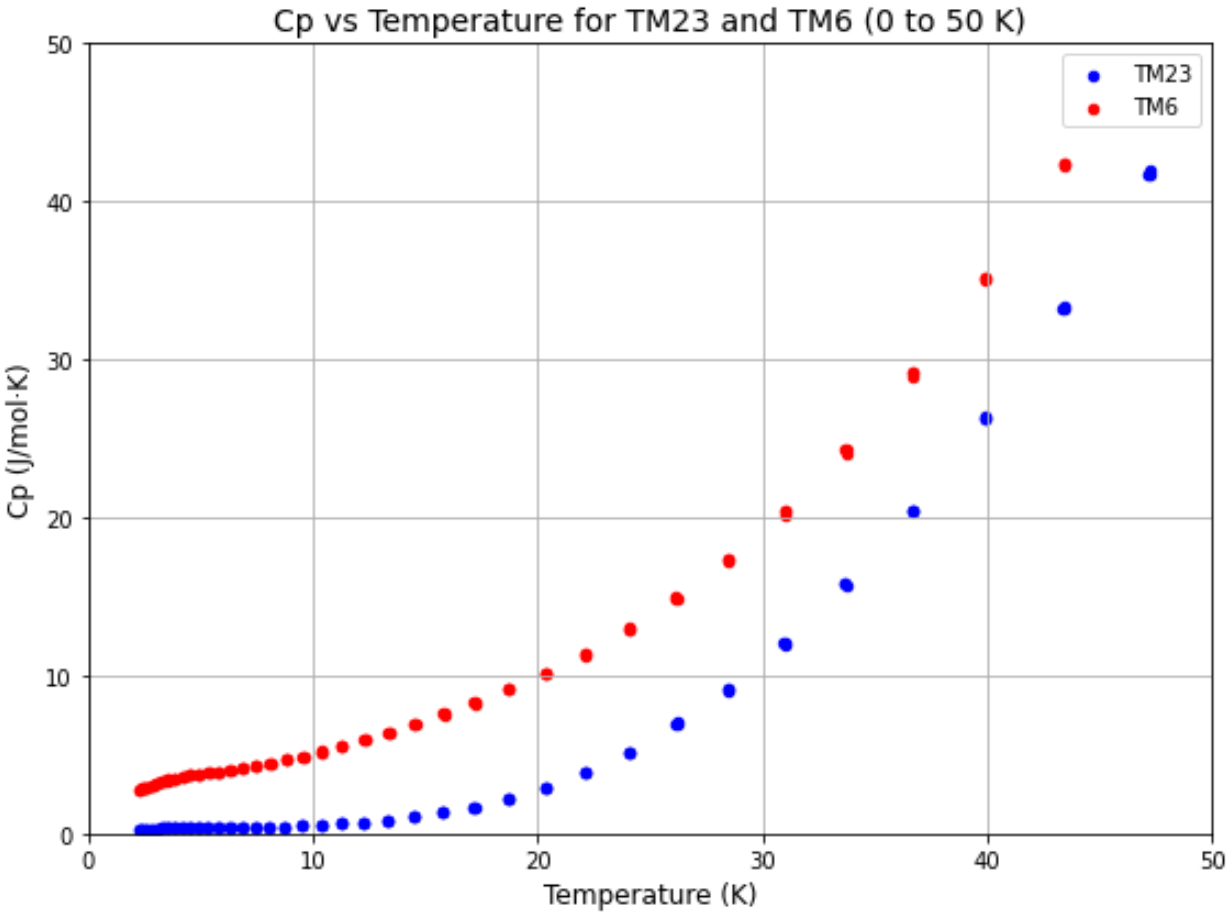

Figure 3E. The Cp difference between foitite (tm6) and dravite (tm23) highlights significant variability in the 0–50 K T range, driven primarily by magnetic contributions. This range has the largest impact on Cp curve differences and dominates uncertainty in both Cp and integrated entropy, as entropy is highly sensitive to 1/T at low T. Measurements were conducted down to 2 K.

Heatmaps. Heatmaps were created by extracting Cp values every 5 K from 0–100 K and every 20 K from 100–800 K using piecewise linear interpolation of each measured Cp curve. At each T, the mean and standard deviation were calculated, and Cp values were converted to Z-scores to standardize and compare curves, highlighting whether Cp is lower (blue) or higher (red) than the mean (Figure 3F). The same process was applied to Cp uncertainties to provide a visual comparison of relative magnitudes (Figure 3G). this shows that our sample show variance which is needed if we want to extract endmember data from these solid solutions.

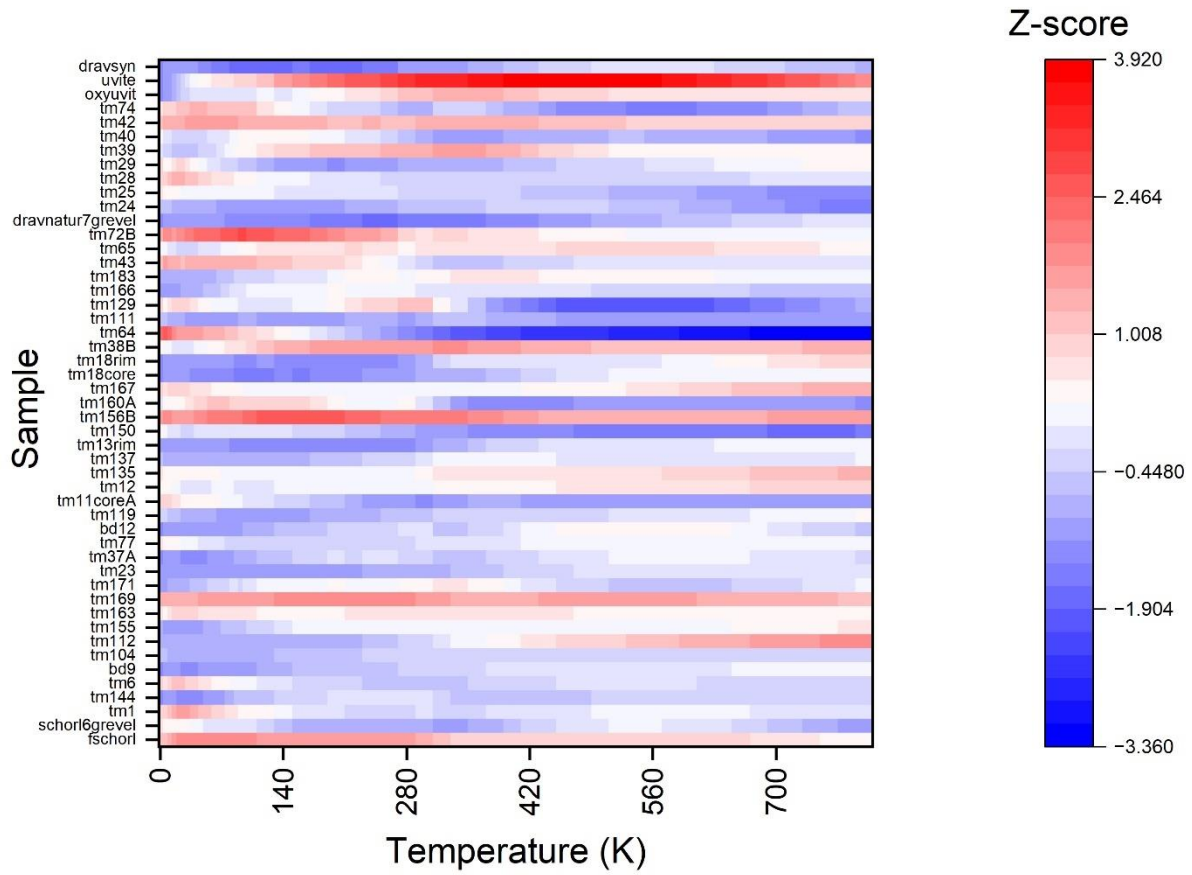

Figure 3F. Heatmap of training set samples showing Cp Z-scores per T compared to the dataset mean, with white indicating values near the mean, blue lower, and red higher, illustrating how relative differences vary with T.

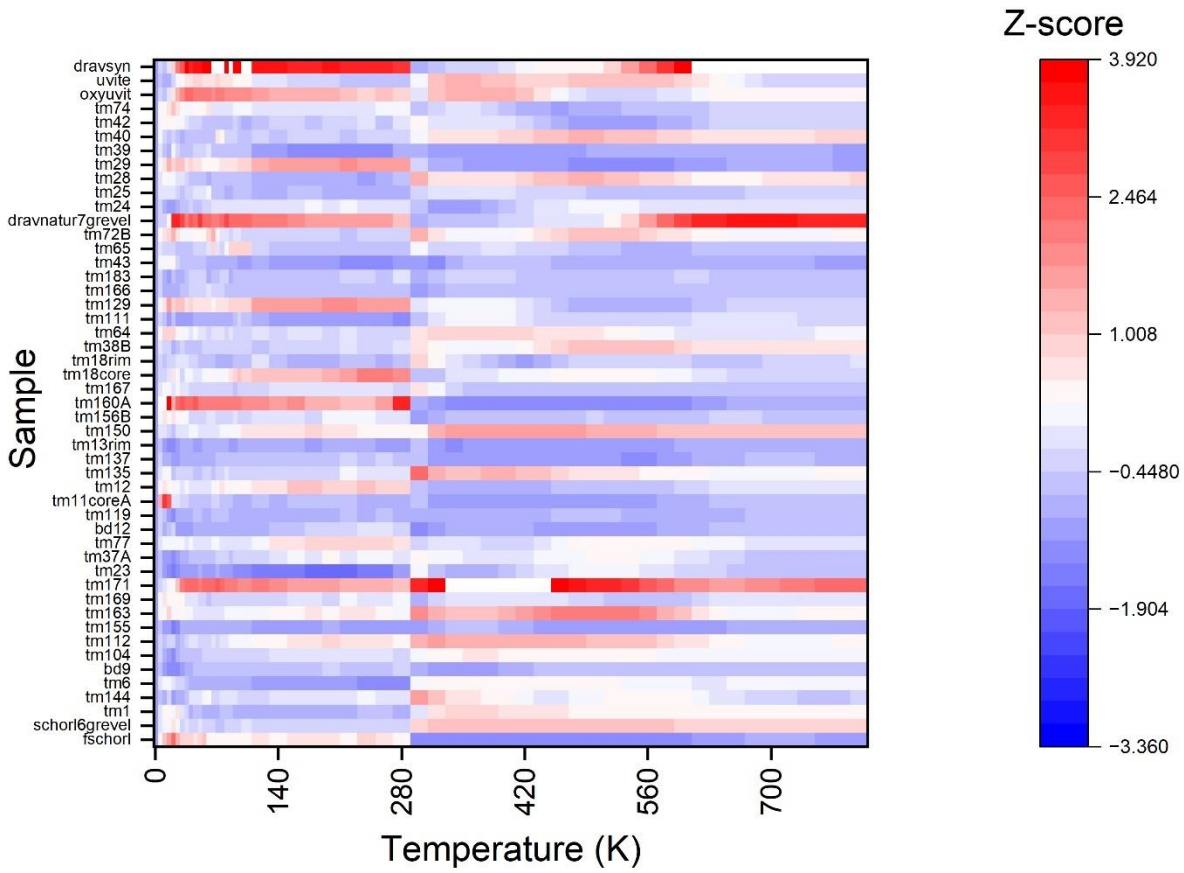

Figure 3G. Heatmap of training set samples showing Cp uncertainties Z-scores per T compared to the dataset mean uncertainty.

Jump between PPMS and DSC

To connect the Cp values between the PPMS and DSC instruments, piecewise linear interpolation was initially used, resulting in either a jump or drop when transitioning from one technique to the other. The source of this discrepancy, whether from the PPMS, DSC, or both, was unknown. Since the goal was the final endmember Cp curves, no immediate correction was applied, assuming the random nature of these jumps would cancel out during regression, yielding smooth endmember Cp curves, see histogram in Figure 3H, whereas individual jumps in relative percentages (rel%) at RT (Room Temperature, 298.15K) are shown in Figure 3I.

The regression on low-temperature Cp data revealed that samples with jumps at 25°C were not flagged as outliers in the PPMS regression used to obtain the standard state entropy. However,

when regressions were performed on the high-temperature Cp functions from 298 to 773.15 K, and the integral of these Cp values over this temperature range was used to calculate $S_{298.15K}^{773.15K}$, all samples with large DSC jumps were identified as significant outliers compared to the rest of the dataset. This discrepancy indicates that the offset observed between PPMS and DSC at room temperature arises from a systematic baseline shift in the DSC Cp signal, not in the PPMS data. This is shown in Figure 3J, where we compare measured and predicted $S_{298.15K}^{773.15K}$, supporting the conclusion that the bias lies in the DSC data.

To address this, a correction factor was calculated at 298.15 K using the integral equation for low-T Cp and the Berman equations for high-T Cp. This additive factor was applied to the DSC data above 298.15 K, aligning it vertically with the PPMS signal. No correction was applied for the slope or other higher derivatives. No horizontal differences between DSC and PPMS data due to T lag were observed. This normalization of the DSC to the PPMS is opposite to the method suggested by Dachs and Benisek (2011), where they recommend correcting PPMS data to align with DSC values at 298.15 K. This correction is superior as it addresses the systematic baseline shift in the DSC Cp signal, likely worsened since Dachs and Benisek's work due to instrument degradation. By normalizing the DSC to the PPMS, we avoid introducing bias and improve the internal consistency of the thermodynamic model, yielding more accurate endmember Cp curves and standard state entropy values.

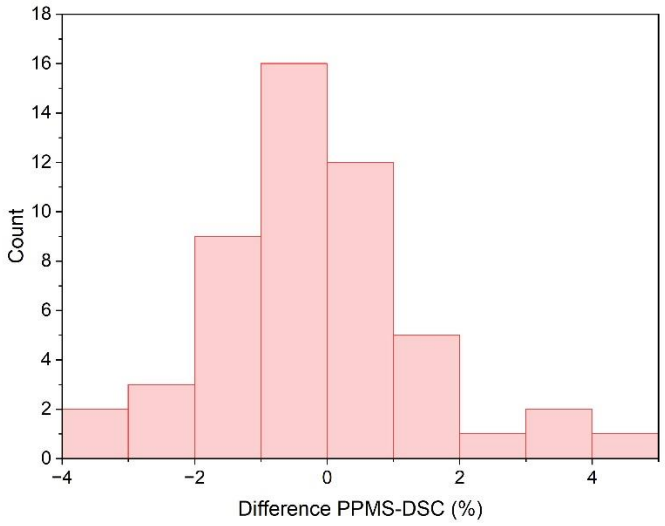

Figure 3H. The jump between PPMS and DSC data at 298.15K in terms of relative percentages.

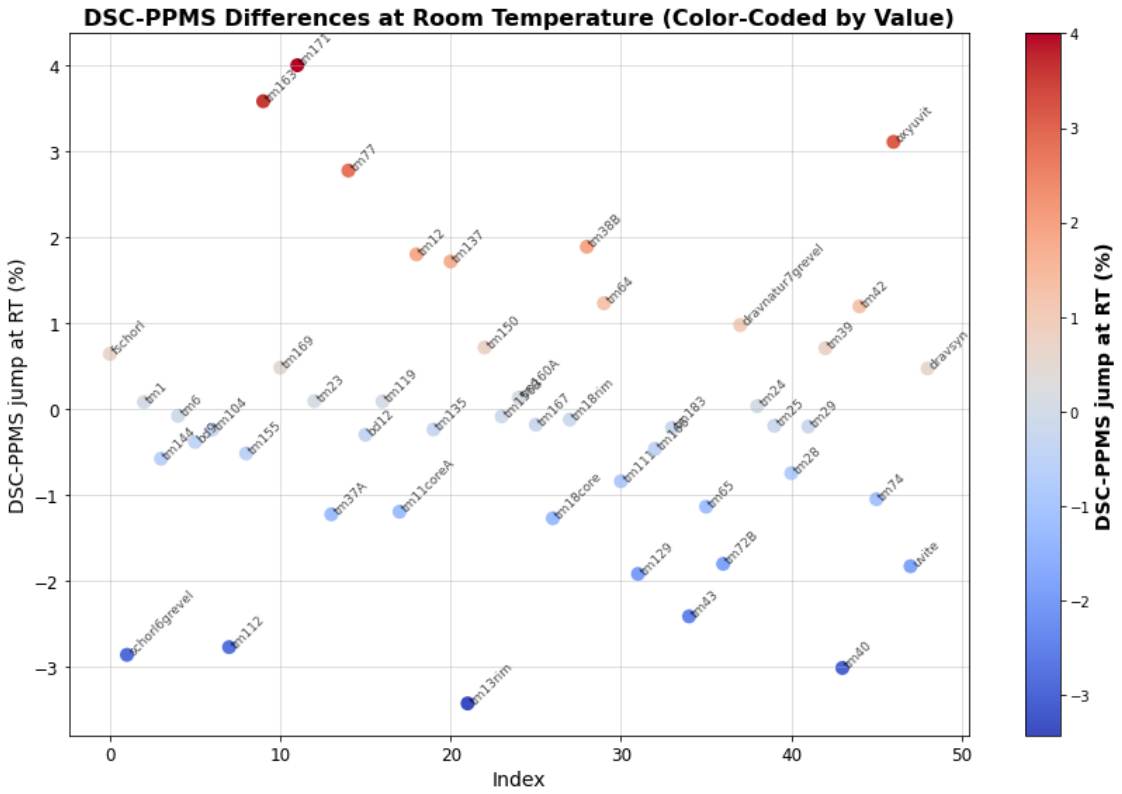

Figure 3I. Relative percentage % differences between PPMS-DSC.

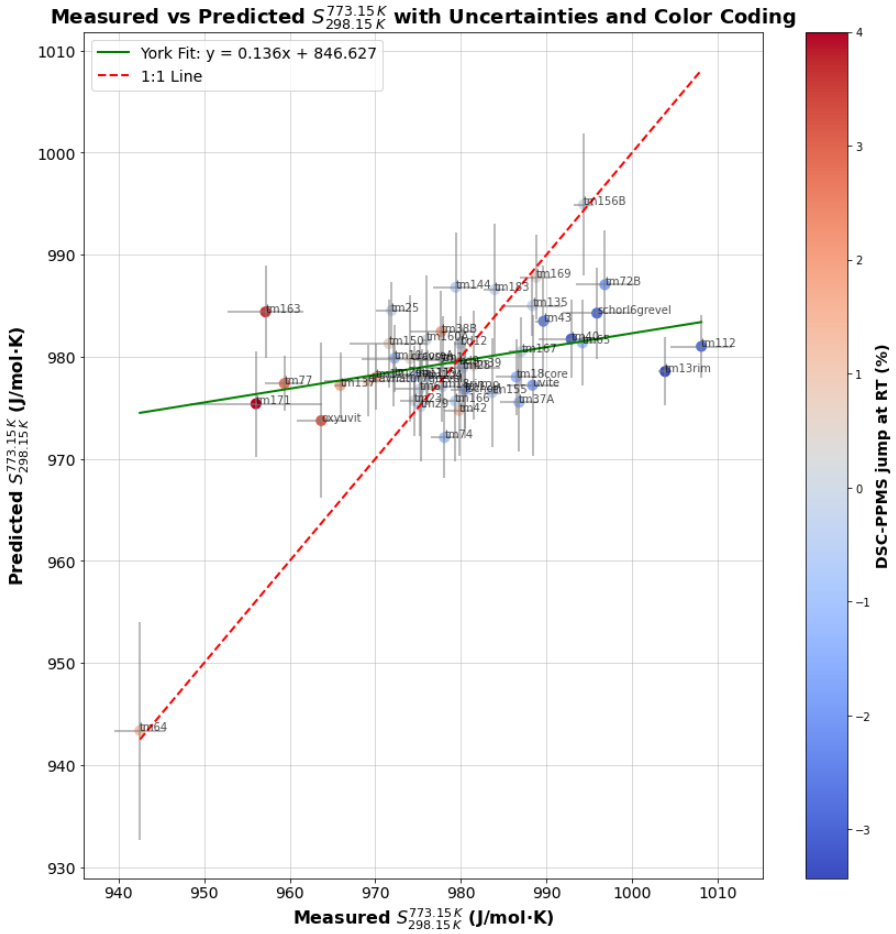

Figure 3J. Predicted $S_{298.15K}^{773.15\,K}$ using uncorrected DSC Berman fits. Samples with overestimated values correspond to positive jumps, while underestimated ones show negative jumps, indicating inaccuracies in the DSC data. A vertical correction was applied, assuming accurate slope determination.

4. TRAINING DATASET REGRESSION: ORDINARY LEAST SQUARES

The heat capacity Cp is related to the Gibbs free energy through the differential:

$$C_p = -T\left(\frac{\partial S}{\partial T}\right)_P = -T\left(\frac{\partial^2 G}{\partial T^2}\right)_P$$

The low-temperature Cp curve is formulated using piecewise linear interpolation:

$$C_p^{\text{predicted}}(T) = \sum_{i=1}^{n} f_{\text{interp},i}(T)$$

where $f_{\text{interp},i}(T)$ represents the linear interpolation function for each temperature segment. Specifically, for each interval $[T_i, T_{i+1}]$, the linear interpolation is given by:

$$f_{\text{interp},i}(T) = f(T_i) + \frac{f(T_{i+1}) - f(T_i)}{T_{i+1} - T_i}(T - T_i)$$

Here, $f(T_i)$ and $f(T_{i+1})$ are the heat capacity values at the boundaries T_i and T_{i+1}, and T is the interpolated temperature within this segment.

The standard state entropy S^0 at 298 k and 1bar can be expressed both as an integral and as a derivative of the Gibbs free energy divided by temperature. First, using the integral of $\frac{C_p}{T}$ over temperature: $S_0 = -\int_{T_0}^{T} \frac{C_p}{T} dT$, which simplifies, given the linear interpolation of $\frac{C_p}{T}$, to:

$$S_0 = -\int_{T_0}^{T} \sum_{i=1}^{n} f_{\text{interp},i}(T') \frac{dT'}{T'}$$

Alternatively, S^0 can be directly calculated as the derivative of G:

$$S_0 = -\left(\frac{\partial G}{\partial T}\right)_{P,T=T_0}$$

ensures that the thermodynamic model is consistent with both the Cp and entropy calculations.

We performed regression analyses on our solid solution dataset to extract the heat capacity (Cp) and entropy (S) functions of thermodynamic endmembers. Both bulk compositional and site-speciation models were derived. To derive endmember Cp and S properties from mixed-composition (impure) samples, we used two distinct methods:

- **Method 1 – Regression at each temperature (Cp-based regression):**
  First we fit linear interpolation functions to our measured Cp curves. Then at each 1K temperature, we regressed the Cp values of all samples against their endmember fractions using a ordinary linear regression model. This yields a Cp value for each endmember at each temperature, effectively reconstructing the Cp(T) function of each endmember. These functions were then interpolated (linearly), and the entropy for each endmember was calculated by numerically integrating Cp/T from to 298.15 K. This method captures fine details and trends in Cp(T) but may risk overfitting due to the large number of regressions.

- **Method 2 – Regression of integrated entropy (S-based regression):**
  Here, we first interpolated and integrated the measured Cp/T curves for each sample to obtain the standard state entropy. These integrated entropy values were then regressed against the endmember fractions, yielding endmember entropies directly. This method is simpler, avoids overfitting, and provides robust estimates, but it loses detailed information on how Cp varies with temperature. This approach was performed in the NCSS software (Appendix 3D), which also generated additional statistical diagnostics such as variance inflation factors, multicollinearity, confidence intervals, Cook's distance, and residual behavior.

In short, Method 1 provides high-resolution temperature-dependent Cp behavior per endmember, while Method 2 is more stable but compresses the data into a single entropy value per sample.

4.1 Bulk Compositional Model: Low-T CP (Method 1)

Bulk compositional endmember low-T Cp curves (0–298.15 K) were obtained using ordinary least squares (OLS) of the combined Cp functions in Mathematica. Parameter estimates were calculated as $\hat{\beta}^{\text{ls}} = (X^T X)^{-1} X^T y$, where X is the design matrix and y the dependent variable and the pseudoinverse method was used to obtain the inverse matrix. Residuals were squared and summed to compute total squared residuals, with fit variance obtained by dividing by degrees of freedom. The covariance matrix was scaled by the variance, and parameter standard errors derived from the square root of its diagonal elements.

Regression was performed in 0.1 K steps, with 0.01 K steps yielding identical results. Figure 3K overlays all endmember Cp curves with their confidence intervals (CI). Standard errors (SE) were combined with a z-score of 1.96 to calculate CIs for the low-T Cp curves of endmembers. CIs are tight for most endmembers but are notably wider for oleB, mdtwB, aorsmB in the bulk compositional model, highlighting their extrapolated nature. Heatmap of Cp Z-scores at 0.1 K intervals compares endmember curves to each other, highlighting T-dependent variations (Figure 3L). Individual endmember Cp curves and standard errors are detailed in Appendix 3E, respectively.

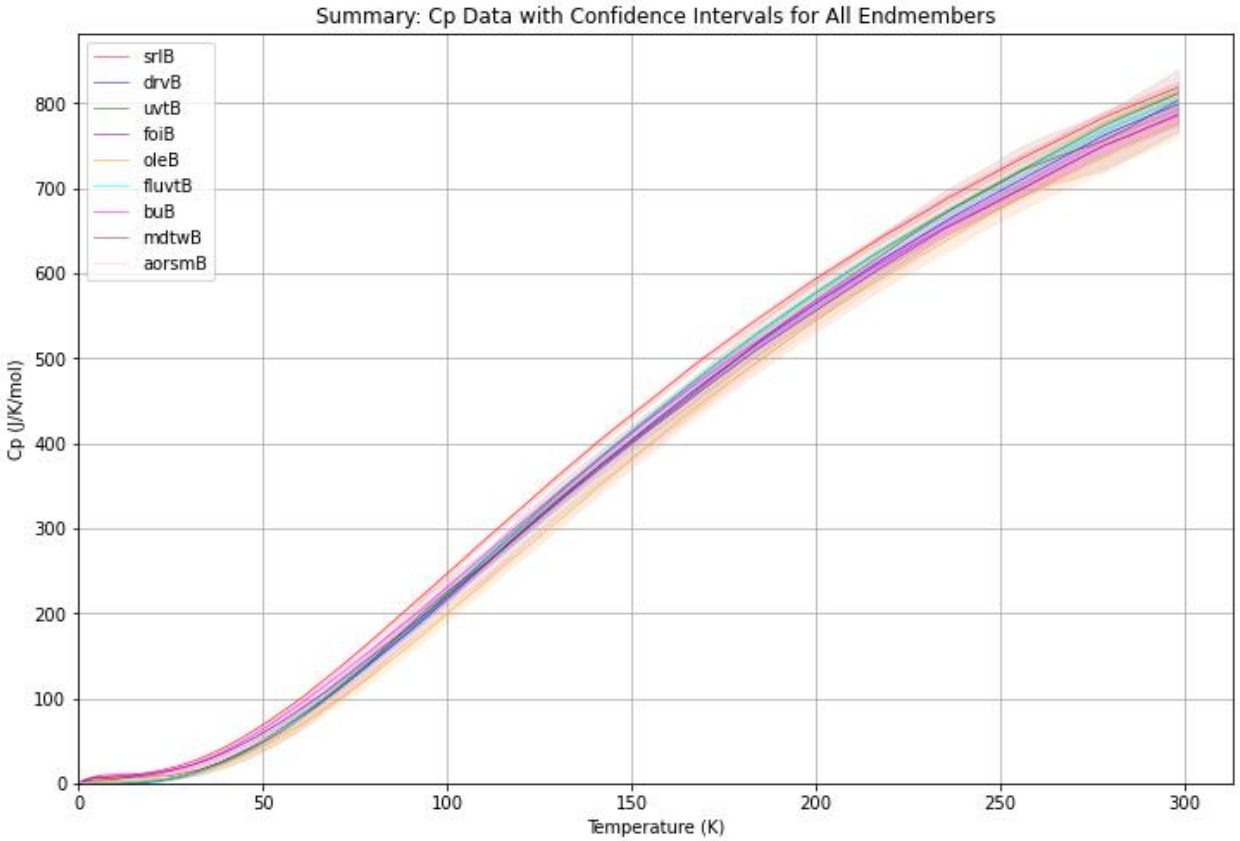

Figure 3K. Bulk compositional endmember low-T Cp curves with their confidence intervals.

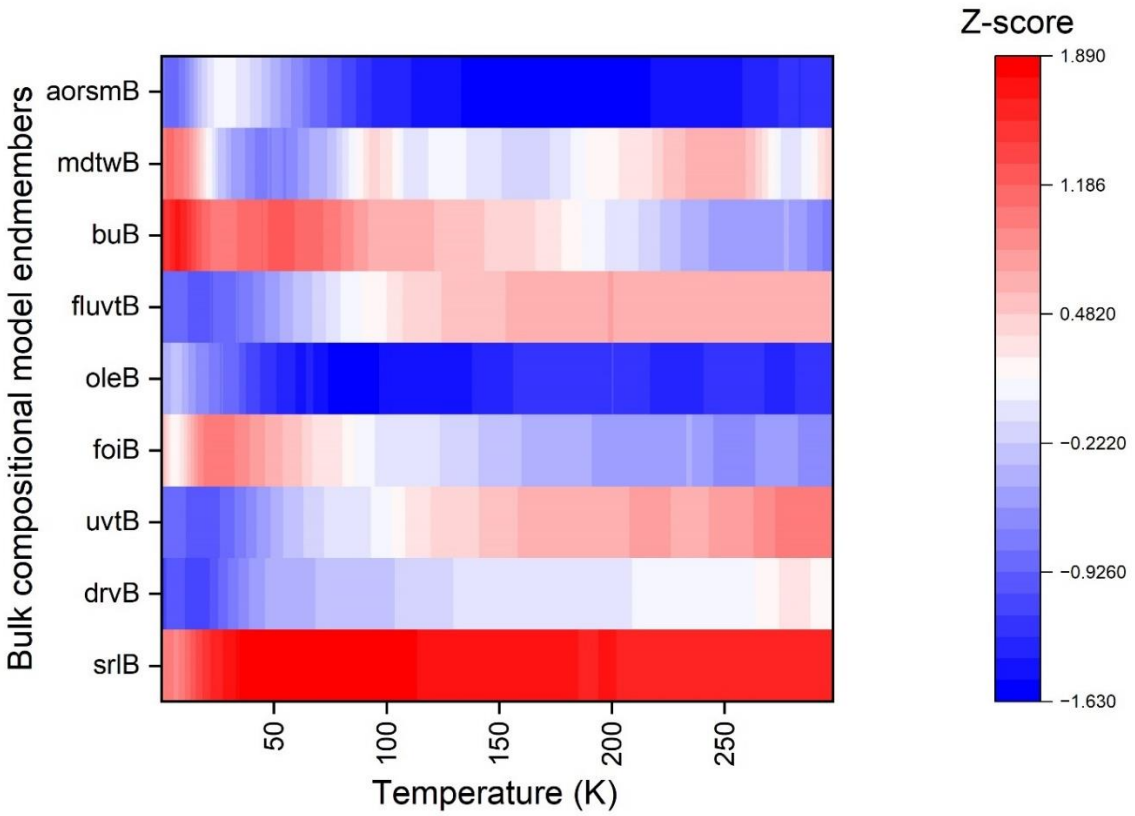

Figure 3L. Heatmap of bulk compositional model Cp curves Z-scores at 0.1 K intervals, comparing each endmember to the mean of all endmembers. White indicates Cp near the mean, blue lower than the mean, and red higher. The plot highlights how relative differences between curves vary with T.

The SE's, nearly linear in absolute values, show sharp increases in relative uncertainty below 50 K, particularly around 15–20 K due to the small magnitudes of Cp in this T range, especially for drvB/uvtB (Figure 3M). If the designer matrix is orthogonal or nearly orthogonal to the regression basis functions, predicted entropy remains unaffected by correlation. However, moderate multicollinearity in oleB (Variance Inflation Factor; VIF = 8.8), foiB (VIF = 8.5), and aorsmB (VIF = 6.4) complicate the independence of the regression coefficients (Figure 3N). The use of aorsmB as the AlT endmember was problematic due to its correlation with oleB, a poorly constrained but essential variable. These VIF values are consistent across bulk compositional model regressions due to their dependence on the designer matrix.

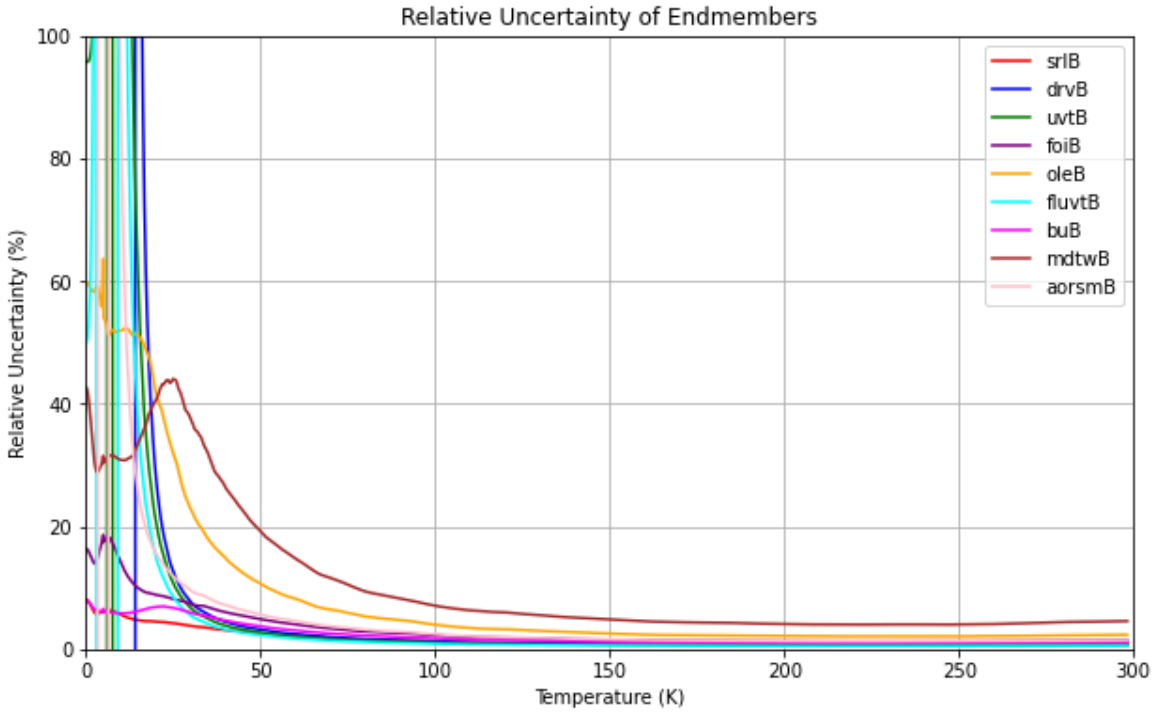

Figure 3M. The relative uncertainty in endmember in low-T Cp (J/K/mol) and its dependence on T.

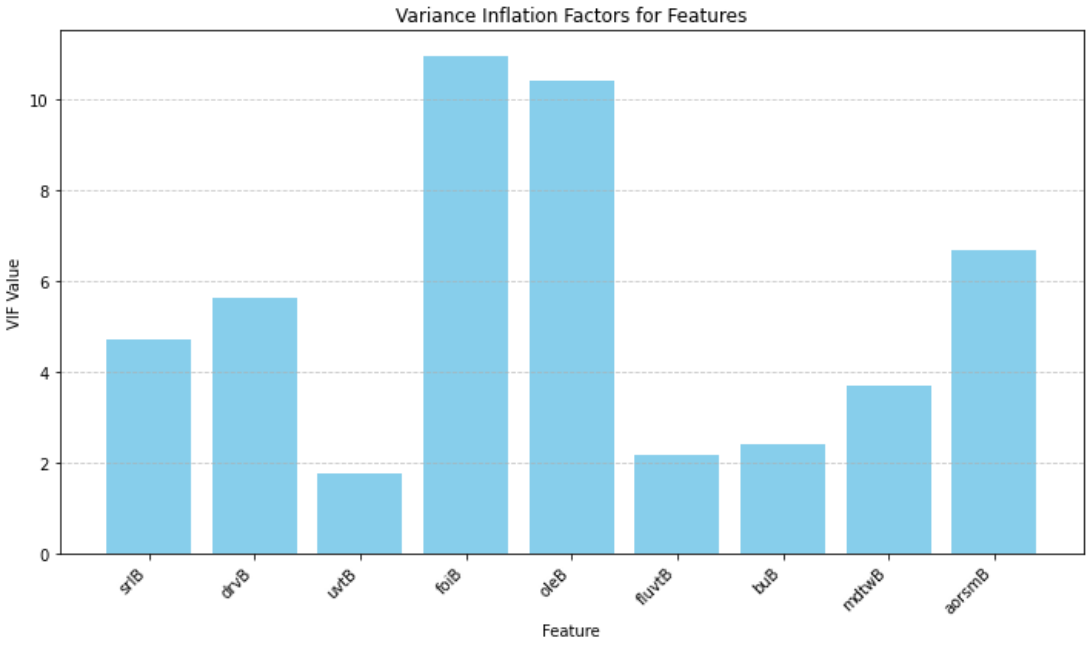

Figure 3N. VIF factors for the bulk compositional model. VIF factors depend on the designer matrix and are therefore equal for all regressions relating to the bulk compositional model.

Endmember interpolation functions ($f_{interp,i}$) were combined with the designer matrix (X) to recalculate Cp curves for each sample as $C_p^{\text{predicted}}(T) = \sum_{i=1}^{n} X_i f_{\text{interp},i}(T)$. These predicted curves were compared to measured Cp curves from training samples to evaluate model bias. Goodness of fit was assessed using the mean squared error (MSE) calculated of the vertical residuals at all 0.1 K intervals (Figure 3O), and relative deviations were computed as the ratio of residuals to measured values. The largest relative deviations of the samples were observed at low T again due to the low magnitudes of Cp (Figure 3P).

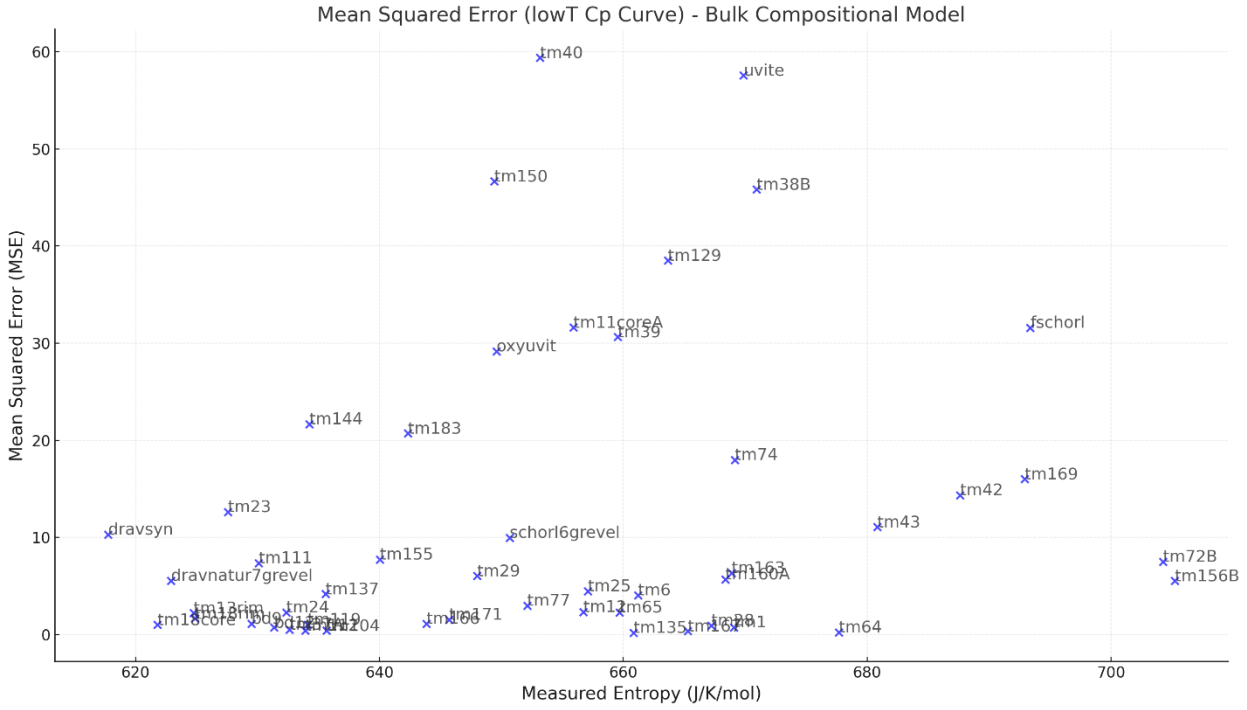

Figure 3O. Mean Squared Error (MSE) of Cp curve versus Measured Entropy (J/K/mol) for the low-T Cp curve regression of the Bulk Compositional Model.

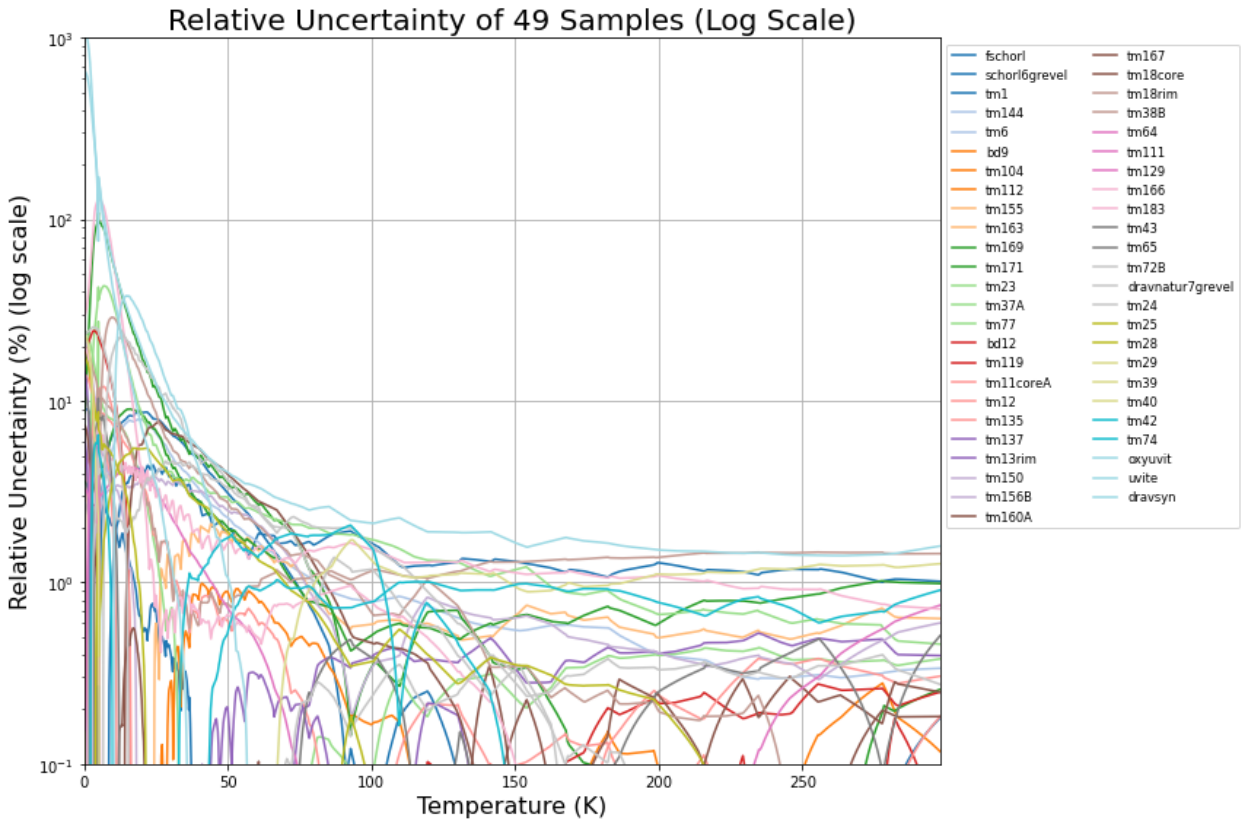

Figure 3P. Relative residuals (%) between measured and predicted low-T Cp curves for the bulk compositional model, plotted on a log scale. Higher uncertainties (>1%) occur below 100 K, while they remain <2% above 100 K.

Endmember Cp curves were piecewise linearly interpolated and integrated over T to compute standard state entropies at 298.15 K, with uncertainties derived by integrating standard errors from the regression covariance matrix at each T (Table 3A).

Table 3A. S^0 of the endmembers obtained using method 1 for the bulk compositional model. Correlation matrix of the S0 bulk model endmembers. Correlation matrix figure for S^0 bulk model.

Endmember	Entropy (J/mol·K)	Uncertainty (J/mol·K)
srlB	714.434	8.497
drvB	633.572	7.728
uvtB	647.370	6.526
foiB	655.825	14.005

Endmember	Entropy (J/mol·K)	Uncertainty (J/mol·K)
oleB	606.501	22.357
fluvtB	647.343	5.395
buB	681.534	11.401
mdtwB	658.136	44.871
aorsmB	609.034	13.795

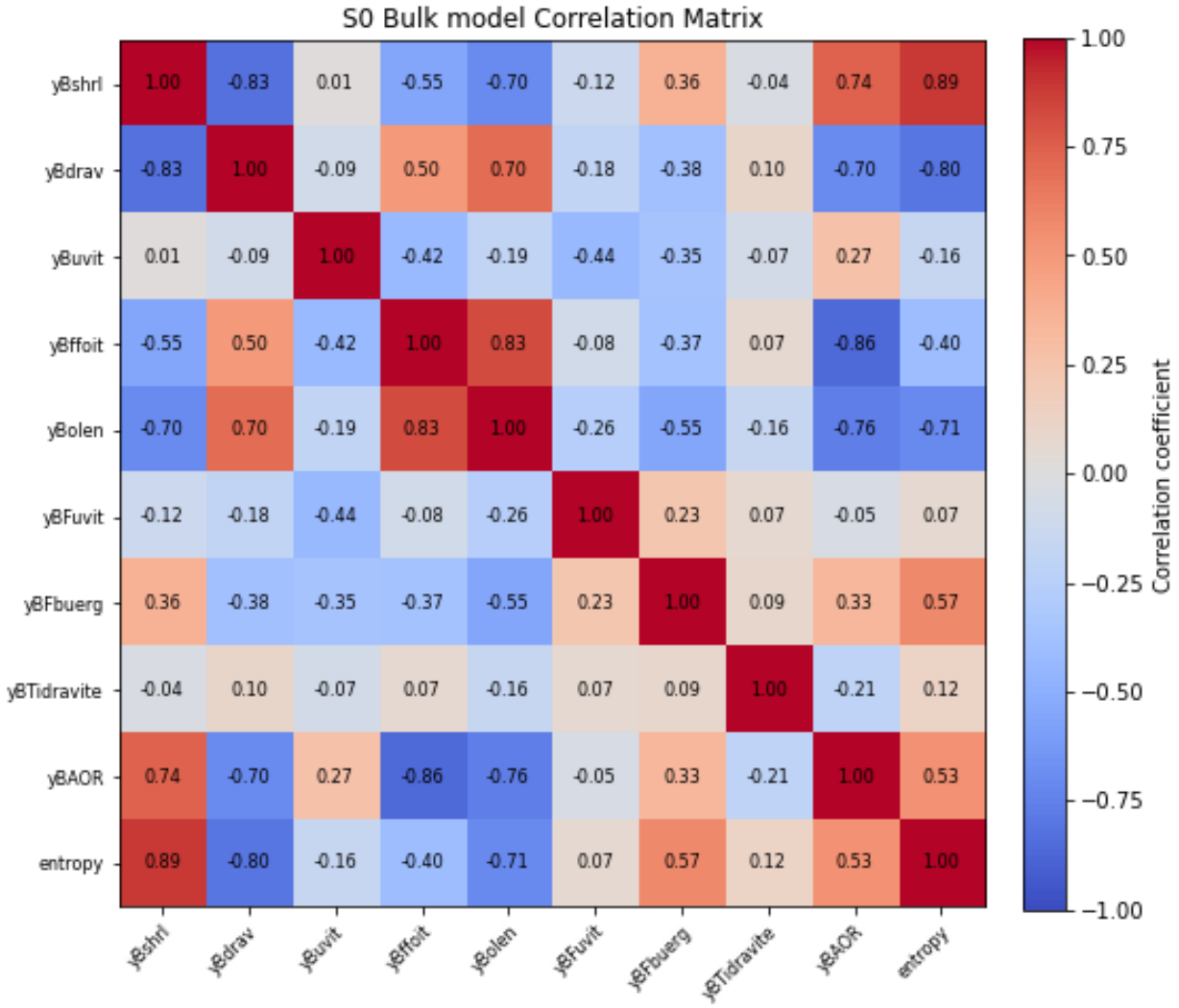

Internal Validation. Predicted and measured Cp curves were also integrated over T to compare entropies, which have been plotted in Figure 3Q. Gibbs free energy differences at 298.15 K were calculated using: $\Delta G = \int_0^{298.15} \Delta C_P dT - T \int_0^{298.15} \frac{\Delta C_P}{T} dT$ where the enthalpy and entropy increments counteract to calculate the ΔG discrepancy introduced by model simplifications. This

excludes S_{conf}, which, being constant and independent of T in our model, only affects ΔG by a constant term S_{conf}·T.

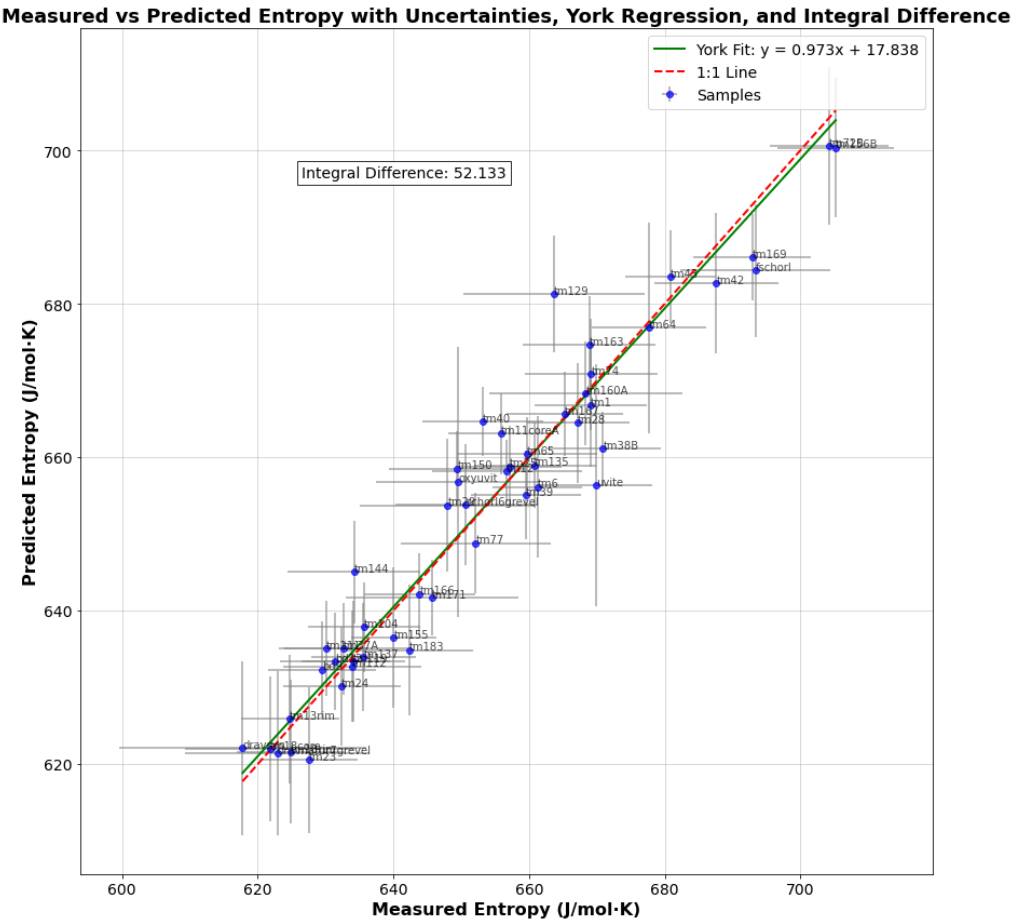

Figure 3Q. Measured versus predicted entropy using Method 1.

A Table with the largest MSE per sample is presented in Appendix 3F, highlighting that most deviations occur at high levels of nonbuergeitic Fe^{3+}. The ΔS difference between measured and predicted values results in ΔG differences of 2 kJ/mol, with synthetic uvite being the outlier with 4 kJ/mol which is the same order of many interaction parameters (1-50 kJ/mol).

Low-T Cp Curve Regression Details To evaluate regressions along the Cp curve, 55 points were generated per sample using piecewise linear interpolation at 5 K intervals up to 100 K and 20 K intervals from 100 to 800 K. NCSS analysis assessed OLS regression metrics and linearity across the T range. Below 21 K, non-transition metal tourmalines (drvB, uvtB, fluvtB, oleB, and

aorsmB) show negligible Cp contributions, with drvB exhibiting unphysical negative values (-0.21J/mol·K), uvtB/fluvtB contributing 0.1–0.2J/mol·K, and oleB 0.7J/mol·K. Significant contributions only appear at 16 K for uvtB, fluvtB, and aorsmB, and at 21 K for drvB and oleB. Residuals at 5 K are non-normal, but they are normally distributed and random at other T, with high-residual samples varying across the range. Surprisingly, R_{PRESS}^2 remains ~0.85 up to 100 K despite higher uncertainties at lower-T, before steadily declining to 0 at 400 K, indicating robustness in the low-T regression. The trend may result from lower-T Cp data, despite higher uncertainties, exhibiting stronger or more distinct patterns that the model captures effectively, maintaining high R_{PRESS}^2. At higher T, reduced variability in Cp may limit the model's explanatory power, leading to the decline. Additionally, the lognormal distribution of data points along the Cp curve resulted in measurements being taken at wider intervals at higher T, potentially increasing inaccuracies due to the reliance on linear interpolation.

Correlations between endmembers and Cp highlight their significant positive or negative contributions in determining Cp values and therefore can be used alongside the Z-score heatmaps in Figure 3L. Strong correlations between srlB-drvB, srlB-S0, and drvB-S0 observed in S^0 OLS (298.15 K) persist at low-T Cp. SrlB-drvB correlations (-0.82) hold over the entire range (0–800 K). SrlB-Cp correlations grow from 0.71 at 1 K to 0.89 at 40 K before decreasing steadily to 0.55 at 300 K and almost 0 by 800 K. DrvB follows a similar trend, starting at -0.64, peaking at -0.75 at 40 K, and dropping to -0.5 at 300 K and near 0 by 800 K.

BuB's Cp correlation starts at 0.63 until 20 K, where it has the highest low-T Cp, likely due to the magnetic anomaly associated with its high Fe^{3+} content, turns negative at 430 K (-0.3), and drops to -0.4 by 800 K, reflecting high magnetic entropy at low T and low high-frequency vibrations at high T. OleB-Cp rises from -0.32 at 0 K to -0.77 at 220 K before nearing 0 by 280 K. AOR increases from 0.27 at 0 K to 0.55 at 36 K, stabilizing until 280 K. FoiB shows no correlation at low T, reaching -0.6 at 300 K, with no correlations beyond this point.

Impact of Low-T Magnetic Anomalies on S^0 in Transition Metal Tourmalines Magnetic entropy significantly affects S^0 through low-T (<30 K) magnetic anomalies in transition metal tourmalines (Figure 3E, foitite sample, for example), with strong (anti-)correlations (srlB−S^0, drvB−S^0, srlB−Cp, drvB−Cp), emphasizing the need for accurate low-T measurements, as

magnetic peaks in low-iron systems dominate Cp and disproportionately influence standard state entropy. These anomalies arise from spin system transitions, influenced by local crystal fields, magnetic ion distributions, and inter-site interactions, potentially introducing non-linear effects relative to endmember fractions, which are not captured in our regressions. In the absence of significant interaction parameters, linear behavior is assumed as an approximation.

Assessing model robustness trough LOOCV Leave-One-Out Cross-Validation (LOOCV), preferred for small datasets (Hastie et al. 2017), recalculates regression coefficients with one sample excluded. While residuals between the excluded sample and the model estimate test error, they often underestimate true errors due to minimal training set changes. Consequently, LOOCV is better suited as a proxy for assessing model robustness, particularly our dataset with extreme samples, as it effectively identifies high-leverage samples with significant residuals that strongly influence the model.

The LOOCV MSE doubles in the bulk compositional model due to the F-buergerite (tm64) outlier, though median residuals decrease, indicating better overall fit without it to the centroid of data. Removing F-buergerite results in large negative residuals, with the model predicting a Cp curve for buergerite with much higher integrated entropy than observed. Synthetic samples in the bulk model show high LOOCV uncertainty, just like F-buergerite due to their extreme compositions, poorly captured by the rest of the training set due to the correlations they aim to break, compounded by sample coupling differences between powdered synthetic and single-crystal natural samples.

4.2 Bulk Compositional Model High-T Cp (Method 1)

Endmember Cp curves Bulk compositional endmember high-T Cp curves (>298.15 K) were obtained using OLS in Mathematica, fitting DSC Cp data prefit with Berman & Brown (1985)'s empirical polynomial equation. OLS was performed at 1 K intervals along the Cp curve to regress endmember values. The Cp(T) endmember curves for the bulk model are shown on top of each other in Figure 3R and individual plots can be found in Appendix 3E. Standard error analysis shows absolute uncertainty linearly increases with T, while relative stays relatively constant (Figure 3T). The confidence intervals (CI) are tight except for oleB and mdtwB.

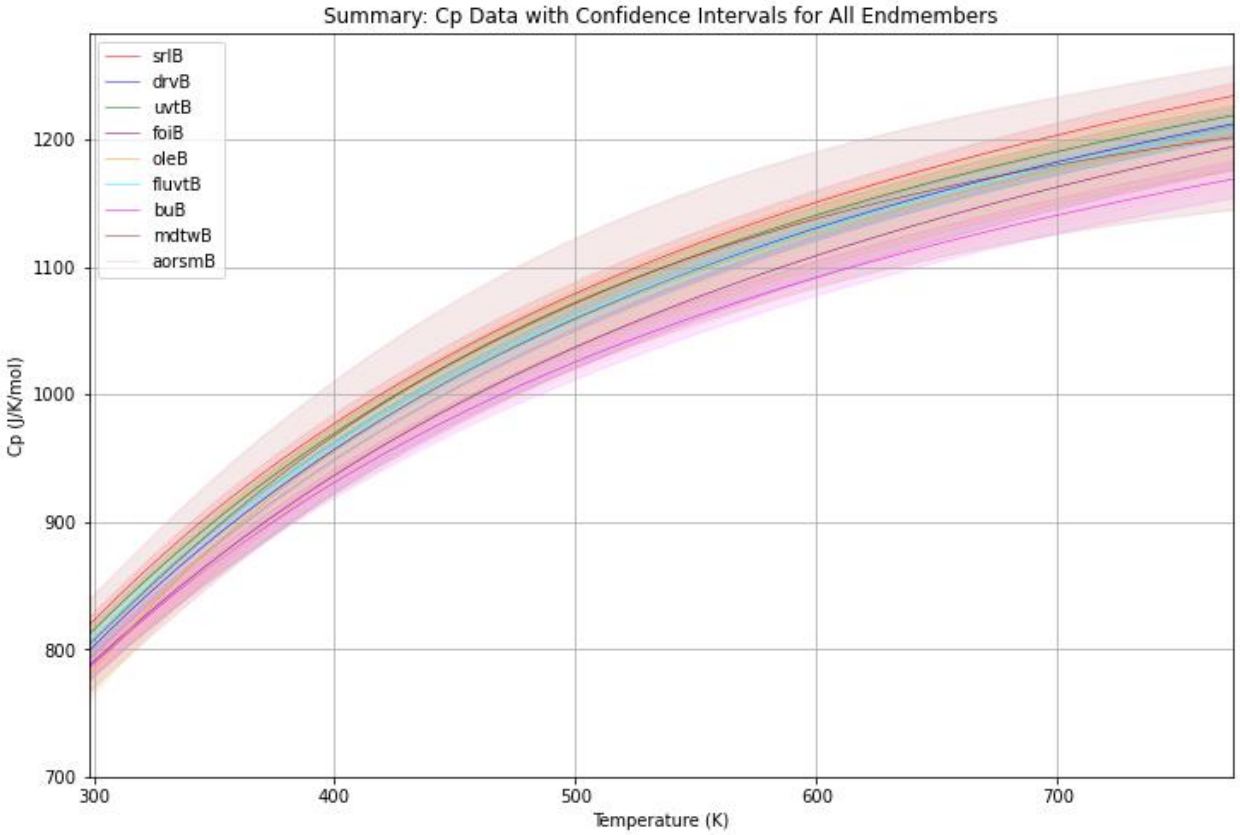

Figure 3R. Bulk compositional endmember high-T Cp curves with their CI.

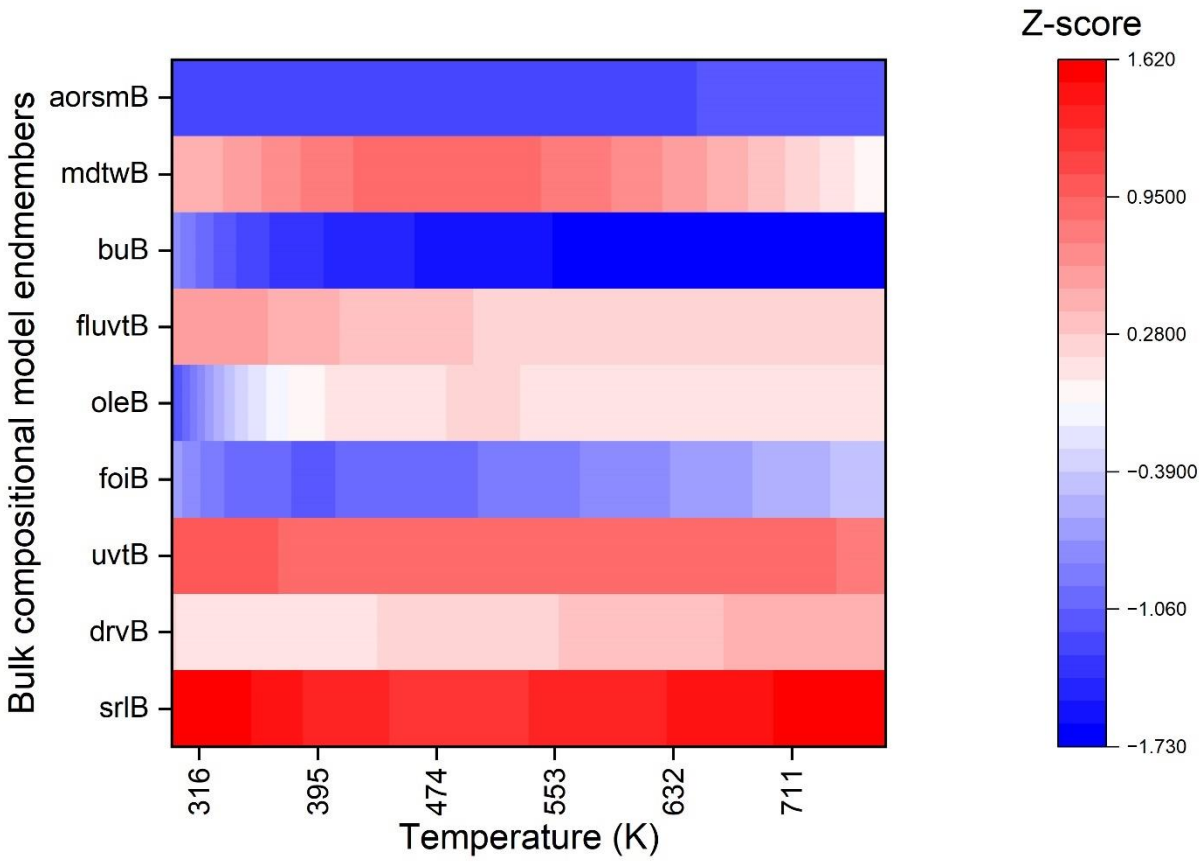

Figure 3S. Heatmap of bulk compositional model high-T Cp curves Z-scores at 1 K intervals, comparing each endmember to the mean of all endmembers.

The heatmap of Z-scores across T reveals that srlB, uvtB, mdtwB and drvB have the highest while foiB, buB, and aorsmB exhibit the lowest high-T Cp curves (Figure 3S). Fluorine lowers Cp compared to non-fluorine due to the loss of high frequency OH vibrations.

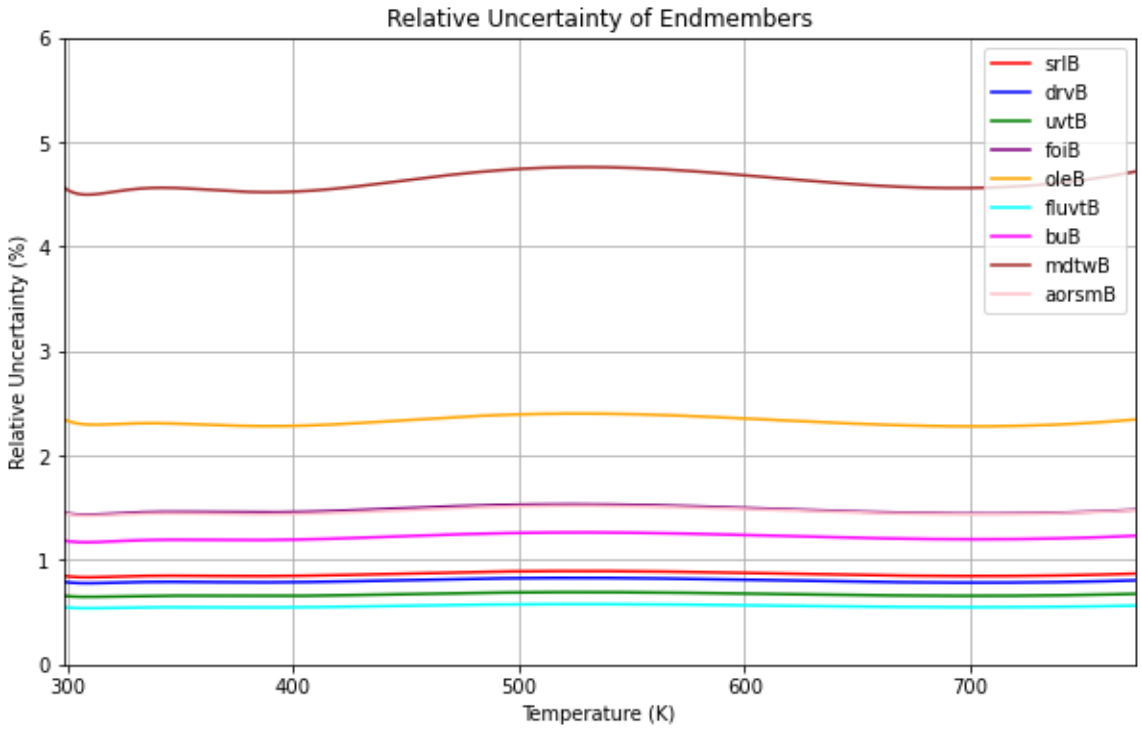

Figure 3T. The relative uncertainty in Cp (J/K/mol) dependence on T. $X(YZ)9Si_xAl_{(1-x)}(VW)_4$.

Residuals from the OLS fit are randomly distributed.

Endmember caloric Equation of State (EoS) All endmember high-T Cp curves and their standard errors were fitted using four empirical caloric EoS: HP (Holland and Powell 1990), Berman (Berman and Brown 1985) , Stix (Stixrude and Lithgow-Bertelloni 2011) , and Supcrt (Johnson et al. 1992). These models differ in coefficients and T dependencies but are all linear in regression coefficients. Singular value decomposition was used for fitting. The chi-squared goodness-of-fit was similar for HP, Berman, and Stix, with better fits from models with more coefficients. Residuals showed no T dependence except in the Supcrt model which is therefore unsuitable for high-T applications. Covariance matrices revealed highly correlated regression coefficients (>0.95) with no physical significance, preventing their use for direct determination of endmember Cp coefficients by regression due to a lack of independence.

$$C_p = c_1 + c_2 \cdot T + \frac{c_3}{T^2} + \frac{c_5}{T^{\frac{1}{2}}} \ (HP) \qquad C_p = c_1 + \frac{c_3}{T^2} + \frac{c_5}{T^{\frac{1}{2}}} + \frac{c_7}{T^3} \ (Berman)$$

$$C_p = c_1 + c_2 \cdot T + \frac{c_3}{T^2} + c_4 \cdot T^2 + \frac{c_5}{T^{\frac{1}{2}}} + \frac{c_6}{T} \ (Stix) \qquad C_p = c_1 + c_2 \cdot T + \frac{c_3}{T^2} \ (Supcrt)$$

All these models can be accommodated within the Perplex generalized empirical caloric EoS used in Perple_X software (Connolly 2005):

$$C_p(T, P_r) = c_1 + c_2 T + \frac{c_3}{T^2} + c_4 T^2 + \frac{c_5}{T^{1/2}} + \frac{c_6}{T} + \frac{c_7}{T^3} + c_8 T^3 \ (Perplex).$$

We use the Berman polynomial, but the additional equations are included in the Mathematica script as a courtesy to the user. The bulk model endmember Berman polynomial coefficients and their covariance matrices can be found in Table 3B, Table 3C.

Table 3B. Bulk model Berman polynomial regression coefficients for the endmember high-T Cp. The high number of significant figures are given as there are strong parameter correlations, rendering standard significance rules inapplicable.

Endmember	x^0 Coefficient (c1)	$x^{-0.5}$ Coefficient (c3)	x^{-2} Coefficient (c5)	x^{-3} Coefficient (c7)
srlB	1.72655×10^3	-1.25681×10^4	-2.91141×10^7	3.91145×10^9
drvB	1.64552×10^3	-1.05030×10^4	-4.07394×10^7	5.83319×10^9
uvtB	1.59346×10^3	-8.58155×10^3	-4.82376×10^7	6.83545×10^9
foiB	1.71539×10^3	-1.34417×10^4	-2.81039×10^7	4.41008×10^9
oleB	1.62643×10^3	-1.05078×10^4	-2.93238×10^7	2.40959×10^9
fluvtB	1.64728×10^3	-1.09333×10^4	-3.31115×10^7	4.33330×10^9
buB	1.61351×10^3	-1.12091×10^4	-3.01809×10^7	4.25520×10^9
mdtwB	1.23174×10^3	3.20011×10^3	-1.06815×10^8	1.55868×10^{10}
aorsmB	1.63565×10^3	-1.14735×10^4	-3.03345×10^7	3.95967×10^9

Table 3C. Bulk model covariance matrices for the Berman fit to endmember high-T Cp. Due to the high correlation between the Berman polynomial coefficients, uncertainty propagation should utilize the covariance matrices instead of the standard deviations of individual coefficients to avoid overinflating uncertainties. Additionally, the correlation matrices of the parameters are plotted. The correlation matrix of the heat capacity at 600 K (Cp_{600}) is also provided.

srlB

$$\begin{bmatrix} 2.88737\times10^{3} & -1.00746\times10^{5} & 6.0799\times10^{8} & -1.04624\times10^{11} \\ -1.00746\times10^{5} & 3.5217\times10^{6} & -2.1362\times10^{10} & 3.68663\times10^{12} \\ 6.0799\times10^{8} & -2.1362\times10^{10} & 1.3157\times10^{14} & -2.29134\times10^{16} \\ -1.04624\times10^{11} & 3.68663\times10^{12} & -2.29134\times10^{16} & 4.01346\times10^{18} \end{bmatrix}$$

drvB

$$\begin{bmatrix} 2.38865\times10^{3} & -8.33445\times10^{4} & 5.02976\times10^{8} & -8.65531\times10^{10} \\ -8.33445\times10^{4} & 2.91342\times10^{6} & -1.76723\times10^{10} & 3.04986\times10^{12} \\ 5.02976\times10^{8} & -1.76723\times10^{10} & 1.08845\times10^{14} & -1.89557\times10^{16} \\ -8.65531\times10^{10} & 3.04986\times10^{12} & -1.89557\times10^{16} & 3.32024\times10^{18} \end{bmatrix}$$

uvtB

$$\begin{bmatrix} 1.70356\times10^{3} & -5.94402\times10^{4} & 3.58716\times10^{8} & -6.17285\times10^{10} \\ -5.94402\times10^{4} & 2.07781\times10^{6} & -1.26037\times10^{10} & 2.17512\times10^{12} \\ 3.58716\times10^{8} & -1.26037\times10^{10} & 7.76268\times10^{13} & -1.3519\times10^{16} \\ -6.17285\times10^{10} & 2.17512\times10^{12} & -1.3519\times10^{16} & 2.36795\times10^{18} \end{bmatrix}$$

foiB

$$\begin{bmatrix} 7.84498\times10^{3} & -2.73726\times10^{5} & 1.65191\times10^{9} & -2.84263\times10^{11} \\ -2.73726\times10^{5} & 9.56845\times10^{6} & -5.80406\times10^{10} & 1.00166\times10^{13} \\ 1.65191\times10^{9} & -5.80406\times10^{10} & 3.57476\times10^{14} & -6.22556\times10^{16} \\ -2.84263\times10^{11} & 1.00166\times10^{13} & -6.22556\times10^{16} & 1.09045\times10^{19} \end{bmatrix}$$

oleB

$$\begin{bmatrix} 1.99915\times10^{4} & -6.97541\times10^{5} & 4.20959\times10^{9} & -7.24395\times10^{11} \\ -6.97541\times10^{5} & 2.43835\times10^{7} & -1.47906\times10^{11} & 2.55254\times10^{13} \\ 4.20959\times10^{9} & -1.47906\times10^{11} & 9.10964\times10^{14} & -1.58647\times10^{17} \\ -7.24395\times10^{11} & 2.55254\times10^{13} & -1.58647\times10^{17} & 2.77883\times10^{19} \end{bmatrix}$$

fluvtB

$$\begin{bmatrix} 1.16422\times10^{3} & -4.06217\times10^{4} & 2.45148\times10^{8} & -4.21855\times10^{10} \\ -4.06217\times10^{4} & 1.41999\times10^{6} & -8.61339\times10^{9} & 1.48649\times10^{12} \\ 2.45148\times10^{8} & -8.61339\times10^{9} & 5.30505\times10^{13} & -9.23891\times10^{15} \\ -4.21855\times10^{10} & 1.48649\times10^{12} & -9.23891\times10^{15} & 1.61827\times10^{18} \end{bmatrix}$$

buB

$$\begin{bmatrix} 5.19888\times10^{3} & -1.81398\times10^{5} & 1.09472\times10^{9} & -1.88382\times10^{11} \\ -1.81398\times10^{5} & 6.34102\times10^{6} & -3.84636\times10^{10} & 6.63798\times10^{12} \\ 1.09472\times10^{9} & -3.84636\times10^{10} & 2.369\times10^{14} & -4.12568\times10^{16} \\ -1.88382\times10^{11} & 6.63798\times10^{12} & -4.12568\times10^{16} & 7.22646\times10^{18} \end{bmatrix}$$

mdtwB

$$\begin{bmatrix} 8.05279\times10^{4} & -2.80977\times10^{6} & 1.69567\times10^{10} & -2.91794\times10^{12} \\ -2.80977\times10^{6} & 9.82192\times10^{7} & -5.95781\times10^{11} & 1.02819\times10^{14} \\ 1.69567\times10^{10} & -5.95781\times10^{11} & 3.66946\times10^{15} & -6.39047\times10^{17} \\ -2.91794\times10^{12} & 1.02819\times10^{14} & -6.39047\times10^{17} & 1.11934\times10^{20} \end{bmatrix}$$

aorsmB

$$\begin{bmatrix} 7.61086\times10^{3} & -2.65557\times10^{5} & 1.60261\times10^{9} & -2.7578\times10^{11} \\ -2.65557\times10^{5} & 9.2829\times10^{6} & -5.63085\times10^{10} & 9.71763\times10^{12} \\ 1.60261\times10^{9} & -5.63085\times10^{10} & 3.46808\times10^{14} & -6.03977\times10^{16} \\ -2.7578\times10^{11} & 9.71763\times10^{12} & -6.03977\times10^{16} & 1.05791\times10^{19} \end{bmatrix}$$

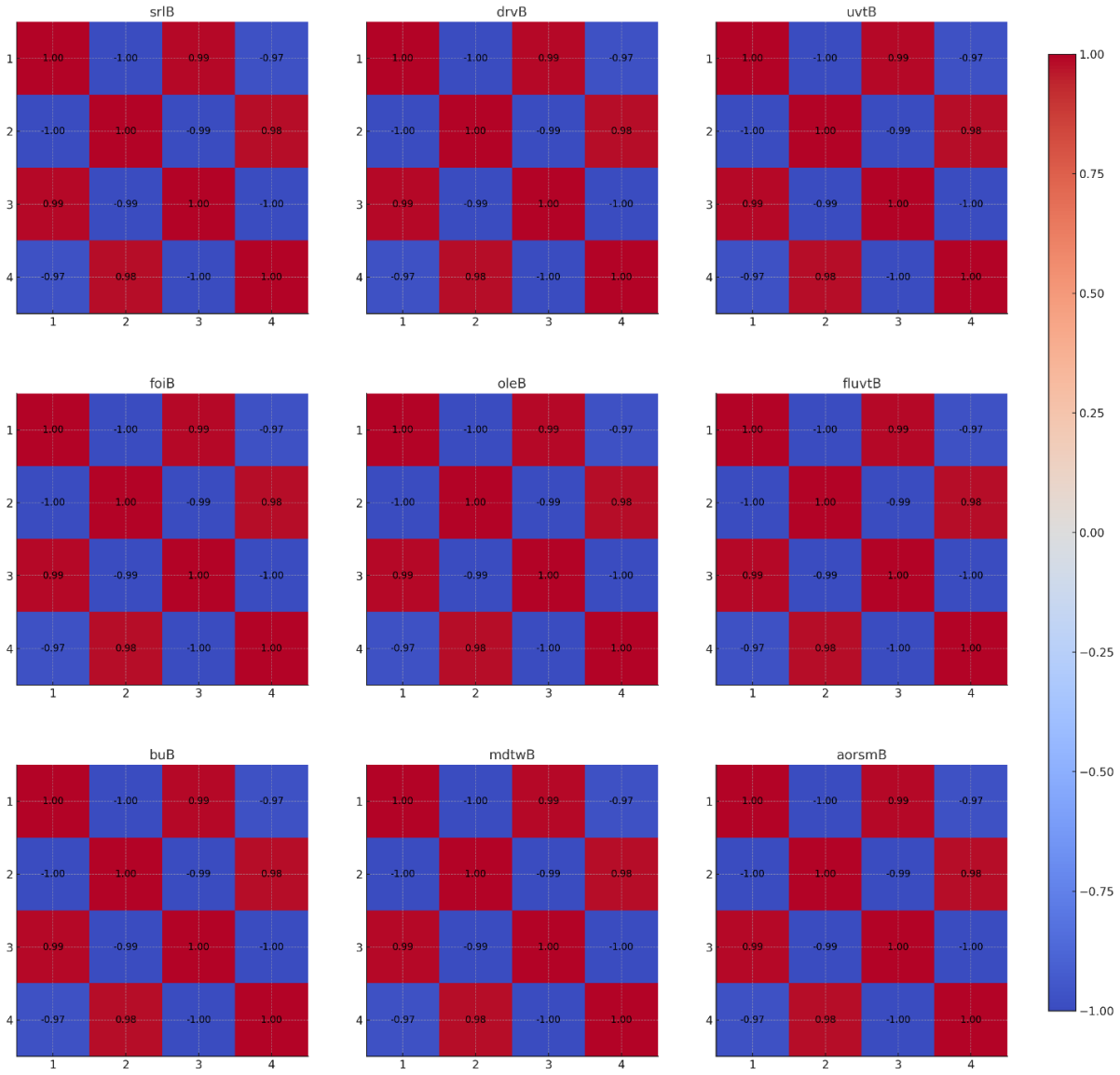
Correlation Matrices with Values
srlB
drvB
uvtB
foiB
oleB
fluvtB
buB
mdtwB
aorsmB
1.00
-1.00
0.99
-0.97
-1.00
1.00
-0.99
0.98
0.99
-0.99
1.00
-1.00
-0.97
0.98
-1.00
1.00
1
2
3
4
1.00
0.75
0.50
0.25
0.00
−0.25
−0.50
−0.75
−1.00

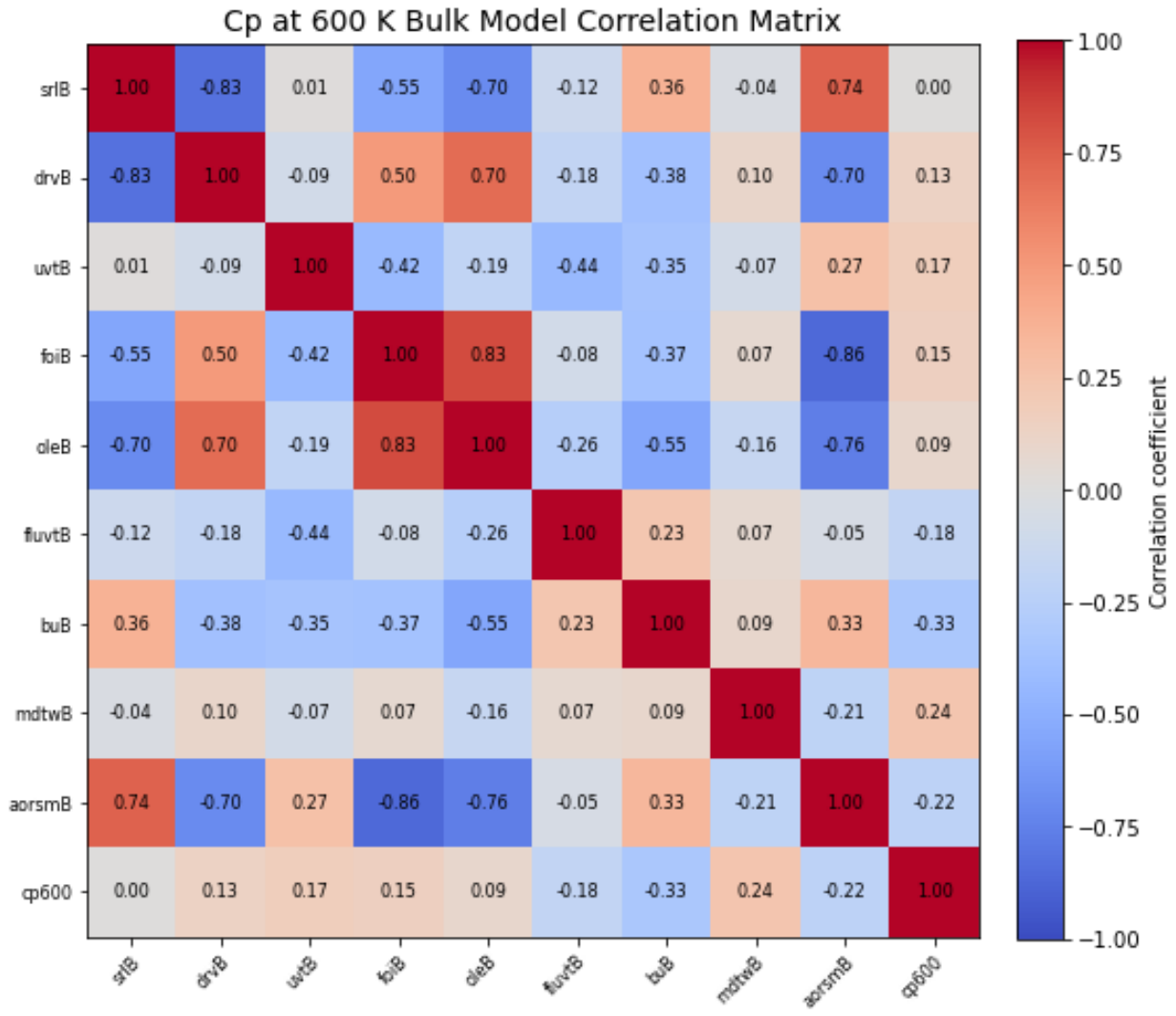

Internal Validation The Berman Cp model regression coefficients for endmembers were used to predict Cp curves for training samples, with uncertainties propagated from the covariance matrix of the polynomial fit, which are likely underestimated due to the assumption of a 'perfect' Berman model. Residuals between predicted and measured Cp were squared and averaged over 298.15–798.15 K, and these sample MSE averaged resulting in a mean MSE of 67.2 (median 37.6). Residuals were random and showed no T dependency, unlike low-T Cp curves. Most samples had relative deviations within 1%, with outliers reaching 2% (Figure 3W).

Predicted Cp curves were piecewise linearly interpolated, integrated over T to compute $S_{298.15\,\mathrm{K}}^{773.15\,\mathrm{K}}$, and compared to measured values, resulting in an entropy MSE of 51.02. Measured $S_{298.15\,\mathrm{K}}^{773.15\,\mathrm{K}}$

exhibits greater variance than predicted Cp/T integrals which leads to systematic bias, as shown in Figure 3U.

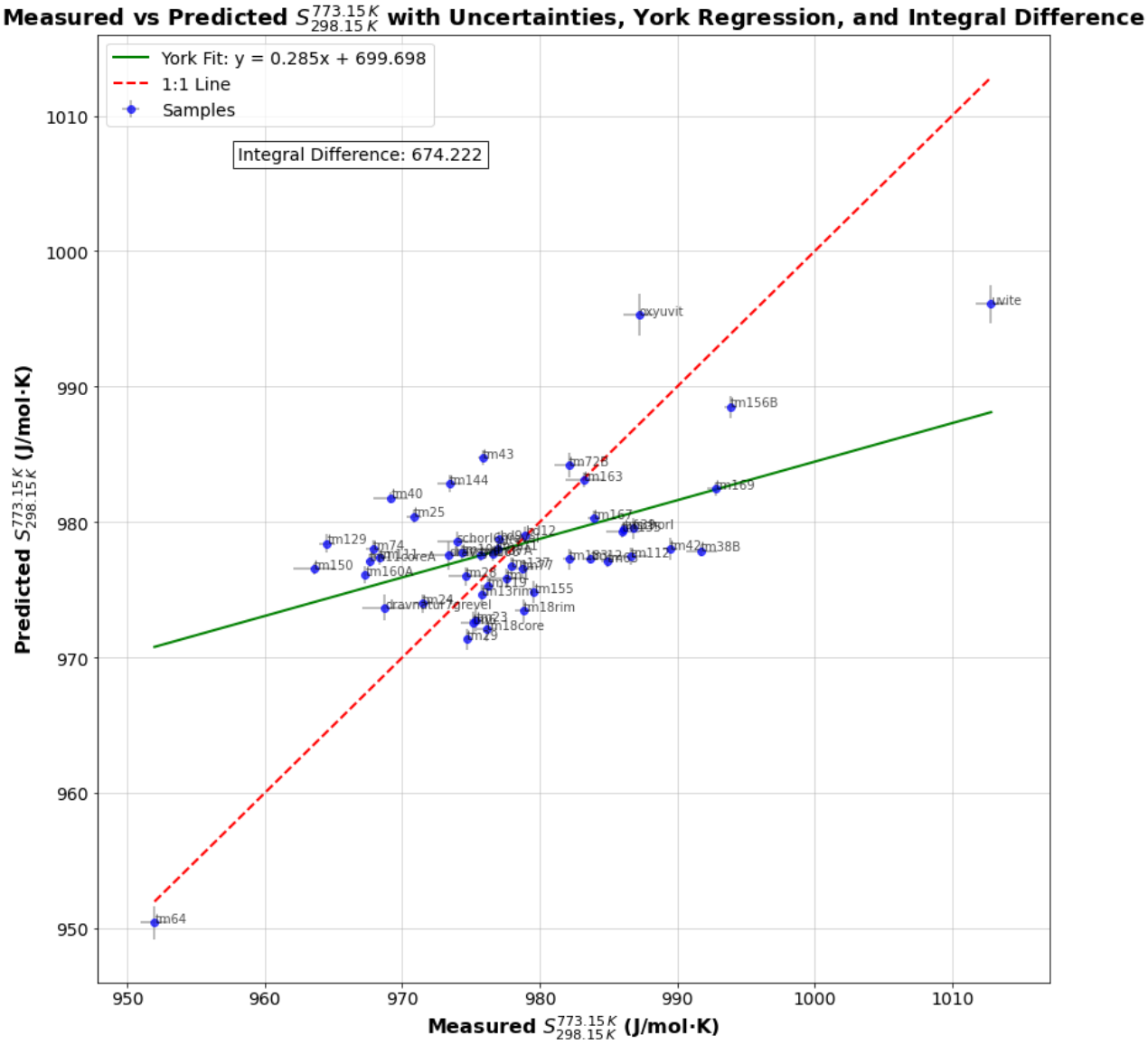

Figure 3U. Measured versus predicted entropy using Method 1. Uncertainties are propagated from the polynomial model fit and therefore assumed a 'perfect' Berman model.

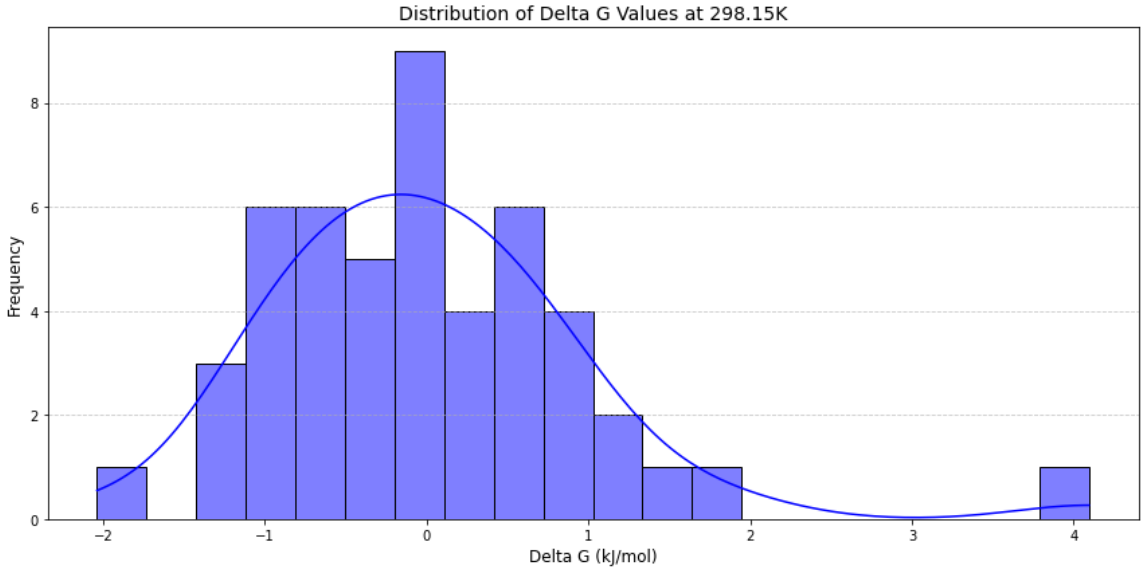
Distribution of Delta G Values at 298.15K
Frequency
Delta G (kJ/mol)

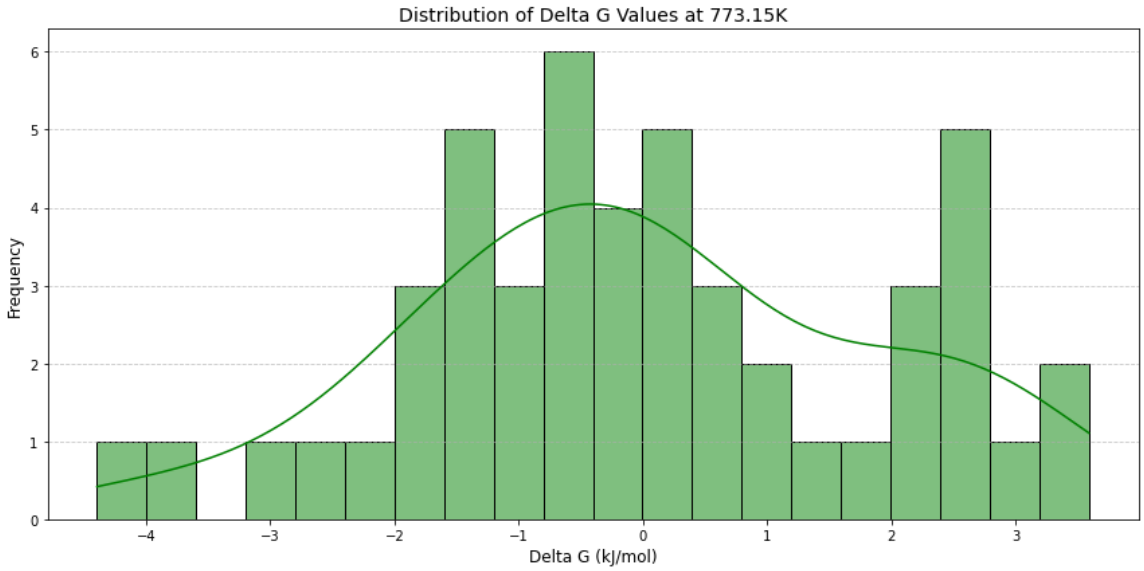
Distribution of Delta G Values at 773.15K
Frequency
Delta G (kJ/mol)

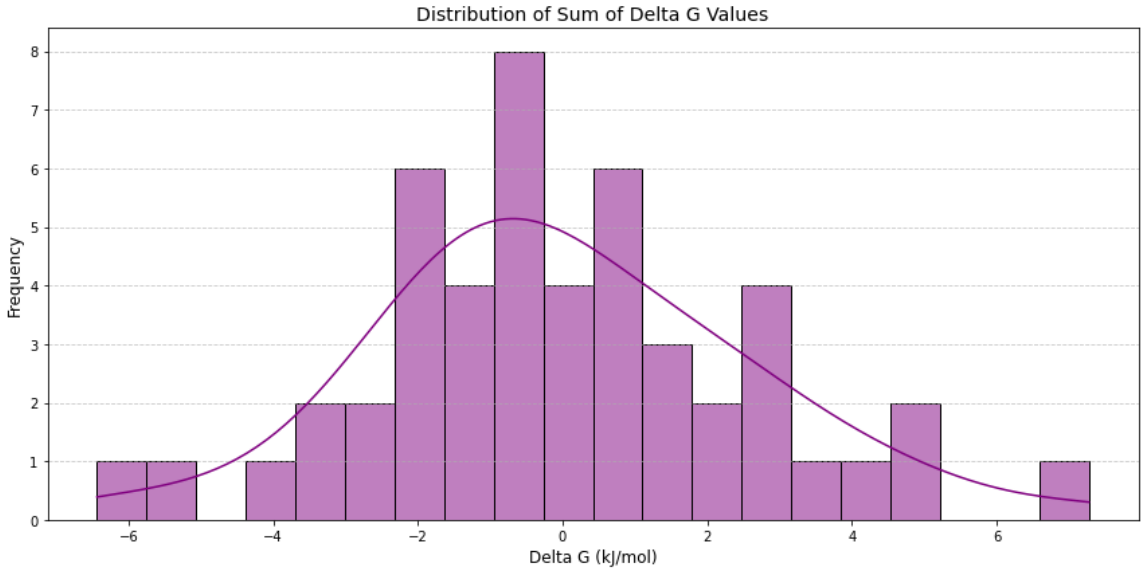
Distribution of Sum of Delta G Values
Frequency
Delta G (kJ/mol)

Figure 3V. Distribution of ΔG differences at 773.15 K arising from discrepancies between measured and predicted Cp for the bulk compositional model. The figure highlights the contributions from differences in S^0, integrated entropy along the high-T Cp curve ($S_{298.15K}^{773.15\,K}$), and their combined impact on ΔG values at 773.15 K.

Gibbs free energy discrepancies due to model simplifications at 773.15 K, excluding standard state enthalpy/entropy and S_{conf}, reached a maximum of 4.5 kJ, again comparable to interaction parameters, underscoring the need for Cp measurements with <1% relative uncertainty for accurate high-T energy calculations in solid solutions (Figure 3V). Adding the two ΔG together per samples shows the total model simplification energies at 773.15 K can be up to 6 kJ/mol (Figure 3V, bottom). This shows that published Cp measurements with more than 2% uncertainty are may not provide the precision required for accurate thermodynamic modelling.

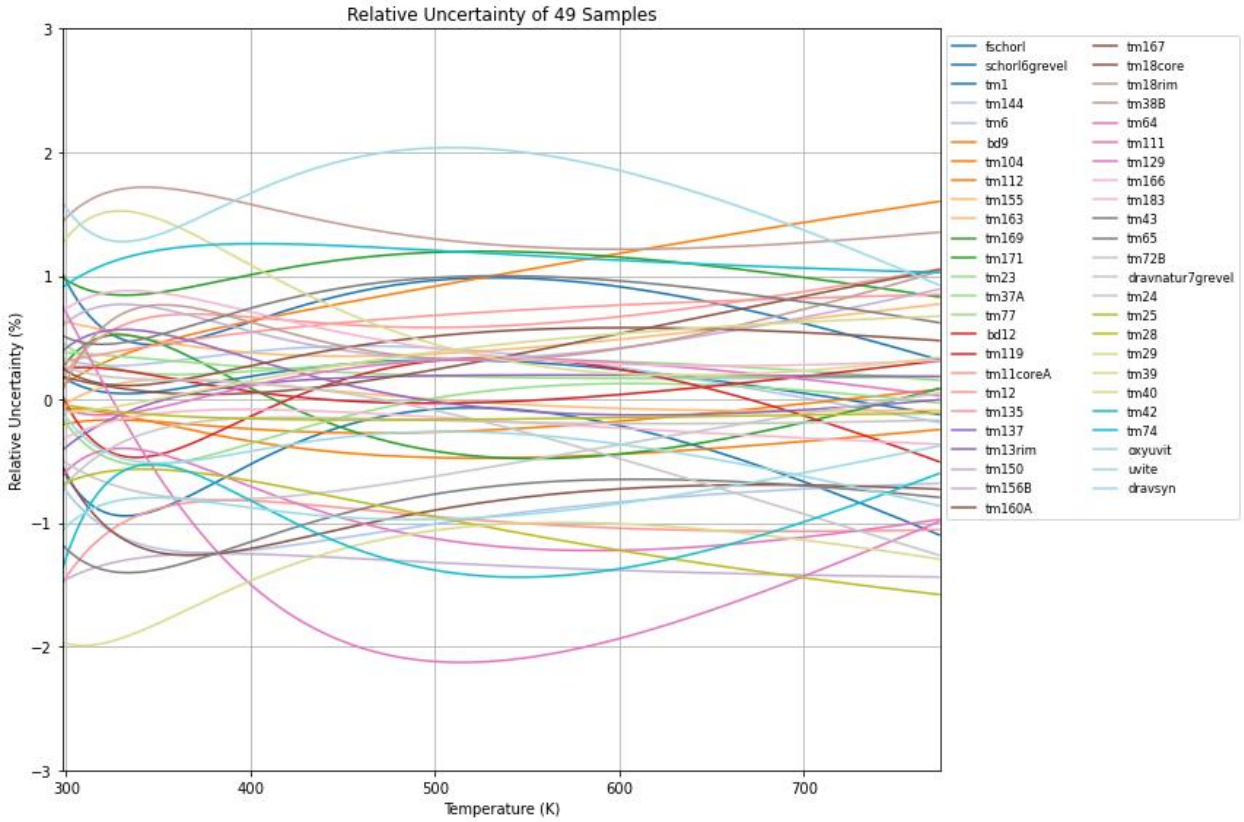

Figure 3W. Relative deviations between training set data and model for high-T Cp.

At 300.15 K, 373.15 K, 573.15 K, and 773.15 K, measured versus predicted Cp comparisons showed good agreement with the 1:1 line (Figure 3X). However, a systematic offset was observed, with the model near uniform high-T Cp values (1190–1220 J/mol·K), while measured values spanned 1180–1250 J/mol·K, creating a horizontal spread at higher T in the 1:1 plot. Appendix 3I figures provide zoomed-in predicted vs. measured Cp plots at each T with York regression fits, showing residuals that are nonrandom and heteroscedastic. The York regression and the integral between the York fit and the 1:1 line confirm the systematic bias of the overprediction for low Cp samples and underprediction for high Cp samples at high T. This discrepancy is not attributable to the Berman polynomial limitations, as both measured and predicted curves were independently fitted to this polynomial, and alternative parameterization (e.g., Perplex polynomial or linear interpolation) yielded similar results.

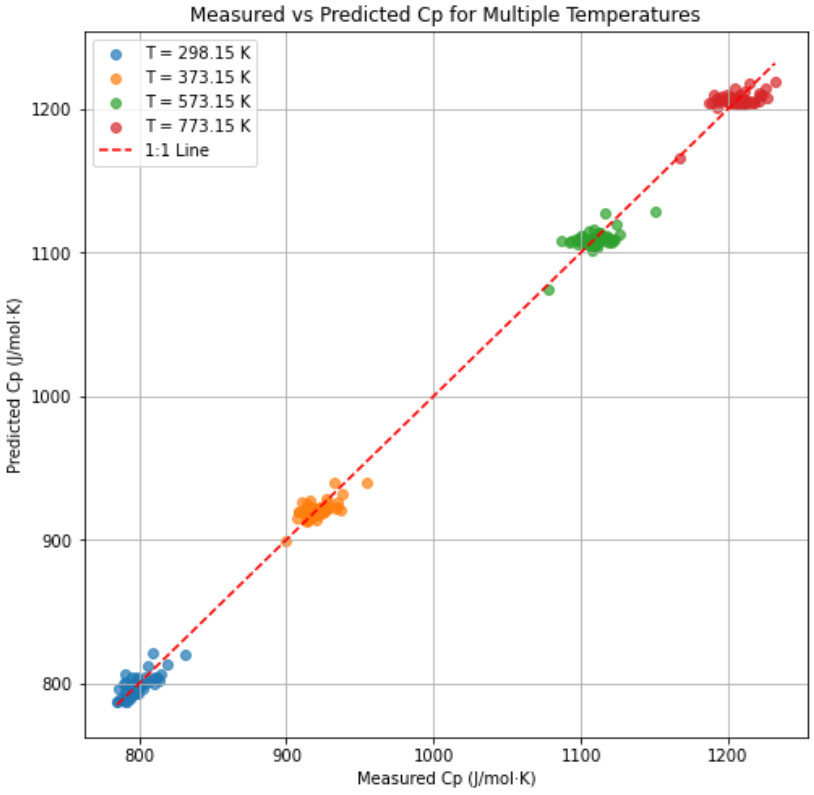

Figure 3X. Predicted versus measured Cp at four different T with the 1:1 line. Note the increasingly horizontal distribution of samples around the 1:1 line at higher T.

LOOCV The LOOCV MSE nearly tripled for the bulk compositional model (67.2 to 149.5), highlighting the high leverage of F-buergerite (Tm64) and synthetic samples also at high T. This emphasizes the Cp model's data dependence and the need for correlation-breaking simple tourmalines to enhance robustness. Weighted least squares (WLS), using the inverse of variance at each point as weights, produced excessively wiggly high-T Cp fits due to disrupted correlations between Cp values across T, rendering the method unusable.

4.3 Speciation Model

The methodology and figures used in the speciation model are identical to those in the bulk compositional model, including the regression analysis, predicted versus measured comparisons, and entropy calculations. These details are provided in Appendix 3H, which presents the figures and analysis for the speciation model in the same format as the bulk compositional model. Appendix 3J contains the individual endmember curves, while Appendix 3F covers the method 1 statistics. Method 2 is detailed in Appendix 3D. Appendix 3I highlights the four-temperature zoom, showing that the speciation model also experiences regression sensitivity loss as the Cp curves flatten at high temperatures. Only final tables with endmember entropies (Table 3D), Berman coefficients (Table 3E) and Berman coefficients covariance matrices (Table 3F) are presented here.

Table 3D. Standard State Entropy of the endmembers obtained using method 1 for the speciation model. Additionally, the correlation matrices of the parameters are plotted.

Endmember Name	Entropy (J/K/mol)	Entropy Uncertainty (J/K/mol)
srl	710.54	18.85
drv	621.85	8.77
uvt	648.33	16.36
fuvt	725.19	40.70
foi	669.94	25.04
ole	656.99	41.44
drvdis	641.39	18.50
odrv	629.22	8.75
fluvt	641.06	6.46
bu	657.44	28.02
mdtw	690.41	43.41
bole	568.46	15.38
aorsm	638.87	26.07
pov	1000.44	120.65

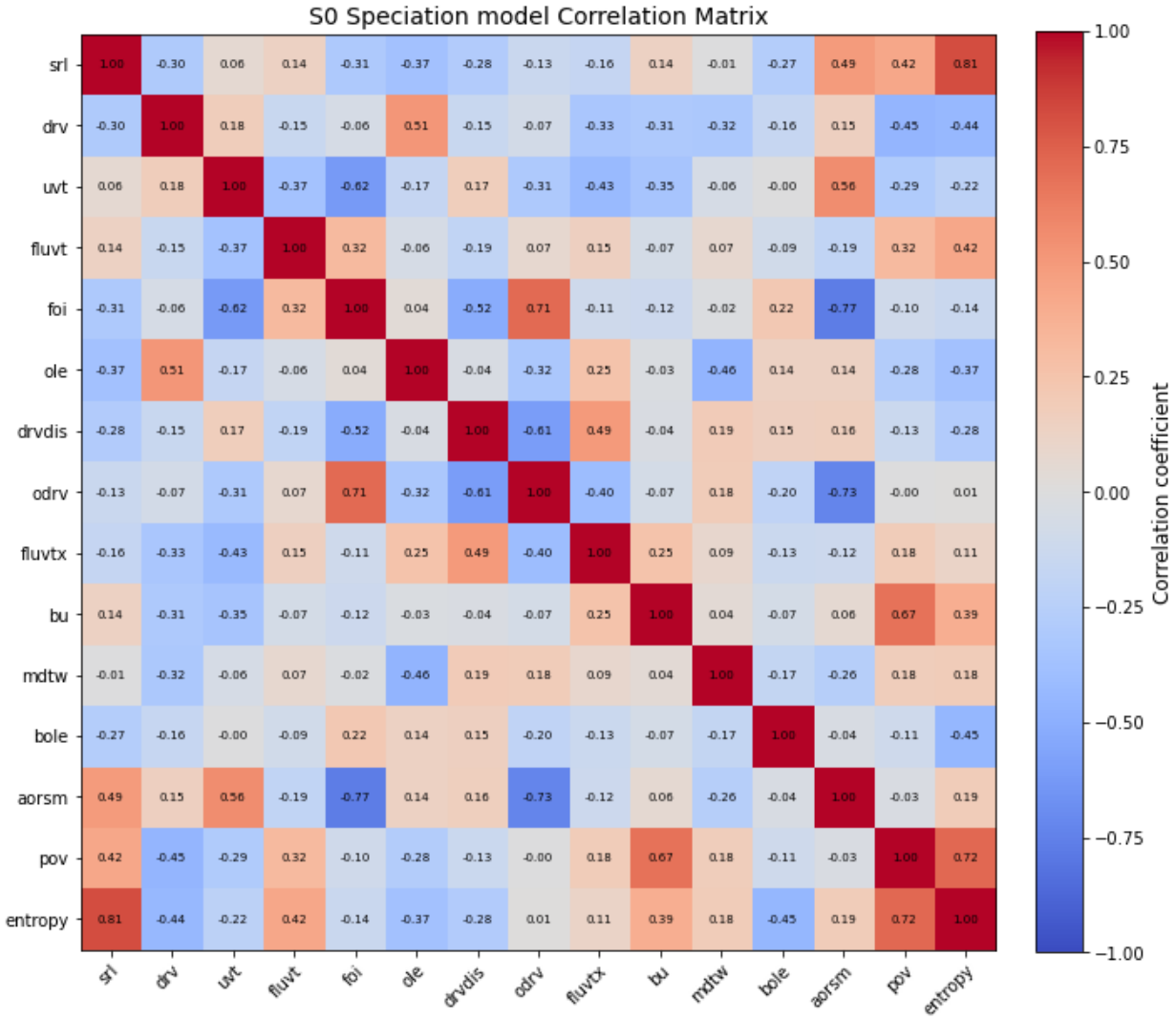
S0 Speciation model Correlation Matrix
srl
drv
uvt
fluvt
foi
ole
drvdis
odrv
fluvtx
bu
mdtw
bole
aorsm
pov
entropy
1.00 -0.30 0.06 0.14 -0.31 -0.37 -0.28 -0.13 -0.16 0.14 -0.01 -0.27 0.49 0.42 0.81
-0.30 1.00 0.18 -0.15 -0.06 0.51 -0.15 -0.07 -0.33 -0.31 -0.32 -0.16 0.15 -0.45 -0.44
0.06 0.18 1.00 -0.37 -0.62 -0.17 0.17 -0.31 -0.43 -0.35 -0.06 -0.00 0.56 -0.29 -0.22
0.14 -0.15 -0.37 1.00 0.32 -0.06 -0.19 0.07 0.15 -0.07 0.07 -0.09 -0.19 0.32 0.42
-0.31 -0.06 -0.62 0.32 1.00 0.04 -0.52 0.71 -0.11 -0.12 -0.02 0.22 -0.77 -0.10 -0.14
-0.37 0.51 -0.17 -0.06 0.04 1.00 -0.04 -0.32 0.25 -0.03 -0.46 0.14 0.14 -0.28 -0.37
-0.28 -0.15 0.17 -0.19 -0.52 -0.04 1.00 -0.61 0.49 -0.04 0.19 0.15 0.16 -0.13 -0.28
-0.13 -0.07 -0.31 0.07 0.71 -0.32 -0.61 1.00 -0.40 -0.07 0.18 -0.20 -0.73 -0.00 0.01
-0.16 -0.33 -0.43 0.15 -0.11 0.25 0.49 -0.40 1.00 0.25 0.09 -0.13 -0.12 0.18 0.11
0.14 -0.31 -0.35 -0.07 -0.12 -0.03 -0.04 -0.07 0.25 1.00 0.04 -0.07 0.06 0.67 0.39
-0.01 -0.32 -0.06 0.07 -0.02 -0.46 0.19 0.18 0.09 0.04 1.00 -0.17 -0.26 0.18 0.18
-0.27 -0.16 -0.00 -0.09 0.22 0.14 0.15 -0.20 -0.13 -0.07 -0.17 1.00 -0.04 -0.11 -0.45
0.49 0.15 0.56 -0.19 -0.77 0.14 0.16 -0.73 -0.12 0.06 -0.26 -0.04 1.00 -0.03 0.19
0.42 -0.45 -0.29 0.32 -0.10 -0.28 -0.13 -0.00 0.18 0.67 0.18 -0.11 -0.03 1.00 0.72
0.81 -0.44 -0.22 0.42 -0.14 -0.37 -0.28 0.01 0.11 0.39 0.18 -0.45 0.19 0.72 1.00
1.00
0.75
0.50
0.25
0.00
−0.25
−0.50
−0.75
−1.00
Correlation coefficient

Table 3E. Speciation model Berman polynomial regression coefficients for endmember high-T Cp. The high number of significant figures are given as there are strong parameter correlations, rendering standard significance rules inapplicable.

Endmember	x^0 Coefficient (c1)	$x^{-0.5}$ Coefficient (c3)	x^{-2} Coefficient (c5)	x^{-3} Coefficient (c7)
srl	1.0892×10^3	9.27407×10^3	-1.48237×10^8	2.26211×10^{10}
drv	1.27704×10^3	2.25033×10^3	-1.12376×10^8	1.72737×10^{10}
uvt	1.07092×10^3	9.26158×10^3	-1.45642×10^8	2.22102×10^{10}
fuvt	5.7365×10^2	2.9335×10^4	-2.85716×10^8	4.58651×10^{10}
foi	1.0618×10^3	8.0897×10^3	-1.33455×10^8	2.03064×10^{10}
ole	7.16118×10^2	2.14646×10^4	-1.96593×10^8	2.76376×10^{10}
drvdis	1.08946×10^3	8.2565×10^3	-1.37159×10^8	2.03493×10^{10}
odrv	1.72823×10^3	-1.34833×10^4	-2.0288×10^7	1.80596×10^9
fluvt	1.72914×10^3	-1.37634×10^4	-1.92416×10^7	2.30223×10^9
bu	5.62016×10^2	2.51396×10^4	-2.40675×10^8	3.83514×10^{10}
mdtw	7.60559×10^2	2.02213×10^4	-2.01319×10^8	3.07205×10^{10}
bole	1.65844×10^3	-1.16786×10^4	-5.39347×10^7	9.29786×10^9
aorsm	2.31906×10^3	-3.55637×10^4	1.15461×10^8	-2.01997×10^{10}
pov	3.2381×10^3	-7.01221×10^4	3.71811×10^8	-6.26094×10^{10}

srl

$$\begin{bmatrix} 1.48856 \times 10^4 & -5.18897 \times 10^5 & 3.12289 \times 10^9 & -5.36558 \times 10^{11} \\ -5.18897 \times 10^5 & 1.81219 \times 10^7 & -1.09626 \times 10^{11} & 1.88898 \times 10^{13} \\ 3.12289 \times 10^9 & -1.09626 \times 10^{11} & 6.73387 \times 10^{14} & -1.17093 \times 10^{17} \\ -5.36558 \times 10^{11} & 1.88898 \times 10^{13} & -1.17093 \times 10^{17} & 2.0478 \times 10^{19} \end{bmatrix}$$

drv

$$\begin{bmatrix} 3.22367 \times 10^3 & -1.12374 \times 10^5 & 6.76299 \times 10^8 & -1.16198 \times 10^{11} \\ -1.12374 \times 10^5 & 3.92452 \times 10^6 & -2.37408 \times 10^{10} & 4.09083 \times 10^{12} \\ 6.76299 \times 10^8 & -2.37408 \times 10^{10} & 1.4583 \times 10^{14} & -2.53578 \times 10^{16} \\ -1.16198 \times 10^{11} & 4.09083 \times 10^{12} & -2.53578 \times 10^{16} & 4.43475 \times 10^{18} \end{bmatrix}$$

uvt

$$\begin{bmatrix} 1.12203 \times 10^4 & -3.91128 \times 10^5 & 2.35393 \times 10^9 & -4.0444 \times 10^{11} \\ -3.91128 \times 10^5 & 1.36597 \times 10^7 & -8.26322 \times 10^{10} & 1.42386 \times 10^{13} \\ 2.35393 \times 10^9 & -8.26322 \times 10^{10} & 5.07577 \times 10^{14} & -8.82606 \times 10^{16} \\ -4.0444 \times 10^{11} & 1.42386 \times 10^{13} & -8.82606 \times 10^{16} & 1.54356 \times 10^{19} \end{bmatrix}$$

fuvt

$$\begin{bmatrix} 6.94389 \times 10^4 & -2.42056 \times 10^6 & 1.45677 \times 10^{10} & -2.50295 \times 10^{12} \\ -2.42056 \times 10^6 & 8.45355 \times 10^7 & -5.11383 \times 10^{11} & 8.81177 \times 10^{13} \\ 1.45677 \times 10^{10} & -5.11383 \times 10^{11} & 3.14123 \times 10^{15} & -5.46216 \times 10^{17} \\ -2.50295 \times 10^{12} & 8.81177 \times 10^{13} & -5.46216 \times 10^{17} & 9.5526 \times 10^{19} \end{bmatrix}$$

foi

$$\begin{bmatrix} 2.62845 \times 10^4 & -9.16250 \times 10^5 & 5.51428 \times 10^9 & -9.47435 \times 10^{11} \\ -9.16250 \times 10^5 & 3.1999 \times 10^7 & -1.93573 \times 10^{11} & 3.3355 \times 10^{13} \\ 5.51428 \times 10^9 & -1.93573 \times 10^{11} & 1.18904 \times 10^{15} & -2.06758 \times 10^{17} \\ -9.47435 \times 10^{11} & 3.3355 \times 10^{13} & -2.06758 \times 10^{17} & 3.61593 \times 10^{19} \end{bmatrix}$$

ole

$$\begin{bmatrix} 7.19787 \times 10^4 & -2.5091 \times 10^6 & 1.51005 \times 10^{10} & -2.59449 \times 10^{12} \\ -2.5091 \times 10^6 & 8.76275 \times 10^7 & -5.30088 \times 10^{11} & 9.13407 \times 10^{13} \\ 1.51005 \times 10^{10} & -5.30088 \times 10^{11} & 3.25612 \times 10^{15} & -5.66194 \times 10^{17} \\ -2.59449 \times 10^{12} & 9.13407 \times 10^{13} & -5.66194 \times 10^{17} & 9.902 \times 10^{19} \end{bmatrix}$$

drvdis

$$\begin{bmatrix} 1.43458 \times 10^4 & -5.0008 \times 10^5 & 3.00964 \times 10^9 & -5.171 \times 10^{11} \\ -5.0008 \times 10^5 & 1.74647 \times 10^7 & -1.0565 \times 10^{11} & 1.82048 \times 10^{13} \\ 3.00964 \times 10^9 & -1.0565 \times 10^{11} & 6.48967 \times 10^{14} & -1.12846 \times 10^{17} \\ -5.171 \times 10^{11} & 1.82048 \times 10^{13} & -1.12846 \times 10^{17} & 1.97353 \times 10^{19} \end{bmatrix}$$

odrv

$$\begin{bmatrix} 3.20874 \times 10^3 & -1.11853 \times 10^5 & 6.73167 \times 10^8 & -1.1566 \times 10^{11} \\ -1.11853 \times 10^5 & 3.90635 \times 10^6 & -2.36308 \times 10^{10} & 4.07188 \times 10^{12} \\ 6.73167 \times 10^8 & -2.36308 \times 10^{10} & 1.45155 \times 10^{14} & -2.52404 \times 10^{16} \\ -1.1566 \times 10^{11} & 4.07188 \times 10^{12} & -2.52404 \times 10^{16} & 4.41421 \times 10^{18} \end{bmatrix}$$

fluvt

$$\begin{bmatrix} 1.74663 \times 10^3 & -6.08857 \times 10^4 & 3.66429 \times 10^8 & -6.29579 \times 10^{10} \\ -6.08857 \times 10^4 & 2.12637 \times 10^6 & -1.28631 \times 10^{10} & 2.21647 \times 10^{12} \\ 3.66429 \times 10^8 & -1.28631 \times 10^{10} & 7.9013 \times 10^{13} & -1.37393 \times 10^{16} \\ -6.29579 \times 10^{10} & 2.21647 \times 10^{12} & -1.37393 \times 10^{16} & 2.40282 \times 10^{18} \end{bmatrix}$$

bu

$$\begin{bmatrix} 3.29042 \times 10^4 & -1.147 \times 10^6 & 6.90302 \times 10^9 & -1.18604 \times 10^{12} \\ -1.147 \times 10^6 & 4.00578 \times 10^7 & -2.42323 \times 10^{11} & 4.17553 \times 10^{13} \\ 6.90302 \times 10^9 & -2.42323 \times 10^{11} & 1.4885 \times 10^{15} & -2.58829 \times 10^{17} \\ -1.18604 \times 10^{12} & 4.17553 \times 10^{13} & -2.58829 \times 10^{17} & 4.52658 \times 10^{19} \end{bmatrix}$$

mdtw

$$\begin{bmatrix} 7.89717 \times 10^4 & -2.75287 \times 10^6 & 1.65676 \times 10^{10} & -2.84656 \times 10^{12} \\ -2.75287 \times 10^6 & 9.61409 \times 10^7 & -5.81588 \times 10^{11} & 1.00215 \times 10^{14} \\ 1.65676 \times 10^{10} & -5.81588 \times 10^{11} & 3.57247 \times 10^{15} & -6.21203 \times 10^{17} \\ -2.84656 \times 10^{12} & 1.00215 \times 10^{14} & -6.21203 \times 10^{17} & 1.0864 \times 10^{20} \end{bmatrix}$$

bole

$$\begin{bmatrix} 9.90723 \times 10^3 & -3.45355 \times 10^5 & 2.07845 \times 10^9 & -3.57109 \times 10^{11} \\ -3.45355 \times 10^5 & 1.20611 \times 10^7 & -7.29619 \times 10^{10} & 1.25722 \times 10^{13} \\ 2.07845 \times 10^9 & -7.29619 \times 10^{10} & 4.48176 \times 10^{14} & -7.79316 \times 10^{16} \\ -3.57109 \times 10^{11} & 1.25722 \times 10^{13} & -7.79316 \times 10^{16} & 1.36292 \times 10^{19} \end{bmatrix}$$

aorsm

$$\begin{bmatrix} 2.84943 \times 10^4 & -9.93279 \times 10^5 & 5.97786 \times 10^9 & -1.02709 \times 10^{12} \\ -9.93279 \times 10^5 & 3.46892 \times 10^7 & -2.09847 \times 10^{11} & 3.61592 \times 10^{13} \\ 5.97786 \times 10^9 & -2.09847 \times 10^{11} & 1.289 \times 10^{15} & -2.2414 \times 10^{17} \\ -1.02709 \times 10^{12} & 3.61592 \times 10^{13} & -2.2414 \times 10^{17} & 3.91992 \times 10^{19} \end{bmatrix}$$

pov

$$\begin{bmatrix} 6.10085 \times 10^5 & -2.12669 \times 10^7 & 1.27991 \times 10^{11} & -2.19907 \times 10^{13} \\ -2.12669 \times 10^7 & 7.42723 \times 10^8 & -4.49298 \times 10^{12} & 7.74195 \times 10^{14} \\ 1.27991 \times 10^{11} & -4.49298 \times 10^{12} & 2.75986 \times 10^{16} & -4.79901 \times 10^{18} \\ -2.19907 \times 10^{13} & 7.74195 \times 10^{14} & -4.79901 \times 10^{18} & 8.39284 \times 10^{20} \end{bmatrix}$$

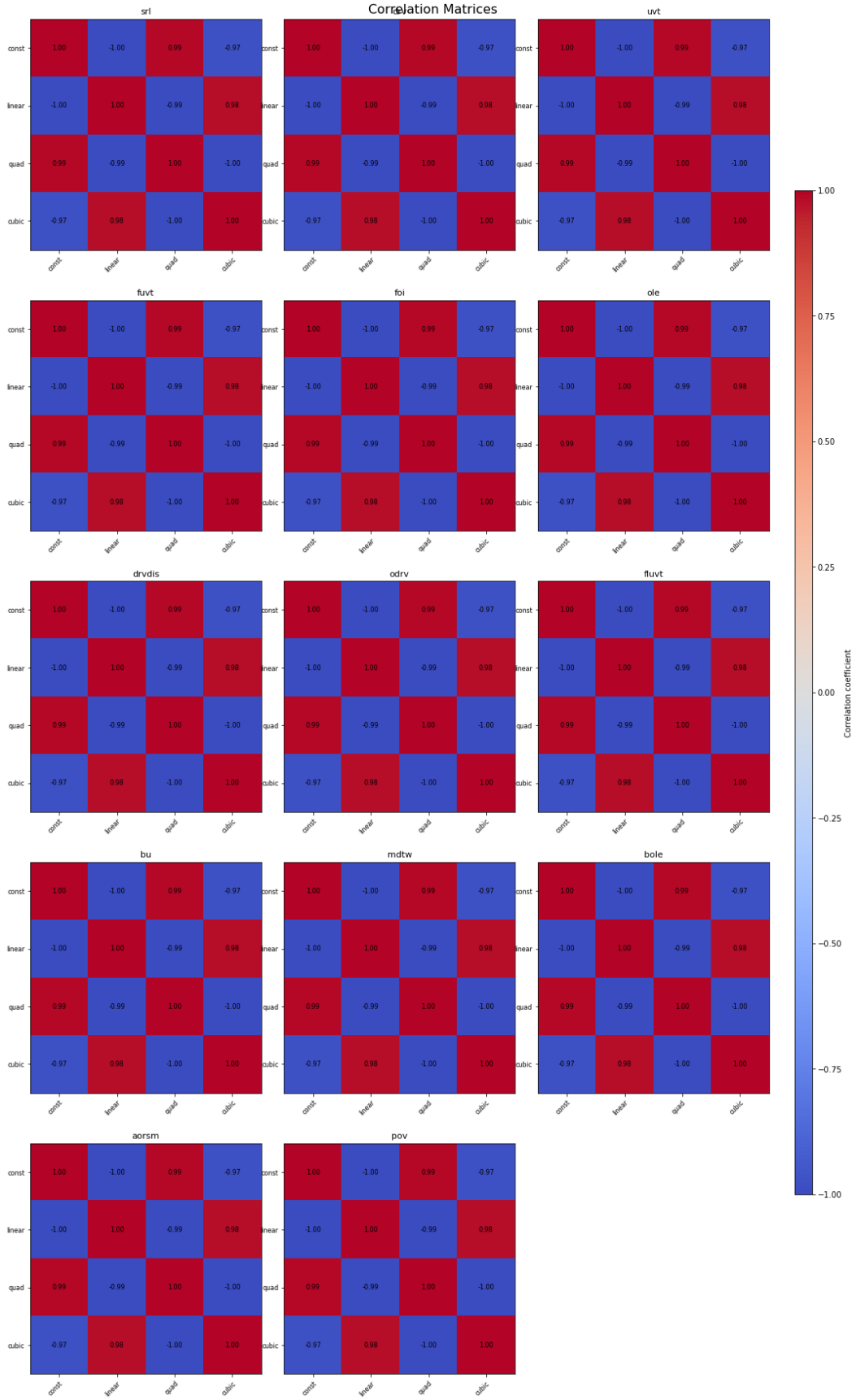
Correlation Matrices
srl
tv
uvt
fuvt
foi
ole
drvdis
odrv
fluvt
bu
mdtw
bole
aorsm
pov
const
linear
quad
cubic
1.00
-1.00
0.99
-0.97
-1.00
1.00
-0.99
0.98
0.99
-0.99
1.00
-1.00
-0.97
0.98
-1.00
1.00
Correlation coefficient
1.00
0.75
0.50
0.25
0.00
−0.25
−0.50
−0.75
−1.00

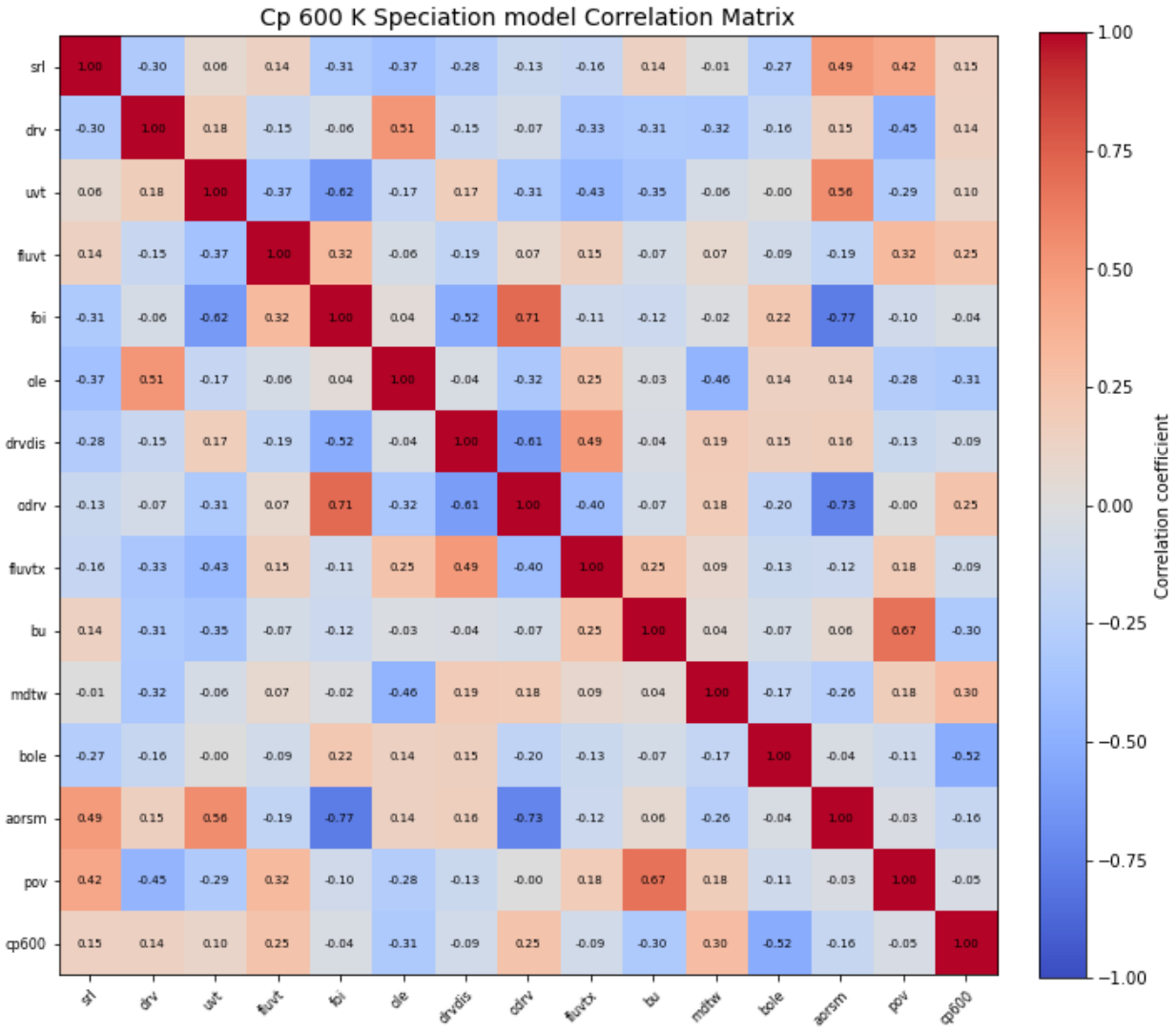

1. DISCUSSION ORDINARY LEAST SQUARES MODELS

Method 1 vs. Method 2 Entropy, as a state function, depends only on the initial and final states of the system. However, deriving entropy from heat capacity data can be influenced by the order of regression and integration, particularly at low T (<298.15 K) where Cp variations contribute disproportionately due to 1/T weighting in the integration. In Method 1, linear interpolation approximates Cp curves, regression derives endmember Cp curves, and integration follows. This approach reduces noise by leveraging regression to average out inconsistencies across samples, and only the Cp curves of the endmembers are integrated, minimizing the potential for cumulative errors (Main text and Appendix 3F) In contrast, Method 2 (Appendix 3D1-3D3) first integrates sample Cp fits to calculate entropy, then applies regression to derive endmember

entropies. While simpler, here, all sample Cp curves are integrated which amplifies errors when the samples fits are imperfect. At high T (>298.15 K), where Cp curves are smoother and dominated by Dulong-Petit behavior, both methods yield comparable results due to reduced sensitivity to interpolation errors.

Dulong-Petit due to Systematic Bias at high T Cp Although the overall accuracy of the predicted $S_{298.15K}^{773.15\,K}$ is reasonable <2 %, significant compositional biases arise in $S_{298.15K}^{773.15\,K}$ and Cp regressions above 500 K. When performing linear regression on Cp curves, the slope (dCp/dT) heavily influences model sensitivity to deviations. At low T, where Cp curves are steep, even small inaccuracies yield large residuals, forcing the regression to align data around the 1:1 line, including extreme samples. At high T, as Cp curves flatten, deviations produce smaller residuals, reducing regression sensitivity. This leads to nearly constant regressed Cp values across compositions, resulting in horizontal spreading and underpredicted variability at high T, while measured data still show subtle differences. This systematic offset reveals the inability of endmember Cp curves from linear regression to capture subtle anharmonic effects or deviations from the Dulong-Petit law, critical for mineral behavior above 773.15 K.

Attempts to increase regression sensitivity in flat regions included removing high-leverage points, weighted regression using inverse dCp/dT, z-score transformations with back-transformation, and nonlinear regression directly fitting Berman coefficients. None eliminated the flattening effect at high T. Only amplifying slope importance by a factor of 20 reduced the horizontal spread, but this increased overall uncertainty (Figure 3Y).

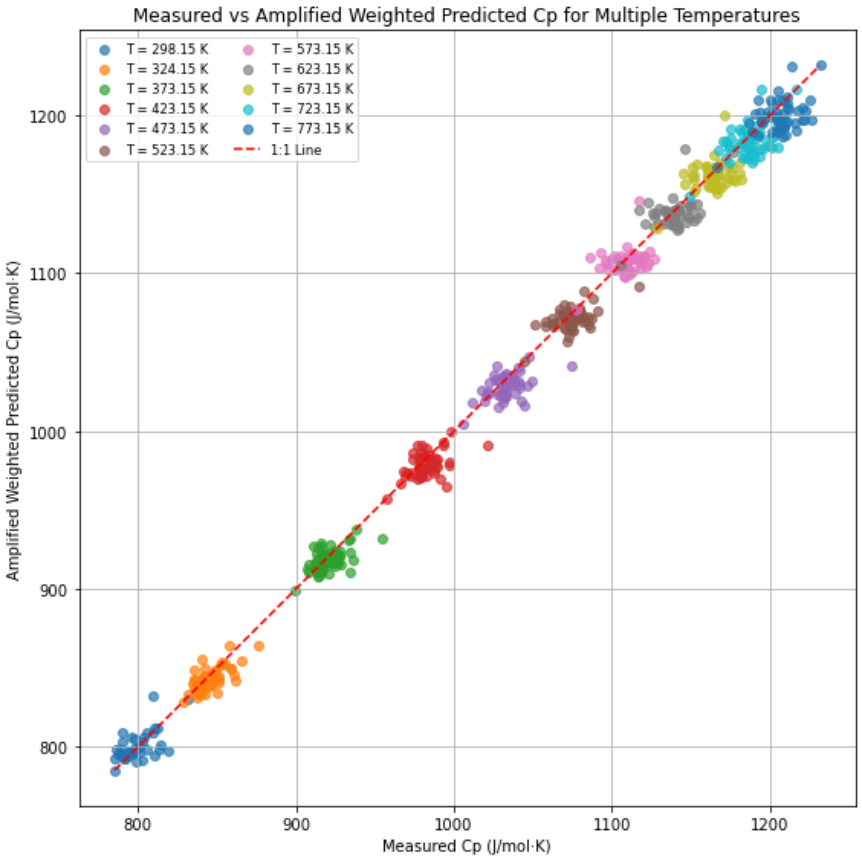

Figure 3Y. Slope weighted linear regression where the weight was multiplied with a factor of 20.

Standardizing the variables does not fully resolve the issue, as low Z-scores, corresponding to regions of the Cp curve with low variability, still result in weak explanatory power or model fit. This highlights a fundamental challenge in modelling high-T Cp curves and their extrapolations. The same problems were experienced for the flat parts of the low-T Cp curve where the relative uncertainties increased many folds due to the low magnitudes but also the regression problems for horizontal Cp/T slopes. The fit minimises absolute deviations, but due to Cp data spanning several orders of magnitude, fractional deviations, based on the inverse of first or second derivative, could prioritise flat gradients. Logarithmic or exponential scaling could down-weight deviations in high Cp regions while capturing finer deviations in flat regions. Alternatively, fitting flat regions separately or setting the standard state at a higher T could improve model balance across both flat and steep sections.

This issue is pervasive across mineral thermodynamic models in Earth sciences, where linear regression is almost ubiquitously employed to derive endmember Cp curves from solution models (Holland and Powell 1990; Gottschalk 1996). Although deviations are small (~30 J/mol·K on total measurement value of ~1200 J/mol·K), when extrapolated to 1200 K (see polyhedron comparison paragraph), they cause minor (~4 rel%) yet significant discrepancies between measured and predicted Cp curves, slightly affecting phase stability calculations at near-melting temperatures. Including physically motivated constraints, such as anharmonicity corrections or separate fits for Cp >500 K, could mitigate these systematic biases

Fe^{3+} Speciation and Z-site Substitution Effects Not Captured by the Bulk Compositional Model The bulk compositional model fails to account for internal speciation effects and site-specific chemical differences, such as the systematic offset in Cp evolution between F-buergerite (Tm64) and other Fe^{3+}-rich tourmalines, revealing its inability to model differences between bu and pov components (refer to Chapter 2 for endmember abbreviations; see Figure 3Z). While both buergerite and povondraite share high Fe^{3+} contents, their compositional differences extend beyond Fe^{3+} speciation: buergerite features Al-dominant Z-sites, whereas povondraite shows Fe^{3+}-Mg substitution at the Z-site. This Z-site chemical variation significantly impacts thermodynamic properties, including molar volume, entropy, and heat capacity, but is not represented in bulk compositional models. Furthermore, uncertainties in buB and oleB fractions are amplified by errors in the hydrogen component, a dependent parameter excluded from reciprocal model endmember definitions, complicating deprotonation thermodynamics modelling. Excluding F-buergerite reduces the LOOCV MSE from 231.5 to 84.5, confirming it as the primary outlier. However, its exclusion increases multicollinearity and disrupts the smooth, Berman-like shape of some endmember curves due to extrapolation, highlighting the poor modelling of tourmalines with significant pov components.

This mirrors the issue encountered in the molar volume model in Chapter 2, where bulk parameter-based endmembers like buB failed to capture the significant differences between bu and pov in V, S^0 and $S_{298.15K}^{773.15\,K}$. Figures 3Z, 3AA, and 3AB illustrate how both Fe^{3+} speciation and Z-site chemical substitution (Al versus Fe^{3+}+Mg) result in distinct thermodynamic behaviors between buergerite- and povondraite-like tourmalines, trends not captured by bulk compositional models."

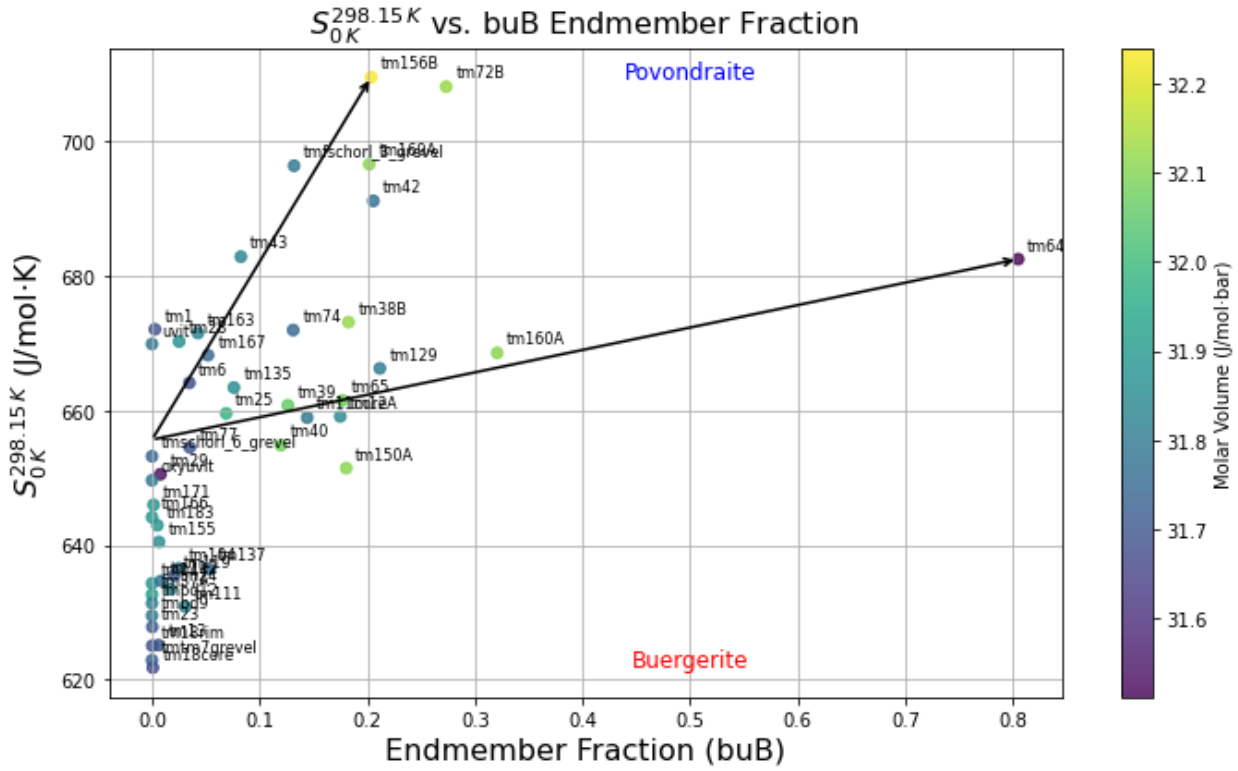

Figure 3Z. A. S_0 versus buB fraction. Two distinct trends are evident: one toward buergerite (bu) and another toward povondraite (pov), reflecting differences in Fe^{3+} speciation and Z-site substitution (Al versus Fe^{3+}+Mg) in tourmalines. Arrows qualitatively indicate samples that, in

the speciation model, have either high pov–low bu or high bu–low pov contents.

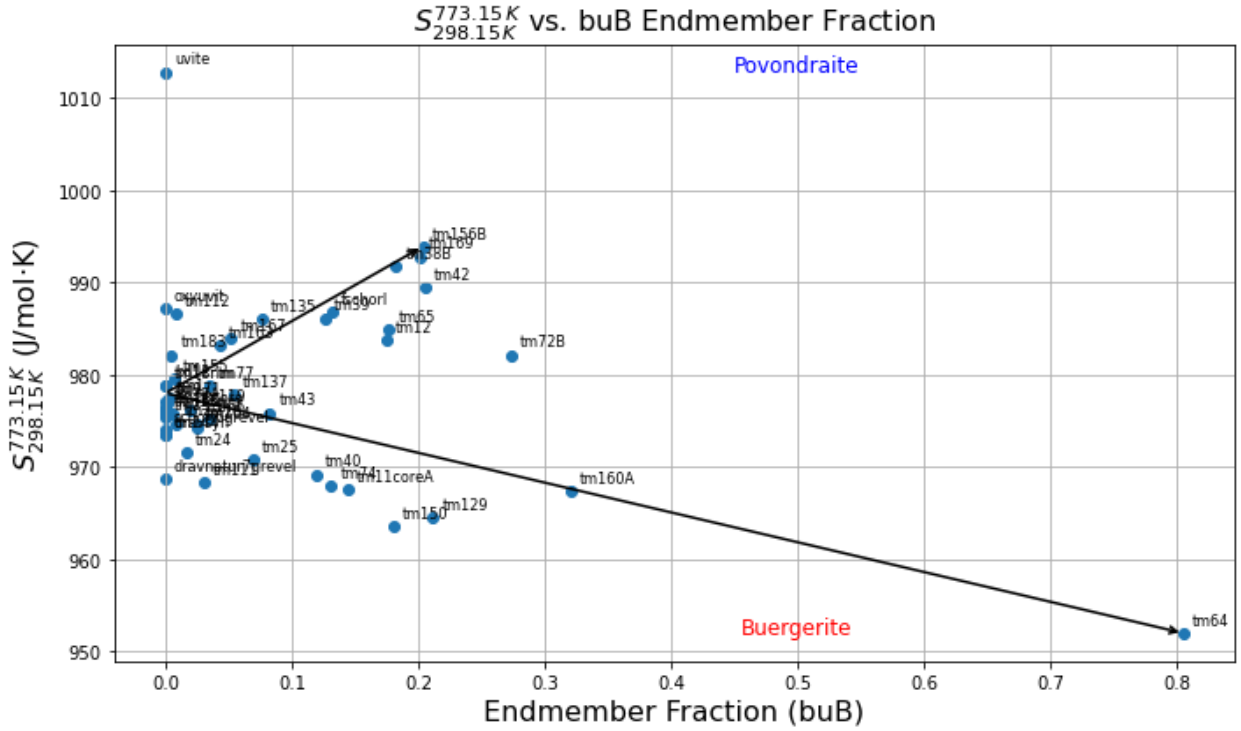

Figure 3AA. $S^{773.15\,K}_{298.15K}$ versus buB fraction. The data show two separate trends toward bu and pov compositions, highlighting how Fe^{3+} speciation coupled with Z-site substitution influences entropy evolution. Arrows qualitatively indicate samples with dominant pov or bu components based on the speciation model.

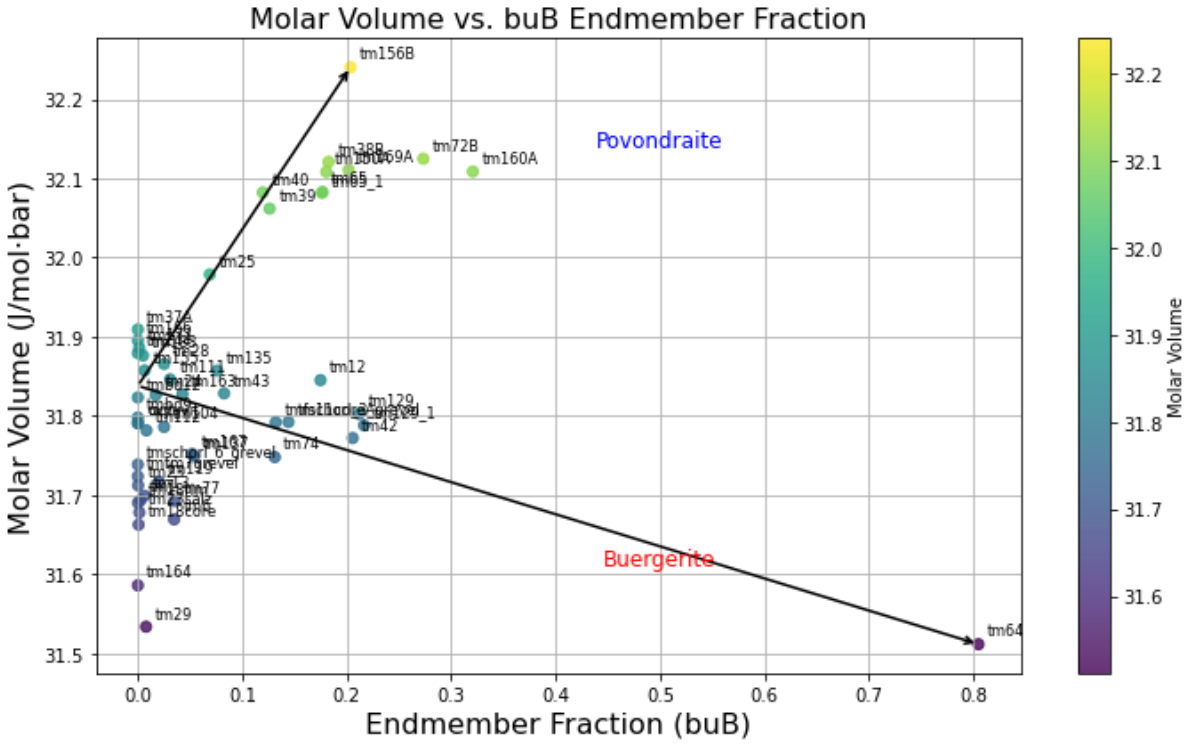

Figure 3AB. Molar volume versus buB fraction. Two distinct trends emerge corresponding to bu and pov behavior, underscoring the effects of Z-site chemical differences in addition to Fe^{3+} speciation. Arrows qualitatively point to samples enriched in pov or bu in the speciation model; light green points indicate intermediate compositions (pov-bu mixtures).

Magnetic Entropy Contributions The standard state entropy of tourmaline is strongly dominated by magnetic contributions from Fe^{2+} and Fe^{3+} spin disorder, as most of the variance in Cp/T curves occurs below ~20 K (Figure 3D). Strong correlations between Fe content and entropy (see Paragraph 4), as well as between low-temperature Cp and schorl composition, suggest that magnetic effects are the primary source of standard state entropy variations. It is therefore natural to compare the magnitude of observed entropy variations with predictions based on maximum magnetic randomization, as discussed in Appendix 3A and 3C.

The theoretical background for magnetic entropy contributions is detailed in Appendix 3M. There, we outline how the maximum magnetic entropy ($S_{max}^{magnetic}$) can be derived from the Boltzmann formula $S = R \ln \Omega$, where Ω depends on the total angular momentum $J = |L–S|,\ldots,L+S$. For high-spin Fe^{3+} ($S = 5/2$, $L = 5/2$) in octahedral environments, crystal field splitting quenches the orbital contribution, yielding $S_{max}^{magnetic} = R \ln(6) \approx 14.89$ J/mol·K. High-spin Fe^{2+}

(S = 2, L = 2) can show incomplete orbital quenching depending on the degree of site distortion, potentially enhancing magnetic entropy beyond the spin-only value R ln(5). In tourmaline, local distortions at the Y site (Ertl et al., 2002), optical evidence of residual spin-orbit coupling (Altieri et al., 2022), and dynamic electron hopping between Fe^{2+} and Fe^{3+} (Mattson and Rossman, 1987) suggest that spin-orbit effects may contribute variably across samples. Although we could not separate the magnetic and lattice contributions in the heat capacity, an analysis that would require low-temperature phonon modelling beyond the scope of this study, the dominance of magnetic entropy is clear. A detailed comparison between the measured entropy and theoretical spin-only or spin–orbit–coupled models remains an important future step to conclusively determine the magnitude of magnetic disorder contributions in tourmaline.

2. ALTERNATIVE REGRESSION METHODS

Various alternative regression methods were applied to the integrated entropy data which were also applied to molar volume data in Chapter 2. The regression methods, including method which include both y and x-uncertainty, and robust approaches, were tested alongside leave-one-out cross-validation (LOOCV) to assess model robustness and performance. These analyses highlight how uncertainties, parameter-to-data ratios, and method-specific sensitivities influenced the prediction accuracy and sensitivity to outliers across bulk and speciation models. However, we do not have a test set for entropy, therefore, OLS is preferred for its unbiased, efficient estimates, minimizing squared residuals under normality assumptions. Alternative methods are detailed in Appendix 3K for reference.

3. COMPARISON TO ESTIMATION MODELS BASED ON THE POLYHEDRON APPROACH

Polyhedron Estimation Method The polyhedron method (The Neumann-Kopp approach for polyhedra instead of elements) estimates mineral entropy and its high T Cp curve by treating coordination polyhedra, such as SiO_4 tetrahedra and AlO_6 octahedra, as independent chemical components (Chermak and Rimstidt 1989), similar to the microscopic Bragg-Williams models, e.g. (Sack and Ghiorso 1994). It decomposes the unit cell's electron density into contributions from these polyhedra, neglecting interactions beyond the first coordination sphere,

polymerization, and bond topology. Entropy is calculated as a linear combination of polyhedral contributions, weighted by stoichiometric coefficients. Polyhedral vibrational modes are modelled using the Einstein lattice method, which assumes independent atomic vibrations in harmonic potentials with single characteristic frequencies, neglecting vibrational coupling and treating phonons as localized to individual atoms rather than as collective excitations (Einstein 1907), see Appendix 3A. The method assumes structure averaged, idealized, and transferable polyhedral geometries without Jahn-Teller distortions and excludes hydrogen bonding, structural distortions, but provides a postprocessing correction for magnetic contributions, and long-range order/disorder effects (Holland 1989; Holland and Powell 1990, 1998).

This method, effective for minerals with isolated or weakly connected corner sharing polyhedra like olivine, has been applied to highly polymerized edge and face sharing tourmaline in the absence of thermodynamic data. Van Hinsberg et al. (2005a, 2005b) calibrated it using a database of 105 end-members from a range of different mineral classes, excluding intermediates to avoid mixing effects, and incorporated polyhedra with hydroxide ligands for improved high T Cp and entropy estimates without volume corrections. Van Hinsberg and Schumacher (2007) extended the model to include B^{III} and B^{iV} polyhedral entropies and high T Cp by analyzing residuals after subtracting nonboron polyhedral contributions from 2 tourmaline solid solutions and additional borosilicate minerals, ignoring mixing effects.

Fluorine was excluded from the original regression model due to limited F-bearing minerals for parameterization. Corrections were applied using the exchange equilibrium: F-phlogopite $+$ OH-pargasite $\rightarrow$ OH-phlogopite $+$ F-pargasite, assuming $\Delta H_{\text{reaction}} \approx 0$ and $\Delta S_{\text{reaction}} \approx 0$. Assuming $\Delta S_{\text{reaction}} \approx 0$, implies a balanced entropy change, where the entropy gained by one mineral offset the loss by another, resulting in a constant transferable ΔS/mol F (Van Hinsberg et al. 2005a, 2005b). F-bearing endmember properties were estimated using the ΔS/mol F difference between fluor and hydroxyl endmembers of phlogopite, with a similar entropic effect assumed for tourmaline.

Corrections Applied to the Training Database of the Polyhedron Method The training database for the polyhedron method has been corrected for non-transferable entropic properties: Magnetic entropy ($S^{max}_{\text{magnetic}} = R\sum n \ln(2s+1)$), where s is the spin quantum number, R is the

gas constant, and n is the number of cations, and the configurational entropy for disorder, $S_{\text{disorder}}^{max} = -mR\sum X_i \ln X_i$, where Xi is the site mole fraction and m is the site multiplicity, both fixed and T independent were subtracted from the entropies of the training set entropies (Van Hinsberg et al. 2005a, 2005b).

For endmember minerals undergoing a tricritical phase transition at T>298 K, thermodynamic properties of the ordered precursor and high-T disordered phases are derived using the mean-field Landau free energy model (Holland and Powell 1990, 1998). The excess properties are described relative to the low-T ordered phase. The ordered phase exhibits a Landau anomaly in Cp, with entropy combining vibrational and configurational contributions. A baseline Cp is subtracted, and the residual peak at Tc is integrated to obtain S_{max}. Excess properties were derived from:

$$\text{For } T < T_c:$$
$$C_p^{\text{ex}} = \frac{TS_{max}}{2\sqrt{T_c}}(T_c - T)^{-\frac{1}{2}}$$
$$S^{\text{cx}} = S_{max}(1 - Q^2)$$
$$\text{with } Q = \left(1 - \frac{T}{T_c}\right)^{\frac{1}{4}}$$
$$\text{For } T > T_c:$$
$$S_{\text{ex}} = S_{\text{max}}, \text{ and } Q = 0.$$

See Appendix 3L for the derivations of these equations

Entropy: Comparison of Speciation Model and Polyhedron Method Measured entropies ranged from 574.16–709.5J/mol·K with uncertainties of 6–18J/mol·K (1–3% relative), a mean of 9.7J/mol·K, and a median of 8.7J/mol·K (~1.5% relative).

Speciation model The least-squares speciation model predicted entropies range from 574 to 710J/mol·K, with propagated uncertainties between 1.5 and 6.4J/mol·K. The average absolute mean propagated uncertainty is 3.18J/mol·K, with an absolute relative uncertainty of 0.4%. Model uncertainties are one-third of the measured uncertainties due to using multiple Cp curves to estimate endmember Cp.

Internal validation showed that residuals between measured and predicted entropies ranges between ±15J/mol·K (2.4% relative), with a mean and median not significantly different from zero, indicating no systematic bias. The average absolute mean residual is 3.86J/mol·K, with a mean absolute relative uncertainty of 0.5% and a median absolute relative uncertainty of 0.3%. A 3.86 J/(K·mol) difference in standard entropy results in a ΔG change of -1.15 kJ/mol at 298 K and -2.98 kJ/mol at 773 K**.** The speciation model's relative residuals are within the propagated uncertainties of measured entropies, except for tm38B, tm111, tm129, tm183, and uvit.

Polyhedron model The polyhedron method (Van Hinsberg et al. 2005a, 2005b; Van Hinsberg and Schumacher 2007) was applied using the thermodynamic model's training set as its test set. Tourmaline mineral formulas were recalculated from the speciation model, ensuring consistent normalization, charge balance, and site occupancies. Differences between models stem solely from thermodynamic formulations, not normalization discrepancies. Site fractions were multiplied with the multiplicities and summed into bulk components (Na^{multi}, Ca^{multi}, Al^{OHO}, Mg^{OHO}, Fe^{2+OHO}, Fe^{3+OHO}, Al^{oct}, Mg^{oct}, Fe^{2+oct}, Fe^{3+oct},Ti^{oct}, Si^{T}, Al^{T}, B^{T}, B^{3}) to form the new chemical component basis. Multi-assignment of Na and Ca describes large alkali (earth) sites with coordination >8. The polyhedron method incorporates OH into the polyhedra, removing it as a separate constituent. It does so as fully OH-coordinated (X-OH) and as partially O and OH-coordinated polyhedra (X-OHO). Van Hinsberg and Schumacher (2007) assigned all tourmaline octahedral sites to be OHO, except for Ti, which was assigned to have no OH groups due to its high charge and was assumed to only occur as Ti-Oct.

The number of Y and Z polyhedra with 0, 1, or 2 OH groups is determined by their connectivity to O1 (W-site) and O3 (V-site) and the OH occupancies X_W and X_V. Y polyhedra connect to one O1 and one O3, while Z polyhedra connect only to O3. The number of Y-sites with 0 OH is $N_{\mathrm{Y,0OH}} = 3 \cdot (1 - X_W) \cdot (1 - X_V)$, reflecting the scenario where neither O1 nor O3 contains OH, with 1 OH is $N_{\mathrm{Y,1OH}} = 3 \cdot [X_W \cdot (1 - X_V) + (1 - X_W) \cdot X_V]$, reflecting cases where either O1 or O3 contains OH but not both, and with 2 OH is $N_{\mathrm{Y,2OH}} = 3 \cdot X_W \cdot X_V$, representing the situation where both O1 and O3 contain OH. For Z-sites, which connect only to O3, the number with 0 OH is $N_{\mathrm{Z,0OH}} = 6 \cdot (1 - X_V)$, , and with 1 OH is $N_{\mathrm{Z,1OH}} = 6 \cdot X_V$. As the polyhedron method does not differeniate between Y and Z sites, and 1OH or 2 OH containing octahedra these were merged.

It was unclear if the OH around cations should be ignored, if we should assumed a ordered or a disordered state between the OH between Y and Z. Van Hinsberg and Schumacher (2007) suggested disordered OH at Y and Z sites results in OHO-coordination for Xtotal≥2.9, but this is questionable as probabilistically disorder actually reduces OH fractions at individual sites, increasing O^{2-} polyhedra at Y and Z sites. In the ordered state, OH^V ensures at least one OH ligand per polyhedron, with Y sites linking to V and W, and Z sites to V. Disorder, however, spreads OH, increasing O^{2-} only polyhedra, contradicting universal OHO-coordination under disorder (Table 3G). The model assumes Ti-oct without Ti-OHO polyhedra due to the high charge introduces small charge imbalance. Order or disorder would not change the overall charge balance of the structure but does break the bond valence sums of the sites.

Table 3G. Polyhedral Calculation in Tourmaline: Ordered vs. OH-Disordered Model for example tourmaline (fschorl).

Polyhedra	Ordered State	Disordered State
X_W	0.437	0.860
X_V	1.000	0.860
Y0OH	0.000	0.0588
Y1OH	1.689	0.7224
Y2OH	1.311	2.2188
Z0OH	0.000	0.840
Z1OH	6.000	5.160

Differences between using different amounts of oct and OHO polyhedra makes big differences as the thermodynamics of these polyhedra differ (Table 3H).

Table 3H. Polyhedral entropies for oct and OHO polyhedra (Van Hinsberg et al. 2005a).

Component	Value	Component	Value
Mg - oct	28.28	**Mg - OHO**	35.83
Fe - oct	42.97	**Fe - OHO**	50.67
Fe3 - oct	30.68	**Fe3 - OHO**	49.14
Al - oct	22.24	**Al - OHO**	38.87

If OH is assumed to hop between sites, the full OHO model of Hinsberg and Schumacher (2007) holds, though strong evidence for this process is lacking. In this model all octahedral sites, except TiO_2, were assumed as XOH. We tested models using Oxy+OHO polyhedra with the ordered formula, the ordered formula with disordered OH on the V and W sites, and pure OHO polyhedra (except Ti^{oct}).

Polyhedral stoichiometry matrices multiplied by polyhedral entropies yield lattice dynamical entropy, while magnetic entropy ($S^{max}_{\text{magnetic}} = R\sum n \ln(2s+1)$) was calculated using Fe^{2+} and Fe^{3+} concentrations assuming orbital quenching for both. The results of the comparison between the speciation model and the polyhedron-based models are summarized in Table 3I.

Table 3I. Comparing the measured versus predicted of the speciation and all polyhedral models.

Model Name	**Mean Absolute Relative Deviation (%)**	**Residual Range (%)**	**Median Residual (%)**
Speciation Model Without S^{conf}	0.5	-2.4 to 2.4	0
Oxy+OHO Polyhedra, Ordered V+W, with $S^{vib} + S^{mag}$	4.1	-0.4 to 18	3.5
Oxy+OHO Polyhedra, Disordered V+W, with $S^{vib} + S^{mag}$	6.2	-2 to 18	6
OHO Polyhedra, with $S^{vib} + S^{mag}$	3.7	-0.4 to 9	3.5

The speciation model outperforms all polyhedron-based models, with a mean absolute residual (0.5%) that is 7.5-12.4 times lower and a narrower residual range. Polyhedron models underestimate entropy, with results strongly influenced by assumptions such as OH order/disorder and polyhedral types. While OHO polyhedra, with Svib + Smag performs best, uncertainties in OH ordering, polyhedral types, and the merging of all OHO polyhedra with more than 1 OH prevent definitive conclusions. Additionally, the calculation of OHO polytopes in the training dataset of the polyhedron method and the associated assumptions of OH order/disorder remains unclear, as this depends on the bond graphs of each respective mineral and whether disorder increases or decreases OHO polyhedra, as shown with tourmaline. The extreme sample buergerite is the one that gives the high residual for the Oxy+OHO so it seems to behave more

like an OHO polyhedra. Figure 3AC shows that at average the polyhedron method underpredicts by 25 J/(K·mol).

The current polyhedral entropies are an average of many mineral systems with both open or dense minerals. Using an Einstein model for each average polyhedron accounts for some variations in vibrational frequencies but still underestimates entropy compared to measured Cp. This is due to the model's inability to capture the full phonon density of states, particularly low-frequency collective vibrations that significantly contribute to entropy at low T.

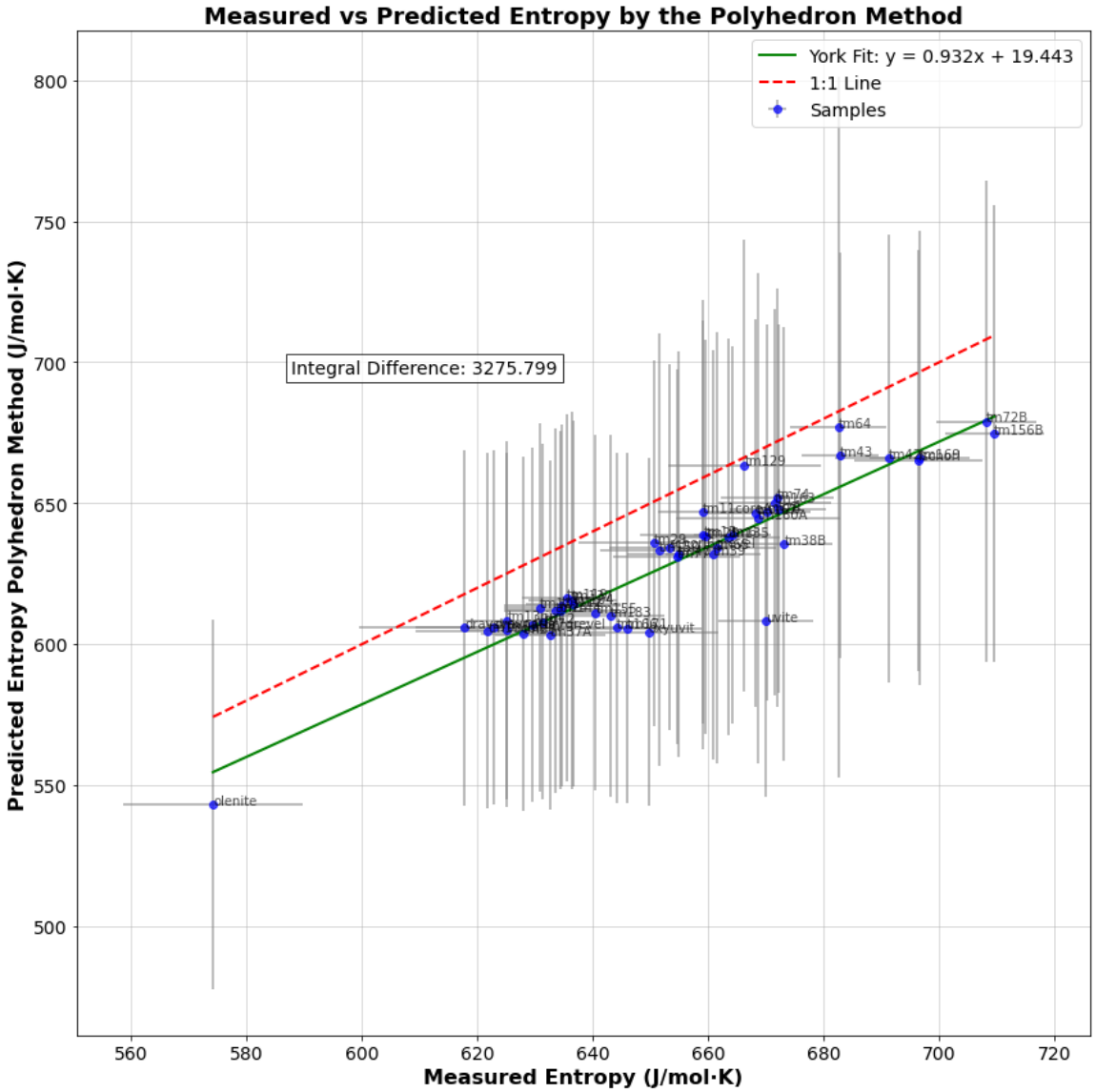

Figure 3AC. Measured vs Predicted Entropy with Uncertainties, York Regression, and Integral Difference for the Polyhedron method with OHO polyhedra without S^{conf}. The method underpredicts by 25 J/(K·mol).

Polyhedron method is similar as using the mean of measured S as a model The polyhedron method performs similarly to the mean of measured entropies as a model for tourmaline, with similar relative errors ranging from -13% to 8%, a mean absolute relative deviation of 3% an average of 0%. Therefore, the polyhedron method can predict the average T evolution and order of relative stability fields of tourmaline compared to other minerals, such as breakdown or first occurrence (net-transfer reactions), but not detailed chemical changes within tourmaline (exchange reactions), as also stated in van Hinsberg and Schumacher (2007) .

This comparison is limited as it contrasts the speciation model's training error with the polyhedron method's test error. A fair comparison requires a separate test set for both methods. However, the near 7-12-fold decrease in mean absolute residual and uncertainty and 3-18 fold reduction in the range of residuals indicate improved predictions of tourmaline thermodynamics.

LOOCV cross-validation of the OLS speciation model, used as a rough indication of test error, shows the relative error range increasing from ±2.4% to -16% to +2.4% due to two synthetic tourmalines (drav_syn, olenite), which uniquely define specific endmember speciation, are excluded from the training set and predicted using the rest. Their high leverage and extreme compositions disrupt correlations, and their exclusion forces reliance on natural sample correlations, leading to poor extrapolation for predicting their extreme compositions, raising the mean absolute deviation to 1.3% while the median remains around 0.5%. Excluding these samples increases the relative error range slightly from ±2.4% to ±3%. Including the sensitivity of the synthetics, the test set error shows a 3-fold reduction in mean residuals compared to the polyhedron method, demonstrating improvement.

The polyhedron method underestimates measured entropies by approximately 25 J/(K·mol). A 25 J/(K·mol) difference in standard entropy results in a ΔG change of -7.45 kJ/mol at 298 K and -19.33 kJ/mol at 773 K**.** Although these new measured data, and the end-member properties

derived from them negate the need for estimated properties, Appendix 3M lists several ways to improve the polyhedron method.

High-T Cp: Comparison of Bulk Compositional Model and Polyhedron Method High-T Cp functions from the bulk compositional model and the polyhedron method were compared to measured Cp values using recalculated tourmaline mineral formulas derived from bulk compositional independent endmembers. This ensures consistent data normalization and isolates differences in thermodynamic formulation. For synthetic compositions, recalculated speciation model values were summed into bulk parameters. Additionally, the Cp functions were extrapolated up to 1200 K to evaluate how both models perform beyond their calibration domain. Figure 3AD shows the comparison between measured Cp and polyhedron method predictions, with both curves fitted using the Berman model for consistency.

Polyhedron Method.

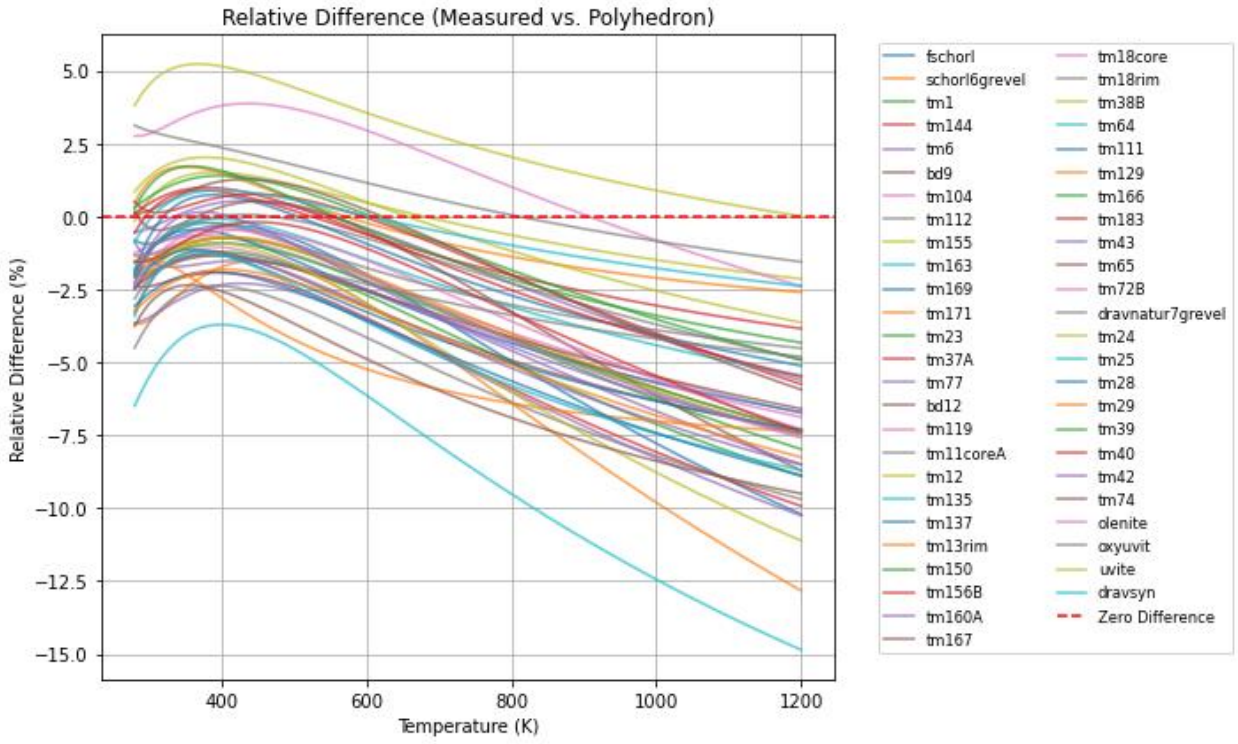

Figure 3AD. Relative difference between measured Cp values and predictions from the polyhedron method, where negative values indicate overprediction. Both measured and predicted Cp data were fitted using the Berman model for consistency.

The bulk compositional and speciation models show relative uncertainties within ±2% up to 773.15 K (Figure 3W), while the polyhedron method has higher residuals, around -7.5% to 5%, and slightly higher for F-buergerite (Figure 3AD). Residuals for the bulk model are 2–3 times lower than the polyhedron method, but the latter performs well given its use of a diverse mineral dataset. Unlike entropy, which is challenging to predict due to its reliance on low-T details, the polyhedron method provides more stable Cp curves, making it suitable for estimation. At lower T, the polyhedron method both over- and underpredicts Cp, but at higher T, many tourmalines show negative relative differences, indicating overprediction (Figure 3AD). This shows that the polyhedron method does not extrapolate well beyond 773.15 K and agrees with the divergence in fractional ^{III}B Cp observed by van Hinsberg and Schumacher (2007) at >800K. With only 3 measured tourmaline high-T Cp curves, these authors were unable to determine which was/were to be preferred and used the mean, but this comparison suggests that the Cp data of Hemingway et al. (1996) are more accurate than those of Kuyunko et al. (1984) and Ogorodova et al. (2004) or the non-^{III}B polyhedra the Hemingway are better constrained.

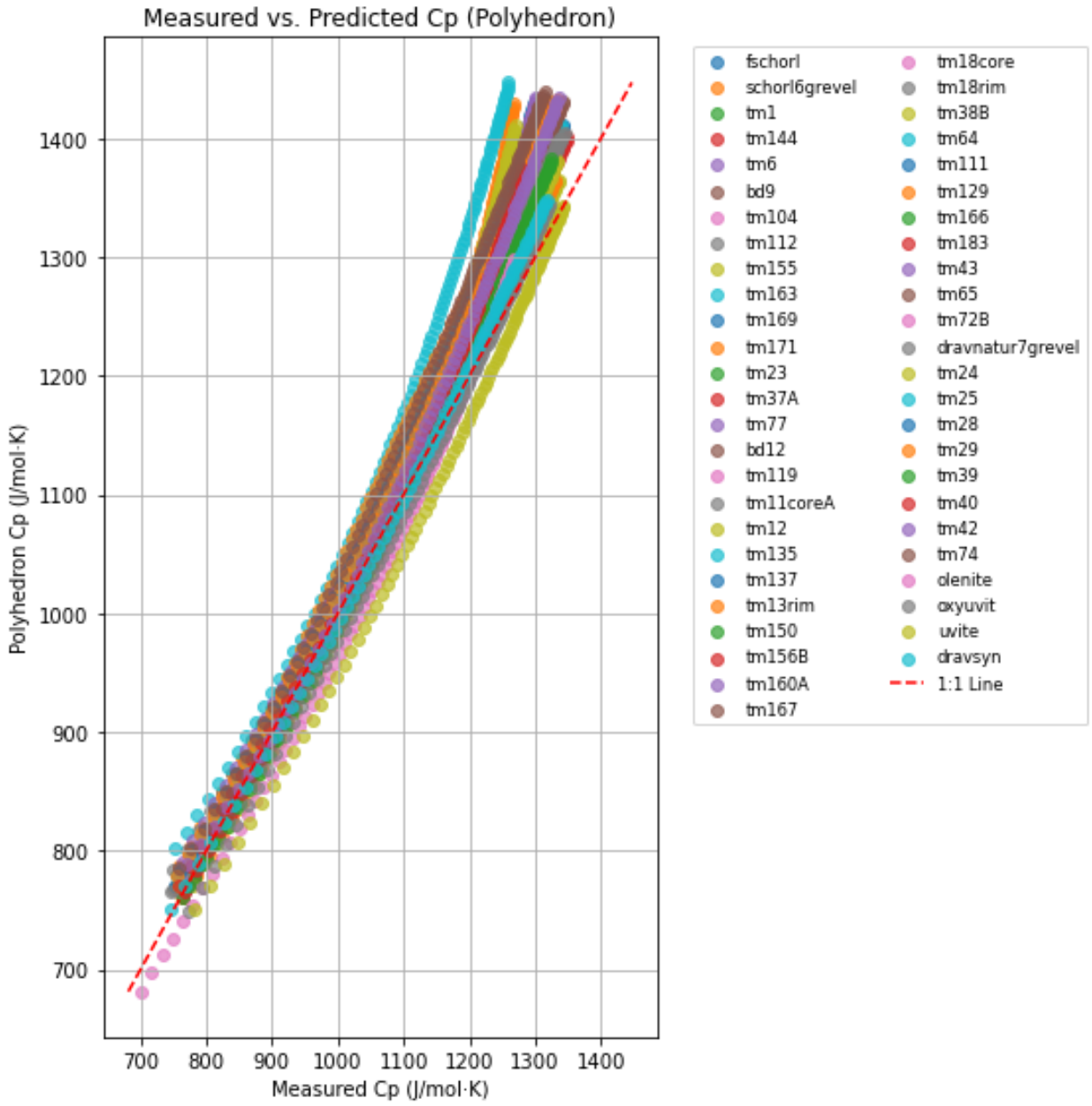

Figure 3AE. Cp curves from the polyhedron model vs. measured Cp, both fitted using the Berman model. The 1:1 line indicates a perfect fit. Measured data is available up to ~1200 J/mol·K, with the remainder extrapolated.

The deviations in Figure 3AD and 3AE result that the polyhedron model at 1000 K has ΔG differences of up to 25 kJ/mol, considering the balance between Cp integration into H and Cp/T integration into −TS (Figure 3AF). While this ΔG is within the order of magnitude of high-T net transfer reactions, it far exceeds the 1–10 kJ/mol range of exchange reactions, indicating that the

polyhedron method can approximate net transfer magnitudes but lacks precision for exchange reactions. Most ΔG differences cluster around 10 kJ/mol, within the exchange reaction range. This assumes the measured Cp values are perfect, which is not the case; however, even if ΔG values are halved and considering that Cp is only part of the whole, the conclusions remain unchanged.

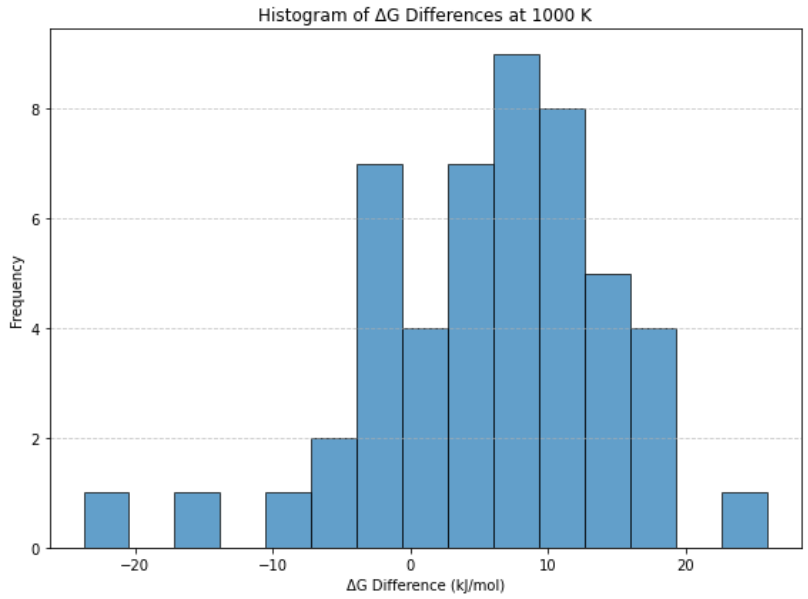

Figure 3AF. ΔG differences at 1000 K resulting from discrepancies between measured and predicted high-T Cp in the polyhedron model, highlighting the impact of model simplifications.

Bulk Composition model. The bulk compositional model maintains ±2% (~±20 J/mol·K) uncertainty up to 773.15 K, but regression-based loss of sensitivity at high T leads to misfits of up to 3% (~30–40 J/mol·K) and one outlier at 4% (~50 J/mol·K) when extrapolated to 1200 K (Figure 3AG, 3AI)). Endmember Cp curves derived from OLS regression on measured solid solutions tend to converge toward the Debye-Petit limit, while measured Cp curves retain slope variations, causing erroneous extrapolations (Figure 3U). This issue affects all thermodynamic databases relying on least-squares regression and requires an internally consistent solution. Despite these extrapolation challenges, the bulk model still outperforms the polyhedron method, which exhibits relative errors up to -15% (Figure 3AD).

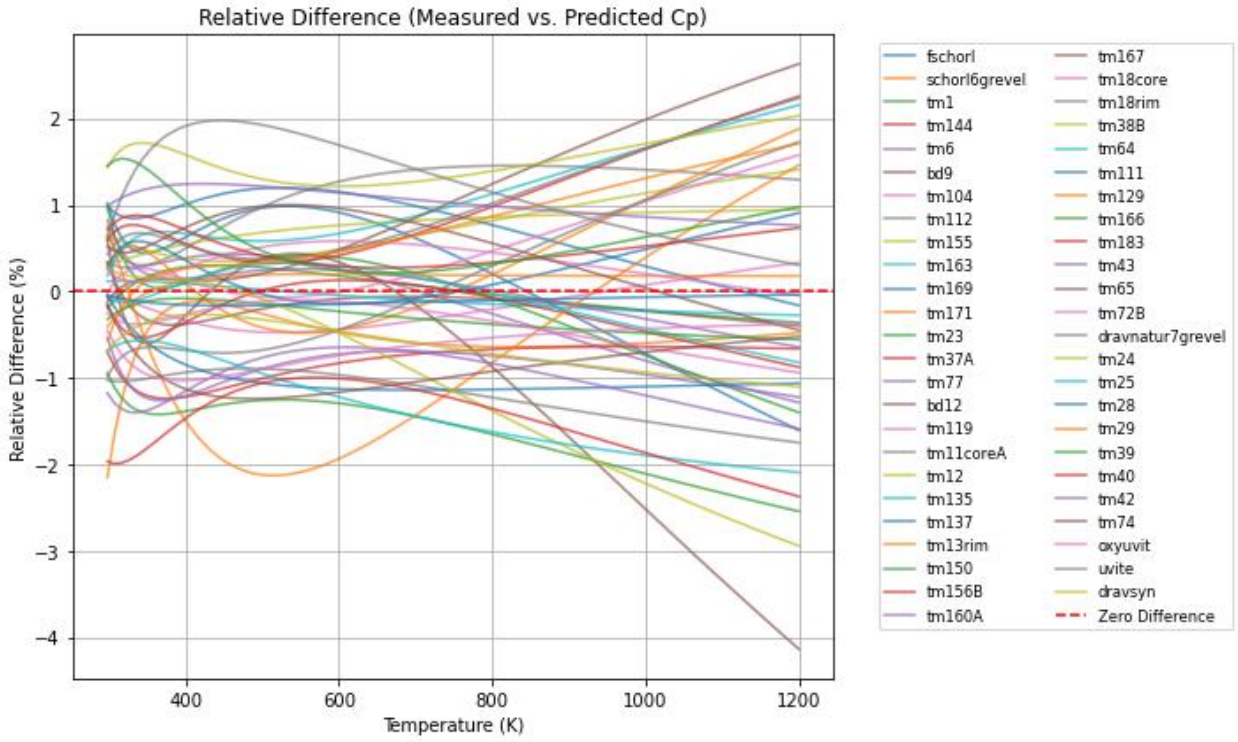

Figure 3AG. Relative difference between measured Cp values and predictions from the bulk compositional method, where negative values indicate overprediction. Both measured and predicted Cp data were fitted using the Berman model for consistency and extrapolated up to 1200 K.

At 1000 K, Cp misfits in the bulk compositional model can cause ΔG deviations up to 8 kJ/mol, balancing Cp integration into H and Cp/T into −TS (Figure 3AH). A 6 kJ/mol uncertainty is significant for exchange reactions (1–10 kJ/mol), introducing high-T uncertainties, but is still acceptable for net transfer reactions (10–50 kJ/mol), which would result in only slight phase boundary errors. We conclude that the bulk (and speciation) models remain reliable predictors up to the melting T of tourmalines (which is at ~850 to 950˚C at 1 bar, see chapter 5).

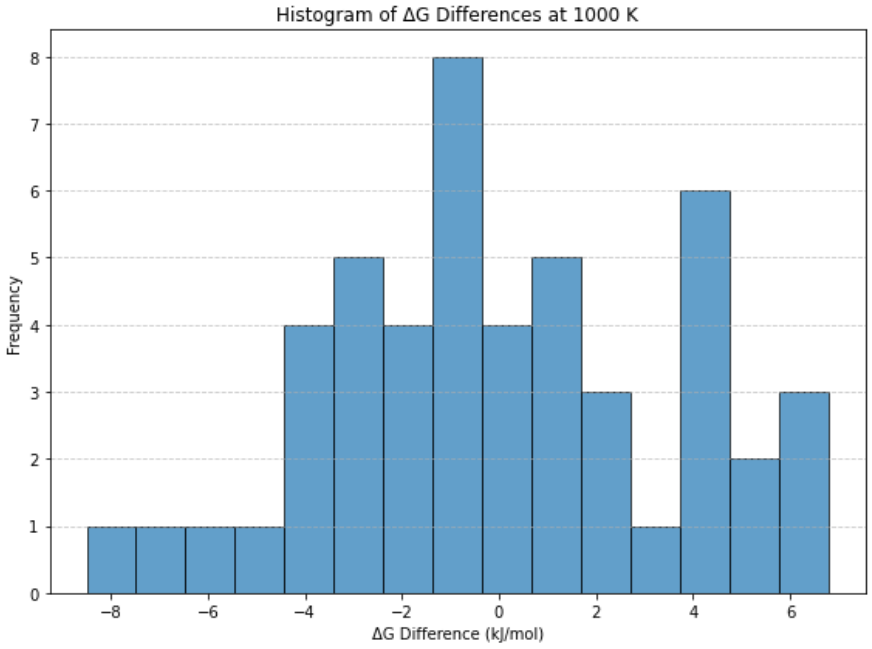

Figure 3AH. ΔG differences at 1000 K resulting from discrepancies between measured and predicted high-T Cp in the bulk compositional model, highlighting the impact of model simplifications.

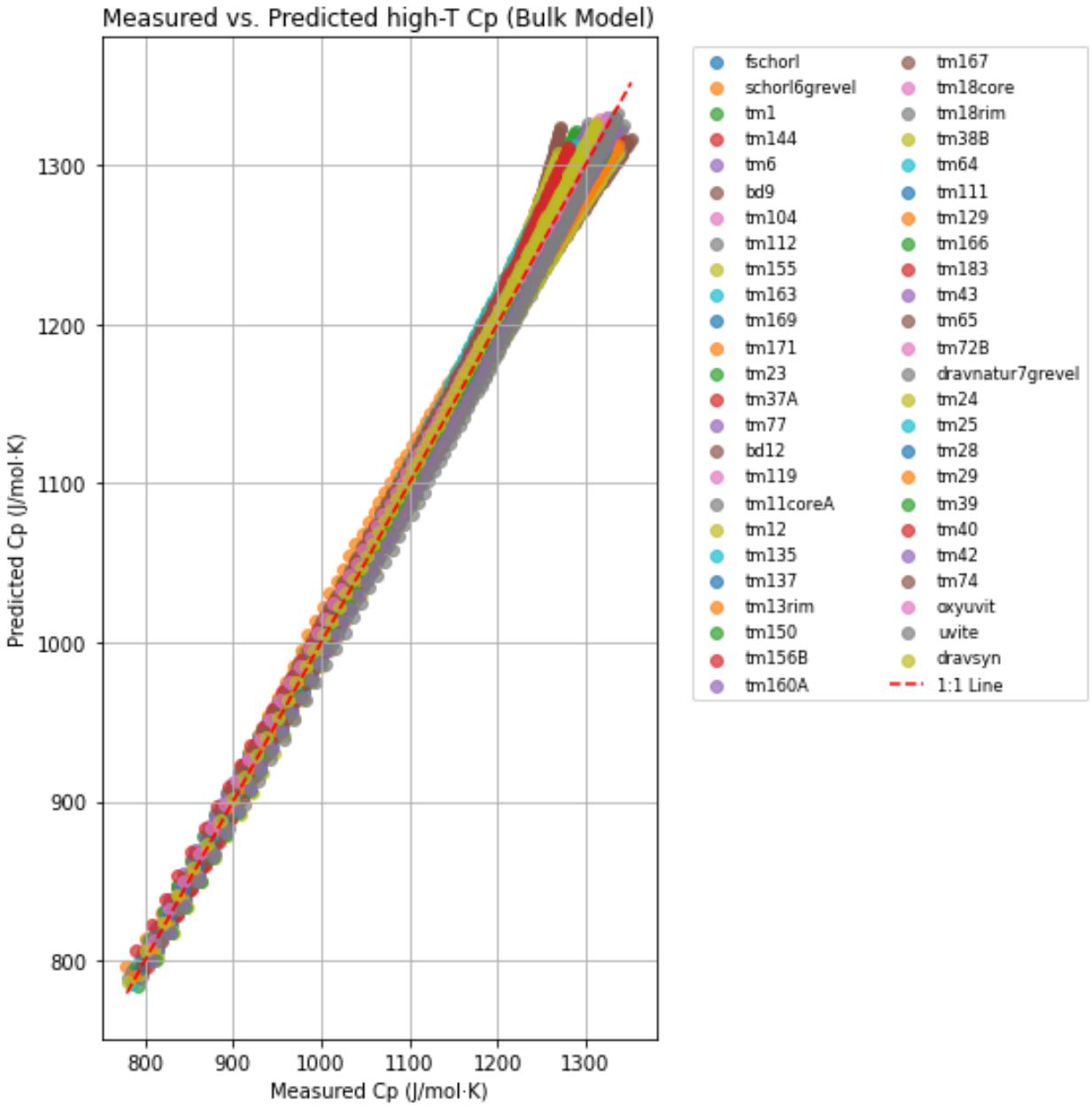

Figure 3AI. Extrapolated Cp curves from the bulk compositional model compared to extrapolated measured Cp curves, with the 1:1 line indicating a perfect fit. Measured data is available up to ~1200 J/mol·K, with the remainder extrapolated.

4. CORRELATIONS BETWEEN STATE VARIABLES

A correlation analysis was done on tourmalines measured using SC-XRD, focusing on natural samples, as synthetics were excluded. Due to multicollinearity and dataset dependencies, these

correlations should be interpreted cautiously, as they do not imply causation and may result from underlying variables affecting both factors. However, they provide a basis for qualitatively assessing entropy differences between tourmalines. The most important correlation scatterplots are presented in Appendix 3N.

Entropy Entropy (S_0) in tourmaline primarily correlates with the Fe/Mg ratio and electron count at the Y and Z sites. Strong correlations were found with schorl, dravite, olenite, Y- and Z-site electron counts, and the Y-O6 bond (except buergerite), which links Y and Z sites to the downward-pointing tetrahedra. In the speciation model, the anti-correlation with dravite is broken, indicating that the Fe-Mg relationship arises from multicollinearity and could be resolved using synthetic endmembers without natural Fe-Mg dependencies. Entropy and enthalpy (see chapter 5) are correlated (0.82), with higher enthalpy (less negative) corresponding to higher entropy, reflecting the trend in silicates where Fe-endmembers have lower formation enthalpies than Mg- or Al^{VI}-endmembers (Holland and Powell 2011). Weaker Fe^{2+} bonds allow more vibrational modes, while stronger Mg and Al^{VI} bonds restrict them. Fe also contributes significantly to magnetic entropy (S^{mag}). Entropy variations show a strong correlation with the presence and magnitude of magnetic Cp/T peaks at low temperature (Figure 3D, Appendix 3A, 3C), confirming that Fe spin disorder dominates the standard-state entropy. Figure 3AJ shows the correlation between Fetotal (apfu) versus entropy. Entropy shows no significant correlation with molar volume but correlates with the hexagonal a-axis, except for buergerite. The a-cell axis similarly depends on the Y-O6 bond length.

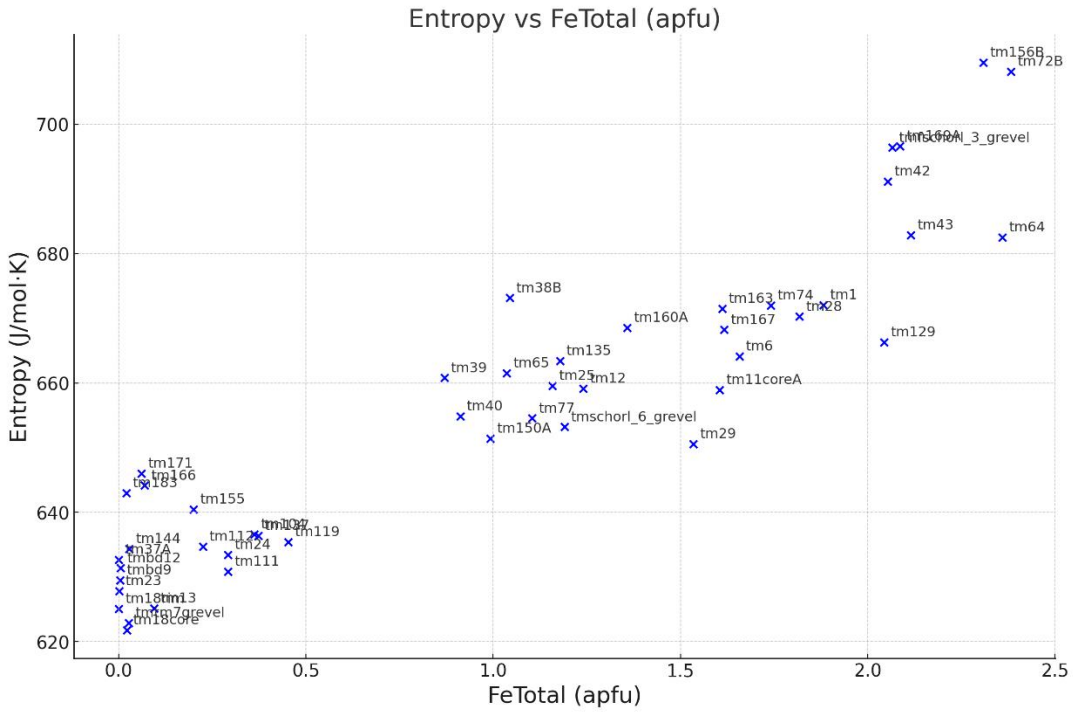

Figure 3AJ. Relationship between FeTotal (apfu) and standard-state entropy (S_0) for tourmaline samples. Sample labels are shown. The strong positive correlation reflects the dominant role of Fe^{2+} and Fe^{3+} spin disorder in contributing to magnetic entropy. Additionally, the high mass of Fe enhances acoustic phonon contributions, while weaker Fe^{2+} bonds allow more optical phonon modes, further increasing entropy.

High-T Cp High-T Cp shows weak to non-existent correlations with mineralogical and other thermodynamic parameters.

Molar Volume Molar volume correlations are complex, with the strongest found with B-olenite (-0.79) and stronger correlations to the hexagonal a-cell axis length (0.78) than the c-cell axis length (0.69). While Fe dominates entropy and enthalpy, Al primarily controls molar volume, with high correlations to total Al (-0.82), AlY (-0.76), and AlZ (-0.73). Structural correlations include T-O4 (0.80) and T-O5 (0.78), connecting the bottom X site to the T site, and Y-O2 (0.85), linking the top X site to Y. The a-cell axis length is closely related to AlY (-0.84), YO3 (Y-Z-V connector), and YO6 (0.86, Y-Z-T connector), where Al on the Y site reduces a-cell length. The c-cell axis length depends on nearly all site occupancies, showing correlations with XO5 (-0.72, bottom X to T), YO2 (0.78, top X to Y), ZO6 (0.75, Y-Z-T connector), TO6 (-0.77,

Y-Z-T connector), and BO2 (0.81, top X to Y and B). Key contributors include Mg (0.72), Al (-0.87), MgZ (0.85), and X-site vacancies (-0.88), mainly affecting bonds involving the X, Z, and T sites.

5. QUALITATIVE ASSESSMENT OF ENTROPY DIFFERENCES IN TOURMALINE

Comparison of the bulk compositional, speciation, and polyhedron models reveals the origins of entropy differences in tourmaline endmembers. The electronic density of states (e-DOS) dictates the force constants and the dynamical matrix, which governs phonon dispersions and the vibrational density of states (v-DOS) (Kittel and McEuen 2018). The v-DOS, representing the number of vibrational states available for phonon occupation, contributes to heat capacity (Cp) and, when integrated over T, to entropy. It includes acoustic phonons (3L) representing whole-unit cell vibrations and optical phonons (3L(n-1)) describing internal unit cell deformations (Dove 1993). Stronger bonds, reflected in higher enthalpy, increase force constants and suppress low-frequency phonon modes, reducing atomic motion and entropy (Stølen and Grande 2004). Weak bonds allow greater atomic flexibility, raising entropy while lowering enthalpy (Grimvall 2001). Larger molar volumes enhance low-T entropy through acoustic vibrations (Debye modes) driven by unit cell mass and volume, while high-T optical phonons (Einstein modes) depend on bond stiffness and local structural deformations (Kieffer 1979). Using Shannon's crystal radii (1976) for octahedral coordination comparing the ions shows that Al^{3+}-O bonds are the strongest due to Al's small ionic radius (~0.675 Å (Shannon, 1976)), high charge density (+3), and strong orbital overlap (Gibbs et al., 2006). Mg^{2+}-O bonds are weaker but stable, with a moderate ionic radius (~0.86 Å (Shannon, 1976)) and purely ionic nature (Gibbs et al., 2006). High spin Fe^{3+}-O bonds, despite a smaller radius (~0.785 Å (Shannon, 1976)) and oxidation state (+3), are less stable due to reduced orbital overlap from Fe^{3+}'s high-spin d^5 configuration, weak d-orbital interactions, and high spin electronic instability (Grodzicki and Lebernegg 2011). Fe^{2+}-O bonds are the weakest, with a large ionic radius (~0.92 Å (Shannon, 1976)) and weakly antibonding orbitals (Grodzicki and Lebernegg 2011). The bond strength ranking is Al^{3+}-O > Mg^{2+}-O > Fe^{3+}-O > Fe^{2+}-O. This interplay offers a simplified model of tourmaline's complex vibrational behavior.

In summary, ionic radius (Shannon, 1976) and bond strength, governed by electrostatics (Brown, 2002) and orbital overlap (Gibbs et al., 2006), control vibrational properties in tourmaline. Strong, short, covalent bonds (e.g., Al–O) stiffen the lattice, raising phonon frequencies and delaying thermal activation. In contrast, weaker, longer, ionic bonds (e.g., Fe^{2+}–O) lower vibrational frequencies, allowing modes to activate at lower temperatures. Smaller unit cells restrict acoustic phonons, while larger cells enable low-energy vibrations. These factors shape the vibrational density of states, and thus entropy and heat capacity evolution.

Bulk compositional effects High spin Fe^{2+} ($3d^6$), with its larger ionic radius in octahedral coordination (~0.92 Å), forms long Fe^{2+}-O bonds with reduced orbital overlap, occupying weakly antibonding orbitals in octahedral coordination, destabilizing bonds and inducing Jahn-Teller distortions (Grodzicki and Lebernegg 2011). At low T, Cp in Fe^{2+}-rich tourmalines is dominated by the magnetic phase transition peak, with S^{mag} as the primary contributor to S^{o} differences between tourmalines, see Figure 3D and 3E. Additionally, Fe's heavier atomic mass lowers the Debye frequency, enhancing low-frequency acoustic modes and increasing Cp and entropy (Figure 3L, srlB), primarily due to mass rather than volume effects (Grimvall 2001). At higher Ts, Cp is dominated by optical phonons with weaker Fe^{2+} bonds shifting optical phonons to lower frequencies and increasing accessible microstates (Grimvall 2001). The 0.82 correlation between enthalpy and entropy and both their correlation with Fe^{2+} reflects this bond-weakening effect (Appendix 3N), as weaker bonds store less potential energy and allow greater vibrational flexibility (Dove, 1993). Thus, Fe^{2+}'s unique combination of weak bonding, heavier mass, and magnetic effects significantly enhances both vibrational and magnetic contributions to Cp and entropy, driving the key thermodynamic differences between Fe^{2+}-rich and other tourmalines, with minimal influence from volume changes.

Fe^{3+} forms stronger, stiffer bonds due to its smaller Shannon ionic radius (~0.785 Å) in ocathedral coordination, which creates shorter more ionic Fe^{3+}-O bonds with greater orbital overlap (Grodzicki and Lebernegg 2011). Its higher oxidation state (+3) enhances electrostatic attraction to oxygen, compensating for reduced covalency and further strengthening the bond. Unlike Fe^{2+}, high-spin Fe^{3+} has a more symmetric electronic configuration, minimizing Jahn-Teller distortions, making Fe^{3+}-O bonds more stable and less sensitive to local distortions (Grodzicki and Lebernegg 2011). Fe^{3+}-rich tourmalines exhibit high Cp at low T due to the

magnetic phase transition associated with Fe^{3+}'s d^5 configuration and spin states, combined with contributions from acoustic phonons (Figure 3L, buB) and possible electronic excitations (second peak at low T, see Figure 3B), but their contributions diminish at higher T due to spin disorder. The stronger Fe^{3+}-O bonds, with higher force constants, elevate optical phonon frequencies, reducing thermally accessible modes and resulting in low high-T Cp compared to softer-bonded Fe^{2+} tourmalines (Figure 3L, Fe^{2+} srlB vs. Fe^{3+} buB) (Grodzicki and Lebernegg 2011).

Mg- and Al-rich tourmalines, with lighter atomic masses and stronger, stiffer bonds, exhibit increase the Debye frequency and shift acoustic phonons to higher frequencies, as described by $\omega \propto \sqrt{k/m}$ (Grimvall 2001). Fewer low-frequency modes are available at low T, resulting in lower Cp and reduced entropy (Figure 3L, drvB, uvtB, oleB). Al-rich tourmalines also have smaller unit cells (Table 2F, bole, ole, aorsm). At higher T, optical phonons dominate Cp, and the high force constants of Mg-O and Al-O bonds gradually activate higher-energy vibrational modes (Figure 3L, drvB, uvtB) (Dove, 1993). This steady activation eventually leads to Cp surpassing that of Fe^{3+}-rich tourmalines (Figure 3L, drvB vs. buB).

Shannon (1976)'s Al-O bond in tetrahedral coordination (0.53 Å) is longer and less covalent than Si-O bond in tetrahedral coordination (0.40 Å) (Gibbs et al., 2006). Al's smaller ionic radius, lower charge and weaker bonding compared to Si, lowers optical phonon frequencies, increases vibrational flexibility, and makes thermal states more accessible at high T, increasing Cp. Compared to the rigid Si–O tetrahedra, Al–O octahedra form larger and more flexible units. This expands the polyhedral environment, increases molar volume, and relaxes the structure, enhancing low-frequency acoustic modes (Dove, 1993). When comparing the olenite and AOR speciation endmembers (Table 2F, ole, aorsm), we observe the opposite effect—likely due to Na^+ being replaced by a vacancy on the X site, which perturbs the structure more significantly than an Al^{3+}–Si^{4+} substitution on a single tetrahedral site. B^{3+} substitution at the T site, with its much smaller ionic Shannon radius (~0.25 Å) in tetrahedral coordination has the opposite effect, it contracts the tetrahedron, strengthens local bonding, and raises optical phonon frequencies, lowering Cp (Figure A3H.9, bole) and reduce molar volume (Table 2F, bole).

In tourmalines, the W site, as a terminal bond, minimally impacts molar volume and entropy. F at the W site stiffens the lattice (Henry and Dutrow, 2011), raising vibrational frequencies and lowering entropy compared to OH as shown by the differences S^0 of uvt and fluvt (Table 3A uvtB vs fluvtB). The V site connects the Y and Z polyhedra, with OH contributing to structural flexibility. Tourmalines like olenite and buergerite, lacking OH on the V site, exhibit extreme thermodynamic effects due to polyhedral stiffening, often coinciding with high 3+ cation content (e.g., Fe^{3+}, Al^{3+}) for charge balance. We propose that OH primarily serves as a charge regulator, with its influence on entropy and molar volume linked to higher-charge ions. The stark differences between oxy and OHO polyhedral (Van Hinsberg et al. 2005a) challenge the idea that OH solely regulates charge. However, OH-deficient tourmalines being better modelled with OHO polyhedra suggests that, in tourmaline, the structural differences between polyhedra with and without OH may be less pronounced than in other mineral systems.

Order-disorder effects The structural impact of Fe^{3+}-Al^{3+} ordering and disordering significantly affects the thermodynamic properties of tourmalines, particularly entropy and molar volume, requiring a speciation model.

Tourmalines with Fe^{3+} at both the distorted Y site and regular Z site, such as povondraite, exhibit high entropy and large molar volumes (Figure A3H.15, A3H.16) due to the replacement of Al (or Mg) compact ridged bonding by (larger), weaker, and more flexible Fe^{3+}-O bonds (Bosi et al. 2023). Al strongly controls molar volume, as shown by its high correlations with total Al (-0.82), AlY (-0.76), and AlZ (-0.73), Appendix 3N. Replacing the stiffer Al-O (or Mg-O) bonds at the Z site increases lattice flexibility, lowers the Debye frequency, and enhances low-energy vibrational modes, contributing to low-T entropy. At high T, when Al begins to contribute to Cp, povondraite is overtaken by Al-rich tourmalines, though extrapolation issues persist (Figure A3H.9) .

Our study shows that Al-rich tourmalines with Fe^{3+} on the Y site and Al^{3+} on the Z site exhibit low entropy and small volumes (Figure 3Z, 3AA, 3AB). Al^{3+}'s smaller ionic radius and strong Al-O bonds contract the unit cell and stiffen the Z site, shifting phonon frequencies higher and reducing vibrational entropy by limiting low-frequency modes (Dove, 1993). Fe^{3+}'s smaller radius and stronger Fe^{3+}-O bonds further contract the Y site compared to larger, weaker-bonded

Mg^{2+} or Fe^{2+} which explain their smaller cell size and entropy than schorl-dravite. The absence of OH groups on the Z site minimises hydrogen bonding and structural distortions, enhancing unit cell contraction.

In contrast, Mg-Al ordering or disordering has minimal effect due to their similar ionic radii in ocathedral coordination (Shannon 1976) and strong, stiff bonds (Gibbs et all, 2006), see Table 2F drvdis vs drv). Fe^{2+} could cause substantial changes when disordered between Y and Z sites, given its larger radius and weaker bonds, though significant Fe^{2+} occupancy on the Z site in tourmalines remains controversial (Ertl et al. 2012; Bosi and Andreozzi 2013) .

The observed correlations between entropy, heat capacity, enthalpy, molar volume, and structural parameters in tourmalines remain qualitative. Ab initio methods, like density functional theory (DFT), are needed to compute the complete and partial vibrational density of states (v-DOS), revealing site-specific vibrational contributions and capturing the full electronic density of states (e-DOS). By comparing the e-DOS of individual elements, DFT provides precise insights into phonon softening, optical and acoustic mode shifts, and their effects on thermodynamic properties. This approach could also help establish correction factors for polyhedral in different mineral systems.

6. CONCLUSION

In conclusion, we present a bulk and speciation model for entropy (S) and high-T Cp in tourmaline, derived from linear regression of direct calorimetric measurements and an internally consistent tourmaline database. These models significantly improve upon the polyhedron approach, offering the first robust thermodynamic framework for tourmaline, with predictive accuracy suitable for net transfer and exchange phase equilibria.

REFERENCES

Altieri, A., Pezzotta, F., Skogby, H., Hålenius, U., and Bosi, F. (2022) Blue growth zones caused by Fe2+ in tourmaline crystals from the San Piero in Campo gem-bearing pegmatites, Elba Island, Italy. Mineralogical Magazine, 86, 910–919.

Benisek, A., and Dachs, E. (2008) The uncertainty in determining the third law entropy by the heat-pulse calorimetric technique. Cryogenics, 48, 527–529.

Berman, R.G., and Brown, T.H. (1985) Heat capacity of minerals in the system Na2O-K2O-CaO-MgO-FeO-Fe2O3-Al2O3-SiO2-TiO2-H2O-CO2: representation, estimation, and high temperature extrapolation. Contributions to Mineralogy and Petrology, 89, 168–183.

Bosi, F., and Andreozzi, G.B. (2013) A critical comment on Ertl et al. (2012): "Limitations of Fe2+ and Mn2+ site occupancy in tourmaline: Evidence from Fe2+- and Mn2+-rich tourmaline." American Mineralogist, 98, 2183–2192.

Bosi, F., Skogby, H., and Hovis, G.L. (2023) Crystal chemistry of povondraite by single-crystal XRD, EMPA, Mössbauer spectroscopy and FTIR. Mineralogical Magazine, 87, 178–185.

Chermak, J.A., and Rimstidt, J.D. (1989) Estimating the thermodynamic properties (Δ G of and Δ H of) of silicate minerals at 298 K from the sum of polyhedral contributions. American Mineralogist, 74, 1023–1031.

Connolly, J.A. (2005) Computation of phase equilibria by linear programming: a tool for geodynamic modelling and its application to subduction zone decarbonation. Earth and Planetary Science Letters, 236, 524–541.

Dachs, E., and Benisek, A. (2011) A sample-saving method for heat capacity measurements on powders using relaxation calorimetry. Cryogenics, 51, 460–464.

Dachs, E., and Bertoldi, C. (2005) Precision and accuracy of the heat-pulse calorimetric technique low-temperature heat capacities of milligram-sized synthetic mineral samples. European Journal of Mineralogy, 17, 251–261.

Dachs, E., Geiger, C.A., Benisek, A., and Grodzicki, M. (2014) Thermodynamic mixing properties and behavior of almandine–spessartine solid solutions. Geochimica et Cosmochimica Acta, 125, 210–224.

Dove, M.T. (1993) Introduction to lattice dynamics, 258 p. Cambridge University Press, Cambridge.

Einstein, A. (1907) Planck's theory of radiation and the theory of specific heat. Annalen der Physik, 22, 180–190.

Ertl, A., Hughes, J.M., Pertlik, F., Foit, F.F., Wright, S.E., Brandstätter, F., and Marler, B. (2002) Polyhedron Distortions in Tourmaline. The Canadian Mineralogist, 40, 153–162.

Ertl, A., Kolitsch, U., Dyar, M.D., Hughes, J.M., Rossman, G.R., Pieczka, A., Henry, D.J., Pezzotta, F., Prowatke, S., and Lengauer, C.L. (2012) Limitations of Fe2+ and Mn2+ site occupancy in tourmaline: evidence from Fe2+-and Mn2+-rich tourmaline. American Mineralogist, 97, 1402–1416.

Geiger, C.A., and Dachs, E. (2018) Recent developments and the future of low- *T* calorimetric investigations in the Earth sciences: Consequences for thermodynamic calculations and databases. Journal of Metamorphic Geology, 36, 283–295.

Gopal, E. (1966) Specific heats at low temperatures, 240 p. Heywood Books, London.

Gottschalk, M. (1996) Internally consistent thermodynamic data for rock-forming minerals in the system SiO2-TiO2-Al2O3-Fe2O3-CaO-MgO-FeO-K2O-Na2O-H2O-CO2. European Journal of Mineralogy, 175–223.

Grimvall, G. (2001) Dependence of thermodynamic properties on atomic masses and bonding in solids. In Solid Solutions in Silicate and Oxide Systems, EMU Notes in Mineralogy, Vol. 3, European Mineralogical Union, Eötvös University Press.

Grodzicki, M., and Lebernegg, S. (2011) Computation and interpretation of Mössbauer parameters of Fe-bearing compounds. In Mössbauer spectroscopy and transition metal chemistry. Springer, Berlin.

Hastie, T., Tibshirani, R., and Friedman, J. (2017) The elements of statistical learning: data mining, inference, and prediction, 715 p. Springer.

Henry, D.J., and Dutrow, B.L. (1996) Metamorphic tourmaline and its petrologic applications. Reviews in Mineralogy and Geochemistry, 33, 503–557.

——— (2018) Tourmaline studies through time: contributions to scientific advancements. Journal of Geosciences, 63, 77–98.

Holland, T.J. (1989) Dependence of entropy on volume for silicate and oxide minerals; a review and predictive model. American Mineralogist, 74, 5–13.

Holland, T.J.B., and Powell, R. (1990) An enlarged and updated internally consistent thermodynamic dataset with uncertainties and correlations: the system K2O–Na2O–CaO–MgO–MnO–FeO–Fe2O3–Al2O3–TiO2–SiO2–C–H2–O2. Journal of metamorphic Geology, 8, 89–124.

Holland, T.J.B., and Powell, R. (1998) An internally consistent thermodynamic data set for phases of petrological interest. Journal of metamorphic Geology, 16, 309–343.

Holland, T.J.B., and Powell, R. (2011) An improved and extended internally consistent thermodynamic dataset for phases of petrological interest, involving a new equation of state for solids. Journal of Metamorphic Geology, 29, 333–383.

Johnson, J.W., Oelkers, E.H., and Helgeson, H.C. (1992) SUPCRT92: A software package for calculating the standard molal thermodynamic properties of minerals, gases, aqueous species, and reactions from 1 to 5000 bar and 0 to 1000 C. Computers & Geosciences, 18, 899–947.

Kennedy, C.A., Stancescu, M., Marriott, R.A., and White, M.A. (2007) Recommendations for accurate heat capacity measurements using a Quantum Design physical property measurement system. Cryogenics, 47, 107–112.

Kieffer, S.W. (1979) Thermodynamics and lattice vibrations of minerals: 1. Mineral heat capacities and their relationships to simple lattice vibrational models. Reviews of Geophysics, 17, 1–19.

Kittel, C., and McEuen, P. (2018) Introduction to solid state physics, 8th ed., 692 p. John Wiley & Sons, Singapore.

Kuyunko, N.S., Semenov, Ë.V., Gurevich, V.M., Kuz'min, V.I., Topor, N.D., and Gorbunov, V.E. (1984) Experimental determination of thermodynamic properties of tourmaline dravite. Geokhimiya, 10, 1458–1465.

Lashley, J.C., Hundley, M.F., Migliori, A., Sarrao, J.L., Pagliuso, P.G., Darling, T.W., Jaime, M., Cooley, J.C., Hults, W.L., Morales, L., and others (2003) Critical examination of heat capacity measurements made on a Quantum Design physical property measurement system. Cryogenics, 43, 369–378.

Mattson, S.M., and Rossman, G.R. (1987) Fe2+-Fe3+ interactions in tourmaline. Physics and Chemistry of Minerals, 14, 163–171.

Miller, A.P. (1988) Theory of Specific Heat of Solids. In CINDAS Data Series, Vol.I-2, Specific Heat of Solids pp. 1–89. Hemisphere Publishing Corporation, New York.

Mraw, S.C. (1988) Differential scanning calorimetry. In CINDAS Data Series, Vol.I-2, Specific Heat of Solids pp. 395–435. Hemisphere Publishing Corporation.

Ogorodova, L.P., Melchakova, L.V., Kiseleva, I.A., and Peretyazhko, I.S. (2004) Thermodynamics of natural tourmaline–elbaite. Thermochimica Acta, 419, 211–214.

Robie, R.A., and Hemingway, B.S. (1995) Thermodynamic properties of minerals and related substances at 298.15 K and 1 bar (10^5 pascals) pressure and at higher temperatures. Bulletin. U.S. Geological Survey.

Rosen, P.F., and Woodfield, B.F. (2020) Standard methods for heat capacity measurements on a quantum design physical property measurement system. The Journal of Chemical Thermodynamics, 141, 105974.

Sack, R.O., and Ghiorso, M.S. (1994) Thermodynamics of multicomponent pyroxenes: I. Formulation of a general model. Contributions to Mineralogy and Petrology, 116, 277–286.

Schliesser, J.M., and Woodfield, B.F. (2015) Lattice vacancies responsible for the linear dependence of the low-temperature heat capacity of insulating materials. Physical Review B, 91, 024109.

Shannon, R.D. (1976) Revised effective ionic radii and systematic studies of interatomic distances in halides and chalcogenides. Foundations of Crystallography, 32, 751–767.

Stixrude, L., and Lithgow-Bertelloni, C. (2011) Thermodynamics of mantle minerals-II. Phase equilibria. Geophysical Journal International, 184, 1180–1213.

Stølen, S., and Grande, T. (2004) Chemical thermodynamics of materials: macroscopic and microscopic aspects, 395 p. John Wiley & Sons, Chichester.

van Hinsberg, V.J. (2006) Tourmaline: Monitor of the P-T-X evolution in rocks. PhD thesis, University of Bristol.

van Hinsberg, V.J., and Schumacher, J.C. (2007a) Intersector element partitioning in tourmaline: a potentially powerful single crystal thermometer. Contributions to Mineralogy and Petrology, 153, 289–301.

van Hinsberg, V.J., and Schumacher, J.C. (2007b) Using estimated thermodynamic properties to model accessory phases: the case of tourmaline. Journal of metamorphic Geology, 25, 769–779.

van Hinsberg, V.J., Vriend, S.P., and Schumacher, J.C. (2005a) A new method to calculate end-member thermodynamic properties of minerals from their constituent polyhedra I: enthalpy, entropy and molar volume. Journal of Metamorphic Geology, 23, 165–179.

——— (2005b) A new method to calculate end-member thermodynamic properties of minerals from their constituent polyhedra II: heat capacity, compressibility and thermal expansion. Journal of Metamorphic Geology, 23, 681–693.

van Hinsberg, V.J., Henry, D.J., and Marschall, H.R. (2011) Tourmaline: an ideal indicator of its host environment. The Canadian Mineralogist, 49, 1–16.

van Hinsberg, V.J., Franz, G., and Wood, B.J. (2017) Determining subduction-zone fluid composition using a tourmaline mineral probe. Geochemical Perspectives Letters, 3, 160–168.

Westrum, E.F. (1988) Calorimetry in the range 5-300K. In Specific Heat of Solids. Hemisphere Publishing Corporation, New York.

Bridging Text Between Manuscripts (Chapter 3-Chapter 4)

From Derivative Constraints to Energetic Anchoring

Chapter 4 completes the thermodynamic framework developed in the preceding chapters by introducing the final component of the Gibbs free energy function: the enthalpy of formation. Chapters 1 and 2 defined the composition and speciation space, enabling a consistent mapping of endmember proportions. Chapter 2 constrained the pressure dependence of Gibbs energy through molar volume, and Chapter 3 addressed its temperature dependence via entropy and heat capacity. Together, these properties define the derivative behavior of the Gibbs free energy, capturing how it varies with pressure and temperature, i.e., the slopes of phase boundaries in P–T–X space. However, without enthalpy of formation, these functions remain unanchored, lacking the absolute energy offset needed to fix phase stability fields in energy space.

Chapter 4 addresses this gap by presenting direct measurements of enthalpies of formation from oxides for a representative subset of tourmaline samples, using high-temperature drop-solution calorimetry. Anchored to the same internally consistent compositional dataset used in earlier chapters, these measurements define the energy baseline upon which the derivative properties act. Because no extensive external test dataset exists for tourmaline enthalpies, model performance is evaluated by comparing regression fits to the training data against previous estimation-based models. The study includes a rigorous Monte Carlo error propagation analysis to assess precision, and a comprehensive sensitivity analysis evaluating the impact of reference materials, thermodynamic cycles, and normalization schemes on model accuracy. This not only quantifies uncertainty but also identifies sources of systematic bias—critical for integrating tourmaline into internally consistent thermodynamic databases.

Furthermore, the derived enthalpy values serve as initial estimates for CALPHAD-style optimisation, where experimental, computational, and natural assemblage data are jointly refined to achieve global consistency. With the addition of Chapter 4, the model transitions from a framework defined by relative slopes to one fully anchored in absolute energy—enabling predictive modelling of tourmaline stability and compositional evolution across geologic conditions.

Thermodynamic model for Tourmaline

"*It is important to realize that in physics today, we have no knowledge of what energy is. We do not have a picture that energy comes in little blobs of a definite amount*. [...] *It is an abstract thing in that it does not tell us the mechanism or the reasons for the various formulas*" (Feynman, 1963).

Energy is precisely measurable and highly useful in calculations; its fundamental nature remains abstract and elusive. Similarly, in thermodynamics, we utilize concepts like entropy and energy effectively in models, even though their underlying physical realities remain beyond direct observation or intuitive understanding.

Feynman, R. P., Leighton, R. B., & Sands, M. (1963). *The Feynman Lectures on Physics, Vol. I: Mainly Mechanics, Radiation, and Heat*. Reading, MA: Addison-Wesley.

Chapter 4. Thermodynamic model for Tourmaline. Enthalpy

Stan Roozen, Vincent van Hinsberg, Xiaofeng Guo, Artur Benisek, Christian Pruner

ABSTRACT Tourmaline's low diffusion rates, preserved zoning patterns, and large stability range make it a key recorder of geochemical processes. Interpreting these patterns requires a thermodynamic model, yet enthalpies of formation remain poorly constrained. This study presents direct enthalpy measurements for 15 natural and 1 synthetic tourmaline using high-temperature drop solution calorimetry in a lead borate solvent at 700°C, with FTIR line-broadening as an indirect proxy for enthalpy of mixing. Precision was evaluated using Monte Carlo error propagation, while accuracy was assessed through sensitivity analysis of the impact of methodological choices, including thermodynamic cycle selection, reference oxides, and normalization schemes. The measured enthalpies are regressed to bulk compositional model endmembers using linear regression, providing the current best estimates, but due to data scarcity have multicollinearity issues. These values serve as starting points for optimisation using the CALPHAD approach and subsequent incorporation of internally consistent thermodynamic databases. No significant enthalpies of mixing were found. refining predictive models of tourmaline stability and geochemical behavior. This advances tourmaline's integration into forward thermodynamic modelling, enhancing its use in interpreting geochemical processes, constraining its formation conditions, and refining mineral equilibrium predictions in natural systems.

1. INTRODUCTION

Tourmaline is a complex borosilicate mineral group with a wide compositional range that reflects its geochemical formation environments (van Hinsberg et al. 2011). Its ability to incorporate diverse elements provides valuable information about phase reactions (Dutrow and Henry 2011), but interpreting this geochemical record requires the ability to predictively model these reactions and hence a thermodynamic model for the tourmaline mineral group. Previous chapters have presented direct measurements of molar volumes, heat capacities, and entropies but we also need enthalpies of formation for the various tourmaline endmembers and interaction energies between these to provide a full thermodynamic description of tourmaline. Accurate enthalpy measurements are essential for understanding tourmaline's stability and geochemical behavior under different pressure, temperature and geochemical conditions. While volume and entropy are absolute properties, enthalpy provides relative energy values compared to other phases at standard state conditions (Anderson 2005). Ensuring internal consistency with these

phases is crucial; otherwise, the validity of including tourmaline in thermodynamic modelling is compromised. Thermodynamic databases (Berman 1988; Holland and Powell 1990; Gottschalk 1996) optimize enthalpy values using the CALPHAD approach, relying on experimental and field-based phase relationships for internal consistency. They refine directly measured enthalpies of reactions, avoiding the large uncertainties associated with the absolute values of the enthalpies of formation from the elements ($\Delta H_{\text{form,el}}$). However, data for tourmaline remain limited. Solely relying on field data can lead to enthalpy values that are highly correlated with other phases, making them empirical fit parameters rather than independent measurements. Instead, here we present directly measured enthalpies of formation for tourmaline species to provide initial estimates with their uncertainty margins. These measurements will provide first-order constraints on the absolute enthalpy values of tourmaline, even if they are later correlated with other phases trough internally consistency optimisation. We aim to use the limited constraints from experiments and natural assemblages as a test set for our model

This study quantifies tourmaline enthalpies from the oxides using high-temperature lead borate drop solution calorimetry , and enthalpies of mixing were indirectly assessed via empirical calibrations using line broadening of FTIR spectroscopy (Boffa Ballaran and Carpenter 2003). We show how different methodological choices, such as the thermodynamic cycle and reference oxides, and normalization schemes, can impact the results. Given that even small compositional variations can significantly affect outcomes, precise compositional data are essential for accurate thermodynamic modelling. Our findings address key uncertainties and challenges, provide valuable insights not only for tourmaline but also for modelling other mineral systems with complex solid solutions.

2. METHODS

Sample characterisation is detailed in Chapter 1. For this study, we used a subset (N=15) of the natural samples for which we measured molar volumes, heat capacities, and entropies. Figure 4A presents their compositions in terms of the independent endmembers of the bulk composition thermodynamic model. Additionally synthetic B-olenite was also measured (1 single

measurement).

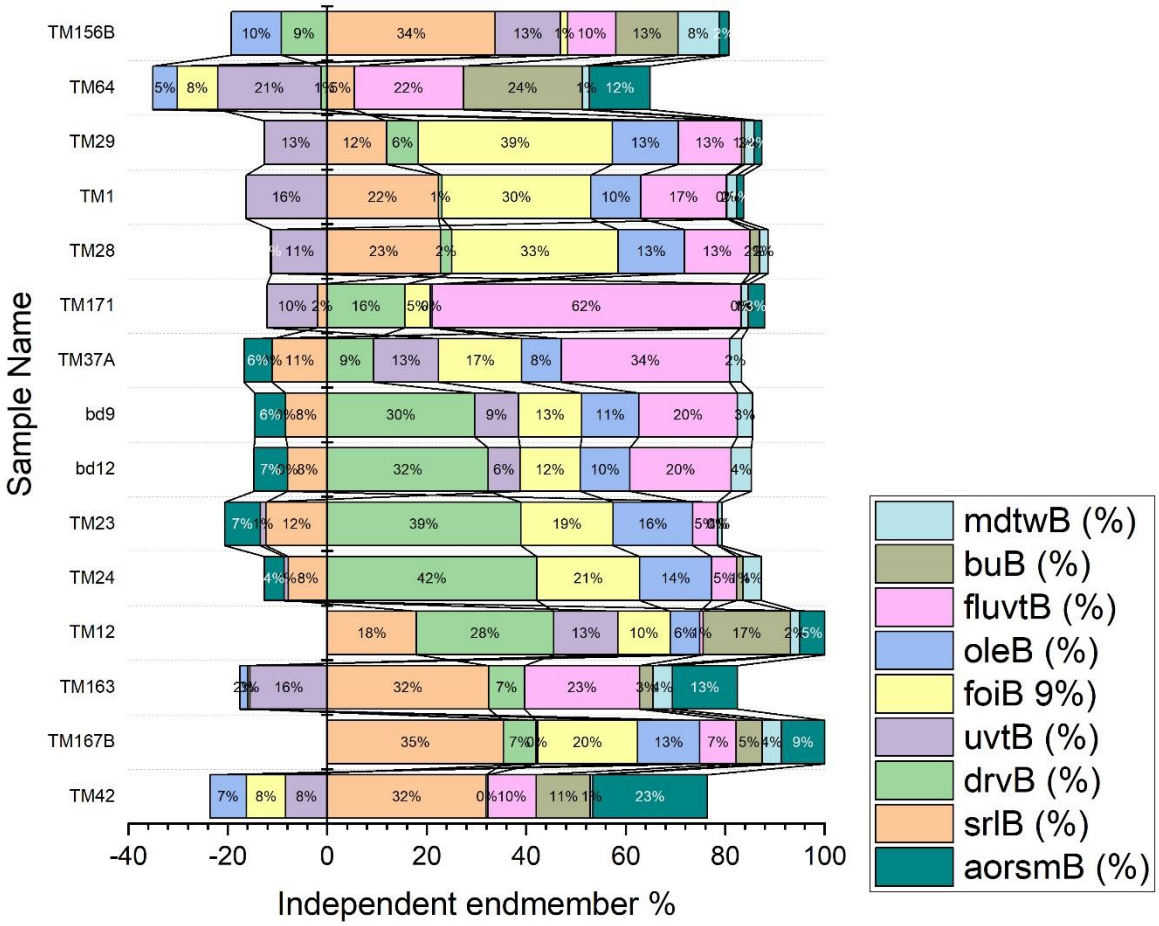

Figure 4A. Independent endmember fractions of the Bulk model for the 15 natural samples selected for enthalpy measurements. Chapter 2 outlines their calculation and defines the Bulk model endmember abbreviations.

2.1 Thermogravimetric Analysis (TGA)

Our drop solution calorimetry thermodynamic cycles assume that no phase transition occurs when the sample is dropped into the 700°C solvent. To evaluate this, we performed TGA-DSC analysis using a Setaram SetSys Evolution thermogravimetric differential scanning calorimeter at the Guo lab at the Alexandra Navrotsky Institute for Experimental Thermodynamics at Washington State University. Tourmaline samples were heated from room temperature to 1100°C at 10°C/min under a flowing N_2 atmosphere (100 ml/min). Two Fe-rich samples were additionally analysed under flowing air (100 ml/min) with otherwise identical conditions.

Temperature and heat calibrations were performed using indium, tin, lead, zinc, and aluminum, by comparing their fusion temperatures and heats to certified values. For both blank and sample runs, we used the same crucible, ensuring that the mass difference with the reference crucible was within 20 mg for each run. Blank-subtracted mass and heat flow data were analysed in Origin to estimate melting temperatures, determined visually from the onset of the endothermic heat flow peak. The heat of melting was not extracted due to tourmalines known incongruent melting behavior, and the product phases were not characterised. Synchronous DSC measurements, included in the results section figures, are for qualitative purposes only due to uncertainties of over 10%. Attempts to correlate these DSC signals with high-precision Cp measurements from Chapter 3 showed significant slope changes, attributed to non-optimised instrumentation and lack of isothermal or sapphire standard measurements. The primary aim of these measurements was to assess if major structural changes occur before the tourmaline reaches the solvent.

2.2 Drop Solution Calorimetry

The mineral sample was finely ground under acetone in an agate mortar for 5-10 minutes which is known to achieve an average particle size of around 20 μm. Intermittent microscopic inspections were conducted to identify and remove any impurities or inclusions, thereby ensuring the purity of the sample and particle size uniformity was also verified and checked to be well above the nanometer scale to avoid surface thermodynamic effect's dominating over bulk thermodynamics (Navrotsky 2001; Navrotsky et al. 2008).

Enthalpy measurements were conducted using a Setaram AlexSYS-1000 calorimeter, which is a Tian-Calvet twin integrated heat flow microcalorimeter with two sample chambers. This instrument is housed at the Guo lab at the Alexandra Navrotsky Institute for Experimental Thermodynamics at Washington State University. The system was set up the night before to stabilize the baseline. Sample powder pellets, weighing between 3-5 mg, were hand-pressed using a custom pellet die and then dropped from room temperature into 20 g of molten lead borate (2PbO-B2O3) contained in a 106 mm long Pt crucible, about 1 cm in diameter, surrounded by a SiO2 glass liner at 700°C. Hand pressing ensured that the powder remained intact during drop without being overly compacted to aid dissolution. The headspace above the

solvent was continuously flushed with O_2 gas at 100 mL/min to maintain a constant gas atmosphere and bubbled through the lead borate melt at 5 mL/min using an Al_2O_3 tube with a Pt extension. This setup ensured mixing of the melt, removal of devolatilized H_2O, and control of the redox state of both the sample and melt (Navrotsky et al. 1994). Measurements were repeated until at least three measurements with less than 5% uncertainty were obtained and/or until the solvent reached a dilution factor of 1:1000. A 1–2-hour wait was necessary for the enthalpy signal to return to baseline before introducing a new sample, making typical sample measurements take about 8-10 hours. The induced temperature change was detected in each chamber by a Pt-PtRh thermopile housed within an Inconel block, which served as an infinite heat sink. The differential electromotive force of the two thermopiles was recorded using a Keithley microvoltmeter. Signal integration involved constructing a background for each enthalpy peak, subtracting this background, and integrating the corrected signal to obtain heat flow data in μV·s. Due to relatively large baseline noise compared to the enthalpy signal, manual setting of the background was user-dependent, emphasizing the need for consistency in handling relative energy differences. The integrated emf over time is proportional to the heat released or absorbed. The calibration factor (J μV^{-1} s^{-1}) for converting measured voltage into kJ/mol was obtained by measuring the heat content, $\int_{RT}^{700^{\circ}C} C_p(T)dT$), through transposed temperature drop calorimetry using 35-50 mg of hand-pressed α-Al_2O_3 powders (pre-calcined at 1673 K) or 15-200 mm Pt wire, and comparing results with literature values in the JANAF table. The error in the calibration factor was kept 0.5%. Calibration and further methodology details are described in earlier studies (Guo et al. 2015, 2016, 2018; Strzelecki et al. 2020, 2024; Goncharov et al. 2022; Reece et al. 2024). At least three measurements that were closest to each other were selected to obtain the mean and 2 standard error. Samples with integrated heat signals deviating by more than 5% from the selected three were considered outliers and excluded, requiring an unfortunate but necessary selective consideration of enthalpy signals. This was essential due to potential issues during the drop, such as incomplete dissolution, sample adhesion to the crucible, or baseline shifts.

2.3 FTIR powder absorption spectra

In the theoretical background Appendix 4A, we explain the physical and chemical basis for the assumption that spectral broadening correlates with enthalpy of mixing, as well as how the FTIR autocorrelation function quantitatively represents this broadening.

For mid-infrared (MIR) spectroscopy (3800 cm^{-1} to 400 cm^{-1}), we prepared KBr pellets with the powdered tourmaline samples. The process began by drying spectroscopic-grade KBr powder at 150°C for 24 hours to eliminate residual moisture. The mineral sample was finely ground under acetone in an agate mortar for 5-10 minutes to achieve uniform particle size and ensure homogeneity. Microscopic inspection was performed intermittently to remove impurities or inclusions, ensuring sample purity. The ground sample was then mixed with KBr in a 1:200 ratio and ground for an additional five minutes to ensure even distribution within the KBr matrix. This mixture was dried again at 150°C for 24 hours before being carefully loaded into a preheated die (100°C) while avoiding powder sticking to the sides. A vacuum pump was applied to the die for 2-5 minutes, followed by a series of loadings using a hydraulic press to a 13 mm diameter piston: 3 tons/cm^2, 7 tons/cm^2 held for 30 seconds to 2 minutes, and finally 10 tons/cm^2 held for 10 minutes. Each loading was released slowly to prevent pellet cracking. The resulting disk pellets were clear and free of water absorption. Due to KBr's hygroscopic nature, the pellets were handled with gloves and immediately stored in a desiccator to prevent moisture absorption.

For far-infrared (FIR) spectroscopy (680 cm^{-1} to 50 cm^{-1}), we prepared polyethylene (PE) pellets containing powdered tourmaline. 2 mg of the powdered sample was weighted and mixed with 75 mg of spectroscopic-grade PE powder. The mixture was carefully ground in an agate mortar, avoiding static buildup, until homogeneous. It was then placed into a die, ensuring no material adhered to the sides, and pressed at a consistent loading of 10 tons using a hydraulic press. These steps ensured the optical clarity and mechanical stability of the PE pellets.

After preparing the sample pellet, they were carefully positioned in the sample holder of the Bruker IFS66 FTIR spectrometer at the Maurizio Musso Vibrational Spectroscopy Lab, Department of Chemistry and Physics of Materials, at the Paris-Lodron University Salzburg with the help of Christian Pruner. The spectrometer is equipped with a heated silicon carbide Globar blackbody source, which emits broadband infrared light. The spectrometer was set up for the desired spectral range: MIR or FIR. For MIR measurements with KBr pellets, the KBr

beamsplitter and MIR pyroelectric TD6S FGSC detector (DTGS) were used. For FIR measurements with PE pellets, the multilayer Mylar beamsplitter (T222/8) and pyroelectric TD6S FIR (DTGS-2) detector were employed; these pyroelectric detectors measure temperature-induced capacitance changes as voltage variations. The chamber was not at vacuum, but the spectrometer was purged with dry air at 200 L/h to reduce water vapor and CO_2 interference, and desiccant material was added to the sample chamber. A 10-minute wait after a sample change was required to establish steady-state environmental conditions.

The FTIR measurements were done of a single set of instrumental conditions. A resolution of 4 cm^{-1} was used for both the background and the sample. The alignment of the Michelson interferometer mirrors was optimised for maximum instrumental gain (amplitude of the ZPD centerburst > 20,000). All measurements were conducted at room temperature with a 10 mm aperture to minimize nonparallel radiation. The interferogram was recorded at a mirror speed of 1.22 kHz, with wavelength calibration using a 632.8 nm HeNe reference laser as an internal standard, and data acquisition in double-sided forward-backward mode. No intensity calibration was performed; normalization was applied as a postprocessing step. A 1-16 kHz low-pass filter reduced noise. These settings resulted in an interferogram comprising 14,218 points, with the Fourier transform providing a frequency domain resolution of 16k points. Phase resolution was set to 16 bits, with Mertz phase correction applied. To reduce FT truncation errors, a Blackman-Harris 3-term apodization function was applied, and zero-filling was used to double the number of data points. Each spectrum was recorded as absorbance, $\alpha = -\log_{10}(I_{sample}/I_{reference})$, where I represent transmission intensity. The spectra were calculated from the Fourier transform of 64 interferometer scans, providing a satisfactory signal-to-noise ratio for both MIR and FIR measurements.

Performing a background scan with a reference KBr/PE pellet in the sample holder and air as the reference yielded a flat signal at approximately 70% transmission. Although the FIR beamsplitter is specified for use up to 30 cm^{-1}, reliable data could not be obtained beyond 50 cm^{-1}, likely due to the wavenumber range limitations of the Globar IR source. For all subsequent measurements, a reference pellet (PE or KBr) was placed in the reference beam path and the sample pellet in the sample path; the reference pellet served to record the baseline, allowing for accurate baseline correction of the sample spectrum. To ensure consistent transmission percentages, the weights of

the reference and sample pellets were kept as close as possible, always within 5 mg. This baseline correction accounts for any instrumental or environmental contributions to the measured signal.

Spectra were acquired with on the sample KBr/PE pellet, and absorbed water + CO_2 was removed using the atmospheric compensation algorithm in the instrument software OPUS. Effective H_2O compensation requires no sample absorption between 3600–4000 cm^{-1}, and CO_2 compensation requires none between 2300–2400 cm^{-1}. While the samples had no peaks in the CO_2 range, sample absorption in the H_2O range may have led to their overcorrection. The spectra were loaded into Spectraglyph 1.2 for postprocessing. We normalised the NIR/MIR and FIR spectra to the same value based on a dominant peak near 400 cm^{-1} visible in both the MIR and FIR spectra. After normalization, the spectra were merged. We cut the spectra from 3800 cm^{-1} and removed any residual CO_2 peaks around 2350 ± 200 cm^{-1} if present. Initial tests indicated that these procedures did not affect the resulting autocorrelation analysis. The only procedure affecting the autocorrelation analysis was the nonlinear advanced background subtraction in Spectraglyph. Consequently, we prepared two sets of merged spectra: one with linear background subtraction and one with nonlinear background subtraction. While the absolute values differed between the sets, the relative differences were similar, as was also found by Boffa Ballaran et al. (1999).

A Mathematica 5.2 script written by Artur Benisek was used for the autocorrelation analysis, selecting the spectrum from 50 cm^{-1} to 2000 cm^{-1}. The FTIR spectra of tourmaline display continuous overlapping peaks from 50 cm^{-1} to 2000 cm^{-1}, with no gaps. The main challenge in using FTIR broadening to correlate with the enthalpy of mixing lies in defining the relevant spectral range (Boffa Ballaran and Carpenter 2003). However, due to the absence of gaps in tourmaline's spectrum, the broadening across the entire FTIR range must be used as a probe for the enthalpy of mixing. This assumes that the dipole changing optical phonons in the 5000 to 200,000 Å range can indirectly detects the strain fields responsible for enthalpy of mixing (see Appendix 4A). The range was chosen to avoid inaccuracies in the OH vibration broadening around 3500 cm^{-1}, which could be affected by water absorption in the sample chamber and the applied atmospheric correction. The autocorrelation function, $\mathrm{Corr}\big(\alpha(\omega), \alpha(\omega')\big) =$

$\int_{-\infty}^{\infty} \alpha(\omega)\alpha(\omega+\omega')d\omega$ measures how the spectrum correlates with itself when shifted by a frequency ω', i.e., lagged version of itself, for a range of lags, for details of its use in FTIR spectroscopy see Salje et al. (2000). This calculation produces a new spectrum where each point represents the correlation of the original spectrum with a shifted version of itself. The central peak of the autocorrelation function is fitted with a Gaussian function, $G(x) = k_0 \exp\left(-\frac{(x-x_0)^2}{2k_2^2}\right)$ and the Gaussian fit is extrapolated to zero lag (ω′=0) (Salje et al. 2000). The parameter k_2 is related to the line width by $\Delta_{corr} = 2\sqrt{2\ln 2}k_2$. This extrapolated value Δ_{corr} accounts for the broadening without interference from adjacent peaks, and represents the weighted average of the line widths of the absorption peaks in the selected IR spectrum segment (Salje et al. 2000).

Grain size and shape can contribute to spectral broadening, but autocorrelation analysis is minimally affected by user-controlled factors like grinding time, pellet preparation, dilution, and resolution (Blanch et al. 2007). No significant spectral differences were observed in KBr pellets with varying concentration ratios (200:1, 100:1, and 500:1). We ground tourmaline to 15–20 µm using an agate mill, ensuring uniform particle size across all samples. While MIR particles >2.5 µm can cause refraction artifacts (McMillan and Hofmeister 1988) and FIR spectra suffer from noise due to low detector sensitivity and H_2O vapour interference, these effects remain consistent. Frequency shifts from TO-LO splitting and surface modes are also potentially present (McMillan and Hofmeister 1988) but since we compare relative spectral differences, not absolute peak positions, autocorrelation remains robust to these factors.

3. THERMOGRAVIMETRIC ANALYSIS (TGA)

Results. A detailed summary of the key features observed in the TGA-DSC experiments is presented in Table 4.A (Figures in Appendix 4B). This table provides an overview of the mass loss behavior of various tourmaline samples under different thermal conditions, highlighting temperature ranges of mass loss steps, weight loss percentages, melting temperatures, and total weight loss values. The data include measurements both in air and non-air environments to assess the influence of oxidation and dehydration processes. Additionally, Karl-Fisher titration

results (Chapter 1) are provided for comparison, offering insights into the consistency between water content estimates from independent methods

Table 4A. Thermogravimetric analysis (TGA) results for selected tourmaline samples. Each sample was heated under either inert (N_2) or oxidative (air) conditions, and mass loss was monitored as a function of temperature. Three distinct mass loss intervals (T1, T2, T3) are reported where applicable, corresponding to devolatilization events observed during heating. The table lists the temperature range (°C) and associated weight loss (%) for each step. The melting temperature indicates the onset of endothermic melting from differential scanning calorimetry (DSC) where available. Total weight loss is the cumulative mass loss over the full TGA run, and values corrected to exclude physically adsorbed water are given in the adjacent column. Karl-Fisher titration values from Chapter 1 provide an independent estimate of structural water. Samples measured in air (oxidizing conditions) are indicated with “air” in the name. Bolded values highlight measurements outside the expected dehydration behavior, possibly indicating experimental artifacts or compositional variability.

Tourmaline	Mass loss T1	Wt% loss 1	Mass loss T2	Wt% loss 2	Mass loss T3	Wt% loss 3	Melting T	Total Weight loss	Total Weight loss (no absorption)	Karl-Fisher
Tm42	455-860	0.12			860-940	2.80	884.5	2.92	2.80	2.87
Tm42 air	200-953.8	0.53			953.8-1032	1.48	997	**2.01**	1.48	**2.87**
Tm29	400-878	0.27			878-945	2.70	900	2.97	2.70	3.26
Tm28 air	200-929.2	0.70			929.2-1024.66	1.67	971.3	**2.37**	1.67	**3.34**
Tm1	25-860	0.62			860-917	2.59	879	3.21	2.59	3.08
Tm1 air	200-953	0.88			953-1031	1.46	1004	**2.34**	1.46	**3.08**
Tm12	200-879	0.28			879-994	2.88	928	3.16	2.88	3.18
Tm24	200-913	0.28			913-1019	3.07	962	3.35	3.07	3.38
Tm23	400-897	0.10			897-1038	3.43	999	3.53	3.43	3.34
Tm37A	200-534	0.38	**534-625**	**1.03**	888-1020	3.24	950	4.65	3.24	2.26
bd9			**270-402**	**1.43**	910-1032	2.96	982	4.39	2.96	3.08
bd12	333-889	0.26			889-1025	3.07	960	3.33	3.07	2.94
Tm171	600-683	0.28			883-1020	3.01	966	3.29	3.01	2.70
Tm156B	200-840	0.33			840-987	2.60	937	2.93	2.60	2.99
Tm64	200-482	0.35			861-1080	1.72	978	2.07	**1.72**	**0.50**
Olenite			**25-800**	**1.93**	800-973	2.12	952	4.05	2.12	4.00
Oxyuvite			**25-861**	**1.11**	861-990	2.59	945	3.70	2.59	4.06

TGA measurements of Tm1 and Tm42 under N_2 and O_2 atmospheres show oxidation-driven changes in tourmaline behavior before melting. Under O_2, a gradual mass loss of 0.5-1 wt% starts after 200°C, with the melting point increasing by 130°C, resembling buergerite. Total weight loss in O_2 is about 1 wt% lower than in N_2. The oxidation of Fe^{2+} to Fe^{3+}, balanced by deprotonation, follows:

$$^{(Y+Z)}Fe^{2+} + {}^{(V+W)}OH + 1/4\ O_2 \rightarrow {}^{(Y+Z)}Fe^{3+} + {}^{(V+W)}O^{2-} + 1/2\ H_2O(g)$$

This process, first identified by Pieczka and Kraczka (2004) and later confirmed by Castañeda et al. (2006) and Bačík et al. (2011), has been observed in Fe-rich tourmalines such as schorl (Filip et al. 2012; Liu et al. 2019; Celata et al. 2023b, 2023a) and Fe-containing varieties (Bosi et al. 2016, 2018, 2019; Altieri et al. 2023). Mossbauer spectra in these studies show increased Fe^{3+}, and IR spectra indicate OH reduction, confirming deprotonation. However, this reaction does not explain the lower H_2O release in O_2 compared to N_2, suggesting the possibility that the incongruent melt or the related hydrous product phases (Wolf and London 1997) might retain water under oxidized conditions, though this remains unverified as the final reaction products were neither preserved nor analysed after the measurements. Under oxidizing conditions, weight loss attributed to water release may have been offset by the formation of iron oxides, resulting in an apparent mass gain. Network former Fe^{3+} in borosilicate melts retain more water than network breaker Fe^{2+} due to hydroxyl stabilization in the higher polymerized structure (Le Losq et al. 2021), but this behavior is absent in buergerite. Melting volatile release under in O_2 is half of what Karl-Fisher titration predicts, possibly indicating a (peritectic or residual) product phase that retains the missing water. Alternatively, reduced oxygen (O^{2-}) may be incorporated into the tourmaline structure, offsetting the weight loss from deprotonation (Vho et al. 2019), but Bosi(2016)'s post heat-treated SC-XRD analysis found no evidence of extra oxygen positions, possibly because interstitial oxygen is undetectable due to its random distribution. The loss of protons would contrast with the low hydrogen diffusion rates in tourmaline (Desbois and Ingrin 2007), however diffusion might change when transitions metal oxide however might speed up when their charge balance function is no longer need. Buergerite also exhibited higher than expected weight loss, with Karl-Fisher measuring 0.5 wt% and actual loss around 2 wt%, suggesting fluorine might be volatilized. Other fluorine-rich tourmalines show similarly higher weight losses, though these vary widely and do not correlate well with fluorine concentration. In

uvite samples tm37A and bd9, abrupt weight losses at 550°C and 300°C, respectively, likely reflect inclusions in the source crystals, resulting in final weights 1.5 wt% lower than expected. Chlorite in bd9 caused the 300°C loss, while magnesite in tm37A released CO_2 at 550°C. These inclusions were visible in the macrocrystals, and care was taken to exclude them during powder preparation, yet some were still incorporated. This suggests TGA is more sensitive than XRD for detecting impurities, which remained difficult to identify under optical microscopy. It's possible that the powders of these samples used in the solution calorimetry have the same 1–2 wt% impurity; however, this is low that it does not significantly affect the enthalpy given the other uncertainties in the drop solution calorimetry method and the thermodynamic cycle. Its effect on the autocorrelation analysis of the FTIR spectra is also considered minimal due to the high peak density and algorithmic removal of CO_2 peaks. Lastly, we observed distinct behavior in the synthetic samples, olenite and oxyuvite. Both samples exhibited an immediate mass loss of about 1-2 wt% at the start of the heating cycle in a continuous manner. When the samples melted, only half of the total volatile mass was lost, yet the total mass loss was consistent with Karl-Fisher titration measurements. This could indicate residual precursor phases, though abrupt signals like those from inclusions would be expected. Instead, it might suggest water in synthetic samples may be structured differently than in natural ones. However, FTIR spectra showed no significant changes in water absorption bands (3400–3700 cm^{-1} O-H stretching, 1600–1650 cm^{-1} H-O-H bending, 600–800 cm^{-1} rotational/translational modes), as both natural and synthetic samples exhibited peaks in these regions. This overlap prevents determining whether additional water-related peaks are present in the synthetic samples. Structural differences in synthetic samples have important implications for thermodynamic modelling, potentially affecting the reliability of their enthalpies in representing natural systems. However, despite TGA inconsistencies, their ability to break correlations in regression models, particularly in complex systems like tourmalines, justifies their continued use.

Discussion: Thermogravimetric analysis (TGA)

We performed a multiple linear regression using the bulk composition thermodynamic model to extrapolate melting temperatures under N_2 for endmember compositions, assuming a linear dependence on compositional variables. While this assumption is uncertain due to potential involvement of unknown product phases in the breakdown reaction, it provides a general trend

for breakdown temperatures across tourmaline compositions. The model shows a low percentage error of around 1% and a root mean square error (RMSE) of 21, indicating it is a reasonable first-order approximation, with all melting temperatures for endmembers statistically significant at $\alpha = 0.05$.

Table 4B. Melting temperatures extrapolated to the bulk compositional model endmembers using ordinary least squares multiple linear regression on the 14 samples for which melting temperatures were obtained. The regression coefficient for each variable represents the predicted melting temperature (in °C) of the pure endmember. The 95% confidence intervals indicate the uncertainty in this extrapolation, based on the standard error of each coefficient.

Regression Coefficient Confidence Intervals

Independent Variable	Regression Coefficient b(i)	Standard Error Sb(i)	95% Confidence Limits of β(i)	
			Lower	Upper
srlB	845.3719	89.07264	598.0666	1092.677
drvB	970.1111	63.79959	792.9751	1147.247
uvtB	941.8365	47.72369	809.3343	1074.339
foiB	825.9313	158.609	385.562	1266.301
oleB	1018.191	330.8616	99.57188	1936.81
fluvtB	950.2298	35.00741	853.0336	1047.426
buB	962.3242	73.19888	759.0916	1165.557
mdtwB	1326.986	359.1925	329.7076	2324.264
aorsmB	927.3766	103.7292	639.3781	1215.375

Note: The T-Value used to calculate the confidence limits was 2.776.

The observed trend indicates that Fe^{2+} endmembers, such as srlB and foiB, have the lowest melting temperatures around 830°C which makes sense as similar trends are observed for other minerals like olivine and pyroxene (Beattie 1993). UvtB, fluvtB, and aorsmB melt around 940°C. DrvB and ferric endmember buB melt at approximately 970°C, with oleB and mdtwB melting at even higher temperatures but with greater uncertainties. Extremely high VIF factors suggests multicollinearity, particularly among srlB (17), foiB (71), oleB (84), and aorsmB (21), highlighting the need for additional data to address notable correlations between drvB and srlB (-

0.82), oleB and srlB (-0.76), drvB and oleB (0.81), and foiB and aorsmB (-0.88), as well as oleB and aorsmB (-0.84). This results in a data-dependent regression, evidenced by the near-zero R^2_{Press}, indicating low predictability. All melting temperatures exceed 700°C, the solvent temperature in the lead borate drop solution calorimetry. Samples must remain stable below this to prevent melting before dissolution, ensuring accurate enthalpy measurements.

4. ENTHALPIC THERMODYNAMIC CYCLES OF TOURMALINE

Drop enthalpies (ΔH_{drop}) for our tourmaline samples are found in Table 4C. The enthalpy of the sample in kJ/mol is calculated by multiplying the heat signal per gram (Q, in kJ/g) (Table 4C, column 2 &3) by the sample's molar mass (M, in g/mol), as calculated from the mineral formula obtained in Chapter 1. Drop solution enthalpy reflects the energy difference between elements in tourmaline and their speciation in the lead borate melt, along with the heat content gained as tourmaline is heated from room temperature to the solvent temperature (including phase changes, oxidation reactions).

This heat content is governed by the statistical occupation of phonon energy states, described by the vibrational density of states (v-DOS). Heat content was measured separately using power-compensated DSC from room temperature to 500°C in Chapter 3. We applied the Berman and Brown (1985) Cp polynomial to fit this data, extrapolated it to 700°C, and integrated over T to calculate the heat content. The covariance matrix of the fit provided an estimate of the uncertainty. No lead platinates, a common issue with transition metal-containing phases (Lilova et al. 2012), formed when using lead borate at 700°C under an O_2 atmosphere, as no reaction materials were observed in the platinum crucible after the experiments.

Table 4C. Drop-solution enthalpy measurements of tourmaline samples in lead-borate solvent at 700 °C. The first column lists the number of drops used per sample for calculating the mean and the total number of drops. Drops which gave inconsistent results were not used for the calculation of the mean. The second and third columns report the measured enthalpies of solution in kJ/g. These were converted to molar values using the molar mass of each sample (not shown). The fourth and fifth columns give the heat contents (H^o(700 °C) – H^o(25 °C)) in kJ/mol, obtained by integrating the caloric equations of state (Cp) from 25 °C up to 700 °C.

Sample	N (used for calcualting mean of drop H)/total drops	Drop solution Enthalpy (kJ/gram)	Drop solution enthalpy 2 SE (kJ/gram)	Heat Content (J/mol, measured Cp integration)	Heat Content ± Error (J/mol, measured Cp integration)
TM42	3/7	0.962226	0.018507	751.16	0.663088
TM167B	4/6	1.092919	0.007688	759.97	0.466916
TM163	3/6	1.007662	0.014326	735.136	1.62575
TM12	5/7	1.042974	0.030646	745.617	0.754499
TM24	4/6	1.135864	0.034376	742.248	0.825856
TM23	4/8	1.142477	0.047764	747.973	0.549563
bd12	6/6	1.20956	0.034858	748.907	0.361851
bd9	3/6	0.837794	0.022529	752.377	0.441771
TM37A	4/4	1.214823	0.014147	755.855	0.72471
TM171	3/4	1.231079	0.017591	735.235	3.16628
TM28	4/5	1.003929	0.024323	752.668	1.66585
TM1	4/4	0.87706	0.028466	749.765	1.37012
TM29	4/5	0.962117	0.009882	750.592	0.145361
TM64	3/6	0.817223	0.008912	721.013	1.14691
TM156B	4/8	1.007609	0.013965	762.848	0.514402
olenite_syn	1/1	0.972197	only 1 measurement	709.889	1.19978

Thermodynamic Cycles In the calorimetric cycle used here, the reaction measured for tourmaline is:

$$\text{Tourmaline}\ (\text{s}, 298\text{K}) \rightarrow \sum \text{Oxides (solution, } 973\text{K})$$

meaning that the crystalline tourmaline at 298 K is dissolved into a high-temperature solvent at 973 K.

Similarly, for each reference oxide, the measured reaction is:

$$\text{Oxide}\ (\text{s}, 298\text{K}) \rightarrow\ \text{Oxide (solution, } 973\text{K)}$$

where the crystalline oxide dissolves into the same solvent at 973 K (Figure 4B).

To obtain the standard enthalpy of formation of tourmaline from its component oxides at 298 K, the drop solution enthalpy of tourmaline is subtracted from the sum of the drop solution enthalpies of the oxides. Subtracting these reactions effectively reconstructs the standard-state reaction at 298 K, as it automatically removes the heat content (enthalpy increase from 298 K to 973 K) of the oxides. Therefore, the heat content of tourmaline is not needed. Our analysis of tourmaline's thermodynamic cycles follows Hess's Law, ensuring consistency in enthalpy calculations. So the enthalpy change for conversion to reference oxides is: $\Delta H^{\circ\text{tourmaline}}_{f,\text{ oxide}} = \Delta H^{\text{oxides}}_{\text{drop solution}} - \Delta H^{\text{tourmaline}}_{\text{drop solution}}$. Formation enthalpy from elements, leveraging the path-independent nature of enthalpy, is given by: $\Delta H^{\circ\text{tourmaline}}_{f,\text{ element}} = \sum\left(\Delta H^{\text{oxide}}_{f,\text{ element}}\right) + \Delta H^{\text{tourmaline}}_{f,\text{ oxide}}$. This method is applicable to non-transition metal oxides. For transition metal oxides, we account for oxidation in the lead borate melt under oxygen. Each thermodynamic cycle must begin with a well-defined initial state and end in a clearly known final state, such as dissolved oxides in a Henryian state, evolved gases, and well-defined oxidation states, to ensure accurate calculations (Navrotsky et al. 1994). Previous studies show that Fe_2O_3 (Lilova et al. 2012), Mn_2O_3 (Fritsch and Navrotsky 1996) , and V_2O_5 (Dorogova et al. 2007) are the final oxidation states of Fe, Mn, and V in lead borate under oxygen at 700°C and 1 bar. To account for the oxidation effect in the thermodynamic cycles, we used the standard-state enthalpy of reaction from Robie and Hemingway (1995) for FeO oxidation: $4\text{FeO} + \text{O}_2 \rightarrow 2\text{Fe}_2\text{O}_3$. The drop enthalpy (not drop solution enthalpy) for FeO was then calculated using: $\text{Drop Enthalpy}_{\text{FeO}} = \Delta H^{298\text{K}}_{\text{reaction}} + \left[2\Delta H^{\text{Fe}_3\text{O}_3}_{\text{heat content}} - \Delta H^{\text{O}_2}_{\text{heat content}}\right]$. The drop solution enthalpy of FeO is given by (Figure 4B): $\text{Drop Solution Enthalpy}_{\text{FeO}} = \frac{\text{Drop Enthalpy}_{\text{FeO}}}{4} + \left(\text{Drop Solution}_{\text{Fe}_2\text{O}_3} - \Delta H^{\text{Fe}_2\text{O}_3}_{\text{heat content}}\right)$. We applied an equivalent approach for MnO and V_2O_3. When calculating the enthalpy of formation from the elements, we used the enthalpies of formation for all non-transition metal oxides and the reduced forms of transition metal oxides. Our methodology assumes complete H_2O

devolatilization, with F and volatile metals like Na remaining in the melt during the reactions (Westrich and Navrotsky 1981).

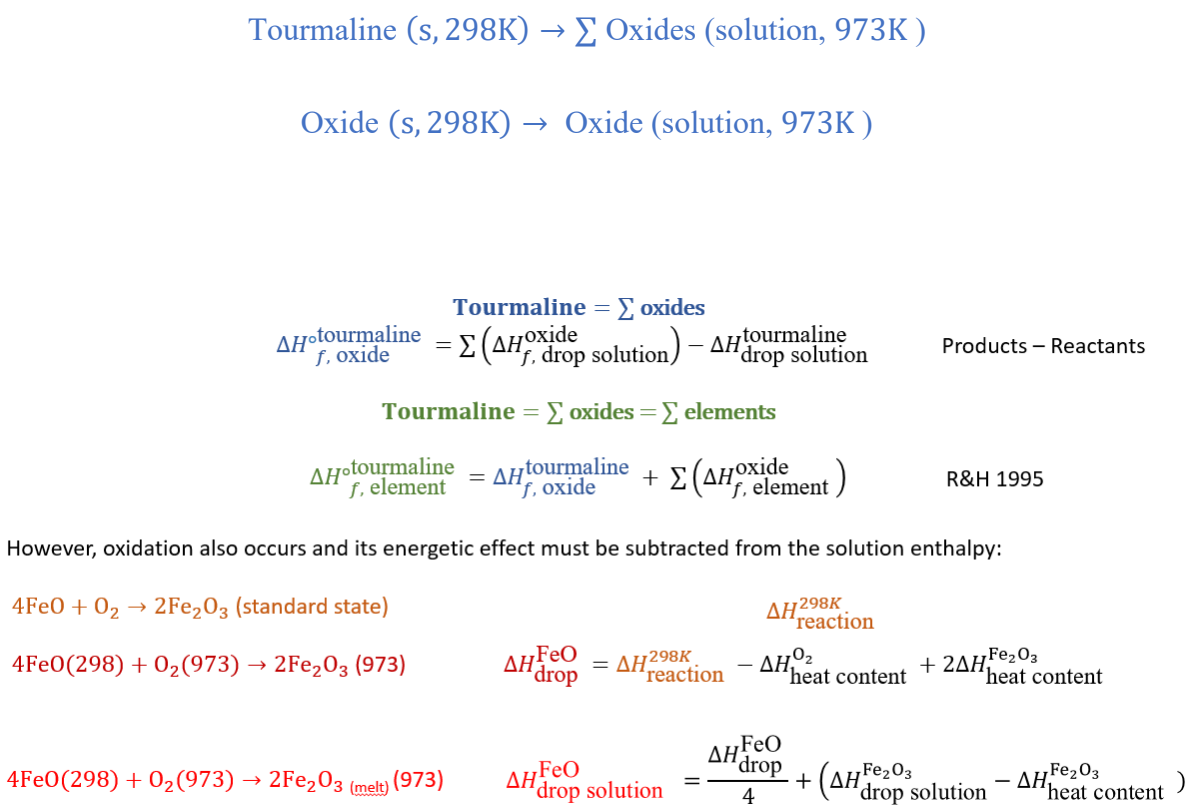

Figure 4B. Thermodynamic Cycle for Formation Enthalpy of Tourmaline This diagram outlines the thermodynamic cycle used to derive the enthalpy of formation of tourmaline. The cycle begins with drop-solution calorimetry measurements of tourmaline and its reference oxides. The formation enthalpy from oxides is calculated as the difference between product and reactant solution enthalpies, using the sign convention appropriate for dissolution (opposite to formation). To obtain the formation enthalpy from the elements, standard enthalpies of formation for the oxides (from Robie and Hemingway, 1995) are added. An oxidation correction is applied via Hess's Law to account for transition metal oxidation during dissolution in lead borate. For example, FeO is oxidized to Fe_2O_3, corrected to 973 K using Cp integrals, and hematite's solution enthalpy is incorporated. Dividing the total corrected enthalpy by 4 yields the drop solution enthalpy of FeO. This cycle leverages the state function nature of enthalpy to isolate measurable steps while highlighting the complexity and error accumulation when multiple oxide references are required.

Step-by-step enthalpy calculation for tourmaline sample TM42. Thermochemical cycle for calculating the enthalpy of formation of tourmaline sample TM42 from the elements. The drop solution enthalpy measured in the calorimeter is combined with the enthalpy of the corresponding oxide mixture and literature enthalpies of formation using Hess's Law. Stepwise values show intermediate calculations and clarify the role of transition-metal and non-transition-metal oxides. The enthalpy of formation values in Step 3 (from oxides) and Step 5 (from elements) are reported at standard reference conditions (298.15 K, 1 bar). of the oxides were subtracted from their drop solution enthalpies to back-calculate the enthalpy at 298.15 K. Importantly, both the drop enthalpy of tourmaline and that of the oxide mixture contain their respective heat contents ($H_{700} - H_{298}$), that is, the energy needed to heat each solid from 298.15 K to the drop temperature (973 K). Therefore, when the two drop enthalpies are subtracted to compute the enthalpy of reaction (tourmaline → oxides), the heat content contributions effectively cancel, making it unnecessary to know or use the heat capacity of tourmaline. This ensures that the final enthalpies are consistently referenced to standard conditions and satisfies Hess's Law.

Step	Description	Formula	Value
0.a	Drop enthalpy of tourmaline (measured)	$\Delta H^{\text{tourmaline}}_{\text{drop solution}}$	0.96223 kJ/g
	Molar Formula Weight	—	1021.1676 g/mol
	Conversion to kJ/mol	0.96223 × 1021.1676	**982.59 kJ/mol**

Step	Description	Formula	Value (kJ/mol)
1	Drop enthalpy of tourmaline (measured)	$\Delta H^{\text{tourmaline}}_{\text{drop solution}}$	982.59
2a	Drop enthalpy of non-TM oxides	$\Delta H^{\text{non-transition metals oxides}}_{\text{drop solution}}$	812.20
2b	Drop enthalpy of transition metal oxides	$\Delta H^{\text{transition metal oxides}}_{\text{drop solution}}$	-92.69
2c	Total oxide enthalpy	$\Delta H^{\text{oxides}}_{\text{drop solution}}$ = 812.20 - 92.69	719.51
3	Enthalpy of formation from the oxides (tourmaline → oxides)	$\Delta H^{\circ\text{tourmaline}}_{f,\text{ oxide}}$ = 982.59 - 719.51	263.08
4	Formation enthalpy of oxides from elements (literature)		-14,251.90
5	Formation enthalpy of tourmaline from elements	$\Delta H^{\circ\text{tourmaline}}_{f,\text{ element}}$ = -14,251.90 - 263.08	-14,514.98

In solution calorimetry, the objective is to determine the stability of a compound relative to a reference state defined by the stable elemental forms. Thermodynamically, all compounds are positioned relative to an elemental hyperplane, a mathematical surface connecting the enthalpies of the pure elements at standard conditions. The enthalpy of formation of a compound corresponds to the vertical distance from this hyperplane at its specific composition. Therefore, the choice of intermediate reference oxides is not based on structural similarity to the compound of interest, but on the use of a compositionally independent and well-characterised set of materials with accurately known enthalpies of formation from the elements. An internally consistent set ensures that all reference phases are tied to the same elemental baseline, that their thermodynamic properties (enthalpy, entropy, volume) are coherent across reactions, and that no inconsistencies arise when combining formation data into reactions or phase equilibria calculations.

The reference oxides we used were NaF and MgF_2 (Westrich and Navrotsky 1981), Na_2O and K_2O (Kiseleva et al. 1996), SiO_2 (Grevel et al. 2005), MgO (Smelik et al. 1994), Al_2O_3 (Navrotsky 2014), CaO (Zhang et al. 2013), TiO_2 (Putnam et al. 1999), Fe_2O_3 (Lilova et al. 2012), Mn_2O_3 (Fritsch and Navrotsky 1996), Li_2O (Xu et al. 1999), V_2O_5 (Dorogova et al. 2007), ZnO (Davies and Navrotsky 1981), SrO (DiCarlo et al. 1993), H_2O (Chase 1998), and B_2O_3 (Wu et al. 2019). We selected these reference oxides because, except for H_2O, they were measured at Navrotsky's solution calorimetry lab, which follows the same protocols and uses the same instruments as the Guo lab at WSU. This ensures consistency within the dataset, though it carries the risk of systematic errors or bias, discussed in the next paragraph. These reference oxides are also the same ones used in major databases to ensure that all experimental data are internally consistent, e.g. (Holland and Powell 1990). For these oxides, we have reliable enthalpies of formation from the elements, which must be especially accurate and precise given the magnitude of the values involved. For these enthalpies of formation, we used the enthalpy of formation of the oxides from the elements from Robie and Hemingway (1995), and when not available, we used Robie et al. (1978). Heat contents were sourced from the NIST-JANAF tables for all oxides, except for MnO, Mn_2O_3, and ZnO (hexagonal), which are absent from the JANAF tables; for these, we also used Robie and Hemingway (1995). Unfortunately, these sources are not internally consistent with one another, but at present, there is no single thermochemical database

that provides a complete and self-consistent set of enthalpies and heat contents for all relevant oxides. Whereas most of these oxides are stable under experimental conditions and were measured directly, some, like Na_2O, K_2O, CaO, and Li_2O, are naturally unstable and were derived from their corresponding (stable) carbonates using additional thermodynamic cycles (Kiseleva et al. 1996; Xu et al. 1999; Zhang et al. 2013). One could argue that the true reference compounds are actually Na_2CO_3, K_2CO_3, $CaCO_3$, and Li_2CO_3, rather than their respective oxides. In this case, it would no longer be referred to as the enthalpy of formation from the oxides, but rather from the compounds. Moreover, Li_2CO_3 was measured at 800°C and extrapolated back to 700°C using heat capacity integrals, as Li_2CO_3 has a melting temperature near 700°C (Xu et al. 1999). This introduces additional uncertainty, as Li speciation in the melt may change over the 100-degree range. The currently obtained oxide enthalpies are therefore best estimates, internally consistent with these carbonates. Similarly, B_2O_3 was derived from drop solution data of boric acid due to the difficulty in obtaining crystalline B_2O_3, as it often occurs in hydrated forms or remains amorphous (Wu et al. 2019). All reference oxides must be anchored relative to each other, meaning that the true reference structures—to which all values are tied—must be extremely well characterised crystal-chemically and calorimetrically.

Ideally, it would have been preferable if no phase changes occurred in the reference oxides up to 700°C to minimize uncertainties in heat content due to transitions, as measuring exact transition enthalpies is challenging. NaF, MgF_2, Na_2O (Na_2CO_3), MgO, K_2O (K_2CO_3), CaO ($CaCO_3$), TiO_2, Li_2O (Li_2CO_3), ZnO, and SrO exhibit no phase transitions under typical conditions. H_2O evaporates at 100°C. Quartz (SiO_2) transitions to β-quartz at 573°C. FeO, often non-stoichiometric, is particularly challenging as it undergoes symmetry changes between 200-300°C and oxidizes to magnetite around 570°C, with further oxidation to hematite around 700°C in an O_2 atmosphere. Fe_2O_3 undergoes a magnetic phase transition at a Néel temperature of 675 °C (Grønvold and Samuelsen 1975; Harrison 2006). Mn_2O_3 transitions from cubic to orthorhombic between 550-600°C, and V_2O_5 melts at 690°C after structural changes starting at 300°C. Boric-acid first dehydrates into metaboric acid around 100°C, then further decomposes into boron oxide (B_2O_3) around 300°C, which melts at approximately 450°C and remains stable in its liquid form up to 700°C. All energy contributions were accounted for using integrated heat capacity curves from JANAF tables. As discussed in the next paragraph, uncertainties in phase transition

enthalpies likely affect thermodynamic cycles by no more than 1–4 kJ/mol. However, their exact impact was not evaluated due to the lack of uncertainty data on heat contents in the JANAF tables. The thermodynamic cycles can be found in Electronic Appendix 4B

Precision: Error propagation Tourmaline is a complex solid solution composed of many oxides. As the number of steps in our thermodynamic cycles increases as more oxides are involved, so does the uncertainty in our calculations. Therefore, it is crucial to perform an uncertainty analysis to determine the cumulative effect of these steps on the uncertainties of our final enthalpy values and ensure the reliability of our thermodynamic models. We performed Monte Carlo (MC) error propagation (Anderson 1976) using the mean and standard error (SE) from the composition and measured drop solution enthalpies of oxides and tourmaline, generating 2000 random samples with Excel's NORM.INV(RAND()) function, which showed that convergence of the MC mean and standard deviation (SD) was reached after 1000 samples. For the mean composition, we used the atoms per formula unit (apfu) derived from the optimised mineral formula based on EMPA, LA-ICP-MS, and Mossbauer spectroscopy, incorporating electron density per site, bond valence sums, and overall charge and site fraction constraints, which was then back-converted to the bulk composition afpu, see Chapter 1. The uncertainty in these apfu was obtained through Monte Carlo error propagation of the EMPA, LA-ICP-MS, and Mossbauer uncertainties into the 31-oxygen normalization scheme, prior to mineral formula optimisation, see Chapter 1 for more details. We included only these uncertainties, excluding those from electron density per site, bond valence, and potential uncertainty-reducing constraints like site fraction or bond valence sums, as accurately weighing these factors is challenging. Thus, the estimate primarily reflects the chemically observed uncertainty after normalization (i.e., charge balancing), affecting both the calculation of reference oxide amounts corresponding to tourmaline and the conversion of measured enthalpies to molar enthalpies by defining the uncertainty in its molar formula weight. In addition to compositional uncertainty, we incorporated the analytical uncertainty from drop solution calorimetry, using the 2SE of the enthalpies of formation for FeO, MnO, and V_2O_3 oxidation reactions, the drop solution enthalpies of the reference oxides, their enthalpies of formation from the elements, and the drop solution enthalpies of the tourmaline. The Monte Carlo analysis of the mean enthalpy of formation from the elements ($\Delta H_f°_{el}$) for tourmalines was conducted by propagating the 2SE

(twice the standard error) of all input data**.** However, the final uncertainty on the $\Delta H_f°_{el}$ estimate was determined using the 2 standard deviations (2SD) of the Monte Carlo iterations, providing a direct measure of the spread in the computed enthalpy values. This approach yielded uncertainties of approximately 30–50 kJ per mol tourmaline on an average $\Delta H_f°_{el}$ of ~−15,000 kJ/mol (0.33 rel%) whereas the measured $\Delta H_f°_{ox}$ account for about half of this uncertainty (15-20 kJ/mol tourmaline) on $\Delta H_f°_{ox}$ of ~-250 kJ/mol (8 rel%). This uncertainty reflects the complexity of tourmaline compositions and aligns with uncertainty values reported by Ogorodova et al. (2012). Uncertainties in the heat contents of the oxides were not included, as the JANAF tables do not provide these values. Table 4D provide the results of the MC analysis.

This uncertainty analysis emphasizes the importance of accurate mineral characterisation, particularly in thermodynamic cycles for enthalpy, where the values are significantly larger than those for molar volumes and entropies. In complex mineral solid solutions, such uncertainty is often overlooked, leading to enthalpy measurements appearing more precise than they are. Error propagation represents a worst-case scenario (Bevington and Robinson 2003), but repeated drop solution measurements, ideally by different researchers and instruments, along with repeated material characterisation, would provide a more accurate uncertainty estimate. A complete covariance matrix of reference oxide uncertainties is essential for accurate uncertainty quantification in thermodynamic cycles. Independent error assumptions in Monte Carlo simulations can overestimate uncertainties by ignoring systematic correlations from shared experimental sources and modelling assumptions (Anderson 1976). Incorporating covariance data will improve precision and reliability in such uncertainty calculations.

While we did not repeated enthalpy measurements, we do have EMPA data from different occasions on the selected tourmaline subset. Renormalizing these using the same 31O norm and deriving molar enthalpies accordingly yields $\Delta H_f°_{el}$ values differing by 50–100 kJ **(**0.3 rel%) and $\Delta H_f°_{ox}$ values differing by 15 kJ (8 rel%) per mol of tourmaline, demonstrating that Monte Carlo error propagation effectively captures variability from repeated compositional analyses. The thermodynamic cycles including the Monte Carlo simulations can be found in Electronic Appendix 4C.

Table 4D. Measured enthalpies of formation from the elements for our sample tourmalines. The first column lists $\Delta H^{\circ\text{tourmaline}}_{f,\text{ oxides}}$ using preferred values for composition and reference oxide enthalpies. The second column is the $\Delta H^{\circ\text{tourmaline}}_{f,\text{ element}}$. The MC mean $\Delta H^{\circ\text{tourmaline}}_{f,\text{ element}}$ is the average from 2000 Monte Carlo trials, incorporating the mean and 2SE of compositions and $\Delta H^{\circ\text{tourmaline}}_{f,\text{ oxides}}$ measurements. 2SD represents the standard deviation of the MC trials. All enthalpy values are at standard state (298.15 K, 1bar)

Sample	$\Delta H^{\circ\text{tourmaline}}_{f,\text{ oxides}}$ (kJ/mol)	$\Delta H^{\circ\text{tourmaline}}_{f,\text{ element}}$ (kJ/mol)	MC Mean $\Delta H^{\circ\text{tourmaline}}_{f,\text{ element}}$ (kJ/mol)	MC $\Delta H^{\circ\text{tourmaline}}_{f,\text{ element}}$ 2SD (kJ/mol)
TM42	-263.08	-14514.98	-14510.46	38.70
TM167B	-406.64	-14876.21	-14875.40	36.64
TM163	-294.36	-14818.09	-14846.22	40.07
TM12	-281.21	-14846.66	-14876.99	54.07
TM24	-292.75	-15178.31	-15229.49	50.81
TM23	-265.45	-15245.90	-15208.28	57.31
bd12	-327.56	-15384.83	-15379.88	52.11
bd9	31.56	-15037.71	-15032.06	42.14
TM37A	-330.10	-15413.66	-15417.50	40.25
TM171	-342.93	-15432.55	-15427.39	58.53
TM28	-330.82	-14720.81	-14704.28	42.87
TM1	-204.16	-14583.82	-14592.17	69.99
TM29	-247.40	-14723.49	-14707.40	36.35
TM64	96.56	-14224.72	-14180.42	46.40
TM156B	-370.13	-14599.14	-14632.88	44.37
olenite_syn	-92.63	-15151.16	-15133.43	122.26

Accuracy: Sensitivity Analysis of Thermodynamic Cycles The Monte Carlo analysis demonstrated precision challenges, while accuracy is assessed here through sensitivity analysis.

Iron Transition metals present challenges in solution calorimetry due to variable valence states, magnetic effects and high oxidation enthalpies. Iron oxides are particularly problematic: Wüstite ($Fe_{1-x}O$, where $0 \leq x \leq 0.125$) exhibits non-stoichiometry and oxidizes to hematite in lead borate at 700° (Lilova et al. 2012). This oxidation process means that accurate enthalpy determination requires knowledge of wüstite's heat content, its oxidation enthalpy to hematite, and hematite's

dissolution enthalpy in lead borate. The specific order of these components does not matter, as long as the thermodynamic cycle remains closed, in accordance with Hess's Law. Lilova et al. (2012) reported stability issues in hematite (α-Fe_2O_3) drop solution measurements in lead borate at 700°C, including Pt crucible discolouration and baseline instabilities, necessitating measurements at 800°C and subsequent extrapolation. This is likely due to α-Fe_2O_3 undergoing a magnetic phase transition around 700°C (Grønvold and Samuelsen 1975). Since our calorimetric work in lead borate is performed at 700°C, this extrapolation introduces uncertainty, further complicated by potential Fe speciation changes in melts at different temperatures.

To address these issues, we conducted a sensitivity analysis by varying iron reference materials and thermodynamic parameters from the literature. Instead of using Robie and Hemingway's (1995) extrapolated enthalpy for hypothetical stoichiometric FeO to determine the wüstite-to-hematite oxidation enthalpy at standard state, we based our framework on the standard-state properties of wüstite ($Fe_{0.94}O$), modifying our tourmaline composition description accordingly. In an alternative cycle, we used Lilova et al. (2012)'s directly measured drop enthalpy of wüstite at 800°C, extrapolated to 700°C using heat content differences from the NIST-JANAF tables. This approach accounts for wüstite heating, oxidation at high temperatures, and Fe_2O_3 disintegration in the melt (Navrotsky 2014). By relying solely on drop calorimetry, it minimises uncertainty propagation from multiple experimental steps in thermodynamic cycles. In contrast, database oxidation enthalpies at standard state compile data from multiple sources, whereas Lilova et al. (2012)'s work is based entirely on drop solution calorimetry, providing a more direct but method-dependent measurement. Additionally, we evaluated different heat content sources, comparing JANAF data with Robie & Hemingway (1995) where available.

These adjustments resulted in a 1–3 kJ difference in the $\Delta H_f°_{el}$ (0.02 rel%) and $\Delta H_f°_{ox}$ (1.2 rel%) per mole of tourmaline. Due to the lack of an ideal iron reference at 700°C in lead borate, we will use Lilova et al. (2012)'s Fe_2O_3 measurement at 800°C, JANAF-NIST heat contents, and Robie & Hemingway's (1995) formation and oxidation enthalpies at standard state for consistency. However, this underscores the need to refine iron reference materials for lead borate calorimetry at 700°C, as most calorimetric work is conducted at this temperature. Since all iron-containing minerals in thermodynamic databases are anchored to FeO and Fe_2O_3, any uncertainty

in these reference data propagates through thermodynamic calculations, directly impacting mineral stability predictions and reaction energetics.

Non transition metals We tested the effect of varying non-transition metal reference oxides using the Holland and Powell (2011) database where available. While their individual uncertainties are lower, they accumulate to $\Delta H_f°_{el}$ uncertainties of 1–3 kJ/mol per mole of tourmaline, comparable to iron, due to the higher proportion of non-transition metals in tourmaline. Fluoride compounds showed the greatest uncertainty due to limited data (Westrich and Navrotsky 1981). For tourmalines that had excess F after all Na was accounted for (as was referenced to NaF), substituting AlF_3 with MgF_2 yielded similar $\Delta H_f°_{el}$ shifts per mol tourmaline as the uncertainties to iron. The $\Delta H_f°_{ox}$ due to the fluoride reference switch showed larger changes by ~15 kJ/mol tourmaline showing that error cancellation can occur.

Gibbsite instead of H_2O as reference oxide for H While H_2O is commonly used, hydroxide is suggested as a potential better reference since structural water contributes differently to ΔH than free H_2O, as reflected in the polyhedron method (Van Hinsberg et al. 2005a, 2005b). Aluminum and hydrogen were referenced using $Al(OH)_3$ (gibbsite) instead of Al_2O_3 and $H_2O(l)$, respectively, so that $Al(OH)_3$ serves as the reference oxide for both Al and H in the thermodynamic cycle. This led to a difference of up to 100 kJ per mole of tourmaline for its $\Delta H_f°_{el}$ (0.66 rel%) and about 10 kJ (4 rel%) per mole of tourmaline for its $\Delta H_f°_{ox}$. This variation stems from the higher enthalpy of formation for gibbsite compared to H_2O. The $Al(OH)_3$ method may account for OH bond breakage, which H_2O evaporation does not, but the 100 kJ difference seems too large to be explained solely by this and may reflect uncertainty in the $Al(OH)_3$ measurement. In contrast, H_2O-related energies are relatively small (around 40 kJ/mol) and its enthalpy of formation from the elements (~200 kJ) is moderate. The larger enthalpy of formation for gibbsite, due to the presence of Al, which makes strong bonds, might obscure small energy changes like H_2O bond breakages, leading to higher uncertainties. Given our better understanding of water-related enthalpies and to stay consistent with Navrotsky group's papers (Navrotsky 2014; Navrotsky and Koryttseva 2023), we prefer to use H_2O as the reference oxide. As Ogorodova et al. (2012)'s thermodynamic cycles involve gibbsite, their enthalpy of formation for tourmaline is not internally consistent with ours.

This underscores the critical need for internal consistency across phases in thermodynamic databases or thermodynamic cycles to ensure accuracy. While instrumental precision can be improved, addressing accuracy requires a coordinated community effort to establish a rigorously consistent reference framework.

Internally consistent database for reference oxides The sensitivity analysis highlights the need for two key components to improve accuracy: (1) an internally consistent database containing the fundamental thermodynamic properties of reference oxides and (2) a comprehensive database compiling drop solution enthalpy of these reference materials in their respective solvents. Establishing both is essential to improving accuracy and consistency in thermodynamic modelling and calorimetric analysis.

Ideally heat contents, $\Delta H_f°_{el}$, and oxidation enthalpies should all be sourced from a single internally consistent database. However, the incompleteness of existing datasets (JANAF-NIST and Robie and Hemingway (1995) and the complex chemistry of tourmaline make a combination of sources almost unavoidable. This lack of a fully internally consistent thermodynamic dataset for reference oxides remains a major challenge for the calorimetry community. Future work should aim to develop a unified, experimentally verified reference oxide database—an internally consistent update of JANAF and Robie & Hemingway (1995), covering a broader compositional space. This database should include a complete covariance uncertainty matrix to enhance the precision and reliability of drop solution calorimetry for determining enthalpies of formation from oxides.

In addition, the drop solution enthalpies of reference oxides should be compiled into a single, accessible database for the calorimetry community. Navrotsky's review papers (Navrotsky 2014; Navrotsky and Koryttseva 2023) provide essential compilations for lead borate and sodium molybdate solvents, a crucial step toward this goal. However, they contain occasional errors—e.g., incorrect references in Table 1 of Navrotsky (2014) and inconsistencies in V_2O_5 measurement temperatures. Expanding this effort with data from multiple laboratories is necessary. Values in compilations (Navrotsky and Koryttseva 2023) often deviate slightly from original studies (see papers above behind the reference oxides), likely due to undocumented

corrections for phase transitions or temperature adjustments. These corrections should be explicitly stated, with current preferred values clearly identified to ensure transparency.

Such an internally consistent reference set for calorimetry should be similar to analytical geochemistry standards, ensuring accuracy. Reference oxides should be fully characterised by multiple labs, with standardized samples distributed for drop solution enthalpy measurements to ensure consistency. While Al_2O_3 or Pt serve as primary standards, periodic measurements of such reference oxides as secondary standards improve their accuracy and provide essential instrumentation checks. This reference database must be continuously updated to maintain consistency across the field.

Such standardization prevents discrepancies arising from differences in reference materials, measurement protocols, or material purity. For example, Wu et al. (2019) reports the enthalpy of formation for B_2O_3 as 46.75 kJ/mol, while Ogorodova et al. (2012) reports 38.77 ± 0.84 kJ/mol, highlighting uncertainties introduced by inter-laboratory variability.

Mineral normalization coherence We also observed large differences in enthalpies when changing the normalization scheme of tourmaline composition (e.g., normalizing to 31 oxygen vs. 18 cations). Given the large $\Delta H_f°_{el}$ for reference oxides, and even their cumulative effect in the calculation of $\Delta H_f°_{ox}$ of tourmaline even minor compositional changes—within the uncertainty of methods like Electron Microprobe, LA-ICP-MS, Karl-Fisher Titration, Mossbauer spectroscopy, and single-crystal XRD—can shift the $\Delta H_f°_{el}$ for tourmalines by 50-100 kJ per mole of tourmaline (0.55 rel%). As we saw in the previous paragraph, differences of that scale were also observed when using EMPA data from the same tourmalines during the initial search for compositions for our thermodynamic model, as well as when comparing the 31-oxygen normalised tourmaline before mineral formula optimisation to the optimised bulk mineral formula. The choice of normalization scheme leads to changes in tourmaline's $\Delta H_f°_{ox}$ by as much as 20 kJ/mol (8% rel%). This underscores the importance of using the same normalization scheme for all tourmalines used to calibrate the thermodynamic models and extend this to the unknowns when applying the model, a concept we refer to here as **mineral normalization coherence**. In earlier chapters, we demonstrated that changes in the assumptions made during mineral normalization, essentially a form of charge balancing, have a greater impact on the final

mineral formula and its uncertainty than the individual propagated uncertainties. This is because the mineral formula optimisation tool tends to guide the results toward similar values, regardless of input data uncertainty. Only when these assumptions are altered does the optimiser produce significantly different values, see Chapter 1. One could argue that mineral normalization coherence is just as crucial, if not more important, than internal consistency within the thermodynamic database itself, see for example sheet 3 of electronic Appendix 4B where the 31O normalisation tourmaline is compared to the recalculated tourmaline composition of the bulk compositional model. Inconsistent normalization schemes can lead to misleading results, affecting both absolute enthalpy values and the relative energies between different tourmaline samples. Phase relationships calculated using a thermodynamic model based on one normalization scheme and an analysed tourmaline based on another are **incomparable**, potentially leading to major inaccuracies in thermodynamic predictions. Since minerals are often measured using different instruments, conditions, and standards, it is challenging to accurately link chemical compositions with enthalpy data. While many databases in earth sciences, such as Holland and Powell (2011) and Berman (1988), are internally consistent, their solid solution model calibrations often lack normalization coherence due to fitting data from various experimental sources that have characterised minerals slightly differently. This issue is compounded by the fact that there is yet to be universal commons on the normalization of complex minerals. This is therefore an inherent limit in modelling accuracy.

5. BULK COMPOSITIONAL MODEL

In this study, the regression targets the $\Delta H^{\circ\text{tourmaline}}_{f,\text{element}}$ of the endemmbers from $\Delta H^{\circ\text{tourmaline}}_{f,\text{element}}$ measured from our solid soluions, i.e., $\Delta H^{\circ\text{tourmaline}}_{f,\text{element}} = \Delta H^{\circ\text{tourmaline}}_{f,\text{element}}(\mathbf{X})$. In principle, this relationship does not need to be purely linear: non-ideal interactions between endmembers could introduce curvature (nonlinearities) into the mixing behavior, captured through excess enthalpy terms (e.g., interaction parameters). However, given the size and distribution of our available dataset, we currently do not attempt to resolve such non-idealities. Instead, we assume a first-order linear approximation between $\Delta H^{\circ\text{tourmaline}}_{f,\text{element}}$ and X, acknowledging that subtle nonlinear mixing effects may remain unresolved. $\Delta H^{\circ\text{tourmaline}}_{f,\text{element}}$ directly links to the full thermodynamic description of the Gibbs free energy. The Gibbs energy is defined as

G=G(P,T,X), where P is pressure, T is temperature, and X represents the endmember proportions. The enthalpy is related to the Gibbs energy by the fundamental thermodynamic relation H=G+TS, where S is entropy. At standard conditions (1 bar and 298.15 K), this simplifies to $G_i^\circ = H_i^\circ - T^\circ S_i^\circ$. Thus, regression of $\Delta H^{\circ\text{tourmaline}}_{f,\text{element}}$ for the endmembers, which, together with S^0 obtained from independent calorimetric constraints (Chapter 3), completely specifies G_i° for each endmember at standard conditions. This anchors the P–T extrapolation needed for phase equilibrium modelling.

We used a bulk composition model to extrapolate the enthalpies of formation of the measured tourmaline solid solutions to their endmembers via multiple linear regression in NCSS (2023), employing a no-intercept constraint, as residual energy is not physically meaningful. We excluded the synthetic B-olenite sample as our bulk model does not model B^T at the moment. The small sample-to-parameter ratio of 1.66 (15/9), results in relatively high uncertainties and multicollinearity, but the model provides a preliminary foundation for a thermodynamic model of tourmaline. The model's fit shows a root mean squared error (RMSE) of 138.15, corresponding to a 0.38% average absolute error. All endmember enthalpies are statistically significant with an alpha of 0.05, but the high standard errors indicate large uncertainty, which is reflected in the wide 95% confidence intervals for the enthalpy estimates. For comparison, the endmember $\Delta H_f{}^\circ_{el}$ uncertainties are 10x times than on the measured values. Complete detail of the NCSS ordinary least square regression with all assumption tests and residual analysis can be found in Appendix 4B.

Table 4E. $\Delta H_f°_{el}$ extrapolated to the bulk compositional model endmembers by ordinary least squares multiple linear regression of the 16 samples for with drop enthalpies were obtained. Figure of the correlation matrix of the bulk model $\Delta H_f°_{el}$ is found below.

Regression Coefficient Confidence Intervals

Independent Variable	$\Delta H_f°_{el}$ Regression Coefficient	$\Delta H_f°_{el}$ Standard Error	95% Confidence Limits of $\Delta H_f°_{el}$	
			Lower	Upper
srlB	-14480.29	478.1794	-15650.35	-13310.23
drvB	-15204.97	362.269	-16091.41	-14318.53
uvtB	-15457.77	310.9338	-16218.6	-14696.94
foiB	-14453.62	593.3715	-15905.54	-13001.69
oleB	-15434.25	1295.456	-18604.12	-12264.38
fluvtB	-15494.47	202.6296	-15990.29	-14998.66
buB	-13956.61	415.7634	-14973.94	-12939.27
mdtwB	-15262.03	2408.87	-21156.32	-9367.74
aorsmB	-15091.78	1004.378	-17549.4	-12634.16

Note: The T-Value used to calculate the confidence limits was 2.447

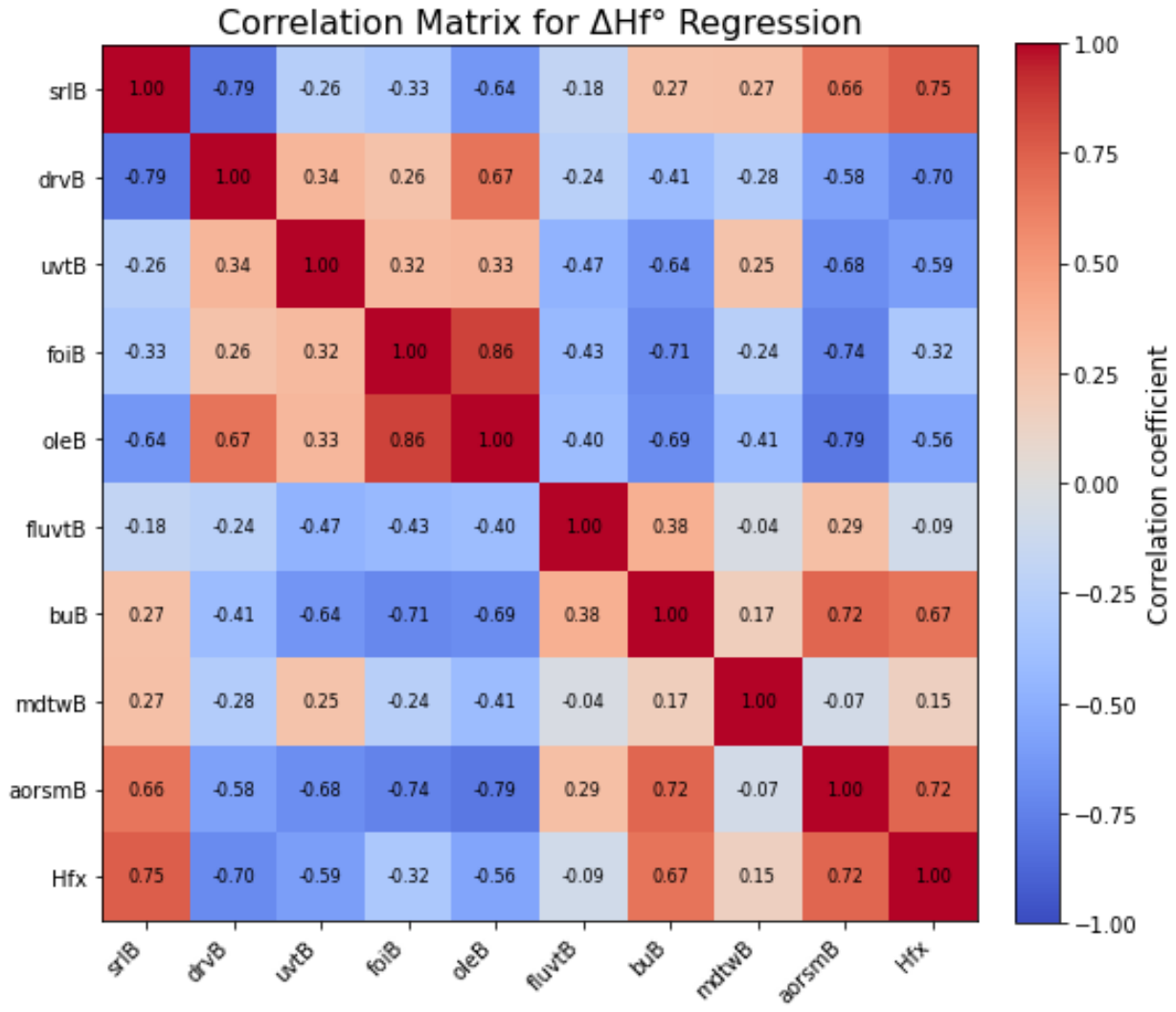

The residuals are not normally distributed, and the R^2_{PRESS} of 0 indicates the model is highly dependent on the data included in each iteration. Significant correlations between endmember enthalpies lead to multicollinearity, as shown by the high VIF factors. This suggests that the data lacks sufficient spread to separate the enthalpic contributions of some endmembers independently. This is unavoidable and can only be solved with more data, and we advocate strongly for more measurements to be made by the community

Table 4F. Summary of the most important statistical parameters of the $\Delta H_f°_{el}$ extrapolation to the bulk compositional model endmembers by ordinary least squares multiple linear regression of the 16 samples for with drop enthalpies were obtained. Correlations show relationships between variables, VIF measures how multicollinearity inflates the variance of regression coefficients, R^2 versus IVs indicates variance explained by other variables, tolerance reflects unexplained variance (1 - R^2), and diagonal (X'X inverse) reflects sensitivity of coefficients to data changes, with larger values suggesting higher instability.

Endmember	Correlations	VIF	R^2 Versus IVs	Tolerance	Diagonal (X'X Inverse)
srlB	drvB (-0.78), oleB (-0.63), aorB (0.66)	12.60	0.9207	0.0793	11.98
drvB	srlB (-0.78), oleB (0.66)	5.44	0.8162	0.1838	6.88
uvtB	buB (-0.64), aorsmB (-0.68)	3.77	0.7347	0.2653	5.07
foiB	oleB (0.86), buB (-0.71), aorsmB (-0.74)	12.40	0.9194	0.0806	18.45
oleB	srlB (-0.63), drvB (0.66), aorsmB (-0.79)	23.84	0.9581	0.0419	87.93
fluvtB	-	1.73	0.4224	0.5776	2.15
buB	uvtB (-0.64), foiB (-0.71), aorsmB (0.72)	5.52	0.8189	0.1811	9.06
mdtwB	-	3.93	0.7455	0.2545	304.04
aorsmB	srlB (0.66), uvtB (-0.68), oleB (-0.79), foiB (-0.74), buB (0.72)	21.35	0.9532	0.0468	52.86

Residual analysis provides an initial indication of which solid solutions are not well modelled by our bulk compositional endmember model. High residuals in relative error percentages are observed for some srlB-foiB solid solutions (tm1: 0.61%, Tm167: 0.66%) and drvB-fluvtB solid solutions (bd12: 0.48%, bd9: 1.86%, tm171: 0.39%), with bd9 showing the largest deviation. Leave-one-out cross-validation reveals that the fluor-buergerite sample (Tm64), which was well fit in the original training set, has an exceptionally high Cook's D (975) and DFFITS (111). This indicates that removing fluor-buergerite from the training set would significantly alter its predicted values and affect all Fe^{3+} and F- thermodynamic predictions, making it a highly influential data point. This shows that near endmember fluor-buergerite behaves very differently from other tourmalines with Fe^{3+}. Other samples with high residuals would similarly lead to different predicted values when excluded. For example, DFBETAS analysis indicates that

Tm167 predominantly influences drvB, foiB, and oleB, while bd9 controls uvtB, foiB, oleB, and fluvtB. Tm171 mainly influences fluvtB, and Tm64 strongly impacts all endmember enthalpies except fluvtB and aorsmB. Additional enthalpy of mixing interaction terms were not considered further, as preliminary subset selection confirmed that none of the additional variables were statistically significant (alpha = 0.05). Their lack of statistical significance does not imply that enthalpy of mixing is absent but rather that our dataset is too limited to constrain these effects with confidence.

We did not apply robust regression, even though it could potentially improve the estimates by reducing sensitivity to outliers. However, multicollinearity in the dataset remains a significant issue, limiting the model's ability to accurately isolate individual effects. Our current regression approach provides an initial estimate for endmember enthalpies, highlighting areas where additional measurements are needed to break correlations and improve the model, rather than offering a complete and final set of enthalpies for detailed thermodynamic modelling.

6. CORRELATION ANALYSIS

We investigated potential empirical relationships between mineralogical and thermodynamic parameters with enthalpy and FTIR $\delta\Delta$ Corr using a correlation matrix. While correlations involving FTIR $\delta\Delta$ Corr were weak to non-existent, we found strong correlations between enthalpy and parameters related to the Fe/Mg ratio, as well as number of electrons at the octahedral Y and Z sites in tourmaline. These include schorl (0.71), dravite (-0.87), olenite (-0.71), AOR (0.77), electron count at the Y site (0.89), electron count at the Z site (0.81), and X-O2 bond distance (0.85), which connects the Y triangle to the X site. Similar strong correlations were observed between Fe/Mg ratios and entropy, resulting in a high correlation between entropy and enthalpy (0.82). This trend is typical in silicates, where the enthalpy of formation for Fe-endmembers is lower than for Mg- or Al^{VI}-endmembers (Holland and Powell 2011). Weaker Fe bonds in the octahedral triangle lead to more vibrational modes, while stronger Mg and Al^{VI} bonds reduce vibrational freedom. The observed anticorrelation between srlB and drvB in both entropy and enthalpy measurements is a direct consequence of using natural samples where $Fe^{2+} \leftrightarrows$ Mg exchange is the dominant exchange vector (van Hinsberg and Schumacher 2011). This anticorrelation has therefore become embedded in all derived enthalpy, entropy, and volume

measurements. Moreover, this correlation is also prevalent in other complex solid solutions involving Fe and Mg (e.g. biotites; annite-phlogopite (Dachs and Benisek 2021; Dachs et al. 2021)). It arises due to the natural compositional variability of these elements, making the relationship effectively unbreakable unless DFT calculations or synthetic samples are employed to independently assess these properties without the inherent correlations present in natural samples.

7. CHALLENGES IN DERIVING ENTHALPIES OF MIXING: INSIGHT FROM FTIR SPECTRA BROADENING

In an attempt to obtain enthalpies of mixing, we used bulk composition and speciation models to extrapolate ΔCorr from FTIR spectra for tourmaline solid solutions to endmembers via multiple linear regression without intercept in NCSS. We performed the regression with and without nonlinear background subtraction of the FTIR data prior to autocorrelation analysis, but since the trends remained consistent despite changes in absolute ΔCorr values, we focused on the non-background-corrected data. The goal was to identify endmember ΔCorr and interaction components δΔCorr that could be correlated with enthalpy of mixing, using the same 49 samples measured for molar volume, heat capacity, and entropy.

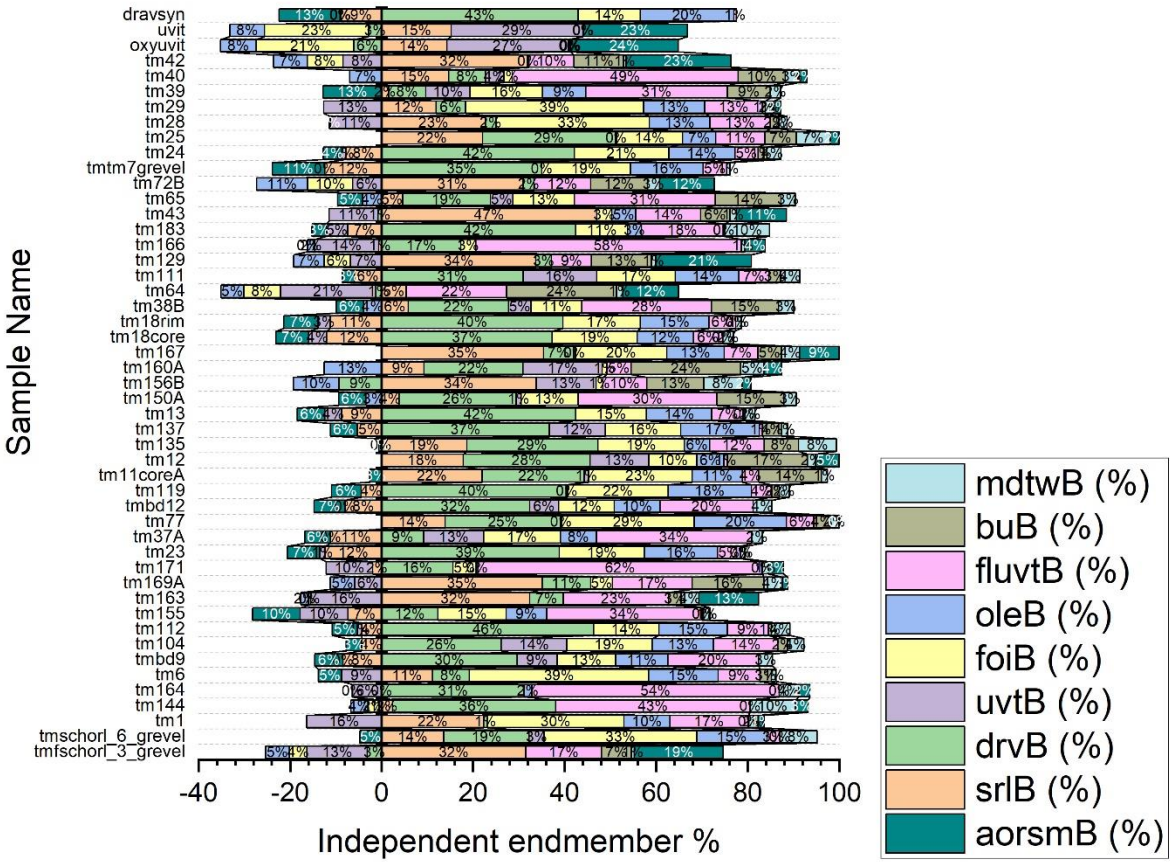

Figure 4C. Independent endmember fractions of the Bulk model for the 49 natural samples selected for FTIR measurements. Chapter 2 outlines their calculation and defines the Bulk model endmember abbreviations.

FTIR spectra of synthetic samples were sharper than those of natural samples. Without synthetic samples, regression models for ΔCorr values against bulk composition and speciation models failed, showing scattered data and average absolute errors over 10%, with no significant endmember or interaction components identified. Including synthetic samples made most endmembers significant, but these results were driven by synthetic samples, primarily fixing uvtB and drvB. In the bulk composition model, srlB, foiB, and aorsmB endmembers remained unfixed due to the lack of synthetic equivalents, with their ΔCorr values influenced by the high X-leverage of the synthetic dravite and uvite samples. In the speciation model, significant differences were observed between ordered and disordered endmembers, but the synthetic

samples were measured by powder-XRD, with long-range order partitioning assumed based on Henry et al. (2011) 's nomenclature rules, meaning they were assumed ordered despite likely being disordered due to short crystallisation times. However, they have sharper FTIR lines indicating limited SRO (see Appendix 4A). When nonsignificant endmembers (oleB and mdtwB for bulk composition; fuvt, ole, mdtw, and pov for speciation) were removed, a single interaction parameter became sometimes significant in some subset selection calculations. However, the specific parameter that became significant varied across models, suggesting it was likely purely by chance. We tested models with an alpha of 0.05, meaning we should expect occasional false positives, as approximately 5% of the time, a variable may appear statistically significant due to random chance rather than a true effect. We used the average ΔCorr of the synthetic samples as anchor points for all endmembers in both models. Despite this, significant interaction components were not identified, as subset selection procedures still failed to yield significant interaction parameters. The lack of systematic trends in FTIR line broadening in the compositional model likely stems from its inability to capture long-range order-disorder in both endmember and solid solution, which is thought to be a key driver for FTIR broadening and related enthalpy of mixing in bulk composition models. Tourmaline has both ordered and disordered endmembers. Similarly, applying anchor points in the speciation model did not lead to significant interaction parameters, likely due to the unproven assumption that ΔCorr values for both ordered and disordered endmembers are the same.

In summary, significant endmember components were identified, but interaction parameters were not significant. There are likely several reasons for this including lack of well-distributed training set, lack of near-endmember compositions, and data scarcity, issues also observed when searching for interaction parameters in molar volume, heat capacity, and entropy data. Still their absence suggests that these parameters are not of high enough magnitude to invalidate models that do not include them, or more likely, correlate with endmember $\Delta H_f°_{el}$ and are therefore build into the endmember data. This means that they are not essential for modelling natural samples. Using the rule of thumb that approximately 5 observations are needed per parameter, our dataset of 50 measurements can only constrain about 10 parameters, and with 9 endmembers $\Delta H_f°_{e,}$ this would leave only 1 interaction parameter. Given that the tourmaline samples were selected to cover a broad compositional range, there is likely insufficient vertical resolution (i.e., limited

data density within specific compositional subsets) for any exchange reaction to emerge as statistically significant. This supports the use of ideal empirical thermodynamic models for natural samples, as the W parameters and long- and short-range disorder appears to be incorporated into averaged endmember properties through a sort of DQF framework. The lack of line broadening distinction between near-endmember compositions and solid solutions in case of natural samples suggests that enthalpies of mixing may not be necessary in these models. The volume paper showed that even with tripled measurements by including molar volumes from the literature (internal consistency issues aside), it remains challenging to derive interaction parameters directly from natural samples. For this reason, many mineral systems rely on synthetic samples along single binaries to derive mixing properties. However, synthesizing tourmaline along a binary is nearly impossible. We hope that future theoretical work, such as DFT calculations, will help determine the interaction parameters needed for further developing the tourmaline model, and at the same time providing a stronger physical basis for the empirical parameters.

8. MODEL VALIDATION AND COMPARISON

Internal Validation Figure 4D shows the measured versus predicted figure for our training set tourmalines. The more negative the Enthalpy the more stable the bonds. Note that F-buergerite sample (tm64) is the least stable of all tourmalines measured. Note also bd9 which has a predicted $\Delta H_f°_{el}$ much lower than her measured one which might indicate a nonideality along the drvB-uvtB binary but data is too scare to make reliable interpretations.

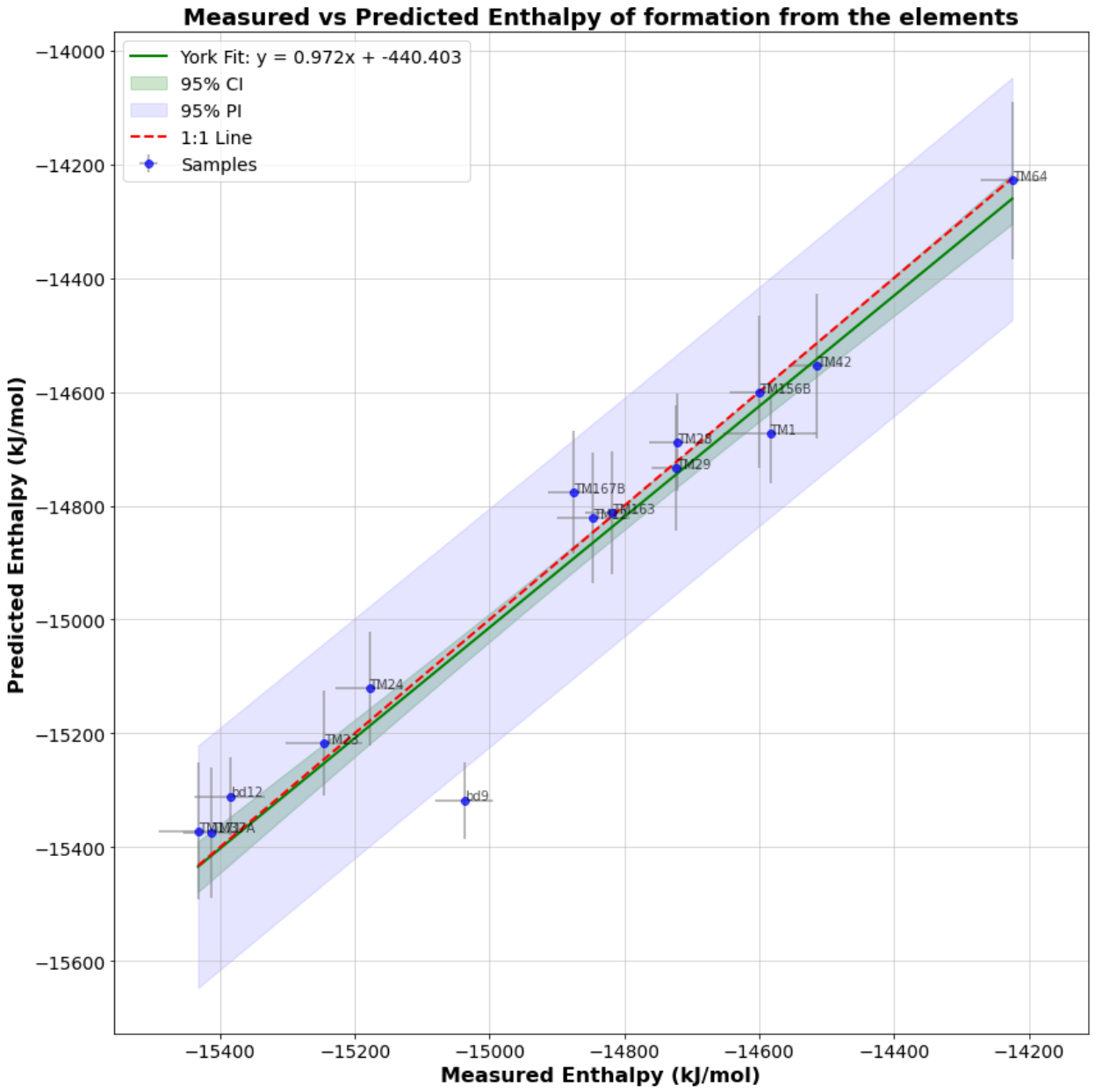

Figure 4D. Measured versus Predicted $\Delta H_f°_{el}$ of our training set tourmalines. Uncertainties are the Monte Carlo 2 standard deviations in case of the measured values.

External Validation At the moment, we only have three tourmaline $\Delta H^{\circ\text{tourmaline}}_{f,\,\text{element}}$ measurements in the literature to compare directly with our values. Our analysis revealed that, due to the lack of normalization coherence and the use of different reference oxides, the original values from Ogorodova et al. (2012) (Dravite: 15,410 ± 24 kJ/mol, Schorl: 14,500 ± 44 kJ/mol) and Kuyunko et al.(1984) (Mg-foitite: -15,437 ± 19 kJ/mol) are incomparable. There are significant

differences in material characterisation to make them compositionally internally consistent with our data. However, we attempted a renormalization of their compositions using a 31 O basis. Using their measured tourmaline drop enthalpies and our reference oxide set, we recalculated their $\Delta H^{\circ\text{tourmaline}}_{f,\text{element}}$ values for tourmaline. For schorl_Ogo, which was measured by drop calorimetry, the recalculated value could be directly incorporated into our cycles. In contrast, dravite_Ogo and Kuyunko were measured by solution calorimetry (no drop). To ensure compatibility with our cycle, we calculated their heat contents between 298 and 973 K by integrating their high-temperature Cp curves, obtaining values of 432.80 kJ/mol and 358.00 kJ/mol, respectively. Ogorodova et al. (2012) (Dravite: -15042.59± 125 kJ/mol, Schorl: 14836.87 ± 44 kJ/mol) and Kuyunko et al. (1984) (Mg-foitite: -14916.23 ± 44 kJ/mol), where the uncertainties are the MC propagated 2SE. The 31O normalised apfu were used to calculate the independent bulk endmember fractions of these tourmalines which can be found in e-Appendix 4D. We then used our $\Delta H^{\circ\text{tourmaline}}_{f,\text{element}}$ bulk model to predict these three tourmaline propagating their undertainties using the covariance matrix of the regression coeffients. This resulted in:

Table 4G. Comparison between measured and predicted standard-state enthalpies of formation (ΔHf°) for the tourmaline samples *schorl_Ogo, dravite_Ogo,* and *kuyunko*. Predicted values and their propagated uncertainties are based on regression from endmember enthalpies. The difference column shows predicted minus measured ΔHf° values.

Sample	**Predicted ΔHf° (kJ/mol)**	**Predicted Uncertainty (kJ/mol)**	**Measured ΔHf° (kJ/mol)**	**Measured Uncertainty (kJ/mol)**	**Differences (kJ/mol)**
schorl_Ogo	-14610.5	265.6775	-14836.9	44	226.3942
dravite_Ogo	-15237.7	136.2131	-15042.59	125	-195.156
kuyunko	-14904.4	362.0905	-14916.23	44	11.81223

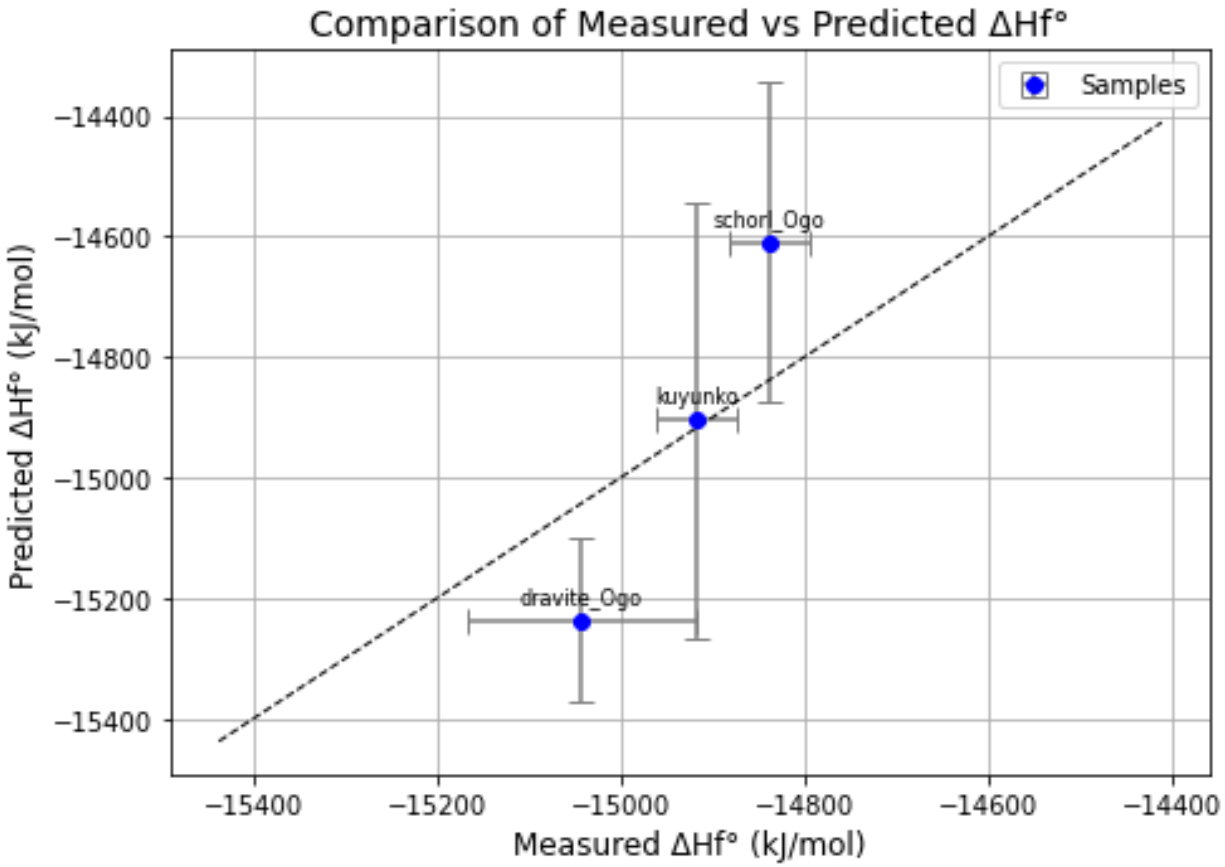

Figure 4E. Measured versus predicted standard-state enthalpies of formation (ΔHf°) for tourmaline test samples. Error bars represent the propagated uncertainty from the endmember regression model. The dashed line indicates the 1:1 line for perfect agreement between predicted and measured values.

The only other thermodynamic model for tourmaline is by Van Hinsberg and Schumacher (2007) which is an improvement on an initial model by Garofalo et al. (2000), which derived their estimates for the enthalpies of formation for their chosen endmember systems using the polyhedral approach as estimation method. This method uses polyhedra, rather than endmembers, as chemical components to build their endmembers. Polyhedral energies are extracted from large mineral databases and are primarily characterised by their element, coordination number, and the presence of hydrogen attached to oxygen within the polyhedra. (Hinsberg and Schumacher 2007) However, the method does not account for energy changes due to crystal topology or electron density deformation around the polyhedron, i.e., next-nearest

neighbor effects. Therefore, the polyhedral energies are not specific to the tourmaline system but represent average energies for similar coordination polyhedra in a broad set of minerals. The enthalpies obtained from this method were subsequently optimised with a small set of experimental data and existing databases (van Hinsberg 2006).

Comparing the enthalpies of formation from this estimated tourmaline model (Table 4H) shows that the uncertainties are of a similar order, and our measurements lie within the 1SE of the polyhedral model (and vice versa), meaning they fall well within each other's confidence intervals. However, the uncertainties are significant in both our bulk compositional model, which is based on only 15 measurements, and the polyhedral model, leading to differences that can still amount to 200-300 kJ. These represent absolute differences, assuming the values were constrained independently, without accounting for the correlations present in our dataset due to multicollinearity.

Table 4H. $\Delta H_f°_{el}$ of select bulk model endmembers compared with the same endmembers as derived from the polyhedron method of van Hinsberg and Schumacher (2007).

End-member	H (kJ/mol)	Error (1SE) (kJ/mol)	H (kJ/mol) Polyhedral	Error (1SE) (kJ/mol) Polyhedral	Difference (kJ/mol)
srlB	-14480	478.179	-14443	340.304	-37.261
drvB	-15205	362.269	-15579.5	325.350	374.506
uvtB	-15458	310.934	-15669.2	313.945	211.383
foiB	-14454	593.372	-14775.2	318.352	321.551
oleB	-15434	1295.460	-15255.7	308.632	-178.548
buB	-13957	415.763	-13752.3	594.539	-204.327

9. CONCLUSIONS

A first comprehensive set of standard enthalpies of formation from the elements ($\Delta H^{\circ \text{tourmaline}}_{f,\,\text{element}}$) for tourmaline is presented, internally consistent both compositionally and energetically with our chosen set of reference oxides. Even though 15 samples were measured, the complexity of tourmaline structure still leads to significant uncertainties in endmember properties these data should be regarded as starting point for optimisation using natural and experimental

compositional constraints in the CALPHAD approach given that the reaction enthalpies $\Delta Hrxn°_{el}$,<< $\Delta H_f°_{el}$ in equivalent approach as was done for amphiboles (Dale et al. 2000, 2005).

The results provide a preliminary thermodynamic framework but highlight challenges such as high uncertainties, multicollinearity, and dataset dependence. The impact of reference oxide selection, normalization schemes, and mixing behavior underscores the need for methodological consistency. Future research should prioritise refining these $\Delta H_f°_{el}$, incorporating more comprehensive datasets and natural constraint. Employing advanced methods like density functional theory (DFT) to enhance the accuracy of endmember and mixing enthalpies provides another promising route. DFT can greatly expand the sample space and provide detailed insights into atomic interactions and energetics, offering a deeper understanding of the physical origin of thermodynamic properties while complementing experimental data. Given the challenges in obtaining reliable mixing parameters from natural samples, theoretical modelling and synthetic samples could yield a more physically grounded understanding of tourmaline's complex solid solutions. Ultimately, these advancements will lead to more accurate thermodynamic models for tourmaline, improving predictions of its stability and geochemical behavior across various environmental conditions.

REFERENCES

Altieri, A., Luppi, R., Skogby, H., Hålenius, U., Tempesta, G., Pezzotta, F., and Bosi, F. (2023) Thermal treatment of the tourmaline Fe-rich princivalleite Na(Mn2Al)Al6(Si6O18)(BO3)3(OH)3O. Physics and Chemistry of Minerals, 50, 27.

Anderson, G.M. (1976) Error propagation by the Monte Carlo method in geochemical calculations. Geochimica et Cosmochimica Acta, 40, 1533–1538.

Anderson, G.M. (2005) Thermodynamics of natural systems, 2nd ed., 648 p. Cambridge University Press, Cambridge.

Bačík, P., Ozdín, D., Miglierini, M., Kardošová, P., Pentrák, M., and Haloda, J. (2011) Crystallochemical effects of heat treatment on Fe-dominant tourmalines from Dolní Bory (Czech Republic) and Vlachovo (Slovakia). Physics and Chemistry of Minerals, 38, 599–611.

Beattie, P. (1993) Olivine-melt and orthopyroxene-melt equilibria. Contributions to Mineralogy and Petrology, 115, 103–111.

Berman, R.G. (1988) Internally-consistent thermodynamic data for minerals in the system Na2O-K2O-CaO-MgO-FeO-Fe2O3-Al2O3-SiO2-TiO2-H2O-CO2. Journal of petrology, 29, 445–522.

Berman, R.G., and Brown, T.H. (1985) Heat capacity of minerals in the system Na2O-K2O-CaO-MgO-FeO-Fe2O3-Al2O3-SiO2-TiO2-H2O-CO2: representation, estimation, and high temperature extrapolation. Contributions to Mineralogy and Petrology, 89, 168–183.

Bevington, P.R., and Robinson, D.K. (2003) Data reduction and error analysis. McGraw-Hill, New York, 320.

Blanch, A.J., Quinton, J.S., Lenehan, C.E., and Pring, A. (2007) Autocorrelation infrared analysis of mineralogical samples: The influence of user controllable experimental parameters. Analytica chimica acta, 590, 145–150.

Boffa Ballaran, T., and Carpenter, M.A. (2003) Line Broadening and Enthalpy: Some Empirical Calibrations of Solid Solution Behaviour from IR Spectra. Phase Transitions, 76, 137–154.

Boffa Ballaran, T., Carpenter, M.A., Geiger, C.A., and Koziol, A.M. (1999) Local structural heterogeneity in garnet solid solutions. Physics and Chemistry of Minerals, 26, 554–569.

Bosi, F., Skogby, H., and Hålenius, U. (2016) Thermally induced cation redistribution in Fe-bearing oxy-dravite and potential geothermometric implications. Contributions to Mineralogy and Petrology, 171, 1–14.

Bosi, F., Skogby, H., Hålenius, U., and Ciriotti, M.E. (2018) Experimental cation redistribution in the tourmaline lucchesiite, CaFe2+3Al6(Si6O18)(BO3)3(OH)3O. Physics and Chemistry of Minerals, 45, 621–632.

Bosi, F., Skogby, H., and Hålenius, U. (2019) Thermally induced cation redistribution in fluor-elbaite and Fe-bearing tourmalines. Physics and Chemistry of Minerals, 46, 371–383.

Castaneda, C., Eeckhout, S.G., Costa, G.M. da, Botelho, N.F., and De Grave, E. (2006) Effect of heat treatment on tourmaline from Brazil. Physics and Chemistry of Minerals, 33, 207–216.

Celata, B., Stagno, V., Capizzi, L.S., Bosi, F., Ballirano, P., D'Arco, A., Stopponi, V., Lupi, S., Scarlato, P., and Skogby, H. (2023a) Schorl breakdown at upper mantle conditions: Insights from an experimental study at 3.5 GPa. Lithos, 438, 106999.

Celata, B., Ballirano, P., Bosi, F., Andreozzi, G.B., and Beckett-Brown, C. (2023b) Thermal behavior of schorl up to breakdown temperature at room pressure. Periodico di Mineralogia, 92.

Chase, M.W. (1998) NIST-JANAF Thermochemical Tables 4th ed. J. of Physical and Chemical Reffernce Data, 1529–1564.

Dachs, E., and Benisek, A. (2021) A new activity model for Fe–Mg–Al biotites: I—Derivation and calibration of mixing parameters. Contributions to Mineralogy and Petrology, 176, 22.

Dachs, E., Roozen, S., and Benisek, A. (2021) A new activity model for Fe–Mg–Al biotites: II—Applications in the K2O–FeO–MgO–Al2O3–SiO2–H2O (KFMASH) system. Contributions to Mineralogy and Petrology, 176, 23.

Dale, J., Holland, T., and Powell, R. (2000) Hornblende–garnet–plagioclase thermobarometry: a natural assemblage calibration of the thermodynamics of hornblende. Contributions to Mineralogy and Petrology, 140, 353–362.

Dale, J., Powell, R., White, R.W., Elmer, F.L., and Holland, T.J.B. (2005) A thermodynamic model for Ca-Na clinoamphiboles in Na2O-CaO-FeO-MgO-Al2O3-SiO2-H2O-O for petrological calculations. Journal of Metamorphic Geology, 23, 771–791.

Davies, P.K., and Navrotsky, A. (1981) Thermodynamics of solid solution formation in NiO-MgO and NiO-ZnO. Journal of Solid State Chemistry, 38, 264–276.

Desbois, G., and Ingrin, J. (2007) Anisotropy of hydrogen diffusion in tourmaline. Geochimica et Cosmochimica Acta, 71, 5233–5243.

DiCarlo, J., Mehta, A., Banschick, D., and Navrotsky, A. (1993) The energetics of la2-xaxnio4-y (A= ba, sr). Journal of Solid State Chemistry, 103, 186–192.

Dorogova, M., Navrotsky, A., and Boatner, L.A. (2007) Enthalpies of formation of rare earth orthovanadates, REVO4. Journal of Solid State Chemistry, 180, 847–851.

Dutrow, B.L., and Henry, D.J. (2011) Tourmaline: a geologic DVD. Elements, 7, 301–306.

Filip, J., Bosi, F., Novák, M., Skogby, H., Tuček, J., Čuda, J., and Wildner, M. (2012) Iron redox reactions in the tourmaline structure: High-temperature treatment of Fe3+-rich schorl. Geochimica et Cosmochimica Acta, 86, 239–256.

Fritsch, S., and Navrotsky, A. (1996) Thermodynamic Properties of Manganese Oxides. Journal of the American Ceramic Society, 79, 1761–1768.

Garofalo, P., Audétat, A., Gunther, D., Heinrich, C.A., and Ridley, J. (2000) Estimation and testing of standard molar thermodynamic properties of tourmaline end-members using data of natural samples. American Mineralogist, 85, 78–88.

Goncharov, V.G., Nisbet, H., Strzelecki, A., Benmore, C.J., Migdisov, A.A., Xu, H., and Guo, X. (2022) Energetics of hydroxylbastnäsite solid solutions, La1- xNdxCO3OH. Geochimica et Cosmochimica Acta, 330, 47–66.

Gottschalk, M. (1996) Internally consistent thermodynamic data for rock-forming minerals in the system SiO2-TiO2-Al2O3-Fe2O3-CaO-MgO-FeO-K2O-Na2O-H2O-CO2. European Journal of Mineralogy, 175–223.

Grevel, K.-D., Kahl, W.-A., Majzlan, J., Navrotsky, A., Lathe, C., and Fockenberg, T. (2005) Thermodynamic properties of magnesiochloritoid. European Journal of Mineralogy, 17, 587–598.

Grønvold, F., and Samuelsen, E.J. (1975) Heat capacity and thermodynamic properties of α-Fe2O3 in the region 300–1050 K. Antiferromagnetic transition. Journal of Physics and chemistry of Solids, 36, 249–256.

Guo, X., Szenknect, S., Mesbah, A., Labs, S., Clavier, N., Poinssot, C., Ushakov, S.V., Curtius, H., Bosbach, D., Ewing, R.C., and others (2015) Thermodynamics of formation of coffinite, $USiO_4$. Proceedings of the National Academy of Sciences, 112, 6551–6555.

Guo, X., Navrotsky, A., Kukkadapu, R.K., Engelhard, M.H., Lanzirotti, A., Newville, M., Ilton, E.S., Sutton, S.R., and Xu, H. (2016) Structure and thermodynamics of uranium-containing iron garnets. Geochimica et Cosmochimica Acta, 189, 269–281.

Guo, X., White, J.T., Nelson, A.T., Migdisov, A., Roback, R., and Xu, H. (2018) Enthalpy of formation of U3Si2: A high-temperature drop calorimetry study. Journal of Nuclear Materials, 507, 44–49.

Harrison, R.J. (2006) Microstructure and magnetism in the ilmenite-hematite solid solution: A Monte Carlo simulation study. American Mineralogist, 91, 1006–1024.

Henry, D.J., Novák, M., Hawthorne, F.C., Ertl, A., Dutrow, B.L., Uher, P., and Pezzotta, F. (2011) Nomenclature of the tourmaline-supergroup minerals. American Mineralogist, 96, 895–913.

Holland, T.J.B., and Powell, R. (1990) An enlarged and updated internally consistent thermodynamic dataset with uncertainties and correlations: the system K2O–Na2O–CaO–MgO–MnO–FeO–Fe2O3–Al2O3–TiO2–SiO2–C–H2–O2. Journal of metamorphic Geology, 8, 89–124.

——— (2011) An improved and extended internally consistent thermodynamic dataset for phases of petrological interest, involving a new equation of state for solids. Journal of Metamorphic Geology, 29, 333–383.

Kiseleva, I., Navrotsky, A., Belitsky, I.A., and Fursenko, B.A. (1996) Thermochemistry of natural potassium sodium calcium leonhardite and its cation-exchanged forms. American Mineralogist, 81, 668–675.

Kuyunko, N.S., Semenov, Y.V., Gurevich, V.M., Kuzmin, V.I., Topor, N.D., and Gorbunov, V.E. (1984) Experimental Determination of the Thermodynamic Properties of Dravite Tourmaline. Geokhimiya, 1458–1465.

Le Losq, C., Cicconi, M.R., and Neuville, D.R. (2021) Iron in Silicate Glasses and Melts: Implications for Volcanological Processes. In R. Moretti and D.R. Neuville, Eds., Geophysical Monograph Series pp. 233–253. Wiley.

Lilova, K.I., Xu, F., Rosso, K.M., Pearce, C.I., Kamali, S., and Navrotsky, A. (2012) Oxide melt solution calorimetry of Fe2+-bearing oxides and application to the magnetite-maghemite (Fe3O4-Fe8/3O4) system. American Mineralogist, 97, 164–175.

Liu, X., Yu, C., Yang, W., Xie, L., and Liang, S. (2019) Thermal decomposition kinetics of Fe-rich tourmaline. European Journal of Mineralogy, 31, 919–928.

McMillan, P.F., and Hofmeister, A.M. (1988) Chapter 4. Infrared and Raman Spectroscopy. In F.C. Hawthorne, Ed., Spectroscopic Methods in Mineralogy and Geology pp. 99–160. De Gruyter.

Navrotsky, A. (2001) Thermochemistry of nanomaterials. In Nanoparticles and the Enviroment Vol. 44, pp. 73–103. Mineralogical Society of America.

——— (2014) Progress and New Directions in Calorimetry: A 2014 Perspective. Journal of the American Ceramic Society, 97, 3349–3359.

Navrotsky, A., and Koryttseva, A. (2023) Acid–base properties of oxides derived from oxide melt solution calorimetry. Molecules, 28, 4623.

Navrotsky, A., Rapp, R.P., Smelik, E., Burnley, P., Circone, S., Chai, L., and Bose, K. (1994) The behavior of H2O and CO2 in high-temperature lead borate solution calorimetry of volatile-bearing phases. American Mineralogist, 79, 1099–1109.

Navrotsky, A., Mazeina, L., and Majzlan, J. (2008) Size-Driven Structural and Thermodynamic Complexity in Iron Oxides. Science, 319, 1635–1638.

Ogorodova, L.P., Melchakova, L.V., Kiseleva, I.A., and Peretyazhko, I.S. (2012) Thermodynamics of natural tourmalines—Dravite and schorl. Thermochimica acta, 539, 1–6.

Pieczka, A., and Kraczka, J. (2004) Oxidized tourmalines—a combined chemical, XRD and Mossbauer study. European Journal of Mineralogy, 16, 309–321.

Putnam, R.L., Navrotsky, A., Woodfield, B.F., Boerio-Goates, J., and Shapiro, J.L. (1999) Thermodynamics of formation for zirconolite (CaZrTi2O7) from T= 298.15 K to T= 1500 K. The Journal of Chemical Thermodynamics, 31, 229–243.

Reece, M.E., Li, J., Strzelecki, A.C., Wen, J., Zhang, Q., and Guo, X. (2024) Surface thermodynamics of yttrium titanate pyrochlore nanomaterials. Nanoscale, 16, 5421–5432.

Robie, R.A., and Hemingway, B.S. (1995) Thermodynamic properties of minerals and related substances at 298.15 K and 1 bar (10^5 pascals) pressure and at higher temperatures. Bulletin. U.S. Geological Survey.

Robie, R.A., Hemingway, B.S., and Fisher, J.R. (1978) Thermodynamic properties of minerals and related substances at 298.15 K and 1 bar (10^5 pascals) pressure and at higher temperatures. Bulletin. U.S. Geological Survey.

Salje, E.K.H., Carpenter, M.A., Malcherek, T., and Boffa Ballaran, T. (2000) Autocorrelation analysis of infrared spectra from minerals. European Journal of Mineralogy, 12, 503–519.

Smelik, E.A., Jenkins, D.M., and Navrotsky, A. (1994) A calorimetric study of synthetic amphiboles along the tremolite-tschermakite join and the heats of formation of magnesiohornblende and tschermakite. American Mineralogist, 79, 1110–1122.

Strzelecki, A.C., Bourgeois, C., Kriegsman, K.W., Estevenon, P., Wei, N., Szenknect, S., Mesbah, A., Wu, D., Ewing, R.C., Dacheux, N., and others (2020) Thermodynamics of $CeSiO_4$: Implications for Actinide Orthosilicates. Inorganic Chemistry, 59, 13174–13183.

Strzelecki, A.C., Cockreham, C.B., Parker, S.S., Mann, S.C., Lhermitte, C., Wu, D., Guo, X., Monreal, M., Jackson, J.M., and Mitchell, J. (2024) A new methodology for measuring the enthalpies of mixing and heat capacities of molten chloride salts using high temperature drop calorimetry. Review of Scientific Instruments, 95.

van Hinsberg, V.J. (2006) Tourmaline: Monitor of the P-T-X evolution in rocks. PhD thesis, University of Bristol.

van Hinsberg, V.J., and Schumacher, J.C. (2007) Using estimated thermodynamic properties to model accessory phases: the case of tourmaline. Journal of Metamorphic Geology, 25, 769–779.

van Hinsberg, V.J., and Schumacher, J.C. (2011) Tourmaline as a petrogenetic indicator mineral in the Haut-Allier metamorphic suite, Massif Central, France. The Canadian Mineralogist, 49, 177–194.

van Hinsberg, V.J., Vriend, S.P., and Schumacher, J.C. (2005a) A new method to calculate end-member thermodynamic properties of minerals from their constituent polyhedra I: enthalpy, entropy and molar volume. Journal of Metamorphic Geology, 23, 165–179.

——— (2005b) A new method to calculate end-member thermodynamic properties of minerals from their constituent polyhedra II: heat capacity, compressibility and thermal expansion. Journal of Metamorphic Geology, 23, 681–693.

van Hinsberg, V.J., Henry, D.J., and Marschall, H.R. (2011) Tourmaline: an ideal indicator of its host environment. The Canadian Mineralogist, 49, 1–16.

Vho, A., Lanari, P., and Rubatto, D. (2019) An Internally-Consistent Database for Oxygen Isotope Fractionation Between Minerals. Journal of Petrology, 60, 2101–2129.

Westrich, H.R., and Navrotsky, A. (1981) Some thermodynamic properties of fluorapatite, fluorpargasite, and fluorphlogopite. American journal of science, 281, 1091–1103.

Wolf, M.B., and London, D. (1997) Boron in granitic magmas: stability of tourmaline in equilibrium with biotite and cordierite. Contributions to Mineralogy and Petrology, 130, 12–30.

Wu, L., Koryttseva, A., Groß, C.B.M., and Navrotsky, A. (2019) Thermochemical investigation of lithium borate glasses and crystals. Journal of the American Ceramic Society, 102, 4538–4545.

Xu, H., Heaney, P.J., Navrotsky, A., Topor, L., and Liu, J. (1999) Thermochemistry of stuffed quartz-derivative phases along the join $LiAlSiO_4$ -SiO_2. American Mineralogist, 84, 1360–1369.

Zhang, Y.-Q., Radha, A.V., and Navrotsky, A. (2013) Thermochemistry of two calcium silicate carbonate minerals: scawtite, Ca7 (Si6O18)(CO3)· 2H2O, and spurrite, Ca5 (SiO4) 2 (CO3). Geochimica et Cosmochimica Acta, 115, 92–99.

Bridging Text Between Manuscripts (Chapter 4-Chapter 5)

Chapter 5 builds upon the compositional foundation and thermodynamic parameter calibration established in Chapters 1 through 4 by integrating the results into a complete solution model for tourmaline. The preceding chapters defined the composition and speciation space and the positions of the training set tourmalines in this space (Chapters 1–2), calibrated the pressure and temperature dependence of Gibbs free energy via molar volume (Chapter 2), entropy and heat capacity (Chapter 3), and anchored the energy functions with measured enthalpies of formation (Chapter 4).

Chapter 5 formalizes this framework by summarizing the two thermodynamic models: a bulk compositional model for use with chemical data alone, and a speciation model incorporating crystallographic site populations. These models define the standard state properties and the caloric equation of state of tourmaline endmembers and propagate uncertainties using full covariance matrices. Importantly, this chapter extends beyond by addressing the configurational entropy term—required to complete the Gibbs free energy formulation. The volumetric equation of state has minimal effect on solid phases over the pressure–temperature range of interest, and as shown by the previous chapters, compositional equations of state could not be meaningfully extracted from the data due to statistical insignificance. Consequently, configurational entropy emerges as the dominant contributor to non-ideality in the Gibbs energy landscape. It is modelled using generalized Bragg-Williams expressions for long-range order (LRO), and through molecular mixing approximations for short-range order (SRO), both grounded in the degrees of freedom defined by site occupancy and charge balance constraint.

In doing so, Chapter 5 closes the thermodynamic cycle initiated in Chapter 1, moving from empirical measurements and calibrated endmember properties toward a predictive, internally consistent solution model suitable for implementation in thermodynamic modelling software. The inclusion of configurational entropy, the treatment of disorder among site multiplicities by randomization, and the explicit discussion of model dimensionality underscore the complexity. This chapter sets the stage for tourmaline's application in phase equilibria modelling, geothermobarometry, and fluid-rock interaction studies.

Thermodynamic model for Tourmaline

Ludwig Bolzmann, who spent much of his life studying statistical mechanics, died in 1906, by his own hand. Paul Ehrenfest, carrying on the work, died similarly in 1933.

Now it is our turn to study statistical mechanics…

The opening paragraph of Goodstein's textbook "States of Matter"

Goodstein, David L. *States of matter*. Courier Corporation, 1985.

Chapter 5. Model Integration and Conclusions

Stan Roozen

1. SUMMARY OF THERMODYNAMIC DATA

This study develops a thermodynamic model for Li-poor tourmalines in the chemical system Na-Ca-Mg-Fe^{2+}-Fe^{3+}-Al-Si-B-O-H-F and the preceding chapters have presented newly measured data for molar volume (chapter 2), entropy and heat capacity (chapter 3) and enthalpy (chapter 4), all grounded in a comprehensive and consistent crystallo-chemical characterisation of the tourmaline samples set (chapter 1) on which these properties were determined. Here, these data are integrated into a tourmaline solution model for use in thermodynamic modelling software and remaining limitations and challenges are presented and discussed.

1.1 Speciation model standard state properties and caloric EoS

The speciation model consists of the following endmembers (Table 5A) and the thermodynamic properties of these endmembers are given in Tables 5B-C. Enthalpy was not defined for the speciation model, because of the limited set of measured enthalpies (see chapter 4).

Table 5A. Speciation independent endmember definitions and independent site fractions**.**

Endmember	1X	3Y	6Z	6T	3B	27O	3V	W
schorl (srl)	Na	Fe_3	Al_6	Si_6	B_3	O_{27}	OH_3	OH
dravite (drv)	Na	Mg_3	Al_6	Si_6	B_3	O_{27}	OH_3	OH
uvite (uvt)	Ca	Mg_3	$MgAl_5$	Si_6	B_3	O_{27}	OH_3	OH
feruvite (fuvt)*	Ca	Fe_3	$FeAl_5$	Si_6	B_3	O_{27}	OH_3	OH
foitite (foi)	Vac	Fe_2Al	Al_6	Si_6	B_3	O_{27}	OH_3	OH
olenite (ole)	Na	Al_3	Al_6	Si_6	B_3	O_{27}	O_3	OH
dravite-disordered (drv-dis)*	Na	Mg_2Al	$MgAl_5$	Si_6	B_3	O_{27}	OH_3	OH
oxy-dravite (odrv)	Na	Al_2Mg_1	$MgAl_5$	Si_6	B_3	O_{27}	OH_3	O
fluor-uvite (fluvt)	Ca	Mg_3	$MgAl_5$	Si_6	B_3	O_{27}	OH_3	F
buergerite (bu)*	Na	Fef_3	Al_6	Si_6	B_3	O_{27}	O_3	OH
magnesium-dutrowite (mdtw)*	Na	$MgTi_2$	Al_6	Si_6	B_3	O_{27}	O_3	O
boron-olenite (bole)	Na	Al_3	Al_6	Si_3B_3	B_3	O_{27}	OH_3	OH
alumina-oxy-rossmanite (aorsm)	Vac	Al_3	Al_6	Si_5Al_1	B_3	O_{27}	OH_3	O
povondraite (pov)	Na	Fef_3	Fef_4Mg_2	Si_6	B_3	O_{27}	OH_3	O

$$\left\{x_{\mathrm{NaX}}, x_{\mathrm{CaX}}, x_{\mathrm{FeY}}, x_{\mathrm{MgY}}, x_{\mathrm{AlY}}, x_{\mathrm{FefY}}, x_{\mathrm{TiY}}, x_{\mathrm{AlZ}}, x_{\mathrm{MgZ}}, x_{\mathrm{FeFZ}}, x_{\mathrm{SiT}}, x_{\mathrm{AlT}}, x_{\mathrm{OHV}}, x_{\mathrm{FW}}\right\}$$

Table 5B. Speciation model molar volume and Entropy at standard state. Note that due to multicollinearity present in the data the uncertainties are not independent and it is better to use

the covariance matrix which for molar volume can be found in Electronic Appendix 2D and the correlation matrix for entropy can be found in Appendix 3D3 (which is the correlation matrix of method 2 but only minimal changes are assumed for method 1)

Endmember	Molar Volume (298K, 1bar) (J/bar/mol) ± Uncertainty	Entropy (298K, 1bar) (J/K/mol) ± Uncertainty
Srl	32.037 ± 0.0422	710.54 ± 18.85
Drv	31.826 ± 0.0465	621.85 ± 8.77
Uvt	32.087 ± 0.0490	648.33 ± 16.36
fuvt	32.362 ± 0.0398	725.19 ± 40.70
foi	31.612 ± 0.0410	669.94 ± 25.04
ole	30.854 ± 0.0986	656.99 ± 41.44
drvdis	31.913 ± 0.0728	641.39 ± 18.50
odrv	31.713 ± 0.0319	629.22 ± 8.75
fluvt	31.915 ± 0.0391	641.06 ± 6.46
bu	31.648 ± 0.1131	657.44 ± 28.02
mdtw	31.910 ± 0.0650	690.41 ± 43.41
bole	29.596 ± 0.0297	568.46 ± 15.38
aorsm	30.964 ± 0.0586	638.87 ± 26.07
pov	34.557 ± 0.0301	1000.44 ± 120.65

Table 5C. Heat capacity coefficients of a Berman and Brown (1985) model fit to speciation endmember curves. Due to strong correlations in the Berman polynomial equations, individual variance uncertainties are not meaningful. Cp polynomial was calibrated using measured Cp between 298-778K. Instead, uncertainties must be assessed using the covariance matrix, provided in Chapter 3.

Endmember	Coefficient (c1)	Coefficient (c3)	Coefficient (c5)	Coefficient (c7)
srl	1.0892×10^{3}	9.27407×10^{3}	-1.48237×10^{8}	2.26211×10^{10}
drv	1.27704×10^{3}	2.25033×10^{3}	-1.12376×10^{8}	1.72737×10^{10}
uvt	1.07092×10^{3}	9.26158×10^{3}	-1.45642×10^{8}	2.22102×10^{10}
fuvt	5.7365×10^{2}	2.9335×10^{4}	-2.85716×10^{8}	4.58651×10^{10}
foi	1.0618×10^{3}	8.0897×10^{3}	-1.33455×10^{8}	2.03064×10^{10}
ole	7.16118×10^{2}	2.14646×10^{4}	-1.96593×10^{8}	2.76376×10^{10}
drvdis	1.08946×10^{3}	8.2565×10^{3}	-1.37159×10^{8}	2.03493×10^{10}
odrv	1.72823×10^{3}	-1.34833×10^{4}	-2.0288×10^{7}	1.80596×10^{9}
fluvt	1.72914×10^{3}	-1.37634×10^{4}	-1.92416×10^{7}	2.30223×10^{9}
bu	5.62016×10^{2}	2.51396×10^{4}	-2.40675×10^{8}	3.83514×10^{10}
mdtw	7.60559×10^{2}	2.02213×10^{4}	-2.01319×10^{8}	3.07205×10^{10}
bole	1.65844×10^{3}	-1.16786×10^{4}	-5.39347×10^{7}	9.29786×10^{9}
aorsm	2.31906×10^{3}	-3.55637×10^{4}	1.15461×10^{8}	-2.01997×10^{10}
pov	3.2381×10^{3}	-7.01221×10^{4}	3.71811×10^{8}	-6.26094×10^{10}

1.2 Bulk compositional model, standard state properties and caloric EoS

The bulk model consists of the following endmembers (Table 5D) and the thermodynamic properties of these endmembers are given in Tables 5E-F. The bulk model does not distinguish between the Y and Z sites, which corresponds with the fact that element distribution over these sites cannot be determined from bulk chemical analyses (*e.g.* EPMA), but requires crystal-structure data.

Table 5D. Bulk independent endmember definitions and independent bulk parameters.

	1X	9(YZ)	6T	3B	27O	4(VW)
schorl (srlB)	Na	Fe_3Al_6	Si_6	B_3	O_{27}	OH_4
dravite (drvB)	Na	Mg_3Al_6	Si_6	B_3	O_{27}	OH_4
uvite (uvtB)	Ca	Mg_4Al_5	Si_6	B_3	O_{27}	OH_4
foitite (foiB)	Vac	Fe_2Al_7	Si_6	B_3	O_{27}	OH_4
olenite (oleB)	Na	Al_9	Si_6	B_3	O_{27}	OH_3
fluor-uvite (fluvtB)	Ca	Mg_4Al_5	Si_6	B_3	O_{27}	OH_3F
buergerite (buB)*	Na	Fef_3Al_6	Si_6	B_3	O_{27}	OH_3
magnesium-dutrowite (mdtwB)*	Na	$MgTi_2Al_6$	Si_6	B_3	O_{27}	O_4
alumina-oxy-rossmanite (aorsmB)	Vac	Al_9	Si_5Al	B_3	O_{27}	OH_3O

{na, ca, fe, mg, al, fef, ti, si, F}.

Table 5E. Bulk model standard state molar volume and Entropy. Note that due to multicollinearity present in the data the uncertainties are not independent and it is better to use the covariance matrix which for molar volume can be found in Electronic Appendix 2E and the correlation matrix for entropy can be found in Appendix 3D2 (which is the covariance matrix of method 2 but only minimal changes are assumed for method 1). For the Enthalpy data with strong multicollinearity due to the sparse dataset the correlation matrix can be found in Appendix 4F.

Mineral	Molar Volume (298K, 1bar) (cm^3/mol) ± Uncertainty	Entropy (298K, 1bar) (J/mol·K) ± Uncertainty	Enthalpy (298K, 1bar) (J/mol) ± Uncertainty
srlB	32.1075 ± 0.0672	714.434 ± 8.497	-14480.29 ± 478.1794
drvB	31.8568 ± 0.0567	633.572 ± 7.728	-15204.97 ± 362.269
uvtB	32.0976 ± 0.0477	647.370 ± 6.526	-15457.77 ± 310.9338
foiB	31.6362 ± 0.1112	655.825 ± 14.005	-14453.62 ± 593.3715
oleB	31.1157 ± 0.1718	606.501 ± 22.357	-15434.25 ± 1295.456
fluvtB	32.0113 ± 0.0389	647.343 ± 5.395	-15494.47 ± 202.6296
buB	32.1980 ± 0.0846	681.534 ± 11.401	-13956.61 ± 415.7634
mdtwB	31.9796 ± 0.3330	658.136 ± 44.871	-15262.03 ± 2408.87
aorsmB	30.8704 ± 0.1101	609.034 ± 13.795	-15091.78 ± 1004.378

Table 5F. Heat capacity coefficients of a Berman and Brown (1985) model fit to bulk endmember curves. Cp polynomial was calibrated using measured Cp between 298-778K Due to strong correlations in the Berman polynomial equations, individual variance uncertainties are not meaningful. Instead, uncertainties must be assessed using the covariance matrix, provided in Chapter 3.

Endmember	Coefficient (c1)	Coefficient (c3)	Coefficient (c5)	Coefficient (c7)
srlB	1.72655×10^{3}	-1.25681×10^{4}	-2.91141×10^{7}	3.91145×10^{9}
drvB	1.64552×10^{3}	-1.05030×10^{4}	-4.07394×10^{7}	5.83319×10^{9}
uvtB	1.59346×10^{3}	-8.58155×10^{3}	-4.82376×10^{7}	6.83545×10^{9}
foiB	1.71539×10^{3}	-1.34417×10^{4}	-2.81039×10^{7}	4.41008×10^{9}
oleB	1.62643×10^{3}	-1.05078×10^{4}	-2.93238×10^{7}	2.40959×10^{9}
fluvtB	1.64728×10^{3}	-1.09333×10^{4}	-3.31115×10^{7}	4.33330×10^{9}
buB	1.61351×10^{3}	-1.12091×10^{4}	-3.01809×10^{7}	4.25520×10^{9}
mdtwB	1.23174×10^{3}	3.20011×10^{3}	-1.06815×10^{8}	1.55868×10^{10}
aorsmB	1.63565×10^{3}	-1.14735×10^{4}	-3.03345×10^{7}	3.95967×10^{9}

In order to propagate the uncertainties in the measured data in thermodynamic modelling, the covariance matrix (Σ) is obtained from the correlation matrix (R) using $\Sigma=DRD$, where D is a diagonal matrix of parameter standard deviations (σ_i). Each element is computed as $\Sigma_{ij}=R_{ij}\cdot\sigma_i\cdot\sigma_j$, ensuring that parameter correlations are scaled by their actual variances. This transformation accounts for parameter uncertainties and dependencies.

2. SOLUTION MODEL INTEGRATION

These standard-state thermodynamic properties provide Gibbs free energies for mechanical mixing. No statistically significant excess Gibbs free energy (G_{ex}) was identified, indicating that the only remaining energetic component needed for a complete thermodynamic solution model for tourmaline is the configurational Gibbs free energy (G_{conf}). This can be incorporated using the integral Gibbs free energy equation:

$$G_{\mathrm{mix}} = G_{\mathrm{mech}} + G_{\mathrm{conf}}$$

where G_{mix} represents the total Gibbs free energy of mixing, G_{mech} accounts for mechanical mixing contributions, and G_{conf} captures the configurational entropy effects.

2.1 Configurational entropy

Configurational entropy (S_{conf}) depends on two key factors: (1) The number of independent components (Thompson Jr. 1982) represents the smallest set of chemical components required to fully describe the solid solution, accounting for stoichiometry constraints such as site occupancy, and charge balance, which is equal to the system's degrees of freedom (DOF) plus one (to make the sum of components add to 1), and (2) the number of equivalent 'sites' (sublattices) available for these independent components to mix, which determines the spatial distribution of these components (Wood and Fraser 1977; Cemic 2005; Connolly 2016). The formula,

$$S_{\text{conf}} = -R \sum_{s} M_s \sum_{i=1}^{n_{\text{ind}s}} x_{i,s} \ln\, x_{i,s}$$

shows that $n_{ind,s}$ (independent components) and M_s (number of sites) jointly determine S^{conf} (Vinograd 2001). It quantifies the number of microstates for a given state (Vinograd 2001), assuming a random distribution of independent chemical components across equivalent sites (Spear 1993). Derived from statistical mechanics, it measures the system's information uncertainty. Jaynes (1957) presents statistical mechanics as a special case of Bayesian inference, where the principle of maximum entropy provides a rigorous criterion for constructing probability distributions from incomplete information. This approach justifies the randomization argument, assigning maximum-entropy states when the order-disorder state is unknown, independently of physical assumptions. Whether the uncertainty lies in long-range ordering (as in a speciation model) or in bulk parameters (as in a macroscopic model), randomization offers the least biased, most noncommittal representation, avoiding unwarranted assumptions and yielding the best possible estimate given the available knowledge. As individual 'site' occupancies are often unmeasurable with current instrumentation, S^{conf} provides a simplified model to represent the uncertainty in the chemical components describing the solid solution.

In convergent ordering, order-disorder entropy is captured in the heat capacity (Cp) polynomial as atomic rearrangements modify the vibrational density of states (v-DOS), shifting phonon excitation levels and altering bonding, force constants, or symmetry, creating anomalies (Vinograd 2001) that can be separated from third-law effects using macroscopic mean-field

models such as Landau free energy expressions (Carpenter 1993; Holland and Powell 1998). This indicates that the configurational entropy (S^{conf}) is T-dependent, can be at least partly measured with calorimetry and be explicitly modelled using Landau free energy expressions.

In nonconvergent ordering, the effect of order-disorder on vibrational density of states (v-DOS) is uncertain, as species redistribution may not significantly alter lattice vibrations, making configurational entropy (S^{conf}) a separate term (Vinograd 2001). However, even when S^{conf} is considered temperature-independent, its contribution to the Gibbs free energy, $\mathbf{-T\cdot S^{conf}}$, is inherently temperature-dependent due to the multiplication by T.

The key question is whether the measured Cp already accounts for the temperature-dependent order-disorder entropy—where $\int Cp\, dT$ contributes to enthalpy and $\int Cp/T\, dT$ to entropy—or if order-disorder has negligible impact on phonon structure, necessitating an additional fixed T-independent S^{conf}.

The common geoscience assumption that nonconvergent ordering does not affect the vibrational density of states (v-DOS), is therefore not measured by calorimetry, and that S^{conf} should be added separately can lead to double-counting in thermodynamic models (Vinograd, 2001), see examples below. This assumption (artificially) separates S^{conf} and S^{vib} as independent quantities. While successful for solid solutions involving homovalent substitutions (Thompson Jr and Waldbaum 1968, 1969b, 1969a; Waldbaum and Thompson Jr 1968, 1969), it has since also been applied to coupled substitutions, despite their need for local charge balancing and extensive short-range order (SRO) (Navrotsky 1994). This is illustrated in Holland and Powell (1996), who present clear examples of LRO convergent and non-convergent ordering behavior within a Bragg-Williams framework. The effects of LRO are directly modelled through changes in the speciation endmember proportions, and both models apply separate configurational entropy calculations under the assumption that Sconf can be separated from the measured heat capacity (Cp) curve. It has been assumed that S^{conf} overestimation can be corrected by adding higher H^{ex} to counterbalance its effect (Waldbaum 1973), but this renders interaction parameters physically meaningless. Originally, Margules parameters (W) had a clear physical meaning as measures of excess energy due to interactions between components at infinite dilution, reflecting how one species perturbs the host lattice when present in trace amounts (Spear 1993; Sluiter and Kawazoe

2002). In modern solid solution models (*e.g.*, White et al. 2007; Holland and Powell 2011; Green et al. 2016), W values are empirically calibrated across finite compositions, and thus lose this original interpretability (Spear 1993; Sluiter and Kawazoe 2002). As a result, solid solution models use empirical Margules parameters (W) that no longer represent interactions at infinite dilution This problem is further exacerbated as enthalpy, highly uncertain and reference-state dependent, is the primary adjustment target in internally consistent database optimisations due to its large magnitude (Holland and Powell 1990), see Chapter 5. Interaction parameters and endmember properties are strongly correlated (see Chapter 3), therefore requiring simultaneous adjustment.

To gauge the magnitude of order-disorder processes, we can examine the entropy changes associated with convergent ordering. Holland and Powell (1998) found integrated disordering peaks ranging from ~11 J/(mol·K) for plagioclase (S^0~200 J/(mol·K)) to ~25 J/(mol·K) for cordierite (S^0~450 J/(mol·K)), representing 5–10% of S^0 (S^0 = standard state entropy at 298 K and 1 bar). For disordered systems like tourmaline, with many active sites where order-disorder potential takes place, configurational contributions might double this range. This corresponds to S^{conf} values of ~32.5 J/(mol·K) (5%), ~65 J/(mol·K) (10%), based on an average measured standard state entropy S^0 ~650 J/(mol·K), leading to uncertainties much larger than typical S^0 measurement errors. If S^{conf} is T-independent, $-TS^{conf}$ increases linearly with T, while H remains constant. Enthalpy dominates at low temperatures, favoring order, but as T rises, the growing entropy term increasingly governs G = H - TS, stabilizing disorder. At 773 K, the above estimates yields $-TS^{conf}$ contributions of approximately −25 kJ/mol (5%), and −50 kJ/mol (10%), highlighting the significant energy range involved in configurational effects and underscoring S^{conf} as a major source of uncertainty in thermodynamic models

LRO and SRO components can explicitly model order-disorder processes, incorporating the H−TS interplay, if their associated clusters/endmembers have defined thermodynamic properties. In the H−TS interplay, enthalpy (H) and entropy (S) compete: enthalpy favors low-energy, ordered states, while the entropy term (−TS) favors disordered, higher-entropy states at elevated temperatures, together determining the most stable phase. The relative energy difference between configurations as a function of T directly models $S^{conf}(T)$. The randomization assumption simplifies models by treating S_{conf} as T-independent, maximizing its contribution, but often

overcorrects by misrepresenting chemical distributions, requiring further adjustments through additional thermodynamic parameters (Will 1998; Connolly 2016). The DOF are fixed by the site and charge balance constraints (Thompson Jr 1969), creating a balance between selecting enough chemical components to adequately describe the solid solution and relying on theoretical models to capture order-disorder effects. More chemical components lower the DOF, constraining configurational variability, whereas using a theoretical model like the randomization model frees up DOF which then can be used represent the wider LRO compositional space. The extent to which the model explicitly incorporates order/disorder effects directly influences its accuracy and flexibility.

Statistical Thermodynamic Models Before exploring new approaches to model short-range order (SRO) effects, it is important to review how SRO is traditionally treated in statistical thermodynamic models. Methods such as the Ising model, cluster expansions, and Monte Carlo simulations explicitly capture local atomic interactions, but their reliance on computational techniques without closed-form thermodynamic expressions limits their integration into global thermodynamic frameworks. This background provides the necessary context for understanding the challenges associated with incorporating SRO into thermodynamic models.
Statistical thermodynamic models extend beyond the Bragg-Williams approximation by incorporating short-range interactions (Cohen 1986). In both microscopic and macroscopic Bragg-Williams models, each crystallographic site is treated as an average site, and its occupancy is scaled by site multiplicity, implicitly assuming that all equivalent sites behave identically. However, once short-range order (SRO) is introduced, this assumption breaks down: interactions between neighboring atoms cause local environments to diverge, making site multiplicities invalid. Each site must then be modelled as a distinct entity, with explicit neighbor-dependent interactions, as in cluster variation or Ising-type models. The cluster variation method (CVM) models local ordering via atomic clusters (Connolly and Williams 1983; de Fontaine and Wolverton 1994; Wolverton and Zunger 1994), using cluster expansions calibrated through computational methods such as DFT using the single/double defect method (Sluiter and Kawazoe 2002; Vinograd et al. 2013) or empirical potentials (Dove et al. 2000; Bosenick et al. 2001b, 2001a; Dove 2001). A variant of the cluster expansion method popular in the geosciences , J formalism, models mixing and ordering in mineral solid solutions by defining effective

pairwise interaction energies (J values) (Dove et al. 2000; Bosenick et al. 2001b; Dove 2001; Vinograd et al. 2004). After the energetic properties of the clusters have been established they can be used in Monte Carlo simulations to determine cluster frequencies and thermodynamic averages (Bosenick et al. 2001a; Warren et al. 2001) or can be analytically calculated using the cluster variation method (Vinograd 2001). Thermodynamic integration of Monte Carlo results extracts thermodynamic parameters but requires simulations for each temperature, pressure, and composition (Warren et al. 2001; Burton and Van de Walle 2006, 2006; Vinograd et al. 2007, 2009). Often, only nearest-neighbor clusters are considered, enforcing symmetric mixing properties (Vinograd et al. 2007). Such interactions are modelled explicitly between individual atoms occupying specific sites rather than averaged over site types as in mean-field approaches like Bragg-Williams. Mixing energy consists of chemical (ordering) and elastic (size-mismatch) contributions, the latter often causing non-linear compositional effects and are responsible for H^{ex} (Vinograd et al. 2004). Size mismatch between SRO clusters is therefore a prime driver of nonideality. CVM demonstrates that assuming full randomization at long-range order overestimates configurational entropy (S_{conf}), particularly at low temperatures. S_{conf} remains valid mainly at high temperatures, where disorder dominates, while ordered domains stabilize at lower temperatures in binary systems (Vinograd 1997; Vinograd et al. 2004, 2007, 2009, 2013). Silicate solid solutions involving homovalent cation substitutions of similar size and charge, such as Fe-Mg in pyroxenes, are well-modelled by LRO Bragg-Williams models, with SRO negligible. However, heterovalent substitutions, such as Al-Mg in phyllosilicates, induce SRO (Sanz and Robert 1992). Similarly, Al-Si mixing on tetrahedral sites leads to strong SRO through Al avoidance (Kerrick and Darken 1975).

One criticism is that Monte Carlo methods inherently favor randomization, which can bias configurational sampling, particularly in systems with strong short- or long-range order, reducing accuracy in predicting ordered states at lower temperatures. While these models offer detailed insights, they compute only a single solid solution at a time for a given P and T and lack closed-form expressions G(P,T,n1,n2..) for differentiation (Gottschalk 2016). Therefore the statistical method does not provide predictive equations which can be used in computational thermodynamics, limiting integration into modelling software like FactSage (Bale et al. 2002),

Theriak-Domino (Capitani and Petrakakis 2010), Perplex (Connolly 2005), or GEM-Selector (Kulik et al. 2013).

SRO in Tourmaline As tourmaline contains all types of coupled substitution, SRO is expected. Short-range order in tourmaline is supported by theoretical calculations and bond valence analysis, where predicted *a-priori* cluster bond lengths are compared to those in other mineral endmember systems to assess the likelihood of SRO stability (Hawthorne 1996, 2002; Bosi 2010, 2011, 2013).

Fourier transform infrared (FTIR) and Raman spectroscopy OH-stretching broadening has been linked to short-range order (SRO), but exact assignments remain empirical and challenging (Hawthorne 2016). Two models are used: the short-range arrangement model assigns OH-stretching bands based on local ^{V}OH and ^{W}OH environments, considering adjacent cations (Gonzalez-Carreño et al. 1988; Hoang et al. 2011; Skogby et al. 2012; Fantini et al. 2014; Berryman et al. 2016; Kutzschbach et al. 2016, 2021; Bronzova et al. 2019), while the site-symmetry model (Watenphul et al. 2016, 2017) assumes ^{V}OH hydrogen atoms rotate around the threefold axis, forming a single phonon mode. This generalizes OH band assignments, treating energy influences as cluster-wide rather than local. Due to overlapping OH signals, empirical assignments remain qualitative. Using simple synthetic samples (Berryman et al. 2016) or *ab initio* calculations (Fuchs et al. 2022; Balan et al. 2023) offers a promising path forward.

Magic angle spinning nuclear magnetic resonance (MAS NMR) would be an additional probe for SRO and has been used on mainly ordered Al-rich tourmalines. This is due to MAS NMR being limited to Fe^{2+}- free tourmaline. (Tsang and Ghose 1973; Marler and Ertl 2002; Lussier et al. 2008, 2009, 2011). Extending MAS NMR to Fe-free Mg-rich tourmalines could provide insights into cation ordering, but challenges like strong quadrupolar broadening, local disorder, and spectral complexity must be addressed, but could theoretically supply proof of disordering of Mg over the Y and Z-sites without relying on bond valence theory arguments.

TEM studies reveal that schorl (P3m1) and buergerite (P31m) differ in ordering and plane group symmetry (Iijima et al. 1973). Ferrow et al. (1993) identified plane groups along ***c*** using HRTEM: elbaite (P31m), Fe-elbaite (P3m1), red elbaite (P6), and dravite-schorl (pseudo-P6), with only elbaite conforming to R3m. Ferrow (1995) noted that fractional site occupancy

complicates TEM interpretation, as contrast depends on atomic overlap, which is minimal along ***c***. Additional studies are needed as simulated TEM images require full chemical characterisation which none of these studies had.

Generalized Bragg Williams model (LRO models) The generalized Bragg-Williams model (Bragg and Williams 1934, 1935) describes LRO in solid solutions by averaging site occupancies and assuming a random distribution of elements across symmetry-equivalent sites, neglecting SRO. Site multiplicities represent averaged sites and partial, rather than full, occupancies describe the solid solution. Chemical components are defined based on an LRO averaged unit cell constrained by space group symmetry, determined via single-crystal X-ray diffraction (sc-XRD). This averaged LRO unit cell represents the system being modelled, and configurational entropy (S^{conf}) independent of caloric, volumetric, or compositional equations of state with fixed values for each endmember quantifies the number of microstates corresponding to a given macrostate and capturing the random arrangements consistent with the averaged LRO structure of the endmember. Therefore, it predicts fixed residual S^{conf} at 0 K.

The number of independent endmembers (n_{ind}) represent the dimensions of the charge-balanced hyperplane polytope (Myhill and Connolly 2021) that concisely describes the tourmaline system and is crucial for S^{conf}. This defines the maximum number of independent components that can distribute freely under site fraction and charge balance constraints. n_{ind} are given by:

$$n_{\text{ind-mbes}} - 1 = n_{\text{site-species}} - (n_{\text{sites}} + c)$$

(Thompson Jr 1969; Myhill and Connolly 2021). Where the right-hand site is the DOF = variables-constraints, c = 1 if charge balance is independent of site constraints (*e.g.*, in tourmaline), and c = 0 otherwise (Myhill and Connolly 2021). The number of independent endmembers (n_{ind}) is one more than the DOF, so their proportions sum to 1. The total S^{conf} remains unchanged under basis transformation to different sets of independent components, as dependent components are fully determined by system constraints (Powell and Holland 1999; Myhill and Connolly 2021).

Negative independent endmember fractions in speciation or bulk models must be transformed into positive independent site fractions/bulk parameters (see Chapter 3) for computational

reasons. These site fractions are linear combinations of the independent endmember fractions but remain positive while preserving the same DOF. This transformation from independent endmember coordination space to independent site fraction/bulk parameter space automatically incorporates stoichiometry, including charge balance and site occupancy constraints. Independent site fractions are essential for calculating S^{conf} , as positive values are required for the ln-term in S^{conf} calculations. Therefore, these mean field multisite stochastic models allow the DOF to be expressed as independent site populations/bulk parameters, which can independently mix across multiple crystallographic sites (Wood and Fraser 1977; Will 1998).

The randomization model maximizes S^{conf} for a given DOF, causing LRO models to overestimate it, as true randomness is rare due to SRO constraints in real systems. Conversely, molecular models (see next paragraph) predict the minimum S^{conf} for the same DOF, representing the two extremes of S^{conf} (Will 1998). Assuming a randomization model simplifies chemical components to their average ones, freeing DOF to better describe the compositional/speciation space of LRO systems. The S^{conf} is one of the largest sources of uncertainty in such models.

In thermodynamic phase calculators like THERMOCALC (Powell et al. 1998), configurational normalization constants are required for disordered endmembers (*e.g.*, uvt, foi) to ensure their activity approaches 1 at pure composition. This correction is necessary because such programs operate with standard states and apply calorimetric, volumetric, and compositional EoS to adjust standard-state reactions to specific P-T-X conditions, effectively computing energy differences between states. However, when using Gibbs free energy minimisation based solely on integral configurational energy (G_{conf}), normalization is generally unnecessary. G_{conf} inherently accounts for all microstates, meaning total configurational energy suffices without comparison to the standard state conditions.

Speciation Generalized Bragg Williams model The speciation model, $XY_3Z_6T_6V_3W$**,** explicitly models six distinct crystallographic sites with 14 DOF corresponding to 14 independent endmembers. Positive independent site fractions were chosen to represent linear combinations of these independent speciation endmembers (Chapter 3):
$x_{\mathrm{NaX}}, x_{\mathrm{CaX}}, x_{\mathrm{FeY}}, x_{\mathrm{MgY}}, x_{\mathrm{AlY}}, x_{\mathrm{FefY}}, x_{\mathrm{TiY}}, x_{\mathrm{AlZ}}, x_{\mathrm{MgZ}}, x_{\mathrm{FeFZ}}, x_{\mathrm{SiT}}, x_{\mathrm{AlT}}, x_{\mathrm{OHV}}, x_{\mathrm{FW}}$. Treating site

species as separate entities in the LRO unit cell classifies these Bragg -Williams models as ionic (Ganguly 2001), though this is somewhat misleading, these site populations represent elements in specific coordination environments, resembling polyhedral units more than isolated ions.

Starting with the square stoichiometric matrix of speciation endmembers in terms of independent site fractions from Chapter 3, we transpose it to express independent site fractions as linear combinations of endmembers:

$$x_{nax} = \text{bole} + \text{bu} + \text{drv} + \text{drvdis} + \text{ole} + \text{odrv} + \text{pov} + \text{srl} + \text{mdtw}$$

$$x_{cax} = \text{fuvt} + \text{fluvt} + \text{uvt}$$

$$x_{fey} = \frac{2\,\text{foi}}{3} + \text{fuvt} + \text{srl}$$

$$x_{mgy} = \text{drv} + \frac{2\,\text{drvdis}}{3} + \text{fluvt} + \frac{\text{odrv}}{3} + \frac{\text{mdtw}}{3} + \text{uvt}$$

$$x_{aly} = \text{aorsm} + \text{bole} + \frac{\text{drvdis}}{3} + \frac{\text{foi}}{3} + \text{ole} + \frac{2\,\text{odrv}}{3}$$

$$x_{fefy} = \text{bu} + \text{pov}$$

$$x_{tiy} = \frac{2\text{mdtw}}{3}$$

$$x_{alz} = \text{aorsm} + \text{bole} + \text{bu} + \text{drv} + \frac{5\text{drvdis}}{6} + \text{foi} + \frac{5\,\text{fuvt}}{6} + \frac{5\text{fluvt}}{6} + \text{ole} + \frac{5\,\text{odrv}}{6} + \text{srl} + \text{mdtw} + \frac{5\text{uvt}}{6}$$

$$x_{mgz} = \frac{\text{drvdis}}{6} + \frac{\text{fluvt}}{6} + \frac{\text{odrv}}{6} + \frac{\text{pov}}{3} + \frac{\text{uvt}}{6}$$

$$x_{fefz} = \frac{2\,\text{pov}}{3}$$

$$x_{sit} = \frac{5\,\text{aorsm}}{6} + \frac{\text{bole}}{2} + \text{bu} + \text{drv} + \text{drvdis} + \text{foi} + \text{fuvt} + \text{fluvt} + \text{ole} + \text{odrv} + \text{pov} + \text{srl} + \text{mdtw} + \text{uvt}$$

$$x_{alt} = \frac{\text{aorsm}}{6}$$

$$x_{OHv} = \text{aorsm} + \text{bole} + \text{drv} + \text{drvdis} + \text{foi} + \text{fuvt} + \text{fluvt} + \text{odrv} + \text{pov} + \text{srl} + \text{uvt}$$

$$x_{Fw} = \text{fluvt}$$

Using these independent site fractions, the general S^{conf} equation yields an average S^{conf} of approximately 48 J/(mol·K) for the tourmalines in the training set (Figure 5A). In Figure 5A, we show that the differences between these S^{conf} models are significant. The associated configurational entropies contribute approximately 10% of the standard state entropy and, at ~1000 K, lower the Gibbs free energy by ~48 kJ/mol—comparable to typical reaction energies—highlighting their thermodynamic importance. Range and standard deviation cannot be calculated here, as the value is fixed by the theoretical model, determined by site multiplicities, site populations, and the choice of independent compositional components, rather than arising from empirical variability.

The speciation model includes LRO order/disorder endmembers, providing insight into potential magnitude of expected configurational energies for tourmaline. The $S_{298.15K}^{773.15\,K}$ differences between drv, drvdis, and odrv are minimal (within 5 J/(mol·K)), while Fe^{3+} and Fe^{2+} + order-disorder on Y and Z sites shows larger differences, such as 100 J/(mol·K) for bu vs. (strongly extrapolated) pov and 20 J/(mol·K) for uvt vs. fuvt, which also might be largely due to bulk composition differences. True ordering energies require basis transformations to independent endmembers having the same bulk composition forming isochemical reactions (e.g., drv and drvdis) to calculate and convert into Q-ordering vectors. This was not attempted due to multicollinearity from data scarcity. This analysis suggests that LRO configurational energy is generally small, but Fe^{3+} ordering could have a significant, potentially major impact.

Bulk compositional Generalized Bragg Williams model In the bulk composition model, $X(YZ)9Si_xAl_{(1-x)}(VW)_4$, with only 9 DOF, some sites were merged, reducing the system to just 4 distinct sites. The model is formally a reciprocal model. The bulk model significantly overestimates S^{conf} as the merging of sites led to extended site populations which can potentially disorder, (X,9(Y+Z),6T, 4(V+W)), which shows that S^{conf} is highly dependent on the model definition. Merging or splitting octahedral sites notably impacts the calculated entropy. Using nine independent bulk parameters as the DOF, representing the linear combination of independent bulk endmembers (Na, Ca, Fe^{2+}, Mg, Al, Fe^{3+}, Ti, Si, and F):

Na= buB + drvB + oleB + srlB + mdtwB

Ca = fluvtB + uvtB

Fe^{2+} = 2 foiB + 3srlB

Mg = 3drvB + 4fluvtB + mdtwB + 4uvtB

Al = 10 aorsmB + 6 buB + 6 drvB + 7 foiB + 5 fluvtB + 9 oleB + 6 srlB + 6 mdtwB + 5uvtB

Fe^{3+} = 3buB

Ti = 2mdtwB

Si = 5 aorsmB + 6buB + 6drvB + 6 foiB + 6 fluvtB + 6 oleB + 6 srlB + 6 mdtwB + 6uvtB

F = fluvtB

the average bulk compositional reciprocal S^{conf} is approximately 71 J/(mol·K) (Figure 6A). Most of this entropy arises from the octahedral sites, assuming maximum disorder among 9 YZ, and the 4 VW sites. In Figure 5A we compare these S^{conf} models.

The randomization assumption is incorrect, for both sites. At the YZ site, elements are known to exhibit site preferences: the Y site favors Mg^{2+}, Fe^{2+}, and Al^{3+}, while the Z site primarily hosts Al^{3+}, with minor Fe^{3+} and Mg^{2+}, and potential Fe^{2+} (Henry et al. 2011; Bosi 2018). The extent of site preference and associated order/disorder remains debated due to challenges in interpreting overlapping Mössbauer and optical spectra (Bosi 2008; Ertl et al. 2012; Filip et al. 2012; Bosi and Andreozzi 2013; Bosi et al. 2015) and depends on the constraints used in the mineral formula optimisations. Heating experiments using FTIR, pXRD, and sc-XRD show electron density redistribution, OH loss, and structural changes, suggesting oxidation and order-disorder effects (Bosi et al. 2016a, 2016b, 2016b, 2018; Ballirano et al. 2022; Celata et al. 2023). However, this would require element mobility, whereas tourmaline has low diffusion rates (Desbois and Ingrin 2007), as also shown by preservation of sharp composition and isotopic breaks (van Hinsberg and Schumacher 2007; Van Hinsberg and Marschall 2007). This potentially implies disorder occurs via local site exchanges, and proton migration (H+ diffusion) to mitigate local charge imbalances, where cation rearrangement within Y and Z sites is driven by thermal vibrations and charge redistribution, maintaining structural integrity without long-range diffusion. Anisotropy in H+ diffusion indicate that this is likely within the ring along the ***c***-

axis (Desbois and Ingrin 2007). Such order disorder without long range diffusion has been shown for Fe – Mg in olivine, and Al – Si order-disorder in feldspars (Redfern 2000).

Concerning the V and W sites, F is confined to the W site (Henry and Dutrow 2011). The V site in tourmaline, bonded to two Z-site and one Y-site octahedron, is unfavorable for F substitution due to its interaction with high-charge cations, which stabilize OH via shared bonding with tetrahedral oxygens. In contrast, the W site (O(1)), linked to a single Y-site octahedron, provides a more symmetrical charge environment, minimizing structural distortion and making F substitution more favorable (Henry and Dutrow 2011). These LRO constraints cannot currently be enforced due to the limited DOF available in the bulk compositional model.

Molecular Mixing models (SRO models) Molecular mixing (simplical) models vary in complexity based on the number and definition of charge-balanced SRO molecular endmembers, which represent specific chemical or structural configurations (Will 1998). The solid solution is modelled as a mixture of these species, ignoring sub-site interactions. In molecular mixing models, the "site" is redefined from a polyhedron to a unit cell, which combine to form the solid solution, similar to how averaged polyhedra construct an average LRO unit cell. This higher structural scale captures local atomic correlations, breaking $R\bar{3}m$ symmetry and reducing the unit cell to P1, reflecting the loss of long-range symmetry and increasing model complexity by explicitly representing short-range interactions. These types of models are not popular for solid solutions (Spear 1993) and have mainly been applied to fluids, *e.g.* the recent dilute silicate - fluid molecular model of Holland et al. 2018). The accuracy of these models depends on the number and type of molecular components, determined analytically or theoretically. S^{conf} is calculated from the random distribution of molecular species across a single "site". Each species corresponds to a vertex of a simplex in compositional space, with their proportions representing the coordinates within that simplex. This approach consistently gives the minimum S^{conf} per DOF.

In SRO models, one might assume that linearity and convexity are broken due to local atomic correlations and nonlinear interactions, meaning thermodynamic properties cannot be expressed as a simple sum of independent endmembers and therefore would need the more elaborate statistical thermodynamic models described above. Fully accounting for dependent endmembers

is infeasible due to the combinatorial explosion of configurations (Okhotnikov et al. 2016a, 2016b; Cadars et al. 2017), requiring approximations using independent SRO endmembers. This assumes linearity as a first-order simplification, which cannot fully capture nonlinearity, but is effective for LRO models, where randomness preserves additivity. Such assumptions are reasonable, as minerals with SRO (P1 symmetry) often exhibit an average LRO unit cell with distinct space group symmetry.

Both bulk compositional and speciation models can be expressed as molecular models, with the number of independent molecular clusters determined by the DOF and the limits of instrumental measurement.

Bulk compositional Molecular Mixing Model The bulk compositional model represents the simplest molecular approach, treating the nine independent bulk endmembers (srlB, drvB, uvtB, foiB, oleB, fluvtB, buB, mdtwB, aorsmB) as fixed-composition SRO molecular clusters that randomly mix on a single "site". This simplification drastically reduces the number of microstates per macrostate, with the model's DOF governed by bulk compositional constraints.

$$\begin{bmatrix} NaFe_3Al_6Si_6B_3O_{27}(OH)_4, NaMg_3Al_6Si_6B_3O_{27}(OH)_4, CaMg_4Al_5Si_6B_3O_{27}(OH)_4, VacFe_2Al_7Si_6B_3O_{27}(OH)_4 \\ , NaAl_9Si_6B_3O_{27}(OH)_3, CaMg_4Al_5Si_6B_3O_{27}(OH)_3F, NaFef_3Al_6Si_6B_3O_{27}(OH)_3, NaMgTi_2Al_6Si_6B_3O_{27}O_4, \\ VacAl_9Si_5AlBB_3O_{27}(OH)_3O \end{bmatrix}$$

No instrument directly measures molecular clusters in tourmalines. Although the model describes molecular clusters, it relies on atomic-level measurements, using equations of chapter 3 to derive independent endmembers from bulk compositional parameters. Independent endmembers which can be negative are mapped to positive independent bulk parameters – Na, Ca, Fe, Mg, Al, Fef, Ti, Si, and F – aligned with the system's thermodynamic DOF, allowing the nine bulk parameters to represent the linear combination of nine independent SRO molecules. These positive values are required for the S^{conf} equation, as ln is undefined for negative or zero values. Treating these parameters as mixing on a single site yields an average S^{conf} of 11.81 J/(mol·K) (see comparison in S^{conf} between different models, Figure 5A).

Speciation Molecular Mixing Model In the speciation model, the DOF increases to 14, allowing 14 SRO clusters to mix on a single site. This model uses site fractions to define SRO

clusters, equating SRO with long-range order (LRO). For the specified speciation endmembers—srl, drv, uvt, fuvt, foi, ole, drv-dis, odrv, fluvt, bu, mdtw, bole, aorsm, pov—this corresponds to the following 14 SRO molecular clusters:

$$\mathrm{NaFe_3Al_6Si_6B_3O_{27}OH_3OH}$$
$$\mathrm{NaMg_3Al_6Si_6B_3O_{27}OH_3OH}$$
$$\mathrm{CaMg_3(MgAl_5)Si_6B_3O_{27}OH_3OH}$$
$$\mathrm{CaFe_3(FeAl_5)Si_6B_3O_{27}OH_3OH}$$
$$\mathrm{Vac(Fe_2Al)Al_6Si_6B_3O_{27}OH_3OH}$$
$$\mathrm{NaAl_3Al_6Si_6B_3O_{27}O_3OH}$$
$$\mathrm{Na(Mg_2Al)(MgAl_5)Si_6B_3O_{27}OH_3OH}$$
$$\mathrm{Na(Al_2Mg)(MgAl_5)Si_6B_3O_{27}OH_3O}$$
$$\mathrm{CaMg_3(MgAl_5)Si_6B_3O_{27}OH_3F}$$
$$\mathrm{NaFef_3Al_6Si_6B_3O_{27}O_3OH}$$
$$\mathrm{Na(MgTi_2)Al_6Si_6B_3O_{27}O_3O}$$
$$\mathrm{NaAl_3Al_6(Si_3B_3)B_3O_{27}OH_3OH}$$
$$\mathrm{VacAl_3Al_6Si_5Al_1B_3O_{27}OH_3O}$$
$$\mathrm{NaFef_3(Fef_4Mg_2)Si_6B_3O_{27}OH_3O}$$

The fourteen positive independent site fractions associated with linear combinations of the molecular clusters are $\{x_{\mathrm{NaX}}, x_{\mathrm{CaX}}, x_{\mathrm{FeY}}, x_{\mathrm{MgY}}, x_{\mathrm{AlY}}, x_{\mathrm{FefY}}, x_{\mathrm{TiY}}, x_{\mathrm{AlZ}}, x_{\mathrm{MgZ}}, x_{\mathrm{FeFZ}}, x_{\mathrm{SiT}}, x_{\mathrm{AlT}}, x_{\mathrm{OHV}}, x_{\mathrm{FW}}\}$. Treating these as mixing on a single site allows S^{conf} to be calculated, yielding an average value of 13.9 J/(mol·K) (Figure 5A). One can see that the addition of these additional molecules does not change the S^{conf} drastically.

Full Molecular Mixing Model The complete molecular model includes all independent SRO molecular clusters, requiring the redefinition of averaged sites (*e.g.*, splitting "3Y" into "Y_1, Y_2, Y_3"), increasing degrees of freedom and explicitly capturing local structural ordering (*cf.* Gottschalk 2016). Determining the number of SRO endmembers consistent with site and charge balance constraints involves vertex enumeration of the charge-balanced hyperplane through the tourmaline polytope, treating each site independently to derive the mineral formula (Myhill and Connolly 2021).

[Na Ca Vac]

[Fe^{2+} Mg Al Fe^{3+} Ti] [Fe^{2+} Mg Al Fe^{3+} Ti] [Fe^{2+} Mg Al Fe^{3+} Ti]

[Al Mg Fe^{2+} Fe^{3+}][Al Mg Fe^{2+} Fe^{3+}] [Al Mg Fe^{2+} Fe^{3+}] [Al Mg Fe^{2+} Fe^{3+}] [Al Mg Fe^{2+} Fe^{3+}] [Al Mg Fe^{2+} Fe^{3+}]

[Si Al B] [Si Al B] [Si Al B] [Si Al B] [Si Al B] [Si Al B]

[OH O] [OH O] [OH O]

[OH O F]

To calculate the number of independent endmembers (n_{ind}), the system's DOF is determined by subtracting the number of constraints from the total variables, where total variables are the sum of species across all sites:

[Na Ca Vac]: 3 species
[Fe^{2+} Mg Al Fe^{3+} Ti]: 5 species (3 sites)
[Al Mg Fe^{2+} Fe^{3+}]: 4 species (6 sites)
[Si Al B]: 3 species (6 sites)
[OH O]: 2 species (3 sites)
[OH O F]: 3 species (1 site)

$$\text{Total variables} = 3 + (5 \cdot 3) + (4 \cdot 6) + (3 \cdot 6) + (2 \cdot 3) + 3 = 69$$

The constraints include 20 site occupancy constraints (1 + 3 + 6 + 6 + 3 + 1 = 20) and one charge balance constraint, independent of the site fraction constraints in tourmaline, for a total of 21 constraints. The DOF are calculated as:

$$\text{DOF} = \text{Total variables} - \text{Total constraints} = 69 - 21 = 48$$

n_{ind} is one more than the DOF, as their proportions must sum to 1, adding an additional vertex to the simplex. Thus, the polytope has 49 independent endmembers, representing the solution space dimension.

This approach significantly increases the number of endmembers and interaction parameters required to fully describe the system, as it aims to capture all possible SRO structures (*cf.* Gottschalk, 2016). However, no current instrumental technique can measure all SRO

configurations in a solid solution, so such models must rely on theoretical calculations like density functional theory (DFT) (Benisek and Dachs 2018, 2020). With computational advances, it is now feasible to calculate these 49 endmembers. For a non-ideal system with 49 independent endmembers, the number of binary interaction parameters is:

$$\binom{49}{2} = \frac{49 \cdot 48}{2} = 1176$$

The number of ternary interaction parameters is:

$$\binom{49}{3} = \frac{49 \cdot 48 \cdot 47}{6} = 18{,}424$$

Each endmember in this framework is ordered so has $S^{conf}=0$, and the solid solution of these SRO clusters can be modelled by defining a single site where all clusters mix. This way all types of order disorder will be explicitly modelled. From a bond valence perspective (*cf.* Brown 2016) molecular models with SRO are more appropriate as they inherently account for nearest-neighbor interactions and treat the entire unit cell as a single entity, similar to bond graphs.

Incomplete Representation of SRO in Simplified Molecular Models The Bulk and Speciation Molecular models represent incomplete SRO polytopes, with nine and fourteen DOF, respectively, capturing only a fraction of the 49 independent molecular clusters required to describe all possible SRO configurations. While this molecular model reduces the resolution and predictive power of thermodynamic frameworks for complex solid solutions (Cohen 1986), these models provide a valuable reference frame by representing the minimum configurational entropy achievable in the system per DOF.

Molecular models use DOF to capture SRO instead of LRO Molecular models prioritise SRO over LRO by redistributing thermodynamic DOF to represent solid solutions as mixtures of predefined SRO molecular clusters, capturing local atomic arrangements, bonding patterns and clustering tendencies. The tradeoff is that this reallocation reduces the DOF available for LRO, limiting compositional space, configurational variability, and microstate diversity. By coupling atomic site populations into predefined groups, these models create correlated parameters,

restricting configurational diversity and failing to capture the full range of atomic-scale interactions.

Although the total DOF remains unchanged, this trade-off allows molecular models to focus on SRO complexities while sacrificing broader configurational variability and independent atomic distributions required for detailed LRO representation.

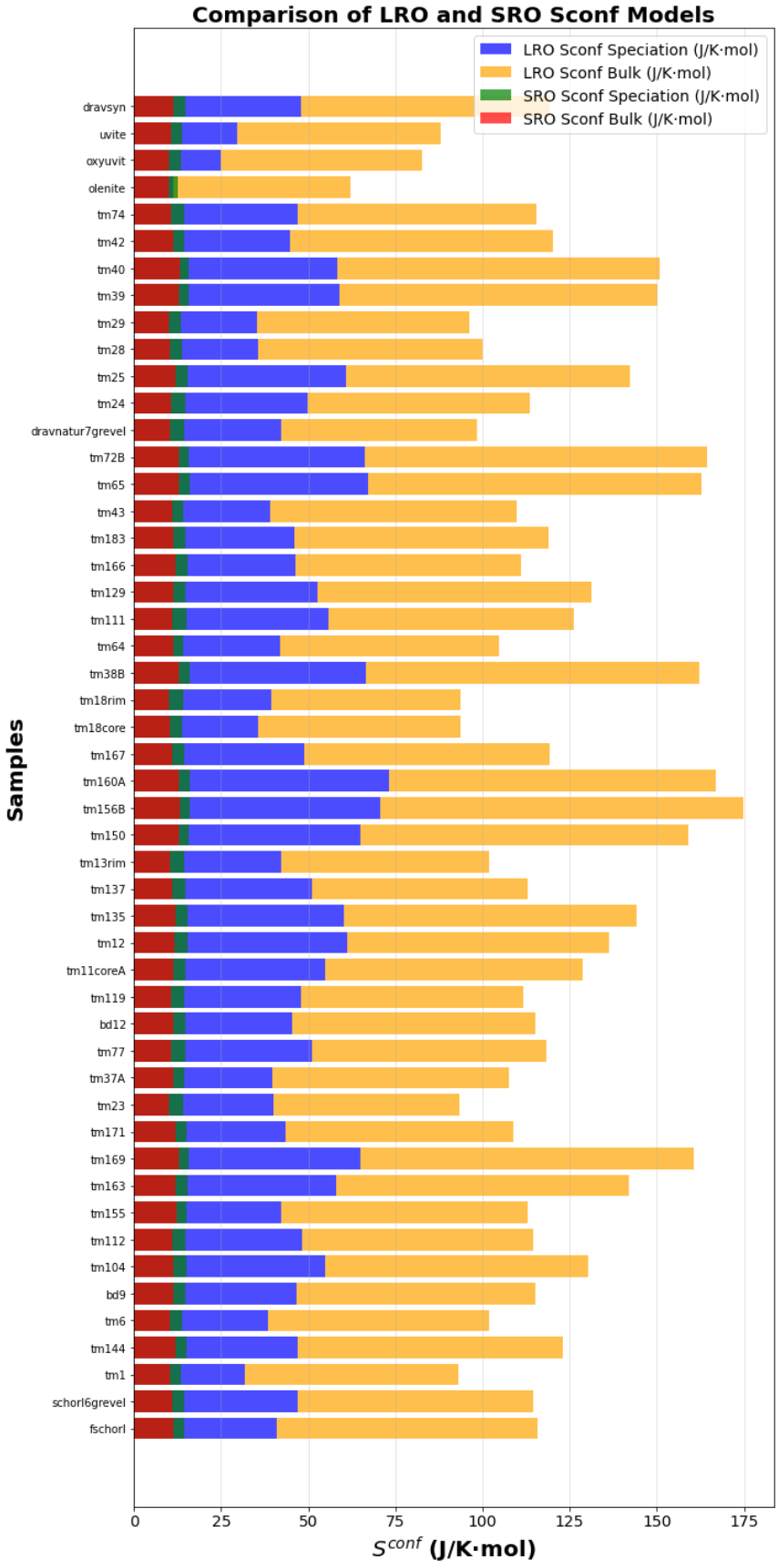
Comparison of LRO and SRO Sconf Models
LRO Sconf Speciation (J/K·mol)
LRO Sconf Bulk (J/K·mol)
SRO Sconf Speciation (J/K·mol)
SRO Sconf Bulk (J/K·mol)
Samples
dravsyn
uvite
oxyuvit
olenite
tm74
tm42
tm40
tm39
tm29
tm28
tm25
tm24
dravnatur7grevel
tm72B
tm65
tm43
tm183
tm166
tm129
tm111
tm64
tm38B
tm18rim
tm18core
tm167
tm160A
tm156B
tm150
tm13rim
tm137
tm135
tm12
tm11coreA
tm119
bd12
tm77
tm37A
tm23
tm171
tm169
tm163
tm155
tm112
tm104
bd9
tm6
tm144
tm1
schorl6grevel
fschorl
0
25
50
75
100
125
150
175
S^{conf} (J/K·mol)

Figure 5A. **Comparison of Configurational Entropy (S^{conf})** The four bars per sample represent independently calculated entropy contributions from different models: LRO S^{conf} Speciation (blue), LRO S^{conf} Bulk (orange), SRO S^{conf} Speciation (green), and SRO S^{conf} Bulk (red). Each bar shows the calculated S^{conf} value in J/(mol·K), with its exact value labeled at the right end of the bar. At 1000 K, differences in S^{conf} translate into Gibbs free energy differences of ~40–60 kJ/mol, comparable to many mineral reaction energies, emphasizing that the choice of configurational entropy model can significantly affect thermodynamic predictions.

Discussion of Configurational Entropy Models and Their Implications All solid solution models in the Earth Sciences face significant uncertainty from the treatment of configurational entropy (S^{conf}), as different models, bulk vs. speciation, LRO vs. SRO, yield differences of up to ~10% of total entropy. At high temperatures (~1000 K), these discrepancies translate into Gibbs free energy shifts of 40–60 kJ/mol, on par with typical reaction energies, thereby affecting phase equilibria and stability predictions.

Because no single approach to modelling S^{conf} is universally validated, most thermodynamic models absorb these differences into excess enthalpy or volume terms during calibration, effectively treating them as hidden fitting parameters. This practice obscures the physical basis of interaction parameters and limits model interpretability.

A more rigorous approach would estimate Sconf from theory (e.g., Monte Carlo simulation, cluster variation methods, or DFT-derived cluster expansions) or optimize it as a separate component within CALPHAD frameworks. Importantly, this is a testable problem. If accurate enthalpy values are available, different Sconf, whose predictions often differ substantially, can be directly compared based on their ability to reproduce experimental phase stability data. The most effective test would involve both a tourmaline near-endmember composition, where configurational entropy is expected to be small and order dominates, and a highly disordered, high-entropy tourmaline composition, where Sconf strongly stabilizes the solid solution.

The fact that tourmaline is observed only as a solid solution, with no true endmembers found in nature, further suggests that configurational entropy plays a fundamental role in stabilizing the structure across its compositional range. Recognizing and explicitly addressing Sconf uncertainty

is therefore crucial for improving the transparency, robustness, and physical realism of thermodynamic models for complex mineral solid solutions.

Size of composition and speciation space

The bulk model is the only solution model we can fully populate as the limited availability of enthalpy data does not permit reliable extrapolation of measured enthalpies to endmember species. Comparing the LRO Bragg-Williams bulk model with the SRO molecular bulk model highlights a fundamental issue in thermodynamic solution models for phases with intermediate complexity (~200 bits, e.g., amphiboles, tourmalines) (Krivovichev 2013; Grew et al. 2016). Bits refer to the Shannon information content of a mineral's crystal structure, quantifying its structural complexity in terms of the number of distinguishable configurations or the amount of information needed to describe its atomic arrangement (Krivovichev 2013). The size of configurational entropy (S^{conf}) is directly linked to the compositional space allowed by the solution model via the DOF allocation.

As shown in Chapter 3, enumerating independent endmembers for the bulk model results in >600 dependent endmembers using the methods of Myhill and Connolly (2021). In the polytope, if Mg and Fe^{2+} occupy the Z-site, all six Z sites can, in theory, be filled by these ions. The polytope expands with each added endmember, extending not only to that composition but also to all linear combinations with other independent endmembers. However, experimental synthesis and mineralogical studies show structural limits on element incorporation (Vereshchagin et al. 2018). Experimental synthesis and crystallographic refinements show that structural limits on element incorporation constrain tourmaline stability (Vereshchagin et al., 2018; Bosi, 2018). Vereshchagin et al. (2018) demonstrated that instability occurs when the sum $\langle Y–O\rangle + \langle Z–O\rangle$ deviates from ~3.03 Å, corresponding to a bond-length ratio $\langle Y–O\rangle/\langle Z–O\rangle$ ~1.03. Beyond this, incomplete crystallisation or other synthesis phases (oxides, silicates) form. Bosi (2018) further showed that when the difference $\langle Y–O\rangle – \langle Z–O\rangle$ exceeds ~0.15 Å, long-range order is disrupted and continuous solid solution is not maintained. Thus, exceeding these structural limits leads to decomposition. As described in Chapter 1, approximately 100 dependent endmembers were identified as unstable through first-order bond-valence analysis. Accessibility to certain compositional regions is highly dependent on accuracy of the thermodynamics. If no significant

interaction parameters are present, such as in our model, extreme compositions may become accessible during Gibbs free energy minimisation.

We observe three key models:

1. The **Bulk LRO Bragg-Williams model**, which overpredicts composition space and overestimates S^{conf}
2. The **Bulk SRO molecular model**, which underpredicts composition space and underestimates S^{conf}
3. The **Speciation model**, which has the largest speciation space but intermediate $S^{conf,}$ though it lacks sufficient enthalpy data for full calibration.

This has advantages and drawbacks. Predicting unrealistic compositions reveals missing thermodynamic constraints, indicating a need for additional data to refine the model. However, it may also reduce model usability for those users that simply want a working thermodynamic model for the central compositional range rather than extremes. The choice of regression method in Chapter 3 impacts this balance; whether to fit the centroid of data accurately or allow greater variance for better generalisation to compositional limits. This bias-variance tradeoff is key in thermodynamic solid-solution models.

Currently, many thermodynamic models in the geosciences are fitted using a subset of experimental data, while the rest is often dismissed as incorrect or inconsistent. While this approach may have some merit, it has resulted in models that lack proper test sets, leaving the task of validation to users attempting to fit their specific rock compositions. Documenting model failures is crucial in such testing to identify gaps, improve robustness, and advance future models. This would be the merit of having a model with a vast composition space as such failures would be clear. However, for users primarily seeking a functional model, one with a more constrained compositional space would be preferable, as it minimises unrealistic predictions while maintaining practical usability.

Similar challenges exist beyond tourmaline. White et al. (2007), Holland and Powell (2011) and Green et al. 2016 restrict solution space based on *a priori* knowledge of the likely compositions that minerals can have. These constraints are informed by extensive mineral data and natural or

experimental compositional measurements, ensuring that the models remain consistent with observed mineral chemistry. This Bayesian-like approach basically integrates additional constrains besides charge balance and site occupancy used to define the composition polytope to prevent unrealistic compositions. In these solution models, such hard limits are fundamental, functioning as implicit model parameters although they are never mentioned as such. Models with these compositional "infinity walls" behave fundamentally differently in software packages where such constraints are enforced, *e.g.* ThermoCalc (Powell et al. 1998) from those without (*e.g.*, Perple_X, Connolly 2005). Removing such limits requires a complete recalibration of thermodynamic properties, as interaction parameters (W) in unconstrained models partially compensate for these restrictions. In other words, when these "infinity walls" are removed, the fitting process yields entirely different thermodynamic parameters, as previously hidden constraints must now be explicitly captured within the interaction terms. Therefore, such compositional space limits are a fundamental part of the solid solution model, as fundamental as their standard state properties and EoS, basically a class of solid solutions models of their own kind. Although these models may appear to have fewer parameters, they are not truly low-parameter models. Many of the constraints, such as infinite W at certain compositional bounds, function as hidden parameters that are just as fundamental to the model as the explicitly calibrated thermodynamic terms. It is doubtful that W parameters alone could accurately replicate infinity walls, as their effect would need to be extremely abrupt. Capturing such sharp compositional boundaries may require splitting the composition space into distinct regions to model this behavior effectively, as seen in approaches like Darken's quadratic formalism (DQF) (Powell 1987). Consequently, models optimised under strict constraints may fail outside their defined compositional space, necessitating model refitting when limits are removed.

Model calibration in this context resembles a least-squares optimisation with crystal-chemical constraints. The key question is whether such additional constraints, such as bond valence networks (Chapter 2), should be incorporated into polytope construction or whether interaction parameters should be carefully calibrated to impose such limits naturally. For example, LRO endmember definition by charge balance allows two atoms to occupy a site (Hawthorne 2021). Short-range order can modify this by locally enforcing bond valence constraints, restricting possible ion arrangements (Hawthorne et al. 2021). Such a constraint is now already imposed

with the model type chosen, i.e., an incomplete SRO molecular model is and extremely restricted example. Comparing the highly restricted molecular model with the extensive compositional space of the Bragg-Williams LRO model will help determine what approach ultimately produces more robust thermodynamic models. Randomization was the best choice when we had no additional information (Jaynes 1957), however, we now do have additional information, which is currently largely unused.

We have already applied crystal chemical constraints and bond valence sum (BVS) calculations in optimizing mineral formulas to define endmembers. For example, the assumed Al-Mg disorder primarily arises from BVS requirements. While one could discuss the reliability of BVS-derived constraints from empirical crystal databases for specific tourmaline structures, our results indicate that disorder is largely dictated by bond valence constraints, with no direct evidence for Mg occupancy on the Z site.

Since these constraints have already been used to define the polytope vertices, it follows logically that they should also be applied to constrain the rest of the polytope.

3. CONCLUSION AND SUMMARY

This study presents a nearly complete thermodynamic solid solution model for tourmaline, enabling its integration into the thermodynamic databases for forward modelling exchange and net transfer reaction with mineral assemblages, fluids, and melts. Two thermodynamic models were developed: a bulk compositional model, applicable when only chemical composition is available, and a speciation model, incorporating site occupancies derived from structural data.

Meeting Research Objectives The research aimed to develop a thermodynamic framework for tourmaline by overcoming past reliance on estimation methods and empirical calibrations. This was achieved by:

- Assembling and characterizing a diverse tourmaline dataset (~50 natural and synthetic samples) to constrain endmember properties.

- Developing a convex polytope representation of tourmaline's compositional and speciation space, allowing rigorous formulation of endmember-dependent thermodynamic functions.
- Using crystal structure and calorimetric measurements (sc-XRD for molar volume, relaxation calorimetry for entropy, Differential scanning calorimetry for heat capacity, and drop solution calorimetry for enthalpy) to obtain direct thermodynamic data.
- Applying multiple regression techniques to derive endmember properties, ensuring consistency while addressing multicollinearity and uncertainty propagation.
- Implementing a LRO Bragg-Williams and SRO molecular model, providing a first-order approximation of configurational entropy.

This study therefore results in a thermodynamic model that significantly improves on previous estimation-based attempts (Garofalo et al. 2000; van Hinsberg and Schumacher 2007). The inclusion of tourmaline in thermodynamic databases represents a major breakthrough, given tourmaline's stability across diverse pressure-temperature conditions and its role as a powerful petrogenetic indicator mineral in geologic systems.

4. IMPLICATIONS AND FUTURE DIRECTIONS

Despite these advancements, several challenges remain. To properly model tourmaline requires that B can exchange among multiple solid, melt and fluid phases, but high-pressure, high-temperature data for B-species in fluids and melts are currently lacking as are thermodynamic data for virtually all other boron-bearing minerals. As a result, boron behavior can only readily be incorporated into geochemical models for close to ambient conditions.

Standard state properties for DFT Density Functional Theory (DFT) is a promising tool for determining thermodynamic properties, particularly enthalpies of formation, essential for further enthalpic calibration of both our models, especially the speciation model. It has been applied to mineral endmembers and excess enthalpy in solid solutions (Benisek and Dachs 2018, 2020, 2024). DFT-derived enthalpies of formation are obtained by computing the energy difference between a fully geometry-optimised mineral structure and a set of reference oxides (e.g., MgO, Al_2O_3, SiO_2, B_2O_3, H_2O). These calculations rely on both converged and consistently chosen

computational parameters to minimize systematic errors in the derived thermodynamic quantities (Benisek and Dachs 2018).

Among the parameters that must be converged, the k-point grid defines the mesh used to sample the Brillouin zone in periodic systems (Benisek and Dachs 2018). A sufficiently dense grid ensures accurate integration over the electronic states, and convergence is tested by increasing the number of k-points until total energy changes are below a defined threshold (Martin, 2004). The plane-wave cutoff energy sets the maximum kinetic energy of the plane waves used to expand the electronic wavefunctions and determines the completeness of the basis set. Convergence is checked by gradually raising the cutoff until calculated energies and atomic forces stabilize (Benisek and Dachs 2020). Geometry optimisation thresholds, particularly force and stress criteria, must also be converged to guarantee that the crystal structure is fully relaxed and not trapped in a metastable configuration; typically, forces should be below 0.01–0.03 eV/Å for accurate thermodynamic results (Benisek and Dachs 2018).

In contrast, some computational parameters are chosen rather than converged, and must be kept consistent across all calculations to allow meaningful energy comparisons. The exchange-correlation functional, such as the Local Density Approximation (LDA) or Generalized Gradient Approximation (GGA), provides an approximate treatment of electron–electron interactions (Benisek and Dachs 2018). The choice of pseudopotentials defines the treatment of core electrons and must match the chosen functional while being appropriate for the element's oxidation state (Martin, 2004). Spin polarization should be included when unpaired electrons are expected, such as in systems containing transition metals, and must be consistently applied across all relevant atoms and structures (Martin, 2004). When strongly correlated electrons are present, a DFT+U correction may be used to correct for on-site Coulomb interactions; the value of U is typically taken from literature or calibrated to reproduce experimental properties (Benisek and Dachs 2018).

While absolute total energies calculated by DFT can contain systematic offsets due to these approximations, energy differences, such as those between a compound and its decomposition products, often benefit from error cancellation, making them more reliable for thermodynamic modelling. Enthalpies of formation from elements from the reference oxide structures are then

derived using thermodynamic databases like JANAF (Benisek and Dachs 2018). DFT provides enthalpies accurate to a few kJ/mol and entropies within a few J/mol/K, making it reliable for modelling reactions with large enthalpy changes. However, its inherent errors become significant in low-enthalpy reactions (~few kJ/mol). It also predicts mineral volumes with 1–2% error (Benisek & Dachs, 2020), making it suitable for thermodynamic databases. Compressibilities can also be obtained via DFT and fitted to volumetric equations of state. The quasi-harmonic approximation (Baroni et al. 2010; Qin et al. 2019) enables thermal expansivity calculations but at a high computational cost, making direct measurement preferable.

Excess enthalpies from DFT DFT enhances the resolution of nonlinear mixing behavior, aiding in the confirmation of deviations from ideality. It provides insights into the heat of mixing in solid solutions, enabling phase equilibrium and solvus predictions, as shown in garnets, feldspars, pyroxenes, and amphiboles (Benisek and Dachs 2020). Excess enthalpies of mixing are determined using methods such as the single defect method, double defect method, and approaches based on microscopic interaction energies.

The single defect method (Sluiter & Kawazoe, 2002) determines mixing parameters in dilute limits where order-disorder effects are negligible. It involves introducing a single substitutional defect in a large supercell to compute excess internal energy (ΔE_{mix}), closely approximating the enthalpy of mixing (ΔH_{mix}) at low pressure due to the negligible volume term ($P\Delta V_{mix}$). This method effectively extracts Margules interaction parameters from DFT and has been successfully applied to solid solutions including pyrope-grossular, diopside-jadeite, and alkali feldspars, showing good agreement with calorimetric data (Benisek and Dachs 2020). The double defect method (Vinograd et al. 2009) extends this by incorporating two, simultaneous and coupled substitutions, refining estimates of cation interactions, clustering effects, and cross-site interaction parameters (*e.g.*, Mg + Si = Al + Al in pyroxenes and biotites). It is particularly useful for minerals with strong cation ordering tendencies, where local charge balance and non-random interactions significantly affect excess enthalpy (Benisek and Dachs 2020). The accuracy of both methods depends on the exchange-correlation functional (LDA, GGA-PBE) and supercell size, with larger supercells generally yielding more reliable results (Benisek and Dachs 2020).

An alternative approach to obtaining macroscopic excess enthalpy parameters (W) from DFT involves first determining microscopic interaction energies (w) for various structures and then applying basis transformations to model macroscopic mixing behavior (Myhill and Connolly 2021). This method circumvents limitations of the single defect method, particularly in systems with strong ordering or local charge balance effects. In this approach, DFT calculations are performed on multiple structurally distinct configurations of a solid solution, where substitutional interactions occur on different crystallographic sites. These calculations yield microscopic interaction energies (w) for each substitutional pair (Benisek and Dachs 2024) and cross site w. The resulting microscopic interaction energies (w) are then transformed into macroscopic parameters (W) using mathematical frameworks like those of Myhill & Connolly (2021). This method provides a systematic framework for decomposing complex substitutional behavior, allowing for more accurate predictions of mixing properties across a wide range of mineral compositions. For the complex reaction involved between tourmaline endmembers see Appendix 5A and 5B for the bulk and speciation models. The interaction energy correlations with mineral elasticity and oxygen packing fraction (Benisek and Dachs 2024) further enhance the applicability of this approach in thermodynamic modelling.

Spectroscopy from DFT Beyond thermodynamics, DFT provides electronic structure insights, enabling spectroscopic property calculations, such as:

- Electron density distributions to reveal charge localization, bonding characteristics, and their link to thermodynamic properties like enthalpy.
- Optical absorption spectra for interpreting electronic transitions in the complex optical spectra of tourmaline.
- Mössbauer spectra, EFG tensors, and Mössbauer parameters.
- Vibrational spectra (FTIR, Raman) for identifying lattice dynamics.

DFT-based spectroscopy is particularly valuable for minerals like tourmaline, where overlapping spectral features complicate experimental interpretation. It enables rigorous deconvolution of spectra, distinguishing site occupancies, bond distortions, and structural variations with atomic-scale precision, which is particularly important for tourmaline Mössbauer measurements, as

these are our best method for constraining Fe^{2+}/Fe^{3+} ratios, but have significant uncertainty at present as discussed in chapter 2.

Thermodynamic Scaling Exploratory calculations to obtain enthalpy and mixing parameters from DFT modelling have been conducted as part of this study and highlighted as a major challenge defining and constructing the supercells required to properly capture intermediate compositions. While DFT provides valuable thermodynamic and spectroscopic parameters, careful validation against experimental calorimetric, volumetric, and spectroscopic data remains essential, especially for complex solid solutions with significant cation ordering due to coupled substitutions. Large unit cell requirements and ordering effects complicate direct DFT applications of tourmaline, highlighting the need for hybrid approaches that integrate DFT with empirical calorimetric scaling.

Short- and long-range order effects in tourmaline require further study, as current models do not fully capture their impact on entropy and enthalpy of mixing. Calculating the 49 independent SRO structure would enable the first SRO molecular model for tourmaline. Combining these results with direct measurements allows for DFT calibration and the construction of an internally consistent thermodynamic model across the full tourmaline compositional space.

Internal Consistency with databases Ensuring internal consistency in thermodynamic databases requires aligning tourmaline properties with other minerals using experimental constraints. The model will be tested against phase assemblages containing tourmaline in nature and experiments, as well as well-constrained Fe-Mg K_D values (*e.g.*, Morgan and London 1989; von Goerne et al. 1999, 2011; van Hinsberg and Schumacher 2009; London 2011). Refinements should prioritise measured properties, adjusting only standard state enthalpy – the most uncertain parameter, while keeping entropy, Cp and volume fixed for reliable Gibbs free energy extrapolations. A Bayesian approach (Khan et al., 2021). integrates prior knowledge with experimental data, capturing parameter correlations and uncertainties more effectively than least-squares regression. This enhances phase equilibria predictions, resolves discrepancies between experimental and modelled stability fields (Connolly & Khan, 2016). Its adaptability allows continuous model updates, enhancing predictions phase equilibria (Khan et al., 2021). By constraining solutions within physically meaningful limits, Bayesian methods mitigate

overfitting and ensure thermodynamic consistency (Connolly, 2016), making them particularly effective for optimizing high-dimensional solid solution models like tourmaline.

Crystal chemical assumptions Crystal chemical assumptions are among the strongest constraints in mineral formula optimisation and must be rigorously validated against experimental data. Due to spectral overlap in optical spectroscopy, FTIR, and Mössbauer, multiple techniques must be combined to refine the tourmaline structural formula. Local bond lengths are essential for constraining site occupancies. X-ray absorption spectroscopy, being element-specific, can determine which sites elements occupy. Additionally, pair distribution functions from diffuse X-ray scattering at synchrotron sources could provide comprehensive bond length data. While likely complex, this spectrum could be decomposed using element-specific X-ray absorption data, resolving debates on site assignments, such as Mg and Fe^{2+} on Y vs. Z and Ti site preferences. Reverse Monte Carlo methods (Tucker et al. 2001; Dove et al. 2002) could further refine unit cell fitting using multiple SRO structures.

The spin-glass state of tourmaline significantly influences its entropy. More data is needed to determine its magnetic state below the transition temperature, particularly for povondraite. Phonon lattice models (*e.g* calibrated using the Fourier transform infrared spectra (Kieffer 1979a, 1979b, 1979c, 1980, 1982) should be fitted to heat capacity (Cp) curves to separate lattice and magnetic contributions. The resulting magnetic Cp curves can then be tested for linearity across the solid solution series. Since such transitions remain challenging to model with DFT, these empirical results can serve as correction factors for computational entropy values.

Tourmaline model Case studies The resulting tourmaline thermodynamic model can be implemented in petrological software like PerpleX (Connolly, 2005) to model tourmaline formation and its exchange with other phases, including fluids (*cf.* Galvez et al. 2015; Connolly and Galvez 2018). Tourmaline chemistry in rocks from the 3.2 Ga Tartoq Belt, SW Greenland, provides insights into Archean seawater composition, crustal fluids during metamorphism in a proposed early subduction setting, and late-stage hydrothermal fluids responsible for high-grade orogenic gold mineralization, as we showed in van Hinsberg et al. (2019). As a well-preserved remnant of Mesoarchean oceanic crust, the Tartoq Belt records seawater interaction, early-type subduction metamorphism, and orogenic gold formation. Tourmaline, present in all units,

exhibits concentric zoning, preserving a time-integrated record of the belt's geological history and would therefore provide an excellent case study for geologic history and fluid chemistry reconstruction.

Advancing Tourmaline Thermodynamic Modelling and Its Geologic Applications Despite its limitations, this study represents a critical step forward, enabling tourmaline's reliable inclusion in thermodynamic modelling for the first time. Future refinements through high-PT studies, improved experimental constraints, and advanced computational methods will enhance predictive accuracy. Addressing a key challenge from the 2011 *Canadian Mineralogist* special issue on tourmaline (van Hinsberg et al. 2011), it enables compositional zoning to be read as a mineral record in space and time. Given tourmaline's ubiquity, this model benefits metamorphic, igneous, and hydrothermal studies, supporting pseudosection thermobarometry, provenance analysis, mineral exploration, and fluid and magma reconstruction.

REFERENCES

Balan, E., Radtke, G., Fourdrin, C., Paulatto, L., Horn, H.A., and Fuchs, Y. (2023) Effect of Fe–Fe interactions and X-site vacancy ordering on the OH-stretching spectrum of foitite. European Journal of Mineralogy, 35, 105–116.

Bale, C.W., Chartrand, P., Degterov, S.A., Eriksson, G., Hack, K., Ben Mahfoud, R., Melançon, J., Pelton, A.D., and Petersen, S. (2002) FactSage thermochemical software and databases. Calphad, 26, 189–228.

Ballirano, P., Celata, B., and Bosi, F. (2022) In situ high-temperature behaviour and breakdown conditions of uvite at room pressure. Physics and Chemistry of Minerals, 49, 40.

Baroni, S., Giannozzi, P., and Isaev, E. (2010) Density-functional perturbation theory for quasi-harmonic calculations. Reviews in Mineralogy and Geochemistry, 71, 39–57.

Benisek, A., and Dachs, E. (2018) The accuracy of standard enthalpies and entropies for phases of petrological interest derived from density-functional calculations. Contributions to Mineralogy and Petrology, 173, 90.

——— (2020) Excess enthalpy of mixing of mineral solid solutions derived from density-functional calculations. Physics and Chemistry of Minerals, 47, 15.

——— (2024) The packing fraction of the oxygen sublattice: its impact on the heat of mixing. Physics and Chemistry of Minerals, 51, 23.

Berman, R.G., and Brown, T.H. (1985) Heat capacity of minerals in the system Na2O-K2O-CaO-MgO-FeO-Fe2O3-Al2O3-SiO2-TiO2-H2O-CO2: representation, estimation, and high temperature extrapolation. Contributions to Mineralogy and Petrology, 89, 168–183.

Berryman, E.J., Wunder, B., Ertl, A., Koch-Müller, M., Rhede, D., Scheidl, K., Giester, G., and Heinrich, W. (2016) Influence of the X-site composition on tourmaline's crystal structure: investigation of synthetic K-dravite, dravite, oxy-uvite, and magnesio-foitite using SREF and Raman spectroscopy. Physics and Chemistry of Minerals, 43, 83–102.

Bosenick, A., Dove, M.T., Myers, E.R., Palin, E.J., Sainz-Diaz, C.I., Guiton, B.S., Warren, M.C., Craig, M.S., and Redfern, S.A.T. (2001a) Computational methods for the study of energies of cation distributions: applications to cation-ordering phase transitions and solid solutions. Mineralogical Magazine, 65, 193–219.

Bosenick, A., Dove, M.T., Heine, V., and Geiger, C.A. (2001b) Scaling of thermodynamic mixing properties in garnet solid solutions. Physics and Chemistry of Minerals, 28, 177–187.

Bosi, F. (2008) Disordering of Fe2+ over octahedrally coordinated sites of tourmaline. American Mineralogist, 93, 1647–1653.

——— (2010) Octahedrally coordinated vacancies in tourmaline: a theoretical approach. Mineralogical Magazine, 74, 1037–1044.

——— (2011) Stereochemical constraints in tourmaline: from a short-range to a long-range structure. The Canadian Mineralogist, 49, 17–27.

——— (2013) Bond-valence constraints around the O1 site of tourmaline. Mineralogical Magazine, 77, 343–351.

——— (2018) Tourmaline crystal chemistry. American Mineralogist, 103, 298–306.

Bosi, F., and Andreozzi, G.B. (2013) A critical comment on Ertl et al. (2012): "Limitations of Fe2+ and Mn2+ site occupancy in tourmaline: Evidence from Fe2+- and Mn2+-rich tourmaline." American Mineralogist, 98, 2183–2192.

Bosi, F., Andreozzi, G.B., Hålenius, U., and Skogby, H. (2015) Experimental evidence for partial Fe2+ disorder at the Y and Z sites of tourmaline: a combined EMP, SREF, MS, IR and OAS study of schorl. Mineralogical Magazine, 79, 515–528.

Bosi, F., Skogby, H., and Balić-Žunić, T. (2016a) Thermal stability of extended clusters in dravite: a combined EMP, SREF and FTIR study. Physics and Chemistry of Minerals, 43, 395–407.

Bosi, F., Skogby, H., and Hålenius, U. (2016b) Thermally induced cation redistribution in Fe-bearing oxy-dravite and potential geothermometric implications. Contributions to Mineralogy and Petrology, 171, 1–14.

Bosi, F., Skogby, H., Hålenius, U., and Ciriotti, M.E. (2018) Experimental cation redistribution in the tourmaline lucchesiite, CaFe 2+ 3 Al 6 (Si 6 O 18)(BO 3) 3 (OH) 3 O. Physics and Chemistry of Minerals, 45, 621–632.

Bragg, W.L., and Williams, E.J. (1934) The effect of thermal agitation on atomic arrangement in alloys. Proceedings of the Royal Society of London. Series A, Containing Papers of a Mathematical and Physical Character, 145, 699–730.

——— (1935) The effect of thermal agitation on atomic arrangement in alloys—II. Proceedings of the Royal Society of London. Series A - Mathematical and Physical Sciences, 151, 540–566.

Bronzova, Y., Babushkina, M., Frank-Kamenetskaya, O., Vereshchagin, O., Rozhdestvenskaya, I., and Zolotarev, A. (2019) Short-range order in Li–Al tourmalines: IR spectroscopy, X-ray single crystal diffraction analysis and a bond valence theory approach. Physics and Chemistry of Minerals, 46, 815–825.

Brown, I.D. (2016) The Chemical Bond in Inorganic Chemistry: The Bond Valence Model, Second Edition., 336 p. Oxford University Press, Oxford, New York.

Burton, B.P., and Van de Walle, A. (2006) First-principles phase diagram calculations for the system NaCl–KCl: the role of excess vibrational entropy. Chemical Geology, 225, 222–229.

Cadars, S., Ahn, N.H., Okhotnikov, K., Shin, J., Vicente, A., Hong, S.B., and Fernandez, C. (2017) Modelling short-range substitution order and disorder in crystals: Application to the Ga/Si distribution in a natrolite zeolite. Solid State Nuclear Magnetic Resonance, 84, 182–195.

Capitani, C. de, and Petrakakis, K. (2010) The computation of equilibrium assemblage diagrams with Theriak/Domino software. American Mineralogist, 95, 1006–1016.

Carpenter, M.A. (1993) Thermodynamics of phase transitions in minerals: a macroscopic approach. In G.D. Price and N.L. Ross, Eds., The Stability of Minerals Vol. 3, pp. 172–215. Springer Netherlands, Dordrecht.

Celata, B., Ballirano, P., Bosi, F., Andreozzi, G.B., and Beckett-Brown, C. (2023) Thermal behavior of schorl up to breakdown temperature at room pressure. Periodico di Mineralogia, 92.

Cemic, L. (2005) Thermodynamics in Mineral Sciences, 386 p. Springer.

Cohen, R.E. (1986) Configurational thermodynamics of aluminous pyroxenes: A generalized pair approximation. Physics and Chemistry of Minerals, 13, 183–197.

Connolly, J.A. (2005) Computation of phase equilibria by linear programming: a tool for geodynamic modelling and its application to subduction zone decarbonation. Earth and Planetary Science Letters, 236, 524–541.

Connolly, J.A.D. (2016) Thermodynamics applied to earth materials, 68 p. Lecture Notes, ETH Zurich.

Connolly, J.A.D., and Galvez, M.E. (2018) Electrolytic fluid speciation by Gibbs energy minimisation and implications for subduction zone mass transfer. Earth and Planetary Science Letters, 501, 90–102.

Connolly, J.W.D., and Williams, A.R. (1983) Density-functional theory applied to phase transformations in transition-metal alloys. Physical Review B, 27, 5169–5172.

de Fontaine, D., and Wolverton, C. (1994) Cluster approach to first-principles thermodynamics of crystals. Progress of Theoretical Physics Supplement, 115, 115–130.

Desbois, G., and Ingrin, J. (2007) Anisotropy of hydrogen diffusion in tourmaline. Geochimica et Cosmochimica Acta, 71, 5233–5243.

Dove, M.T. (2001) Computer simulations of solid solutions. In Solid Solutions in Silicate and Oxide Systems Vol. 3.

Dove, M.T., Bosenick, A., Myers, E.R., Warren, M.C., and Redfern, S.A.T. (2000) Modelling in relation to cation ordering. Phase Transitions, 71, 205–226.

Dove, M.T., Tucker, M.G., Wells, S.A., and Keen, D.A. (2002) Reverse Monte Carlo methods. In Energy Modelling in Minerals Vol. 4.

Ertl, A., Kolitsch, U., Dyar, M.D., Hughes, J.M., Rossman, G.R., Pieczka, A., Henry, D.J., Pezzotta, F., Prowatke, S., and Lengauer, C.L. (2012) Limitations of Fe2+ and Mn2+ site occupancy in tourmaline: evidence from Fe2+-and Mn2+-rich tourmaline. American Mineralogist, 97, 1402–1416.

Fantini, C., Tavares, M.C., Krambrock, K., Moreira, R.L., and Righi, A. (2014) Raman and infrared study of hydroxyl sites in natural uvite, fluor-uvite, magnesio-foitite, dravite and elbaite tourmalines. Physics and Chemistry of Minerals, 41, 247–254.

Ferrow, E.A. (1995) Computer-simulated high-resolution transmission electron microscopy (HRTEM) in tourmaline. Journal of Microscopy, 177, 68–76.

Ferrow, E.A., Wallenberg, L.R., and Skogby, H. (1993) Compositional control of plane group symmetry in tourmalines: an experimental and computer simulated TEM, crystallographic image processing and Mossbauer spectroscopy study. European Journal of Mineralogy, 479–492.

Filip, J., Bosi, F., Novák, M., Skogby, H., Tuček, J., Čuda, J., and Wildner, M. (2012) Iron redox reactions in the tourmaline structure: High-temperature treatment of Fe3+-rich schorl. Geochimica et Cosmochimica Acta, 86, 239–256.

Fuchs, Y., Fourdrin, C., and Balan, E. (2022) Theoretical OH stretching vibrations in dravite. European Journal of Mineralogy, 34, 239–251.

Galvez, M.E., Manning, C.E., Connolly, J.A., and Rumble, D. (2015) The solubility of rocks in metamorphic fluids: A model for rock-dominated conditions to upper mantle pressure and temperature. Earth and Planetary Science Letters, 430, 486–498.

Ganguly, J. (2001) Thermodynamic modelling of solid solutions. In Solid Solutions in Silicate and Oxide Systems. Eotvos University Press.

Garofalo, P., Audétat, A., Günther, D., Heinrich, C.A., and Ridley, J. (2000) Estimation and testing of standard molar thermodynamic properties of tourmaline end-members using data of natural samples. American Mineralogist, 85, 78–88.

Gonzalez-Carreño, T., Fernandez, M., and Sanz, J. (1988) Infrared and electron microprobe analysis of tourmalines. Physics and Chemistry of Minerals, 15, 452–460.

Gottschalk, M. (2016) Beyond the Margules equation: a universal thermodynamic equation for solid solutions including coupled substitution, long- and short-range order. European Journal of Mineralogy, 28, 219–244.

Green, E.C.R., White, R.W., Diener, J.F.A., Powell, R., Holland, T.J.B., and Palin, R.M. (2016) Activity-composition relations for the calculation of partial melting equilibria in metabasic rocks. Journal of Metamorphic Geology, 34, 845–869.

Grew, E.S., Krivovichev, S.V., Hazen, R.M., and Hystad, G. (2016) Evolution of structural complexity in boron minerals. The Canadian Mineralogist, 54, 125–143.

Hawthorne, F.C. (1996) Structural mechanisms for light-element variations in tourmaline. The Canadian Mineralogist, 34, 123–132.

——— (2002) Bond-valence constraints on the chemical composition of tourmaline. The Canadian Mineralogist, 40, 789–797.

——— (2016) Short-range atomic arrangements in minerals. I: The minerals of the amphibole, tourmaline and pyroxene supergroups. European Journal of Mineralogy, 28, 513–536.

——— (2021) Proof that a dominant endmember formula can always be written for a mineral or a crystal structure. The Canadian Mineralogist, 59, 159–167.

Hawthorne, F.C., Mills, S.J., Hatert, F., and Rumsey, M.S. (2021) Ontology, archetypes and the definition of ‘mineral species.’ Mineralogical Magazine, 85, 125–131.

Henry, D.J., and Dutrow, B.L. (2011) The incorporation of fluorine in tourmaline: Internal crystallographic controls or external environmental influences? The Canadian Mineralogist, 49, 41–56.

Henry, D.J., Novák, M., Hawthorne, F.C., Ertl, A., Dutrow, B.L., Uher, P., and Pezzotta, F. (2011) Nomenclature of the tourmaline-supergroup minerals. American Mineralogist, 96, 895–913.

Hoang, L.H., Hien, N.T.M., Chen, X.B., Minh, N.V., and Yang, I. (2011) Raman spectroscopic study of various types of tourmalines. Journal of Raman Spectroscopy, 42, 1442–1446.

Holland, T.J.B., Green, E.C.R., and Powell, R. (2018) Melting of Peridotites through to Granites: A Simple Thermodynamic Model in the System KNCFMASHTOCr. Journal of Petrology, 59, 881–900.

Holland, T.J.B., and Powell, R. (1990) An enlarged and updated internally consistent thermodynamic dataset with uncertainties and correlations: the system K2O–Na2O–CaO–MgO–MnO–FeO–Fe2O3–Al2O3–TiO2–SiO2–C–H2–O2. Journal of metamorphic Geology, 8, 89–124.

Holland, T.J.B., and Powell, R. (1998) An internally consistent thermodynamic data set for phases of petrological interest. Journal of metamorphic Geology, 16, 309–343.

Holland, T.J.B., and Powell, R. (2011) An improved and extended internally consistent thermodynamic dataset for phases of petrological interest, involving a new equation of state for solids. Journal of Metamorphic Geology, 29, 333–383.

Iijima, S., Cowley, J.M., and Donnay, G. (1973) Hochauflösende Elektronenmikroskopie von Turmalinkristallen. Tschermaks mineralogische und petrographische Mitteilungen, 20, 216–224.

Jaynes, E.T. (1957) Information Theory and Statistical Mechanics. Physical Review, 106, 620–630.

Kerrick, D.M., and Darken, L.S. (1975) Statistical thermodynamic models for ideal oxide and silicate solid solutions, with application to plagioclase. Geochimica et Cosmochimica Acta, 39, 1431–1442.

Kieffer, S.W. (1979a) Thermodynamics and lattice vibrations of minerals: 1. Mineral heat capacities and their relationships to simple lattice vibrational models. Reviews of Geophysics, 17, 1–19.

——— (1979b) Thermodynamics and lattice vibrations of minerals: 2. Vibrational characteristics of silicates. Reviews of Geophysics, 17, 20.

——— (1979c) Thermodynamics and lattice vibrations of minerals: 3. Lattice dynamics and an approximation for minerals with application to simple substances and framework silicates. Reviews of Geophysics, 17, 35.

——— (1980) Thermodynamics and lattice vibrations of minerals: 4. Application to chain and sheet silicates and orthosilicates. Reviews of Geophysics, 18, 862.

——— (1982) Thermodynamics and lattice vibrations of minerals: 5. Applications to phase equilibria, isotopic fractionation, and high-pressure thermodynamic properties. Reviews of Geophysics, 20, 827.

Krivovichev, S.V. (2013) Structural complexity of minerals: information storage and processing in the mineral world, 77, 275–326.

Kulik, D.A., Wagner, T., Dmytrieva, S.V., Kosakowski, G., Hingerl, F.F., Chudnenko, K.V., and Berner, U.R. (2013) GEM-Selektor geochemical modelling package: revised algorithm and GEMS3K numerical kernel for coupled simulation codes. Computational Geosciences, 17, 1–24.

Kutzschbach, M., Wunder, B., Rhede, D., Koch-Müller, M., Ertl, A., Giester, G., Heinrich, W., and Franz, G. (2016) Tetrahedral boron in natural and synthetic HP/UHP tourmaline: evidence from Raman spectroscopy, EMPA, and single-crystal XRD. American Mineralogist, 101, 93–104.

Kutzschbach, M., Wunder, B., Wannhoff, I., Wilke, F.D., Couffignal, F., and Rocholl, A. (2021) Raman spectroscopic quantification of tetrahedral boron in synthetic aluminum-rich tourmaline. American Mineralogist, 106, 872–882.

London, D. (2011) Experimental synthesis and stability of tourmaline: a historical overview. The Canadian Mineralogist, 49, 117–136.

Lussier, A.J., Aguiar, P.M., Michaelis, V.K., Kroeker, S., Herwig, S., Abdu, Y., and Hawthorne, F.C. (2008) Mushroom elbaite from the Kat Chay mine, Momeik, near Mogok, Myanmar: I. Crystal chemistry by SREF, EMPA, MAS NMR and Mössbauer spectroscopy. Mineralogical Magazine, 72, 747–761.

Lussier, A.J., Aguiar, P.M., Michaelis, V.K., Kroeker, S., and Hawthorne, F.C. (2009) The occurrence of tetrahedrally coordinated Al and B in tourmaline: An 11B and 27Al MAS NMR study. American Mineralogist, 94, 785–792.

Lussier, A.J., Abdu, Y., Hawthorne, F.C., Michaelis, V.K., Aguiar, P.M., and Kroeker, S. (2011) Oscillatory zoned liddicoatite from Anjanabonoina, central Madagascar. I. Crystal chemistry and structure by SREF and 11B and 27Al MAS NMR spectroscopy. Canadian Mineralogist, 49, 63–88.

Marler, B., and Ertl, A. (2002) Nuclear magnetic resonance and infrared spectroscopic study of excess-boron olenite from Koralpe, Styria, Austria. American Mineralogist, 87, 364–367.

Morgan, G.B., and London, D. (1989) Experimental reactions of amphibolite with boron-bearing aqueous fluids at 200 MPa: implications for tourmaline stability and partial melting in mafic rocks. Contributions to Mineralogy and Petrology, 102, 281–297.

Myhill, R., and Connolly, J. (2021) Notes on the creation and manipulation of solid solution models. Contributions to Mineralogy and Petrology, 176.

Navrotsky, A. (1994) Physics and chemistry of earth materials, 413 p. Cambridge University Press, Cambridge.

Okhotnikov, K., Charpentier, T., and Cadars, S. (2016a) Supercell program: a combinatorial structure-generation approach for the local-level modelling of atomic substitutions and partial occupancies in crystals. Journal of Cheminformatics, 8, 17.

——— (2016b) Supercell program tutorial.

Powell, R. (1987) Darken's quadratic formalism and the thermodynamics of minerals. American Mineralogist, 72, 1–11.

Powell, R., and Holland, T. (1999) Relating formulations of the thermodynamics of mineral solid solutions; activity modelling of pyroxenes, amphiboles, and micas. American Mineralogist, 84, 1–14.

Powell, R., Holland, T., and Worley, B. (1998) Calculating phase diagrams involving solid solutions via non-linear equations, with examples using THERMOCALC. Journal of Metamorphic Geology, 16, 577–588.

Qin, T., Zhang, Q., Wentzcovitch, R.M., and Umemoto, K. (2019) qha: A Python package for quasiharmonic free energy calculation for multi-configuration systems. Computer Physics Communications, 237, 199–207.

Redfern, S.A.T. (2000) Order-Disorder Phase Transitions. Reviews in Mineralogy and Geochemistry, 39, 105–133.

Sanz, J., and Robert, J.-L. (1992) Influence of structural factors on 29Si and 27Al NMR chemical shifts of phyllosilicates 2: 1. Physics and Chemistry of Minerals, 19, 39–45.

Skogby, H., Bosi, F., and Lazor, P. (2012) Short-range order in tourmaline: a vibrational spectroscopic approach to elbaite. Physics and Chemistry of Minerals, 39, 811–816.

Sluiter, M.H.F., and Kawazoe, Y. (2002) Prediction of the mixing enthalpy of alloys. Europhysics Letters, 57, 526.

Spear, F.S. (1993) Metamorphic phase equilibria and pressure–temperature–time paths. Mineralogical Society of America Monograph., 799.

Thompson Jr, J.B. (1969) Chemical reactions in crystals. American Mineralogist: Journal of Earth and Planetary Materials, 54, 341–375.

Thompson Jr., J.B. (1982) Chapter 1. Composition space: An algebraic and geometric appoach. In J.M. Ferry, Ed., Characterisation of Metamorphism through Mineral Equilibria pp. 1–32. De Gruyter.

Thompson Jr, J.B., and Waldbaum, D.R. (1968) Mixing properties of sanidine crystalline solutions: I. Calculations based on ion-exchange data. American Mineralogist: Journal of Earth and Planetary Materials, 53, 1965–1999.

——— (1969a) Analysis of the two-phase region halite-sylvite in the system NaCl- KCl. Geochimica et Cosmochimica Acta, 33, 671–690.

——— (1969b) Mixing properties of sanidine crystalline solutions: III. Calculations based on two-phase data. American Mineralogist: Journal of Earth and Planetary Materials, 54, 811–838.

Tsang, T., and Ghose, S. (1973) Nuclear magnetic resonance of 1H, 7Li, 11B, 23Na, and 27Al in tourmaline (elbaite). American Mineralogist, 58, 224–229.

Tucker, M.G., Dove, M.T., and Keen, D.A. (2001) Application of the reverse Monte Carlo method to crystalline materials. Journal of applied crystallography, 34, 630–638.

van Hinsberg, V.J., and Schumacher, J.C. (2007a) Intersector element partitioning in tourmaline: a potentially powerful single crystal thermometer. Contributions to Mineralogy and Petrology, 153, 289–301.

van Hinsberg, V.J., and Schumacher, J.C. (2007b) Using estimated thermodynamic properties to model accessory phases: the case of tourmaline. Journal of Metamorphic Geology, 25, 769–779.

van Hinsberg, V.J., and Marschall, H.R. (2007c) Boron isotope and light element sector zoning in tourmaline: Implications for the formation of B-isotopic signatures. Chemical Geology, 238, 141–148.

van Hinsberg, V.J., and Schumacher, J.C. (2009) The geothermobarometric potential of tourmaline, based on experimental and natural data. American Mineralogist, 94, 761–770.

van Hinsberg, V.J., Henry, D.J., and Marschall, H.R. (2011) Tourmaline: an ideal indicator of its host environment. The Canadian Mineralogist, 49, 1–16.

Vereshchagin, O.S., Frank-Kamenetskaya, O.V., Rozhdestvenskaya, I.V., and Zolotarev, A.A. (2018) Incorporation of 3d elements in tourmalines: structural adjustments and stability. European Journal of Mineralogy, 30, 917–928.

Vinograd, V.L. (1997) Application of stochastic processes to modelling of ordered cationic distributions in aluminosilicates.

——— (2001) Configurational entropy of binary silicate solid solutions.

Vinograd, V.L., Sluiter, M.H.F., Winkler, B., Putnis, A., Halenius, U., Gale, J.D., and Becker, U. (2004) Thermodynamics of mixing and ordering in pyrope–grossular solid solution. Mineralogical Magazine, 68, 101–121.

Vinograd, V.L., Gale, J.D., and Winkler, B. (2007) Thermodynamics of mixing in diopside–jadeite, CaMgSi2O6–NaAlSi2O6, solid solution from static lattice energy calculations. Physics and Chemistry of Minerals, 34, 713–725.

Vinograd, V.L., Sluiter, M.H.F., and Winkler, B. (2009) Subsolidus phase relations in the CaCO 3 – MgCO 3 system predicted from the excess enthalpies of supercell structures with single and double defects. Physical Review B, 79, 104201.

Vinograd, V.L., Brandt, F., Rozov, K., Klinkenberg, M., Refson, K., Winkler, B., and Bosbach, D. (2013) Solid–aqueous equilibrium in the BaSO4–RaSO4–H2O system: first-principles calculations and a thermodynamic assessment. Geochimica et Cosmochimica Acta, 122, 398–417.

von Goerne, G., Franz, G., and Wirth, R. (1999) Hydrothermal synthesis of large dravite crystals by the chamber method. European Journal of Mineralogy, 11, 1061–1077.

von Goerne, G., Franz, G., and van Hinsberg, V.J. (2011) Experimental determination of Na–Ca distribution between tourmaline and fluid in the system CaO–Na2O–MgO–Al2O3–SiO2–B2O3–H2O. The Canadian Mineralogist, 49, 137–152.

Waldbaum, D.R. (1973) The configurational entropies of Ca2MgSi2O7-Ca2SiAl2O7 melilites and related minerals. Contributions to Mineralogy and Petrology, 39, 33–54.

Waldbaum, D.R., and Thompson Jr, J.B. (1968) Mixing properties of sanidine crystalline solutions: II. Calculations based on volume data. American Mineralogist: Journal of Earth and Planetary Materials, 53, 2000–2017.

——— (1969) Mixing properties of sanidine crystalline solutions: IV. Phase diagrams from equations of state. American Mineralogist: Journal of Earth and Planetary Materials, 54, 1274–1298.

Warren, M.C., Dove, M.T., Myers, E.R., Bosenick, A., Palin, E.J., Sainz-Diaz, C.I., Guiton, B.S., and Redfern, S.A.T. (2001) Monte Carlo methods for the study of cation ordering in minerals. Mineralogical Magazine, 65, 221–248.

Watenphul, A., Schlüter, J., Bosi, F., Skogby, H., Malcherek, T., and Mihailova, B. (2016) Influence of the octahedral cationic-site occupancies on the framework vibrations of Li-free tourmalines, with implications for estimating temperature and oxygen fugacity in host rocks. American Mineralogist, 101, 2554–2563.

Watenphul, A., Malcherek, T., Wilke, F.D., Schlüter, J., and Mihailova, B. (2017) Composition–thermal expandability relations and oxidation processes in tourmaline studied by in situ Raman spectroscopy. Physics and Chemistry of Minerals, 44, 735–748.

White, R.W., Powell, R., and Holland, T.J.B. (2007) Progress relating to calculation of partial melting equilibria for metapelites. Journal of metamorphic Geology, 25, 511–527.

Will, T.M. (1998) Phase Equilibria in Metamorphic Rocks, 315 p. Vol. 71. Springer, Berlin, Heidelberg.

Wolverton, C., and Zunger, A. (1994) Comparison of two cluster-expansion methods for the energetics of Pd-V alloys. Physical Review B, 50, 10548–10560.

Wood, B.J., and Fraser, D.G. (1977) Elementary thermodynamics for geologists. 318 p. Oxford university Press.

Appendices Chapter 1

APPENDIX 1B. EMPA Details

EMPA Matrix correction details

Averaged k-ratios far from 1 (F (0.010), Na (0.138), Si (0.572), Mg (0.370), Al (1.481), K (0.004), Ca (0.059), Ti (0.005), Fe (0.078), Mn (0.005), Cr (0.000)) and density differences between primary standards and tourmaline emphasized the need for accurate matrix corrections. To linearize the calibration curve and relate measured k-ratios directly to concentration ratios, second-generation X-Phi ZAF corrections were applied, incorporating ϕ(ρz)-based absorption adjustments for matrix differences between tourmaline and standards, i.e., $k_i = \frac{I_i}{I_i^{\text{std}}} = \frac{c_i}{c_i^{\text{std}}}[ZA]\text{F}$ via:

$$k_i = \frac{I_i}{I_i^{\text{std}}} = \frac{c_i \int_0^{\infty} \phi_j(\rho z)\exp\left[-\left(\frac{\mu}{\rho}\right)\rho z\csc(\psi)\right] d\rho z}{c_i^{\text{std}} \int_0^{\infty} \phi_j^{\text{std}}(\rho z)\exp\left[-\left(\frac{\mu}{\rho}\right)^{\text{std}}\rho z\csc(\psi)\right] d\rho z} \times \frac{(1+\sum f_c + f_b)}{(1+\sum f_c + f_b)^{\text{std}}}$$

where the Beer-Lambert exponential term $\exp\left[-\left(\frac{\mu}{\rho}\right)\rho z\csc(\psi)\right]$ multiplied with the ϕ(ρz) distributions adjusts for photo-electronic absorption (ZA in ZAF), with μ/ρ as the mass absorption coefficient (MAC), ρz the depth, and ψ the take-off angle (Llovet et al., 2021).

X-Phi employs Gaussian ϕ(ρz) for x-ray depth production (Merlet 1992, 1994; Lavrent'ev et al. 2004) and MAC30 values from Heinrich (1987) for 30° takeoff angle, but for boron initial values from Henke et al. (1982) were empirical corrected using a borides database (Bastin and Heijligers 1986). Using MAC30 at 40° may cause slight errors, especially for light elements due to absorption path differences. The fluorescence correction $\frac{(1+\Sigma f_c+f_b)}{(1+\Sigma f_c+f_b)^{std}}$ accounts for enhancement from characteristic and continuum fluorescence, backscattering, and ionization potential differences between the sample and standard (F in ZAF) (Llovet et al. 2021). The matrix correction is calculated iteratively until convergence, as the absorption depends on the averaged MAC, via the additive rule (Llovet et al. 2023), which is influenced by unknown concentrations (Reed 2005). Fixed estimates of B_2O_3 (10%) and H_2O (2.5%) were essential for accurate matrix corrections, as their inclusion lowered SiO_2 (-0.6 wt%) and increased Al_2O_3 (+0.4 wt%), FeO (+0.2 wt%), or MgO (+0.16 wt%), due to boron's dilution effect which absorbs

fewer heavy-element x-rays but affects Si Kα absorption. EMPA measurements of tourmaline excluding light elements in matrix corrections may show higher Si in the T-site, and also in JEOL versus CAMECA instruments due to more pronounced Mg and Si peak shifts (Llovet et al. 2021). Due to the high and uncertain MAC values of light elements like fluorine in matrices like oxygen and calcium, EMPA measurements are more uncertain, further compounded by peak shifts, Fe interference, and absorption by carbon coating (Llovet et al. 2021). The variance of light element MAC values between matrix correction algorithm (Llovet et al. 2023) is shown by the difference of about 0.3% when we use PAP (Pouchou and Pichoir 1991) instead of X-Phi for Si (effected by B).

EMPA LOD details Average detection limits for each major element were calculated using the Goldstein method (Goldstein et al. 2003), which defines the limit as 3σ above the background. While the Ancey method (Ancey et al. 1978), based on Poisson statistics, rendered all our F measurements below limit of detection (LOD), we opted for Goldstein due to the consistency of repeated measurements, even those "below Ancey's LOD".

****

EMPA Condition File.

Xtal information

Xtal parameters:

F Ka	Sp1	LTAP	(2d= 25.745	K= 0.002180)
Na Ka	Sp4	TAP	(2d= 25.745	K= 0.002180)
Si Ka	Sp2	LTAP	(2d= 25.745	K= 0.002180)
Mg Ka	Sp2	LTAP	(2d= 25.745	K= 0.002180)
Al Ka	Sp4	TAP	(2d= 25.745	K= 0.002180)
K Ka	Sp3	LPET	(2d= 8.75	K= 0.000144)
Ca Ka	Sp3	LPET	(2d= 8.75	K= 0.000144)
Ti Ka	Sp3	LPET	(2d= 8.75	K= 0.000144)
Fe Ka	Sp5	LLIF	(2d= 4.0267	K= 0.000058)
Mn Ka	Sp5	LLIF	(2d= 4.0267	K= 0.000058)
Cr Ka	Sp5	LLIF	(2d= 4.0267	K= 0.000058)

Pha parameters :

Elt. Line	Spec	Xtal	Bias (V)	Gain	Dtime (µs)	Blin (mV)	Wind (mV)	Mode
F Ka	Sp1	LTAP	1301	2991	3	825	2922	
Na Ka	Sp4	TAP	1297	2959	3	820	4180	
Si Ka	Sp2	LTAP	1307	3023	3	830	4170	
Mg Ka	Sp2	LTAP	1307	3023	3	830	4170	
Al Ka	Sp4	TAP	1297	2959	3	820	4081	
K Ka	Sp3	LPET	1856	1042	3	740	3728	
Ca Ka	Sp3	LPET	1856	1042	3	1060	3940	
Ti Ka	Sp3	LPET	1856	1042	3	534	3480	
Fe Ka	Sp5	LLIF	1841	445	3	699	2054	
Mn Ka	Sp5	LLIF	1841	445	3	953	2252	
Cr Ka	Sp5	LLIF	1841	445	3	802	2144	

****

Acquisition information

Elt. Line	Spec	Xtal	Peak Time/Repeat	Pk Time	Bg Off1 Range		Bg Off2 #Channels	Slope/IBg (cps/nA)	Bg Time	Calibrat
F Ka	Sp1	LTAP	71296	20	-1800	1400	10	CAF2_20kV_FKa-Sp1-LTAP3	13.0	
Na Ka	Sp4	TAP	46358	20	-2200	2040	10	AALB_20kV_NaKa-Sp4-TAP3	24.3	
Si Ka	Sp2	LTAP	27742	20	-2200	1800	10	Diop_20kV_SiKa-Sp2-LTAP_CaKa-Sp3-LPET3	946.2	
Mg Ka	Sp2	LTAP	38529	20	-1900	1300	10	Diop_20kV_MgKa-Sp2-LTAP3	162.6	
Al Ka	Sp4	TAP	32471	20	-1740	1500	10	Sanidine_20kV_AlKa-Sp4-TAP_SiKa-Sp2-LTAP_KKa-Sp3-LPET3	111.1	
K Ka	Sp3	LPET	42767	20	-1450	1200	10	Sanidine_20kV_AlKa-Sp4-TAP_SiKa-Sp2-LTAP_KKa-Sp3-LPET3	281.4	
Ca Ka	Sp3	LPET	38386	20	-1320	1450	10	Diop_20kV_SiKa-Sp2-LTAP_CaKa-Sp3-LPET3	634.3	
Ti Ka	Sp3	LPET	31412	10	-2030	1050	5	TiO2_20kV_TiKa-Sp3-LPET3	2868.8	
Fe Ka	Sp5	LLIF	48082	20	-1200	1300	10	Fe2O3_20kV_FeKa-Sp5-LLIF3	929.7	
Mn Ka	Sp5	LLIF	52196	20	-1150	1150	10	Spess_20kV_MnKa-Sp5-LLIF3	353.5	
Cr Ka	Sp5	LLIF	56862	20	-1050	1050	10	CHRO_20kV_CrKa-Sp5-LLIF3	327.7	

Eds Time = 60s

****

APPENDIX 1D. Karl fisher titration details

The titration setup consists of an RF generator, sample chamber, CuO oven, temperature display, and moisture meter. Samples, placed in platinum crucibles, were heated to 1000°C in a high-frequency induction furnace. An argon stream, dried with a molecular sieve, carried volatiles from the sample to the titration cell through a Cu contact at 300°C.

Measurement System Water content was measured with a Mitsubishi CA-200 moisture meter, featuring separate anolyte and catholyte cells. The anolyte cell contains Aquamicron AX solution (up to 100 mg H_2O capacity), while the catholyte cell holds Aquamicron CXU, separated by a diaphragm that forms the electrochemical generator electrode (Scholz 2012).

Karl Fischer Reaction

In the anolyte cell, the Karl Fischer reaction occurs as follows (Fischer 1935):

$$I_2 + SO_2 + 3Base + ROH + H_2O \rightarrow (2Base \cdot HI) + (Base + HSO_4R)$$

where iodine, sulphur dioxide, base, and methanol (solvent) react with water. Iodine is generated electrochemically by anodic oxidation:

$$2I^- - 2e \rightarrow I_2$$

Balanced by a reduction in the catholyte compartment, positive hydrogen ions are reduced to hydrogen. Each molecule of iodine reacts with a molecule of water, detected by a double platinum electrode, which regenerates iodine through electrolysis (Meyer and Boyd 1959). Faraday's laws link iodine production to water quantity (1 mg H_2O = 10.712 Coulombs), measured by current integration.

End-Point Detection

The endpoint is indicated by electrodes maintaining an alternating current, where a decrease in voltage signals excess iodine (Scholz 2012).

APPENDIX 1E. Mossbauer details

Limits of the single Lorenzian Model Physically interpretable tourmaline hyperfine interactions ideally require a static Hamiltonian per Fe SRO cluster, but underdetermination necessitates empirical fits. Each SRO cluster has distinct Lorentzian peaks, as seen in MO studies on octahedral clusters (Evans 2004, 2005) and silicates like omphacite, where local distortions shift quadrupole splittings up to 0.3 mm/s (Katerinopoulou et al. 2013). Although Lorentzian fits suit uniform Fe environments, tourmaline's varied Fe-O, OH, F, and second-neighbor cation configurations broaden and overlap peaks, making multiple Lorentzian fits non-unique (Pieczka et al. 1998; Pieczka and Kraczka 2004). Systems without SRO preference produce Gaussian-distributed set of Lorentzian peaks, while preferred clusters and electron hopping result in non-Gaussian broadening (Rancourt and Ping 1991; Rancourt 1994). Andreozzi (2008) noted broadening but incorrectly applied an excessive Lorentzian linewidth, which overestimates wings and underestimates peaks due to its $1/x^2$ decay and lead to matrix correction errors. The Lorentzian linewidth of 0.194 mm/s should remain fixed as it is derived from Heisenberg's uncertainty principle, where the minimum ^{57}Fe transition linewidth of 0.097 mm/s doubles through the convolution of absorption (Γa) and emission (Γs) (Gütlich et al. 2010). Minor deviations (±0.05 mm/s) can occur from sample thickness effects, but further adjustments lack physical basis (Rancourt 1994).

Data Normalization To relate Fe^{2+}/Fe^{3+} doublet area ratios in Mössbauer spectra to concentration ratios, a matrix correction C accounts for differences in linewidth Γ, saturation correction G, and recoil-free fractions f (Lamb-Mössbauer factor). The relation $\frac{A_1}{A_2} = C\frac{N_1}{N_2}$, uses $C = \frac{\Gamma_1 G_1 f_1}{\Gamma_2 G_2 f_2}$ (Bancroft 1973). Assumptions like $\Gamma1=\Gamma2$, G1=G2 and f1=f2 are often made or assumed to cancel out via Γ_1*G1*f_1 = Γ_2*G2*f_2 (Hawthorne 1988) but require verification.

To balance spectral distortion and signal-to-noise, we used a 5 mg/cm² Fe absorber, exceeding the 0.5 mg/cm² thin limit (Ping and Rancourt 1992), which may introduce 5–10% area errors affecting all doublets (Rancourt et al. 1993). To correct for these thickness effects without full deconvolution or having to solve the full transmission integral we adjusted Lorentzian linewidths (±0.03 of 0.2 mm/s) using the same Γ for each doublet , which keeps G1/G2≈1 (Fultz 2011). Such simplified corrections suffice for ratio calculations but make exact site assignments from

doublets uncertain. Individual doublet line broadening (Andreozzi et al. 2008) renders Γ1≠Γ2 and complicates G1/G2≈1 and consistency in the matrix correction.

Assuming f=f for $^{VI}Fe^{2+}$ and $^{VI}Fe^{3+}$ may seem reasonable, but size and distortion differences (Ertl et al. 2002) indicate otherwise. The recoil-free fraction f varies with site geometry and valence (Dyar et al. 2008), affecting partial vibrational density of states (p-vDOS). Fe^{3+}, being smaller and more charged, forms a rigid lattice, enhancing recoil-free absorption, while Fe^{2+}, with longer, flexible bonds and Jahn-Teller distortion, reduces f (Grodzicki and Lebernegg 2011). Incorrect assumptions can cause errors up to 30%, averaging 15% (Whipple 1974), and depend on site and composition (De Grave and Van Alboom 1991). No f differences for tourmaline were estimated using Debye models fitting to temperature-dependent center shifts, though these oversimplify mineral complexity and require accurate doublets (Saegusa 1978). First-principles or NRIXS provide p-vDOS allowing f to be derived from the thermalized mean squared displacement ⟨u2⟩ with Bose-Einstein weightings, as $f = e^{(u^2)k^2}$ with k as the gamma-ray wave vector (Dauphas et al. 2018). NRIXS Bulk Fe^{2+} in schorl show 74.83% recoil-free fraction (Nie et al. 2021), but due to data absence on Fe^{3+} in tourmaline and site dependency, f=f was maintained, adding uncertainty to the Fe^{3+}/Fe^{2+} ratios, common in all tourmaline Mössbauer studies. Fractionation of ^{57}Fe between sites and valences is assumed negligible.

Intervalence charge transfer (IVCT) IVCT in tourmaline, studied via optical and Mössbauer spectroscopy, involves Mn^{2+}-Ti^{4+}, Fe^{2+}-Ti^{4+}, and Fe^{2+}-Fe^{3+} mechanisms. Optical studies show that Fe^{2+}-Fe^{3+} IVCT enhances Fe^{2+} bands without forming new peaks, intensifies at low temperatures, weakens Fe^{3+} features, and causes the black colour in Fe-rich varieties (Faye et al. 1974), unlike Fe^{2+}-Ti^{4+}, which forms new IVCT peaks. This effect is stronger in tourmaline than in other minerals and lacks a theoretical basis and mechanism (Mattson and Rossman 1987) (e.g., polaron hopping, band-like behavior, or covalent exciton formation). Mössbauer spectroscopy with slower timescales (~10^{-8} to 10^{-10} s) than optical spectroscopy (~10^{-15} s), reveals broad spectra and intermediate isomer shifts, indicating electron delocalisation and thermally activated hopping without an electric field. Sharp spectra from limited low-temperature (~20–80 K) data (Scorzelli et al. 1976; Ferrow et al. 1988; Ferrow 2009) suggest potential electron localization, supporting the thermal nature of electron hopping, though phonon mode effects may also contribute. Mössbauer IVCT interpretation is challenged by cation variability, Y and Z site

symmetry differences, and weak support for doublet averaging (Ferrow 2009), with Fe interaction with Ti^{4+}, Mn^{3+}, or vacancies producing nonaveraging peaks due to varying electric field gradients. The ionic model's integer charge assumption overlooks covalency, leading to delocalized electron density and blurred valence distinctions, which are dynamically influenced by temperature, composition, and electronic density of states (e-DOS) in solid solutions. Similar broad features appear in EPR (Babińska et al. 2008) , XANES (Levy et al. 2018), and XPS (Li 2022).

APPENDIX 1E. Mossbauer Figures

This Appendix contains all Mossbauer Figures.

Tm28

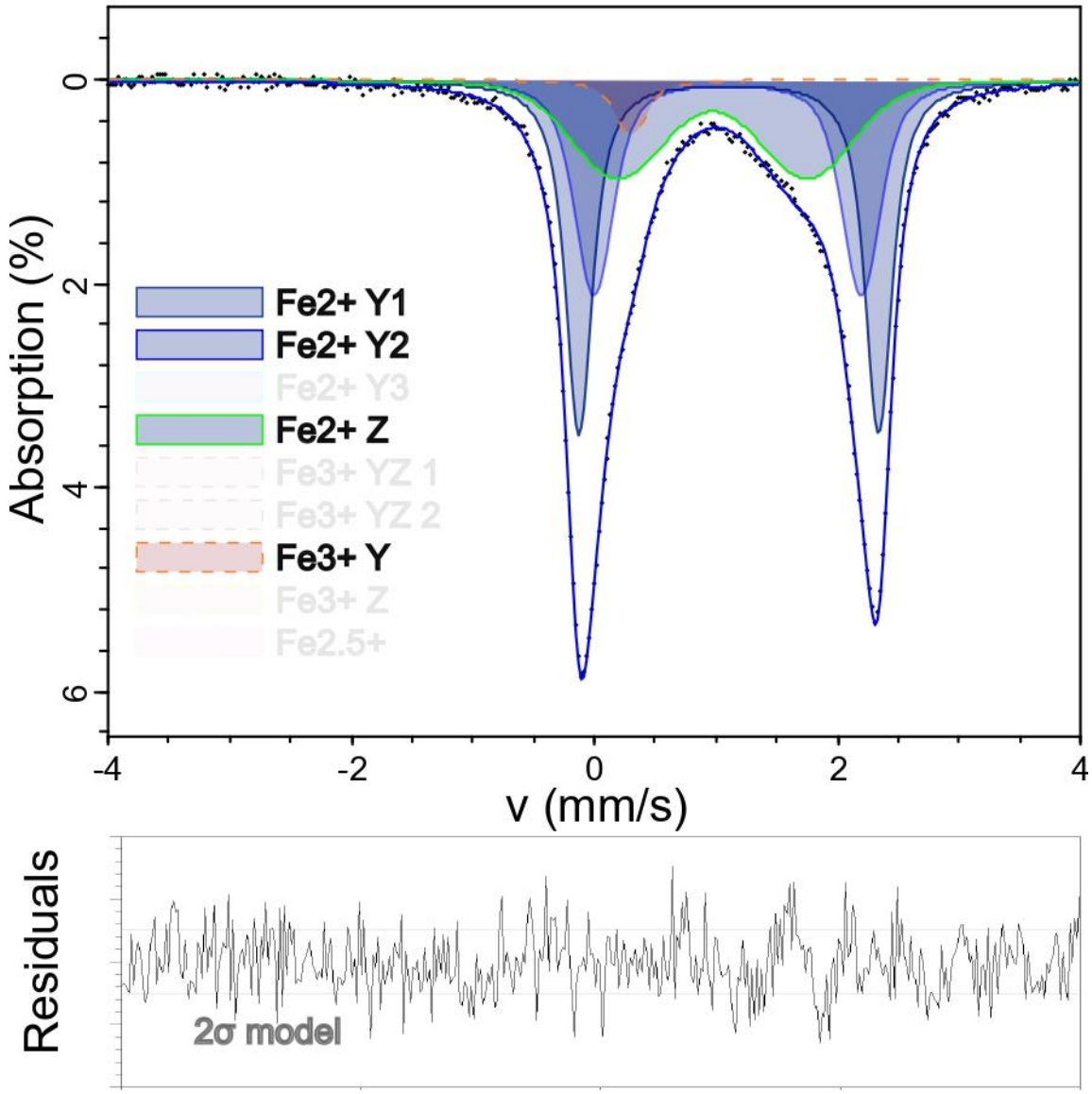
Absorption (%)
0
2
4
6
Fe2+ Y1
Fe2+ Y2
Fe2+ Y3
Fe2+ Z
Fe3+ YZ 1
Fe3+ YZ 2
Fe3+ Y
Fe3+ Z
Fe2.5+
-4
-2
0
2
4
v (mm/s)
Residuals
2σ model

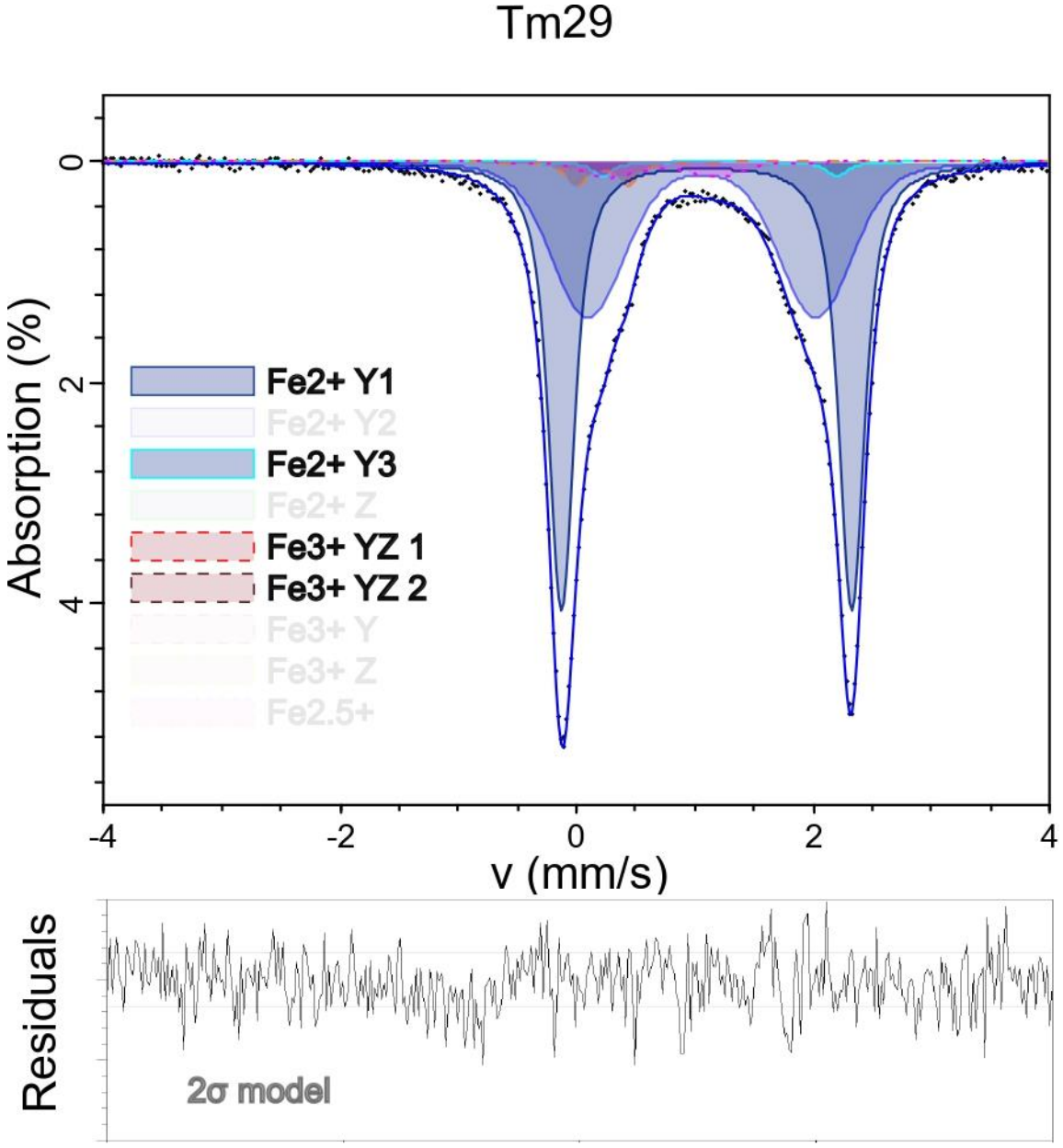
Tm29
Absorption (%)
0
2
4
Fe2+ Y1
Fe2+ Y2
Fe2+ Y3
Fe2+ Z
Fe3+ YZ 1
Fe3+ YZ 2
Fe3+ Y
Fe3+ Z
Fe2.5+
-4
-2
0
2
4
v (mm/s)
Residuals
2σ model

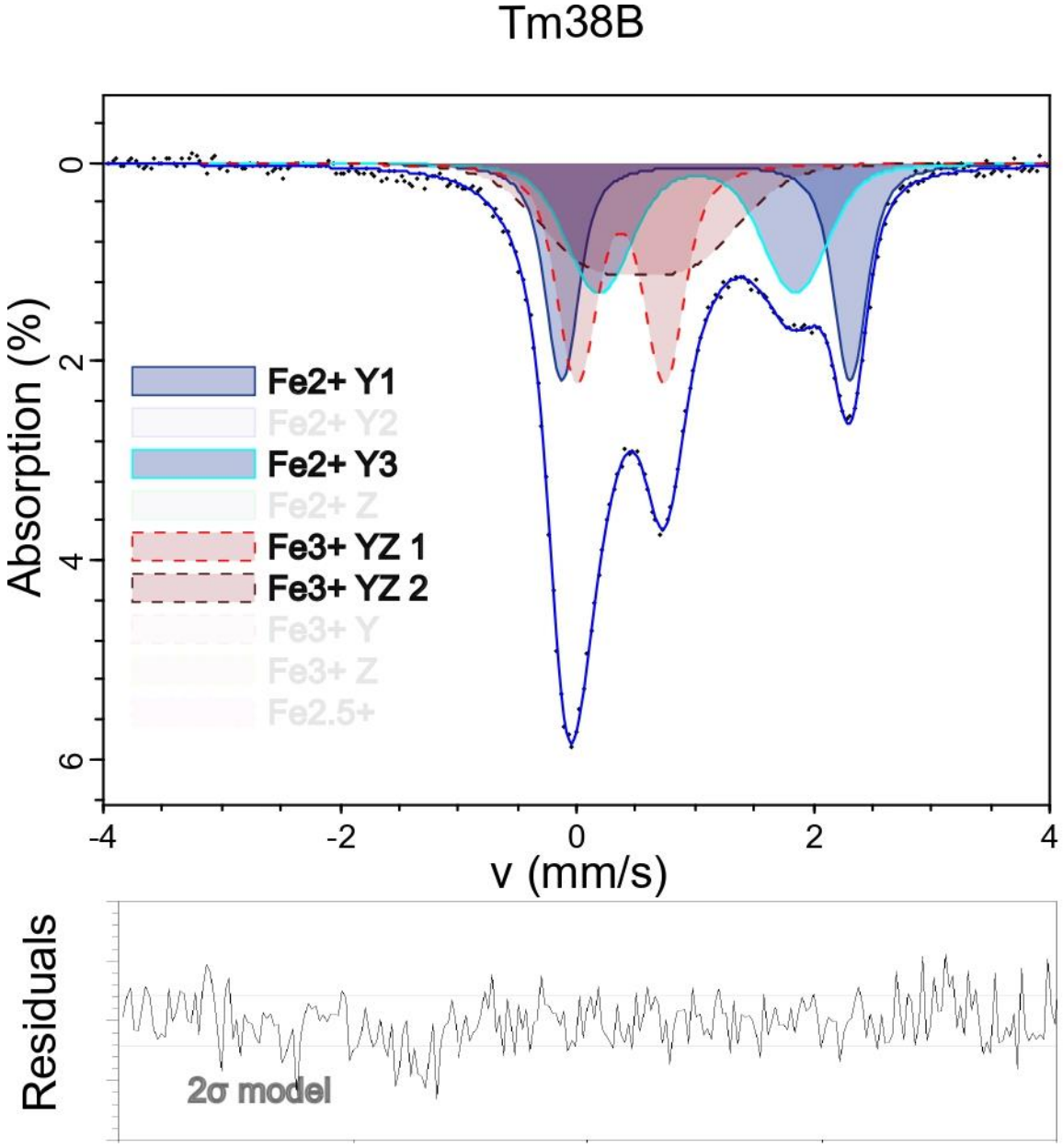
Tm38B
Absorption (%)
0
2
4
6
Fe2+ Y1
Fe2+ Y2
Fe2+ Y3
Fe2+ Z
Fe3+ YZ 1
Fe3+ YZ 2
Fe3+ Y
Fe3+ Z
Fe2.5+
-4
-2
0
2
4
v (mm/s)
Residuals
2σ model

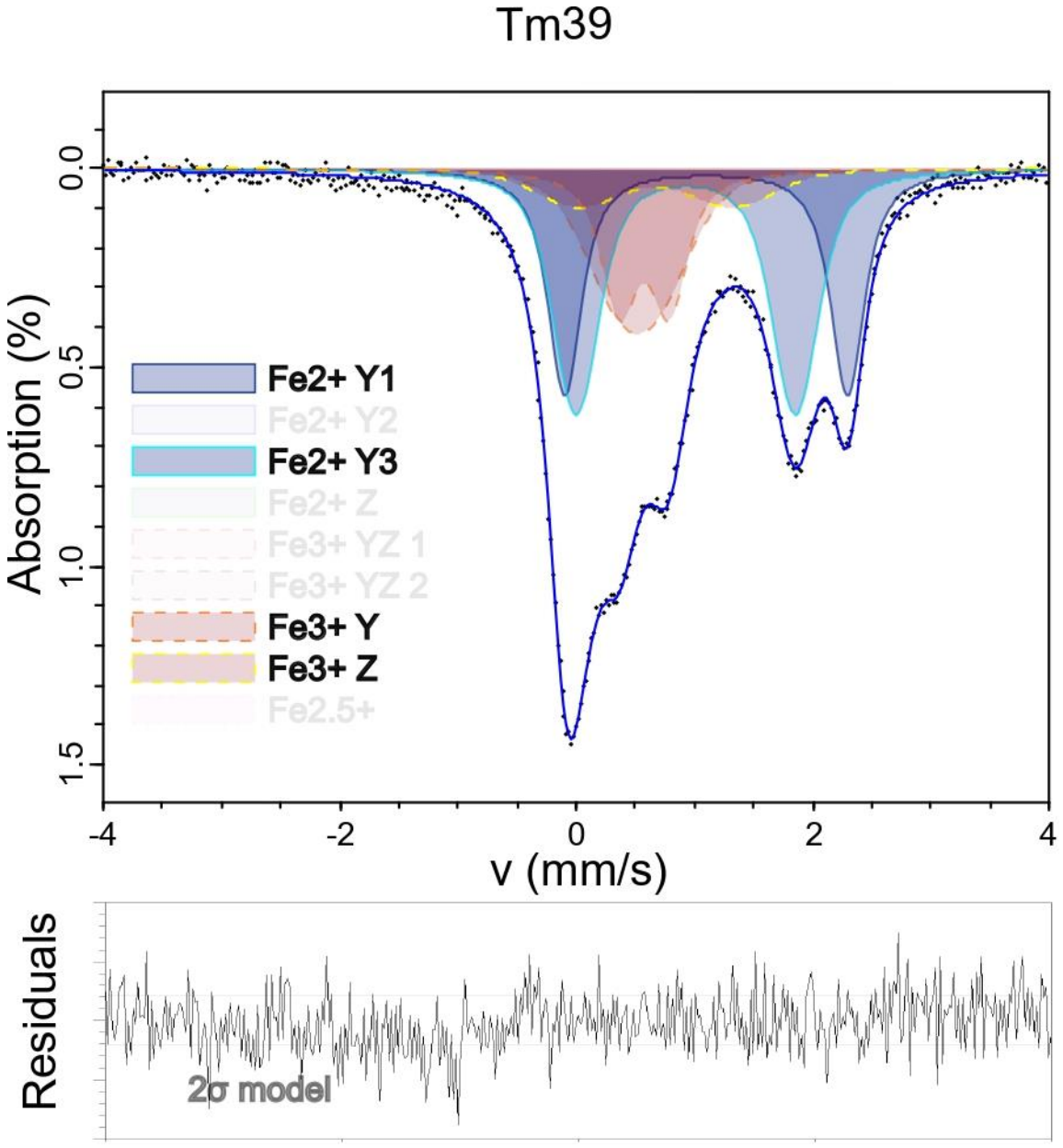
Tm39
Absorption (%)
0.0
0.5
1.0
1.5
Fe2+ Y1
Fe2+ Y2
Fe2+ Y3
Fe2+ Z
Fe3+ YZ 1
Fe3+ YZ 2
Fe3+ Y
Fe3+ Z
Fe2.5+
-4
-2
0
2
4
v (mm/s)
Residuals
2σ model

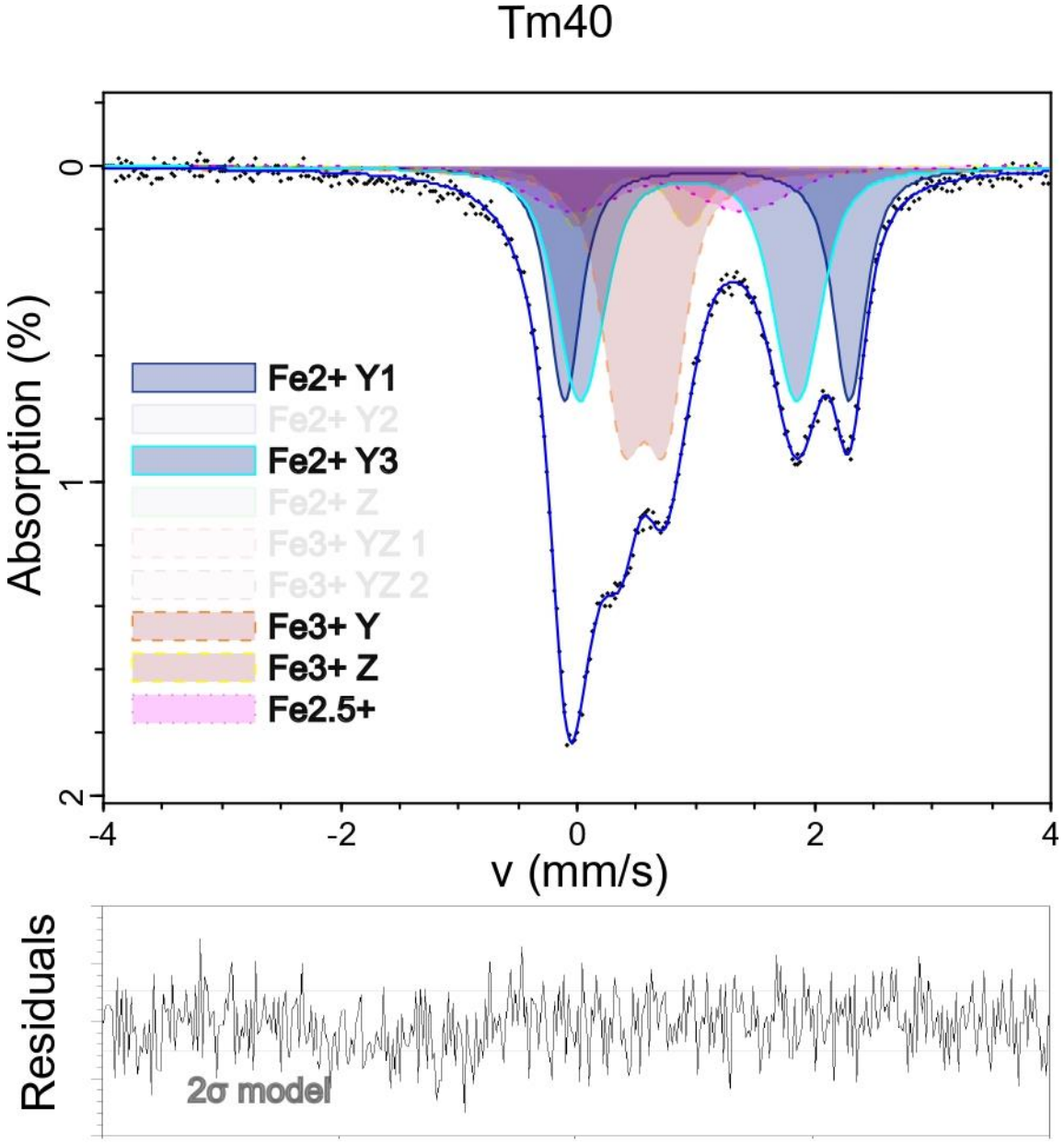
Tm40
Absorption (%)
0
1
2
-4
-2
0
2
4
v (mm/s)
Fe2+ Y1
Fe2+ Y2
Fe2+ Y3
Fe2+ Z
Fe3+ YZ 1
Fe3+ YZ 2
Fe3+ Y
Fe3+ Z
Fe2.5+
Residuals
2σ model

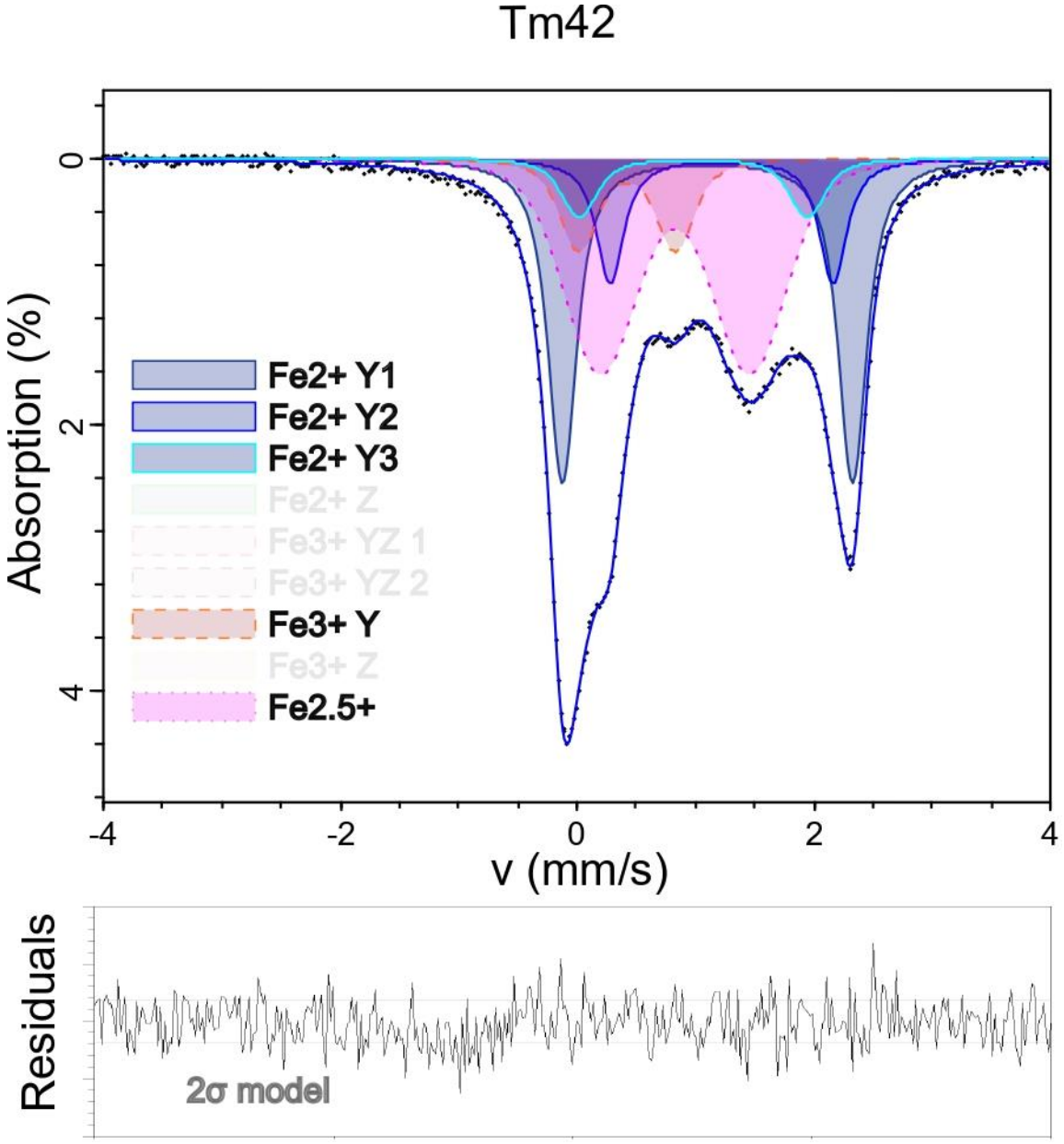
Tm42
Absorption (%)
0
2
4
Fe2+ Y1
Fe2+ Y2
Fe2+ Y3
Fe2+ Z
Fe3+ YZ 1
Fe3+ YZ 2
Fe3+ Y
Fe3+ Z
Fe2.5+
-4
-2
0
2
4
v (mm/s)
Residuals
2σ model

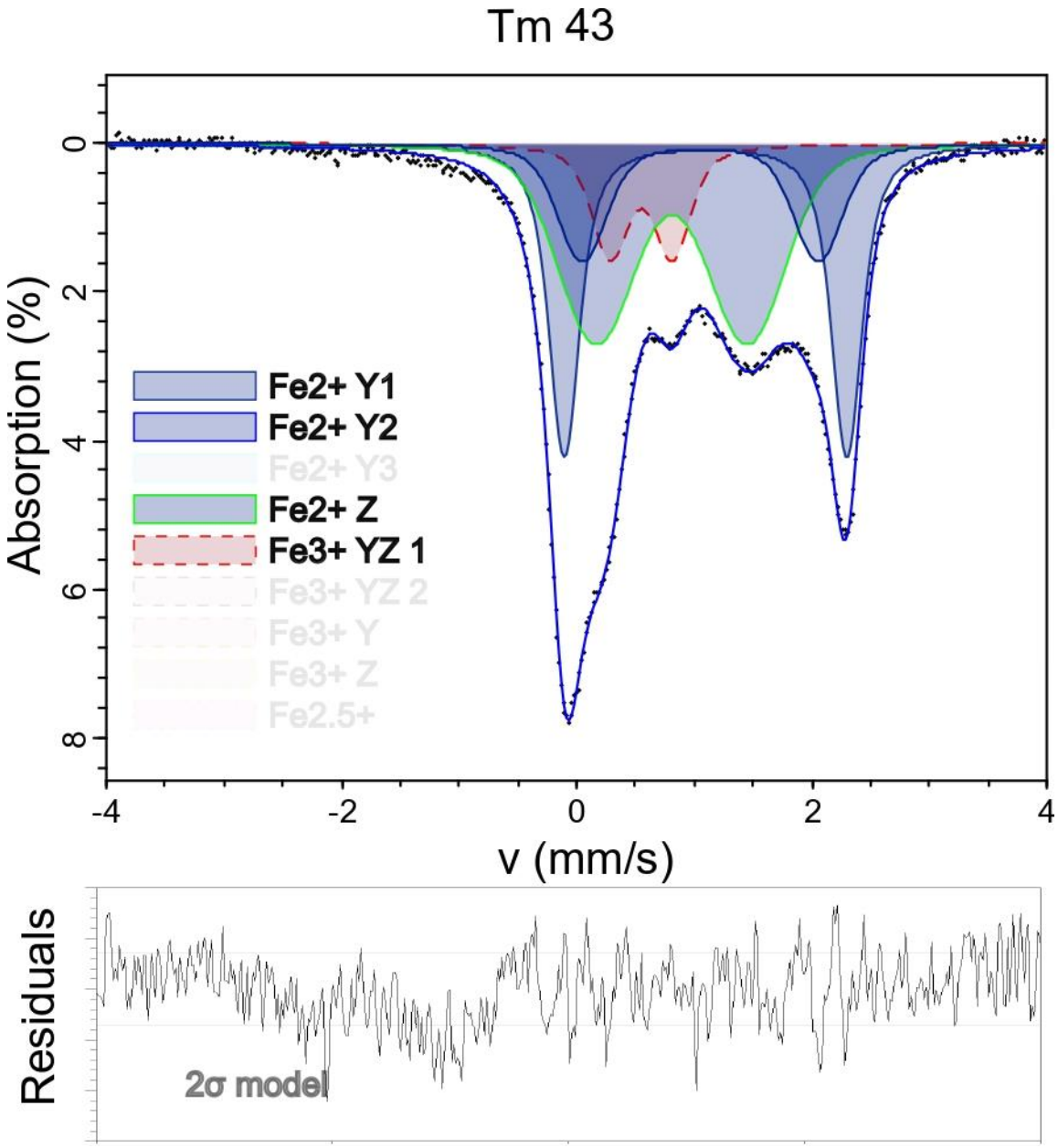
Tm 43
Absorption (%)
0
2
4
6
8
Fe2+ Y1
Fe2+ Y2
Fe2+ Y3
Fe2+ Z
Fe3+ YZ 1
Fe3+ YZ 2
Fe3+ Y
Fe3+ Z
Fe2.5+
-4
-2
0
2
4
v (mm/s)
Residuals
2σ model

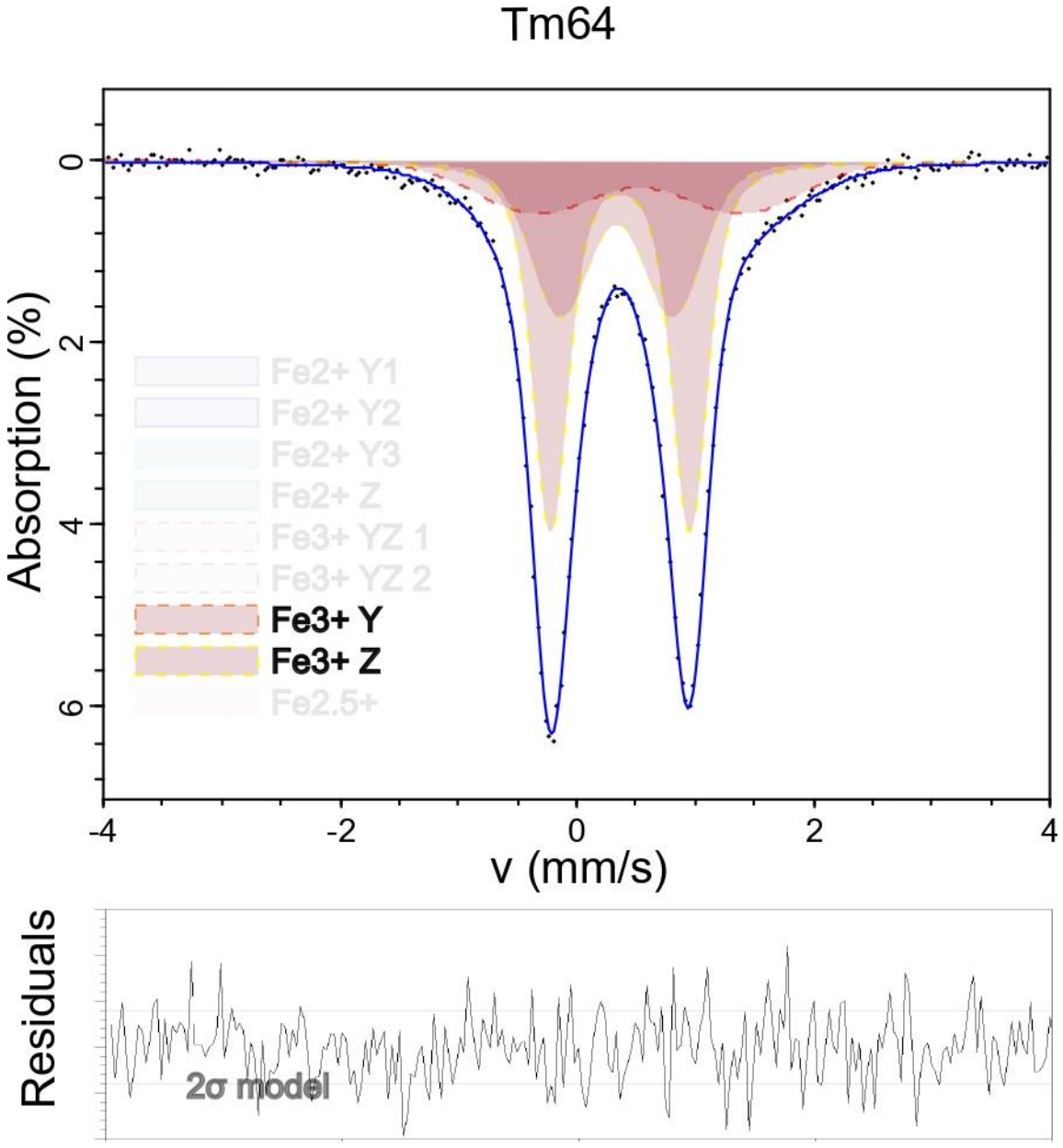
Tm64
Absorption (%)
0
2
4
6
Fe2+ Y1
Fe2+ Y2
Fe2+ Y3
Fe2+ Z
Fe3+ YZ 1
Fe3+ YZ 2
Fe3+ Y
Fe3+ Z
Fe2.5+
-4
-2
0
2
4
v (mm/s)
Residuals
2σ model

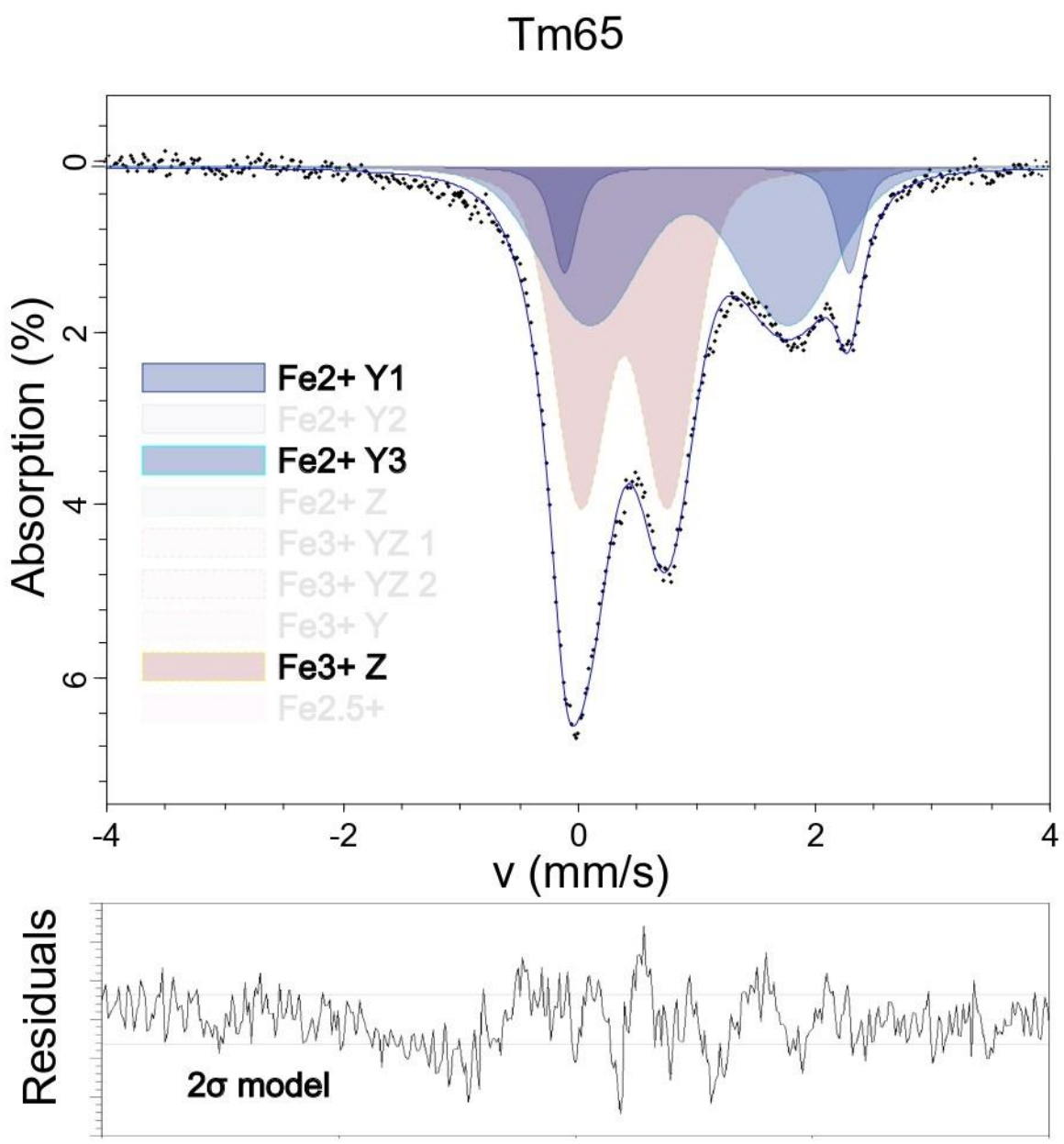
Tm65
Absorption (%)
0
2
4
6
Fe2+ Y1
Fe2+ Y2
Fe2+ Y3
Fe2+ Z
Fe3+ YZ 1
Fe3+ YZ 2
Fe3+ Y
Fe3+ Z
Fe2.5+
-4
-2
0
2
4
v (mm/s)
Residuals
2σ model

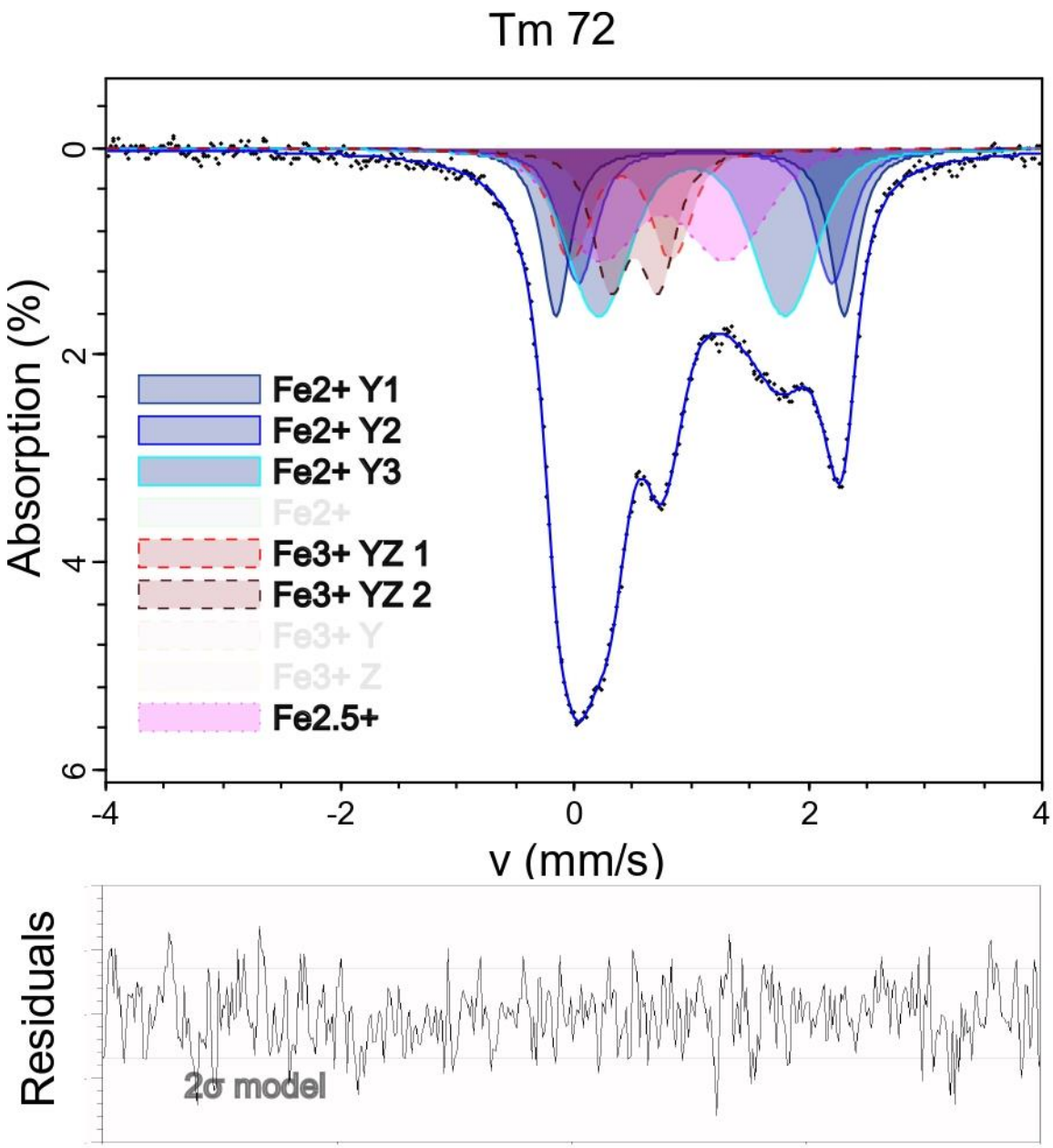
Tm 72
Absorption (%)
0
2
4
6
-4
-2
0
2
4
v (mm/s)
Fe2+ Y1
Fe2+ Y2
Fe2+ Y3
Fe2+
Fe3+ YZ 1
Fe3+ YZ 2
Fe3+ Y
Fe3+ Z
Fe2.5+
Residuals
2σ model

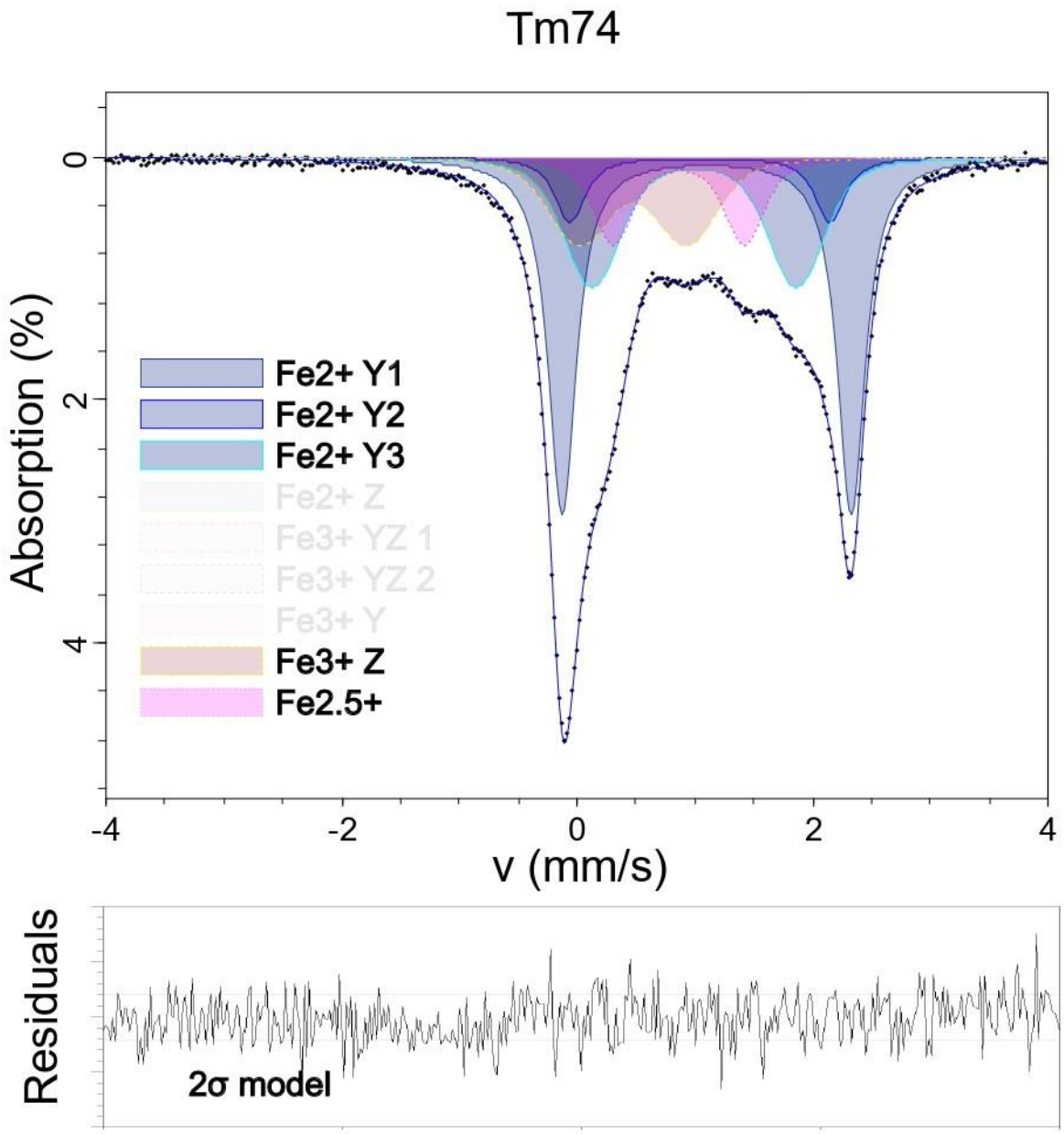
Tm74
Absorption (%)
0
2
4
Fe2+ Y1
Fe2+ Y2
Fe2+ Y3
Fe2+ Z
Fe3+ YZ 1
Fe3+ YZ 2
Fe3+ Y
Fe3+ Z
Fe2.5+
-4
-2
0
2
4
v (mm/s)
Residuals
2σ model

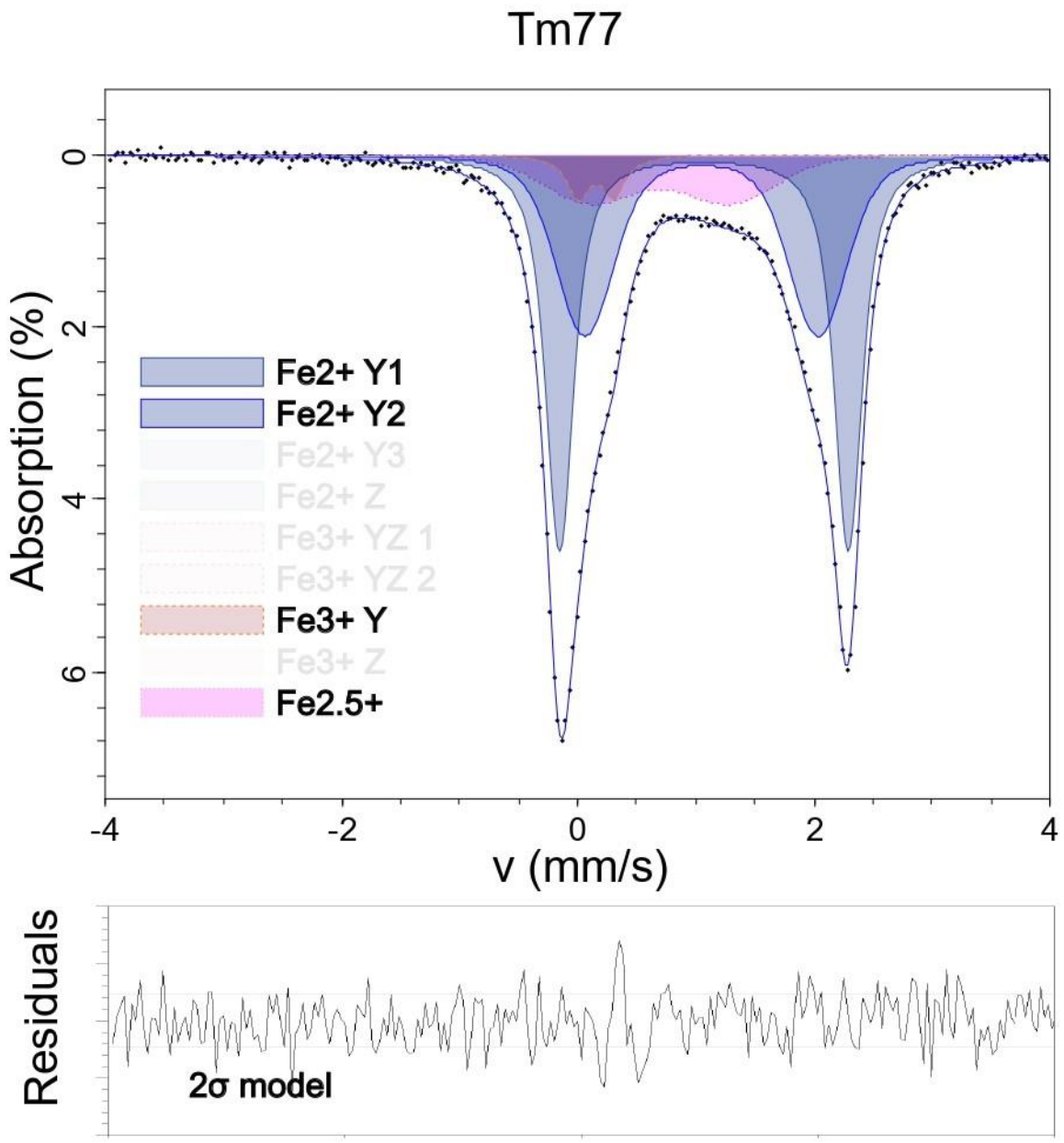
Tm77
Absorption (%)
0
2
4
6
Fe2+ Y1
Fe2+ Y2
Fe2+ Y3
Fe2+ Z
Fe3+ YZ 1
Fe3+ YZ 2
Fe3+ Y
Fe3+ Z
Fe2.5+
-4
-2
0
2
4
v (mm/s)
Residuals
2σ model

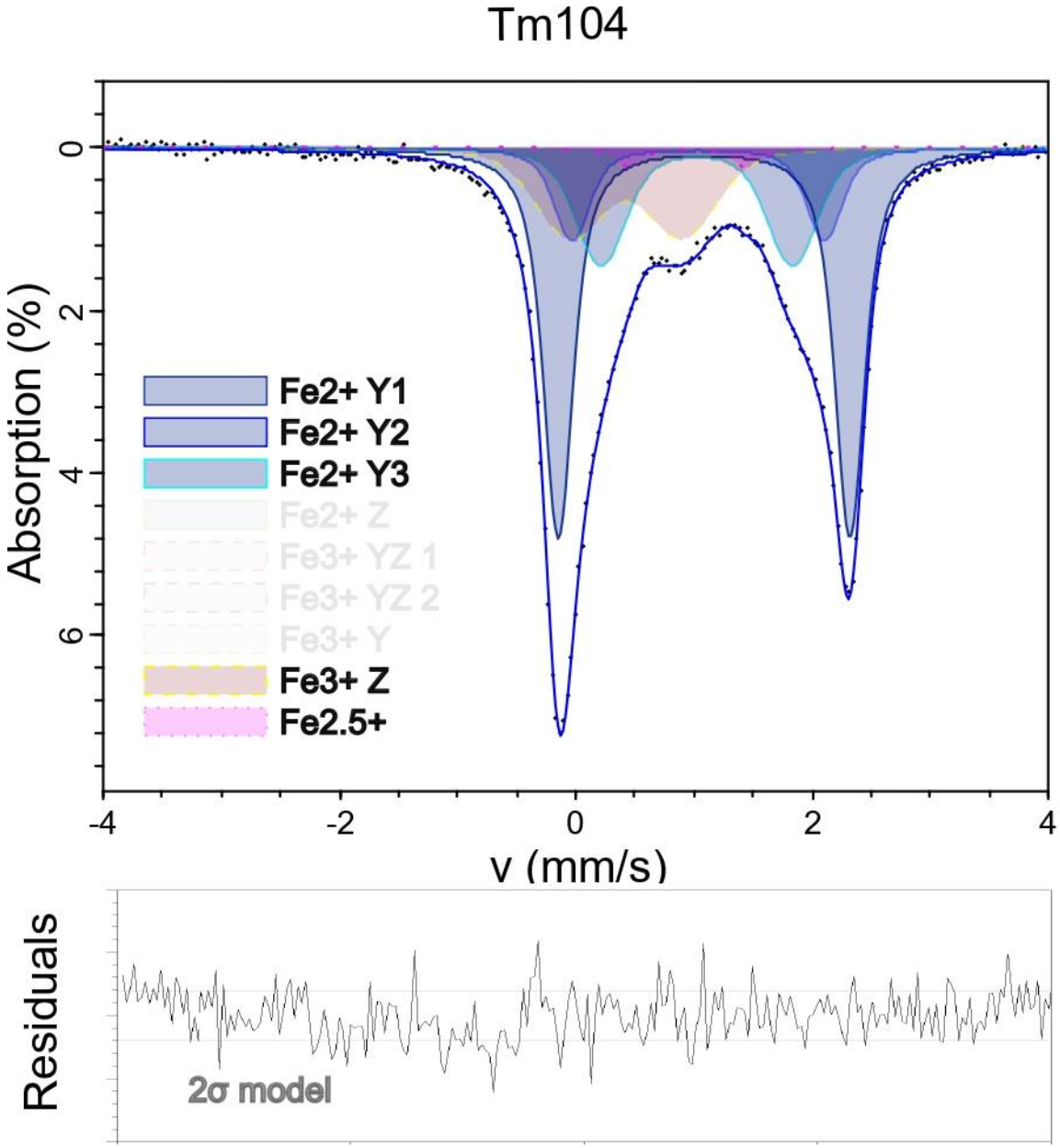
Tm104
Absorption (%)
0
2
4
6
Fe2+ Y1
Fe2+ Y2
Fe2+ Y3
Fe2+ Z
Fe3+ YZ 1
Fe3+ YZ 2
Fe3+ Y
Fe3+ Z
Fe2.5+
-4
-2
0
2
4
v (mm/s)
Residuals
2σ model

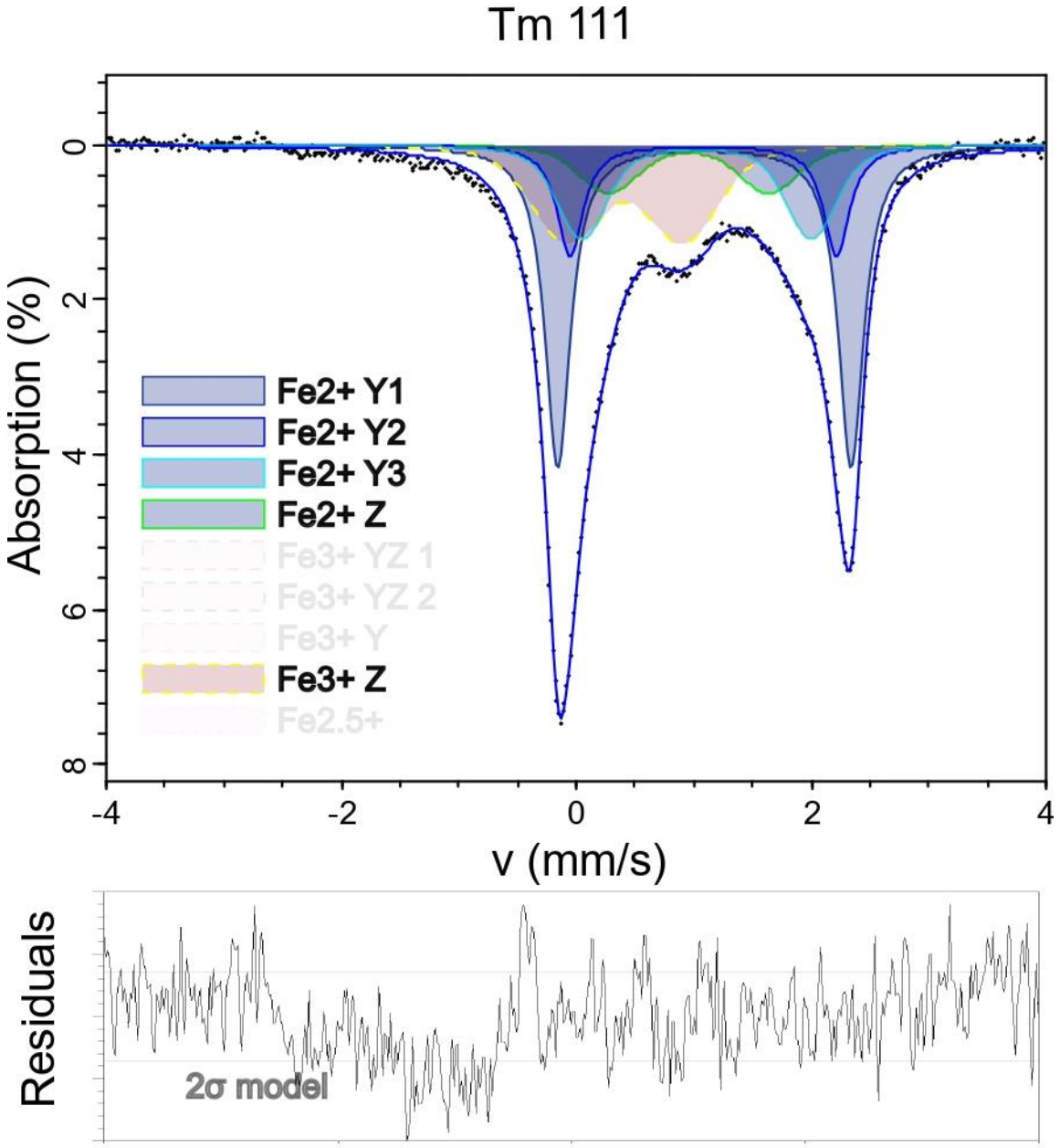
Tm 111
Absorption (%)
0
2
4
6
8
-4
-2
0
2
4
v (mm/s)
Fe2+ Y1
Fe2+ Y2
Fe2+ Y3
Fe2+ Z
Fe3+ YZ 1
Fe3+ YZ 2
Fe3+ Y
Fe3+ Z
Fe2.5+
Residuals
2σ model

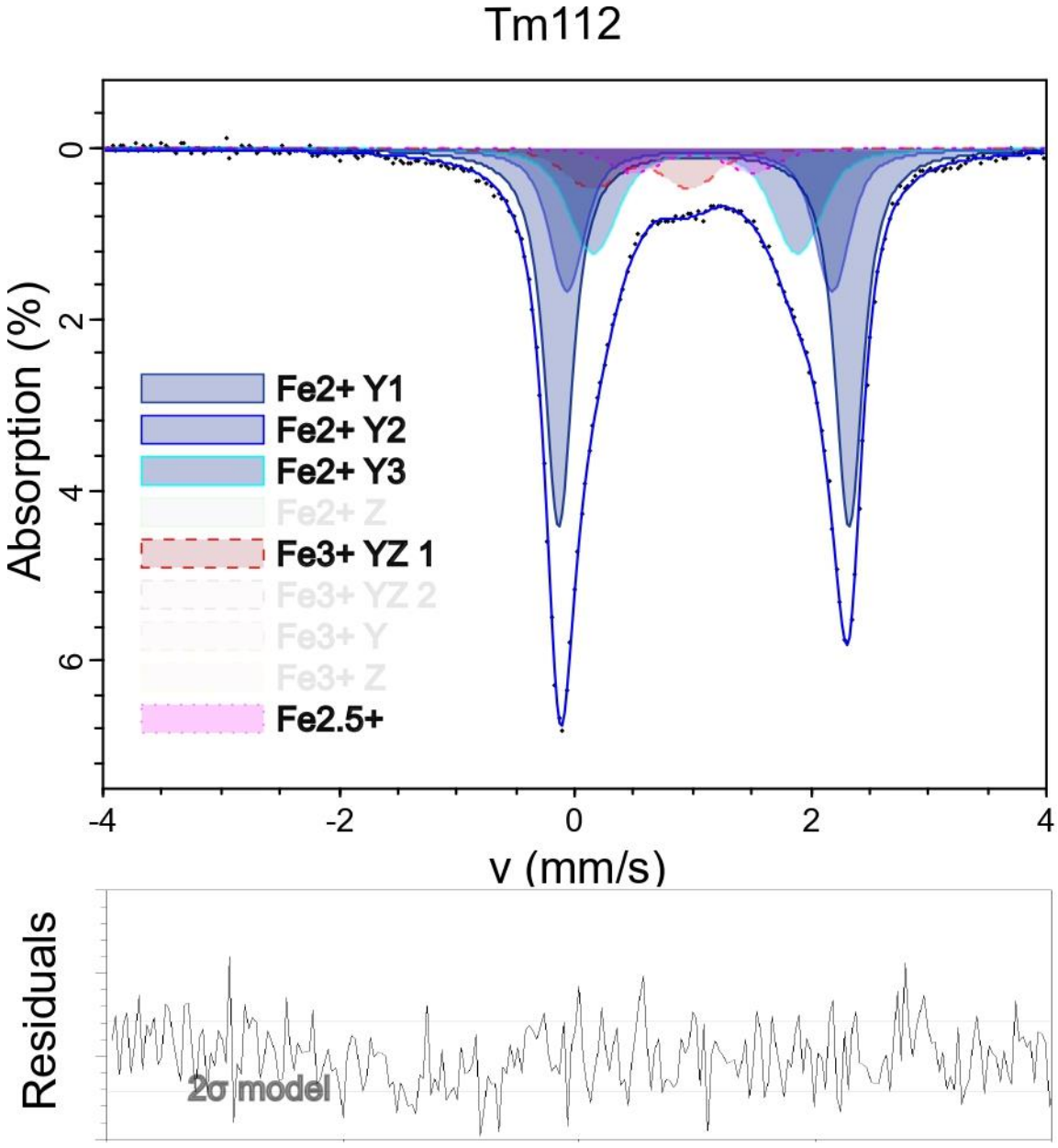
Tm112
Absorption (%)
0
2
4
6
Fe2+ Y1
Fe2+ Y2
Fe2+ Y3
Fe2+ Z
Fe3+ YZ 1
Fe3+ YZ 2
Fe3+ Y
Fe3+ Z
Fe2.5+
-4
-2
0
2
4
v (mm/s)
Residuals
2σ model

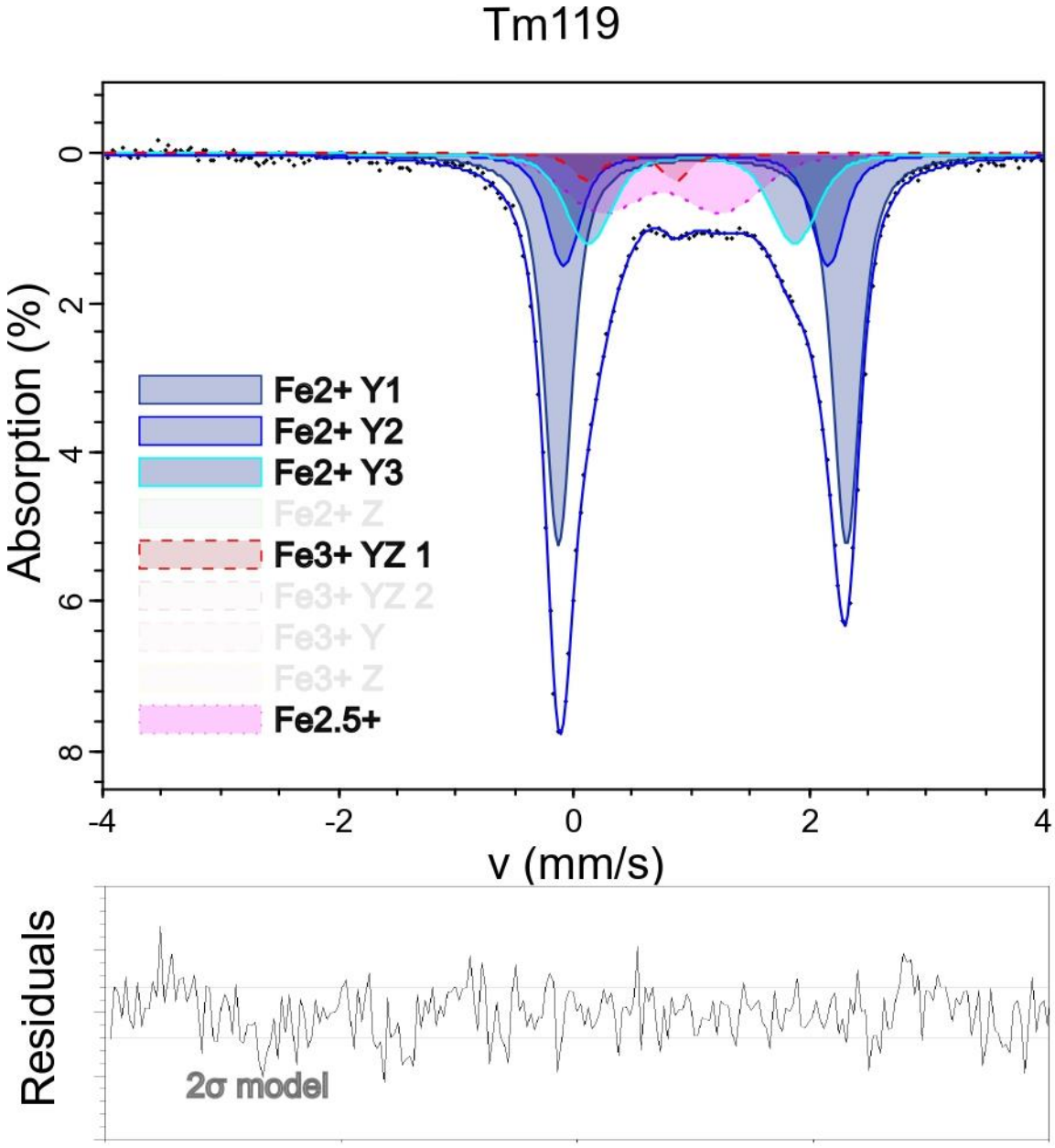
Tm119
Absorption (%)
0
2
4
6
8
Fe2+ Y1
Fe2+ Y2
Fe2+ Y3
Fe2+ Z
Fe3+ YZ 1
Fe3+ YZ 2
Fe3+ Y
Fe3+ Z
Fe2.5+
-4
-2
0
2
4
v (mm/s)
Residuals
2σ model

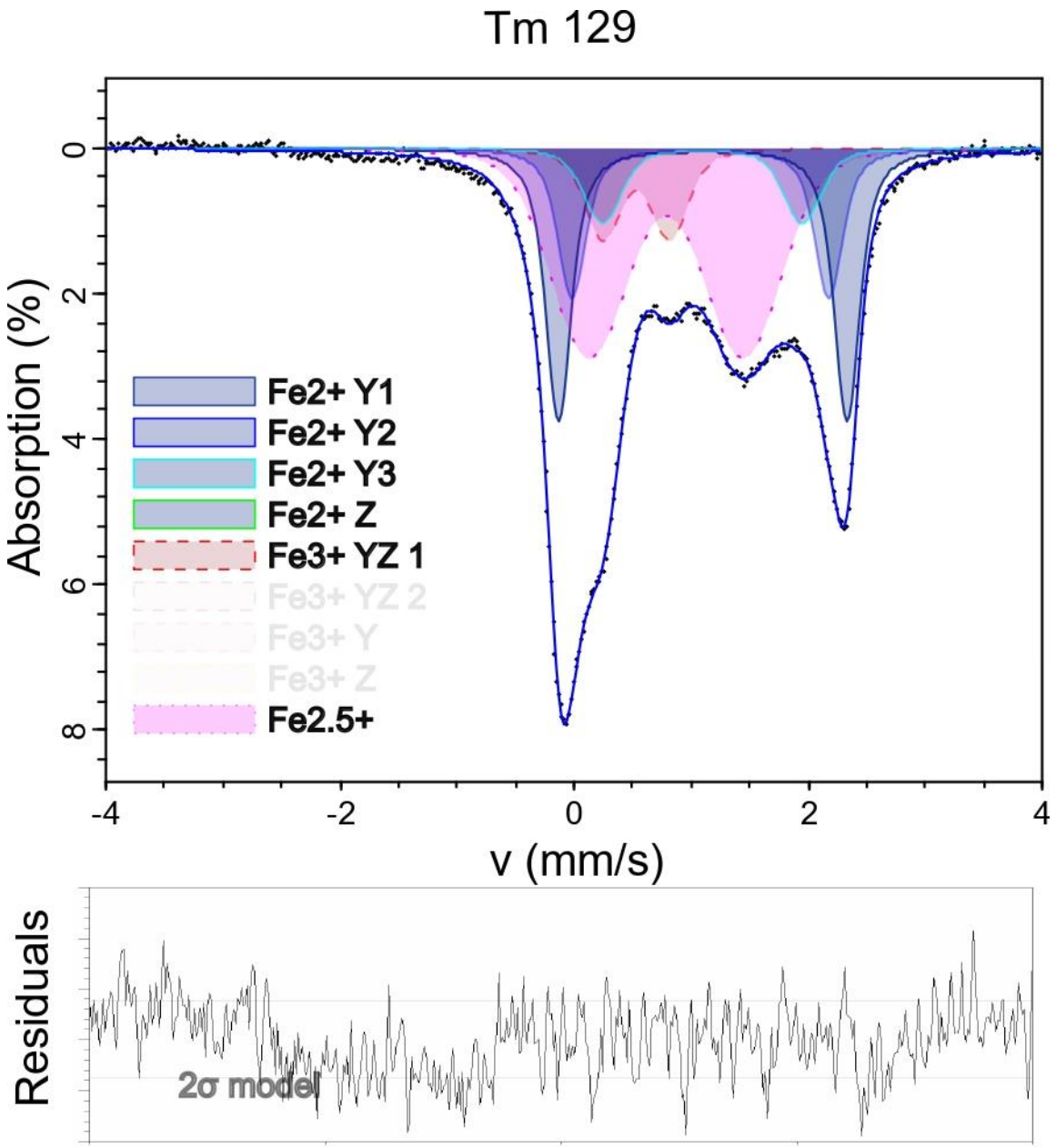
Tm 129
Absorption (%)
0
2
4
6
8
Fe2+ Y1
Fe2+ Y2
Fe2+ Y3
Fe2+ Z
Fe3+ YZ 1
Fe3+ YZ 2
Fe3+ Y
Fe3+ Z
Fe2.5+
-4
-2
0
2
4
v (mm/s)
Residuals
2σ model

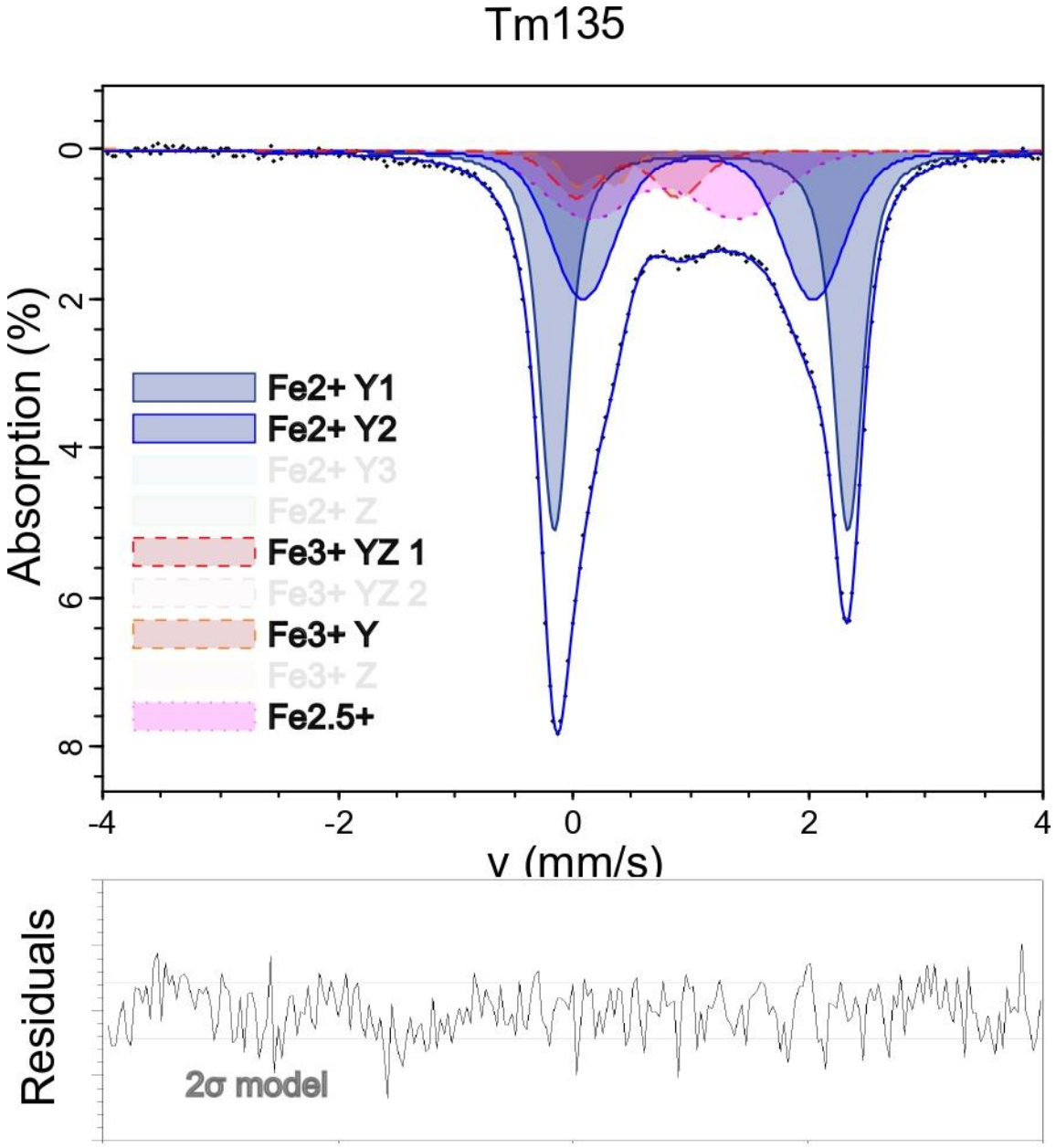
Tm135
Absorption (%)
0
2
4
6
8
Fe2+ Y1
Fe2+ Y2
Fe2+ Y3
Fe2+ Z
Fe3+ YZ 1
Fe3+ YZ 2
Fe3+ Y
Fe3+ Z
Fe2.5+
-4
-2
0
2
4
v (mm/s)
Residuals
2σ model

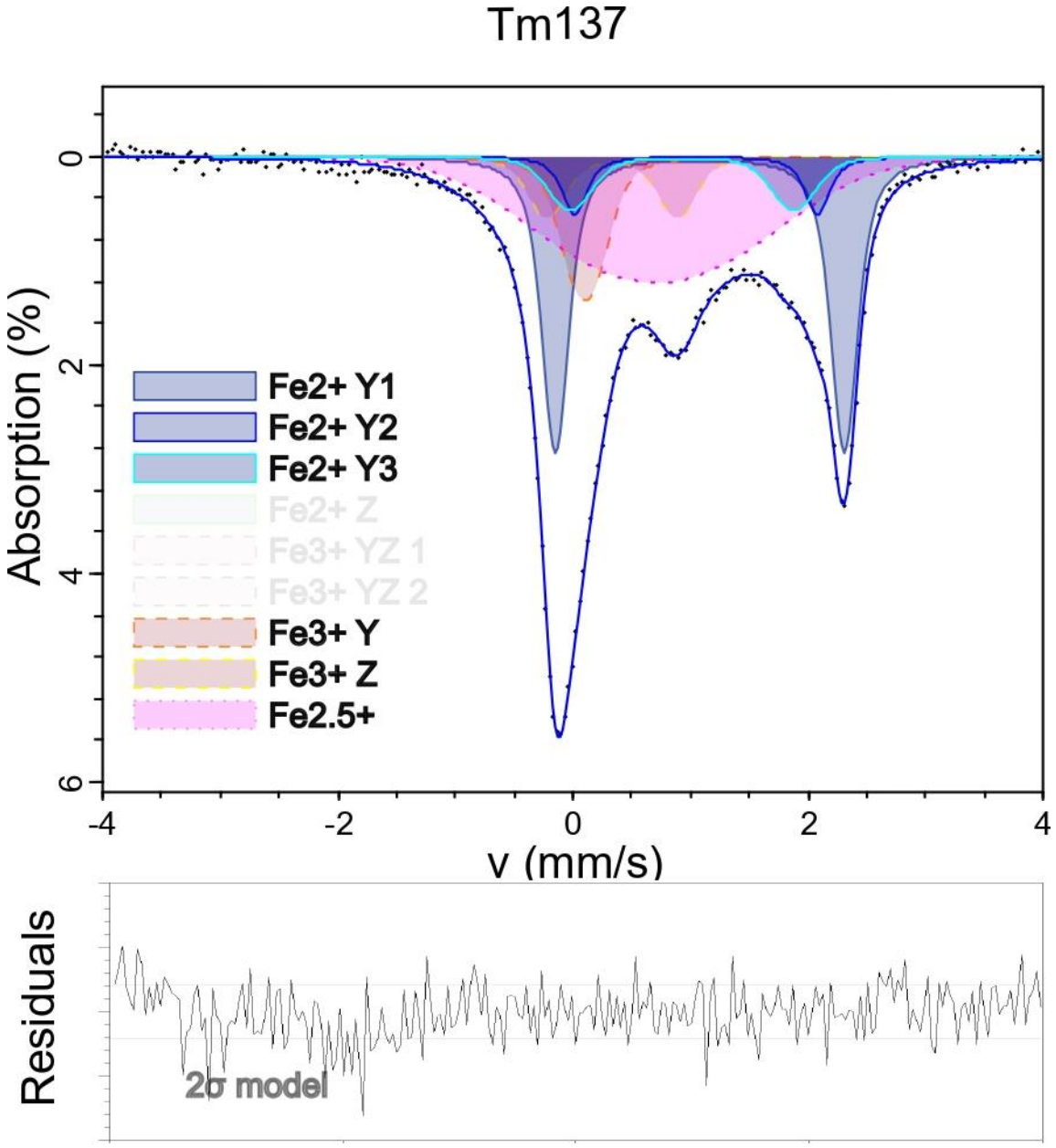
Tm137
Absorption (%)
0
2
4
6
Fe2+ Y1
Fe2+ Y2
Fe2+ Y3
Fe2+ Z
Fe3+ YZ 1
Fe3+ YZ 2
Fe3+ Y
Fe3+ Z
Fe2.5+
-4
-2
0
2
4
v (mm/s)
Residuals
2σ model

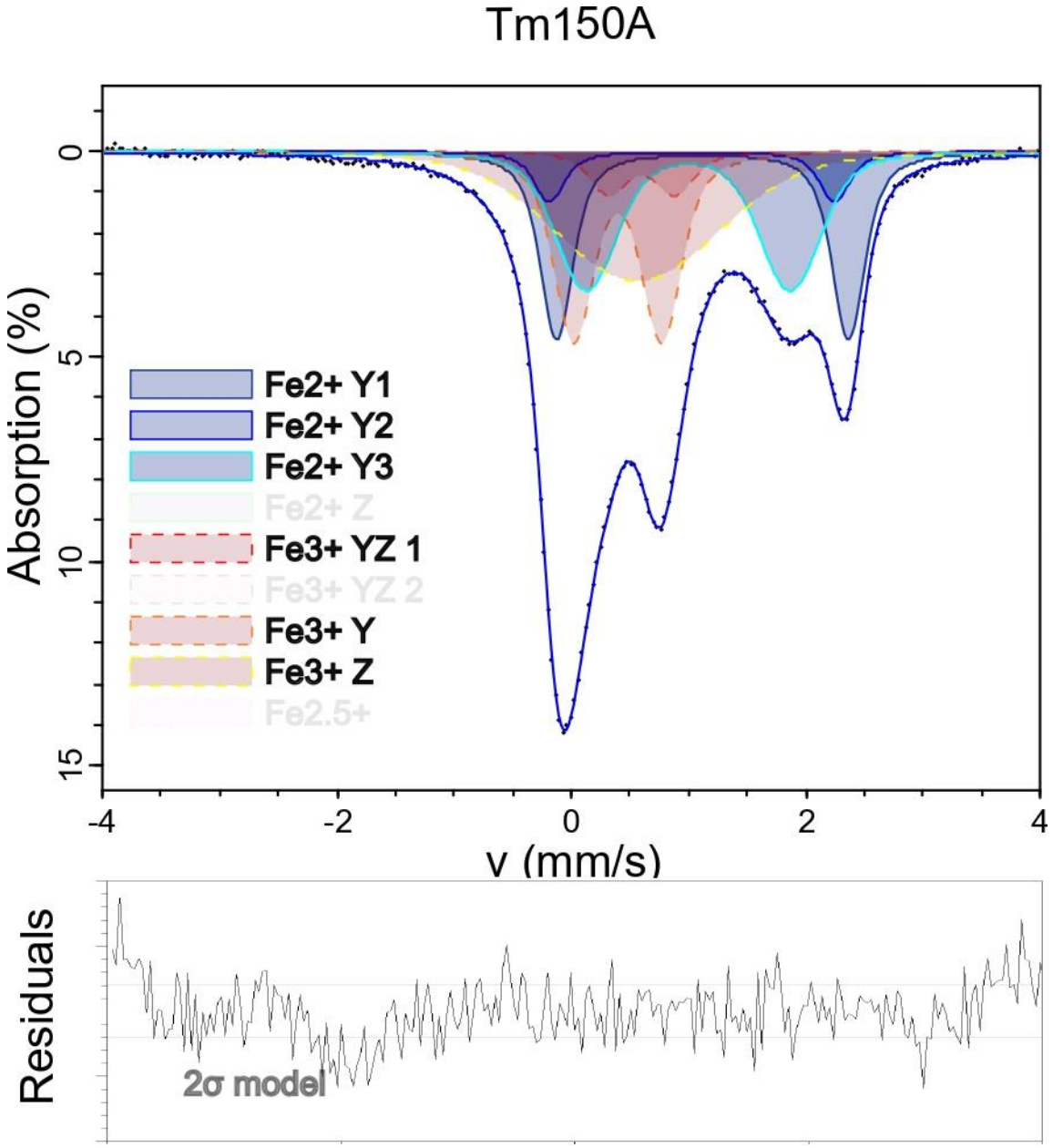
Tm150A
Absorption (%)
0
5
10
15
Fe2+ Y1
Fe2+ Y2
Fe2+ Y3
Fe2+ Z
Fe3+ YZ 1
Fe3+ YZ 2
Fe3+ Y
Fe3+ Z
Fe2.5+
-4
-2
0
2
4
v (mm/s)
Residuals
2σ model

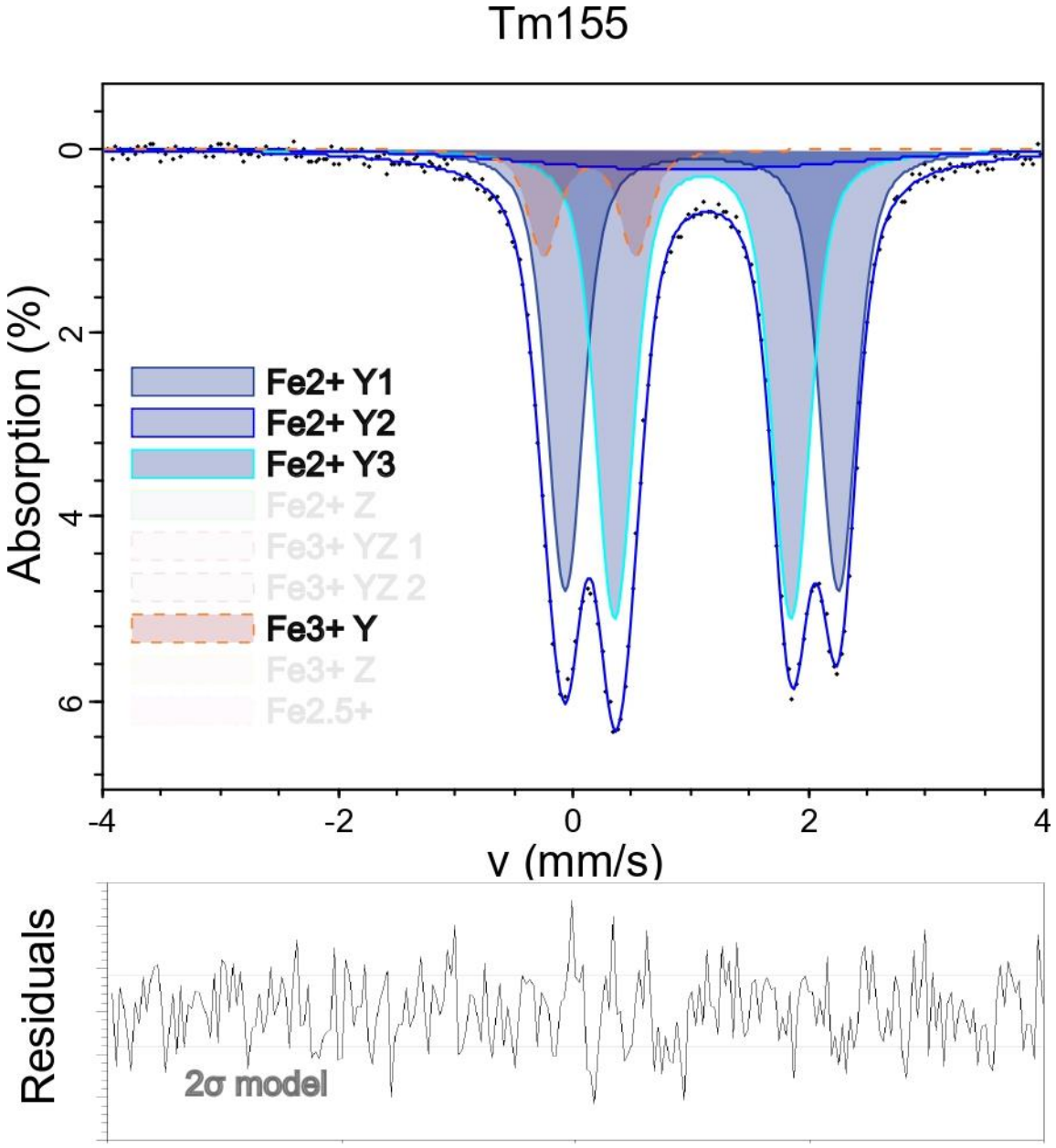
Tm155
Absorption (%)
0
2
4
6
Fe2+ Y1
Fe2+ Y2
Fe2+ Y3
Fe2+ Z
Fe3+ YZ 1
Fe3+ YZ 2
Fe3+ Y
Fe3+ Z
Fe2.5+
-4
-2
0
2
4
v (mm/s)
Residuals
2σ model

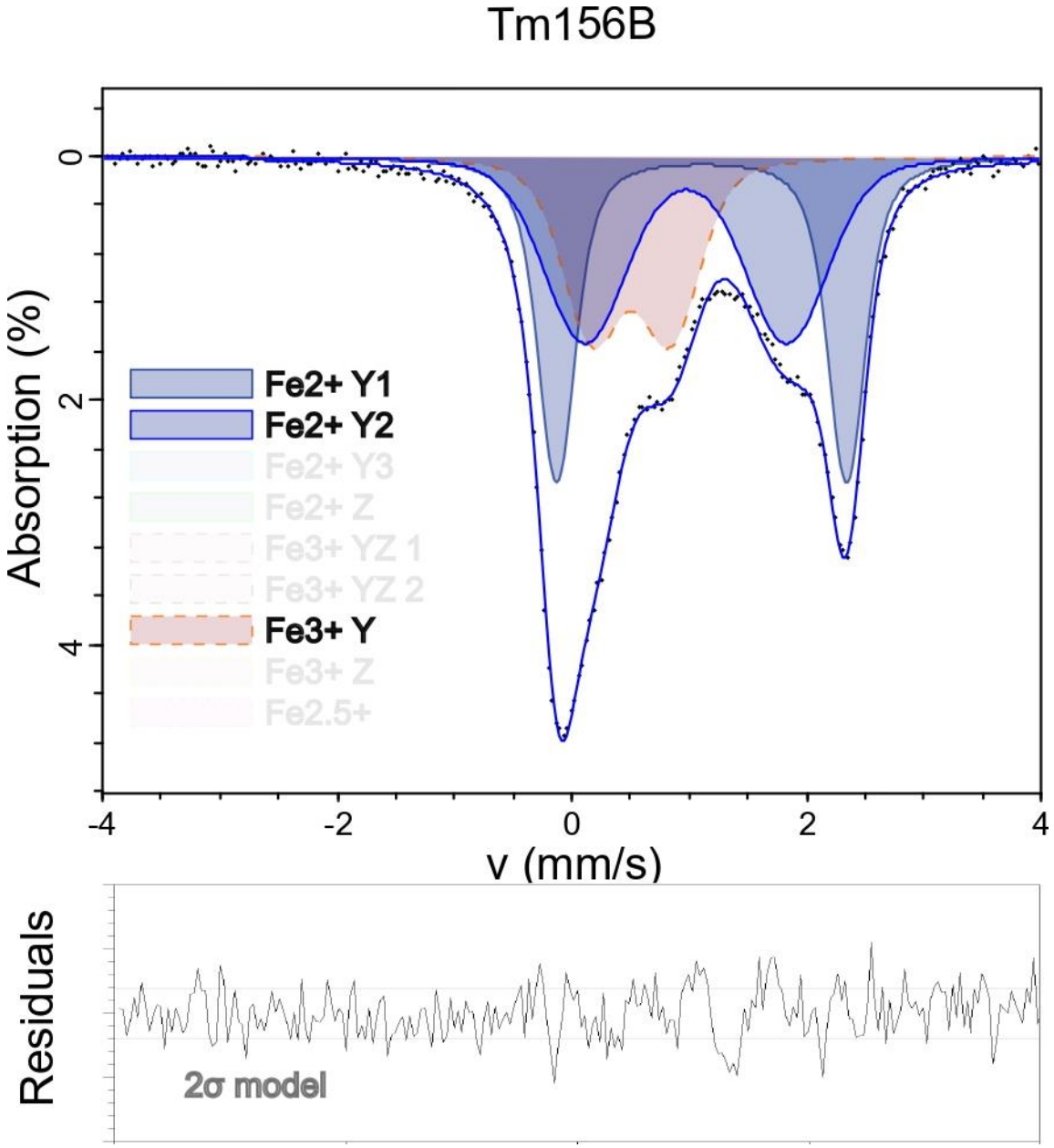
Tm156B
Absorption (%)
0
2
4
Fe2+ Y1
Fe2+ Y2
Fe2+ Y3
Fe2+ Z
Fe3+ YZ 1
Fe3+ YZ 2
Fe3+ Y
Fe3+ Z
Fe2.5+
-4
-2
0
2
4
v (mm/s)
Residuals
2σ model

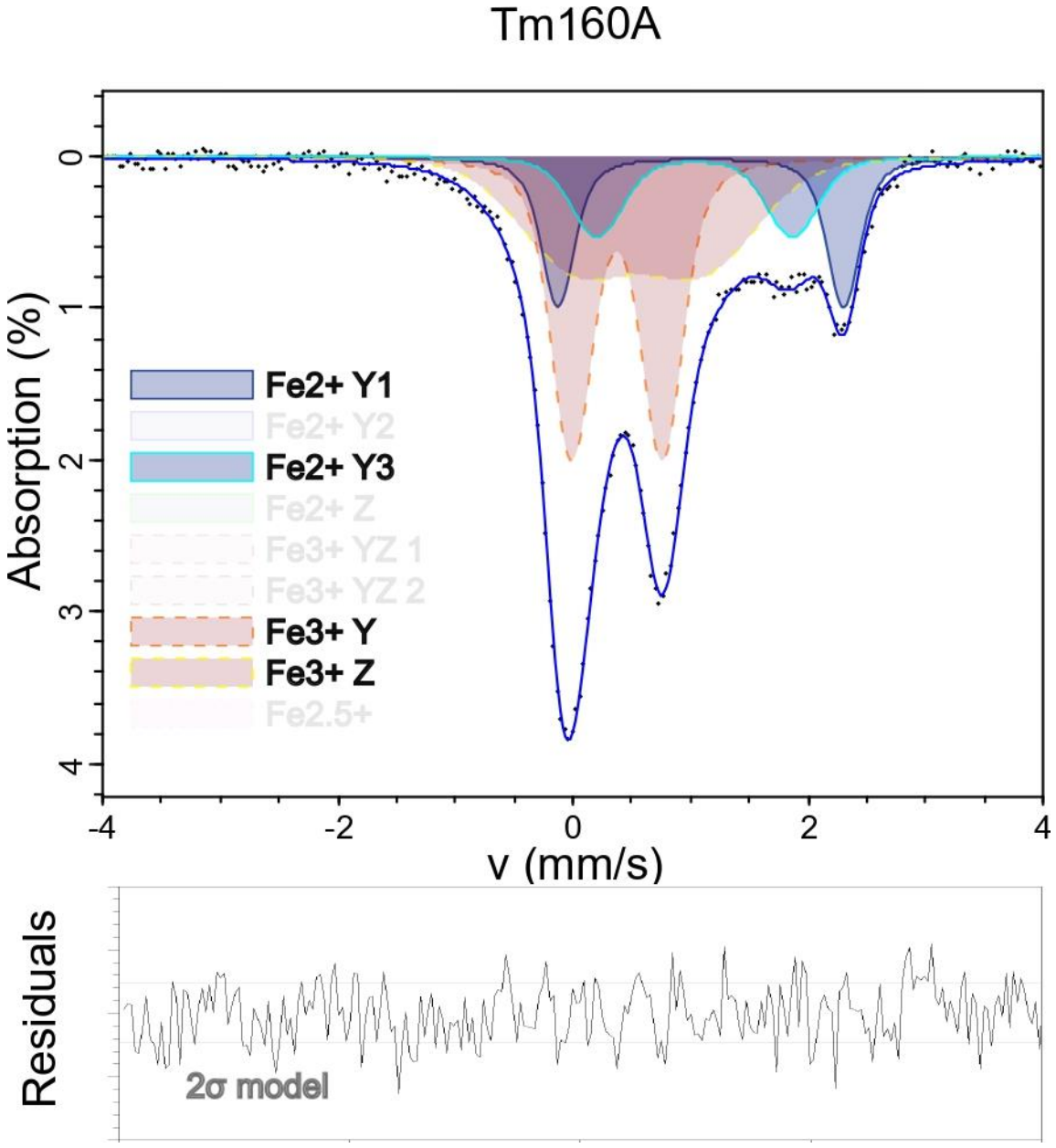
Tm160A
Absorption (%)
0
1
2
3
4
Fe2+ Y1
Fe2+ Y2
Fe2+ Y3
Fe2+ Z
Fe3+ YZ 1
Fe3+ YZ 2
Fe3+ Y
Fe3+ Z
Fe2.5+
-4
-2
0
2
4
v (mm/s)
Residuals
2σ model

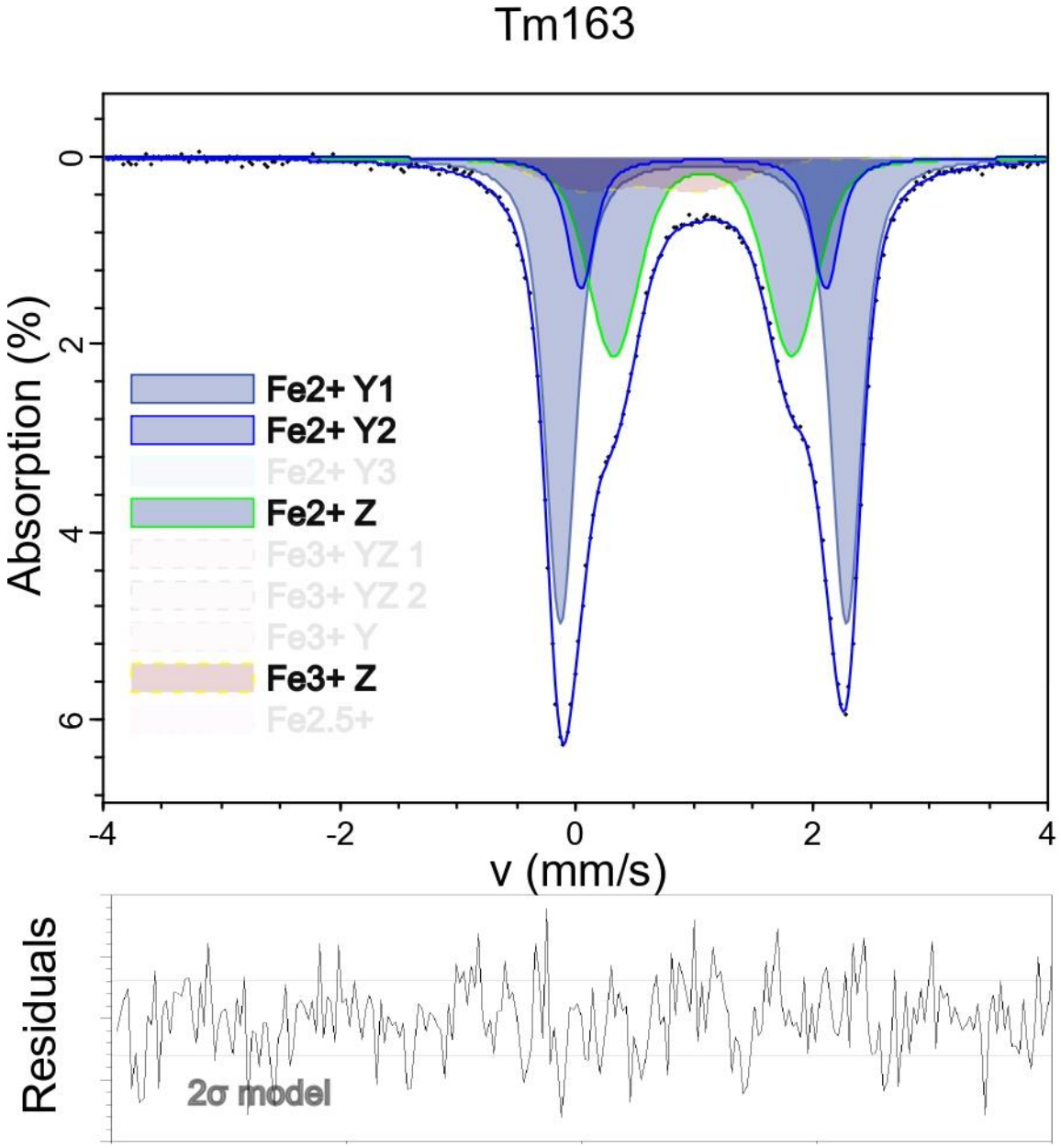
Tm163
Absorption (%)
0
2
4
6
Fe2+ Y1
Fe2+ Y2
Fe2+ Y3
Fe2+ Z
Fe3+ YZ 1
Fe3+ YZ 2
Fe3+ Y
Fe3+ Z
Fe2.5+
-4
-2
0
2
4
v (mm/s)
Residuals
2σ model

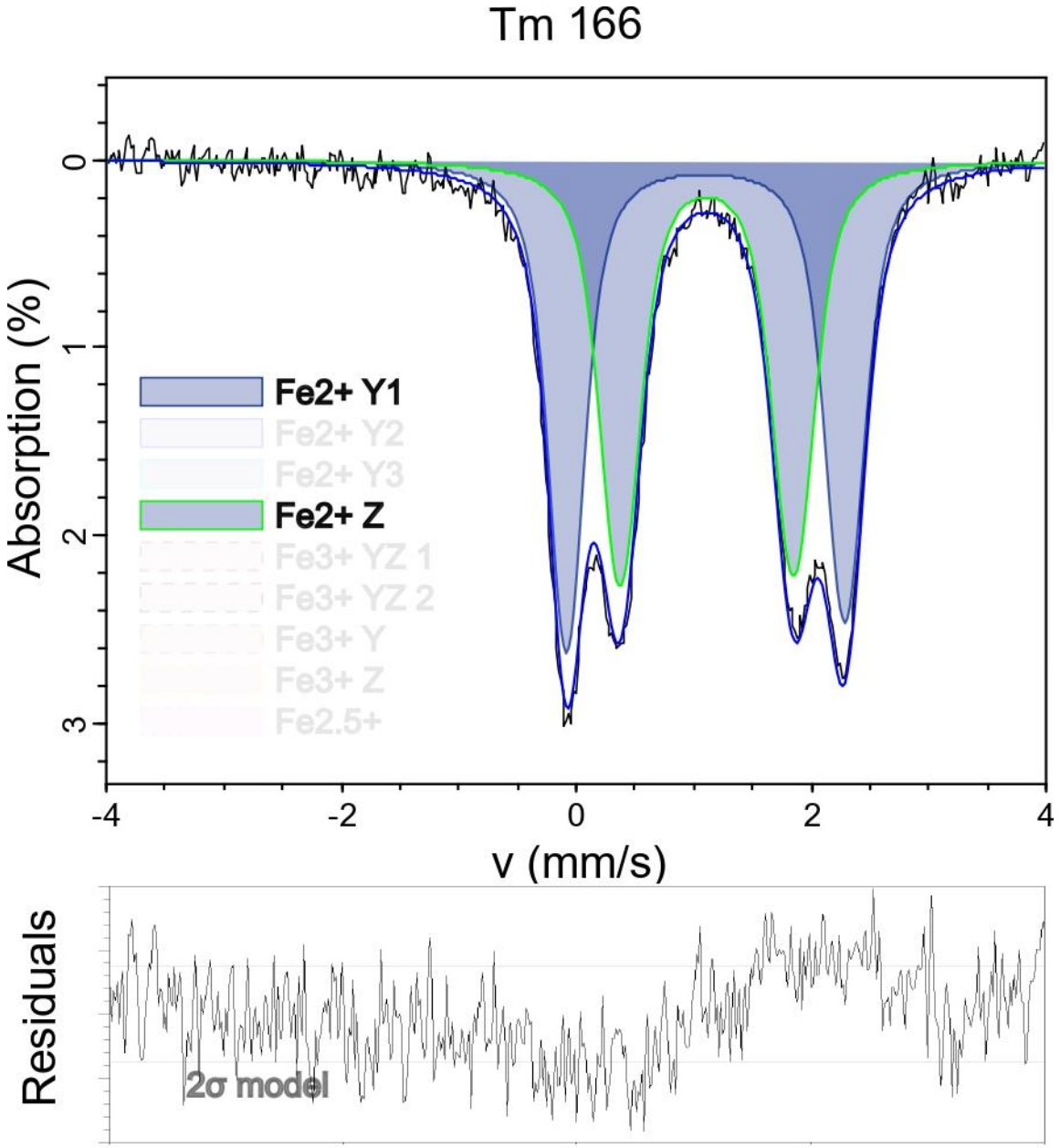
Tm 166
Absorption (%)
0
1
2
3
Fe2+ Y1
Fe2+ Y2
Fe2+ Y3
Fe2+ Z
Fe3+ YZ 1
Fe3+ YZ 2
Fe3+ Y
Fe3+ Z
Fe2.5+
-4
-2
0
2
4
v (mm/s)
Residuals
2σ model

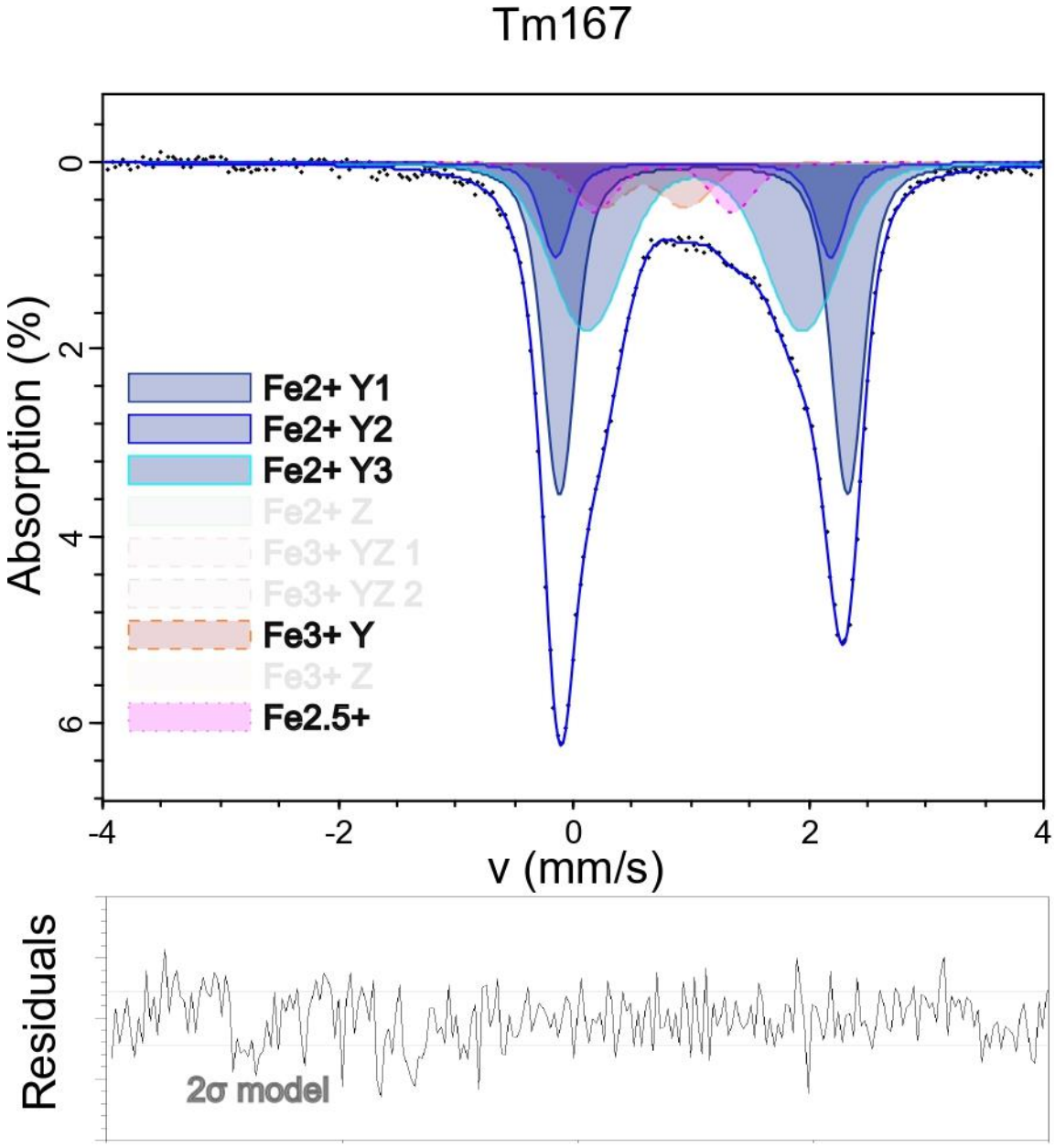
Tm167
Absorption (%)
0
2
4
6
Fe2+ Y1
Fe2+ Y2
Fe2+ Y3
Fe2+ Z
Fe3+ YZ 1
Fe3+ YZ 2
Fe3+ Y
Fe3+ Z
Fe2.5+
-4
-2
0
2
4
v (mm/s)
Residuals
2σ model

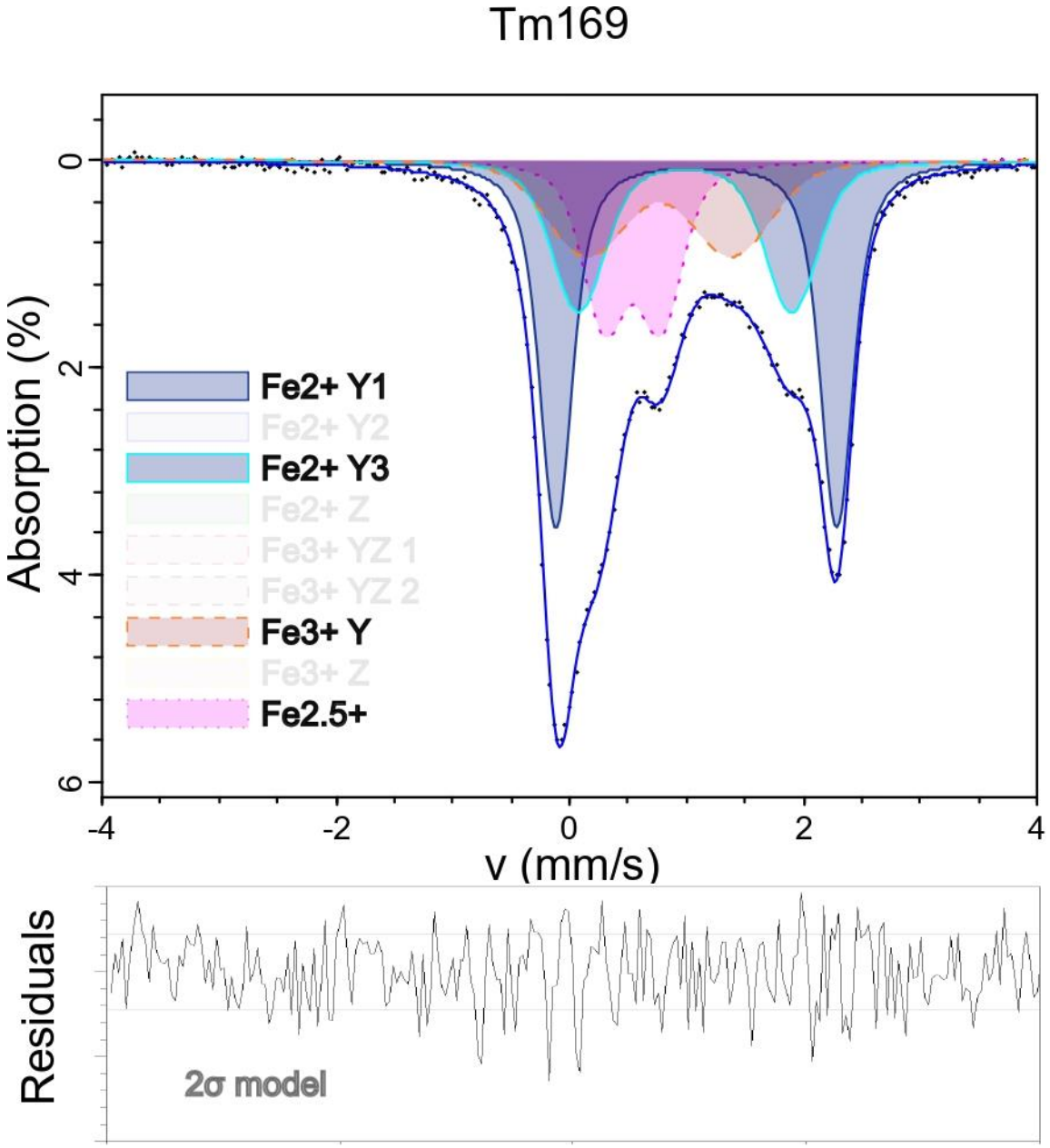
Tm169
Absorption (%)
0
2
4
6
Fe2+ Y1
Fe2+ Y2
Fe2+ Y3
Fe2+ Z
Fe3+ YZ 1
Fe3+ YZ 2
Fe3+ Y
Fe3+ Z
Fe2.5+
-4
-2
0
2
4
v (mm/s)
Residuals
2σ model

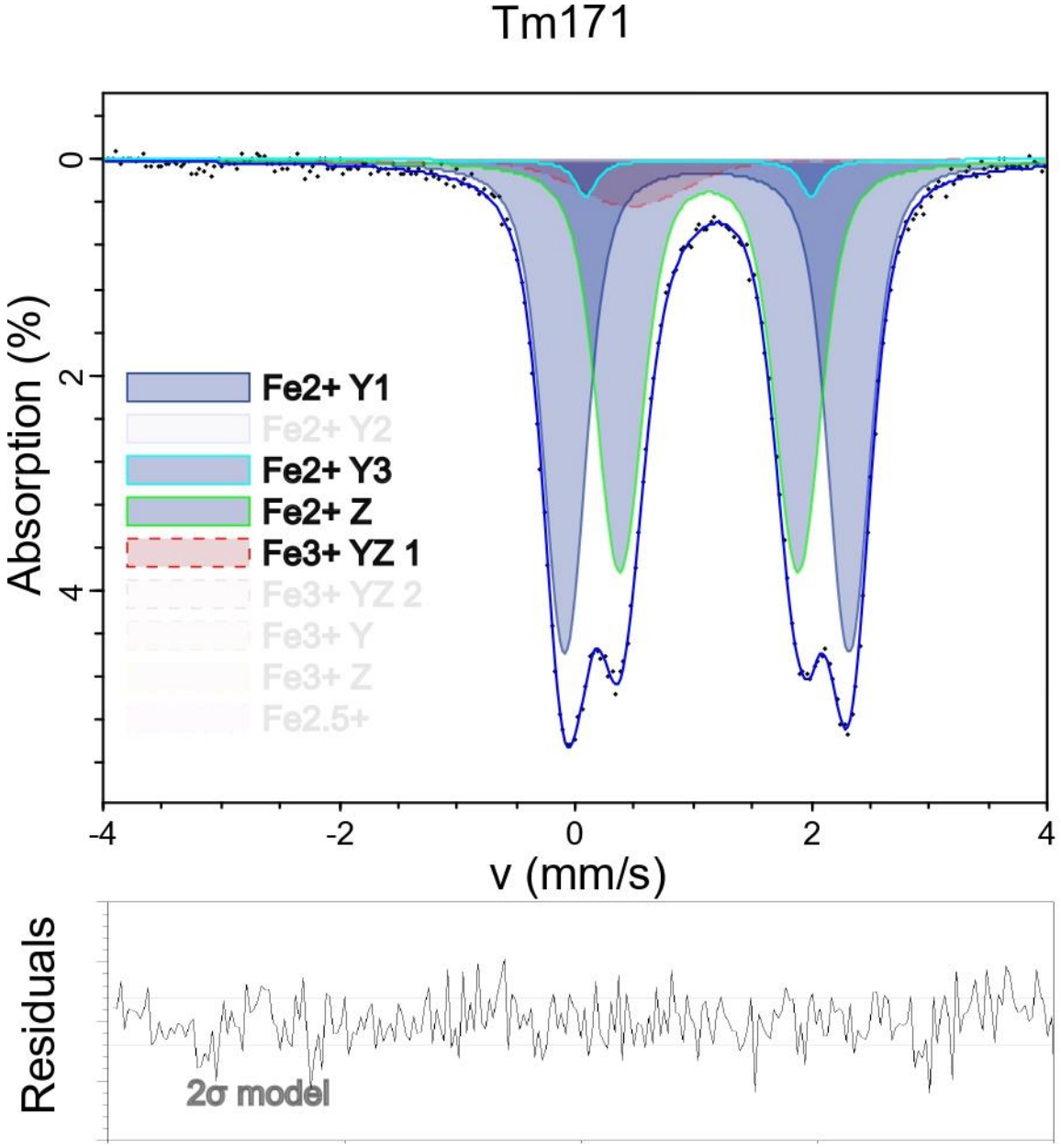
Tm171
Absorption (%)
0
2
4
Fe2+ Y1
Fe2+ Y2
Fe2+ Y3
Fe2+ Z
Fe3+ YZ 1
Fe3+ YZ 2
Fe3+ Y
Fe3+ Z
Fe2.5+
-4
-2
0
2
4
v (mm/s)
Residuals
2σ model

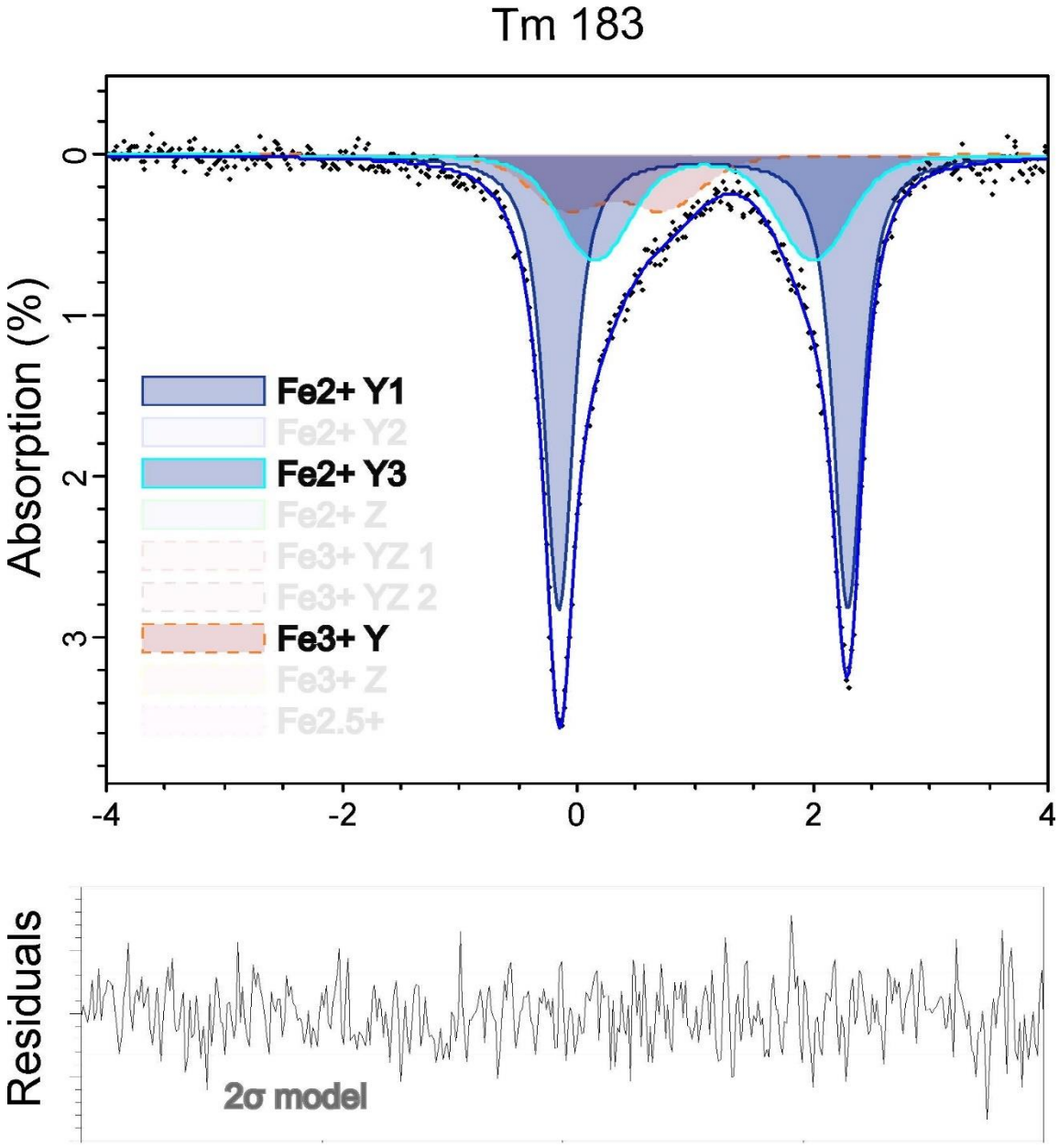
Tm 183
Absorption (%)
0
1
2
3
-4
-2
0
2
4
Fe2+ Y1
Fe2+ Y2
Fe2+ Y3
Fe2+ Z
Fe3+ YZ 1
Fe3+ YZ 2
Fe3+ Y
Fe3+ Z
Fe2.5+
Residuals
2σ model

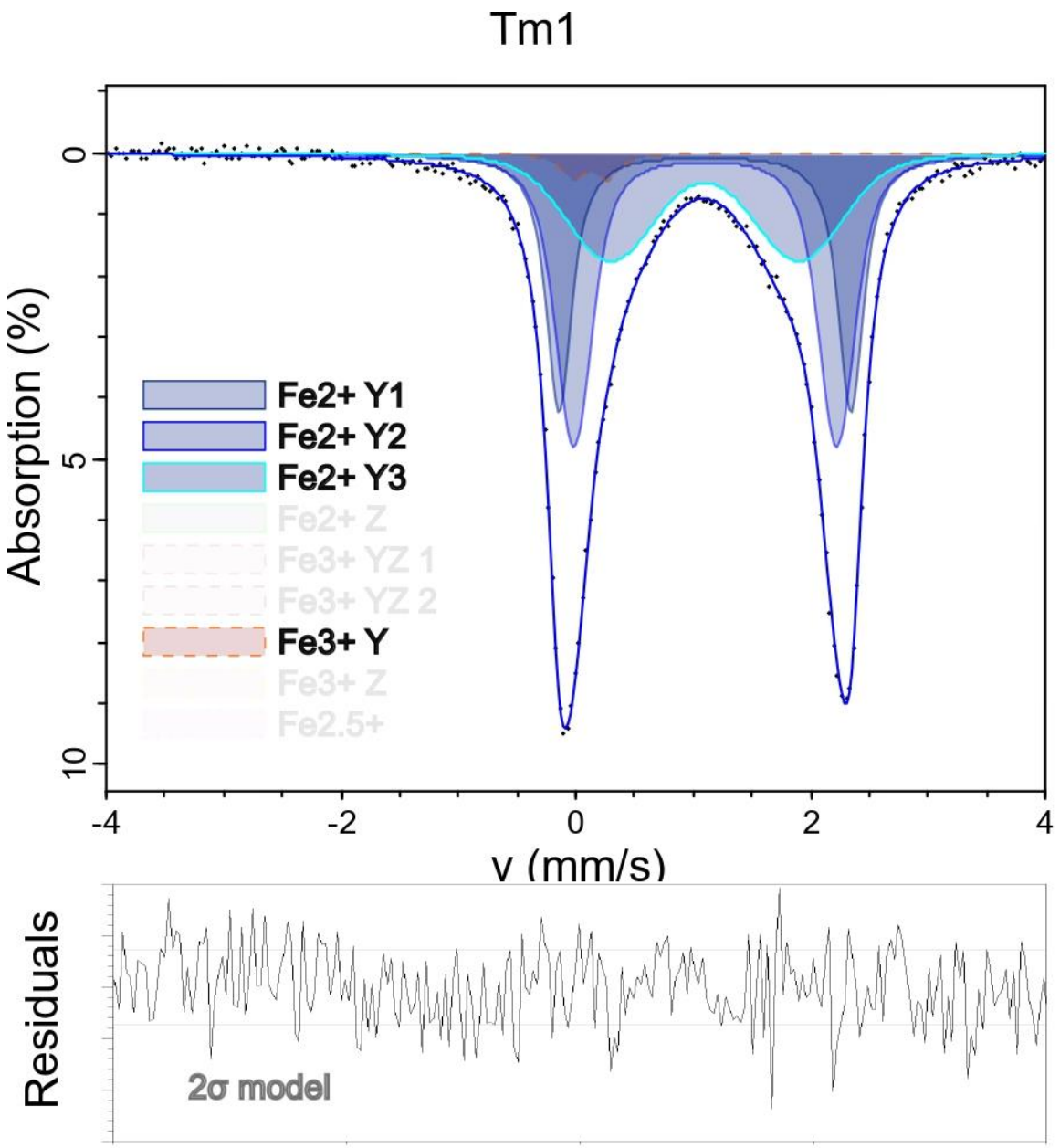
Tm1
Absorption (%)
0
5
10
Fe2+ Y1
Fe2+ Y2
Fe2+ Y3
Fe2+ Z
Fe3+ YZ 1
Fe3+ YZ 2
Fe3+ Y
Fe3+ Z
Fe2.5+
-4
-2
0
2
4
v (mm/s)
Residuals
2σ model

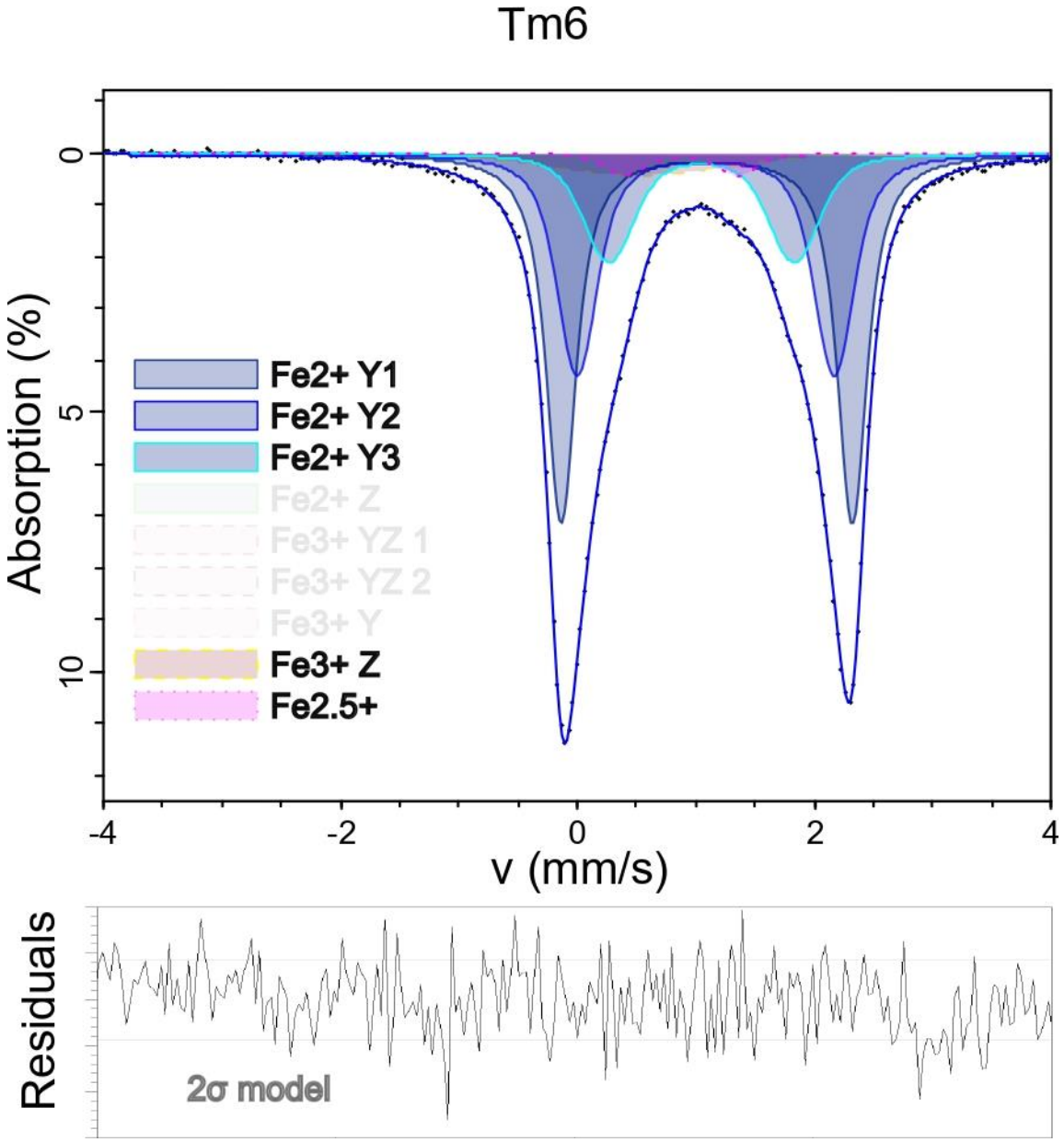
Tm6
Absorption (%)
0
5
10
Fe2+ Y1
Fe2+ Y2
Fe2+ Y3
Fe2+ Z
Fe3+ YZ 1
Fe3+ YZ 2
Fe3+ Y
Fe3+ Z
Fe2.5+
-4
-2
0
2
4
v (mm/s)
Residuals
2σ model

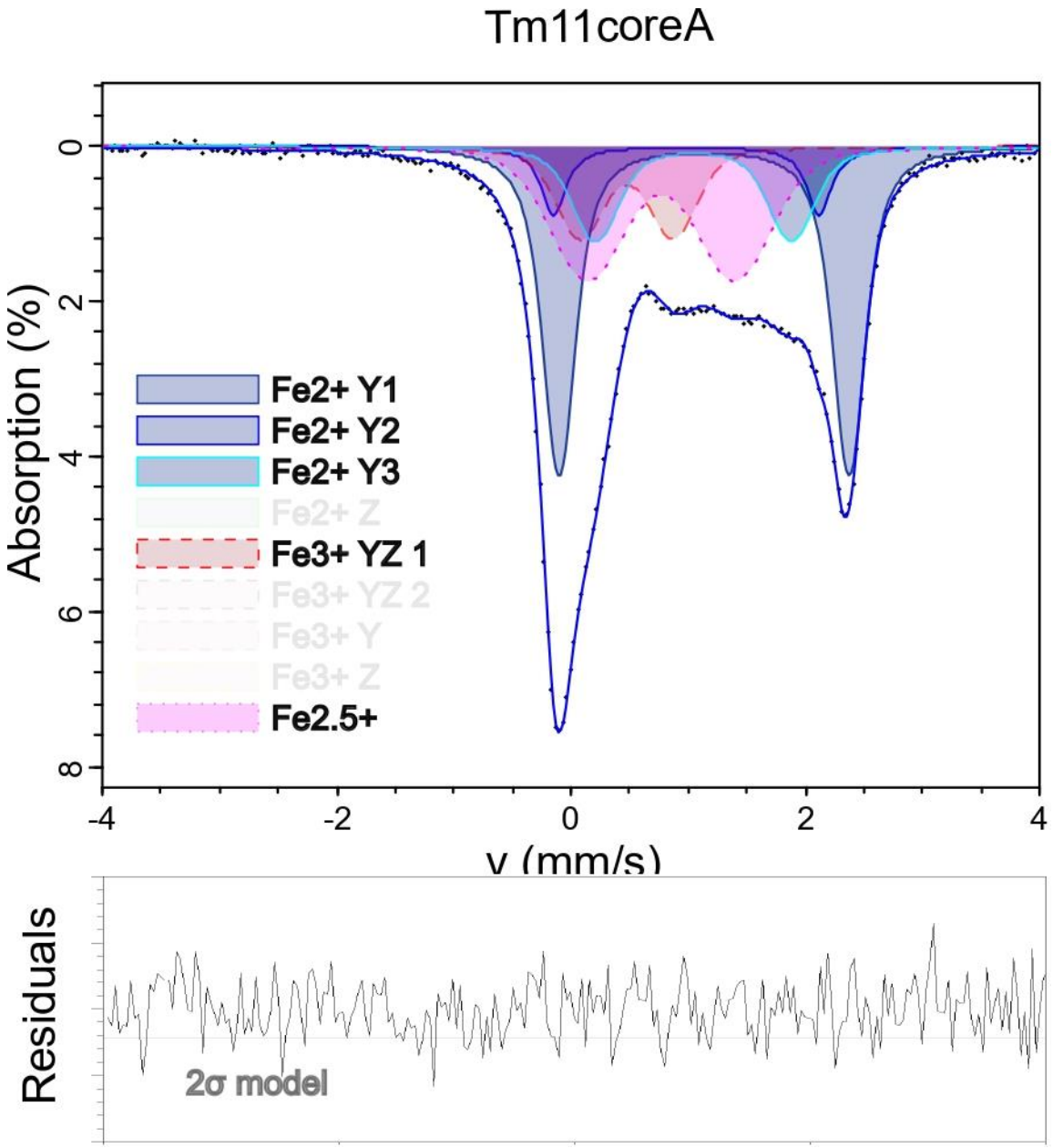
Tm11coreA
Absorption (%)
0
2
4
6
8
Fe2+ Y1
Fe2+ Y2
Fe2+ Y3
Fe2+ Z
Fe3+ YZ 1
Fe3+ YZ 2
Fe3+ Y
Fe3+ Z
Fe2.5+
-4
-2
0
2
4
v (mm/s)
Residuals
2σ model

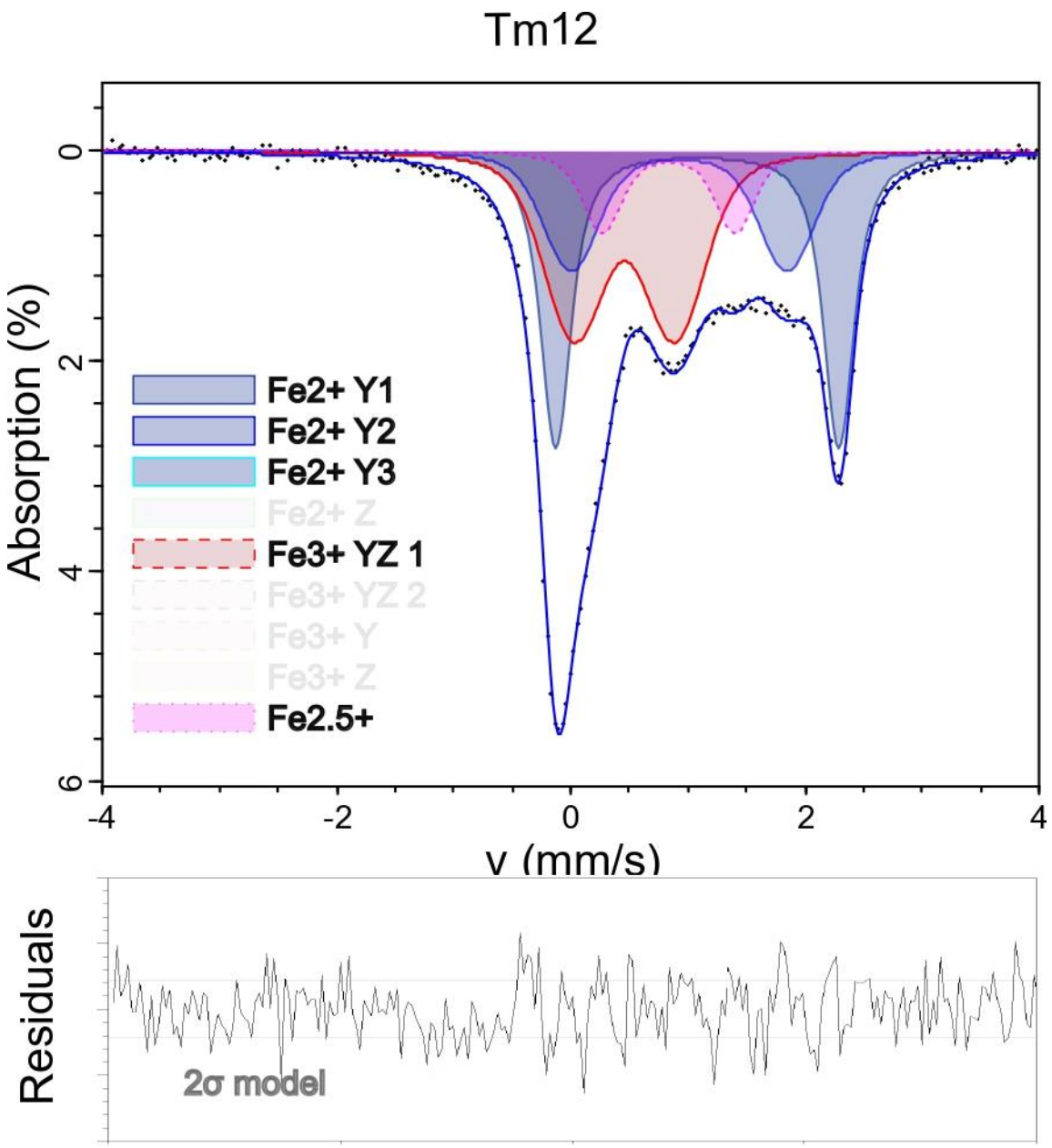
Tm12
Absorption (%)
0
2
4
6
-4
-2
0
2
4
v (mm/s)
Fe2+ Y1
Fe2+ Y2
Fe2+ Y3
Fe2+ Z
Fe3+ YZ 1
Fe3+ YZ 2
Fe3+ Y
Fe3+ Z
Fe2.5+
Residuals
2σ model

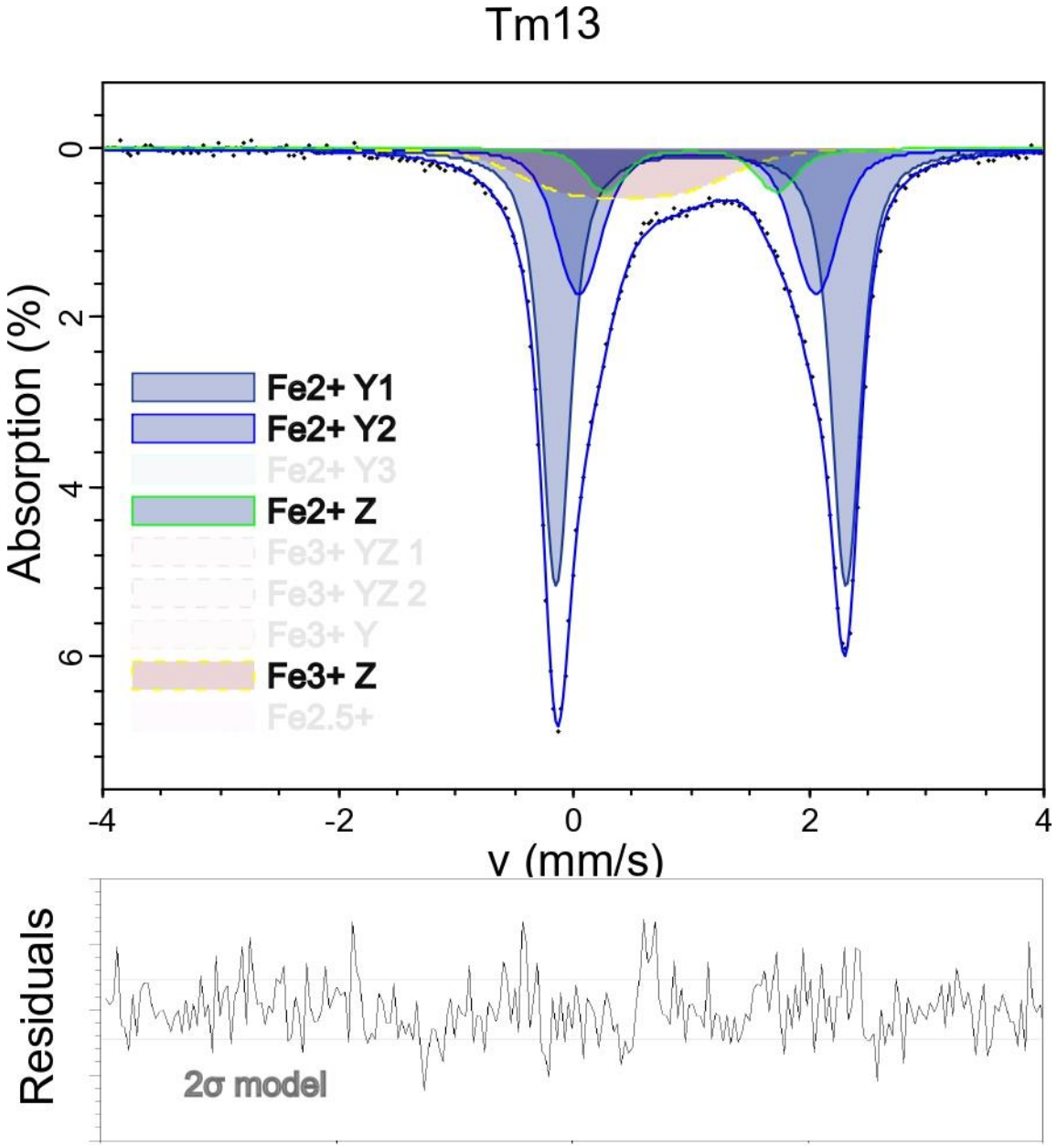
Tm13
Absorption (%)
0
2
4
6
Fe2+ Y1
Fe2+ Y2
Fe2+ Y3
Fe2+ Z
Fe3+ YZ 1
Fe3+ YZ 2
Fe3+ Y
Fe3+ Z
Fe2.5+
-4
-2
0
2
4
v (mm/s)
Residuals
2σ model

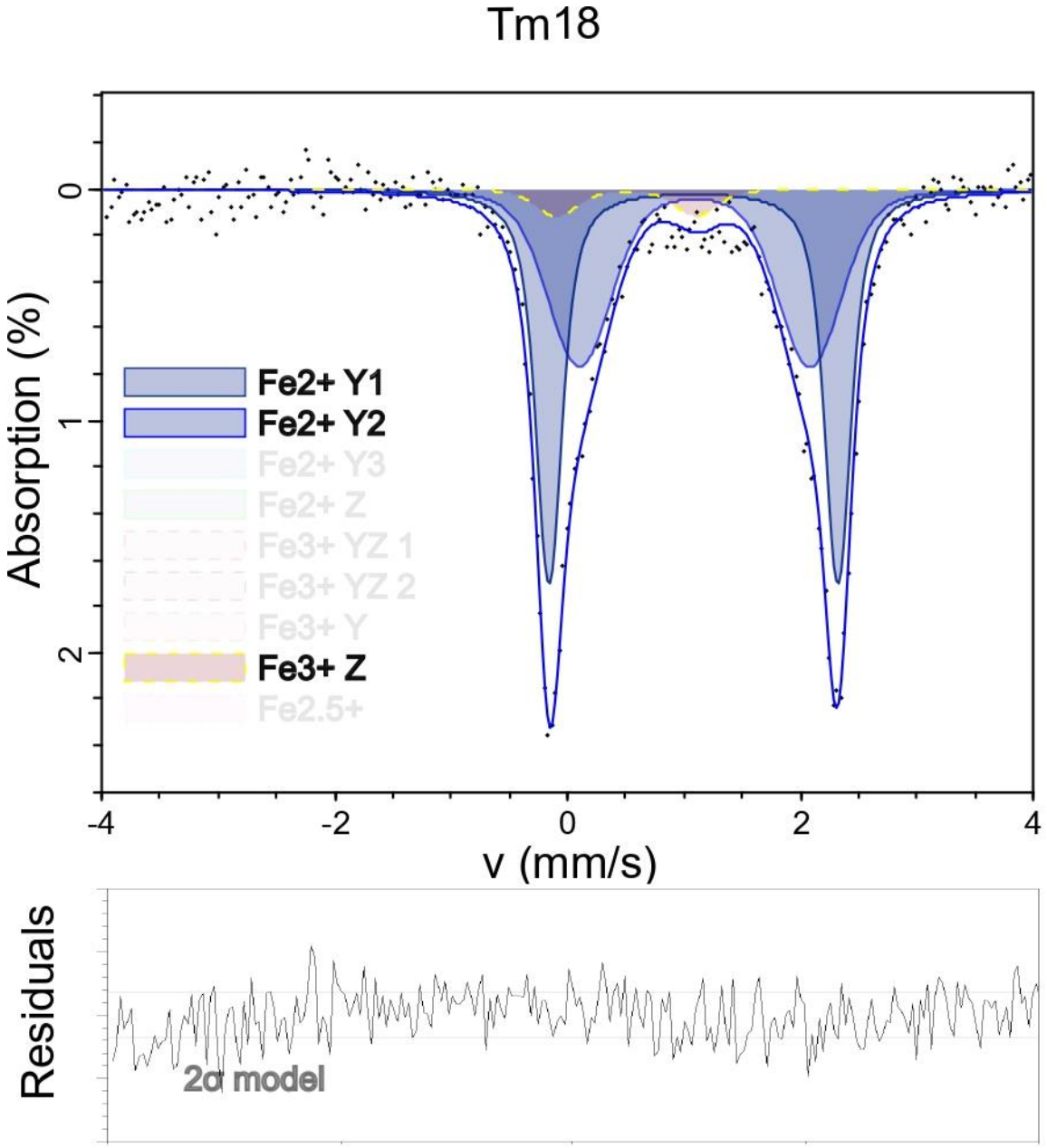
Tm18
Absorption (%)
0
1
2
Fe2+ Y1
Fe2+ Y2
Fe2+ Y3
Fe2+ Z
Fe3+ YZ 1
Fe3+ YZ 2
Fe3+ Y
Fe3+ Z
Fe2.5+
-4
-2
0
2
4
v (mm/s)
Residuals
2σ model

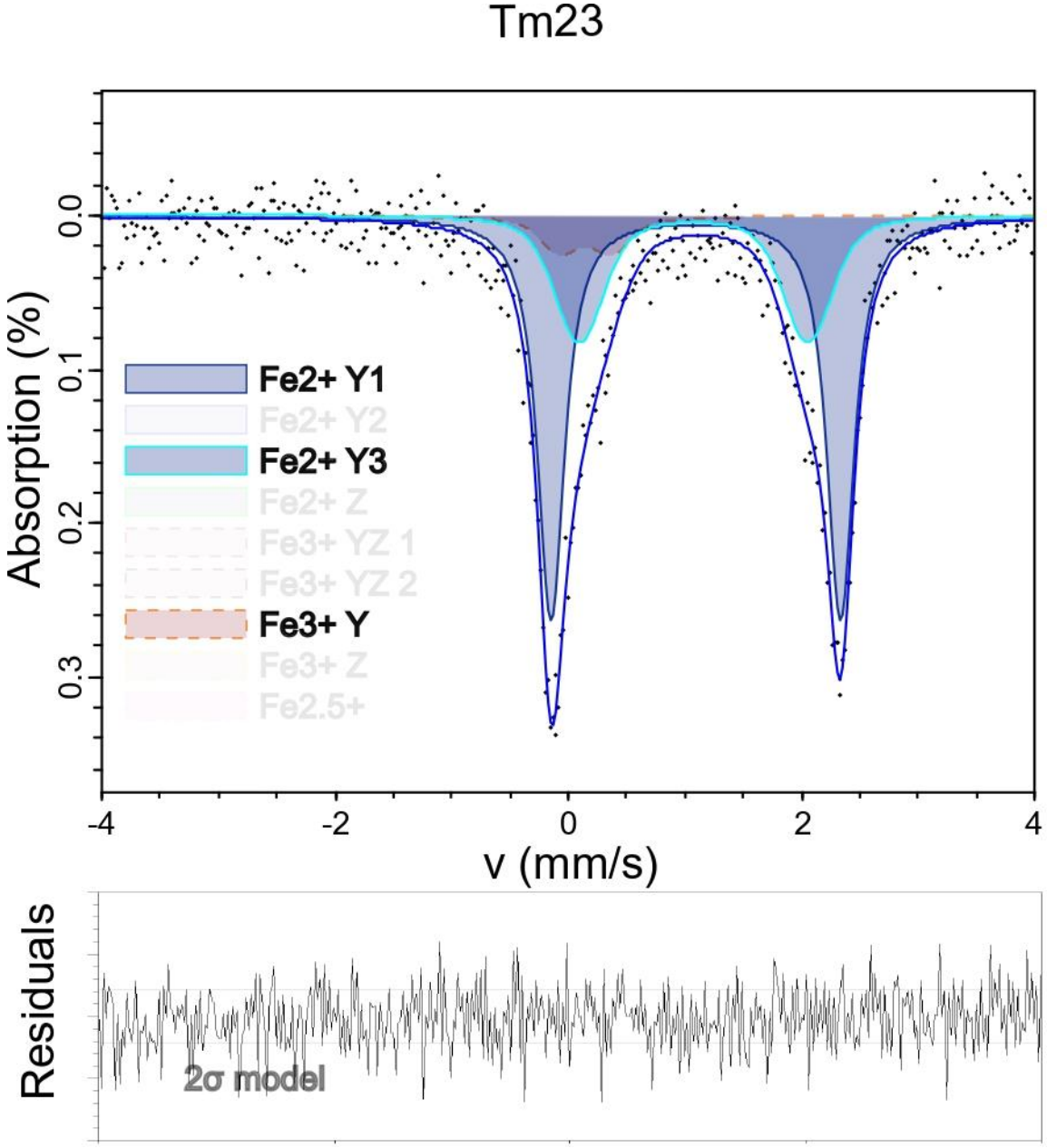
Tm23
Absorption (%)
0.0
0.1
0.2
0.3
Fe2+ Y1
Fe2+ Y2
Fe2+ Y3
Fe2+ Z
Fe3+ YZ 1
Fe3+ YZ 2
Fe3+ Y
Fe3+ Z
Fe2.5+
-4
-2
0
2
4
v (mm/s)
Residuals
2σ model

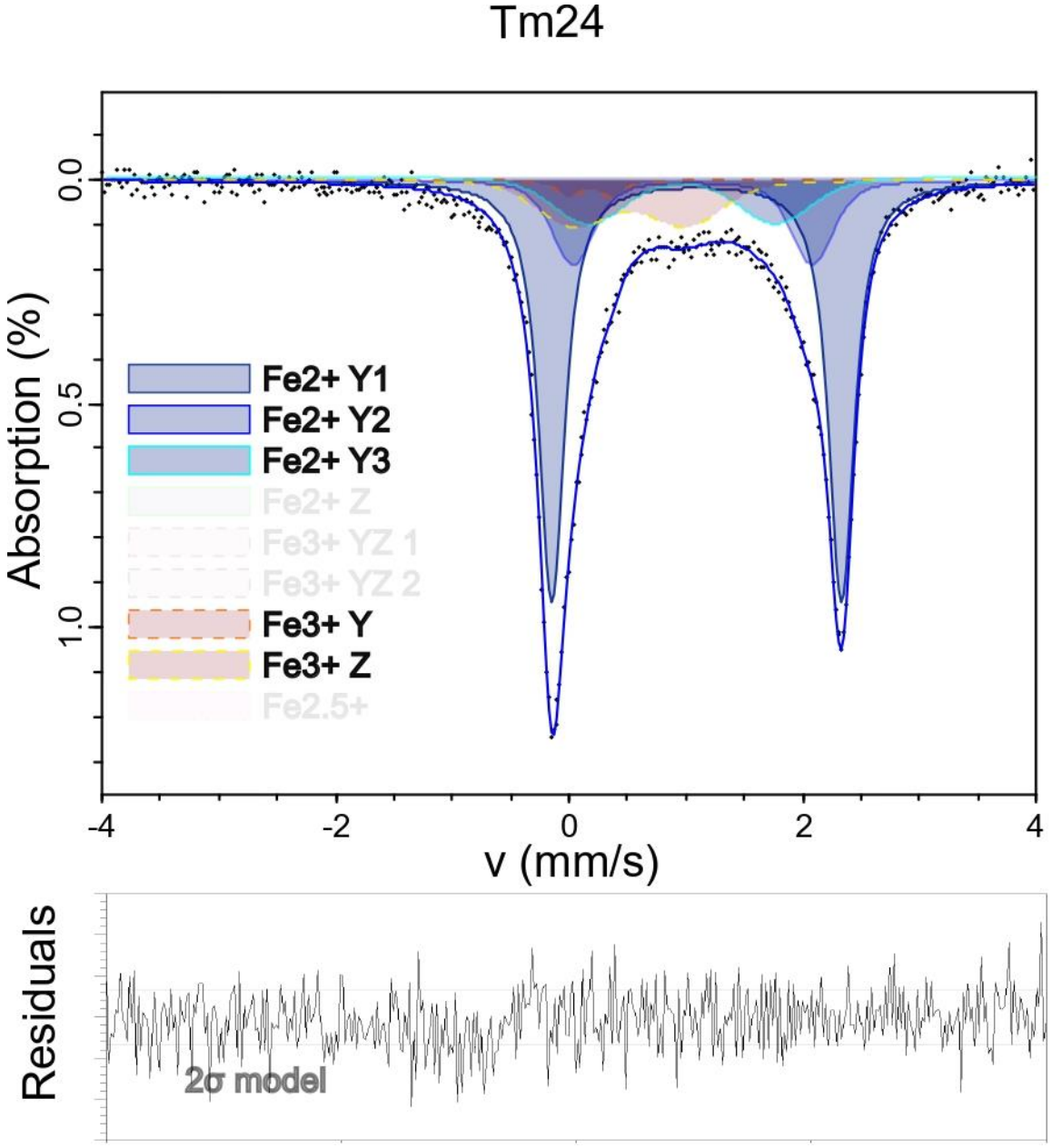
Tm24
Absorption (%)
0.0
0.5
1.0
Fe2+ Y1
Fe2+ Y2
Fe2+ Y3
Fe2+ Z
Fe3+ YZ 1
Fe3+ YZ 2
Fe3+ Y
Fe3+ Z
Fe2.5+
-4
-2
0
2
4
v (mm/s)
Residuals
2σ model

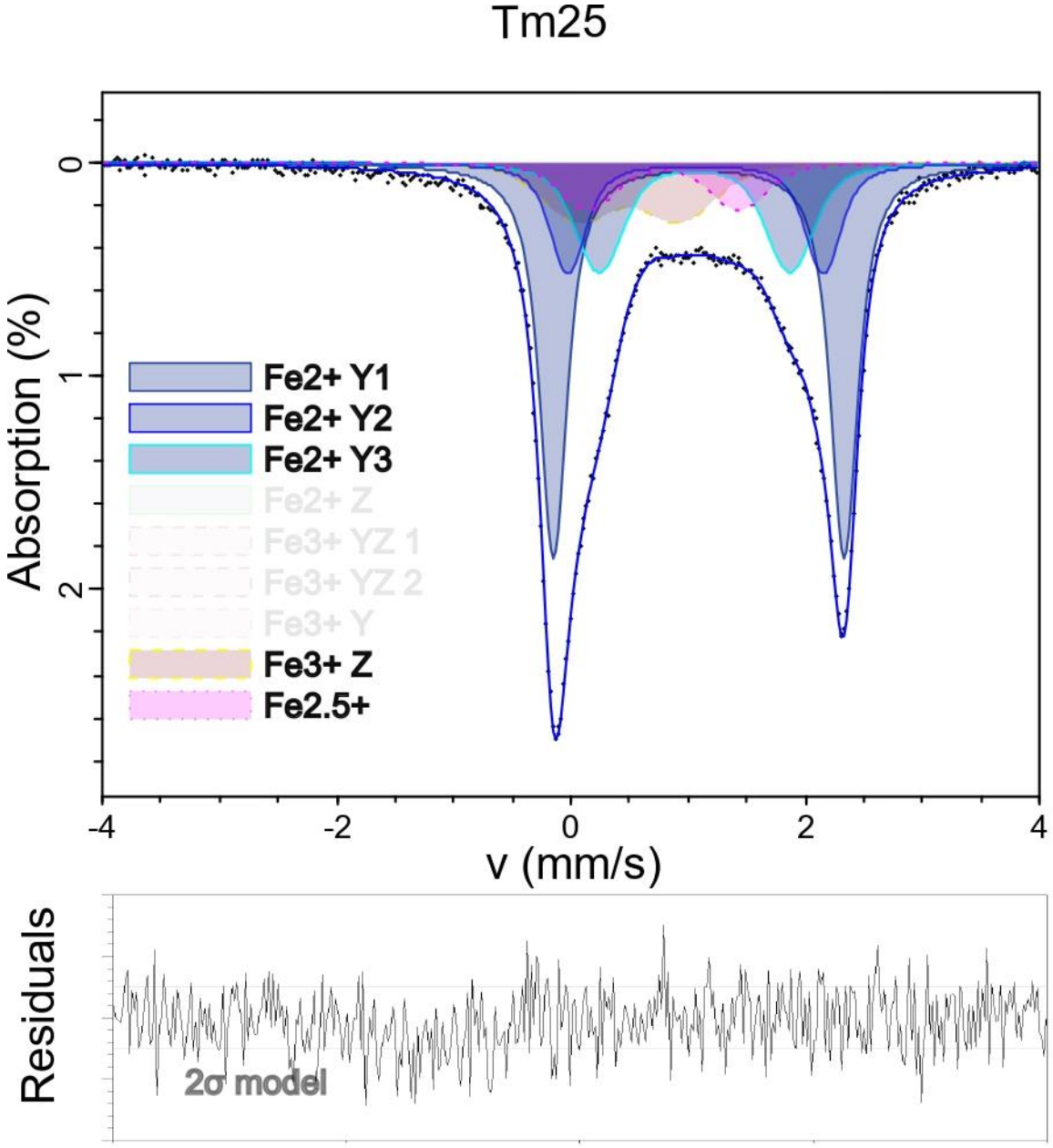
Tm25
Absorption (%)
0
1
2
Fe2+ Y1
Fe2+ Y2
Fe2+ Y3
Fe2+ Z
Fe3+ YZ 1
Fe3+ YZ 2
Fe3+ Y
Fe3+ Z
Fe2.5+
-4
-2
0
2
4
v (mm/s)
Residuals
2σ model

APPENDIX 1F. p-XRD details

Rietveld refinement theoretical background (Redhammer 2021) The measured intensities of a powder diffraction pattern are related to the structure factors by the equation $I_{hkl} = s \cdot K \cdot L(\theta) \cdot P(\theta) \cdot A \cdot E \cdot H \cdot |F_{hkl}^2|$, where s is a scale factor, K combines various constants, L(θ) is the Lorentz correction that accounts for geometric factors and the time the reciprocal lattice vector spends at the reflection position, P(θ) is the polarization correction, A is the absorption correction, E is the extinction correction, and H is the multiplicity, which accounts for the superposition of diffraction peaks caused by scattering from equivalent reciprocal lattice point. The structure factor, F_{hkl} is given by:

$F_{hkl} = \sum_{n=0}^{n=N} f_n \cdot occ \cdot \exp\left[2\pi i(hx_n + ky_n + lz_n)\right] \cdot \exp\left(-B\frac{\sin^2\theta}{\lambda^2}\right)$, where fn is the atomic scattering factor, occ the occupancy of the n-th atom, and (xn,yn,zn) are the fractional atomic coordinates of the n-th atom. The term $\exp(-B\sin 2\theta/\lambda^2)$ represents the temperature factor, which accounts for the thermal vibrations of atoms, and λ is the wavelength of the X-ray radiation. Accurate determination of crystal occupancies must consider Wyckoff positions to correctly represent the number of equivalent atoms in the unit cell.

In Rietveld refinement, a theoretical powder diffraction spectrum Y(calc) is generated using models for background, peak shape, peak width, instrumental configuration, and crystal structure. This Y(calc) is compared to the observed spectrum Y(obs), and the model parameters are refined using a weighted non-linear least squares method. The equation Y(calc) = $s\sum_{nkl} L_K \cdot P_k \cdot H \cdot A \cdot E \cdot S_r \cdot PO_k \cdot |F_{hkl}|^2 \cdot G(2\theta - 2\theta_k) + y_{ib}$ includes terms for surface roughness (S_r) and preferred orientation (PO), with G(2θ−2θk) representing the reflection profile function. For multiphase samples, Y(calc) is the sum of contributions from each phase, and the scale factors are proportional to their respective phase percentages; $w_i = \frac{s_i \cdot (ZMV)_i}{\sum_{k=1}^{n} s_k \cdot (ZMV)_k}$. Where s are the scale factors, The density ρ (g cm^{-3}) of a phase is calculated as ρ=ZMV , where Z is the number of formula units per unit cell, M is the molecular mass of the formula unit, and V is the unit cell volume. If the sample contains amorphous or unidentified phases, the calculated phase proportions may be overestimated.

APPENDIX 1K1. Bond Valence Table

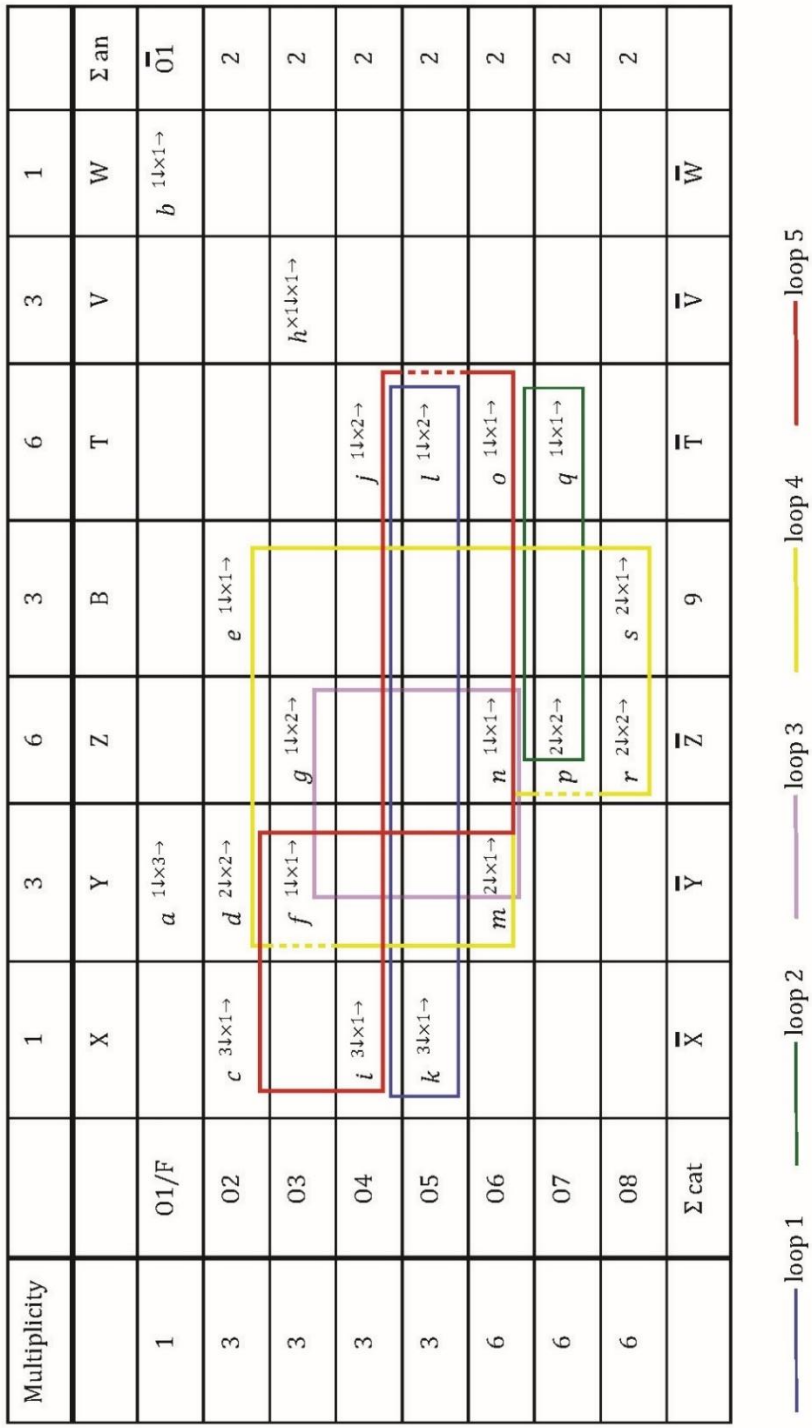

APPENDIX 1K2. Bond Valence Table for X-vacant tourmaline

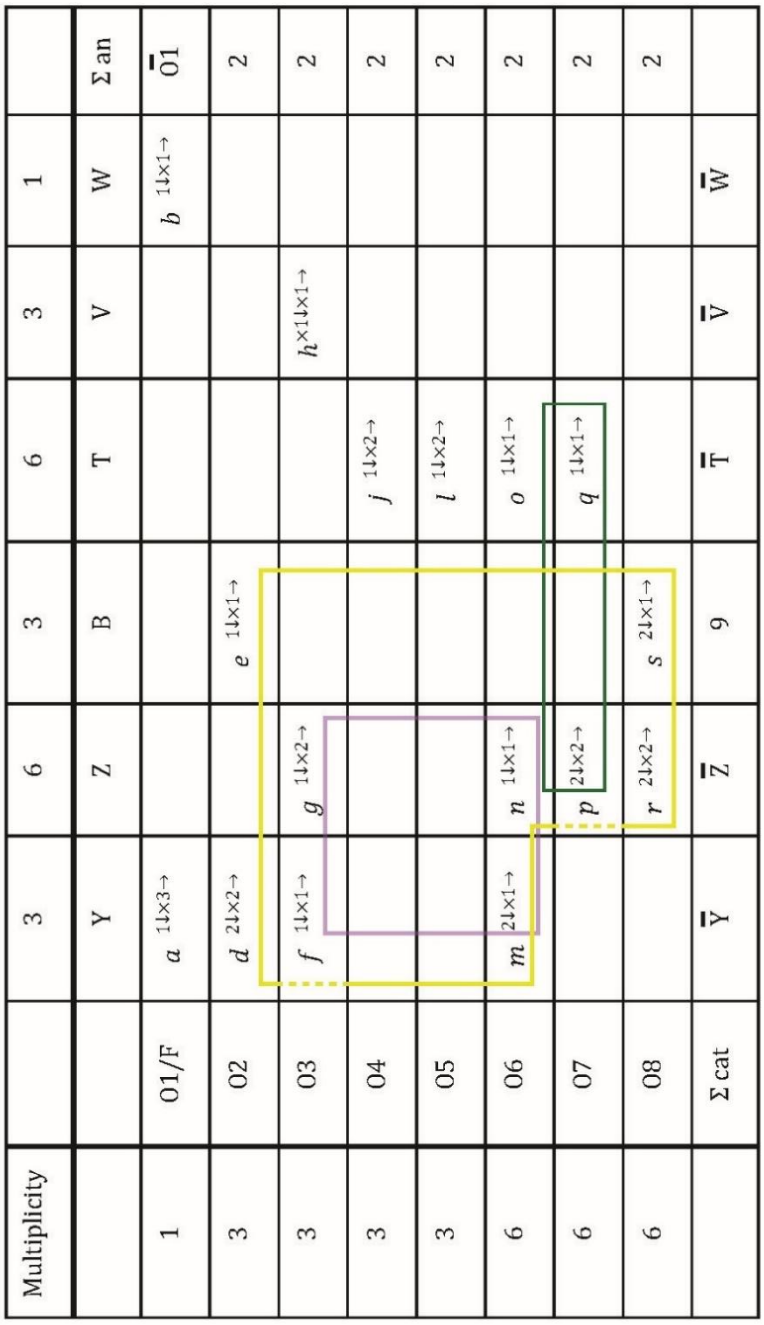

APPENDIX 1L. Stability indices Bond Valence Theory

Stability Indices Gagné & Hawthorne (2020) For comparison, we calculated Δtopo and Δcrystal (=Δelectrosteric) for the unit cell by expanding Gagné & Hawthorne (2020) polyhedral formulation. While Gagné's unit cell Δcrystal formula resembles the Bond Strain Index (BSI) (e.g., Eq. 7 in Gagné and Hawthorne (2016)), it differs in order of operations: BSI squares before summing and then takes the square root, while Δcrystal applies the absolute value before summing, affecting bond strain accumulation. The formulas used were:

$$\Delta_{\text{topo}} = \frac{\sum\left(\text{Catmult}\,{}_1^{\,T} \cdot w_1^T \cdot \left| I - \text{Pauling} \right| \right)}{\sum\left(\text{Catmult}\,{}_1^{\,T} \cdot w_1^T \right)}$$

$$\Delta_{\text{crystal}} = \frac{\sum\left(\text{Catmult}\,{}_1^{\,T} \cdot w_1^T \cdot \left| I - \text{BVtable}\,{}_1^{\,T} \right| \right)}{\sum\left(\text{Catmult}\,{}_1^{\,T} \cdot w_1^T \right)}$$

Polyhedral versions (Gagné and Hawthorne 2020):

$$\Delta_{\text{topo\_poly\_gagne}}(j) = \frac{\sum\left(\text{multiPoly} \cdot \left| I_{\text{Poly}} - \text{Pauling}_{\text{Poly}} \right|\right)}{n_{\text{coord}}}$$

$$\Delta_{\text{crystal\_poly\_gagne}}(j) = \frac{\sum\left(\text{multiPoly} \cdot \left| I_{\text{Poly}} - \text{BVtable}_{\text{Poly}} \right|\right)}{n_{\text{coord}}}$$

These indices, not being physical observables, don't require specific scaling—what matters is quantifying deviations from theoretical regularity. Consistency in operation order, as in the BSI formula, ensures normalization and comparability, and this is the reason we prefer our versions of the equations over the formulations provided in Gagné & Hawthorne (2020).

APPENDIX 1M. Bosi and Lucchesi (2004) method

Bosi and Lucchesi (2004) method to obtain mean local bond lengths in tourmaline Local Mean bond lengths for the elements were obtained from a database of optimised tourmaline structures by Bosi & Lucchesi (2004). Mean local bond length for T, Y and Z sites were calculated as functions of site fractions Xi and local mean bond lengths:

$$\langle Z-0\rangle \text{ calc } = \Sigma X_{\mathrm{i}}\langle Z-0\rangle_{\mathrm{i}}$$
$$\langle Y-0\rangle \text{ calc } = \Sigma X_{\mathrm{i}}\langle Y-0\rangle_{\mathrm{i}}$$
$$\langle T-0\rangle \text{ calc } = \Sigma X_{\mathrm{i}}\langle T-0\rangle_{\mathrm{i}}$$

Observed mean bond lengths:

$$\langle Z-O\rangle obs = (ZO3 + ZO6 + ZO7D + ZO7E + ZO8 + ZO8E)/6$$
$$\langle Y-0\rangle obs = (Y0\mathrm{I} + 2\cdot Y02 + Y03 + 2\cdot Y06)/6$$
$$\langle T-0\rangle obs = (T04 + T05 + T06 + T07)/4$$

The O6 site was chosen as a reference for bond length calculations due to its shared connectivity with Z-, Y-, and T-sites, standardizing measurements and reducing errors from positional shifts caused by variable fractional coordinates in tourmaline, ensuring consistent accuracy. The bond lengths were calculated using the general formula for the distance between two points in a 3D space:

$$d^2 = a^2(x_1-x_2)^2 + b^2(y_1-y_2)^2 + c^2(z_1-z_2)^2 + 2ab\cos(\gamma)\,(x_1-x_2)(y_1-y_2) + 2ac\cos(\beta)\,(x_1-x_2)(z_1-z_2) + 2bc\cos(\alpha)(y_1-y_2)(z_1-z_2)$$

Which simplifies in the hexagonal system since a=b, α=β=90∘, and γ=120∘ to:

$$d^2 = a^2[(x_1-x_2)^2 + (y_1-y_2)^2 - (x_1-x_2)(y_1-y_2)] + c^2(z_1-z_2)^2.$$

This equation derived the specific bond lengths between cation sites and O6, such as the Z-O6 bond length:

$$(ZO_6)^2 = a^2[(x_Z-x_{O6})^2 + (y_Z-y_{O6})^2 - (x_Z-x_{O6})(y_Z-y_{O6})] + c^2(z_Z-z_{O6})^2.$$

For Y-O6:

$$(YO_6)^2 = a^2\left[(x_Y-x_{O6})^2 + \left(\tfrac{1}{2}x_Y-y_{O6}\right)^2 - (x_Y-x_{O6})\left(\tfrac{1}{2}x_Y-y_{O6}\right)\right] + c^2(z_Y-z_{O6})^2$$

The factor $\frac{1}{2}x_Y$ arises from Y sharing its y-coordinate with two O6 anions due to symmetry.

For T-O6:

$$(TO_6)^2 = a^2[(x_T - x_{O6})^2 + (y_T - y_{O6})^2 - (x_T - x_{O6})(y_T - y_{O6})] + c^2(z_T - z_{O6})^2$$

Simplifying by fixing the z-coordinates z_Z, and z_Y and z_T (=1) reduces non-linear dependencies. Although these fractional coordinates can vary in tourmaline, this approach simplifies the bond length equations. Defining:

$$ZZZ = [(x_{\mathrm{Z}} - x_{\mathrm{O6}})^2 + (y_{\mathrm{Z}} - y_{\mathrm{O6}})^2 - (x_{\mathrm{Z}} - x_{\mathrm{O6}})(y_{\mathrm{Z}} - y_{\mathrm{O6}})]$$
$$YYY = [(x_{\mathrm{Y}} - x_{\mathrm{O6}})^2 + (1/2x_{\mathrm{Y}} - y_{\mathrm{O6}})^2 - (x_{\mathrm{Y}} - x_{\mathrm{O6}})(1/2x_{\mathrm{Y}} - y_{\mathrm{O6}})]$$
$$TTT = [(x_{\mathrm{T}} - x_{\mathrm{O6}})^2 + (y_{\mathrm{T}} - y_{\mathrm{O6}})^2 - (x_{\mathrm{T}} - x_{\mathrm{O6}})(y_{\mathrm{T}} - y_{\mathrm{O6}})]$$
$$SZ = ZO3 + ZO7D + ZO7E + ZO8 + ZO8E$$
$$SY = 1/2(YO1) + YO2 + 1/2(YO3)$$
$$ST = TO4 + TO5 + TO7$$

the equations for $\langle Z - O\rangle obs, \langle Y - O\rangle obs, \langle T - O\rangle obs$ can be rewritten as functions of lattice parameters a, c, and the fractional coordinate zO6.

$$(ZZZ)a^2 + (z_Z - z_{O6})^2c^2 = [6 < Z - O > obs - (SZ)]^2$$

$$(YYY)a^2 + (z_Y - z_{O6})^2c^2 = [3 < Y - 0 > obs - (SY)]^2$$

$$(TTT)a^2 + (1 - z_{\mathrm{O6}})^2c^2 = [4\langle T - 0\rangle\, obs - (ST)]^2$$

Fixing z_Z, z_Y, and z_T= simplifies mean bond length equations by reducing complex quadratic terms to linear relationships in terms of a, c, and zO6. This allows for solving using linear methods instead of non-linear optimisation. This system of three equation with three unknown (a, c, zO6) can be solved to get equation for a, c and ZO6 expressed in terms of $\langle T - 0\rangle obs, \langle Y - 0\rangle obs$ and $\langle Z - 0\rangle$obs see long expressions in the Appendix of Bosi & Lucchesi (2004).

The equations for a, c, and zO6 can now also be solved using the calculated $\langle T - 0\rangle calc$, $\langle Y - 0\rangle calc$, and $\langle Z - 0\rangle calc$, derived from site fractions and local bond lengths $\langle T - 0\rangle_{\mathrm{i}}$, $\langle Y - 0\rangle_{\mathrm{i}}$ and $\langle Z - 0\rangle_{\mathrm{i}}$. Initial values for these local bond lengths are based on the Shannon (1976) ionic radii. The optimisation adjusts these local bond lengths until the calculated a, c, and zO6 match the observed values by minimizing the objective function

$$G(X_i, D_i) = \frac{\sum F(X_i)}{(\text{number samples})}$$

In this objective function the Xi are fixed?. Simultaneous optimisation of mean bond lengths, unit cell parameters, and zO6 was necessary as direct multiple linear regression of the local mean bond lengths per elements using only site fractions and mean bond lengths does not maintain required symmetry constraints.

Appendix 1N. A-priory bond lengths

These tables present the range of a-priori bond lengths for cations at the X, Y, Z, and T sites in nomenclature tourmaline endmembers, calculated using bond valence methods. Each range reflects how variations in local coordination and neighboring site occupancy affect ideal bond lengths under full site occupancy. For each element, the tables list the minimum and maximum bond lengths, the total range, and the endmembers defining these extremes. Variability is largest for larger, more polarizable cations (e.g., Na, Ca, Mg) and smallest for rigidly bonded cations like Al and Si.

Table A1N.1. A-priory bond length of LRO endmembers.

Table 1. X Site Bond Length Ranges (Full Occupancy)

Element	Bond Length Range	Difference	Tourmalines Contributing to the Range	Tourmaline with Minimum Bond Length	Tourmaline with Maximum Bond Length
Ca	2.5306 - 2.5564	0.0258	[Ca][Fe]$_3$[Mg$_{1/6}$Al$_{5/6}$]$_6$[Si]$_6$[OH]$_3$[OH], [Ca][Mg]$_3$[Al$_{5/6}$Mg$_{1/6}$]$_6$[Si]$_6$[OH]$_3$[F], [Ca][Mg]$_3$[Al]$_6$[Si]$_6$[OH]$_3$[O], [Ca][Mg]$_3$[Al$_{5/6}$Mg$_{1/6}$]$_6$[Si]$_6$[OH]$_3$[OH]	[Ca][Fe]$_3$[Al]$_6$[Si$_{5/6}$Al$_{1/6}$]$_6$[OH]$_3$[OH]	[Ca][Fe]$_3$[Al]$_6$[Si]$_6$[OH]$_3$[O]
Na	2.6224 - 2.6699	0.0475	[Na][Fe$_{5/6}$Ti$_{1/6}$]$_3$[Al]$_6$[Si]$_6$[OH]$_3$[O], [Na][Al]$_3$[Al]$_6$[Si$_{4/6}$B$_{2/6}$]$_6$[OH]$_3$[O], [Na][Fef]$_3$[Al$_{4/6}$Fe$_{2/6}$]$_6$[Si]$_6$[OH]$_3$[O], [Na][Fef]$_3$[Al]$_6$[Si]$_6$[O]$_3$[F], [Na][Mg]$_3$[Al]$_6$[Si]$_6$[OH]$_3$[F], [Na][Fe]$_3$[Al]$_6$[Si]$_6$[OH]$_3$[F],	[Na][Fef]$_3$[Al$_{4/6}$Mg$_{2/6}$]$_6$[Si]$_6$[OH]$_3$[O]	[Na][Mg]$_3$[Al]$_6$[Si]$_6$[OH]$_3$[OH]

Element	Bond Length Range	Difference	Tourmalines Contributing to the Range	Tourmaline with Minimum Bond Length	Tourmaline with Maximum Bond Length
			[Na][$Mg_{5/6}Ti_{1/6}$]$_3$[Al]$_6$[Si]$_6$[OH]$_3$[O], [Na][Al]$_3$[Al]$_6$[Si]$_6$[O]$_3$[OH], [Na][$Al_{2/3}Mg_{1/3}$]$_3$[$Al_{5/6}Mg_{1/6}$]$_6$[Si]$_6$[OH]$_3$[O], [Na][$Fe_{2/3}Al_{1/3}$]$_3$[Al]$_6$[Si]$_6$[OH]$_3$[O], [Na][Fef]$_3$[$Fef_{4/6}Mg_{2/6}$]$_6$[Si]$_6$[OH]$_3$[O], [Na][Fe]$_3$[Al]$_6$[Si]$_6$[OH]$_3$[OH]		

Table 2. Y Site Bond Length Ranges (Full Occupancy)

Element	Bond Length Range	Difference	Tourmalines Contributing to the Range	Tourmaline with Minimum Bond Length	Tourmaline with Maximum Bond Length
Al	1.9136 - 1.9148	0.0004	[V][Al]$_3$[Al]$_6$[$Si_{5/6}Al_{1/6}$]$_6$[OH]$_3$[O], [Na][Al]$_3$[Al]$_6$[Si]$_6$[O]$_3$[OH], [Na][Al]$_3$[Al]$_6$[$Si_{4/6}B_{2/6}$]$_6$[OH]$_3$[O]	[Na][Al]$_3$[Al]$_6$[$Si_{4/6}B_{2/6}$]$_6$[OH]$_3$[O]	[Na][Al]$_3$[Al]$_6$[Si]$_6$[O]$_3$[OH]
Fe	2.1463 - 2.1938	0.0475	[Ca][Fe]$_3$[Al]$_6$[$Si_{5/6}Al_{1/6}$]$_6$[OH]$_3$[OH], [Ca][Fe]$_3$[$Mg_{1/6}Al_{5/6}$]$_6$[Si]$_6$[OH]$_3$[OH], [Na][Fe]$_3$[Al]$_6$[Si]$_6$[OH]$_3$[OH], [Na][Fe]$_3$[Al]$_6$[Si]$_6$[OH]$_3$[F]	[Na][Fe]$_3$[Al]$_6$[Si]$_6$[OH]$_3$[F]	[Ca][Fe]$_3$[Al]$_6$[Si]$_6$[OH]$_3$[O]
Fef	2.0098 - 2.0208	0.0110	[Na][Fef]$_3$[$Al_{4/6}Fe_{2/6}$]$_6$[Si]$_6$[OH]$_3$[O], [Na][Fef]$_3$[$Fef_{4/6}Mg_{2/6}$]$_6$[Si]$_6$[OH]$_3$[O], [Na][Fef]$_3$[Al]$_6$[Si]$_6$[O]$_3$[F]	[Na][Fef]$_3$[Al]$_6$[Si]$_6$[O]$_3$[F]	[Na][Fef]$_3$[$Al_{4/6}Mg_{2/6}$]$_6$[Si]$_6$[OH]$_3$[O]
Mg	2.0819 - 2.1391	0.0572	[Na][Mg]$_3$[Al]$_6$[Si]$_6$[OH]$_3$[OH], [Na][Mg]$_3$[Al]$_6$[Si]$_6$[OH]$_3$[F], [Ca][Mg]$_3$[$Al_{5/6}Mg_{1/6}$]$_6$[Si]$_6$[OH]$_3$[OH], [Ca][Mg]$_3$[$Al_{5/6}Mg_{1/6}$]$_6$[Si]$_6$[OH]$_3$[F], [Ca][Mg]$_3$[Al]$_6$[Si]$_6$[OH]$_3$[O]	[Ca][Mg]$_3$[$Al_{5/6}Mg_{1/6}$]$_6$[Si]$_6$[OH]$_3$[F]	[Ca][Mg]$_3$[Al]$_6$[Si]$_6$[OH]$_3$[O]

Table 3. Z Site Bond Length Ranges (Full Occupancy)

Element	Bond Length Range	Difference	Tourmalines Contributing to the Range	Tourmaline with Minimum Bond Length	Tourmaline with Maximum Bond Length
Al	1.9059 - 1.9096	0.0037	[Ca][Fe]$_3$[Al]$_6$[Si$_{5/6}$Al$_{1/6}$]$_6$[OH]$_3$[OH], [V][Al]$_3$[Al]$_6$[Si$_{5/6}$Al$_{1/6}$]$_6$[OH]$_3$[O], [Na][Mg]$_3$[Al]$_6$[Si]$_6$[OH]$_3$[OH], [Na][Fe$_{5/6}$Ti$_{1/6}$]$_3$[Al]$_6$[Si]$_6$[OH]$_3$[O], [Na][Fef]$_3$[Al]$_6$[Si]$_6$[O]$_3$[F], [Na][Mg]$_3$[Al]$_6$[Si]$_6$[OH]$_3$[F], [Na][Fe]$_3$[Al]$_6$[Si]$_6$[OH]$_3$[F], [V][Fe$_{2/3}$Al$_{1/3}$]$_3$[Al]$_6$[Si]$_6$[OH]$_3$[OH], [Na][Mg$_{5/6}$Ti$_{1/6}$]$_3$[Al]$_6$[Si]$_6$[OH]$_3$[O], [V][Mg$_{2/3}$Al$_{1/3}$]$_3$[Al]$_6$[Si]$_6$[OH]$_3$[OH], [Ca][Mg]$_3$[Al]$_6$[Si]$_6$[OH]$_3$[O], [Na][Al]$_3$[Al]$_6$[Si]$_6$[O]$_3$[OH], [V][Fe$_{1/3}$Al$_{2/3}$]$_3$[Al]$_6$[Si]$_6$[OH]$_3$[O], [Na][Fe$_{2/3}$Al$_{1/3}$]$_3$[Al]$_6$[Si]$_6$[OH]$_3$[O], [Na][Fe]$_3$[Al]$_6$[Si]$_6$[OH]$_3$[OH]	[Ca][Fe]$_3$[Al]$_6$[Si]$_6$[OH]$_3$[O]	[Na][Al]$_3$[Al]$_6$[Si$_{4/6}$B$_{2/6}$]$_6$[OH]$_3$[O]

Table 4. T Site Bond Length Ranges (Full Occupancy)

Element	Bond Length Range	Difference	Tourmalines Contributing to the Range	Tourmaline with Minimum Bond Length	Tourmaline with Maximum Bond Length
Si	1.6193 - 1.6254	0.0061	[Na][Fef]$_3$[Al$_{4/6}$Mg$_{2/6}$]$_6$[Si]$_6$[OH]$_3$[O], [Na][Mg]$_3$[Al]$_6$[Si]$_6$[OH]$_3$[OH], [Na][Fe$_{5/6}$Ti$_{1/6}$]$_3$[Al]$_6$[Si]$_6$[OH]$_3$[O], [Na][Fef]$_3$[Al$_{4/6}$Fe$_{2/6}$]$_6$[Si]$_6$[OH]$_3$[O], [Na][Fef]$_3$[Al]$_6$[Si]$_6$[O]$_3$[F], [Na][Mg]$_3$[Al]$_6$[Si]$_6$[OH]$_3$[F], [Na][Fe]$_3$[Al]$_6$[Si]$_6$[OH]$_3$[F],	[V][Fe$_{2/3}$Al$_{1/3}$]$_3$[Al]$_6$[Si]$_6$[OH]$_3$[OH]	[Ca][Fe]$_3$[Mg$_{1/6}$Al$_{5/6}$]$_6$[Si]$_6$[OH]$_3$[OH]

Element	Bond Length Range	Difference	Tourmalines Contributing to the Range	Tourmaline with Minimum Bond Length	Tourmaline with Maximum Bond Length
			[Ca][Mg]$_3$[Al$_{5/6}$Mg$_{1/6}$]$_6$[Si]$_6$[OH]$_3$[F], [Ca][Fe]$_3$[Al]$_6$[Si]$_6$[OH]$_3$[O], [Na][Mg$_{5/6}$Ti$_{1/6}$]$_3$[Al]$_6$[Si]$_6$[OH]$_3$[O], [V][Mg$_{2/3}$Al$_{1/3}$]$_3$[Al]$_6$[Si]$_6$[OH]$_3$[OH], [Ca][Mg]$_3$[Al]$_6$[Si]$_6$[OH]$_3$[O], [Na][Al]$_3$[Al]$_6$[Si]$_6$[O]$_3$[OH], [Na][Al$_{2/3}$Mg$_{1/3}$]$_3$[Al$_{5/6}$Mg$_{1/6}$]$_6$[Si]$_6$[OH]$_3$[O], [V][Fe$_{1/3}$Al$_{2/3}$]$_3$[Al]$_6$[Si]$_6$[OH]$_3$[O], [Na][Fe$_{2/3}$Al$_{1/3}$]$_3$[Al]$_6$[Si]$_6$[OH]$_3$[O], [Na][Fef]$_3$[Fef$_{4/6}$Mg$_{2/6}$]$_6$[Si]$_6$[OH]$_3$[O], [Na][Fe]$_3$[Al]$_6$[Si]$_6$[OH]$_3$[OH], [Ca][Mg]$_3$[Al$_{5/6}$Mg$_{1/6}$]$_6$[Si]$_6$[OH]$_3$[OH]		

REFERENCES CITED IN APPENDICES

Ancey, M., Bastenaire, F., Tixier, R., Maurice, F., and Meny, I. (1978) Applications of statistical methods in microanalysis. Microanalysis and scanning electron microscopy, 319–343.

Andreozzi, G.B., Bosi, F., and Longo, M. (2008) Linking Mossbauer and structural parameters in elbaite-schorl-dravite tourmalines. American Mineralogist, 93, 658–666.

Babińska, J., Dyrek, K., Pieczka, A., and Sojka, Z. (2008) X and Q band EPR studies of paramagnetic centres in natural and heated tourmaline. European Journal of Mineralogy, 20, 233–240.

Bancroft, G.M. (1973) Mössbauer spectroscopy: an introduction for inorganic chemists and geochemists. 271 p. McGraw-Hill.

Bastin, G.F., and Heijligers, H.J.M. (1986) Quantitative electron probe microanalysis of boron in binary borides p. 118. Netherlands.

Bosi, F., and Lucchesi, S. (2004) Crystal chemistry of the schorl-dravite series. European Journal of Mineralogy, 16, 335–344.

Dauphas, N., Hu, M.Y., Baker, E.M., Hu, J., Tissot, F.L.H., Alp, E.E., Roskosz, M., Zhao, J., Bi, W., Liu, J., and others (2018) SciPhon: a data analysis software for nuclear resonant

inelastic X-ray scattering with applications to Fe, Kr, Sn, Eu and Dy. Journal of Synchrotron Radiation, 25, 1581–1599.

De Grave, E., and Van Alboom, A. (1991) Evaluation of ferrous and ferric Mössbauer fractions. Physics and chemistry of minerals, 18, 337–342.

Dyar, M.D., Schaefer, M.W., Sklute, E.C., and Bishop, J.L. (2008) Mössbauer spectroscopy of phyllosilicates: Effects of fitting models on recoil-free fractions and redox ratios. Clay Minerals, 43, 3–33.

Ertl, A., Hughes, J.M., Pertlik, F., Foit, F.F., Wright, S.E., Brandstätter, F., and Marler, B. (2002) Polyhedron Distortions in Tourmaline. The Canadian Mineralogist, 40, 153–162.

Evans, R.J. (2005) Hyperfine electric field gradient tensors at Fe2+ sites in octahedral layers: Toward understanding oriented single-crystal Mossbauer spectroscopy measurements of micas. American Mineralogist, 90, 1540–1555.

Evans, T.P. (2004) A method for calculating effective bulk composition modification due to crystal fractionation in garnet-bearing schist: implications for isopleth thermobarometry. Journal of Metamorphic Geology, 22, 547–557.

Faye, G.H., Manning, P.G., Gosselin, J.R., and Tremblay, R.J. (1974) The optical absorption spectra of tourmaline; importance of charge-transfer processes. The Canadian Mineralogist, 12, 370–380.

Ferrow, E. (2009) Non-integral hybrid ions in tourmaline: buffering and geo-thermometry. European Journal of Mineralogy, 21, 241–250.

Ferrow, E.A., Annersten, H., and Gunawardane, R.P. (1988) Mössbauer effect study on the mixed valence state of iron in tourmaline. Mineralogical Magazine, 52, 221–228.

Fischer, K. (1935) Neues Verfahren zur maßanalytischen Bestimmung des Wassergehaltes von Flüssigkeiten und festen Körpern. Angewandte Chemie, 48, 394–396.

Fultz, B. (2011) “Mössbauer Spectrometry” in Characterisation of Materials, Elton Kaufmann, Editor. John Wiley, New York.

Gagné, O.C., and Hawthorne, F.C. (2016) Chemographic exploration of the milarite-type structure. The Canadian Mineralogist, 54, 1229–1247.

Gagné, O.C., and Hawthorne, F.C. (2020) Bond-length distributions for ions bonded to oxygen: Results for the transition metals and quantification of the factors underlying bond-length variation in inorganic solids. IUCrJ, 7, 581–629.

Goldstein, J.I., Newbury, D.E., Echlin, P., Joy, D.C., Lyman, C.E., Lifshin, E., Sawyer, L., and Michael, J.R. (2003) Scanning Electron Microscopy and X-ray Microanalysis: Third Edition. Springer US, Boston, MA.

Grodzicki, M., and Lebernegg, S. (2011) Computation and interpretation of Mössbauer parameters of Fe-bearing compounds. Mössbauer spectroscopy and transition metal chemistry. Springer, Berlin.

Gütlich, P., Bill, E., and Trautwein, A.X. (2010) Mössbauer spectroscopy and transition metal chemistry: fundamentals and applications. Springer

Hawthorne, F.C. (1988) Chapter 8. Mossbauer Spectroscopy. In F.C. Hawthorne, Ed., Spectroscopic Methods in Mineralogy and Geology pp. 255–340. De Gruyter.

Heinrich, K.F.J. (1987) Mass absorption coefficients for electron probe microanalysis. Proc. 11th Int. Congr. on X-Ray Optics and Microanalysis, 67–119.

Henke, B.L., Lee, P., Tanaka, T.J., Shimabukuro, R.L., and Fujikawa, B.K. (1982) Low-energy x-ray interaction coefficients: Photoabsorption, scattering, and reflection: E = 100–2000 eV Z = 1–94. Atomic Data and Nuclear Data Tables, 27, 1–144.

Katerinopoulou, A., Grodzicki, M., Tippelt, G., and Amthauer, G. (2013) Mössbauer spectroscopy and molecular orbital calculations on iron bearing omphacite. Mineralogy and Petrology, 107, 281–287.

Lavrent'ev, Yu.G., Korolyuk, V.N., and Usova, L.V. (2004) Second Generation of Correction Methods in Electron Probe X-ray Microanalysis: Approximation Models for Emission Depth Distribution Functions. Journal of Analytical Chemistry, 59, 600–616.

Levy, E.A., Henry, D.J., Roy, A., and Dutrow, B.L. (2018) Determination of ferrous–ferric iron contents in tourmaline using synchrotron-based XANES. Journal of Geosciences (Czech Republic), 63, 167.

Li, M. (2022) Characterisation of Blue Tourmaline from Madagascar for Exploring Its Colour Origin. Advances in Condensed Matter Physics, 2022, 1–7.

Llovet, X., Moy, A., Pinard, P.T., and Fournelle, J.H. (2021) Electron probe microanalysis: A review of recent developments and applications in materials science and engineering. Progress in Materials Science, 116, 100673.

Llovet, X., Pöml, P., Moy, A., and Fournelle, J.H. (2023) Assessing the Accuracy of Mass Attenuation Coefficients for Soft X-ray EPMA. Microscopy and Microanalysis, 29, 540–551.

Mattson, S.M., and Rossman, G.R. (1987) Fe2+-Fe3+ interactions in tourmaline. Physics and Chemistry of Minerals, 14, 163–171.

Merlet, C. (1992) Quantitative Electron Probe Microanalysis: New Accurate Φ (ρz) Description. In A. Boekestein and M.K. Pavićević, Eds., Electron Microbeam Analysis pp. 107–115. Springer, Vienna.

——— (1994) An Accurate Computer Correction Program for Quantitative Electron Probe Microanalysis. Mikrochimica Acta, 114, 363–376.

Meyer, A.S., and Boyd, C.M. (1959) Determination of Water by Titration with Coulometrically Generated Karl Fischer Reagent. Analytical Chemistry, 31, 215–219.

Nie, N.X., Dauphas, N., Alp, E.E., Zeng, H., Sio, C.K., Hu, J.Y., Chen, X., Aarons, S.M., Zhang, Z., and Tian, H.-C. (2021) Iron, magnesium, and titanium isotopic fractionations between garnet, ilmenite, fayalite, biotite, and tourmaline: Results from NRIXS, ab initio, and study of mineral separates from the Moosilauke metapelite. Geochimica et Cosmochimica Acta, 302, 18–45.

Pieczka, A., and Kraczka, J. (2004) Oxidized tourmalines—a combined chemical, XRD and Mossbauer study. European Journal of Mineralogy, 16, 309–321.

Pieczka, A., Kraczka, and Zabinski (1998) Mossbauer spectra of Fe3+-poor schorls: reinterpretation on the basis of the ordered structure model. Journal of Geosciences, 43, 69–74.

Ping, J.Y., and Rancourt, D.G. (1992) Thickness effects with intrinsically broad absorption lines. Hyperfine Interactions, 71, 1433–1436.

Pouchou, J.-L., and Pichoir, F. (1991) Quantitative Analysis of Homogeneous or Stratified Microvolumes Applying the Model “PAP.” In K.F.J. Heinrich and D.E. Newbury, Eds., Electron Probe Quantitation pp. 31–75. Springer US, Boston, MA.

Rancourt, D. (1994) Mossbauer spectroscopy of minerals: I. Inadequacy of Lorentzian-line doublets in fitting spectra arising from quadrupole splitting distribution. Physics and Chemistry of Minerals, 21, 244–249.

Rancourt, D.G., and Ping, J.Y. (1991) Voigt-based methods for arbitrary-shape static hyperfine parameter distributions in Mössbauer spectroscopy. Nuclear Instruments and Methods in Physics Research Section B: Beam Interactions with Materials and Atoms, 58, 85–97.

Rancourt, D.G., McDonald, A.M., Lalonde, A.E., and Ping, J.Y. (1993) Mössbauer absorber thicknesses for accurate site populations in Fe-bearing minerals. American Mineralogist, 78, 1–7.

Redhammer, G. J. (2021) Structure: Scattering Techniques. In O. Diwald and T. Berger, Eds., Metal Oxide Nanoparticles, 2 Volume Set: Formation, Functional Properties, and Interfaces. John Wiley & Sons.

Reed, S.J.B. (2005) Electron microprobe analysis and scanning electron microscopy in geology. Cambridge university press.

Saegusa, N. (1978) Mossbauer Study of Tourmaline. PhD Thesis, Australian National University.

Scholz, E. (2012) Karl Fischer titration: determination of water. Springer

Scorzelli, R.B., Baggio-Saitovitch, E., and Danon, J. (1976) Mössbauer spectra and electron exchange in tourmaline and staurolite. Le Journal de Physique Colloques, 37, C6-801.

Shannon, R.D. (1976) Revised effective ionic radii and systematic studies of interatomic distances in halides and chalcogenides. Foundations of Crystallography, 32, 751–767.

Whipple, E.R. (1974) Quantitative Mössbauer spectra and chemistry of iron. PhD Thesis, Massachusetts Institute of Technology.

Appendices Chapter 2

Appendix 2A. Endmember fraction Box and Violin plots

TRAINING SET FIGURES

Bulk compositional model

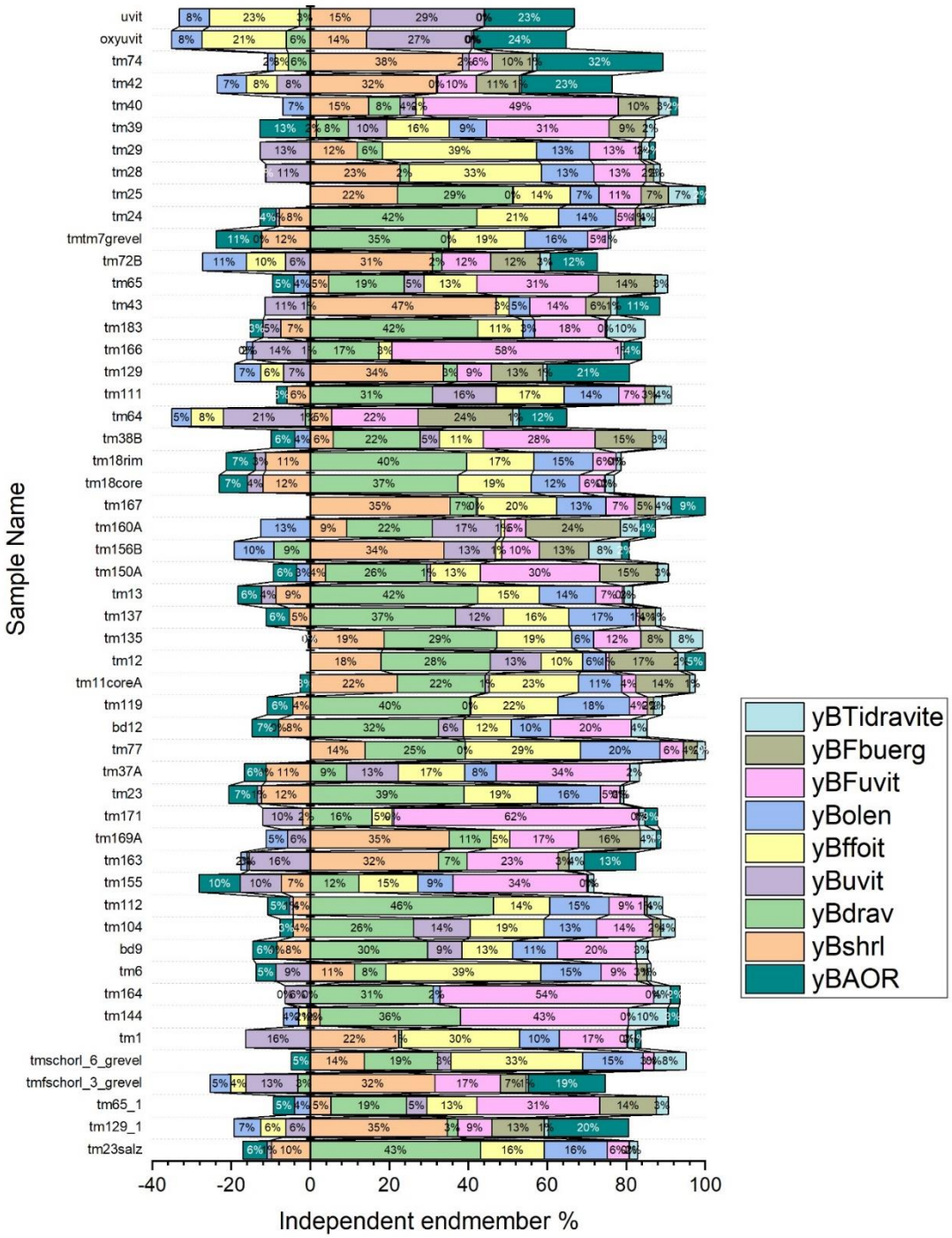

Figure 2A.1. Bulk compositional model training set endmember fractions

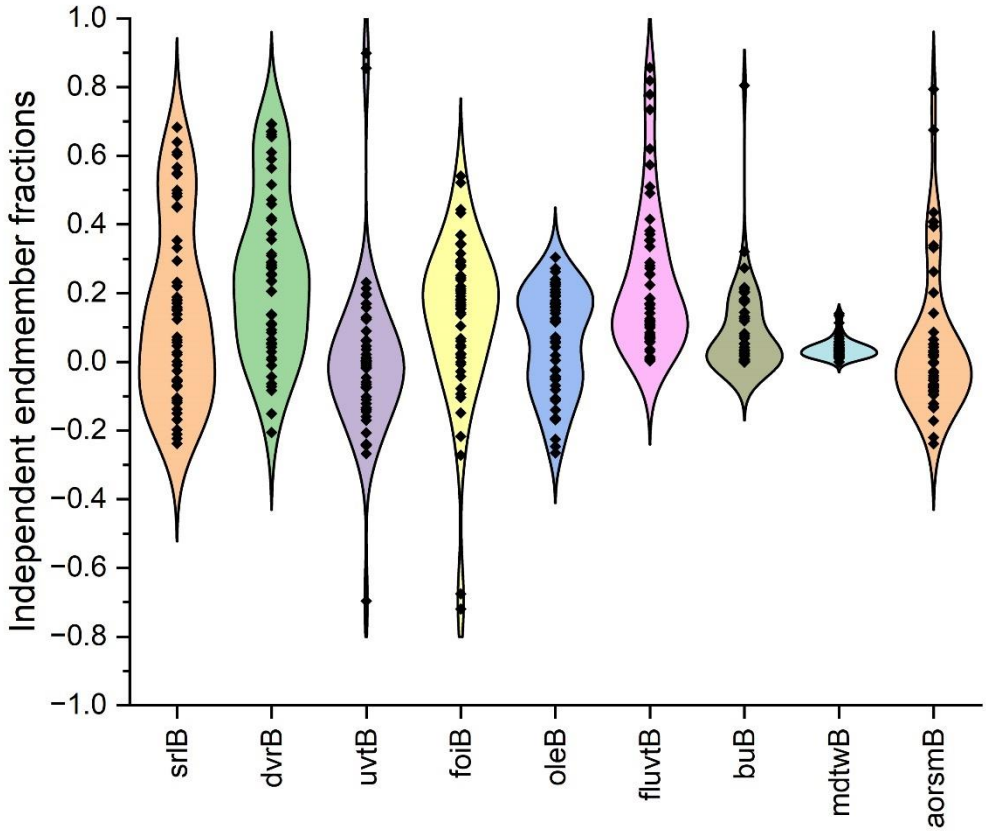

Figure 2A.2. Violin plots showing the distributions of the bulk compositional model training set endmember fractions

Speciation model

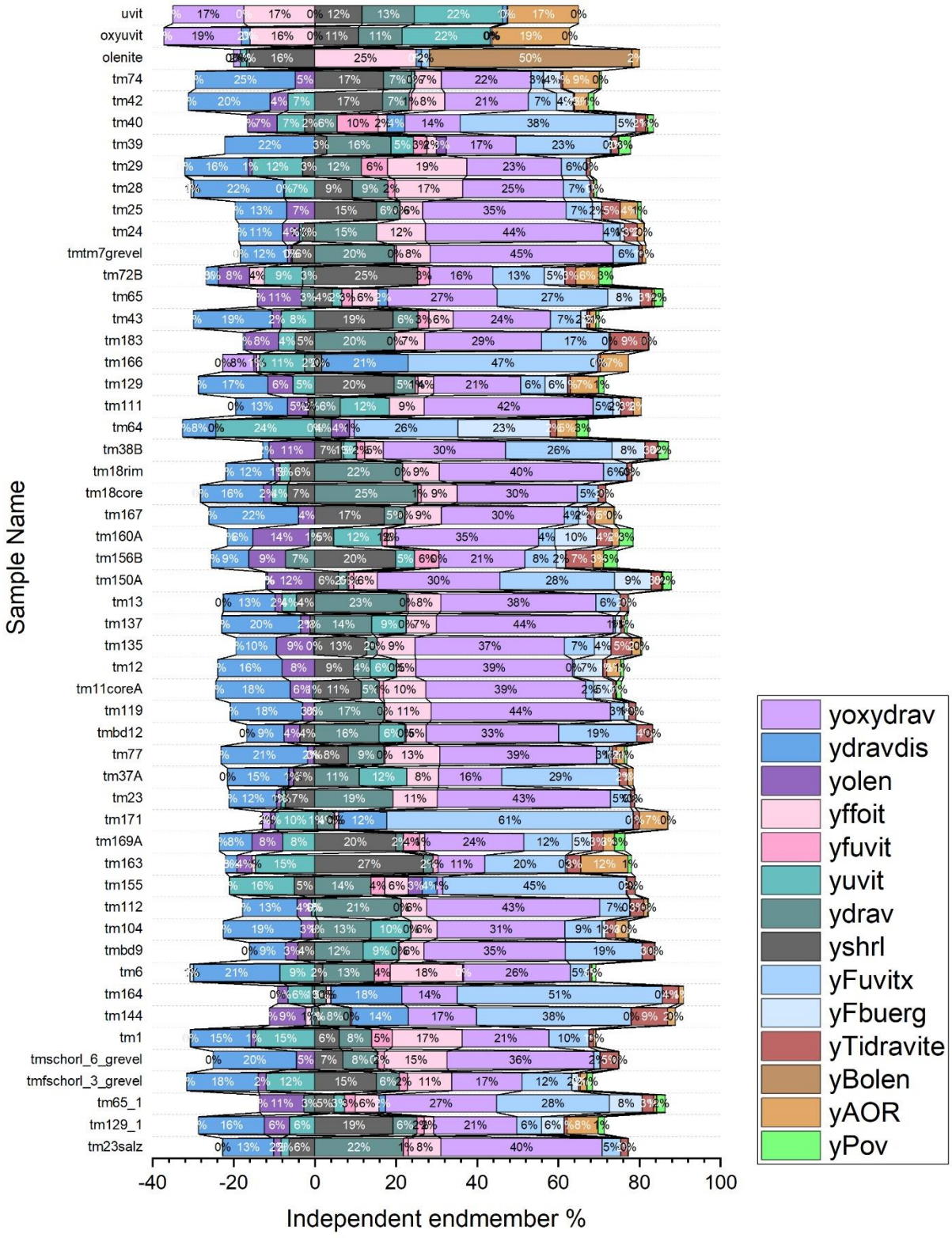

Figure 2A.3 Speciation model training set endmember fractions

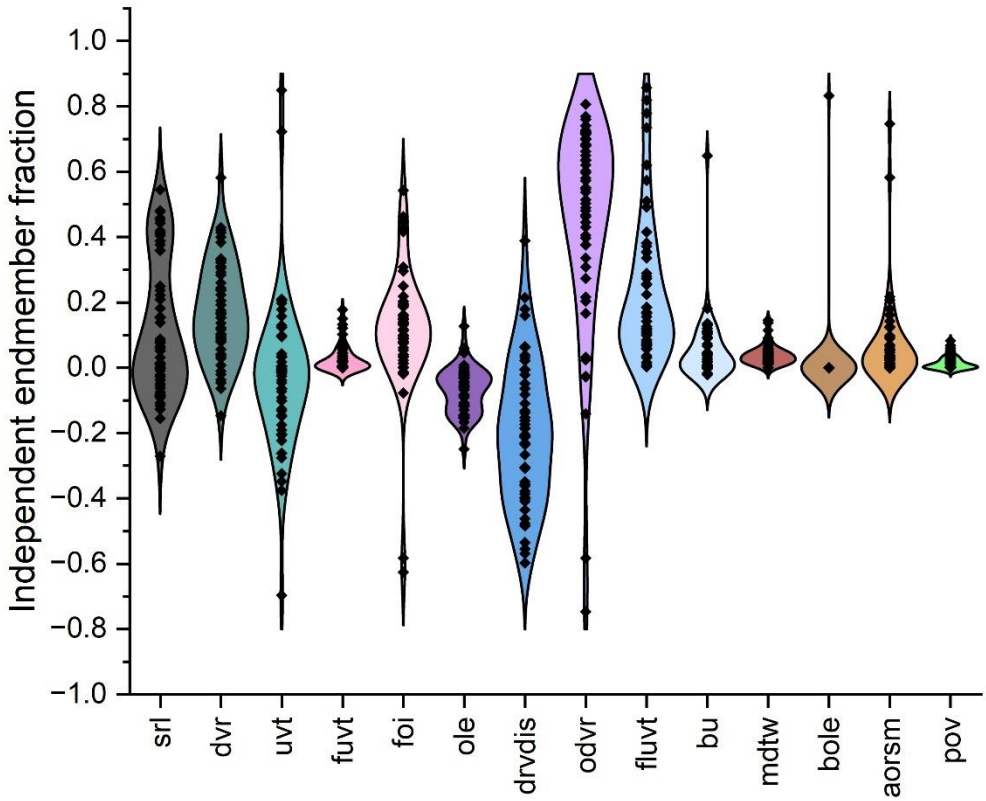

Figure 2A.4. Violin plots showing the distributions of the speciation model training set endmember fractions

TEST SET FIGURES

Bulk compositional model

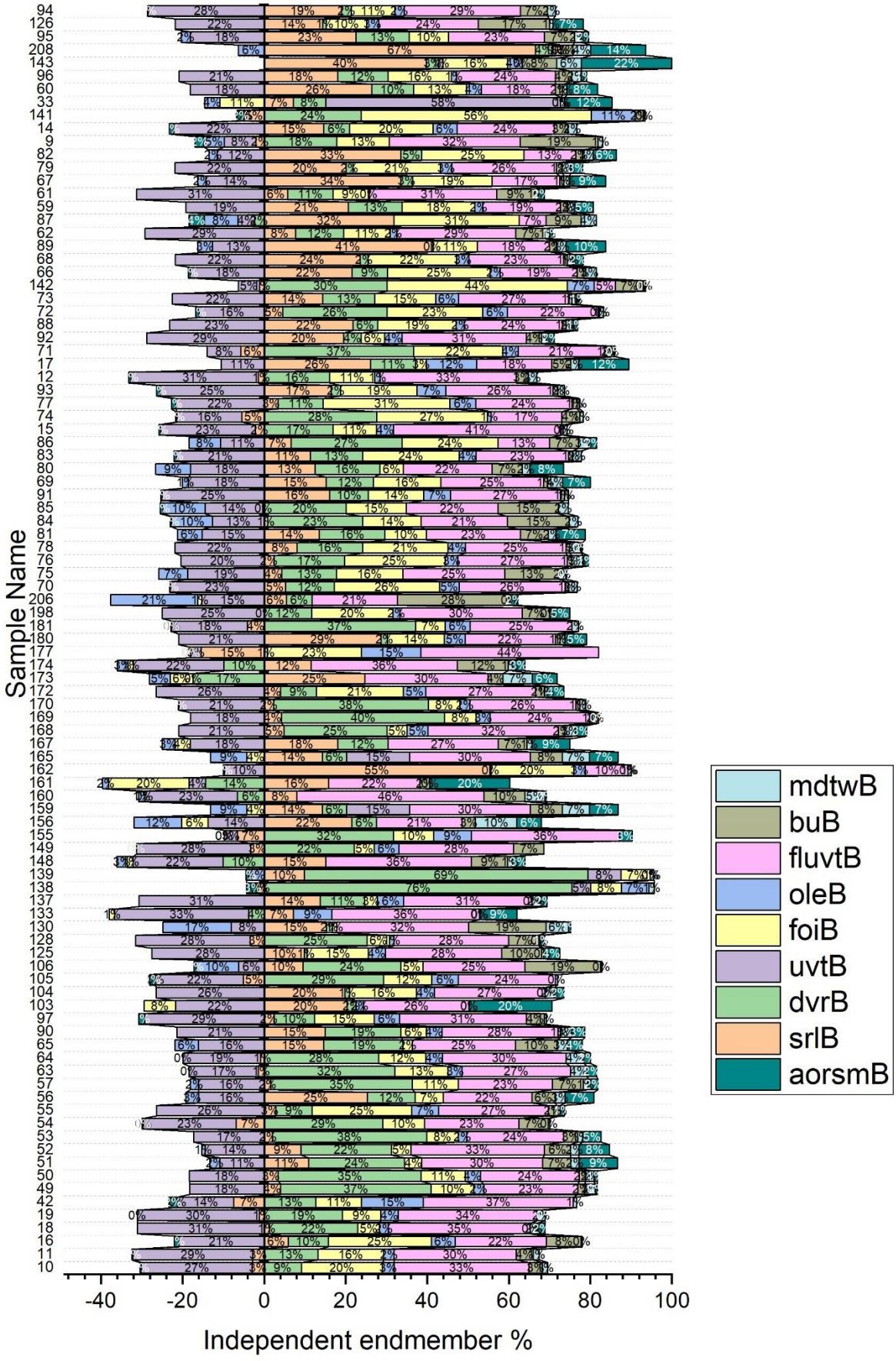
Sample Name
Independent endmember %
-40
-20
0
20
40
60
80
100
mdtwB
buB
fluvtB
oleB
foiB
uvtB
dvrB
srlB
aorsmB

Figure 2A.5. Bulk compositional model test set endmember fractions

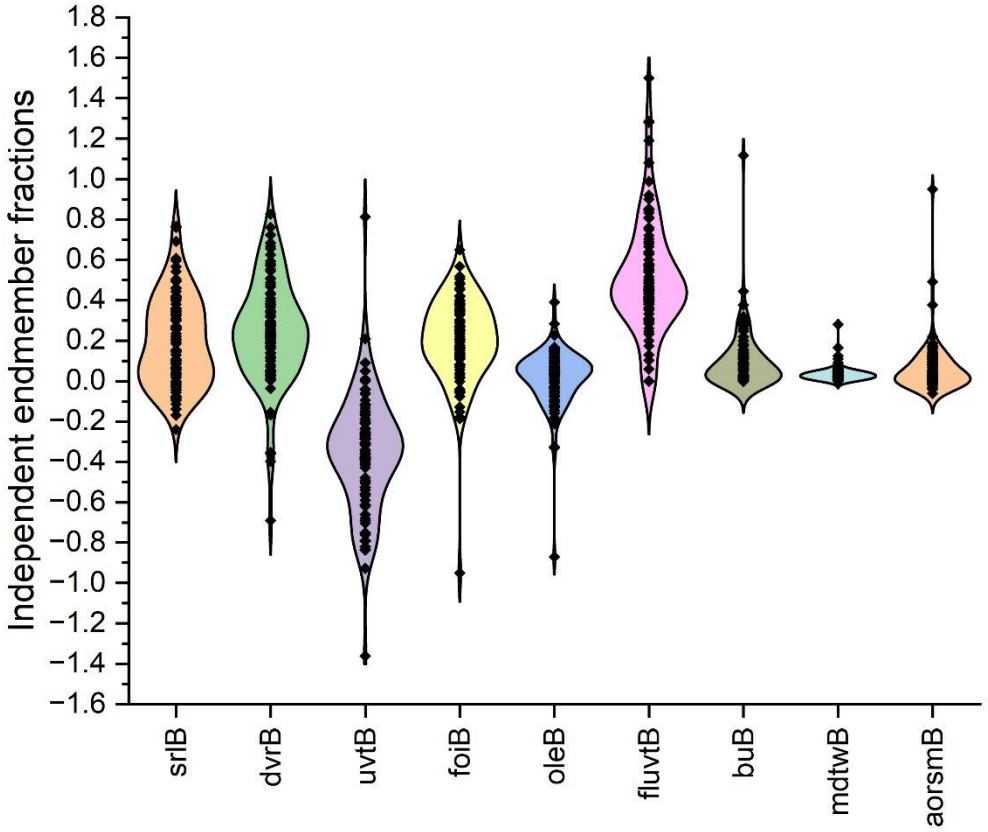

Figure 2A.6. Violin plots showing the distributions of the bulk composition model test set endmember fractions.

Speciation model.

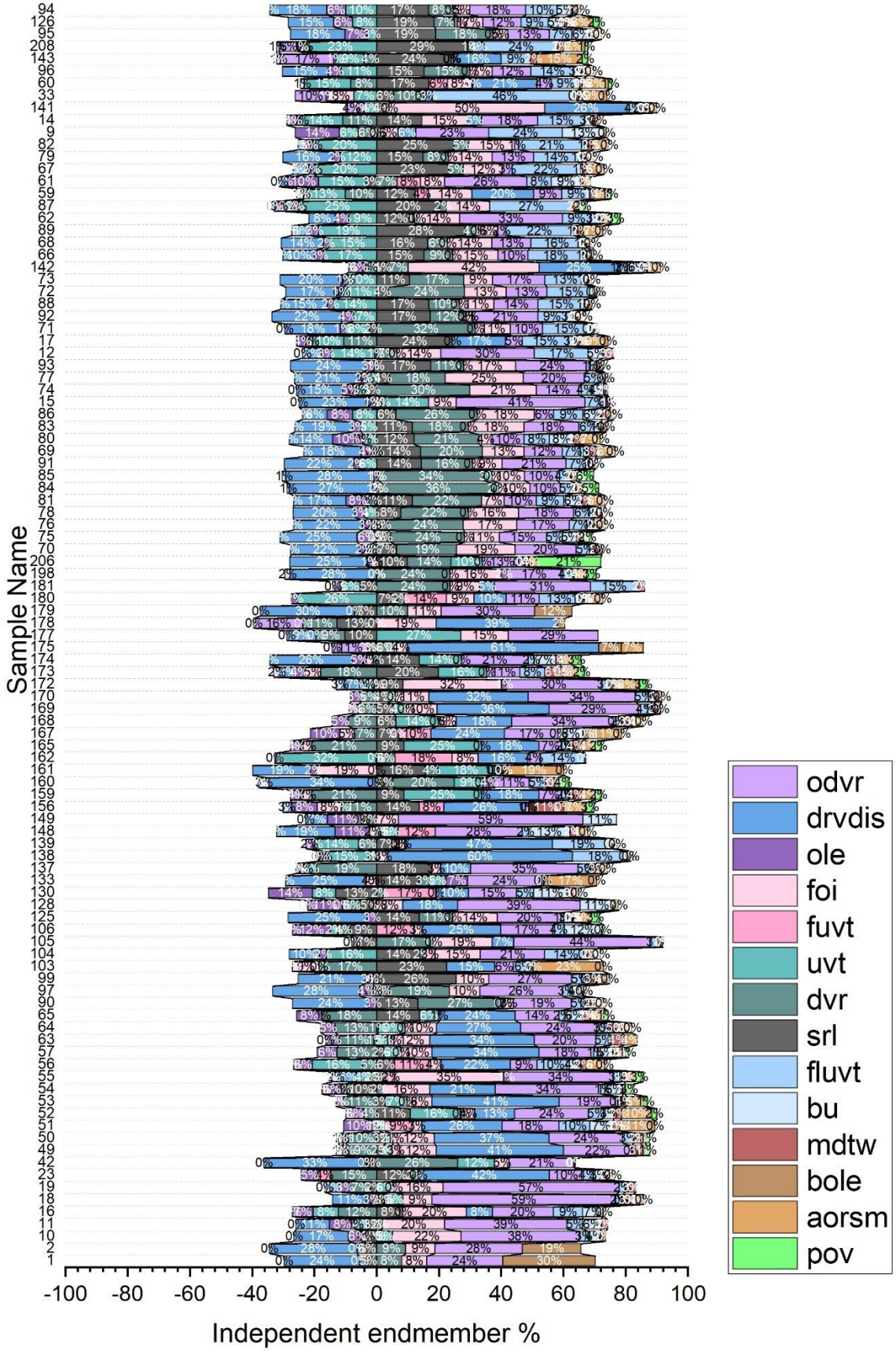
Sample Name
Independent endmember %
-100
-80
-60
-40
-20
0
20
40
60
80
100
odvr
drvdis
ole
foi
fuvt
uvt
dvr
srl
fluvt
bu
mdtw
bole
aorsm
pov

Figure 2A.7. Speciation model test set endmember fractions.

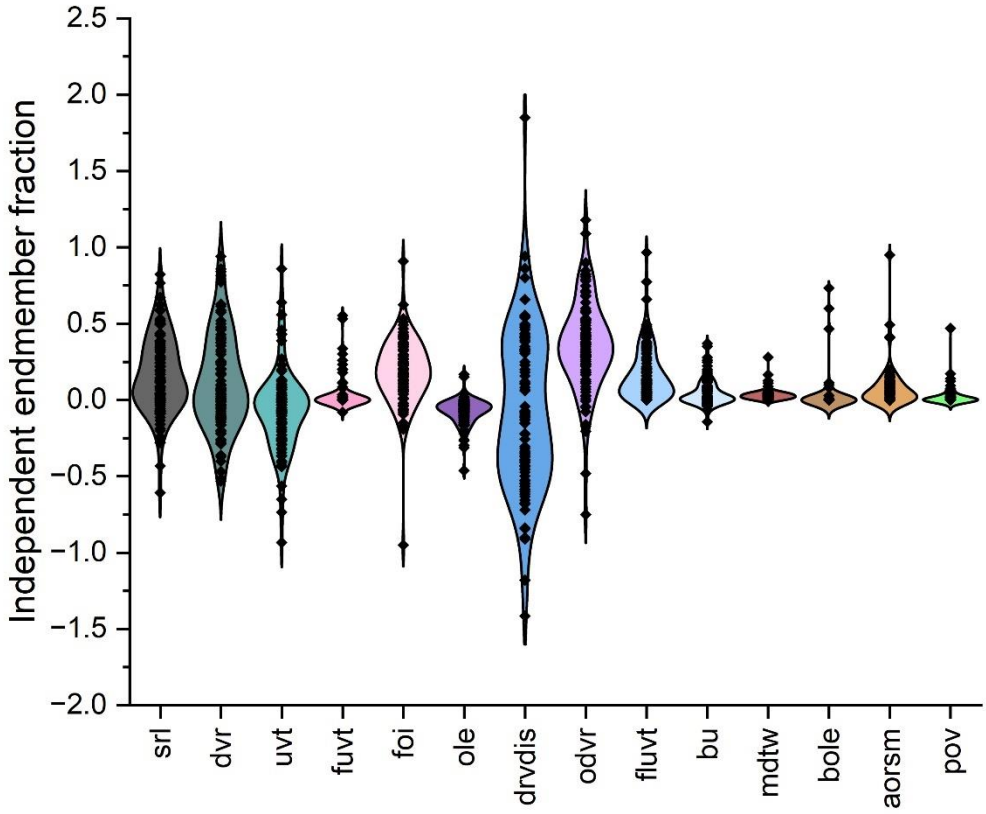

Figure 2A.8. Violin plots showing the distributions of the speciation model test set endmember fractions.

APPENDIX. COMBINED DATASET

Bulk compositional model

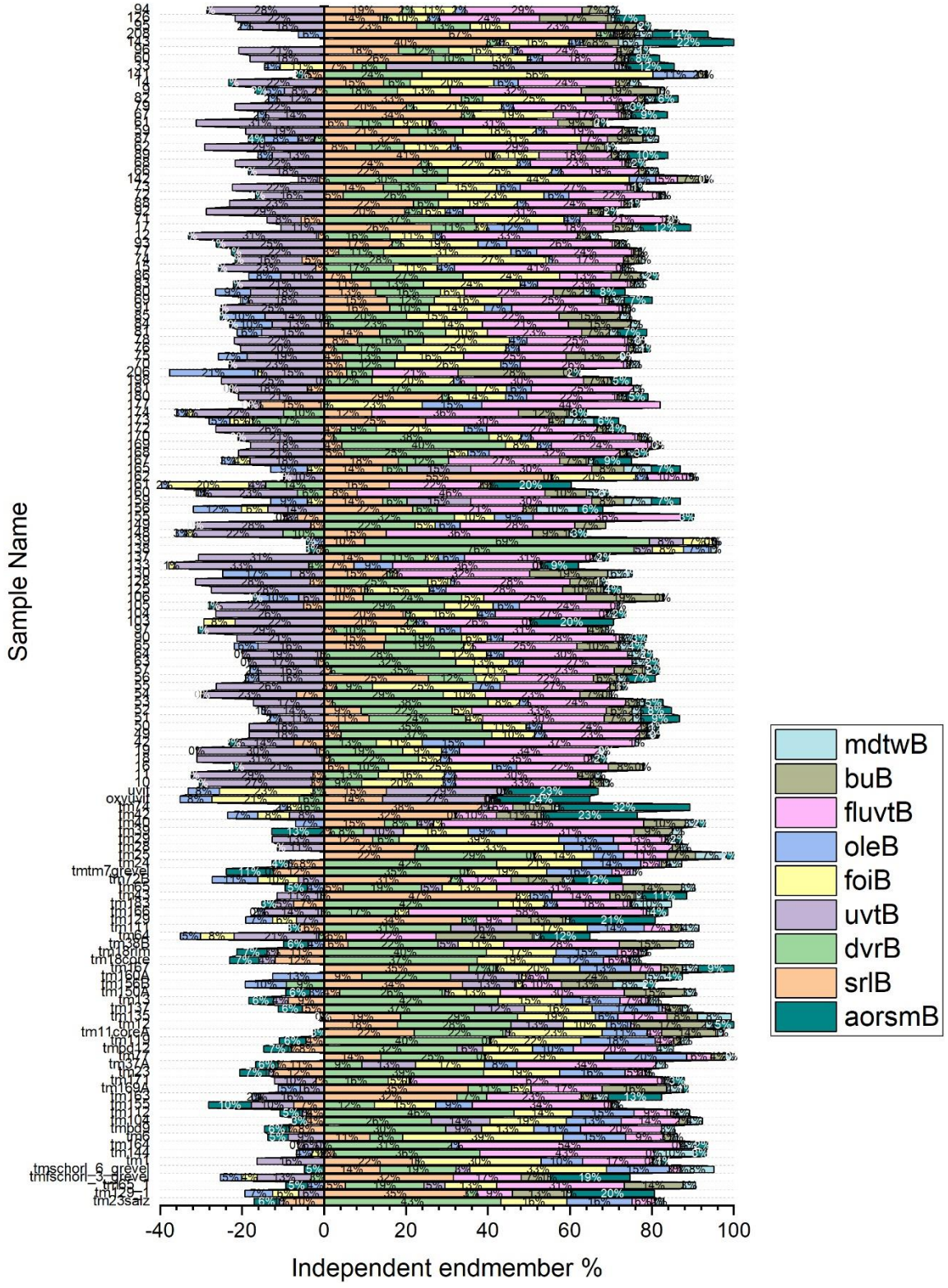
Sample Name
Independent endmember %
-40
-20
0
20
40
60
80
100
mdtwB
buB
fluvtB
oleB
foiB
uvtB
dvrB
srlB
aorsmB

Figure 2A.9. Bulk composition model combined dataset endmember fractions.

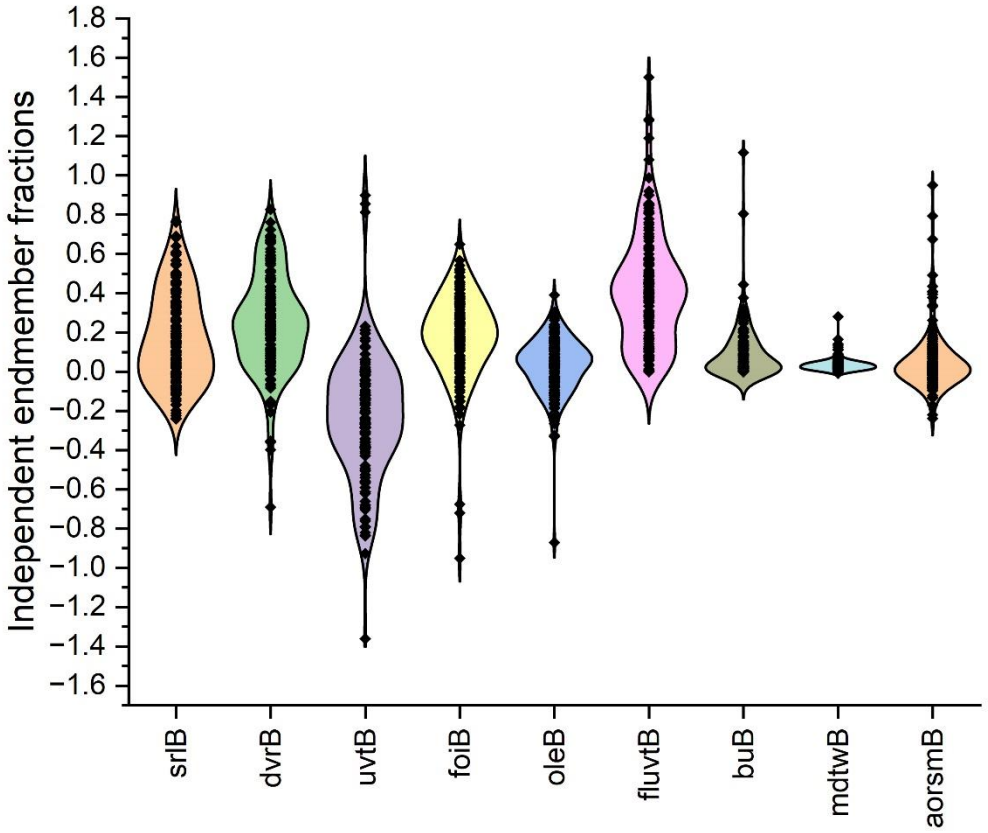

Figure 2A.10. Violin plots showing the distributions of the bulk compositional model combined dataset endmember fractions.

Speciation model

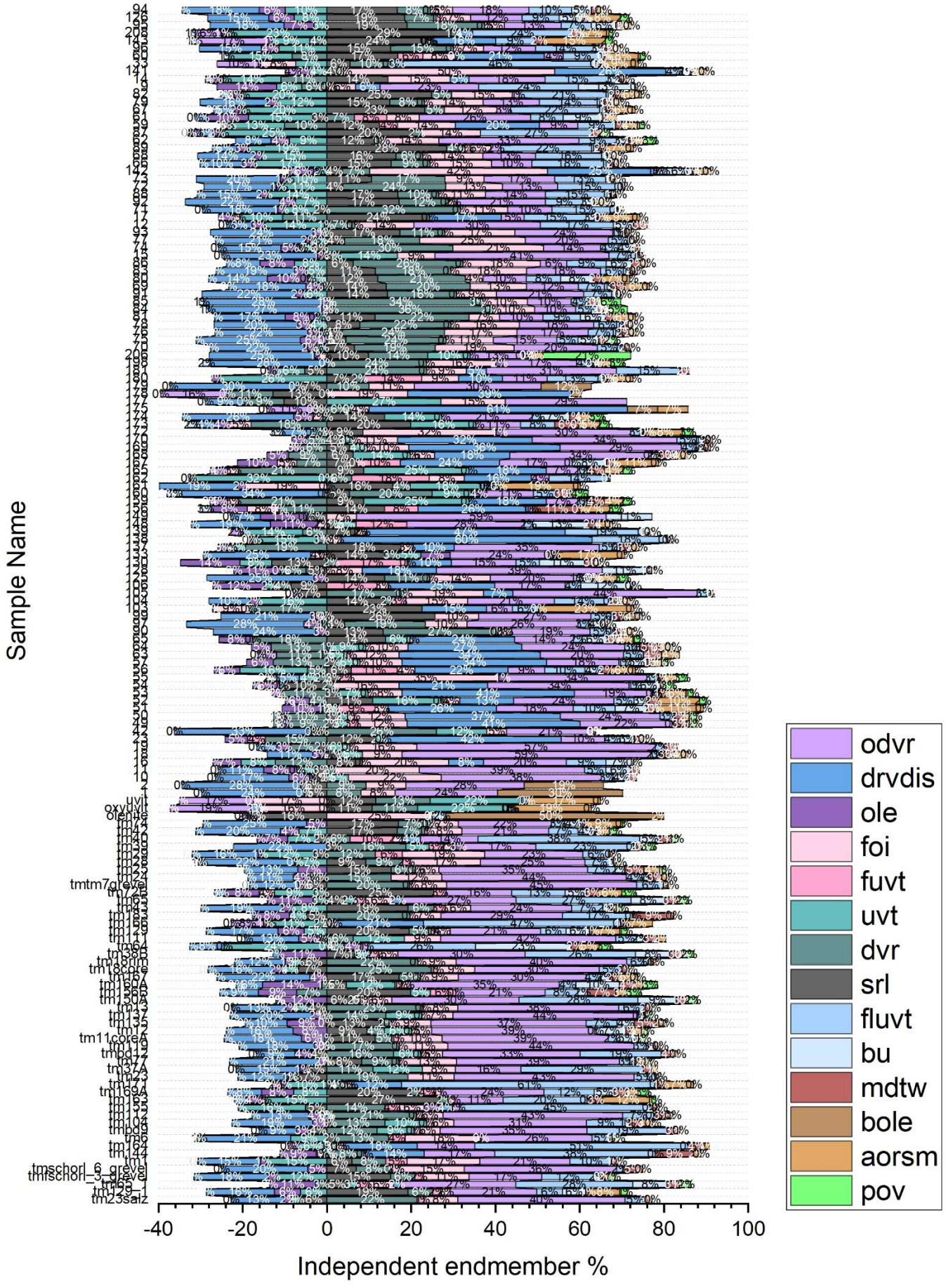
Sample Name
Independent endmember %
-40
-20
0
20
40
60
80
100
odvr
drvdis
ole
foi
fuvt
uvt
dvr
srl
fluvt
bu
mdtw
bole
aorsm
pov

Figure 2A.11. Speciation model combined dataset endmember fractions.

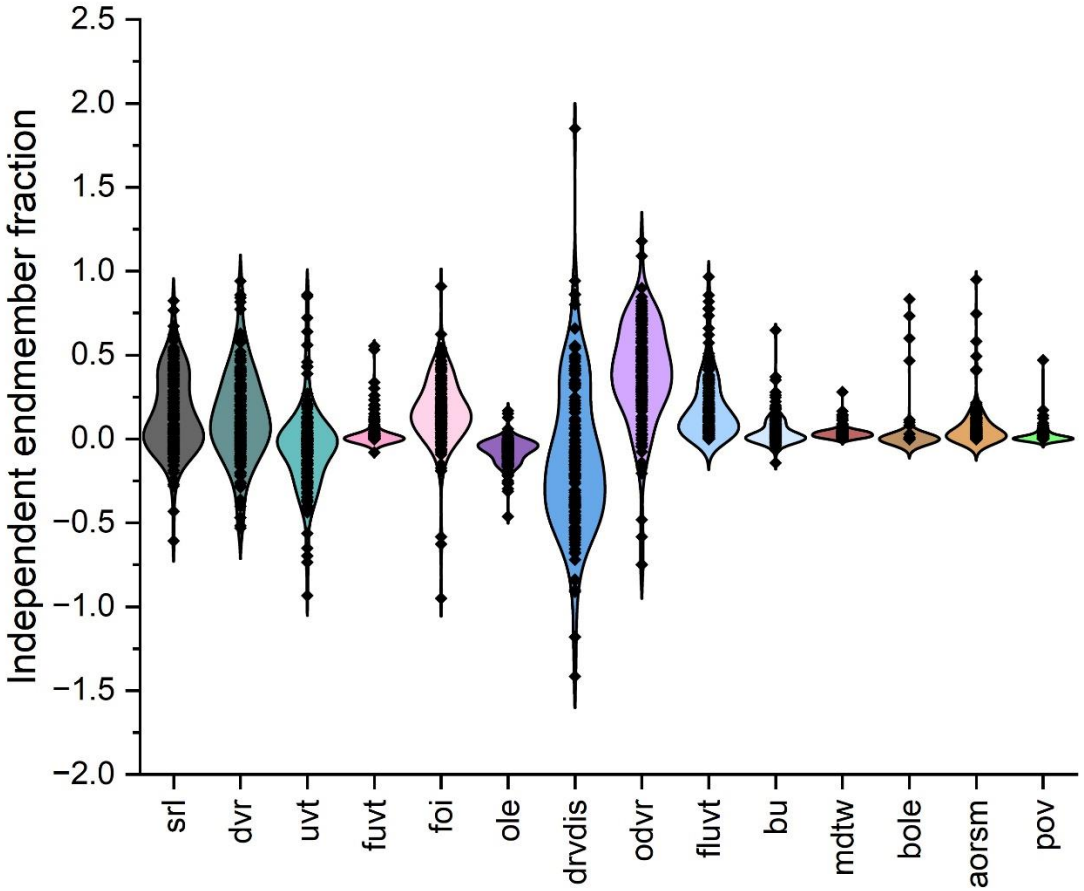

Figure 2A.12. Violin plots showing the distributions of the speciation model combined dataset endmember fractions.

Appendix 2B. Details of regression methods

We examine advanced regression methods, or supervised learners, each defined by distinct complexity-reducing assumptions, numerical techniques, and their balance between bias (underfitting) and variance (overfitting).

Ordinary Least Squares (OLS) OLS models systems with a global linear function $Y = X^T \beta + \varepsilon$, capturing relationships among predictors and responses (Hastie et al. 2017). If the predictors (X) have constraints, such as summing to a constant, all values cannot be zero, rendering the intercept—representing Y when all predictors are zero—physically meaningless. OLS has low variance, potentially high bias, and generalizes well but risks underfitting (Hastie et al. 2017). OLS find coefficients $\hat{\beta}^{\text{ls}}$ by minimizing the squared difference, $\text{RSS}(\hat{\beta}^{\text{ls}}) = (\mathbf{y} - \mathbf{X}\hat{\beta}^{\text{ls}})^T(\mathbf{y} - \mathbf{X}\hat{\beta}^{\text{ls}})$ (Hastie et al. 2017). Differentiating $\text{RSS}(\hat{\beta}^{\text{ls}})$ with respect to $\hat{\beta}^{\text{ls}}$ and setting it to zero yields the normal equation $\hat{\beta}^{\text{ls}} = (X^T X)^{-1} X^T y$ (Hastie et al. 2017). Solving the matrix inversion in the normal equation employs different techniques based on X's characteristics: LU decomposition for square full-rank matrices, QR for rectangular or near-singular matrices, and SVD decomposition $\hat{\beta}^{\text{ls}} = \mathbf{V}\mathbf{\Sigma}^{-1}\mathbf{U}^{\mathbf{T}}\text{y}$ with $[U, \Sigma, V] = \text{svd}([X])$ for improved numerical stability in ill-conditioned or near-singular cases (Trefethen and Bau 2022) . The fitted values are $\hat{\mathbf{y}} = \mathbf{X}\hat{\beta}^{\text{ls}} = \mathbf{H}\,\mathbf{y}$, where the hat matrix $\mathbf{H} = \mathbf{X}(\mathbf{X}^T\mathbf{X})^{-1}\mathbf{X}^T$ computes the orthogonal projection of y onto the column space of X (Hastie et al. 2017). The diagonal elements of H, known as leverage scores, quantify each observation's influence on the fitted values.

OLS requires linearity in parameters, a full-rank, non-singular, positive-definite design matrix for a unique solution, and uncorrelated, homoscedastic, Gaussian residuals for valid inference (Freedman 2009). Proper model specification, including avoiding omitted variables and measurement errors in predictors, ensures unbiased estimates (Freedman 2009). Nonorthogonal predictors due to the narrow subspace collection lead to multicollinearity, which introduces correlation among regression coefficients, making it difficult to attribute changes in the thermodynamic property to specific endmembers (Hastie et al. 2017). Violations such as multicollinearity, heteroscedasticity, or correlated residuals destabilize estimates and compromise inference. The solution provided is valid only within the complexity-reducing constraints assumed (Hastie et al. 2017).

The variance-covariance matrix of regression parameters is $\text{Var}(\widehat{\hat{\beta}^{\text{ls}}}) = (\mathbf{X}^T\mathbf{X})^{-1}\sigma^2$, assuming constant σ^2, estimated as $\hat{\sigma}^2 = \frac{1}{N-p-1}\sum_{i=1}^{N}(y_i - \hat{y}_i)^2$ (Wurm 2021), where n and p are the number of observations and parameters. OLS assumptions enable inference, such as hypothesis testing and

confidence intervals. The F-statistic tests the significance of coefficient groups by measuring the change in residual sum of squares per added parameter, normalised by variance (Hastie et al. 2017).

Weighted Least Squares (WLS) WLS extends LS to handle heteroscedasticity by weighting y inversely to its variances, assuming no deviations in X ($W_X = 0$) and no correlations between X and y ($W_{Xy} = 0$)(NCSS 2023). The solution is: $\hat{\beta}^{\text{wls}} = (X^T W_y^{-1} X)^{-1} X^T W_y^{-1} y$ where W_y is the diagonal variance matrix of y (NCSS 2023). WLS minimises the weighted sum of squared residuals.

Total Least Squares (TLS) TLS is a globally fitting method for linear equations that accounts for measurement uncertainties in all variables (Markovsky and Van Huffel 2007). TLS minimises the perpendicular distances between data points and the regression hyperplane, assuming equal variances in X and y. The solution is derived via singular value decomposition (SVD) on the combined matrix [X, y], i.e., $[U, \Sigma, V] = \text{svd}([X, y])$:

$$[\boldsymbol{X} \quad \boldsymbol{y}] = [\boldsymbol{U}_p \quad \boldsymbol{u}_q] \begin{bmatrix} \boldsymbol{\Sigma}_p & \\ & \sigma_q \end{bmatrix} \begin{bmatrix} \boldsymbol{V}_{pp} & \boldsymbol{v}_{pq} \\ \boldsymbol{v}_{qp} & v_{qq} \end{bmatrix}^{\top}$$

(Gavin 2025). Here Up and Vpp are N×p and p×p orthogonal matrices, where N is the number of observations and p the number of regression coefficients. The columns of U span the column space of [X,y], representing directions of maximum variance in observations, while the columns of V span the row space representing variance in variables. Σ is a (p+1)-dimensional diagonal matrix, with singular values $\sigma 1 \geq \sigma 2 \geq \sigma q \geq 0$ of the matrix $[\boldsymbol{X} \quad \boldsymbol{y}]$ (Gavin 2025). All other values are scalars associated with the augmentation by y. The closest rank-n approximation to $[\boldsymbol{X} \quad \boldsymbol{y}]$, defined as $[\boldsymbol{X} \quad \boldsymbol{y}] + [\tilde{\boldsymbol{X}} \quad \tilde{\boldsymbol{y}}]$, minimises the Frobenius norm of the residuals and modifies $[\boldsymbol{X} \quad \boldsymbol{y}]$ such that the smallest singular value becomes 0, while preserving the original singular vectors from the SVD:

$$\left[\boldsymbol{X} + \tilde{\boldsymbol{X}}, \boldsymbol{y} + \tilde{\boldsymbol{y}}\right] = [\boldsymbol{U}_p \quad \boldsymbol{u}_q] \begin{bmatrix} \boldsymbol{\Sigma}_p & \\ & 0 \end{bmatrix} \begin{bmatrix} \boldsymbol{V}_{pp} & \boldsymbol{v}_{pq} \\ \boldsymbol{v}_{qp} & v_{qq} \end{bmatrix}^{\top}.$$

(Gavin 2025). By rearranging and simplifying this rank-n approximation, the TLS solution is derived by utilising the smallest principal components from the V matrix as:

$$\hat{\beta}^{\text{tls}} = -v_{\text{pq}} v_{qq}^{-1}$$

where v_{pq} represents the first n elements, and v_{qq} is the (n+1)-th element of the last column of the right singular vector matrix V (Gavin 2025). The covariance matrices of the regression coefficients are

calculated by mse* $(\mathbf{X}^{\mathrm{T}}\mathbf{X}- \sigma^2_{n+1}\, \boldsymbol{I})^{-1}$ with σ_{n+1}, the smallest singular value of augmented matrix [X, $\boldsymbol{y}$] (Wurm 2021).

The predicted values $\hat{y}_{\mathrm{TLS}}$ for the training dataset are calculated as $\hat{y}_{\mathrm{TLS}} = [\boldsymbol{X} + \widetilde{\boldsymbol{X}}\,]\,\hat{\beta}^{\mathrm{tls}}$, requiring both $\hat{\beta}^{\mathrm{tls}}$ and the perturbations $\widetilde{\boldsymbol{X}}$ in the endmember fractions (Gavin 2025). Since the TLS solution is based on a perturbed basis, $\hat{\beta}^{\mathrm{tls}}$ cannot be directly compared to OLS coefficients, complicating its application to parameterized functional forms where predictions are needed at fixed new X. Formally, TLS cannot predict ŷ for new X (Gavin 2025). However, when perturbations $\widetilde{\boldsymbol{X}}$ are minimal, TLS regression coefficients can be applied within an OLS-based predictive model. This only works when the units of the predictors are higher than the units of the predictors as one problem with TLS estimates is that they depend on the units in which variables are measured. This does make the method success depend on the choose of units. The method does give more flexibility to fitting however how flexible should it be?

Scaled Total Least Squares (scaled-TLS) extends TLS by allowing different variances for X and y while assuming homoscedasticity within each (Wurm 2021).

Generalized Total Least Squares (GTLS) GTLS assumes a fixed covariance matrix for all regression coefficients or observations, acting as a covariance-weighted TLS, see Wurms (2021) and references therein. Row (P_C) and column (P_R) correlation matrices can be used for weighting . Using Cholesky factorization, GTLS is reformulated into an ordinary TLS problem for solution:

$$C_C^{\mathrm{T}} C_C = P_C \qquad C_R^{\mathrm{T}} C_R = P_R$$

, the GTLS weight matrices, $W_C = C_C^{-1}$ (column) and $W_R = C_R^{-1}$ (row), convert the GTLS problem into a weighted TLS problem solvable via SVD (Rhode et al. 2014; Wurm 2021).

$$\hat{\beta}^{\mathrm{tls}\prime} = \mathrm{tls}\left(\boldsymbol{W_R}^{\mathrm{T}}[\boldsymbol{X}, \boldsymbol{y}]\boldsymbol{W_C}\right)$$

The final regression coefficients are derived by rescaling the weighted TLS solution (Wurm 2021):

$$\hat{\beta}^{\mathrm{gtls}} = \mathrm{gtls}([X, y], P_C, P_R) = \frac{W_{C11}\hat{\beta}^{\mathrm{tls}\prime} - W_{C12}}{W_{C22}}.$$

Where the W_{C11}, W_{C12} and W_{C22} are obtained from $\boldsymbol{W}_C = \begin{pmatrix} n & 1 \\ \boldsymbol{W}_{C11} & \boldsymbol{W}_{C12} \\ \mathbf{0} & \boldsymbol{W}_{C22} \end{pmatrix} \begin{matrix} n \\ 1 \end{matrix}$

the covariance matrix of the regression coefficient is calculated using

$\boldsymbol{\Sigma}_{\boldsymbol{x},\mathrm{gtls}}([X,\boldsymbol{y}]) = \frac{\boldsymbol{W}_{C11} \cdot \boldsymbol{\Sigma}_{x,\mathrm{tls}}(W_R^{\mathrm{T}}[X,y]W_C) \cdot \boldsymbol{W}_{C11}^{\mathrm{T}}}{\boldsymbol{W}_{C22}^2}$ (Rhode et al. 2014; Wurm 2021).

Iteratively Reweighted Least Squares (Robust regression) We performed robust regressions using MATLAB 2022a's robustfit to assess outlier influence, using weight functions based on residuals to reduce their impact (Huber 1981; "Matlab" 2022):

Table 2B.1. Weight functions used by the robustfit algorithm in Matlab2022a.

Weight Function	Equation	Tuning Constant	Description
andrews	$w = (\lvert r \rvert < \pi) \cdot \frac{\sin(r)}{r}$	1.339	Zero weight for residuals outside $[-\pi, \pi]$; weights decrease smoothly as the residual grows, using a sine function
bisquare	$w = (\lvert r \rvert < 1) \cdot (1 - r^2)^2$	4.685	Reduces weight with increasing r^2 (a.k.a. biweights). Decreases sharply to zero beyond a cutoff.
cauchy	$w = \frac{1}{1 + r^2}$	2.385	Slowly reduces weight inversely proportional to the square; always assigns nonzero influence to outliers
fair	$w = \frac{1}{1 + \lvert r \rvert}$	1.400	Reduces weight inversely to the absolute residual
huber	$w = \frac{1}{\max(1, \lvert r \rvert)}$	1.345	Full weight for small residuals; linear decrease for large residuals
logistic	$w = \frac{\tanh(r)}{r}$	1.205	Smooth logistic reduction in weight as residual increases
talwar	$w = 1 \times (\lvert r \rvert < 1)$	2.795	Full weight below a threshold, zero beyond
welsch	$w = \exp(-r^2)$	2.985	Exponential weight reduction; diminishes outlier influence without exclusion

The tuning constant defines the cutoff for reducing weights on outliers, balancing robustness against sensitivity and ensuring inliers retain influence. Regression coefficients are initialized using OLS to calculate starting residuals ("Matlab" 2022). In iterative WLS, weights are updated based on residual size—smaller residuals receive higher weights, while larger ones contribute less (Huber 1981). Coefficients and residuals are recalculated at each step until convergence, indicated by minimal changes in coefficients.

York regression The York et al. (2004) regression method, widely used in geochronology (e.g., Isoplot (Ludwig 1991; Vermeesch 2018)), is a 2D iterative reweighted least squares (IRLS) method for errors-in-variables regression, providing an alternative to total least squares (TLS). Unlike TLS, York minimises a weighted vertical residual loss function (York 1966):

$$\chi^2 = \sum_{i=1}^{n} W_i(Y_i - bX_i - a)^2$$

where Wi is the weight (York et al. 2004):

$$W_i = \frac{\omega(X_i)\omega(Y_i)}{\omega(X_i) + b^2\omega(Y_i) - 2br_i\sqrt{\omega(X_i)\omega(Y_i)}}.$$

Here, $\omega(X_i)$ and $\omega(Y_i)$ are inverses of variances, and r_i is the correlation coefficient. Starting with an OLS estimate of the slope b, the method iteratively updates weights and recalculates the regression coefficients until convergence. Weighted means of X and Y ($\bar{X} = \frac{\sum_{i=1}^{n} W_i X_i}{\sum_{i=1}^{n} W_i}$ and $\bar{Y} = \frac{\sum_{i=1}^{n} W_i Y_i}{\sum_{i=1}^{n} W_i}$) are computed (York et al. 2004). These weighted means are subtracted from the actual values in order to normalize them $V_i = Y_i - \bar{Y}$, and $U_i = X_i - \bar{X}$. The W_i, U_i, V_i are used to calculate $\beta_i = W_i\left[\frac{U_i}{\omega(Y_i)} + \frac{bV_i}{\omega(X_i)} - (bU_i + V_i)\frac{r_i}{\alpha_i}\right]$ and these parameters combined are used to calculate the weighted sums necessary to obtain an improved estimate of regression coefficient b (York et al. 2004):

$$b = \frac{\sum W_i\beta_i V_i}{\sum W_i\beta_i U_i}, a = \bar{Y} - b\bar{X},$$

Then for each X_i and Y_i we can calculate the least square adjusted values x_i and y_i with $x_i = \bar{X} + \beta_i$ and $y_i = \bar{Y} + b\beta_i$. The adjusted xi are used together with Wi to calculate the weighted $\bar{x} = \frac{\sum W_i x_i}{\sum W_i}$ and ui = xi -

$\bar{x}$, which are the parameters needed to calculate the uncertainties of the regression coefficients (York et al. 2004):

$$\sigma_b^2 = \frac{1}{\sum W_i u_i^2}$$

$$\sigma_a^2 = \frac{1}{\sum W_i} + \overrightarrow{x^2}\sigma_b^2,$$

One assumption of York method is that the uncertainties in x and y are normally distributed (York et al. 2004). Goodness-of-fit is assessed using reduced χ^2 (a.k.a. Mean Square of the Weighted Deviates; MSWD) (Wendt and Carl 1991):

$$\chi_\nu^2 = \frac{\chi^2}{n-2} = \frac{\sum W_i (Y_i - bX_i - a)^2}{n-2}.$$

If weighted residuals follow a χ^2 distribution, χ^2 equals the degrees of freedom (ν=n−p) on average, so $\chi_\nu^2 \approx 1$ for an ideal fit (Wendt and Carl 1991); $\chi_\nu^2 > 1$ indicates underestimated uncertainties or poor fit, while $\chi_\nu^2 < 1$ suggests overestimated uncertainties or overfitting. The confidence interval $\chi_\nu^2 > 1 + 2\sqrt{2/f}, P < 0.05$. Wendt and Carl (1991), accounts for statistical variability in χ_ν^2, permitting slightly higher thresholds for small df with values beyond this indicating a poor fit or underestimated uncertainty. The York method retains compatibility with conventional WLS metrics, simplifying posterior regression diagnostics.

Regression Diagnostics WLS to use for York regression

PRESS The sum of squares of predictions (PRESS) is computed via leave-one-out cross-validation for York regression fits on both training and test datasets (Quenouille 1956). For a dataset with n observations, each observation is excluded one by one, and a regression equation is built using the remaining n−1 observations to predict the omitted response. The PRESS residual is the difference between the actual and predicted values, calculated as (NCSS 2023):

$$\text{PRESS} = \sum_{i=1}^{n} w_j \left(y_i - \hat{y}_{i(i)}\right)^2.$$

Smaller PRESS indicates better generalisation and model robustness.

Residual Analysis Residual analysis identified leverage and poorly represented samples using these metrics, See NCSS (2023) for details:

$$\mathbf{H} = \mathbf{X}_{\text{col}}(\mathbf{X}'_{\text{col}}\mathbf{W}\mathbf{X}_{\text{col}})^{-1}\mathbf{X}'_{\text{col}}\mathbf{W}$$

$$\text{DFFITS}_j = \frac{\hat{y}_j - \hat{y}_j(j)}{s(j)\sqrt{h_{jj}}}$$

$$Cook\ D_j = \frac{\sum_{i=1}^{N} w_j\left[\hat{y}_j - \hat{y}_j(j)\right]^2}{ps^2}$$

$$\text{CovRatio}_j = \frac{\det[cov(\beta(j))]}{\det\left[cov(\beta)\ \right]}$$

$$D_{FBETAS_{kj}} = \frac{\beta_k - \beta_k(j)}{s(j)\sqrt{(\mathbf{X}'\mathbf{W}\mathbf{X})^{-1}}}$$

Here, (j) indicates the York fit without observation j. H measures the weighted leverage of each sample on the regression model, DFFITS quantifies the change in an observation's predicted value when it is omitted, Cook's D assesses the impact of omitting a sample on all predicted values, CovRatio evaluates changes in the covariance matrix of regression coefficients when a sample is omitted, and DFBETAS indicates the influence of a sample on individual regression coefficients k when excluded j (NCSS 2023). These statistics were normalised (subtracting the median and dividing by the MAD) to identify outliers, visualized via a heatmap highlighting influential samples, revealing composition-dependent biases in the training and test datasets in the selfwritten Matlab scripts.

REFERENCES

Freedman, D.A. (2009) Statistical models: theory and practice, 2nd ed., 448 p. Cambridge University Press.

Gavin, H.P. (2025) Total Least Squares, 11 p. Lecture Notes CEE 629 System Identification, Duke University.

Hastie, T., Tibshirani, R., and Friedman, J. (2017) The elements of statistical learning: data mining, inference, and prediction, 715 p. Springer.

Huber, P.J. (1981) Robust Statistics., 320 p. John Wiley & Sons, Inc, New York.

Ludwig, K.R. (1991) ISOPLOT; a plotting and regression program for radiogenic-isotope data; version 2.53. US Geological Survey.

Markovsky, I., and Van Huffel, S. (2007) Overview of total least-squares methods. Signal processing, 87, 2283–2302.

Matlab (2022). The MathWorks Inc., Natick, Massachusetts.

NCSS (2023) Multiple Regression, 72 p. NCSS Helpfile, chapter 305.

Quenouille, M.H. (1956) Notes on bias in estimation. Biometrika, 43, 353–360.

Rhode, S., Usevich, K., Markovsky, I., and Gauterin, F. (2014) A recursive restricted total least-squares algorithm. IEEE Transactions on Signal Processing, 62, 5652–5662.

Trefethen, L.N., and Bau, D. (2022) Numerical Linear Algebra, Twenty-fifth Anniversary Edition. Society for Industrial and Applied Mathematics, Philadelphia, PA.

Vermeesch, P. (2018) IsoplotR: A free and open toolbox for geochronology. Geoscience Frontiers, 9, 1479–1493.

Wendt, I., and Carl, C. (1991) The statistical distribution of the mean squared weighted deviation. Chemical Geology, 86, 275–285.

Wurm, M. (2021) A universal and fast method to solve linear systems with correlated coefficients using weighted total least squares. Measurement Science and Technology, 33, 015017.

York, D. (1966) Least-squares fitting of a straight line. Canadian Journal of Physics, 44, 1079–1086.

York, D., Evensen, N.M., Martínez, M.L., and De Basabe Delgado, J. (2004) Unified equations for the slope, intercept, and standard errors of the best straight line. American journal of physics, 72, 367–375.

Appendix 2C. OLS Regression Analysis

Table 2C.1 $X(YZ)_9Si_xAl_{(1-x)}(VW)_4$ model without interaction parameters**.**

Table 0. Descriptive Statistics.

Variable	Count	Standard Deviation	Mean	Minimum	Maximum
srlB	52	0.1437	0.2666	-0.2376	0.6829
drvB	52	0.2537	0.2416	-0.2054	0.6935
uvtB	52	0.0028	0.2347	-0.6961	0.8989
foiB	52	0.1251	0.2416	-0.7191	0.5411
oleB	52	0.0566	0.1513	-0.2647	0.3046
fluvtB	52	0.2409	0.2216	0.0026	0.8569
buB	52	0.0882	0.1337	0.0000	0.8047
mdtwB	52	0.0396	0.0302	0.0000	0.1410
aorsmB	52	0.0495	0.2121	-0.2382	0.7940
Molar Volume (J/mol/bar)	52	0.1621	31.84	31.51	32.24

Table 1. Model Fit Statistics.

Sample Size	R^2	Mean Square Error (MSE)	Square Root of MSE	Average Percent Error	R^2Press	Residual Normality
52	1	0.0048	0.069	0.136	0.65	Not Normal

Table 2. Regression Coefficients.

Independent Variable	Coefficient (b(i))	Standard Error (Sb(i))	95% CI Lower	95% CI Upper
srlB	32.2600	0.0755	32.1078	32.4123
drvB	31.9559	0.0636	31.8275	32.0842
uvtB	32.1924	0.0536	32.0844	32.3004
foiB	31.8305	0.1249	31.5787	32.0823
oleB	30.7905	0.1929	30.4014	31.1795
fluvtB	31.9544	0.0437	31.8663	32.0425
buB	31.9170	0.0950	31.7254	32.1086
mdtwB	31.5006	0.3739	30.7466	32.2545
aorsmB	30.7689	0.1237	30.5195	31.0183

Table 3. Correlations Between Endmember Volumes.

Endmember Pair	Correlation Coefficient
srlB and drvB	-0.83
oleB and srlB	-0.69
drvB and oleB	0.68
foiB and oleB	0.83
aorsmB and srlB	0.75
aorsmB and drvB	-0.68
aorsmB and foiB	-0.86
aorsmB and oleB	-0.75

Table 4. Multicollinearity VIF Factors.

Endmember	VIF Factor

Endmember	VIF Factor
foiB	9.78
oleB	9.16
aorsmB	7.39

Table 5. Residual Analysis.

Observation	Residual	Hat Diagonal (h)	Cook's D	DFFITS	CovRatio
tm164	-0.27	-	0.29	-2.11	2.02
tm24	0.12	-	-	-	-
tm25	0.11	-	-	-	-
tm28	0.11	-	-	-	-
tm29	-0.12	-	0.17	-1.28	-
tm156B	-	0.39	-	-	2.02
tm43	-	0.30	-	-	-
tm64	-	0.94	3.96	-6.05	15.07
tm183	-	0.35	-	-	-
oxyuvite	-	0.48	-	-	2.31
uvit	-	0.39	-	-	-

Table 6. DFBETAS (>0.28).

Observation	Affected Variables
tm164	drvB, uvtB, foiB, fluvtB (strong), buB, aorsmB
tm1	foiB
tm171	fluvtB
tm64	All except fluvtB
tm166	fluvtB
tm183	srlB, mdtwB
tm25	mdtwB
tm28	foiB
tm29	srlB, foiB (strong), oleB
tm39	uvtB, oleB, fluvtB, buB

OLS REGRESSION ANALYSIS.

Table 2C.2 $X(YZ)_9Si_xAl_{(1-x)}(VW)_4$ model with interaction parameters**.**

Table 1. Model Fit Statistics.

Sample Size	R^2	Mean Square Error (MSE)	Square Root of MSE	Average Percent Error	R^2Press	Residual Normality
52	1	0.0039	0.0625	0.123	0.66	Normal

Table 2. Regression Coefficients.

Independent Variable	Coefficient (b(i))	Standard Error (Sb(i))	95% CI Lower	95% CI Upper
srlB	32.2057	0.0707	32.063	32.3484
drvB	32.1520	0.0852	31.9799	32.3242
uvtB	32.1098	0.0622	31.9842	32.2353
foiB	31.7031	0.1283	31.4439	31.9623
oleB	30.5885	0.1923	30.2002	30.9768

Independent Variable	Coefficient (b(i))	Standard Error (Sb(i))	95% CI Lower	95% CI Upper
fluvtB	32.1204	0.0921	31.9344	32.3065
buB	31.7374	0.1267	31.4816	31.9933
mdtwB	31.7992	0.3555	31.0812	32.5172
aorsmB	30.7690	0.1134	30.5400	30.9980
WdrvB-fluvtB	-1.2770	0.4236	-2.1326	-0.4215
WfoiB-fluvtB	0.7117	0.3105	0.0847	1.3387

Table 3. Correlations Between Endmember Volumes.

Endmember Pair	Correlation Coefficient
srlB and drvB	-0.83
oleB and srlB	-0.69
drvB and oleB	0.68
foiB and oleB	0.83
aorsmB and srlB	0.75
aorsmB and drvB	-0.68
aorsmB and foiB	-0.86
aorsmB and oleB	-0.75
WdrvB-fluvtB and fluvtB	0.64
WfoiB-fluvtB and buB	-0.60

Table 4. Multicollinearity VIF Factors.

Endmember	VIF Factor
foiB	12.54
oleB	11.03
aorsmB	7.54
WdrvB-fluvtB	9.89

Table 5. Residual Analysis.

Observation	Residual	Hat Diagonal (h)	Cook's D	DFFITS	CovRatio
tm164	-0.18	-	0.55	-2.91	4.71
tm155	-	0.76	0.18	-1.39	4.71
tm64	-	0.95	3.91	-6.65	15.60
tm166	-	-	0.13	1.25	-
tm29	-0.12	-	0.16	-1.40	-
tm74	-	-	0.11	1.17	-
uvit	-	-	0.13	-1.19	-
oxyuvite	-	0.48	-	-	2.47

Table 6. DFBETAS (>0.28).

Observation	Affected Variables
tm1	aorsmB, W parameters
tm164	All parameters
tm155	All except aorsmB, WdrvB-fluvtB, srlB, drvB
tm171	fluvtB
tm64	All except WdrvB-fluvtB
tm166	All except drvB, srlB, uvtB, aorsmB
tm183	mdtwB

Observation	Affected Variables
tm25	mdtwB
tm28	foiB
tm29	srlB, foiB (strong), oleB, aorsmB
tm74	drvB, uvtB, buB, aorsmB, WdrvB-fluvtB

OLS REGRESSION ANALYSIS.

Table 2C.3. $X(YZ)_9Si_xAl_{(1-x)}(VW)_4$ model without interaction parameters using the combined dataset**.**

Table 0. Descriptive Statistics.

Variable	Count	Mean	Standard Deviation	Minimum	Maximum
srlB	149	0.1768	0.2386	-0.24	0.7667
drvB	149	0.2485	0.2514	-0.69	0.8264
uvtB	149	-0.2326	0.3223	-1.36	0.8989
foiB	149	0.1774	0.2260	-0.95	0.6494
oleB	149	0.0293	0.1478	-0.87	0.3905
fluvtB	149	0.4135	0.2921	0	1.5
buB	149	0.0941	0.1400	0	1.1167
mdtwB	149	0.0369	0.0345	0	0.2806
aorsmB	149	0.0561	0.1594	-0.238	0.95
Molar Volume (J/mol/bar)	149	31.8114	0.2005	31.16	33.02

Table 1. Model Fit Statistics.

Sample Size	R^2	Mean Square Error (MSE)	Root MSE	Average Percent Error	R^2Press	Residual Normality
149	1	0.0065	0.0809	0.159	0.79	Not Normal

Table 2. Regression Coefficients.

Independent Variable	Coefficient (b(i))	Standard Error (Sb(i))	95% CI Lower	95% CI Upper
srlB	32.2109	0.0438	32.1242	32.2975
drvB	31.8811	0.0294	31.8229	31.9393
uvtB	32.0942	0.0350	32.0251	32.1633
foiB	31.5882	0.0453	31.4987	31.6777
oleB	31.1132	0.0730	30.9689	31.2575
fluvtB	31.9883	0.0341	31.9208	32.0558
buB	32.1628	0.0674	32.0296	32.2961
mdtwB	31.6753	0.2197	31.2409	32.1097
aorsmB	30.6837	0.0755	30.5344	30.8330

Table 3. Correlations Between Endmember Volumes.

Endmember Pair	Correlation Coefficient
srlB and drvB	-0.75
uvtB and fluvtB	-0.75
oleB and buB	-0.68
oleB and Molar Volume	-0.68

Endmember Pair	Correlation Coefficient
foiB and aorsmB	-0.76

Table 4. Multicollinearity VIF Factors.

Endmember	VIF Factor
All <3.3	

Table 5. Residual Analysis.

Observation	Residual	Hat Diagonal (h)	Cook's D	DFFITS	CovRatio
tm164	-0.29	-	0.06	-	-
tm64	-0.29	0.36	1.35	-3.77	1.66
tm24	0.15	-	-	-	-
tm25	0.12	-	-	-	-
tm28	0.15	-	-	-	-
tm74	0.11	-	-	-	-
oxyuvite	-	0.25	0.07	-	-
uvit	-	0.20	-	-	-
103	-0.13	-	-	-	-
133	-	0.22	-	-	-
148	-	0.12	-	-	-
156	-	0.39	0.05	-	1.66
161	-	0.29	-	-	1.50
168	0.12	-	-	-	-
169	0.10	-	-	-	-
170	0.10	-	-	-	-
173	-	0.14	-	-	-
174	-	0.13	-	-	-
177	0.10	-	-	-	-
206	0.20	0.44	1.07	3.242	1.50
15	-0.11	-	-	-	-
17	0.21	-	0.03	-	-
92	-0.1	-	-	-	-
9	-0.46	-	0.15	-1.30	-
14	-0.13	-	-	-	-
33	-0.19	-	0.08	-	-

Table 7. DFBETAS (Threshold > 0.163)

Observation	Affected Variables
tm164	All except srlB, oleB, and mdtwB
tm37A	uvtB, fluvtB
tm183	mdtwB
tm24	oleB, fluvtB, mdtwB
tm25	mdtwB
tm28	foiB
tm74	aorsmB, odrvB
tm64	oleB, fluvtB, buB, mdtwB
103	aorsmB

Observation	Affected Variables
138	drvB
139	srlB, drvB
156	uvtB, fluvtB, mdtwB
160	drvB, mdtwB
162	srlB
169	drvB
170	drvB
177	srlB, drvB, uvtB, foiB, fluvtB
181	drvB
206	drvB, oleB, buB (strong), aorsmB
86	foiB, oleB
15	fluvtB
17	srlB, foiB, oleB, buB
92	srlB, foiB, aorsmB
87	foiB
9	uvtB, foiB, fluvtB, buB, mdtwB
33	uvtB, fluvtB, mdtwB

OLS REGRESSION ANALYSIS.

Table 2C.4. $X(YZ)_9Si_xAl_{(1-x)}(VW)_4$ model with interaction parameters using the combined dataset.

Table 0. Significant Interaction Parameters from Subset Selection

Independent Variable	Coefficient (b(i))	Standard Error (Sb(i))	T-Statistic	P-Value	Reject H0 at α = 0.05?	Power-
srlB	32.0626	0.0511	627.922	0.0000	Yes	1.0000
drvB	31.9672	0.0557	574.113	0.0000	Yes	1.0000
uvtB	32.1764	0.0397	809.569	0.0000	Yes	1.0000
foiB	31.6773	0.0489	647.677	0.0000	Yes	1.0000
oleB	31.2184	0.0791	394.867	0.0000	Yes	1.0000
fluvtB	32.0692	0.0361	889.369	0.0000	Yes	1.0000
buB	31.6972	0.1178	269.091	0.0000	Yes	1.0000
mdtwB	31.8263	0.2082	152.860	0.0000	Yes	1.0000
aorsmB	30.7758	0.0804	382.674	0.0000	Yes	1.0000
WsrlB-buB	1.6419	0.3703	4.434	0.0000	Yes	0.9927
WdrvB-buB	1.1901	0.2938	4.051	0.0001	Yes	0.9804
WdrvB-fluvtB	-0.6646	0.1835	-3.622	0.0004	Yes	0.9491
WdrvB-uvtB	-0.6416	0.1815	-3.535	0.0006	Yes	0.9395
WdrvB-foiB	-0.4704	0.1593	-2.953	0.0037	Yes	0.8346

Table 1. Model Fit Statistics.

Sample Size	R^2	Mean Square Error (MSE)	Root MSE	Average Percent Error	R^2Press	Residual Normality
149	1	0.005	0.07	0.156	0.83	Not Normal

Table 2. Regression Coefficients.

Independent Variable	Coefficient (b(i))	Standard Error (Sb(i))	95% CI Lower	95% CI Upper

Independent Variable	Coefficient (b(i))	Standard Error (Sb(i))	95% CI Lower	95% CI Upper
srlB	32.0626	0.0511	31.9616	32.1636
drvB	31.9672	0.0557	31.8571	32.0774
uvtB	32.1764	0.0397	32.0978	32.2550
foiB	31.6773	0.0489	31.5806	31.7740
oleB	31.2184	0.0791	31.0621	31.3748
fluvtB	32.0692	0.0361	31.9979	32.1405
buB	31.6972	0.1178	31.4642	31.9301
mdtwB	31.8262	0.2082	31.4145	32.2380
aorsmB	30.7758	0.0804	30.6167	30.9348
WsrlB-buB	1.6419	0.3703	0.9096	2.3741
WdrvB-buB	1.1901	0.2938	0.6090	1.7712
WdrvB-fluvtB	-0.6646	0.1835	-1.0277	-0.3018
WdrvB-uvtB	-0.6416	0.1815	-1.0006	-0.2827
WdrvB-foiB	-0.4704	0.1593	-0.7854	-0.1554

Table 3. Correlations Between Endmember Volumes.

Endmember Pair	Correlation Coefficient
srlB and drvB	-0.7525
uvtB and fluvtB	-0.7563
foiB and aorsmB	-0.7652
oleB and Molar Volume (J/mol/bar)	-0.6828
WsrlB-buB and buB	0.7548
WdrvB-uvtB and uvtB	-0.8510
WdrvB-foiB and foiB	0.7165

Table 4. Multicollinearity VIF Factors.

Endmember	VIF Factor
WdrvB-fluvtB	21.73
WdrvB-uvtB	12.66
buB	7.38
WsrlB-buB	6.71
drvB	5.32

Table 5. Residual Analysis: Residual and Model Fit Metric Changes Due to Interaction Parameters

Observation	Residual Change	Hat Diagonal Change	Cook's D Change	DFFITS Change	CovRatio Change
173	0.11	-	-	-	-
177	0.14	+0.13	-	-0.8	-
206	0.11	+0.1	-0.7	-0.97	-
tm64	-	+0.3	-0.7	+0.7	+1.75
tm72B	-	+0.16	+0.11	-1.23	-

Table 6. DFBETAS (>0.163): effects on W's.

Observation	Influenced Parameters
129	WsrlB-buB (-0.20)

Observation	Influenced Parameters
164	WdrvB-fluvtB (-0.60), WdrvB-uvtB (-0.62), WdrvB-foiB (-0.25)
tm64	WsrlB-buB (1.42), WdrvB-buB (1.87), WdrvB-fluvtB (-0.85), WdrvB-uvtB (-0.59), WdrvB-foiB(-0.34)
tm72B	WsrlB-buB (-0.57), WdrvB-buB (-0.23)
oxyuvite	WdrvB-fluvtB(-0.16), WdrvB-uvtB (-0.32)
128	WdrvB-uvtB (0.22)
138	WdrvB-fluvtB(0.42), WdrvB-uvtB (0.26), Wdrv-foit (0.36)
139	WdrvB-fluvtB(0.23), WdrvB-foiB(0.19)
160	WsrlB-buB (-0.18), WdrvB-fluvtB(-0.30), WdrvB-uvtB (-0.23), WdrvB-foiB(-0.25)
173	WdrvB-buB (-0.24), WdrvB-fluvtB(0.80), WdrvB-uvtB (0.83), WdrvB-foiB(0.49)
174	WdrvB-buB (-0.42), WdrvB-fluvtB(-0.19), WdrvB-foiB(-0.16)
177	WdrvB-foiB(0.18)
206	WsrlB-buB (0.75), WdrvB-buB (0.95)
15	WdrvB-fluvtB(-0.18)
9	WsrlB-buB (1.49), WdrvB-buB (0.44), WdrvB-fluvtB (-0.46), WdrvB-uvtB (-0.55), WdrvB-foiB(-0.40)
33	WdrvB-foiB(0.33)

OLS REGRESSION ANALYSIS.

Table 2C.5. $X(YZ)_9Si_xAl_{(1-x)}(VW)_4$ model with subregular interaction parameters using the combined dataset**.**

Table 1. Model Fit Statistics.

Sample Size	R^2	Mean Square Error (MSE)	Root MSE	Average Percent Error	R^2Press	Residual Normality
149	1	0.0056	0.075	0.154	0.76	Not Normal

Table 2. Regression Coefficients.

Independent Variable	Coefficient (b(i))	Standard Error (Sb(i))	95% CI Lower	95% CI Upper
slrB	32.1255	0.0513	32.0239	32.2270
drvB	31.9755	0.0565	31.8637	32.0873
uvtB	32.1800	0.0406	32.0996	32.2603
foiB	31.6687	0.0502	31.5695	31.7679
oleB	31.2316	0.0816	31.0703	31.3929
fluvtB	32.0650	0.0366	31.9925	32.1374
buB	31.8112	0.1060	31.6016	32.0207
mdtwB	31.8761	0.2141	31.4526	32.2994
aorsmB	30.7580	0.0818	30.5962	30.9197
WdrvB-buB	0.8708	0.2755	0.3260	1.4156
WdrvB-fluvtB	-0.6413	0.1865	-1.0102	-0.2724
WdrvB-uvtB	-0.6184	0.1842	-0.9828	-0.2540
WdrvB-foiB	-0.4738	0.1642	-0.7986	-0.1490
WslrB-srlB-buB	1.1376	0.5243	0.1005	2.1747
WslrB-buB-buB	1.3871	0.4580	0.4812	2.2930

OLS REGRESSION ANALYSIS.

Table 2C.6 $XY_3Z_6T_6V_3W$ model without interaction parameters.

Table 0. Descriptive Statistics.

Variable	Count	Mean	Standard Deviation	Minimum	Maximum
srl	53	0.1166	0.2097	-0.2701	0.5452
drv	53	0.1705	0.1515	-0.1470	0.5817
uvt	53	-0.0263	0.2322	-0.6965	0.8494
fuvt	53	0.0280	0.0419	0.0000	0.1780
foi	53	0.1142	0.1943	-0.6256	0.5427
ole	53	-0.0690	0.0696	-0.2487	0.1274
drvdis	53	-0.2038	0.2189	-0.5970	0.3886
odrv	53	0.4460	0.3233	-0.7466	0.8067
fluvt	53	0.2370	0.2213	0.0032	0.8569
bu	53	0.0497	0.0981	-0.0215	0.6492
mdtw	53	0.0393	0.0310	0.0000	0.1455
bole	53	0.0157	0.1144	-0.0007	0.8328
aorsm	53	0.0660	0.1332	0.0000	0.7466
pov	53	0.0160	0.0211	0.0000	0.0824
Molar Volume (J/mol/bar)	53	31.8000	0.3199	29.8234	32.2403

Table 1. Model Fit Statistics.

Sample Size	R^2	Mean Square Error (MSE)	Square Root of MSE	Average Percent Error	R^2Press	Residual Normality
53	1	0.0058	0.077	0.142	0	Not Normal

Table 2. Regression Coefficients

Independent Variable	Coefficient (b(i))	Standard Error (Sb(i))	95% CI Lower	95% CI Upper
srl	31.9482	0.2529	31.4367	32.4597
drv	31.7589	0.2094	31.3353	32.1825
uvt	32.1568	0.1807	31.7913	32.5222
fuvt	32.1492	0.3859	31.3687	32.9296
foi	31.7070	0.2919	31.1164	32.2974
ole	30.9781	0.3788	30.2119	31.7443
drvdis	31.8729	0.2330	31.4017	32.3441
odrv	31.6974	0.0935	31.5083	31.8866
fluvt	31.9845	0.0646	31.8538	32.1152
bu	31.4036	0.3294	30.7374	32.0699
mdtw	31.7836	0.4038	30.9669	32.6004
bole	29.5442	0.1459	29.2492	29.8392
aorsm	31.1208	0.3270	30.4593	31.7822
pov	35.6274	1.1422	33.3171	37.9378

Table 3. Correlations Between Endmember Volumes

Endmember Pair	Correlation Coefficient
foi and uvt	-0.62

Endmember Pair	Correlation Coefficient
odrv and foi	0.71
foi and aorsm	-0.76
odrv and aorsm	-0.71
pov and bu	0.68
bole and Molar Volume	-0.86

Table 4. Multicollinearity VIF Factors

Endmember	VIF Factor
srl	24.86
drv	8.89
uvt	15.56
foi	28.42
drvdis	22.99
odrv	8.07
bu	9.23
aorsm	16.76

Table 5. Residual Analysis

Observation	Residual	Hat Diagonal (h)	Cook's D	DFFITS	CovRatio
tm164	-0.31	-	0.26	-2.71	-
tm24	0.10	-	-	-	-
tm25	0.13	-	-	-	-
tm28	0.13	-	0.09	1.16	-
tm29	-0.12	-	0.19	-1.69	-
tm64	-	0.98	2.45	-5.81	98.12
olenite	-	1.00	21013	536.88	1824375
oxyuvit	-	0.61	-	-	3.49
uvit	-	0.60	0.13	-1.19	3.21

Table 6. DFBETAS (Threshold >0.30)

Observation	Affected Variables
tm164	All except fuvt, mdtw, and ole
tm144	mdtw
tm156B	mdtw
tm150A	drv
tm160A	pov
tm64	ole, fluvt, bu, mdtw
tm28	All except fluvt, bu, mdtw, aorsm
tm29	srl, fuvt, fluvt, ole, aorsm
tm40	fuvt, fluvt, ole, pov
tm42	fuvt, odrv
olenite	bole (strong)
uvite	srl, drv, uvt, drvdis, bu

OLS REGRESSION ANALYSIS.

Table 2C.7. $XY_3Z_6T_6V_3W$ model without interaction parameters using the combined dataset**.**

Table 0. Descriptive Statistics

Variable	Count	Mean	Standard Deviation	Minimum	Maximum
srl	157	0.1463	0.2367	-0.6067	0.8248
drv	157	0.1270	0.2869	-0.9867	0.9416
uvt	157	-0.0476	0.2575	-0.9324	0.8600
fluvt	157	0.0309	0.0832	-0.0800	0.5546
foi	157	0.1608	0.2111	-0.9500	0.9100
ole	157	-0.0729	0.0810	-0.4623	0.1689
drvdis	157	-0.1110	0.4646	-1.4143	1.8500
odrv	157	0.3853	0.3082	-0.7500	1.1800
fluvt	157	0.1899	0.1945	0.0000	0.9670
bu	157	0.0482	0.0888	-0.1424	0.6492
mdtw	157	0.0357	0.0346	0.0000	0.2809
bole	157	0.0189	0.1069	-0.0007	0.8328
aorsm	157	0.0707	0.1260	-0.0000	0.9500
pov	157	0.0179	0.0458	-0.0000	0.4700
Molar Volume (J/mol/bar)	157	31.7545	0.3715	29.7100	33.0200

Table 1. Model Fit Statistics.

Sample Size	R^2	Mean Square Error (MSE)	Root MSE	Average Percent Error	R^2Press	Residual Normality
149	1	0.0089	0.0945	0.199	0.91	Not Normal

Table 2. Regression Coefficients.

Independent Variable	Coefficient (b(i))	Standard Error (Sb(i))	95% CI Lower	95% CI Upper
srl	32.2215	0.0666	32.0898	32.3531
drv	31.9271	0.0477	31.8327	32.0214
uvt	32.1432	0.0591	32.0264	32.2601
fuvt	32.6133	0.1270	32.3622	32.8644
foi	31.5301	0.0471	31.4370	31.6232
ole	30.9624	0.1602	30.6457	31.2791
drvdis	31.9376	0.0367	31.8651	32.0101
odrv	31.6456	0.0309	31.5846	31.7066
fluvt	31.9946	0.0452	31.9053	32.0840
bu	31.7001	0.1341	31.4351	31.9651
mdtw	31.4303	0.2593	30.9177	31.9429
bole	29.4129	0.0793	29.2562	29.5696
aorsm	30.5382	0.1079	30.3248	30.7515
pov	34.2256	0.1795	33.8708	34.5803

Table 3. Correlations Between Endmember Volumes.

Endmember Pair	Correlation Coefficient
drv and drvdis	-0.73
foi and aorsm	-0.69

Endmember Pair	Correlation Coefficient
bole and Molar Volume	-0.83

Table 4. Multicollinearity VIF Factors.

Variable	VIF Value
drvdis	5.0
uvt	4.0
srl	3.3
aorsm	3.2

Table 5. Residual Analysis.

Observation	Residual	Hat Diagonal	Cook's D	DFFITS	CovRatio
tm64	-	0.89	-	-	11.00
tm164	-0.30	-	0.05	-0.91	
olenite	0.27	0.40	0.69	3.27	-
oxyuvite	-	0.27	0.076	1.03	-
uvt	-	0.21	-	-	-
1	-	0.31	0.03	-	-
2	-	0.21	-	-	-
9	-0.40	-	0.22	-1.89	-
14	-0.16	-	-	-	-
23	0.39	-	0.15	1.57	-
87	0.18	-	0.04	-	-
103	-0.13	-	0.03	-	-
130	-	0.35	-	-	1.66
148	-	0.20	-	-	-
155	-0.14	-	0.03	-	-
156	-0.15	0.41	0.24	-	-
159	-0.15	-	-	-	-
160	-	0.25	-	-	-
161	-	0.38	-	-	1.78
162	-	0.34	-	-	1.64
173	-	0.19	-	-	-
175	-0.27	-	0.076	-1.00	-
178	-	0.37	-	-	1.69
179	-0.23	0.19	0.12	-1.33	-
206	0.07	0.71	0.25	1.88	3.28

Table 6. DFBETAS (>0.16)

Observation	Affected Variables
tm164	foi, fluvt
tm171	fluvt
tm23	odrv
tm37A	fluvt
tm166	fluvt
tm183	srl, fluvt, mdtw

Observation	Affected Variables
tm24	srl, uvt, fluvt, odrv, aorsm
tm28	foi
olenite	srl, uvt, foi, odrv, bu, bole (Strong)
oxyuvite	drv, uvt, odrv, aorsm
1	bole
2	bole
10	drv, foi, drvdis
23	All except fluvt and pov
103	srl, drv, uvt, fluvt, odrv, bu, aorsm
137	odrv
138	drv, drvdis, odrv
148	fluvt, bu
155	uvt, fluvt, ole, drvdis, odrv, fluvt, mdtw
156	All except fluvt, ole, bole, pov
159	srl, uvt, aorsm
162	fluvt
173	mdtw
175	All except fluvt, foi, mdtw, pov
178	foi, odrv
179	All except foi, fluvt, mdtw, pov
206	srl, uvt, fluvt, foi, ole, bu, mdtw, pov
85	pov
93	srl, uvt, aorsm
92	srl
142	foi
87	All except srl, fluvt, foi, mdtw, bole, aorsm
9	All except foi, bu, bole, pov
33	fluvt

Appendix 2D. Model Selection Bulk Model

Bulk compositional model $X(YZ)_9Si_xAl_{(1-x)}(VW)$

Table 2D.1. Bulk Model. Best performing models based on a single statistic

Weighted Optimisation Results

Unweighted y residual metrics.

Minimum MSE: 0.006957 (Model_Method: Bulk_noW_robust cauchy)
Minimum MAE: 0.051623 (Model_Method: Bulk_noW_robust cauchy)
Minimum MAD: 0.050339 (Model_Method: Bulk_noW_robust cauchy)
Maximum Adj_R_squared: 0.794640 (Model_Method: Bulk_noWno164 gtls block diag)

Weighted York residual metrics.
Minimum wMSE: 0.005127 (Model_Method: Bulk_noW_robust cauchy)
Minimum wMAE: 0.046395 (Model_Method: Bulk_noW_robust cauchy)
Minimum wMAD: 0.001323 (Model_Method: Bulk_noWno164 cwtls block diag)
Maximum AdjR_: 0.754749 (Model_Method: Bulk_noWno164 gtls row column)
Maximum RsquaredPress: 0.746464 (Model_Method: Bulk_noWno164 gtls row column)

Bias Integral.
Minimum IntegralBetweenYorkand1_1: 0.028353 (Model_Method: Bulk_noW cwtls block diag)

Table 2D.2. Bulk model Z-score heuristics combining the sample amount averaged index performance on the training and test sets. For the meaning of the different Z scores and how they are summed into one heuristic, see main text. Best performing robust regression method and x-uncertainty regression methods with lowest sum Z scores are in bold and yellow.

Model Method	MSE_Z	MAE_Z	MAD_Z	Adj R Squared Z	Integral Between York and 1_1_Z	wMSE_Z	AdjR_Z	Rsquared Press Z	Sum Z Scores
Bulk_noWno164 cwtls block diag	**-0.78**	**-0.51**	**-0.75**	**-0.81**	**-3.59**	**-0.42**	**-1.29**	**-1.37**	**-9.52**
Bulk_noWno164 gtls block diag	-0.93	-1.24	-1.13	-0.96	-0.60	-0.81	-1.73	-1.79	-9.20
Bulk_noWno164 gtls fullW	-0.89	-1.15	-1.03	-0.92	-1.02	-0.57	-1.68	-1.74	-8.99
Bulk_noW_robust cauchy	**-0.98**	**-1.60**	**-1.57**	**-0.92**	**0.90**	**-1.49**	**-1.19**	**-1.19**	**-8.03**
Bulk_noW_robust welsch	-0.93	-1.51	-1.50	-0.85	1.01	-1.44	-1.07	-1.07	-7.36
Bulk_noW_robust bisquare	-0.92	-1.48	-1.47	-0.83	0.97	-1.40	-1.02	-1.01	-7.15
Bulk_noW_robust andrews	-0.91	-1.47	-1.46	-0.82	0.97	-1.39	-1.01	-1.00	-7.11
Bulk_noWno164 TLS	-0.88	-0.96	-0.92	-0.93	-0.40	-0.80	-0.97	-1.01	-6.87
Bulk_noWno164 OLS	**-0.88**	**-0.96**	**-0.92**	**-0.93**	**-0.40**	**-0.79**	**-0.96**	**-1.00**	**-6.84**
Bulk_noWno164 gtls cov data	-0.88	-0.95	-0.92	-0.93	-0.38	-0.79	-0.95	-1.00	-6.81

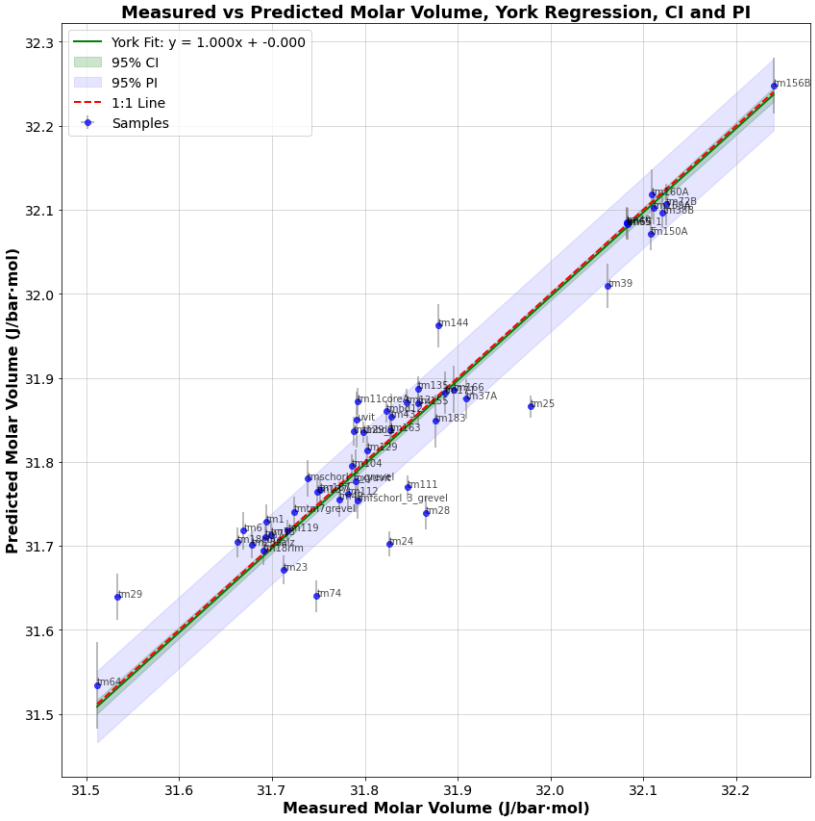
Measured vs Predicted Molar Volume, York Regression, CI and PI
York Fit: y = 1.000x + -0.000
95% CI
95% PI
1:1 Line
Samples
Predicted Molar Volume (J/bar·mol)
Measured Molar Volume (J/bar·mol)
32.3
32.2
32.1
32.0
31.9
31.8
31.7
31.6
31.5
31.5
31.6
31.7
31.8
31.9
32.0
32.1
32.2

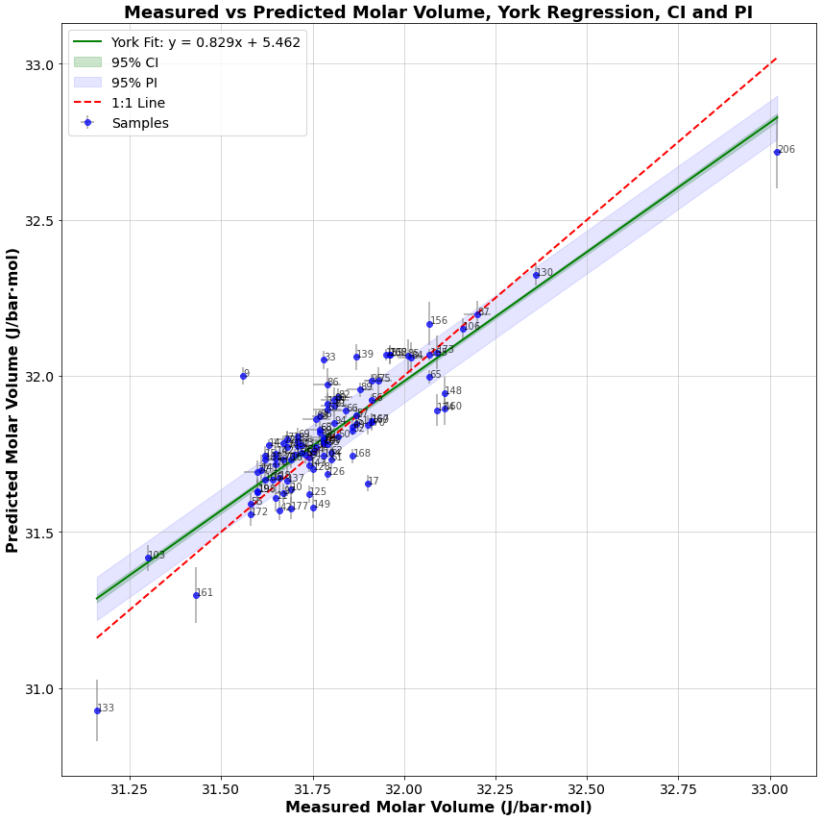
Measured vs Predicted Molar Volume, York Regression, CI and PI
York Fit: y = 0.829x + 5.462
95% CI
95% PI
1:1 Line
Samples
Predicted Molar Volume (J/bar·mol)
Measured Molar Volume (J/bar·mol)
33.0
32.5
32.0
31.5
31.0
31.25
31.50
31.75
32.00
32.25
32.50
32.75
33.00

Figure 2D.1. Bulk model. OLS without interaction parameters and tm164. A) training set fit. B) test set fit. Green bands show confidence intervals for the mean response, while blue bands represent prediction intervals for individual measurements

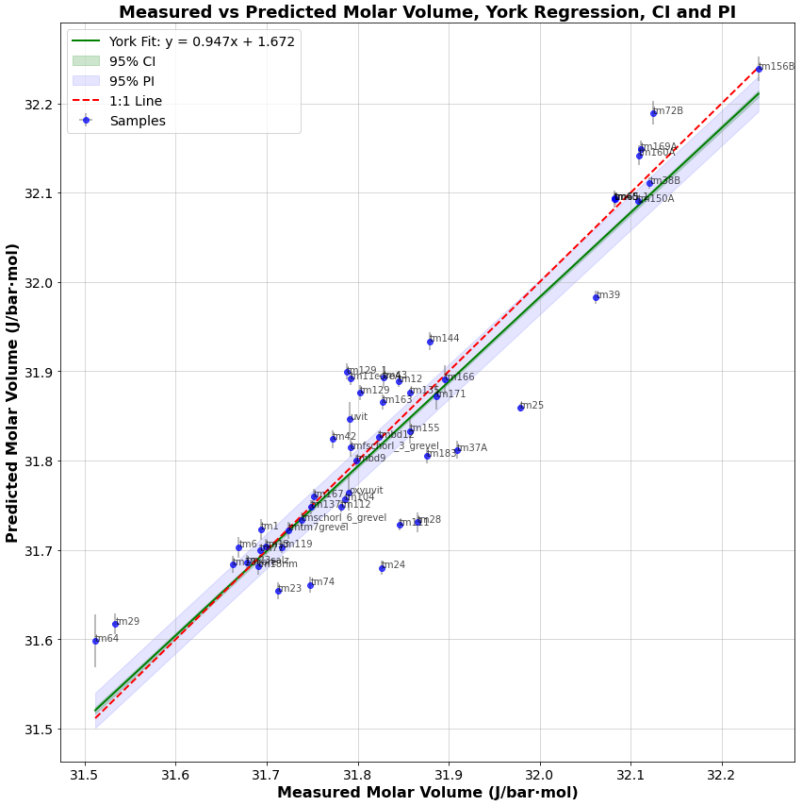
Measured vs Predicted Molar Volume, York Regression, CI and PI
York Fit: y = 0.947x + 1.672
95% CI
95% PI
1:1 Line
Samples
Predicted Molar Volume (J/bar·mol)
Measured Molar Volume (J/bar·mol)

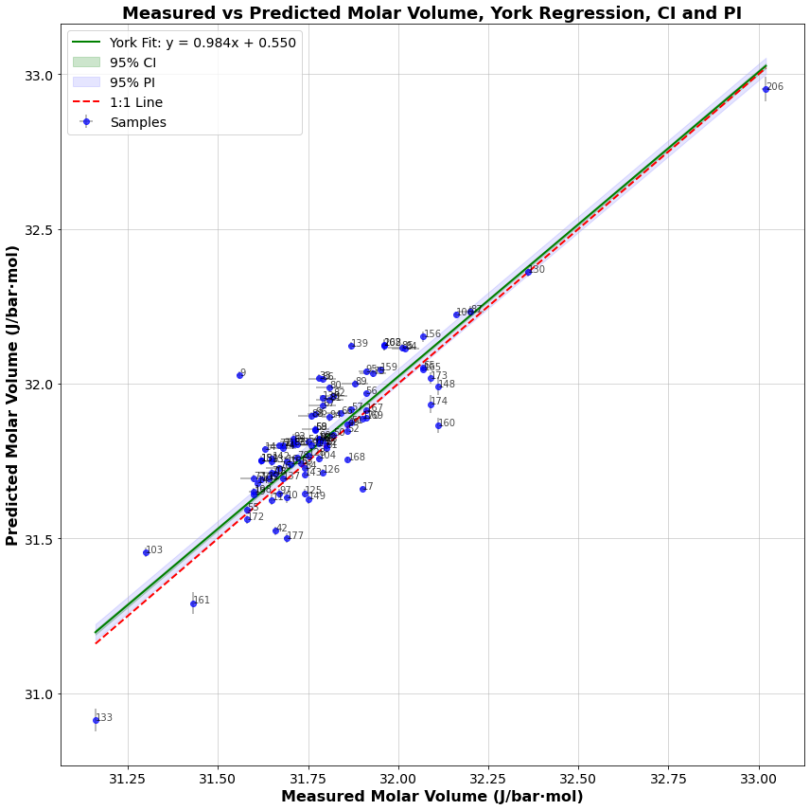
Measured vs Predicted Molar Volume, York Regression, CI and PI
York Fit: y = 0.984x + 0.550
95% CI
95% PI
1:1 Line
Samples
Predicted Molar Volume (J/bar·mol)
Measured Molar Volume (J/bar·mol)

Figure 2D.2. Bulk model. CWTLS without interaction parameters and tm164. A) training set fit. B) test set fit. Green bands show confidence intervals for the mean response, while blue bands represent prediction intervals for individual measurements

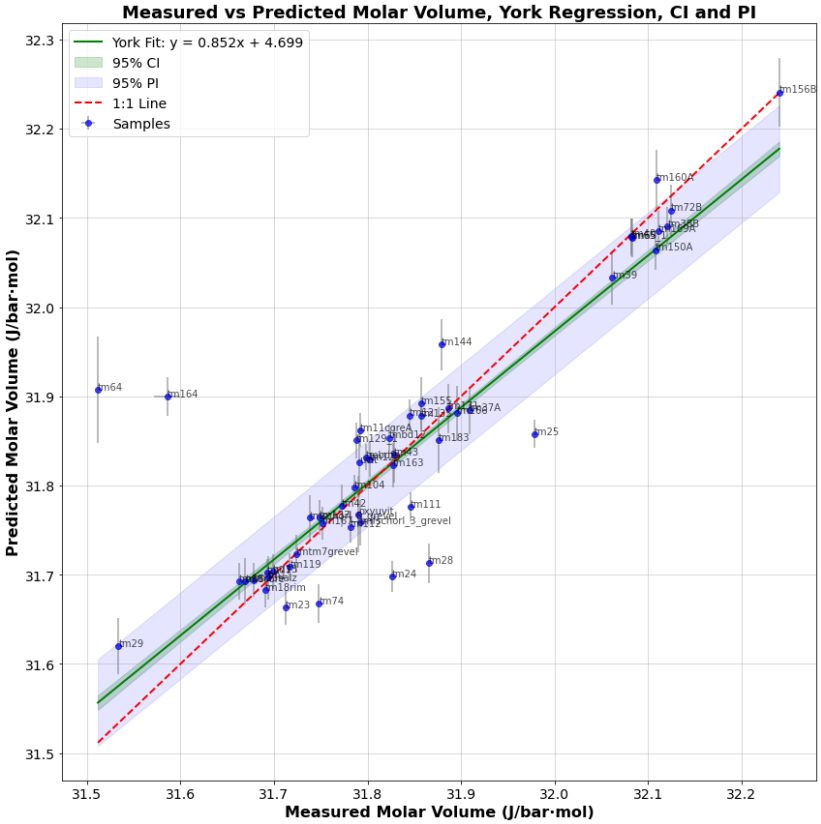
Measured vs Predicted Molar Volume, York Regression, CI and PI
York Fit: y = 0.852x + 4.699
95% CI
95% PI
1:1 Line
Samples
Predicted Molar Volume (J/bar·mol)
Measured Molar Volume (J/bar·mol)

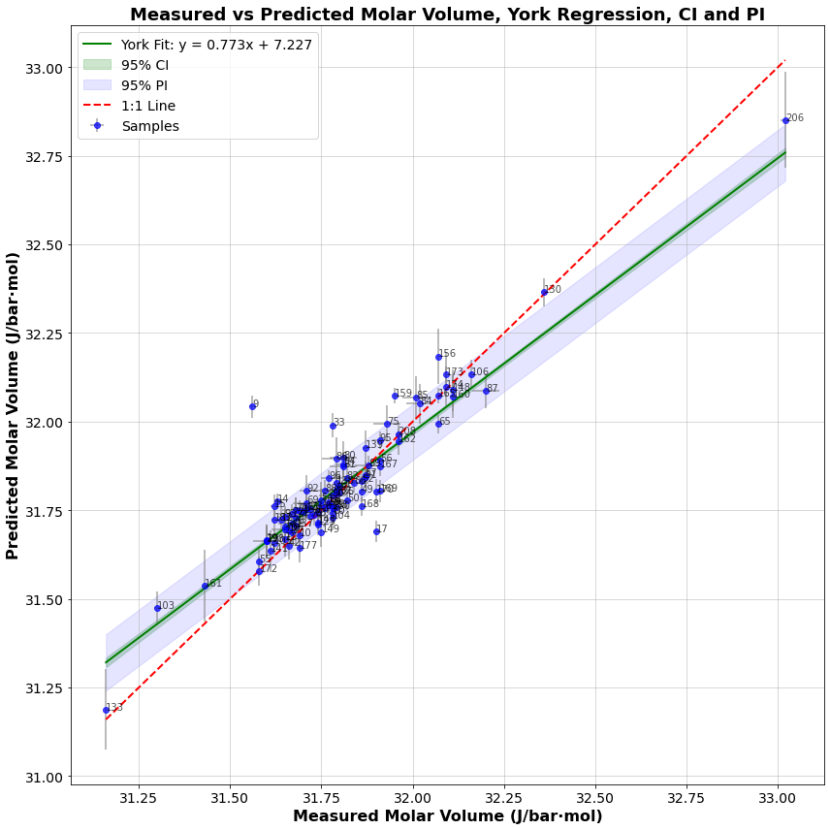
Measured vs Predicted Molar Volume, York Regression, CI and PI
York Fit: y = 0.773x + 7.227
95% CI
95% PI
1:1 Line
Samples
Predicted Molar Volume (J/bar·mol)
Measured Molar Volume (J/bar·mol)

Figure 2D.3. Bulk model. Cauchy robust fit without interaction parameters. A) training set fit. B) test set fit. Green bands show confidence intervals for the mean response, while blue bands represent prediction intervals for individual measurements

Appendix 2E. Model Selection Speciation model

Table 2E.1. Speciation Model. Best performing models based on a single statistic

Unweighted y residual metrics.

Minimum MSE: 0.013006 (Model_Method: Speciation_noW cwtls block diag)
Minimum MAE: 0.080412 (Model_Method: Speciation_noW cwtls block diag)
Minimum MAD: 0.068460 (Model_Method: Speciation_noW cwtls block diag)
Maximum Adj_R_squared: 0.891693 (Model_Method: Speciation_noW cwtls block diag)

Weighted York residual metrics.
Minimum wMSE: 0.005334 (Model_Method: Speciation_noW cwtls block diag)
Minimum wMAE: 0.051389 (Model_Method: Speciation_noW cwtls block diag)
Minimum wMAD: 0.002261 (Model_Method: Speciation_noW cwtls block diag)
Maximum AdjR_: 0.927919 (Model_Method: Speciation_noW cwtls block diag)
Maximum RsquaredPress: 0.925424 (Model_Method: Speciation_noW cwtls block diag)

Bias Integral.
Minimum IntegralBetweenYorkand1_1: 0.146839 (Model_Method: Speciation_noW gtls y scaled)

Table 2E.2. Speciation model. Top 10 Model-method combination based oon total Z-score minimisation. Z-score heuristics combining the sample-amount averaged index performance on the training and test sets. For the meaning of the different Z scores and how they are summed into one heuristic, see main text. Best performing robust regression method and x-uncertainty regression methods with lowest sum Z scores are in bold and yellow.

Model Method	MSE_Z	MAE_Z	MAD_Z	Adj R Squared Z	Integral Between York and 1_1_Z	wMSE_Z	AdjR_Z	Rsquared Press Z	Sum Z Scores
Speciation_noW cwtls block diag	**-0.96**	**-1.34**	**-1.60**	**-0.94**	**-1.07**	**-1.06**	**-1.85**	**-1.87**	**-10.69**
Speciation_noWno164 xyscaledTLS	-0.63	-0.84	-0.95	-0.67	-0.64	-0.76	-0.92	-0.94	-6.35
Speciation_noWno164 gtls	-0.63	-0.84	-0.94	-0.67	-0.63	-0.75	-0.91	-0.93	-6.30

Model Method	MSE_Z	MAE_Z	MAD_Z	Adj R Squared Z	Integral Between York and 1_1_Z	wMSE_Z	AdjR_Z	Rsquared Press Z	Sum Z Scores
cov data y scaled									
Speciation_noW cwtls fullW	-0.52	-0.41	-0.71	-0.50	-0.98	-0.67	-0.95	-0.99	-5.73
Speciation_noW_robust WLS	**-0.61**	**-0.81**	**-0.87**	**-0.60**	**-0.60**	**-0.63**	**-0.73**	**-0.76**	**-5.60**
Speciation_noW xyscaledTLS	-0.56	-0.74	-0.84	-0.56	-0.69	-0.60	-0.73	-0.76	-5.48
Speciation_noW gtls cov data y scaled	-0.56	-0.74	-0.83	-0.56	-0.68	-0.60	-0.72	-0.75	-5.44
Speciation_Wcombi_robust WLS	-0.33	-0.48	-0.69	-0.30	-0.42	-0.69	-0.85	-0.85	-4.61
Speciation_Wcombi gtls cov data y scaled	-0.27	-0.40	-0.63	-0.24	-0.48	-0.66	-0.84	-0.84	-4.37
Speciation_Wcombi xyscaledTLS	-0.24	-0.37	-0.63	-0.21	-0.51	-0.66	-0.84	-0.85	-4.31

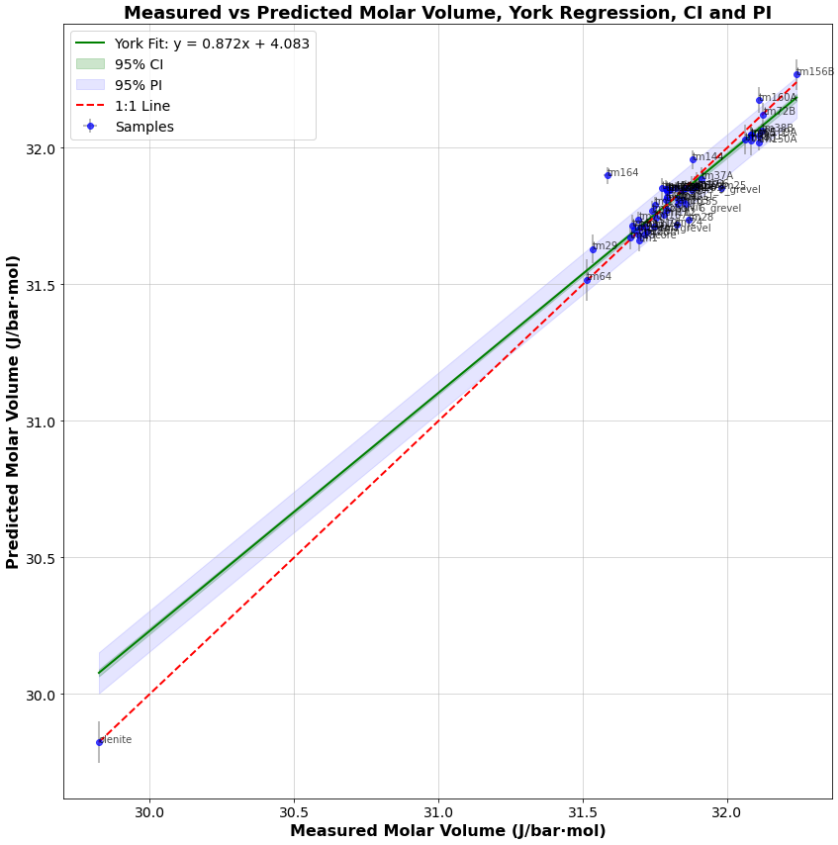
Measured vs Predicted Molar Volume, York Regression, CI and PI
York Fit: y = 0.872x + 4.083
95% CI
95% PI
1:1 Line
Samples
Predicted Molar Volume (J/bar·mol)
Measured Molar Volume (J/bar·mol)
30.0
30.5
31.0
31.5
32.0

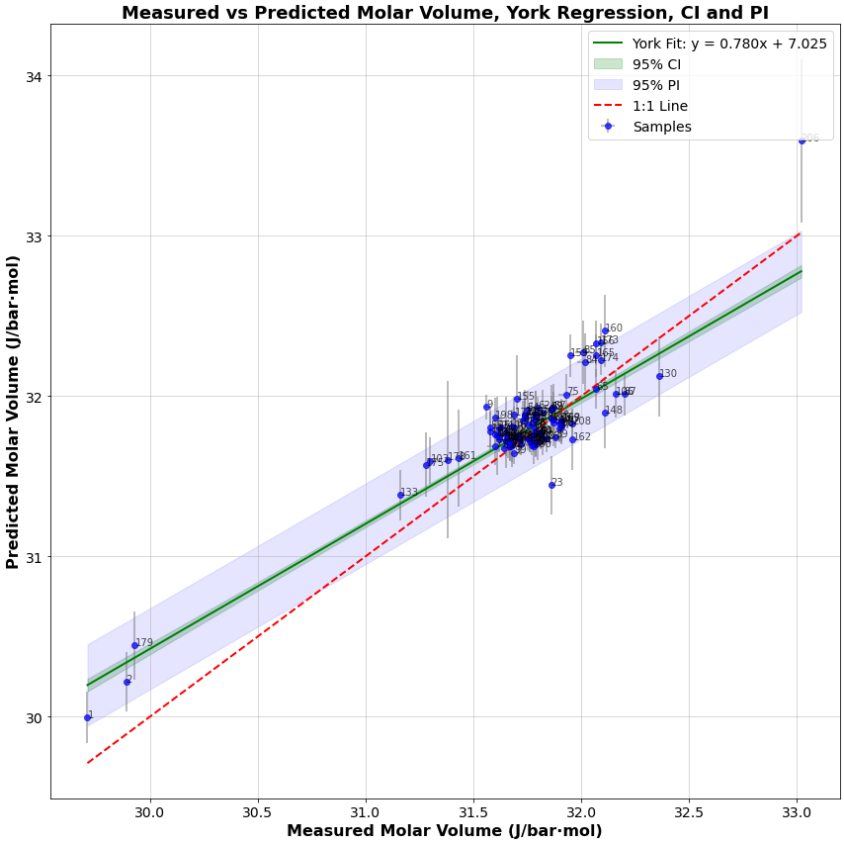
Measured vs Predicted Molar Volume, York Regression, CI and PI
York Fit: y = 0.780x + 7.025
95% CI
95% PI
1:1 Line
Samples
Predicted Molar Volume (J/bar·mol)
Measured Molar Volume (J/bar·mol)
30
31
32
33
34
30.0
30.5
31.0
31.5
32.0
32.5
33.0

Figure 2E.1. Speciation model. OLS without interaction parameters. A) training set fit. B) test set fit. Green bands show confidence intervals for the mean response, while blue bands represent prediction intervals for individual measurements

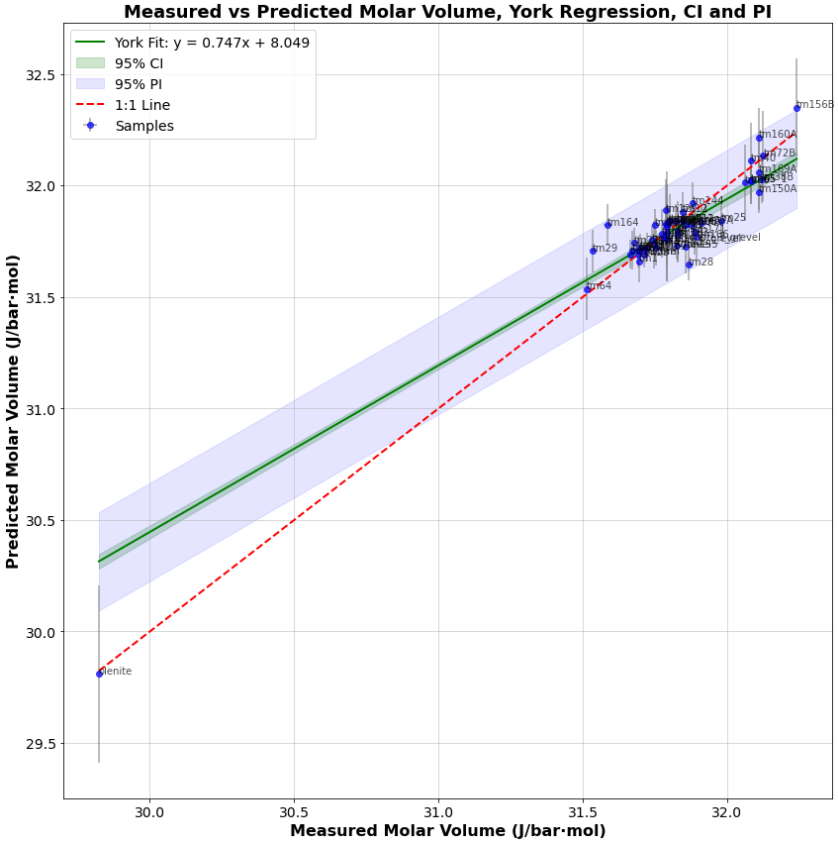
Measured vs Predicted Molar Volume, York Regression, CI and PI
York Fit: y = 0.747x + 8.049
95% CI
95% PI
1:1 Line
Samples
Predicted Molar Volume (J/bar·mol)
Measured Molar Volume (J/bar·mol)

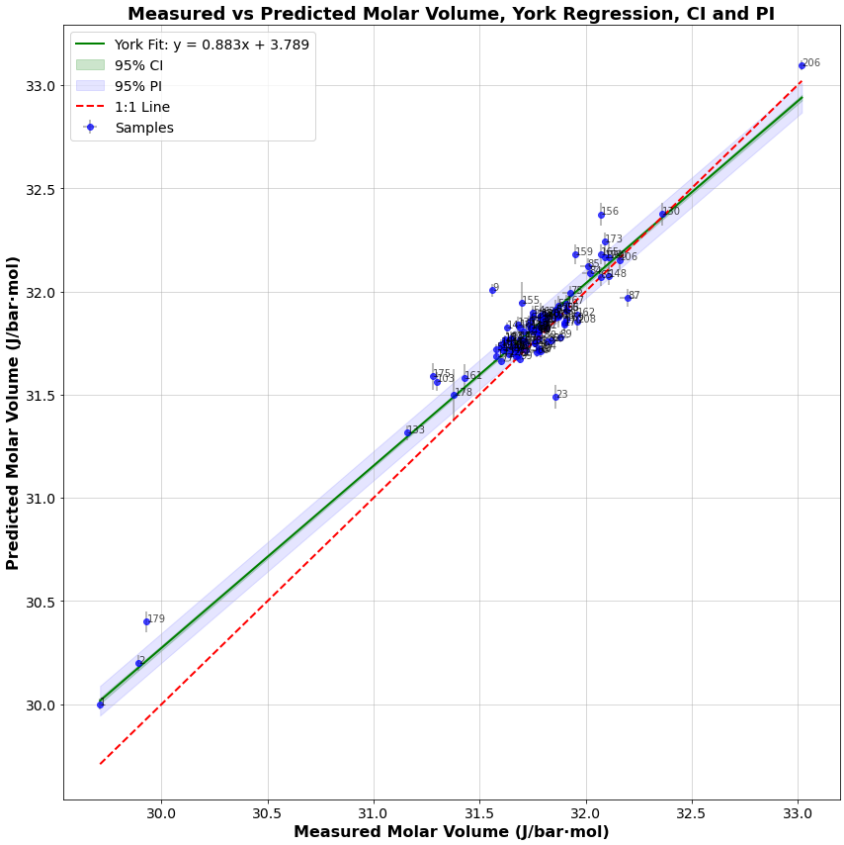
Measured vs Predicted Molar Volume, York Regression, CI and PI
York Fit: y = 0.883x + 3.789
95% CI
95% PI
1:1 Line
Samples
Predicted Molar Volume (J/bar·mol)
Measured Molar Volume (J/bar·mol)

Figure 2E.2. Speciation model. OLS without interaction parameters. A) training set fit. B) test set fit. Green bands show confidence intervals for the mean response, while blue bands represent prediction intervals for individual measurements

Appendix 2F. Model Assessment

Bulk compositional model.

Table 2F.1. Cauchy Robust Regression without interaction parameters including outlier tm164; Internal and External validation.

Internal validation using the training data. The results of the internal validation of the $X(YZ)_9Si_xAl_{(1-x)}(VW)$ model.

Table 1. Model Fit Statistics.

Mean Squared Error (MSE)	Mean Absolute Error (MAE)	Median Absolute Deviation (MAD)	Adjusted R^2
0.007	0.045	0.0457	0.67

Table 2. York Regression Metrics

Weighted MSE (wMSE)	Weighted MAE (wMAE)	Weighted MAD (wMAD)	Adjusted Weighted R^2	Overall Weighted PRESS R^2	Bias Integral
0.004	0.04	0.0015	0.75	0.75	0.0062

External validation using the test data. The results of the external validation of the $X(YZ)_9Si_xAl_{(1-x)}(VW)$ model.

Table 1. Model Fit Statistics.

Mean Squared Error (MSE)	Mean Absolute Error (MAE)	Median Absolute Deviation (MAD)	Adjusted R^2
0.007	0.055	0.053	0.84

Table 2. York Regression Metrics

Weighted MSE (wMSE)	Weighted MAE (wMAE)	Weighted MAD (wMAD)	Adjusted Weighted R^2	Overall Weighted PRESS R^2	Bias Integral
0.005	0.05	0.002	0.68	0.67	0.51

Speciation model.

Table 2F.2. CWTLS without interaction parameters with outlier tm164.

Internal validation using the training data.

Table 1. Model Fit Statistics.

Mean Squared Error (MSE)	Mean Absolute Error (MAE)	Median Absolute Deviation (MAD)	Adjusted R^2
0.0050	0.0521	0.0521	0.9317

Table 2. York Regression Metrics

Weighted MSE (wMSE)	Weighted MAE (wMAE)	Weighted MAD (wMAD)	Adjusted Weighted R^2	Overall Weighted PRESS R^2	Bias Integral
0.0036	0.0454	0.0011	0.9014	0.8992	0.0061

External validation using the training data.

Table 1. Model Fit Statistics.

Mean Squared Error (MSE)	Mean Absolute Error (MAE)	Median Absolute Deviation (MAD)	Adjusted R^2
0.017	0.096	0.077	0.87

Table 2. York Regression Metrics

Weighted MSE (wMSE)	Weighted MAE (wMAE)	Weighted MAD (wMAD)	Adjusted Weighted R^2	Overall Weighted PRESS R^2	Bias Integral
0.006	0.0546	0.0029	0.942	0.94	0.276

Appendices Chapter 3

Appendix 3A. Theoretical framework Entropy and Cp(T)

Caloric equation of state Cp(T)**.** The caloric equation of state, $C_p(T)$, and its integral to standard state conditions (vibrational entropy S) reveal Gibbs free energy (G) changes with temperature, where $C_p = -T\left(\frac{\partial^2 G}{\partial T^2}\right)_P$, $S = -\left(\frac{\partial G}{\partial T}\right)_P$. Direct Cp and S measurements anchor these first- (slope) and second-derivative (curvature) properties in the T dimension in thermodynamic database optimisations using phase equilibria, reducing parameter correlations and enabling independent refinement of high-uncertainty parameters like enthalpy (H), which sets the absolute magnitude of G in P-T space (Ganguly 2008).

In solid solutions, Cp macroscopically parameterizes thermal behavior and microscopically reflects the energy required to excite quasiparticles to higher states. For tourmaline, energy states include lattice vibrations (phonons) and, in magnetically ordered state, spin waves (magnons). At very low temperatures, limited energy levels for distinguishable particles (e.g., electronic, spin, phonon, or spin waves) can lead to Schottky anomalies (Miller 1988). The thermodynamic heat capacity of a mineral is determined by the average properties of the combined density of states of all thermally excitable energy levels and their occupation (Kieffer 1979).

Third law of Thermodynamics The third law of thermodynamics states that as T→0, the entropy S of a perfect crystal without disorder approaches a common value (Anderson 2005), conventionally set as S(0)=0 J/(K·mol) (Melrose 1970). As T→0, vibrational modes freeze into their ground states, leaving no accessible microstates for phono quasiparticles to distribute upon. This freezing causes both the heat capacity Cp and the vibrational entropy S^{vib} to approach zero. Although the system retains zero-point energy due to quantum mechanical constraints, this energy does not contribute to entropy, ensuring that S^{vib} vanishes. Consequently, the entropy expression $S(T) = \int_0^T \frac{C_p}{T} dT$ converges without indefinition (Gopal 1966). Therefore, to satisfy the third law and ensure accurate entropy calculations, both Cp and S^{vib} must be extrapolated to 0 J/(K·mol) at 0 K.

For perfect crystalline substances, the total entropy $S = S_{\text{vib}} + S_{\text{conf}}$ approaches zero as the crystal exists in a single microstate, where S= $k_B \ln\ \Omega$ and Ω=1. However, in solid solutions, disorder persists at low T, making S^{conf} finite and referred to as residual entropy (Anderson

2005). Since this finite entropy is not measurable by calorimetry unless the disorder can be quenched, e.g. (Benisek and Dachs 2015; Benisek et al. 2023) , it must be estimated using theoretical statistical mechanics, making it dependent on the statistical model used to describe the system.

Collective Excitations and Transitions in Crystals: The Role of Phonons and Magnons in Thermal, Magnetic, and Phase transition behavior

Phonons: Vibrational Contributions The vibrational contribution to heat capacity is modelled using the harmonic approximation, treating thermal vibrations as the superposition of independent quantum mechanical harmonic oscillations, represented by quasiparticles called phonons (Dove 1993). Phonons describe collective atomic vibrations and behave like an ideal gas of non-interacting particles. Key assumptions include the Born-Oppenheimer approximation, where the electronic ground state distribution instantaneously follows nuclear motion, and periodic boundary conditions (Born–van Karman), ensuring Cp remains consistent regardless of unit cell choice (Born and Huang 1954) (i.e., closely linked to the validity of the configurational entropy equation). Quantum mechanics governs energy level spacing, while statistical mechanics defines their occupancy under specific P-T conditions.

Simple lattice dynamic models There are two simple endmember lattice dynamical models for monoatomic solids.

Einstein model (Einstein 1907). In the Einstein model, the solid is treated as a collection of uncoupled linear oscillators, each vibrating at the same frequency, ω_E (the Einstein frequency), neglecting the wave nature of phonons and localizing them on individual atoms. The vibrational density of states (V-DOS) is a delta function: $g(\omega)=3N\delta(\omega-\omega E)$, where N is the number of atoms, and 3N accounts for three degrees of freedom per atom (Navrotsky 1994) . The specific heat capacity C_V is given by: $C_V = 3Nk_B \left(\frac{\hbar\omega_E}{k_B T}\right)^2 \frac{e^{\hbar\omega_E/k_B T}}{\left(e^{\hbar\omega_E/k_B T}-1\right)^2}$, which derives from applying Bose-Einstein statistics to quantum harmonic oscillators, describing the phonon energy level occupancy in a solid as function of temperature. At low temperatures ($T \ll \theta_E$, where $\theta_E = \frac{\hbar\omega_E}{k_B}$, the Einstein temperature), C_V approaches zero exponentially, reflecting the freezing out of

phonon modes. Although the model poorly captures the commonly observed T^3 behavior at low temperatures, it matches experimental data well at higher temperatures.

Einstein model in Polyhedron method Estimation methods like the polyhedron method, which applies the Kopp-Neumann law to polyhedral chemical constituents instead of individual atoms, rely on a simplified Einstein model to predict endmember thermodynamic properties (Holland 1989). However, its linear nature cannot account for interaction effects. For materials with phonons of significantly different frequencies—arising from variations in bonding, atomic masses, or crystallographic directions—a single Einstein frequency is insufficient. Instead, multiple Einstein terms, each with a distinct frequency ω_i can be summed to account for different atomic motions (e.g., along various crystal axes or involving distinct atomic species):

$$C_V = 3k_B \sum_{i=1}^{M} f_i \left(\frac{\hbar\omega_i}{k_B T}\right)^2 \frac{\exp(\hbar\omega_i/k_B T)}{(\exp(\hbar\omega_i/k_B T) - 1)^2}$$

Here, M is the number of distinct Einstein frequencies, fi is the fraction of modes (or effective number of atoms) oscillating at ω_i, and the condition $\sum_{i=1}^{M} f_i = N$ ensures the total number of degrees of freedom is conserved.

Debye model (Debye 1912)**.** The Debye model is a lattice dynamic model that assumes atoms are coupled and vibrate collectively at various frequencies. It treats phonons as elastic waves with a linear dispersion relation $\omega = v_s k$, where v_s is the speed of sound, valid up to the Debye frequency ω_D. The vibrational density of states (V-DOS) is proportional to ω^2 for frequencies below ω_D and zero above it (Stølen and Grande 2004):

$$g(\omega) = \frac{9N}{\omega_D^3}\omega^2 \text{ for } \omega \leq \omega_D$$

The specific heat capacity C_V is given by:

$$C_V = 9Nk_B\left(\frac{T}{\theta_D}\right)^3 \int_0^{\frac{\theta_D}{T}} \frac{x^4 e^x}{(e^x - 1)^2} dx$$

where θ_D is the Debye temperature ($\theta_D = \hbar\omega_D/k_B$), and the integral is over the reduced variable $x = \hbar\omega/k_BT$. The Debye model effectively captures low-temperature heat capacity, influenced by low-frequency acoustic vibrations, with wavelengths much larger than interatomic distances, resembling an elastic continuum (Kieffer 1979). The Debye temperature marks the point where all vibrational modes contribute to the heat capacity. These models are useful for simple structures, but minerals are more complex, composed of discrete atoms and are not monoatomic.

Generalized lattice dynamics model Phonon DOS is derived from dispersion relations obtained by diagonalizing the dynamic matrix, which depends on force constants and e-DOS (Dove 1993). Phonon frequencies, calculated from the dynamic matrix eigenvalues, define acoustic branches with in-phase oscillations, starting at zero and linear at low k, and optical branches with out-of-phase oscillations and nonzero frequencies at the Brillouin zone center but flatter dispersion (Dove 1993). Acoustic branches dominate low frequencies, while optical branches contribute at higher frequencies. Crystal anisotropy splits these branches into one longitudinal and two transverse modes, based on displacement direction relative to the wave vector (Dove 1993). Sampling phonon frequencies across the Brillouin zone and counting states per frequency interval constructs the DOS, representing the number of phonon states per unit frequency, summing contributions from all branches (Kittel and McEuen 2018).

The Born and von Karman lattice dynamics model (Born and Von Kármán 1912) uses the true V-DOS derived from dispersion relations, unlike the simple approximations in basic lattice models. The Cv is given by:

$$C_V = \int_0^\infty k_B \left(\frac{\hbar\omega}{k_BT}\right)^2 \frac{\exp(\hbar\omega/k_BT)}{(\exp(\hbar\omega/k_BT) - 1)^2} g(\omega)d\omega$$

where k_B is the Boltzmann constant, ħ is the reduced Planck's constant, and ω is the angular frequency of the phonons and $g(\omega)$ the phonon density of states. The term $\left(\frac{\hbar\omega}{k_BT}\right)^2$ scales the contribution of each phonon mode by its energy relative to thermal energy, while the Bose-Einstein factor $\frac{\exp(\hbar\omega/k_BT)}{(\exp(\hbar\omega/k_BT)-1)^2}$ accounts for the occupancy of each mode at thermal equilibrium (Miller 1988). High-frequency modes contribute less to C_V due to the exponential suppression, while low-frequency modes dominate at lower temperatures.

Empirical Fits for Low-Temperature Lattice Heat Capacity Models The low-T heat capacity of crystalline solids is modelled using the Debye T^3 law for acoustic phonons, with higher-order anharmonic terms (T^5, T^7) added to account for optical phonons and interactions, expressed as (Rosen and Woodfield 2020):

$$C_{\text{lattice}} = aT^3 + bT^5 + cT^7.$$

For systems with low-energy vibrational gaps in the v-DOS, an exponential term is included:

$$C_{\text{gap}} = B_{\text{gap}} T^m e^{-\frac{\Delta}{T}},$$

where Δ is the gap energy and m is material-dependent (Schliesser and Woodfield 2015). However, our FTIR spectra of tourmaline (chapter 4) do not show any gaps making this an unlikely contribution.

Magnons: Magnetic Contributions Magnetic contributions to heat capacity in tourmalines with open-shell transition metals arise from electron spins. In paramagnetic materials, random spin orientation prevents magnetic heat capacity. In ferromagnetic and antiferromagnetic materials, quantum exchange interactions create ordered spin arrangements. Perturbing a spin propagates disturbances as spin waves, absorbing heat (Gopal 1966). The quantized energy of these waves, called magnons, behaves as bosons and follows Bose-Einstein statistics. Their heat capacity contribution is calculated using the Born and von Karman Cv formula, similar to phonons.

The density of states differs from phonons differing nature of the magnon dispersion relations, influenced by the type of magnetic exchange interactions, magnetic ordering (ferro/antiferromagnetism), and anisotropies. Exchange interactions include: 1) direct exchange from orbital overlap of neighboring atoms, 2) superexchange via intermediaries, 3) double exchange through hopping, 4) dipole-dipole interactions, 5) Dzyaloshinskii-Moriya (DM) interaction from spin-orbit coupling, and 6) frustration, where geometric constraints prevent energy minimisation, leading to noncollinear spin arrangements (Blundell 2001).

Simple magnon dynamics models The magnon contribution to heat capacity (C_V) in ordered magnetic materials is estimated using simplified dispersion models. In ferromagnets, direct

exchange creates a quadratic dispersion with magnon DOS scaling as $\omega^{1/2}$, resulting in $C_V \propto T^{3/2}$ at low-T, described by: $C_V = \beta T^3 + \delta T^{\frac{3}{2}}$, where the T^3 term arises from phonons and β and δ depend on the material (Miller 1988). A plot of $C_V/T_{3/2}$ versus $T^{3/2}$ should appear linear. In antiferromagnets, linear dispersion produces a DOS proportional to ω^2, yielding $C_V \propto T^3$ identical to phonons. Separation from lattice contributions is only feasible in insulators with a Néel temperature much lower than the Debye temperature, indicated by Cp/T versus T^2 plots (Miller 1988). Indirect exchanges (superexchange), double exchange, and frustration alter magnon dispersions, leading to anomalous Cp behavior that deviates from standard $T^{3/2}$ or T^3 laws (Blundell 2001). In anisotropic systems, an exponential spin gap term is added:

$$C_{\text{magnon}} = AT^n + B_{\text{magnon}}\, T^m e^{-\frac{\Delta}{T}}.$$

(Schliesser and Woodfield 2015). These terms capture both collective excitations and localized spin-wave effects, improving accuracy for complex materials

Generalized magnon dynamics model The Heisenberg model describes magnetic interactions in a spin lattice through exchange interactions characterised by J (Tsang et al. 1971). For ferromagnetic systems, isotropic interactions (Jx=Jy=Jz) are assumed with the Hamiltonian:

$$H = -\sum_{\langle i,j \rangle} J_{ij} \mathbf{S}_i \cdot \mathbf{S}_j,$$

where $\mathbf{S}_i$ and $\mathbf{S}_j$ are spin operators at sites i and j, summed over neighboring pairs (Blundell 2001). For antiferromagnetic systems, anisotropic effects are significant, modelled by the Hamiltonian:

$$H = -\sum_{\langle i,j \rangle} \left(J_x S_i^x S_j^x + J_y S_i^y S_j^y + J_z S_i^z S_j^z \right)$$

where Jx,Jy,Jz represent direction-dependent exchange interactions, see Zherebetskyy et al. (2012) for a silicate example. Exchange interactions, from mechanisms like direct, superexchange, or double exchange, contribute individual or get averaged into an effective J

(Geiger et al. 2019). Additional terms, such as Dzyaloshinskii-Moriya or higher-order effects, extend the Heisenberg model for complex magnetism (Blundell 2001).

Magnetic Phase transition At high temperatures, thermal agitation disrupts spin alignments, causing paramagnetic behavior in materials with transition metals. Near the critical temperature, magnetic order-disorder transitions, such as lambda-type singularities in second-order transitions, significantly affect heat capacity. Macroscopic mean field models fit transition curves but simplify by ignoring explicit microscopic interactions. Mean field models like the Weiss molecular field (Weiss 1914), Bragg-Williams approach (Bragg and Williams 1934), and Landau power series expansion (Landau 1937) simplify spin interactions by assuming a field dependent on the system's average magnetic moment (Redfern 2000) . In ferromagnets, the Curie temperature marks the transition to paramagnetism, while in antiferromagnets, the Néel temperature signals antiferromagnetic ordering.

Spin Glass Behavior Spin glasses are magnetic systems with short-range order (SRO) where spins are randomly arranged and interact in a frustrated manner, creating a complex energy landscape (Miller 1988). Unlike ferromagnets (aligned spins) or antiferromagnets (alternating spins) the lack of long-range order and the presence of frustration and disorder in spin glasses result in localized spin wave-like excitations with a broad energy spectrum, reflecting variations in local magnetic environments. Near the spin glass transition temperature, heat capacity peaks as the system can suddenly access a large number of nearly degenerate configurations requiring minimal energy for transitions.

Landau treatment of the (spin glass) magnetic phase transition The linear Cp term at low-T can be explained using Landau phenomenological mean field theory (Landau 1937), which can be seen as a generalisation of the Weiss model for ferromagnetism and the Bragg-Williams model for order-disorder transitions. This theory, applicable to magnetic phase transitions, including spin glass systems, describes critical transitions using the Landau free energy (energy tailored to describe critical transitions) expanded in terms of the order parameter M (magnetization) near the antiferromagnetic Néel temperature (T_N):

$$F(M) = F_0 + \frac{1}{2}a(T)M^2 + \frac{1}{4}bM^4$$

(Landau 1937). Where F_0 is the free energy in the absence of the order parameter, $a(T)$ is a temperature-dependent coefficient and b is a temperature-independent, positive coefficient for stability. For the AFM to PM transition, $a(T)$ changes sign at TN: $a(T) = a_0(T - T_N)$. Minimizing the free energy $\frac{\partial F}{\partial M} = a(T)M + bM^3 = 0$ gives M=0 in the paramagnetic phase ($T>T_N$) and in the AFM phase ($T<T_N$), non-zero solutions for M can be found by solving $M(a(T) + bM^2) = 0$ which gives $M = \sqrt{\frac{a_0(T_N - T)}{b}}$. Substituting M into the Landau free energy equation gives $F \approx F_0 - \frac{a_0^2(T_N - T)^2}{4b}$. Cp is then $C_p = -T\frac{\partial^2}{\partial T^2}\left(-\frac{a_0^2(T_N - T)^2}{4b}\right) = \frac{a_0^2 T}{2b}$ a linear term with T (Landau 1937, pp451, Blundell 2001, pp 115). However, Landau theory oversimplifies, predicting a vertical jump in Cp at T_N, while experiments show a gradual decrease due to short-range spin order not covered by mean field theory (Holland and Powell 1990).

Localized States and Specific Heat: Understanding the Schottky Anomaly in Paramagnetic Materials

Schottky anomaly A Schottky anomaly in specific heat (Cp) arises from thermal excitations of distinguishable particles between two discrete, non-degenerate energy levels, often observed in systems with localized electronic or spin states where internal fields lift degeneracies (Miller 1988). Localized states, created by impurities, defects, or strong electron-electron interactions within the valence band near the band gap, become thermally populated at low temperatures when thermal energy matches the energy gap (Δ). This reduces the system to an effective two-level state, as most energy levels are "frozen out". These energy levels can include electronic, spin, phonon, or magnon states, (Rosen and Woodfield 2020), but a two-level system is rare for phonons and magnons due to their nonlocal, collective excitations and continuous low-temperature DOS. Schottky theory assumes independent ions, making it suitable for localized electronic or spin states in paramagnetic materials, where weak spin-spin coupling and internal fields create discrete energy levels. It also applies to magnetic impurities, which introduce localized states, unlike magnetically ordered systems with collective excitations. In this idealized two-level system, the DOS consists of two delta functions at the energy levels, simplifying analysis. The heat capacity contribution is modelled as:

$$C_p = R\left(\frac{\Delta}{T}\right)^2\left(\frac{g_0}{g_1}\right)\frac{\exp\left(\frac{\Delta}{T}\right)}{\left[1+(g_0+g_1)\exp\left(\frac{\Delta}{T}\right)\right]^2}$$

(Gopal 1966). Here, R is the gas constant, and g0 and g1 are ground and excited states degeneracies. The introduction of more energy levels would significantly increase the complexity of the analysis. Since Cp is an integrative property, it does not directly reveal specific energy levels, their separations, or degeneracies. Theoretical models and experimental techniques like spectroscopy and magnetic susceptibility are needed to interpret Schottky Cp data accurately. The Schottky anomaly peak occurs at a temperature approximately equal to Δ/kB (Stølen and Grande 2004), providing an indirect method to estimate the energy gap, but other level interactions or degeneracies can shift the peak slightly. The peak height reflects the degeneracies of the states involved (Gopal 1966). At temperatures much lower than Δ/kB , Cp increases exponentially as $C_p \propto \exp\left(-\frac{\Delta}{k_B T}\right)$, while at temperatures much higher than Δ/k_B , it follows a T^{-2} decay as the population difference between levels diminishes (Miller 1988).

If the Schottky anomaly occurs between 2-5 K, it dominates Cp since its magnitude is on the order of R, much larger than lattice or electronic contributions (10^{-2}) (Miller 1988). Even in magnetically ordered systems with magnons, the anomaly can still be resolved. At higher temperatures, separating the Schottky anomaly from magnetic or lattice contributions becomes difficult, but comparison with similar structures lacking the anomaly can help. Below 2 K, the high-temperature tail of the anomaly is modelled with bT^3(phonon) +DT^{-2} (Schottky), and a CpT^2 versus T^5 plot yields a straight line (Miller 1988).

Schottky anomalies can arise from electron hopping between Fe^{2+} and Fe^{3+} ions, where electrons transition between oxidation states, creating discrete energy levels. Thermal excitation at low temperatures populates these states, producing a characteristic heat capacity peak associated with the tunneling energy gap (Miller 1988).

Experimental Distinctions Between Schottky Anomalies and Magnetic Phase Transitions

Experimental distinctions between a Schottky anomaly and a magnetic phase transition include the sensitivity to external magnetic fields and the type of complementary measurements. In a

magnetic phase transition, Cp behavior is field-dependent, with shifts in critical temperature or changes in the anomaly magnitude; In contrast, a Schottky anomaly remains largely unaffected by magnetic fields unless they significantly alter the local energy levels (López et al. 2002). Magnetic transitions can be further confirmed with susceptibility or magnetization measurements, which show peaks or changes at the transition temperature, often with critical scaling or hysteresis during heating and cooling, e.g. (Filip et al. 2008). Additionally, low-temperature neutron diffraction reveals the long-range magnetic order.

REFERENCES

Anderson, G.M. (2005) Thermodynamics of natural systems, 2nd ed., 648 p. Cambridge University Press, Cambridge.

Benisek, A., and Dachs, E. (2015) The vibrational and configurational entropy of disordering in Cu3Au. Journal of Alloys and Compounds, 632, 585–590.

Benisek, A., Dachs, E., Carpenter, M.A., Joachim-Mrosko, B., Vielreicher, N.M., and Wildner, M. (2023) Vibrational entropy of disordering in omphacite. Physics and Chemistry of Minerals, 50, 36.

Blundell, S. (2001) Magnetism in condensed matter, 238 p. Oxford University Press, Oxford.

Born, M., and Huang, J. (1954) The Dynamical Theory of Crystal Lattices, 420 p. Clarendon, Oxford.

Born, M., and Von Kármán, T. (1912) Über schwingungen in raumgittern. Physikalishe Zeitschrift, 13, 297–309.

Bragg, W.L., and Williams, E.J. (1934) The effect of thermal agitation on atomic arrangement in alloys. Proceedings of the Royal Society of London. Series A, Containing Papers of a Mathematical and Physical Character, 145, 699–730.

Debye, P. (1912) Zur Theorie der spezifischen Wärmen. Annalen der Physik, 344, 789–839.

Dove, M.T. (1993) Introduction to the theory of lattice dynamics, 258 p. Cambridge University Press, Cambridge.

Einstein, A. (1907) Die Plancksche Theorie der Strahlung und die Theorie der spezifischen Wärme. Annalen der Physik, 327, 180–190.

Filip, J., Dachs, E., Tucek, J., Novak, M., and Bezdicka, P. (2008) Low-temperature calorimetric and magnetic data for natural end-members of the axinite group. American Mineralogist, 93, 548–557.

Ganguly, J. (2008) Thermodynamics in Earth and Planetary Sciences, 501 p. Springer International Publishing, Berlin.

Geiger, C.A., Grodzicki, M., and Dachs, E. (2019) An analysis of the magnetic behavior of olivine and garnet substitutional solid solutions. American Mineralogist, 104, 1246–1255.

Gopal, E. (1966) Specific heats at low temperatures, 240 p. Heywood Books, London.

Holland, T.J. (1989) Dependence of entropy on volume for silicate and oxide minerals; a review and predictive model. American Mineralogist, 74, 5–13.

Holland, T.J.B., and Powell, R. (1990) An enlarged and updated internally consistent thermodynamic dataset with uncertainties and correlations: the system K2O–Na2O–CaO–MgO–MnO–FeO–Fe2O3–Al2O3–TiO2–SiO2–C–H2–O2. Journal of metamorphic Geology, 8, 89–124.

Kieffer, S.W. (1979) Thermodynamics and lattice vibrations of minerals: 1. Mineral heat capacities and their relationships to simple lattice vibrational models. Reviews of Geophysics, 17, 1–19.

Kittel, C., and McEuen, P. (2018) Introduction to solid state physics, 8th ed., 692 p. John Wiley & Sons, Singapore.

Landau, L.D. (1937) On the theory of phase transitions. Zhurnal Eksperimental'noi i Teoreticheskoi Fiziki, 7, 926.

López, J., De Lima, O.F., Lisboa-Filho, P.N., and Araujo-Moreira, F.M. (2002) Specific heat at low temperatures and magnetic measurements in Nd0.5Sr0.5MnO3 and R0.5Ca0.5MnO3 (R = Nd , Sm, Dy, and Ho) samples. Physical Review B, 66, 214402.

Melrose, M.P. (1970) Statistical mechanics and the third law. Journal of Chemical Education, 47, 283.

Miller, A.P. (1988) Theory of Specific Heat of Solids. In CINDAS Data Series, Vol.I-2, Specific Heat of Solids pp. 1–89. Hemisphere Publishing Corporation, New York.

Navrotsky, A. (1994) Physics and chemistry of earth materials, 413 p. Cambridge University Press, Cambridge.

Redfern, S.A. (2000) Order-disorder phase transitions. Reviews in Mineralogy and Geochemistry, 39, 105–133.

Rosen, P.F., and Woodfield, B.F. (2020) Standard methods for heat capacity measurements on a quantum design physical property measurement system. The Journal of Chemical Thermodynamics, 141, 105974.

Schliesser, J.M., and Woodfield, B.F. (2015) Lattice vacancies responsible for the linear dependence of the low-temperature heat capacity of insulating materials. Physical Review B, 91, 024109.

Stølen, S., and Grande, T. (2004) Chemical thermodynamics of materials: macroscopic and microscopic aspects, 395 p. John Wiley & Sons, Chichester.

Tsang, T., Thorpe, A.N., and Donnay, G. (1971) Magnetic susceptibility and triangular exchange coupling in the tourmaline mineral group. Journal of Physics and Chemistry of Solids, 32.7, 1441–1448.

Weiss, M.P. (1914) Sur la nature du champ moléculaire. Annales de physique, 9, 134–162.

Zherebetskyy, D., Lebernegg, S., Amthauer, G., and Grodzicki, M. (2012) Magnetic structure of almandine. Physics and Chemistry of Minerals, 39, 351–361.

Appendix 3B. Theoretical framework Calorimetry

Relaxation calorimetry Theory (Dachs and Bertoldi 2005; Rosen and Woodfield 2020)**.** Relaxation calorimetry with a Quantum Design PPMS uses a relaxation method to measure heat capacity by monitoring the temperature of a small sample with a short relaxation time to a heat sink when the heater is switched off. relaxation curves are measured by heating the sample with a controlled heat pulse and monitoring its exponential temperature decay (Dachs and Bertoldi 2005). Heat capacity is determined from the time constant of the exponential temperature decay, allowing precise measurements between 2.5 K to 298 K, referred to as the lowT-Cp signal.

The following description of the relaxation calorimetry method is a summary of what is more extensively described in Dachs and Bertoldi (2005) and Dachs and Geiger (2006): The process begins with an addenda measurement to account for the heat capacity of the sample platform and components like Apiezon N grease. The platform's temperature response to a heat pulse is modelled with a one-tau (τ) model using the energy balance equation:

$$c_{\mathrm{pl}} \frac{dT_{\mathrm{p}}(t)}{dt} = P_{\mathrm{in}}(t) - K_w\big(T_{\mathrm{pl}}(t) - T_b\big)$$

where c_{pl} is the platform heat capacity, Pin(t) is input power, K_w is the thermal conductance of wires, and $T_{pl}(t)$ and T_b are platform and bath temperatures, respectively. The platform's temperature rise and relaxation are fitted to an exponential function, yielding the time constant τ:

$$\tau = \frac{c_{\mathrm{pl}}}{K_w}$$

The sample measurement uses the two-tau model to account for thermal interactions between the platform and the sample. The heat capacities of both components are considered, with the thermal response described by two coupled equations:

$$c_{\mathrm{pl}} \frac{dT_{\mathrm{p}}(t)}{dt} = P_{\mathrm{in}}(t) - K_w\big(T_{\mathrm{pl}}(t) - T_b\big) - K_g\left(T_{\mathrm{pl}}(t) - T_s(t)\right)$$

for the platform, and

$$c_s \frac{dT_x(t)}{dt} = K_g \left(T_{\mathrm{pl}}(t) - T_s(t) \right)$$

for the sample, where cs is the sample's heat capacity, K_g is the thermal conductance due to the grease, and Ts(t) is the sample temperature.

By eliminating Ts(t), a second-order differential equation describes the temperature response during heater-on and heater-off periods. The analytical solutions are:

$$T_{\mathrm{on}}(t) = T_b + \frac{P_0}{K_w} + \frac{P_0}{2\beta K_w} \left(e^{-\frac{t}{\tau_2}} - e^{-\frac{t}{\tau_1}} \right) \text{ for } 0 \le t \le t_0$$

$$T_{\mathrm{off}}(t) = T_b + \frac{4\beta P_0}{K_w} \left(\frac{e^{-(t-t_0)//_2} - e^{-\left(t-t_{t_0}\right)//_1}}{2 - \frac{1}{\beta}\left(e^{-t_0/e_2} - e^{-t_0/\tau_1}\right)} \right) \text{ for } t > t_0$$

where τ1 and τ2 are the time constants:

$$\tau_1 = \frac{1}{\alpha - \beta}, \tau_2 = \frac{1}{\alpha + \beta},$$

with:

$$\alpha = \frac{c_{\mathrm{pl}}}{K_g} + \frac{c_s}{K_g} + \frac{c_{\mathrm{p}} c_s}{K_w}, \beta = \sqrt{\alpha^2 - \frac{4 c_{\mathrm{p}} c_s}{K_w}}.$$

This model enables precise heat capacity determination by fitting temperature responses to these equations using nonlinear least-square fitting routines.

During low-temperature magnetic first-order order-disorder phase transitions, significant heat capacity peaks and critical fluctuations may disrupt stable heat flow dynamics, leading to deviations from exponential decay (Lashley et al. 2003). These transitions may also face challenges from internal equilibration times, reducing model accuracy for precise heat capacity values near critical regions (Rosen and Woodfield 2020). Fortunately, in our case we have second order phase transitions which do not have such sharp features.

DSC theory DSC measures the differential heat flow (ΔQ) between sample and reference pans during temperature scanning, directly correlating to the sample's heat capacity (Mraw 1988). Independent heaters on a common heat sink maintain a constant temperature difference, monitored by thermocouples, and the power-compensated DSC adjusts the heater power to maintain temperature equilibrium. The differential heat flow is described as: $\frac{dQ_s}{dt} - \frac{dQ_r}{dt} = \frac{dT}{dt}\left(C_{p,s} - C_{p,r}\right)$, where $C_{p,s}$ and $C_{p,r}$ are the heat capacities and Q_s and Q_r are the powers supplied to the respective pans of the sample and reference. The reference chamber remains constant empty pan, while the sample chamber can be empty, contain a reference material, or hold the sample (Höhne et al. 2003). After dynamic equilibrium is reached ($\frac{dT}{dt} = \frac{dT_s}{dt} = \frac{dT_r}{dt}$), user-defined scan rate), the sample temperature lags behind the thermometer due to platform and pan thermal resistance, scan rate, and R×ΔT, causing minor horizontal shifts in the Cp curve (a few tenths of Kelvin) (Mraw 1988), which are negligible except during transitions, absent for tourmaline. Consistent use of cooling bath, purge gas, and sample pans ensures uniform temperature lag for blank, reference and sample and its effect mostly removed with the black subtraction.

DSC Instrumental drift correction Figures

Heat flow versus time signal of the DSC before and after drift correction. See main text for details.

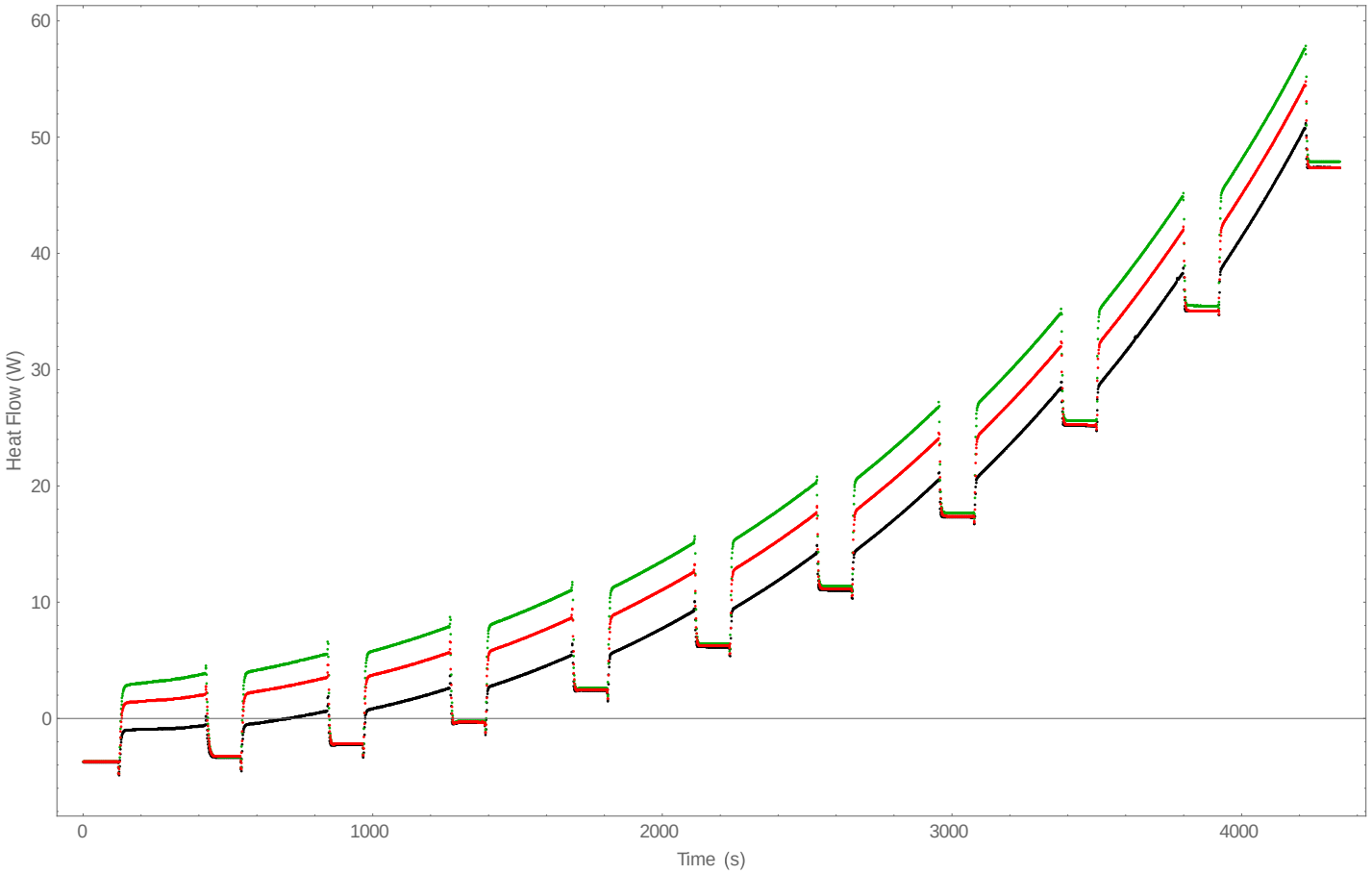

Figure A3B.1. DSC signal before drift correction. Isothermal sections should be the same for blank (black), reference (green) and sample (red). The fact they are not the same indicates instrumental drift.

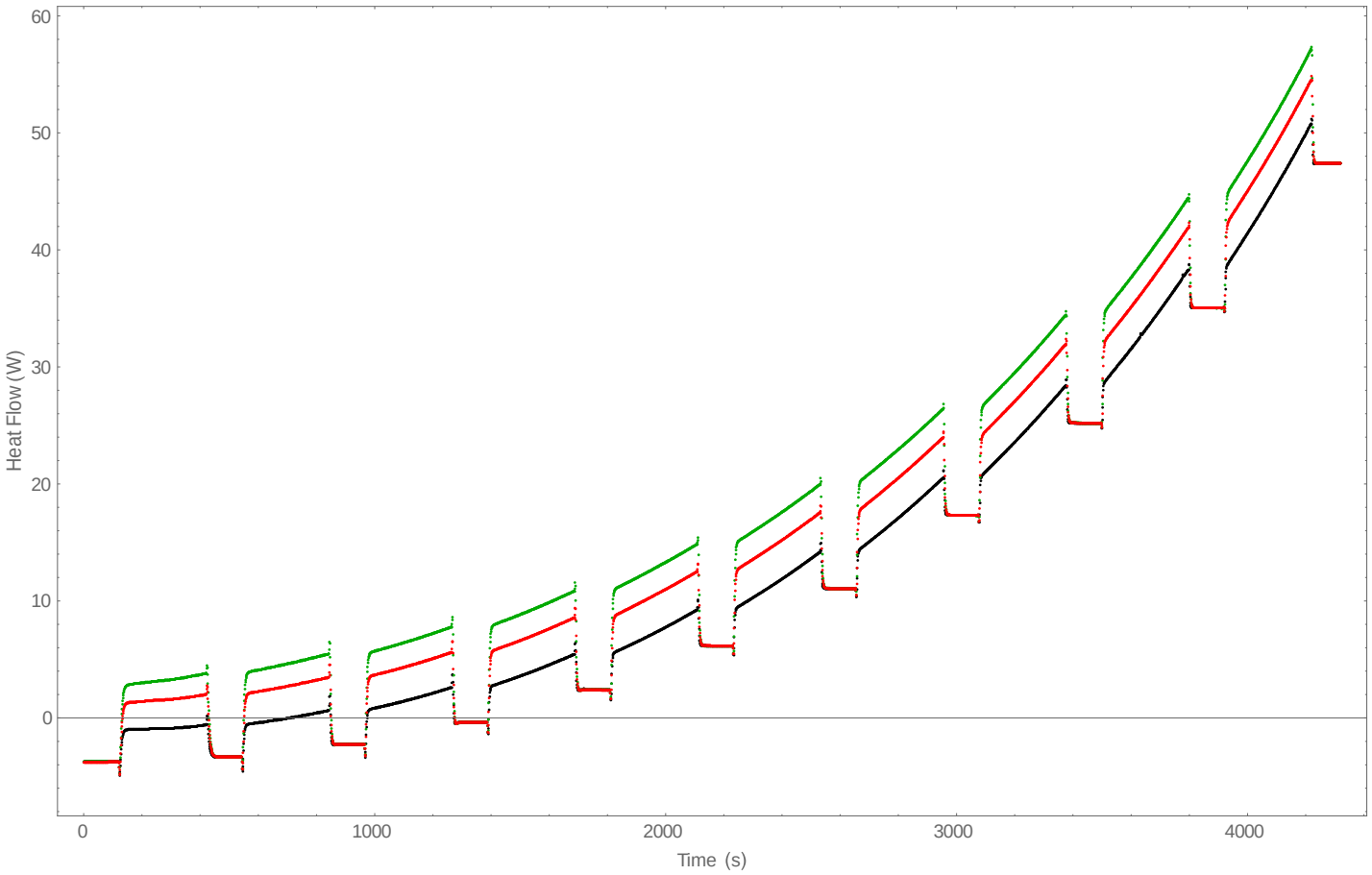

Figure A3B.2. DSC signal after drift correction. Isotermal sections are made the same for blank (black), reference (green) and sample (red).

REFERENCES

Dachs, E., and Bertoldi, C. (2005) Precision and accuracy of the heat-pulse calorimetric technique low-temperature heat capacities of milligram-sized synthetic mineral samples. European Journal of Mineralogy, 17, 251–261.

Dachs, E., and Geiger, C.A. (2006) Heat capacities and entropies of mixing of pyrope-grossular (Mg3Al2Si3O12-Ca3Al2Si3O12) garnet solid solutions: A low-temperature calorimetric and a thermodynamic investigation. American Mineralogist, 91, 894–906.

Höhne, G.W.H., Hemminger, W.F., and Flammersheim, H.-J. (2003) Differential Scanning Calorimetry. Springer, Berlin, Heidelberg.

Lashley, J.C., Hundley, M.F., Migliori, A., Sarrao, J.L., Pagliuso, P.G., Darling, T.W., Jaime, M., Cooley, J.C., Hults, W.L., Morales, L., and others (2003) Critical examination of heat capacity measurements made on a Quantum Design physical property measurement system. Cryogenics, 43, 369–378.

Mraw, S.C. (1988) Differential scanning calorimetry. In CINDAS Data Series, Vol.I-2, Specific Heat of Solids pp. 395–435. Hemisphere Publishing Corporation.

Rosen, P.F., and Woodfield, B.F. (2020) Standard methods for heat capacity measurements on a quantum design physical property measurement system. The Journal of Chemical Thermodynamics, 141, 105974.

Appendix 3C. Magnetic Spin Glass Transition Proof The magnetic structure of tourmaline, particularly its variation across the solid solution, remains poorly understood. Magnetic susceptibility measurements show that buergerite, Fe^{2+} and Fe^{3+} rich schorl at first order can be analysed using the Heisenberg spin-exchange model. Strong crystal field quenching in high-spin Fe^{3+} (d^5, S=5/2) and the dominance of spin-allowed Fe^{2+} (d^6, S=2) transitions in optical spectroscopy (Mattson and Rossman 1987; Altieri et al. 2022) indicate suppressed orbital contributions due to quenching and lifted orbital degeneracy, respectively. This leaves primarily spin-driven magnetic interactions for both valence states. A single exchange constant J is used to describe both Fe^{3+} and Fe^{2+} interactions, a simplification, as $^{VI}Fe^{2+}$ is sensitive to Jahn-Teller distortions and crystal field effects. The Heisenberg Hamiltonian $\mathcal{H} = -\sum_{\langle i,j \rangle} J_{ij} \mathbf{S}_i \cdot \mathbf{S}_j$, captures short-range magnetic exchange. Y-Y, Z-Z, and Y-Z pathways correspond to the exchange constants J, J′, and J″, respectively. More theoretical detail can be found in Appendix 3A.

In buergerite weak magnetic anisotropy and dominant Y-Y exchange (J/kB=7.5 K (Tsang et al. 1971) up to J/kb ~ 20 K (Mattson and Rossman 1984)) govern short-range antiferromagnetic interactions (Weiss T ~ -100 K). The inability to fit high- and low-T susceptibility with a single J reflects site or cluster dependent interactions and model fits improve when an additional weaker J exchange is added (Tsang et al. 1971; Mattson and Rossman 1984). In Fe^{2+} -rich schorl, the magnetic susceptibility is anisotropic, likely due to exchange anisotropy and/or Jahn-Teller distortions of Fe^{2+} in Y or Z sites. The average exchange J^{avg}/kB and combined strength (2J′+J″)/kB≈8 K provide a good fit to the data (Tsang et al. 1971). In Fe^{3+} rich schorl with minor Y-site Fe^{2+} the susceptibility is again isotropic, and the simultaneous fit to both schorls led to J/kB=7.5 K, J′/kB=1 K, and J″/kB=6K. In both schorls, the Curie-Weiss T θ θ=+9 K indicates weak ferromagnetic or frustrated antiferromagnetic coupling. This simplified framework, with uncertain site occupancy due to a lack of structural measurements for the schorls, qualitatively suggests multiple pathways, with J's Y-Y > Z-Z >Y-Z (Tsang et al. 1971).

A single neutron powder diffraction measurement at 4.2 K confirms the absence of magnetic LRO in buergerite down to 4.2 K, attributing this to geometric frustration within the triangular Y-site lattice and weak inter-triangle coupling, which confine interactions to short-range order and suppress magnetic coherence and preventing a single antiferromagnetic ground state (Tippe and Hamilton 1971).

Using well-characterised samples, Fillip et al. (2012), demonstrated the effect of disorder. Untreated schorl has a low Curie constant Cmol=13.2 emuK/molOe and a Weiss T θ=−32 K, indicating moderate antiferromagnetic interactions, while fully oxidized at 700C under air shows a larger Curie constant (172.5 emuK/molOe) and more negative θ=−165 K, reflecting stronger antiferromagnetic coupling. These results align with Tsang et al. (1971) and Mattson and Rossman (1984), for schorl and buergerite. The heated schorl, treated at 700°C under reduction, retains a similar Fe^{3+}/Fe^{2+} ratio but with increased disorder, maintaining a weak Curie constant Cmol=20.1 emuK/molOe, but an extreme θ=−592 K. The small Curie constant indicates weak or sparse magnetic moments, while the large negative Weiss T point to strong short-range antiferromagnetic interactions, due to frustration. Hysteresis loops at 2 K (-70 to +70 kOe) show narrow, symmetric loops with negligible coercivity, confirming antiferromagnetic behavior in all samples. Minimal differences between the untreated and heated reduced samples were observed, whereas the fully oxidized sample shows low-field saturation, reflecting reduced frustration and easier spin alignment.

The pronounced decrease in Mössbauer peak width from 298 K to 5 K in ferric-rich tourmaline is attributed to enhanced cross-relaxation between Fe^{3+} and Fe^{2+} ions at low T (Mattson and Rossman 1984). Energy transfer from Fe^{3+} to Fe^{2+}, which relaxes rapidly via spin-lattice mechanisms, narrows the peaks. This effect is not structural or compositional, as indicated by T-independent quadrupole splitting and the absence of broad peaks. Instead, it is driven by stronger Fe^{2+}-Fe^{3+} interactions at lower T, supported by intensified Fe^{2+} optical absorption bands under similar conditions (Mattson and Rossman 1984, 1987).

Additional unpublished 5 K Mössbauer spectra of Fe-rich tourmalines from the thesis of Saegusa (1978) (Figure A3C.1) reveal a magnetic sextet, indicating magnetic ordering at low T, though the influence of magnetic inclusions cannot be excluded.

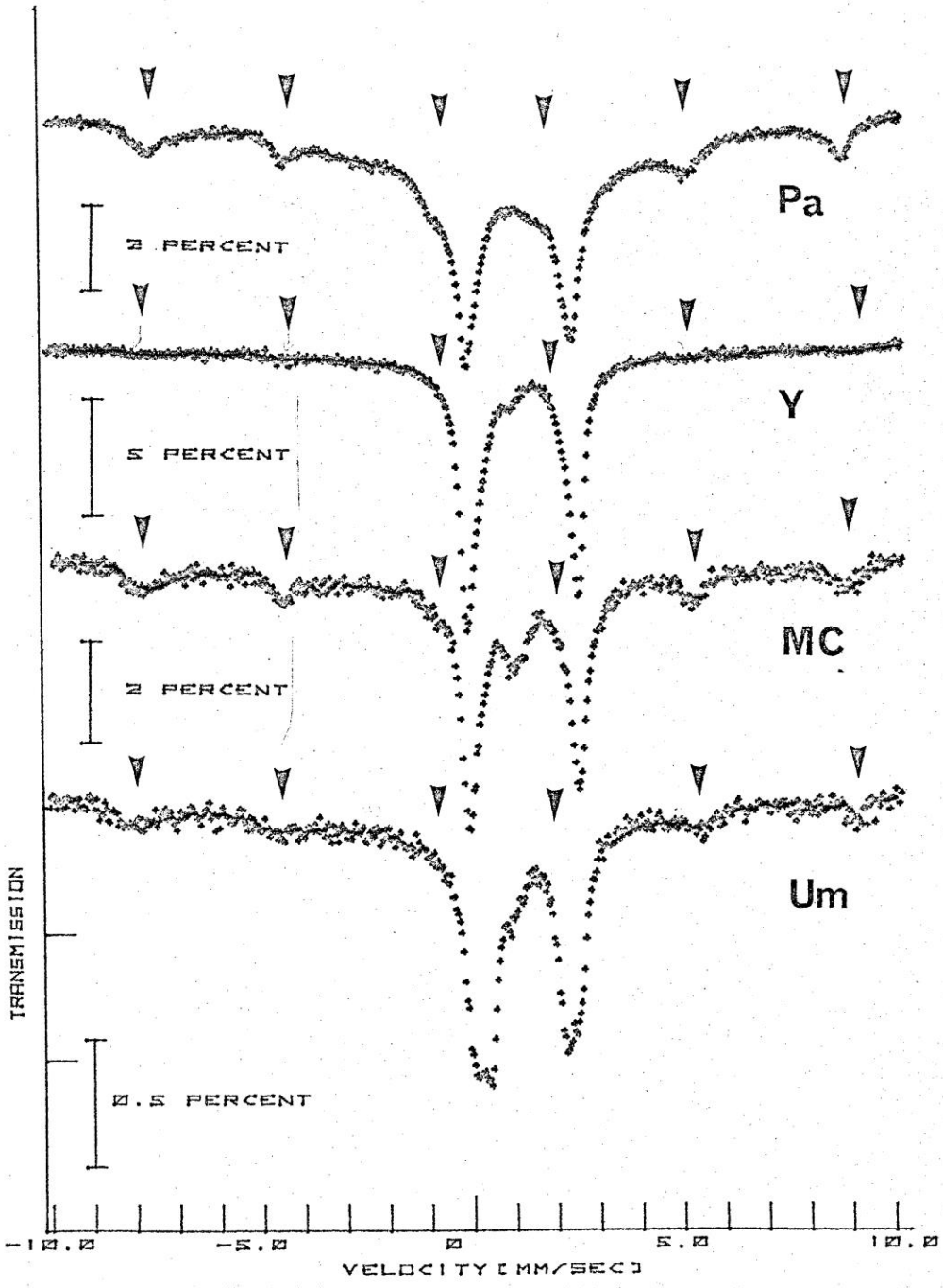

fig. 4.18. Mössbauer spectra of samples UM, MC, Y and Pa at 10K in larger velocity scale. Arrows indicate the positions of magnetic hyperfine spectrum.

Figure A3C.1. Mössbauer spectra of tourmaline samples Pa (Fe: 2.73 apfu), Y (Fe: 1.92 apfu), MC (Fe: 0.795 apfu), and UM (Fe: 0.6 apfu). Downward-pointing arrays indicate a magnetic sextet, possibly from magnetic ordering in tourmaline at 5 K. However magnetic inclusions can also be the culprit. Figure (4.18) and sample spectra from thesis of Saegusa (1978).

Optical spectroscopy in the paramagnetic state reveals short-range interactions, with Fe^{3+}-rich schorl showing intensified Fe^{2+}-Fe^{3+} interactions, where Fe^{2+} absorption bands are enhanced by Fe^{3+} without new visible Fe^{3+} bands (Mattson and Rossman 1987). Strong polarization effects, particularly in the E⊥c direction, distinguish site-specific interactions (e.g., trimer or helical Y-Z configurations). Ferric tourmalines also lack Fe^{3+} bands and exhibit intense absorption bands at 485 nm (E⊥c) and 540 nm (E∥c), attributed to Fe^{3+}-Fe^{3+} ion-pair interactions within Y-Y trimer and helix sites, driven by antiferromagnetic exchange (Mattson and Rossman 1984). The exchange spectra, particularly for Fe^{2+}-Fe^{3+}, are P- and T-dependent (Taran and Rossman 2002). A caveat to tourmaline's spectroscopic analysis is its reliance on accurate spectral fitting, complicated by overlapping optical and Mössbauer features. Optical and Mössbauer studies at 5 K are needed to assess whether these exchange interactions persist or intensify at low T.

The Cp anomaly indicates a magnetic spin glass phase transition, driven by short-range antiferromagnetic interactions, geometric frustration, and localized spin dynamics (Tippe and Hamilton 1971; Tsang et al. 1971; Filip et al. 2012). The magnetism arises from strong Y, secondary Z-site coupling, and weak Y-Z interactions. Trigonal symmetry and weak triangle-helix connections prevent long-range order, with the overall response reflecting localized exchanges. The analysis of the frustrated spin glass is complicated by the superposition of SRO clusters each with variations in Fe ratios, non-magnetic substitutions, and spatial arrangements, creating distinct exchange strengths and non-linear effects. In addition, phonon- or photon-activated Fe^{2+}-$Fe^{3+}$and Fe^{3+}- Fe^{3+} interactions, introduces dynamic effects and site-specific variability. Spin-glass behavior significantly affects S^0 in tourmaline, and many solid solutions with dilute Fe may exhibit this effect, making it crucial to account for in thermodynamic models.

The origin of the second Cp peak in F-buergerite around 2.5 K is uncertain. One possibility is staggered magnetic spin glass transitions on distinct octahedral sites. Alternatively, it could be a Schottky anomaly from thermal excitations between discrete energy levels, such as electronic or

spin states (see Appendix 3A). This is consistent with the 2–5 K range and peak magnitude, which aligns with the order of R. Potential mechanisms include electron hopping between Fe^{2+} and Fe^{3+} ions or energy level splitting due to internal magnetic fields. Differentiating a Schottky anomaly from a magnetic phase transition requires complementary techniques, such as Cp analysis under a magnetic field, since Schottky peaks are largely field-independent, unlike magnetic transitions. (Blundell 2001).

REFERENCES

Altieri, A., Pezzotta, F., Skogby, H., Hålenius, U., and Bosi, F. (2022) Blue growth zones caused by Fe2+ in tourmaline crystals from the San Piero in Campo gem-bearing pegmatites, Elba Island, Italy. Mineralogical Magazine, 86, 910–919.

Blundell, S. (2001) Magnetism in condensed matter, 238 p. Oxford University Press, Oxford.

Filip, J., Bosi, F., Novák, M., Skogby, H., Tuček, J., Čuda, J., and Wildner, M. (2012) Iron redox reactions in the tourmaline structure: High-temperature treatment of Fe3+-rich schorl. Geochimica et Cosmochimica Acta, 86, 239–256.

Mattson, S.M., and Rossman, G.R. (1984) Ferric iron in tourmaline. Physics and Chemistry of Minerals, 11, 225–234.

——— (1987) Fe2+-Fe3+ interactions in tourmaline. Physics and Chemistry of Minerals, 14, 163–171.

Saegusa, N. (1978) Mossbauer Study of Tourmaline. PhD Thesis, Australian National University.

Taran, M.N., and Rossman, G.R. (2002) High-temperature, high-pressure optical spectroscopic study of ferric-iron-bearing tourmaline. American Mineralogist, 87, 1148–1153.

Tippe, A., and Hamilton, W.C. (1971) A neutron-diffraction study of the ferric tourmaline, buergerite. American Mineralogist, 56, 101–113.

Tsang, T., Thorpe, A.N., and Donnay, G. (1971) Magnetic susceptibility and triangular exchange coupling in the tourmaline mineral group. Journal of Physics and Chemistry of Solids, 32.7, 1441–1448.

Appendix 3D. Method 2 Bulk and Speciation Model

1. BULK COMPOSITIONAL MODEL: ENTROPY AT 298 K (METHOD 2)

Method 2 derived endmember entropies OLS regression a set of sample entropies obtained prior via integration over T of the linear interpolation low-T Cp sample curves, minimizing sensitivity to low-T Cp variations while yielding a robust regression model, i.e., R_{Press}^2=0.87. The details of the regression, done in NCSS, can be found in the end of the Appendix. The model achieved an MSE of 41.62 higher than the better fit obtained by regressing the low-T Cp curves directly (MSE=32.8). Residuals followed a normal distribution.

SrlB (718.48 J/mol·K) and drvB (632.97 J/mol·K) were the most critical endmembers, with their correlated Fe-Mg exchange (r=−0.82) explaining most of the variance (R^2=0.88) underscored by strong positive and negative correlations of entropy with srlB (+0.88) and drvB (−0.79), respectively. Other endmembers, such as uvtB (647.22 J/K·mol), foiB (658.77 J/K·mol), and oleB (608.38 J/K·mol), play secondary roles

Influential observations such as the synthetics, F-buergerite (tm64) and Fe^{3+} rich tourmalines exhibit high leverage and residuals, respectively, significantly impacting predictions. Figure A3D.1 illustrates the internal validation of Method 2, comparing measured versus predicted entropy using both the standard error (SE) of the confidence interval (CI) and the SE of the prediction interval (PI). The LOOCV indicate F-buergerite and synthetic uvite predictions diverging significantly from the rest of the dataset.

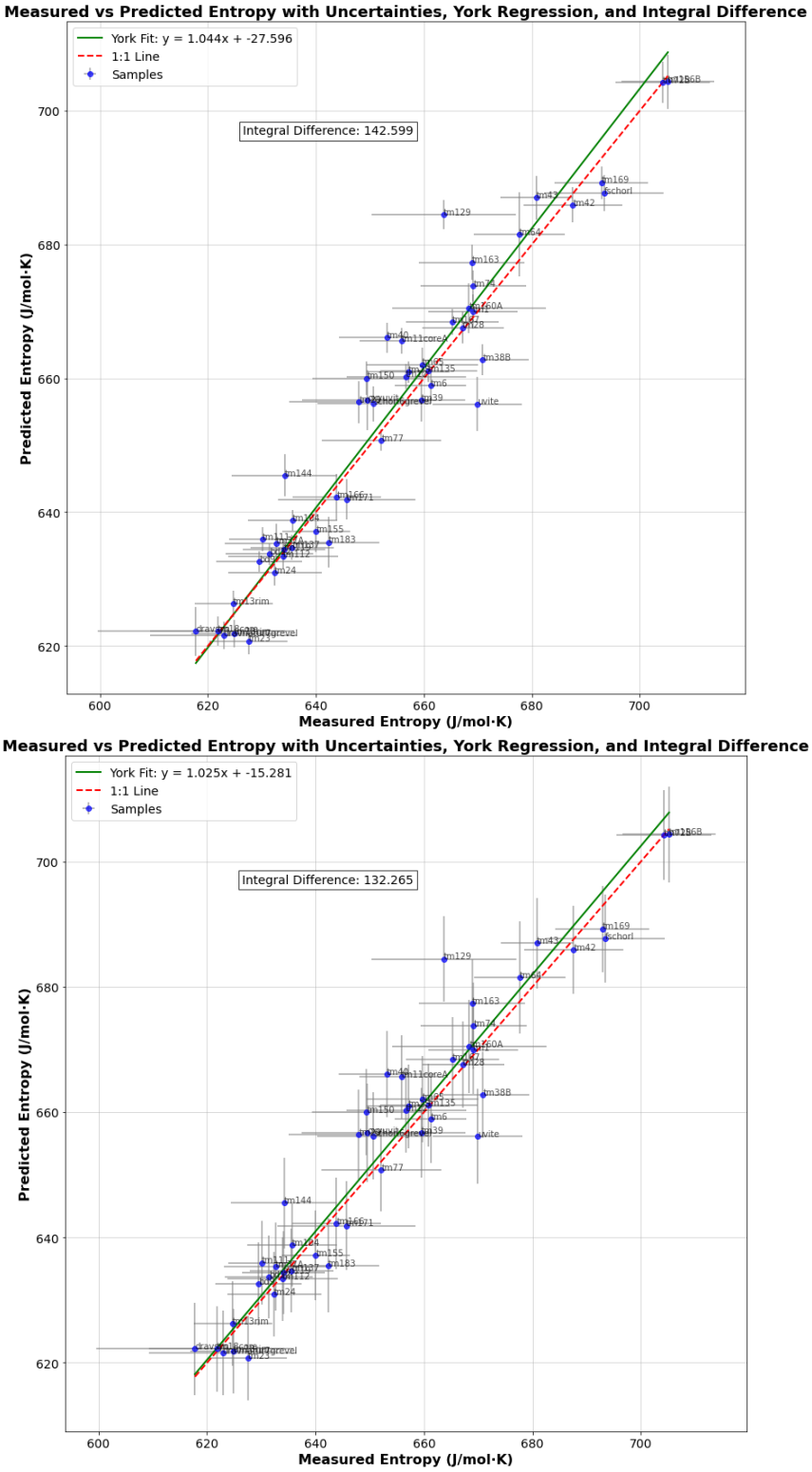

Figure A3D.1. Measured versus predicted entropy using Method 2. A) using the SE of the confidence interval. B) using the SE of the prediction interval.

Comparing Figure 3Q and Figure A3D.1. shows that Method 1 provides a superior fit, with lower MSE and reduced compositional bias measured by the integral between the York fit and the 1:1 line, whether using confidence or prediction interval standard errors. We recommend regression on the low-T Cp curve followed by integration, as it allows Cp and entropy predictions below 298.15 K and improves training set fits. However, without a test set, potential overfitting cannot be ruled out, potentially making Method 1 less reliable for low-T Cp predictions far from the calibration set, where robust methods such as performing the regression on the S^0 directly might perform better.

2. BULK COMPOSITIONAL MODEL: $S_{298.15K}^{773.15\,K}$ (METHOD 2)

We performed an OLS regression on the vibrational entropy gained prior by integrating Cp/T from 298.15 K to 773.15 K, ignoring S_o and S^{conf}, equivalent to Method 2 low-T Cp regression. SrlB and drvB maintain a strong negative correlation (-0.82), while other endmember correlations vanish, and no endmember fractions correlate with $S_{298.15K}^{773.15\,K}$, consistent with Dulong-Petit behavior. Endmembers with X and V site vacancies, like foiB, aorsmB, and buB, show lower integrated Cp values, with Fe^{3+}-rich buB having the lowest and Fe^{2+}-rich srlB the highest, reflecting limited phonon excitation of high-frequency OH vibrations in OH-poor tourmaline. Outlier diagnostics highlight influential points, notably F-buergerite (tm64), impacting regression coefficients. DrvB emerges as the primary source of variance, with hierarchical subset selection confirming no excess Cp above 298.15 K. In contrast to low-T Cp, the measured versus predicted plot demonstrates that Method 1 and Method 2 yield identical results, indicating that the order of integration and regression does not affect the outcome. This consistency likely arises from the smooth and less variable nature of the high-T Cp curve.

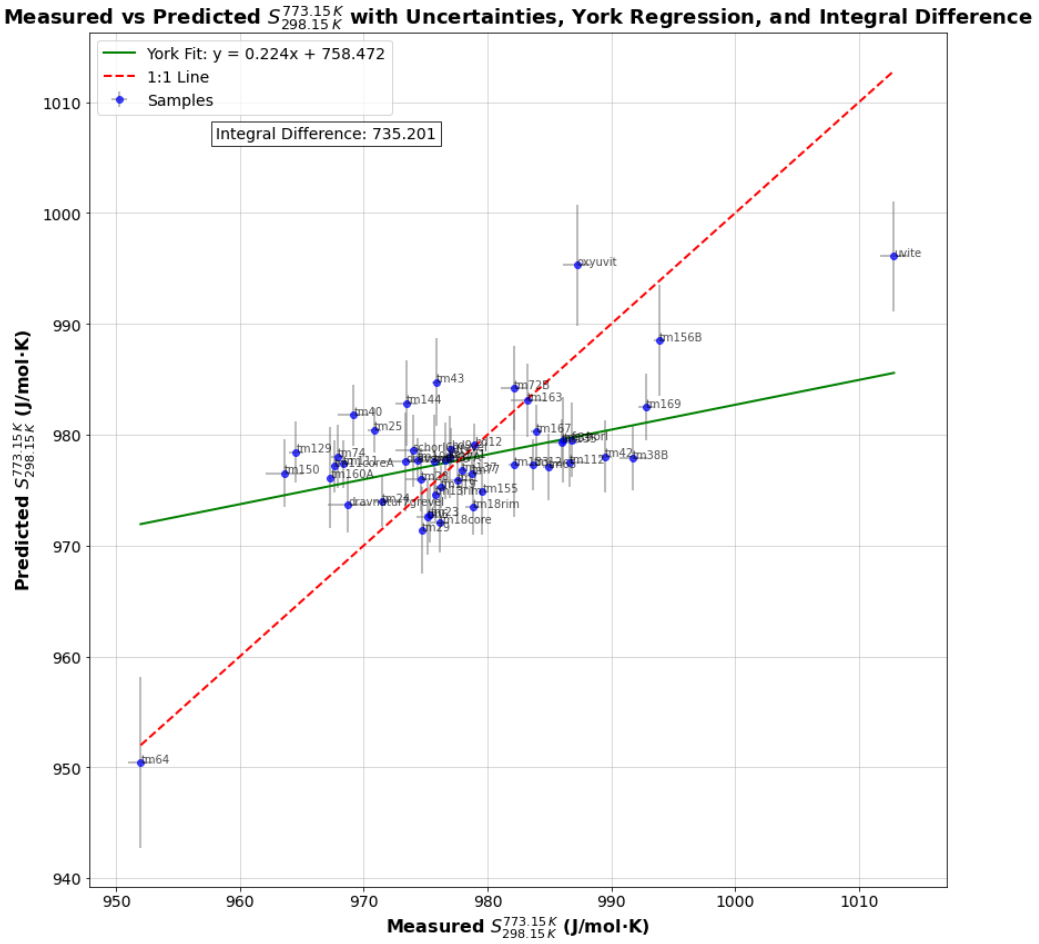

Figure A3D.2. Measured versus predicted $S^{773.15\,K}_{298.15K}$ using Method 2. Prediction uncertainty based on the confidence interval. This figure is identical to Method 1(Figure 3U) showing that the order of integration and regression does not matter for high-T Cp data.

1. SPECIATION MODEL: ENTROPY AT 298 K (METHOD 2)

Method 2 derived endmember entropies via integration over temperature (T) of linear interpolation low-T Cp sample curves, with subsequent OLS regression performed using NCSS on the $XY_3Z_6T_6V_3W$ basis set and a sample size of 50. The model's mean entropy was 653.28 J/mol·K, with a standard deviation of 25.64 J/mol·K, and an entropy range from 574.16 to 709.54 J/mol·K. Model fit statistics showed an MSE of 40.66 which is larger than method 1. An R_{PRESS}^2 of 0 indicate the lack of robustness and the data dependent nature of the regression model. Residuals followed a normal distribution. The correlation matrix showed that correlations between srl and drv, and drv and S_0 in the bulk compositional model were broken in

the speciation model. However, srl-S_0 remained at 0.81, and pov-S_0 was high at 0.71, indicating these endmembers largely influence S_0 in the solid solution. Outlier diagnostics identified synthetic B-olenite as highly influential due to its unique bole component, along with synthetic samples (oxyuvite, uvit, dravsyn) whose exclusion would alter predictions. In the measured versus predicted plot (Figure A3D.3) there is a slight improvement in compositional bias with method 1 compared to method 2. Differences between predicted entropies of the training set samples is at average overestimated in method 2 with an maximus difference of 5 J/mol·K.

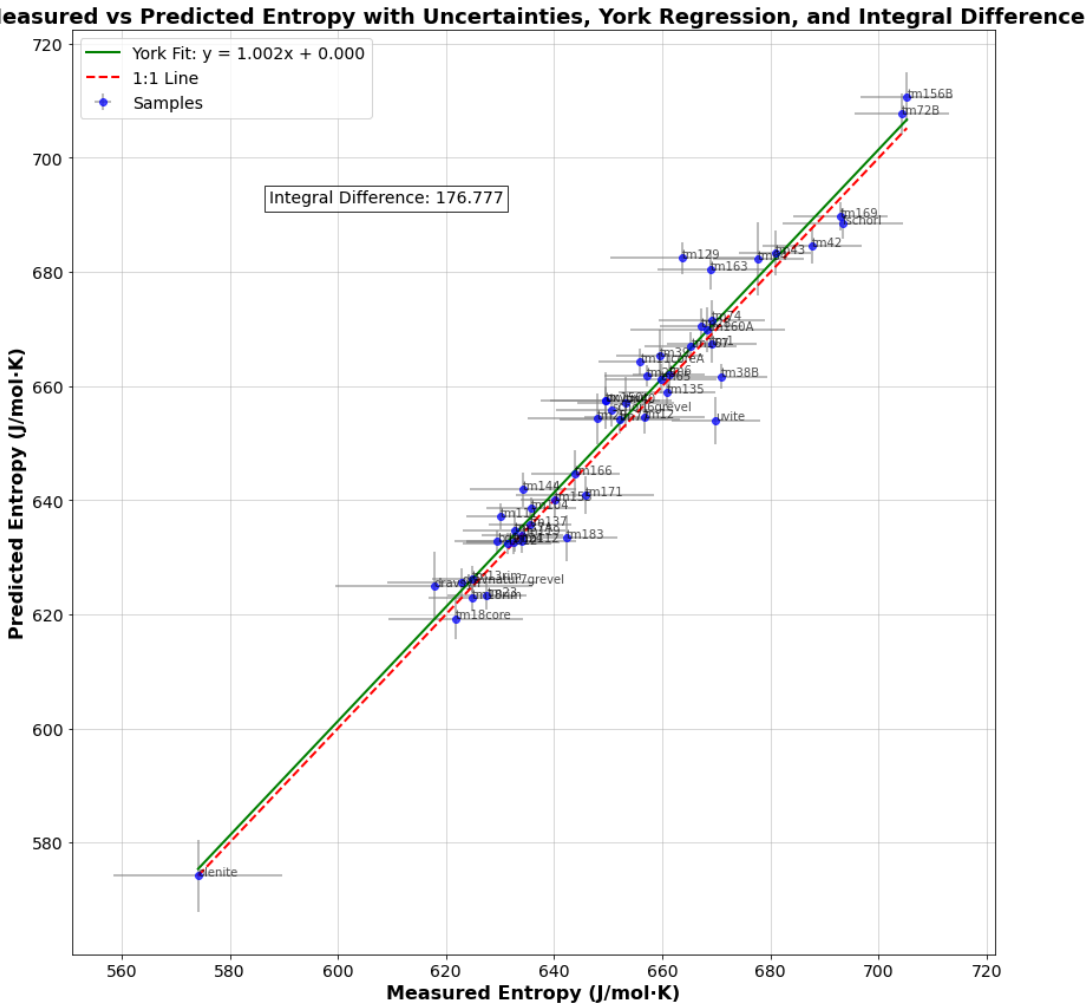

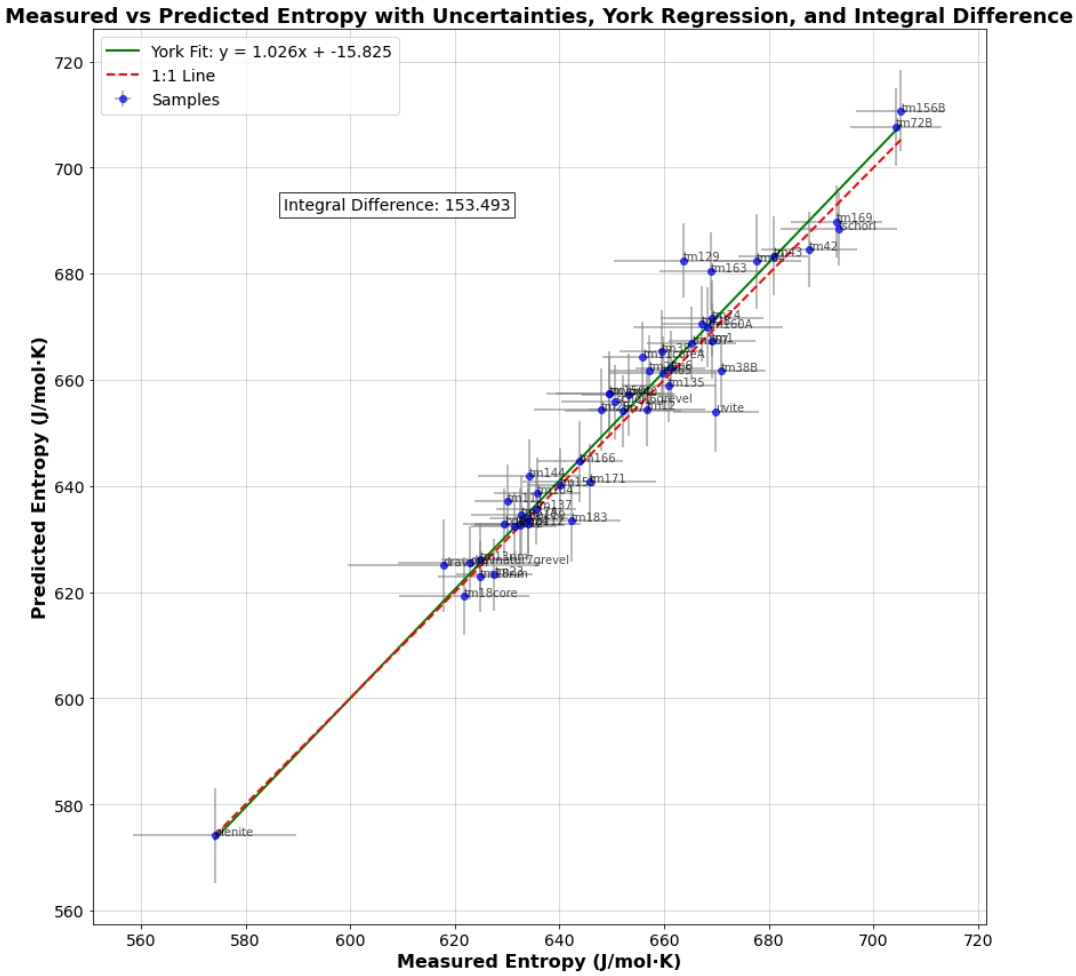

Figure A3D.3. Measured versus predicted entropy using method 2 using CI and PI uncertainties.

1. SPECIATION MODEL: $S_{298.15K}^{773.15\,K}$ (METHOD 2)

The NCSS OLS regression on the $S_{298.15K}^{773.15\,K}$ obtained by Cp/T integration of the sample Cp curves also yielded endmember $S_{298.15K}^{773.15\,K}$. The mean Cp is 976.8 J/mol·K with a standard deviation of 12.76 J/mol·K, showing limited variance. The model's MSE is 64.8, similar to Method 1. Key regression coefficients show strong associations with pov (1045.22 J/mol·K), fuvt (1010.09 J/mol·K), and ole (1010.98 J/mol·K), while bole (919.58 J/mol·K) and aorsm (961.91 J/mol·K) have lower coefficients. Compared to the bulk composition model, integrated Cp for srl, drv, uvt, foi, fluvt, and sorsm are similar. Ole is larger in the speciation model (1010 J/mol·K) than in the bulk model (976 J/mol·K). Ole is larger (1010 J/mol·K) and Buergerite smaller (941 J/mol·K) in the speciation model compared to the bulk model (976 J/mol·K and 951

J/mol·K, respectively), while mdtw increased to 1012 J/mol·K from 987 J/mol·K. Drv, drvdis, and odrv show similar integrated high-T Cp

The pattern observed in the bulk compositional model, where endmembers with X and V site vacancies, such as foiB, aorsmB, and buB, show lower Cp values, remains true. However, in the speciation model, ole, which had intermediate Cp values just below vacancy-free endmembers in the bulk compositional model, now has a higher $S_{298.15K}^{773.15\,K}$ than many endmembers without vacancies, indicating that speciation effects might play a role as well.

Strong multicollinearity affects endmember independence, leading to correlations like uvt and foi (-0.62), odrv and foi (0.70), foi and aorsm (-0.77), odrv and drvdis (-0.60), odrv and aorsm (-0.72), bu and pov (0.67). The correlation of B-Olenite with Cp (-0.66) shows significant influence on $S_{298.15K}^{773.15\,K}$.

The model's R^2 of 0 shows it is not robust and data-dependent, particularly on synthetic data and F-Buergerite, which significantly influence many endmembers. Similar to the bulk compositional model, Method 1 and Method 2 yield identical results, indicating the order of integration and regression does not affect the outcome. The hierarchical subset selection procedure indicates no significant interaction parameters, and excess Cp at T > 298.15K is absent.

APPENDIX. REGRESSION ANALYSIS DETAILS

Least Squares Entropy NCSS
bulk Compositional Model, $X(YZ)9Si_xAl_{(1-x)}(VW)_4$

Table 1. Model Fit Statistics

Model	MSE	Average Percent Error (%)	R^2	Press	Residual Normality
Reciprocal Model	41.62	0.68	0.87		Normal

Table 2. Regression Coefficient Confidence Intervals

Reciprocal Model with AlT Speciation

Independent Variable	Coefficient (b(i))	Standard Error (Sb(i))	Lower 95% CI	Upper 95% CI
srlB	718.48	6.69	704.96	732.00
drvB	632.97	6.09	620.66	645.27
uvtB	647.21	5.14	636.82	657.59
foiB	658.76	11.03	636.46	681.05
oleB	608.37	17.61	572.78	643.95
uvtB	647.36	4.25	638.77	655.95
buB	686.81	8.98	668.66	704.96
mdtwB	664.25	35.34	592.83	735.67
aorsmB	609.77	10.86	587.81	631.73

Table 3. Correlations Between Endmembers and Entropy

Variables	Correlation Coefficient
srlB and drvB	−0.82
Entropy and srlB	+0.88
Entropy and drvB	−0.79
srlB and oleB	−0.69
Entropy and oleB	−0.70

Table 4. Variance Inflation Factors (VIF)

Variable	VIF Value
oleB	8.8
foiB	8.5
aorsmB	6.4

Table 5. Outliers and Influence Diagnostics

Observation	Percentage Difference (%)	Residual	Cook's D(>0.08)	Hat Diagonal (>0.42)	DFFITS
tm144	1.76	−11.17	-	-	−1.15

Observation	Percentage Difference (%)	Residual	Cook's D(>0.08)	Hat Diagonal (>0.42)	DFFITS
tm38B	1.54	+10.37	-	-	-
tm129	2.73	−18.20	0.13	-	−1.25
tm40	1.71	−11.26	-	-	-
uvit	2.05	+13.73	0.54	-	2.41
Tm64				0.94	2.95
oxyuvit			0.25	0.48	-1.5
Tm183			0.12		1.07

Table 6. Observations with High DFBETAS (>0.28)

Observation	Affected Variables
tm144	uvtB, buB, mdtwB
tm6	foiB
tm169	srlB, aorsmB, fluvtB
tm150	drvB, foiB, oleB, mdtwB
tm156B	drvB, aorsmB, mdtwB
tm38B	drvB, uvtB, oleB, mdtwB
tm64	All except fluvtB
tm129	srlB, drvB, uvtB, foiB, oleB
tm183	All except drvB, foiB, oleB
tm43	srlB
tm29	foiB, aorsmB
tm40	uvtB, fluvtB
oxyuvit	uvtB, aorsmB
uvit	uvtB (strong), foiB, oleB, fluvtB
dravsyn	srlB, foiB, oleB, aorsmB

APPENDIX. REGRESSION ANALYSIS

Least Squares Integrated High-T Cp Curve NCSS.
bulk Compositional Model, $X(YZ)9Si_xAl_{(1-x)}(VW)_4$.

Table 1. Model Fit Statistics

Model	MSE	Average Percent Error (%)	R^2	Press	Residual Normality
Reciprocal Model	62.50	0.59		0	Normal

Table 2. Regression Coefficient Confidence Intervals

Reciprocal Model with Al^T Speciation

Independent Variable	Coefficient (b(i))	Standard Error (Sb(i))	Lower 95% CI	Upper 95% CI
srlB	1000.42	8.20	983.85	1017.00
drvB	980.98	7.46	965.91	996.06
uvtB	991.71	6.30	978.98	1004.44
foiB	962.18	13.52	934.87	989.50
oleB	976.65	21.58	933.04	1020.26
uvtB	982.51	5.21	971.98	993.03
buB	951.34	11.00	929.10	973.57
mdtwB	987.51	43.31	899.98	1075.03
aorsmB	956.58	13.31	929.68	983.49

Table 3. Correlations Between Endmember Variables

Endmember Pair	Correlation Coefficient
srlB and drvB	-0.82
srlB and aorsmB	0.74
srlB and oleB	-0.69
drvB and oleB	0.69
drvB and aorsmB	-0.69
foiB and oleB	0.82
aorsmB and foiB	-0.86
oleB and aorsmB	-0.76

Table 4. Variance Inflation Factors (VIF)

Variable	VIF Value
oleB	8.8
foiB	8.5
aorsmB	6.4

Table 5. Outliers and Influence Diagnostics

Observation	Absolute Percent Error (%)	Residual	Hat Diagonal	DFFITS	Cook's D
tm169A	1.04	-10.35	-	-	-
tm150A	1.34	-12.91	-	-	-
tm38B	1.40	13.90	-	-	-
tm129	1.43	-13.90	-	-	-
tm40	1.30	-12.61	-	-	-
tm42	1.15	11.40	-	-	-
tm74	1.05	-10.16	-	-	-
uvit	1.65	16.70	0.39	2.39	-
tm156B	-	-	0.39	-	-
tm64	-	-	0.94	3.68	1.51
tm183	-	-	0.35	-	-
oxuvit	-	-	0.48	-1.38	-

Table 6. Observations with High DFBETAS (>0.28)

Observation	Affected Variables
tm144	mdtwB
tm169A	srlB, aorsmB
tm150	drvB, oleB, mdtwB
tm150A	drvB, oleB, mdtwB
tm156B	mdtwB
tm160A	foiB, oleB, buB
tm38B	oleB
tm64	All except fluvtB
tm43	srlB, foiB, oleB, aorsmB
tm39	uvtB, fluvtB, oleB
tm40	fluvtB
oxuvt	uvtB, aorsmB
uvit	uvtB (strong), fluvtB, aorsmB

APPENDIX. REGRESSION ANALYSIS

Least Squares Entropy NCSS
Speciation Model, $XY_3Z_6T_6V_3W$

Table 0. Descriptive Statistics

Metric	Value
Sample Size	50
Mean Entropy	653.28
Standard Deviation Entropy	25.64
Minimum Entropy	574.16
Maximum Entropy	709.54

Table 1. Model Fit Statistics

Model	MSE	Average Percent Error (%)	R^2	Press	Residual Normality
Speciation Model	40.66	0.58		0	Normal

Table 2. Regression Coefficient Confidence Intervals

Speciation Model.

Independent Variable	Coefficient (b(i))	Standard Error (Sb(i))	Lower 95% CI	Upper 95% CI
srl	716.74	14.87	686.59	746.89
drv	621.67	6.92	607.64	635.70
uvt	650.05	12.91	623.87	676.23
fuvt	732.73	32.11	667.61	797.85
foi	675.64	19.75	635.58	715.71
ole	664.34	32.69	598.04	730.64
drvdis	643.99	14.59	614.39	673.59
odrv	630.19	6.90	616.19	644.19
fluvt	640.69	5.09	630.36	651.01
bu	665.16	22.10	620.33	709.98
mdtw	697.89	34.24	628.44	767.33
bole	567.62	12.13	543.03	592.22
aorsm	639.49	20.57	597.78	681.20
pov	1006.53	95.17	813.51	1199.55

Table 3. Correlations Between Endmember Variables

Endmember Pair	Correlation Coefficient
srl and drv	-0.82
srl and ole	-0.69

Endmember Pair	Correlation Coefficient
srl and Entropy	0.81
drv and ole	0.69
drv and aorsm	-0.69
foi and ole	0.82
aorsm and foi	-0.77
ole and aorsm	-0.76
drvdis and odrv	-0.60
bu and pov	0.67

Table 4. Variance Inflation Factors (VIF)

Variable	VIF Value
srl	11.5
uvt	11.40
drvdis	12.1
aorsm	9.36
foi	18.8

Table 5. Outliers and Influence Diagnostics

Observation	Absolute Percent Error (%)	Residual	Hat Diagonal (>0.52)	DFFITS	Cook's D (>0.08)
tm38B	1.70	11.46	-	-	-
tm129	2.43	-16.20	-	-1.55	0.13
Tm183					0.18
Tm163					12`
uvit	2.36	15.86	0.39	3.27	0.55
tm64	-	-	0.98	0.36	0.36
oxyuvit	-	-	0.61	-2.54	0.42
dravsyn	-	-	0.85	-8.47	3.94
olenite	-	-	-	3152	311051

Table 6. Observations with High DFBETAS (>0.30)

Observation	Affected Variables
tm144	mdtw
tm163	uvt, odrv, bu, aorsm
tm171	fuvt
tm64	ole, bu, mdtw
tm129	All except drv, fuvt, bole, aorsm, pov
tm183	All except drv, foi, fuvt, ole, aorsm, pov
tm29	fuvt

Observation	Affected Variables
tm39	fuvt, pov
olenite	mdtw, Strong Influence on bole
oxyuvt	srl, drv, drvdis, bu, aorsm
uvit	All except foi, fuvt, mdtw, aorsm, bole
dravsyn	All except fuvt, pov

APPENDIX. REGRESSION ANALYSIS

Least Squares Integrated High-T Cp Curve NCSS Speciation Model, $XY_3Z_6T_6V_3W$

Table 0. Descriptive Statistics

Metric	Value
Sample Size	50
Mean Cp	976.80
Standard Deviation	12.76
Minimum Cp	917.81
Maximum Cp	1012.83

Table 1. Model Fit Statistics

Model	MSE	Average Percent Error (%)	R^2	Press	Residual Normality
Speciation Model	64.8	0.54	0		Normal

Table 2: Regression Coefficient Confidence Intervals

Speciation Model.

Independent Variable	Coefficient (b(i))	Standard Error (Sb(i))	Lower 95% CI	Upper 95% CI
srl	1003.39	18.76	965.34	1041.44
drv	982.36	8.73	964.65	1000.06
uvt	992.98	16.29	959.95	1026.02
fuvt	1010.09	40.52	927.91	1092.28
foi	968.63	24.93	918.07	1019.19
ole	1010.98	41.26	927.31	1094.66
drvdis	985.08	18.42	947.73	1022.44
odrv	979.15	8.71	961.48	996.82
fluvt	978.60	6.43	965.57	991.64
bu	941.42	27.89	884.85	997.99
mdtw	1012.67	43.21	925.03	1100.31

Independent Variable	Coefficient (b(i))	Standard Error (Sb(i))	Lower 95% CI	Upper 95% CI
bole	919.58	15.31	888.54	950.62
aorsm	961.91	25.96	909.27	1014.56
pov	1045.22	120.11	801.62	1288.82

Table 3. Correlations Between Endmember Variables

Endmember Pair	Correlation Coefficient
uvt and foi	-0.62
odrv and foi	0.70
foi and aorsm	-0.77
odrv and drvdis	-0.60
odrv and aorsm	-0.72
bu and pov	0.67
bole and Cp	-0.66

Table 4. Variance Inflation Factors (VIF)

Variable	VIF Value
srl	11.5
uvt	11.40
drvdis	12.1
aorsm	9.36
foi	18.8

Table 5. Outliers and Influence Diagnostics

Observation	Absolute Percent Error (%)	Residual	Hat Diagonal	DFFITS	Cook's D
tm12	1.05	10.4	-	-	-
Tm150A	1.08	-10.45			
tm38B	1.54	15.34	-	-	-
tm129	1.22	-11.77	-	-1.55	0.13
tm42	1.33	13.22	-	-	-
Tm156B			0.46		
tm64	-	-	0.98	-1.96	0.28
Tm166			0.43		
Tm183			0.40		
Tm29			0.48		
Tm39			0.49		
Tm40			0.49	-1.46	
olenite	-	-	1.00	682.00	33828.00
oxyuvit	-	-	0.61	-2.16	0.32
uvit	1.63	16.63	0.42	2.54	0.38

Observation	Absolute Percent Error (%)	Residual	Hat Diagonal	DFFITS	Cook's D
dravsyn	-	-	0.85	-7.18	3.04

Table 6. Observations with High DFBETAS (>0.30)

Observation	Affected Variables
tm144	mdtw
tm12	bu, pov
tm169A	srl, aorsm
tm160A	srl, ole, bolenite, pov
tm38B	uvt
tm64	ole, bu, mdtw
tm129	uvt, ole, drvdis, mdtw
tm183	odrv, mdtw
tm43	srl, fuvt, foi, fuvt, bu, bole, aorsm, pov
tm40	fuvt, foi, ole, drvdis, fuvt, mdtw, bolenite, aorsm, pov
tm42	fuvt, ole, drvdis, odrv, mdtw
tm74	ole, drvdis
olenite	Strongly on bole
oxyuvt	srl, drv, aorsm
uvit	All except foi, fuvt, mdtw, bole, aorsm
dravsyn	Strongly on all except fuvt, pov

Appendix 3E. Bulk Model endmember curves

This Appendix contains all the Bulk model endmember Cp curves.

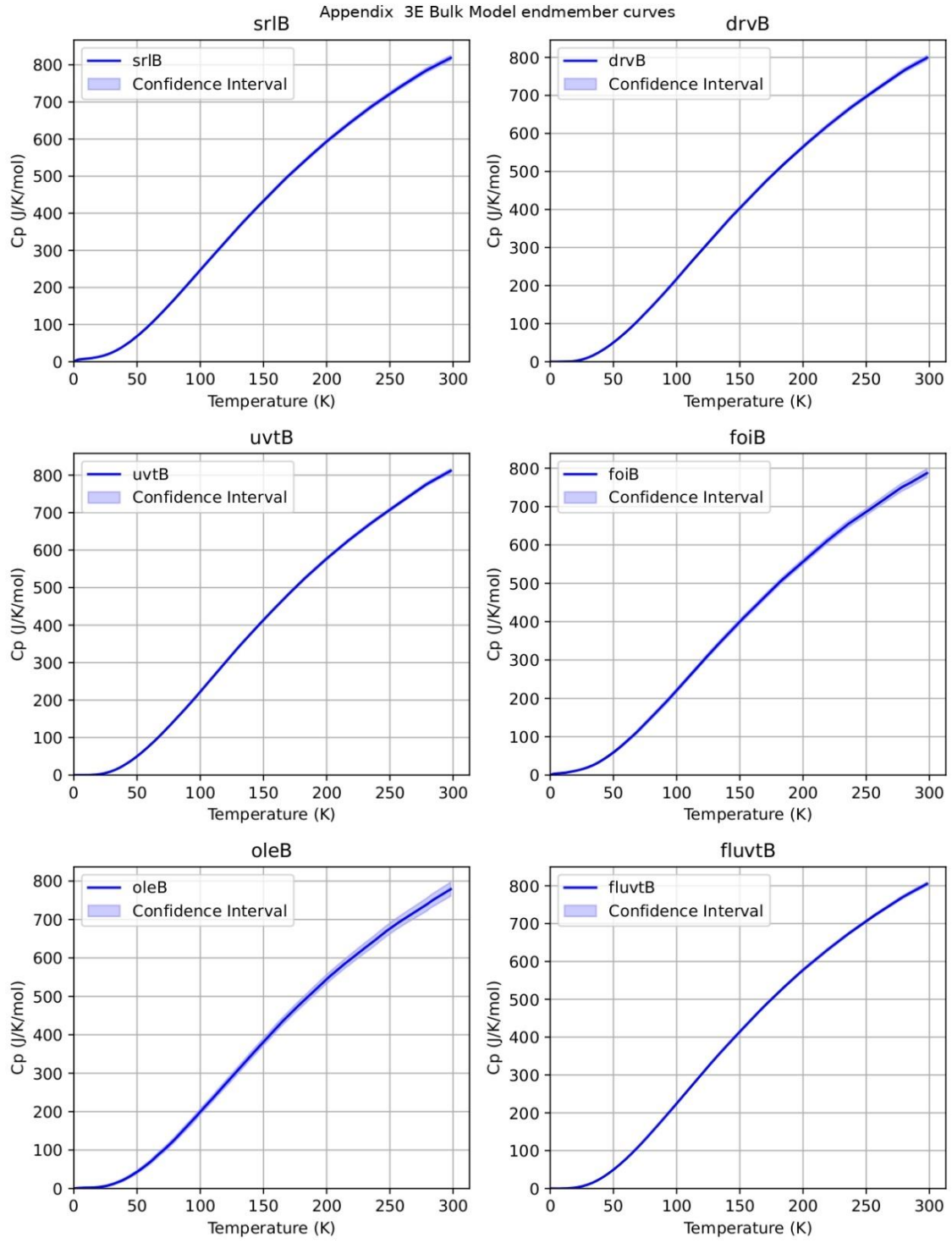

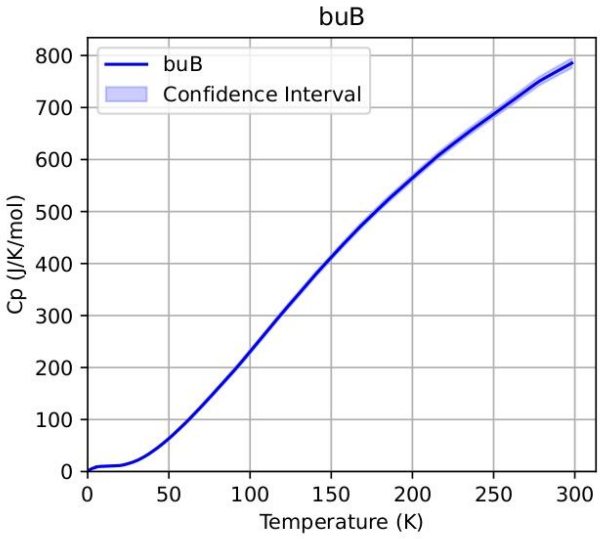
buB
buB
Confidence Interval
Cp (J/K/mol)
Temperature (K)
0
100
200
300
400
500
600
700
800
0
50
100
150
200
250
300

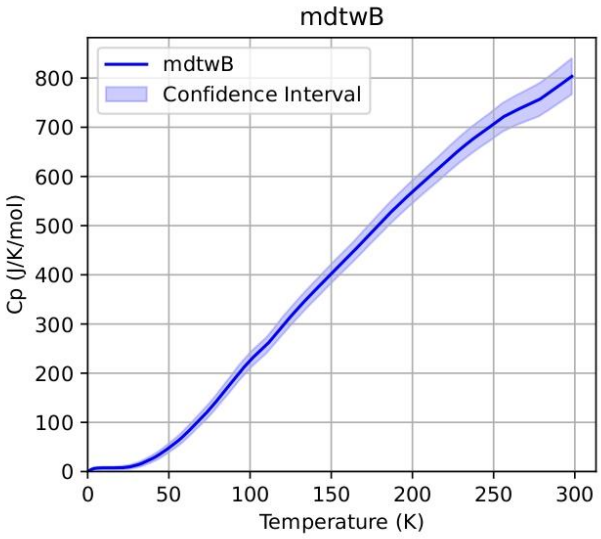
mdtwB
mdtwB
Confidence Interval
Cp (J/K/mol)
Temperature (K)
0
100
200
300
400
500
600
700
800
0
50
100
150
200
250
300

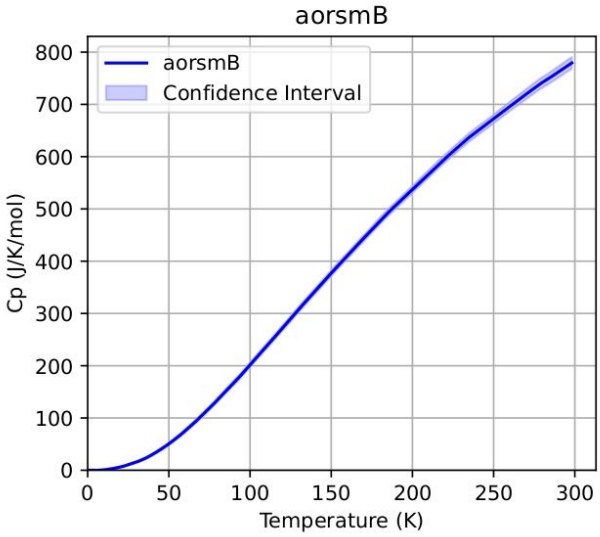
aorsmB
aorsmB
Confidence Interval
Cp (J/K/mol)
Temperature (K)
0
100
200
300
400
500
600
700
800
0
50
100
150
200
250
300

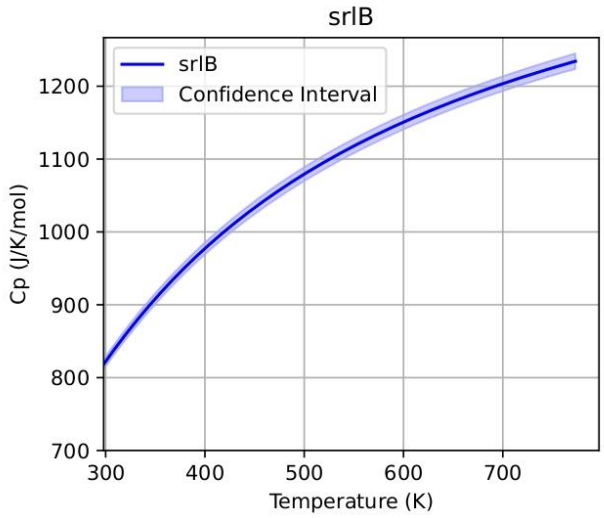
srlB
srlB
Confidence Interval
Cp (J/K/mol)
Temperature (K)
700
800
900
1000
1100
1200
300
400
500
600
700

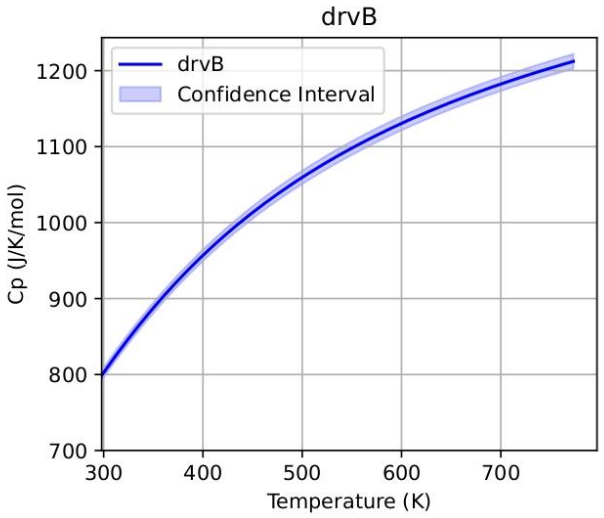
drvB
drvB
Confidence Interval
Cp (J/K/mol)
Temperature (K)
700
800
900
1000
1100
1200
300
400
500
600
700

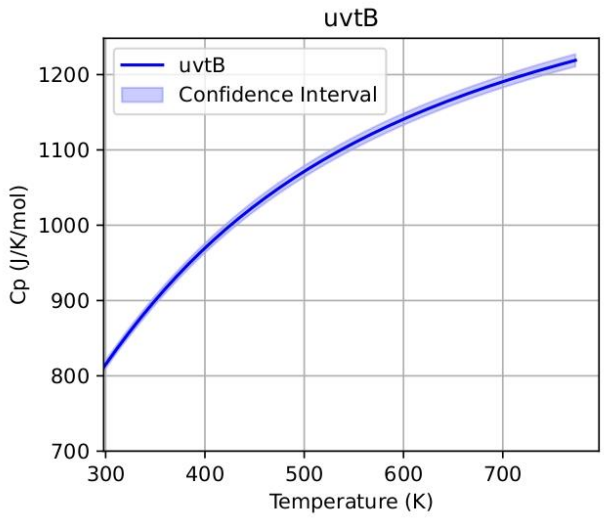
uvtB
uvtB
Confidence Interval
Cp (J/K/mol)
Temperature (K)
700
800
900
1000
1100
1200
300
400
500
600
700

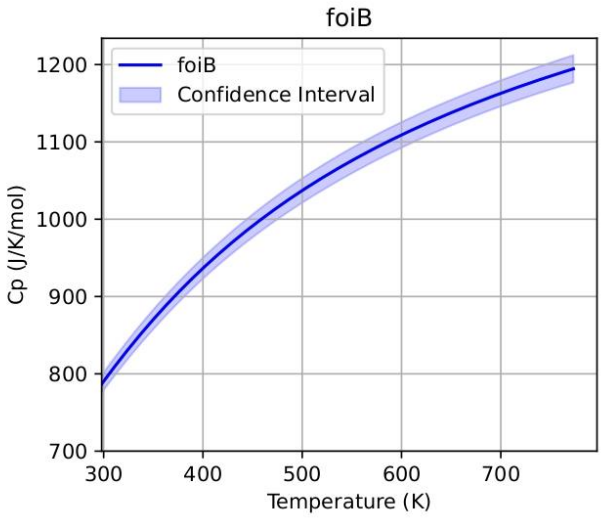
foiB
foiB
Confidence Interval
Cp (J/K/mol)
Temperature (K)
700
800
900
1000
1100
1200
300
400
500
600
700

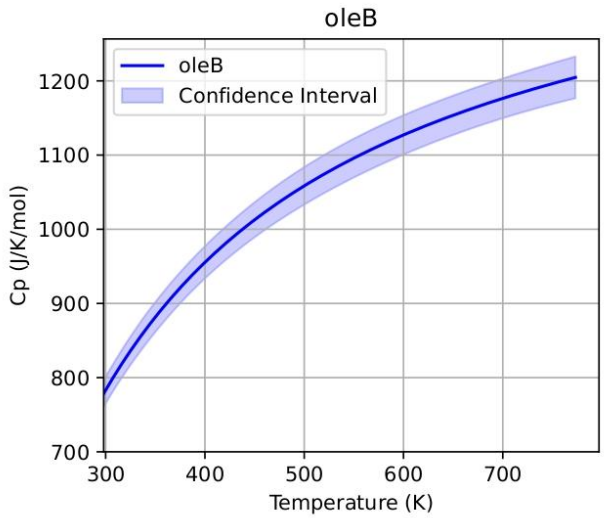
oleB
oleB
Confidence Interval
Cp (J/K/mol)
Temperature (K)
700
800
900
1000
1100
1200
300
400
500
600
700

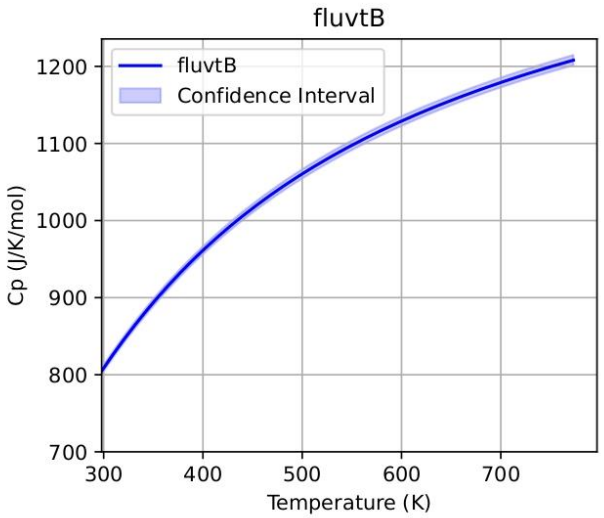
fluvtB
fluvtB
Confidence Interval
Cp (J/K/mol)
Temperature (K)
700
800
900
1000
1100
1200
300
400
500
600
700

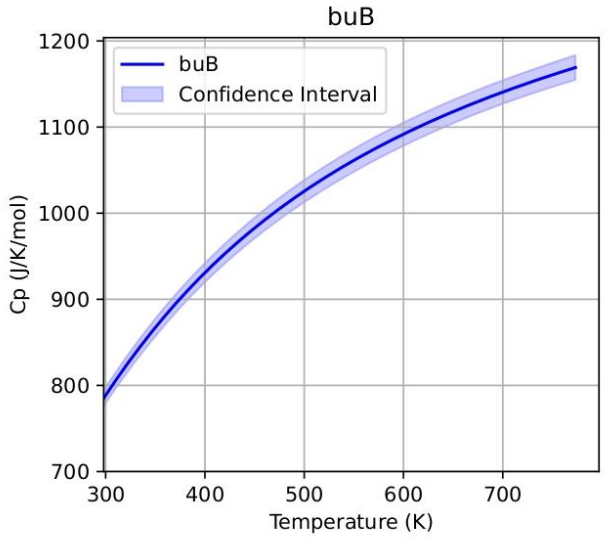
buB
buB
Confidence Interval
Cp (J/K/mol)
Temperature (K)
1200
1100
1000
900
800
700
300
400
500
600
700

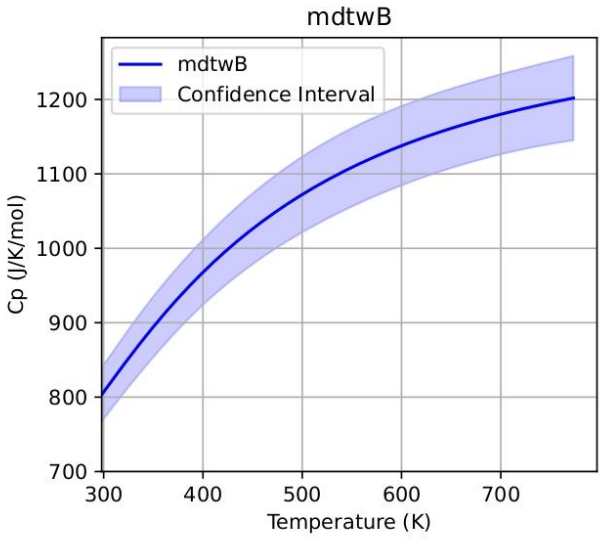
mdtwB
mdtwB
Confidence Interval
Cp (J/K/mol)
Temperature (K)
1200
1100
1000
900
800
700
300
400
500
600
700

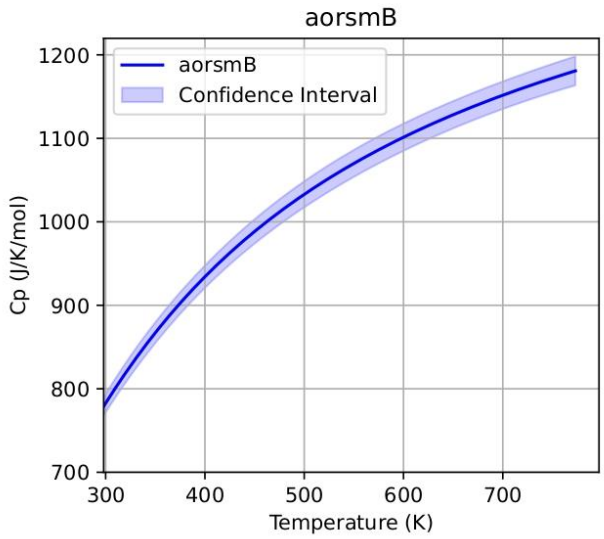
aorsmB
aorsmB
Confidence Interval
Cp (J/K/mol)
Temperature (K)
1200
1100
1000
900
800
700
300
400
500
600
700

Appendix 3F. Method 1 Statistics Summary Bulk and Speciation

Low-T Cp curve regression

Model	Largest MSE	LOOCV MSE
$X(YZ)_9Si_xAl_{(1-x)}(VW)_4$	31.5 fschorl, 21.68 tm144, 31.62 tm11coreA, 46.6 tm150, 45.8 tm38B, **0.25 tm64**, 38.5 tm129, 20.72 tm183, 30.6 tm39,59.3 tm40, 29.14 oxyuvit,57.5 uvite	47.1 fschorl, 37.3 tm144 , 38.3 tm11coreA, 64.9 tm150, 61.0 tm38B, **97.0 tm64**, 49.8 tm129, 49.3 tm183, 52.4 tm39,77.0 tm40, 108.2 oxyuvit,156.9 uvite
$XY_3Z_6T_6V_3W$	27.7 fschorl, 22.4 tm11coreA, 30.0 tm150, 55.0 tm38B, 35.0 tm129, 27.9 tm183, 28.9 oxyuvit, 94.9 uvite	42.0652 fschorl, 29.5423 tm11coreA, 41.0307 tm150, 71.6864 tm38B, **321.662 tm64**, 53.8623 tm129, 77.8844 tm183, $2.57011*10^7$ olenite, 190.7 oxyuvit, 283.0 uvite, 864.8 dravsyn

---

Table 1. Model Comparison for Entropy and MSE

Model	Mean Relative %	Mean MSE	Median MSE	MSE Entropy	Median MSE Entropy
$X(YZ)_9Si_xAl_{(1-x)}(VW)_4$	-1.05%	12.13	5.5	32.8	10.6
$XY_3Z_6T_6V_3W$	-0.67%	10.7	5.4	28.5	5.9

Table 2. LOOCV Metrics

Model	LOOCV Mean MSE	LOOCV Median MSE	LOOCV MSE Entropy	LOOCV Median MSE Entropy
$X(YZ)_9Si_xAl_{(1-x)}(VW)_4$	22.7	3.32	60.2	14.3
$XY_3Z_6T_6V_3W$	47.6	4.26	118.3	11.4

High-T Cp curve regression

Model	Largest MSE	LOOCV MSE
$X(YZ)_9Si_xAl_{(1-x)}(VW)_4$	5.5 tm64, 337.5 uvite, 300.3 tm129, 200.9 tm150, 73.6 oxyuvit, 210.0 tm38B, 170.7 tm40, 150.8 tm42, 84.2 tm160A, 147.6 tm112, 150.0 tm25	2090.0 tm64, 920.2 uvite, 390.5 tm129, 282.1 tm150, 273.3 oxyuvit, 284.6 tm38B, 222.7 tm40, 217.5 tm42, 187.2 tm160A, 174.2 tm112, 169.1 tm25
$XY_3Z_6T_6V_3W$	138.3 tm112, 2.6 tm163, 4.0 tm171, 2.1 tm13rim, 0.2 tm64, 1.8 tm166, 124.1 tm65, 314.6 uvite,78.5 dravsyn	932.9 tm112, 887.4 tm163, 549.0 tm171, 786 tm13rim, 1010 tm64, 829.2 tm166, 504.5 tm65, 592.1 uvite, 3556.2 dravsyn

Table 1. Model Comparison for Entropy and MSE

Model	Mean Relative %	Mean MSE	Median MSE	MSE Entropy	Median MSE Entropy
$X(YZ)_9Si_xAl_{(1-x)}(VW)_4$	-1.05%	67.2	37.6	51.02	42.3
$XY_3Z_6T_6V_3W$	-0.00005	61.1	31.2	46.6	21.1

Table 2. LOOCV Metrics

Model	LOOCV Mean MSE	LOOCV Median MSE	LOOCV MSE Entropy	LOOCV Median MSE Entropy
$X(YZ)_9SixAl_{(1-x)}(VW)_4$	149	44.6	60.2	39.10
$XY_3Z_6T_6V_3W$	217	59.1	162.1	55.5

LOOCV mean is calculated excluding synthetic B-olenite sample.

Appendix 3G. Bulk Model. 4 Temperature Zoom in Predicted vs Measured

This Appendix contains all the Bulk Model. 4 Temperature Zoom in Predicted vs Measured for 298.15, 373.15, 573.15 and 773.15K.

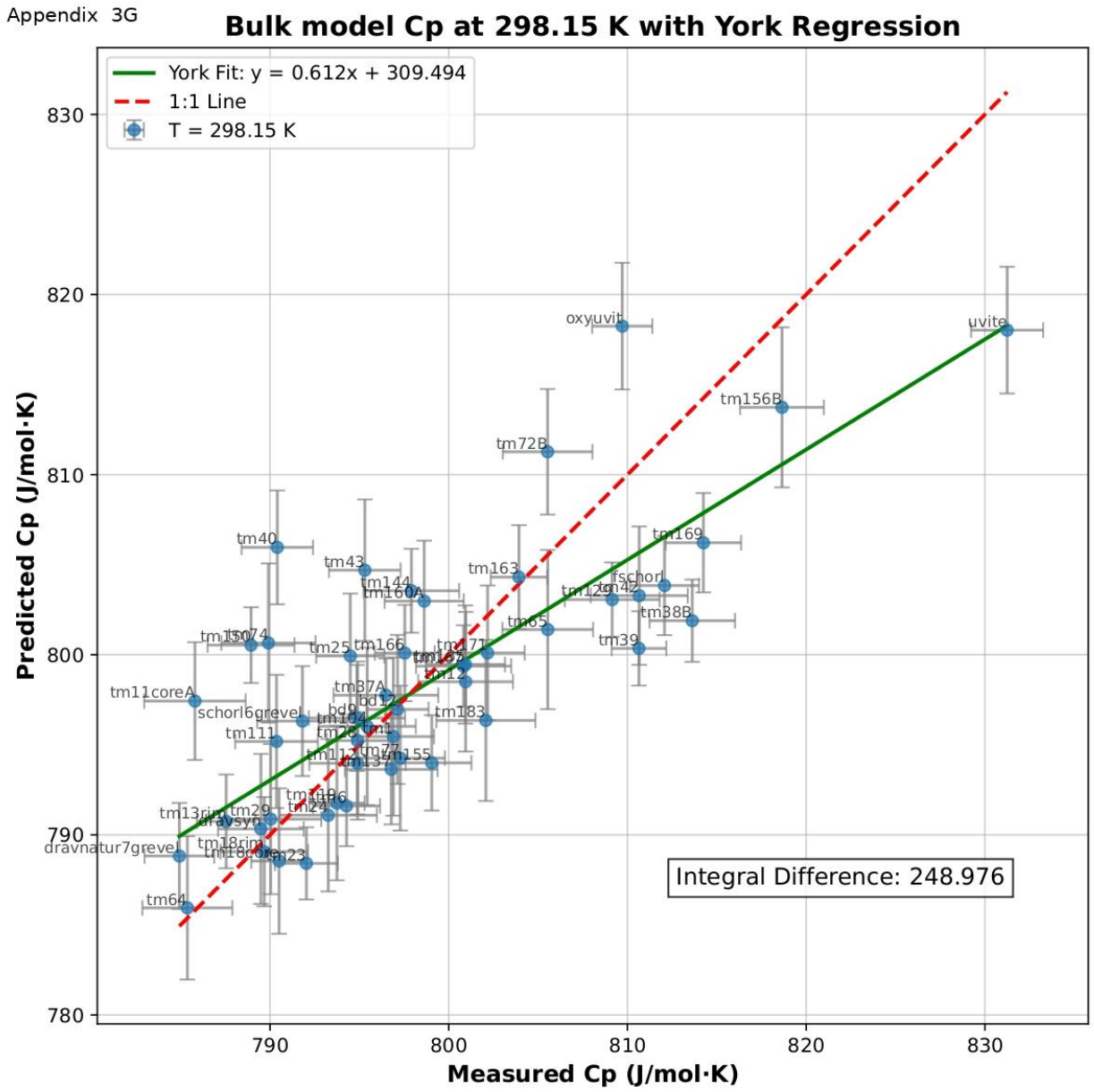

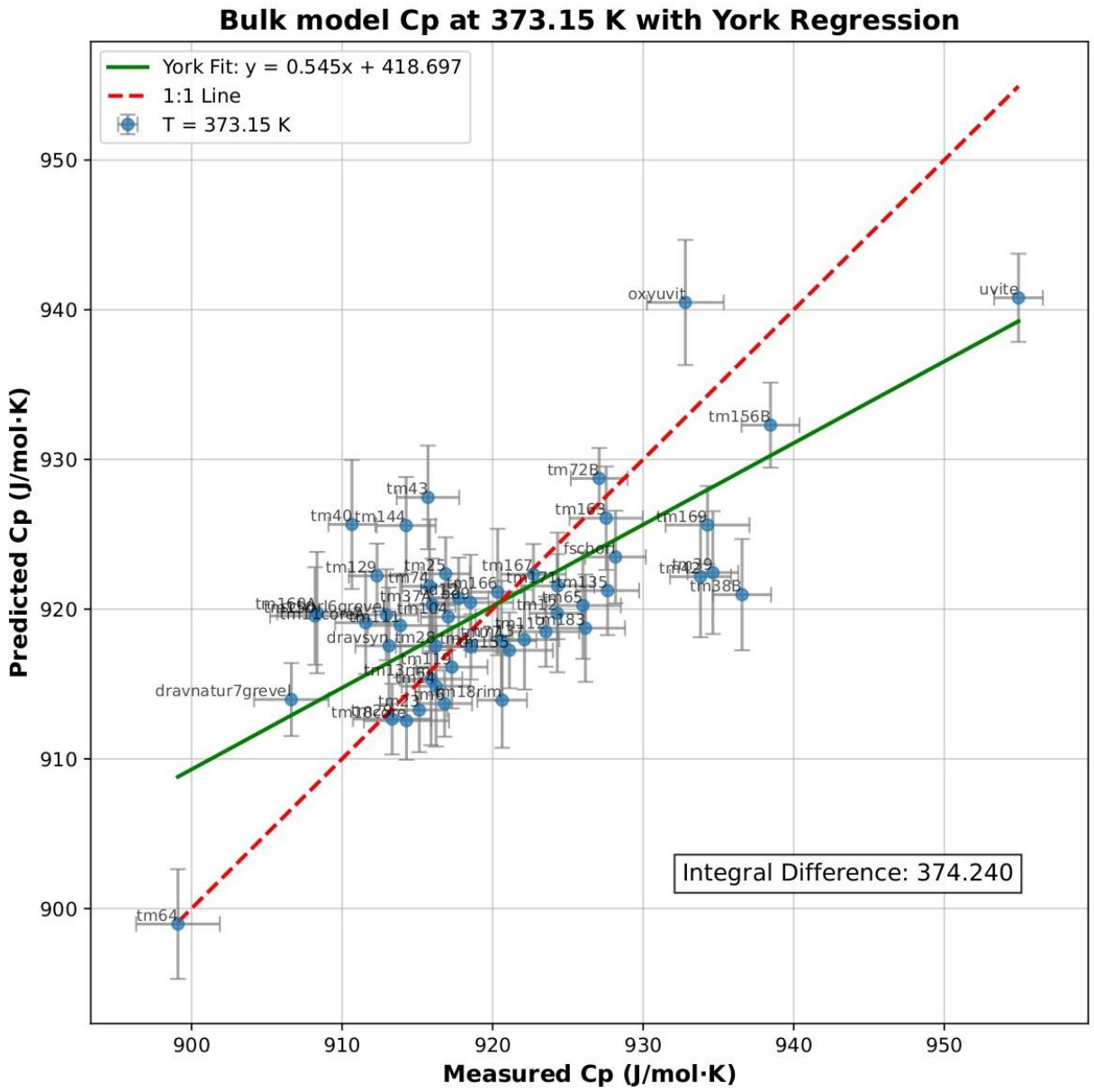
Bulk model Cp at 373.15 K with York Regression
York Fit: y = 0.545x + 418.697
1:1 Line
T = 373.15 K
Predicted Cp (J/mol·K)
Measured Cp (J/mol·K)
Integral Difference: 374.240
oxyuvit
uvite
tm156B
tm72B
tm43
tm40
tm144
tm169
tm129
tm25
tm167
tm135
tm38B
tm165
tm183
dravsyn
dravnatur7grevel
tm18rim
tm64
900
910
920
930
940
950

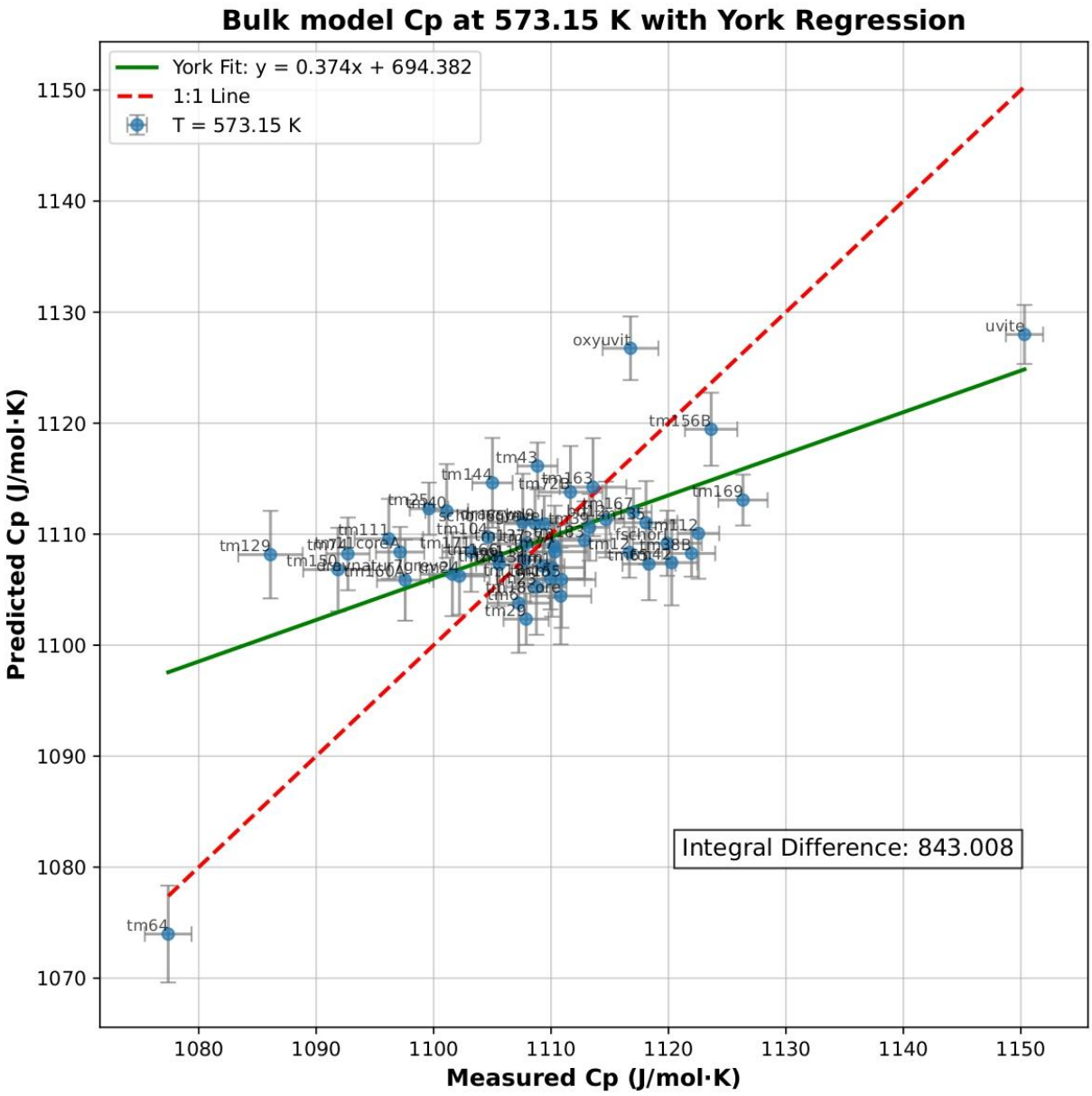
Bulk model Cp at 573.15 K with York Regression
York Fit: y = 0.374x + 694.382
1:1 Line
T = 573.15 K
Predicted Cp (J/mol·K)
Measured Cp (J/mol·K)
Integral Difference: 843.008
oxyuvit
uvite
tm156B
tm169
tm43
tm144
tm163
tm129
tm64
tm29
1070
1080
1090
1100
1110
1120
1130
1140
1150

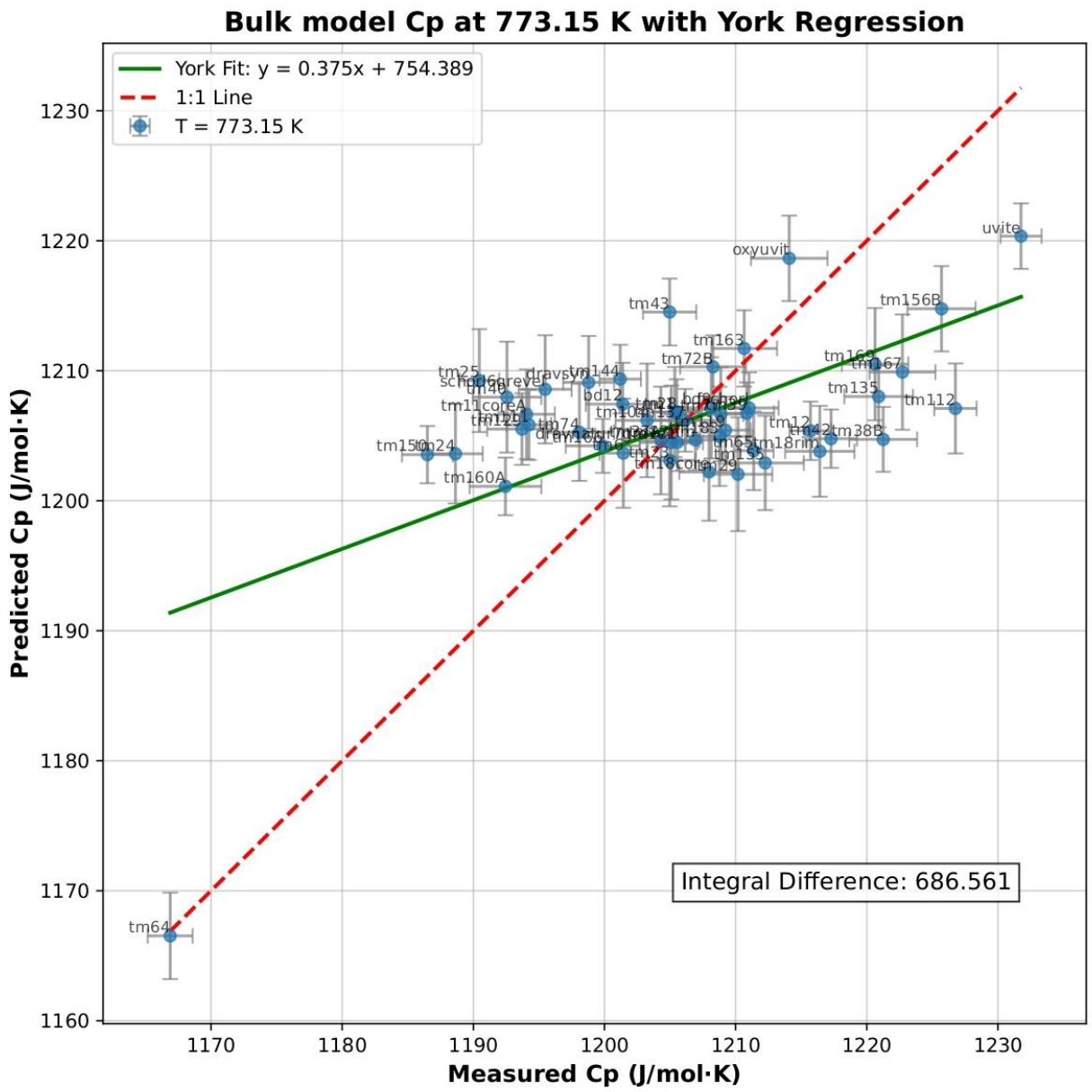
Bulk model Cp at 773.15 K with York Regression
York Fit: y = 0.375x + 754.389
1:1 Line
T = 773.15 K
Integral Difference: 686.561
Predicted Cp (J/mol·K)
Measured Cp (J/mol·K)
1160
1170
1180
1190
1200
1210
1220
1230
uvite
oxyuvit
tm43
tm156B
tm163
tm72B
tm169
tm167
tm135
tm112
tm38B
tm160A
tm64

Appendix 3H. Speciation Model Regression

2. SPECIATION MODEL: LOW-T CP (METHOD 1)

The same methods described for the bulk model were also applied using the speciation model. Method description is therefore not repeated. Endmember fraction ranges can be found in chapter 2 and show good coverage for drv, uvt, odrv, flvt, bu, bole, and aorsm (0.6-0.9), intermediate for srl, foi, and drvdis (0.35-0.55), and poor for fuvt (0.18), ole (0.12), mdtw (0.14), and pov (0.08). The later are extrapolated with higher uncertainties.

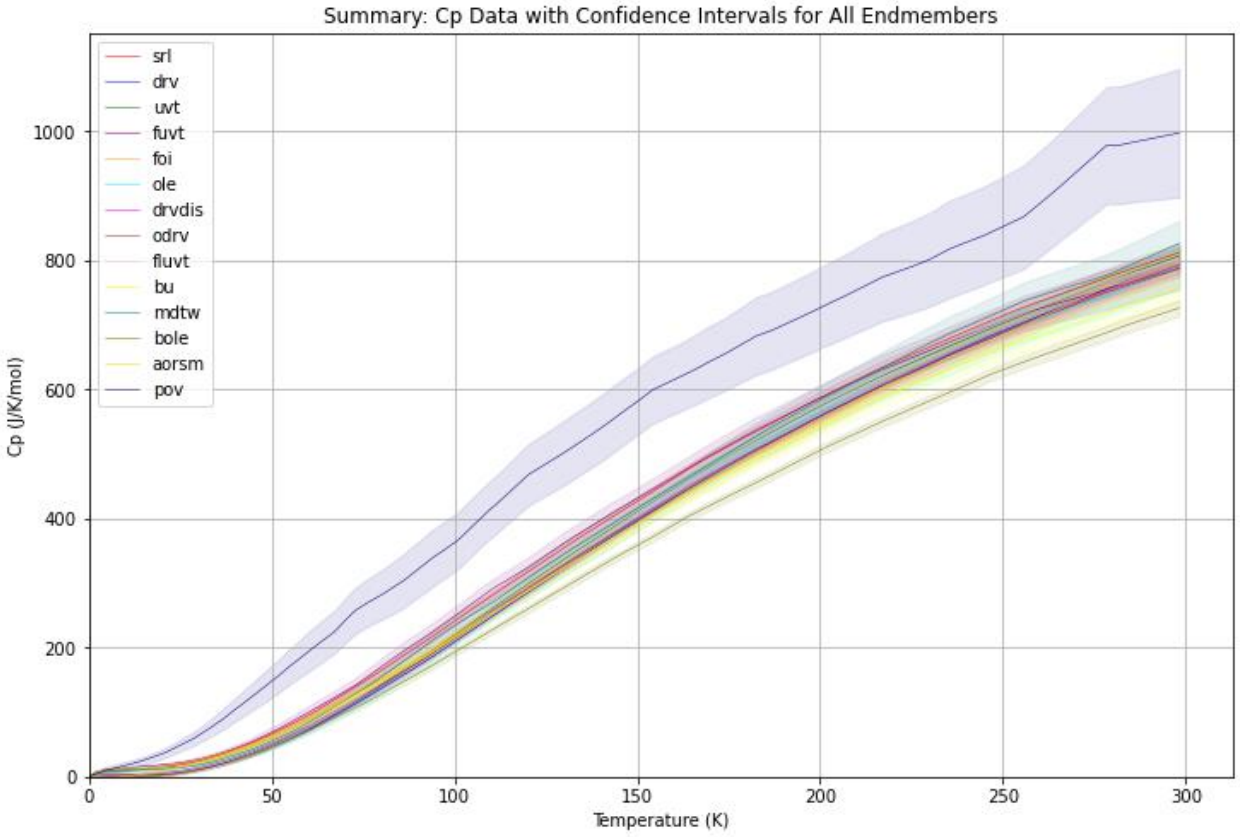

Figure A3H.1. Speciation endmember low-T Cp curves with their confidence intervals.

Figure A3H.1 shows the speciation endmember curves. The individual curves can be found in Appendix 3J. All confidence limits are tight except for fuvt and pov in the speciation model, with pov exhibiting the highest Cp curve, entropy, and uncertainty. The stark contrast between the highly extrapolated Cp curve for pov (highest Cp) and the other tourmalines highlights its distinct behavior and the non-smooth cp curve its elevated uncertainty. Pov dominates the

heatmap as well (Figure A3H.2). Other endmember low-T cp curves behave similarity to their bulk composition equivalent. Minimal differences between drv, odrv and drvdis mainly occur <150K.

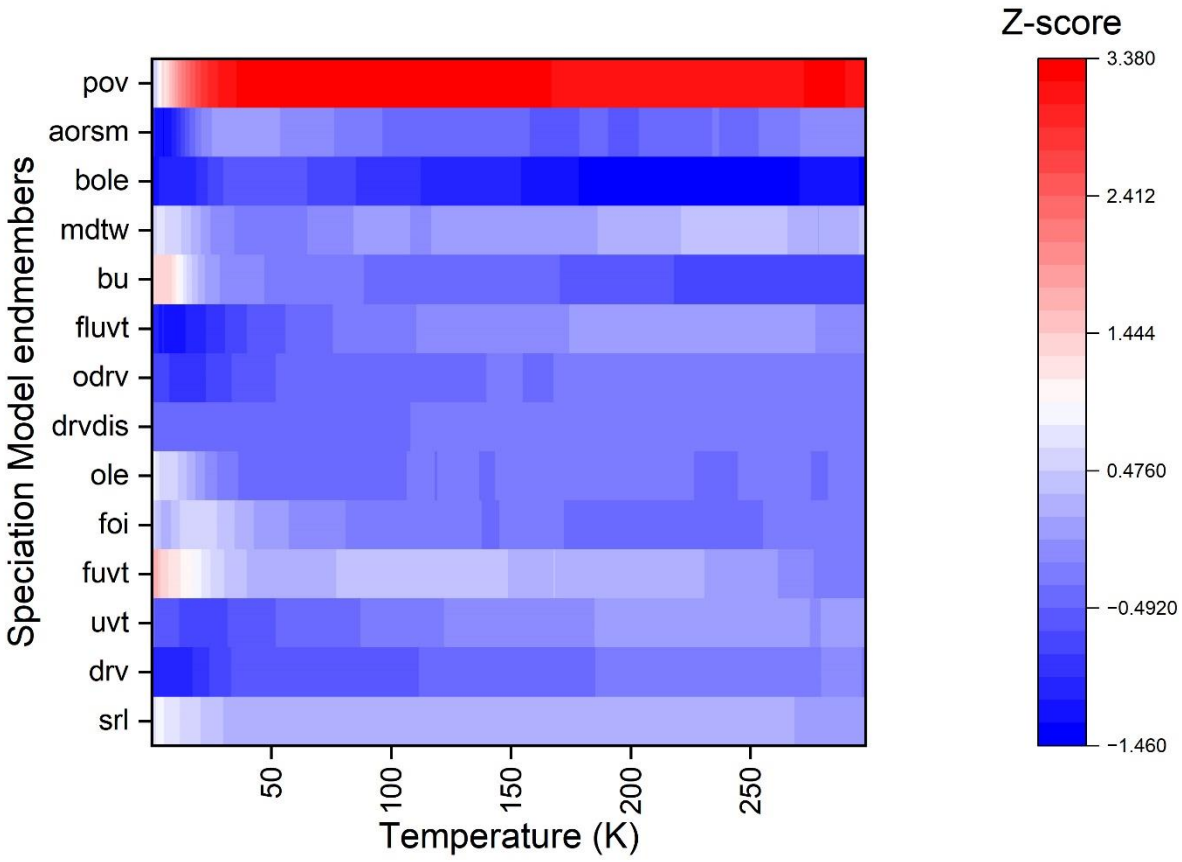

Figure A3H.2. Heatmap of speciation model Cp curves Z-scores at 0.1 K intervals, comparing each endmember to the mean of all endmembers. White indicates Cp near the mean, blue lower than the mean, and red higher. The plot highlights how relative differences between curves vary with temperature.

The SE's, nearly linear in absolute values, again show sharp increases in relative uncertainty below 50 K (Figure A3H.3), particularly around 15–20 K due to the small magnitudes of Cp in this temperature range, especially for drv/uvt. Severe multicollinearity in srl (VIF=15.1), uvt (VIF=11.5), foi (VIF=25.2), ole (VIF=12.0), drvdis (VIF=23.3), odrv (VIF=17.64), bu (VIF=7.2), aorsm (VIF=11.8), and pov (VIF=7.7) complicate the independence of the regression

coefficients and hint to data scarcity and insufficient datapoint to constrain all the endmembers (Figure A3H.4). The similarity between ordered and disordered endmembers, such as drv, drvdis, and odrv, simplifies the derivation of isochemical reaction equations but increases collinearity, which hinders the independent estimation of endmember properties and induces spurious correlations between them. This challenge is relevant to nearly all thermodynamic models involving ordered endmembers, particularly in solid solution models in the H&P database (Holland and Powell 2011; White et al. 2014; Green et al. 2016) .

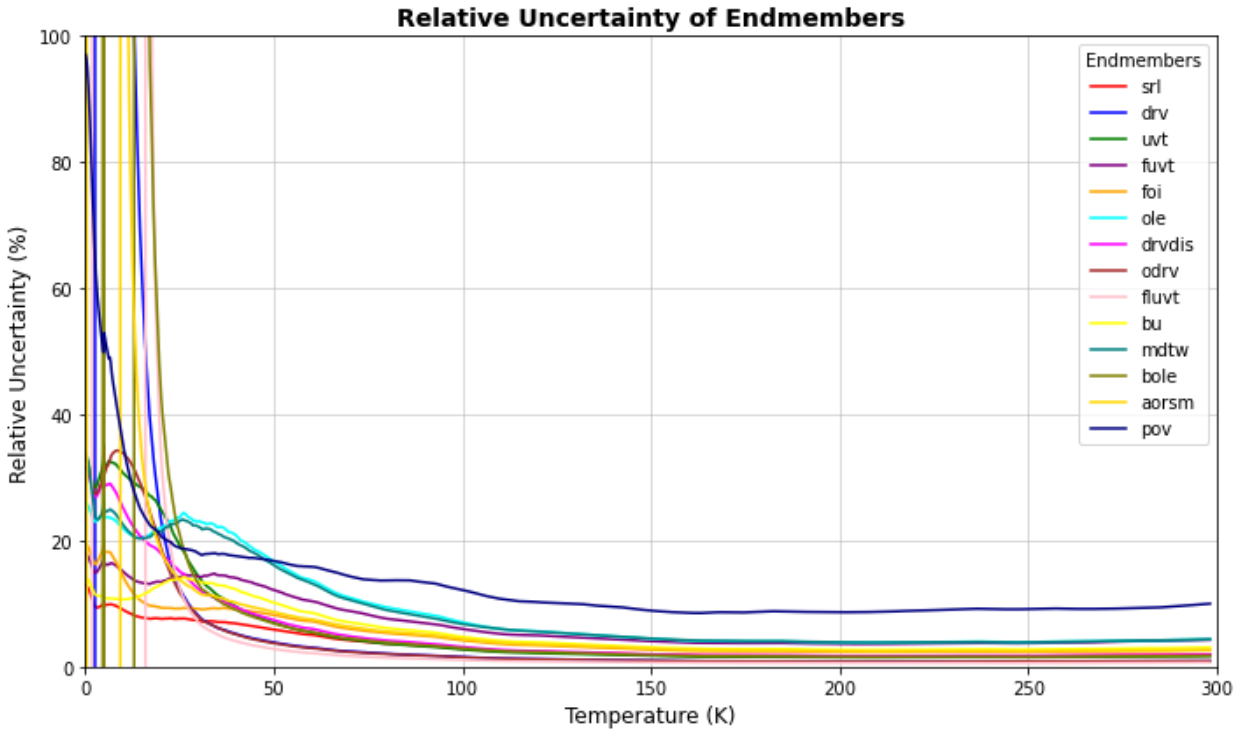

Figure A3H.3. The relative uncertainty in endmember in low-T Cp (J/K/mol) and its dependence on T.

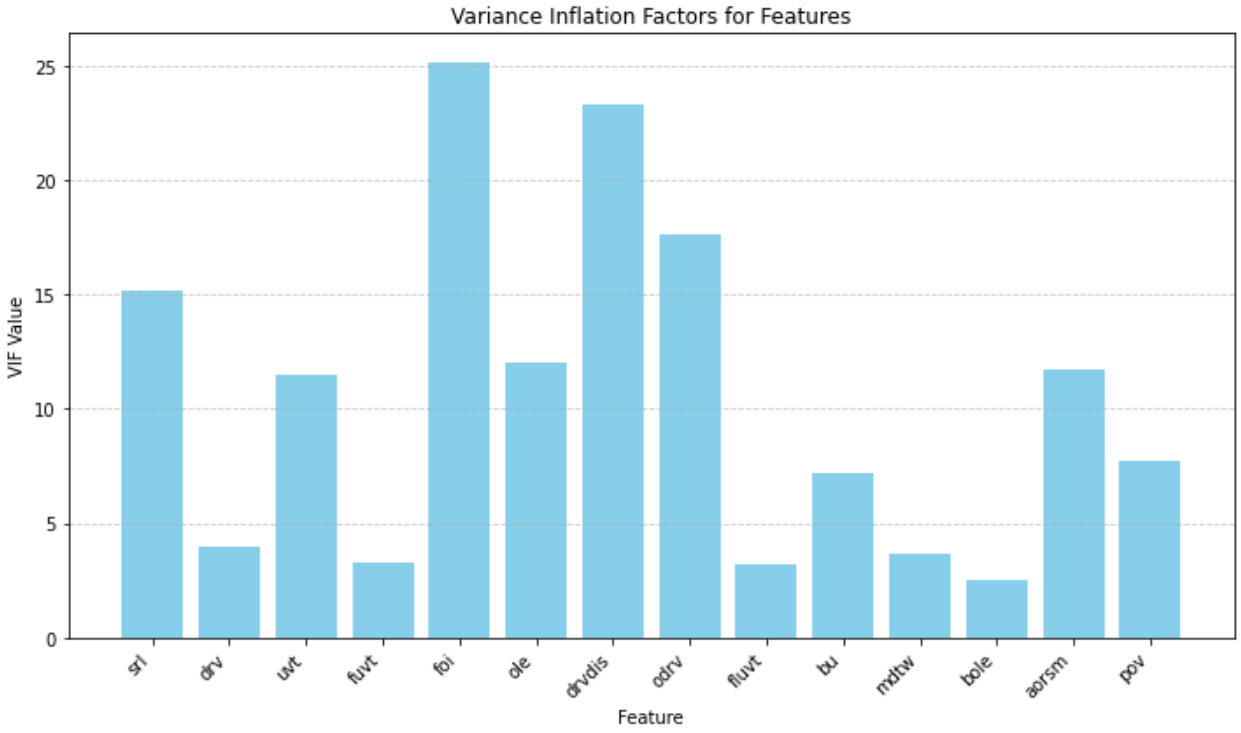

Figure A3H.4. VIF factors for the speciation model. VIF factors depend on the designer matrix and are therefore equal for all regressions relating to the speciation model.

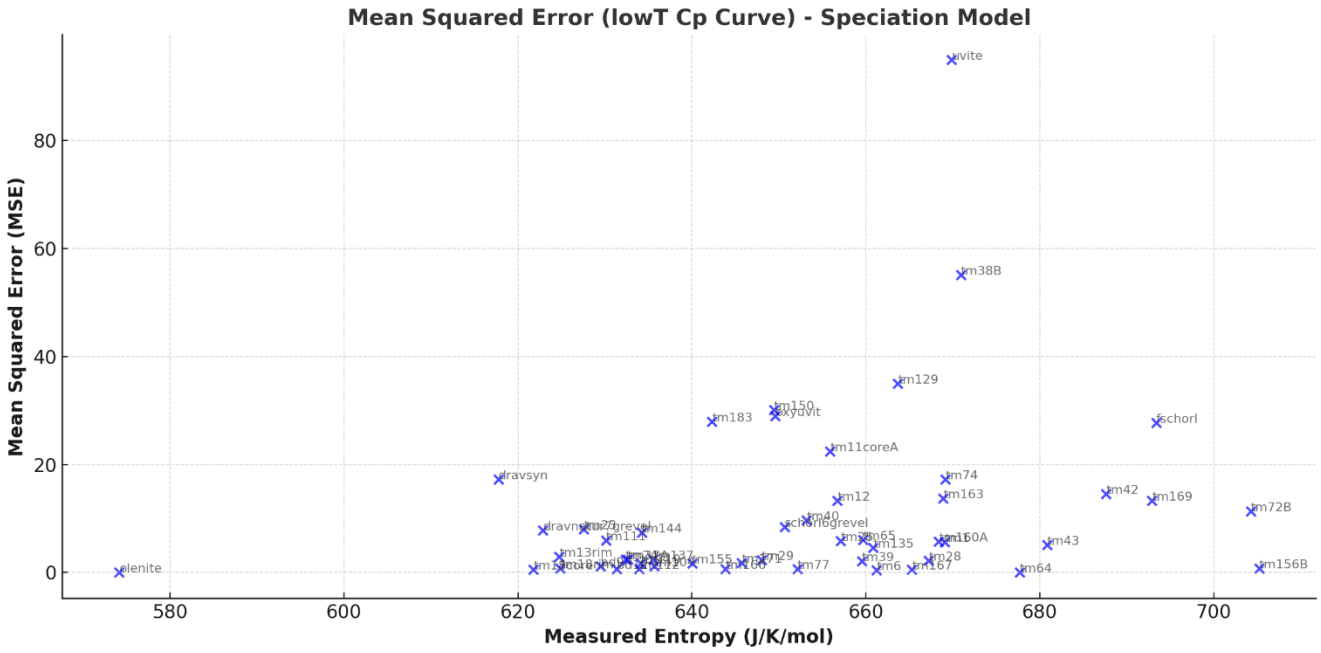

Figure A3H.5 Mean Squared Error (MSE) of Cp curve versus Measured Entropy (J/K/mol) for the low-T Cp curve regression of the speciation model.

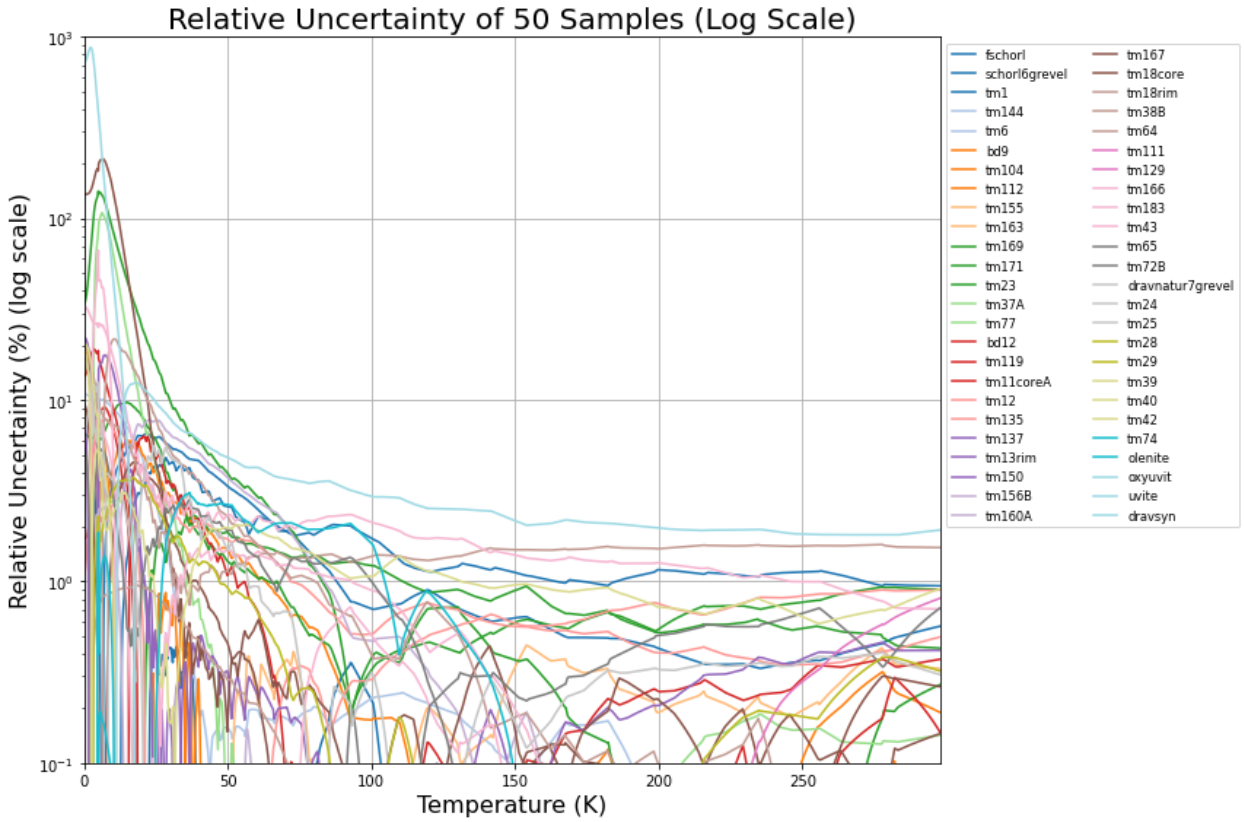

Figure A3H.6 Relative residuals (%) between measured and predicted low-T Cp curves for the speciation model, plotted on a log scale. Higher uncertainties (>1%) occur below 100 K, while they remain <2% above 100 K.

Endmember Cp curves were piecewise linearly interpolated and integrated over T to compute standard state entropies at 298.15 K, with uncertainties derived by integrating standard errors from the regression covariance matrix at each temperature.

Table A3H.1. Standard State Entropy of the endmembers obtained using method 1 for the speciation model.

Endmember Name Entropy (J/K/mol) Entropy Uncertainty (J/K/mol)

Endmember Name	Entropy (J/K/mol)	Entropy Uncertainty (J/K/mol)
srl	710.54	18.85
drv	621.85	8.77
uvt	648.33	16.36
fuvt	725.19	40.70
foi	669.94	25.04
ole	656.99	41.44
drvdis	641.39	18.50
odrv	629.22	8.75
fluvt	641.06	6.46
bu	657.44	28.02
mdtw	690.41	43.41
bole	568.46	15.38
aorsm	638.87	26.07
pov	1000.44	120.65

Bulk compositional vs Speciation S^0. The comparison between the bulk compositional and speciation models is valid, as the training set differs only by an additional synthetic B-olenite sample and basis set formulation differences. S_0 values for srl, uvt, and fluvt are nearly identical in both models. However, the S_0 of ordered drv is predicted to be 10 J/K/mol smaller, while dravdis is 10 J/K/mol larger. Odrv lies between these values, aligning with bulk composition drvB S_0, indicating a 20 J/K/mol S_0 difference between Mg/Al ordering states on the Y and Z sites. Due to strong multicollinearity, these values are not statistically independent, making interpretation of individual effects less reliable. Foi's S_0 is higher than foiB but within the bulk compositional CI. Ole's S_0 is much higher, outside the bulk compositional CI, and 25 J/K/mol smaller than aorsm in the speciation model. Bu's S_0 is lower, while mdtw's is larger than in the bulk compositional model.

Internal Validation. Predicted and measured Cp curves were integrated over T to compare entropies, as shown in Figure A3H.7. Entropies MSE was 28.5 (median 5.9). Gibbs free energy differences due to model simplifications at 298.15 K remained mainly within 2 kJ for the speciation model, consistent with the bulk compositional model. Significant outliers include the synthetic uvite sample and Fe^{3+}-rich tm38B, which were also outliers in the bulk compositional model. Residuals for tourmalines with high nonbuergeritic Fe^{3+} content decreased significantly but did not vanish entirely.

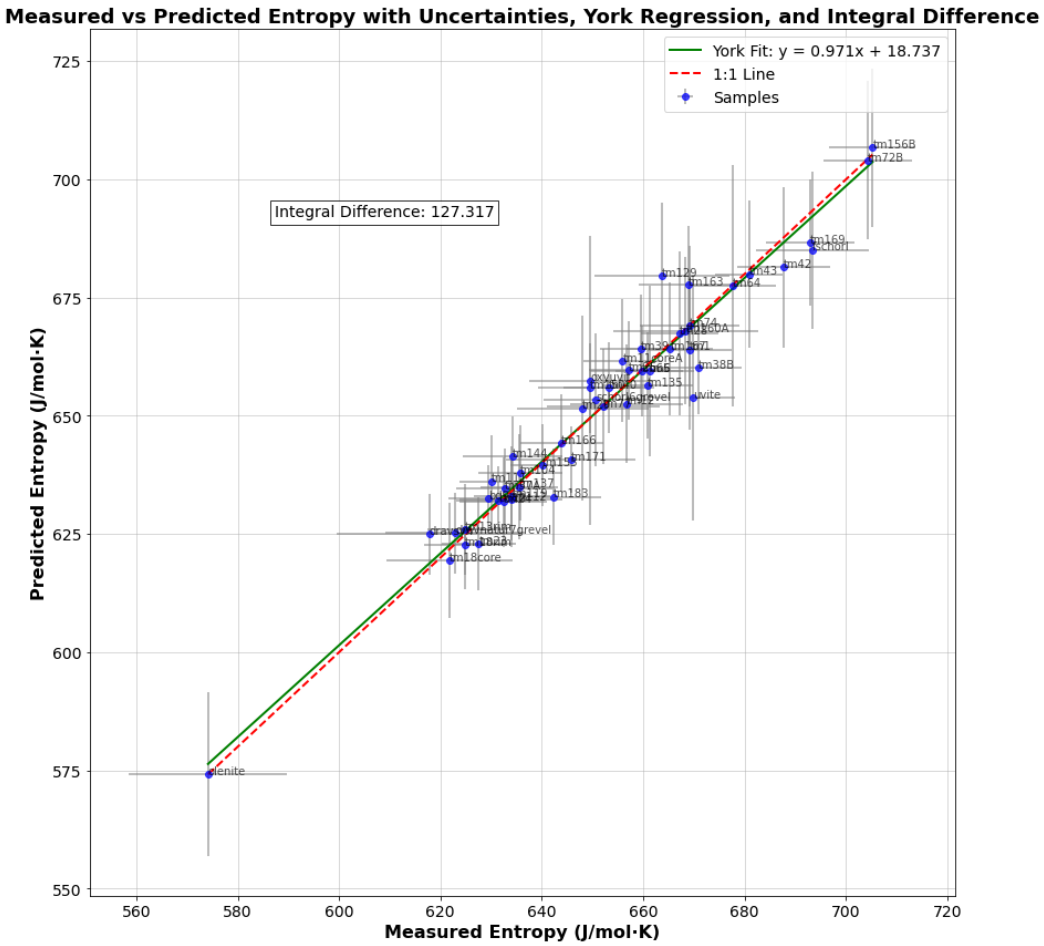

Figure A3H.7. Measured versus predicted entropy using Method 1

Low-T Cp Curve Regression Details. To evaluate regressions along the Cp curve, 55 points were generated per sample using piecewise linear interpolation at 5 K intervals up to 100 K and 20 K intervals from 100 to 800 K to evaluate regression metrics and linearity.

At low T (1–21 K), endmembers such as ordered drv, fluvt, bole, aorsm, and pov are not significant. bole, aorsm, and drv exhibit unphysical negative Cp values (-0.29, -0.02, -0.03 J/K/mol, respectively), while fluvt (0.04 J/K/mol) and olenite (0.8 J/K/mol) have very low Cp values. Pov has a high Cp (2.5 J/K/mol), but this results from highly uncertain extrapolation. The previously observed correlation (~0.75) between srl-drv and drv-S^0 (~ -0.7 J/K/mol) in the bulk compositional models is absent at low T Cp in the speciation model, likely due to the division of bulk drv into ordered and disordered forms. R_{PRESS}^2 is ~0.90 at 1 K, drops to 0 at 61 K, rises to 0.7 at 80 K, and again falls to 0 at 100 K.

Strong multicollinearity is observed among speciation endmembers in the speciation model, unlike the bulk composition model. In the molar volume model, this issue was resolved only by including a literature dataset, which does not exist for entropy. At 1 K, multicollinearity results in significant correlations among speciation endmembers include foi-uvt (-0.62), foi-aorsm (-0.77), foi-odrv (0.7), drvdis-odrv (-0.60), odrv-aorsm (-0.72), and bu-pov (0.67). Additionally, endmember-Cp correlations, such as srl-Cp (0.62) and pov-Cp (0.69), highlight their strong contributions to Cp. These correlations increase with temperature, reaching srl-Cp (0.8) and pov-Cp (0.73) at 100 K, but decrease to 0.57 and 0.26 at 310 K, and 0.34 and 0 at 800 K. bole correlations shift from 0 at 1 K to -0.73 at 240 K, stabilize until 450 K, and decline to -0.5 at 800 K. Buergerite starts at 0.52, switches sign near 298 K, and becomes -0.36 at 800 K.

LOOCV. The speciation model is less robust than the bulk model, with MSE and derived entropy quadrupling in LOOCV and their median doubling due to high-leverage samples like buergerite and synthetics, which often single-handedly define endmembers. These samples are well fit by the model but poorly predicted when excluded.

3. SPECIATION MODEL HIGH-T Cp (METHOD 1)

Endmember Cp curves. Speciation endmember high-T Cp curves (>298.15 K) can be found in Figure A3H.8. Standard error analysis shows absolute uncertainty linearly increases with temperature, while relative stays relatively constant. The confidence intervals are broader than in the bulk compositional model however behave smoothly, except for pov which is very poorly

constrained.

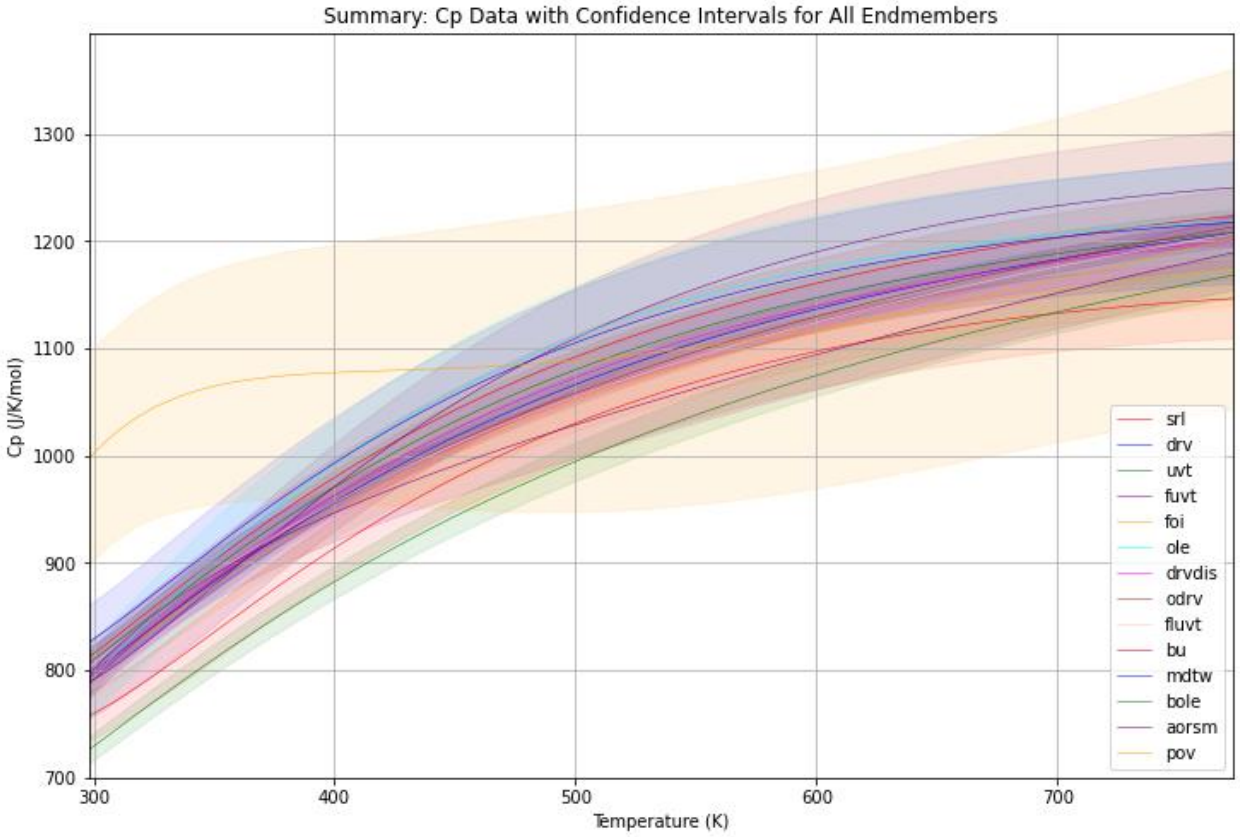

Figure A3H.8. Speciation endmember high-T Cp curves with their confidence intervals.

$XY_3Z_6T_6V_3W$

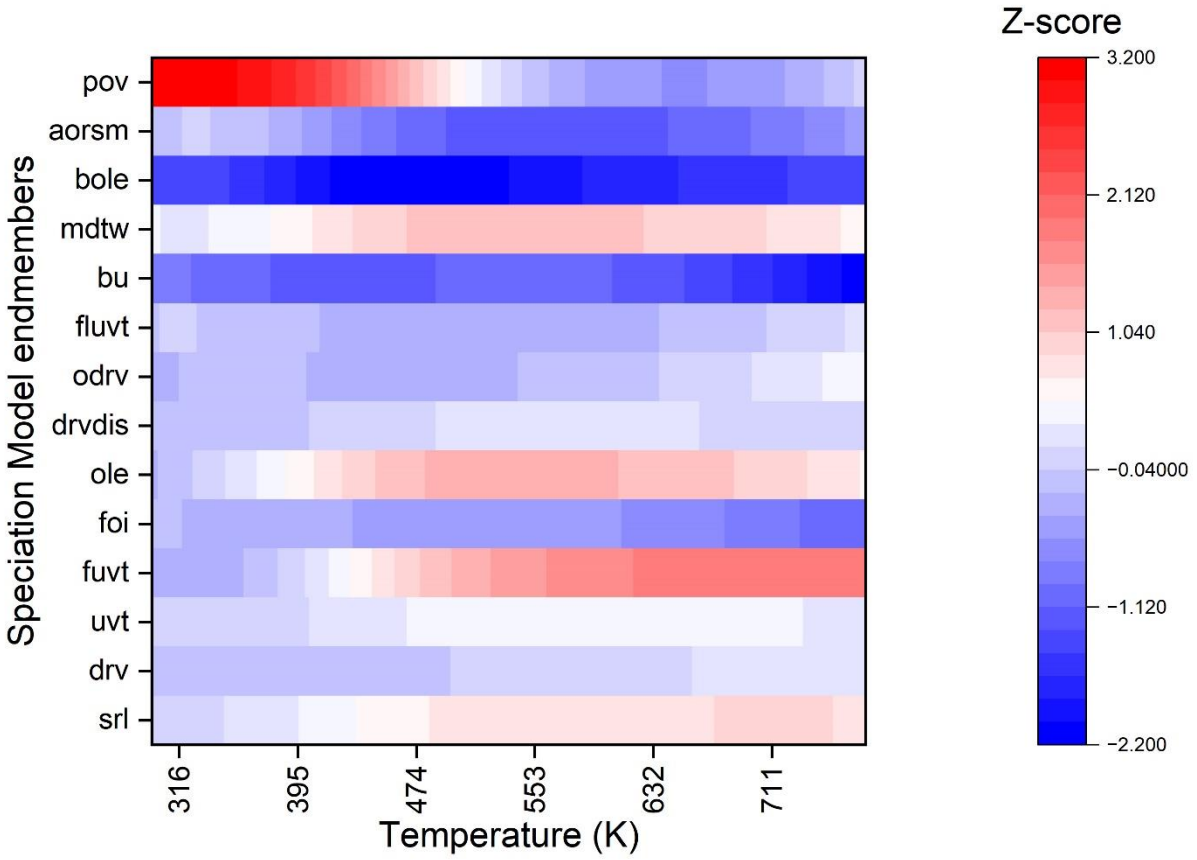

Figure A3H.9: Heatmap of speciation model high-T Cp curves Z-scores at 1 K intervals, comparing each endmember to the mean of all endmembers. $XY_3Z_6T_6V_3W$

The heatmap of Z-scores across temperatures shows that pov, mdtw, ole, and fuvt exhibit the highest high-T Cp curves, while foi, bu, and bole have the lowest (Figure A3H.9). In the bulk compositional model, uvtB has high Cp curves, but in the speciation model, it shows intermediate values. This is likely due to the iron-rich versions of these endmembers in the speciation model having their own separate endmembers.

.

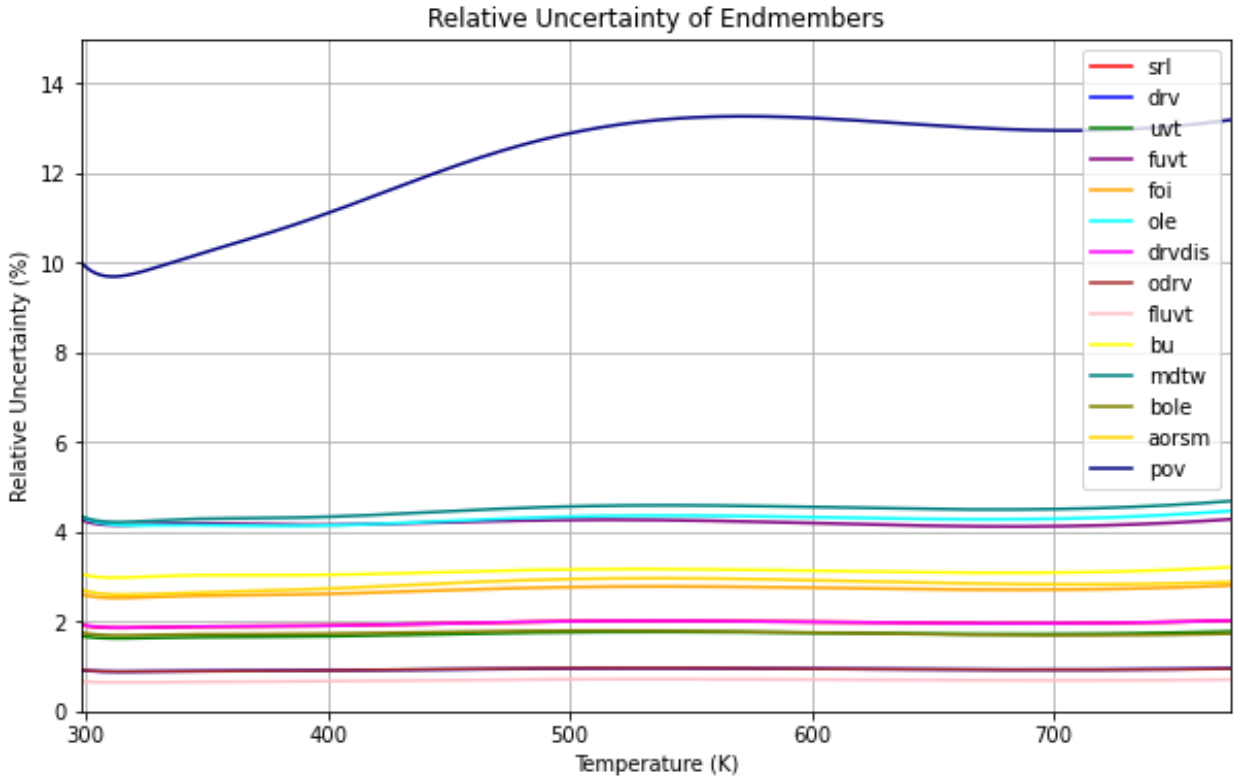

Figure A3H.10. The relative uncertainty in Cp (J/K/mol) dependence on T. $XY_3Z_6T_6V_3W$. Uncertainty is high for the pov endmember.

Internal Validation. The Berman Cp model regression coefficients for endmembers were used to predict Cp curves for training samples, with a mean MSE of 61.1 (median 31.2), similar to the bulk compositional model. Residuals showed no temperature dependency and relative deviations within 1%, with outliers reaching 2% (Figure A3H.13). The mean $S_{298.15K}^{773.15\,K}$ MSE is 46.6, with a median of 21.1, half that of the bulk compositional model, indicating that while outliers are not better fit, the centroid of the data is. This is also reflected in the delta G values, where outliers remain similar but centroid free energies differences decrease (Figure A3H.12).

Predicted versus measured plots show that in the speciation model, compositional bias is much less extreme than in the bulk model, with more samples clustering around the 1:1 line (Figure A3H.10). In contrast to the bulk model, predicted differences between endmembers at high T still exist, suggesting the speciation model extrapolates better to high T. However, direct comparison of integral differences between the two models is not possible due to the inclusion of the low-entropy synthetic B-Olenite sample.

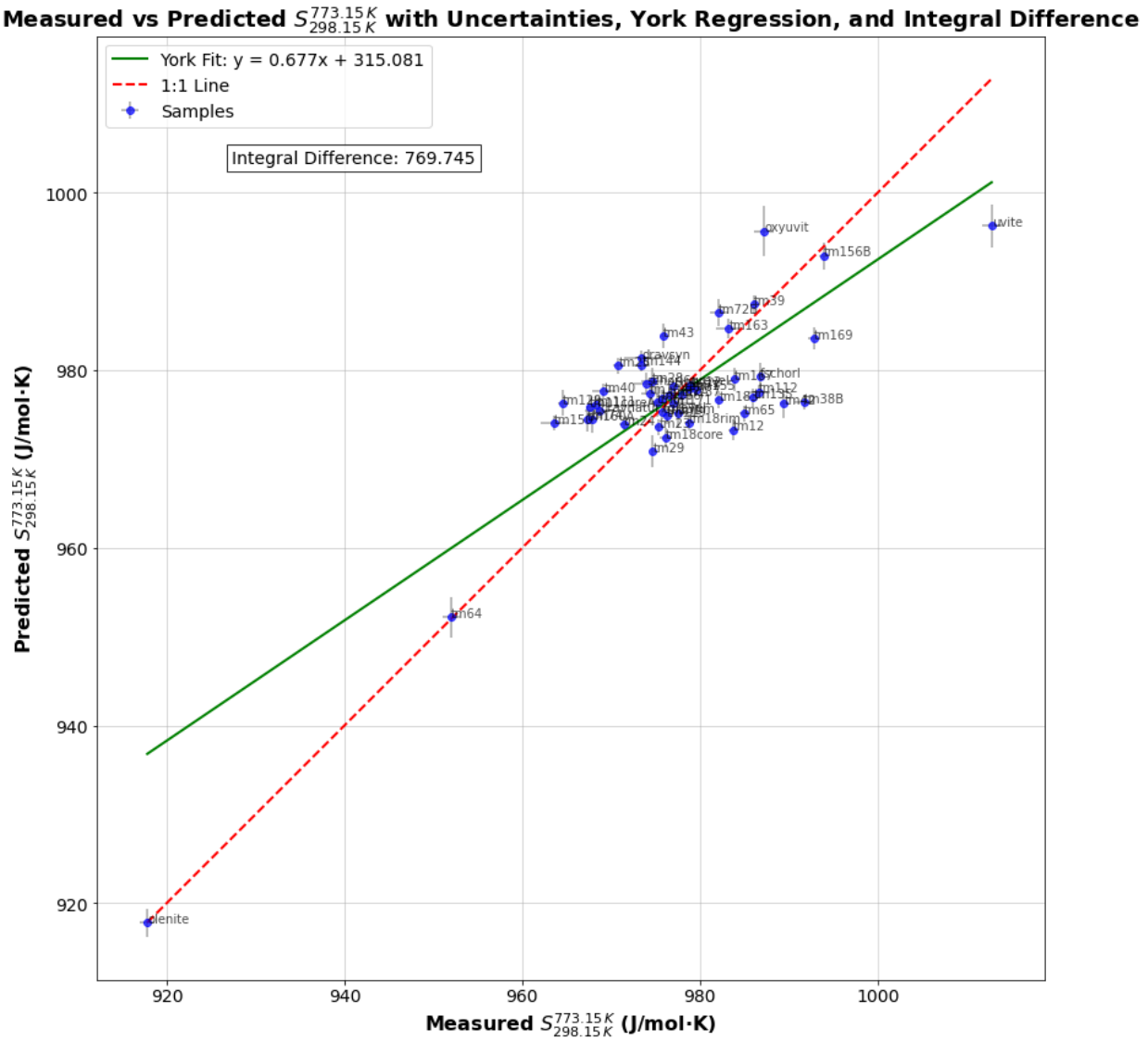

Figure A3H.11. Measured versus predicted entropy using Method 1. Uncertainties are propagated from the polynomial model fit and therefore assumed a 'perfect' Berman model.

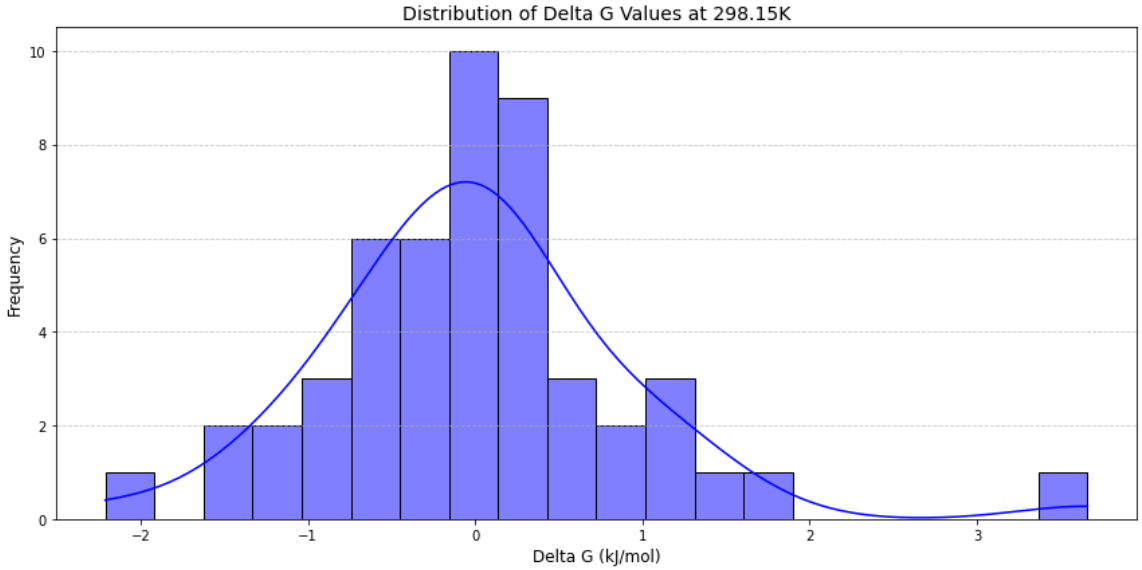
Distribution of Delta G Values at 298.15K
Frequency
Delta G (kJ/mol)

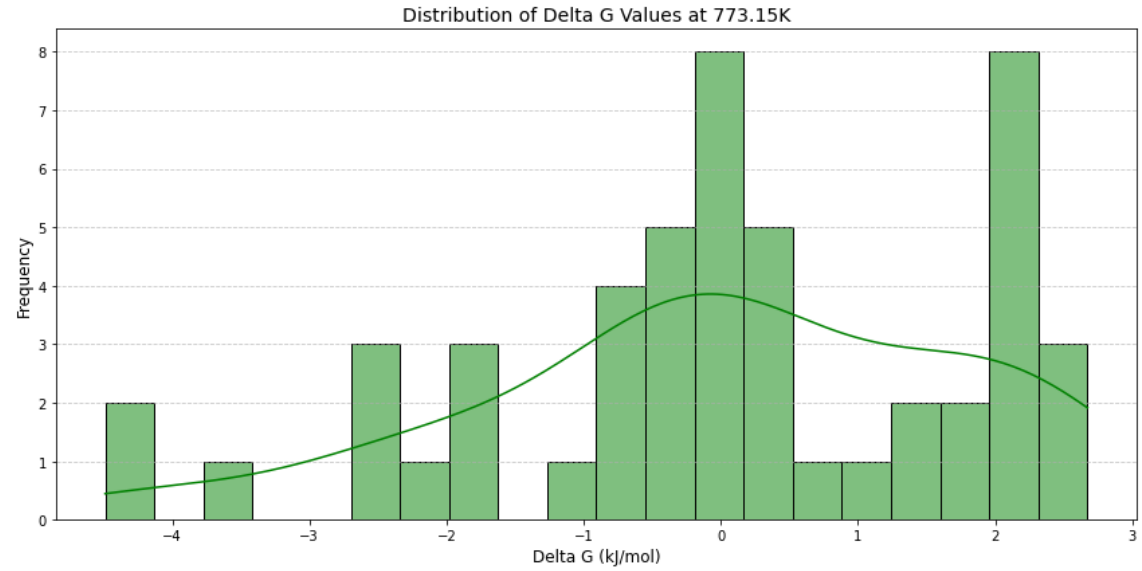
Distribution of Delta G Values at 773.15K
Frequency
Delta G (kJ/mol)

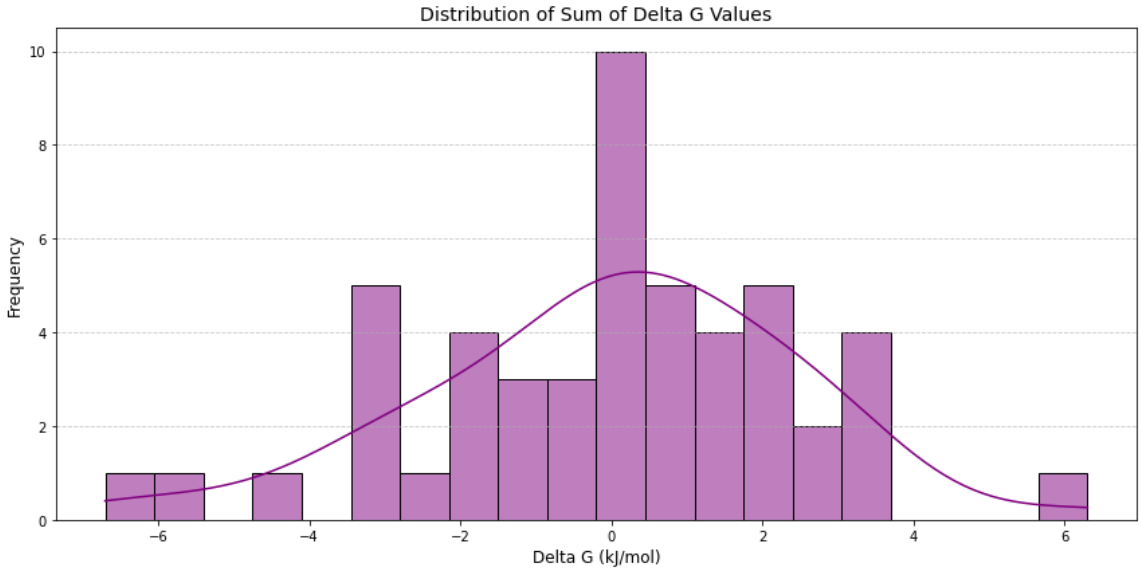
Distribution of Sum of Delta G Values
Frequency
Delta G (kJ/mol)

Figure A3H.12. Distribution of ΔG differences at 773.15 K arising from discrepancies between measured and predicted Cp for the speciation model. The figure highlights the contributions from differences in standard state entropy (S_0), integrated entropy along the high-T Cp curve ($S_{298.15K}^{773.15\,K}$), and their combined impact on ΔG values at 773.15 K.

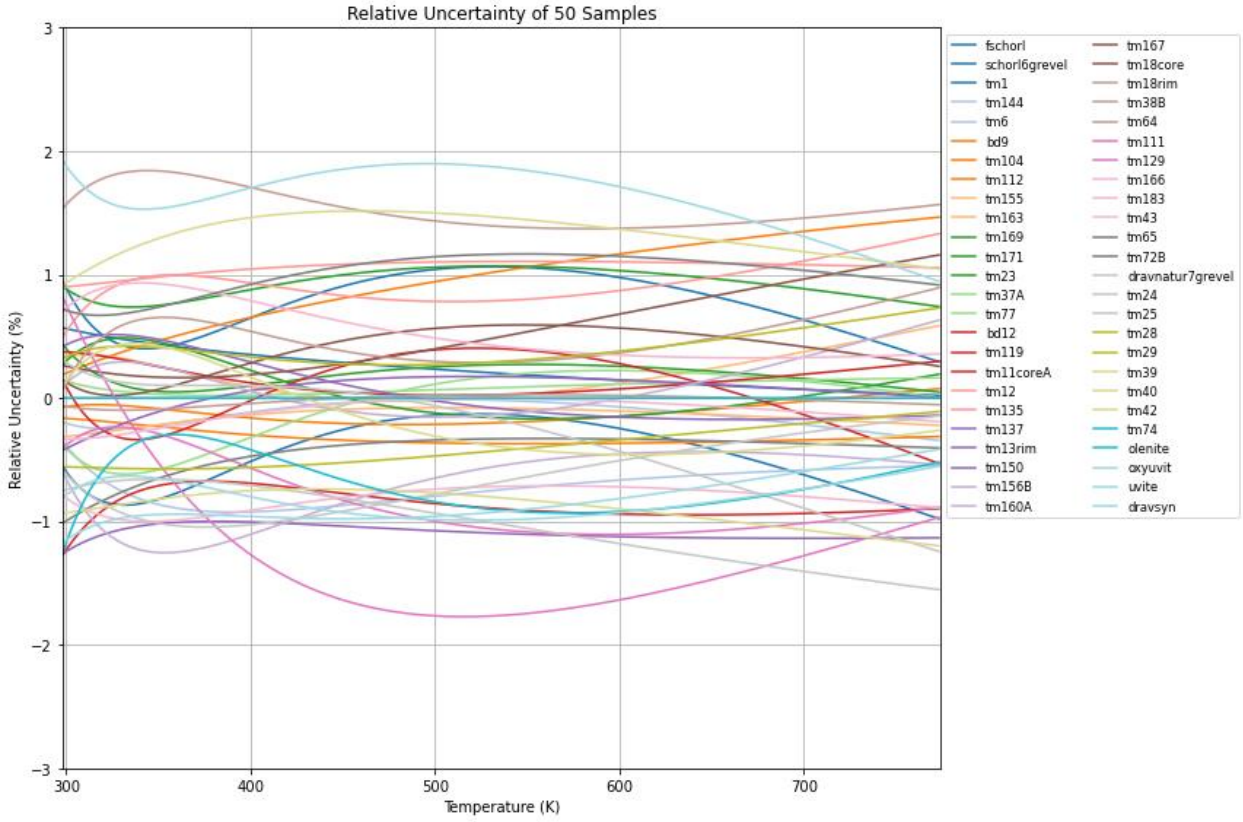

Figure A3H.13. Relative deviations between training set data and model for high-T Cp. $XY_3Z_6T_6V_3W$.

At 300.15 K, 373.15 K, 573.15 K, and 773.15 K, measured versus predicted Cp comparisons showed good agreement with the 1:1 line (Figure A3H.14). While the systematic offset observed in the bulk compositional model is also present in the speciation model, the compositional bias is reduced, indicating that adding additional endmembers improves sensitivity in the flat parts of the high-T Cp curve. Therefore, speciation models may extrapolate better to high temperatures than bulk compositional models.

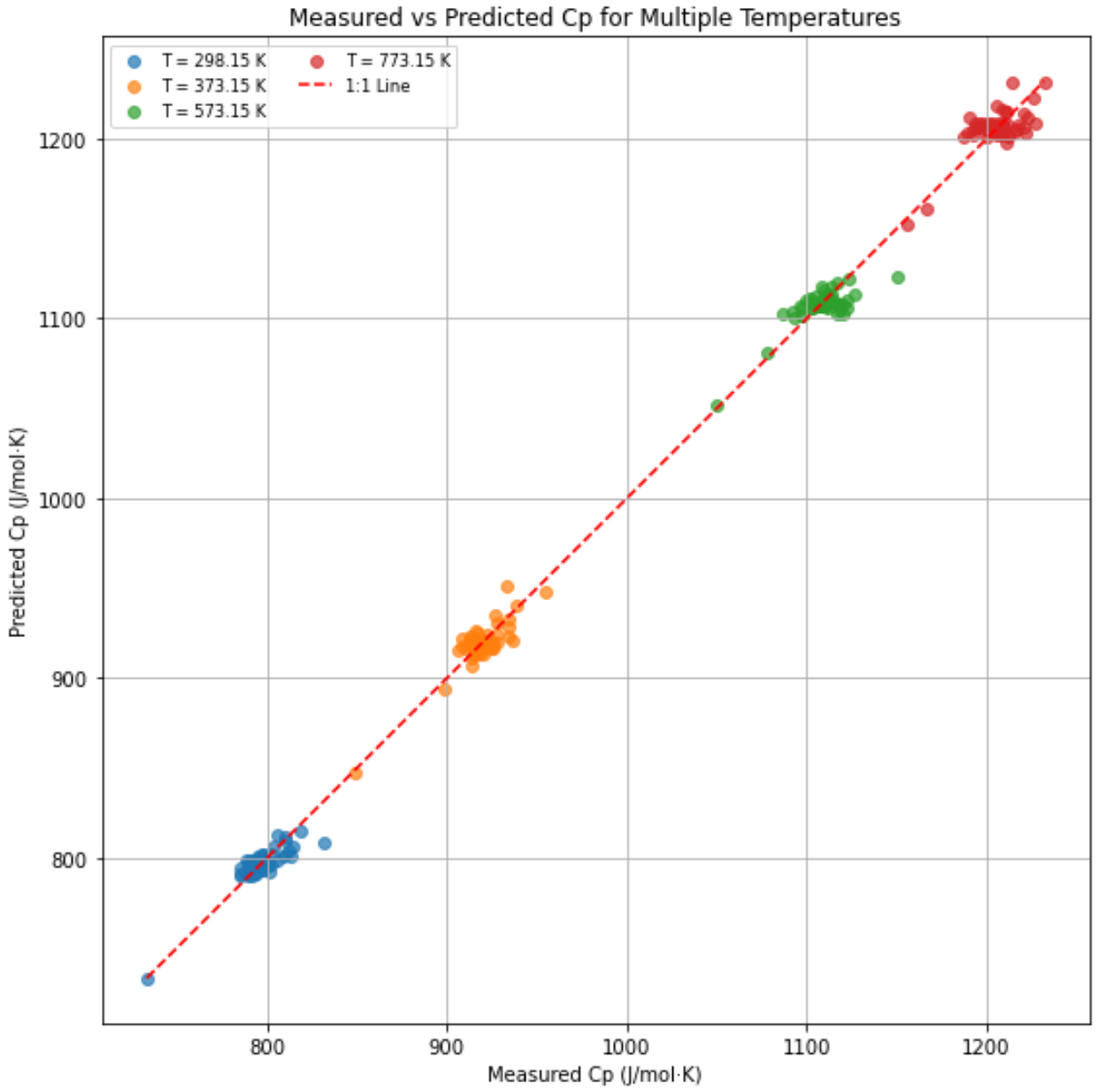

Figure A3H.14. Predicted versus measured Cp at four different T with the 1:1 line, highlighting the more horizontal distribution of samples at higher T, though less pronounced than in the bulk compositional model.

LOOCV The LOOCV MSE for high-T Cp and $S_{298.15K}^{773.15\,K}$ quadrupled instead of tripled for the speciation model showing that the speciation model is more data dependent. This makes sense as many endmembers in the speciation model are dictated by only 1-2 samples and therefore is not robust when such samples are removed from the training set data.

Fe^{3+} Speciation effects Figure A3H.14 a) and b) shows that bu and pov have drastically different effects on molar volume, S_0, and $S_{298.15K}^{773.15\,K}$.

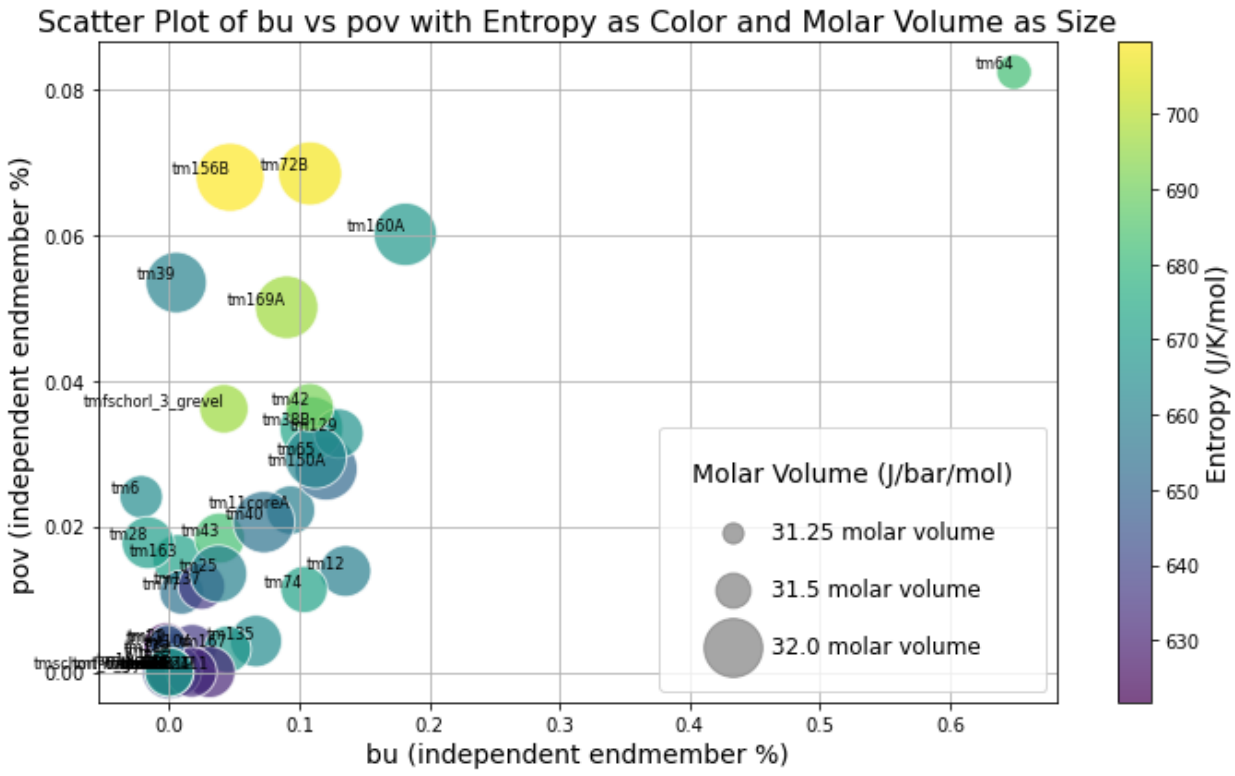

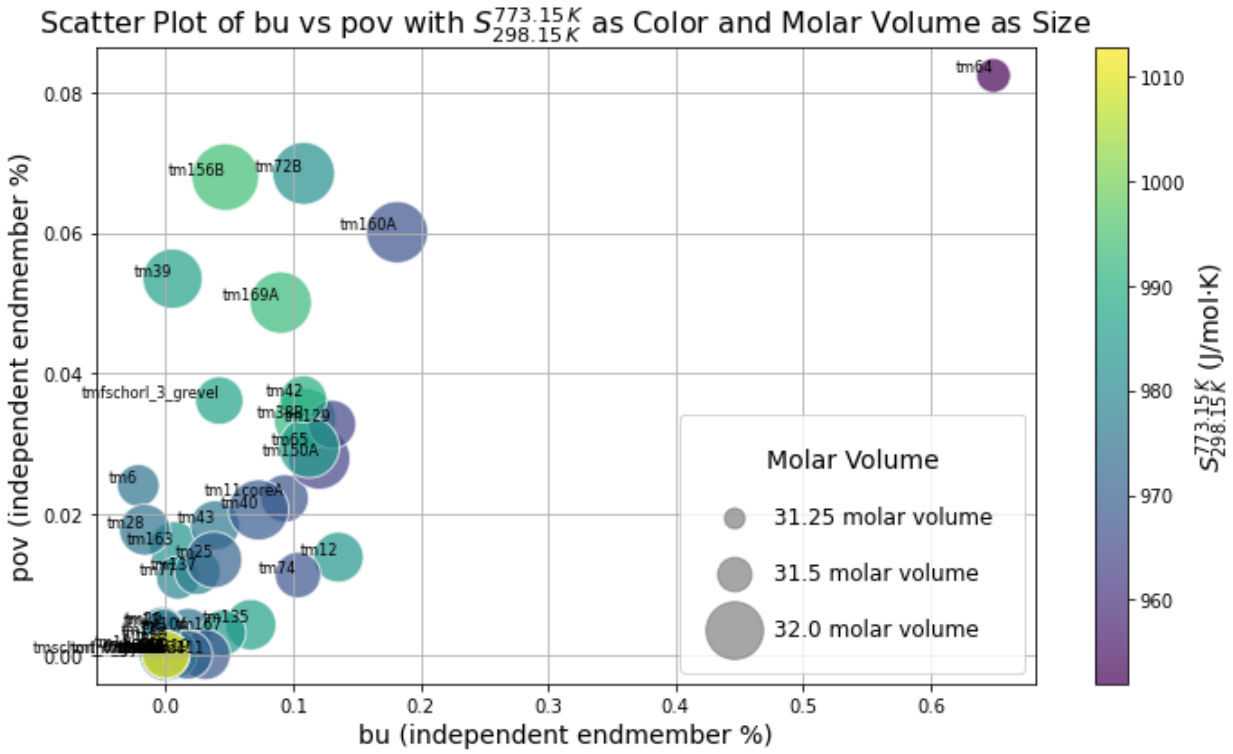

Figure A3H.15. Pov versus bu endmember fraction. Size of points indicate molar volume whereas the colour indicates in a) standard state entropy and in b) $S^{773.15\,K}_{298.15K}$. Note the difference in scale for the pov and bu axis. The figures do show how pov and bu have drastically different properties.

REFERENCES

Green, E.C.R., White, R.W., Diener, J.F.A., Powell, R., Holland, T.J.B., and Palin, R.M. (2016) Activity-composition relations for the calculation of partial melting equilibria in metabasic rocks. Journal of Metamorphic Geology, 34, 845–869.

Holland, T.J.B., and Powell, R. (2011) An improved and extended internally consistent thermodynamic dataset for phases of petrological interest, involving a new equation of state for solids. Journal of Metamorphic Geology, 29, 333–383.

White, R.W., Powell, R., Holland, T.J.B., Johnson, T.E., and Green, E.C.R. (2014) New mineral activity-composition relations for thermodynamic calculations in metapelitic systems. Journal of Metamorphic Geology, 32, 261–286.

Appendix 3I. Speciation Model 4 Temperature Zoom in Predicted vs Measured

This Appendix contains all the Speciation Model. 4 Temperature Zoom in Predicted vs Measured for 298.15, 373.15, 573.15 and 773.15K.

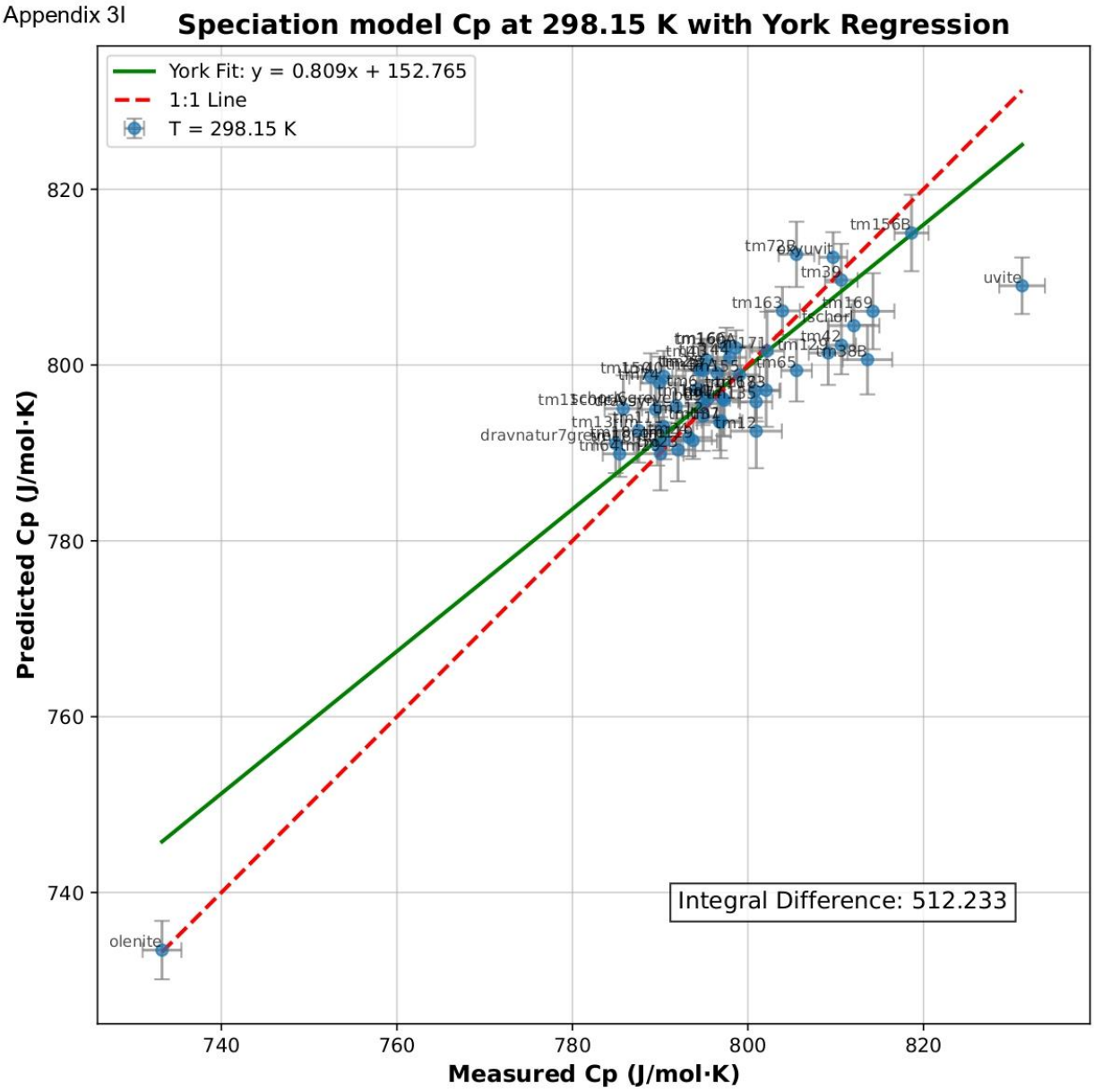

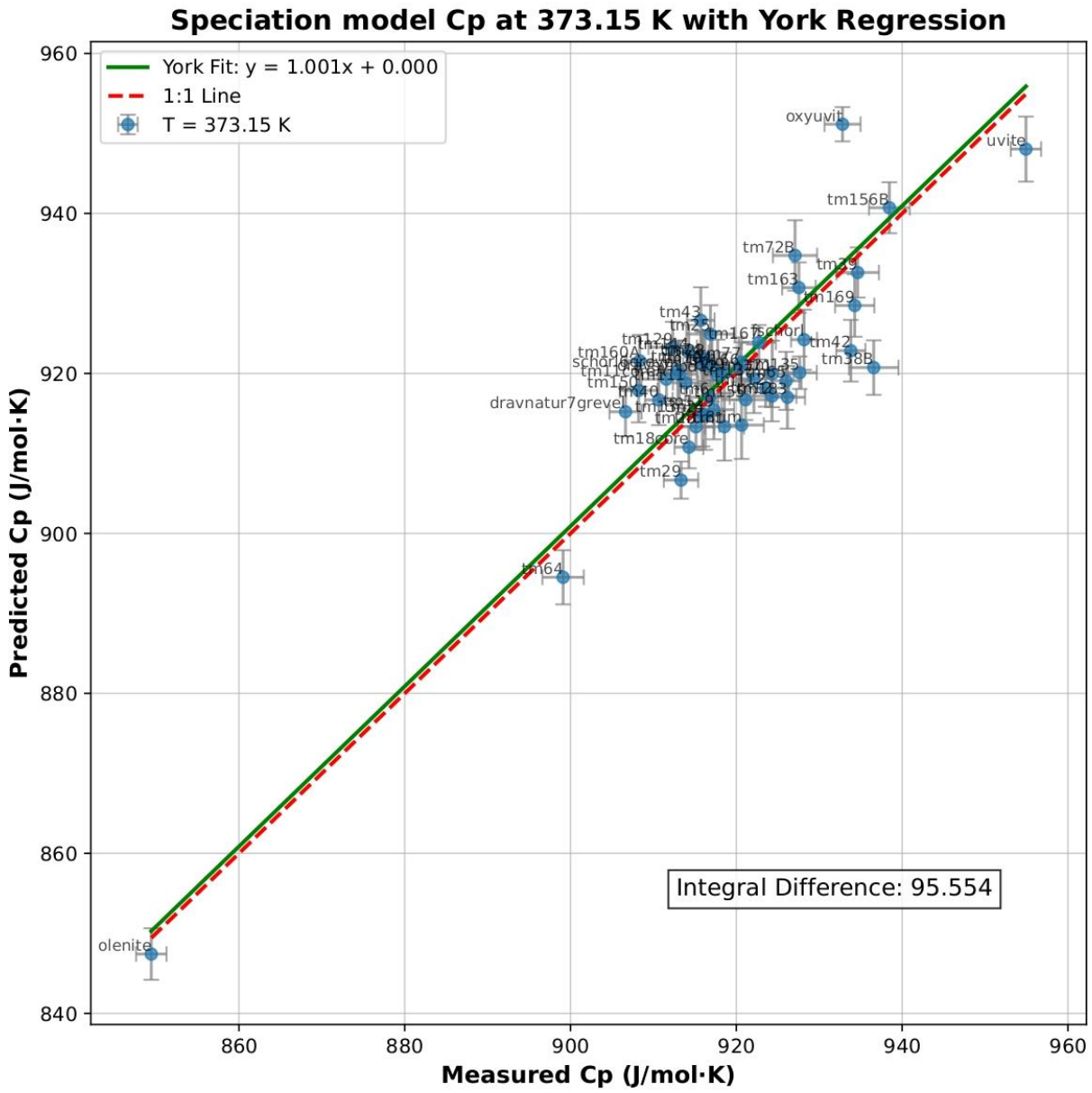
Speciation model Cp at 373.15 K with York Regression
York Fit: y = 1.001x + 0.000
1:1 Line
T = 373.15 K
Integral Difference: 95.554
Predicted Cp (J/mol·K)
Measured Cp (J/mol·K)
960
940
920
900
880
860
840
860
880
900
920
940
960
oxyuvite
uvite
tm156B
tm72B
tm163
tm169
tm43
tm42
tm38B
dravnatur7grevel
tm29
tm164
olenite

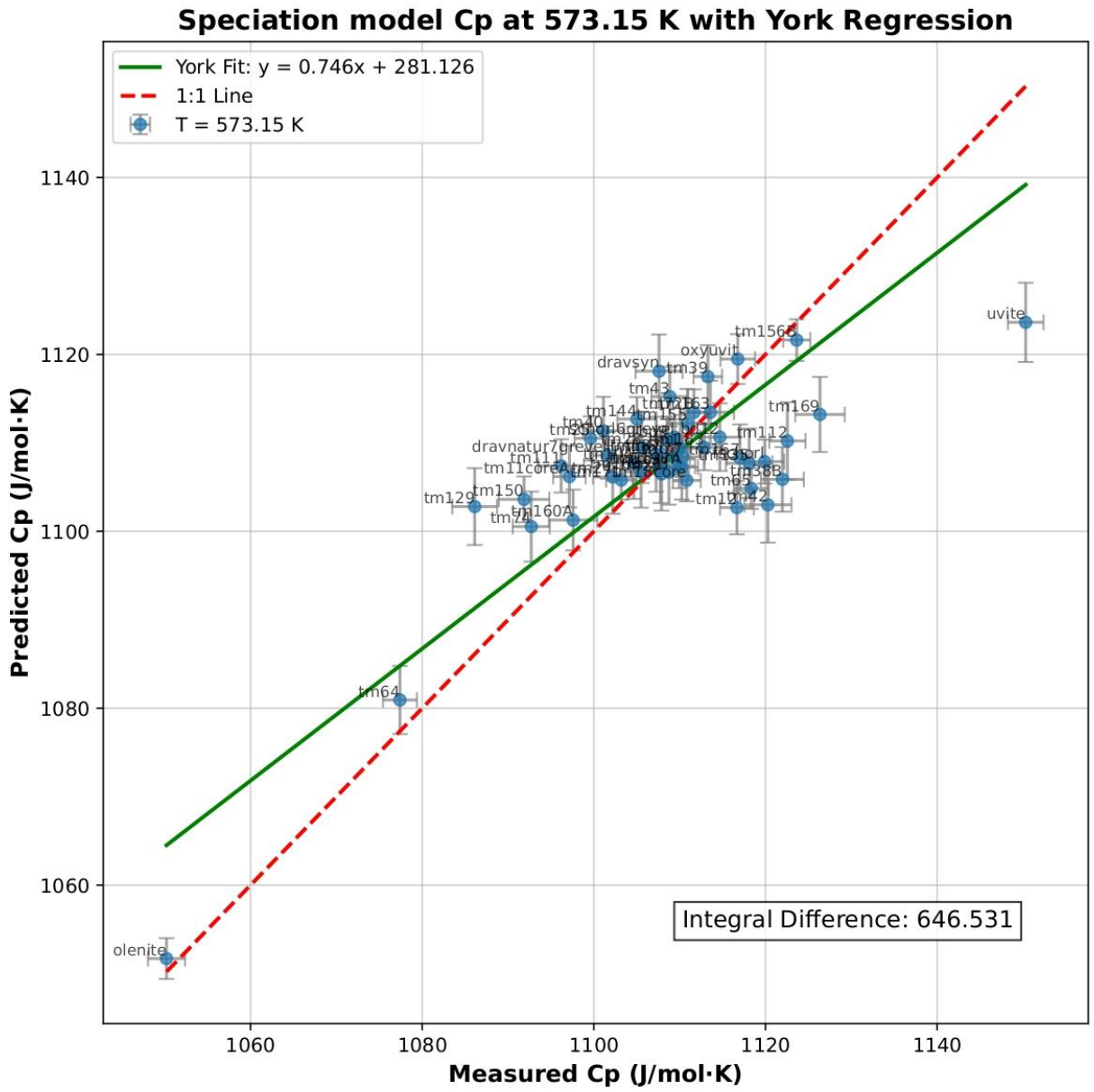
Speciation model Cp at 573.15 K with York Regression
York Fit: y = 0.746x + 281.126
1:1 Line
T = 573.15 K
Predicted Cp (J/mol·K)
Measured Cp (J/mol·K)
1060
1080
1100
1120
1140
Integral Difference: 646.531
uvite
olenite
tm64
tm129
tm150
tm160A
tm74
tm156B
oxyuvit
dravsyn
tm39
tm43
tm169
tm112
tm42
tm93
tm38B

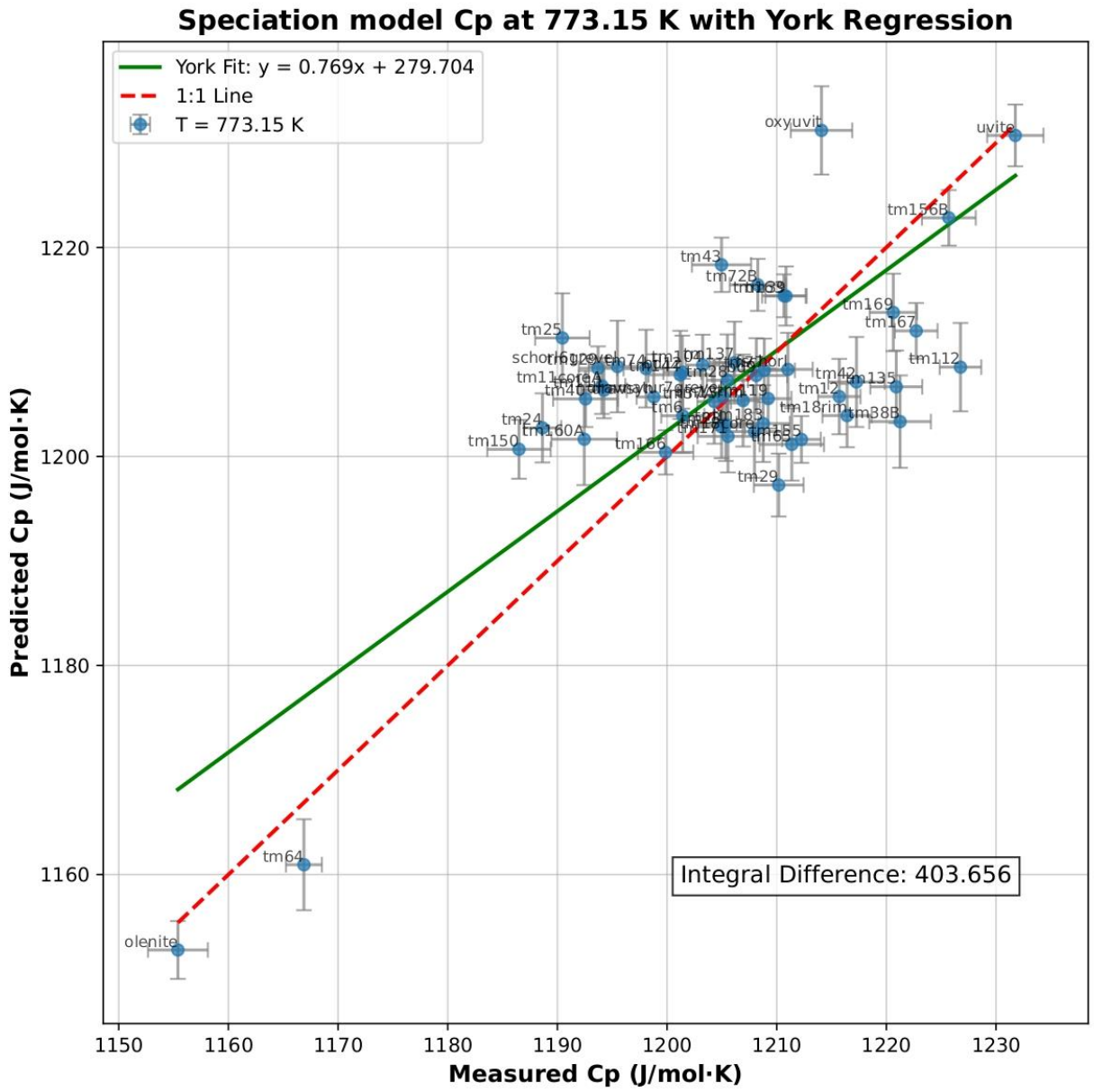
Speciation model Cp at 773.15 K with York Regression
York Fit: y = 0.769x + 279.704
1:1 Line
T = 773.15 K
Predicted Cp (J/mol·K)
Measured Cp (J/mol·K)
Integral Difference: 403.656
oxyuvit
uvite
tm156B
tm43
tm72B
tm169
tm167
tm25
tm112
tm42
tm135
tm12
tm18rim
tm88B
tm24
tm160A
tm150
tm29
tm64
olenite
1150
1160
1170
1180
1190
1200
1210
1220
1230
1160
1180
1200
1220

Appendix 3J. Speciation Model endmember curves

This Appendix contains all the Speciation model endmember Cp curves.

Appendix 3J Speciation Model Cp curves

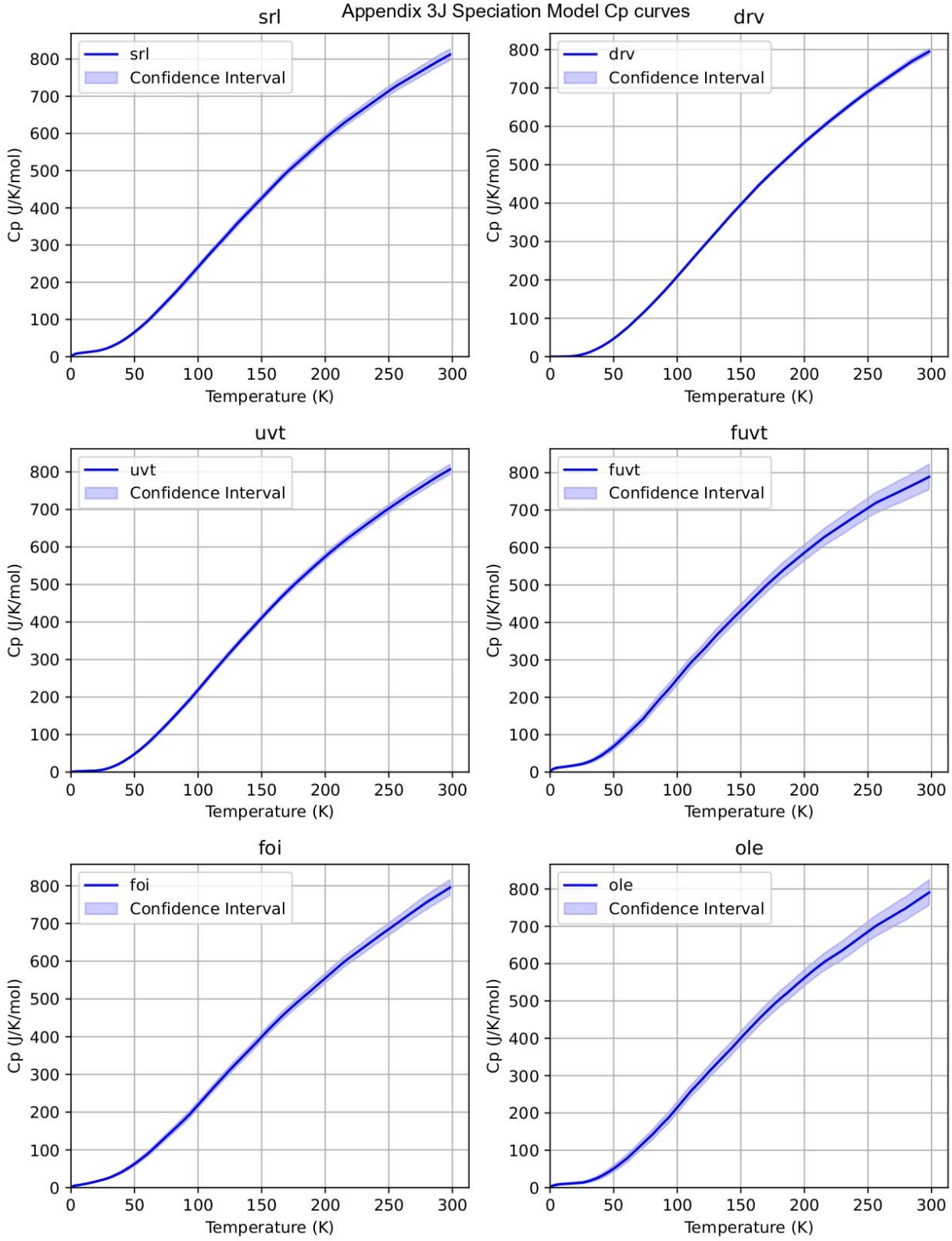

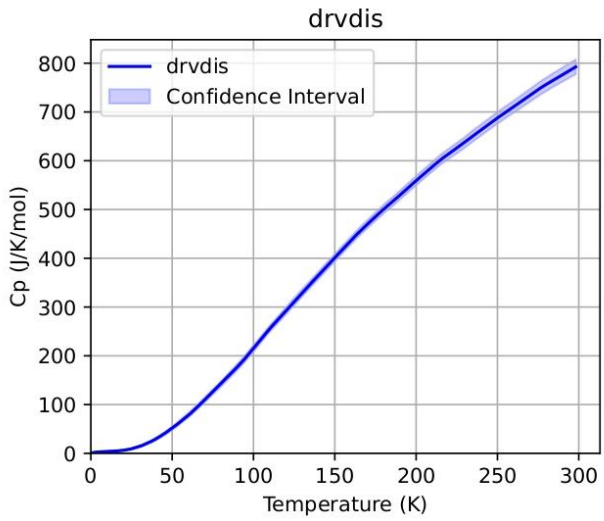
drvdis
drvdis
Confidence Interval
Cp (J/K/mol)
Temperature (K)

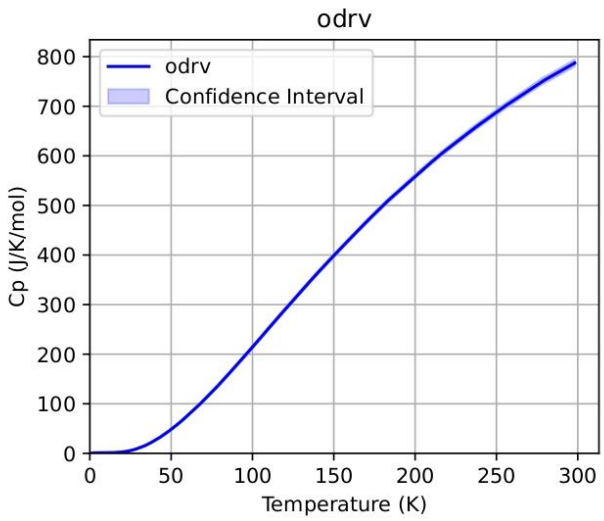
odrv
odrv
Confidence Interval
Cp (J/K/mol)
Temperature (K)

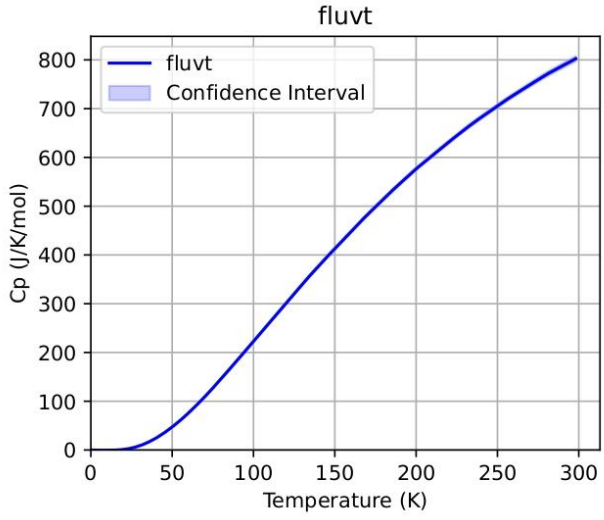
fluvt
fluvt
Confidence Interval
Cp (J/K/mol)
Temperature (K)

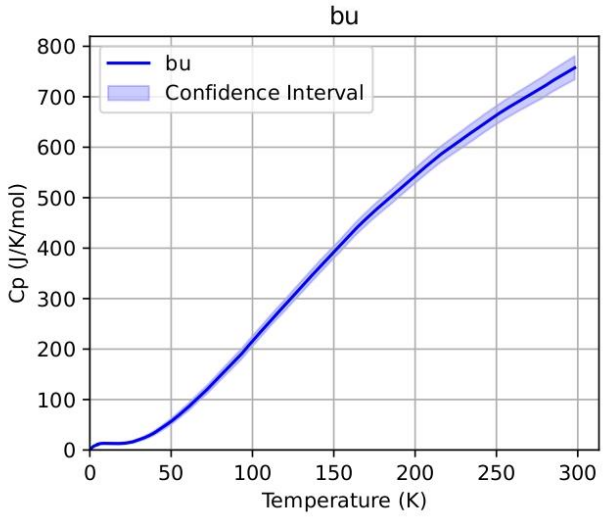
bu
bu
Confidence Interval
Cp (J/K/mol)
Temperature (K)

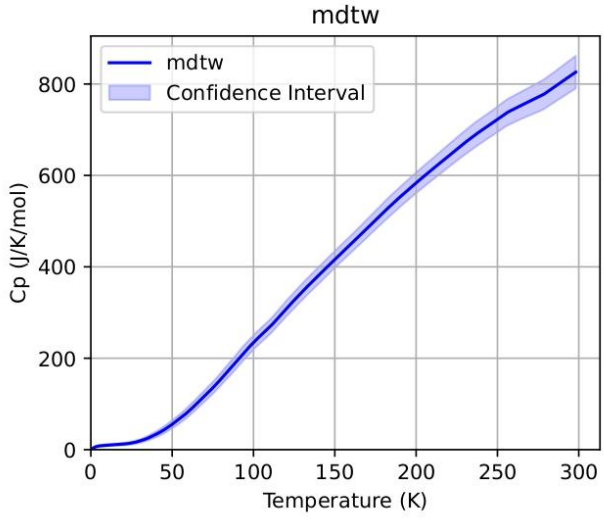
mdtw
mdtw
Confidence Interval
Cp (J/K/mol)
Temperature (K)

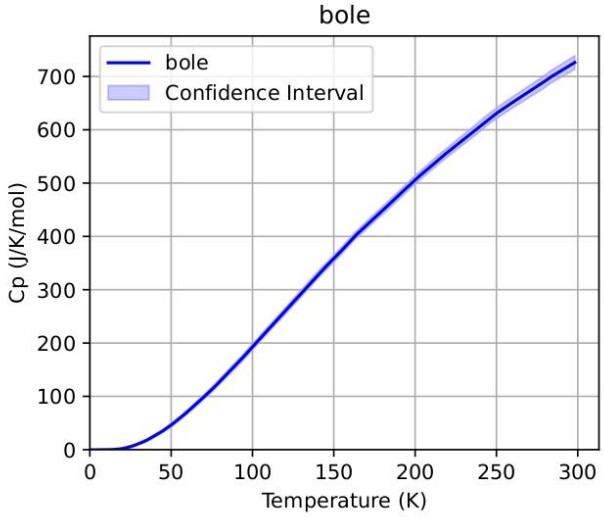
bole
bole
Confidence Interval
Cp (J/K/mol)
Temperature (K)

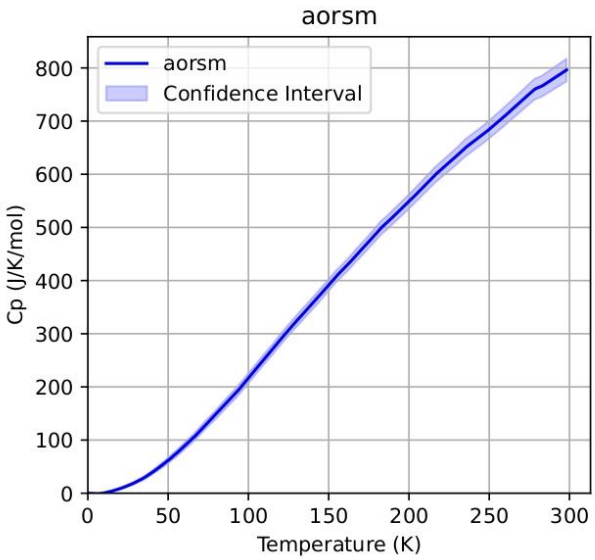
aorsm
aorsm
Confidence Interval
Cp (J/K/mol)
Temperature (K)
0
100
200
300
400
500
600
700
800
0
50
100
150
200
250
300

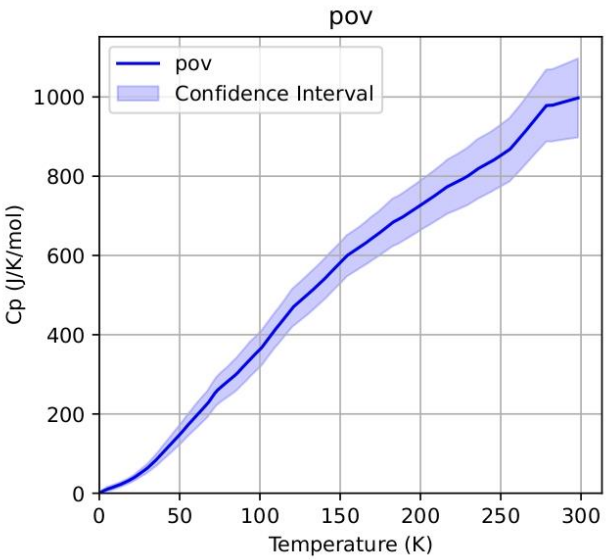
pov
pov
Confidence Interval
Cp (J/K/mol)
Temperature (K)
0
200
400
600
800
1000
0
50
100
150
200
250
300

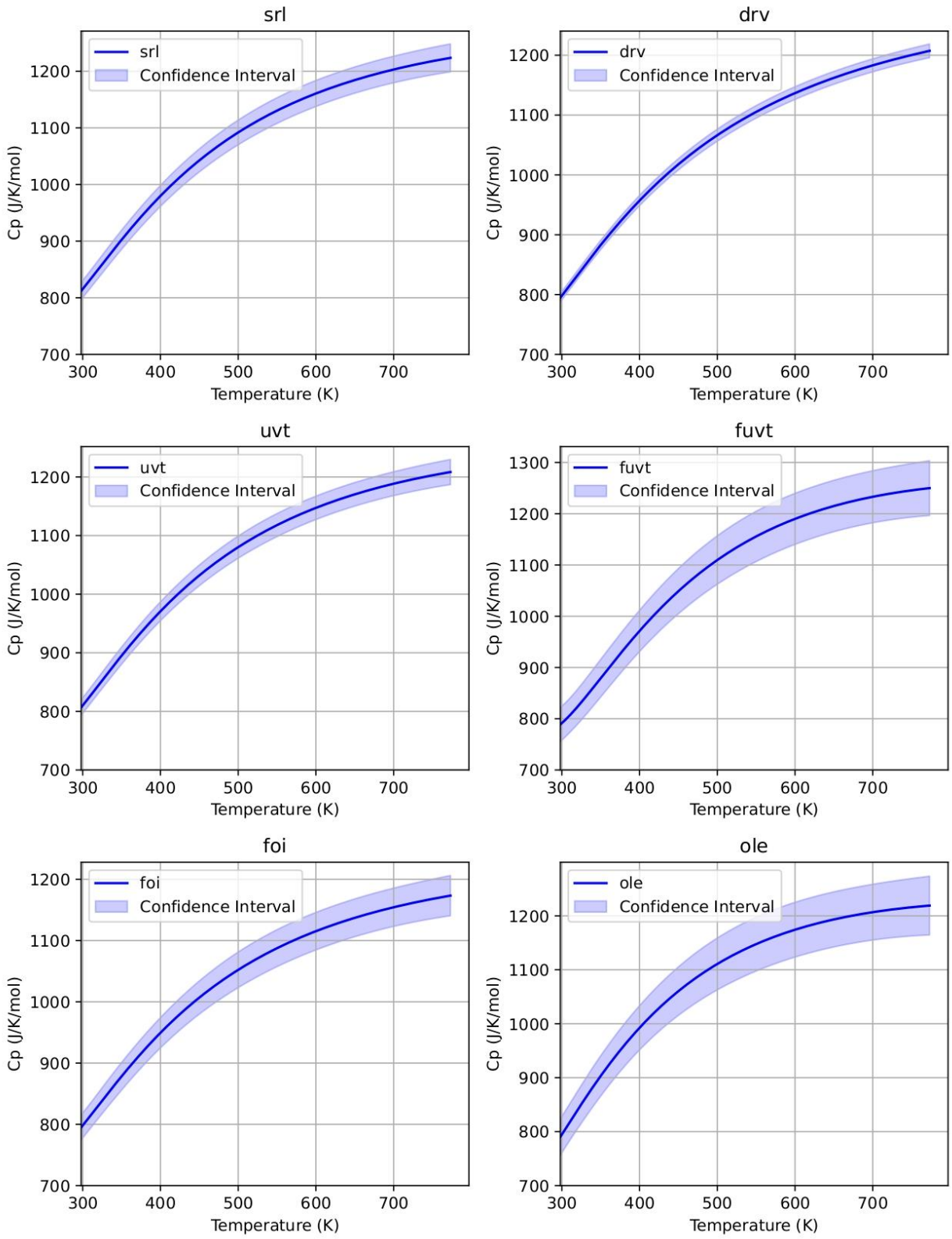
srl
srl
Confidence Interval
Cp (J/K/mol)
Temperature (K)
drv
drv
Confidence Interval
Cp (J/K/mol)
Temperature (K)
uvt
uvt
Confidence Interval
Cp (J/K/mol)
Temperature (K)
fuvt
fuvt
Confidence Interval
Cp (J/K/mol)
Temperature (K)
foi
foi
Confidence Interval
Cp (J/K/mol)
Temperature (K)
ole
ole
Confidence Interval
Cp (J/K/mol)
Temperature (K)

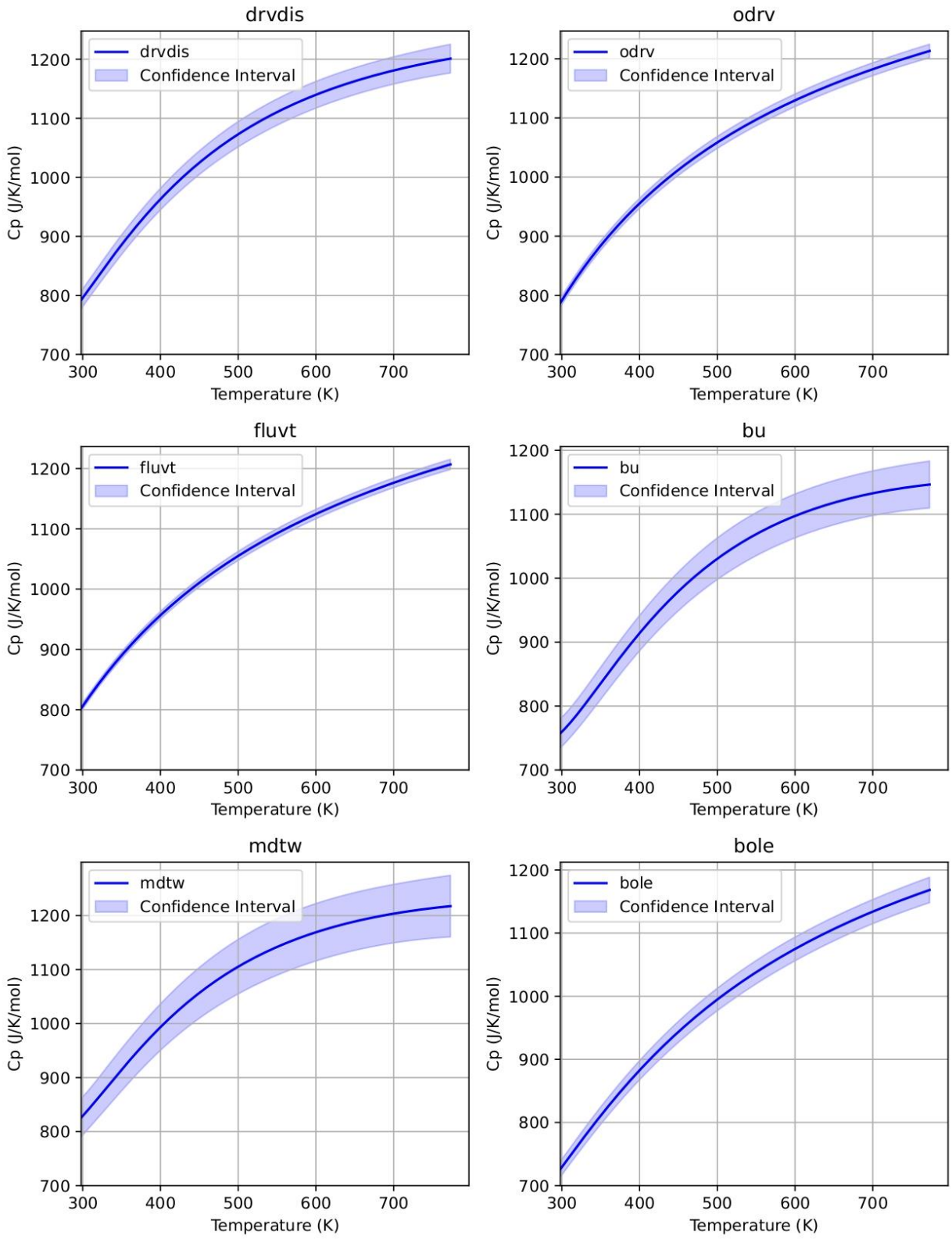
drvdis
drvdis
Confidence Interval
odrv
odrv
Confidence Interval
fluvt
fluvt
Confidence Interval
bu
bu
Confidence Interval
mdtw
mdtw
Confidence Interval
bole
bole
Confidence Interval
Cp (J/K/mol)
Temperature (K)
700
800
900
1000
1100
1200
300
400
500
600
700

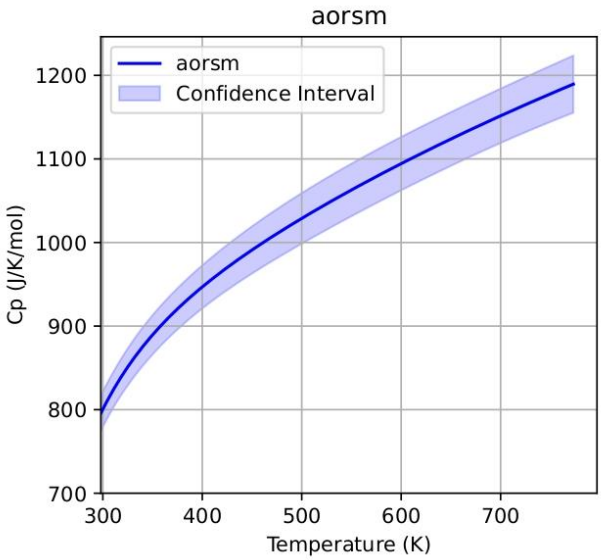
aorsm
aorsm
Confidence Interval
Cp (J/K/mol)
Temperature (K)
1200
1100
1000
900
800
700
300
400
500
600
700

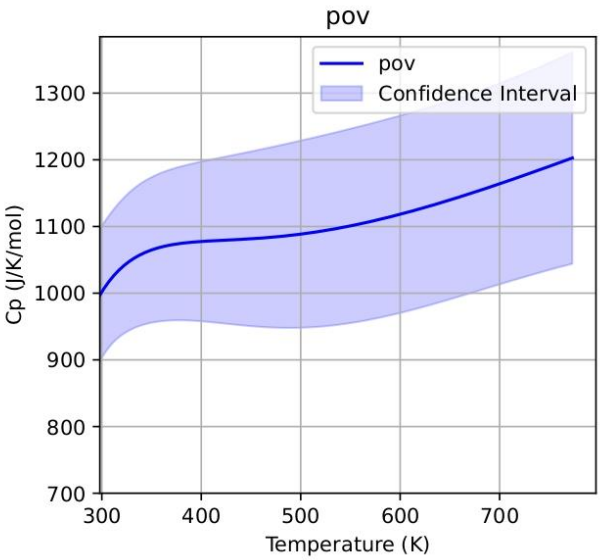
pov
pov
Confidence Interval
Cp (J/K/mol)
Temperature (K)
1300
1200
1100
1000
900
800
700
300
400
500
600
700

Appendix 3K. Alternative Regression Methods

ALTERNATIVE REGRESSION METHODS

We applied alternative fitting methods to OLS on entropies obtained by integrating piecewise linear interpolation of the measured Cp curve, following the method in chapter 3 for molar volume data. The techniques, including x uncertainties for both the bulk and speciation models, consisted of total least squares (TLS), x-scaled TLS, x and y-scaled TLS, y-scaled generalized TLS (gtls-y-scaled), generalized TLS with covariance matrix from the full dataset (gtls-cov-data), gtls-cov-data-y-scaled, gtls-row-column, gtls-block-diag, cwtls-block-diag, gtls-fullW, and cwtls-fullW. We used the MATLAB scripts from chapter 3 modified from Wurm (2021), which combine these x-uncertainty methods with additional robust regression methods, and included a leave-one-out cross-validation procedure (LOOCV) to assess model robustness, which, in data-scarce situations, is dominated by the removal of high-leverage samples that disrupt centroid correlations. This favors models that fit the centroid but does not assess predictive capability or extrapolation to new data.

As in chapter 3 for molar volume regressions, we used the absolute uncertainties. While uncertainties in molar volumes and endmembers were similar (0.1), the larger entropy uncertainties (~1-5 J/K/mol) introduced a bias, making the regression more sensitive to entropy than to x uncertainties. This bias was less pronounced in the speciation model due to its higher cumulative x-uncertainty from more endmembers. We did not normalize, but the difference in magnitudes adjusted the tolerance, allowing CWTLS to work with a higher regularisation parameter to ensure nonsingular, positive definite matrices. In the future, normalizing x and y variables would help equalize their importance, though there are more x variables than y variables.

Bulk Compositional Model The LOOCV MSE is highest for OLS (65), and similarly low for x-uncertainty methods (>52), and robust methods (>52). However, the exact robustness varies depending on the specific variant of the method, reflecting differences in how each approach handles data fitting (Table 3K1, Table 3K2). In case of x-uncertainty methods CWTLS-fullW using the full weight matrix including the covariances of block diagonal covariances had the

lowest LOOCV MSE and in case of robust methods the iteratively reweighted least squares (IWLS) with Cauchy weighting yielded the lowest LOOCV MSE, MAE, MAD, adjusted R^2, and compositional bias integral in case of the robust methods (Table 3K1, Table 3K2). Compared to OLS, the Cauchy robust model predicted LOOCV for F-Buergerite (tm64) more accurately, staying closer to the true value. This is because both high-pov and high-bu samples are high-leverage outliers, and the centroid fit captures a balance between the two main data trends (Figure 3Z). The higher compositional bias integrals of the CWTLS methods indicate they fit extreme data more aggressively, leading to higher LOOCV MSE when these outliers are excluded.

In cross-validation studies, the performance of regression methods such as OLS, CWTLS, and robust methods (e.g., Cauchy) highlights their differing capacities for generalisation and sensitivity to dataset characteristics. For the bulk compositional models, OLS, which minimises the sum of squared residuals without accounting for data point uncertainties or multicollinearity, treating all data points equally, tends to overfit high leverage extreme data points. This is reflected in its high LOOCV MSE, as single-point removal often disrupts its overfitted structure, particularly in datasets with outliers or high variability. In contrast, x-uncertainty methods such as CWTLS incorporates weights and constraints to address data uncertainties and correlations, striking a balance between generalisation and fit. It offers greater flexibility to fit the data and improve generalisation but remains sensitive to dataset structure, due to the unequal treatment of data points, which can result in significant effects from single-point removal during LOOCV. Robust methods, such as IWLS designed to minimize the influence of outliers by down-weighting extreme residuals, excel in LOOCV scenarios. By prioritizing the central trend, they avoid overfitting and maintain the smallest LOOCV MSE, offering the best generalisation performance for the average tourmaline. However extreme samples are not well predicted and therefore the chemical subspace where such empirical models can be used in extremely limited.

Table 3K.1. Bulk Model: LOOCV MSE and Mean Residual Analysis. The LOOCV MSE and mean residuals assess the performance and robustness of different regression methods. Negative mean residuals indicate general underestimation, while positive values suggest general overestimation. LOOCV MSE highlights model sensitivity to extreme outliers, reflecting method

robustness. The most robust models balance low MSE with minimal bias in residual means and are indicated with yellow. OLS is the reference method.

Regression Method	LOOCV MSE	Mean Residual
OLS-regression then integrate	60.20	
OLS	**65.00**	**0.48**
TLS	59.10	0.23
xscaledTLS	61.29	0.31
xy-scaled-TLS	62.68	-0.12
gtls-y-scaled	61.11	-0.18
gtls-cov-data	61.03	0.31
gtls-cov-data-y-scaled	63.92	-0.09
gtls-row-column	61.74	0.31
gtls-block-diag	61.73	-0.42
cwtls-block-diag	54.54	-0.38
gtls-fullW	85.43	-0.58
cwtls-fullW	**52.24**	**-0.34**
robust andrews	64.20	-0.29
robust bisquare	64.00	-0.29
robust cauchy	**52.66**	**-0.11**
robust fair	54.72	0.03
robust huber	52.85	-0.13
robust logistic	53.17	-0.10
robust talwar	66.62	0.35
robust welsch	59.71	-0.18
WLS	65.53	0.02

Table 3K.2. Bulk model Z-score heuristics using the LOOCV as an estimate for the test set show which models have lowest training set uncertainty and is most robust. For the meaning of the different Z scores and how they are summed into one heuristic, see Chapter 3. Best performing robust regression method and x-uncertainty regression methods with lowest sum Z scores are in bold and yellow.

Model Method	MSE_Z	MAE_Z	MAD_Z	Adj R Squared Z	Integral Between York and 1_1_Z	wMSE_Z	AdjR_Z	Rsquared Press Z	Sum Z Scores
robust cauchy	**-1.12**	**-1.37**	**-1.40**	**-1.12**	**-0.18**	**-0.93**	**-1.22**	**-1.18**	**-8.51**
robust huber	-1.14	-1.09	-1.11	-1.14	-0.33	-1.04	-1.19	-1.17	-8.21
robust logistic	-1.07	-1.25	-1.27	-1.07	-0.30	-0.83	-0.99	-0.95	-7.72
cwtls fullW	**-1.10**	**-2.01**	**-2.00**	**-1.10**	**2.66**	**0.03**	**-1.53**	**-1.55**	**-6.61**
robust fair	-0.90	-0.79	-0.80	-0.90	-0.57	-0.84	-0.84	-0.81	-6.45
cwtls block diag	-0.88	-1.30	-1.31	-0.88	2.67	0.19	-0.98	-0.93	-3.42
robust welsch	-0.15	-0.44	-0.40	-0.15	0.26	-0.33	-0.75	-0.74	-2.69
TLS	-0.40	0.30	0.32	-0.40	-0.71	-0.57	0.31	0.26	-0.88
gtls	0.28	-0.10	-0.12	0.28	-0.28	0.66	-0.83	-0.69	-0.80

Model Method	MSE_Z	MAE_Z	MAD_Z	Adj R Squared Z	Integral Between York and 1_1_Z	wMSE_Z	AdjR_Z	Rsquared Press Z	Sum Z Scores
block diag									
gtls cov data	-0.15	0.52	0.54	-0.15	-0.60	-0.63	0.29	0.24	0.05

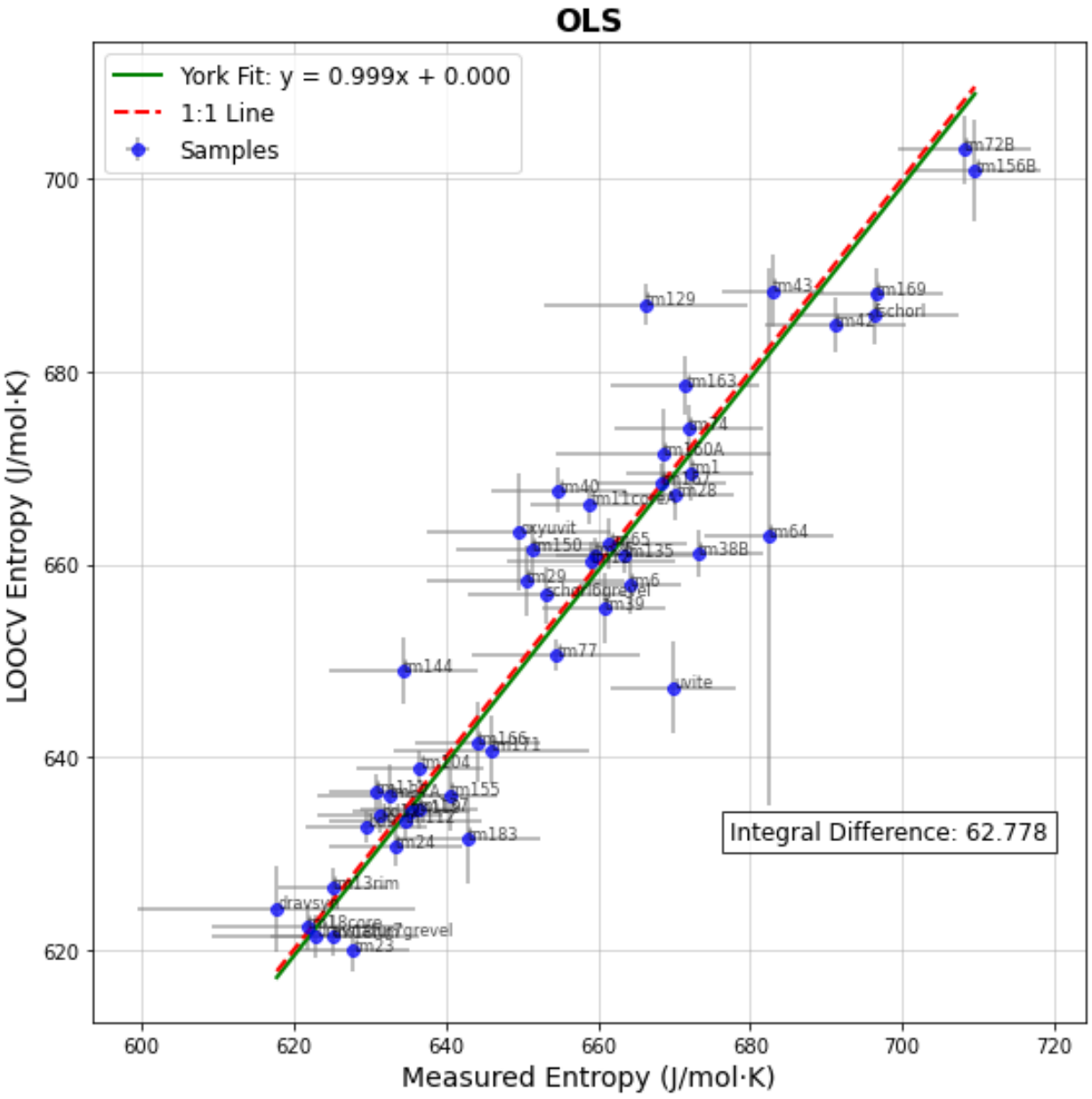

Figure 3K.1. Bulk model measured entropy versus LOOCV Entropy with Uncertainties, York Regression, and Integral Difference for OLS. Notice the high LOOCV MSE of F-buergerite (tm64).

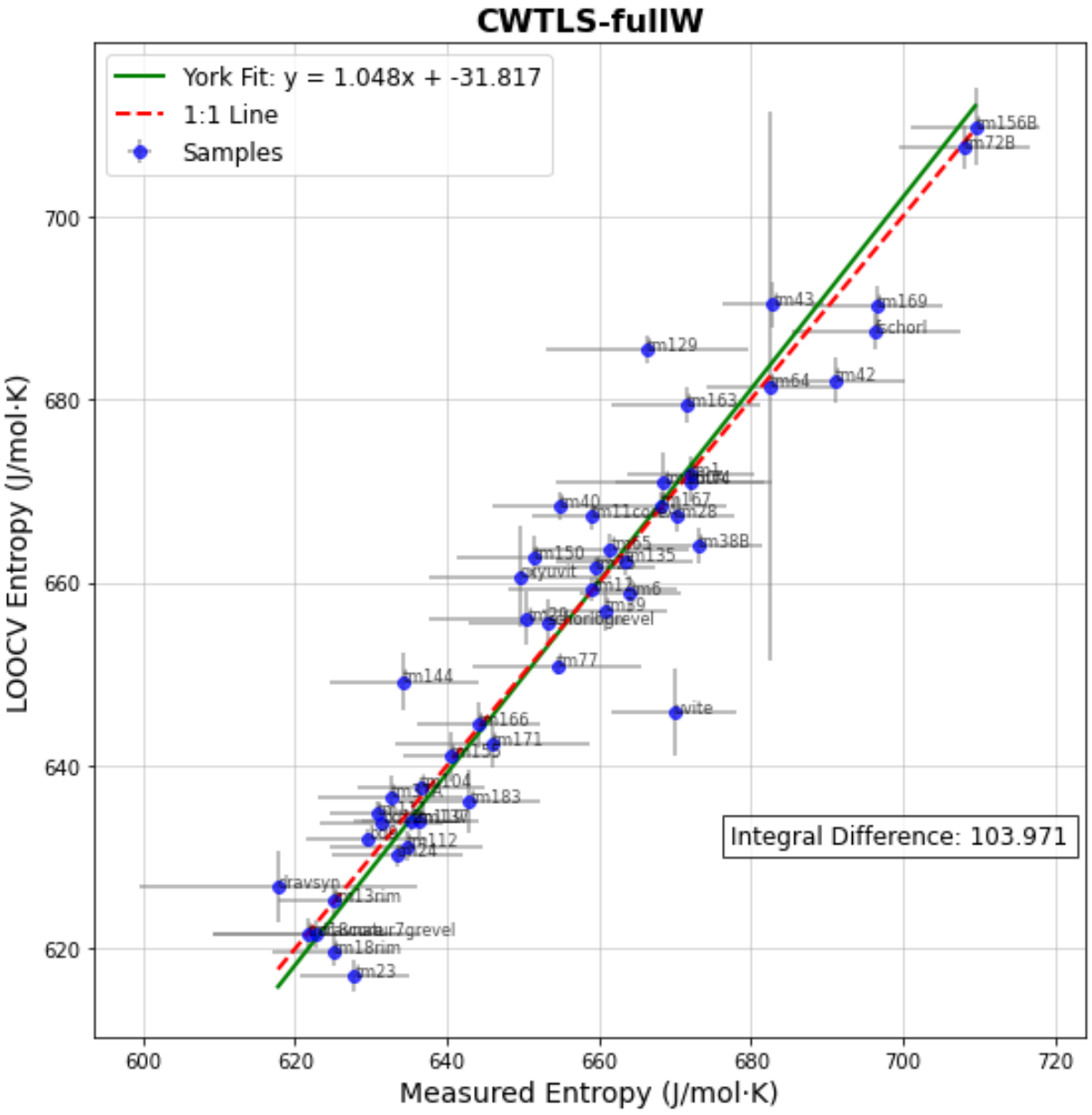

Figure 3K.2. Bulk model measured entropy versus LOOCV Entropy with Uncertainties, York Regression, and Integral Difference for CWTLS using the Full weight matrix with block diagonal covariances of each sample and covariances of the covariances. While overall fit is good there is compositional bias as demonstrated by the high integral difference between the York line and the 1:1 line.

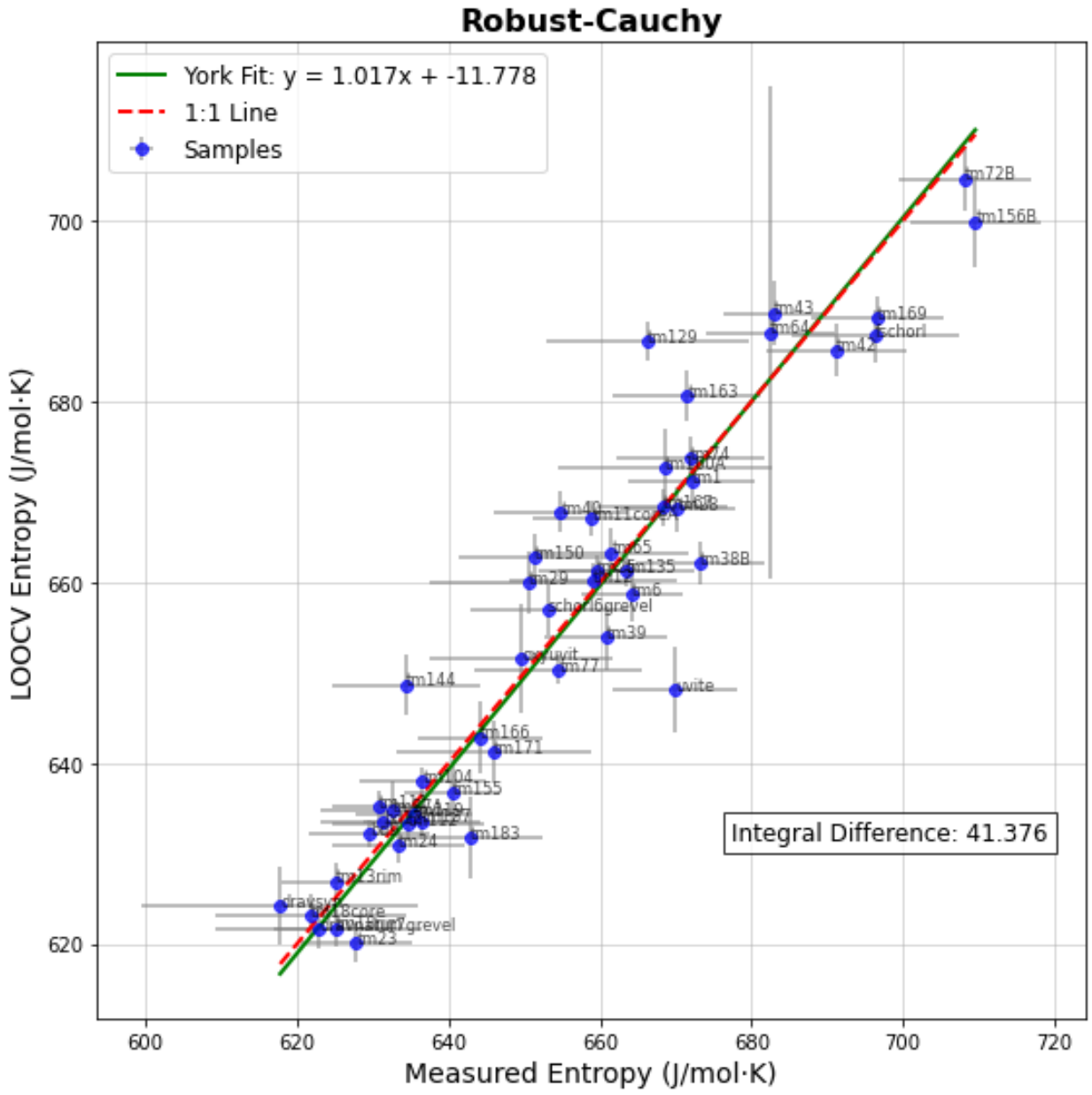

Figure 3K.3. Bulk model measured entropy versus LOOCV Entropy with Uncertainties, York Regression, and Integral Difference for robust regression using the Cauchy weight function. The most robust method.

Speciation Model

In the speciation model, OLS is highly data-dependent, with single samples often dictating endmember regression coefficients, leading to higher LOOCV MSE than in the bulk compositional model. The synthetic B-Olenite sample was excluded from the LOOCV MSE

calculation. Like the bulk model, the inclusion of x-uncertainty in case of CWTLS-fullW decreased LOOCV MSE in the speciation model, suggesting that added flexibility increased its robustness. As the parameter-to-data increases, model sensitivity rises, and CWTLS is still prone to overfitting as its flexibility amplify its responsiveness to dataset structure, leading to a relatively high LOOCV MSE. Note that all other x-uncertainty method do worse due to its data structure dependence. This sensitivity arises from the disruption of weighted constraints during single-point removal, as influential points often dictate the speciation endmember, destabilizing predictions. OLS, despite its limitations, benefits from its simplicity by treating all data points equally in high-parameter settings, avoiding the overfitting tendencies of the other x-uncertainty models and yielding moderate LOOCV MSE. Robust methods, due to their resistance to overfitting and ability to focus on the underlying trend of the bulk of the data—primarily the natural samples with inherent correlations—minimize sensitivity to noise or compositional extremes.

Table 3K.3. Speciation Model: LOOCV MSE and Mean Residual Analysis.

Method	**LOOCV MSE**	**LOOCV mean(residual)**
OLS-regression then integrate	118.30	
OLS	**119.76**	**-0.73**
TLS	134.59	-1.60
xscaledTLS	133.25	-1.56
xy-scaled-TLS	126.82	-1.57
gtls-y-scaled	127.35	-1.60
gtls-cov-data	134.40	-1.58
gtls-cov-data-y-scaled	127.14	-1.50
gtls-row-column	134.52	-1.60
gtls-block-diag	158.52	-0.09
cwtls-block-diag	145.17	-1.04
gtls-fullW	149.42	-0.18

Method	LOOCV MSE	LOOCV mean(residual)
cwtls-fullW	**114.71**	**-0.92**
robust andrews	87.91	0.64
robust bisquare	88.02	0.63
robust cauchy	149.42	0.99
robust fair	**98.54**	**-0.69**
robust huber	97.26	-0.32
robust logistic	96.50	-0.38
robust talwar	122.73	-0.86
robust welsch	110.95	0.97
WLS	116.74	-1.11

Table 3K.4. Speciation model Z-score heuristics using the LOOCV as an estimate for the test set show which models have lowest training set uncertainty and is most robust. For the meaning of the different Z scores and how they are summed into one heuristic, see Chapter 3. Best performing robust regression method and x-uncertainty regression methods with lowest sum Z scores are in bold and yellow.

Model Method	MSE_ Z	MAE_ Z	MAD_ Z	Adj R Squared Z	Integral Between York and 1_1_Z	wMSE_ Z	AdjR_ Z	Rsquared Press Z	Sum Z Scores
robust fair	**-1.25**	**-1.46**	**-1.59**	**-1.25**	**-0.90**	**-1.01**	**-1.00**	**-1.00**	**-9.46**
robust logistic	-1.33	-1.56	-1.67	-1.32	-0.69	-0.93	-0.95	-0.95	-9.41
robust huber	-1.30	-1.45	-1.55	-1.29	-0.69	-0.89	-0.88	-0.89	-8.94
WLS	-0.28	-0.99	-0.85	-0.28	-0.06	-0.93	-0.94	-0.98	-5.32
robust bisquare	-1.49	-0.67	-0.71	-1.53	0.58	-0.16	-0.34	-0.31	-4.63
robust andrews	-1.58	-0.80	-0.90	-1.61	0.59	0.34	0.04	0.07	-3.85
OLS	**-0.30**	**-0.25**	**-0.31**	**-0.27**	**-0.90**	**-0.33**	**-0.24**	**-0.23**	**-2.84**
gtls cov data y scaled	0.24	-0.49	-0.28	0.24	0.44	-0.82	-0.90	-0.94	-2.52
xyscaledTLS	0.21	-0.42	-0.21	0.21	0.56	-0.79	-0.88	-0.92	-2.23
gtls y scaled	0.24	-0.37	-0.16	0.24	0.60	-0.78	-0.87	-0.92	-2.03

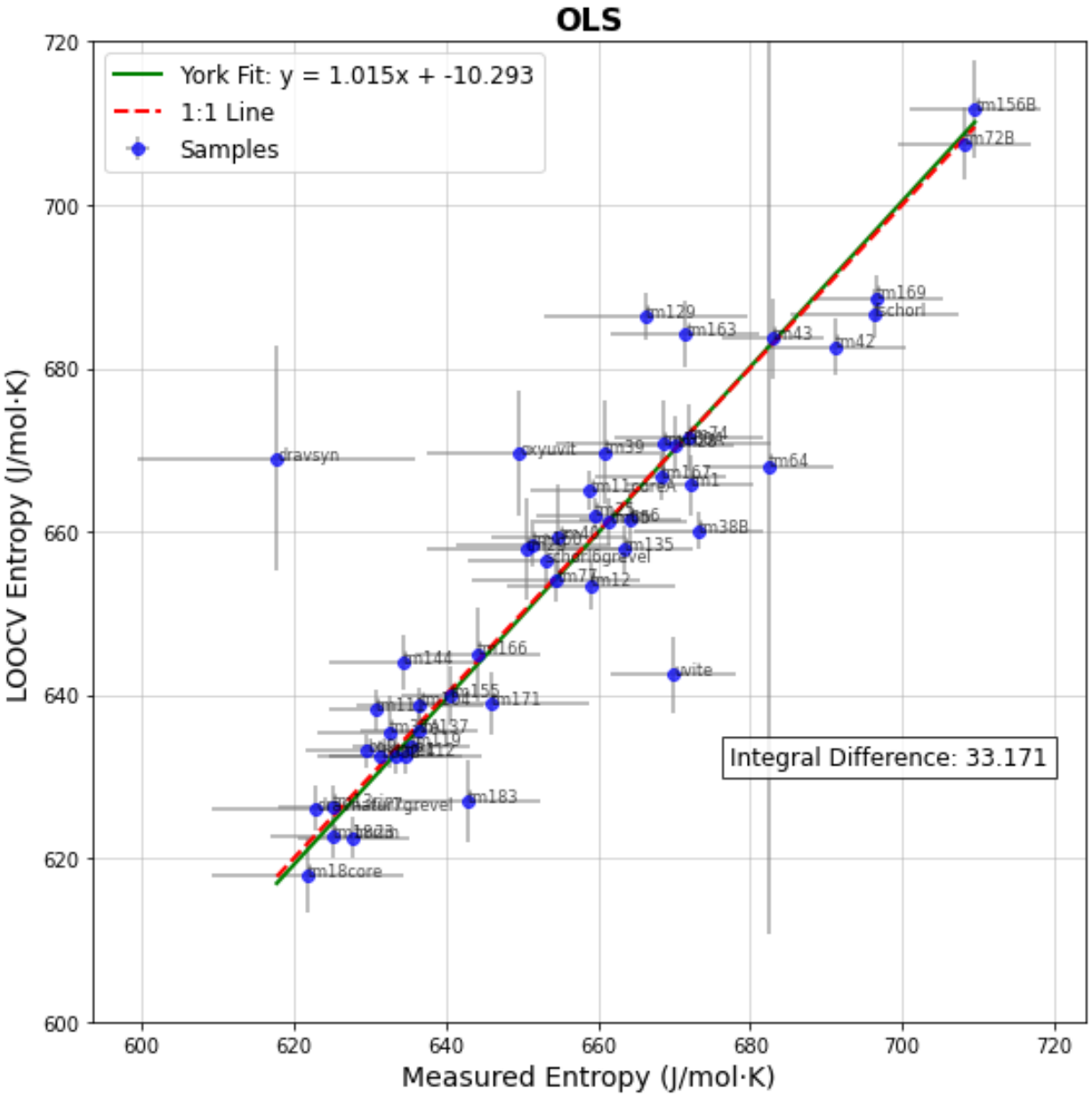

Figure 3K.4. Speciation model measured entropy versus LOOCV Entropy with Uncertainties, York Regression, and Integral Difference for OLS. Notice the high LOOCV MSE of F-buergerite (tm64).

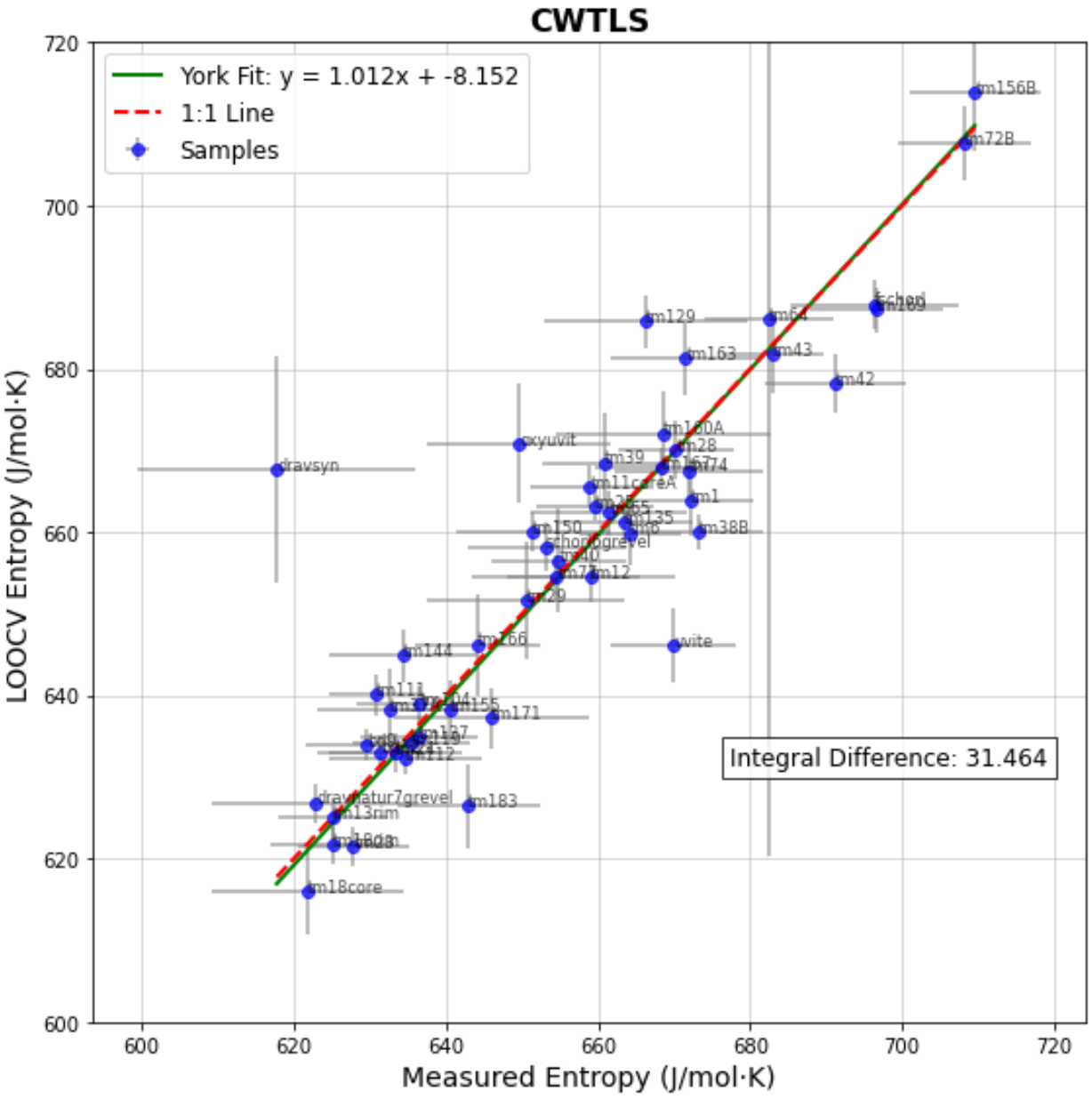

Figure 3K.5. Speciation model measured entropy versus LOOCV Entropy with Uncertainties, York Regression, and Integral Difference for CWTLS using the Full weight matrix with block diagonal covariances of each sample and covariances of the covariances.

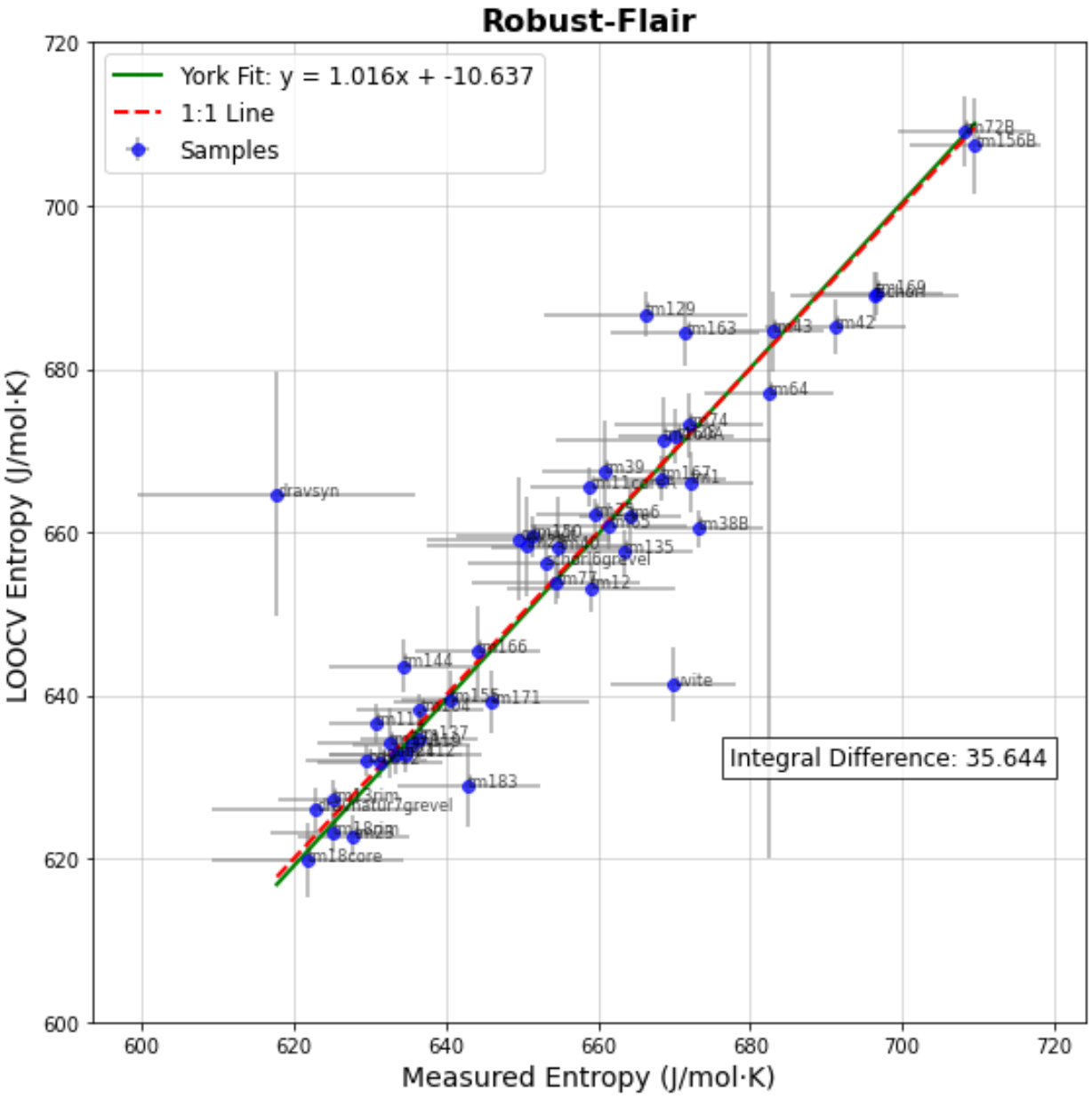

Figure 3K.6. Speciation model measured entropy versus LOOCV Entropy with Uncertainties, York Regression, and Integral Difference for robust regression using the Flair weight function.

Each regression technique has its strengths and limitations, and the best model can only be determined with a separate test set. Model performance depends on dataset structure and the number of parameters, meaning the optimal method in one case may not be the best in another. For instance, OLS tends to overfit noise in bulk models but is relatively robust in high-parameter settings due to its simplicity. Robust methods fit central data well but are limited by extreme compositional bias, affecting their ability to predict outliers. CWTLS, with its added flexibility, often generalizes effectively but is highly sensitive to dataset structure, particularly in high-parameter models. These nuances highlight the importance of tailoring regression methods to the specific characteristics of each dataset rather than relying on a one-size-fits-all approach.

Without a test set, we cannot determine which method performs best. LOOCV, while useful for assessing robustness, falls short of providing an accurate estimate of test set error in small datasets with few correlation-breaking outliers. This leads to the trivial conclusion that robust methods are the most robust. In the absence of a test set, OLS is preferred for its unbiased, efficient estimates, minimizing squared residuals under normality assumptions. Its simplicity, robustness, and reliability make it an optimal baseline. Overfitting of high-leverage samples is considered beneficial, as it provides the correlation-breaking samples necessary for obtaining independent regression estimates. If the model is truly overfitting, this can be tested by future entropy measurements of extreme tourmaline compositions, observing how well it performs on tourmalines that are far removed from the calibration dataset.

REFERENCES

Wurm, M. (2021) A universal and fast method to solve linear systems with correlated coefficients using weighted total least squares. Measurement Science and Technology, 33, 015017.

Appendix 3L. Derivation of Holland and Powell (1990) Landau tricritical

Derivation of Holland and Powell (1990) tricritical S and Cp equations from Landau free energy expression.

Define the Landau Free Energy The general Landau free energy expansion is: $G(Q) = G_0 + a(T - T_c)Q^2 + bQ^4 + cQ^6 + \cdots$, where Q is the order parameter, a, b, and c are constants, and Tc is the critical temperature (Landau 1937). For a tricritical transition (b=0): $G(Q) = G_0 - \frac{a}{2}(T_c - T)Q^2 + \frac{c}{6}Q^6$, here a>0 and c>0. Excess properties are modelled by: $\Delta G(Q) = -\frac{a}{2}(T_c - T)Q^2 + \frac{c}{6}Q^6$, after subtracting the vibrational heat capacity baseline (cp^{vib}) and removing G^0, which does not affect the phase transition (Holland and Powell 1990).

The stability criterion $T_c = c/a$ ensures the free energy $G(Q) = -\frac{a}{2}(T_c - T)Q^2 + \frac{c}{6}Q^6$ remains bounded by balancing the destabilizing Q^2 term, which changes sign at Tc, with the stabilizing Q^6 term at large Q. The entropy maximum criterion S_{max}=a/2 arises from maximal thermal fluctuations at T_c, where the temperature-dependent Q^2 term leads to a peak in entropy and heat capacity (Holland and Powell 1990).

Experimentally, cp(T) measurements require subtracting the lattice contribution to isolate tricritical behavior. The peak of the corrected cp(T) curve indicates T_c, and integrating cp confirms S_{max}=a/2. Fitting the curve to the Landau model determines c, a, and their ratio c/a.

To derive the expression for Q in terms of Tc when $T_c = c/a$,

Derivation expression Q

1. Equilibrium Condition: Minimize G(Q), by setting $\frac{\partial G(Q)}{\partial Q} = 0$:

$$\frac{\partial G(Q)}{\partial Q} = -a(T_c - T)Q + cQ^5 = 0$$

Simplify:

$Q[-a(T_c - T) + cQ^4] = 0.$

Solutions : $Q = 0$ (stable for $T > T_c$)
$Q^4 = \frac{a}{c}(T_c - T)$(for $T < T_c$).

2. Substitute $T_c = \frac{c}{a}$:

$$Q^4 = \frac{a}{c}\left(\frac{c}{a} - T\right)$$

Simplify: $Q^4 = \frac{a}{c} \cdot \frac{c-aT}{a} = 1 - \frac{T}{T_c}$..

3. Solve for Q:

$$Q = \left(1 - \frac{T}{T_c}\right)^{1/4}$$

Derivation of ΔS

1. Free Energy and Entropy Relation:

$$S = -\frac{\partial G}{\partial T}$$

2. Differentiate G(Q) w.r.t. T**:**

From G, only the first term depends on T, $-\frac{a}{2}(T_c - T)Q^2$:

$$\frac{\partial G}{\partial T} = -\frac{\partial}{\partial T}\left[-\frac{a}{2}(T_c - T)Q^2\right] = -\frac{a}{2}Q^2$$

3. We include a reference standard state entropy contribution S0 (when Q=0), making it a ΔS:

$$\Delta S = \frac{a}{2}(1 - Q^2)$$

As $Smax = \frac{a}{2}$

$$\Delta S = Smax(1 - Q^2)$$

Derivation of Cp equation

1. Expand Q^2

From $Q = \left(1 - \frac{T}{T_c}\right)^{1/4}$, squaring gives: $Q^2 = \left(1 - \frac{T}{T_c}\right)^{1/2}$.

Substituting Q^2 into $\Delta S = Smax(1 - Q^2)$:

$$S = S_{max}\left(1 - \left(1 - \frac{T}{T_c}\right)^{1/2}\right)$$

2. Relate S to Cp:

The heat capacity is:

$$C_p = T\frac{dS}{dT}$$

3. Differentiate **S:**

$$\frac{dS}{dT} = S_{max} \cdot \frac{d}{dT}\left[1 - \left(1 - \frac{T}{T_c}\right)^{\frac{1}{2}}\right]$$

Using the chain rule

$$\frac{d}{dT}\left[\left(1 - \frac{T}{T_c}\right)^{\frac{1}{2}}\right] = \frac{1}{2}\left(1 - \frac{T}{T_c}\right)^{-\frac{1}{2}} \cdot \frac{d}{dT}\left(1 - \frac{T}{T_c}\right)$$

The derivative of $1 - \frac{T}{T_c}$ with respect to T is:

$$\frac{d}{dT}\left(1 - \frac{T}{T_c}\right) = -\frac{1}{T_c}.$$

Thus:

$$\frac{d}{dT}\left[\left(1 - \frac{T}{T_c}\right)^{\frac{1}{2}}\right] = \frac{1}{2}\left(1 - \frac{T}{T_c}\right)^{-\frac{1}{2}} \cdot \left(-\frac{1}{T_c}\right)$$

Simplify:

$$\frac{d}{dT}\left[\left(1-\frac{T}{T_c}\right)^{\frac{1}{2}}\right]=-\frac{1}{2T_c}\left(1-\frac{T}{T_c}\right)^{-\frac{1}{2}}$$

$$\frac{dS}{dT}=S_{max}\cdot\left[-\frac{1}{2T_c}\left(1-\frac{T}{T_c}\right)^{-\frac{1}{2}}\right]$$

4: Substitute $\frac{dS}{dT}$ into Cp

$$C_p=T\cdot\left(-\frac{S_{max}}{2T_c}\left(1-\frac{T}{T_c}\right)^{-\frac{1}{2}}\right)$$

Simplify:

$C_p=-\frac{TS_{max}}{2T_c}\left(1-\frac{T}{T_c}\right)^{-1/2}$.

5. Rewrite in Terms of Tc – T.

Rewrite $1-\frac{T}{T_c}$ as $\frac{T_c-T}{T_c}$:

$C_p=-\frac{TS_{max}}{2T_c}\cdot\left(\frac{T_c-T}{T_c}\right)^{-1/2}$.

Simplify:

$$\left(\frac{T_c-T}{T_c}\right)^{-\frac{1}{2}}=\sqrt{T_c}\cdot(T_c-T)^{-\frac{1}{2}}$$

Substitute this back:

$$C_p=-\frac{TS_{max}}{2T_c}\cdot\sqrt{T_c}\cdot(T_c-T)^{-\frac{1}{2}}$$

Combine terms:

$$C_p = -\frac{TS_{max}\sqrt{T_c}}{2T_c^{\frac{3}{2}}} \cdot (T_c - T)^{-\frac{1}{2}}$$

Simplify $T_c^{3/2}$:

$$C_p = \frac{TS_{max}}{2\sqrt{T_c}}(T_c - T)^{-1/2}$$

REFERENCES

Holland, T.J.B., and Powell, R. (1990) An enlarged and updated internally consistent thermodynamic dataset with uncertainties and correlations: the system K2O–Na2O–CaO–MgO–MnO–FeO–Fe2O3–Al2O3–TiO2–SiO2–C–H2–O2. Journal of metamorphic Geology, 8, 89–124.

Landau, L.D. (1937) On the theory of phase transitions. Zhurnal Eksperimental'noi i Teoreticheskoi Fiziki, 7, 926.

Appendix 3M. Improvements suggestions for the Polyhedron Method

Debye model inclusion The polyhedron method's vibrational model, based on Einstein oscillators with fixed frequencies for each polyhedron, fails to capture the continuous vibrational density of states in a coupled lattice crystal (Holland 1989). A Debye-like correction factor is needed to transition from discrete frequencies to a continuous vibrational spectrum of an endmember unit cell. Volume corrections have been proposed using $S_j = \sum n_i S_i + k\left(V_j - \sum n_i V_i\right)$, where k is a scaling constant correlates entropy to volume changes, as predicted by Debye theory (Holland 1989). While effective for moderately complex structures, this correction fails for highly polymerized systems (Van Hinsberg et al. 2005a, 2005b; Van Hinsberg and Schumacher 2007). In tourmaline, where high-T optical phonons depend more on bond stiffness and polyhedral distortions than volume expansion (see next paragraph), an alternative approach is needed to account for cooperative lattice vibrations.

Magnetic entropy overestimation The maximum magnetic entropy is derived from the Boltzmann formula $S_{max}^{\text{magnetic}} = R\ln\ \Omega$, where $\Omega = 2J + 1$ where $J = |L - S|, \ldots, L + S$ is the total angular momentum quantum number combining spin S and orbital L contributions through spin-orbit coupling (Blundell 2001). This model assumes equally accessible states in the paramagnetic phase at high T, where thermal energy exceeds state energy gaps.

For high-spin Fe^{3+} $\left(S = \frac{5}{2}, L = \frac{5}{2}\right)$ in octahedral environments, the symmetric d^5 configuration and weak Jahn-Teller effects result in crystal field splitting that quenches L, leaving the entropy dominated by spin $S_{max}^{\text{magnetic}} = R\ln(6) = 14.89\ \text{J/mol}\cdot\text{K}$. In rare cases, distortions can preserve partial orbital contributions, described by an effective L_{eff}, where $S_{max}^{\text{magnetic}} = R\ln\left[(2S + 1)(2L_{\text{eff}} + 1)\right]$, applies under weak spin-orbit coupling (Blundell 2001), which would make $S_{max}^{\text{magnetic}}$ much larger.

For high-spin Fe^{2+} (S = 2, L = 2) the asymmetric d^6 configuration and Jahn-Teller effects can prevent full quenching of L, enhancing spin-orbit coupling (Blundell 2001). In perfect octahedral symmetry, crystal field splitting fully quenches L, and the spin-only entropy $S_{max}^{\text{magnetic}} = R\ln(5)$ applies. Distorted environments allow residual L_{eff} from 0 to 2. In tourmaline, stronger

distortions at the Y site and the rigid symmetry of the Z site and nearest neighbor inductive effects create varying Fe^{2+} environments (Ertl et al. 2002) as demonstrated by Mössbauer spectroscopy (Andreozzi et al. 2008). Optical spectroscopy reveals significant t_{2g}–e_g splitting dominated by spin-allowed transitions, favoring orbital quenching. Weak signals suggest spin-forbidden transitions, indicating residual L_{eff} (Altieri et al. 2022).

In SRO or spin glass systems, local distortions cause L_{eff} or J to vary across regions, with the solid solution behaving as an average. The average can be tested by fitting a lattice dynamics model to the heat capacity curve, isolating and integrating the magnetic contribution to determine if it aligns with S, S+L_{eff}, or J formulations of S^{mag}. Additionally, electron delocalisation in tourmaline is indicated by intensified Fe^{2+} optical peaks in the presence of Fe^{3+} (Mattson and Rossman 1987). Electron hopping between Fe^{2+} and Fe^{3+} could dynamically affect the crystal fields and spin orbit coupling.

The polyhedron method estimates S^{mag} in tourmalines with Fe^{2+} and Fe^{3+} as $x_{Fe^{2+}} \cdot R \cdot \ln(5) + x_{Fe^{3+}} \cdot R \cdot \ln(6)$, where x is the apfu value. This assumes fully quenched orbital contributions, but crystal field effects and distortions could increase L_{eff}, expanding microstates despite spin-orbit coupling's tendency to reduce them.

Rethinking of Order-Disorder correction in Training dataset Subtracting a T-independent, heavily model-dependent S^{conf} constant from measured entropies in the training database of van Hinsberg (2005) introduces significant noise into thermodynamic property derivations, especially for the few disordered samples used and when the appropriate S^{conf} is unclear, particularly in minerals with high site multiplicities and diverse elemental populations. This practice can lead to unphysical negative polyhedron entropies, as observed for the B^{III} polyhedron (Hinsberg and Schumacher 2007). While bulk compositional endmember formulas in the training dataset are detailed in van Hinsberg (2005a), the structural formulas used for S^{conf} calculations of disordered endmembers remain unknown. The reference state for minerals used to derive polyhedral thermodynamic properties assumes order, but anion sites were treated as disordered, introducing uncorrected S^{conf}.

Configurational Entropy The treatment of S^{conf} in the polyhedron method requires refinement due to inconsistencies in its application**.** S^{conf} depends on the number of independent component and equivalent sites (Ms) for mixing and is calculated using the Bolzmann formula:

$$S_{\text{conf}} = -R \sum_{s} M_s \sum_{i=1}^{n_{\text{indi},s}} x_{i,s} \ln\, x_{i,s}$$

To calculate n_{ind} the formula is:

$$n_{ind} = \text{ total species } - (\text{ number of sites } + \text{ charge balance constraint }) + 1$$

Which is the degree of freedom (variables-constraints) + 1 to add a dependent endmember so the simplex sums to 1 (Myhill and Connolly 2021).

The charge balance constraint is problematic, as polyhedra like Al^{OHO} imply >1 OH groups and are not necessarily charge balanced.

A fundamental question remains: does the polyhedron method, i.e., summing polyhedra, represent short-range order (SRO) molecular clusters or can long-range order (LRO) unit cells be derived as well? SRO models minimize S^{conf} by mixing charge-balanced molecules (Will 1998) on individual sites, while LRO models maximize it by assuming complete randomization (e.g., Bragg-Williams, (Bragg and Williams 1934, 1935)). This distinction significantly influences the treatment of configurational entropy.

LRO S^{conf} For an endmember configuration with 1 X-site**,** 9 YZ-sites**,** and 6 T-sites, as the V and W sites are incorporated into the species, The species distributions are:

X-site: 3 species – Na^{multi}, Ca^{multi}, and vacancy (vac).
YZ-site: 5 species – Al^{OHO}, Mg^{OHO}, Fe^{2+OHO}, Fe^{3+OHO} and Ti^{oct},
T-site: 3 species – Si^{T}, Al^{T}, B^{T}

With a total of 11 species (3+5+3), 3 distinct sites, and a charge balance constraint (c) of 1, we calculate:

$$n_{ind} = 11 - (3 + 1) + 1 = 8$$

This calculation provides the independent components required for accurate S^{conf} determination.

The independent polyhedra would be Na^{multi}, Ca^{multi}, Al^{OHO}, Mg^{OHO}, Fe^{2+OHO}, Fe^{3+OHO}, Ti^{oct}, Si^{T}. S^{conf} using these 8 independent bulk parameters and 3 sites with their site multiplicities on the tourmaline training dataset results in an average S^{conf} of 63.35 J/K/mol.

SRO S^{conf} Using the independent polyhedra Na^{multi}, Ca^{multi}, Al^{OHO}, Mg^{OHO}, Fe^{2+OHO}, Fe^{3+OHO}, Ti^{oct}, Si^{T} as positive polyhedra as linear combinations of the molecular clusters the S^{conf} using these 8 independent bulk parameters and 1 site on the tourmaline training dataset results in an average S^{conf} of 10.8 J/K/mol.

OOH and Oxy Ambiguity also arises in treating components like OOH and Oxy as distinct and whether ordered or disordered OH groups should be assumed. If Al^{oct}, Mg^{oct}, Fe^{2+oct}, and Fe^{3+oct} are added as mixing components on the YZ site:

X-site: 3 species (Na^{multi}, Ca^{multi}, vac).
YZ-site: 9 species (Al^{OHO}, Mg^{OHO}, Fe^{2+OHO}, Fe^{3+OHO}, Ti^{oct}, Al^{oct}, Mg^{oct}, Fe^{2+oct}, Fe^{3+oct}).
T-site: 3 species (Si^{T}, Al^{T}, B^{T}).

Total species = 15
Using n_{ind} formula $n_{\text{ind}} = 15 - (3 + 1) + 1 = 12$

The 12 independent components would include Na^{multi}, Ca^{multi}, all 9 YZ species, and Si^{T}. Adding these increases S^{conf} due to the greater configurational randomness. However, this only modifies the values slightly, in case of the ordered V+W formula; Bulk LRO S^{conf} = 65.37 and SRO S^{conf} = 10.98. In case of the disordered V+W formula which changes the distribution of Oxy and OHO polyhedra would result in Bulk LRO S^{conf} = 87.24 and SRO S^{conf} = 12.36.

The bulk compositional generalized Bragg-Williams model overestimates randomness and inflates entropy values. For example, adding the bulk compositional S^{conf} derived above to measured Cp curves, which lack theoretical S^{conf}, results in overpredictions. This is because the assumption of complete randomization is incorrect; elements exhibit site preferences due to long-range order (LRO) constraints. For instance, Mg^{2+}, Fe^{2+}, and Al^{3+} favor the larger Y site, while the smaller Z site primarily hosts Al^{3+}, with minor Fe^{3+}, Mg^{2+}, and minimal Fe^{2+} (Bosi 2018). F is largely restricted to the W site. These preferences are not enforced in bulk compositional models due to limited degrees of freedom (DOF). As we have the measured mineral formula, we also attempted to add the speciation model S^{conf}, however also here this leads to an overpredicting of S^{conf} (~47 J/K/mol).

Integrating short-range order (SRO) S^{conf} into the polyhedron method is feasible and improves accuracy by halving the mean absolute deviation (Table 3M.1).

Table 3M.1. Adding molecular (SRO) model S^{conf} to the polyhedron method estimates.

Model Name	**Mean Absolute Relative Deviation (%)**	**Residual Range (%)**	**Median Residual (%)**
With S^{conf}.			
Oxy+OHO Polyhedra, Ordered V+W, with $S^{vib} + S^{mag} + S^{conf}$	2.9	-1.2 to 19	1.8
Oxy+OHO Polyhedra, Disordered V+W, with $S^{vib} + S^{mag} + S^{conf}$	4.8	0.3 to 18	4.5
OHO Polyhedra, with $S^{vib} + S^{mag} + S^{conf}$	2.3	-1 to 8	1.8

A molecular mixing model is suitable since polyhedra, as molecular clusters, inherently involve mixing. Under this approach, polyhedra are treated as charge-neutral entities without any form of polymerization, aligning the model with realistic mixing behavior while retaining essential site-specific constraints via the DOF. However, since the polyhedron method tends to underestimate thermodynamic properties and molecular configurational entropy is inherently small, adding this

correction could merely serve as an arbitrary adjustment to improve the fit without a strong physical basis.

REFERENCES

Altieri, A., Pezzotta, F., Skogby, H., Hålenius, U., and Bosi, F. (2022) Blue growth zones caused by Fe2+ in tourmaline crystals from the San Piero in Campo gem-bearing pegmatites, Elba Island, Italy. Mineralogical Magazine, 86, 910–919.

Andreozzi, G.B., Bosi, F., and Longo, M. (2008) Linking Mossbauer and structural parameters in elbaite-schorl-dravite tourmalines. American Mineralogist, 93, 658–666.

Blundell, S. (2001) Magnetism in condensed matter, 238 p. Oxford University Press, Oxford.

Bosi, F. (2018) Tourmaline crystal chemistry. American Mineralogist, 103, 298–306.

Bragg, W.L., and Williams, E.J. (1934) The effect of thermal agitation on atomic arrangement in alloys. Proceedings of the Royal Society of London. Series A, Containing Papers of a Mathematical and Physical Character, 145, 699–730.

——— (1935) The effect of thermal agitaion on atomic arrangement in alloys—II. Proceedings of the Royal Society of London. Series A - Mathematical and Physical Sciences, 151, 540–566.

Ertl, A., Hughes, J.M., Pertlik, F., Foit, F.F., Wright, S.E., Brandstätter, F., and Marler, B. (2002) Polyhedron Distortions in Tourmaline. The Canadian Mineralogist, 40, 153–162.

Holland, T.J. (1989) Dependence of entropy on volume for silicate and oxide minerals; a review and predictive model. American Mineralogist, 74, 5–13.

Mattson, S.M., and Rossman, G.R. (1987) Fe2+-Fe3+ interactions in tourmaline. Physics and Chemistry of Minerals, 14, 163–171.

Myhill, R., and Connolly, J. (2021) Notes on the creation and manipulation of solid solution models. Contributions to Mineralogy and Petrology, 176.

van Hinsberg, V.J., and Schumacher, J.C. (2007) Intersector element partitioning in tourmaline: a potentially powerful single crystal thermometer. Contributions to Mineralogy and Petrology, 153, 289–301.

van Hinsberg, V.J., and Schumacher, J.C. (2007) Using estimated thermodynamic properties to model accessory phases: the case of tourmaline. Journal of metamorphic Geology, 25, 769–779.

van Hinsberg, V.J., Vriend, S.P., and Schumacher, J.C. (2005a) A new method to calculate end-member thermodynamic properties of minerals from their constituent polyhedra I: enthalpy, entropy and molar volume. Journal of Metamorphic Geology, 23, 165–179.

——— (2005b) A new method to calculate end-member thermodynamic properties of minerals from their constituent polyhedra II: heat capacity, compressibility and thermal expansion. Journal of Metamorphic Geology, 23, 681–693.

Will, T.M. (1998) Phase Equilibria in Metamorphic Rocks, 315 p. Vol. 71. Springer, Berlin, Heidelberg.

Appendix 3N. State Variable Correlations

- This Appendix contains all the state variables correlations. Note ‘a cell’ means the hexagonal cell a axis.

.

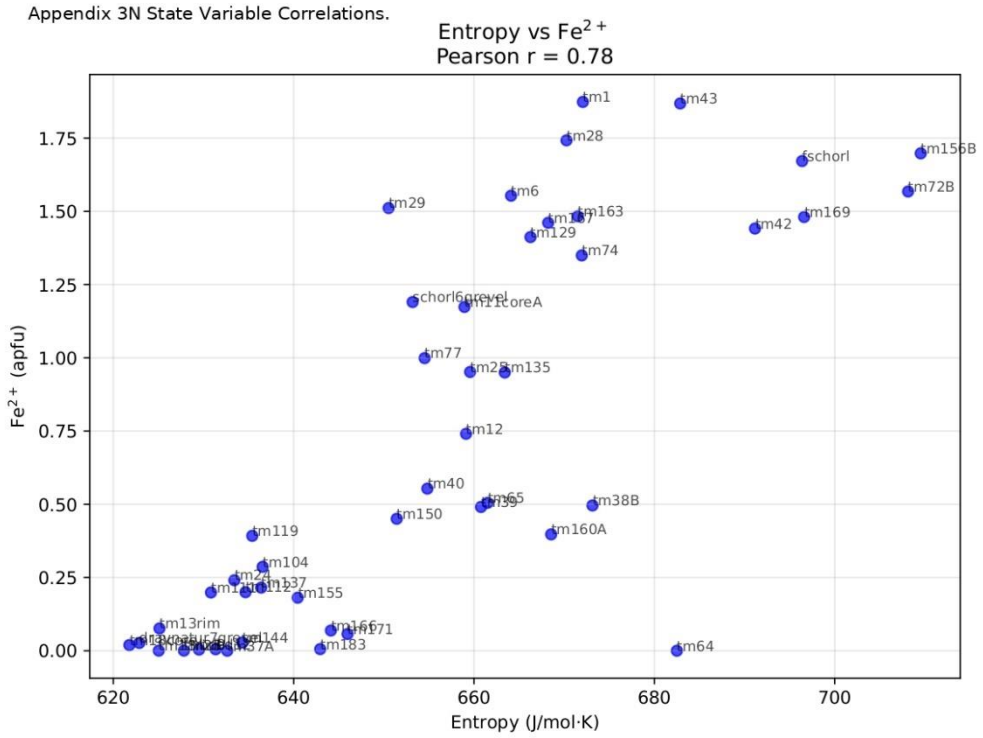

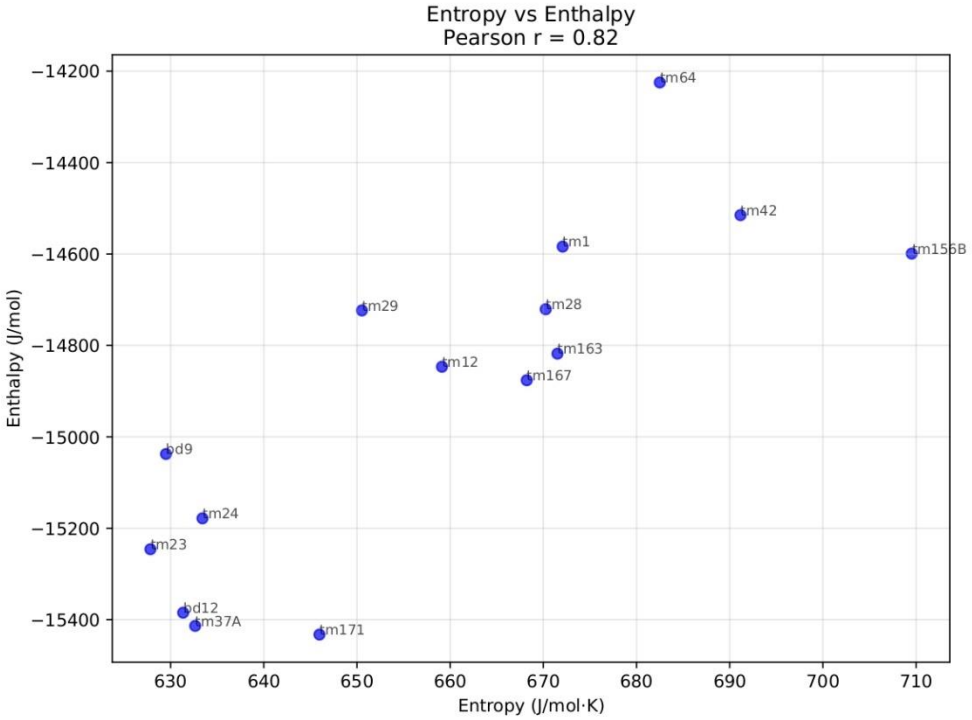
Entropy vs Enthalpy
Pearson r = 0.82
Enthalpy (J/mol)
Entropy (J/mol·K)
tm64
tm42
tm1
tm156B
tm29
tm28
tm163
tm12
tm167
bd9
tm24
tm23
bd12
tm37A
tm171

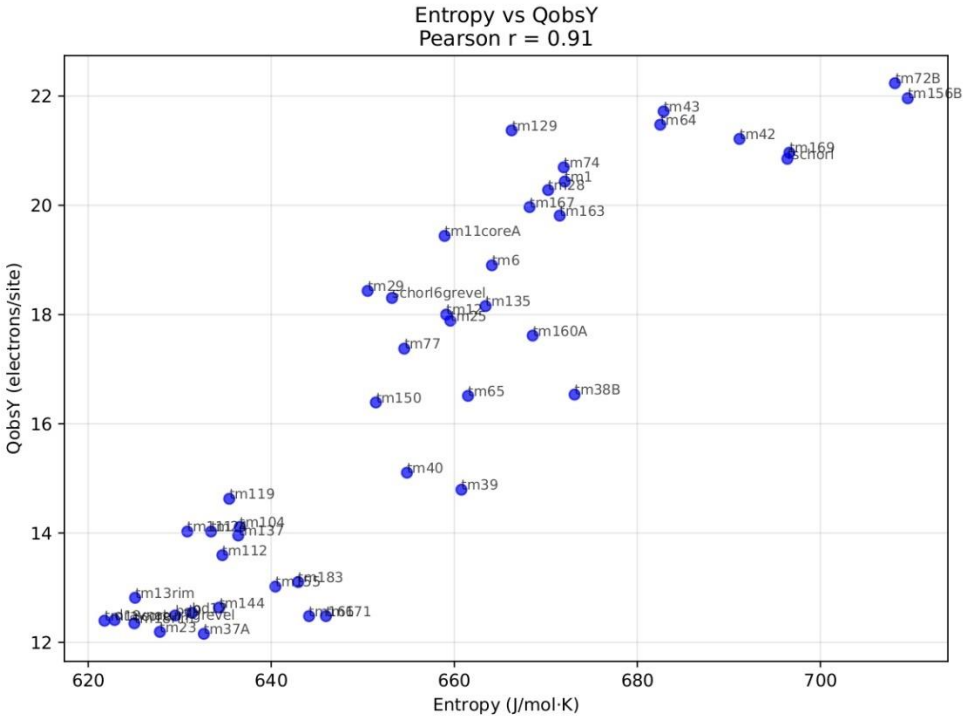
Entropy vs QobsY
Pearson r = 0.91
QobsY (electrons/site)
Entropy (J/mol·K)
tm72B
tm156B
tm43
tm64
tm129
tm42
tm169
tm74
tm1
tm28
tm167
tm163
tm11coreA
tm6
tm29
tchorl6grevel
tm135
tm25
tm160A
tm77
tm150
tm65
tm38B
tm40
tm39
tm119
tm137
tm112
tm13rim
tm144
tm23
tm37A

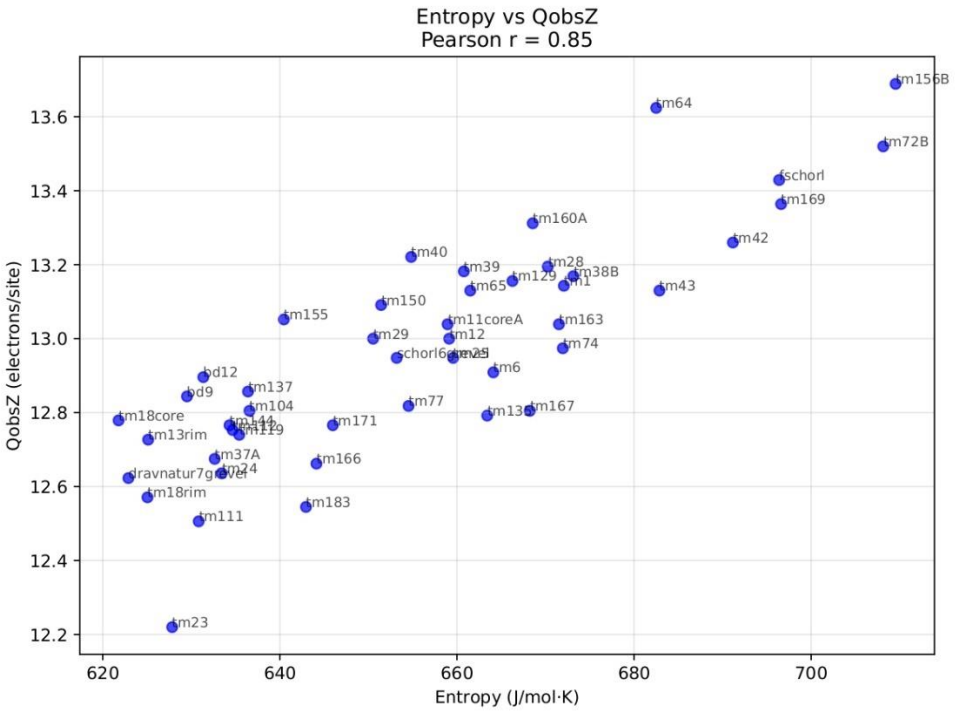
Entropy vs QobsZ
Pearson r = 0.85
QobsZ (electrons/site)
Entropy (J/mol·K)
tm156B
tm64
tm72B
fschorl
tm169
tm160A
tm42
tm40
tm39
tm28
tm38B
tm129
tm1
tm65
tm43
tm150
tm155
tm11coreA
tm163
tm29
tm12
tm74
tm6
bd12
bd9
tm137
tm77
tm104
tm18core
tm135
tm167
tm171
tm13rim
tm37A
tm166
tm24
tm18rim
tm183
tm111
tm23

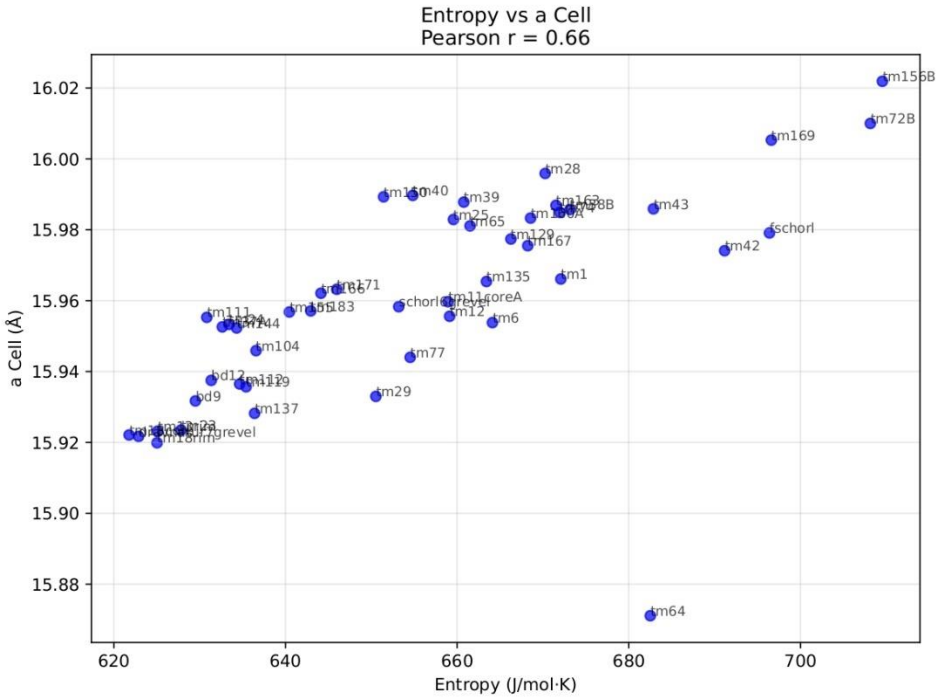
Entropy vs a Cell
Pearson r = 0.66
a Cell (Å)
Entropy (J/mol·K)
tm156B
tm72B
tm169
tm28
tm40
tm39
tm43
tm25
tm65
fschorl
tm129
tm167
tm42
tm135
tm1
tm171
tm166
tm11coreA
tm12
tm6
tm111
tm104
tm77
bd12
bd9
tm29
tm137
tm64

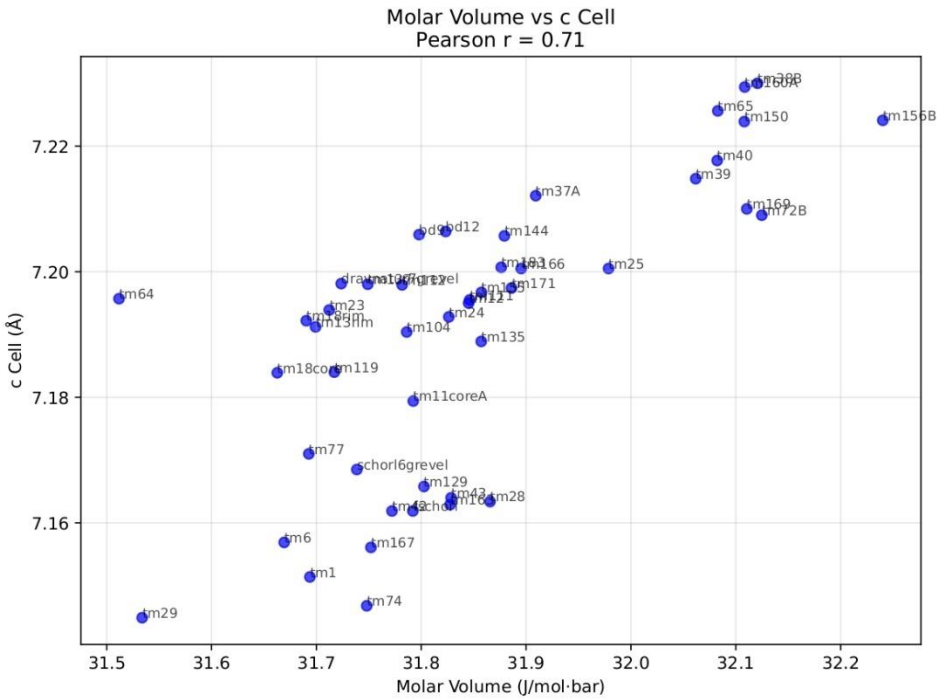
Molar Volume vs c Cell
Pearson r = 0.71
c Cell (Å)
Molar Volume (J/mol·bar)
7.22
7.20
7.18
7.16
31.5
31.6
31.7
31.8
31.9
32.0
32.1
32.2
tm65
tm150
tm156B
tm40
tm39
tm37A
tm169
tm72B
tm144
tm25
tm64
tm171
tm24
tm104
tm135
tm119
tm11coreA
tm77
schorl6grevel
tm129
tm28
tm6
tm167
tm1
tm74
tm29

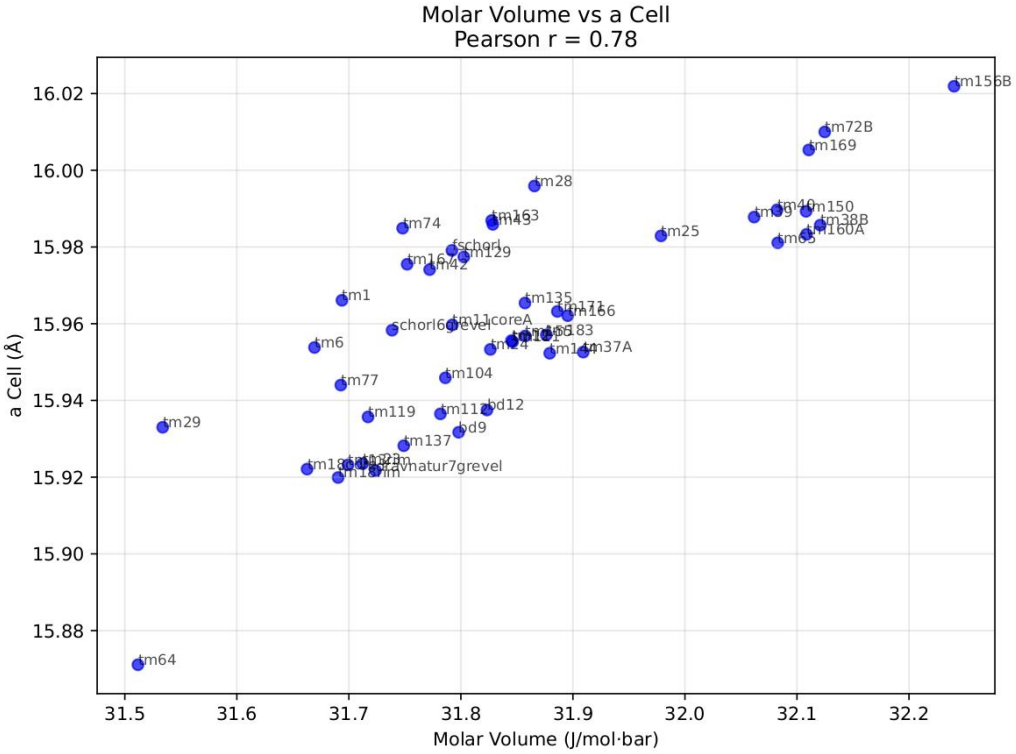
Molar Volume vs a Cell
Pearson r = 0.78
a Cell (Å)
Molar Volume (J/mol·bar)
16.02
16.00
15.98
15.96
15.94
15.92
15.90
15.88
31.5
31.6
31.7
31.8
31.9
32.0
32.1
32.2
tm156B
tm72B
tm169
tm28
tm40
tm150
tm38B
tm160A
tm74
tm25
tm29
tm64
tm1
tm135
tm6
tm77
tm104
tm119
tm37A
bd12
bd9
tm137
tm183
tm111
tm43
tm42
tm129
tm167
tm163
tm39
tm144
tm155
tm12
tm24
tm18rim
tm13rim
tm18core
tm23rim
tm23core
tm13core
tm11coreA
schorl6grevel
schorl
dravnatur7grevel

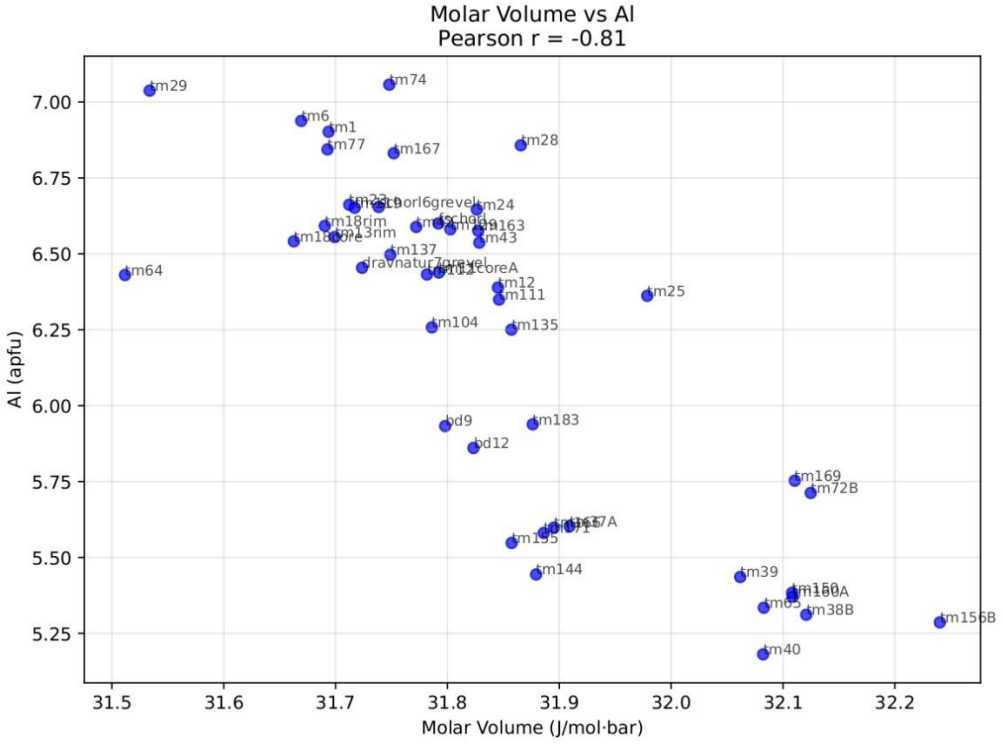
Molar Volume vs Al
Pearson r = -0.81
Al (apfu)
Molar Volume (J/mol·bar)
7.00
6.75
6.50
6.25
6.00
5.75
5.50
5.25
31.5
31.6
31.7
31.8
31.9
32.0
32.1
32.2
tm29
tm74
tm6
tm1
tm77
tm167
tm28
tm64
tm25
tm104
tm135
tm183
bd9
bd12
tm169
tm72B
tm155
tm144
tm39
tm38B
tm156B
tm40
tm24
tm18rim
tm13rim
tm137
tm163
tm43
tm12
tm111
schorl6grevel
schorl
dravnatur7grevel
tm11coreA

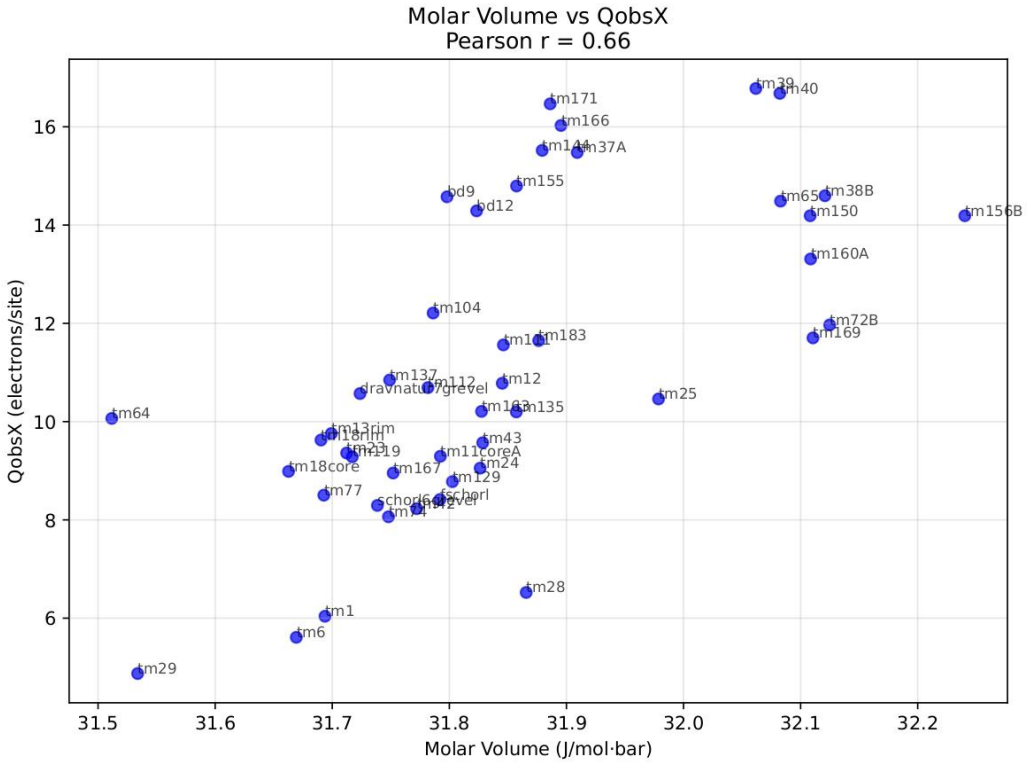
Molar Volume vs QobsX
Pearson r = 0.66
QobsX (electrons/site)
Molar Volume (J/mol·bar)
16
14
12
10
8
6
31.5
31.6
31.7
31.8
31.9
32.0
32.1
32.2
tm39
tm40
tm171
tm166
tm144
tm37A
tm155
bd9
bd12
tm65
tm38B
tm150
tm156B
tm160A
tm104
tm72B
tm169
tm183
tm137
tm112
tm12
dravnatu7grevel
tm25
tm64
tm135
tm43
tm11coreA
tm24
tm129
tm167
tm18core
tm77
tm1
tm6
tm29
tm28

Appendices Chapter 4

Appendix 4A. Theoretical Framework: Empirical Link Between Broadening of FTIR Spectra and Enthalpy of Mixing and Disorder

Influence of Strain and its Length Scale on the Enthalpy of Mixing in Solid Solutions The enthalpy of mixing (ΔH_{mix}) in solid solutions reflects the differences in energy of the solution compared to a mechanical mixture of long-range ordered (LRO) endmembers. This difference depends on electronic and elastic components (Vinograd 2001). Elastic component is mainly due to as atomic (or cluster/endmember) sizes, introduces strain fields, and leads to a balance between short-range order (SRO) and configurational disorder in the crystal lattice. Local distortions and strain fields from cation substitutions affect average bond lengths and angles (Bosenick et al. 2001). The elastic contribution results from lattice deformation and is always positive, scaling with volume differences between substituting species (atoms, SRO clusters, endmembers) (Geiger 2001). The correlation between ΔH_{mix} and volume differences is primarily driven by this elastic component, which remains composition-dependent (O'Neil and Navrotsky 1984; Vinograd 2001). The electronic component depends on orbital character (ionic or polarizable), and charge differences between substituting cations, which affect the electronic density of states (e-DOS) in the unfolded band structure. The chemical contribution arises from changes in atomic pairs, three-body interactions, clusters, and thermal disorder (Vinograd 2001). Even with constant total cluster energy, shifts in their proportions affect enthalpy. Both factors are not well captured by LRO ideal endmember formulations (Ganguly 1976; Cohen 1986; Wolverton and Zunger 1995; Bosenick et al. 2001; Carpenter and Ballaran 2001; Geiger 2001; Urusov 2001; Vinograd 2001). Elastic strain, where the lattice is "bent" or "compressed," has been described macroscopically by 'order parameters' (Ballaran 2003), bypassing the need for microscopic details. Many researchers have attempted to develop microscopic models of such strain fields and link elastic strain energy theoretically to the enthalpy of mixing, aiming to derive empirical or phenomenological equations (Geiger 2001; Christian 2002). However, the theoretical framework for determining the length scale of these strain fields and how to measure them directly remains unclear which complicates the selection of the spectral range where these effects are expected to influence spectroscopic measurements (Boffa Ballaran et al. 1999; Salje et al. 2000).

For a long time, oxides and silicates were considered largely ionic (Gale 2001), dominated by long-range Coulombic forces and, as such, the LRO unit cell provided the base for thermodynamic model building (Ganguly and Saxena 2012). However, nearest and next-nearest neighbors, as well as different short-range order (SRO) clusters, play a crucial role in defining structures and their thermodynamic properties (Navrotsky 1994a, 1994b). Melting preserves coordination polyhedra and bond lengths, with enthalpies of fusion being larger than solid-solid transitions but smaller than vaporization enthalpies (Navrotsky 1994b). Nearest neighbor and next nearest neighbor effects significantly influence NMR, ESR, EXAFS, XANES, and Mössbauer spectra by modifying local electronic structure and bonding interactions at the short-range order (SRO) scale (Navrotsky 1994b) . In NMR, neighboring atoms affect shielding and resonance frequencies (Kirkpatrick et al. 1985), while ESR signals are altered by exchange interactions and dipolar coupling (Calas 1988). EXAFS and XANES probe local scattering and absorption changes tied to bond lengths (Brown et al. 1988), coordination, and valence states, while Mössbauer spectra are shaped by electric field gradients and magnetic hyperfine interactions (Hawthorne 1988). These techniques provide critical insight into SRO structures, essential for understanding structural, electronic, and magnetic properties in complex materials.

DFT calculations show that electron density distribution is closely correlated with nearest neighbors (Vinograd et al. 2009), supporting the success of polyhedral models (Van Hinsberg et al. 2005a, 2005b) and molecular orbital calculations to describe periodic crystal systems. It is therefore argued that the strain fields responsible for the macroscopic enthalpy of mixing are due to variations in SRO clustering (Vinograd 2001). The partial occupancy of a site in a unit cell is derived from the bulk compositional mineral description and is impossible and supercells are therefore required to describe solid solutions. When the SRO clusters are considered in the mineral this leads to the breakdown of Bloch's theorem, i.e., it would lose it's periodicity and parameters including as unit cell volumes no longer have meaning as for each SRO cluster, the molar volume would be different. Each SRO cluster will have its own e-DOS and the band structure of supercells of various of these SRO structures combined would need to be unfolded to compare it with the band structure of the pure ordered endmember components.

In most spectroscopic methods, sharp lines broaden into absorption bands due to interactions with the surrounding environment. The more variable the local environment, the broader the

absorption peak, reflecting a range of slightly different energy states (White 1974). For example, Al-Si ordering in the ring silicate, cordierite, has been extensively studied using various techniques, including XRD, solution calorimetry, NMR, IR, and Raman spectroscopy (Putnis 1980; Fyfe et al. 1983; Putnis and Bish 1983; McMillan et al. 1984). Each of these techniques emphasizes different aspects of the ordering process, offering unique insights. Capturing the mesoscale supercell with SRO clusters in cordierite is challenging due to its complex framework, which permits variable cation ordering, channel occupancy, and dynamic disorder across different scales, limiting resolution by a single spectroscopic or diffraction technique. Many solid solutions with disordered or SRO structures, such as feldspars, pyroxenes, and spinels, exhibit supercells larger than 50–100 Å (Vinograd 1997, 2001). The character and dynamics of these systems are not fully understood because no spectroscopy can directly probe the 20 to 100 Å scale, and, therefore, no instrumental technique can currently unequivocally detect these SRO clusters (Navrotsky 1994a).

This theoretical analysis indicates that if strain fields arise from the distribution of SRO structures, they would span large length scales, comparable to multiple unit cells. Given that vibrational properties of SRO distributions involve many unit cell lengths, IR and Raman spectra in the MIR and FIR region are the most suitable candidates for probing these effects (Boffa Ballaran et al. 1999; Salje et al. 2000).

FTIR Spectroscopy basics In Fourier Transform Infrared Spectroscopy (FTIR) (McMillan et al. 1984; McMillan 1985; McMillan and Hofmeister 1988), broadband infrared (IR) light from an IR source is split by a beamsplitter into two beams—one directed to a stationary mirror and the other to a moving mirror. The differing path lengths of these beams, created by the moving mirror, result in an interference pattern when the beams are recombined. This interferogram contains all contributions of IR frequencies simultaneously, varied by moving the mirror, allowing rapid spectral data collection (McMillan 1985). The recombined light then passes through the sample, where certain frequencies are absorbed depending on the lattice dynamics of the sample. The interferogram of many frequency contributions are, through a Fourier transform, converted back into an IR spectrum displaying light absorption over the range of frequencies (King et al. 2004). IR light excites phonons from their vibrational ground state to higher quantized vibrational states through perturbations caused by the interaction between the

oscillating electric field vector of the light and the instantaneous dipole moment (u= Q*r, where Q is the charge and r is the separation distance) vector of the cooperative lattice distortions, phonons, within the unit cell (McMillan and Hofmeister 1988). The individual peaks in the FTIR spectrum are therefore the energies of vibrational transitions, which are called the frequencies of the vibrational modes. The phonons responsible for dipole changes can only interact with IR light when their wavelength is comparable to that of the incoming light. The wavelength of IR light ranges from approximately 5000 to 200,000 Å (2000 to 50 cm^{-1}), while the typical size of a unit cell in a crystal is on the order of tens of angstroms (Å). Because of this significant difference in scale, IR light predominantly interacts with long-wavelength phonons, particularly those near the center of the Brillouin zone where the wavevector k is close to zero (i.e., $k \rightarrow 0$, $\lambda \rightarrow \infty$) (Kieffer 1979). Due to this long-wavelength interaction, dispersion effects, which are changes in the frequency of phonons as a function of k, are usually not observed in IR spectra. In a crystal lattice of N atoms per unit cell, the 3 acoustic phonon branches involve collective atom movement in the same direction without dipole changes, whereas $3N-3$ optical branches involve relative atom displacements that alter the dipole moment and interact with light (Kieffer 1979). This is why IR spectroscopy typically does not provide information about the entire phonon dispersion curve but rather focuses on the zone-center optical phonons (Dove 1993). The intensities of these peaks are dependent on the dipole moment change of the vibrations, i.e., the more ionic the atoms involved in the vibration, the stronger its intensity. Although the frequencies and intensities of FTIR spectra are relatively well understood, broadening of these peaks is not.

Broadening of IR and Raman spectra, unlike frequencies and intensities, cannot currently be predicted well using DFT methods (Clark et al. 2005). This is because DFT methods primarily describe endmember structures and do not account for the effects due to disordered or mixed structures that would result in broadening.

Theory FTIR powder spectrum broadening

Measuring the enthalpy of mixing directly by drop calorimetry is challenging due to the uncertainties mostly from the thermodynamic cycles being of the same order of magnitude of the ΔH_{mix}. No statistically significant ΔH_{mix} was found in subset selection analysis of the dataset

presented here. However, the vibrational spectrum depends on interatomic forces, so the band-unfolded e-DOS (electronic part of the enthalpy of mixing) indirectly affects the vibrational properties of minerals. Different e-DOS result in different dynamical matrices, altering forces and eigenvalues, which changes phonon dispersion relationships (Dove 1993). If Bloch's theorem is satisfied, integrating these relationships over the Brillouin zone yields a different v-DOS (Navrotsky 1994a). In supercells with multiple SRO clusters, each cluster has its own e-DOS and v-DOS, leading to broadening when these are superimposed. Distributions of SRO should thus cause specific patterns of line broadening by modifying local bonding environments and elastic strain fields. While mineral or site specific adjustment can enhance or reduce the spectral broadening, in general, a less dilute solid solution with diverse SRO clusters should produce broader spectra due to the superposition of diverse v-DOS. The zone-center optical phonons measured by FTIR should show such broadening.

Macroscopically, Salje (2000) underscores that the scaling between vibrational damping and the order parameter Q is essential for understanding phase transitions, cation ordering, and structural changes using FTIR spectra. Damping shortens vibrational lifetimes through interactions with defects, disordered atoms and multitudes of SRO clusters, leading to broader powder FTIR peaks (Salje et al. 2000). The extent of broadening reflects the level of damping from these material interactions. Such broadening by extrinsic factors such as local structural heterogeneities, compositional fluctuations, and defects would likely be inhomogeneous, i.e., only effect certain phonon branches (Jenkins et al. 2018). Additionally, homogeneous broadening from intrinsic factors like phonon-phonon interactions and anharmonic effects may also occur (Salje et al. 2000). Band broadening in disordered and amorphous materials has been linked to the loss of translational symmetry, which allows dispersion effects to manifest in infrared spectra (Shuker and Gammon 1970). The loss of long-range order in these materials results in a breakdown of the strict IR selection rules that govern crystalline solids. Consequently, broader and more complex spectral features can emerge, as phonon modes that would be forbidden in a perfect crystal may become active in disordered systems (Shuker and Gammon 1970).

Peak broadening has been proposed to correlate with the enthalpy of mixing, primarily due to local strain energies affecting the v-DOS (Ballaran 2003). The relationship between line broadening $\Delta\nu$ and the enthalpy of mixing ΔH_{mix} can be expressed as: $\Delta H_{mix} \propto \Delta\nu^2$ (Boffa

Ballaran and Carpenter 2003). Similar quadratic relationships have also been found theoretically and empirically in lattice strain theory in the case of trace element substitutions, bond valence theory, computational studies and links the strain part of the enthalpy of mixing with volume mismatches (Greenwood 1979; Davies and Navrotsky 1983; Bosenick et al. 2001; Blundy and Wood 2003; Stølen and Grande 2003; Bosi 2014) and dominant Q2 term in Landau serie expansion for excess enthalpy of phase transitions. Autocorrelation analysis quantifies spectral broadening by correlating the spectrum with itself. The autocorrelation function Corr(α,ω′) is defined as: $\mathrm{Corr}\ (\alpha, \omega') = \int_{-\infty}^{\infty} \alpha(\omega)\alpha(\omega + \omega')d\omega$ where $\alpha(\omega)$is the spectrum of interest and $\alpha(\omega + \omega')$is the same spectrum offset by ω as implemented by (Salje et al. 2000; Jenkins et al. 2014, 2018). This function produces a symmetric spectrum from a potentially complex and asymmetric one, allowing for systematic comparison of relative differences in spectral broadening due to lattice strain from order/disorder and compositional solid solution. $\delta\Delta$ Corr is calculated as the deviation from linearity of ΔCorr between two endmembers (Etzel and Benisek 2008). This allows precise and systematic quantification of broadening, making autocorrelation analysis a robust tool for investigating strain-induced spectral changes, see (Rodehorst et al. 2004; Etzel et al. 2007; Jenkins et al. 2014).

Broadening has been shown to differ depending on the spectral range analysed, with its specifics varying by mineral (Boffa Ballaran and Carpenter 2003). For example, broadening per wavenumber does not change significantly in (almandine-grossular) (Boffa Ballaran et al. 1999) or plagioclase (albite-anorthite), but it does in pyroxene (augite-jadeite) and (clinoenstatite-clinoferrosilite) (Boffa Ballaran and Carpenter 2003). The difference is that substitutions in the former effect all polyhedrons whereas in pyroxene, substitutions effect one polyhedron but not the other. As lower wavenumber phonons correlate with longer strain field scales, lower frequencies in FTIR have shown clearer correlations with enthalpy of mixing (Boffa Ballaran and Carpenter 2003), although Jenkins (2018) demonstrated that mid-infrared (MIR) regions also relate to mixing enthalpies in carbonates. The accuracy of these correlations is complicated by factors such as crystallite size, strain introduced during sample grinding, and the differences in strain fields observed in Raman versus IR spectra (Geisler et al. 2016; Jenkins et al. 2018). While empirical correlations have been established between FTIR spectral broadening and enthalpy of mixing for several minerals (Boffa Ballaran et al. 1999; Boffa Ballaran and Carpenter 2003;

Rodehorst et al. 2004; Etzel and Benisek 2008; Jenkins et al. 2014, 2018; Geisler et al. 2016), no universal relationship applies to all minerals over all wavenumbers, necessitating mineral group-specific studies. The connection between spectral broadening and excess energy depends on relative, rather than absolute, broadening differences. Dapiaggi et al. (2005) related microscopic strain, measured by synchrotron powder XRD at 5 K, to the enthalpy of mixing in the pyrope-grossular garnet binary. Using Rietveld refinement with the fundamental parameter approach, they established empirical correlations between strain and enthalpy of mixing at the scale of multiple unit cells, offering a more direct measurement of strain (Redhammer 2021). This study benefits from XRD line broadening, which has a well-established theoretical framework, making it more quantifiable than broadening in FTIR or Raman spectra, where phonon interactions and local bonding effects introduce complexities.

REFERENCES

Ballaran, T.B. (2003) Line Broadening and Enthalpy: Some Empirical Calibrations of Solid Solution Behaviour from IR Spectra. Phase Transitions, 76, 137–154.

Blundy, J., and Wood, B. (2003) Partitioning of trace elements between crystals and melts. Earth and Planetary Science Letters, 210, 383–397.

Boffa Ballaran, T., and Carpenter, M.A. (2003) Line Broadening and Enthalpy: Some Empirical Calibrations of Solid Solution Behaviour from IR Spectra. Phase Transitions, 76, 137–154.

Boffa Ballaran, T., Carpenter, M.A., Geiger, C.A., and Koziol, A.M. (1999) Local structural heterogeneity in garnet solid solutions. Physics and Chemistry of Minerals, 26, 554–569.

Bosenick, A., Dove, M.T., Heine, V., and Geiger, C.A. (2001) Scaling of thermodynamic mixing properties in garnet solid solutions. Physics and Chemistry of Minerals, 28, 177–187.

Bosi, F. (2014) Bond valence at mixed occupancy sites. I. Regular polyhedra. Acta Crystallographica Section B Structural Science, Crystal Engineering and Materials, 70, 864–870.

Brown, G.E., Calas, G., Waychunas, G.A., and Petiau, J. (1988) Chapter 11. X-ray absorption spectroscopy and its applications in minerology and geochemistry. In F.C. Hawthorne, Ed., Spectroscopic Methods in Mineralogy and Geology pp. 431–512. De Gruyter.

Calas, G. (1988) Chapter 12. Electron Paramagentic Resonance. In F.C. Hawthorne, Ed., Spectroscopic Methods in Mineralogy and Geology pp. 513–572. De Gruyter.

Carpenter, M.A., and Ballaran, T.B. (2001) The influence of elastic strain heterogeneities in silicate solid solutions. In Solid Solutions in Silicate and Oxide Systems Vol. 3.

Christian, J. (2002) The theory of transformations in metals and alloys, 1200 p. Pergamon.

Clark, S., Segall, M., Pickard, C., Hasnip, P., Probert, M., Refson, K., and Payne, M. (2005) First principles methods using CASTEP. Zeitschrift für Kristallographie, 220.

Cohen, R.E. (1986) Configurational thermodynamics of aluminous pyroxenes: A generalized pair approximation. Physics and Chemistry of Minerals, 13, 183–197.

Dapiaggi, M. (2005) Microscopic strain in synthetic pyrope-grossular solid solutions determined by synchrotron X-ray powder diffraction at 5 K: The relationship to enthalpy of mixing behavior. American Mineralogist, 90, 506–509.

Davies, P.K., and Navrotsky, A. (1983) Quantitative correlations of deviations from ideality in binary and pseudobinary solid solutions. Journal of Solid State Chemistry, 46, 1–22.

Dove, M.T. (1993) Introduction to lattice dynamics, 258 p. Cambridge University Press, Cambridge.

Etzel, K., and Benisek, A. (2008) Thermodynamic mixing behavior of synthetic Ca-Tschermak–diopside pyroxene solid solutions: III. An analysis of IR line broadening and heat of mixing behavior. Physics and Chemistry of Minerals, 35, 399–407.

Etzel, K., Benisek, A., Dachs, E., and Cemič, L. (2007) Thermodynamic mixing behavior of synthetic Ca-Tschermak–diopside pyroxene solid solutions: I. Volume and heat capacity of mixing. Physics and Chemistry of Minerals, 34, 733–746.

Fyfe, C.A., Gobbi, G.C., Klinowski, J., Putnis, A., and Thomas, J.M. (1983) Characterisation of local atomic environment and quantitative determination of changes in site occupancies during the formation of ordered synthetic cordierite by 29 Si and 27 Al magic-angle spinning nmr spectroscopy. Journal of the Chemical Society, Chemical Communications, 556–558.

Gale, J.D. (2001) Simulating the crystal structures and properties of ionic materials from interatomic potentials. Molecular modelling theory: applications in the geosciences, 42, 37–62.

Ganguly, J. (1976) The energetics of natural garnet solid solution: II. Mixing of the calcium silicate end-members. Contributions to Mineralogy and Petrology, 55, 81–90.

Ganguly, J., and Saxena, S.K. (2012) Mixtures and mineral reactions Vol. 19. Springer

Geiger, C.A. (2001) Thermodynamic mixing properties of binary oxide and silicate solid solutions determined by direct measurements: the role of strain. In Solid Solutions in Silicate and Oxide Systems, EMU Notes in Mineralogy, Vol. 3, European Mineralogical Union, Eötvös University Press.

Geisler, T., Popa, K., and Konings, R.J. (2016) Evidence for Lattice Strain and Non-ideal Behavior in the (La1-xEux)PO4 Solid Solution from X-ray Diffraction and Vibrational Spectroscopy. Frontiers in Earth Science, 4, 64.

Greenwood, H.J. (1979) Some linear and non-linear problems in petrology. Geochimica et Cosmochimica Acta, 43, 1873–1885.

Hawthorne, F.C. (1988) Chapter 8. MOSSBAUER SPECTROSCOPY. In F.C. Hawthorne, Ed., Spectroscopic Methods in Mineralogy and Geology pp. 255–340. De Gruyter.

Jenkins, D.M., Carpenter, M.A., and Zhang, M. (2014) Experimental and infrared characterisation of the miscibility gap along the tremolite-glaucophane join. American Mineralogist, 99, 730–741.

Jenkins, D.M., Holmes, Z.F., Ishida, K., and Manuel, P.D. (2018) Autocorrelation analysis of the infrared spectra of synthetic and biogenic carbonates along the calcite–dolomite join. Physics and Chemistry of Minerals, 45, 563–574.

Kieffer, S.W. (1979) Thermodynamics and lattice vibrations of minerals: 1. Mineral heat capacities and their relationships to simple lattice vibrational models. Reviews of Geophysics, 17, 1–19.

King, P.L., Ramsey, M.S., McMillan, P.F., and Swayze, G. (2004) Laboratory Fourier transform infrared spectroscopy methods for geologic samples. Infrared Spectroscopy in Geochemistry, Exploration, and Remote Sensing, 33, 57–91.

Kirkpatrick, R.J., Smith, K.A., Schramm, S., Turner, G., and Yang, W.-H. (1985) Solid-state nuclear magnetic resonance spectroscopy of minerals. Annual Review of Earth and Planetary Sciences, 13, 29.

McMillan, P. (1985) Vibrational spectroscopy in the mineral sciences. In Microscopic to Macroscopic Atomic Enviroments to Mineral Thermodyanmics Vol. 14, pp. 9–63. Mineralogical Society of America.

McMillan, P., Putnis, A., and Carpenter, M.A. (1984) A Raman spectroscopic study of Al-Si ordering in synthetic magnesium cordierite. Physics and Chemistry of Minerals, 10, 256–260.

McMillan, P.F., and Hofmeister, A.M. (1988) Chapter 4. Infrared and Raman Spectroscopy. In F.C. Hawthorne, Ed., Spectroscopic Methods in Mineralogy and Geology pp. 99–160. De Gruyter.

Navrotsky, A. (1994a) Physics and chemistry of earth materials, 413 p. Cambridge University Press, Cambridge.

——— (1994b) Repeating patterns in mineral energetics. American Mineralogist, 79, 589–605.

O'Neil, H.S.C., and Navrotsky, A. (1984) Cation distributions and thermodynamic properties of binary spinel solid solutions. American Mineralogist, 69, 733–753.

Putnis, A. (1980) The distortion index in anhydrous Mg-cordierite. Contributions to Mineralogy and Petrology, 74, 135–141.

Putnis, A., and Bish, D.L. (1983) The mechanism and kinetics of Al, Si ordering in Mg-cordierite. American Mineralogist, 68, 60–65.

Redhammer, G.J. (2021) Structure: Scattering Techniques. In Metal Oxide Nanoparticles pp. 303–347. John Wiley & Sons, Ltd.

Rodehorst, U., Carpenter, M.A., Ballaran, T.B., and Geiger, C.A. (2004) Local structural heterogeneity, mixing behaviour and saturation effects in the grossular?spessartine solid solution. Physics and Chemistry of Minerals, 31.

Salje, E.K.H., Carpenter, M.A., Malcherek, T., and Boffa Ballaran, T. (2000) Autocorrelation analysis of infrared spectra from minerals. European Journal of Mineralogy, 12, 503–519.

Shuker, R., and Gammon, R.W. (1970) Raman-Scattering Selection-Rule Breaking and the Density of States in Amorphous Materials. Physical Review Letters, 25, 222–225.

Stølen, S., and Grande, T. (2004) Chemical thermodynamics of materials: macroscopic and microscopic aspects, 395 p. John Wiley & Sons, Chichester

Urusov, V.S. (2001) The phenomenological theory of solid solutions. In Solid Solutions in Silicate and Oxide Systems, EMU Notes in Mineralogy, Vol. 3, European Mineralogical Union, Eötvös University Press.

Van Hinsberg, V.J., Vriend, S.P., and Schumacher, J.C. (2005a) A new method to calculate end-member thermodynamic properties of minerals from their constituent polyhedra I: enthalpy, entropy and molar volume. Journal of Metamorphic Geology, 23, 165–179.

——— (2005b) A new method to calculate end-member thermodynamic properties of minerals from their constituent polyhedra II: heat capacity, compressibility and thermal expansion. Journal of Metamorphic Geology, 23, 681–693.

Vinograd, V.L. (1997) Application of stochastic processes to modelling of ordered cationic distributions in aluminosilicates.

——— (2001) Configurational entropy of binary silicate solid solutions.

Vinograd, V.L., Sluiter, M.H.F., and Winkler, B. (2009) Subsolidus phase relations in the CaCO 3 – MgCO 3 system predicted from the excess enthalpies of supercell structures with single and double defects. Physical Review B, 79, 104201.

White, W.B. (1974) Order–disorder Effects. In V.C. Farmer, Ed., The Infrared Spectra of Minerals Vol. 4, p. 0. Mineralogical Society of Great Britain and Ireland.

Wolverton, C., and Zunger, A. (1995) Ising-like Description of Structurally Relaxed Ordered and Disordered Alloys. Physical Review Letters, 75, 3162–3165.

Appendix 4B. TGA-DSC signals

- This Appendix contains all the TGA-DSC Figures.

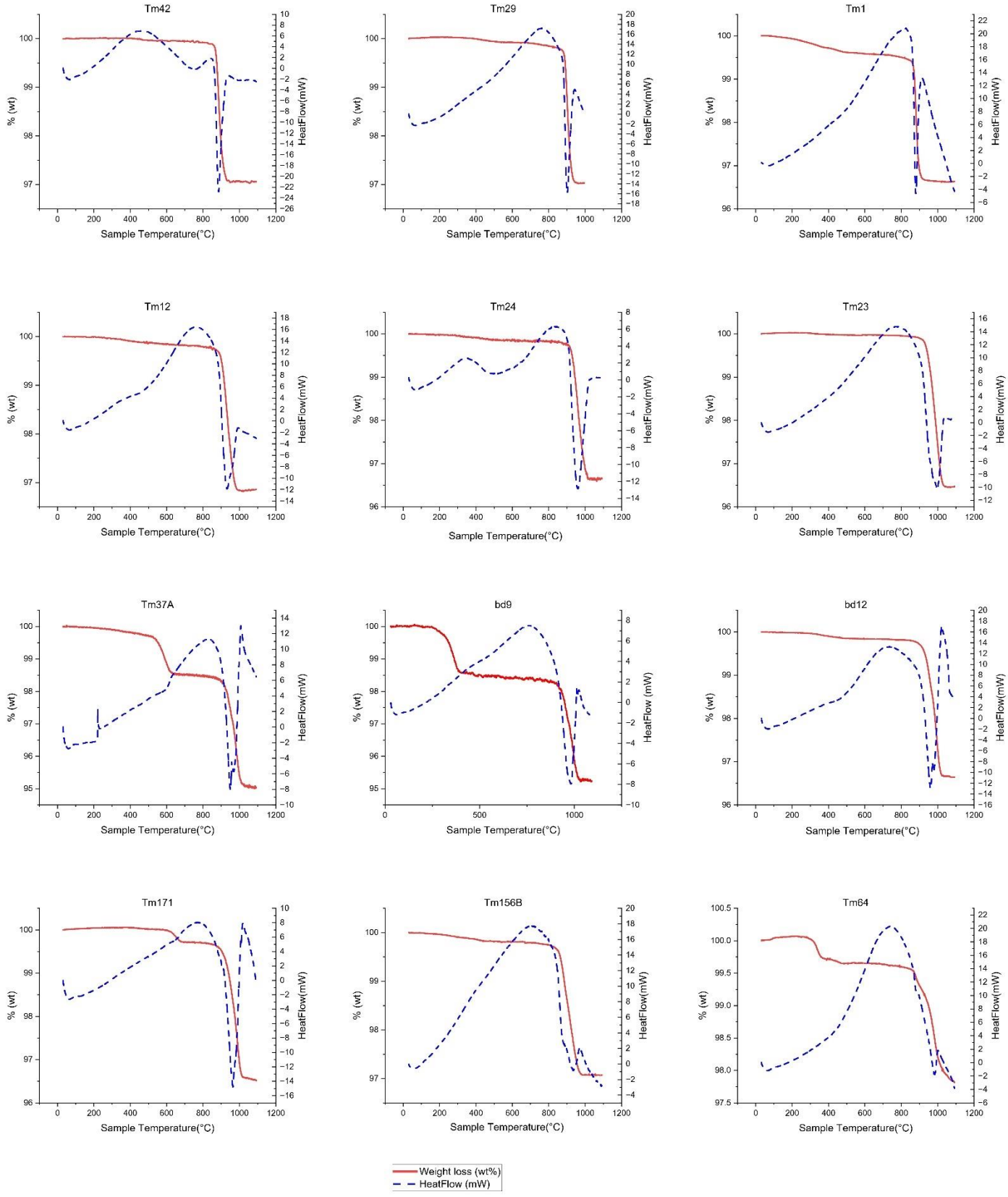
Tm42
Tm29
Tm1
Tm12
Tm24
Tm23
Tm37A
bd9
bd12
Tm171
Tm156B
Tm64
% (wt)
HeatFlow(mW)
HeatFlow (mW)
Sample Temperature(°C)
Weight loss (wt%)
HeatFlow (mW)

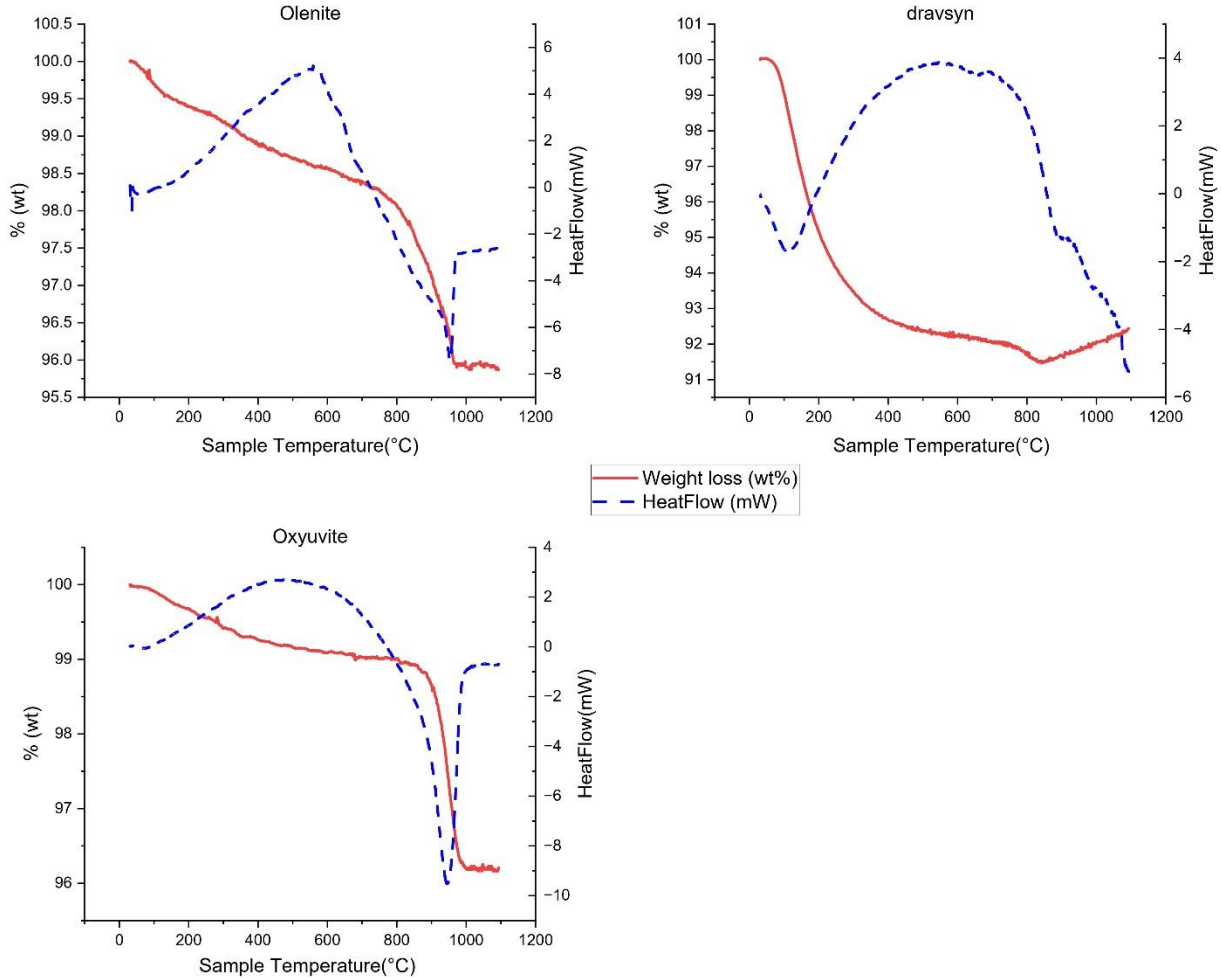
Olenite
dravsyn
Oxyuvite
% (wt)
HeatFlow(mW)
Sample Temperature(°C)
Weight loss (wt%)
HeatFlow (mW)

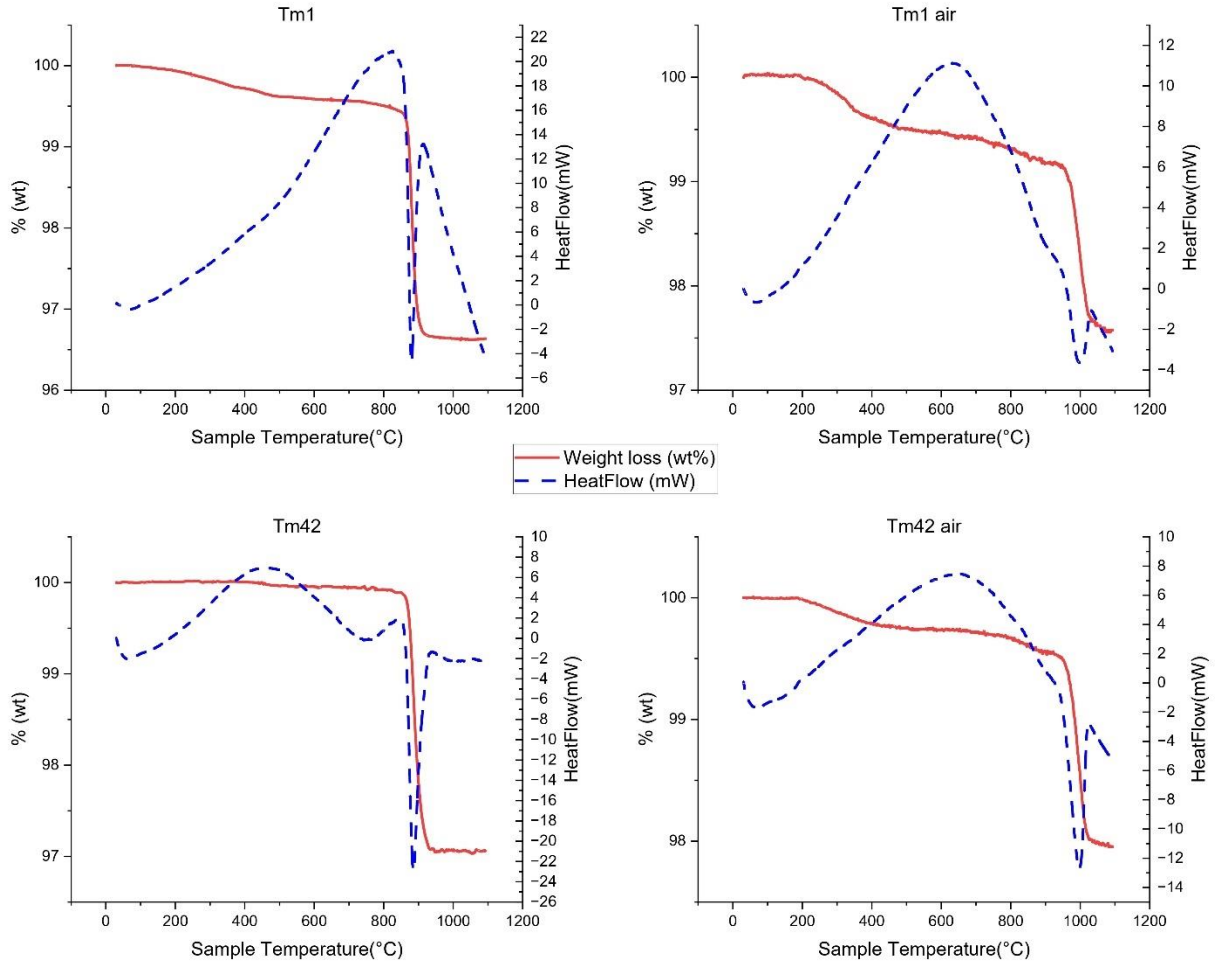
Tm1
% (wt)
HeatFlow(mW)
Sample Temperature(°C)
Tm1 air
% (wt)
HeatFlow(mW)
Sample Temperature(°C)
Weight loss (wt%)
HeatFlow (mW)
Tm42
% (wt)
HeatFlow(mW)
Sample Temperature(°C)
Tm42 air
% (wt)
HeatFlow(mW)
Sample Temperature(°C)

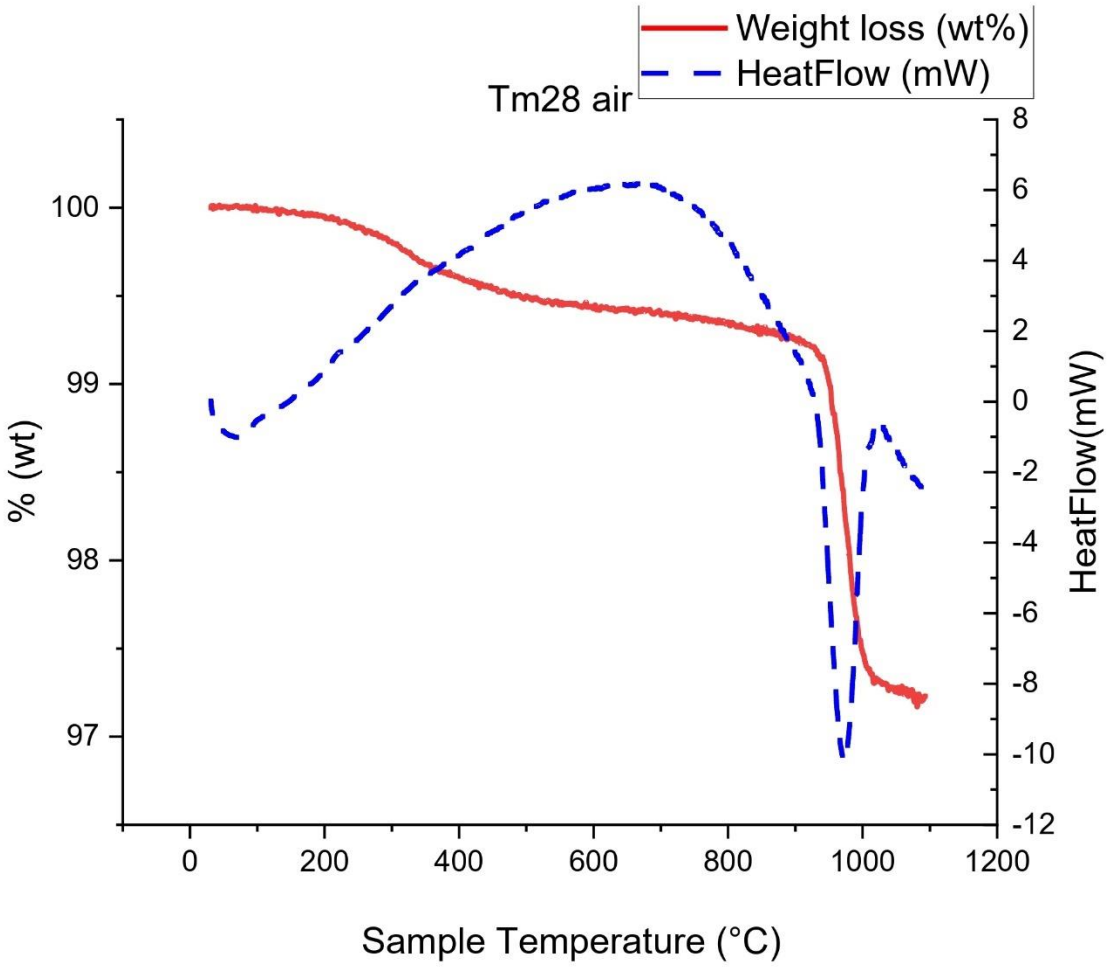
Weight loss (wt%)
HeatFlow (mW)
Tm28 air
% (wt)
HeatFlow(mW)
Sample Temperature (°C)
100
99
98
97
8
6
4
2
0
-2
-4
-6
-8
-10
-12
0
200
400
600
800
1000
1200

Appendices Chapter 5

Appendix 5A. Bulk model exchange reactions relating the endmembers

- This Appendix contains all the Bulk model exchange reaction between endmembers.

"srlB"	"drvB"	−3 "fe" + 3 "mg"
"srlB"	"uvtB"	−"al" + "ca" − 3 "fe" + 4 "mg" − "na"
"srlB"	"foiB"	"al" − "fe" − "na" + "vac"
"srlB"	"oleB"	3 "al" − 3 "fe" + 3 "O" − 3 "OH"
"srlB"	"fluvtB"	−"al" + "ca" + "F" − 3 "fe" + 4 "mg" − "na" − "OH"
"srlB"	"buB"	−3 "fe" + 3 "fef" + 3 "O" − 3 "OH"
"srlB"	"mdtwB"	−3 "fe" + "mg" + 4 "O" − 4 "OH" + 2 "Ti"
"drvB"	"uvtB"	−"al" + "ca" + "mg" − "na"
"drvB"	"foiB"	"al" + 2 "fe" − 3 "mg" − "na" + "vac"
"drvB"	"oleB"	3 "al" − 3 "mg" + 3 "O" − 3 "OH"
"drvB"	"fluvtB"	−"al" + "ca" + "F" + "mg" − "na" − "OH"
"drvB"	"buB"	3 "fef" − 3 "mg" + 3 "O" − 3 "OH"
"drvB"	"mdtwB"	−2 "mg" + 4 "O" − 4 "OH" + 2 "Ti"
"uvtB"	"foiB"	2 "al" − "ca" + 2 "fe" − 4 "mg" + "vac"
"uvtB"	"oleB"	4 "al" − "ca" − 4 "mg" + "na" + 3 "O" − 3 "OH"
"uvtB"	"fluvtB"	"F" − "OH"
"uvtB"	"buB"	"al" − "ca" + 3 "fef" − 4 "mg" + "na" + 3 "O" − 3 "OH"
"uvtB"	"mdtwB"	"al" − "ca" − 3 "mg" + "na" + 4 "O" − 4 "OH" + 2 "Ti"
"foiB"	"oleB"	2 "al" − 2 "fe" + "na" + 3 "O" − 3 "OH" − "vac"
"foiB"	"fluvtB"	−2 "al" + "ca" + "F" − 2 "fe" + 4 "mg" − "OH" − "vac"
"foiB"	"buB"	−"al" − 2 "fe" + 3 "fef" + "na" + 3 "O" − 3 "OH" − "vac"
"foiB"	"mdtwB"	−"al" − 2 "fe" + "mg" + "na" + 4 "O" − 4 "OH" + 2 "Ti" − "vac"
"oleB"	"fluvtB"	−4 "al" + "ca" + "F" + 4 "mg" − "na" − 3 "O" + 2 "OH"
"oleB"	"buB"	−3 "al" + 3 "fef"
"oleB"	"mdtwB"	−3 "al" + "mg" + "O" − "OH" + 2 "Ti"
"fluvtB"	"buB"	"al" − "ca" − "F" + 3 "fef" − 4 "mg" + "na" + 3 "O" − 2 "OH"
"fluvtB"	"mdtwB"	"al" − "ca" − "F" − 3 "mg" + "na" + 4 "O" − 3 "OH" + 2 "Ti"
"buB"	"mdtwB"	−3 "fef" + "mg" + "O" − "OH" + 2 "Ti"

Appendix 5B. Speciation model exchange reactions relating the endmembers

This Appendix contains all the Speciation model exchange reaction between endmembers.

"srl"	"drv"	−3 "xfey" + 3 "xmgy"
"srl"	"uvt"	−"xalz" + "xcax" − 3 "xfey" + 3 "xmgy" + "xmgz" − "xnax"
"srl"	"fluvt"	−"xalz" + "xcax" + "xfez" − "xnax"
"srl"	"foi"	"xaly" − "xfey" − "xnax" + "xvx"
"srl"	"ole"	3 "xaly" − 3 "xfey" − 3 "xOHv" + 3 "xOv"
"srl"	"drvdis"	"xaly" − "xalz" − 3 "xfey" + 2 "xmgy" + "xmgz"
"srl"	"odrv"	2 "xaly" − "xalz" − 3 "xfey" + "xmgy" + "xmgz" − "xOHw" + "xOw"
"srl"	"fluvt"	−"xalz" + "xcax" − 3 "xfey" + "xFw" + 3 "xmgy" + "xmgz" − "xnax" − "xOHw"
"srl"	"bu"	3 "xfefy" − 3 "xfey" − 3 "xOHv" + 3 "xOv"
"srl"	"mdtw"	−3 "xfey" + "xmgy" − 3 "xOHv" − "xOHw" + 3 "xOv" + "xOw" + 2 "xTiy"
"srl"	"bole"	3 "xaly" + 3 "xbt" − 3 "xfey" − 3 "xsit"
"srl"	"aorsm"	"xalt" + 3 "xaly" − 3 "xfey" − "xnax" − "xOHw" + "xOw" − "xsit" + "xvx"
"srl"	"pov"	−6 "xalz" + 3 "xfefy" + 4 "xfefz" − 3 "xfey" + 2 "xmgz" − "xOHw" + "xOw"
"drv"	"uvt"	−"xalz" + "xcax" + "xmgz" − "xnax"
"drv"	"fluvt"	−"xalz" + "xcax" + 3 "xfey" + "xfez" − 3 "xmgy" − "xnax"
"drv"	"foi"	"xaly" + 2 "xfey" − 3 "xmgy" − "xnax" + "xvx"
"drv"	"ole"	3 "xaly" − 3 "xmgy" − 3 "xOHv" + 3 "xOv"
"drv"	"drvdis"	"xaly" − "xalz" − "xmgy" + "xmgz"
"drv"	"odrv"	2 "xaly" − "xalz" − 2 "xmgy" + "xmgz" − "xOHw" + "xOw"
"drv"	"fluvt"	−"xalz" + "xcax" + "xFw" + "xmgz" − "xnax" − "xOHw"
"drv"	"bu"	3 "xfefy" − 3 "xmgy" − 3 "xOHv" + 3 "xOv"
"drv"	"mdtw"	−2 "xmgy" − 3 "xOHv" − "xOHw" + 3 "xOv" + "xOw" + 2 "xTiy"
"drv"	"bole"	3 "xaly" + 3 "xbt" − 3 "xmgy" − 3 "xsit"
"drv"	"aorsm"	"xalt" + 3 "xaly" − 3 "xmgy" − "xnax" − "xOHw" + "xOw" − "xsit" + "xvx"
"drv"	"pov"	−6 "xalz" + 3 "xfefy" + 4 "xfefz" − 3 "xmgy" + 2 "xmgz" − "xOHw" + "xOw"
"uvt"	"fluvt"	3 "xfey" + "xfez" − 3 "xmgy" − "xmgz"
"uvt"	"foi"	"xaly" + "xalz" − "xcax" + 2 "xfey" − 3 "xmgy" − "xmgz" + "xvx"
"uvt"	"ole"	3 "xaly" + "xalz" − "xcax" − 3 "xmgy" − "xmgz" + "xnax" − 3 "xOHv" + 3 "xOv"
"uvt"	"drvdis"	"xaly" − "xcax" − "xmgy" + "xnax"
"uvt"	"odrv"	2 "xaly" − "xcax" − 2 "xmgy" + "xnax" − "xOHw" + "xOw"
"uvt"	"fluvt"	"xFw" − "xOHw"
"uvt"	"bu"	"xalz" − "xcax" + 3 "xfefy" − 3 "xmgy" − "xmgz" + "xnax" − 3 "xOHv" + 3 "xOv"
"uvt"	"mdtw"	"xalz" − "xcax" − 2 "xmgy" − "xmgz" + "xnax" − 3 "xOHv" − "xOHw" + 3 "xOv" + "xOw" + 2 "xTiy"
"uvt"	"bole"	3 "xaly" + "xalz" + 3 "xbt" − "xcax" − 3 "xmgy" − "xmgz" + "xnax" − 3 "xsit"
"uvt"	"aorsm"	"xalt" + 3 "xaly" + "xalz" − "xcax" − 3 "xmgy" − "xmgz" − "xOHw" + "xOw" − "xsit" + "xvx"
"uvt"	"pov"	−5 "xalz" − "xcax" + 3 "xfefy" + 4 "xfefz" − 3 "xmgy" + "xmgz" + "xnax" − "xOHw" + "xOw"
"fluvt"	"foi"	"xaly" + "xalz" − "xcax" − "xfey" − "xfez" + "xvx"
"fluvt"	"ole"	3 "xaly" + "xalz" − "xcax" − 3 "xfey" − "xfez" + "xnax" − 3 "xOHv" + 3 "xOv"
"fluvt"	"drvdis"	"xaly" − "xcax" − 3 "xfey" − "xfez" + 2 "xmgy" + "xmgz" + "xnax"
"fluvt"	"odrv"	2 "xaly" − "xcax" − 3 "xfey" − "xfez" + "xmgy" + "xmgz" + "xnax" − "xOHw" + "xOw"
"fluvt"	"fluvt"	−3 "xfey" − "xfez" + "xFw" + 3 "xmgy" + "xmgz" − "xOHw"
"fluvt"	"bu"	"xalz" − "xcax" + 3 "xfefy" − 3 "xfey" − "xfez" + "xnax" − 3 "xOHv" + 3 "xOv"
"fluvt"	"mdtw"	"xalz" − "xcax" − 3 "xfey" − "xfez" + "xmgy" + "xnax" − 3 "xOHv" − "xOHw" + 3 "xOv" + "xOw" + 2 "xTiy"
"fluvt"	"bole"	3 "xaly" + "xalz" + 3 "xbt" − "xcax" − 3 "xfey" − "xfez" + "xnax" − 3 "xsit"
"fluvt"	"aorsm"	"xalt" + 3 "xaly" + "xalz" − "xcax" − 3 "xfey" − "xfez" − "xOHw" + "xOw" − "xsit" + "xvx"
"fluvt"	"pov"	−5 "xalz" − "xcax" + 3 "xfefy" + 4 "xfefz" − 3 "xfey" − "xfez" + 2 "xmgz" + "xnax" − "xOHw" + "xOw"

"foi"	"ole"	2 "xaly" − 2 "xfey" + "xnax" − 3 "xOHv" + 3 "xOv" − "xvx"
"foi"	"drvdis"	− "xalz" − 2 "xfey" + 2 "xmgy" + "xmgz" + "xnax" − "xvx"
"foi"	"odrv"	"xaly" − "xalz" − 2 "xfey" + "xmgy" + "xmgz" + "xnax" − "xOHw" + "xOw" − "xvx"
"foi"	"fluvt"	− "xaly" − "xalz" + "xcax" − 2 "xfey" + "xFw" + 3 "xmgy" + "xmgz" − "xOHw" − "xvx"
"foi"	"bu"	− "xaly" + 3 "xfefy" − 2 "xfey" + "xnax" − 3 "xOHv" + 3 "xOv" − "xvx"
"foi"	"mdtw"	− "xaly" − 2 "xfey" + "xmgy" + "xnax" − 3 "xOHv" − "xOHw" + 3 "xOv" + "xOw" + 2 "xTiy" − "xvx"
"foi"	"bole"	2 "xaly" + 3 "xbt" − 2 "xfey" + "xnax" − 3 "xsit" − "xvx"
"foi"	"aorsm"	"xalt" + 2 "xaly" − 2 "xfey" − "xOHw" + "xOw" − "xsit"
"foi"	"pov"	− "xaly" − 6 "xalz" + 3 "xfefy" + 4 "xfefz" − 2 "xfey" + 2 "xmgz" + "xnax" − "xOHw" + "xOw" − "xvx"
"ole"	"drvdis"	− 2 "xaly" − "xalz" + 2 "xmgy" + "xmgz" + 3 "xOHv" − 3 "xOv"
"ole"	"odrv"	− "xaly" − "xalz" + "xmgy" + "xmgz" + 3 "xOHv" − "xOHw" − 3 "xOv" + "xOw"
"ole"	"fluvt"	− 3 "xaly" − "xalz" + "xcax" + "xFw" + 3 "xmgy" + "xmgz" − "xnax" + 3 "xOHv" − "xOHw" − 3 "xOv"
"ole"	"bu"	− 3 "xaly" + 3 "xfefy"
"ole"	"mdtw"	− 3 "xaly" + "xmgy" − "xOHw" + "xOw" + 2 "xTiy"
"ole"	"bole"	3 "xbt" + 3 "xOHv" − 3 "xOv" − 3 "xsit"
"ole"	"aorsm"	"xalt" − "xnax" + 3 "xOHv" − "xOHw" − 3 "xOv" + "xOw" − "xsit" + "xvx"
"ole"	"pov"	− 3 "xaly" − 6 "xalz" + 3 "xfefy" + 4 "xfefz" + 2 "xmgz" + 3 "xOHv" − "xOHw" − 3 "xOv" + "xOw"
"drvdis"	"odrv"	"xaly" − "xmgy" − "xOHw" + "xOw"
"drvdis"	"fluvt"	− "xaly" + "xcax" + "xFw" + "xmgy" − "xnax" − "xOHw"
"drvdis"	"bu"	− "xaly" + "xalz" + 3 "xfefy" − 2 "xmgy" − "xmgz" − 3 "xOHv" + 3 "xOv"
"drvdis"	"mdtw"	− "xaly" + "xalz" − "xmgy" − "xmgz" − 3 "xOHv" − "xOHw" + 3 "xOv" + "xOw" + 2 "xTiy"
"drvdis"	"bole"	2 "xaly" + "xalz" + 3 "xbt" − 2 "xmgy" − "xmgz" − 3 "xsit"
"drvdis"	"aorsm"	"xalt" + 2 "xaly" + "xalz" − 2 "xmgy" − "xmgz" − "xnax" − "xOHw" + "xOw" − "xsit" + "xvx"
"drvdis"	"pov"	− "xaly" − 5 "xalz" + 3 "xfefy" + 4 "xfefz" − 2 "xmgy" + "xmgz" − "xOHw" + "xOw"
"odrv"	"fluvt"	− 2 "xaly" + "xcax" + "xFw" + 2 "xmgy" − "xnax" − "xOw"
"odrv"	"bu"	− 2 "xaly" + "xalz" + 3 "xfefy" − "xmgy" − "xmgz" − 3 "xOHv" + "xOHw" + 3 "xOv" − "xOw"
"odrv"	"mdtw"	− 2 "xaly" + "xalz" − "xmgz" − 3 "xOHv" + 3 "xOv" + 2 "xTiy"
"odrv"	"bole"	"xaly" + "xalz" + 3 "xbt" − "xmgy" − "xmgz" + "xOHw" − "xOw" − 3 "xsit"
"odrv"	"aorsm"	"xalt" + "xaly" + "xalz" − "xmgy" − "xmgz" − "xnax" − "xsit" + "xvx"
"odrv"	"pov"	− 2 "xaly" − 5 "xalz" + 3 "xfefy" + 4 "xfefz" − "xmgy" + "xmgz"
"fluvt"	"bu"	"xalz" − "xcax" + 3 "xfefy" − "xFw" − 3 "xmgy" − "xmgz" + "xnax" − 3 "xOHv" + "xOHw" + 3 "xOv"
"fluvt"	"mdtw"	"xalz" − "xcax" − "xFw" − 2 "xmgy" − "xmgz" + "xnax" − 3 "xOHv" + 3 "xOv" + "xOw" + 2 "xTiy"
"fluvt"	"bole"	3 "xaly" + "xalz" + 3 "xbt" − "xcax" − "xFw" − 3 "xmgy" − "xmgz" + "xnax" + "xOHw" − 3 "xsit"
"fluvt"	"aorsm"	"xalt" + 3 "xaly" + "xalz" − "xcax" − "xFw" − 3 "xmgy" − "xmgz" + "xOw" − "xsit" + "xvx"
"fluvt"	"pov"	− 5 "xalz" − "xcax" + 3 "xfefy" + 4 "xfefz" − "xFw" − 3 "xmgy" + "xmgz" + "xnax" + "xOw"
"bu"	"mdtw"	− 3 "xfefy" + "xmgy" − "xOHw" + "xOw" + 2 "xTiy"
"bu"	"bole"	3 "xaly" + 3 "xbt" − 3 "xfefy" + 3 "xOHv" − 3 "xOv" − 3 "xsit"

"bu"	"aorsm"	"xalt" + 3 "xaly" − 3 "xfefy" − "xnax" + 3 "xOHv" − "xOHw" − 3 "xOv" + "xOw" − "xsit" + "xvx"
"bu"	"pov"	−6 "xalz" + 4 "xfefz" + 2 "xmgz" + 3 "xOHv" − "xOHw" − 3 "xOv" + "xOw"
"mdtw"	"bole"	3 "xaly" + 3 "xbt" − "xmgy" + 3 "xOHv" + "xOHw" − 3 "xOv" − "xOw" − 3 "xsit" − 2 "xTiy"
"mdtw"	"aorsm"	"xalt" + 3 "xaly" − "xmgy" − "xnax" + 3 "xOHv" − 3 "xOv" − "xsit" − 2 "xTiy" + "xvx"
"mdtw"	"pov"	−6 "xalz" + 3 "xfefy" + 4 "xfefz" − "xmgy" + 2 "xmgz" + 3 "xOHv" − 3 "xOv" − 2 "xTiy"
"bole"	"aorsm"	"xalt" − 3 "xbt" − "xnax" − "xOHw" + "xOw" + 2 "xsit" + "xvx"
"bole"	"pov"	−3 "xaly" − 6 "xalz" − 3 "xbt" + 3 "xfefy" + 4 "xfefz" + 2 "xmgz" − "xOHw" + "xOw" + 3 "xsit"
"aorsm"	"pov"	−"xalt" − 3 "xaly" − 6 "xalz" + 3 "xfefy" + 4 "xfefz" + 2 "xmgz" + "xnax" + "xsit" − "xvx"

MASTER REFERENCE LIST

Allen, D.M. (1974) The Relationship Between Variable Selection and Data Augmentation and a Method for Prediction. Technometrics, 16, 125–127.

Altieri, A., Pezzotta, F., Skogby, H., Hålenius, U., and Bosi, F. (2022) Blue growth zones caused by Fe2+ in tourmaline crystals from the San Piero in Campo gem-bearing pegmatites, Elba Island, Italy. Mineralogical Magazine, 86, 910–919.

Altieri, A., Luppi, R., Skogby, H., Hålenius, U., Tempesta, G., Pezzotta, F., and Bosi, F. (2023) Thermal treatment of the tourmaline Fe-rich princivalleite Na(Mn2Al)Al6(Si6O18)(BO3)3(OH)3O. Physics and Chemistry of Minerals, 50, 27.

Ancey, M., Bastenaire, F., Tixier, R., Maurice, F., and Meny, I. (1978) Applications of statistical methods in microanalysis. In Microanalysis and scanning electron microscopy pp. 319–343.

Andersen, D.J., and Lindsley, D.H. (1988) Internally consistent solution models for Fe-Mg-Mn-Ti oxides; Fe-Ti oxides. American Mineralogist, 73, 714–726.

Anderson, G.M. (1976) Error propagation by the Monte Carlo method in geochemical calculations. Geochimica et Cosmochimica Acta, 40, 1533–1538.

Anderson, G.M. (2005) Thermodynamics of natural systems, 2nd ed., 648 p. Cambridge University Press, Cambridge.

Andreozzi, G.B., Bosi, F., and Longo, M. (2008) Linking Mossbauer and structural parameters in elbaite-schorl-dravite tourmalines. American Mineralogist, 93, 658–666.

Andreozzi, G.B., Bosi, F., Celata, B., Capizzi, L.S., Stagno, V., and Beckett-Brown, C.E. (2020) Crystal-chemical behavior of Fe2+ in tourmaline dictated by structural stability: insights from a schorl with formula NaY(Fe2+2Al)Z(Al5Fe2+)(Si6O18)(BO3)3(OH)3(OH,F) from Seagull batholith (Yukon Territory, Canada). Physics and Chemistry of Minerals, 47, 25.

Anovitz, L.M., and Hemingway, B.S. (1996) Thermodynamics of boron minerals; summary of structural, volumetric and thermochemical data. Reviews in Mineralogy and Geochemistry, 33, 181–261.

Appel, P.W.U. (1984) Tourmaline in the early Archaean Isua supracrustal belt, West Greenland. The Journal of Geology, 92, 599–605.

Asimow, P.D., and Ghiorso, M.S. (1998) Algorithmic modifications extending MELTS to calculate subsolidus phase relations. American Mineralogist, 83, 1127–1132.

Babińska, J., Dyrek, K., Pieczka, A., and Sojka, Z. (2008) X and Q band EPR studies of paramagnetic centres in natural and heated tourmaline. European Journal of Mineralogy, 20, 233–240.

Bačík, P. (2015) Cation ordering at octahedral sites in schorl-dravite series tourmalines. The Canadian Mineralogist, 53, 571–590.

——— (2018) The crystal-chemical autopsy of octahedral sites in Na-dominant tourmalines: Octahedral metrics model unconstrained by the Y, Z-site disorder assignment. Journal of Geosciences, 63, 137–154.

Bačík, P., and Fridrichová, J. (2021) Cation partitioning among crystallographic sites based on bond-length constraints in tourmaline-supergroup minerals. American Mineralogist, 106, 851–861.

Bačík, P., Ozdín, D., Miglierini, M., Kardošová, P., Pentrák, M., and Haloda, J. (2011) Crystallochemical effects of heat treatment on Fe-dominant tourmalines from Dolní Bory (Czech Republic) and Vlachovo (Slovakia). Physics and Chemistry of Minerals, 38, 599–611.

Bačík, P., Uher, P., Ertl, A., Jonsson, E., Nysten, P., Kanickỳ, V., and Vaculovič, T. (2012) Zoned REE Enriched Dravite from a Granitic Pegmatite in Forshammar Bergslagen Province, Sweden an EMPA XRD and LA–ICP-MS Study. The Canadian Mineralogist, 50, 825–841.

Bačík, P., CemPírek, J., Uher, P., Novák, M., Ozdín, D., Filip, J., Škoda, R., Breiter, K., Klementová, M., and ĎuĎa, R. (2013) Oxy-schorl, Na(Fe2+2Al) Al6Si6O18(BO3)3(OH)3O, a new mineral from Zlatá Idka, Slovak Republic and Přibyslavice, Czech Republic. American Mineralogist, 98, 485–492.

Balan, E., Radtke, G., Fourdrin, C., Paulatto, L., Horn, H.A., and Fuchs, Y. (2023) Effect of Fe–Fe interactions and X-site vacancy ordering on the OH-stretching spectrum of foitite. European Journal of Mineralogy, 35, 105–116.

Bale, C.W., Chartrand, P., Degterov, S.A., Eriksson, G., Hack, K., Ben Mahfoud, R., Melançon, J., Pelton, A.D., and Petersen, S. (2002) FactSage thermochemical software and databases. Calphad, 26, 189–228.

Ballaran, T.B. (2003) Line Broadening and Enthalpy: Some Empirical Calibrations of Solid Solution Behaviour from IR Spectra. Phase Transitions, 76, 137–154.

Ballirano, P., Celata, B., and Bosi, F. (2022) In situ high-temperature behaviour and breakdown conditions of uvite at room pressure. Physics and Chemistry of Minerals, 49, 40.

Bancroft, G.M. (1973) Mössbauer spectroscopy: an introduction for inorganic chemists and geochemists. 271 p. McGraw-Hill.

Baroni, S., Giannozzi, P., and Isaev, E. (2010) Density-functional perturbation theory for quasi-harmonic calculations. Reviews in Mineralogy and Geochemistry, 71, 39–57.

Bastin, G.F., and Heijligers, H.J.M. (1986) Quantitative electron probe microanalysis of boron in binary borides p. 118. Netherlands.

Beattie, P. (1993) Olivine-melt and orthopyroxene-melt equilibria. Contributions to Mineralogy and Petrology, 115, 103–111.

Benisek, A., and Dachs, E. (2008) The uncertainty in determining the third law entropy by the heat-pulse calorimetric technique. Cryogenics, 48, 527–529.

——— (2015) The vibrational and configurational entropy of disordering in Cu3Au. Journal of Alloys and Compounds, 632, 585–590.

——— (2018) The accuracy of standard enthalpies and entropies for phases of petrological interest derived from density-functional calculations. Contributions to Mineralogy and Petrology, 173, 90.

——— (2020) Excess enthalpy of mixing of mineral solid solutions derived from density-functional calculations. Physics and Chemistry of Minerals, 47, 15.

——— (2024) The packing fraction of the oxygen sublattice: its impact on the heat of mixing. Physics and Chemistry of Minerals, 51, 23.

Benisek, A., Dachs, E., Carpenter, M.A., Joachim-Mrosko, B., Vielreicher, N.M., and Wildner, M. (2023) Vibrational entropy of disordering in omphacite. Physics and Chemistry of Minerals, 50, 36.

Berman, R.G. (1988) Internally-consistent thermodynamic data for minerals in the system Na2O-K2O-CaO-MgO-FeO-Fe2O3-Al2O3-SiO2-TiO2-H2O-CO2. Journal of petrology, 29, 445–522.

Berman, R.G., and Brown, T.H. (1985) Heat capacity of minerals in the system Na2O-K2O-CaO-MgO-FeO-Fe2O3-Al2O3-SiO2-TiO2-H2O-CO2: representation, estimation, and high temperature extrapolation. Contributions to Mineralogy and Petrology, 89, 168–183.

Berryman, Wunder, B., Rhede, D., Schettler, G., Franz, G., and Heinrich, W. (2016) P-T-X controls on Ca and Na distribution between Mg–Al tourmaline and fluid. Contributions to Mineralogy and Petrology, 171, 31.

Berryman, E., Wunder, B., and Rhede, D. (2014) Synthesis of K-dominant tourmaline. American Mineralogist, 99, 539–542.

Berryman, E.J., Wunder, B., Wirth, R., Rhede, D., Schettler, G., Franz, G., and Heinrich, W. (2015) An experimental study on K and Na incorporation in dravitic tourmaline and insight into the origin of diamondiferous tourmaline from the Kokchetav Massif, Kazakhstan. Contributions to Mineralogy and Petrology, 169, 28.

Berryman, E.J., Wunder, B., Ertl, A., Koch-Müller, M., Rhede, D., Scheidl, K., Giester, G., and Heinrich, W. (2016) Influence of the X-site composition on tourmaline's crystal structure: investigation of synthetic K-dravite, dravite, oxy-uvite, and magnesio-foitite using SREF and Raman spectroscopy. Physics and Chemistry of Minerals, 43, 83–102.

Berryman, E.J., Zhang, D., Wunder, B., and Duffy, T.S. (2019) Compressibility of synthetic Mg-Al tourmalines to 60 GPa. American Mineralogist, 104, 1005–1015.

Bevington, P.R., and Robinson, D.K. (2003) Data reduction and error analysis. 320 p, McGraw-Hill, New York.

Biagioni, C., Bosi, F., Mauro, D., Skogby, H., Dini, A., and Zaccarini, F. (2023) Dutrowite, Na(Fe2+2.5Ti0.5)Al6(Si6O18)(BO3)3(OH)3O, a new mineral from the Apuan Alps (Tuscany, Italy): the first member of the tourmaline supergroup with Ti as a species-forming chemical constituent. European Journal of Mineralogy, 35, 81–94.

Biernacka, J. (2019) Insight into diagenetic processes from authigenic tourmaline: An example from Carboniferous and Permian siliciclastic rocks of western Poland. Sedimentary geology, 389, 73–90.

Blanch, A.J., Quinton, J.S., Lenehan, C.E., and Pring, A. (2007) Autocorrelation infrared analysis of mineralogical samples: The influence of user controllable experimental parameters. Analytica chimica acta, 590, 145–150.

Bloodaxe, E.S., Hughes, J.M., Dyar, M.D., Grew, E.S., and Guidotti, C.V. (1999) Linking structure and chemistry in the Schorl-Dravite series. American Mineralogist, 84, 922–928.

Blundell, S. (2001) Magnetism in condensed matter, 238 p. Oxford University Press, Oxford.

Blundy, J., and Wood, B. (2003) Partitioning of trace elements between crystals and melts. Earth and Planetary Science Letters, 210, 383–397.

Boffa Ballaran, T., and Carpenter, M.A. (2003) Line Broadening and Enthalpy: Some Empirical Calibrations of Solid Solution Behaviour from IR Spectra. Phase Transitions, 76, 137–154.

Boffa Ballaran, T., Carpenter, M.A., Geiger, C.A., and Koziol, A.M. (1999) Local structural heterogeneity in garnet solid solutions. Physics and Chemistry of Minerals, 26, 554–569.

Born, M., and Huang, J. (1954) The Dynamical Theory of Crystal Lattices, 420 p. Clarendon, Oxford.

Born, M., and Von Kármán, T. (1912) Über schwingungen in raumgittern. Physikalishe Zeitschrift, 13, 297–309.

Bosenick, A., Dove, M.T., Myers, E.R., Palin, E.J., Sainz-Diaz, C.I., Guiton, B.S., Warren, M.C., Craig, M.S., and Redfern, S.A.T. (2001a) Computational methods for the study of

energies of cation distributions: applications to cation-ordering phase transitions and solid solutions. Mineralogical Magazine, 65, 193–219.

Bosenick, A., Dove, M.T., Heine, V., and Geiger, C.A. (2001b) Scaling of thermodynamic mixing properties in garnet solid solutions. Physics and Chemistry of Minerals, 28, 177–187.

Bosi, F. (2008) Disordering of Fe2+ over octahedrally coordinated sites of tourmaline. American Mineralogist, 93, 1647–1653.

——— (2010) Octahedrally coordinated vacancies in tourmaline: a theoretical approach. Mineralogical Magazine, 74, 1037–1044.

——— (2011) Stereochemical constraints in tourmaline: from a short-range to a long-range structure. The Canadian Mineralogist, 49, 17–27.

——— (2013) Bond-valence constraints around the O1 site of tourmaline. Mineralogical Magazine, 77, 343–351.

——— (2014a) Bond valence at mixed occupancy sites. I. Regular polyhedra. Acta Crystallographica Section B Structural Science, Crystal Engineering and Materials, 70, 864–870.

——— (2014b) Mean bond-length variation in crystal structures: a bond-valence approach. Acta Crystallographica Section B Structural Science, Crystal Engineering and Materials, 70, 697–704.

——— (2018) Tourmaline crystal chemistry. American Mineralogist, 103, 298–306.

Bosi, F., and Andreozzi, G.B. (2013) A critical comment on Ertl et al. (2012): “Limitations of Fe2+ and Mn2+ site occupancy in tourmaline: Evidence from Fe2+- and Mn2+-rich tourmaline.” American Mineralogist, 98, 2183–2192.

Bosi, F., and Lucchesi, S. (2004) Crystal chemistry of the schorl-dravite series. European Journal of Mineralogy, 16, 335–344.

——— (2007) Crystal chemical relationships in the tourmaline group: Structural constraints on chemical variability. American Mineralogist, 92, 1054–1063.

——— (2013b) Oxy-dravite, Na(Al2Mg)(Al5Mg)(Si6O18)(BO3)3(OH)3O, a new mineral species of the tourmaline supergroup. American Mineralogist, 98, 1442–1448.

Bosi, F., Andreozzi, G.B., Federico, M., Graziani, G., and Lucchesi, S. (2005) Crystal chemistry of the elbaite-schorl series. American Mineralogist, 90, 1784–1792.

Bosi, F., Balić-Žunić, T., and Surour, A.A. (2010) Crystal structure analyses of four tourmaline specimens from the Cleopatra’s Mines (Egypt) and Jabal Zalm (Saudi Arabia), and the role of Al in the tourmaline group. American Mineralogist, 95, 510–518.

Bosi, F., Andreozzi, G.B., Hålenius, U., and Skogby, H. (2015) Experimental evidence for partial Fe2+ disorder at the Y and Z sites of tourmaline: a combined EMP, SREF, MS, IR and OAS study of schorl. Mineralogical Magazine, 79, 515–528.

Bosi, F., Skogby, H., and Balić-Žunić, T. (2016a) Thermal stability of extended clusters in dravite: a combined EMP, SREF and FTIR study. Physics and Chemistry of Minerals, 43, 395–407.

Bosi, F., Skogby, H., and Hålenius, U. (2016b) Thermally induced cation redistribution in Fe-bearing oxy-dravite and potential geothermometric implications. Contributions to Mineralogy and Petrology, 171, 1–14.

Bosi, F., Reznitskii, L., Hålenius, U., and Skogby, H. (2017a) Crystal chemistry of Al–V–Cr oxy-tourmalines from Sludyanka complex, Lake Baikal, Russia. European Journal of Mineralogy, 29, 457–472.

Bosi, F., Skogby, H., Ciriotti, M.E., Gadas, P., Novák, M., Cempírek, J., Všianskỳ, D., and Filip, J. (2017b) Lucchesiite, CaFe2+3Al6 (Si6O18)(BO3)3(OH)3O, a new mineral species of the tourmaline supergroup. Mineralogical Magazine, 81, 1–14.

Bosi, F., Skogby, H., Hålenius, U., and Ciriotti, M.E. (2018) Experimental cation redistribution in the tourmaline lucchesiite, CaFe2+3Al6(Si6O18)(BO3)3(OH)3O. Physics and Chemistry of Minerals, 45, 621–632.

Bosi, F., Skogby, H., and Hålenius, U. (2019b) Thermally induced cation redistribution in fluor-elbaite and Fe-bearing tourmalines. Physics and Chemistry of Minerals, 46, 371–383.

Bosi, F., Biagioni, C., Pezzotta, F., Skogby, H., Hålenius, U., Cempírek, J., Hawthorne, F.C., Lussier, A.J., Abdu, Y.A., and Day, M.C. (2022) Uvite, CaMg3(Al5Mg)(Si6O18)(BO3)3(OH)3(OH), a new, but long-anticipated mineral species of the tourmaline supergroup from San Piero in Campo, Elba Island, Italy. Mineralogical Magazine, 86, 767–776.

Bosi, F., Skogby, H., and Hovis, G.L. (2023a) Crystal chemistry of povondraite by single-crystal XRD, EMPA, Mössbauer spectroscopy and FTIR. Mineralogical Magazine, 87, 178–185.

Bosi, F., Biagioni, C., and Oberti, R. (2019) On the Chemical Identification and Classification of Minerals. Minerals, 9, 591.

Boyd, F.R., and England, J.L. (1960) Apparatus for Phase-Equilibrium Measurements at Pressures up to 50 Kilobars and Temperatures up to 1750°C. Journal of Geophysical Research, 65, 741.

Boyd, S.P., and Vandenberghe, L. (2004) Convex optimisation, 716 p. Cambridge University Press, Cambridge, UK.

Bragg, W.L., and Williams, E.J. (1934) The effect of thermal agitation on atomic arrangement in alloys. Proceedings of the Royal Society of London. Series A, Containing Papers of a Mathematical and Physical Character, 145, 699–730.

——— (1935) The effect of thermal agitation on atomic arrangement in alloys—II. Proceedings of the Royal Society of London. Series A - Mathematical and Physical Sciences, 151, 540–566.

Brese, N.E., and O'Keeffe, M. (1991) Bond-valence parameters for solids. Acta Crystallographica Section B: Structural Science, 47, 192–197.

Bronzova, Y., Babushkina, M., Frank-Kamenetskaya, O., Vereshchagin, O., Rozhdestvenskaya, I., and Zolotarev, A. (2019) Short-range order in Li–Al tourmalines: IR spectroscopy, X-ray single crystal diffraction analysis and a bond valence theory approach. Physics and Chemistry of Minerals, 46, 815–825.

Brown, G.E., Calas, G., Waychunas, G.A., and Petiau, J. (1988) Chapter 11. X-ray absorption spectroscopy and its applications in minerology and geochemistry. In F.C. Hawthorne, Ed., Spectroscopic Methods in Mineralogy and Geology pp. 431–512. De Gruyter.

Brown, I.D. (2016) The Chemical Bond in Inorganic Chemistry: The Bond Valence Model, Second Edition., 336 p. Oxford University Press, Oxford, New York.

Brown, I.D., and Altermatt, D. (1985) Bond-valence parameters obtained from a systematic analysis of the inorganic crystal structure database. Acta Crystallographica Section B: Structural Science, 41, 244–247.

Burton, B.P., and Van de Walle, A. (2006) First-principles phase diagram calculations for the system NaCl–KCl: the role of excess vibrational entropy. Chemical Geology, 225, 222–229.

Byerly, G.R., and Palmer, M.R. (1991) Tourmaline mineralization in the Barberton greenstone belt, South Africa: early Archean metasomatism by evaporite-derived boron. Contributions to Mineralogy and Petrology, 107, 387–402.

Cadars, S., Ahn, N.H., Okhotnikov, K., Shin, J., Vicente, A., Hong, S.B., and Fernandez, C. (2017) Modelling short-range substitution order and disorder in crystals: Application to the Ga/Si distribution in a natrolite zeolite. Solid State Nuclear Magnetic Resonance, 84, 182–195.

Calas, G. (1988) Chapter 12. Electron Paramagentic Resonance. In F.C. Hawthorne, Ed., Spectroscopic Methods in Mineralogy and Geology pp. 513–572. De Gruyter.

Cámara, F., Ottolini, L., and Hawthorne, F.C. (2002) Crystal chemistry of three tourmalines by SREF, EMPA, and SIMS. American Mineralogist, 87, 1437–1442.

Capitani, C. de, and Petrakakis, K. (2010) The computation of equilibrium assemblage diagrams with Theriak/Domino software. American Mineralogist, 95, 1006–1016.

Carpenter, M.A. (1993) Thermodynamics of phase transitions in minerals: a macroscopic approach. In G.D. Price and N.L. Ross, Eds., The Stability of Minerals Vol. 3, pp. 172–215. Springer Netherlands, Dordrecht.

Carpenter, M.A., and Ballaran, T.B. (2001) The influence of elastic strain heterogeneities in silicate solid solutions. In Solid Solutions in Silicate and Oxide Systems, EMU Notes in Mineralogy, Vol. 3, European Mineralogical Union, Eötvös University Press.

Castaneda, C., Eeckhout, S.G., Costa, G.M. da, Botelho, N.F., and De Grave, E. (2006) Effect of heat treatment on tourmaline from Brazil. Physics and Chemistry of Minerals, 33, 207–216.

Celata, B., Stagno, V., Capizzi, L.S., Bosi, F., Ballirano, P., D'Arco, A., Stopponi, V., Lupi, S., Scarlato, P., and Skogby, H. (2023a) Schorl breakdown at upper mantle conditions: Insights from an experimental study at 3.5 GPa. Lithos, 438, 106999.

Celata, B., Ballirano, P., Bosi, F., Andreozzi, G.B., and Beckett-Brown, C. (2023b) Thermal behavior of schorl up to breakdown temperature at room pressure. Periodico di Mineralogia, 92.

Cemic, L. (2005) Thermodynamics in Mineral Sciences, 386 p. Springer.

Cempírek, J., Novák, M., Ertl, A., Hughes, J.M., Rossman, G.R., and Dyar, M.D. (2006) Fe-bearing olenite with tetrahedrally coordinated Al from an abyssal pegmatite at Kutná Hora, Czech Republic: structure, crystal chemistry, optical and XANES spectra. The Canadian Mineralogist, 44, 23–30.

Chase, M.W. (1998) NIST-JANAF Thermochemical Tables 4th ed. J. of Physical and Chemical Reffernce Data, 1529–1564.

Chatterjee, N.D., Krüger, R., Haller, G., and Olbricht, W. (1998) The Bayesian approach to an internally consistent thermodynamic database: theory, database, and generation of phase diagrams. Contributions to Mineralogy and Petrology, 133, 149–168.

Cheng, W., and Ganguly, J. (1994) Some aspects of multicomponent excess free energy models with subregular binaries. Geochimica et cosmochimica acta, 58, 3763–3767.

Chermak, J.A., and Rimstidt, J.D. (1989) Estimating the thermodynamic properties (Δ G of and Δ H of) of silicate minerals at 298 K from the sum of polyhedral contributions. American Mineralogist, 74, 1023–1031.

Christian, J. (2002) The theory of transformations in metals and alloys, 1200 p. Pergamon.

Clark, S., Segall, M., Pickard, C., Hasnip, P., Probert, M., Refson, K., and Payne, M. (2005) First principles methods using CASTEP. Zeitschrift für Kristallographie, 220.

Cohen, R.E. (1986) Configurational thermodynamics of aluminous pyroxenes: A generalized pair approximation. Physics and Chemistry of Minerals, 13, 183–197.

Connolly, J.A.D. (1990) Multivariable phase diagrams; an algorithm based on generalized thermodynamics. American Journal of Science, 290, 666–718.

Connolly, J.A.D. (2005) Computation of phase equilibria by linear programming: a tool for geodynamic modelling and its application to subduction zone decarbonation. Earth and Planetary Science Letters, 236, 524–541.

Connolly, J.A.D. (2016) Thermodynamics applied to earth materials, 68 p. Lecture Notes, ETH Zurich.

Connolly, J.A.D., and Galvez, M.E. (2018) Electrolytic fluid speciation by Gibbs energy minimisation and implications for subduction zone mass transfer. Earth and Planetary Science Letters, 501, 90–102.

Connolly, J.W.D., and Williams, A.R. (1983) Density-functional theory applied to phase transformations in transition-metal alloys. Physical Review B, 27, 5169–5172.

Creagh, D.C. (2006) X-ray Dispersion corrections. In International Tables for Crystallography Vol. C, Table 4.2.6.8, pp. 255–257. Springer, Dordrecht.

Creagh, D.C., and Hubbell, J.H. (2006) X-Ray Absorption (or Attenuation) Coefficients. In International Tables for Crystallography Vol. C, Table 4.2.4.3, pp. 230–236. Springer, Dordrecht.

Dachs, E., and Benisek, A. (2011) A sample-saving method for heat capacity measurements on powders using relaxation calorimetry. Cryogenics, 51, 460–464.

——— (2019) A new activity model for Mg–Al biotites determined through an integrated approach. Contributions to Mineralogy and Petrology, 174, 76.

——— (2021) A new activity model for Fe–Mg–Al biotites: I—Derivation and calibration of mixing parameters. Contributions to Mineralogy and Petrology, 176, 22.

——— (2024) A new activity model for biotite and its application. Contributions to Mineralogy and Petrology, 179, 93.

Dachs, E., and Bertoldi, C. (2005) Precision and accuracy of the heat-pulse calorimetric technique low-temperature heat capacities of milligram-sized synthetic mineral samples. European Journal of Mineralogy, 17, 251–261.

Dachs, E., and Geiger, C.A. (2006) Heat capacities and entropies of mixing of pyrope-grossular (Mg3Al2Si3O12-Ca3Al2Si3O12) garnet solid solutions: A low-temperature calorimetric and a thermodynamic investigation. American Mineralogist, 91, 894–906.

Dachs, E., Geiger, C.A., Benisek, A., and Grodzicki, M. (2014) Thermodynamic mixing properties and behavior of almandine–spessartine solid solutions. Geochimica et Cosmochimica Acta, 125, 210–224.

Dachs, E., Roozen, S., and Benisek, A. (2021) A new activity model for Fe–Mg–Al biotites: II—Applications in the K2O–FeO–MgO–Al2O3–SiO2–H2O (KFMASH) system. Contributions to Mineralogy and Petrology, 176, 23.

Dale, J., Holland, T., and Powell, R. (2000) Hornblende–garnet–plagioclase thermobarometry: a natural assemblage calibration of the thermodynamics of hornblende. Contributions to Mineralogy and Petrology, 140, 353–362.

Dale, J., Powell, R., White, R.W., Elmer, F.L., and Holland, T.J.B. (2005) A thermodynamic model for Ca-Na clinoamphiboles in Na2O-CaO-FeO-MgO-Al2O3-SiO2-H2O-O for petrological calculations. Journal of Metamorphic Geology, 23, 771–791.

Dapiaggi, M. (2005) Microscopic strain in synthetic pyrope-grossular solid solutions determined by synchrotron X-ray powder diffraction at 5 K: The relationship to enthalpy of mixing behavior. American Mineralogist, 90, 506–509.

Dauphas, N., Hu, M.Y., Baker, E.M., Hu, J., Tissot, F.L.H., Alp, E.E., Roskosz, M., Zhao, J., Bi, W., Liu, J., and others (2018) SciPhon: a data analysis software for nuclear resonant inelastic X-ray scattering with applications to Fe, Kr, Sn, Eu and Dy. Journal of Synchrotron Radiation, 25, 1581–1599.

Davies, P.K., and Navrotsky, A. (1981) Thermodynamics of solid solution formation in NiO-MgO and NiO-ZnO. Journal of Solid State Chemistry, 38, 264–276.

Davies, P.K., and Navrotsky, A. (1983) Quantitative correlations of deviations from ideality in binary and pseudobinary solid solutions. Journal of Solid State Chemistry, 46, 1–22.

de Fontaine, D., and Wolverton, C. (1994) Cluster approach to first-principles thermodynamics of crystals. Progress of Theoretical Physics Supplement, 115, 115–130.

De Grave, E., and Van Alboom, A. (1991) Evaluation of ferrous and ferric Mössbauer fractions. Physics and chemistry of minerals, 18, 337–342.

Debye, P. (1912) Zur Theorie der spezifischen Wärmen. Annalen der Physik, 344, 789–839.

Desbois, G., and Ingrin, J. (2007) Anisotropy of hydrogen diffusion in tourmaline. Geochimica et Cosmochimica Acta, 71, 5233–5243.

DiCarlo, J., Mehta, A., Banschick, D., and Navrotsky, A. (1993) The energetics of la2-xaxnio4-y (A= ba, sr). Journal of Solid State Chemistry, 103, 186–192.

Dorogova, M., Navrotsky, A., and Boatner, L.A. (2007) Enthalpies of formation of rare earth orthovanadates, REVO4. Journal of Solid State Chemistry, 180, 847–851.

Dove, M.T. (1993) Introduction to lattice dynamics, 258 p. Cambridge University Press, Cambridge.

——— (2001) Computer simulations of solid solutions. In Solid Solutions in Silicate and Oxide Systems, EMU Notes in Mineralogy, Vol. 3, European Mineralogical Union, Eötvös University Press.

Dove, M.T. (2011) Introduction to the theory of lattice dynamics. In École thématique de la Société Française de la Neutronique pp. 123–159.

Dove, M.T., Bosenick, A., Myers, E.R., Warren, M.C., and Redfern, S.A.T. (2000) Modelling in relation to cation ordering. Phase Transitions, 71, 205–226.

Dove, M.T., Tucker, M.G., Wells, S.A., and Keen, D.A. (2002) Reverse Monte Carlo methods. In Energy Modelling in Minerals Vol. 4.

Dutrow, B.L., and Henry, D.J. (2011) Tourmaline: a geologic DVD. Elements, 7, 301–306.

——— (2016) Fibrous tourmaline: a sensitive probe of fluid compositions and petrologic environments. The Canadian Mineralogist, 54, 311–335.

Dutrow, B.L., Foster, C.T., and Henry, D.J. (1999) Tourmaline-rich pseudomorphs in sillimanite zone metapelites: Demarcation of an infiltration front. American Mineralogist, 84, 794–805.

Dyar, M.D., Schaefer, M.W., Sklute, E.C., and Bishop, J.L. (2008) Mössbauer spectroscopy of phyllosilicates: Effects of fitting models on recoil-free fractions and redox ratios. Clay Minerals, 43, 3–33.

Einstein, A. (1907) Die Plancksche Theorie der Strahlung und die Theorie der spezifischen Wärme. Annalen der Physik, 327, 180–190.

Einstein, Albert (1907) Planck's theory of radiation and the theory of specific heat. Annalen der Physik, 22, 180–190.

Ertl, A. (2023) Are the [6]-coordinated sites in tourmaline in certain cases partially vacant? Mineralogy and Petrology, 117, 201–207.

Ertl, A., and Hughes, J.M. (2002) The crystal structure of an aluminum-rich schorl overgrown by boron-rich olenite from Koralpe, Styria, Austria. Mineralogy and Petrology, 75, 69–78.

Ertl, A., Hughes, J.M., Pertlik, F., Foit, F.F., Wright, S.E., Brandstätter, F., and Marler, B. (2002) Polyhedron Distortions in Tourmaline. The Canadian Mineralogist, 40, 153–162.

Ertl, A., Hughes, J.M., Brandstätter, F., Dyar, M.D., and Prasad, P.S.R. (2003) Disordered mg-bearing olenite from a granitic pegmatite at goslarn, austria: a chemical, structural, and infrared spectroscopic study. The Canadian Mineralogist, 41, 1363–1370.

Ertl, A., Tillmanns, E., Ntaflos, T., Francis, C., Giester, G., Körner, W., Hughes, J.M., Lengauer, C., and Prem, M. (2008) Tetrahedrally coordinated boron in Al-rich tourmaline and its

relationship to the pressure–temperature conditions of formation. European Journal of Mineralogy, 20, 881–888.

Ertl, A., Marschall, H.R., Giester, G., Henry, D.J., Schertl, H.-P., Ntaflos, T., Luvizotto, G.L., Nasdala, L., and Tillmanns, E. (2010) Metamorphic ultrahigh-pressure tourmaline: Structure, chemistry, and correlations to PT conditions. American Mineralogist, 95, 1–10.

Ertl, A., Schuster, R., Hughes, J.M., Ludwig, T., Meyer, H.-P., Finger, F., Dyar, M.D., Ruschel, K., Rossman, G.R., and Klötzli, U. (2012a) Li-bearing tourmalines in Variscan granitic pegmatites from the Moldanubian nappes, Lower Austria. European Journal of Mineralogy, 24, 695–715.

Ertl, A., Kolitsch, U., Dyar, M.D., Hughes, J.M., Rossman, G.R., Pieczka, A., Henry, D.J., Pezzotta, F., Prowatke, S., and Lengauer, C.L. (2012b) Limitations of Fe2+ and Mn2+ site occupancy in tourmaline: evidence from Fe2+-and Mn2+-rich tourmaline. American Mineralogist, 97, 1402–1416.

Ertl, A., Baksheev, I.A., Giester, G., Lengauer, C.L., Prokofiev, V.Y., and Zorina, L.D. Bosiite, NaFe3(Al4Mg2)(Si6O18)(BO3)3(OH)3O, a new ferric member of the tourmaline supergroup from the Darasun gold deposit, Transbaikalia, Russia., 28 European Journal of Mineralogy 581–591 (2016).

Ertl, A., Henry, D.J., and Tillmanns, E. (2018) Tetrahedral substitutions in tourmaline: a review. European Journal of Mineralogy, 30, 465–470.

Etzel, K., and Benisek, A. (2008) Thermodynamic mixing behavior of synthetic Ca-Tschermak–diopside pyroxene solid solutions: III. An analysis of IR line broadening and heat of mixing behavior. Physics and Chemistry of Minerals, 35, 399–407.

Etzel, K., Benisek, A., Dachs, E., and Cemič, L. (2007) Thermodynamic mixing behavior of synthetic Ca-Tschermak–diopside pyroxene solid solutions: I. Volume and heat capacity of mixing. Physics and Chemistry of Minerals, 34, 733–746.

Evans, R.J. (2005) Hyperfine electric field gradient tensors at Fe2+ sites in octahedral layers: Toward understanding oriented single-crystal Mossbauer spectroscopy measurements of micas. American Mineralogist, 90, 1540–1555.

Evans, T.P. (2004) A method for calculating effective bulk composition modification due to crystal fractionation in garnet-bearing schist: implications for isopleth thermobarometry. Journal of Metamorphic Geology, 22, 547–557.

Fantini, C., Tavares, M.C., Krambrock, K., Moreira, R.L., and Righi, A. (2014) Raman and infrared study of hydroxyl sites in natural uvite, fluor-uvite, magnesio-foitite, dravite and elbaite tourmalines. Physics and Chemistry of Minerals, 41, 247–254.

Faye, G.H., Manning, P.G., Gosselin, J.R., and Tremblay, R.J. (1974) The optical absorption spectra of tourmaline; importance of charge-transfer processes. The Canadian Mineralogist, 12, 370–380.

Ferrow, E. (2009) Non-integral hybrid ions in tourmaline: buffering and geo-thermometry. European Journal of Mineralogy, 21, 241–250.

Ferrow, E.A. (1995) Computer-simulated high-resolution transmission electron microscopy (HRTEM) in tourmaline. Journal of Microscopy, 177, 68–76.

Ferrow, E.A., Annersten, H., and Gunawardane, R.P. (1988) Mössbauer effect study on the mixed valence state of iron in tourmaline. Mineralogical Magazine, 52, 221–228.

Ferrow, E.A., Wallenberg, L.R., and Skogby, H. (1993) Compositional control of plane group symmetry in tourmalines: an experimental and computer simulated TEM, crystallographic image processing and Mossbauer spectroscopy study. European Journal of Mineralogy, 479–492.

Filatov, M. (2009) First principles calculation of Mössbauer isomer shift. Coordination Chemistry Reviews, 253, 594–605.

Filip, J., Dachs, E., Tucek, J., Novak, M., and Bezdicka, P. (2008) Low-temperature calorimetric and magnetic data for natural end-members of the axinite group. American Mineralogist, 93, 548–557.

Filip, J., Bosi, F., Novák, M., Skogby, H., Tuček, J., Čuda, J., and Wildner, M. (2012a) Iron redox reactions in the tourmaline structure: High-temperature treatment of Fe3+-rich schorl. Geochimica et Cosmochimica Acta, 86, 239–256.

Fischer, K. (1935) Neues Verfahren zur maßanalytischen Bestimmung des Wassergehaltes von Flüssigkeiten und festen Körpern. Angewandte Chemie, 48, 394–396.

Freedman, D.A. (2009) Statistical models: theory and practice, 2nd ed., 448 p. Cambridge University Press.

Fritsch, S., and Navrotsky, A. (1996) Thermodynamic Properties of Manganese Oxides. Journal of the American Ceramic Society, 79, 1761–1768.

Fuchs, Y., Lagache, M., and Lixares, J. (1998) Fe-tourmaline synthesis under different T and fO_2 conditions. American Mineralogist, 83, 525–534.

Fuchs, Y., Fourdrin, C., and Balan, E. (2022) Theoretical OH stretching vibrations in dravite. European Journal of Mineralogy, 34, 239–251.

Fultz, B. (2011) “Mössbauer Spectrometry” in Characterisation of Materials, Elton Kaufmann, Editor. John Wiley, New York.

Fyfe, C.A., Gobbi, G.C., Klinowski, J., Putnis, A., and Thomas, J.M. (1983) Characterisation of local atomic environment and quantitative determination of changes in site occupancies during the formation of ordered synthetic cordierite by 29Si and 27Al magic-angle spinning NMR spectroscopy. Journal of the Chemical Society, Chemical Communications, 556–558.

Gadas, P., Novák, M., Cempírek, J., Filip, J., Vašinová Galiová, M., Groat, L.A., and Všianskỳ, D. (2014) Mineral assemblages, compositional variation, and crystal structure of feruvitic tourmaline from a contaminated anatectic pegmatite at Mirošov near Strážek, Moldanubian Zone, Czech Republic. The Canadian Mineralogist, 52, 285–301.

Gagné, O.C., and Hawthorne, F.C. (2015) Comprehensive derivation of bond-valence parameters for ion pairs involving oxygen. Acta Crystallographica Section B: Structural Science, Crystal Engineering and Materials, 71, 562–578.

Gagné, O.C., and Hawthorne, F.C. (2016) Chemographic exploration of the milarite-type structure. The Canadian Mineralogist, 54, 1229–1247.

Gagné, O.C., and Hawthorne, F.C. (2017) Mean bond-length variations in crystals for ions bonded to oxygen. Acta Crystallographica Section B: Structural Science, Crystal Engineering and Materials, 73, 1019–1031.

——— (2020) Bond-length distributions for ions bonded to oxygen: Results for the transition metals and quantification of the factors underlying bond-length variation in inorganic solids. IUCrJ, 7, 581–629.

Gagné, O.C., Mercier, P.H., and Hawthorne, F.C. (2018) A priori bond-valence and bond-length calculations in rock-forming minerals. Acta Crystallographica Section B: Structural Science, Crystal Engineering and Materials, 74, 470–482.

Gale, J.D. (2001) Simulating the crystal structures and properties of ionic materials from interatomic potentials. Molecular modelling theory: applications in the geosciences, 42, 37–62.

Galvez, M.E., Manning, C.E., Connolly, J.A., and Rumble, D. (2015) The solubility of rocks in metamorphic fluids: A model for rock-dominated conditions to upper mantle pressure and temperature. Earth and Planetary Science Letters, 430, 486–498.

Ganguly, J. (1976) The energetics of natural garnet solid solution: II. Mixing of the calcium silicate end-members. Contributions to Mineralogy and Petrology, 55, 81–90.

——— (2001) Thermodynamic modelling of solid solutions. In Solid Solutions in Silicate and Oxide Systems. Eotvos University Press.

——— (2008) Thermodynamics in Earth and Planetary Sciences, 501 p. Springer International Publishing, Berlin.

Ganguly, J., and Saxena, S.K. (2012) Mixtures and mineral reactions, 291 p. Vol. 19. Springer.

Garofalo, P., Audétat, A., Gunther, D., Heinrich, C.A., and Ridley, J. (2000) Estimation and testing of standard molar thermodynamic properties of tourmaline end-members using data of natural samples. American Mineralogist, 85, 78–88.

Gatta, G.D., Bosi, F., McIntyre, G.J., and Skogby, H. (2014) First accurate location of two proton sites in tourmaline: A single-crystal neutron diffraction study of oxy-dravite. Mineralogical Magazine, 78, 681–692.

Gauss, C.F. (1823) Theoria combinationis observationum erroribus minimis obnoxiae. Henricus Dieterich.

Gavin, H.P. (2025) Total Least Squares, 11 p. Lecture Notes CEE 629 System Identification, Duke University.

Geiger, C.A. (2001) Thermodynamic mixing properties of binary oxide and silicate solid solutions determined by direct measurements: the role of strain. In Solid Solutions in Silicate and Oxide Systems, EMU Notes in Mineralogy, Vol. 3, European Mineralogical Union, Eötvös University Press.

Geiger, C.A., and Dachs, E. (2018) Recent developments and the future of low- *T* calorimetric investigations in the Earth sciences: Consequences for thermodynamic calculations and databases. Journal of Metamorphic Geology, 36, 283–295.

Geiger, C.A., Grodzicki, M., and Dachs, E. (2019) An analysis of the magnetic behavior of olivine and garnet substitutional solid solutions. American Mineralogist, 104, 1246–1255.

Geisler, T., Popa, K., and Konings, R.J. (2016) Evidence for Lattice Strain and Non-ideal Behavior in the (La1-xEux)PO4 Solid Solution from X-ray Diffraction and Vibrational Spectroscopy. Frontiers in Earth Science, 4, 64.

Ghiorso, M.S., and Sack, O. (1991) Fe-Ti oxide geothermometry: thermodynamic formulation and the estimation of intensive variables in silicic magmas. Contributions to Mineralogy and Petrology, 108, 485–510.

Gibbs, G.V., Ross, N.L., Cox, D.F., and Rosso, K.M. (2014) Insights into the crystal chemistry of Earth materials rendered by electron density distributions: Pauling's rules revisited. American Mineralogist, 99, 1071–1084.

Gibbs, G.V., Hawthorne, F.C., and Brown, G.E. (2022) Pauling's rules for oxide-based minerals: A re-examination based on quantum mechanical constraints and modern applications of bond-valence theory to Earth materials. American Mineralogist, 107, 1219–1248.

Gibbs, J.W. (1957) The Collected Works of J. Willard Gibbs: In Two Volumes, 925 p. Yale University Press.

Goldstein, J.I., Newbury, D.E., Echlin, P., Joy, D.C., Lyman, C.E., Lifshin, E., Sawyer, L., and Michael, J.R. (2003) Scanning Electron Microscopy and X-ray Microanalysis: Third Edition. Springer US, Boston, MA.

Goncharov, V.G., Nisbet, H., Strzelecki, A., Benmore, C.J., Migdisov, A.A., Xu, H., and Guo, X. (2022) Energetics of hydroxylbastnäsite solid solutions, La1-xNdxCO3OH. Geochimica et Cosmochimica Acta, 330, 47–66.

Gonzalez-Carreño, T., Fernandez, M., and Sanz, J. (1988) Infrared and electron microprobe analysis of tourmalines. Physics and Chemistry of Minerals, 15, 452–460.

Gopal, E. (1966) Specific heats at low temperatures, 240 p. Heywood Books, London.

Gottschalk, M. (1996) Internally consistent thermodynamic data for rock-forming minerals in the system SiO2-TiO2-Al2O3-Fe2O3-CaO-MgO-FeO-K2O-Na2O-H2O-CO2. European Journal of Mineralogy, 175–223.

——— (2016) Beyond the Margules equation: a universal thermodynamic equation for solid solutions including coupled substitution, long- and short-range order. European Journal of Mineralogy, 28, 219–244.

Green, E.C.R., White, R.W., Diener, J.F.A., Powell, R., Holland, T.J.B., and Palin, R.M. (2016) Activity-composition relations for the calculation of partial melting equilibria in metabasic rocks. Journal of Metamorphic Geology, 34, 845–869.

Greenwood, H.J. (1979) Some linear and non-linear problems in petrology. Geochimica et Cosmochimica Acta, 43, 1873–1885.

Grevel, K.-D., Kahl, W.-A., Majzlan, J., Navrotsky, A., Lathe, C., and Fockenberg, T. (2005) Thermodynamic properties of magnesiochloritoid. European Journal of Mineralogy, 17, 587–598.

Grew, E.S., Krivovichev, S.V., Hazen, R.M., and Hystad, G. (2016) Evolution of structural complexity in boron minerals. The Canadian Mineralogist, 54, 125–143.

Grew, E. S., and Anovitz, L. M. (1996). Borosilicates (exclusive of tourmaline) and boron in rock-forming minerals in metamorphic environments. Reviews in Mineralogy, 33, 387-502.

Grimvall, G. (2001) Dependence of thermodynamic properties on atomic masses and bonding in solids. In Solid Solutions in Silicate and Oxide Systems, EMU Notes in Mineralogy, Vol. 3, European Mineralogical Union, Eötvös University Press.

Grodzicki, M., and Lebernegg, S. (2011) Computation and interpretation of Mössbauer parameters of Fe-bearing compounds. In Mössbauer spectroscopy and transition metal chemistry. Springer, Berlin.

Grønvold, F., and Samuelsen, E.J. (1975) Heat capacity and thermodynamic properties of α-Fe2O3 in the region 300–1050 K. Antiferromagnetic transition. Journal of Physics and chemistry of Solids, 36, 249–256.

Günther, D., and Hattendorf, B. (2005) Solid sample analysis using laser ablation inductively coupled plasma mass spectrometry. TrAC Trends in Analytical Chemistry, 24, 255–265.

Guo, X., Szenknect, S., Mesbah, A., Labs, S., Clavier, N., Poinssot, C., Ushakov, S.V., Curtius, H., Bosbach, D., Ewing, R.C., and others (2015) Thermodynamics of formation of coffinite, $USiO_4$. Proceedings of the National Academy of Sciences, 112, 6551–6555.

Guo, X., Navrotsky, A., Kukkadapu, R.K., Engelhard, M.H., Lanzirotti, A., Newville, M., Ilton, E.S., Sutton, S.R., and Xu, H. (2016) Structure and thermodynamics of uranium-containing iron garnets. Geochimica et Cosmochimica Acta, 189, 269–281.

Guo, X., White, J.T., Nelson, A.T., Migdisov, A., Roback, R., and Xu, H. (2018) Enthalpy of formation of U3Si2: A high-temperature drop calorimetry study. Journal of Nuclear Materials, 507, 44–49.

Gütlich, P., Bill, E., and Trautwein, A.X. (2010) Mössbauer spectroscopy and transition metal chemistry: fundamentals and applications, 568 p. Springer.

Hamilton, D. t, and Henderson, C.M.B. (1968) The preparation of silicate compositions by a gelling method. Mineralogical magazine and journal of the Mineralogical Society, 36, 832–838.

Handt, A. von der, and Mosenfelder, J. (2019) Soft X-ray Emission Spectroscopy of Borosilicate Glasses and Minerals by SXES and EPMA-WDS. Microscopy and Microanalysis, 25, 270–271.

Harrison, R.J. (2006) Microstructure and magnetism in the ilmenite-hematite solid solution: A Monte Carlo simulation study. American Mineralogist, 91, 1006–1024.

Hastie, T., Tibshirani, R., and Friedman, J. (2017) The elements of statistical learning: data mining, inference, and prediction, 715 p. Springer.

Hawthorne, F.C. (1988) Chapter 8. Mossbauer Spectroscopy. In F.C. Hawthorne, Ed., Spectroscopic Methods in Mineralogy and Geology Vol. 18, pp. 255–340. De Gruyter.

——— (1996) Structural mechanisms for light-element variations in tourmaline. The Canadian Mineralogist, 34, 123–132.

——— (2002) Bond-valence constraints on the chemical composition of tourmaline. The Canadian Mineralogist, 40, 789–797.

Hawthorne, F.C. (2012) The use of end-member charge arrangements in defining new mineral species and hetrovalent substitutions in complex minerals. Canadian Mineralogist, 40, 699–710.

Hawthorne, F.C. (2016) Short-range atomic arrangements in minerals. I: The minerals of the amphibole, tourmaline and pyroxene supergroups. European Journal of Mineralogy, 28, 513–536.

——— (2021) Proof that a dominant endmember formula can always be written for a mineral or a crystal structure. The Canadian Mineralogist, 59, 159–167.

Hawthorne, F.C., and Dirlam, D.M. (2011) Tourmaline the indicator mineral: From atomic arrangement to Viking navigation. Elements, 7, 307–312.

Hawthorne, F.C., Ungaretti, L., and Oberti, R. (1995) Site populations in minerals; terminology and presentation of results of crystal-structure refinement. The Canadian Mineralogist, 33, 907–911.

Hawthorne, F.C., Mills, S.J., Hatert, F., and Rumsey, M.S. (2021) Ontology, archetypes and the definition of 'mineral species.' Mineralogical Magazine, 85, 125–131.

Heinrich, K.F.J. (1987) Mass absorption coefficients for electron probe microanalysis. Proc. 11th Int. Congr. on X-Ray Optics and Microanalysis, 67–119.

Helffrich, G., and Wood, B.J. (1989) Subregular model for multicomponent solutions. American Mineralogist, 74, 1016–1022.

Helgeson, H.C., Kirkham, D.H., and Flowers, G.C. (1981) Theoretical prediction of the thermodynamic behavior of aqueous electrolytes by high pressures and temperatures; IV, Calculation of activity coefficients, osmotic coefficients, and apparent molal and standard and relative partial molal properties to 600 degrees C and 5kb. American Journal of Science, 281, 1249–1516.

Hemingway, B.S., and Evans Jr, H.T. (1996) Thermal expansion of some borate and borosilicate minerals (fluoborite, danburite, sinhalite, datolite, elbaite, dravite, kornerupine, dumortierite, ferro-axinite, and manganaxinite) between 25 and about 1200 degrees C. US Geological Survey.

Henke, B.L., Lee, P., Tanaka, T.J., Shimabukuro, R.L., and Fujikawa, B.K. (1982) Low-energy x-ray interaction coefficients: Photoabsorption, scattering, and reflection: E = 100–2000 eV Z = 1–94. Atomic Data and Nuclear Data Tables, 27, 1–144.

Henry, D.J., and Dutrow, B.L. (1990) Ca substitution in Li-poor aluminous tourmaline. The Canadian Mineralogist, 28, 111–124.

——— (1996) Metamorphic tourmaline and its petrologic applications. Reviews in Mineralogy and Geochemistry, 33, 503–557.

——— (2011) The incorporation of fluorine in tourmaline: internal crystallographic controls or external environmental influences? The Canadian Mineralogist, 49, 41–56.

Henry, D.J., and Dutrow, B.L. (2012) Tourmaline at diagenetic to low-grade metamorphic conditions: Its petrologic applicability. Lithos, 154, 16–32.

Henry, D.J., and Dutrow, B.L. (2018) Tourmaline studies through time: contributions to scientific advancements. Journal of Geosciences, 63, 77–98.

Henry, D.J., and Guidotti, C.V. (1985) Tourmaline as a petrogenetic indicator mineral- An example from the staurolite-grade metapelites of NW Maine. American mineralogist, 70, 1–15.

Henry, D.J., Sun, H., Slack, J.F., and Dutrow, B.L. (2008) Tourmaline in meta-evaporites and highly magnesian rocks: perspectives from Namibian tourmalinites. European Journal of Mineralogy, 20, 889–904.

Henry, D.J., Novák, M., Hawthorne, F.C., Ertl, A., Dutrow, B.L., Uher, P., and Pezzotta, F. (2011) Nomenclature of the tourmaline-supergroup minerals. American Mineralogist, 96, 895–913.

——— (2013) Erratum: Nomenclature of the tourmaline-supergroup minerals (American Mineralogist (2011) 96 (895-913. American Mineralogist, 98, 524.

Hildebrand, J.H. (1929) Solubility XII. Regular Solutions. Journal of the American Chemical Society, 51, 66–80.

Hoang, L.H., Hien, N.T.M., Chen, X.B., Minh, N.V., and Yang, I. (2011) Raman spectroscopic study of various types of tourmalines. Journal of Raman Spectroscopy, 42, 1442–1446.

Höhne, G.W.H., Hemminger, W.F., and Flammersheim, H.-J. (2003) Differential Scanning Calorimetry. Springer, Berlin, Heidelberg.

Holland, T., and Powell, R. (1996a) Thermodynamics of order-disorder in minerals; I, Symmetric formalism applied to minerals of fixed composition. American Mineralogist, 81, 1413–1424.

——— (1996b) Thermodynamics of order-disorder in minerals; II, Symmetric formalism applied to solid solutions. American Mineralogist, 81, 1425–1437.

——— (2003) Activity–composition relations for phases in petrological calculations: an asymmetric multicomponent formulation. Contributions to Mineralogy and Petrology, 145, 492–501.

Holland, T.J. (1989) Dependence of entropy on volume for silicate and oxide minerals; a review and predictive model. American Mineralogist, 74, 5–13.

Holland, T.J.B., and Powell, R. (1985) An internally consistent thermodynamic dataset with uncertainties and correlations: 2. Data and results. Journal of metamorphic Geology, 3, 343–370.

Holland, T.J.B., and Powell, R. (1990) An enlarged and updated internally consistent thermodynamic dataset with uncertainties and correlations: the system K2O–Na2O–CaO–MgO–MnO–FeO–Fe2O3–Al2O3–TiO2–SiO2–C–H2–O2. Journal of metamorphic Geology, 8, 89–124.

Holland, T.J.B., and Powell, R. (1998) An internally consistent thermodynamic data set for phases of petrological interest. Journal of metamorphic Geology, 16, 309–343.

Holland, T.J.B., and Powell, R. (2011) An improved and extended internally consistent thermodynamic dataset for phases of petrological interest, involving a new equation of state for solids. Journal of Metamorphic Geology, 29, 333–383.

Holland, T.J.B., Green, E.C.R., and Powell, R. (2018) Melting of Peridotites through to Granites: A Simple Thermodynamic Model in the System KNCFMASHTOCr. Journal of Petrology, 59, 881–900.

Huber, P.J. (1981) Robust Statistics., 320 p. John Wiley & Sons, Inc, New York.

Iijima, S., Cowley, J.M., and Donnay, G. (1973) Hochauflösende Elektronenmikroskopie von Turmalinkristallen. Tschermaks mineralogische und petrographische Mitteilungen, 20, 216–224.

Jaynes, E.T. (1957) Information Theory and Statistical Mechanics. Physical Review, 106, 620–630.

Jenkins, D.M., Carpenter, M.A., and Zhang, M. (2014) Experimental and infrared characterisation of the miscibility gap along the tremolite-glaucophane join. American Mineralogist, 99, 730–741.

Jenkins, D.M., Holmes, Z.F., Ishida, K., and Manuel, P.D. (2018) Autocorrelation analysis of the infrared spectra of synthetic and biogenic carbonates along the calcite–dolomite join. Physics and Chemistry of Minerals, 45, 563–574.

Jochum, K.P., Nohl, U., Herwig, K., Lammel, E., Stoll, B., and Hofmann, A.W. (2005) GeoReM: A New Geochemical Database for Reference Materials and Isotopic Standards. Geostandards and Geoanalytical Research, 29, 333–338.

Johnson, J.W., Oelkers, E.H., and Helgeson, H.C. (1992) SUPCRT92: A software package for calculating the standard molal thermodynamic properties of minerals, gases, aqueous species, and reactions from 1 to 5000 bar and 0 to 1000 C. Computers & Geosciences, 18, 899–947.

Katerinopoulou, A., Grodzicki, M., Tippelt, G., and Amthauer, G. (2013) Mössbauer spectroscopy and molecular orbital calculations on iron bearing omphacite. Mineralogy and Petrology, 107, 281–287.

Kennedy, C.A., Stancescu, M., Marriott, R.A., and White, M.A. (2007) Recommendations for accurate heat capacity measurements using a Quantum Design physical property measurement system. Cryogenics, 47, 107–112.

Kent, A., and Ungerer, A. (2005) Production of barium and light rare earth element oxides during LA-ICP-MS microanalysis. Journal of Analytical Atomic Spectrometry, 20.

Kerrick, D.M., and Darken, L.S. (1975) Statistical thermodynamic models for ideal oxide and silicate solid solutions, with application to plagioclase. Geochimica et Cosmochimica Acta, 39, 1431–1442.

Kieffer, S.W. (1979a) Thermodynamics and lattice vibrations of minerals: 1. Mineral heat capacities and their relationships to simple lattice vibrational models. Reviews of Geophysics, 17, 1–19.

——— (1979b) Thermodynamics and lattice vibrations of minerals: 2. Vibrational characteristics of silicates. Reviews of Geophysics, 17, 20.

——— (1979c) Thermodynamics and lattice vibrations of minerals: 3. Lattice dynamics and an approximation for minerals with application to simple substances and framework silicates. Reviews of Geophysics, 17, 35.

——— (1980) Thermodynamics and lattice vibrations of minerals: 4. Application to chain and sheet silicates and orthosilicates. Reviews of Geophysics, 18, 862.

——— (1982) Thermodynamics and lattice vibrations of minerals: 5. Applications to phase equilibria, isotopic fractionation, and high-pressure thermodynamic properties. Reviews of Geophysics, 20, 827.

King, P.L., Ramsey, M.S., McMillan, P.F., and Swayze, G. (2004) Laboratory Fourier transform infrared spectroscopy methods for geologic samples. Infrared Spectroscopy in Geochemistry, Exploration, and Remote Sensing, 33, 57–91.

Kirkpatrick, R.J., Smith, K.A., Schramm, S., Turner, G., and Yang, W.-H. (1985) Solid-state nuclear magnetic resonance spectroscopy of minerals. Annual Review of Earth and Planetary Sciences, 13, 29.

Kiseleva, I., Navrotsky, A., Belitsky, I.A., and Fursenko, B.A. (1996) Thermochemistry of natural potassium sodium calcium leonhardite and its cation-exchanged forms. American Mineralogist, 81, 668–675.

Kittel, C., and McEuen, P. (2018) Introduction to solid state physics, 8th ed., 692 p. John Wiley & Sons, Singapore.

Krivovichev, S.V. (2013) Structural complexity of minerals: information storage and processing in the mineral world, 77, 275–326.

Krosse, S. (1995) Hochdrucksynthese, stabilität und eigenschaften der borsilikate dravit und kornerupin sowie darstellung und stabilitätsverhalten eines neuen Mg-Al-borates. PhD Thesis.

Kuhn, H.-R., and Günther, D. (2004) Laser ablation-ICP-MS: particle size dependent elemental composition studies on filter-collected and online measured aerosols from glass. Journal of Analytical Atomic Spectrometry, 19, 1158–1164.

Kulik, D.A., Wagner, T., Dmytrieva, S.V., Kosakowski, G., Hingerl, F.F., Chudnenko, K.V., and Berner, U.R. (2013) GEM-Selektor geochemical modelling package: revised algorithm and GEMS3K numerical kernel for coupled simulation codes. Computational Geosciences, 17, 1–24.

Kutzschbach, M., Wunder, B., Rhede, D., Koch-Müller, M., Ertl, A., Giester, G., Heinrich, W., and Franz, G. (2016) Tetrahedral boron in natural and synthetic HP/UHP tourmaline: evidence from Raman spectroscopy, EMPA, and single-crystal XRD. American Mineralogist, 101, 93–104.

Kutzschbach, M., Wunder, B., Wannhoff, I., Wilke, F.D., Couffignal, F., and Rocholl, A. (2021) Raman spectroscopic quantification of tetrahedral boron in synthetic aluminum-rich tourmaline. American Mineralogist, 106, 872–882.

Kuyunko, N.S., Semenov, Y.V., Gurevich, V.M., Kuzmin, V.I., Topor, N.D., and Gorbunov, V.E. (1984a) Experimental Determination of the Thermodynamic Properties of Dravite Tourmaline. Geokhimiya, 1458–1465.

Lagarec, K., and Rancourt, D. (1998) Recoil User Manual -- Mossbauer spectral analysis software for Windows.

Landau, L.D. (1937) On the theory of phase transitions. Zhurnal Eksperimental'noi i Teoreticheskoi Fiziki, 7, 926.

Lashley, J.C., Hundley, M.F., Migliori, A., Sarrao, J.L., Pagliuso, P.G., Darling, T.W., Jaime, M., Cooley, J.C., Hults, W.L., Morales, L., and others (2003) Critical examination of heat capacity measurements made on a Quantum Design physical property measurement system. Cryogenics, 43, 369–378.

Lavrent'ev, Yu.G., Korolyuk, V.N., and Usova, L.V. (2004) Second Generation of Correction Methods in Electron Probe X-ray Microanalysis: Approximation Models for Emission Depth Distribution Functions. Journal of Analytical Chemistry, 59, 600–616.

Lawson, C.L., and Hanson, R.J. (1974) Solving Least Squares Problems. Society for Industrial and Applied Mathematics.

Le Losq, C., Cicconi, M.R., and Neuville, D.R. (2021) Iron in Silicate Glasses and Melts: Implications for Volcanological Processes. In R. Moretti and D.R. Neuville, Eds., Geophysical Monograph Series pp. 233–253. Wiley.

Levy, E.A., Henry, D.J., Roy, A., and Dutrow, B.L. (2018) Determination of ferrous–ferric iron contents in tourmaline using synchrotron-based XANES. Journal of Geosciences (Czech Republic), 63, 167.

Li, M. (2022) Characterisation of Blue Tourmaline from Madagascar for Exploring Its Colour Origin. Advances in Condensed Matter Physics, 2022, 1–7.

Li, Y., Kowalski, P.M., Blanca-Romero, A., Vinograd, V., and Bosbach, D. (2014) Ab initio calculation of excess properties of La1−x(Ln, An)xPO4 solid solutions. Journal of Solid State Chemistry, 220, 137–141.

Lilova, K.I., Xu, F., Rosso, K.M., Pearce, C.I., Kamali, S., and Navrotsky, A. (2012) Oxide melt solution calorimetry of Fe2+-bearing oxides and application to the magnetite-maghemite (Fe3O4-Fe8/3O4) system. American Mineralogist, 97, 164–175.

Liu, Xin, Vinograd, V.L., Nichenko, S., Kulik, D.A., Lu, X., and Winkler, B. (2019) Emulation of short-range ordering within the Compound Energy Formalism: Application to the calcite-magnesite solid solution. Calphad, 64, 115–125.

Liu, Xiaowen, Yu, C., Yang, W., Xie, L., and Liang, S. (2019) Thermal decomposition kinetics of Fe-rich tourmaline. European Journal of Mineralogy, 31, 919–928.

Liu, Y., Hu, Z., Gao, S., Günther, D., Xu, J., Gao, C., and Chen, H. (2008) In situ analysis of major and trace elements of anhydrous minerals by LA-ICP-MS without applying an internal standard. Chemical Geology, 257, 34–43.

Llovet, X., Moy, A., Pinard, P.T., and Fournelle, J.H. (2021) Electron probe microanalysis: A review of recent developments and applications in materials science and engineering. Progress in Materials Science, 116, 100673.

Llovet, X., Pöml, P., Moy, A., and Fournelle, J.H. (2023) Assessing the Accuracy of Mass Attenuation Coefficients for Soft X-ray EPMA. Microscopy and Microanalysis, 29, 540–551.

Loan, C.F., and Pitsianis, N. (1993) Approximation with Kronecker Products. In M.S. Moonen, G.H. Golub, and B.L.R. Moor, Eds., Linear Algebra for Large Scale and Real-Time Applications pp. 293–314. Springer Netherlands, Dordrecht.

London, D. (2011) Experimental synthesis and stability of tourmaline: a historical overview. The Canadian Mineralogist, 49, 117–136.

Longerich, H.P., Jackson, S.E., and Günther, D. (1996) Inter-laboratory note. Laser ablation inductively coupled plasma mass spectrometric transient signal data acquisition and analyte concentration calculation. Journal of analytical atomic spectrometry, 11, 899–904.

López, J., De Lima, O.F., Lisboa-Filho, P.N., and Araujo-Moreira, F.M. (2002) Specific heat at low temperatures and magnetic measurements in Nd0.5Sr0.5MnO3 and R0.5Ca0.5MnO3 (R = Nd , Sm, Dy, and Ho) samples. Physical Review B, 66, 214402.

Ludwig, K.R. (1991) ISOPLOT; a plotting and regression program for radiogenic-isotope data; version 2.53. US Geological Survey.

Lussier, A., Ball, N.A., Hawthorne, F.C., Henry, D.J., Shimizu, R., Ogasawara, Y., and Ota, T. (2016) Maruyamaite, K(MgAl2)(Al5Mg)Si6O18(BO3)3(OH)3O, a potassium-dominant

tourmaline from the ultrahigh-pressure Kokchetav massif, northern Kazakhstan: Description and crystal structure. American Mineralogist, 101, 355–361.

Lussier, A.J., Aguiar, P.M., Michaelis, V.K., Kroeker, S., Herwig, S., Abdu, Y., and Hawthorne, F.C. (2008) Mushroom elbaite from the Kat Chay mine, Momeik, near Mogok, Myanmar: I. Crystal chemistry by SREF, EMPA, MAS NMR and Mössbauer spectroscopy. Mineralogical Magazine, 72, 747–761.

Lussier, A.J., Aguiar, P.M., Michaelis, V.K., Kroeker, S., and Hawthorne, F.C. (2009) The occurrence of tetrahedrally coordinated Al and B in tourmaline: An 11B and 27Al MAS NMR study. American Mineralogist, 94, 785–792.

Lussier, A.J., Abdu, Y., Hawthorne, F.C., Michaelis, V.K., Aguiar, P.M., and Kroeker, S. (2011) Oscillatory zoned liddicoatite from Anjanabonoina, central Madagascar. I. Crystal chemistry and structure by SREF and 11B and 27Al MAS NMR spectroscopy. The Canadian Mineralogist, 49, 63–88.

MacDonald, D.J., and Hawthorne, F.C. (1995) The crystal chemistry of Si= AI substitution in tourmaline. Canadian Mineralogist, 33, 849–858.

Mahalanobis, P.C. (1936) On the generalized distance in statistics. Proceedings of the National Institute of Science of India, 2, 49–55.

Margules, M.S. (1895) On the composition of saturated vapors of mixtures. Akademie der Wissenschaften in Wien, Mathematisch-Naturwissenschaftliche Klasse Abteilung II, 104, 1234–1239.

Markovsky, I. (2010) Bibliography on total least squares and related methods. Statistics and its interface, 3, 329–334.

Markovsky, I., and Van Huffel, S. (2007) Overview of total least-squares methods. Signal processing, 87, 2283–2302.

Marler, B., and Ertl, A. (2002) Nuclear magnetic resonance and infrared spectroscopic study of excess-boron olenite from Koralpe, Styria, Austria. American Mineralogist, 87, 364–367.

Marler, B., Borowski, M., Wodara, U., and Schreyer, W. (2002) Synthetic tourmaline (olenite) with excess boron replacing silicon in the tetrahedral site: II. Structure analysis. European Journal of Mineralogy, 14, 763–771.

Marschall, H.R., Ertl, A., Hughes, J.M., and McCammon, C. (2004) Metamorphic Na- and OH-rich disordered dravite with tetrahedral boron, associated with omphacite, from Syros, Greece: chemistry and structure. European Journal of Mineralogy, 16, 817–823.

Maslen, E.N., Fox, A.G., and O'Keefe, M.A. (2006) X-Ray Scattering. In International Tables for X-ray Crystallography Vol. C, Tables 6.1.1.4, pp. 555–564. Dordrecht, Springer.

Massonne, H.J., and Schreyer, W. (1986) High-pressure syntheses and X-ray properties of white micas in the system K2O-MgO-Al2O3-SiO2-H2O. Neues Jahrbuch Für Mineralogie. Abhandlungen, 153, 177–215.

Matlab (2022). The MathWorks Inc., Natick, Massachusetts.

Mattson, S.M., and Rossman, G.R. (1984) Ferric iron in tourmaline. Physics and Chemistry of Minerals, 11, 225–234.

——— (1987) Fe2+-Fe3+ interactions in tourmaline. Physics and Chemistry of Minerals, 14, 163–171.

McCormack, S.J., and Navrotsky, A. (2021) Thermodynamics of high entropy oxides. Acta Materialia, 202, 1–21.

McMillan, P. (1985) Vibrational spectroscopy in the mineral sciences. In Microscopic to Macroscopic Atomic Enviroments to Mineral Thermodyanmics Vol. 14, pp. 9–63. Mineralogical Society of America.

McMillan, P., Putnis, A., and Carpenter, M.A. (1984) A Raman spectroscopic study of Al-Si ordering in synthetic magnesium cordierite. Physics and Chemistry of Minerals, 10, 256–260.

McMillan, P.F., and Hofmeister, A.M. (1988) Chapter 4. Infrared and Raman Spectroscopy. In F.C. Hawthorne, Ed., Spectroscopic Methods in Mineralogy and Geology pp. 99–160. De Gruyter.

Melrose, M.P. (1970) Statistical mechanics and the third law. Journal of Chemical Education, 47, 283.

Merlet, C. (1992) Quantitative Electron Probe Microanalysis: New Accurate Φ (ρz) Description. In A. Boekestein and M.K. Pavićević, Eds., Electron Microbeam Analysis pp. 107–115. Springer, Vienna.

——— (1994) An Accurate Computer Correction Program for Quantitative Electron Probe Microanalysis. Mikrochimica Acta, 114, 363–376.

Meyer, A.S., and Boyd, C.M. (1959) Determination of Water by Titration with Coulometrically Generated Karl Fischer Reagent. Analytical Chemistry, 31, 215–219.

Miller, A.P. (1988) Theory of Specific Heat of Solids. In CINDAS Data Series, Vol.I-2, Specific Heat of Solids pp. 1–89. Hemisphere Publishing Corporation, New York.

Montgomery, D.C., Peck, E.A., and Vining, G.G. (2021) Introduction to linear regression analysis, 672 p. John Wiley & Sons.

Morgan, G.B., and London, D. (1989) Experimental reactions of amphibolite with boron-bearing aqueous fluids at 200 MPa: implications for tourmaline stability and partial melting in mafic rocks. Contributions to Mineralogy and Petrology, 102, 281–297.

Mraw, S.C. (1988) Differential scanning calorimetry. In CINDAS Data Series, Vol.I-2, Specific Heat of Solids pp. 395–435. Hemisphere Publishing Corporation.

Muggianu, Y.-M., Gambino, M., and JP, B. (1975) Enthalpies de formation des alliages liquides bismuth-étain-gallium à 723 K. Choix d'une représentation analytique des grandeurs d'excès intégrales et partielles de mélange. Journal de Chimie Physique, 83–88.

Mukhopadhyay, B., Basu, S., and Holdaway, M.J. (1993) A discussion of Margules-type formulations for multicomponent solutions with a generalized approach. Geochimica et Cosmochimica Acta, 57, 277–283.

Myhill, R., and Connolly, J. (2021) Notes on the creation and manipulation of solid solution models. Contributions to Mineralogy and Petrology, 176.

Myhill, R., Cottaar, S., Heister, T., Rose, I., Unterborn, C., Dannberg, J., and Gassmoeller, R. (2023) BurnMan–a Python toolkit for planetary geophysics, geochemistry and thermodynamics. Journal of Open Source Software, 8, 5389.

Navrotsky, A. (1994a) Physics and chemistry of earth materials, 413 p. Cambridge University Press, Cambridge.

——— (1994b) Repeating patterns in mineral energetics. American Mineralogist, 79, 589–605.

——— (1997) Progress and new directions in high temperature calorimetry revisited. Physics and Chemistry of Minerals, 24, 222–241.

——— (2001) Thermochemistry of nanomaterials. In Nanoparticles and the Environment Vol. 44, pp. 73–103. Mineralogical Society of America.

——— (2014) Progress and New Directions in Calorimetry: A 2014 Perspective. Journal of the American Ceramic Society, 97, 3349–3359.

Navrotsky, A., and Koryttseva, A. (2023) Acid–base properties of oxides derived from oxide melt solution calorimetry. Molecules, 28, 4623.

Navrotsky, A., Rapp, R.P., Smelik, E., Burnley, P., Circone, S., Chai, L., and Bose, K. (1994) The behavior of H2O and CO2 in high-temperature lead borate solution calorimetry of volatile-bearing phases. American Mineralogist, 79, 1099–1109.

Navrotsky, A., Mazeina, L., and Majzlan, J. (2008) Size-Driven Structural and Thermodynamic Complexity in Iron Oxides. Science, 319, 1635–1638.

NCSS (2023a) Multiple Regression, 72 p. NCSS Helpfile, chapter 305.

——— (2023b) Subset Selection in Multiple Regression. NCSS Helpfile, chapter 307.

Nie, N.X., Dauphas, N., Alp, E.E., Zeng, H., Sio, C.K., Hu, J.Y., Chen, X., Aarons, S.M., Zhang, Z., and Tian, H.-C. (2021) Iron, magnesium, and titanium isotopic fractionations between garnet, ilmenite, fayalite, biotite, and tourmaline: Results from NRIXS, ab initio, and study of mineral separates from the Moosilauke metapelite. Geochimica et Cosmochimica Acta, 302, 18–45.

Ogorodova, L. P., Melchakova, L.V., Kiseleva, I.A., and Peretyazhko, I.S. (2004) Thermodynamics of natural tourmaline–elbaite. Thermochimica acta, 419, 211–214.

Ogorodova, L. P., Melchakova, L.V., Kiseleva, I.A., and Peretyazhko, I.S. (2012) Thermodynamics of natural tourmalines—Dravite and schorl. Thermochimica acta, 539, 1–6.

Okhotnikov, K., Charpentier, T., and Cadars, S. (2016a) Supercell program: a combinatorial structure-generation approach for the local-level modelling of atomic substitutions and partial occupancies in crystals. Journal of Cheminformatics, 8, 17.

——— (2016b) Supercell program tutorial.

O'Neil, H.S.C., and Navrotsky, A. (1984) Cation distributions and thermodynamic properties of binary spinel solid solutions. American Mineralogist, 69, 733–753.

Ota, T., Kobayashi, K., Katsura, T., and Nakamura, E. (2008) Tourmaline breakdown in a pelitic system: implications for boron cycling through subduction zones. Contributions to Mineralogy and Petrology, 155, 19–32.

Palmer, M.R., London, D., Morgan, G.B., and Babb, H.A. (1992) Experimental determination of fractionation of11B/10B between tourmaline and aqueous vapor: A temperature- and pressure-dependent isotopic system. Chemical Geology: Isotope Geoscience section, 101, 123–129.

Paton, C., Hellstrom, J., Paul, B., Woodhead, J., and Hergt, J. (2011) Iolite: Freeware for the visualisation and processing of mass spectrometric data. Journal of Analytical Atomic Spectrometry, 26, 2508–2518.

Paul, B., Petrus, J., Savard, D., Woodhead, J., Hergt, J., Greig, A., Paton, C., and Rayner, P. (2023) Time resolved trace element calibration strategies for LA-ICP-MS. Journal of Analytical Atomic Spectrometry, 38, 1995–2006.

Pechoušek, J., Jančík, D., Frydrych, J., Navařík, J., and Novák, P. (2012) Setup of Mössbauer spectrometers at RCPTM pp. 186–193. Presented at the MOSSBAUER SPECTROSCOPY IN MATERIALS SCIENCE - 2012: Proceedings of the International Conference MSMS-12, Olomouc, Czech Republic.

Pieczka, A. (1996) Studium mineralogiczne turmalinów Polski: Mineralogical study of Polish tourmalines. Wydawnictwo Oddziału Polskiej Akademii Nauk, Kraków.

Pieczka, A., and Kraczka, J. (2004) Oxidized tourmalines—a combined chemical, XRD and Mossbauer study. European Journal of Mineralogy, 16, 309–321.

Pieczka, A., Kraczka, and Zabinski (1998) Mossbauer spectra of Fe3+-poor schorls: reinterpretation on the basis of the ordered structure model. Journal of Geosciences, 43, 69–74.

Pieczka, A., Ertl, A., Sęk, M.P., Twardak, D., Zelek, S., Szełęg, E., and Giester, G. (2018) Oxy-dravite from Wołowa Góra Mountain, Karkonosze massif, SW Poland: Crystallochemical and structural studies. Mineralogical Magazine, 82, 913–928.

Ping, J.Y., and Rancourt, D.G. (1992) Thickness effects with intrinsically broad absorption lines. Hyperfine Interactions, 71, 1433–1436.

Pouchou, J.-L., and Pichoir, F. (1991) Quantitative Analysis of Homogeneous or Stratified Microvolumes Applying the Model "PAP." In K.F.J. Heinrich and D.E. Newbury, Eds., Electron Probe Quantitation pp. 31–75. Springer US, Boston, MA.

Powell, R. (1987) Darken's quadratic formalism and the thermodynamics of minerals. American Mineralogist, 72, 1–11.

Powell, R., and Holland, T. (1993) On the formulation of simple mixing models for complex phases. American Mineralogist, 78, 1174–1180.

——— (1999) Relating formulations of the thermodynamics of mineral solid solutions; activity modelling of pyroxenes, amphiboles, and micas. American Mineralogist, 84, 1–14.

Powell, R., and Holland, T.J.B. (1988) An internally consistent dataset with uncertainties and correlations: 3. Applications to geobarometry, worked examples and a computer program. Journal of metamorphic Geology, 6, 173–204.

Powell, R., Holland, T., and Worley, B. (1998) Calculating phase diagrams involving solid solutions via non-linear equations, with examples using THERMOCALC. Journal of Metamorphic Geology, 16, 577–588.

Puerta, J., and Martin, P. (1981) Three and four generalized Lorentzian approximations for the Voigt line shape. Applied optics, 20, 3923–3928.

Putnam, R.L., Navrotsky, A., Woodfield, B.F., Boerio-Goates, J., and Shapiro, J.L. (1999) Thermodynamics of formation for zirconolite (CaZrTi2O7) from T=298.15K to T=1500K. The Journal of Chemical Thermodynamics, 31, 229–243.

Putnis, A. (1980) The distortion index in anhydrous Mg-cordierite. Contributions to Mineralogy and Petrology, 74, 135–141.

Putnis, A., and Bish, D.L. (1983) The mechanism and kinetics of Al, Si ordering in Mg-cordierite. American Mineralogist, 68, 60–65.

Qin, T., Zhang, Q., Wentzcovitch, R.M., and Umemoto, K. (2019) qha: A Python package for quasiharmonic free energy calculation for multi-configuration systems. Computer Physics Communications, 237, 199–207.

Quenouille, M.H. (1956) Notes on bias in estimation. Biometrika, 43, 353–360.

Rancourt, D. (1994) Mossbauer spectroscopy of minerals: I. Inadequacy of Lorentzian-line doublets in fitting spectra arising from quadrupole splitting distribution. Physics and Chemistry of Minerals, 21, 244–249.

Rancourt, D.G., and Ping, J.Y. (1991) Voigt-based methods for arbitrary-shape static hyperfine parameter distributions in Mössbauer spectroscopy. Nuclear Instruments and Methods in Physics Research Section B: Beam Interactions with Materials and Atoms, 58, 85–97.

Rancourt, D.G., McDonald, A.M., Lalonde, A.E., and Ping, J.Y. (1993) Mössbauer absorber thicknesses for accurate site populations in Fe-bearing minerals. American Mineralogist, 78, 1–7.

Redfern, S.A. (2000) Order-disorder phase transitions. Reviews in Mineralogy and Geochemistry, 39, 105–133.

Redhammer, G. J. (2021) Structure: Scattering Techniques. In O. Diwald and T. Berger, Eds., Metal Oxide Nanoparticles, 2 Volume Set: Formation, Functional Properties, and Interfaces. John Wiley & Sons.

Reece, M.E., Li, J., Strzelecki, A.C., Wen, J., Zhang, Q., and Guo, X. (2024) Surface thermodynamics of yttrium titanate pyrochlore nanomaterials. Nanoscale, 16, 5421–5432.

Reed, S.J.B. (2005) Electron microprobe analysis and scanning electron microscopy in geology. Cambridge university press.

Renner, J., Zerbian, A., and Stöckhert, B. (1997) Microstructures of synthetic polycrystalline coesite aggregates. The effect of pressure, temperature, and time. Lithos, 41, 169–184.

Rhode, S., Usevich, K., Markovsky, I., and Gauterin, F. (2014) A recursive restricted total least-squares algorithm. IEEE Transactions on Signal Processing, 62, 5652–5662.

Robbins, C.R., and Yoder Jr, H.S. (1962) Stability relations of dravite, a tourmaline. Carnegie Inst. Wash. Yearbook, 61, 106–108.

Robie, R.A., and Hemingway, B.S. (1995) Thermodynamic properties of minerals and related substances at 298.15 K and 1 bar (10^5 pascals) pressure and at higher temperatures. Bulletin. U.S. Geological Survey.

Robie, R.A., Hemingway, B.S., and Fisher, J.R. (1978) Thermodynamic properties of minerals and related substances at 298.15 K and 1 bar (10^5 pascals) pressure and at higher temperatures. Bulletin. U.S. Geological Survey.

Rodehorst, U., Carpenter, M.A., Ballaran, T.B., and Geiger, C.A. (2004) Local structural heterogeneity, mixing behaviour and saturation effects in the grossular?spessartine solid solution. Physics and Chemistry of Minerals, 31.

Rodríguez-Carvajal, J. (1993) Recent advances in magnetic structure determination by neutron powder diffraction. Physica B: Condensed Matter, 192, 55–69.

Rosen, P.F., and Woodfield, B.F. (2020) Standard methods for heat capacity measurements on a quantum design physical property measurement system. The Journal of Chemical Thermodynamics, 141, 105974.

Sack, R.O. (2017) Fahlore thermochemistry: Gaps inside the (Cu,Ag)10(Fe,Zn)2(Sb,As)4S13 cube. Petrology, 25, 498–515.

Sack, R.O., and Ghiorso, M.S. (1994) Thermodynamics of multicomponent pyroxenes: I. Formulation of a general model. Contributions to Mineralogy and Petrology, 116, 277–286.

Saegusa, N. (1978) Mossbauer Study of Tourmaline. PhD Thesis, Australian National University.

Salje, E.K.H., Carpenter, M.A., Malcherek, T., and Boffa Ballaran, T. (2000) Autocorrelation analysis of infrared spectra from minerals. European Journal of Mineralogy, 12, 503–519.

Sanz, J., and Robert, J.-L. (1992) Influence of structural factors on 29Si and 27Al NMR chemical shifts of phyllosilicates 2: 1. Physics and Chemistry of Minerals, 19, 39–45.

Schliesser, J.M., and Woodfield, B.F. (2015) Lattice vacancies responsible for the linear dependence of the low-temperature heat capacity of insulating materials. Physical Review B, 91, 024109.

Scholz, E. (2012) Karl Fischer titration: determination of water. Springer

Schreyer, W., Wodara, U., Marler, B., Van Aken, P.A., Seifert, F., and Robert, J.-L. (2000) Synthetic tourmaline (olenite) with excess boron replacing silicon in the tetrahedral site: I. Synthesis conditions, chemical and spectroscopic evidence. European Journal of Mineralogy, 12, 529–541.

Scorzelli, R.B., Baggio-Saitovitch, E., and Danon, J. (1976) Mössbauer spectra and electron exchange in tourmaline and staurolite. Le Journal de Physique Colloques, 37, C6-801.

Scribner, E.D., Cempírek, J., Groat, L.A., Evans, R.J., Biagioni, C., Bosi, F., Dini, A., Hålenius, U., Orlandi, P., and Pasero, M. (2021) Magnesio-lucchesiite, CaMg3Al6(Si6O18)(BO3)3(OH)3O, a new species of the tourmaline supergroup. American Mineralogist, 106, 862–871.

Shannon, R. D. (1976) Revised effective ionic radii and systematic studies of interatomic distances in halides and chalcogenides. Foundations of Crystallography, 32, 751–767.

Sheldrick, G.M. (2015) Crystal structure refinement with SHELXL. Acta Crystallographica Section C: Structural Chemistry, 71, 3–8.

Shuker, R., and Gammon, R.W. (1970) Raman-Scattering Selection-Rule Breaking and the Density of States in Amorphous Materials. Physical Review Letters, 25, 222–225.

Skogby, H., Bosi, F., and Lazor, P. (2012) Short-range order in tourmaline: a vibrational spectroscopic approach to elbaite. Physics and Chemistry of Minerals, 39, 811–816.

Slack, J.F. (1996) Tourmaline associations with hydrothermal ore deposits. Reviews in Mineralogy and Geochemistry, 33, 559–643.

Slack, J.F., and Trumbull, R.B. (2011) Tourmaline as a recorder of ore-forming processes. Elements, 7, 321–326.

Sluiter, M.H., and Kawazoe, Y. (2000) Prediction of solution enthalpies of substitutional impurities in aluminium. Modelling and Simulation in Materials Science and Engineering, 8, 221.

Sluiter, M.H.F., and Kawazoe, Y. (2002) Prediction of the mixing enthalpy of alloys. Europhysics Letters, 57, 526.

Smelik, E.A., Jenkins, D.M., and Navrotsky, A. (1994) A calorimetric study of synthetic amphiboles along the tremolite-tschermakite join and the heats of formation of magnesiohornblende and tschermakite. American Mineralogist, 79, 1110–1122.

Spear, F.S. (1993) Metamorphic phase equilibria and pressure–temperature–time paths. Mineralogical Society of America Monograph., 799.

Spear, F.S., Rumble, D., and Ferry, J. M. (1982) Chapter 3. Linear Algebraic Manipulation of N-Dimentional Composition Space. In John M. Ferry, Ed., Characterisation of Metamorphism through Mineral Equilibria pp. 53–104. De Gruyter.

Stixrude, L., and Lithgow-Bertelloni, C. (2011) Thermodynamics of mantle minerals-II. Phase equilibria. Geophysical Journal International, 184, 1180–1213.

Stølen, S., and Grande, T. (2004) Chemical thermodynamics of materials: macroscopic and microscopic aspects, 395 p. John Wiley & Sons, Chichester.

Strzelecki, A.C., Bourgeois, C., Kriegsman, K.W., Estevenon, P., Wei, N., Szenknect, S., Mesbah, A., Wu, D., Ewing, R.C., Dacheux, N., and others (2020) Thermodynamics of $CeSiO_4$: Implications for Actinide Orthosilicates. Inorganic Chemistry, 59, 13174–13183.

Strzelecki, A.C., Cockreham, C.B., Parker, S.S., Mann, S.C., Lhermitte, C., Wu, D., Guo, X., Monreal, M., Jackson, J.M., and Mitchell, J. (2024) A new methodology for measuring the enthalpies of mixing and heat capacities of molten chloride salts using high temperature drop calorimetry. Review of Scientific Instruments, 95.

Tajčmanová, L., Connolly, J. a. D., and Cesare, B. (2009) A thermodynamic model for titanium and ferric iron solution in biotite. Journal of Metamorphic Geology, 27, 153–165.

Taran, M.N., and Rossman, G.R. (2002) High-temperature, high-pressure optical spectroscopic study of ferric-iron-bearing tourmaline. American Mineralogist, 87, 1148–1153.

Taylor, M.C., Copper, M.A., and Hawthorne, F.C. (1995) Local change-compensation in hydroxyl-deficient uvite. The Canadian Mineralogist, 33, 1215–1221.

Thompson Jr., J.B. (1967) Thermodynamic properties of simple solutions. In P.H. Abelson, Ed., Researches in geochemistry vol. 2 Vol. 2, pp. 340–361. J. Wiley and Sons, New York, NY.

Thompson Jr., J.B. (1969) Chemical reactions in crystals. American Mineralogist: Journal of Earth and Planetary Materials, 54, 341–375.

Thompson Jr., J.B. (1982a) Chapter 1. Composition space: An algebraic and geometric appoach. In J.M. Ferry, Ed., Characterisation of Metamorphism through Mineral Equilibria pp. 1–32. De Gruyter.

——— (1982b) Chapter 2. Reaction Space: An Algebraic and Geometric Approach. In J.M. Ferry, Ed., Characterisation of Metamorphism through Mineral Equilibria pp. 33–52. De Gruyter.

Thompson Jr., J.B., and Waldbaum, D.R. (1968) Mixing properties of sanidine crystalline solutions: I. Calculations based on ion-exchange data. American Mineralogist: Journal of Earth and Planetary Materials, 53, 1965–1999.

——— (1969a) Analysis of the two-phase region halite-sylvite in the system NaCl- KCl. Geochimica et Cosmochimica Acta, 33, 671–690.

——— (1969b) Mixing properties of sanidine crystalline solutions: III. Calculations based on two-phase data. American Mineralogist: Journal of Earth and Planetary Materials, 54, 811–838.

Tippe, A., and Hamilton, W.C. (1971) A neutron-diffraction study of the ferric tourmaline, buergerite. American Mineralogist, 56, 101–113.

Trefethen, L.N., and Bau, D. (2022) Numerical Linear Algebra, Twenty-fifth Anniversary Edition. Society for Industrial and Applied Mathematics, Philadelphia, PA.

Tsang, T., and Ghose, S. (1973) Nuclear magnetic resonance of 1H, 7Li, 11B, 23Na, and 27Al in tourmaline (elbaite). American Mineralogist, 58, 224–229.

Tsang, T., Thorpe, A.N., and Donnay, G. (1971) Magnetic susceptibility and triangular exchange coupling in the tourmaline mineral group. Journal of Physics and Chemistry of Solids, 32.7, 1441–1448.

Tucker, A. (1994) Applied combinatorics, 447 p. John Wiley & Sons, Inc.

Tucker, M.G., Dove, M.T., and Keen, D.A. (2001) Application of the reverse Monte Carlo method to crystalline materials. Journal of applied crystallography, 34, 630–638.

Urusov, V.S. (2001) The phenomenological theory of solid solutions. In Solid Solutions in Silicate and Oxide Systems, EMU Notes in Mineralogy, Vol. 3, European Mineralogical Union, Eötvös University Press.

Van Hinsberg, V.J. (2006) Tourmaline: Monitor of the P-T-X evolution in rocks. PhD thesis, University of Bristol.

Van Hinsberg, V.J. (2011) Preliminary experimental data on trace-element partitioning between tourmaline and silicate melt. The Canadian Mineralogist, 49, 153–163.

Van Hinsberg, V.J., and Marschall, H.R. (2007) Boron isotope and light element sector zoning in tourmaline: Implications for the formation of B-isotopic signatures. Chemical Geology, 238, 141–148.

Van Hinsberg, V. J., and Schumacher, J.C. (2007) Intersector element partitioning in tourmaline: a potentially powerful single crystal thermometer. Contributions to Mineralogy and Petrology, 153, 289–301.

——— (2007b) Using estimated thermodynamic properties to model accessory phases: the case of tourmaline. Journal of metamorphic Geology, 25, 769–779.

Van Hinsberg, V.J., and Schumacher, J.C. (2009) The geothermobarometric potential of tourmaline, based on experimental and natural data. American Mineralogist, 94, 761–770.

——— (2011) Tourmaline as a petrogenetic indicator mineral in the Haut-Allier metamorphic suite, Massif Central, France. The Canadian Mineralogist, 49, 177–194.

Van Hinsberg, V.J., Vriend, S.P., and Schumacher, J.C. (2005a) A new method to calculate end-member thermodynamic properties of minerals from their constituent polyhedra I: enthalpy, entropy and molar volume. Journal of Metamorphic Geology, 23, 165–179.

——— (2005b) A new method to calculate end-member thermodynamic properties of minerals from their constituent polyhedra II: heat capacity, compressibility and thermal expansion. Journal of Metamorphic Geology, 23, 681–693.

Van Hinsberg, V.J., Schumacher, J.C., Kearns, S., Mason, P.R., and Franz, G. (2006) Hourglass sector zoning in metamorphic tourmaline and resultant major and trace-element fractionation. American Mineralogist, 91, 717–728.

Van Hinsberg, V.J., Henry, D.J., and Marschall, H.R. (2011a) Tourmaline: an ideal indicator of its host environment. The Canadian Mineralogist, 49, 1–16.

Van Hinsberg, V.J., Henry, D.J., and Dutrow, B.L. (2011b) Tourmaline as a petrologic forensic mineral: A unique recorder of its geologic past. Elements, 7, 327–332.

Van Hinsberg, V. J., Franz, G., and Wood, B.J. (2017) Determining subduction-zone fluid composition using a tourmaline mineral probe. Geochemical Perspectives Letters, 3, 160–168.

Van Hinsberg, V.J., Schumacher, J.C., Slack, J.F., and Marschall, H.R. (2017) Trace elements in tourmaline. Tourmaline 2017 conference, Czech Republic.

Vereshchagin, O.S., Frank-Kamenetskaya, O.V., Rozhdestvenskaya, I.V., and Zolotarev, A.A. (2018) Incorporation of 3d elements in tourmalines: structural adjustments and stability. European Journal of Mineralogy, 30, 917–928.

Vermeesch, P. (2018) IsoplotR: A free and open toolbox for geochronology. Geoscience Frontiers, 9, 1479–1493.

Vho, A., Lanari, P., and Rubatto, D. (2019) An Internally-Consistent Database for Oxygen Isotope Fractionation Between Minerals. Journal of Petrology, 60, 2101–2129.

Vinograd, V.L. (1997) Application of stochastic processes to modelling of ordered cationic distributions in aluminosilicates.

——— (2001) Configurational entropy of binary silicate solid solutions.

Vinograd, V.L., Sluiter, M.H.F., Winkler, B., Putnis, A., Halenius, U., Gale, J.D., and Becker, U. (2004) Thermodynamics of mixing and ordering in pyrope–grossular solid solution. Mineralogical Magazine, 68, 101–121.

Vinograd, V.L., Gale, J.D., and Winkler, B. (2007) Thermodynamics of mixing in diopside–jadeite, CaMgSi2O6–NaAlSi2O6, solid solution from static lattice energy calculations. Physics and Chemistry of Minerals, 34, 713–725.

Vinograd, V.L., Sluiter, M.H.F., and Winkler, B. (2009) Subsolidus phase relations in the CaCO3 – MgCO3 system predicted from the excess enthalpies of supercell structures with single and double defects. Physical Review B, 79, 104201.

Vinograd, V.L., Brandt, F., Rozov, K., Klinkenberg, M., Refson, K., Winkler, B., and Bosbach, D. (2013) Solid–aqueous equilibrium in the BaSO4–RaSO4–H2O system: first-principles calculations and a thermodynamic assessment. Geochimica et Cosmochimica Acta, 122, 398–417.

Violet, C.E., and Pipkorn, D.N. (1971) Mössbauer line positions and hyperfine interactions in α iron. Journal of Applied Physics, 42, 4339–4342.

Von Goerne, G., Franz, G., and Wirth, R. (1999) Hydrothermal synthesis of large dravite crystals by the chamber method. European Journal of Mineralogy, 11, 1061–1077.

Von Goerne, G., Franz, G., and Robert, J.L. (1999) Upper thermal stability of tourmaline + quartz in the system MgO-Al2O3-SiO2-B2O3-H2O and Na2O-MgO-Al2O3-SiO2-B2O3-H2O-HCl in hydrothermal solutions and siliceous melts. The Canadian Mineralogist, 37, 1025–1039.

Von Goerne, G., Franz, G., and van Hinsberg, V.J. (2011) Experimental determination of Na–Ca distribution between tourmaline and fluid in the system CaO–Na2O–MgO–Al2O3–SiO2–B2O3–H2O. The Canadian Mineralogist, 49, 137–152.

Waldbaum, D.R. (1973) The configurational entropies of Ca2MgSi2O7-Ca2SiAl2O7 melilites and related minerals. Contributions to Mineralogy and Petrology, 39, 33–54.

Waldbaum, D.R., and Thompson Jr, J.B. (1968) Mixing properties of sanidine crystalline solutions: II. Calculations based on volume data. American Mineralogist: Journal of Earth and Planetary Materials, 53, 2000–2017.

——— (1969) Mixing properties of sanidine crystalline solutions: IV. Phase diagrams from equations of state. American Mineralogist: Journal of Earth and Planetary Materials, 54, 1274–1298.

Warding, G., & Schreyer, W. (1978). Synthesis and crystal chemistry of kornerupine in the system MgO-Al2O3-SiO2-B2O3-H2O. Contributions to Mineralogy and Petrology. 67(3), 247-259.

Warren, M.C., Dove, M.T., Myers, E.R., Bosenick, A., Palin, E.J., Sainz-Diaz, C.I., Guiton, B.S., and Redfern, S.A.T. (2001) Monte Carlo methods for the study of cation ordering in minerals. Mineralogical Magazine, 65, 221–248.

Watenphul, A., Schlüter, J., Bosi, F., Skogby, H., Malcherek, T., and Mihailova, B. (2016) Influence of the octahedral cationic-site occupancies on the framework vibrations of Li-free tourmalines, with implications for estimating temperature and oxygen fugacity in host rocks. American Mineralogist, 101, 2554–2563.

Watenphul, A., Malcherek, T., Wilke, F.D., Schlüter, J., and Mihailova, B. (2017) Composition–thermal expandability relations and oxidation processes in tourmaline studied by in situ Raman spectroscopy. Physics and Chemistry of Minerals, 44, 735–748.

Weiss, M.P. (1914) Sur la nature du champ moléculaire. Annales de physique, 9, 134–162.

Weller, O.M., Holland, T.J., Soderman, C.R., Green, E.C., Powell, R., Beard, C.D., and Riel, N. (2024) New thermodynamic models for anhydrous alkaline-silicate magmatic systems. Journal of Petrology, 65, egae098.

Wendt, I., and Carl, C. (1991) The statistical distribution of the mean squared weighted deviation. Chemical Geology, 86, 275–285.

Westrich, H.R., and Navrotsky, A. (1981) Some thermodynamic properties of fluorapatite, fluorpargasite, and fluorphlogopite. American journal of science, 281, 1091–1103.

Westrum, E.F. (1988) Calorimetry in the range 5-300K. In Specific Heat of Solids. Hemisphere Publishing Corporation, New York.

Whipple, E.R. (1974) Quantitative Mössbauer spectra and chemistry of iron. PhD Thesis, Massachusetts Institute of Technology.

White, R.W., Powell, R., and Holland, T.J.B. (2007) Progress relating to calculation of partial melting equilibria for metapelites. Journal of metamorphic Geology, 25, 511–527.

White, R.W., Powell, R., Holland, T.J.B., Johnson, T.E., and Green, E.C.R. (2014) New mineral activity-composition relations for thermodynamic calculations in metapelitic systems. Journal of Metamorphic Geology, 32, 261–286.

White, W.B. (1974) Order–disorder Effects. In V.C. Farmer, Ed., The Infrared Spectra of Minerals Vol. 4, p. 0. Mineralogical Society of Great Britain and Ireland.

Will, T.M. (1998) Phase Equilibria in Metamorphic Rocks, 315 p. Vol. 71. Springer, Berlin, Heidelberg.

Williamson, B.J., Spratt, J., Adams, J.T., Tindle, A.G., and Stanley, C.J. (2000) Geochemical Constraints from Zoned Hydrothermal Tourmalines on Fluid Evolution and Sn Mineralization: an Example from Fault Breccias at Roche, SW England. Journal of Petrology, 41, 1439–1453.

Wodara, U. (1996) Synthese und Eigenschaften von Turmalinen im System Na2O-Al2O3-SiO2-B2O3-H2O. Unpublished Diploma thesis, Ruhr Universitat Bochum.

Wohl, K. (1953) Thermodynamic evaluation of binary and ternary liquid systems. Chemical Engineering Progress, 49, 218–221.

Wojdyr, M. (2022) GEMMI: A library for structural biology. Journal of Open Source Software, 7, 4200.

Wolf, M.B., and London, D. (1997) Boron in granitic magmas: stability of tourmaline in equilibrium with biotite and cordierite. Contributions to Mineralogy and Petrology, 130, 12–30.

Wolverton, C., and Zunger, A. (1994) Comparison of two cluster-expansion methods for the energetics of Pd-V alloys. Physical Review B, 50, 10548–10560.

——— (1995) Ising-like Description of Structurally Relaxed Ordered and Disordered Alloys. Physical Review Letters, 75, 3162–3165.

Wood, B.J., and Fraser, D.G. (1977) Elementary thermodynamics for geologists. 318 p. Oxford university Press.

Wood, B.J., and Nicholls, J. (1978) The thermodynamic properties of reciprocal solid solutions. Contributions to Mineralogy and Petrology, 66, 389–400.

Wright, S.E., Foley, J.A., and Hughes, J.M. (2000) Optimisation of site occupancies in minerals using quadratic programming. American Mineralogist, 85, 524–531.

Wu, L., Koryttseva, A., Groß, C.B.M., and Navrotsky, A. (2019) Thermochemical investigation of lithium borate glasses and crystals. Journal of the American Ceramic Society, 102, 4538–4545.

Wurm, M. (2021) A universal and fast method to solve linear systems with correlated coefficients using weighted total least squares. Measurement Science and Technology, 33, 015017.

Xu, H., Heaney, P.J., Navrotsky, A., Topor, L., and Liu, J. (1999) Thermochemistry of stuffed quartz-derivative phases along the join $LiAlSiO_4$ -SiO_2. American Mineralogist, 84, 1360–1369.

York, D. (1966) Least-squares fitting of a straight line. Canadian Journal of Physics, 44, 1079–1086.

York, D., Evensen, N.M., Martínez, M.L., and De Basabe Delgado, J. (2004) Unified equations for the slope, intercept, and standard errors of the best straight line. American journal of physics, 72, 367–375.

Zhang, Y.-Q., Radha, A.V., and Navrotsky, A. (2013) Thermochemistry of two calcium silicate carbonate minerals: scawtite, Ca7(Si6O18)(CO3)·2H2O, and spurrite, Ca5(SiO4)2(CO3). Geochimica et Cosmochimica Acta, 115, 92–99.

Zherebetskyy, D., Lebernegg, S., Amthauer, G., and Grodzicki, M. (2012) Magnetic structure of almandine. Physics and Chemistry of Minerals, 39, 351–361.